12th INTERNATIONAL EXERGY, ENERGY AND ENVIRONMENT SYMPOSIUM (IEEES-12)

December 20 – 24, 2020
Education City, Doha, Qatar

PROCEEDINGS BOOK

KAHRAMAA
المؤسسة العامة القطرية للكهرباء والماء
Qatar General Electricity & Water Corporation

جامعة حمد بن خليفة
HAMAD BIN KHALIFA UNIVERSITY
كلية العلوم والهندسة
College of Science & Engineering

الصندوق القطري لرعاية البحث العلمي
Qatar National Research Fund
Member of Qatar Foundation

12th INTERNATIONAL EXERGY, ENERGY AND ENVIRONMENT SYMPOSIUM (IEEES-12)

December 20 – 24, 2020
Education City, Doha, Qatar

PROCEEDINGS BOOK

EDITORS

Yusuf Bicer

Mehmet Akif Ezan

İbrahim Dincer

ISBN: 978-625-409-817-8

INDEX

ABOUT HAMAD BIN KHALIFA UNIVERSITY

Hamad Bin Khalifa University (HBKU), a member of Qatar Foundation for Education, Science, and Community Development (QF), was founded in 2010 to continue fulfilling QF's vision of unlocking human potential.

HBKU is a homegrown research and graduate studies University that acts as a catalyst for positive transformation in Qatar and the region while having a global impact.

Located within Education City, HBKU seeks to provide unparalleled opportunities where inquiry and discovery are integral to teaching and learning at all levels utilizing a multidisciplinary approach across all focus areas.

HBKU is committed to actively contribute to achieving the Qatar National Vision 2030 by building and cultivating human capacity through an enriching academic experience and an innovative research ecosystem. Through applying creativity to knowledge, students will have the opportunity to discover innovative solutions that are locally relevant and have a global impact.

At Hamad Bin Khalifa University – our students, faculty, staff, partners, and leadership – all share a common belief in the power of higher education and research to make a positive impact in the developmen of nations.

FOREWORDS

Dean's Welcoming Message

On behalf of the College of Science and Engineering (CSE) at Hamad Bin Khalifa University, it is our honor to host and help organize this prestigious international event, the 12th International Exergy, Energy and Environment Symposium (IEEES-12). I would like to extend my warmest greetings to all the attendees of this excellent event.

The 12th International Exergy, Energy and Environment Symposium (IEEES-12) is an initiative aimed at bringing together academics, researchers, scientists, technocrats and practicing engineers, in the confluence between several related disciplines ranging from energy to environment.

This international symposium serves as a forum that promulgates ideas, experience, and knowledge of fellow researchers and engineers working on sustainable energy and environment systems across the globe.

IEEES-12 will cover a diverse range of cutting-edge topics, including Renewable Energy Technologies, Solar Energy, Oil and Gas Technologies, Smart Grids, Green and Electrified Transportation, Alternative and Clean Fuels, Hydrogen and Fuel Cell Technologies, Nuclear Energy, Desalination Technologies, Waste Water Treatment and Environmental Technologies.

The symposium is intended to increase the visibility and advancement of futuristic and cleaner technologies such as green energy, renewable energy, environmental science and e-mobility. Other highlights are smart cities, green buildings, energy management systems, and desalination technologies.

It also addresses societal and environmental threats, unveiling the challenges in the life cycle assessment, CO_2 reduction technologies, bio-waste utilization, wastewater treatment, nuclear energy and fuels for transportation.

We look forward to welcoming you.

Dr. Mounir Hamdi
Dean of the College of Science and Engineering
Hamad Bin Khalifa University

FOREWORDS

Kahramaa President's Welcoming Message

Doha is all set to open the 12th series of the International Exergy, Energy and Environment Symposium (IEEES-12). The conference, whose genesis was in Izmir, Turkey almost 17 years ago as its first edition, has been running successfully ever since. IEEES is focused on the theoretical and practical aspects of Exergy, Energy, and Environment (3E's) for a sustainable future.

The symposium will be highly significant, as it will discuss several Global Sustainable Agenda and Sustainable Development goals (SDGs), including methods to procure a better incorporation of the massive research conducted in the area of environmental sciences. It is a unique opportunity for exchanging ideas, experiences, and information in areas where the world faces critical challenges in sustainable development. The 12th International Exergy, Energy and Environment Symposium (IEEES-12) will facilitate close cooperation and intellectual exchange amongst many experts from academia, leading Research & Development institutions, government agencies, private sectors, industries, among others.

IEEES-12 will shed light on a diverse range of cutting-edge topics, such as Environmental Technologies, Renewable Energy Technologies, and Oil and Gas Technologies. It is also a chance to visualize sustainability and preservation related projects and solutions such as Smart Grids, Green and Electrified Transportation, Alternative and Clean Fuels, Hydrogen and Fuel Cell Technologies, Nuclear Energy, Desalination Technologies, Wastewater Treatment, and Solar Energy. Tackling these issues falls in close alignment with Qatar National Vision (QNV) 2030, and the government is committed to ensure long-term human, economic, social, and environmental sustainability.

I take the opportunity to welcome you all to the symposium and hope that all the experts and professionals present here will brainstorm for ideas to overcome environmental, resource, efficiency, cost, energy security, and sustainability-related issues and challenges. It is regrettable that the current circumstances have prevented our physical gathering and deprived us of the chance of being your hosts in the beautiful city of Doha. However, I am hopeful that we will proceed together, armed with faith and determination, to overcome these difficult times, and I hope everyone will find IEEES- 12 enjoyable, informative, pragmatic, and solution- oriented.

Last but not least, I would like to express my warmest thanks to the organizers for their exemplary efforts in arranging this colossal intellectual gathering and wish all participants a very fruitful meeting.

HE Eng. Essa Bin Hilal Al-Kuwari,
President, Qatar General Electricity & Water Corporation "KAHRAMAA"

FOREWORDS

Chair's Welcoming Message

It is our great honor to welcome you to the 12th International Exergy, Energy and Environment Symposium (IEEES-12) which is virtually organized by Hamad Bin Khalifa University, in Qatar from December 20-24, 2020. The IEEES has been organized successfully as a leading symposium in the area since 2003 and previous editions have been held auspiciously in various parts of the world, from Poland
to India.
IEEES-12 will be a remarkable event with an even wider reach in terms of technical content including plenary sessions, keynote talks, and several specialized parallel sessions focusing on energy, exergy and environmental topics across diverse disciplines. We anticipate that this conference will provide a forum for the exchange of technical information, dissemination of high-quality research results, the presentation of new policies and scientific progress toward achieving sustainable development. It is our hope that the symposium will lead to effective, fruitful discussions and collaborations between participants from different disciplines, institutes and sectors from all over the world. The scientific part of IEEES-12 will include talks by keynote and invited speakers,
as well as oral and poster presentations from participants. Conference proceedings will be published after reviewing the manuscripts submitted. High quality papers will be considered, in extended form, for possible publication in specific reputable international journals mentioned on the website.

We endeavor to ensure that IEEES-12 will be a valuable, impactful and enjoyable event.

Yusuf Bicer
On Behalf of the Organizing Committee
Symposium Chair

ORGANIZING COMMITTEE

Founding Chair

Ibrahim Dincer
Ontario Tech University, Canada

Symposium Chair

Yusuf Bicer
Hamad Bin Khalifa University, Qatar

Executive Organizing Committee

Mohamed M. Abdallah
Hamad Bin Khalifa University, Qatar

Ahmad S. Abushaika
Hamad Bin Khalifa University, Qatar

Tareq A. Al-Ansari
Hamad Bin Khalifa University, Qatar

Sami G. Al-Ghamdi
Hamad Bin Khalifa University, Qatar

Luluwag Al-Fagih
Hamad Bin Khalifa University, Qatar

Adel Elomri
Hamad Bin Khalifa University, Qatar

Mounir Hamdi
Hamad Bin Khalifa University, Qatar

Muammer Koc
Hamad Bin Khalifa University, Qatar

Hamish R. MacKey
Hamad Bin Khalifa University, Qatar

Gordon McKay
Hamad Bin Khalifa University, Qatar

LOCAL AND INTERNATIONAL ORGANIZING COMMITTEE

Ibrahim Ari
Hamad Bin Khalifa University, Qatar

Islam Safak Bayram
University of Strathclyde, Glasgow, UK

Can Ozgur Colpan
Dokuz Eylul University, Turkey

Rami El-Emam
Austria

Mehmet Akif Ezan
Dokuz Eylul University, Turkey

Rima Isaifan
Hamad Bin Khalifa University, Qatar

Farrukh Khalid
Hamad Bin Khalifa University, Qatar

Shoukat Alim Khan
Hamad Bin Khalifa University, Qatar

Onder Kizilkan
Isparta University of Applied Sciences, Turkey

Tahir A.H. Ratlamwala
National University of Sciences and Technology (NUST), Pakistan

Nurettin Sezer
Hamad Bin Khalifa University, Qatar

INTERNATIONAL SCIENTIFIC COMMITTEE

Ahmed Abdala
Texas A&M University at Qatar, Qatar

Fares A. Almomani
Qatar University, Qatar

Said Ahzi
Hamad Bin Khalifa University /
Qatar Environment and Energy
Research Institute, Qatar

Fethi Aloui
Universite Polytechnique Hauts-de-France
(UPHF), INSA HDF, LAMIH UMR CNRS
8201, France

Husam Baalousha
Hamad Bin Khalifa University /
Qatar Environment and Energy
Research Institute, Qatar

Adrian Bejan
Duke University, USA

Yunus Cengel
University of Nevada, Reno, USA

Wei-Hsin Chen
National Cheng Kung University, Taiwan

Nimir Elbashir
Texas A&M University at Qatar, Qatar

Yasar Demirel
University of Nebraska–Lincoln, USA

Ibrahim Dincer
Ontario Tech University, Canada

Greg F. Naterer
Memorial University
of Newfoundland, Canada

Mohamed Gadalla
American University of Sharjah, UAE

Edwin Geo
SRM Institute, India

Saud Ghani
Qatar University, Qatar

Yousef Haik
Texas A & M University-Kingsville

Feridun Hamdullahpur
University of Waterloo, Canada

Hicham Hamoudi
Hamad Bin Khalifa University /
Qatar Environment and Energy
Research Institute, Qatar

Arif Hepbasli
Yasar University, Turkey

Rima Isaifan
Hamad Bin Khalifa University, Qatar

Ramazan Kahraman
Qatar University, Qatar

Majeda Khraisheh
Qatar University, Qatar

Marwan Khraisheh
Texas A&M University at Qatar

Muammer Koc
Hamad Bin Khalifa University, Qatar

Xianguo Li
University of Waterloo, Canada

INTERNATIONAL SCIENTIFIC COMMITTEE

Peter D. Lund
Aalto University, Finland

Abdulnasser Mabrouk
Hamad Bin Khalifa University / Qatar Environment and Energy Research Institute, Qatar

Belabbes Merzougui
Hamad Bin Khalifa University / Qatar Environment and Energy Research Institute, Qatar

Adnan Midilli
Yildiz Technical University, Turkey

Meng Ni
Hong Kong Polytechnic University, Hong Kong

Sandro Nižetić
University of Split, Croatia

Mustafa Ozilgen
Yeditepe University, Turkey

Bestami Ozkaya
Yildiz Technical University, Turkey

Marc A. Rosen
Ontario Tech University, Canada

Bahri Sahin
Yildiz Technical University, Turkey

Ziad Saghir
Ryerson University, Canada

Zekai Sen
Istanbul Medipol University, Turkey

S.A. Sherif
University of Florida, USA

Ramazan Solmaz
Bingol University, Turkey

Lounes Tadrist
University of Aix-Marseille, France

George Tsatsaronis
Technical University of Berlin, Germany

Ilhami Yildiz
Dalhousie University, Canada

ACKNOWLEDGEMENT

The IEEES-12 Organizing Committee expresses its sincere appreciation
to the following organizations:

Co-organizer and Strategic Partner

KAHRAMAA
كهرماء
المؤسسة العامة القطرية للكهرباء والماء
Qatar General Electricity & Water Corporation

Sponsor

الصندوق القطري لرعاية البحث العلمي
Qatar National Research Fund
Member of Qatar Foundation

Partners

OntarioTech UNIVERSITY

NATIONAL HYDROGEN ASSOCIATION
H2
TURKEY

12th INTERNATIONAL EXERGY, ENERGY AND ENVIRONMENT SYMPOSIUM (IEEES-12)

December 20 – 24, 2020
Education City, Doha, Qatar

VIRTUAL SYMPOSIUM PROGRAM

DAY 1

December 20, 2020 | SUNDAY | Webex short link: https://bit.ly/3mbIsPy *(Password: 20-20)*

OPENING SESSION

Time (GMT+3)	Welcome Remarks
3:30 pm-4:00 pm	**Dr. Ahmad M. Hasnah** President Hamad Bin Khalifa University **H.E. Essa Al-Kuwari** President Qatar General Electricity & Water Corporation Member of Board of Trustees, Hamad Bin Khalifa University **Dr. Ibrahim Dincer** Founding Chair of Symposium Ontario Tech University **Dr. Mounir Hamdi** Dean, College of Science and Engineering Hamad Bin Khalifa University **Dr. Hisham M. Sabir** Director, Technical, Qatar National Research Fund (QNRF) **Dr. Yusuf Bicer** Chair of the Symposium Hamad Bin Khalifa University

PLENARY SESSION – 1

Time (GMT+3)	Presentation
4:00 pm - 4:45 pm	Energy-Climate Change-Sustainability Triangle: How Can We Move Together Toward Achieving a Global Solution? **Keynote Speaker – Prof. Dr. Feridun Hamdullahpur** Professor, President and Vice-Chancellor University of Waterloo, Canada
4:45 pm - 5:00 pm	**Break**
5:00 pm - 5:45 pm	Novel Methods for Production of Hydrogen for Industrial Applications **Keynote Speaker – Prof. Dr. Ibrahim Dincer** Professor, Ontario Tech University, Canada

END OF THE DAY

DAY 2

December 21, 2020 | MONDAY | Webex short link: https://bit.ly/3mlSNIB *(Password: 20-20)*

PLENARY SESSION – 2

Time (GMT+3)	Presentation
8:30 am – 9:15 am	Integrated Footprints Accounting for Sustainability, Emissions and Plastic **Keynote Speaker – Prof. Dr. Jiři Jaromir Klemeš** Professor, Brno University of Technology, Czech Republic
9:15 am – 9:30 am	**Break**
9:30 am – 10:15 am	Intricacies of the 2nd Law and Its Application to LNG Liquefaction and Regasification Facilities **Keynote Speaker - Prof. Dr. Yunus Çengel** Professor Emeritus, University of Nevada, Reno, NV, USA
10:15 am – 10:30 am	**Break**

PRESENTATIONS SESSION – 1

Session Chair: Dr. Luluwah Al-Fagih

Time (GMT+3)	Presentation
10:45 am – 11:00 am	**IEEES12- P338** Data-Driven Materials Discovery **Fadwa El-Mellouhi**
11:00 am – 11:15 am	**IEEES12- P289** Simulation Model for Designing an Optimal Site Specific Renewable Energy Based Electric Vehicle (EV) Charging Station – a Case Study in Qatar **Abdulla Al Wahedi, Yusuf Bicer**
11:15 am – 11:30 am	**IEEES12- P188** Al Rayyan's Wind Energy Potential to Satisfy Ahmed Bin Ali Stadium's Energy Demand During the 2022 FIFA World Cup in Qatar **Carlos Mendez, Yusuf Bicer**
11:30 am – 11:45 am	**IEEES12- P085** Wind Speed Analysis by Using Mixed Extreme Value Distributions **Hassan Tahir, Weidong Zhao, Arsalan Ahmed**
11:45 am – 12:00 pm	**IEEES12- P372** Impact of Fossil Fuel Subsidies on Renewable Energy Sector **Sikandar Abdul Qadir, Furqan Tahir, Luluwah Al-Fagih**
12:00 pm – 12:15 pm	**IEEES12- P193** MOPSA and SPECO Approaches for Thermo-economic Assessment of a Combined Power Cycle Using Renewable and Conventional Fuels **Cuneyt Uysal, Hasan Ozcan**
12:15 pm – 12:30 pm	**IEEES12- P219** Sustainable Energy Use and Decarbonization Potential in the Hungarian Residential Building Sector **Tamas Palvolgyi, Attila Buzasi**
12:30 pm – 12:45 pm	**IEEES12- P310** Renewable Penetration to Turkey's Electric Power Grid **İzzet Alagöz, Mehmet Bulut, Mehmet Biçer**

POSTERS SESSION - 1

Time (GMT+3)	Presentation
12:45 pm – 12:50 pm	**IEEES12- P321** Application of Artificial Neural Networks for Solar Multi-parameters Prediction; A Case Study of Nigeria **Olusola Bamisile, Ariyo Oluwasanmi, Sandra Obiora, Eric Okonkwo, Gaylord Asoronye, Qi Huang**

12:50 pm – 12:55 pm	**IEEES12- P138** Integration of Kalina Cycle with CPVT for Multi-generation and Hydrogen Production: An Energy, Exergy and Environmental Performance Study **Olusola Bamisile, Qi Huang, Eric Okonkwo, Tareq Al-Ansari, Patrick Ayambire, Victor Adebayo, Tahir Ratlamwala**
12:55 pm – 1:00 pm	**IEEES12- P200** Research on Spatial Non-Uniformity of Power Distribution for Solar Radiation Simulation **Bartosz Stanek, Łukasz Bartela, Daniel Węcel, Anna Skorek-Osikowska**
1:00 pm – 1:05 pm	**IEEES12- P006** Blade design for horizontal axis wind turbine **David Esteban Albadan Molano**
1:05 pm – 1:10 pm	**IEEES12- P027** Assessment of TPHs and PAHs in the Marine Sediment Relating to Oil and Gas Extraction Activity on the Western Coastline of Qatar **Maryam Abdulla, Azenith Castillo, Christopher Collins, Tom Sizmur**
1:10 pm – 1:15 pm	**IEEES12- P097** Natural Gas Portfolio Optimization for Thermopower and Petrochemical Feeds **Henrique Plaudio, Brenno Menezes, Fernando Pessoa**
1:15 pm – 1:20 pm	**IEEES12- P270** Revisit of Modeling Techniques for Foam Flow in Porous Media **Lei Ding, Dominique Guerillot, Mirna Maklad**
1:20 pm – 1:25 pm	**IEEES12- P098** CO_2 Emission through Road Gradient and Real-Time Traffic Monitoring for Vehicle Routing Problems **Eduardo Escamilla, Marzieh Khakifirooz, Brenno Menezes, Mahdi Fathi**
1:25 pm – 1:30 pm	**IEEES12- P376** Quantified literature database for Methane Dehydroaromatization - an opportunity for statistical and artificial intelligence to unravel hidden intercorrelations **Nagat Elrefaei, Anchu Ashok, Ma'Moun Al-Rawashdeh**

PRESENTATIONS SESSION – 2

Session Chair: Dr. Ahmed Abdala

Time (GMT+3)	Presentation
1:30 pm – 1:45 pm	**IEEES12- P151** Performance Comparison of Machined from Bulk and Fabricated via Powder Metallurgy Approach Crofer®22 APU Interconnects for SOFC Applications **Ömer Necati Cora, Bülent Öztürk, Alparslan Topcu**
1:45 pm – 2:00 pm	**IEEES12- P235** Fuel Cell Electric Vehicles: Current Prospects and Challenges Beyond 2020 **Ömer Necati Cora**
2:00 pm – 2:15 pm	**IEEES12- P155** Development of a Solar Energy Based Multigeneration Plant with SOFC for Hydrogen Production **Nejat Tukenmez, Fatih Yilmaz, Murat Ozturk**
2:15 pm – 2:30 pm	**IEEES12- P154** Investigation of Performance Improvement of Geothermal Energy Assisted Power, Heating and Hydrogen Generation Plants with Thermoelectric Generator **Nejat Tukenmez, Fatih Yilmaz, Murat Ozturk**
2:30 pm – 2:45 pm	**IEEES12- P222** Sintering Inhibitors of Iron Powder Particles used for Hydrogen Production **Fotouh Al-Ragom**
2:45 pm – 3:00 pm	**IEEES12- P266** Ni-B and Zr-Ni-B In-Situ Catalytic performance for Hydrogen Generation from Sodium Borohydride, Ammonia Borane and Their Mixtures **Deniz Lim, Göksel Özkan, Gülay Özkan**
3:00 pm – 3:15 pm	**IEEES12- P267** Investigation of Ni2B Additive as a Molten Carbonate Fuel Cell Anode Material **Erdi Başarır, Göksel Özkan, Gülay Özkan**
3:15 pm – 3:30 pm	**IEEES12- P237** Physical and Electrochemical Analysis of Calcium Co-Doped GDC and its Use as Electrolyte in IT-SOFC **Ieeba Khan, Suddhasatwa Basu**

PRESENTATIONS SESSION – 3

Session Chair: Dr. Islam Safak Bayram

Time (GMT+3)	Presentation
3:30 pm – 4:00 pm	Performance Improvement of Silicon Photovoltaic Panels by Application of Cooling Techniques **Invited Talk – Prof. Dr. Sandro Nižetić** Professor, University of Split, Croatia
4:00 pm – 4:15 pm	**IEEES12- P165** Comparative Study for Solar Powered Systems in Pakistan **Tahir Abdul Hussain, Sohaib Ahmed, Muhammad Umer Khan, Moiz Ahmed, Osama Tahir**
4:15 pm – 4:30 pm	**IEEES12- P030** Optimized PV Power Curtailment Technique with Absolute Fairness to Eliminate Voltage Rise in Low Voltage Distribution Systems **Ali Elrayyah**
4:30 pm – 4:45 pm	**IEEES12- P139** Investigation of GaAsPN/GaP Quantum Dots Structures for Solar Cells Applications **Abdelkader Aissat, Said Nacer Jean Pierre Vilcot**
4:45 pm – 5:00 pm	**IEEES12- P178** Recovery of the Cubic Structure in Mixed Cation Perovskite Thin Films via Machine Learning Assistance **Adnan Ali, Heesoo Park, Abdelhak Belaidi, Brahim Aissa and Fedwa El-Mellouhi**
5:00 pm – 5:15 pm	**IEEES12- P029** Optimal Solar Hybridization of a Grid-Connected Gas Turbine Combined Cycle Power Plant: A Case Study **Mohammad Mohammadzadeh, Mohammad Tajik Mansouri, Mehdi Rahimi**
5:15 pm – 5:30 pm	**IEEES12- P343** Using BAT Algorithms for Techno-economic Analysis of Grid-Connected PV System and Comparison with PSO and WOA methods **Abdurazaq Elbaz, Muhammet Tahir Güneşer**
5:30 pm – 5:45 pm	**IEEES12- P140** Optimal Sizing of a Residential Grid-Interactive PV with Battery Storage Using HOMER **Stephen Marais, Kanzumba Kusakana**
5:45 pm – 6:00 pm	**IEEES12- P169** Exergoeconomic Performance Evaluation of a PV/T Assisted Wastewater Source Heat Pump System **Mustafa Araz, Arif Hepbasli, Huseyin Gunerhan**
6:00 pm – 6:15 pm	**IEEES12- P324** Enviro-economical Assessment of Hydrogen Fuel cell buses **Pouria Ahmadi, Nader Javani, Alireza Khoshnevisan**
6:15 pm – 6:30 pm	**IEEES12- P250** The Energetic and Environmental Parameters' effect on The Valuation of Bulk Carriers **Murat Koray, M.Ziya Söğüt**
6:30 pm – 6:45 pm	**IEEES12- P037** Development of Transition Metal/Alloy Nanoparticles/Nanoclusters for Water Splitting as a Sustainable Source of Energy **Tanveer Ulhaq, Tareq Al-Ansari**
06:45 pm – 07:00 pm	**IEEES12- P062** Integration of Solid Oxide Fuel Cell with Flare System in Natural Gas Plant **Khalid Al-Khori, Yusuf Bicer, Muammer Koc**
7:00 pm – 7:15 pm	**IEEES12- P232** Maximizing Energy Production for Solar PVs Installed on Complex Curvature Roofs to Mitigate Partial Shading Effect **Saoud Al-Janahi, Omar Ellabban, Sami G. Al-Ghamdi**
7:15 pm – 7:30 pm	**IEEES12- P269** Performance investigation of the reactor cascading effect on ammonia synthesis **Haris Ishaq, Ibrahim Dincer**
7:30 pm – 7:45 pm	**IEEES12- P254** Economic Analysis of Generated Boil-Off Gas of Various Liquefied Energy Carriers During Energy Storage and Transport **Mohammed Al-Breiki, Yusuf Bicer**

END OF THE DAY

DAY 3

December 22, 2020 | TUESDAY | Webex short link: https://bit.ly/34bZKWv *(Password: 20-20)*

PRESENTATIONS SESSION – 4

Session Chair: Dr. Sami G. Al-Ghamdi

Time (GMT+3)	Presentation
8:30 am – 8:45 am	**IEEES12- P259** Architecture design and Energy Performance of a modular Nearly Zero Energy Building Mohammed Ahachad, Mustapha Mahdaoui, Mustapha Ouardouz, Rachid El Alaiji, Fatima Bahraoui, **Youssef Berroho, Nouredine Tlemsani**
8:45 am – 9:00 am	**IEEES12- P010** Complexity and Use in the Built Environment: Post-occupancy Evaluation and Proposed Design Alterations for Qatar University's Most Iconic Building **Mark David Major, Doha Elsaman, Lolwa Al-Mohannadi, Meera Al-Khulifi, Shaikha Al-Thani**
9:00 am – 9:15 am	**IEEES12- P079** Minimum Insulation Thickness to Prevent the Condensation of Building External Walls in a Different Direction **Okan Kon, İsmail Caner**
9:15 am – 9:30 am	**IEEES12- P032** Sustainable Buildings Components: A Technical Review of Green Roofs (GFs) **Sara Zaina, Fodil Fadli**
9:30 am – 9:45 am	**IEEES12- P246** Cost and Thermal Aspects of Solar Driven Heating Assistance Options for Residential Buildings **Ümit Deniz Akyavuz, Hasan Özcan**
9:45 am – 10:00 am	**IEEES12- P077** Energy-Efficient Retrofitting Strategies for Hospital Building for Heating Season **İsmail Caner, Nadir İlten**
10:00 am – 10:15 am	**IEEES12- P361** The Effect of Air Layer Thickness on Insulation Thickness Applied to Buildings with Sandwich Walls **Okan Kon, Ismail Caner**
10:15 am – 10:30 am	**IEEES12- P363** Comfort as the Dead State of Buildings: A Preliminary Discussion **Valentina Bonetti**

PRESENTATIONS SESSION – 5

Session Chair: Dr. Tareq Al-Ansari

Time (GMT+3)	Presentation
10:45 am – 11:00 am	**IEEES12- P175** Turkeys Industrial Waste Heat to Power Potential for Power and Hydrogen Generation **Hasan Ozcan, Funda Ates**
11:00 am – 11:15 am	**IEEES12- P016** Study of Methane Enrichment in a Biogas Fuelled HCCI Engine **Feroskhan M, Saleel Ismail, Panchal Shreyash Hemant**
11:15 am – 11:30 am	**IEEES12- P208** Potential of Biocrude Production from Camel Manure via Hydrothermal Liquefaction: A Qatar Case Study **Mohammad Alherbawi, Prakash Parthasarathy, Tareq Al-Ansari and Gordon Mckay**
11:30 am – 11:45 am	**IEEES12- P262** An Experimental Study on Gas-to-Liquids (GTL) and Biogas Dual Fuel Operation of a Diesel Engine **Saket Verma, L M Das, S C Kaushik**
11:45 am – 12:00 pm	**IEEES12- P297** CSP-hybrid staged-gasification of solid waste to produce hydrogen enriched syngas: ASPEN Plus simulation **Shahid Hussain Ansari, Xinying Liu, K. L. Nkhonjera**

12:00 pm – 12:15 pm	**IEEES12- P181** Synthetic Natural Gas Production in Power-to-Gas Approaches Involving Biomass Gasification and Anaerobic Digestion **Anna Skorek-Osikowska, Jose Luis Galvez-Martos**
12:15 pm – 12:30 pm	**IEEES12- P056** Exergy Analysis of a Biogas-Diesel Fueled Dual Fuel Engine **Feroskhan M, Sreekanth M, Saleel Ismail**
12:30 pm – 12:45 pm	**IEEES12- P040** Performance and emission characteristics of a biogas fueled dual-fuel engine with various DEE fractions **Prashant Dhar Dwivedi, Prashant Das, Hrushikesh V Bhalerao, Sumanth Samsani, Subham Balyan, Yasonandan Vadlamudi, Saleel Ismail, Feroskhan M**

POSTERS SESSION - 2

Time (GMT+3)	Presentation
12:45 pm – 12:50 pm	**IEEES12- P148** Removal of Crystal Violet Dye from Water by Sand of Algerian Sahara **Arris Sihem, Ndermouchi Aida, Bencheikh Lehocine Mossaab, Meniai H-A**
12:50 pm – 12:55 pm	**IEEES12- P149** Characterization of natural carob used for removal of crystal Violet dye from wastewater **Arris Sihem, Bencheikh Lehocine Mossaab, Meniai H-A**
12:55 pm – 1:00 pm	**IEEES12- P101** Underwater Solar Irradiance and Performance analysis of various Silicon Solar Cells with Change in Water Conditions: A Comparative Study **Prasanth K. Enaganti, Prabhat K. Dwivedi, Alok K. Srivastava, Sanket Goel**
1:00 pm – 1:05 pm	**IEEES12- P184** CFD Investigation of Falling Film Flow over Horizontal Tube **Furqan Tahir, Abdelnasser Mabrouk, Muammer Koc**
1:05 pm – 1:10 pm	**IEEES12- P129** Development of Virtual Sensors for Prediction of Flue Gas Composition of a Cement Plant through Ensemble Learning Technique **Usman Khan Jadoon, Iftikhar Ahmad, Arshad Hussain and Brenno C. Menezes**
1:10 pm – 1:15 pm	**IEEES12- P130** Simulation-Based Design and Analysis of Fluidized Bed Membrane Reactor for Naphtha Reforming Process **Adnan Ahmad Bhatti, Iftikhar Ahmad, Arshad Hussain, Brenno C. Menezes**
1:15 pm – 1:20 pm	**IEEES12- P367** Geospatial assessment of *Jatropha curcas* plantation in Qatar: A GIS modelling approach **Mohammad Alherbawi, Maryam Haji, Hazrath Bilal Khan, Gordon Mckay, Tareq Al-Ansari**
1:20 pm – 1:25 pm	**IEEES12- P185** 3D Analysis of Film Thickness Distribution in a Horizontal Type Falling Film Evaporator **Furqan Tahir, Abdelnasser Mabrouk, Muammer Koc**

PLENARY SESSION – 3

Time (GMT+3)	Presentation
1:30 pm – 2:15 pm	Modern Methods for the Comprehensive Evaluation and Improvement of Energy Conversion Systems **Keynote Speaker – Prof. Dr. George Tsatsaronis** Professor, Technical University of Berlin, Germany
2:15 pm – 2:30 pm	**Break**
2:30 pm – 3:00 pm	Thermal Optimization of Heat Transfer Performance Using Nanotechnology: A Hybrid Thermal and Environmental Application **Invited Talk – Prof. Dr. Ziad Saghir** Professor, Ryerson University, Canada
3:00 pm – 3:30 pm	**Break**

PRESENTATIONS SESSION – 6

Session Chair: Dr. Hamish Mackey

Time (GMT+3)	Presentation
3:30 pm – 3:45 pm	**IEEES12- P204** Effects of Microstructure Shape Parameters on Water Removal in a PEMFC Lotus-Like Flow Channel **Xie Xuan, Yin Bifeng, Xu Sheng**
3:45 pm – 4:00 pm	**IEEES12- P086** Commodities Relationships Effect on Adopting Pro-Environmental Measures **Reem Mamoon Mohmed, Frank Himpel**
4:00 pm – 4:15 pm	**IEEES12- P176** Energy-enviro Investigation of Solar Powered Self-Sustainable Minimal Liquid-Solid Discharge Toilet **Policherla Venkata Sai, K S Reddy**
4:15 pm – 4:30 pm	**IEEES12- P160** Formulation of Indicators for Sustainable Groundwater Development in Qatar **Salah Ajjur, Husam Baalousha**
4:30 pm – 4:45 pm	**IEEES12- P104** Biochar: A Sustainable Approach for Water Stress and Plant Growth **Snigdhendubala Pradhan, Hamish R. Mackey, Tareq Al-Ansari, Gordon McKay**
4:45 pm – 5:00 pm	**IEEES12- P166** Assessing the Environment Impacts of Grocery Bags **Tahir Abdul Hussain, Adeel Asghar, Hammad Parvez, Shoaib Shahbaz, Abeer Farooq**
5:00 pm – 5:15 pm	**IEEES12- P360** Synthesis and characterization of carbonized nano-micro materials from agricultural and industrial wastes **Maria Kanwal, Rao Arsalan Khushnood, Abdul Ghafar**
5:15 pm – 5:30 pm	**IEEES12- P127** Effects and critical analysis for Carbon Emission Estimation in the Transportation Sector **Ruba Al- Foraih, Sreekant K J**
5:30 pm – 5:45 pm	**IEEES12- P341** Urban sprawl and its impact on the environment: case of the Greater El Jadida, (Morocco) **Ikram El Mjiri, Abdelmejid Rahimi, Abdelkrim Bouasria**
5:45 pm – 6:00 pm	**IEEES12- P377** Prospects of CO2 Utilization after Carbon Capture Process **Binash Imteyaz, Sikandar Abdul Qadir, Furqan Tahir**
6:00 pm – 6:15 pm	**IEEES12- P082** De-watering of Microalgae through Auto-flocculation for Sustainable Biofuels Production **Naim Rashid, Bongsoo Lee, Yong-Keun Chang**
6:15 pm – 6:30 pm	**IEEES12- P225** Evaluation of regional climate innovation potential in Hungary **Maria Szalmane Csete, Orsolya Barna**
6:30 pm – 6:45 pm	**IEEES12- P135** Removal of Toxic Cadmium From Water Using a Binary Site ion Exchange Resin Derived From Waste Printed Circuit Board **Meng Xu, Haya Alyasi, Junaid Saleem, Ning Chao, Chi Wai Hui, Hamish Mackey, Tareq Al Ansari, Gordon McKay**
6:45 pm – 7:00 pm	**IEEES12- P174** A Predictive Model for the Thermal Conductivity of Nanofluids Using Machine Learning Algorithms **Humphrey Adun, Ifeoluwa Wole-Osho, Eric Okonkwo**
7:00 pm – 7:15 pm	**IEEES12- P284** Synthesis and Testing of Hybrid Micro-Nano Coatings for Advance Nucleate Boiling **Shoukat Alim Khan, Muammer Koc, Sami G. Al-Ghamdi**
7:15 pm – 7:30 pm	**IEEES12- P303** Utilization of the osmotic power potential of desalination brine **Nurettin Sezer, Yusuf Bicer, Muammer Koc**
7:30 pm – 7:45 pm	**IEEES12- P323** Thermodynamic analysis of a polygeneration system designed for Controlled Environment Poultry Farming **Muhammad Luqman, Tareq A. Al-Ansari**
7:45 pm – 8:00 pm	**IEEES12- P378** Energy and Water Conservation Index Application for Optimizing the Conservation of Energy and Water at Facility **Andreas Prasetyadi, Budi Setyahandana**
8:00 pm – 8:15 pm	**IEEES12- P261** Thermodynamic Comparison of Cooling Options for Clean SOFC-Powered Locomotives **Khaled Al-Hamed, Ibrahim Dincer**

END OF THE DAY

DAY 4

December 23, 2020 | WEDNESDAY | Webex short link: https://bit.ly/37gpgvO *(Password: 20-20)*

PRESENTATIONS SESSION – 7

Session Chair: Dr. Gordon McKay

Time (GMT+3)	Presentation
8:30 am – 9:00 am	Plasma Gasification for Better Environmental Sustainability **Invited Talk – Prof. Dr. Adnan Midilli** Professor, Yildiz Technical University, Turkey
9:00 am – 9:15 am	**IEEES12- P171** Experimental Study on a Thermoacoustic-Stirling Engine with Acoustic Field Adjustment **Isares Dhuchakallaya, Patcharin Saechan**
9:15 am – 9:30 am	**IEEES12- P359** Study on challenges and opportunities of Dish type Solar Stirling engine at UAE conditions **Ben Alex Baby, N. M. Zajith Ali, Y. Raja Sekhar**
9:30 am – 9:45 am	**IEEES12- P011** Acetylene as an Alternative Fuel for IC Engines- Production Methodology and Performance Tests **Sri Sathya Sai S V, Rahul Ranganath, Shane Shaju, Ajay J Nayar**
9:45 am – 10:00 am	**IEEES12- P342** Thermodynamic Analysis of an Automobile's Air Conditioning System Assisted by Exhaust Gas and Solar Energy **Santi Sarkar, Goutam Khankari, Sujit Karmakar**
10:00 am – 10:15 am	**IEEES12- P074** Error Correction of Estimation Techniques in a Synchro-Phasor Measurement Unit **Hamid Bentarzi, Mahboubi Meriam, Ouadi Abderrahmane, Abdelmoumene Abdelakder**
10:15 am – 10:30 am	**IEEES12- P038** Resource Provisioning in Plug-in Electric Vehicle Charging Lots **Islam Safak Bayram, Raka Jovanovic, Michael Devetsikiotis**

PRESENTATIONS SESSION – 8

Session Chair: Dr. Rahul Bhosale

Time (GMT+3)	Presentation
10:45 am – 11:00 am	**IEEES12- P123** Thermodynamic Analysis of a Hybrid Multi-generation System Using Solar and Wind Power **Tahir Abdul Hussain Ratlamwala, Danish Ashfaque, Abdul Basit Aftab**
11:00 am – 11:15 am	**IEEES12- P369** Comparative 3-E (Energy, Exergy, and Environmental) Analysis of Partial Oxy-Coal and Air-Coal Combustion based 500 MWe Supercritical Thermal Power Plants with CO2 Capture **Soumya Jyoti Chatterjee, Sujit Karmakar**
11:15 am – 11:30 am	**IEEES12- P019** Solar Thermal Vapor Adsorption - Exergy Analysis **M Natarajan Muthuswamy, Raja Sekhar Yendaluru, C Chiranjeevi, Tangellapalli Srinivas**
11:30 am – 11:45 am	**IEEES12- P352** Entropy Generation and Exergy Analysis under transient condition for Large Diameter Natural Circulation Loops **Elton Dylan Nazareth, Arunachala U Chandavar, Rajat A Chandavar**
11:45 am – 12:00 pm	**IEEES12- P167** Comparative Economic and Exergoeconomic Analysis of a Hybrid Cascade Refrigeration System Using Ammonia-Propane, Propane-Propylene and Isobutane-Propane Refrigerant Pairs **Kaushalendra Kumar Singh, Rajesh Kumar, Anjana Gupta**
12:00 pm – 12:15 pm	**IEEES12- P201** Exergy Analysis of Tunnel Furnace and Tunnel Dryer **Gurhan Tahtali, Hayati Olgun, Mustafa Gunes and Arif Hepbasli**
12:15 pm – 12:30 pm	**IEEES12- P291** Preliminary Investigation of the Experimental CO2 Cascade Heat Pump System From Exergetic Point of View **Mansour Ndiaye, Onder Kizilkan, Koshiro Uchi, Petter Neksa, Hiroshi Yamaguchi**
12:30 pm – 12:45 pm	**IEEES12- P072** Exergy and CO2 Emissions Analysis of an Emerging Alternative Iron and Steel Making Process **Binay Kumar, Gour Gopal Roy, Prodip Kumar Sen**

POSTERS SESSION - 3

Time (GMT+3)	Presentation
12:45 pm – 12:49 pm	**IEEES12- P115** 3-D Computational Study on a Spray Cooled Solar Photovoltaic Panel **Martin Raju, Abhilash Suryan, Sandro Nizetic**
12:49 pm – 12:53 pm	**IEEES12- P328** Application of Magnetite Iron Oxide Nanoparticles (Fe_3O_4) Grafted with Silica Nanoparticles (SiO_2) for separation of Oil from Oil/Water Emulsions **Wamda Elmobarak, Fares Almomani**
12:53 pm – 12:57 pm	**IEEES12- P302** Spectral analysis of LBM-LES numerical data on lid-driven cavity **Fethi Aloui, Insaf Mehrez, Ramla Gheith**
12:57 pm – 1:01 pm	**IEEES12- P307** Heating Rate Effect on Tetrapak Paper Pyrolysis: Thermogravimetric Analysis **Fethi Aloui, Emna Berrich, Afef Bouazizi, Imene Bekri, Ezzedine Srasra**
1:01 pm – 1:05 pm	**IEEES12- P102** Vegan Burger Recipe Optimization for Meat Quality Nutrition in the Food Industry **Brenno Menezes, Mohamed Sawaly, Tareq Al Ansari**
1:05 pm – 1:09 pm	**IEEES12- P247** Cobalt Based Catalysts for Water Oxidation or Oxygen Evolution Reaction **Afreenuzzaman Badruzzaman, Afdhal Yuda, Anchu Ashok, Anand Kumar**
1:09 pm – 1:13 pm	**IEEES12- P248** Anode Catalysts for Methanol Oxidation Reaction in Direct Methanol Fuel Cell **Afdhal Yuda, Anchu Ashok, Anand Kumar**
1:13 pm – 1:17 pm	**IEEES12- P124** Electro-Thermochemical Water-Splitting Cycle for Hydrogen Production **Fares Almomani**
1:17 pm – 1:21 pm	**IEEES12- P022** Fuel Life Cycle Assessment of Non-Passenger Diesel Vehicles in Qatar **Hanadi Al Thani, Muammer Koc, Sami Al-Ghamdi, Rima Isaifan**
1:21 pm – 1:25 pm	**IEEES12- P353** Techno-economic Assessment of a Synthetic Fuel Production Facility by Utilizing the Hydrogenation with CO_2 Captured from Biogas **Alperen Tozlu**
1:25 pm – 1:30 pm	**IEEES12- P373** Powertrain Analysis of Heavy Duty Electric Vehicle with Wheeled and Tracked Alternatives **Eda Alpaslan, Can Özgür Çolpan, Mustafa Umut Karaoğlan**

PRESENTATIONS SESSION – 9

Session Chair: Dr. Adel Elomri

Time (GMT+3)	Presentation
1:30 pm – 1:45 pm	**IEEES12- P368** Techno-Economic Analysis of a 500MWe Supercritical Coal-based Thermal Power Plant with Solar Assisted MEA-based CO_2 Capture **Rajesh Kumar, Sujit Karmakar**
1:45 pm – 2:00 pm	**IEEES12- P214** Impact of Energy Subsidies on the Economic Viability of Rooftop Photovoltaic Systems in Qatar **Omar Alrawi, Islam S. Bayram, Muammer Koc, Sami G. Al-Ghamdi**
2:00 pm – 2:15 pm	**IEEES12- P159** Potential Energy Optimisation of the Coefficient of Performance of a Residential Air Source Heat Pump Water Heater **Stephen Tangwe, Kanzumba Kusakana**
2:15 pm – 2:30 pm	**IEEES12- P058** Metaheuristic Approaches for Solving the Energy Optimization Problem of Multiple Stage Evaporator System **Drishti Yadav, Om Prakash Verma**
2:30 pm – 2:45 pm	**IEEES12- P059** Metaheuristic-Driven Optimization for Solution of Dynamic Model of Multiple Stage Evaporator System of Paper Mills **Drishti Yadav, Om Prakash Verma**

2:45 pm – 3:00 pm	**IEEES12- P144** A sustainable HVAC and architectural design for historical churches: A case study of San Marcello Al Corso **Mohammad Mohammadzadeh, Navid Hadifar, Bahareh Mohammadzadeh**
3:00 pm – 3:15 pm	**IEEES12- P162** Microwave Melting Salt Slurries by Serpentinite Granule for Thermal Energy Storage **Yıldırım Tosun**
3:15 pm – 3:30 pm	**IEEES12- P305** The Effect of Entering Angle on Machinability of PH 13-8 Mo **Ahmet Serdar Güldibi, Halil Demir**

PRESENTATIONS SESSION – 10

Session Chair: Dr. Farrukh Khalid

Time (GMT+3)	Presentation
3:45 pm – 4:15 pm	Some Fundamental Investigations for the Energetic Optimization of Stirling Engines **Invited Talk – Prof. Dr. Fethi Aloui** Professor, Polytechnic University Hauts-de-France, France
4:15 pm – 4:25 pm	**Break**
4:25 pm – 4:55 pm	A review on energy storage technologies with a focus on thermal energy storage: State of the art and prospects **Invited Talk – Prof. Dr. Lounes Tadrist** Professor, Aix-Marseille University, France
4:55 pm – 5:00 pm	**Break**
5:00 pm – 5:15 pm	**IEEES12- P299** Development of an Assessment Methodology for Smart Cities: Canadian Cities as Case Studies **Azzam Abu-Rayash, Ibrahim Dincer**
5:15 pm – 5:30 pm	**IEEES12- P331** Energy and Exergy Analysis of a Solar Driven Trigeneration System for Ammonia Synthesis, Electricity Generation and Fresh Water Production **Murat Emre Demir, Ibrahim Dincer**
5:30 pm – 5:45 pm	**IEEES12- P226** Direct synthesis of formic acid energy carrier from captured carbon dioxide and utilization in a direct formic acid fuel cell **Nour Mardini, Yusuf Bicer**
5:45 pm – 6:00 pm	**IEEES12- P278** Borohydride Oxidation on Copper alloys deposited on carbon by Electroless coating **Harsha Uskaikar, Brenda Dias Barreto, Sheela Berchmans**
6:00 pm – 6:15 pm	**IEEES12- P213** Potential Carbon Reduction From Atmosphere Via Urbanized Local Trees in Qatar **Salma Habib, Sami G. Al-Ghamdi**
6:15 pm – 6:30 pm	**IEEES12- P268** Exergetic Investigation of a New Integrated Ammonia Based System **Osamah Siddiqui, Ibrahim Dincer**
6:30 pm – 6:45 pm	**IEEES12- P224** Enhanced Thermal Conductivity of Polyethylene Composites Using Granulated Graphene **Chaudhry Usman, Abdelnasser Mabrouk, Ahmed Abdala**
6:45 pm – 7:00 pm	**IEEES12- P230** Kinetic Studies of Camel Manure Using Thermogravimetric Analysis **Prakash Parthasarathy, Samar Elkhalifa, Tareq Al-Ansari and Gordon McKay**
7:00 pm – 7:15 pm	**IEEES12- P327** Sustainable Dairy Farm Waste Management – A Polygeneration and Hydrogen Energy-Based Approach **Muhammad Luqman, Tareq Al-Ansari**
7:15 pm – 7:30 pm	**IEEES12- P335** Renewable energy based polygeneration system with hydrogen storage for remote decentralized coastal community **Shoukat Alim Khan, Sami Al-Ghamdi**
7:30 pm – 7:45 pm	**IEEES12- P336** Design Quality for Green Building Delivery **Ayman Raouf , Sami G Al-Ghamdi**
7:45 pm – 8:00 pm	**IEEES12- P125** Preliminary Energy Audit of a Residential Engineering University Campus **Muhammad Sohail Malik, Aleem Ahmed Khan**

END OF THE DAY

DAY 5

December 24, 2020 | THURSDAY | Webex short link: https://bit.ly/3oNT2ho *(Password: 20-20)*

PRESENTATIONS SESSION – 11

Session Chair: Dr. Muammer Koc

Time (GMT+3)	Presentation
8:30 am – 9:00 am	Field Evaluation of Membrane Distillation Technologies for Desalination of Highly Saline Brines **Invited Talk – Dr. Altaf Hussain** ConocoPhillips Global Water Sustainability Centre, Qatar Science & Technology Park
9:00 am – 9:15 am	**IEEES12- P113** Numerical Analysis of a Hybrid Thermal Energy Storage System for Low Temperature Applications **B Swaraj Kumar, James Varghese**
9:15 am – 9:30 am	**IEEES12- P142** Numerical Analysis of 3-D Vanadium Redox Flow Battery with Flow Field **Snigdha Saha, Gajanan Dattarao Surywanshi, Patnaikuni Venkata Suresh**
9:30 am – 9:45 am	**IEEES12- P111** Novel Passive Heat Transport Device for Solar Indoor Cooking: A Numerical Study **K. Varun, U.C. Arunachala, M. S. Manjunath**
9:45 am – 10:00 am	**IEEES12- P116** Strategic and Flexible LNG Production Under Uncertain Future Demand **Noor Yusuf, Tareq Al-Ansari, Rajesh Govindan, Luluwah Al Fagih**
10:00 am – 10:15 am	**IEEES12- P239** Energy Use Identification for Adapted Production in Africa **Aminata Kanta, Lounes Tadrist, Rachid Outbib**
10:15 am – 10:30 am	**IEEES12- P132** The Advantages of Microwave Technology in Commercially Biodiesel Production **Veli Gokhan Demir, Nadir İlten, Hakan Serhad Soyhan, Ismail Caner**

PRESENTATIONS SESSION – 12

Session Chair: Dr. Arif Hepbasli

Time (GMT+3)	Presentation
10:45 am – 11:00 am	**IEEES12- P370** Investigation of Using Hemp as a Thermal Insulation Material in the Building Envelope in Terms of Thermal Comfort **Okan Kon, Ismail Caner, Samet Arda**
11:00 am – 11:15 am	**IEEES12- P236** Assessment of Three Electrochemical Energy Storage Methods for Residential Applications in Hot Climates **Manal Alshafi, Yusuf Bicer**
11:15 am – 11:30 am	**IEEES12- P274** Reliability Analysis of V- Trough Solar Air Heater (V-TASH) with Thermal Storage using Hourly Average Solar Radiation Data **Suniraj Ba, Eswaramoorthy Muthusamy**
11:30 am – 11:45 am	**IEEES12- P073** Experimental Investigation of Heat Transfer Characteristics of a Gravitational Water Vortex Flow **Muhammad Tayyab, Taqi Ahmad Cheema, Ali Al Atas Khan, Muhammad Talha Riaz**
11:45 am – 12:00 pm	**IEEES12- P312** Parametric Study of a Parabolic Trough Collector Based Solar Thermal System for Improving Asphalt Paving Sustainability **Yassine Hrimech, Abdallah Saad, Radia Ait El Cadi, Moaad Aboumalik and Mohamed Essaaidi**
12:00 pm – 12:15 pm	**IEEES12- P180** Life Cycle Assessment of Ammonia Synthesis from Thermo-Catalytic Solar Cracking of Liquified Natural Gas (LNG) **Amro M. O. Mohamed, Sami G. Al-Ghamdi, Yusuf Bicer**

12:15 pm – 12:30 pm	**IEEES12- P110** Thermo-Hydraulic and Exergy Analysis of Parabolic Trough Collector with Wire Matrix Turbulator: An Experimental Investigation **K. Varun, U.C. Arunachala**
12:30 pm – 12:45 pm	**IEEES12- P172** Exergy Analysis of MgO-Water Nanofluid as a Coolant for Sinusoidal Mini-Channel Heat Sink **Muhammad Usman Sajid, Yusuf Bicer, Hafiz Muhammad Ali**

POSTERS SESSION - 4

Time (GMT+3)	Presentation
12:45 pm – 12:50 pm	**IEEES12- P187** Study on Nitrogen doped Carbon paper electrodes for vanadium Redox Flow Battery Applications **Muthumeenal Arunachalam, Ahmed Sodiq, Fatima Fasmin, Belabbes Merzougui**
12:50 pm – 12:55 pm	**IEEES12- P249** Recent Progress in Catalyst Development for Water Gas Shift Reaction **Parisa Ebrahimi, Anand Kumar, Majeda Khraisheh**
12:55 pm – 1:00 pm	**IEEES12- P300** Model and Flow Sheet Improvements for Coal fired Power Plants Equipped with a CO_2 Capture Process Using Monoethanolamine **Fethi Aloui, Tanguy Hahn, Jian Chen, Weiyang Fei**
1:00 pm – 1:05 pm	**IEEES12- P301** Theoretical Investigations of Stirling Engine Performances for Different Working Fluids **Fethi Aloui, Houda Hachem and Ramla Gheith**
1:05 pm – 1:10 pm	**IEEES12- P020** Mitigation of urban air pollution with green vegetation for sustainable cities: A review **Taif Alsalama, Muammer Koç Rima Isaifan**
1:10 pm – 1:15 pm	**IEEES12- P371** Impact of Hazardous Domestic Waste on Human Health in Qatar: Policy Proposal for Integration into The Environmental Law **Taif Alsalama, Muammer Koç Rima Isaifan**
1:15 pm – 1:20 pm	**IEEES12- P223** Energy Saving in an Academic Institution through Passive Daylighting Strategy **Manju G Nair, Aparna S, Abhilash Suryan, Sandro Nizetic**
1:20 pm – 1:25 pm	**IEEES12- P034** Facile Synthesis of Binary Phosphide as Active and Durable Catalyst for Electrochemical Oxygen Evolution **Assem Mohamed, Yahia Shoeb, Amina Al Jaber, Siham Alqaradawi**
1:25 pm – 1:30 pm	**IEEES12- P282** Influence of Boundary Conditions on the Exergetic Optimization of a Thermal Energy Storage Unit Combined with an Organic Rankine Cycle (ORCTES) **Andreas König-Haagen, Dieter Brüggemann**

PRESENTATIONS SESSION – 13

Session Chair: Dr. Mehmet Akif Ezan

Time (GMT+3)	Presentation
1:30 pm – 1:45 pm	**IEEES12- P287** Economic and Social Sustainability in Low-Carbon Energy Transitions: Computer Simulations of a Proof-of-Concept Study **Ibrahim Ari, Muammer Koc**
1:45 pm – 2:00 pm	**IEEES12- P177** Supply Security in Critical Energy Infrastructures for Reliable Energy Grids **İsa Avcı, Cevat Özarpa, Yusuf Biçer**
2:00 pm – 2:15 pm	**IEEES12- P316** Transient Behavior of a Solar-Aided Shell-and-Tube Type Latent Heat TES Unit **Nezir Yagiz Cam, Ersin Alptekin, Levent Bilir and Mehmet Akif Ezan**
2:15 pm – 2:30 pm	**IEEES12- P203** Enhancements in Coal Burning in a Tunnel Furnace **Gurhan Tahtali, Hayati Olgun**

2:30 pm – 2:45 pm	**IEEES12- P374** Simulation of Heavy Duty Electric Vehicle Powertrain with Wheeled and Half Tracked Alternatives **Mustafa Umut Karaoğlan**
2:45 pm – 3:00 pm	**IEEES12- P143** Integration of Petroleum Refinery and Petrochemical Plants for Condensate Feedstock: Challenges and Opportunities **Salman Ashkanani, Brenno Castrillon Menezes**
3:00 pm – 3:15 pm	**IEEES12- P164** Production of Zeolite/ Biochar Active Carbon Composite Pellets for Hydrogen Sorption **Yıldırım Tosun**
3:15 pm – 3:30 pm	**IEEES12- P356** An Effective Hardware–In-The-Loop Testing Technology for an Electro-Mechanical System: Application on Drill String System **Abdelbasset Krama**

PRESENTATIONS SESSION – 14

Session Chair: Dr. Tahir A.H. Ratlamwala

Time (GMT+3)	Presentation
3:45 pm – 4:00 pm	**IEEES12- P347** Energetic analysis of human body for Indian conditions **Arvind Kumar Patel, Satish Pal Singh Rajput**
4:00 pm – 4:15 pm	**IEEES12- P078** The Life Cycle Assessment Related to Insulation Thickness of External Walls of The Hospital Buildings **İsmail Caner, Nadir İlten, Okan Kon**
4:15 pm – 4:30 pm	**IEEES12- P366** Exergetic analysis of trigeneration system using Heliostat and PTC solar technique as energy source **Krishna Mani Mishra, Onkar Singh**
4:30 pm – 4:45 pm	**IEEES12- P083** Entropy Generation of a FLiBe Molten Salt Modular Nuclear Reactor Cooled by Supercritical Carbondi-oxide **Muhammed Emin Topal, Adnan Midilli**
4:45 pm – 5:00 pm	**IEEES12- P346** Building transferable Reactive Force Field potentials: towards an enhanced understanding of metal dusting corrosion initiation **El Tayeb Bentria, Omotayo Salawu, Charlotte S. Becquart, Normand Mousseau, Othmane Bouhali, Fedwa El-Mellouhi**
5:00 pm – 5:15 pm	**IEEES12- P334** Exergy Loss Calculation in a Power Generation System for a Research Hospital **Murat Hacıosmanoğlu, Adnan Midilli**
5:15 pm – 5:30 pm	**IEEES12- P217** Comparison of Multi-Input Single-Output Isolation-free DC-DC Converter Toplogies for Hybrid Power Plants **Sakir Kuzey, Muhammet Tahir Guneser, Cihat Seker**
5:30 pm – 5:45 pm	**IEEES12- P024** Fabrication and Characterization of Sensor Devices Based on Graphene Decorated with Metal-Oxide Nanorods **Ahmad I. Ayesh, Rayyan E. Ahmed, Mai A. Al-Rashid, Rafah Ahmed Alarrouqi, Belal Saleh, Tahir Abdulrehman, Yousef Haik, Leena A. Al-Sulaiti**
5:45 pm – 6:00 pm	**IEEES12- P133** Flowsheet Development for the Steam Gasification of Camel Manure With Subsequent of CO_2 Capturing Using CaO: An ASPEN Plus® Modelling **Muhammad Shahbaz, Tareq Al-Ansari, Ahmed AlNous, Gordon Mckay**

PRESENTATIONS SESSION – 15

Session Chair: Dr. Adnan Midilli

Time (GMT+3)	Presentation
6:00 pm – 6:15 pm	**IEEES12- P207** Parametric study and ANN modeling of Liquid feed Direct Ethanol Fuel cells **Vineesh Ravi, Caraline Ann Jacob, Yohans Varghese, Sreeja P**
6:15 pm – 6:30 pm	**IEEES12- P134** A Novel Multi-Generation System with Reverse Osmosis for a Greenhouse in the Sabkha-Tah Region of Western Sahara in Morocco **Eric Okonkwo, Yasser M. Abdullatif, Tareq Al- Ansari, Yusuf Bicer**
6:30 pm – 6:45 pm	**IEEES12- P231** Thermodynamic Optimization of a Biomass-based Integrated Gasification Combined Cycle with Post Combustion Carbon Capture using Potassium Carbonate **Ikhlas Ghiat, Ahmed Alnouss, Tareq Al-Ansari**
6:45 pm – 7:00 pm	**IEEES12- P256** A Survey of International Security Standards for Smart Grids, Industrial Control System and Critical Infrastructure **Isa Avcı, Cevat Özarpa**
7:00 pm – 7:15 pm	**IEEES12- P313** Integrated sustainability assessment of a multigeneration system **Ugur Akbulut, Ibrahim Dincer**
7:15 pm – 7:30 pm	**IEEES12- P243** Evaluation of Oxygen and Steam Fed Biomass Gasification within Energy, Water and Food Nexus **Ahmed Alnouss, Tareq Al-Ansari, Gordon McKay**
7:30 pm – 7:45 pm	**IEEES12- P017** An Overview of the Solar Potential in Qatar: From Theory to Practice **Abdulsalam Al-Kholidi, Mohamed Alshaghdari, Habib Hamam**
7:45 pm – 8:00 pm	**IEEES12- P009** Recommendations for Exploiting the Solar Energy Potential in Albania **Abdulsalam Alkholidi, Habib Hamam, Aleksander Biberaj**

8:00 pm – 8:30 pm	**Closing and Award Ceremony**

END OF THE SYMPOSIUM

12th INTERNATIONAL EXERGY, ENERGY AND ENVIRONMENT SYMPOSIUM (IEEES-12)

December 20 – 24, 2020
Education City, Doha, Qatar

PRESENTED ARTICLES

Innovative Cooling Technique Mono and Hybrid Nanofluid in Porous Mini-channel: Experimental and Numerical Approach

M. Ziad Saghir[1*], M. Mansur Rahman[2]
[1] Department of Mechanical Engineering, Ryerson University, Canada
[2] Dept of Mathematics, Sultan Qaboos University, Oman
*Email: zsaghir@ryerson.ca

ABSTRACT
As a result of increasing power demands and the decreasing size of computational hardware, the need for an effective cooling technique is more urgent now than ever. Despite this need, there is insufficient research on porous metal foams operating as liquid cooling heat sinks within electronic systems, and documented cases where the results are reported and verified using both experimental and numerical analyses. An experiment has been conducted in a microchannel filled with porous metal foam and mono nanofluid. The heat transfer enhancement was investigated for different flow rate and for different concentration of mono nanofluid of water and Al_2O_3 nanoparticles ranging from 0.1% to 0.6%. Three different heat fluxes were tested in the experiment. Numerical comparison with experimental data showed a good agreement. Pressure drop, as well as the friction factor were investigated in details. The numerical model was repeated for hybrid nanofluid of Al_2O_3 and Cu. Results revealed an improvement in heat enhancement leading to believe that such a mixture is suitable for heat removal. Detailed performance of heat enhancement between pure water and mono nanofluid and hybrid nanofluid will be discussed in details.

KEYWORDS: Nanofluid, Forced convection, Hybrid fluid, Heat enhancement, Micro-channel, Porous medium

I. INTRODUCTION
Thermal energy storage (TES) systems are used to store or release thermal energy temporarily for later usage. The main purpose for the use of TES materials are due to fluctuating energy supply and demands along with varying production costs. Ramachandran et al. conducted a study on the thermal performance of the following hybrid fluid combinations: 25% - 75%, 50% - 50% and 75% - 25% aluminum oxide / copper oxide nanoparticles respectively, with 0.1% volume concentration. The use of hybrid nanofluids will provide an enhancement in the heat transfer coefficient and the Nusselt number for a lower Reynolds number. Hybrid nanofluid is prepared by mixing the nanocomposite powder with deionized water. The hybrid nanofluid with 25% aluminum oxide and 75% copper oxide combination had a thermal resistance that was 44.25% lower than that of deionized water. A reduction in temperature was observed for the hybrid fluid containing 75% copper oxide and 25% aluminum oxide nanoparticles. This is due to the additional mass of the hybrid fluid brought upon by the copper particles, and so a larger hybrid fluid mass will result in a greater temperature drop. Studies on different hybrid fluid combinations, volume concentrations and various nanoparticles are often performed to obtain optimal thermophysical characteristics.

Suresh et al. conducted research on the Nusselt number and friction factors for alumina and copper oxide hybrid fluid with 0.1% volume concentration for flows in the laminar regime. The widespread use of alumina and copper oxide nanoparticles is due to their fluid's excellent thermal properties, stability and it is relatively inexpensive. The lower than the average thermal conductivity of the aluminum oxide nanoparticles in comparison to most metallic particles is offset by the incorporation of the copper oxide fluid. The excellent physical stability and chemical inertness are properties of the former nanoparticles mentioned above. Thermal conductivity significantly depends on the size, shape and type of nanoparticles materials. Nusselt number enhancements are observed despite the volume concentrations at a very low 0.1%. The thermal conductivity increase of the hybrid fluid has a small effect on the improvement of the heat transfer coefficient. It is possible that the random particle motion otherwise known as Brownian motion has significantly increased both the fluid's viscosity and thermal conductivity near the centerline. A flat velocity profile is a result of the increase in the hybrid fluid's viscosity which has led to a decrease in the difference between the average tube wall and bulk mean temperature. This reduction in the temperature difference in conjunction with the thermal conductivity improvement provided by the copper oxide nanoparticles has improved the overall heat transfer coefficient of the fluid. The hybrid nanofluid of aluminum and copper oxide particles exhibited remarkably greater heat transfer coefficient and Nusselt number compared to aluminum oxide nanofluid.

In addition, it manifested a lower thermal resistance to convective heat transfer than that of alumina/water nanofluid. The hybrid fluids are characterized by high viscosity caused by the formation of clusters, consequently it demonstrates a higher friction factor than that of deionized water. Therefore, hybrid fluids will also require a large pumping power than pure water. Hameed et al. performed a comparative study on both the heat transfer and friction characteristics for Alumina-copper and Alumina-CNT hybrid nanofluids in laminar flow regime. When considering the convective heat transfer coefficient in forced convection, there is a large dependence on the fluid velocity and its thermophysical properties. Thus, it is crucial to select a nanofluid that offers an overall optimal set of property values. Therefore, the purpose of the research

conducted by Hameed et al. is to add onto the prior research conducted on various nanofluids and its heat transfer effectiveness, with hopes of determining the most effective hybrid fluid. The heat transfer enhancement as well as the Nusselt number for the Alumina-CNT hybrid fluid was significantly greater than that of Alumina-Cu hybrid fluid and Alumina nanofluid. The Alumina hybrid fluids with copper and carbon nanotubes had higher pressure drops that than of Alumina nanofluids. The Alumina-CNT hybrid fluid demonstrated the largest friction factor enhancement out of the tested hybrid fluids, and so it requires the most pumping power out of the fluids.

II. EXPERIMENTAL DESCRIPTION

An experimental apparatus was developed to analyze the effect of pore density on the heat transfer characteristics within micro-channel porous media operating as heat sinks subjected to a forced flow. The test section consists of a porous micro-channel fluid chamber where the flow enters, a porous chamber containing the porous material, and a fluid chamber to allow the fluid to exit. The chamber is sealed to prevent any water leakage. An aluminum metal block was located below the porous material and a thermo paste material was inserted at the connecting point to allow good heat conduction. Thermocouples were inserted 1mm below this interface. The experimental setup used in the data collection process is similar to the one previously used by Bayomy et al. however, the present apparatus includes variations in the geometric properties of the foam samples. These foam samples consisted of 6061-T6 aluminum manufactured by ERG Aerospace. The pore densities used was 40 PPI. The working fluid used within the system was nanofluid with 0.1% concentration of Al_2O_3. This fluid was recirculated through the apparatus to form a closed loop system. The metal block containing the three porous channels was cut to match the dimensions of the heater included within the apparatus (37.5mm x 37.5 mm). This sizing is consistent with the dimensions of an “Intel Core i7” processor.

The overall experimental setup and the numerical model were illustrated in Fig. 1. The heater was controlled using a dial. This allowed the experimenters to vary the current passing through the heater. This current was used to adjust and control the heat flux entering the system. A voltmeter and ammeter were connected to the heater to determine the actual heat flux entering the system. Ten T-type thermocouples were used in the construction of the apparatus. Eight of these thermocouples were used to read and record the temperature distribution across the surface of the heater. The remaining two were used to record the inlet and outlet temperatures of the fluid passing through the metal foam.

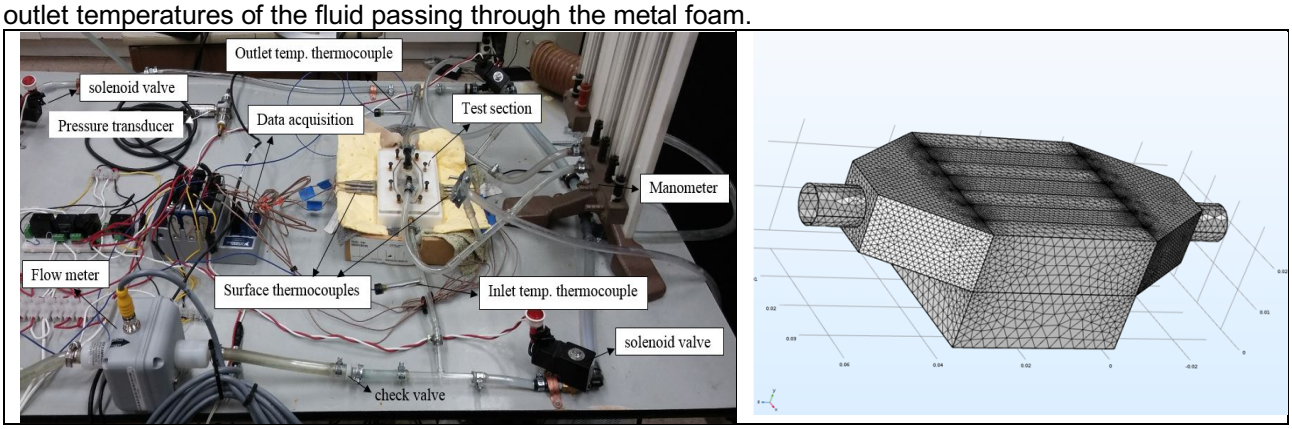

Fig. 1 Experimental Setup and finite element model.

III. FINITE ELEMENT MODELLING AND BOUNDARY CONDITIONS

The finite element modeling assumptions are taken into consideration, the Brinkman- Forchheimer equation and energy equation which describe the fluid flow and heat transfer inside porous micro are solved using the following formulation:

$$\frac{\rho_f}{\varepsilon}\left(\frac{\partial U}{\partial t}+(U\cdot\nabla)\frac{U}{\varepsilon}\right)=\nabla.\left(-pI+\frac{\mu_f}{\varepsilon}(\nabla U+(\nabla U)^T)\right)-(\frac{\mu_f}{K}+\beta_f|U|)U+F \quad (1)$$

$$\nabla\cdot\left(\rho_f U\right)=0 \quad (2)$$

$$(\rho c_p)_{eff}\cdot\frac{\partial T}{\partial t}+(\rho c_p)_f\, U\cdot\nabla T=\nabla.\left(k_{eff}.\nabla T\right) \quad (3)$$

Where ρ_f represents the fluid density, c_p represents the fluid specific heat, ε represents the porosity of the aluminum metal foam, p represents the pressure, U represents the velocity field vector, β_f represents the Forchheimer coefficient, T represents the temperature, μ_f represents the water dynamic viscosity, K represents the permeability of the aluminum foam and k_{eff} represents the effective thermal conductivity of the aluminum metal foam when filled with fluid. An accurate representation of the structural parameters of the metal foam is

important for the estimation of effective thermal conductivity. For the fluid flow at the entrance of the porous channel and at the exit is solved using the Navier Stokes equation combined with the energy equation.

IV. RESULTS AND DISCUSSIONS

Different model scenario will be presented in this paper. The fluid used in our experimental section consist of water mixed with Al_2O_3 nanoparticles. The concentration of these nanoparticles was 0.1%. The forced convection is applied to the three porous micro-channels model as shown in Fig. 1. The porosity is 0.91 and a permeability of 40 PPI is used. The experimental results are compared with the numerical data to show the accuracy of the numerical model. The second segment of this paper is to repeat the experiment by using a hybrid mixture of water-Al_2O_3 and Cu. The aim is to examine the effect of thermal conductivities improvement on the heat enhancement. The model will be solved numerically and a comparison with the mono nanofluid will be conducted.

IV.1 Heat enhancement using mono nanofluid with 0.1% of Al_2O_3

The experiment was conducted on four different flow rates of mono nanofluid of 0.23 US gallon per minute (USGPM), 0.18 USGPM, 0.15 USGPM and 0.1 USGPM, respectively. The heat flux applied at the bottom of the plate was the other variable investigated in this experiment. It consists of three different heat fluxes of around 12 W/cm^2, around 7 W/cm^2 and finally around 5W/cm^2. Fig. 2 presents the temperature variation 1mm below the three-channel flow when the flow rate is set at 0.23 USGM. It was observed that the trend between the experimental and the numerical model is accurate and the difference between the experimental and numerical results is due to many reasons. Amongst them, the accuracy of the thermocouples, the accuracy of the flow rate measurement and the accuracy of the heat flux reading. For more details about the uncertainty analysis refer to the study in ref. [4]. Here T_{in} in the inlet temperature which varied between each run.

IV.2 Heat enhancement using hybrid fluid with different concentration of Al_2O_3 and Cu

While preparing the experiment to be conducted using hybrid nanofluid, the performance of the hybrid fluid against mono nanofluid is investigated numerically using the finite element technique. Different flow rate of 0.1 USGM, 0.15 USGM, 0.18 USGPM and finally 0.23 USGPM were implemented. Two types of fluid are considered in this study. The first is a mono nanofluid of 0.1% Al_2O_3 with water and the second is 0.1% of a mixture of Al_2O_3 and Cu with water (i.e. hybrid nanofluid). A comparison between the two types of fluid confirmed that the hybrid fluid has a heat enhancement exceeding the mono nanofluid by an average of 1%. This performance of hybrid fluid varies nonlinearly with the flow rate. Fig. 3 presents the ratio of heat enhancement of hybrid fluid over the mono nanofluid for a constant heat flux of 5 W/cm^2 at different flow rate.

V. CONCLUSIONS

This study investigated the potential of using hybrid fluid as an alternative to mono nanofluid for heat enhancement. Experimental tests were conducted on four different flow rates; however, four different compositions were used for the numerical study. The results revealed that the hybrid fluid has a heat enhancement exceeding the mono nanofluid, suggested that it is more ideal to use it in porous media than mono nanofluid

Acknowledgements
The authors acknowledge the full support of National Science Research Council, Canada and Ryerson University for funding this project.

References

Ramachandran, R. , Ganesan, K., Rajkumar, M. R. , Asirvatham, L. G. and Wongwises, S.,2016. “Comparative study of the effect of hybrid nanoparticle on the thermal performance of cylindrical screen mesh heat pipe”, Int. Commun. Heat Mass Transfer., **76**, 294–300.

Suresh, S. , Venkitaraj, K. P. , Selvakumar, P. and Chandrasekar, M. 2012. “Effect of Al_2O_3 – Cu / water hybrid nanofluid in heat transfer”, Experimental Thermal Fluid Science, **38**, 54–60.

Hameed, M. S. , Rajive, S. S. and Singh, K. 2019. “Comparative study of heat transfer and friction characteristics of water-based Alumina – copper and Alumina – CNT hybrid nanofluids in laminar flow through pipes”, Journal of Thermal Analytical. Calorimetry., **136**, no. 1, 243–253

Bayomy, A.M, Saghir, M. Z. and Yousefi, T. 2016. "Electronic cooling using water flow in aluminum metal foam heat sink: Experimental and numerical approach", International Journal of Thermal Sciences, **109**, 182-200.

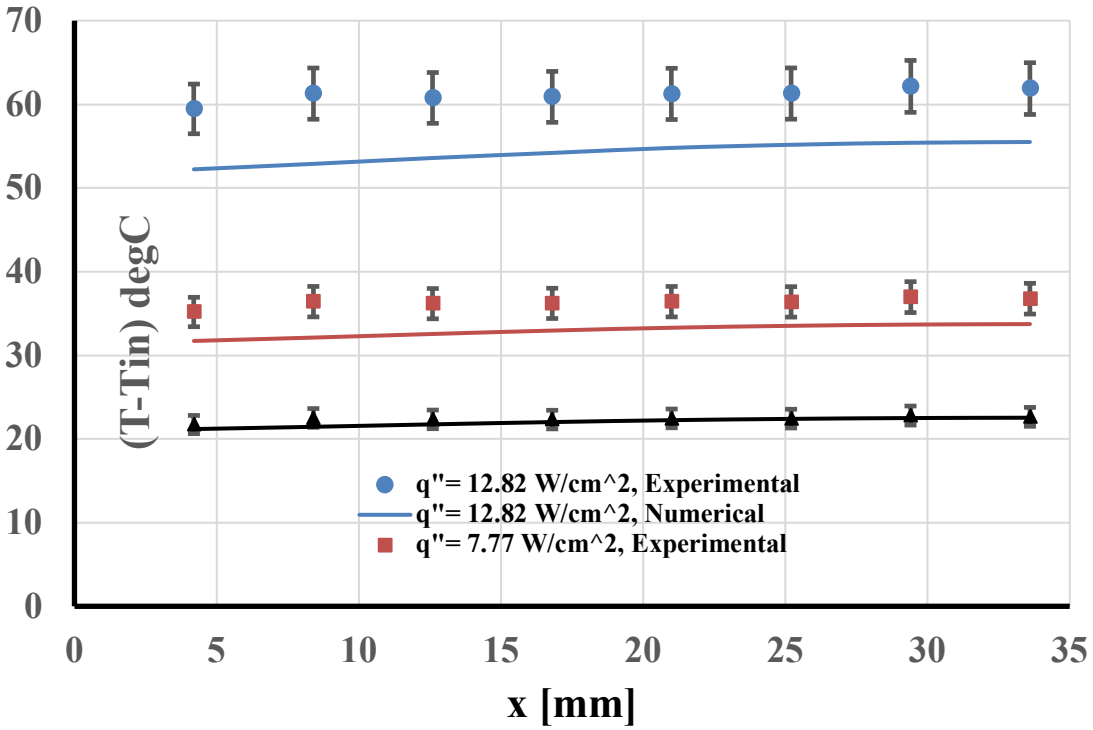

Fig 2. Temperature Variation 1 mm below the microchannel (flow rate=0.23 USGPM)

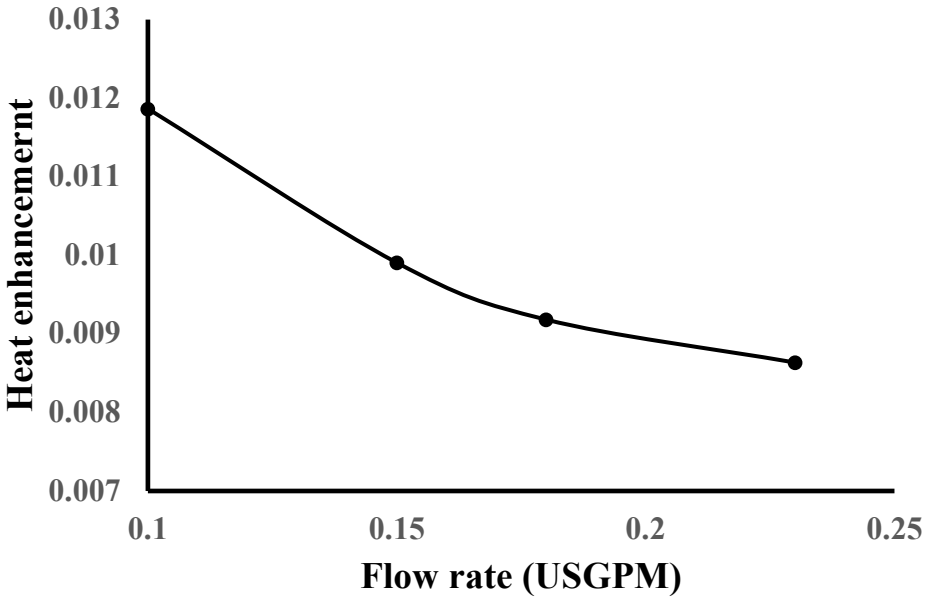

Fig 3. Heat enhancement of hybrid fluid over mono nanofluid as function of the flow rate

Recommendations for Exploiting the Solar Energy Potential in Albania

Abdulsalam Alkholidi[1, 2], Habib Hamam[3] Aleksander Biberaj[4]

[1]Electrical Engineering Department, Faculty of Engineering, Sana'a University, Yemen

[2]Canadian Institute of Technology (CIT), Tirana, Albania

[3]Faculty of Engineering, Moncton University, NB, Canada, E1A 3E9

[4]Faculty of Information Technology, Polytechnic University of Tirana, Tirana, 1001, Albania

* E-mails: abdulsalam.alkholidi@gmail.com

Abstract:

The purpose of this paper is to illustrate the solar energy potential in Albania and propose solutions to develop and encourage a solar energy market in this country, where the economy has been gradually increasing in the last decade. The potential for a renewable energy sector in Albania is promising, mainly because of the important presence of wind and solar energy resources. Moreover, we discuss the importance of exploiting photovoltaic systems in mountainous regions and villages-where public electricity is unavailable - to be widely used in heating, lighting, and irrigation, as well as to support grid systems. Furthermore, the advantages of photovoltaic technology are introduced and illustrated to motivate public establishments and government-owned electrical sectors to use and develop this technology.

Keywords: heating, education, clinics, home lighting, irrigation, mountainous areas.

1. Introduction

Albania a European country located in the Balkan region (Table 1), with a land surface of 27,398 km^2 and a water surface of 1,350 km^2 It is the 146-th largest nation in the world with a total area of 28,748 km^2 [1] Tirana is the capital, Albania has an estimated population of 2.88 million according to UN data. In this work, we present an illustration the solar energy potential in Albania and advances solutions for developing a solar energy market in this country, where the economy has been gradually increasing in the last decade. The remainder of the present paper is organized as follows. After the present brief introduction, an overview of related works and statistical studies is given in Section 2. The solar potential of Albania is addressed in Section 3. An important ongoing project is introduced in Section 4, followed by recommendations in Section 5. After discussion in Section 6, concluding remarks are given in Section 7.

2. Related works

According to a recent study conducted by IRENA, the costs of renewable energy systems are fast dropping down to be competitive with the conventional power production technology, not to say less expensive [2]. As a consequence, fossil fuel prices have dropped down in the last decade, and renewable energy technology prices are falling because of the recent development of a grwing renewable energy global market. Just to lick one example, solar PV systems and solar panel technology in Europe has decreased by approximately 80% from 2010 to 2016 [2]. As a consequence, this decrease led to competitive prices, even in countries with low-quality solar resources such as Germany. It has been recently reported that in this country a utility-scale solar Photovoltaic (PV) auction yielded an average cost of 5.6 Eurocents/kWh [2].

In a recent work [3], a rough assessment of payback time of PV panels, in different sizes and locations, was reported. The study took into consideration the time required for evaluating the incentive mechanism and the PV market economy. The objective is to determine whether the PV system is equivalent to grid systems. This PV technology is of nature to be a standard of developing solar energy systems in the world [3]. It estimated by the studythat the economic situation may result in a decline in the PV market. However, the study also foresees a possible delay in the progress of Grid Parity, though, its finalization is inevitable [3].

The authors of reference [4] investigated projetcs of long-term surface solar radiation (SSR) in the Greece's capital Athens. In the period of 1954 to 2012, measurements of the SSR were conducted. The analysis is based on dataset of monthly SSR deduced from a record of sunshine during the period of 1900 to 1953. The results of the analysis pointed out that a slight change of approximately 0.02% of SSR was observed. In comparision with other studies conducted in Mediterranean countries, the analysis of SSR change in Athensrevealed the lower percentage of this change. The report also pointed out that for the period after 1954, the evaluation of SSR indicated that the reported SSR change in all-sky and clear-sky conditions is due to some extent to cloudiness and to a large part to aerosol load change [4].
Reference [5] focused the deployment of solar and wind energy in Europe. Special attentions was given to the lead strategy behind the growth of the exploitation of these resources in the European Union (EU). EU opted for a long-term plan to attain 27% of its energy production in 2030 by using green natural resources. In this work, Data are

collected from a veriety of sources, including establishments, government officials, and policymakers, that are involved in the development of solar and wind energy. It has been reported in 2016, that more than 12% of the electricity demand in UE was covered by wind and solar sources. Since the target is 27% by 2030, there was a significant progress towards this target [5].

In our work, special attention to solar energy potential and the advantages and drawbacks of its exploitation. The current development of PV technology is seen as one of the effective solutions to meet the incessantly increasing demand for electric power production. Researchers focused on the rapid growth of solar technology and the many challenges and technical difficulties that persist, including low efficiency of PV cells, poor system balance and economic barriers, including high cost and scarcity manifesto of funding mechanisms. In order to help open novel routes regarding solar energy research and practices, a future roadmap for the field of solar research is discussed [6].

Report [7] highlights the importance of photovoltaic solar which has become the main source of electricity on several large markets. 2017 was an exceptionally successful year for PV systems technology. This technology gained ground over other competing technologies, such as nuclear power and fossil fuels [8].

In 2017, twenty-nine (29) countries exceeded the GW threshold with regard to the photovoltaic power installed. Seven (7) countries now exceed the barrier of 10 GW of total capacity, for more than 40 GW and China alone represents 131 GW. Germany, which has led the rankings for several years, had a decline in its leadership position in 2015 and is now fourth (42 GW). Japan is in the third position (49 GW) behind the United States (51 GW). With more than 111 GW of total capacity, Europe is largely surpassed by the Asian leader which exploits more than 219 GW [9].

In report [10], the authors studied the growth, consumption and share of renewable energies in different countries. They focused on the years 2010 and 2011.Obtained data were combined with the official data for three years 2009, 2012, and 2013, and a linear trend forecast was included based on the combined data.

The measured and / or calculated data clearly show the growth in the exploitation of renewable energies outside EU. The gas crisis of 2009 strengthened the importance of the exploitation of renewable energies, particularly in the Balkan countries. As a result, policy makers have been pushed to develop a renewable energy market to overcome with the energy crisis..

3. Solar Potential in Albania

Albania is located in the Western part of the Balkan Peninsula, at the eastern coast of the Adriatic and Ionian seas. It is situated between latitudes 39°38' - 42°38' and longitudes 19°16' - 21°04' and shares a border with Greece to the South and Southeast, Macedonia to the East, Kosovo to the Northeast, and Montenegro to the Northwest [11]. Albania has a significant renewable energy potential from hydro, wind, and, solar resources. In north-eastern Albania, including Bajram Curri, Kruje, Kukës, Peshkopi and Pukë, the amount of solar irradiation is around 1200 kWh / m2 / year. It reaches 1600 kWh / m2 / year in the Myzeqe region. In the north-west (Durrës, Kavaja, Fier, Volorë, Vlora, Saranda, Tirana and Berate), it varies from 1500 kWh / m2 / year to 1700 kWh / m2 / year (Fig. 1) [12, 13]. The potential for solar irradiation in Albania is therefore promising. The amount of average daily solar irradiation varies from 3.2 kWh / m2 / day in the northeast to 4.6 kWh / m2 / day in the southwest. As a result, the average daily solar irradiation in Albania is approximately 4.1 kWh / m2 / day. It is obvious that solar energy in Albania has great potential [12].

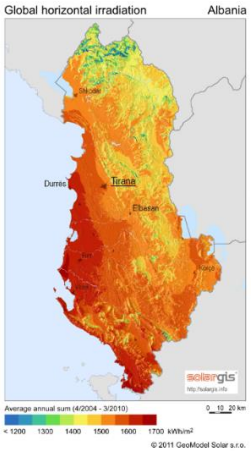

Fig. 1. Solar irradiation map of Albania, SolarGIS 2011.

Therefore, the solar irradiation and solar energy potential in Albania is promising. There is considerable potential to

develop grid-based photovoltaic systems through the country for lighting, heating, irrigation purpose, telecom, and education sector in the rural arreas. This can also be developed in rural and mountainous community as for example (Korab, 2,764 m, Maja Jezercë, 2,694 m, Radohima, 2,568 m, Tomorr, 2,416 m, Maja e thatë, 2,406 m, Shkëlzen, 2,404, and Koritnik, 2393m, ASL, etc) [14]. Currently, the solar energy market growth is increased exponentially in Albania during the last decade thanks to several reasons namely stability in the country and increading the economic growth.

In Tirana, the annual sunshine is about 2,544 hours in average [15]. The geography of Albania is defined by its location. This country is considered as a small primarily mountainous country in Southern Europe, facing the Adriatic and Ionian seas within the Mediterranean Sea. Table 1 shows some geographical statistics for Albania:

Table 1: Geographic statistics about Albania [1].

Item	Description
Continent	Europe
Location	Southeastern Europe, bordering the Adriatic Sea and Ionian Sea, between Greece to the South and Montenegro and Kosovo to the North
Coordinates	41°00′ N 20°00′ E
Area	28,748 km^2
Coastline	362 km (225mi)
Population	3,038,594 (#137)
Population density	110.91/km^2
GDP (PPP)	$33.90 Billion
GPD per Capita	11,900$
Climate	Mild temperate; cool, cloudy, wet winters; hot, clear, dry summers; interior is cooler and wetter

The surface area in the Western coast is affected by a maritime weather, where the average daily temperatures in the cold season is approximately below zero and warm in the summer. The Eastern area is affected by continental air masses; the temperature is ofetn below zero through the winter (the most recorded temperature was - 26°C). In summer, the valley of Albania is hot, where the average daily temperature is about 35°C. Albanian climate is similar to a Mediterranean countries and is featured by a considerable number of sunny days, about 290 days/year, where in the North and in the East, and approximately 325 days/year in the South and Southwest [16].

Table 3: Daily average solar radiation in big cities in Albania in (kJ/m^2) [17]

City Name	Jan.	Feb.	March	April	May	June	July	August	Sept.	Oct.	Nov.	Dec.
Peshkopia	9813	11584	13952	15127	17192	19225	20704	19815	18838	14189	1261	11566
Shkodra	10857	12316	14119	15771	17425	19253	20836	20069	18855	14450	12977	12235
Durres	13205	13523	14347	17604	18637	20228	22277	23199	20305	17750	15347	14677
Tirana	12066	13292	14243	16007	18555	20538	21598	21896	19854	16564	13604	13250
Vlora	14239	13894	13733	17726	19207	21376	22926	24093	23217	19791	17799	15347
Saranda	12868	15445	16633	18511	20405	22758	23443	24101	23237	17390	16857	14820

The average daily solar irradiation for the large cities in Albania is presented in Table 3. The data indicates that solar energy potential is encouraging in all seasons except winter.

4. Ongoing project

Newly, Albania launched a modern project named the “Country Program of Albania” in light of the transformation the global market for solar water heating and the promotion of an initiative by the government. (since 2010 there was a cooperation between the Ministry of Environment, the Ministry of Energy and Industry, and the UNDP). This important project is a part of the GEF/UNDP/UNEP Global Solar Water Heating Market Transformation and Strengthening Initiative [18].

5. Recommendations for energy exploitation

Socio economic benefits [19-22]:

- Creating new job opportunities.
- Motivate new generation engineers and technicians to work in the field of solar technology.
- Expanding and developing a PV systems market.
- Taking protective measures to keep the environment.
- Enhancing the education sector by using PV systems.
- Supporting medical units in the rural and mountainous communities.
- Reducing the migration from rural areas to urban.
- Using the PV water pumping system in irrigation.
- Encouraging and enhancing the small businesses.
- Motivating visiting rural and mountainous areas.
- Ameliorating the living conditions of rural habitants.

Recommendations:

- Increasing the exploitation of solar water heating system.
- Expanding the exploitation of solar energy in the irrigation sector.
- Exemption or at least minimizing taxation for all renewable energy technology.
- Investing more in green energy.
- Including renewable energy in the cirrucula of universities, institutes, and schools.
- Maximizing community awareness of the importance of PV systems.
  Encouraging consumers to use solar energy widely.

Lessons learned [7, 22]:

- Prioritizing the most efficiency PV modules.
- Comparing the efficiency metrics for different suppliers (greater electricity generation).
- PV modules certification – there are several various standards to selecting the best module.
- PV module output – over time, the efficiency of the PV module decreases. Customers must select the best PV panels, taking into account, its inspection for panel degradation and its warranty.
- Expanding customer's use of PV technology, such as solar ovens, solar cell-phone chargers, solar powered tents and backpacks, etc.
- Focusing on the growth of the solar energy technology market.
- Broadening the use of solar energy, especially in the field of heating.
- Addressing the lack of investment in renewable energy.
- Addressing the scarcity of scientific research in the field of renewable energy in Albania.
- Designing and implementing PV systems or solar farms, while ensuring a solid design and installation and high quality components to enhance the system's performance.
- Ensuring a PV system exploitation and the good use of PV components to increase the longevity of the system.

6. Conclusion

Solar power energy potential in Albania was presented and recommendations for its exploitation were provided. This sector is highly promising for investors in the field of irrigation, mainly due to water availability, for the development solar water heating systems, and for residential customers in villages and in urban communities. Based on the data provided in this paper, we foresee a rapid growth of the renewable energy sector in Albania.

References:

[1] World atlas. Albanian Geography, https://www.worldatlas.com/webimage/countrys/europe/albania/alland.htm. [Accessed on 07 August 2018

[2] European Union and IRENA. Renewable Energy for the European Union, Based on REmap analysis, ISNB 978-92-9260-007-5; February 2018. Downloaded on 30.07.2018. <https://www.irena.org//media/Files/IRENA/Agency/Publication/2018/Feb/IRENA_REmap_EU_2018.pdf>. [Accessed on 30 July 2018]

[3] Giovanni Mazzanti, Ezio Santini, Donatella Zaccagnini. Towards grid parity of solar energy in Italy: the payback time trend of photovoltaic plants during the Last Years. pp 1-8, 2012. IEEE, **DOI:** 10.1109/PESGM.2012.6345426.

[4] Stelios Kazadzis et al.. Long-term series and trends in surface solar radiation in Athens, Greece. Atmospheric chemistry and physics, 18, pp 2395–2411. https://doi.org/10.5194/acp-18-2395-2018, 2018.

[5] Roberto Local Arantegui, Arnulf Jäger-Waldu. Photovoltaics and wind status in the European Union after the Paris Agreement. Renewable and Sustainable Energy Reviews 81 (2018) 2460–2471. http://dx.doi.org/10.1016/j.rser.2017.06.052; 2018.

[6] Ehsanul Kabir, Pawan, Kumar, Sandeep Kumar, Adedeji Adelodun, Ki-Hyun Kim. Solar energy: potential and future prospects. Renewable and Sustainable Energy Reviews 82 (2018) 894–900. http://dx.doi.org/10.1016/j.rser.2017.09.094; 2018.

[7] REN21. Renewables 2017 Global Status Report. Paris: REN21 Secretariat; 2017. ISBN 978-3-9818107-6-9.
[8] Frankfurt School-UNEP Centre for Climate & Sustainable Energy Finance (FS-UNEP Centre) and Bloomberg New Energy Finance (BNEF), Global Trends in Renewable Energy Investment 2018 (Frankfurt: April 2018), p. 12; 2018 <http://fs-unep-centre.org/sites/default/files/publications/gtr2018v2.pdf>. [Accessed on 15 July 2018].
[9] IEA international energy agency. Snapshot of global photovoltaic markets, Photovoltaic power systems programe, report IEA PVPS T1-33:2018, ISBN 978-3-906042-72-5, page 4; 2018 <http://www.iea-pvps.org/fileadmin/dam/public/report/statistics/IEA-PVPS_-_A_Snapshot_of_Global_PV_-_1992-2017.pdf>. [Accessed on 07 August 2018]
[10] Stefan Dunjic, Simon Pezzutto, Alyona Zubaryeva. Renewable energy development trends in the Western Balkan. Renewable and Sustainable Energy Reviews 65 (2016) 1026–1032. http://dx.doi.org/10.1016/j.rser.2016.05.051.
[11] Renewable energy resources and energy efficiency in Albania. <http://aea-al.org/wp-content/uploads/2012/04/RENEWABLE-ENERGY-ALBANIA.pdf>. 2012. [Accessed on 24 September 2018].
[12] Albania Energy Association (AEA). Albania Solar Energy, http://aea-al.org/albania-solar-energy/; 2013 [Accessed on 21 September 2018].
[13] SOLARGIS. Download solar resource maps and GIS data 180+ Countries, Selected region Albania, https://solargis.com/maps-and-gis-data/download/albania. [Accessed on 21 September 2018].
[14] List of mountains in Albania, https://en.wikipedia.org/wiki/List_of_mountains_in_Albania. [Accessed on 22 September 2018].
[15] Liz Osborn. Sunniest Cities in Europe, https://www.currentresults.com/Weather-Extremes/Europe/sunniest-cities.php. [Accessed on 28 August 2018].
[16] Climate. Albania, http://www.albantours.info/en/welcome-to-albania/land-information/climate.html, (SHUKALB: Water Supply and) Sewerage Utility of Albania (FB11); Tirana, 2014 [Accessed on 12 September 2018].
[17] Albania overview; 2012. <http://www.akbn.gov.al/wp-content/uploads/2013/11/images_pdf_publikime_Broshura_Energjite_e_Rinovueshme.pdf>. [Accessed on 25 August 2018].
[18] UNDP. Empowered lives Resilient nations. The Country Programme of Albania under the Global Solar Water Heating Market Transformation and Strengthening Initiative; Tirana March 2017. <http://www.al.undp.org/content/dam/albania/docs/misc/Best%20Practice%20from%20SWH%20Project_Eng.pdf>. [Accessed on 17 August 2018]
[19] A. Alkholidi and H. Hamam (2019) "Solar Energy Potentials in Southeastern European Countries: A Case Study", Intern. J. of Smart Grid 3, 1-8, 2019.
[20] Hadwan M, Alkholidi A. Solar power energy solutions for Yemeni rural villages and desert communities. Renew Sustain Energy Rev 2016; 57:838–49. http://dx.doi.org/ 10.1016/j.rser.2015.12.125.
[21] Republic of Albania. Economic reform program 2018-2020, 31 January 2018. https://financa.gov.al/wp-content/uploads/2018/06/Economic_Reform_Programme_2018-2020-1.pdf [Accessed on 17 April 2019].
[22] REN21. 2018. Renewables 2018 Global Status Report (Paris: REN21 Secretariat). ISBN 978-3-9818911-3-3. http://www.ren21.net/wp-content/uploads/2018/06/17-8652_GSR2018_FullReport_web_final_.pdf [Accessed on 17 April 2019].
[23] NASA. Global climate change, Vital signs of the planet, Global temperature, Global land-ocean temperature index, Data source: NASA's Goddard Institute for Space Studies (GISS), NASA's Goddard Institute for Space Studies (GISS). Credit: NASA/GISS. https://climate.nasa.gov/vital-signs/global-temperature/; 2017 [Accessed on 09 September 2018].

Complexity and Use in the Built Environment: Post-occupancy Evaluation and Proposed Design Alterations for Qatar University's Most Iconic Building

Dr. Mark David Major, AICP, CNU-A[1]
Doha Elsaman[2]
Lolwa Al-Mohannadi[2]
Meera Al-Khulifi[2]
Shaikha Al-Thani[2]

E-mail: m.major@qu.edu.qa

Abstract
Constructed in the 1980s using a modular design concept by Egyptian architect Kamal El-Kafrawi, the Building Corridors (BCR) at Qatar University (QU) is the most iconic building on the campus, even incorporated in the university's official logo.[3] However, the BCR Corridors are also notorious for presenting way-finding difficulties for end-users. These navigation problems derive from the repetitive similarity of individual parts in the modular design; stairwells, screens, and temporary installations creating impediments to user readability and visibility; and, the relationship of the BCR Corridors to the immediate surrounding context of the university campus. Recently, faculty and student researchers at QU conducted a post-occupancy evaluation (PoE) of the BCR Corridors. The PoE study included 1) direct observations of movement flows including entry counts at the building perimeter and static occupation of space (i.e., sitting, standing, and interacting) in common areas, 2) extensive room use and photographic surveys, and 3) computer modeling of the spatial layout in the building using space syntax. Space syntax is an international research program of academics and industry practitioners scientifically investigating, mathematically quantifying, and better understanding the role of built space in society from a single building to entire cities based on network science (Hillier and Hanson, 1984; Hillier, 1996; Hanson, 1998; Turner et. al., 2001; Major, 2018). Space syntax is based on a set of techniques for the simple representation and mathematical measurement of architectural and urban space (Hillier et. al., 1987; Hillier & Penn, 1987; Hillier et. al, 1995; Major et. al, 2019). The purpose of the study was to: 1) better understand the observed patterns of movement and space use especially with reference to the widely-known problems for navigation and way-finding in the BCR Corridors; and, 2) develop design alteration proposals (some cosmetic, others substantial) to enable easier use of the building complex.

Keywords: educational buildings, innovation, navigation, post-occupancy evaluation, space syntax

Introduction

The BCR Corridors at QU are notorious for the way-finding difficulties of end-users. These navigation problems arise due to the repetitive similarity of individual parts in its modular design, highly localized impediments to readability and visibility such as shading device screens and temporary installations, and the relationship different parts composing the BCR Corridors to the immediate surrounding context of the QU campus.The Comfort/Complexity and Use in Building Evaluation (CUBE) studies in the DAUP-CENG at QU are part of a multi-year research strategy to generate data about movement and space use on an incremental building-by-building and year-by-year basis of the university building facilities. The long-term goal is to 1) develop a comprehensive dataset about post-occupancy use and movement flows on behalf of the QU Campus Facilities Department, and 2) deploy space syntax as a design tool in the evaluation of new building designs, design interventions in existing buildings, and campus master planning. The objective is to provide an analytical basis for promoting student performance and faculty research collaboration/innovation based on movement, casual social interaction, and healthy work environments in a world-class campus of higher education. In the CUBE[1] study, Major et al. (2019) graphically illustrated building program/use and movement/space use patterns, quantifying the relationship between movement and spatial layout, and the significance of other end-user activities such as sitting and interacting in common areas of the QU Women's Engineering Building. It also included identifying adaptive re-use of classrooms and storage spaces for laboratory and office uses, leading to a shortage of storage in the building. There was a consistent relationship (R^2=0.68, $p < 0.001$) between sitting and interacting unrelated to accessibility or metric area, i.e., the availability of seating was the dominant factor for casual encounter, mostly of students. Finally, there was a weak but consistent relationship (R^2=0.38, $p < 0.001$) between spatial layout and movement flows using space syntax, allowing for the strongly programmatic differences (classrooms vs. faculty offices) in different wings of the building (Major et al., 2019). The findings in CUBE[1] were largely consistent with previous results of space syntax research over the last 30 years for generative layouts such as office buildings, colleges, and research laboratories.

The BCR Corridors complex (Arts, Science, and Engineering Corridors) is the second case study of CUBE. Currently, the BCR Corridors primarily houses the faculty, staff, students, classrooms, research laboratories, and academic/service support facilities for much of the College of Engineering at QU. Constructed in the 1980s using a

[1] Assistant Professor of Architecture and Urban Design, Department of Architecture and Urban Planning, College of Engineering, Qatar University, PO Box 2713, Doha, State of Qatar
[2] Department of Architecture and Urban Planning, College of Engineering, Qatar University, PO Box 2713, Doha, State of Qatar
[3] Conceptually, enabling *ad infinitum* expansion in the future.

modular design concept by Egyptian architect Kamal El-Kafrawi, the BCR Corridors complex is the most iconic building on the campus, even incorporated in the university's official logo.[4] It formed a critical component of the original campus masterplan by Kamal El-Kafrawi in consultation with Ove Arup & Partners and United Nations Educational, Scientific and Cultural Organization (UNESCO) in a planning and construction phase from 1973-1985. Today, QU is home to over 9,000 students (excluding Foundation Studies) and over 1,100 faculty representing 52 nationalities. At QU, approximately 65% of students are Qatari, and more 70% are female. Completion of the first building constructed for the new QU (then Gulf University) occurred in 1982, and the BCR Corridors was part of the first set of buildings built on the campus in the early 1980s. The design was a shortlisted project for the Aga Khan Award for Architecture during the 1989 Cycle. An interconnected grid of octagonal forms grouped along ten (A-J) linear corridors composes the modular design of the BCR Corridors. Subdivision of the modules themselves provides for functional spaces in the complex. The corridors provide the primary circulation in the plan in an approximate east-west direction and access to vertical circulation in section, primarily via multiple outdoor stairwells but also interior elevators for disabled persons. Many outdoor segments of the corridors have screens serving as shading devices for people in movement through the complex. At ground level between modules, there are covered (or partially covered) courtyards serving as outdoor communal areas and providing a degree of cross-circulation in a ~north-south direction through the complex.

Methodology

The study involved two rounds of observation in February and November 2019. The hot and arid climate of the desert environment of Qatar has a direct bearing on the seasonal use of university buildings. The exterior climate during these two rounds was sunny, pleasant, and 22-27º C in February with no precipitation and sunny, warm, and 34-24º C in November with only two days of rainfall. The approximate total metric area of the BCR Corridors including outdoor communal areas floors is ~42,750 square meters with ~28,750 square meters at ground level and ~14,000 square meters at the first floor on 2.875 hectares of land. The study involved convex mapping for ~1,550 convex spaces on two floors, including the communal areas/corridors on the ground and the first floor. The occupation of space tends to be convex where everyone can see *and* be seen by everyone else. A convex space is a defined polygon in the plan where all points are visible to all other points in that space. The collection of all convex spaces in a building is the *convex map*, which tends to be an effective representation in building design and post-occupancy evaluations using space syntax. In total, this represents an average of ~27.5 square meters (or <300 square feet) per convex space in the BCR Coridors. The largest convex spaces in the BCR Corridors are fourteen (14) outdoor communal areas, all the same size and shape; ~100 square meters adjacent to the vertical stairwell access points available in all the corridors except between Corridor B and C. Outdoor communal areas of this size are available between Corridors A and B (1), C and D (1), D and E (1), E and F (2), F and G (3), G and H (3), H and I (2), and I and J (1). The smallest convex spaces are threshold spaces ~0.75 square meters in size, almost all of which (47 in total) define transitions from inside-to-outside of the modules along the corridors. A high degree of complexity and repetitive similarly in the convex map of the BCR Corridors is a significant contributor to the navigation and way-finding problems in the complex. The problem is especially acute at the ground level. The similarly broken up convexity of the outdoor communal spaces between the modules are additionally complex due to the extrusion of vertical access stairwells, built form protrusions arising out of the use of octagon-shaped modules, hardscaping/landscape features requiring deviation around in moving through the complex, and the use of vertical screens as shading devices. Because of this, there are ~50% more convex spaces at the ground level (1,045) compared to the first floor (505).

Fieldwork included counts of people entering the BCR Corridors at twenty (20) access points. Based on these 2-minute counts at the top and bottom of each hour from 7:00 am to 5:00 pm representing an entire day of entry into the building, researchers estimate that the BCR Corridors have ~14,670 users per day. In gross terms, this is 22% higher than the QU Women's Engineering Building (case study for CUBE[1]) with an estimate of ~12,000 users per day. However, the building footprint of the BCR Corridors is nearly four times larger, and the overall floor area is more than two-and-a-half times larger (+/-42,750 square meters compared to +/-16,000 square meters). It suggests that the BCR Corridors are significantly underperforming for the gross number of users by comparison, especially for a building of its size. However, the BCR Corridors are also on the male side of the campus, whereas the Women's Engineering Building is on the female side. More than 70% of QU students are female. On the that side of the campus, female students dominate the user profile (91%) of the QU Women's Engineering Building. Students represent ~48% of all users in the BCR Corridors, an overwhelming majority are male students (80%). Faculty/administrative personnel represent ~29% of all users with males again constituting a majority (82.5%) of this user type. Seven percent (7%) and sixteen percent (16.0%) of the users are security and service personnel, respectively, again are almost entirely male in both cases (95.5%). Though female students only represent ~10% of all users in the BCR Corridors, researchers did note the proportion of female students appears to increase along the perimeter of the complex in all directions. At the same time, there are fewer female students *inside* the BCR Corridors. Based on the entry counts, approximately 40% of all users enter from the western corner of the complex near a greenhouse with most of them (30%) heading southeast using the outdoor communal circulation paralleling the southwestern edge adjacent to the female campus. There is no discernible difference in the ratio between male

[4] Conceptually, enabling *ad infinitum* expansion in the future.

and female users (relative to overall QU student population demographics) entering from this direction, so it is not an effect of the multiple access points to the female campus. About 27% of all users enter the BCR Corridors centrally on the northeastern perimeter near the access points for Corridor E and F. More than half of them either use the communal areas - adjacent to the Annex wing - as a cut-through route to go to further north to the university mosque, library, or other locations nearby. Alternatively, many directly access Corridor F, which passes entirely through the complex from the male to the female campus. Similarly, another 10% use the communal areas through the Annex wing further to the northeast as a cut-through route for the same purposes. In both cases, a few people access modules of the Annex wing in the complex. Entries at the rest of the additional ten (10) access points to the BCR Corridors have evenly distributions, representing 4% or less of total entries for each, and less than 25% in gross terms.

Based on these entry/exit counts, researchers conducted movement trace observations of a typical one hundred (100) people during the first ten minutes of their visit or until reaching a destination, whichever came first. We calibrated these observations from each access point based on observed levels of use. The movement traces demonstrate a few things about movement in the BCR Corridors. First, people more heavily use the northern portions of the complex (north of Corridor E) than the southern Corridors A-D. Second, only a small part of this movement makes use of the first floor within the first 10 minutes of a visit. What does, occurs almost exclusively on the first floors of Corridor G and I. Finally, an overwhelming majority of the movement in the BCR Corridors is through-movement accessing some other part of the campus in all directions. It seems especially true along Corridor F (main pass-through route from the male to the female campus) and somewhat through Corridor B as well. This includes a noticeable level of cut-through movement in a north-south direction through the outdoor communal areas of the Annex wing as previously stated.

Analysis

Building Program and Use

A survey of building use demonstrates a high allocation of rooms for offices and laboratories, with many labs also providing open space work stations for multiple persons. There appear to be less than thirty (30) dedicated classrooms in the BCR Corridors. Allocation of almost all primary spaces in each module is for three uses (labs, offices, and classrooms) with other types (service/storage spaces, library, meeting rooms) forming secondary uses. Given the modular nature of the design, it is not easy to discern any overall pattern to building uses, either along corridors in a northeast-to-southwest direction or in a counter direction along the most extended length of the building footprint except on the first floor. On the first floor, there appears to be an alternating pattern of classrooms, offices, and labs along the longest length of each module, providing some degree of local cross-circulation from corridor to corridor via these spaces and associated hallways. It is most evident in the use of local hallways for offices and lab spaces in the most central sequence of modules from Corridor A-J on the first floor and the subdivision of small rooms accessed from these hallways. However, this occurs in other parts of the BCR Corridors complex as well, though somewhat less extensively. The survey tends to reflect the aggregated nature of the room use over time and the age of the complex itself as one of the oldest buildings on the campus. This means adaptation of rooms for specific uses when such spaces become available, wherever they might be in the layout, appears to be the determining factor. A building use strategy for the BCR Corridors could adopt a more urban-level type of distribution. For example, classrooms loaded along the most heavily used corridors such as Corridor F. It seems difficult to accomplish this without first completely emptying the complex of occupants and engaging in large-scale alterations/renovations of the entire spatial layout to develop a more logical distribution, related to the overall scale and size of its building footprint. The future opening of the new College of Engineering Building north of the QU Main Library might offer such an opportunity for developing such a new building use strategy in the BCR Corridors in concert with the large-scale renovation of the university's most iconic building. However, this will require considerable foresight and careful planning including identifying who and what university entities might occupy the BCR Corridors after completion of the new College of Engineering Building.

Non-programmed Static Space Use

Researchers conducted direct observations of non-programmed static use of 1,225 people based on the static snapshot technique for standing, sitting, and interacting people in all common spaces during an entire day from 7:00 am to 5:00 pm. Classrooms were excluded. Sitting is heavily skewed to interior common areas of the modules themselves. There is a large density of interactive sitting on the first floor at the southwestern edge of Corridor H in an open space laboratory. There is another noticeable cluster of interacting sitting and standing occurring at the southwest edge of Corridor B on the ground floor where there is a classroom immediately adjacent, which is the only classroom in this part of the complex. Otherwise, sitting distributes evenly across the entire complex in these interior common areas of the modules on both floors. There is a cluster of interactive standing (primarily male students) occurring on the first floor of Corridor H in the northern portions of the complex where there are two classrooms. This position also provides an excellent view to watch other people passing below, especially the northernmost location, where researchers observed a considerable level of cut-through movement in the communal areas at the ground level. Finally, the most significant cluster of interactive sitting and (primarily) standing in the entire complex occurs in the southwestern communal area between Corridor G and F. This 'hot spot' appears to occur due to a variety of factors associated with the spatial layout and building use. First, the primary classroom in

this part of the complex is adjacent in G122. Second, 40% of the users enter the BCR Corridors from this southwest direction. Finally, both Corridor G and F are the most extended lines of movement in the BCR Corridors from the northeast to the southwest, with Corridor F providing a direct line of movement from the male to the female campus. The combination of these formal and use factors makes this communal area between Corridor G and F a highly strategic location for causal encounters. Based on researchers' experience, this location is also one of the most critical places for navigation and way-finding disorientation. It is possible (though not directly observed) that some interactive standing in this area involves building users aiding visitors to find specific locations, especially the G122 classroom itself. It is due to two factors. First, it is disorienting to discover that Corridor G does not pass entirely through to the female campus but terminates on an elevator and enclosed courtyard, requiring people to turn back on themselves and deviate to Corridor F to complete a trip to the female campus. Second, the temporary installation of a large-scale engine in the center of the last module of Corridor F blocks the view to the doors providing access to the female campus. It initially makes users uncertain whether they will have to deviate again to continue to the female campus. The way-finding confusion occurs in the communal space before crossing the threshold into the last module, where the most intense observed levels of interactive sitting and (especially) standing occurs in the entire complex.

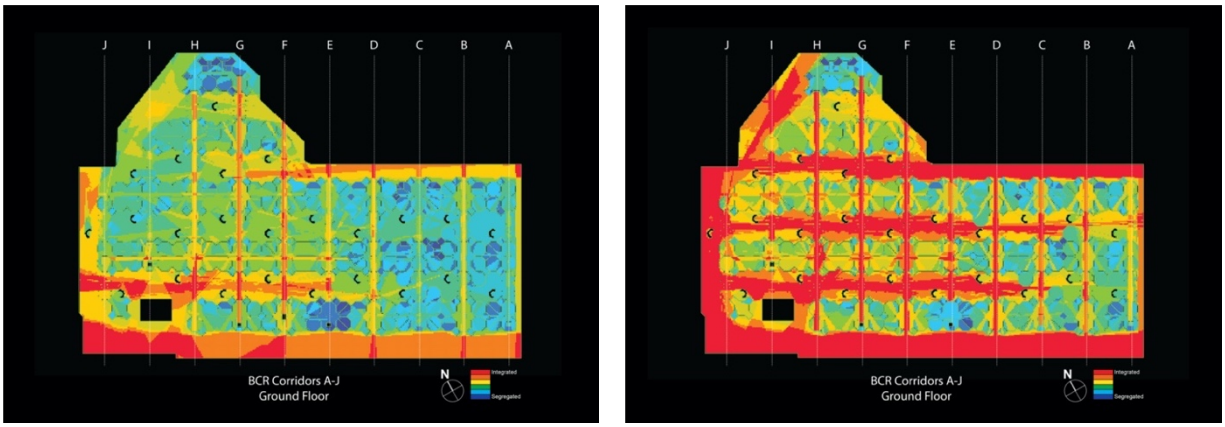

Figure 1. Visibility graph analysis (VGA) of integration (radius=n) set to a common range on the ground floor of the BCR Corridors for (left) existing and (right) proposed with the removal of all shading screen devices and temporary installations (Source: QUST-2-CENG-2019-12).

Space Syntax Modeling of Ground Level at the BCR Corridors

For this study, researchers conducted extensive computer modeling of the spatial layout in the plan of both floors in the BCR Corridors complex using space syntax representations including 1) auto-generation of 'all line' axial analysis; and, 2) visibility graph analysis. In this brief paper, we concentrate on the second. It involves defining a grid over the plan of the complex, in this case approximately 0.28 m^2 or the typical personal space of a normal human being. The computer draws the 360˚ visual field from each grid element, and measure the configurational relationship of every visual field to all other visual fields in the complex in terms of integration (radius=n) (Turner et al., 2001). Modeling of the ground floor of the BCR Corridors as 1) existing and 2) proposed with the removal of all shading device screens and temporary installations offering impediments to movement and sight occurred in the study. Analysis of the existing spatial layout on the ground floor of the BCR Corridors demonstrates the importance of Corridor F and G for circulation from the northeast-to-southwest. It also shows the effect of the elevator/termination point in Corridor G, and temporary installation in Corridor F. Both prevent lines of sight from penetrating completely through the BCR Corridors from the male to the female campus. The lines of sight along Corridor E are the only ones to directly access the perimeter of the complex on the female side of the campus. However, this line of sight is less strategically important than those in Corridors F and E due to the overall shape of the building footprint and the uses/spaces available in the Annex wing. Analysis of the existing layout also highlights the importance of the outdoor perimeter spaces. First, on the male side of the campus in the northeast. Second, those in the southwest through the outdoor communal areas associated with Corridors E-I. As previously shown in the entry counts, more than 70% of all entries to the BCR Corridors occur in these two locations. By comparison, all internal and outdoor spaces associated with Corridor A-D are highly segregated in the complex, with only the line of movement passing through Corridor D from one edge of the complex to the other being of moderate value. Visibility analysis of the proposed layout on the ground floor of the BCR Corridors with the shading screen devices and temporary installations removed and set to a standard range of values demonstrates dramatically the benefits of cosmetic changes on the spatial layout of the building complex. It generates are a series of highly-integrated northwest-to-southeast visual fields. They pass through all outdoor communal areas as well as the perimeter spaces on both the male and female campus. More importantly, the cross-circulation provided in all corridors become highly integrated with constructing a much more straightforward and easily understood grid structure in the layout. The internal spaces of Corridors A-D remain segregated. The proposed changes introduce a significant degree of integration in both the circulation spaces of the corridors and outdoor areas. Maximum integration increases from 7.45 to 9.16 (+23%). In contrast, maximum segregation only increases from 1.96 to 2.19 (+12%), indicating the simplifying the layout introduces more differentiation between spaces, which can help to assist in navigation and way-finding for end-users.

Discussion

This brief paper only summarizes the amount of data collected and space syntax modeling of the BCR Corridors. Researchers will continue to mine the data and modeling for more detailed information over the next year, perhaps even longer, to develop further research. Based on this study, we made the following design recommendations:

- Removal of all vertical shading screen devices in the complex.
- Removal of all temporary installations, especially the engine in Corridor F.
- Adoption of a more comprehensive building/room use strategy in the BCR Corridors when vacated by the current occupants upon opening the new College of Engineering Building involving loading of the most heavily-used spaces (classrooms and services including any retail outlets such as cafes and coffee shops) along Corridors F and (possibly) E. It might also include loading quieter spaces such as offices, library spaces, and laboratories in internal spaces of Corridors A-D in the more segregated locations of the complex.
- Opening additional access to the female campus at the end of Corridor G with a security desk at the new entry point with simultaneous closure of the security gate in the outdoor space north of Corridor G due to its repetitive nature. An additional access point in Corridor G will enable the creation of a strongly-integrated, dual-axis with Corridor F from one perimeter of the complex to the other in a northeast-to-southwest direction.
- Adopting a new signage system in the BCR Corridors, changing from the alphabet-based signage and room numbering to a color-coded version, i.e., Green Corridor, Red Corridor, Blue Corridor, Blue 122, Green 112, etc. Subtle painting of common elements in the corridors as well as the use of color-coded signage could supplement this color-coded signage system.

Conclusion

Constructed in the 1980s using a modular design concept by Egyptian architect Kamal El-Kafrawi, the BCR Corridors at QU is the most iconic building on the campus. However, the BCR Corridors are also notorious for presenting way-finding difficulties for end-users. These navigation problems derive from the repetitive similarity of individual parts in the modular design; stairwells, screens, and temporary installations creating impediments to user readability and visibility; and, the relationship to the immediate surrounding context of the QU campus. Faculty and student researchers at QU conducted a post-occupancy evaluation (PoE) of the BCR Corridors in 2019. The PoE study included 1) direct observations of movement flows including entry counts at the building perimeter and static occupation of space (i.e., sitting, standing, and interacting) in common areas, 2) extensive room use and photographic surveys, and 3) computer modeling of the spatial layout in the building using space syntax. The study demonstrated it was possible to: 1) better understand the observed patterns of movement and space use especially with reference to the widely-known problems for navigation and way-finding in the BCR Corridors; and, 2) develop design alteration proposals (some cosmetic, others substantial) to enable easier use of the building complex.

Acknowledgements

This research was supported by an internal grant of Qatar University (Grant ID: QUST-2-CENG-2019-12). Heba O. Tannous, Research Associate in the DAUP-CENG at QU assisted compiling the results of the ARCT 420 student observations included in this paper. Students on the ARCT 420 Environment-Behavior Studies course during the Spring 2019 semester in the Department of Architecture and Urban Planning, College of Engineering at Qatar University conducted several of the observations in this research. These students are Fatima R. AL-Ashraf, Muneera Y. Al-Hail, Maha M. Al-Kaabi, Noof R. Al-Marri, Noor R. Al-Mohannadi, Aljaze R. Al-Naimi, Noora H. Al-Nassor, Lulwa A. Al-Noaimi, Moza A. Al-Obaidan, Fatima F. Alawadi, Reem M. Ali, Radwa A. Aljack, Alanoud A. Almotawa and Rowaida M. Elnahhas.

Bibliography

Aga Khan Award for Architecture. (1992) Qatar University Project Summary. Edited by the Aga Khan Award for Architecture. Geneva: Aga Khan Award for Architecture. Accessed: 24 December 2019: https://archnet.org/sites/288/publications/620.

El-Wakil, A.W. (1992b) *Qatar University Drawings*. Courtesy of Architect (submitted to the Aga Khan Award for Architecture). Accessed: 24 December 2019: https://archnet.org/sites/288/publications/624.

El-Wakil, A.W. (1992a) *Photographs of Qatar University*. Courtesy of Architect (submitted to the Aga Khan Award for Architecture), 1992. Accessed: 24 December 2019: https://archnet.org/sites/288/publications/623.

Hanson, J. (1998) *Decoding Homes and Houses*. Cambridge: Cambridge University Press.

Hillier, B. (1996) *Space is the Machine: A Configurational Theory of Architecture*. Cambridge: Cambridge University Press.

Hillier, B., Major, M.D., Desyllas, J., Karimi, K., Campos, B., Stonor, T. (1995) *Tate Gallery, Millbank: A Study of the Existing Layout and New Masterplan Proposal*. University College London: Unit for Architectural Studies Report, 31 pp.

Hillier, B. and Penn, A. (1991) Visible Colleges: Structure and randomness in the place of discovery. *Science in Context*, 4 (1) pp. 23-50.

Hiller, B., Hanson, J., Graham, H. (1987) "Ideas are in Things: An Application of Space Syntax Method to Discovering Housing Genotypes," *Environment and Planning D: Planning and Design*, 14: 363–385.

Hillier, B. and Hanson, J. (1984) *The Social Logic of Space*. Cambridge: Cambridge University Press.

Khosla, R. (1992) *Qatar University On-site Review Report* (Edited by Aga Khan Award for Architecture). Geneva: Aga Khan Award for Architecture. Accessed: 24 December 2019: https://archnet.org/sites/288/publications/619.

Major, M.D., Indraganti, M., Ahmed, A.M., Tannous, H.O., Al-Marri, A., Al-Noami, L., Al-Obaidan, M. (2019) "Comfort and Use in Building Evaluation: Information Modelling and post-occupancy in the built environment," *12th International Space Syntax Symposium Proceedings*. Beijing, China: Beijing Jiao Tong University, 8-13 July 2019, 283:1-14.

Major, M.D. (2018) *The Syntax of City Space: American Urban Grids* (with Foreword by Ruth Conroy Dalton). New York/London: Routledge Books/Taylor & Francis Group, ISBN-10: 1138301566, ISBN-13: 978-1138301566.

Sailer K. Koutsolampros, P., Austwick, M., Varoudis, T., Hudson-Smith A. (2016). "Measuring Interaction in Workplaces," *Architecture and Interaction: Human Computer Interaction in Space and Place*. New York/London: Springer International Publishing.

Turner, A., Doxa, M., O'Sullivan, D., Penn, A. (2001) From Isovists to Visibility Graphs: A Methodology for the Analysis of Architectural Space. *Environment and Planning B: Planning and Design*, 28(1): 103–121.

Acetylene as an Alternative Fuel for IC Engines- Production Methodology and Performance Tests

[1*] Sri Sathya Sai S V, [2] Rahul Ranganath, [3] Shane Shaju, [4] Ajay J Nayar
[1,2,3] PES University, Dept. of Mechanical Engineering, 100 ft Ring Rd, BSK-3rd Stage, Bengaluru, 560085, India
[4] PES University, Former Faculty, Dept. of Mechanical Engineering, 100 ft Ring Rd, BSK-3rd Stage, Bengaluru, 560085, India

* E-mails: sathyasai2339@gmail.com; rahulranganath18@gmail.com; shaneshaju@gmail.com; ajayjnair@gmail.com

Abstract
The prime objective of this research work is twofold, which would ultimately ascertain Acetylene gas as a viable alternative fuel in the place of conventional fossil fuels. The first part is the production of acetylene gas at different experimental conditions in order to determine the most favorable yield conditions. The method appertaining to the generation of acetylene from the heat emanating reaction between water and calcium carbide is adopted, taking into account its simplistic and expedient nature. Several trials were conducted by varying the type of water (normal, salt and distilled) used in the reaction and also, at different temperatures. Analyzing the trend of the production curves, the optimal yield was substantiated. The other important part of the research work was subjecting acetylene to various performance tests in an internal combustion engine, testing its compatibility to be used as a fuel. These tests were conducted on a 1.1 kW rated Greaves MK 12/2 HSPP engine. This engine was coupled to an alternator and various performance parameters, such as brake power and rotational speed were attained by varying the electrical loads at periodic intervals. These studies were performed on gasoline and kerosene as well, for comparison purposes. It was noted that that the rotational speed of the engine running on acetylene was around 23% higher than the speed with gasoline, at maximum electrical load of 1000W. Brake power, which follows a similar trend, was found to be greater with acetylene as the primary fuel. Theoretical prediction of indicated power by making use of calculated adiabatic indices leads to the calculation of frictional power. Notable increases in thermal efficiency by 8.4% and 12.4% favored acetylene over gasoline and kerosene respectively. An extensive study was thus accomplished and acetylene is advocated to help bridge the gap between conventional IC engines and hybrid-electric engines.

Keywords: Alternative fuel, acetylene, water, calcium carbide, rotational speed, brake power, indicated power, frictional power, thermal efficiency.

I. Introduction

Fuels undeniably hold a fundamental role in all kinds of industries. They aid in the production of energy which helps in the progress of a country economically. Ever since the Industrial Revolution, fossil fuels hold ardent roles in every industry. They have a major drawback associated with them which is the release of harmful pollutants like Nitrogen Oxides (NO_X) and Sulphur Oxides (SO_X). These pollutants end up playing a detrimental role in the onset of environmental degradation. Fossil fuels are also non-renewable, taking millions of years to form. If not preserved, they would become extinct sooner rather than later. Unreliability due to constant fluctuation in the fossil fuel market calls for the need for a clean and environmentally benign alternative fuel which can ensure the smooth and efficient working of engines. Gaseous fuels have added advantages over their liquid and solid counterparts, which releases a minimal amount of ash and soot after combustion. They also burn with fewer particulates and have fewer mineral impurities associated with them. One such excellent gaseous alternative fuel is Acetylene gas. Acetylene gas has numerous properties that would benefit us immensely. It is non-toxic in nature, odorless and burns easily as indicated by its relatively low heating value (Francis, W., & Peters, M. C., 1980). Producing acetylene is an expedient process and is relatively simple. One of the most feasible process of producing acetylene gas is by the heat liberating chemical reaction between calcium carbide and water in a stoichiometric ratio (Wulff, Joseph, et al., 2000), which was incorporated in our research work. Agricultural and automobile industries would benefit highly from making use of a pollution-free and economical fuel.

II. Methodology

(i) Production of Acetylene:

The exothermic reaction between calcium carbide and water in a stoichiometric ratio is as follows:

$$CaC_2 + 2H_2O \rightarrow C_2H_2\,(g) + Ca(OH)_2 \quad (1)$$

Theoretically, from one gram of calcium carbide (CaC_2) and a stoichiometric amount of water, we obtain 384 milliliters of acetylene gas (from Ideal Gas Equation, PV=nRT). Experimentally, numerical estimation of the volume of acetylene formed was achieved by incorporating the water-displacement method. The quantities of calcium carbide and water were predetermined. Tests were carried out by varying the temperature of water reacting with calcium carbide. It was then determined that the optimal yield of acetylene was at a room temperature of 26.7°C.

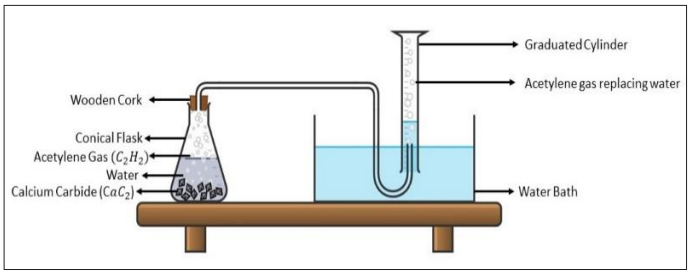

Fig.1. Production of acetylene gas using water-displacement method

Experiments were then conducted by varying the type of water used. Calcium carbide was made to react with normal tap water, distilled water and finally saltwater. Here, the maximum amount of acetylene was found to be generated with normal tap water. It was thereby experimentally ascertained that the optimal yield of acetylene gas was with normal tap water, at an average temperature of around 26°C. The results are tabulated below:

Table 1. Amount(s) of acetylene produced with different types of water at room temperature

Type of water	Amt. of Calcium Carbide (g)	Volume of water (mL)	Volume of Acetylene (mL)
Normal	*1*	*5*	*335*
Distilled	*1*	*5*	*270*
Salt	*1*	*5*	*235*

By juxtaposing the theoretical calculation with the experimental data obtained for normal tap water, it can be concluded that the difference between the theoretical value and the practical yield is approximately 50 mL.

(ii) Performance analysis of an IC engine running on acetylene gas:
Tests were conducted by running an IC engine on acetylene gas, whose performance parameters were compared with those of gasoline and kerosene. The engine which was made use of was the Greaves MK 12/2 HSPP, which had a power rating of 1.1 kW, a speed rating of 3000 RPM and HP of 1.5/1.95. A suitable 2 kW and 3000-3200 RPM rated alternator was coupled to the output shaft of the engine. An alternator was chosen over a mechanical dynamometer as it gives dynamic and fast responses with accurate readings. Suitable electrical loads were applied on the engine and the voltage and current for each iteration (40W to 1000W) was noted by using a voltmeter and an ammeter which in turn was used to calculate the brake power of the engine using $\mathrm{B.P} = \frac{\mathrm{V}\times\mathrm{I}}{\eta_{\mathrm{alternator}}\times 1000}$ kW (Colin R. Ferguson & Allan T. Kirkpatrick, 2016). A non-contact type tachometer was also used to measure the rotational speed of the engine.

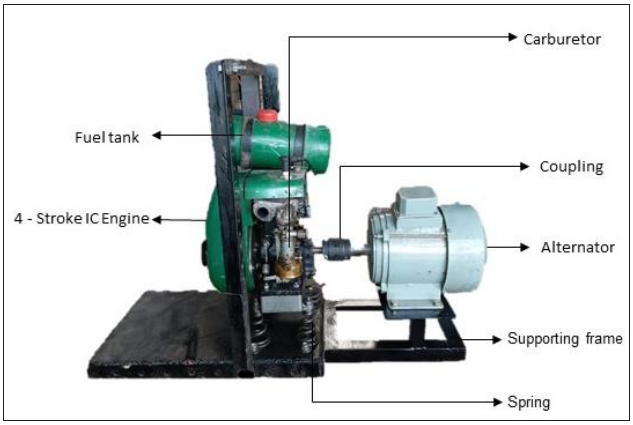

Fig.2. Greaves MK 12/2 HSPP Engine – Alternator Test Rig used for experimentation

III. Analysis

The most vital performance parameters of any engine are brake power, indicated power, frictional power, thermal efficiency, and the rotational speed (Richard Stone, 1999). As the rotational speed and brake power were computed experimentally, all the other parameters had to be calculated theoretically. To do so, P-V diagrams were plotted for all three fuels and the salient points of the Otto cycles (Torii, S., Yano, T., & Yukio, T., 1991) were obtained directly by making use of the isentropic relations in terms of the adiabatic indices. An important mention to be made here is

that of the role of adiabatic indices (Yunus A. Cengel & Michael A. Boles, 2015). The adiabatic index, γ (Sharma, P. K., Kuinkel, H., Shrestha, P., & Poudel, S., 2012) of a gas is the ratio of heat capacity at constant pressure (C_P) to heat capacity at constant volume (C_V). These adiabatic indices were manually calculated by using the stoichiometric combustion equation (Mishra, D., 2010) in which the values of C_P and C_V for all compounds of the fuels were calibrated individually. The resulting P-V diagram provided the values of work done, using which the respective mean effective pressures were calculated. The availability of brake power and indicated power eased the calculation of the frictional power (Ganesan. V., 2007).

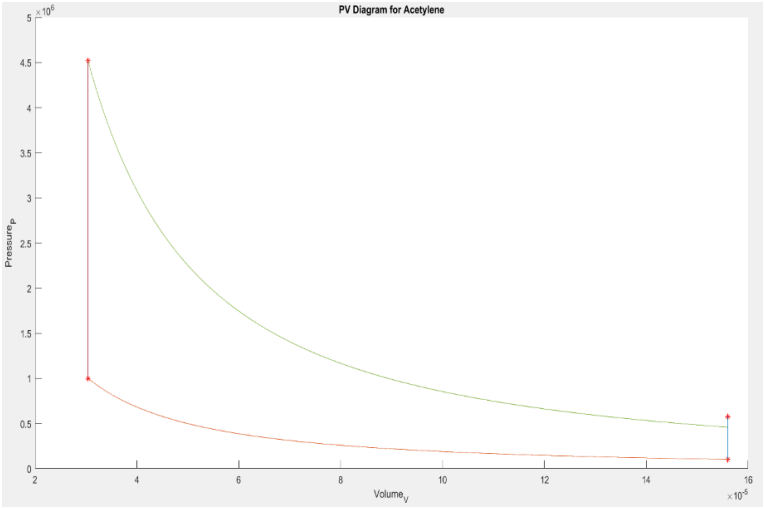

Fig. 3. Otto Cycle for Acetylene gas plotted using theoretical adiabatic indices

The thermal efficiency corresponding to each of the three fuels was also inferred from the respective Otto cycles. Thermal efficiency is obtained from the equation $\eta_{thermal} = \frac{W_N}{q_{2-3}} = 1 - \frac{T_4 - T_1}{T_3 - T_2}$ (Turns, S. R., 2012). The important features from the P-V diagram are emphasized in the table below:

Table 2. Pressure and Temperature values at salient points from the Otto cycle for Acetylene gas

Location	1	2	3	4
Temperature (K)	*300*	*577.12*	*2607.57*	*1749.50*
Pressure (MPa)	*0.101325*	*1.005*	*4.5207*	*0.5909*

IV. Results and discussions

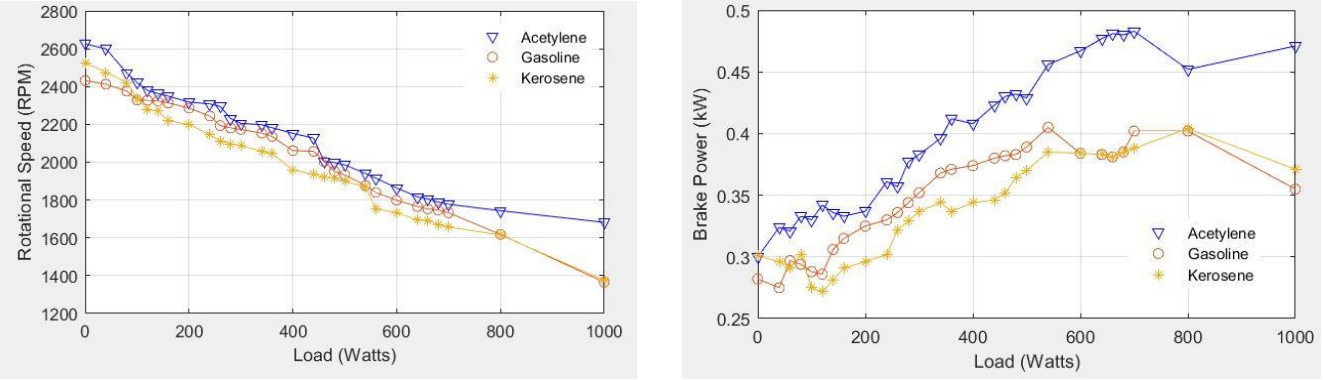

Fig. 4a and 4b. Rotational speed v/s Load and Brake Power v/s Load

At the applied maximum load of 1000 W, the speed of acetylene was found to be 1682 RPM. Speeds of gasoline and kerosene were 1365 RPM and 1375 RPM respectively. It can be noted that acetylene has a speed which is 23.2% and 22.3% higher than the other fuels respectively. This in itself proves a major point regarding acetylene as a viable alternative, as higher speed indicates greater power. This can be confirmed by referring to the graph (Fig.4b) which shows the variation in brake power. The brake power of acetylene was 0.471 kW, which is 32.6%

greater than that of gasoline (0.355 kW) and 26.95% greater than that of kerosene (0.371 kW). At the same loading conditions, acetylene produces a higher power output with greater running speeds. Similar trends were observed for indicated power as well. The thermal efficiency of acetylene worked out to be 30.84% which was significantly higher than gasoline (28.449%) and kerosene (27.45%). The percentage increase in thermal efficiency between acetylene and gasoline turned out to be 8.4%, while that between acetylene and kerosene was 12.34%. This leap advocates the fact that acetylene is a strong contender in the race for alternative fuels. Another important aspect to be noted while considering an alternative fuel is the cost factor. Acetylene gas excels at this front as well, as its production is relatively inexpensive when compared to fossil fuels. Economical fuels are preferred to be used in automobiles. We are well aware of the fact that as the commercially available fuels are in increasing demand, their cost would also experience a gradual rise. In India, on an average, one liter of gasoline costs around INR 77. Kerosene, although cheaper than gasoline, is a bit expensive as well. Acetylene, on the other hand, is a very economical fuel. One kilogram of CaC_2 costs around INR 75 commercially. When it reacts with an optimal amount of water, we obtain around 300-350 liters of acetylene. From these statistics, by employing acetylene as a daily driver, we would approximately pay 95% lesser than what we pay for one liter of gasoline, which is a stupendous feat by itself.

V. Conclusions

In this work, the fundamental idea of acetylene as a viable alternative fuel was validated with various theoretical and experimental data. It was hence promoted to be a worthy replacement over fossil fuels. The reaction between calcium carbide and water at different operating conditions was investigated. One of the conclusions was that the optimal production of acetylene gas was obtained from normal tap water at 26.7°C (room temperature) showing the ease by which it can be produced. Various performance tests were conducted on an IC engine by choosing acetylene as the primary fuel and comparing it with the conventional fossil fuels. A couple of performance plots were generated in order to substantiate that it can be a strong contender in the race for sustainable sources of energy. There are multiple alternatives to generate power such as solar energy, electricity, fuel cells, hydrogen fuel, biogas, etc., which would render internal combustion engines completely obsolete in the years to come. Using an alternative such as acetylene could help bridge the large gap during this inevitable transition. Storage and transportation of acetylene gas would fall under the scope of future research.

Acknowledgments

Before all else, we would like to express our gratitude and appreciation towards our mentor and co-author, Mr. Ajay Nayar who guided us wholeheartedly throughout the entirety of this research work. Special thanks to Dr. Rex Joseph, Dept. of Electrical Engineering, who encouraged us through all the qualms of the project work and provided invaluable suggestions for the engine-alternator setup. We are also grateful to our co-guide, Mrs. Meghana Athadkar for constantly supporting us through the course of this work. We would finally like to thank the management of PES University for their constant support.

References

Ferguson, C. R., & Kirkpartrick, A. T. (2016). “Internal Combustion Engines: Applied Thermosciences (3rd ed.).” John Wiley & Sons Ltd., Sussex, United Kingdom

Francis, W., & Peters, M. C. (1980). “Fuel and Fuel Technology (2nd ed.).”

Ganesan. V. (2007). “Internal Combustion Engine (3rd ed.).” Singapore: McGraw Hill Book Company.

Mishra, D (2010). “Fundamentals of Combustion.”

Richard Stone (1999). “Introduction to Internal Combustion Engines.” Macmillan Press Ltd., London, United Kingdom.

Sharma, P. K., Kuinkel, H., Shrestha, P., & Poudel, S. (2012). “Use of Acetylene as an Alternative Fuel in IC Engines.” Rentech Symposium Compendium, V1.

Torii S., Yano T. & Yukio T. (1991). “Adiabatic Flame Temperature and Specific Heat of Combustion Gases.” Repository.

Turns, S. R. (2012). “An Introduction to Combustion: Concepts and Applications.” New York: McGraw-Hill.

Wulff, Joseph, et al. (2000). “Internal Combustion System Using Acetylene Fuel - Go-Tec.” FPO IP Research & Communities, Patent Number- 6076487.

Yunus A. Cengel & Michael A. Boles (2015). “Thermodynamics: An Engineering Approach (8th ed.).” McGraw-Hill Education, New York, United States of America.

Study of Methane Enrichment in a Biogas Fuelled HCCI Engine

[1]Feroskhan M, [2*]Saleel Ismail, [1]Panchal Shreyash Hemant

[1]School of Mechanical and Building Sciences, VIT Chennai, Tamilnadu, India
[2]Department of Mechanical Engineering, NIT Calicut, Kerala, India

* E-mail: saleel@nitc.ac.in

Abstract

Biogas is one of the promising alternative fuels for IC engines. However, the presence of CO_2 in biogas reduces its calorific value and ignitability. Removal of CO_2 from biogas is called methane enrichment. In this study, a conventional single cylinder CI engine is modified for HCCI operation. Biogas is used as the primary fuel. It is premixed with air in the intake manifold and inducted into the cylinder. DEE is used as the secondary fuel to initiate auto-ignition. It is injected at the inlet port and manifold and injection timing and duration are varied using an electronic control module. Performance and emission characteristics such as brake thermal efficiency, equivalence ratio, HC, CO, NO_x and smoke emissions are compared for operation with raw biogas (50% methane) and methane enriched biogas (100% methane) for various biogas flow rates and engine torques. Methane enrichment improves brake thermal efficiency, HC and CO emissions. Ultra-low NO_x and smoke emissions can be obtained using raw biogas as well as methane enriched biogas. The maximum improvement in brake thermal efficiency is observed at high biogas flow rate. 12% improvement in brake thermal efficiency is observed while using a biogas flow rate of 10 lpm.

Keywords: Methane enrichment, HCCI, DEE, Smoke, NO_x and Biogas.

I. Introduction

Internal Combustion engines are conventionally operated on crude oil-derived fuels such as gasoline and diesel. Against the background of depletion of petroleum deposits, today there is a paradigm shift towards alternative fuels in order to meet the energy demands of the modern world. Researchers in the energy field are coming up with different ways to use renewable alternative fuels in conventional engines (Kumar et al., 2019; Rosha et al., 2019). Ever-stringent emission norms regulating NO_x and CO emissions and environmental concerns also prompt researchers to use alternative fuels (Algayyim et al., 2019). Rising fuel cost is another motivating factor. Additionally, renewable energy resources are more evenly distributed geographically compared to fossil fuels and hence hold the potential to be secure energy sources in near future (Khoiyangbam et al., 2011). In summary, alternative fuels have various advantages over conventional fuels such as faster combustion, very less greenhouse gas emissions as well as carbon residue, ease of production and greater sustainability to provide long term economic benefits(Feroskhan, 2017). So globally, there is a pressing need of finding sustainable solutions by synthesizing alternative fuels. (Linzenich et al., 2019).

One such alternative fuel which is now widely used is biogas. It can be produced easily from urban and rural bio-waste, oil seeds etc. by anaerobic digestion or using algae (Tippayawong and Thanompongchart, 2010). Anaerobic digestion is one of the best methods to produce biogas as it is pollution-free and minimizes the release of foul odor and harmful pathogenic bacteria. Biogas can be used as a fuel for both CI and SI engines (Mohamed Ibrahim et al., 2015; Porpatham et al., 2012). In CI engines, it is mostly used in the dual-fuel mode. A conventional diesel engine can be readily converted to dual-fuel configuration by connecting a gas blender to its intake manifold. The dual-fuel engines can work without engine modifications and also can consume a wide range of gaseous fuels. In this mode, a pilot fuel (a small amount of diesel) is injected after the compression of the charge, which consists of a mixture if biogas and air, causing ignition (Swami Nathan et al., 2010). The main disadvantage of dual-fuel engines is that the HC and CO emissions are very high (Barik and Murugan, 2014). In addition to that, as biogas contains nearly 40% CO_2 (rest 60% being methane) the thermal efficiency is quite low.. Biogas can be directly substituted as an alternative fuel in SI engines, but there are considerable problems of low thermal efficiency and high HC and CO emissions due to the presence of CO_2 in the fuel.

To tackle some of these problems, now-a-days a new alternative engine combustion concept called Homogeneous Charge Compression Ignition (HCCI) is utilized. HCCI engines have the ability to achieve high thermal efficiency (Sudheesh and Mallikarjuna, 2010). The combustion process in HCCI involves auto-ignition of lean air-fuel mixtures by compression. Auto-ignition occurs at several locations simultaneously. Due to this, the combustion temperatures are low - thus NO_x production is minimal. In an HCCI engine, charge dilution is done to ensure controlled burning rates and thus limit pressure rise. There are a few drawbacks of using HCCI, e.g. it leads to greater knock at higher rates of combustion. NO_x and smoke emissions are virtually absent, although HC and CO emissions remain high. Also, HCCI has a limited range of operating conditions.

In this study, a conventional single cylinder CI engine is modified for HCCI operation. Biogas is used as the primary fuel. It is premixed with air in the intake manifold and inducted into the cylinder. Diethyl Ether (DEE) is used as the secondary fuel to initiate auto-ignition. It can be injected either at the inlet port or in the manifold. As

the presence of CO_2 limits the use of biogas in engines, the effectiveness of its removal (termed methane enrichment) in improving the engine performance and emissions merits investigation. Performance and emission characteristics such as brake thermal efficiency, equivalence ratio, HC, CO, NO_x and smoke emissions are compared for operation with raw biogas (50% methane) and methane enriched biogas (100% methane) for various biogas flow rates and engine torques.

II. Experimental Setup and Procedure

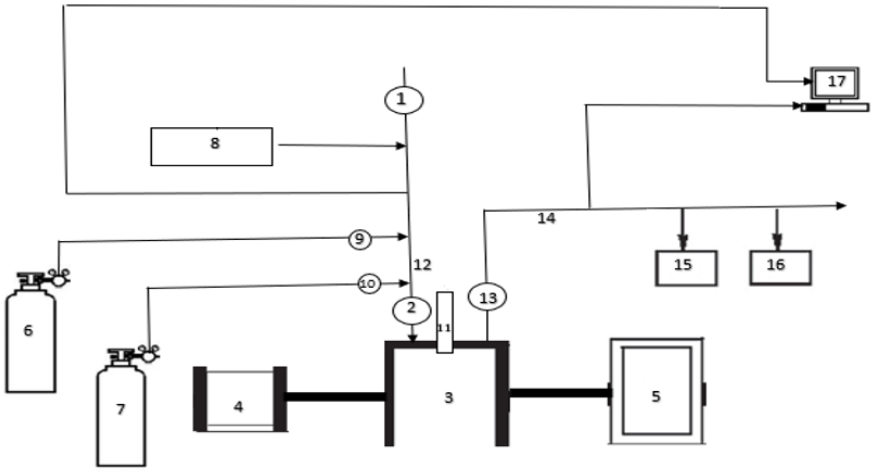

1-Manifold injection 2-Port injection 3-Engine 4- Starter motor 5- Eddy current dynamometer 6- CH_4 cylinder 7- CO_2 cylinder 8-DEE tank 9,10-Inlet manifold gas injection 11-Diesel injector (deactivated) 12- Intake manifold 13-Exhaust gas temperature sensor 14-Exhaust manifold 15- AVL smoke analyzer 16-AVL gaseous emission analyzer 17-Monitoring system.

Fig. 1: Experimental setup

Fig. 1 shows the schematic diagram of the experimental setup used. Experiments were conducted on a naturally aspirated, single cylinder, four stroke, water cooled CI engine which is modified to operate on the HCCI mode. Table 1 shows the engine specifications. A starter motor is coupled with engine which is then directly connected to the eddy current dynamometer. Methane and CO_2 are stored in separate cylinders and their flows are regulated by pressure regulators. The gas streams are fed via individual fuel lines into the engine intake manifold where they get mixed. DEE, used as the ignition improver, can be injected at (1) intake manifold or at (2) intake port. Exhaust gas samples are fed to smoke and gas emission analyzers.

Table 1: Engine specifications

Parameter	Value
Engine	Kirloskar AV1-XL
Engine speed	1900 rpm
Bore	87.5 mm
Stroke	80 mm
Cubic capacity	481 cc
Peak pressure	73.6 bar
Number & arrangement of cylinders	1-Vertical
Working cycle	4-stroke
Combustion principle	HCCI
Compression ratio	17:1
Maximum power	5.97 kW
Maximum torque	25 Nm

III. Results and discussions

The effects of the following parameters are compared the subsequent discussion:
a) Flow rate of biogas – this is expressed as the sum of methane (Q_{CH4}) and CO_2 (Q_{CO2}) flow rates. e.g. 10 + 10 represents the combination of 10 litre/min of methane and 10 litre/min of CO_2, resulting in a net biogas flow rate of 20 litre/min.

b) Methane enrichment – e.g. 10 + 10 represents raw biogas with 50% methane fraction and 10 + 0 represents methane enriched biogas with 100% methane fraction, i.e. with CO_2 completely removed.
c) Location of DEE injection – port vs. manifold.

III.a. Brake thermal efficiency

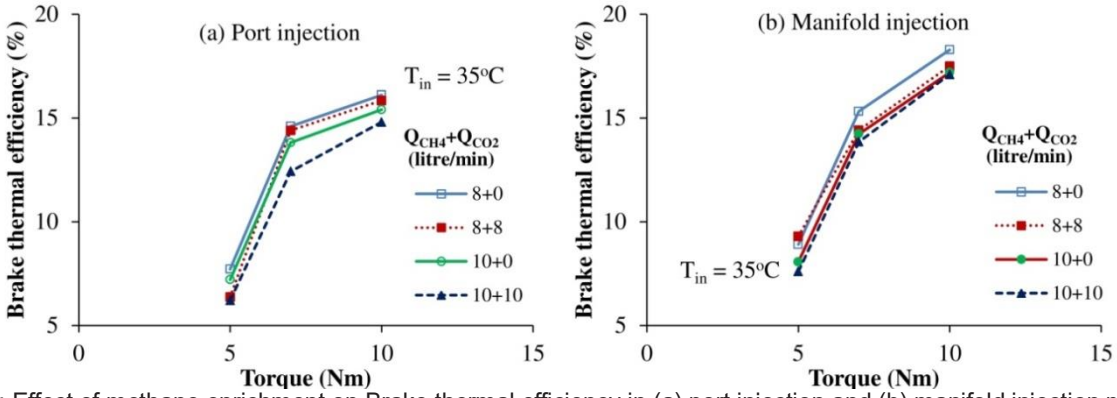

Fig. 2: Effect of methane enrichment on Brake thermal efficiency in (a) port injection and (b) manifold injection method

Fig. 2 shows that efficiency increases slightly with methane enrichment due to the removal of inert gas CO_2 which improves combustion and reduces diesel consumption. Efficiency drops with increase in biogas flow rate as more air gets displaced, some fuel remains unutilized and combustion deteriorates. Manifold injection shows better efficiency compared to port injection method due to better homogeneity.

III.b. Overall equivalence ratio

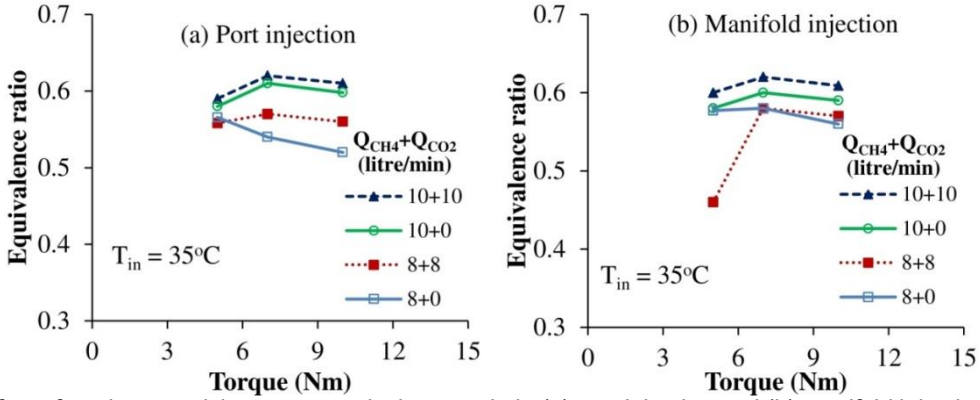

Fig. 3: Effect of methane enrichment on equivalence ratio in (a) port injection and (b) manifold injection method

Fig. 3 depicts the variations of equivalence ratio. Methane enrichment enhances air intake and reduces fuel consumption, resulting in low equivalence ratio. Increasing biogas flow rate has the opposite effect.

III.c. HC emissions

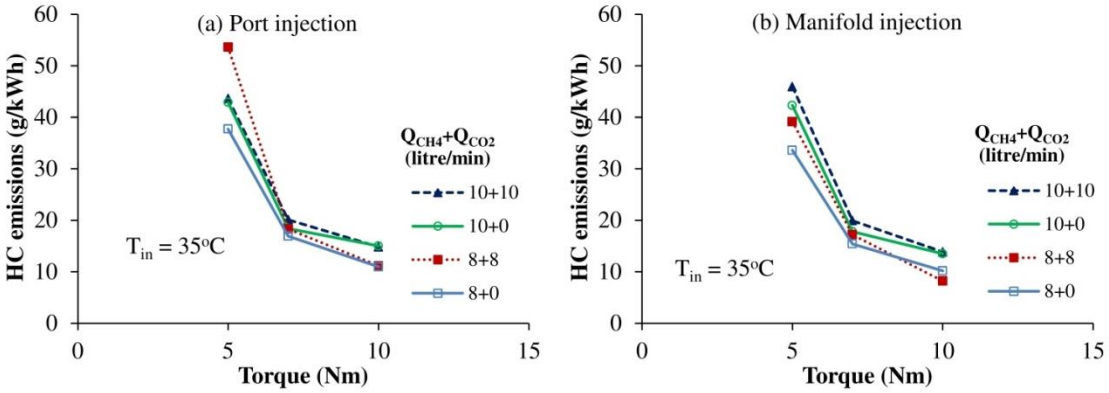

Fig. 4: Effect of methane enrichment on HC emissions in (a) port injection and (b) manifold injection method

Fig. 4 shows that methane enrichment provides lower HC emissions due to reduced fuel consumption and more complete combustion. Increasing biogas flow rate has the opposite effect. 10% of improvement in HC emissions is

observed with manifold injection compared to port injection owing to improved mixture homogeneity.

III.d. CO emissions

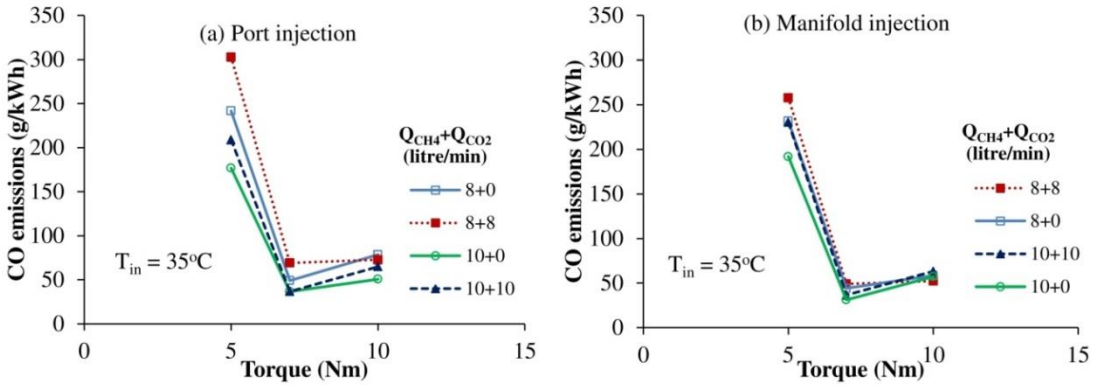

Fig. 5: Effect of methane enrichment on CO emissions in (a) port injection and (b) manifold injection method

Fig. 5 shows that methane enrichment generally helps in mitigating CO emissions by up to 17%. With higher biogas flow rates, a large quantity of the supplied fuel remains unburned owing to insufficient air. This causes more HC emissions (see Fig. 4), but lower CO in general. The effect of DEE injection location is not significant.

III.e. NO_x emissions

HCCI operation is characterized by low temperature combustion. NO_x emissions were close to zero in most of the cases by virtue of the suppression of the thermal NO_x formation mechanism..

III.f. Smoke emissions

Ultra-low smoke emission is observed due to the homogenous nature of the biogas-air mixture.

IV. Conclusion

This study shows that careful choice of the intake parameters such as biogas flow rate and methane fraction can effectively control various performance indices of the HCCI engine. Methane enrichment improves brake thermal efficiency, HC and CO emissions. Ultra-low NO_x and smoke emissions can be obtained using raw biogas as well as methane enriched biogas. The maximum improvement in brake thermal efficiency is observed at high biogas flow rate.

References

Algayyim, S.J.M., Wandel, A.P., Yusaf, T., Al-Lwayzy, S., 2019. Butanol-acetone mixture blended with cottonseed biodiesel: Spray characteristics evolution, combustion characteristics, engine performance and emission. Proc. Combust. Inst. 37, 4729–4739. doi:10.1016/j.proci.2018.08.035

Barik, D., Murugan, S., 2014. Investigation on combustion performance and emission characteristics of a DI (direct injection) diesel engine fueled with biogas-diesel in dual fuel mode. Energy 72, 760–771. doi:10.1016/j.energy.2014.05.106

Feroskhan, M.S.I., 2017. A review on the purification and use of biogas in compression ignition engines. Int. J. Automot. Mech. Eng. 14, 4383–4400. doi:https://doi.org/10.15282/ijame.14.3.2017.1.0348

Khoiyangbam, R.S., Gupta, N., Kumar, S., 2011. Biogas Technology: towards sustainable development. The Energy and Resources Institute (TERI).

Kumar, A.N., Kishore, P.S., Raju, K.B., Kasianantham, N., Bragadeshwaran, A., 2019. Engine parameter optimization of palm oil biodiesel as alternate fuel in CI engine. Environ. Sci. Pollut. Res. 26, 6652–6676. doi:10.1007/s11356-018-04084-z

Linzenich, A., Arning, K., Bongartz, D., Mitsos, A., Ziefle, M., 2019. What fuels the adoption of alternative fuels? Examining preferences of German car drivers for fuel innovations. Appl. Energy 249, 222–236. doi:10.1016/j.apenergy.2019.04.041

Mohamed Ibrahim, M., Varuna Narasimhan, J., Ramesh, A., 2015. Comparison of the predominantly premixed charge compression ignition and the dual fuel modes of operation with biogas and diesel as fuels. Energy 89, 990–1000. doi:10.1016/j.energy.2015.06.033

Porpatham, E., Ramesh, A., Nagalingam, B., 2012. Effect of compression ratio on the performance and combustion of a biogas fuelled spark ignition engine. Fuel 95, 247–256. doi:DOI 10.1016/j.fuel.2011.10.059

Rosha, P., Mohapatra, S.K., Mahla, S.K., Cho, H.M., Chauhan, B.S., Dhir, A., 2019. Effect of compression ratio on combustion, performance, and emission characteristics of compression ignition engine fueled with palm (B20)biodiesel blend. Energy 178, 676–684. doi:10.1016/j.energy.2019.04.185

Sudheesh, K., Mallikarjuna, J.M., 2010. Diethyl ether as an ignition improver for biogas homogeneous charge compression ignition (HCCI) operation - An experimental investigation. Energy 35, 3614–3622. doi:10.1016/j.energy.2010.04.052

Swami Nathan, S., Mallikarjuna, J.M., Ramesh, a., 2010. An experimental study of the biogas-diesel HCCI mode of engine operation. Energy Convers. Manag. 51, 1347–1353. doi:10.1016/j.enconman.2009.09.008

Tippayawong, N., Thanompongchart, P., 2010. Biogas quality upgrade by simultaneous removal of CO_2 and H_2S in a packed column reactor. Energy 35, 4531–4535. doi:10.1016/j.energy.2010.04.014

An overview of the Solar Potential in Qatar: From Theory to Practice

[1,2*]Abdulsalam Alkholidi, [3]Mohammed Alshaghdari [4]Habib Hamam

[1]Electrical Engineering Department, Faculty of Engineering, Sana'a University, Yemen

[2]Canadian Institute of Technology (CIT), Tirana, Albania

[3] College of Engineering, Qatar University, Doha, Qatar

[4]Faculty of Engineering, Moncton University, NB, Canada, E1A 3E9

* E-mails: abdulsalam.alkholidi@gmail.com

Abstract:

The Arabian Gulf countries is considered as one of the richest areas in the world in terms of solar irradiation. We could find rapid economic growth in Qatar in the past few decades, and Qatar has shown significant growth in the renewable energy sector in the past five years. The present work is a review of several scientific papers and reports related to solar energy potential in Qatar as well as ongoing and future projects. Recently, several research works have been taken-up to develop this important renewable energy sector. The objective of this paper is to illustrate some of published research in solar energy, what have been achieved so far practically and focus on the most important areas of utilization of solar energy, development of short-term plan to integrate them in the reality, namely: solar distillation, solar cooling, solar pumping, solar furnaces, solar cooking, e-vehicles and generation of solar energy to support Bedouin backpackers in the GCC countries. The investment in the manufactring of high efficiency solar cells in the state is one of the goals of this study. This study recommends fabricating PV cells and modules in Qatar due to that all necessary conditions are available using for example Singapore approach in the localization of technology.

Keywords: renewable energy, solar energy, PV technology, solar energy projects of Qatar, solar powered vehicles.

1. Introduction

The Arabian Peninsula is one of the richest areas in the world in terms of solar irradiation, and the average sunshine duration in Qatar is approximately 9.5 hours per day. Therefore, the use of solar energy is absolutly prudent, keeping the future in mind. In fact, the remarkable growth in utilisation of photovoltaic systems in the GCC countries has increased dramatically in the last one decade. In Qatar, there are several plans to develop this solar energy sector, and domestication of this technology. One of the efforts is the integrated PV manufacturing plant [1]. In Doha industrial zone, Qatar Solar Energy has officialy opened a 300MW PV module production plant, and is considered as the first integrated PV manufacturing plant in the Middle East and North Africa (MENA) area. One of the potential areas where in the solar technology could be utilized is powering the vehicles - the demand for solar powered electric vehicles has increased significantly. Solar-powered cars have spread over many countries, including China, and demand is expected to increase in many other countries in the coming years. Solar vehciles depend on a solar array that uses PV cells to convert sunlight irradiation into electricity. Therefore, it is wise to establish a Research Center to develop and manufacture electric vehicles in this region. Another area is "solar-powered irrigation system", which is usually used in the desert and away from the electrical grid systems. This is an automatic irrigation system, where the irrigation pump is operated using solar energy. It becomes tedious to manually operate the irrigation system and keep monitoring the water level. Hence, the system uses solar power by using photo-voltaic cells instead of conventional electricity. It may be noted that all the resources such as capital investment, required climate and high quality raw materials are available for initiating such projects.

Geographical Potential: The solar irradiation incident on the fraction of the earth's surface is named as the geographical potential and is suitable for the development of solar facilities. The geographical potential could be determined by the following equation:

$$G_i = 10^3 \times I_i \times h \times A_{a.i} \quad (1)$$

Where G_i(kWh/y) is the geographical potential of cell i, I_i(W/m^2) is the time-averaged irradiance in cell *i* (extracted from the NASA irradiation data), *h (h/y)* is the number of hours in a year, and $A_{a.i}$ (km^2) is the available area for PV installation in cell i. We have adapted this equation to use it for solar irradiance dataset presented in this paper as follows:

$$G_i = 365 \times R_i \times A_{a.i} \quad (2)$$

Where R_i(kWh/m^2 per day) is the daily irradiance in cell *i*, while 365 denotes the number days in a year. We note that the variables in Eq. (2) are known except the area and we can calculate it by two different ways centralized and decentralized systems. For more details of geographical potential, readers may refer to the following reference [2].

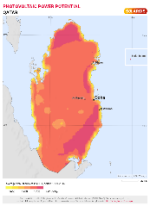

Fig. 1. Photovoltaic power potential – Qatar [3].

Figure 1 presents the solar resource maps of Qatar according to SOLARGIS [4]. We note that the average annual sum of PVOUT starts from 1999 to 2016 is showing tolerance from 1650 to 1750 kwh/kwp.

2. Literature Review

Several scientific, technical and annual reports are published in the field of solar energy in Qatar and in other GCC countries as indicated in [5-15]. Rapid population growth in the Middle East and North Africa (MENA) region is accompanied by rapid development in the socio. As a result, required infrastructure and the necessary services should be expanded, where more than half of the population is under 24 years of age. Accordingly, the electricity demand is increasing day by day [5]. According to the world energy scenarios-2019, the energy demand growth in the MENA region is among the highest in the world after China and India. Consequently, the renewable energy sector will grow significantly, especially in some countries such as Morocco and the United Arab Emirates.

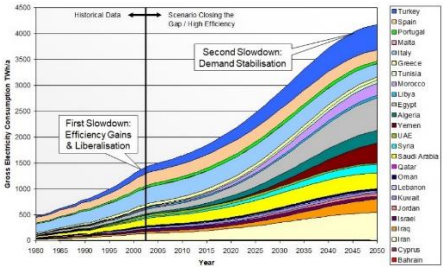

Fig 2. Social sustainability challenge: growing electricity demand in MENA [6].

The future of solar energy in the GCC region will be prosperous for many reasons, most importantly political stability, economic growth as well as the growing demand for energy. According to the Institute of Thermodynamics Technique, located in Germany the social sustainability challenge for growing electricity demand in MENA is presented in Figure. 2.

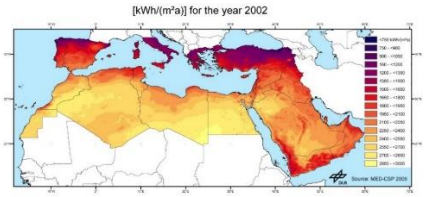

Fig. 3. Annual sum of Direct Normal Irradiation (DNI) [kWh/m^{2}a)] for the year 2002 in the MENA [7].

Figure 3 shows the annual sum of DNI [kWh/m^{2}a)] for the year 2002 in the MENA.

In the past few decades, the economic situation of the GCC countries has been dominated by oil, gas and petroleum industries. During this period, these countries have begun to develop solar energy sector and make optimal use of renewable energy resources. Due to significant growth in Qatar since the last one decade, it has become one of the fastest developing power markets in the region. This study is based on the review of several articles available on the public domain, and deals with solar energy, its optimal utilization, and share PV systems in the power generation sector and prospects for expanding its use as a long-term plan.

Perez-Astudillo and Bachoura [8] from Qatar Environment and Energy Research Institute published their article on DNI, GHI and DHI based on solar irradiation measurements of Doha. Three sorts of irradiations were measured and analyzed in this work for a period of six months from December 2012 to May 2013: Direct Normal Irradiation (DNI), Global Horizontal Irradiation (GHI) and Diffuse Horizontal Irradiation (DHI). The averages of DNI, GHI and DHI are 200.4, 225.2 and 94.7 W/m2, respectively, with the highest monthly averages found in February (DNI=234.9 W/m2), May (GHI=302 W/m2) and April (DHI=129.9 W/m2). The days with the highest averages of DNI, GHI and DHI were all found in May, with 407.5, 355.2 and 193.8 W/m2, respectively.

$$\mathbf{GHI} = \mathrm{DHI} + \mathrm{DIF} \qquad (3)$$

$$\mathbf{DNI} = \mathrm{DHI} / \sin\alpha \qquad (4)$$

Where (DIF) is a diffuse irradiation

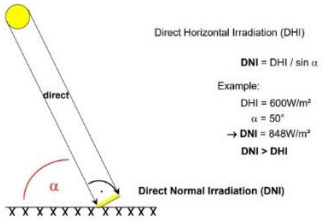

Fig. 4. Direct Normal Irradiation (DNI).

Figure 4 illustrates the direct normal irradiation (DNI). We note that the direct normal irradiation is the sum of diffuse horizontal irradiation (DHI) and diffuse irradiation as indicated in the Eqs. 3&4 [9].

Luis Martín-Pomares et al. analyzed the long- term PV systems power production potential in Qatar as demonstrated in [10] to evaluate the new horizons of solar production. They used kriging techniques data gathered

from satellite maps of monthly/yearly averages of global horizontal and direct normal irradiations. This study is based on 11 years of hourly solar radiation data obtained from satellite sensor and computed using an improved version of Heliosat-3 model. The satellite data has been compared with ground radiometric measurements.

In a recently published article [11] by Islam Safak Bayram the impact of Electricity Vehicle Charging (PEV) on power generation is illustrated for the state of Qatar as a case study under various penetration and charging schedule scenarios by using a stochastic simulation model. The worst-case scenario is evaluated using 5-min electricity load profiles and peak-consumption day is chosen where the results showed that uncontrolled charging would exceed grid generation capacity. The study concluded that to exploit the solar-PEV, charging is recommended. This approach is validated by analyzing the actual load and global horizontal irradiance measurements. This recommendation is important because the region is rich in solar radiation throughout the year, except a few months during winter. This study also indicates that charging PEVs before 11 am would reduce peak consumption. By this method, PEVs can be used to reduce associated costs and flatten the “duck curves”.

The study conducted by Zeineb Abdmouleh et al [12] tackled the motivation and willingness to invest in renewable energy (RE) installation in Qatar. The investigation found that only 74.64% of the respondents are motivated to sell electricity back to the grid in the future if they have the opportunity. However, the cost of RE can be one of the main barriers for its competitiveness to conventional sources of energy. Survey results presented in this study also indicate that only 42.25% of the respondents have interest only when the tariff of electricity coming from RE is cheaper than the current tariffs while the rest of respondents were interested about RE even when RE tariffs will be equal to current tariffs. Nowadays, renewable energy systems are becoming more and more competitive compared to finite sources. Accordingly, 78.17% of the respondents accept that RE can complement the use of fossil fuels (oil/gas) in Qatar. Study shows that the most preferred RE technologies to install at homes are: solar water heater (97.87%), solar electric panels (93.33%), day-lighting and smart systems (91.11%), solar-ready air-conditioners and smart wind turbine. We noted that the interest in PV systems compared to wind energy is justified due to high potential of solar irradiation in Qatar compared to that of wind energy and thanks to easy installation of PV systems and its noiseless nature, compared to wind energy (wind farm is a threat to birds). This study also indicated following additional limitions of using renewable energy in Qatar are:
- The expensive cost of installations
- Lack of information and awareness about the importance of using PV systems
- Unattractive and intermittent.

Nassma Mohandes et al. [13] concentrated on solar energy adaptation for residential areas in Qatar. The goal of the proposed approach is to integrate PV systems in the households thanks to reducing of PV systems technology worldwide. This study also talks about reducing the smoke pollution in the environment, introducing a carbon tax, spreading utilization of PV systems technology and innovation and development of this solar energy. This study also gives direction for expanding solar energy in the residential neighborhoods due to its cost factor as well as the elimination of subsidies and increasing the electricity tariff for the electric power sector or exemption leads to the expansion of use of PV systems. The subsequent PV adoption rates will help facilitate national electricity generation targets of 2% of PV systems by 2020 and 20% by 2030.

As stated by IRENA, the GCC region is home to excellent solar energy potential. Qatar sustainable energy target for 2020 is 200-500 MW of solar energy production. Figure 5 indicates the renewable power planned by the GCC countries. We note that the total addition is 6732 MW, and in that Qatar has a share of 700 MW [14].

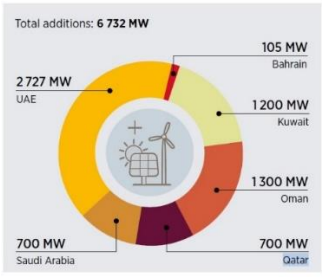

Fig. 5. Renewable power planned for GCC countries.

Table 1 shows the Utility-scale renewable energy projects in Qatar as of January 2019. We note that the solar PV technology for Al-Kharsaag solar PV project is generation of 700 MW power, while the Mesaieed Waste to Energy project produce is 38 MW.

Table 1. Utility-scale renewable energy projects in Qatar as of January 2019 [14].

Qatar	Al-Kharsaag	Solar PV	700 MW
	Mesaieed Waste to Energy	Waste to energy	38 MW

Some statistics about solar energy production in Qatar is provided in Table 2.

Table 2. Solar energy details in Qatar [14].

Installed renewables-based capacity (2017)	43 MW
Share of renewables in total installed power generation capacity (2017)	0.4%
Project pipeline as of November 2018 solar PV power by 2020, with a total of 700 MW by the early 2020s	350 MW

Indeed, over the past five years, Qatar has invested heavily in solar energy where by the end of 2018, Qatar General Electricity and Water Corporation (KAHRAMAA) launched a call for prequalification proceedings of bidders for a 500 MW solar tender. The solar tender will select a company to design, build, own, finance, operate and transfer a 500-MW solar photovoltaic (PV) plant near Al Kharsaa. KAHRAMAA will buy the output under a 25-year Power Purchase Agreement (PPA). The expected Commercial Operation Date (COD) will be in December 2020 [15]. IRENA estimated that the renewable energy capacity of Qatar is approximately 3100 MW by 2030 as demonstrated in Table 3.

Table 3. Estimated renewable energy capacity in (MW) by 2030 in Qatar, Kuwait and Oman.

Country	CSP	PV (utility scale)	PV (rooftop)	Wind	Waste to energy	Total	Source
Qatar	600	2250	150	-	100	3100	IRENA assumption
Kuwait	1000	5800	1000	200	-	8000	Based on inputs from country expert
Oman	770	2 420	990	1210	110	5500	Target of 2.6 GW by 2025, followed by 600 MW added every year to 2030
Note: CSP = concentrated solar power; PV = photovoltaic; GCC = Gulf Cooperation Council.							

3. Discussion of reviewed literature

After reviewing many scientific papers published in prestigious journals as well as many specialized reports in the field of renewable energy, we have concluded that Qatar is heading in the right way in the field of using solar energy; this is also obvious from the results of many projects Qatar that has handled in the past few years. Also, Qatar has the potential of producing/using e-vehicles, keeping further the climate change scenario. All these studies provided a logical roadmap for the present and future use of solar energy in Qatar as Qatar has enormous potential of solar radiation throughout the year. Our contribution is to focus on the localization and utilization of solar energy technology in Qatar, expand its use, spreading awareness among citizens and residents in the schools and universities and promoting the technology and its advantages in various media. In the next section we provided some ideas on how to localize solar technology in Qatar and setting the agenda of Work Breakdown Structure (WBS) of this strategic project. We also propose to take into account the Singapore experience in the localization of technology, considering the similarity of both the countries in surface area as well as population.

4. Solar energy project in Qatar from theory to practice

4.1 Defining the project

The five fundamental steps to define a PV system project are [16]:

- Defining the project scope
- Establishing project priorities
- Creating the work breakdown structure
- Integrating WBS with the Organization
- Coding the WBS for the Information System

4.2 Fabrication and development of solar energy technology scenario

Photovoltaic industry is a leading technology in the worldwide and considered as a future technology that has the huge potential to support grid systems where their costs are decreasing regularly (thanks to the development of semiconductor technology) [17-18]. Designer engineers developed a new generation of PV cells and modules with high efficiency levels and reducedng cell manufacturing cost [19]. The PV cells and other inputs are combined together to create the PV module as a sub-assembly, which is then assembled together with the balance of system (BoS) components to create the PV module with BoS [20]. In order to establish and manufacture PV technology in Qatar, we propose the following procedures:

1- Take a decision to fabricate PV cells and modules in Qatar and resettle (establish) this technology: Materials, conversion principles and devices, and processing and assembly
2- Create national laboratory for fabrication of high performance PV technology, taking into account advantage of Singapore or Chinese methods in technology resettle

3- Setting project goals
4- Define the project vision and mission
5- Prepare study feasibility of this project
6- Motivate stakeholders and government sectors to invest in this project
7- Cooperate with famous fabrication industries of this technology
8- Attract high professional experts in this field
9- Cooperate between proposed PV laboratory with academic establishments and related research centers
10- Apply:
- Short-term plan to start manufacturing of PV cells and modules and expand manufacturing processes step by step
- Long-term plan to attract investment and provide stability of policy instruments
11- Concentrate on local market needs as a first step, then
12- Fabricate competitive PV cells for local, regional and international market

Photovoltaic is the process of converting sunlight directly into electricity by using semiconducting materials that exhibit photovoltaic effect. It is a very smart process to generate environmentally-friendly green energy. PV systems have a wide range of applications - carbon emission-free, clean and silent renewable energy production, and not release any harmful air or water pollution into the environment, and endanger animal or human health [21].

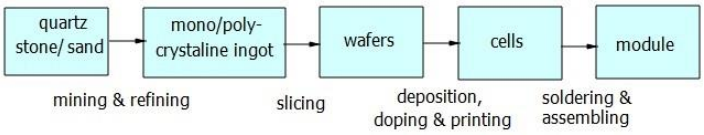

Fig. 6. Product/process chart for wafer-based solar PV technology.

A high-level product/process chart for wafer-based solar PV technology is demonstrated in Fig. 6 [22].

4.3 Proposed strategic plan to develop PV technology [23]:

- Applied scientific research: this means concentrate on specific applications of PV systems
- Improve the performance and reduce fabricated cost compared to competitive products
- Increase the efficiency by minimizing manufacturing defects and increase the reliability of fabricated PV cells and modules
- Study the PV market and minimize the market barriers

4.4 Benefit of this strategic project:

- Reduce carbon emission and keep the nature clean: it is eco-friendly
- Socio-economic benefits: economic growth
- Employment: new jobs creation
- Solar energy to enhance grid systems
- Resettle the PV technology

5. Analysis

Due to high temperature in the Arabian Peninsula, large number of imported vehicles, electricity generators as well as the emission of smoke from oil and gas production plants and its refining and dust emitted from the deserts, life will become difficult in the next few years. Therefore, it is wise to seriously consider the gradual transformation of sustainable energy, wherein all the potentials are available and the climate is ideal to use solar energy. The real purpose of using renewable energy is not only the economic aspect but the maintenance of a clean environment for the long-term plan starting from now. All studies presented in this paper are concentrated on utilization of RE, in particular, solar energy. Hence, we reviewed, studied and analyzed the obtained results and recommendations as well. As researchers in this field, we suggest that the research to be linked and funded by the industrial sector and the Central Planning Organization (CPO). The objective is to harmonize the research centers with the industrial and development sectors in the country. Accordingly, we propose to use Chinese or Singaporean approaches to localize and develop PV technology and vigorously compete in the domestic, regional and global markets. Based on inputs from local experts, it is shown that Kuwait will achieve 8000 MW power of renewable energy, mostly generated by PV (utility scale) (about 5800 MW), Oman is expected to exceed 5500 MW according to target of 2.6 GW by 2025, followed by 600 MW added every year till 2030, while the total renewable energy is expected to be 700, 25000 and 30000 MW power, respectively by Bahrain, KSA and UAE. The estimated total renewable energy capacity which will be generated by 2030 is 72300 MW. From these statistics it is apparent that the renewable energy sector will develop dramatically in the GCC countries. As a result, it will provide jobs in the field of renewable energy of all kind, where it is expected to exceed 220000 by 2030 in GCC region; Qatar's share will be around 4%. We note that this number (4%) is modest compared to that of neighboring countries. Most of these jobs will be in the field of solar power (it could reach 89% of total jobs [14]).

Recommendations:

- Persuade decision makers about the importance of renewable energy

- Develop and fabricate solar PV technology in Qatar
- Increase the efficiency of fabricated solar cell
- Improve the factors affecting the performance of PV cells
- Attract high level experts from worldwide in the field of PV technology
- Motivate researchers to improve the efficiency of solar cells for commercial purpose
- Integrate between academic establishment and research centers with PV industry
- Concentrate on high efficiency silicon solar cells
- Cooperate with leading companies in this field as well as with research centers
- Increase the growth of PV market locally and regionally.

6. Conclusion

After having carried out an extensive review of published scientific information on solar energy research related to Qatar, this study recommends the use of e-vehicle and use of PV systems in houses and streets in the next 10 years in order to reduce the carbon emission and improve the air quality and keep the nature clean. Otherwise, life will become unbearable not only in Qatar but also in the GCC countries, causing heavy pollution. This study encourages the utilization of PV technology in GCC countries as a green energy choice, confirming the cost effectiveness of the system for desert electrification. It is also illustrating the design procedure to provide a practical study to support Bedouins backpackers. We also suggest manufacturing of special solar panels, solar chargers, solar power bank that could be adapted carrying on the back of the camel to help Bedouins to use the necessary devices as cellular phones, i-pads, low consumption power TV, etc. The paper proposes to develop and accelarate using the following applications of solar energy: solar distillation, solar cooling, solar pumping, solar furnaces, solar cooking, and e-vehicles using PV systems.

References:

[1] https://www.qatarsolar-energy.com/
[2] Athina Korfiati et al. Estimation of the global solar energy potential and photovoltaic cost with the use of open data. International Journal of Sustainable Energy Planning and Management Vol. 09 2016 17-30. dx.doi.org/10.5278/ijsepm.2016.9.3.
[3] https://solargis.com/maps-and-gis-data/download/qatar.
[4] https://solargis.com.
[5] World Energy Council. World Energy Scenarios 2019, Exploring Innovation Pathways to 2040, 2019.
[6] https://www.dlr.de/tt/de/desktopdefault.aspx/tabid-2885/4422_read-53076/.
[7] https://www.dlr.de/tt/desktopdefault.aspx/tabid-2885/4422_read-16596/g.
[8] D. Perez-Astudilloa, D. Bachour. DNI, GHI and DHI ground measurements in Doha, Qatar. Elsevier, Energy Procedia 49 (2014) 2398 – 2404, 2014.
[9] Franz Trieb. Renewable Energy Resources. MBA Energy Management, Deutches ZentrumVienna, September 9-10, 2010.
[10] Luis Martín-Pomaresa et al., Analysis of the long-term solar potential for electricity generation in Qatar. Renewable and Sustainable Energy Reviews 73 (2017) 1231–1246. http://dx.doi.org/10.1016/j.rser.2017.01.125.
[11] Islam Safak Bayram. A stochastic simulation model to assess the impacts of electric eehicle charging on power generation: A case study for Qatar. Qatar Environment and Energy Research Institute, Hamad Bin Khalifa University, Doha, Qatar, IEEE, 2019.
[12] Zeineb Abdmouleh, Adel Gastli, Lazhar Ben-Brahim. Survey about public perception regarding smart grid, energy efficiency & renewable energies applications in Qatar. Renewable and Sustainable Energy Reviews 82, 168–175, http://dx.doi.org/10.1016/j.rser.2017.09.023, 2018.
[13] Nasma Mohandes, Antonio Sanfilippo, and Marwa Al Fakhri. Modeling residential adoption of solar energy in the Arabian Gulf region. Renewable Energy, https://doi.org/10.1016/j.renene.2018.07.048, ELSEVIER, 2018.
[14] IRENA, Renewable energy market analysis: GCC 20019, ISBN 978-92-9260-096-9.
[15] Tsvetomira Tsanova, Renewables Now, Solar tender for 500 MW in Qatar enters prequalification stage, May 04, 2018 8:14 CEST, https://renewablesnow.com/news/solar-tender-for-500-mw-in-qatar-enters-prequalification-stage-611345/.
[16] Erik W. Larson and Clifford F. Gray. Project management the managerial process, fifth edition, McGraw-Hill, 2011.
[17] Solar energy technologies office, U.S. Department of Energy. 2018 Portfolio.
[18] A strategic research agenda for photovoltaic solar energy technology, edition 2, 2011, European Union, 2011, ISBN 978-92-79-20172-1, doi:10.2788/15824.
[19] IRENA (2019), Future of solar photovoltaic: development, investment, technology, grid integration and socio-economic aspects (A global Energy Transformation paper), International Renewable Energy, November 2019.
[20] Z.W. Zhong, B. Song, P.E. Loh, LCAs of a polycrystalline photovoltaic module and a wind turbine. Renewable Energy 36 (2011) 2227e2237.
[21] A strategic research agenda for photovoltaic solar energy technology, edition 2, 2011, European Union, 2011, ISBN 978-92-79-20172-1, doi:10.2788/15824.
[22] Pier Stapersma, Clingendael international energy program (CIEP), Solar PV a strategic world. CIEP paper 2015-04.
[23] United States Department of Energy, Office of Energy Efficiency and Renewable Energy, 2016-2020 Strategic Plan and Implementation Framework, EERE 2016–2020 STRATEGIC PLAN.

SOLAR THERMAL VAPOR ADSORPTION EXPERIMENTAL SIMULATION SETUP – ENERGY ANALYSIS

[1*]M.Natarajan, [1]Y. Rajasekhar, [1]C.Chiranjeevi, [2]T. Srinivas
[1]Department of Thermal and Energy, Vellore Institute of Technology, Vellore.
[2]Department of Mechanical Engineering, Dr. B.R, Ambethakar National Institute of Technology, Jalendhar, Punjab, India.

* E-mails: natrajpad@gmail.com

Abstract
Solar thermal adsorption refrigeration systems use solar energy to produce refrigeration effect. This system enables us to provide air conditioning and refrigeration in remote places. Most common refrigerants used in solar adsorption refrigeration systems are water and methanol. Being noiseless, non-corrosive and environmental friendly, there is lots of research going on to increase the efficiency in order to attain performance equal to vapour compressor refrigeration system. This paper emphasize on experimental study of single stage adsorption system. This report presents the experimental investigation of a novel solar adsorption refrigeration system. The system is tested activated carbon-ethanol, in VIT campus, Vellore (12.9718° N, 79.1589° E). Simulations for irradiation and refrigerant properties are done in MATLAB software to study the operating parameters. The novel design consists of an evacuated tubular collector (ETC), which is used the adsorbent bed, and a copper tube with fins and 1 mm wide holes is inserted in ETC to facilitate the passage of the refrigerant. The experiments were carried out in the month of March, 2018. The activated carbon-ethanol system was enhanced by a (LTC) Linear Trough Concentrator and attained solar COP and SCE of 0.034 and 534.2 kJ/kg, respectively. Energy analysis of the simulated results were carried out and results are discussed.

Keywords: Vapour Adsorption, Refrigeration, Solar energy, energy analysis, Activated

I. Introduction

Solar adsorption refrigeration system is an alternative to vapour compression system. Waste energy or low grade energy (solar) is used to produce heating/cooling. The replacement of synthetic refrigerants and zero production of carbon dioxide has made this system more eco- friendly system and sustainable. Adsorption refrigeration system works on the principles of adsorption and desorption which produce cooling effect and produce adsorbate vapour respectively. Activated carbon is the most commonly used adsorbent due to high surface area, total pore volume and average pore diameter. It is formed by carbonization of coal, fossil, coconut shell and so on. It is activated chemically or by steam. The porosity of this adsorbent depends on the activation temperature and carbonization process. The specific area of activated carbon is between 500 and 1500 m2/g (Wang et al., 2009). Activated carbons are available in pellets, granular and in fiber form. (Tamainot-Telto et al., 2009) performed a thermodynamic analysis of various carbon based adsorbents to select the optimum adsorbent- refrigerant pair. Modified DunbininRadushkevich (D-R) equation is used to generate the adsorption isotherms for each sample. In this paper 26 samples of carbons, mainly coconut and coal-based type of different shape and size (monolithic, granular, compacted granular, fiber, compacted fiber, cloth, compacted cloth and powder) properties are measured experimentally. (Wang et al., 2006) investigated various combinations of adsorbent and adsorbate such as, activated carbon-methanol, activated carbon-ammonia and composite adsorbentammonia. The adsorbent is studied in both granular and consolidated form. The composite adsorbents used are a mix of activated carbon and CaCl2 at different mass ratios. It is observed that consolidate form has higher thermal conductivity compared to granular form. Composite adsorbent has improved COP, SCPv and SCP by 1.8 times, 4.7 times and 14 times respectively compared to activated carbon-methanol system. The fiber form of activated carbon has better performance due to its high adsorption capacity and thermal conductivity. (Wang et al., 1997) did a comparative study between activated carbon and activated carbon fiber. Activated carbon fiber has COP, refrigerant capacity and adsorption time, 1.1 to 1.2 times, 3 times and 1/5 to 1/10 times that of normal activated carbon, respectively. (El-Sharkawy et al., 2009) investigated experimentally the isothermal characteristics of methanol onto activated carbons Maxsorb III and Tsurumi activated charcoal. Experiments are conducted at evaporator temperatures of 5, 10 and 15 oC. The experimental isotherms obtained are then compared with the theoretical ones obtained using the Dubinin Raduskevich (D-R) equation, and showed a maximum error of 5%. It is found that Maxsorb III has adsorption capacity 1.76 times higher than activated charcoal. Comparisons using theoretical calculations show that Maxsorb III-methanol pair has upper hand among other carbonaceous adsorbent/methanol pair for both air-conditioning and ice making. (Ambarita and Kawai, 2016) did a study on different combination of adsorbent bed, which is activated carbon and activated alumina. Each sample is tested for three days in Medan city, Indonesia. The study shows that even though activated alumina has high adsorption activated carbon has more performance because desorption pressure of activated alumina is high. High pressure bed means high temperature which is not possible to attain by at plate collector. The paper concludes that 100% activated carbon gives good performance at 100 o C.

II. Experimental Procedure

The basic working principle of an solar adsorption refrigeration system are adsorption and desorption of the

adsorbate on and from the adsorbent surfaces respectively. The simple process includes two isosteric processes and two isobaric processes. Taking the system to start from the desorption stage; the adsorbent bed maintained inside the solar collector is heated up. This heating of adsorbent bed, gives the adsorbate energy which it uses to separate itself from the adsorbent bed. This vapour adsorbate is then condensed and collected. The liquid adsorbate is then send through a evaporator with the help of nozzle or orifice to decrease pressure. Now, when the adsorbent cools down to a needed temperature (usually around 2030°C), the adsorbent bed starts to adsorb the vapour in the closed system, thereby decreasing the pressure of the system. To equalize this decrease in pressure created in the system, the liquid adsorbate from the condenser tank evaporates in the evaporator, taking the latent heat from the refrigeration box. The now evaporated liquid adsorbate equalizes the pressure and vapour is again adsorbed by the adsorbent. This again creates a pressure difference in the system, thereby making more of adsorbate to evaporate taking the latent heat from the refrigeration box. The fluid present in the refrigeration box is henceforth cooled. This cycle goes on until maximum adsorption takes place and the adsorbent bed cannot adsorb anymore of the adsorbate. This happens generally in the night time. In the morning, the adsorbent bed is heated again using solar radiations directly or indirectly. The adsorbent releases the adsorbate and the later condenses in the condenser and the cycle repeats itself cooling down the fluid present in the refrigeration box.

Our project deals with direct heating of adsorbent bed and the solar collector used is an ETC with copper coating integrated with LTC and is able to provide the temperature upto 250°C. High temperatures are needed for higher desorption. The more desorption, the more space for adsorption in the next cycle.

The adsorption refrigeration system in its simplest form consists of closed container with adsorbent and adsorbate (solar collector), a condenser and an evaporator. Adsorption is the separation of substance from one phase followed by the accumulation of them on another surface. The force of interaction holds the molecules of liquid or gas to the surface of the solid. The adsorbent and the adsorbate are selected according to the working condition. The simple process includes two isosteric processes and two isobaric processes. Our setup consists of the following integrated parts:

1. ETC as absorber tube.
2. LTC as concentrator.
3. Radiator as condenser.
4. Condenser tank

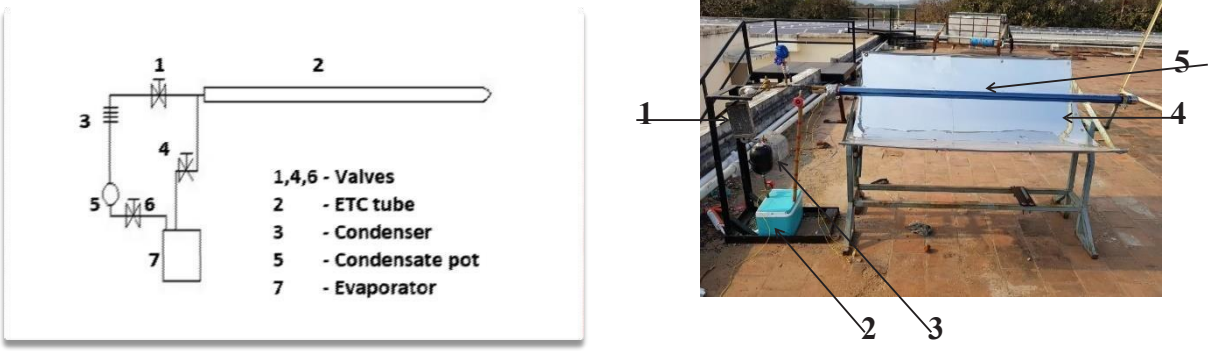

Fig. 1: Schematic diagram of solar vapour adsorption refrigeration system

Table 1. Technical Specification of Experimental set up of Solar Vapour Adsorption Refrigeration system

System	*Equipment*	*Specifications*
Radiation Absorber Tube	*Evacuated Tube Collector*	*1.8m length and copper coated.*
Concentrator	*Linear Trough Concentrator*	*1.5m x 0.9m*
Condenser	*Radiator Type*	*0.18m x 0.12m*
Ice Box	*Insulated ice box*	*6 litres capacity*
Adsorbate	*Ethanol, water*	*1.5 litre*
Adsorbent	*Activated carbon*	*1.3kg*

Closed ETC with aluminum cap and filled with Activated Carbon as adsorbent bed and ethanol used as adsorbate.
Adsorption: Cooling temperatures of water in refrigeration box and

Table 2. Experimental Readings for Adsorption on Activated Carbon (ETC with Aluminium Cap)

Time (hrs)	*Bed Temperature (°C)*	*Chilled Water Temperature (°C)*
20:00	*35*	*28*
20:30	*33*	*22*
21:00	*31.5*	*18.8*
21:30	*30.7*	*18.4*
22:00	*30*	*16.4*
22:30	*29.7*	*16.1*
23:00	*29.4*	*15.1*
23:30	*28.7*	*14.5*
00:00	*28*	*13.4*
00:30	*27.5*	*13.2*
01:00	*26.9*	*12.8*
01:30	*26.7*	*12.2*
02:00	*26.7*	*12.1*
02:30	*26.7*	*9.7*
03:00	*26.6*	*6.7*

III. Results and discussions

The following graph (Fig. 2) shows the variation of temperature with time for an empty ETC. From the graph it can be seen that the values of temperatures rise with time until 11-12 pm and stay constant for one or two hours depending on the day. After this the temperature drops down continuously. The maximum temperature reached to 376°C. This shows the potential of solar power when used with ETC enhanced with the help of LTC.

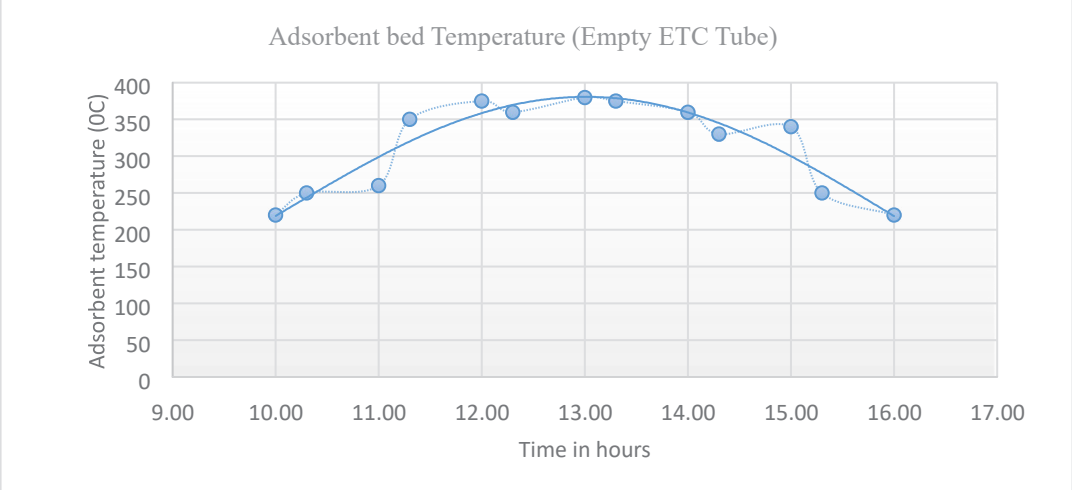

Fig. 2: Absorbent bed temperature for whole day (empty ETC tube)

The following graph (Fig. 3) shows the variation of adsorbent bed temperature with time during adsorption for activated carbon-ethanol working pair. It can be seen that bed temperature decreases very slowly with time due to less heat transfer to surrounding. The following graph (Fig. 3) shows the variation of chilling water temperature with time during adsorption period. The Minimum temperature of 6.7°C was attained by the water in the refrigeration box at 3a.m. There is a drastic drop in temperature in the initial and final cooling stages. The Coefficient of performance of our proposed activated carbon and ethanol working pair solar vapour adsorption refrigeration system is estimated as 0.034.

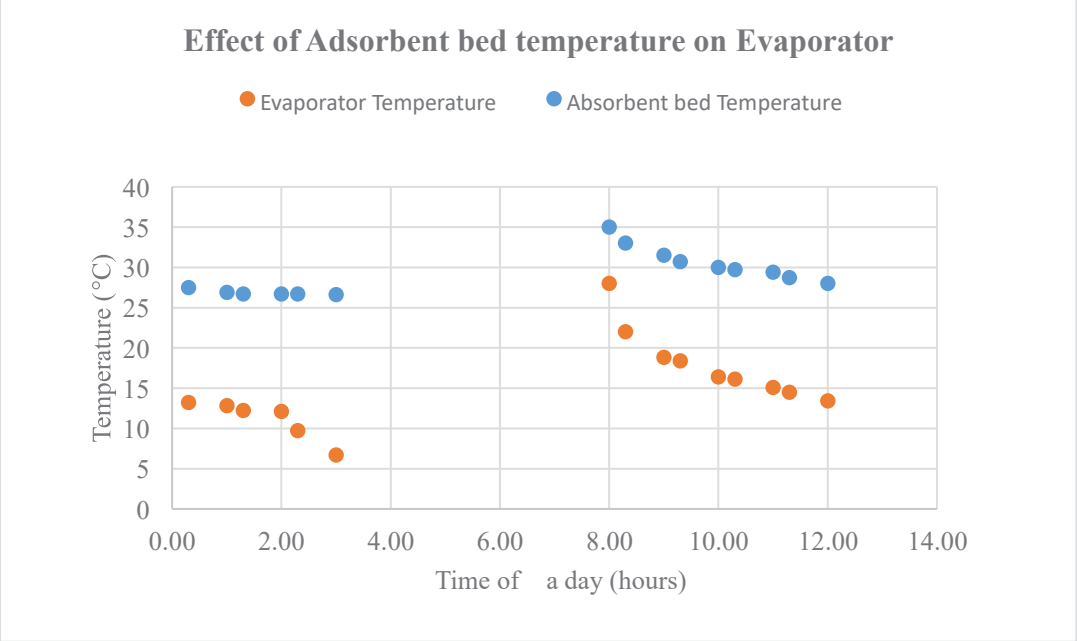

Fig. 3: Effect of Absorbent bed temperature with time of day on Evaporator temperature (ETC tube filled with activated carbon – Adsorption effects)

IV. Conclusions

The silica gel-water working pair solar adsorption refrigeration system is able to attain a Solar COP, cooling energy and SCE of 0.169, 275.88 kJ and 275.88 kJ/kg, respectively. The activated carbon-ethanol working pair solar adsorption refrigeration system is able to attain a Solar COP, cooling energy and SCE of 0.034, 534.204 kJ and 410.9 kJ/kg, respectively. The system is an alternative to conventional compressor type systems and can be used without any high grade energy like electricity. This makes it more suitable for use in remote places and also in space applications. The refrigerants (ethanol and water) used are harmless to the environment and are easily available.

Acknowledgements

We want to thank VIT University for providing us with the resources for carrying out this project. We would like to thank the solar thermal Power Engineering laboratory In-charges and CO2 Research Centre for their valuable guidelines.

References

Ambarita, H., Kawai, H., 2016. Experimental study on solar-powered adsorption refrigeration cycle with activated alumina and activated carbon as adsorbent. Case Stud. Therm. Eng. 7, 36–46. https://doi.org/10.1016/j.csite.2016.01.006

El-Sharkawy, I.I., Hassan, M., Saha, B.B., Koyama, S., Nasr, M.M., 2009. Study on adsorption of methanol onto carbon based adsorbents. Int. J. Refrig. 32, 1579–1586. https://doi.org/10.1016/j.ijrefrig.2009.06.011

Tamainot-Telto, Z., Metcalf, S.J., Critoph, R.E., Zhong, Y., Thorpe, R., 2009. Carbon–ammonia pairs for adsorption refrigeration applications: ice making, air conditioning and heat pumping. Int. J. Refrig. 32, 1212–1229. https://doi.org/10.1016/j.ijrefrig.2009.01.008

Wang, L.W., Wang, R.Z., Lu, Z.S., Chen, C.J., Wang, K., Wu, J.Y., 2006. The performance of two adsorption ice making test units using activated carbon and a carbon composite as adsorbents. Carbon N. Y. 44, 2671–2680. https://doi.org/10.1016/j.carbon.2006.04.013

Wang, L.W., Wang, R.Z., Oliveira, R.G., 2009. A review on adsorption working pairs for refrigeration. Renew. Sustain. Energy Rev. 13, 518–534. https://doi.org/10.1016/j.rser.2007.12.002

Wang, R.Z., Jia, J.P., Zhu, Y.H., Teng, Y., Wu, J.Y., Cheng, J., Wang, Q.B., 1997. Study on a new solid absorption refrigeration pair: Active carbon fiber—methanol. J. Sol. Energy Eng. Trans. ASME 119, 214–218. https://doi.org/10.1115/1.2888021

Optimal solar hybridization of a grid-connected gas turbine combined cycle power plant: a case study

[1*]Mohammad Mohamamadzadeh, [2]Mohammad Tajik Mansouri, [2]Mehdi Rahimi

[1*] Department of Mechanical and Aerospace Engineering, University of Rome "La Sapienza" Via Eudossiana, 18 00184 Rome, Italy

[2] Niroo Research Institute (NRI), Tehran, Iran

* *mohamadzadeh.mo@gmail.com*

Abstract

The world is moving toward sustainability, but it may require many years for sustainable energy systems to dominate the market. Many fossil fuel power plants are in commission right now and will be in service for decades to come. Integrating solar thermal to fossil fuel power plants can diminish emitted greenhouse gases and fuel consumption. The efficient integration of solar energy into conventional power plants plays a vital role in persuading investors and owners to provide finance on such projects. The biggest challenge facing the process of integration is the capital cost of modifications for making conventional combined cycle powerplants capable of integration. In this paper, three configurations have been proposed for adding solar thermal energy to the heat recovery steam generator (HRSG) of a gas turbine combined cycle GTCC power plant. The attempt is made to determine the best configuration of the solar cycle regarding the performance, thermodynamic efficiencies and economic indices in a way that the primary cycle faces with the least modifications and capital costs while it provides the highest cash flow and augmented power during the operation lifetime.

Keywords: First-law analysis; Exergy analysis; Economic assessment; ISCC; Optimization;

I. Introduction

Gas turbine combined cycle (GTCC) power plants are attractive in power generation as they use the residual heat of flue gas from gas turbines for generating electricity in steam turbines. In recent years integrated solar combined cycle (ISCC) systems have been offered as a method of adding solar heat to the common GTCCs. Many studies have implied the positive effect of solar integration, and some plants came into operation, the Archimede power plant in Sicily, Italy (Falchetta et al., n.d.) and Hassi R'Mel in Algeria are in service today. Moving toward the carbon-neutral economy mentioned as the primary goal of recent international and regional agreements such as Paris agreement ("Paris Agreement," n.d.) and European Union roadmap for low carbon economy by 2050 ("2050 Energy Strategy - European Commission," n.d.).

Availability at no cost and being environmentally-friendly have made solar energy known among the best alternatives for nonrenewable resources (Wei et al., 2016). However, due to the high cost of operation and the non-reliability of solar energy during some periods of the year, integration with fossil fuels has been suggested for the optimal operation of the systems (Ameri and Mohammadzadeh, 2018). An ISCC system is a combined cycle power plant with a solar parabolic trough cycle which provides auxiliary heat to the primary system. Many researchers have studied the concept, and some configurations have offered for improving performance and system efficiency (Borello et al., 2013).

Exergy analysis of power plants has been discussed in many studies in recent years (Dinçer and Rosen, 2012). Exergy analysis of the HRSG's components has carried out by Mansouri et al. (Mansouri et al., n.d.). they conducted thermodynamic analyses of the HRSG in a combined cycle power plant for finding the effect of HRSG's pressure levels on exergy efficiency. It is concluded that the increase in pressure levels has an adverse effect on exergy efficiency and increases the irreversibility of the system.

In another study (Gülen, 2015), Gülen analyzed different solar integration methods using central receivers, parabolic troughs and linear Fresnel in comprehensive second law analysis of ISCCs. He mentioned HP steam production "a clear winner" over cost and performance among other types of steam available in the system i.e. (Low pressure, intermediate pressure). Also, the parabolic trough has mentioned the most favorable option regarding its maturity and dominance in the market.

II. Research methodology

Solar cycle integrated configurations proposed for adding solar auxiliary heat to the system, to have the least capital cost of modifications some constraints have been imposed on the system.

Iran's climate has numerous advantages for utilizing solar energy. High solar irradiation and numerous sunny days are some of the mentioned climatic features. In this study, simulations and assessments have been done on the Qom combined cycle power plant in Iran. The models have been verified with the power plant's real-time data to resemble the primary system with the highest accuracy.

Three cases developed for finding the best configuration for adding the solar auxiliary heat to the HRSG. Cases one, two, and three are designed to add solar thermal energy from parabolic troughs to an auxiliary economizer, evaporator and superheater, respectively.

Due to the cost minimization approach of the study, the following constraints met by the system.

1. Turbine inlet temperature (TIT) of the steam turbine is fixed the same as primary value due to material restrictions and the necessity to redesign steam turbines. 2. The condenser has a limited capacity so that the total flow rate of the system restricted to 119 Kg/s. The main goal of adding auxiliary heat has set to transform LP steam into HP steam. 3. The gas turbines have provided the system's baseload while the solar auxiliary heat added to

boost power generation when the sunlight is available. 4. All developed cycles received an equal amount of heat from the solar cycle.

The first case (figure1), has been designed to increase the temperature of the feed water in the solar auxiliary economizer. In the proposed model, a portion of the feed water has been separated and went through the solar economizer and re-joined the main flow before entering the high-pressure evaporator (HPB).

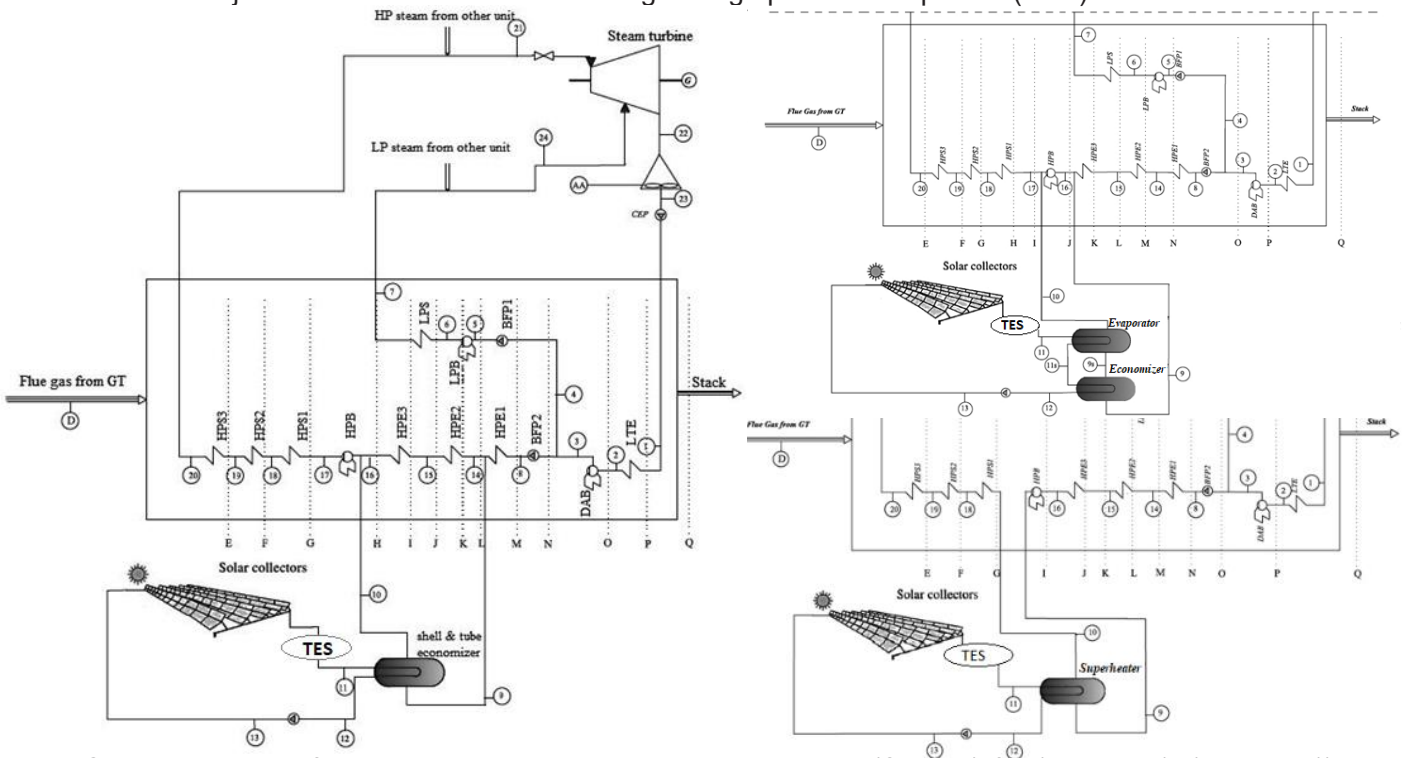

Fig. 1. Schematic diagram of the double pressure solar integrated Rankine cycle (Cases 1(left),2(right-above),3(right-below))

In the second case, the solar cycle auxiliary heat has been used in an auxiliary evaporator in which the added solar heat evaporates of a portion of feed water, subsequently, the saturated steam leaves the solar cycle and enters the HRSG's first high-pressure superheater (HPS1).

In the third case, the saturated steam flows through the solar superheater, and solar thermal heat has been used to superheat steam.

III. Thermodynamic analysis:

III.I.I First and second law analysis:

The system's energy and mass balance equations derived for every component of the system. Steady-state, Steady-flow condition assumed in evaluations, and mass flow rate and thermodynamic characteristics of the streams calculated. To find the main source of irreversibility and losses in the system,it is crucial to conduct the second law analysis on the cycle and its components. Exergy analysis includes four parts; physical, chemical, kinetic, and potential. Kinetic and potential terms can be neglected when the system does not face significant changes in speed and altitude (Akrami et al., 2018).

III.II Economic Analysis:

Table 1 illustrates the fixed parameters used in the economic assessment.

Table 1. Fixed parameters in economic analysis.

Parameter	Value	Parameter	Value
Plant economic life (years)	20	Operating hours per year (full load equivalent)	7400
Average general inflation rate (%)	4.5	The unit cost of natural gas ($/GJ-LHV)	3.97
Discount rate for NPV calculation (%)	15	The unit cost of electricity ($/MWh)	55
Date of commercial operation	2019	Fixed O&M cost ($ / kWnet)	20

The following assumptions have been made in calculations:

1. Air and gases analyzed based on the ideal-gas principles. 2. Significant enthalpy losses have been observed in collectors and exhausts. Other components' losses have been neglected in the calculations due to their minimal effect. 3. The system's dead-state condition has fixed at $P_0 = 1.01$ bar and $T_0 = 298.15$ K.

IV. Results and discussions

IV.I. Exergy analysis results

IV.II. HRSG analysis

Many studies have emphasized the high exergy destruction in the HRSG; Thus, A comprehensive evaluation has done on the HRSG for finding efficiencies, losses, heat absorption, and sources of irreversibility in the system.

Figures 2 and 3 illustrate the comparison between exergy efficiency and exergy destruction of the HRSG's

components, respectively. HRSG's total exergy destruction and total second law efficiency for each case are shown in figure 4. Note that in the calculation of the efficiencies, the absorbed heat by the solar collectors has been considered as the system input heat.

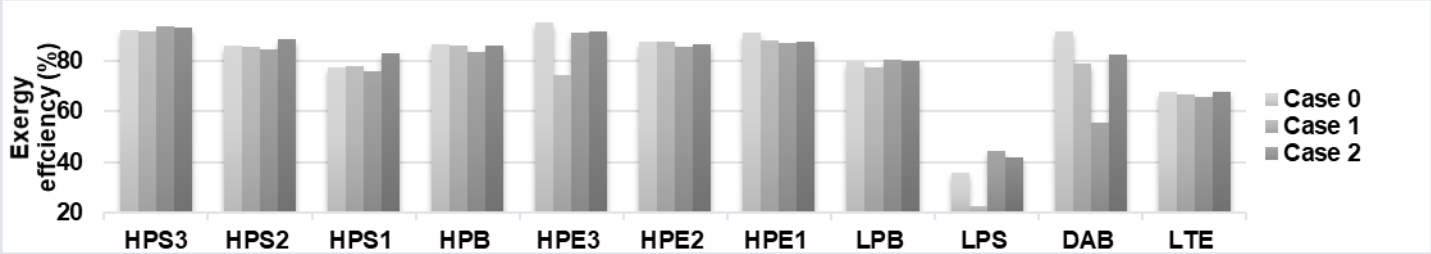

Fig. 2. Exergy efficiency for the HRSG components

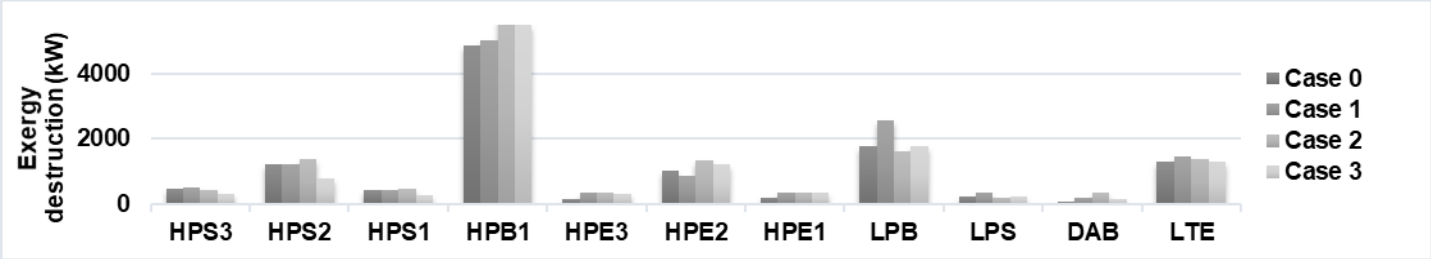

Fig. 3. Exergy destruction of the HRSG components

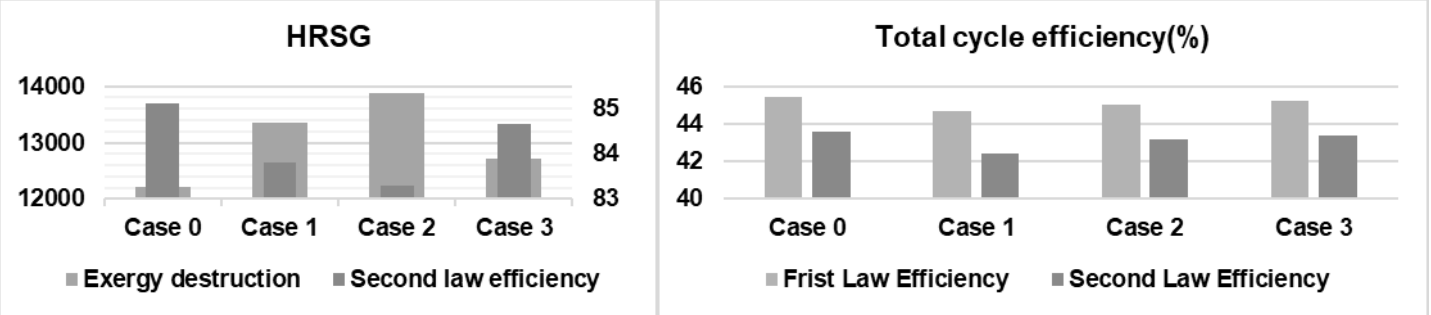

Fig. 4. Exergy destruction and Second law efficiency of the HRSG and total cycle efficiencies.

To find irreversibilities in the HRSG, the amount of absorbed heat should be calculated for each component. The amount of absorbed heat by the water/steam in the HRSG's components has shown in figure 5 for each case.

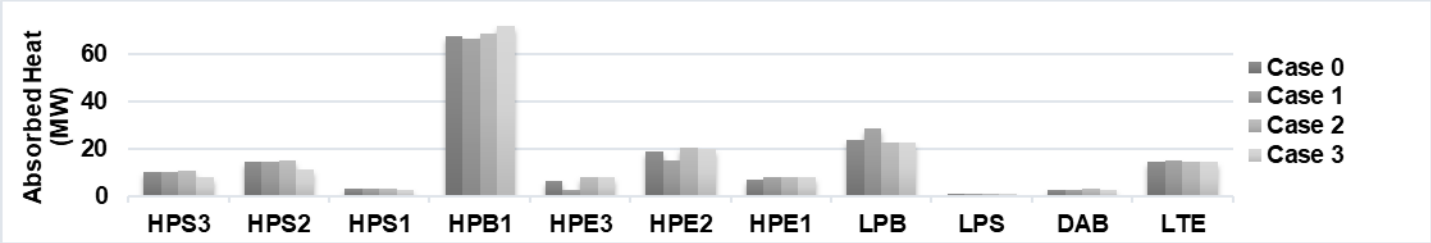

Fig. 5. Absorbed heat by the HRSG components

It is evident that the HP evaporator (HPB), and the LP evaporator (LPB) absorbed the highest flue gas heat compared to other components; therefore, the two elements have the most significant irreversibility in the HRSG. In case 1 auxiliary heat provided by the solar cycle is utilized in an economizer; therefore, a portion of the flue gas heat is conserved for the next sections, including the LP part; Consequently, the LP section received high-temperature flue gas and pinch point increased in LPB. Therefore, the LP steam generation increased. Table 2 compares the total energy and exergy parameters of cases.

Table 2. Energy and exergy parameters of the cases.

Parameter	Unit	Case 0	Case 1	Case 2	Case3
Gross power output of the plant	MW	294.682	297.344	299.49	300.86
Net electric efficiency	%	45.43	44.69	45.01	45.22
Overall exergy efficiency	%	43.55	42.43	43.16	43.37
Annual electricity exported	GWh	2324	2350	2367	2378
Annual CO2 emission	kilo tonne	1035	1035	1035	1035
Specific CO2 emission	kg/kWh	0.445	0.44	0.437	0.435
HP mass flow rate	kg/s	89	93.27	97.67	98.68
LP mass flow rate	kg/s	23	25.8	19.81	20.57
Total mass flow rate	kg/s	112.13	119.07	117.48	119.25

The same phenomenon happens in case 3 for the HPB, where the flue gas with a higher temperature passes HPB

and increases pinch point; Consequently, the mass flow rate of HP steam increases. Higher thermodynamic efficiencies and better performance are calculated for this case.

IV.IV. Economic results

The economic analysis was performed on the cycle, considering fixed-parameters given in Table 1, the results of the economic analysis are shown in Table 3.

Table 3. Outcomes of the economic analysis.

CCPP configuration	Total investment (USD*1000)	Specific investment (USD per kW)	Levelized cost of electricity (USD/kWh)	Years of payback of equity (years)	Net present value (USD)
Case 1	282,682.4	974	0.0466	3.93	95,513,000
Case 2	282,495.5	964.5	0.0461	3.786	102,281,100
Case 3	281,654.9	959.6	0.046	3.6	103,422,400

It is evident in Table 3; Among solar configurations, case 3 has shown better values in the evaluated indices.

V. Conclusions

In this study, a comprehensive thermodynamic analysis carried out for finding the best configuration of the solar cycle in a grid-connected combined cycle. To have a minimum modification in the primary system, a set of constraints met by the system. Qom combined cycle power plant in the dry and hot region of Iran has been simulated. Thermodynamic and exergy analyses have carried out for each configuration, and the best option has been chosen regarding the overall performance, efficiencies, and economic indices.

Solar auxiliary heat in cases one, two, and three have been utilized in an auxiliary economizer, evaporator, and superheater, respectively.

The results show by adding solar cycle auxiliary heat closer to the high-pressure superheaters of the HRSG, flue gas heat will be conserved for the later sections such as HP evaporator with the most absorbed heat. Pinch point increases and the HP evaporator recovers more heat. Consequently, the mass flow rate of HP steam increases. Higher efficiencies and a better overall performance observed in case 3.

The solar thermal heat augmentation results in a 2.7 MW, 4.8 MW, and 6.18 MW boost in the net power for cases one, two, and three, respectively. Exergy analysis showed that cases one, two, and three have an exergy efficiency of 42.43%, 43.16%, and 43.37%, respectively. Therefore, case three has the highest efficiency and the best performance among other proposed configurations. Also, the same case stands ahead in economic assessment

References

2050 Energy Strategy - European Commission [WWW Document], n.d. URL https://ec.europa.eu/energy/en/topics/energy-strategy-and-energy-union/2050-energy-strategy (accessed 10.13.18).

Akrami, E., Khazaee, I., Gholami, A., 2018. Comprehensive analysis of a multi-generation energy system by using an energy-exergy methodology for hot water, cooling, power and hydrogen production. Appl. Therm. Eng. 129, 995–1001. https://doi.org/10.1016/J.APPLTHERMALENG.2017.10.095

Ameri, M., Mohammadzadeh, M., 2018. Thermodynamic, thermoeconomic and life cycle assessment of a novel integrated solar combined cycle (ISCC) power plant. Sustain. Energy Technol. Assessments 27. https://doi.org/10.1016/j.seta.2018.04.011

Borello, D., Corsini, A., Rispoli, F., Tortora, E., Borello, D., Corsini, A., Rispoli, F., Tortora, E., 2013. A Co-Powered Biomass and Concentrated Solar Power Rankine Cycle Concept for Small Size Combined Heat and Power Generation. Energies 6, 1478–1496. https://doi.org/10.3390/en6031478

Dinçer, I., Rosen, M. (Marc A.., 2012. EXERGY : Energy, Environment and Sustainable Development. Elsevier Science.

Falchetta, M., Mazzei, D., Crescenzi, T., SolarPACES, L.M.-P. of the, 2009, undefined, n.d. Design of the Archimede 5 MW molten salt parabolic trough solar plant.

Gülen, S.C., 2015. Second law analysis of integrated solar combined cycle power plants. J. Eng. Gas Turbines Power 137. https://doi.org/10.1115/1.4028741

Mansouri, M., Ahmadi, P., … A.K.-E.C. and, 2012, undefined, n.d. Exergetic and economic evaluation of the effect of HRSG configurations on the performance of combined cycle power plants. Elsevier.

Paris Agreement [WWW Document], n.d. . United Nations Treaty Collect. URL https://treaties.un.org/Pages/ViewDetails.aspx?src=TREATY&mtdsg_no=XXVII-7-d&chapter=27&lang=_en&clang=_en (accessed 10.13.18).

Wei, W., Sun, K., Hu, Y.H., 2016. Direct conversion of CO2 to 3D graphene and its excellent performance for dye-sensitized solar cells with 10% efficiency. J. Mater. Chem. A 4, 12054–12057. https://doi.org/10.1039/c6ta04008j

Effective Droop Control to Mitigate PV-Related Voltage Rise in LV Systems through Reactive Power Balancing and Fair Power Curtailment

Ali Elrayyah
Hamad Bin Khalifa University, Qatar Environment and Energy Research Institite, Doha, Qatar
aelrayyah@hbku.edu.qa

Abstract
The development of effective control techniques to manage PV sources in low voltage distribution networks (LV-DNs) is essential to harness their full benefits without any negative impact on system stability and power quality. The implementation of power-voltage droop based schemes by PV sources is very effective in achieving autonomous voltage rise mitigation. In this paper, a droop based PV control system is presented that ensures fairness among the PV sources all the time. To determine the parameters of the droop relations, a procedure is proposed that does not require the sensitivity matrices as it is based on performing standards load flow analysis.

Keywords: Photovoltaic, voltage rise, reactive power, curtailment fairness, droop control

I. Introduction

In low voltage distribution networks (LV-DNs), voltage related operational challenges tend to have more impact on system reliability and power quality than other kinds of challenges [1, 2]. One of these challenges is the voltage rise due to the reverse power flow from the PV sources [3]. The installed PV capacity could be kept low enough to avoid the occurrence of reverse power flow and subsequently the voltage rise [4, 5]. However, the voltage rise occurrence might not be too frequent, and therefore, limiting the PV capacity in LV-DN would restrict its potential unnecessarily. One technique that receives wide acceptance due its low cost and effectiveness in mitigating the voltage rise is the PV real power curtailment [6]. Adjusting the PV real power supply can significantly help in regulating the voltage in LV-DN. To be effective, the curtailment process needs to ensure high reliability, low cost and fairness among the sources.

To achieve the required fairness, a method in [7] is proposed where communication between PV sources is needed to achieve the needed performance. Clearly, having mitigation techniques that operate autonomously through the use of locally available measurement ensures the highest level of reliability.

In this paper, an effective approach to determine the droop parameters for voltage rise mitigation in LV-DNs is proposed. The proposed approach could be applied very easily by analyzing the load flow analysis outcomes of the considered system and thus there is no need to define sensitivity matrices. The approach is presented in a generalized form that includes PV sources with any ratios between their powers to be supplied.

II. PROPOSED APPROACH FOR EFFECTIVE SETTING OF THE DROOP PARAMETERS

Figure 1 shows the considered structure of the PV sources.

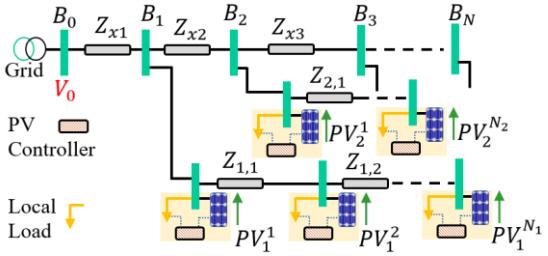

Fig. 1 PV sources and their control systems within a LV-DN

In droop based power curtailment this technique, the allowable power to be fed-back to the grid is defined as:

$$P_{x,y}^{lm} = P_{x,y}^{mx} - K_{x,y}^{drp} max\left(0, V_{x,y} - V_{x,y}^{lm}\right) \quad (1)$$

where $P_{x,y}^{lm}$ is the allowable power, $P_{x,y}^{mx}$ is the maximum power that the PV source can produce, $K_{x,y}^{drp}$ is the droop coefficient, $V_{x,y}^{lm}$ is difined voltage limit and $V_{x,y}$ is actual voltage. $K_{x,y}^{drp}$ and $V_{x,y}^{lm}$ need to be set for all the PV sources such that the required proportional fairness is maintained and the upper voltage limit is not violated.

To analyze voltage in LV-DN nodes, consider the segment of the LV-DN shown in Fig.2 .

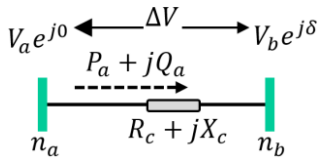

Fig. 2. Voltage drop due inter-nodes power flow

Through simple circuit analysis [8] it can be shown that

$$(V_a - V_b \cos\delta) = \frac{R_c}{V_a} P_a + \frac{X_c}{V_a} Q_a \quad (2)$$

R_c and X_c are small in power systems which makes the phase difference between the adjacent nodes small and $\cos\delta \approx 1$. A generalized approximated expression for the voltage difference can be obtained using the relation

$$V_a - V_b \cos\delta \approx V_a - V_b \approx \frac{R_c P_a}{V_0} + \frac{X_c Q_a}{V_0} = \Delta V_{a,b} \quad (3)$$

Consider the LV-DN shown in Fig. 3. For the feeder connected to B_1, there are N_1 PV sources each one of them supplies an amount of power equal to $\alpha_1 P^r$. Similarly, there are N_2 PV sources connected to B_2 with real power of $\alpha_2 P^r$ fed-back to the grid from each one of them. Two sources are attached to B_3 and the power supplied by each one of the two is given by $\alpha_3 P^r$. The factors α_1, α_2 and α_3 are chosen according to the required ratios of the power supplied by the various PV sources. The voltage rise at the node $n_{3,2}$ ($\Delta V_{3,2}$) can be estimated by summing up the voltage drop over all the resistors between the that node and the bus B_0 which is given by:

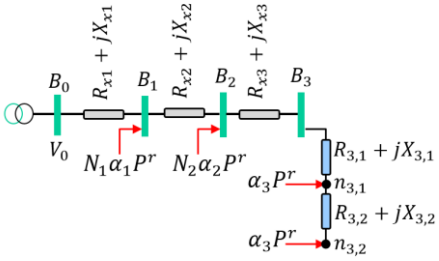

Fig. 3. Voltage rise estimation due to PV at LV-DNs feeders

$$\Delta V_{3,2} = V_{3,2} - V_0 \approx \frac{P^r}{V_0}\left[\alpha_3 R_{3,2} + 2\alpha_3\left(R_{3,1} + R_{x3}\right) + (2\alpha_3 + N_2\alpha_2)R_{x2} + (2\alpha_3 + N_2\alpha_2 + N_1\alpha_1)R_{x1}\right] = \frac{P^r}{V_0} R_{3,2}^{eq} \quad (4)$$

$$R_{3,2}^{eq} = \alpha_3 R_{3,2} + 2\alpha_3\left(R_{3,1} + R_{x3}\right) + (2\alpha_3 + N_2\alpha_2)R_{x2} + (2\alpha_3 + N_2\alpha_2 + N_1\alpha_1)R_{x1} \quad (5)$$

Following similar steps, the voltage rise at the node $n_{3,1}$ ($\Delta V_{3,1}$) can be estimated through the following relation:

$$\Delta V_{3,1} = \frac{P^r}{V_0} R_{3,1}^{eq}, R_{3,1}^{eq} = 2\alpha_3\left(R_{3,1} + R_{x3}\right) + (2\alpha_3 + N_2\alpha_2)R_{x2} + (2\alpha_3 + N_2\alpha_2 + N_1\alpha_1)R_{x1} \quad (6)$$

From (4) and (6), the voltage rise depends on $R_{3,2}^{eq}/V_0$ and $R_{3,1}^{eq}/V_0$. It is thus possible to determine the amount of PV power that would results in an unacceptable voltage rise through the use of the equivalent resistances ($R_{x,y}^{eq}$).

Obtaining the values of the equivalent resistance $\mathbf{R_{x,y}^{eq}}$

The need to determine the values of the equivalent resistances $R_{x,y}^{eq}$ can be a source of complication for the proposed method. Fortunately, the values of the equivalent resistances can be obtained using very simple method that requires the outcome of load flow analysis performed for the considered system.

From (4) and (6), the voltage difference between any two points depends on the value of $P^r R_{x,y}^{eq}/V_o$. To obtained the values of $R_{x,y}^{eq}$, the values of α_i for $i = 1, 2, \cdots$ for the PV sources at the various nodes need first to be specified. Then, load flow analysis needs to be performed where every PV sources is assumed to supply an amount of power equals to $\alpha_i P^r$ where α_i is the relative proportion of the PV source power and P^r is any positive value. After performing the load flow analysis, the voltage $V_{x,y}^r$ at each node is obtained and the value of $R_{x,y}^{eq}$ can easily be estimated from the relation

$$R_{x,y}^{eq} = \left(V_{x,y}^r - V_0\right)V_0/P^r \quad (7)$$

This relation is obtained directly from the relation in (6). Since the value of $R_{x,y}^{eq}$ does not depend on P^r as indicated in (5) and (6), the value obtained in (8) can be used in the algorithm presented in this Section to determine the droop parameter.

III. Case Study

To verify the effectiveness of the proposed method, a simulation study is presented in this section for the 13-bus system shown in Fig. 4. The nominal voltage at the SRF nodes is taken as 400 V and the maximum allowed voltage rise is assumed to be 5%. The considered LV-DN has 10 secvondary radial feeders (SRFs) each one of them has 10 PV sources installed. The medium voltage line impedances Z^L per km is assumed as 1.08+0.302i Ω while the lengths of the segments $Z_{1,2}^L$, $Z_{2,3}^L$, $Z_{3,4}^L$, $Z_{4,5}^L$, $Z_{5,6}^L$, $Z_{1,7}^L$, $Z_{7,8}^L$, $Z_{8,9}^L$, $Z_{7,10}^L$, $Z_{10,11}^L$, $Z_{11,12}^L$ and $Z_{12,13}^L$ are taken to be 2, 2, 2, 2, 2, 3, 2, 2, 3, 3, 4 and 3 km, respectively. The impedance of the feeders lines is taken as 0.551+0.088i Ω per km. The main transformer of the distribution system (33/11 kV) has power rating of 30 MVA and its per unit impedance is 0.01991+0.0459i Ω and each one of the distribution transformers (11/0.4 kV) has rated power of 1 MVA and per unit impedance equals to 0.00430+0.0976i Ω. All feeders have the same impedance and the same total length of 2 km. The power $P_{x,y}^r$ is fed-back to the grid from the yth nodes at SRF connected to the

bus B_x. The value of α is assumed to be 1 except for $P^r_{13,6}$, $P^r_{13,7}$, $P^r_{13,8}$, $P^r_{13,9}$ and $P^r_{13,10}$ where its assumed to be equals to 0.5.

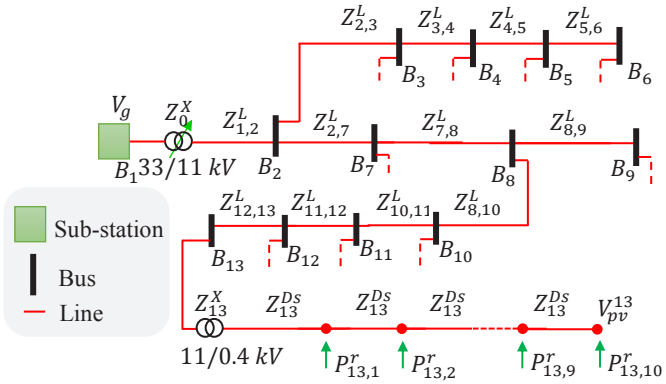

(a) Fig. 4. Considered 13-bus power system

The proposed approach is implemented to determine the values of $V^{lm}_{x,y}$ and $K^{drp}_{x,y}$. Figure 5 shows the values of $V^{lm}_{x,y}$ for the nodes within the feeder connected at the buses B_{11}, B_{12} and B_{13}. It is clear that the value of $V^{lm}_{x,y}$ increases as we move toward the feeders endpoints.

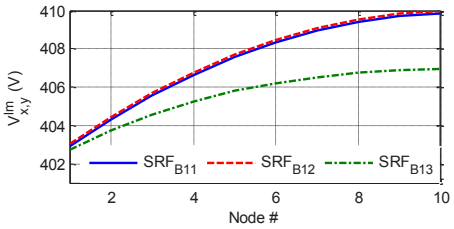

(b) Profile of $V^{lm}_{x,y}$ for the SRFs connected to B_{11}, B_{12} and B_{13}

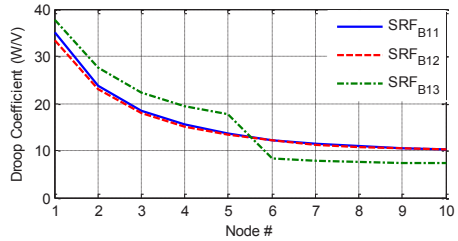

(a) Profile of $K^{drp}_{x,y}$ for the SRFs connected to B_{11}, B_{12} and B_{13}

Fig. 5 Settings of droop parameters using the proposed approach for some PV sources in the simulation power system

In this simulation, each of the PV sources that have $\alpha = 1$ is assumed to have the capability to supply 2 kW while the ones that have $\alpha = 0.5$ can supply 1 kW. The local load with each PV source is assumed to decrease till it becomes zero and as that happens, the power fed-back to grid is observed. The maximum voltage among all nodes of LV-DN for the different load values is shown in Fig. 6(a) where it is always maintained below the upper value of 420 V as the loads vary. Figure 7(b) shows the power supplied by two PV sources; where one of them has $\alpha = 1$ while its 0.5 for the other. Clearly, the proportional fairness between the two sources is maintained at all load values. Note also that when the load is high, no voltage rise is experienced and the voltages at all nodes are below the values given by $V^{lm}_{x,y}$. However, when the load becomes lower than 1.75 kW, this condition is violated and the droop control starts to take actions which changes the slop of the PV power vs. load value curve as indicated clearly in Fig. 6(a) and 6(b). This verifies the effectiveness of the proposed method in maintaining the required voltage limit within LV-DNs.

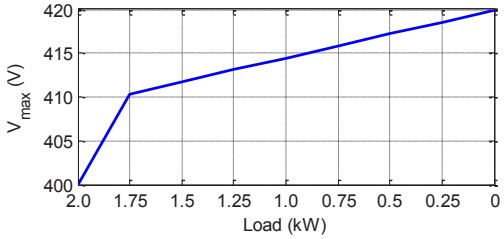

6(a) Highest voltage within the simulated LV-DN

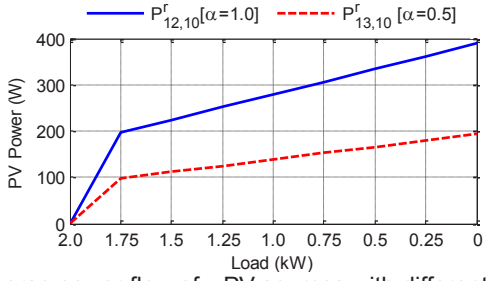

6(b) Reverse power flow of PV sources with different values of αs

Fig. 6. Effectiveness of the proposed method in maintaing the required voltage level and fairness among the PV sources

Figure 7 presents another demonstration for the fairness among the power fed-back by the various PV sources. The highest and lowest PV source power divided by its corresponding values of α are plotted for the various values of the load. Figure 7 shows that the differences between the maximum and minimum values are very small which indicates that the accurate fairness is maintained in the system.

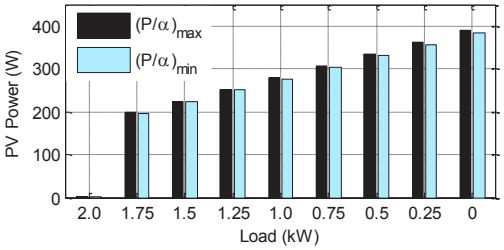

Fig. 7. Highest and lowest values for P/ α for all the source within the simulated LV-DN

IV. Conclusions

In this paper, a novel power-voltage droop based PV controller to perform fair power curtailment is presented. As the droop controllers operate autonomously, their parameters need to be set carefully such that curtailment fairness among the various PV sources is achieved. The proposed method ensures the fairness even when there is variation reactive power consumed by the local loads. By using the outcome of standard load flow analysis, the droop parameters of all PV sources can be obtained through simple computations. The performance of the proposed techniques is verified in the paper through a case study.

References

[1] F. Olivier, P. Aristidou, D. Ernst and T. Van Cutsem, “Active Management of Low-Voltage Networks for Mitigating Over voltages Due to Photovoltaic Units”, IEEE Trans. Smart Grid, vol. 7, no. 2, pp. 926–936, 2016.

[2] F. Trindade, T. Sonnewend, M. Lopes and W. Freitas, “Mitigation of fast voltage variations during cloud transients in distribution systems with PV solar farms,” IEEE Trans. Power Del., in press.

[3] G. Mokhtari, A. Ghosh, G. Nourbakhsh and G. Ledwich, “Smart robust resources control in LV network to deal with voltage rise issue”, IEEE Trans. Sustain. Energy, vol. 4, no. 4, pp. 1043–1050, 2013.

[4] Y. Ueda, K. Kurokawa, T. Tanabe, K. Kitamura and H. Sugihar, “Analysis results of output power loss due to the grid voltage rise in grid-connected photovoltaic power generation system”, IEEE Trans. Ind. Electron., vol. 55, no. 7, pp. 2744–2751, 2008.

[5] R. Tonkoski, D. Turcotte and T. H. M. EL-Fouly, “Impact of high PV penetration on voltage profiles in residential neighborhoods”, IEEE Trans. Sustain. Energy, vol. 3, no. 3, pp. 518–527, 2012.

[6] A. Moawwad, Khadkikar and J. L. Kirtley, “A new P-Q-V droop control method for an interline photovoltaic (I-PV) power system,” IEEE Trans. Power Del., vol. 28, no. 2, pp. 658-668, Apr. 2013.

[7] S. Alyami, Y. Wang, C. Wang, J. Zhao and B. Zhao, “Adaptive real power capping method for fair overvoltage regulation of

[8] J. Appen, T. Stetz, M. Braun and A. Schmiegel, “Local voltage control strategies for PV storage systems in distribution grids”, IEEE Trans. Smart Grid, vol. 5, no. 2, pp. 1002–1009, 2014.

Sustainable Buildings Components: A Technical Review of Green Roofs (GFs)

[1*]Sara Zaina, [1] Fodil Fadli
[1] Qatar University, College of Engineering, Department of Architecture and Urban Planning, Doha, Qatar

* E-mails: sara.zaina@qu.edu.qa; f.fadli@qu.edu.qa

Abstract
Urban development involves environmental, socio-cultural and economic concerns that are affecting human well-being, comforts, and the sustainability levels of cities. Greening the city and its buildings is not a new notion, in fact it is an old-traditional system that is re-discovered to address and improve deleterious impact on the urban environment in a sustainable and natural way. Greening has its roots in the natural environment, and it can also be incorporated significantly within architecture and design, particularly applied as a part of the roof and wall. The horizontal and vertical systems are becoming popular as they are evolving. In the last years, the quantity of studies distributed in the scientific writing on this point, including both roofs and living walls, has rapidly expanded. The process of injecting the concept of design and development of green components in design allows for a more healthy-sustainable urban space and improves the overall quality of life. This paper develops a technical review adopting a classification of different types of roofs. It also provides a comprehensive analysis of sustainable building (SB) components focusing on green roofs (GFs). It uses the SWOT (Strengths, Weaknesses, Opportunities, and Threats) analytical approach. The technical analyticall review of these systems would be valuable to architects, planners and urban designers, to investigate the most suitable green design possibilities in Doha, Qatar.

Keywords: Sustainable Buildings (SBs), Construction Components, Green Roofs (GFs), SWOT analysis

I. Introduction

Greening the building is not a new notion, in fact it is an old-traditional system that is re-discovered to address and improve deleterious impact on the urban environment. Greening has its roots in biological nature and it can also be incorporated significantly within architecture and design, particularly applied as an aspect for the wall and roof (Fadli et al., 2019, 2016; Zaina, 2017). This paper offers an analytical review of green building systems using SWOT analysis tool, which can be of value to urban planners.

Doha faces a myriad of threats originating from the expansion of its suburban and urban environments. It is one of the fast-growing cities in Qatar. This first growth and urbanization have changed the landscapes into impervious surfaces, thus increasing the volume of runoff from rainfall. Additionally, the increased development and urbanization of the city is associated with increased energy use; which results in climate change. Poor air quality is also another threat as a result of fast development. Furthermore, the industrial development in Qatar is currently at an unprecedented rate. These developments have placed the environment at risk as they pose a threat on ecosystem services and biological diversity. To mitigate these changes, Qatar is developing regulatory bodies, legislations and management agencies to manage the ecosystem and to instigate efforts towards conservation. These entireties of these implementations have not been achieved due to lack of enough scientific expertise and may also be attributed from the effects of the early stage of environmental development in the country. Despite the efforts, the question that has remained among policy makers lies in whether these legislations and regulation bodies will be able to reduce the effects that industrialization has caused to the ecosystem and offer the right protection (Susca, Gaffin, & Dell'Osso, 2011). The paper addresses the advantages that will be achieved when GFs are implemented in Qatar. Literature shows that GF technology has a potential to address all these problems and more (Dunnett and Kingsbury, 2008). The geographical location of Doha makes a suitable beneficiary of GF technology. GF are widely known for their energy saving abilities across many nations all over the globe. Green building components have the ability to implement a passive cooling technique in preventing the inbound solar radiation from penetrating the building construction components.

II. History of Greening the Building

The combination of plants by means of architecture is not a new notion, and neither are GFs or green walls. Long time ago, both natural and man-made formed landscapes are incorporated into the urban texture. Greening the building is a mean of sustainable architecture that minimizes the negative impact of buildings on the environment using energy and material efficiency. Within this reason, high greenspace structures have existed as long as humankind remained involved with architecture (Velazquez, 2005).

Around 2100 B.C., the sloping walls of the Ziggurat of Nanna, were covered with shrubs and trees. Around 600 B.C. the "Hanging Gardens of Babylon" built by King Nebuchadnezzar included luxurious terrace and roof gardens. Dating from the Viking era the earth-sheltered huts have been found in Ireland and Scotland. Moreover, sod-covered roofs were used in Scandinavia and Iceland, around 1000 A.D.. Later, in the early nineteenth century settlers in both Canada and northern United States presented grass roofs and walls. Furthermore, "garden cities" remained advanced from Persia to Renaissance period Paris, and later from Russia to Berlin, London, and New York (Velazquez, 2005).

Famous architects such as Frank Lloyd Wright, Roberto Burle and Le Corbusier encouraged the advantage of GF gardens and applied them in their projects. In 1930s successful modern GFs included the five well-known

Rockefeller Roof Gardens in New York, and the Derry and Tom's Garden in London (EnglishNature, 2003).

Today, GFs and green walls can be found in Europe and around the globe. However, the development of the green building structures from an expression of vernacular architecture to a practical sustainable roof construction option occurred in modern Germany. In the 1980s, Germany adopted this type of technology in its sustainable design and building practices mainly for the benefits of both the society and environment. When there were great developments especially urban developments, there was more storm water runoff among other negative effects of urbanization (Maley et al., 1990). Germany thus adopted the technology of GFs to help mitigate these effects of run-offs. It is projected that Germany now has over 800 GF projects (Wark and Wark, 2003). Since then, several nations in North American and Europe incorporated GFs as part of the building design to reduce impacts of imperviousness brought by urban development and growth. Thus, this study seeks to show that Qatar can effectively adopt the GF technology in its vast urban region through a sustainable manner.

III. Classification of Green Architectural Components: The Green Roofs (GFs)

A GF is a roof that is fully or partially protected with plants to primarily reduce storm water runoffs and even lower the cooling costs. It consists of soil, vegetation, and watertight roofing systems. The live vegetation is planted over a waterproof material on the building. Green rooftops can also include irrigation systems and additional layers of root barriers (Dowdey, 2017). They are also referred to as eco-roofs or roof gardens. GF can also refer to cool roof with photovoltaic modules which are a form of green technology.

There are two main types of GFs developed into four different designs adopted in building structures. The two main types include (figure 1); (1) extensive GFs which tend to have a very shallow soil profile with soil depths which range from 10-25cm which are planted with succulent soil community to increase some environmental benefits; and (2) Intensive GFs, which are rather complex with very deep soil profiles of 30cm to very deep heights (Dowdey, 2017). The landscapes on the structures are meant for reaction and active use thus they have a more mature landscape with shrubs and even trees. The four types of roofs discussed in this section include: extensive modular, extensive built up, biodiverse, and intensive GFs.

Fig. 1. construction of extensive and intensive GF types (Greenheights, 2012)

Extensive modular GFs: This type of design functions to reap benefits which GFs offer at very minimal costs and low maintenance. It involves a very thin layer of growing medium which supports low growing, stress-tolerant plants which are able to grow on their own and look after themselves (Liu and Minor, 2005). It should be applied on very large projects as in small projects it is very costly. It is mainly used for ecological protection such as lower carbon emissions.

Extensive built up GFs: This type of GFs involves three separate components, that is, drainage layer, the growing medium and the plant layer. These components are installed on site. Because of these features, they are more cost effective than the modular GFs and as such can be used in large projects. There are also diversified weights and heights for this type of roof. The whole planting process can involve either pre-grown mat, seeding or plug plants. It functions mainly to provide an ecological protection layer for air and water quality among other key aspects (Hossain et al., 2019).

Biodiverse GFs: These are low maintenance roofs that are designed to replace or create natural habitats. Their unique design offers support for particular types of flora and fauna, birds, and bats (Moore, 1986). Planting involves mostly native species such as grasses, hardy succulents, herbs and wildflowers. This type of roof's weight varies based on the needs of the plant species that are required. It weighs 90 – 225 kg/m2 with a build-up height of 70 – 200 mm.

Intensive GFs: This type of design is very heavy and thick with high vegetation weighing 200 kg/m2 + with a build up the height of 150-1500 mm. It is suitable for those areas requiring the planting of lawn and bushes, small trees and shrubs. They can also be combined with hard landscapes and water features. It is mostly applied in recreational areas and roof gardens. This type of roof must be regularly maintained and irrigated (Fadli et al., 2019).

Table 1. extensive vs. intensive green roofs; (Hossain et al., 2019; Velazquez, 2005)

Extensive vs. Intensive Green Roofs	
Low Profile/ Ecoroofs	High Profile/ Roof Gardents
Thickness 10-25cm	Thickness 30cm and deeper
Low growing plants	Large plants, shrubs, and trees
Less plants variety: alpine types, herbs, succulents, grasses and mosses	Huge plants variety, depending on design, loads and budget
Ofen not accessible	Often accessbile: designed for human recreation
Slopes up to 30° and higher	Relatively flat
Low weight 60-150kg/m^2	Greater weight 200-500kg/m^2
Low capital cost 130-165$/$m^2$	High capital cost 540$/ m^2 +
Low irrigation, nutrient and maintenance	High irrigation, fertigation and maintenance
Retains water from 27-45l/m^2	Retains water from 70-130l/m^2

IV. Green Roofs: a SWOT Analysis

To improve the urban environmental quality, the best encounter with the highest returns will be gained through utilizing existing roof tops. Table 2 offers a summary of the factors correlated to extensive and intensive GFs according the SWOT principles including both internal and external factors.

Table 2. SWOT analysis for extensive and intensive GFs

		Positive	Negative
Extensive GFs	Internal Factors	Strengths - Low thickness - Low weight - Less nutrients - Low maintenance - Low capital cost	Weaknesses - Not accessible (slopes up to 30° & higher)
	External Factors	Opportunities - Low irrigation	Threats - Low growing and less variety of plants
Intensive GFs	Internal Factors	Strengths - Accessible (flat)	Weaknesses - High thickness - Greater weight - High capital cost - High fertigation - High maintenance
	External Factors	Opportunities - Large growing & more variety of plants	Threats - High irrigation

Extensive green roofs

Internal factors consist of the strengths and weaknesses interior to the building. Low thickness, weight, nutrients, maintenance and cost are all strengths of an extensive GF system. An extensive GF tend to have a very shallow soil profile with soil depths which range from 10-25cm which are planted with succulent soil community to increase some environmental benefits. Extensive GF can be considered as building material or roof finishing, the package structure is a maximum of 15cm high, needs almost no maintenance, irrigation or nutrients. The weakness of an extensive GF is that it is not accessible in most situations, as it slopes up to 30° and higher. The expenses of developing GFs relied on the parts, including the growing medium, nature of roof membrane, amount of drainage system and plants. As shown in the report led by Environmental Protection Agency (2009), it was predicted that the preliminary costs for an extensive GF is US$10/$m^2$. The maintenance costs of extensive GF reduce when the roof is entirely covered by plants.

External factors consist of the opportunities and threats presented by the environment exterior to the building. Although the choice of vegetation is a threat due to the low growing and restricted variety of plants due to the maintenance conditions and minimalistic construction components; however, this is an opportunity for an extensive GF system as plants should have short and soft roots and should be able to live without consistent irrigation. Sedum plant type are usually used as it require 7cm of substrate (Vijayaraghavan, 2016).

Intensive green roofs

Internal factors consist of the strengths and weaknesses interior to the building. Easy accessibility is a strength of an intensive GF system as roof is flat. Alternatively, high thickness, weight, fertigation, maintenance and cost are all weaknesses of an intensive GF system. Intensive GFs, which are rather complex with very deep soil profiles of 30cm to very deep heights (Dowdey, 2017). In many cases' buildings should be constructively designed to carry the extra weight (Vijayaraghavan, 2016). With a package more than 20 cm and a wide variety of vegetation choices such as bushes, grass or trees, need a lot of maintenance including fertilizing and weeding. As shown in the report conducted by Environmental Protection Agency (2009), it was estimated that the initial expenses for an intensive roof is upto US$270/$m^2$. The maintenance costs of intensive GF remain constant when plants cover the entire roof.

External factors consist of the opportunities and threats presented by the environment exterior to the building. Large growing and more variety of plants is an opportunity for environment and the ecosystem. Although, an intensive GF system offers a variety of plantations; however, this is a threat as it requires a lot of watering.

V. Discussion

Extensive and intensive GFs have almost similar advantages for the urban environmental condition with a dissimilar effect. For nearly all encounters, intensive GFs will be an enhanced resolution than extensive GFs, but intensive roofs usually require helpful alterations and are consequently difficult and low-priced for retrofitting usage, if conceivable at all. Extensive GFs can be well viewed as a structural element or green urban infrastructure with advantages for the urban environmental condition. Thus, the accountability aimed at the decision whether to apply GFs for the community or the public advantage is necessity to continue public.

Moreover, not every urban district has similar environmental difficulties. A compact city area requires a bigger coverage of green area for both water storage and cooling; however, a rural area can have adequate parks or greens to avoid environmental variation impacts. It is generally advantageous to study which local portion is the most appropriate for its local challenge to come up with the most preferred planning solution.

In this paper the capacity of GFs is checked under conditions of Qatar, where GFs can be helpful for numerous environmental change impacts simultaneously, other climates can utilize GFs for another objective. The urban heat island (UHI) effect will result in a serious of environmental danger.

V. Conclusions

In urban areas surfaces are wrapped by concrete, stone, and tarmac, where there is a limited network of green areas. Furthermore, the hot climate of Qatar is portrayed by the outrageous climate states of high outdoor air temperature and solar radiation which cause enormous heat gains through buildings. In such a climate, buildings consume a huge portion of energy to cool the space by air-conditioning systems. In addition, the man-made environment in urban areas increase the air temperatures and atmospheric humidity, thus, causing the UHI effect. At the city scale, the UHI effect contributes to the global warming and high air pollution in the atmosphere.

By adopting GFs in Qatar the urban environmental quality could be improved by reducing cooling energy consumption, cooling and enhancing the air moisture content, extracting CO_2 and pollutants, reducing rainwater run-off and improving the biodiversity.

A general SWOT analysis is made providing an overview of the factors related to extensive and intensive GFs including both internal and external factors. The internal factors consist of strengths and weaknesses internal to the building; whereas, the external factors consist of opportunities and threats presented by the environment external to the building. Extensive GFs are generally the objective of scientific examination as it is less expensive than intensive GFs. Furthermore, its weight adding to the structure is lower than intensive GFs; thus, extensive GFs are more known. However, extensive GFsencounter harsh climatic conditions, for example limited precipitation, shallow growing substrate and high solar radiation; in this manner it constrains the plants selections. These aspects become difficulties in developing extensive GFs; where full watering system can be fitted on intensive GFs. Hence, water productivity is not the serious issue for intensive GFs.

If GFs are extremely required for future encounters, GF types should be considered with respect to local contribution (vegetation possibilities, climatological conditions, etc), rather than the overall advantageous, to focus on the most effective possibility in the varied range of GFforms. In the intital phase of executing, GFs are to be made an obligatory necessity (for retrofitting and/or new building structures). Local authorities should remain liable for an effective GF approach. To proceed with this approach productively, further examination on local climatological needs with respect to its social setting is expected to utilize explicit, sensible and effective goals and strategies in urban planning. Moreover, data, communication and furthermore assessment of practical GFs should be well set up to counter the dangers of an absence of information and scepticism to inevitably improve GF market, developers, engineers and industry, and proceed in a positive spiral.

Acknowledgements

The authors would like to acknowledge the support of Qatar University for creating an environment that encourages scientific research. This research study was developed as part of a PhD Thesis related to green architectural components including both roofs and walls. Finally, the authors thank the anonymous reviewers for their constructive comments, which contributed to the improvement of this paper. The authors are solely responsible for the statements made herein.

References

Dowdey, S., 2017. What is a Green Roof? [WWW Document]. URL https://science.howstuffworks.com/environmental/green-science/green-rooftop.htm (accessed 11.4.19).

Dunnett, N., Kingsbury, N., 2008. Planting green roofs and living walls - Ghent University Library. Timber Press, Portland.

EnglishNature, 2003. Green Roofs: their existing status and potential for conserving biodiversity in urban areas (ENRR498).

Fadli, F., Bahrami, P., Susorova, I., Tabibzadeh, M., Zaina, S., El-Ekhteyar, E.-S., 2016. Bio-Facades; An Innovative Design Solution Towards Sustainable Architecture in Hot Arid Zones. Hamad bin Khalifa University Press (HBKU Press). https://doi.org/10.5339/qfarc.2016.eepp3394

Fadli, F., Zaina, S., Bahrami, P., 2019. Smart biofaçades; An innovative living construction technology, in: Sustainable Construction Materials and Technologies.

Greenheights, 2012. greenerheights | Elevating urban sustainability [WWW Document]. URL https://greenerheights.wordpress.com/ (accessed 11.7.19).

Hossain, M.A., Shams, S., Amin, M., Reza, M.S., Chowdhury, T.U., 2019. Perception and barriers to implementation of intensive and extensive green roofs. Buildings 9. https://doi.org/10.3390/buildings9040079

Liu, K., Minor, J., 2005. NRC Publications Archive Archives des publications du CNRC. Perform. Eval. an Extensive Green Roof 1–11. https://doi.org/10.1039/B910216G

Maley, S., Elizabeth, Kay, 1990. Gardening in the Gulf.

Moore, E., 1986. Gardening in the middle east. Stacey International Publishers, London.

Velazquez, L.S., 2005. Organic Greenroof Architecture: Sustainable Design for the New Millennium.

Vijayaraghavan, K., 2016. Green roofs: A critical review on the role of components, benefits, limitations and trends. Renew. Sustain. Energy Rev. https://doi.org/10.1016/j.rser.2015.12.119

Wark, C., Wark, W., 2003. Green roof specifications and standards. Constr. Specif. 56.

Zaina, S., 2017. The Assessment of Microclimatic Conditions, Users' Psychological Adaptation and Physical Aspects of the Space: Enhancing Spatial Quality of Outdoor Public Space (OPS). ABA J. https://doi.org/10.1002/ejsp.2570

Resource Provisioning in Plug-in Electric Vehicle Charging Lots

[1*]I Safak Bayram, [2]Raka Jovanovic, [3]Michael Devetsikiotis
[1] University of Strathclyde, Faculty of Engineering, Department of Electronic and Electrical Engineering, Glasgow, UK G1 1QX
[2] Qatar Environment and Energy Research Institute, Hamad Bin Khalifa University, Doha, Qatar, 34110
[3]Department of Electrical and Computer Engineering, The University of New Mexico, Albuquerque, NM, 87106
* E-mails: safak.bayram@strath.ac.uk, rjovanonic@hbku.edu.qa, mdevets@unm.edu

Abstract
As the interest in plug-in electric vehicles increase, the design of sustainable charging facilities becomes critical to support mass-market uptake. In this paper, we consider two design problems for plug-in electric vehicle (PEV) charging lots. In the first one, it is assumed that the charging lot is located at a workplace and PEV arrival statistics are estimated in advance. The goal is to calculate the size of the total incomer feeder from the substation to charging lot. In the second problem, we consider the case where the parking lot is located in a busy area and the station is fed by a fixed capacity. In this case, the goal is to calculate the optimal arrival rate that maximizes a revenue function composed of financial parameters such as waiting and electricity costs. In both cases, PEV arrival and departures are assumed to follow a Poisson process and unique optimal solutions are analytically calculated. Presented case studies provide useful insights in this early stage of designing the charging stations of the future.

Keywords: Plug-in electric vehicles, resource planning, stochastic modeling

I. Introduction

With the goal of reducing the carbon footprint of the transportation sector and improve urban air-quality, there has been a global push towards plug-in electric vehicles (PEVs). When such vehicles are charged with electricity produced by clean renewable sources, policy-makers get one step closer to reach 2050 net-zero emission goals set by a number countries such as the United Kingdom and most members of the European Union (Davis, 2018). On the other hand, the integration of a high percentage of renewable generation into to the power grid poses a new set of challenges related to system stability, power quality, and faster asset aging (Bayram I. S., 2019). Moreover, the extra demand exerted on the power grid to enable electric miles further stresses grid operations and threatens the success of PEV penetration goals (Richardson, 2013). Hence, design and operation of charging infrastructures that can absorb PEV load variation is critical. To that, this paper considers two typical design problems for electric vehicle charging lots and presents a framework to calculate optimal system resource to meet demand.

The charging of PEVs typically take place in three different types of places (Falvo, 2014). The first one is home or garage charging in which PEVs are charged with a level 1 chargers (typical rating of 1.4 kW) at the customer premises. Due to long parking hours (8+ hours) such chargers transfer enough power to complete a daily trip. The second type of charging takes place in parking lots which are typically located at university campuses, workplaces, and hospitals. In this case, level 2 chargers (6-10 kW) are used to fuel PEVs that are parked for 2-8 hours. The last option is DC fast chargers which mimic gas-stations and serve vehicles within 30 minutes. In this paper, we consider large parking lots and address two typical design problems, namely optimal resource allocation for parking lots and optimal admission control.

Modeling, optimization, and control of PEV loads at large-scale charging lots has been a primary focus of several studies including (Bayram I. S., 2013), (Zhang, 2015), (Ioakimidis, 2018), and (Jovanovic, 2019). Work presented in (Bayram I. S., 2013) calculates system capacity for a large scale PEV charging lot using the effective bandwidth approach. They show that due to statistical gains, resources that need to be allocated per charger are significantly less than the peak demand. On the other hand, the presented model does not capture financial aspects of a typical charging network such as waiting times and electricity prices. (Zhang, 2015) presents a two stage dynamic programming framework to optimally charge PEVs under varying electricity prices. (Ioakimidis, 2018) develops an optimisation framework to reduce peak electricity demand at a university campus by charging and discharging parked PEVs on campus. (Jovanovic, 2019) considers optimal scheduling at park and ride facilities to reduce power system ramping requirements and smoothing duck curves. Next, we present two design problems and present case studies to provide insights.

II. Design Problem 1: Optimal Resource Calculation

In the first design problem, we consider a PEV parking lot located at a workplace premise for employees. In this case, the number of vehicles visiting the parking lot can be estimated from parking permits or historic arrival patterns. Therefore, the goal is to calculate the size of the total power demand feeding a number of vehicles. We assume the station operates under the following stochastic assumptions. PEVs arrive to the charging lot according to a Poisson process with rate λ. This is a common assumption in the literature, see References (Bayram I. S., 2017) and (Fan, 2015). It is important to note that service durations are independent of the arrivals and charging services, they follow exponential amount of time with mean service rate of μ. Since, there is only one feeder providing power to the lot, the station is modeled as a M/M/1 queueing system. It is further assumed that μ is the decision variable, while λ is known in advance.

In the proposed model two types of financial costs occur. We denote a service cost rate by c_p which is related to amount of the power drawn from the grid. Second, we denote a waiting-cost with c_w for customers. This is related to delays in the charging service and measured by cost per unit time per customer. It is noteworthy that the average long-term cost is equal to the expected steady state cost, which is true if and only if $\mu > \lambda$ (otherwise long-run cost becomes ∞) (Stidham Jr, 2009). Hence, without loss of generality, we assume that $\mu > \lambda$. To that end, the objective is to minimize the long-term average cost represented by

$$C(\mu) = c_p\mu + c_w W(\mu)\,, \tag{1}$$

where $W(\mu)$ denotes the expected number of PEVs in the parking lot. It is further assumed that the charging of PEVs is a first in first out (FIFO) process, therefore, from (Adan, 2001), the expected number of PEVs can be written as

$$W(\mu) = \frac{\lambda}{\mu - \lambda}. \tag{2}$$

To that end, the optimisation problem can be written as

$$\min_{\mu:\mu>\lambda} C(\mu) = c_p\mu + c_w \frac{\lambda}{\mu - \lambda}. \tag{3}$$

It is important to note that the second derivative of the objective function in respect to parameter μ is

$$C^{''}(\mu) = \frac{2c_w\lambda}{(\mu-\lambda)^3} > 0, \forall \mu > \lambda\,, \tag{4}$$

hence, $C(\mu)$ is a convex in service-rate $\mu \in (\lambda, \infty)$. Furthermore, the cost function $C(\mu)$ goes to infinity, as $\mu \downarrow \lambda$ and $\mu \uparrow \infty$. Therefore, the optimal values can be calculated by taking the derivative of the cost function and setting it to zero. That is,

$$C^{'}(\mu) = c_p - \frac{c_w\lambda}{(\mu-\lambda)^2} = 0. \tag{5}$$

It is easy to see that the unique optimal service rate μ^* can be written as

$$\mu^* = \lambda + \sqrt{\frac{c_w\lambda}{c_p}}. \tag{6}$$

By plugging the optimal value into the cost function, the optimal objective value can be written as

$$C(\mu^*) = c_p\lambda + 2\sqrt{\lambda c_p c_w}. \tag{7}$$

In Fig. 1, we present a case study of the proposed model with the following parameter settings: $\lambda = 10$, $c_p = 2$, and $c_w = 4$. The presented results show the convexity of the problem. It can be noticed that as the service rate increases, the PEVs get access to chargers faster. Therefore, the waiting time approaches to zero. It is important to note that, the waiting cost could be a nonlinear function. In this case, the convexity assumption can be valid only for certain ranges of the service rate.

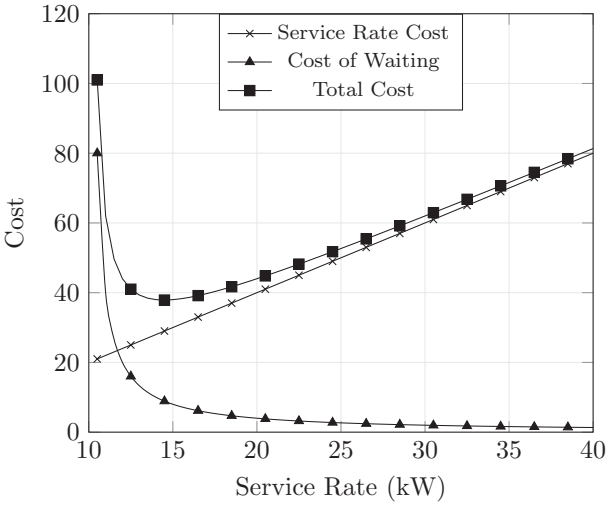

Fig. 1: System cost as a function of charging rate.

III. Design Problem 2: Optimal Demand Calculation

In the second design problem, it is assumed that the charging facility has a fixed charging rate. This time, the facility is a public charging lot, hence, we aim to calculate the optimal arrival rate of PEVs such that a revenue function is maximized. Let c_r denote the reward per arriving PEV. Similar to the previous case, the waiting cost is denoted by c_w. Let us denote the expected net benefit per unit of time by $B(\lambda)$. Then, we can write

$$B(\lambda) = \lambda c_r - c_w\left(\frac{\lambda}{\mu-\lambda}\right), 0 < \lambda < \mu. \tag{8}$$

As explained earlier, if $\mu \leq \lambda$, then, the number of PEVs waiting to be charged will be infinite (total cost equals ∞). Hence without loss of generality, it is assumed that $\lambda < \mu$. To that end, the optimization problem can be formulated as below

$$\max_{\lambda\in[0,\mu)} B(\lambda)\ s.t. \lambda \geq 0 \tag{9}$$

This optimization problem is more complicated than the one presented in equation (3) due to the constraint $\lambda \geq 0$. Note that, $B(\lambda)$ approaches to ∞ as the arrival rate of PEVs gets closer to the service rate, $\lambda \uparrow \mu$, hence, the upper limit of the feasible limit is not a major concern. We continue our analyses, similar to the previous case, by differentiating the benefit function twice with respect to the decision variable related to the arrival rate as below

$$B^{''}(\lambda) = \frac{2c_w\mu}{(\mu-\lambda)^3} < 0, \forall \mu > \lambda. \tag{10}$$

Notice that, $B(\lambda)$ is strictly concave and differentiable. The optimal value can occur for either of the followings:

$$\begin{cases} \lambda = 0, & B^{'}(0) \leq 0 \\ \lambda > 0, & B^{'}(\lambda) > 0 \text{ and } B^{'}(0) > 0 \end{cases} \tag{11}$$

To that end, using equation (8), the optimal unique solution $\lambda^* \in (0, \mu)$ can be written for the two cases as:

$$\begin{cases} Case\ I: & \lambda^* = 0,\ if\ c_r \leq c_w/\mu \\ Case\ II: & \lambda^* = \mu - \sqrt{\mu c_w/c_r},\ if\ c_r > c_w/\mu \end{cases} \tag{12}$$

It is noteworthy that $\mu > \sqrt{\mu c_w/c_r}$ if and only if $c_r > c_w/\mu$, hence the optimal arrival rate can be rewritten as,

$$\lambda^* = \left(c_p\lambda + 2\sqrt{\lambda c_p c_w}\right)^+, \tag{13}$$

where λ^+ is by defitnition, $\max(0, \lambda)$. Next, we present two cases studies to calculate optimal arrival rates given in equation (12). The results are presented in Fig. 2(a) and (b).

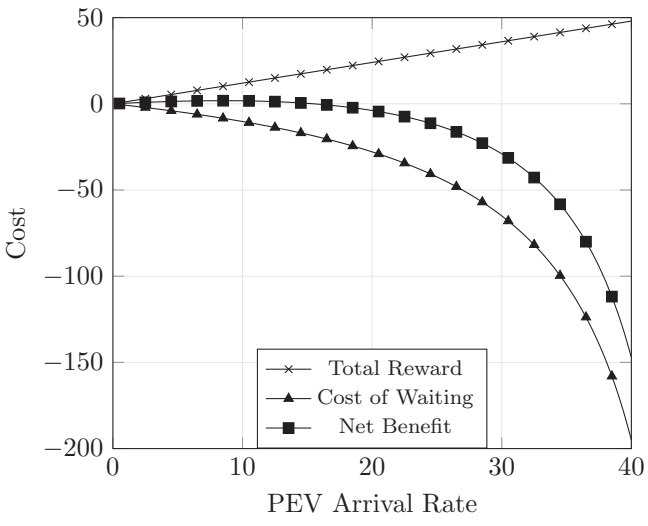

(a) Case I $c_r \leq c_w/\mu$

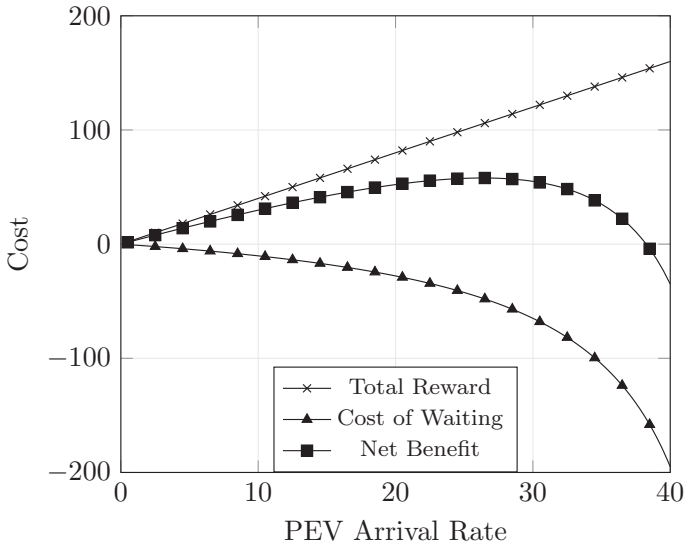

(b) Case II $c_r > c_w/\mu$

Fig. 2. Optimal Arrival Rate Calculations

IV. Conclusions

In this paper, we consider design problems in a large scale PEV charging lot. As a first case, we assumed that the charging lot is located in a place where the customer arrivals are known as a priori. We formulated the capacity planning problem as a convex optimization problem and presented a case study. In the second problem, we assumed that the station is located in a busy region. This time, the station draws the highest possible capacity from the grid. The goal of the station operator is to calculate optimal arrival rates that can maximize the station's profit. The presented results provide insight into charging station operations and some guidelines for designing sustainable charging infrastructures.

Acknowledgements

This publication was made possible by NPRP12S-0214-190083 from the Qatar National Research Fund (a member of Qatar Foundation). The statements made herein are solely the responsibility of the authors.

References

Adan, I. &. (2001). *Queueing Theory.* Eindhoven: University of Technology Department of Mathematics and Computing Science.

Bayram, I. S. (2013). Electric power resource provisioning for large scale public EV charging facilities. *IEEE International Conference on Smart Grid Communications*, (pp. 133-138).

Bayram, I. S. (2017). *Plug-in electric vehicle grid integration.* Artech House.

Bayram, I. S. (2019). Demand-Side Management for PV Grid Integration. In *Solar Resources Mapping* (pp. 313-325).

Davis, S. L. (2018). Net-zero emissions energy systems. *Science*, 6396.

Falvo, M. C. (2014). EV charging stations and modes: International standards. *Symposium on Power Electronics, Electrical Drives, Automation and Motion*, (pp. 1134-1139).

Fan, P. S. (2015). Operation analysis of fast charging stations with energy demand control of electric vehicles. *EEE Transactions on Smart Grid, 6*(4), 1819-1826.

Ioakimidis, C. S. (2018). Peak shaving and valley filling of power consumption profile in non-residential buildings using an electric vehicle parking lot. *Energy*, 148-158.

Jovanovic, R. &. (2019). Scheduling Electric Vehicle Charging at Park-and-Ride Facilities to Flatten Duck Curves. . *IEEE Vehicle Power and Propulsion Conference*, (pp. 1-5).

Richardson, D. B. (2013). Electric vehicles and the electric grid: A review of modeling approaches, Impacts, and renewable energy integration. *Renewable and Sustainable Energy Reviews*, 247-254.

Stidham Jr, S. (2009). *Optimal design of queueing systems.* Chapman and Hall/CRC.

Zhang, L. &. (2015). Optimal management for parking-lot electric vehicle charging by two-stage approximate dynamic programming. *IEEE Transactions on Smart Grid*, 1722-1730.

Performance and emission characteristics of a biogas fueled dual fuel engine with various DEE fractions

[1]Prashant Dhar Dwivedi, [1]Prashant Das, [1]Hrushikesh V Bhalerao, [1]Sumanth Samsani, [1]Subham Balyan, [1]Yasonandan Vadlamudi, [2]Saleel Ismail and [1*]Feroskhan M

[1]School of Mechanical and Building Sciences, VIT Chennai, Tamilnadu, India
[2]Department of Mechanical Engineering, NIT Calicut, Kerala, India

* E-mail: feroskhan.m@vit.ac.in

Abstract

Biogas is preferred as an alternative gaseous fuel on account of its ease of production, low price and a significant reduction in net carbon emissions. The use of biogas in dual-fuel mode in Compression Ignition (CI) engines helps in reducing particulate matter and NO_x emissions simultaneously. The extent of completeness of combustion can be enhanced by increasing the oxygen content of the fuel. This is usually achieved by blending oxygenated compounds such as Di-Ethyl Ether (DEE) with diesel. DEE is a liquid at ambient conditions and has a cetane number of 125, making it easy to handle and an ideal choice for CI engines. This study involves the experimental evaluation of the performance and emission characteristics of a single-cylinder, water-cooled, four-stroke, constant-speed CI engine operated in dual fuel mode with biogas as the primary fuel and diesel-DEE blends containing up to 9% DEE by volume as the secondary (pilot) fuel across the engine load range. The flow rate and composition of biogas are also varied. It is observed that using a 3% DEE-diesel blend along with low intake of methane-deficient biogas improves brake thermal efficiency by up to 3%. Blended diesel shows better NO_x and CO emissions.

Keywords: Biogas, Dual fuel, DEE, Efficiency, Smoke and NO_x.

I. Introduction

A diesel engine, which is used for many applications such as Automobiles, Tractors, Earthmovers etc., is considered one of the most efficient types of heat engines. The major reason for taking diesel engine into account is its durability, higher thermal efficiency, low cost of the diesel fuel and favorable torque characteristics. Techniques like selective catalytic reduction (SCR), exhaust gas recirculation (EGR), water injection, diesel oxidation catalyst (DOC), Particulate filters adopted nowadays, in diesel engine meets the increasingly rigorous emission norms. Another way to approach for sufficing these emission standards can be the partially replacing of fuels like hydrogen, biogas etc (Chuayboon et al., 2014; Tuner, 2016). Gaseous fuels have an upper hand with respect to emissions, efficiency and combustion of the engine. Biogas is used in both SI and CI engines (Mohamed Ibrahim et al., 2015; Porpatham et al., 2012; Swami Nathan et al., 2010). Biogas in CI engine improves NO_x and smoke emissions (Barik and Murugan, 2014; Feroskhan and Ismail, 2016).

Dimethyl ether (DME), CH3OCH3, which is the lowest carbon-ether chain, is considered to improve ignition with replacement or addition in diesel engines successfully, leading to less smoke and nitrogen oxides (NOx) emissions (Liu et al., 2012; Park et al., 2014). Thus, it can be used in everyday vehicles with the help of some modifications in fuel-injection system, which are required to adjust the gaseous fuel properties of blend, but the fuel delivery systems are not as efficient in distribution of high quantities of fuels in gaseous form as opposed to liquid fuels presently.

Thus, the solution to this problem can be found within using diethyl ether (DEE), which has properties quite similar to di-methyl ether (DME) for use in CI engine as a blend, but is generally used in liquid form as compared to gaseous in DME, thus overcoming the problems associated with the current fuel-delivery system. It can be easily produced from ethanol, a biomass product formed through a dehydrating process, producing a bio-fuel or bio-DEE. DEE has several useful properties for diesel engines which are favorable, which includes a good cetane number (of about 125), reasonable energy density, low autoignition temperature, high miscibility with diesel fuel and broad flammability limits. But, its high volatility, its anesthetic effect on human well-being and its tendency for peroxidation in storage, raise some serious concerns.

The major problem associated with the biodiesel is its auto ignition temperature and high viscosity. To elevate the fuel bound oxygen along with the reduction in major drawbacks and to maintain the reasonable level of lubricity, oxygenated additives like diethyl ether and n-butanol are usually blended in small portions. Numerous researches have been done on diesel-DEE blend to improve the emission and performance characteristics. Mahalingam et al. (2018), after studying the effect of DEE on mahuva-methyl ester and found that, smoke and CO emissions were decreased by more than 50% on adding DEE. Venu and Madhavan (2017) also studied the effect of 5% DEE addition with soybean biodiesel in a diesel blend. They noticed a significant lowering in CO emissions and better BSFC on adding DEE into the diesel– biodiesel blend. Therefore, apart from its usage as a cold-start aid in engines, it also assists the engine in performance improvements while also reducing emissions when used as a supplement in diesel fuel. Unlike using DME fuel counterpart, the testing of DEE in combustion ignition diesel engines concerning emissions and performance is very limited. Thus, it can be determined that on addition of DEE,

there is improvement in emission and performance characteristics of diesel engine.

This study involves the experimental evaluation of the performance and emission characteristics of a CI engine operated in dual fuel mode with biogas as the primary fuel and diesel-DEE blends containing up to 9% DEE by volume as the secondary (pilot) fuel across the engine load range. The flow rate and composition of biogas are also varied.

II. Experimental Setup and Procedure

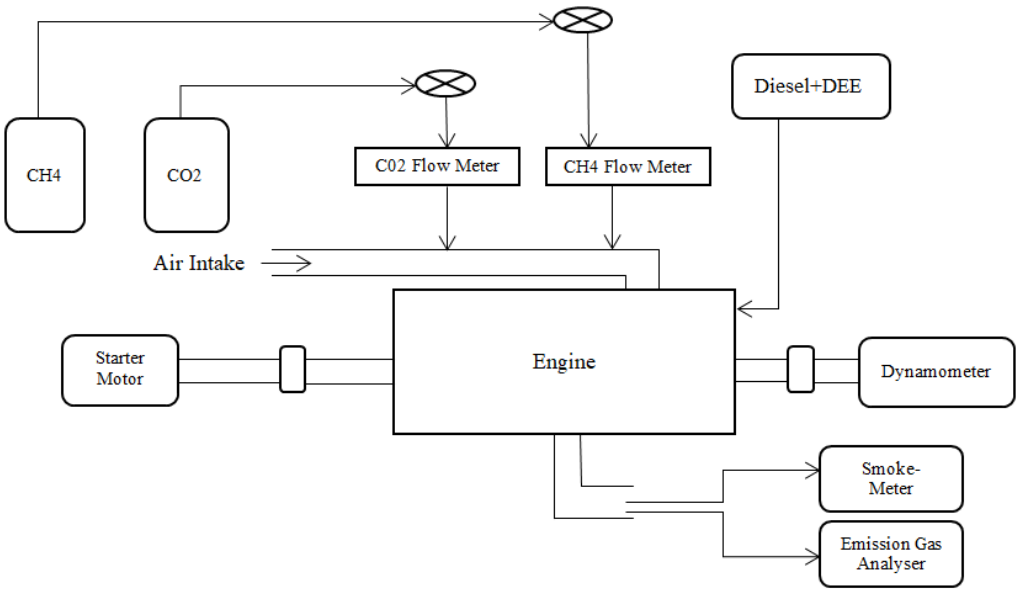

Fig. 1: Experimental Setup

The block diagram of the experimental setup is provided in Fig. 1. Conventional four-stroke, water-cooled, compression ignition (CI) engine is altered to operate as dual-fuel engine. There is an electric sensor which monitors speed and a sensor for load monitoring which are visible to the users on the display provided. Through knobs present on the panel, the operator can change the required values as per the reading. Biogas is obtained by mixing CH_4 and CO_2 together, that are kept in separate cylinders, which are equipped with flow-control valves and specifically rectified thermal mass flow meters. This helps in controlling the flow rates as well as the CH_4: CO_2 ratio. The mixture is fed into the incoming air stream. The engine is started with the help of an electric motor. Diesel fuel is blended with 3%, 6% and 9% DEE (Di-Ethyl Ether) and fuel is injected into the engine. The other equipment includes an eddy current dynamometer, 5-gas emission analyzer and smoke analyzer.

III. Methodology

The engine is started with diesel and then biogas is substituted for biogas-diesel duel fuel operation. The experimental study is conducted to evaluate the performance and exhaust emission characteristics of dual fuel blends at 0%, 3%, 6%, 9% of DEE addition by %vol in diesel. Performance and emission characteristics are calculated for all four fractions of DEE at various biogas flow rates (8 lpm and 12 lpm) and methane fractions (60% and 100%). Table 1 shows properties of various samples used in this study.

Table 1 Properties of sample

Sl. No	Properties	Sample I (Diesel)	Sample II (DEE)	Sample III (D97+DEE3)	Sample IV (D94+DEE6)	Sample V (D91+DEE9)
1	Flash Point	52 °C	-20 °C	52 °C	51 °C	48 °C
2	Fire Point	58 °C	28 °C	57 °C	56 °C	56 °C
3	Cloud Point	5 °C	-5 °C	5 °C	5 °C	5 °C
4	Pour Point	- 6.5 °C	-13 °C	- 6.5 °C	- 6.5 °C	- 6.5 °C
5	Density	833 Kg/m^3	762 Kg/m^3	831 Kg/m^3	827 Kg/m^3	822 Kg/m^3
6	Kinematic Viscosity	3.4 mm^2/s @40°C	0.38 mm^2/s @40°C	3.4 mm^2/s @40°C	3.3 mm^2/s @40°C	3.3 mm^2/s @40°C
7	Calorific Value	40,900 kJ/kg	26,900 kJ/kg	40,590 kJ/kg	40,400 kJ/kg	40,360 kJ/kg

IV. Results and discussions

IV.a. Brake thermal efficiency

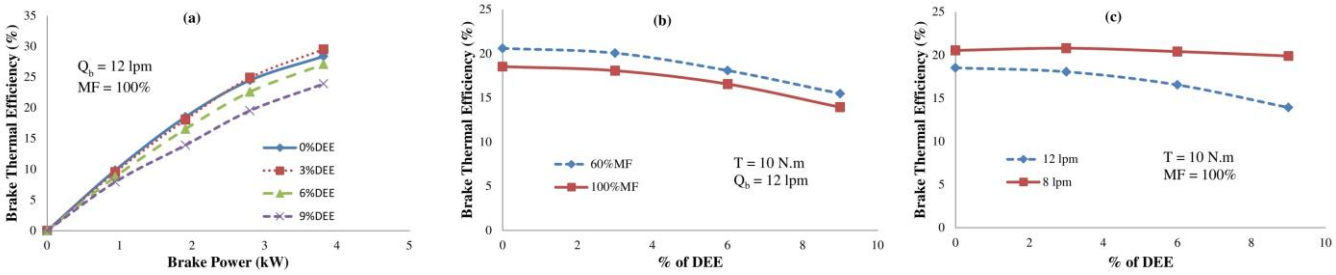

Fig. 2: Effect of (a) DEE addition, (b) methane fraction and (c) biogas flow rate on brake thermal efficiency

The effect of DEE addition, methane fraction and biogas flow rate on brake thermal efficiency for various input parameter is shown in Fig. 2. It can be seen from the figure that as the load increases brake thermal efficiency increases and with higher %DEE, there is a lowered value of brake thermal efficiency (refer Fig. 2(a)). Increase in methane fraction and biogas flow rate reduces pilot fuel consumption and reduces brake thermal efficiency.

IV.b. HC emissions

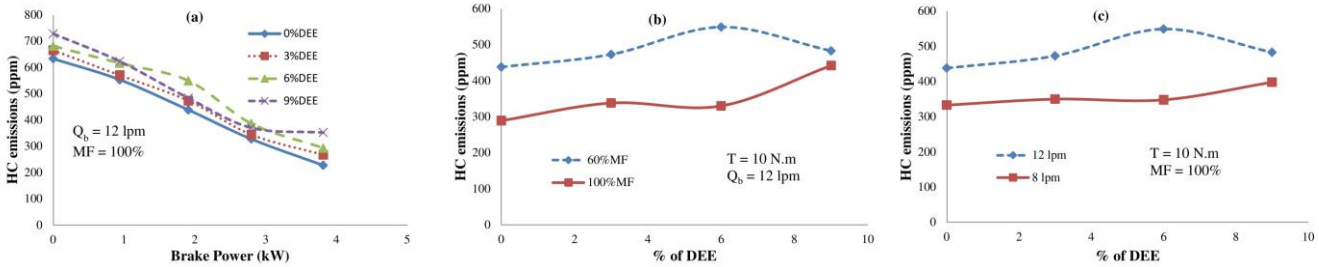

Fig. 3: Effect of (a) DEE addition, (b) methane fraction and (c) biogas flow rate on HC emissions

The effect of DEE addition, methane fraction and biogas flow rate on HC emissions for various input parameter is shown in Fig. 3. From the Fig. 3(a), it can be observed that increase in brake power reduces HC emission due to improvement in combustion. Increase in %DEE inceases HC emissions due to high carbon content in DEE fuel. Low HC emission is observed at high methane fraction and low biogas flow rate.

IV.c. CO emissions

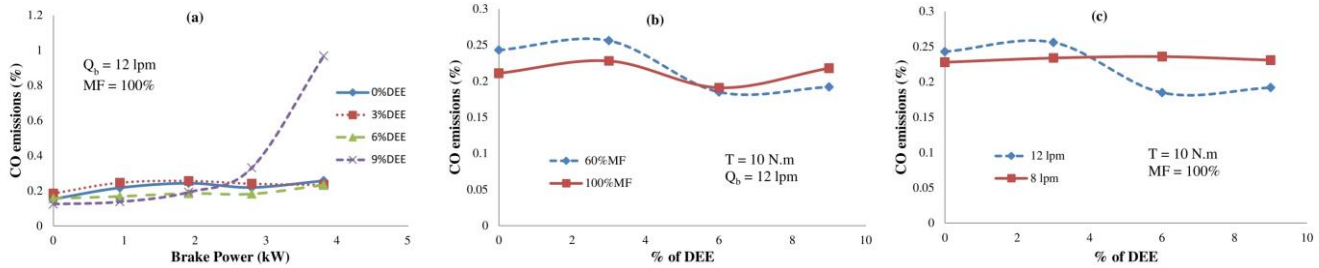

Fig. 4: Effect of (a) DEE addition, (b) methane fraction and (c) biogas flow rate on CO emissions

The effect of DEE addition, methane fraction and biogas flow rate on CO emissions for various input parameter is shown in Fig. 4. At lower load, DEE addition reduces CO emissions. There is no clear trend in Fig. 4(b) and (c).

IV.d. NO_x emissions

The effect of DEE addition, methane fraction and biogas flow rate on NO_x emissions for various input parameter is shown in Fig. 5. From the Fig. 5(a), it is observed that increase in load increases NO_x emissions due to high combustion temperature. Addition of DEE increases combustion temperature and hence it increases NO_x emissions. Increase in methane fraction reduces DEE blended pilot fuel and reduces combustion temperature. It reflected in lower NO_x emissions in Fig. 5(b). High biogas flow rate with high %DEE blended diesel increases combustion temperature NO_x emissions (Refer Fig. 5(c)).

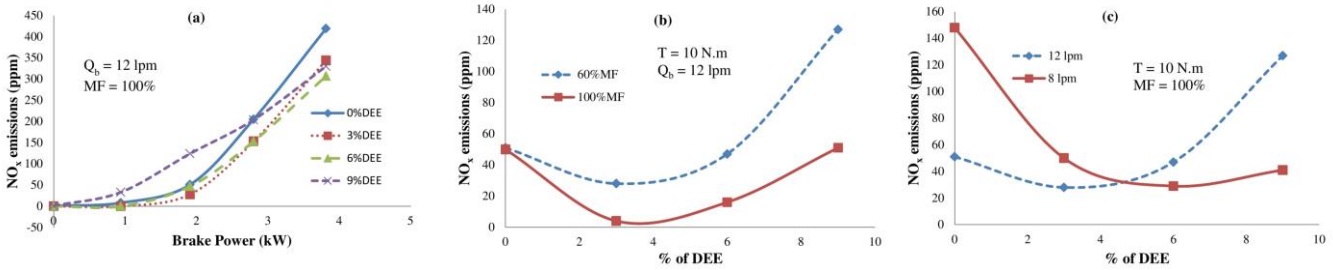

Fig. 5: Effect of (a) DEE addition, (b) methane fraction and (c) biogas flow rate on NO_x emissions

IV.e. Smoke emissions

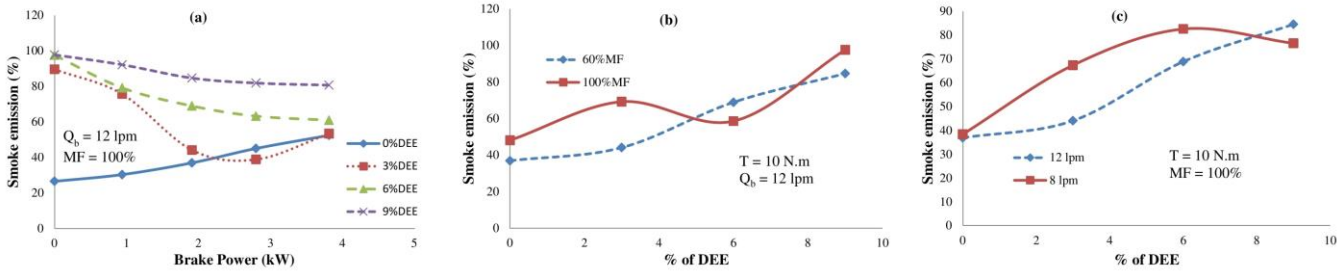

Fig. 6: Effect of (a) DEE addition, (b) methane fraction and (c) biogas flow rate on smoke emissions

The effect of DEE addition, methane fraction and biogas flow rate on smoke emissions for various input parameter is shown in Fig. 6. Increase in brake power reduces smoke emissions in case of DEE blended diesel. High biogas flow rate reduces smoke emissions due to lower consumption of pilot fuel.

V. Conclusions

This study shows that careful choice of the intake parameters such as biogas flow rate, methane fraction and % of DEE in diesel can effectively control various performance indices of the dual fuel engine. It is observed that using a 3% DEE-diesel blend along with low intake of methane-deficient biogas improves brake thermal efficiency by up to 3%. Blended diesel shows better NO_x and CO emissions.

References

Barik, D., Murugan, S., 2014. Investigation on combustion performance and emission characteristics of a DI (direct injection) diesel engine fueled with biogas-diesel in dual fuel mode. Energy 72, 760–771. doi:10.1016/j.energy.2014.05.106

Chuayboon, S., Prasertsan, S., Theppaya, T., Maliwan, K., Prasertsan, P., 2014. Effects of CH4, H-2 and CO2 Mixtures on SI Gas Engine. 2013 Int. Conf. Altern. Energy Dev. Ctries. Emerg. Econ. (2013 Aedcee) 52, 659–665. doi:10.1016/j.egypro.2014.07.122

Feroskhan, M., Ismail, S., 2016. Investigation of the effects of biogas composition on the performance of a biogas – diesel dual fuel CI engine. Biofuels 7269. doi:10.1080/17597269.2016.1168025

Liu, J., Yang, F., Wang, H., Ouyang, M., 2012. Numerical study of hydrogen addition to DME/CH4 dual fuel RCCI engine. Int. J. Hydrog. ….

Mahalingam, A., Devarajan, Y., Radhakrishnan, S., Vellaiyan, S., Nagappan, B., 2018. Emissions analysis on mahua oil biodiesel and higher alcohol blends in diesel engine. Alexandria Eng. J. 57, 2627–2631. doi:10.1016/j.aej.2017.07.009

Mohamed Ibrahim, M., Varuna Narasimhan, J., Ramesh, A., 2015. Comparison of the predominantly premixed charge compression ignition and the dual fuel modes of operation with biogas and diesel as fuels. Energy 89, 990–1000. doi:10.1016/j.energy.2015.06.033

Park, S.H., Yoon, S.H., Cha, J., Lee, C.S., 2014. Mixing effects of biogas and dimethyl ether (DME) on combustion andemission characteristics of DME fueled high-speed diesel engine. Energy 66, 413–422. doi:10.1016/j.energy.2014.02.007

Porpatham, E., Ramesh, A., Nagalingam, B., 2012. Effect of compression ratio on the performance and combustion of a biogas fuelled spark ignition engine. Fuel 95, 247–256. doi:DOI 10.1016/j.fuel.2011.10.059

Swami Nathan, S., Mallikarjuna, J.M., Ramesh, a., 2010. An experimental study of the biogas-diesel HCCI mode of engine operation. Energy Convers. Manag. 51, 1347–1353. doi:10.1016/j.enconman.2009.09.008

Tuner, M., 2016. Review and Benchmarking of Alternative Fuels in Conventional and Advanced Engine Concepts with Emphasis on Efficiency, CO 2 , and Regulated Emissions. SAE Tech. Pap. doi:10.4271/2016-01-0882

Venu, H., Madhavan, V., 2017. Influence of diethyl ether (DEE) addition in ethanol-biodiesel-diesel (EBD) and methanol-biodiesel-diesel (MBD) blends in a diesel engine. Fuel 189, 377–390. doi:10.1016/j.fuel.2016.10.101

Exergy Analysis of a biogas fuelled dual engine

[1]Feroskhan M, [*1]Sreekanth M and [2]Saleel Ismail

[1]School of Mechanical and Building Sciences, VIT Chennai, Tamilnadu, India
[2]Department of Mechanical Engineering, NIT Calicut, Kerala, India

* E-mail: manavalla.sreekanth@vit.ac.in

Abstract

Since the fuel's heating value is different from its total exergy (chemical as well as thermo-mechanical exergy), an exergy analysis provides a finer insight into the processes and throws light on areas where excessive exergy destruction is taking place. This helps in focussing on those areas where more useful energy is being lost. In the present study, biogas-diesel fuelled dual fuel engine is used for exergy analysis. Simulated biogas (mixture of methane and CO_2) is used instead of raw biogas. A single cylinder water cooled four stroke CI engine is used. Biogas is inducted through intake manifold and diesel is injected by using conventional diesel injector. Purified form of biogas (Methane) and variable methane:CO_2 ratios are used. Methane flow rate, methane enrichment and load are considered as input variables. In this study, along with the energy analysis, a detailed exergy analysis has been carried out and the 2nd law efficiency as well as the exergy destruction in each case has been found. The 2nd law efficiency was slightly lower than the 1st law efficiency and ranged from 16 to 39%. Exergy destruction is found to be in the range from 47 to 80%. Methane enrichment and increase in load provide lower exergy destruction. Lower biogas flow rate (3 lpm) provides better performance with lower energy destruction compared to diesel-only mode. Increase in biogas flow rate increases the percentage of energy destruction.

Keywords: Biogas, Dual fuel, Exergy, second law efficiency, energy destruction.

I. Introduction

Energy analysis gives only quantitative information about the performance of a heat engine while exergy analysis throws light on the quality aspects as well and helps in identifying the source of exergy loss which can aid in taking informed remedial action. In the recent past, few researchers have taken up experimental studies on Energy and Exergy analysis of in diesel engines fuelled with different blends. Khoobbakth et al. (2016) have studied the influence of load, speed and blend levels of bio-diesel and ethanol in diesel and found that exergy efficiency increased with increase of all the parameters studied. Maximum exergy efficiency of 36.92% was observed for a blend containing 0.17 litre biodiesel, 0.08 litre ethanol and 1 litre of diesel. Kul and Kahraman (2016) conducted experiments on biodiesel-diesel blends containing 5% bioethanol. They varied the quantity of diesel and biodiesel quantities and the speed (1000-3000 rpm) and found that the maximum exergy efficiency to be 29.38% for the 92% Diesel and 3% biodiesel blend. Interestingly, they found that the highest thermal and exergy efficiency was achieved for 100% diesel and blending actually resulted in the drop of efficiencies. Krishnamoorthi and Malayalamurthi (2017) studied the emission and exergetic behaviour of fuel blends in a variable compression ratio diesel engine. They used various combinations by blending aegle marmelos oil and diethyl ether with diesel which was varied from 50-100%. At 40% aegle marmelos oil and 10% diethyl ether blend, considerable improvement in thermal efficiency, exergy efficiency and low NOx were observed. Maximum exergy efficiency was found to be 63.88% at a compression ratio of 17.5. Paul et al (2017) experimentally studied the influence of 50% biodiesel (Pongamia piñata methyl ester) as a blend in diesel and ethanol. Best performance was observed at 35% diesel, 15% ethanol and 50% biodiesel. However, they noticed a marginal increase in NOx for this blend. Hoseinpour et al. (2017) tried gasoline fumigation in a DI diesel engine using waste cooking oil as biodiesel. Gasoline fumigation showed to increase energy and exergy efficiency at medium to high loads. Krishnamoorthi and Malayalamurthi (2018) further investigated the performance and emission behaviour of blends containing bael oil, diethyl ether and diesel. Best performance was observed at 30% bael oil and 10% diethyl ether blend with an exergy efficiency of 62.17% at full load. Odibi et al. (2019) investigated the effect of oxygenated fuels on a diesel engine using waste cooking biodiesel and triacetin. They observed that oxygenated fuels improved thermal efficiency. Also, Oxygen Ratio (ratio of total oxygen in air and fuel to the stoichiometric oxygen) was found to be a better representation of the air fuel combination compared to equivalence ratio. Increase in Oxygen Ratio decreases fuel exergy as well as the exhaust exergy. Taghavifar et al. (2019) performed a detailed numerical study on a diesel engine performance which uses dimethanol-methanol blends in an HCCI engine. They found that 10% methanol and 30% dimethyl ether gives highest exergetic performance while 30% methanol and 20% dimethyl ether gives the best thermal efficiency. Ma et al. (2020) used diesel-methanol blends in a dual fuel engine. They stated that due to the high latent heat of vaporization of methanol, the heat transfer exergy losses were low. They also found that the exhaust chemical exergy loss decreases with a rise in the intake air temperature and also improves exergy efficiency.
Overall, several experimental as well as few numerical studies were carried out to study the performance of various fuel blends with diesel and optimum operating conditions/blends were identified to obtain maximum exergy efficiency and good emission performance. However, to the best of the authors' knowledge, there was no article in

open literature which reports the results of exergy analysis in Biogas-Diesel blends. Hence, the present study sets out to study this by varying the proportion of biogas in a single cylinder water cooled four stroke diesel engine.

Biogas provides many advantages over other biomass-derived fuels. It can be transported as a compressed gas in cylinders or via pipelines easily (Tippayawong and Thanompongchart, 2010). Biogas typically contains 25 to 50% by volume of carbon dioxide (Feroskhan and Ismail, 2016). Since carbon dioxide is non-combustible, it also reduces the calorific value and energy density of biogas on the basis of volume. Therefore, the presence of CO_2 results in decreased flammability and flame intensity relative to pure methane. Self-ignition temperature of biogas is high and thus it prevents knocking in SI engines (Porpatham et al., 2012). But this makes difficulty to fire in CI engines. One possible way of addressing these drawbacks is to remove CO_2 content from the biogas (Ryckebosch et al., 2011), popularly known as methane enrichment.

The inducted biogas-air mixture can be ignited in CI engines either by injecting a small amount of diesel, or by compressing it until self-ignition occurs. These are respectively called the Dual Fuel and Homogenous Charge Compression Ignition (HCCI) modes. The present work concentrates only on dual fuel mode. In dual fuel mode, in the intake manifold, biogas is mixed with air and induced into the engine cylinder, where it is subjected to compression. A small quantity of diesel, called the pilot fuel, is injected into the top dead center (TDC). The pilot fuel's self ignition initiates a flame that passes through the combustion chamber, consuming the mixture of biogas and air.

II. Experimental Setup and Procedure

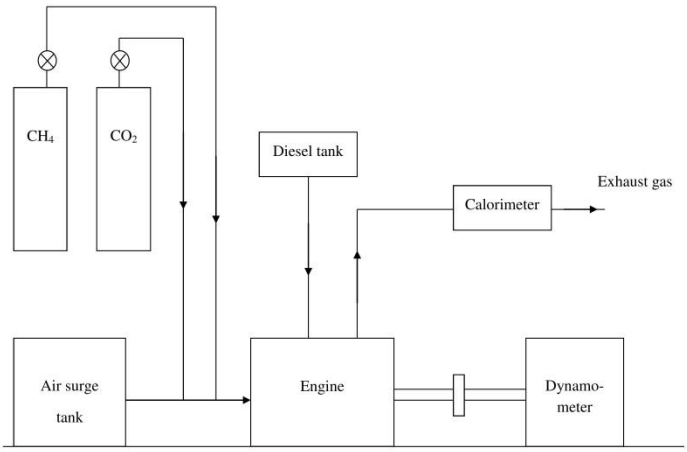

Fig. 1: Experimental Setup

Fig. 1 shows the schematic diagram of the experimental setup used in this study. A 4 stroke water colled single cylinder CI engine (8 HP, 1900 rpm) is modified to operate in dual fuel mode. Methane and CO_2 gases are stored in individual cylinders and its volume flow rates can be varied independently to make the variable composition of methane-enriched biogas. The dynamometer is attached to the engine to measure the brake power. Air flow rate, and diesel flow rate are measured using orifice meter and burette respectively. Rotameters are used to measure the flow rates of methane and CO_2. Caloriemeter is used to measure the heat loss to the exhaust gas.
Load, methane flow rate and methane enriched biogas are main variable in this study. Load is varied from 0 to 20 kg, which covers entire load range. Methane flow rate is varied from 0 to 10 lpm. 0 represents diesel-only operation. 2 cases of methane enriched biogas are analysed such as i) 12 lpm of methane + 4 lpm of CO_2 and ii) 12 lpm of methane + 1.5 lpm of CO_2. Effect of load, methane flow rate and methane enrichment on first law efficiency, second law efficiency and percentage of fuel enegy destroyed are discussed.

III. Energy and Exergy Analysis

The Energy and Exergy analysis is carried out according to the methodology and equations suggested by Kul and Kahraman (2016). The Thermo-mechanical and Chemical exergies of the exhaust gases are computed using the flow-sheeting software Cycle-Tempo by feeding its mass flow rate, temperature and composition. The dead state conditions were taken as 1 atmosphere and 25℃ and the air is assumed to contain 75.65% N_2, 20.3% O_2, 3.12 H_2O, 0.03% CO_2 and 0.9% Ar. The chemical exergy factor for biogas (methane) is taken as 1.04 as suggested for natural gas by Kotas (1985).

IV. Results and discussions

IV.1. First law efficiency

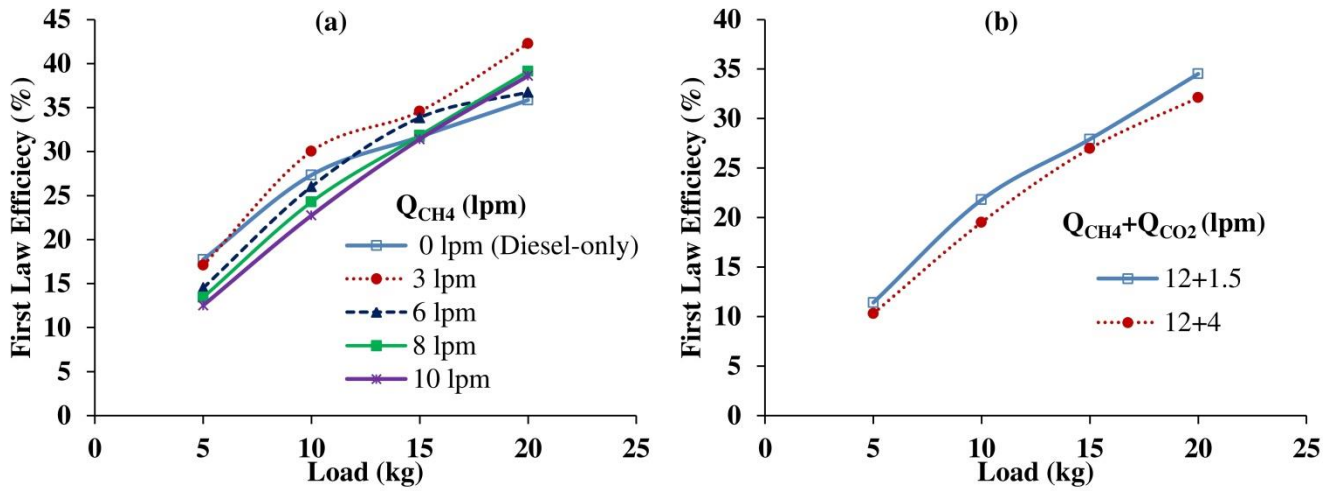

Fig. 2: Effect of (a) methane flow rate and (b) methane enrichment on First law efficiency

The variations in the first law efficiency for different methane flow rates are given in Fig. 2(a). First law based brake thermal efficiency at low loads can be observed to be low due to reduced power output and a high heat loss due to coolant flow. The inlet air with methane makes a very lean mixture, which may result in delayed burning or may not burn at all, when methane intake is less at low loads, where the excess air is high. The excessive exhaust and unaccounted losses in dual fuel operation substantiates this. However, the excess air quantity is lower at higher loads, resulting in more methane-air combustible mixtures. Methane combustion not only contributes to the use of excess air, but also increases the vaporization and burning rates of the diesel injected. This manifests as higher thermal efficiency of dual fuel mode at high loads in comparison to diesel-only mode. Fig. 2(b) shows the variance of the first law efficiency for methane enriched biogas. Methane flow rate of 12 litres per minute was used to study the effect of the biogas composition (methane: CO_2 ratio) on thermal efficiency and the CO_2 flow rate was varied in the range of 1.5-4 lpm. This resulted in a 90-70 percent difference in the methane fraction. The graph shows that improvement in efficiency is due to methane enrichment.

IV.2. Second law efficiency

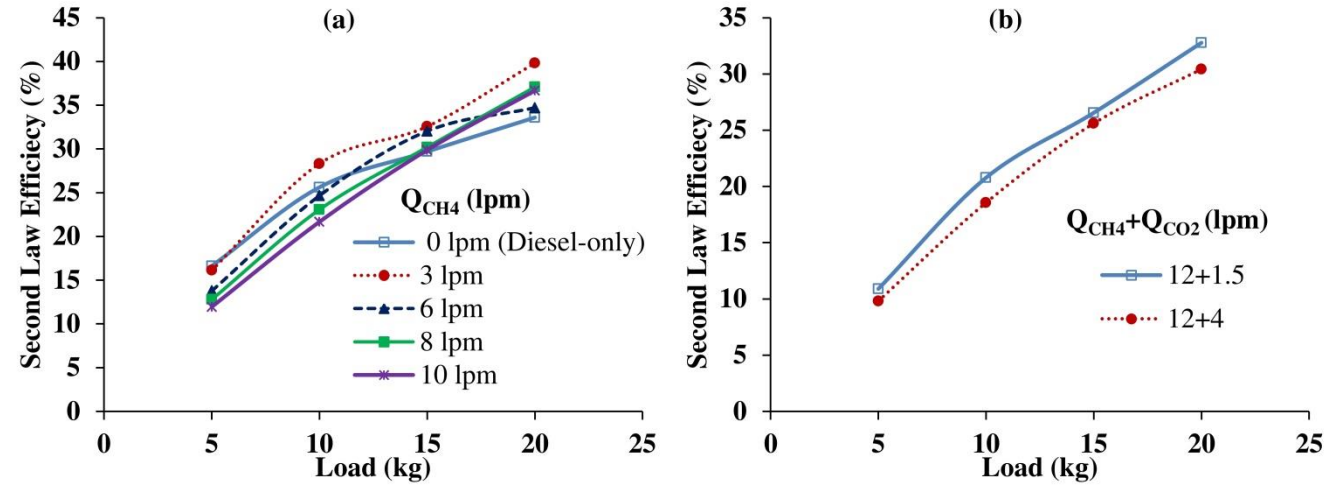

Fig. 3: Effect of (a) methane flow rate and (b) methane enrichment on second law efficiency

The effect of load and methane flow rate on the 2nd law efficiency is shown in Fig. 3(a). The 2nd law efficiency was slightly lower than the 1st law efficiency and ranged from 16 to 39% for 3 lpm of methane flow rate. Fig. 3(b) shows the variations of second law efficiency with respective to load and methane enrichment. Both first law and second law efficiency show the same trend.

IV.3. Percentage of fuel exergy destroyed

Effect of methane flow rate on fuel exergy destroyed is shown in Fig. 4(a). Low methane flow rate shows lowest fuel exergy destroyed. This is due to replacement of excess air quantity. High methane flow rate increases the percentage of fuel exergy destroyed due to high equivalence ratio. Effect of methane enrichment on fuel exergy destroyed is shown in Fig. 4(b). Removal of CO_2 reduces the fuel exergy destroyed due to improvement in its calorific value and ignitability.

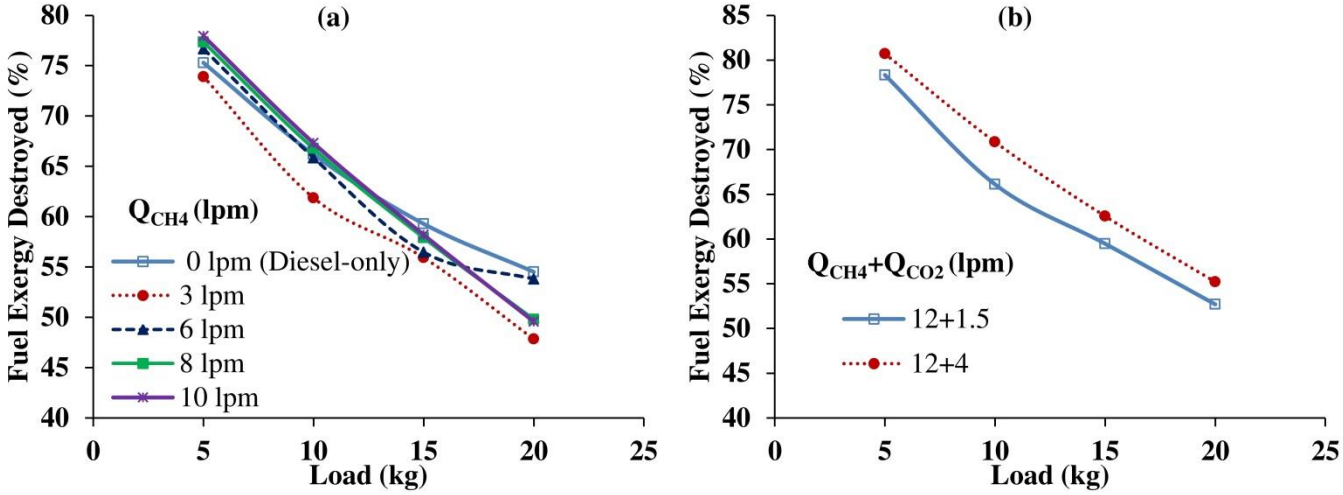

Fig. 4: Effect of (a) methane flow rate and (b) methane enrichment on percentage of fuel exergy destroyed

V. Conclusions

i. The 2nd law efficiency ranged from 16 to 39% in the range of this study.
ii. Both the 1st and 2nd law efficiencies increase due to increase in methane enrichment.
iii. High biogas flow rate results in higher fuel exergy destruction due to increased equivalence ratio.
iv. Exergy destruction due to combustion was predominant and ranged from 47 to 80% of the fuel exergy.
v. Significant improvement in the engine performance would be possible if the irreversibilities due to the combustion process could be reduced.

References

Feroskhan, M., Ismail, S., 2016. Investigation of the effects of biogas composition on the performance of a biogas – diesel dual fuel CI engine. Biofuels 7269. doi:10.1080/17597269.2016.1168025

Hoseinpour, M., Sadrnia, H., Tabasizadeh, M., Ghobadian, B., 2017. Energy and exergy analyses of a diesel engine fueled with diesel, biodiesel-diesel blend and gasoline fumigation. Energy 141, 2408–2420. doi:10.1016/j.energy.2017.11.131

Khoobbakht, G., Akram, A., Karimi, M., Najafi, G., 2016. Exergy and Energy Analysis of Combustion of Blended Levels of Biodiesel, Ethanol and Diesel Fuel in a di Diesel Engine. Appl. Therm. Eng. 25, 720–729. doi:10.1016/j.applthermaleng.2016.01.022

Kotas, T.J., 1985. Exergy analysis of simple processes, in: The Exergy Method of Thermal Plant Analysis. doi:10.1016/b978-0-408-01350-5.50011-8

Krishnamoorthi, M., Malayalamurthi, R., 2018. Availability analysis, performance, combustion and emission behavior of bael oil - diesel - diethyl ether blends in a variable compression ratio diesel engine. Renew. Energy 119, 235–252. doi:10.1016/j.renene.2017.12.015

Krishnamoorthi, M., Malayalamurthi, R., 2017. Experimental investigation on performance, emission behavior and exergy analysis of a variable compression ratio engine fueled with diesel - aegle marmelos oil - diethyl ether blends. Energy 128, 312–328. doi:10.1016/j.energy.2017.04.038

Kul, B.S., Kahraman, A., 2016. Energy and exergy analyses of a diesel engine fuelled with biodiesel-diesel blends containing 5% bioethanol. Entropy 18, 387. doi:10.3390/e18110387

Ma, B., Yao, A., Yao, C., Wu, T., Wang, B., Gao, J., Chen, C., 2020. Exergy loss analysis on diesel methanol dual fuel engine under different operating parameters. Appl. Energy 261, 114483. doi:10.1016/j.apenergy.2019.114483

Odibi, C., Babaie, M., Zare, A., Nabi, M.N., Bodisco, T.A., Brown, R.J., 2019. Exergy analysis of a diesel engine with waste cooking biodiesel and triacetin. Energy Convers. Manag. 198, 111912. doi:10.1016/j.enconman.2019.111912

Paul, A., Panua, R., Debroy, D., 2017. An experimental study of combustion, performance, exergy and emission characteristics of a CI engine fueled by Diesel-ethanol-biodiesel blends. Energy 141, 839–852. doi:10.1016/j.energy.2017.09.137

Porpatham, E., Ramesh, A., Nagalingam, B., 2012. Effect of compression ratio on the performance and combustion of a biogas fuelled spark ignition engine. Fuel 95, 247–256. doi:DOI 10.1016/j.fuel.2011.10.059

Ryckebosch, E., Drouillon, M., Vervaeren, H., 2011. Techniques for transformation of biogas to biomethane. Biomass and Bioenergy 35, 1633–1645. doi:10.1016/j.biombioe.2011.02.033

Taghavifar, H., Nemati, A., Walther, J.H., 2019. Combustion and exergy analysis of multi-component diesel-DME-methanol blends in HCCI engine. Energy 187, 115951. doi:10.1016/j.energy.2019.115951

Tippayawong, N., Thanompongchart, P., 2010. Biogas quality upgrade by simultaneous removal of CO2 and H2S in a packed column reactor. Energy 35, 4531–4535. doi:10.1016/j.energy.2010.04.014

Metaheuristic approaches for solving the Energy optimization problem of Multiple Stage Evaporator System

[1*]Drishti Yadav, [2*]Om Prakash Verma
[1*, 2*]Department of Instrumentation and Control Engineering, Dr B R Ambedkar National Institute of Technology, G.T. Road, Amritsar Bypass, Jalandhar (Punjab) - 144011, India
E-mails: [1*]drish131196@gmail.com, [2*]vermaop@nitj.ac.in

Abstract

With the colossal proliferation of energy requirements, bourgeoning global warming concerns and flourishing expenses of energy supplies, the present era proclaims towards the utilization of renewable energy sources for guaranteeing sustainability. In addition, the emphasis is on the enhancement in energy efficiency of energy-intensive industries. Black liquor derived as a waste residual stream during the Kraft recovery process in Pulp and Paper mills is an incipient biomass energy resource. With an eye to produce a combustible material, black liquor is evaporated to high dryness in a Multiple Stage Evaporator (MSE) system which is the premier energy intensive unit in Pulp and Paper mills. Thus, Energy optimization of MSE system is an attention-grabbing concern pertaining to the contemporary global energy scenario. This kindles our attention to maximize Steam Economy (SE) and abate Steam Consumption (SC) by precise steady-state modeling and simulation of MSE. The energy efficiency parameters SE and SC are governed by numerous operating parameters comprising liquor flow rates, amount of fresh steam input, and temperatures of the vapor generated at each stage. Hence, the optimum values of these parameters reflect the optimum process energy efficiency. With this insight, the present work reconnoiters the non-linear modeling and simulation of Heptads' Effect MSE operated in the backward feed flow configuration. We present an innovative solution in quest of optimum unknown process operating parameters *via* metaheuristic optimization approaches. Optimizers including Particle Swarm Optimization and Ant Colony Optimization have been exploited for energy optimization of MSE. The simulated results demonstrate the robustness, efficiency and exploratory capabilities of these metaheuristic approaches to search the best estimates of unknown process variables. Tabular, evocative and graphical demonstrations have been utilized for comparative analysis of these metaheuristic approaches with reference to various performance parameters of MSE.

Keywords: Multiple Stage Evaporator, Energy Optimization, Steam Economy, Steam Consumption, Metaheuristics, Particle Swarm Optimization, Ant Colony Optimization

Nomenclature and Acronyms

λ	Latent heat of vaporization (kJ/kg)	MSE	Multiple Stage Evaporator
A	Heat transfer area (m^2)	PSO	Particle Swarm Optimization
ACO	Ant Colony Optimization	SC	Steam Consumption (kg/s)
BFF	Backward Feed Flow	SE	Steam Economy
f	Feed	SNLAE	Simultaneous Non-Linear Algebraic Equation
h_L *or h*	Enthalpy of black liquor (kJ/kg)	*T*	Temperature of Vapor produced (˚C)
H	Enthalpy of vapor (kJ/kg)	*U*	Overall heat transfer coefficient (kW/m^2˚C)
HEE	Heptads' Effect Evaporator	*V*	Vapor flow rate (kg/s)
J	Objective function	*x*	Liquor Concentration
L	Flow rate of black liquor (kg/s)	*z*	Decision variables

I. Introduction

Multiple Stage Evaporators (MSEs) employed in the Kraft Recovery Process of Paper mills to concentrate the weak black liquor for its use as biofuel are leading energy-intensive systems. The present-day worldwide energy scenario accentuates on the optimization of energy efficiency of MSE *i.e.*, the energy efficiency parameters, Steam Economy (SE) and Steam Consumption (SC). SE depends on various unknown parameters such as vapor temperatures, flow rates of liquor at various stages and amount of fresh steam supplied (SC). A gigantic volume of literature on modeling, simulation and optimization of MSE is accessible (Bhargava *et al.*, 2008a; Kaya & Sarac, 2007; Sharan & Bandyopadhyay, 2016a; Sharan & Bandyopadhyay, 2016b; Verma *et al.*, 2016). Various approaches have been employed to simulate the non-linear models of MSE (Bhargava *et al.*, 2008b; Gautami & Khanam, 2012; Verma *et al.*, 2017a; Verma *et al.*, 2018b; Verma *et al.*, 2017b; Verma *et al.*, 2018a; Verma & Manik, 2017c). Furthermore, metaheuristic approaches namely Ant Colony Optimization (ACO) and Particle Swarm Optimization (PSO) have established their prospective for solution to a diverse variety of complex optimization problems in recent years due to the inefficiency and inaccuracy of prevailing numerical techniques.

Within the above framework, in the present analysis, an attempt has been made to optimize the energy efficiency of MSE by maximizing SE and minimizing SC. For this, a heptads' effect evaporator (HEE) based MSE system in the backward feed flow (BFF) configuration operating in a North Indian paper mill (Saharanpur, Uttar Pradesh, India) has been considered. The optimum values of unknown process parameters are efficiently tracked down by means of metaheuristic-optimization algorithms ACO and PSO. The non-linear mathematical model of MSE consists of simultaneous non-linear algebraic equations (SNLAEs) with fourteen unknown decision variables (6-Vapor temperatures, T_i, i= 2 - 7, 7-Liquor flow rates, L_i, i = 1 - 7 and flow rate of steam input (SC), V_1). These

SNLAEs are transformed into optimization problem to obtain the optimum values of decision variables by ACO and PSO, thereby yielding optimum energy efficiency parameters SE and SC.

II. Process Description

The heptad's effect MSE system operating in the BFF configuration is depicted in Fig.1. Here, weak black liquor and the fresh steam are fed to 7th and 1st stages respectively. The vapor generated at each stage is fed to the consecutive stage as heat source. The concentrated liquor as a product is recovered from the 1st stage. The operating parameters of the MSE system have been presented in Table 1 (the data has been taken from the aforementioned North Indian paper mill).

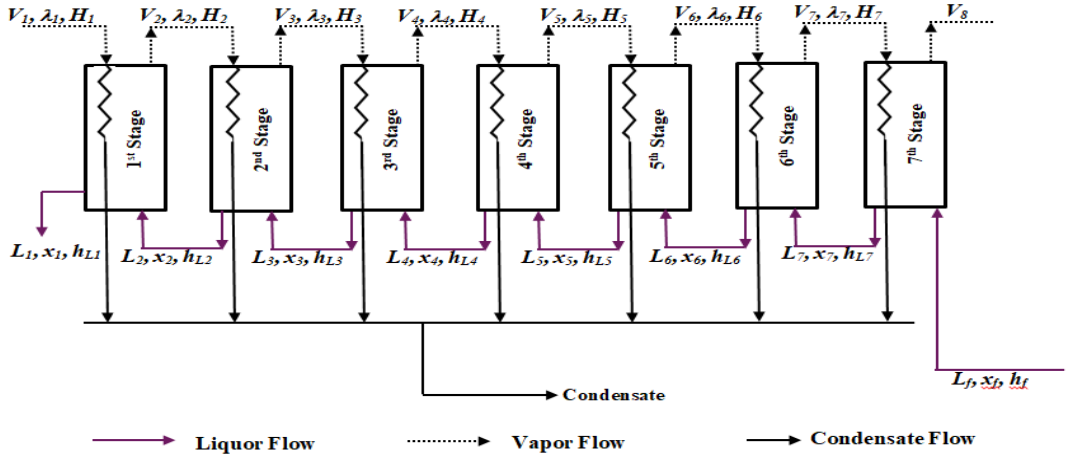

Fig. 1. Schematic diagram of a heptad's effect backward feed flow configured MSE

Table 1. Operating parameters for the considered MSE system

Parameter(s)	Value(s)
Number of stages	7
Concentration of inlet black liquor, x_f	0.118
Flow rate of inlet weak black liquor, L_f	15.611 kg/s
Vapor temperature at last stage	52˚C
Enthalpy of inlet black liquor, h_f	254.8 kJ/kg
Area of stages (A_1 to A_7)	540, 540, 660, 660, 660, 660, 690 m^2

III. Development of non-linear mathematical model in steady state

The non-linear mathematical model of MSE can be developed by considering a few assumptions such as negligible fouling within the evaporator, negligible heat loss between vapor chest and tube, and negligible boiling point elevations. The model development is carried out by employing the energy balance equations at each stage by considering the energy entering into and leaving from the steam chest of each evaporator stage (Verma *et al.*, 2017b). Applying the energy balance to the first stage of MSE given in Fig. 1, we have

[Energy due to the Liquor entering from the 2nd stage] + [Energy due to Steam entering the 1st stage] = [Energy due to the Vapor leaving the 1st stage] + [Energy due to the Liquor leaving the 1st stage]

which yields Eq. (1).

$$V_1\lambda_1 + L_2h_2 = L_1h_1 + V_2H_2 \quad \textbf{(1)}$$

By applying total material balance around the first stage, we obtain: $V_2 = L_2 - L_1$. Therefore, Eq. (1) can be further expressed by Eq. (2) as:

$$V_1\lambda_1 + L_1(H_2 - h_1) + L_2(h_2 - H_2) = 0 \quad \textbf{(2)}$$

Employing the heat balance equation to the first stage of the system, we achieve Eq. (3):

$$U_1A_1(T_1 - T_2) - V_1\lambda_1 = 0 \quad \textbf{(3)}$$

Similarly, for the rest of the stages (i = 2 - 6), the rate of steam input, V_i may be replaced by means of total material balance across the i^{th} stage as: $V_{i+1} = L_{i+1} - L_i$. The derived equations are represented by Eqs. (4) - (5):

$$(L_i - L_{i-1})\lambda_i + L_i(H_{i+1} - h_i) + L_{i+1}(h_{i+1} - H_{i+1}) = 0 \quad \textbf{(4)}$$

$$U_iA_i(T_i - T_{i+1}) - (L_i - L_{i-1})\lambda_i = 0 \quad \textbf{(5)}$$

Similarly, for the last (seventh) stage, the model may be rendered through Eqs. (6) - (7):

$$(L_7 - L_6)\lambda_7 + L_7(H_8 - h_7) + L_f(h_f - H_8) = 0 \quad \textbf{(6)}$$

$$U_7 A_7 (T_7 - T_f) - (L_7 - L_6)\lambda_7 = 0 \quad \textbf{(7)}$$

Finally, it may be concluded that each stage of the MSE yields two algebraic equations. On account of the non-linear behavior of various thermo-physical correlations (such as latent heat of vaporization (λ), enthalpy of vapor (H) and enthalpy of liquor (h_L *or* h)) (Verma *et al.*, 2017b), the resulting mathematical model is non-linear in nature. These correlations depend on the concentration of black liquor (x_i) and unknown parameters, T_i (i = 2 - 7). As a result, we obtain SNLAEs for the HEE consisting of fourteen equations.

IV. Formulation of optimization problem : Transformation of SNLAEs into Objective function

In order to optimize the energy efficiency of HEE, the developed SNLAEs represented by $f_e(z)$ = 0 (e = 1 - 14) are transformed into the optimization problem by using the merit function ***J(z)*** given by Eq. (8). Consequently, ***J(z)*** is the non-linear objective function to be optimized for evaluation of the optimum values of unknown decision variables ***z***, *i.e.*, V_1, T_i (i = 2 – 7) and L_i (i = 1 – 7). The formulated optimization model is simulated in the MATLAB programming environment using the aforesaid metaheuristic approaches and using the conditions given by Eqs. (9)-(10). The boundary conditions of T_i and L_i are provided in Table 2 (Verma *et al.*, 2017b). Temperature of vapor generated at 1st stage is kept constant at 147˚C. For SC, the selected feasible bound is V_1 (kg/s)∈[0:3]. SE is evaluated by taking the ratio of total vapor generated to the amount of fresh steam supplied *i.e.*, V_1. Mathematically, SE is expressed by Eq. (11) such that optimum SE is computed via the optimum values of the unknown parameters L_1 and V_1.

$$J(z) = \sum_{e=1}^{14} abs(f_e(z)) \quad \textbf{(8)}$$

$$T_i > T_{i+1},\ (i = 2-7),\quad T_7 > 52\,(T_8),\quad L_{i+1} > L_i,\ (i = 1-7) \quad \textbf{(9)}$$

$$T_i > 0,\ (i = 2-7) \ \text{ and } \ L_i > 0,\ (i = 1-7) \quad \textbf{(10)}$$

$$SE = \frac{\sum_{i=2}^{8} V_i}{V_1} = \frac{L_f - L_1}{V_1} \quad \textbf{(11)}$$

Table 2. Boundary conditions for various operating parameters for i^{th} stage for the considered HEE

Vapor Temperatures	$T_i(°C) \in [100:110;\ 70:85;\ 66:74;\ 60:70;\ 55:65;\ 52:63],\ (i = 2-7)$
Liquor Flow rates	$L_i(kg/s) \in [2:5;\ 3.5:6;\ 4.5:7;\ 6.5:9;\ 9:11;\ 10.5:13;\ 13:15],\ (i = 1-7)$

V. Optimization Strategies

Due to the accessibility of inclusive and in-depth discussion about ACO and PSO in ample volume of research works, only a brief outline has been presented here.

Ant Colony Optimization (ACO)

ACO is principally inspired by the foraging actions of real ants. The unintended communication between ants by means of pheromone traces facilitates the estimation of optimal routes from their nest and the source of foodstuff. Accordingly, this proficiency of real ant colonies leading to the evolvement of artificial ant colonies has been efficiently utilized for the estimation of approximate solutions of real-time complex optimization problems. In this work, the objective function *J(z)* is simulated by using ACO by taking maximum iterations of 1000 as the stopping criterion. Algorithm 1 given in Table 3 provides a brief summary of the generalized ACO Algorithm.

Table 3. Metaheuristic Approaches

Algorithm 1: ACO	**Algorithm 2: PSO**
Objective function *J(z)* Set the ACO parameters Create initial population of ants Initialize pheromone traces and parameters **while** (*stopping criterion*) Calculate fitness of each ant For each ant, compute the fitness Determine the best position of each ant Find the best global ant Update the Pheromone trace **end while**	Objective function *J(z)* Set the PSO parameters Initialize locations and velocity of particles. **while** (*stopping criterion*) Calculate fitness of particles Select Personal best and Global best Update velocity and position of particles Evaluate fitness of particles. If the fitness increases, update Personal best and Global best **end while** Output the best solution as Gbest

Particle swarm optimization (PSO)

The objective function *J(z)* is simulated by using PSO in order to examine and explore its search space by tuning the trajectories of individual agents (particles *i.e.* initial solutions). The core objective is to find the global best amid all the current best solutions until there is no improvement in the objective function value or a certain number of iterations have been performed. In this work, maximum iteration (1000) is chosen as the stopping criterion. The PSO Algorithm is summarized in Algorithm 2 given in Table 3.

VI. Results and discussions

The optimum SE and SC (*i.e.* V_1) evaluated using ACO and PSO are presented in Table 4 along with other estimated process parameters including L_i, T_i for comparative analysis. The results are obtained by performing 20 independent runs of each metaheuristic approach. Additionally, a comparative visualization of optimum values of energy efficiency parameters acquired via these algorithms is exemplified in Fig. 2. The simulation results demonstrate that SE and SC obtained by PSO are 5.733 and 2.172 kg/s respectively. The SE obtained by PSO is better compared to that obtained by ACO (*i.e.*, 5.676). Fig. 3 shows a bar-graph illustration for comparative analysis of SE of HEE based MSE with previous reported literature works, the present simulated results and real-time plant estimates. As evident from Fig. 3, the present investigation offers better results relative to erstwhile research works.

Table 4. Simulation Results of the HEE system for the considered data.

Process Parameters	Metaheuristic approach	Stage Number						
		1	2	3	4	5	6	7
L_i (in kg/s)	ACO	3.42	5.21	6.86	8.55	10.24	11.94	13.62
	PSO	3.15	5.11	7.00	9.00	10.70	12.25	13.75
T_i (in ˚C)	ACO	147.00	97.54	72.78	66.91	61.42	57.83	54.44
	PSO	147.00	100.00	72.73	66.00	60.00	56.75	53.99
SE	ACO				**5.676**			
	PSO				**5.733**			
SC (V_1) (in kg/s)	ACO				**2.145**			
	PSO				**2.172**			

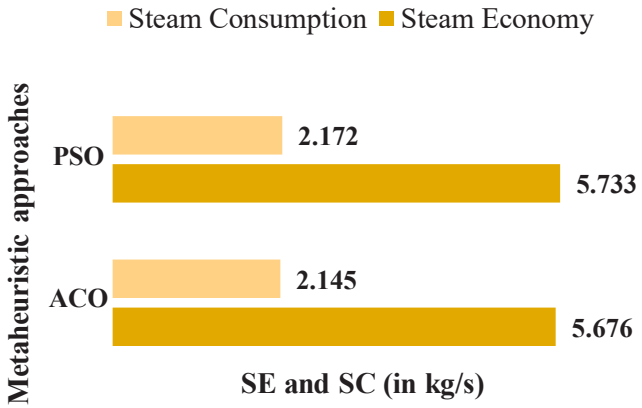

Fig. 2. Comparative illustration of energy efficiency parameters estimated via ACO and PSO

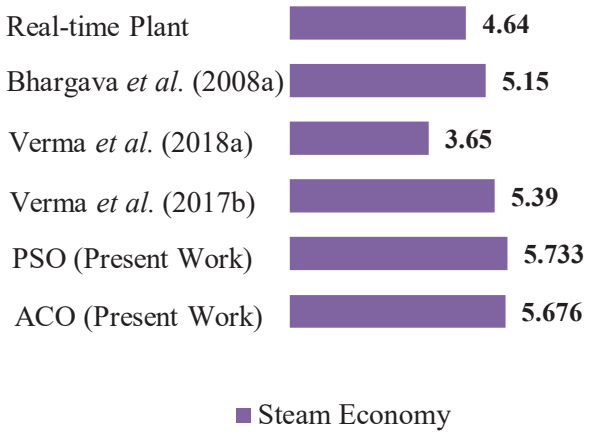

Fig. 3. Comparison of SE obtained in present work with erstwhile literature and real-time plant estimate

VII. Conclusions

The present work attempts to solve the energy optimization problem of MSE via metaheuristic approaches. The mathematical model of HEE comprising of SNLAEs is simulated using ACO and PSO in the MATLAB environment to search optimum values of unknown process parameters, consequently yielding optimum energy efficiency parameters SE and SC. This work demonstrates that ACO and PSO efficiently search the best operating conditions and validate their potential in simulating complex non-linear models that are frequently encountered in several industrial processes. Further, the present work is limited to ideal condition assumptions wherein boiling point elevation, heat loss, scaling and fouling effects, foaming etc. have not been considered and provides the scope for future research.

References

Bhargava, R., Khanam, S., Mohanty, B., & Ray, A. K. (2008a). Simulation of flat falling film evaporator system for concentration

of black liquor. *Computers & Chemical Engineering*, 32(12), 3213-3223.

Bhargava, R., Khanam, S., Mohanty, B., & Ray, A. K. (2008b). Selection of optimal feed flow sequence for a multiple effect evaporator system. *Computers & Chemical Engineering*, *32*(10), 2203-2216.

Gautami, G., & Khanam, S. (2012). Selection of optimum configuration for multiple effect evaporator system. *Desalination*, *288*, 16-23.

Kaya, D., & Sarac, H. I. (2007). Mathematical modeling of multiple-effect evaporators and energy economy. *Energy*, *32*(8), 1536-1542.

Sharan, P., & Bandyopadhyay, S. (2016a). Energy integration of multiple effect evaporators with background process and appropriate temperature selection. *Industrial & Engineering Chemistry Research*, *55*(6), 1630-1641.

Sharan, P., & Bandyopadhyay, S. (2016b). Energy optimization in parallel/cross feed multiple-effect evaporator based desalination system. *Energy*, *111*, 756-767.

Verma, O. P., & Manik, G. (2017c). Solution of SNLAE model of backward feed multiple effect evaporator system using genetic algorithm approach. *International Journal of System Assurance Engineering and Management*, *8*(1), 63-78.

Verma, O. P., Manik, G., & Mohammed, T. H. (2017a). Energy management in multi stage evaporator through a steady and dynamic state analysis. *Korean Journal of Chemical Engineering*, 34(10), 2570-2583.

Verma, O. P., Manik, G., Jain, V. K., Jain, D. K., & Wang, H. (2018a). Minimization of energy consumption in multiple stage evaporator using Genetic Algorithm. *Sustainable Computing: Informatics and Systems*, *20*, 130-140.

Verma, O. P., Mohammed, T. H., Mangal, S., & Manik, G. (2016). Mathematical modeling of multistage evaporator system in Kraft recovery process. In *Proceedings of Fifth International Conference on Soft Computing for Problem Solving* (pp. 1011-1042). Springer, Singapore.

Verma, O. P., Mohammed, T. H., Mangal, S., & Manik, G. (2017b). Minimization of energy consumption in multi-stage evaporator system of Kraft recovery process using Interior-Point Method. *Energy*, *129*, 148-157.

Verma, O. P., Mohammed, T. H., Mangal, S., & Manik, G. (2018b). Optimization of steam economy and consumption of heptad's effect evaporator system in Kraft recovery process. *International Journal of System Assurance Engineering and Management*, *9*(1), 111-130.

Metaheuristic-driven optimization for solution of dynamic model of Multiple Stage Evaporator System of Paper mills

[1*]Drishti Yadav, [2*]Om Prakash Verma
[1*, 2*]Department of Instrumentation and Control Engineering, Dr B R Ambedkar National Institute of Technology, G.T. Road, Amritsar Bypass, Jalandhar (Punjab) - 144011, India
E-mails: [1*]drish131196@gmail.com, [2*]vermaop@nitj.ac.in

Abstract
Multiple Stage Evaporators (MSEs) used in paper mills for concentrating the black liquor to produce a combustible material are premier energy intensive units. The enhancement in energy efficiency of MSE is prominently accentuated attributable to the contemporary energy scenario. Moreover, a tight and appropriate control is essential in order to encounter the necessities for a worthy product quality along with the assurance of optimum energy efficiency. A thorough understanding of the system dynamics is indispensable for the design of an accurate and appropriate control algorithm for effective set-point tracking and disturbance rejection. In order to investigate the open-loop dynamics of MSE, it is mandatory to ascertain the steady-state operating parameters for simulating the dynamic model of the system. Henceforth, in advance of analyzing the system transience, the steady-state analysis has been performed. The optimum steady-state operating parameters are acquired by simulating the nonlinear steady-state model encompassing simultaneous non-linear algebraic equations (SNLAEs). The present work investigates the non-linear dynamic modeling of Heptads' stage based MSE and further, it has been simulated to obtain the transient response of the system. The dynamic model involves simultaneous non-linear ordinary differential equations (SNLODEs) of first order. These SNLODEs are represented as an optimization problem by means of elementary ideas of Fourier series expansion along with metaheuristic approach to yield their approximate solutions. The rigorous simulation of the dynamic model aids in the analysis of open-loop dynamic behavior of the overall system. For simulation work, Water Cycle Algorithm (WCA), a metaheuristic approach has been exploited to solve these SNLAEs and SNLODEs. The simulation results of steady-state and dynamic models of MSE succor in the selection and design of an efficient control algorithm for optimizing steam economy and monitoring the quality of the product.

Keywords: Energy Optimization, Metaheuristics, Multiple Stage Evaporator, Steam Economy, Non-linear Dynamic Model, Water Cycle Algorithm

Nomenclature and Acronyms

λ	Latent heat of vaporization (kJ/kg)	R	Residual function
A	Heat transfer area (m^2)	SC	Steam Consumption (kg/s)
ACO	Ant Colony Optimization	SNLAE	Simultaneous Non-Linear Algebraic Equation
BFFC	Backward Feed Flow Configuration	SNLODE	Simultaneous Non-Linear Ordinary Differential Equation
BL	Black Liquor	*T*	Temperature of Vapor produced (˚C)
f	Feed	*U*	Overall heat transfer coefficient (kW/m^2˚C)
h_L *or h*	Enthalpy of black liquor (kJ/kg)	*V*	Vapor flow rate (kg/s)
H	Enthalpy of vapor (kJ/kg)	W	Weight function
HSE	Heptads' Stage Evaporator	WCA	Water Cycle Algorithm
J	Objective function	WRF	Weighted Residual Function
L	Flow rate of black liquor (kg/s)	*x*	Liquor Concentration
MSE	Multiple Stage Evaporator	*z*	Decision variables

I. Introduction

In order to guarantee optimum energy efficiency and an effective control of Multiple Stage Evaporators (MSEs) employed for enhancing the concentration of weak black liquor (BL), the comprehensive knowledge of system behavior is essential. Moreover, the study of system dynamics for controller design is considerably ruled by the system behavior in the steady-state. This emphasizes on an inclusive understanding of the solution of mathematical model of MSE in both steady and dynamic states. Various researchers have attempted to simulate the mathematical model of MSE under steady-state (Bhargava *et al.*, 2008; Kaya & Sarac, 2007; Verma *et al.*, 2016a; Verma *et al.*, 2017b; Verma & Manik, 2017c; Verma *et al.*, 2018a; Verma *et al.*, 2018b). In addition, a considerable amount of literature is available on the dynamic simulation and control of MSE (Verma *et al.*, 2016b; Verma *et al.*, 2017a; Verma & Manik, 2018c; Verma *et al.*, 2018d). In addition, approximate solutions to ordinary differential equations can be obtained by metaheuristic approaches such as Particle Swarm Optimization, Cuckoo Search Algorithm and Water Cycle Algorithm (WCA) (Babaei, 2013; Sadollah *et al.*, 2015).

The present investigation attempts to solve the dynamic model consisting of SNLODEs by utilizing the rudimentary concepts of Fourier series expansion and Water Cycle Algorithm (WCA), a novel metaheuristic approach. The initial conditions required to solve SNLODEs are acquired by the steady-state process parameters obtained by simulating the non-linear steady state model of MSE *via* WCA. This work utilizes a heptads' stage

evaporator (HSE) based MSE operating in the backward feed flow configuration (BFFC) installed at a North Indian paper mill (Saharanpur, Uttar Pradesh, India). The solution of SNLODEs of the dynamic model of MSE yields the time variation of concentration of Black Liquor and temperature of vapor generated at each stage of MSE.

II. Process Description and Mathematical modeling

Fig.1 shows the schematic of heptad's stage MSE system operating in the BFFC wherein the weak Black Liquor is introduced to the 7th stage with the fresh steam being fed to the 1st stage. Each stage utilizes the vapor generated at the previous stage as source of heat. The 1st stage yields the concentrated Black Liquor to be used as a fuel. Table 1 presents the operating parameters of the considered MSE picked from the aforementioned North Indian paper mill.

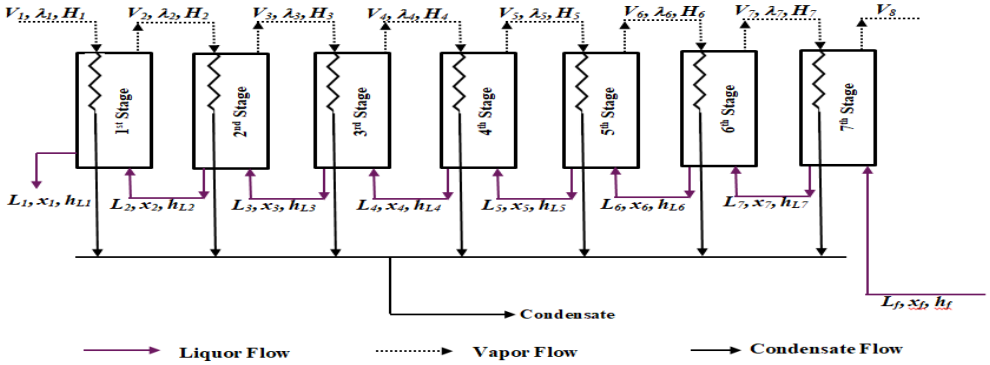

Fig. 1. Schematic of HSE based MSE in BFFC

Table 1. Operating parameters of MSE

Parameter(s)	Value(s)
Number of stages	7
Temperature of inlet BL, T_f	65˚C
Temperature of inlet fresh steam, T_s	147˚C
Vapor temperature at first stage, T_1	147˚C
Concentration of inlet BL, x_f	0.118
Flow rate of inlet weak BL, L_f	15.611 kg/s
Vapor temperature at last stage	52˚C
Enthalpy of inlet BL, h_f	254.8 kJ/kg
Area of stages (A_1 to A_7)	540, 540, 660, 660, 660, 660, 690 m^2
Mass hold up for each stage, M (kg)	0.833

Non-linear Mathematical model in Steady-state

The non-linear mathematical model under steady-state consists of SNLAEs encompassing fourteen equations with fourteen unknown decision variables z (V_1, T_i (i = 2 – 7) and L_i (i = 1 – 7)). The model development has been previously carried out (Verma *et al.*, 2017b) and the SNLAEs developed in the erstwhile literature (Verma *et al.*, 2017b) are utilized here for simulation purpose. These SNLAEs are expressed by Eqs. (1) - (6).

For Stage 1:

$$V_1\lambda_1 + L_1(H_2 - h_1) + L_2(h_2 - H_2) = 0 \quad (1)$$

$$U_1A_1(T_1 - T_2) - V_1\lambda_1 = 0 \quad (2)$$

For stages i = 2 – 6:

$$(L_i - L_{i-1})\lambda_i + L_i(H_{i+1} - h_i) + L_{i+1}(h_{i+1} - H_{i+1}) = 0 \quad (3)$$

$$U_iA_i(T_i - T_{i+1}) - (L_i - L_{i-1})\lambda_i = 0 \quad (4)$$

For Stage 7:

$$(L_7 - L_6)\lambda_7 + L_7(H_8 - h_7) + L_f(h_f - H_8) = 0 \quad (5)$$

$$U_7A_7(T_7 - T_f) - (L_7 - L_6)\lambda_7 = 0 \quad (6)$$

Non-linear Mathenatical model in Dynamic-state

The non-linear dynamic model encompasses SNLODEs of first order with concentrations (x_i, i = 1 - 7) and vapor temperatures (T_i, i = 2 - 7) as dependent variables and time as the independent parameter. The fourteen differential equations, *i.e,* the SNLODEs developed in the erstwhile literature (Verma *et al.*, 2017a) using the thermo-physical correlations (λ, H and h_L *or* h) (Verma *et al.*, 2017b) are utilized here for simulation of dynamic model of MSE. These SNLODEs expressed by Eqs. (1) - (6) are given as follows:

At stage

$$\frac{dx_1}{dt} = \frac{L_2(x_2 - x_1) + x_1V_1}{M_1} \quad (7)$$

1:
$$\frac{dT_1}{dt} = \frac{[\{L_2\,(4.187 - 2.26098\,x_2)(T_2 - T_1)\} + V_1\lambda(T_s) + V_2(4.187T_1 - H(T_1)]}{M_1\,(4.187 - 2.26098\,x_1)} \quad \textbf{(8)}$$

$$\frac{dx_i}{dt} = \frac{L_{i+1}(x_{i+1} - x_i) + x_i V_i}{M_i}, \text{ for } i = 2 \text{ to } 6 \quad \textbf{(9)}$$

At stage 2 - 6:
$$\frac{dT_i}{dt} = \frac{[\{L_{i+1}\,(4.187 - 2.26098\,x_{i+1})(T_{i+1} - T_i)\} + V_i\lambda(T_{i-1}) + V_{i+1}(4.187T_i - H(T_i)]}{M_i\,(4.187 - 2.26098\,x_i)}, \text{ for } i = 2 \text{ to } 6 \quad \textbf{(10)}$$

At stage 7:
$$\frac{dx_7}{dt} = \frac{L_f(x_f - x_7) + x_7 V_7}{M_7} \quad \textbf{(11)}$$

$$\frac{dT_7}{dt} = \frac{[\{L_f\,(4.187 - 2.26098\,x_f)(T_f - T_7)\} + V_7\lambda(T_6) + V_8(4.187T_7 - H(T_7)]}{M_7\,(4.187 - 2.26098\,x_7)} \quad \textbf{(12)}$$

III. Optimization strategy: Water Cycle Algorithm (WCA)

For the estimation of optimum steady-state process parameters, WCA, a nature-inspired metaheuristic optimization method, has been utilized in this work, to optimize the objective function, ***J(z)***. WCA is principally enthused by nature and its elementary concepts are highlighted on the characteristics of hydrological (water) cycle and downhill course of rivers and streams headed for the sea in the real world. Here, we present only a brief pseudo code for the WCA as demonstrated in Algorithm 1 due to the availability of humungous amount of literature works related to WCA.

Algorithm 1: Steps for WCA

Objective function ***J(z)*** or ***WRF***
1. Set the WCA parameters.
2. Create random initial population and form the initial streams (raindrops), rivers, and sea.
3. Evaluate the value (cost) of each raindrop.
4. Compute the intensity of flow for rivers and sea.
5. Interchange the position of river with a stream yielding the best solution. Similarly, interchange the position of river with the sea in case a river finds better solution than the sea.
6. Check the evaporation condition.
7. Start the raining process if the evaporation condition is met.
8. Reduce the value of the evaporation condition constant.
9. If the stopping criterion is met, end the algorithm. Otherwise, go back to Step 5.

Solution of Steady-state model

The steady-state process parameters are computed by converting the SNLAEs (Eqs. (1) - (6)) into objective function ***J(z)*** given by Eq. (13). ***J(z)*** is optimized to yield the steady-state process parameters *z* (V_1, T_i (i = 2 – 7) and L_i (i = 1 – 7)) by WCA using the conditions given by Eqs. (14)-(15). For Steam Consumption (SC) *i.e.*, the flow rate of steam input, the selected feasible bound is V_1 (kg/s) ∈ [0:3]. Table 2 provides the boundary conditions of T_i and L_i used for optimizing ***J(z)*** (Verma *et al.*, 2017b).

$$J(z) = \sum_{e=1}^{14} abs(f_e(z)) \quad \textbf{(13)}$$

$$T_i > T_{i+1},\ (i = 2-7), \quad T_7 > 52\,(T_8) \quad \textbf{(14)}$$

$$T_i > 0,\ (i = 2-7) \text{ and } L_i > 0,\ (i = 1-7) \quad \textbf{(15)}$$

Table 2. Boundary conditions for Vapor temperatures and Liquor flow rates for i^{th} stage of the considered HEE

Vapor Temperatures	$T_i(°C) \in [100:110;\ 70:85;\ 66:74;\ 60:70;\ 55:65;\ 52:63],\ (i = 2-7)$
Liquor Flow rates	$L_i(kg/s) \in [2:5;\ 3.5:6;\ 4.5:7;\ 6.5:9;\ 9:11;\ 10.5:13;\ 13:15],\ (i = 1-7)$

Solution of Non-linear dynamic model

The non-linear dynamic model of MSE comprising of SNLODEs are represented as an optimization problem (Babaei, 2013; Sadollah *et al.*, 2015). The steady-state process parameters obtained by simulation of non-linear steady-state model serve as the initial conditions of SNLODEs. The dependent variables of SNLODEs *i.e.* x_i (i = 1 - 7) and T_i (i = 1 - 7) can be expressed as the partial sum of the Fourier series (finite simple terms of sine and cosine functions) with center t_0, as given by Eqs. (16)-(17) (Babaei, 2013; Sadollah *et al.*, 2015).

$$x_i(t) \approx X_{i_{appx.}}(t) = a_0 + \sum_{m=1}^{NT}\left(a_m \cos\frac{m\pi(t - t_0)}{L} + b_m \sin\frac{m\pi(t - t_0)}{L}\right), i = 1 - 7 \quad \textbf{(16)}$$

$$T_i(t) \approx T_{i_{appx.}}(t) = c_0 + \sum_{m=1}^{NT}\left(c_m \cos\frac{m\pi(t-t_0)}{L} + d_m \sin\frac{m\pi(t-t_0)}{L}\right), i = 1-7 \quad \textbf{(17)}$$

Here, [x(t), T(t)] and [X_{appx},T_{appx}] represent the precise analytical solutions and the approximate solutions respectively. *L* signifies the size of solution interval conforming to the single NLODE and is set to t_n–t_0 (t_0 and t_n are the initial and final points of the solution interval). *NT* represents the number of approximation terms in Fourier series. Here, *L* is chosen to be 0.0005 hr and *NT* is set to 6. The unknown coefficients in Eqs. (16)-(17) (*i.e.*, a_0, a_m, b_m, c_0, c_m, and d_m) serve as the design variables. The objective function of the SNLODEs is the Weighted Residual function *(WRF)* (given by Eq. (18)) to be minimized. *W(t)* and *R(t)* are the weight and residual functions respectively. By substituting the approximate functions [X_{appx},T_{appx}] and their derivatives $X'_{appx.}$ *and* $T'_{appx.}$ in the implicit form of Eq. (19), *R(t)* is obtained. For simplicity, the weight function *W(t)* is taken as 1. Here, the trapezoidal method has been utilized in order to obtain the numerical solution of the objective function (WRF). The initial conditions of SNLODEs serve as the constraints of the formulated optimization problem. For handling constraint violations, penalty factors of 20000 and 100 are used for x_i and T_i respectively. The computation of optimum values of the design variables with minimal value of WRF is the ultimate goal of the optimization task carried out by WCA.

$$WRF = \int |W(t)| \times |R(t)|\, dt \quad \textbf{(18)}$$

$$R(t) = f(t, X_i(t), X_i'(t), T_i(t), T_i'(t)) \quad \textbf{(19)}$$

IV. Results and discussions

The steady-state process parameters including L_i, T_i and V_1 obtained by optimizing the objective function *J(z) via* WCA (20 independent runs, 1000 iterations) are presented in Table 3 along with other estimated process parameters and various thermo-physical parameters (λ, *H* and h_L or h) for comparative analysis. These simulated results under steady-state are utilized for solving the dynamic model (SNLODEs) *via* WCA (10 independent runs, 1000 iterations). The approximate solutions of SNLODEs obtained via WCA are illustrated in Fig. 2 and Fig. 3. On account of the consideration of limited number of approximation terms of the Fourier series expansion (*NT* = 6), the best approximation results are not achieved since the minimum value of the cost function (*WRF*) obtained is 3.2886e+03. However, better results may be obtained by increasing *NT*, thereby improving the solutions by computing improved optimal values of the design variables (Fourier coefficients).

Table 3. Steady-state process parameters: Simulation Results of Steady-state model

Parameters	Stage 1	Stage 2	Stage 3	Stage 4	Stage 5	Stage 6	Stage 7
L_i (in kg/s)	3.34	5.20	6.91	8.63	10.33	12.02	13.67
T_i (in ˚C)	147.00	100.00	73.22	67.08	61.41	57.77	54.39
Overall SC (V_1) (in kg/s)	2.126						

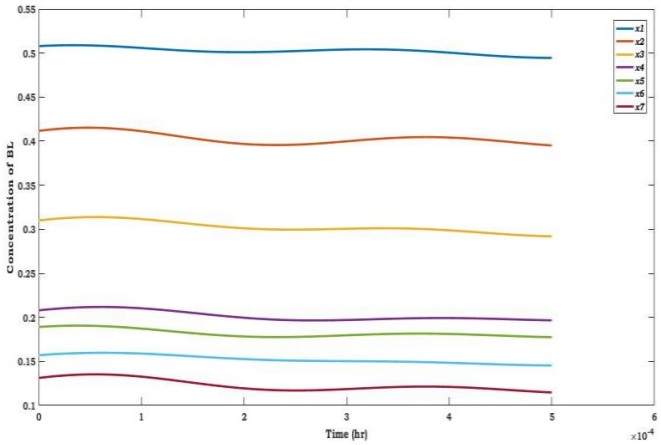

Fig. 2. Approximate solution of Concentration of Black Liquor acquired at each stage of MSE using WCA

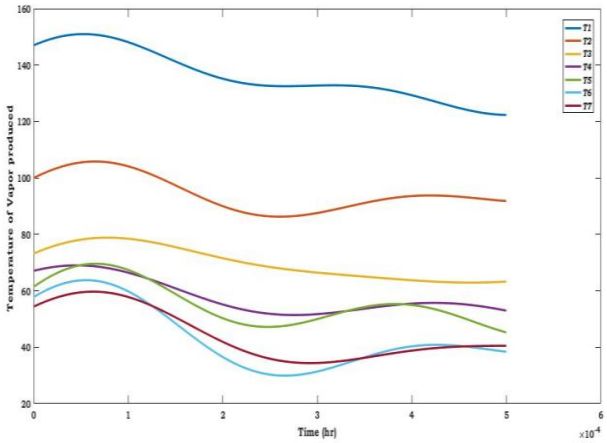

Fig. 3. Approximate solution of Temperature of vapor generated at each stage of MSE using WCA

V. Conclusions

The present work attempts to solve the non-linear dynamic model of MSE using WCA, a metaheuristic approach. The simulation results present an approximate solution to the SNLODEs involved in the dynamic model. These approximate solutions of SNLODEs could assist the scholars in the design of suitable controller for ensuring optimum energy efficiency of MSE along with effective set-point tracking and disturbance rejection. However, the present results can be significantly improved by increasing the number of approximation terms of the Fourier series expansion used for approximation, thereby providing the scope for further work.

References

Babaei, M. (2013). A general approach to approximate solutions of nonlinear differential equations using particle swarm optimization. *Applied Soft Computing*, *13*(7), 3354-3365.

Bhargava, R., Khanam, S., Mohanty, B., & Ray, A. K. (2008). Simulation of flat falling film evaporator system for concentration of black liquor. *Computers & Chemical Engineering*, 32(12), 3213-3223.

Kaya, D., & Sarac, H. I. (2007). Mathematical modeling of multiple-effect evaporators and energy economy. *Energy*, *32*(8), 1536-1542.

Sadollah, A., Eskandar, H., Yoo, D. G., & Kim, J. H. (2015). Approximate solving of nonlinear ordinary differential equations using least square weight function and metaheuristic algorithms. *Engineering Applications of Artificial Intelligence*, *40*, 117-132.

Verma, O. P., & Manik, G. (2017c). Solution of SNLAE model of backward feed multiple effect evaporator system using genetic algorithm approach. *International Journal of System Assurance Engineering and Management*, *8*(1), 63-78.

Verma, O. P., Manik, G., & Mohammed, T. H. (2017a). Energy management in multi stage evaporator through a steady and dynamic state analysis. *Korean Journal of Chemical Engineering*, 34(10), 2570-2583.

Verma, O. P., Manik, G., Jain, V. K., Jain, D. K., & Wang, H. (2018a). Minimization of energy consumption in multiple stage evaporator using Genetic Algorithm. *Sustainable Computing: Informatics and Systems*, *20*, 130-140.

Verma, O. P., Mohammed, T. H., Mangal, S., & Manik, G. (2016a). Mathematical modeling of multistage evaporator system in Kraft recovery process. In *Proceedings of Fifth International Conference on Soft Computing for Problem Solving* (pp. 1011-1042). Springer, Singapore.

Verma, O. P., Mohammed, T. H., Mangal, S., & Manik, G. (2017b). Minimization of energy consumption in multi-stage evaporator system of Kraft recovery process using Interior-Point Method. *Energy*, *129*, 148-157.

Verma, O. P., Mohammed, T. H., Mangal, S., & Manik, G. (2018b). Optimization of steam economy and consumption of heptad's effect evaporator system in Kraft recovery process. *International Journal of System Assurance Engineering and Management*, *9*(1), 111-130.

Verma, O. P., Haji, T. M., Mangal, S., & Manik, G. (2016b). Modeling the dynamics of heptads' effect evaporator system in the Kraft recovery processes. *International Journal of Control Theory and Applications*, *9*(11), 5287-5300.

Verma, O. P., Mohammed, T. H., Mangal, S., & Manik, G. (2018c). Modeling, simulation and control of the dynamics of a Heptads' effect evaporator system used in the Kraft recovery processes. *Transactions of the Institute of Measurement and Control*, *40*(7), 2278-2290.

Verma, O. P., Manik, G., & Jain, V. K. (2018d). Simulation and control of a complex nonlinear dynamic behavior of multi-stage evaporator using PID and Fuzzy-PID controllers. *Journal of Computational Science*, *25*, 238-251.

Integration of Solid Oxide Fuel Cell with Flare System in Natural Gas Plant

Khalid Al-Khori*, Yusuf Biçer, Muammer Koç
Division of Sustainable Development (DSD), College of Science and Engineering (CSE),
Hamad Bin Khalifa University (HBKU), Qatar Foundation (QF), Doha, Qatar

* E-mails: *kalkhori@mail.hbku.edu.qa

Abstract

The oil and gas industry produces a lot of destructive gasses that cause irreversible natural effects and mainly from the flare gas releases. Gas flaring is one of the most harmful reasons for worldwide contaminations, which has a global warming effect and causes environmental changes. Thus, lessening or disposing of the consumption of flare gases is a decisive strategy to annul the GHG gas level increments. Likewise, the use of flare emissions promises a clean power generation opportunity in oil and gas plants. Accordingly, flare gas reduction, and utilization is fundamental since it meets both natural and financial effectiveness objectives. A few flare gas utilization choices are available, for example, gas-to-liquid (GTL) conversion in addition to others. One of the promising technologies right now is the Solid Oxide Fuel Cell (SOFC).

SOFC has been demonstrated to be a profoundly useful electrochemical device that legitimately changes over substance power into electrical power with the possibility to expand framework efficiencies and to lessen releases of harmful gases. The SOFC can be incorporated into the flare structure where the flare gas is utilized as a fuel to the SOFC to produce power. This application in gas plants will require some adaptation by considering the safety and wellbeing of the plant. A techno-economic analysis is performed for this application and the outcomes show that a decrease of practically 70% in the outflows from the flare is possible and it can generate power up to 20 MW for the gas plant utilizing a waste fuel. This consideration will improve and energize the integration of SOFC devices in oil and gas plants for greener operations.

Keywords: Electricity, emissions, flare, natural gas, SOFC.

I. Introduction

Though natural gas is known to be a cleaner, non-renewable energy source contrasted with oil and viewed as a progress vitality asset for many decades to come, Natural gas activity plants additionally necessarily add to the global warming alteration because of flaring. The flare gas releases from petroleum gas extraction plants are enormous. Henceforth, lessening or taking out the consumption of flare gases is an incredible and positive technique to abolish the greenhouse substance level increments. The amount of petroleum gas being flared globally is around 150 billion m^3 that is discharged to the environment with nearly 400 Mt of CO_2 eq. Every year. Likewise, the disadvantages of petroleum gas as a result of flaring contribute a considerable segment of difficulties in oil and gas plants (Emam, 2015). Flaring, as described by (Dewar, 2013), is a controlled technique for an open fire burning to dispose of undesirable/additional gases, which are created from a few units inside the plants because of various reasons like over-pressure or emergency shutdown (Dewar, 2013). The reduction and recuperation of flare gas are crucial since it prompts accomplishing the goals of both technical and financial effectiveness. A few flare gas usage arrangements are conceivable (Oriji and Moses, 2017). This measure of spent energy can be recovered by utilizing the waste gases, which will assist with lessening GHG (Anajafi and Sangsaraki, 2015). Fuel cells utilize gaseous fuel to create power and they are viewed as power transformation devices where an electrochemical reaction happens between the fuel and the air. They are known for their high-performance conversion and low releases (Masih et al., 2010).

The SOFC is among different sorts of fuel cells. One of the most advantages of SOFC over other types is its capacity to work with a wide range of fuels; among these, hydrogen, various hydrocarbons, and even coal can be considered. This article centers around multi-dimensional examination for the combination of SOFC into flare gas within the natural gas plants as a cleaner power generation tool that does not just build the energy effectiveness in gas plants but also lessens the releases by utilizing flare gases. This integration of SOFC in the flare framework will diminish emissions harming substance releases from the flare stack. Moreover, using the flare gas through the SOFC generates the power to be utilized for on-shore and offshore platforms of the gas handling plant.

II. System Description

An ordinary plant with a capacity of 2 Billion Standard Cubic Feet of methane, will discharge around 5 MSCFD of gas through the flare. This gas is mostly methane, and some H_2S, NOx, SOx, and CO_2. The details of flare gas formations in a general gas plant are given in Table 1.

Table 1: Components of typical purge gas

Composition	CH_4	C_2H_6	C_{6+}	CO_2	H_2S	N_2
Mol. %	92.528	1.750	0.092	0.547	0.00046	4.387

Since it has over 90% of methane, it is a suitable fuel for SOFC. Besides, Figure 1 shows the fundamental schematic of incorporating SOFC in the flare framework.

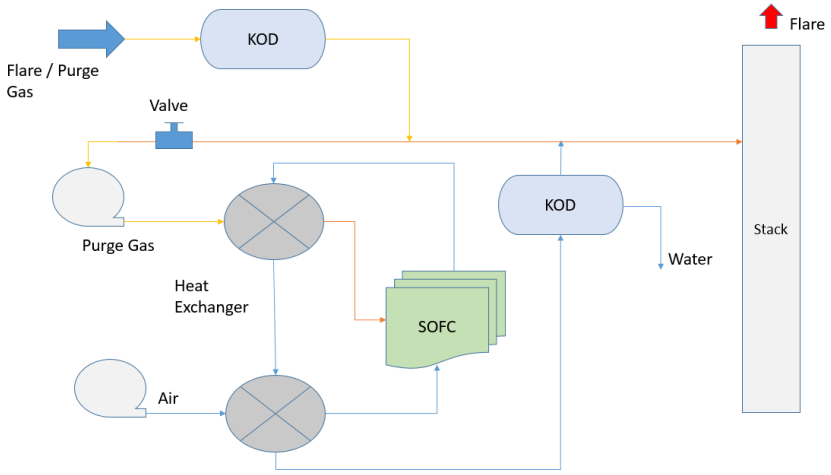

Figure 1: Integrating SOFC with a flare system

The SOFC model is constructed by determining all parameters of SOFC. All conditions, such as reforming and power created from the SOFC and energy balance equations along with thermodynamic parameters, can be seen in another study done by the authors (Al-Khori et al., 2019). The fuel and air are required to be warmed and pressurized to meet the SOFC stack prerequisite and to accomplish that, the excess heat from SOFC is utilized to achieve the temperatures of the fuel and air through heat exchangers. Small size compressors are utilized to reach the pressure needed for fuel and air.

The yield gases from the SOFC framework during activity are chiefly CO_2 where no other destructive gases are delivered because of the electrochemical responses emanations and this is a result of high functioning temperatures of SOFC activity. The emissions are determined based on Environmental Protection Agency (EPA, 2016) and table 4 from AP-2 (EPA, 2018), where it shows the emission factors for GHG gases taken from AP-2 ((EPA, 2018). The electrical force will be delivered in the SOFC framework and exhaust gas from the SOFC will be directed back to the flare stack. Any resentful in the process bringing about an increasingly huge flare gas stream in the emergency cases will sidestep the SOFC framework, and flare gas will be directed to flare stack according to a unique plan. This is put to guarantee the safety guidelines are still met.

III. Analysis

A tie in will be taken from the flare gas headers after the Knock out drums to feed the fuel to the SOFC unit. For onshore, out of an aggregate of 5 MMSCFD of the flare gas, 3.5 MMSCFD is used to feed SOFC and the 1.5 MMSCFD is directed to the flare stack. To keep up the heating value of the flare gas, not all the flare gas can be directed to the SOFC. For offshore, the aggregate flare gas is 0.15 MMSCFD where 0.105 MMSCFD is directed as fuel to SOFC and the rest will go to the flare. The flare gas recuperation in the two areas is dropped from 100% to 70%, with the end goal that the heating value of blended gas (SOFC exhaust gas + remaining flare gas) in stacks fulfills the flare gas stream and heating value needs. In this manner, Husa connections (Astbury, 2007) is utilized to ascertain the gas amount necessity and a different application is performed to evaluate the Lower Explosive Limit (LEL) and Upper Explosive Limit (UEL) of current fuel gas utilized for flare dependent on Le Chatelier's Rule of Flammability (Yaws, 2001).

Table 2: Heating values, explosion limits and mass flow rates of SOFC and flare gas units

Parameters	Onshore	Offshore	Units
Total flare gas	5	0.15	MMSCFD
Flare gas heating value	990	1120	Btu/SCF
Blended Gas LEL	4.87	4.44	%
Blended Gas UEL	14.86	14.44	%
SOFC fuel	70	70	% of total flare gas

IV. Results and discussions

After the flare gas stream estimation, the flare gas recovery is dropped to meet a worth with the end goal that the warming estimation of blended flare gas (flare remaining gas + SOFC exhaust gas) in stacks fulfilling the flare gas stream and warming worth necessities. The heating value, according to (Sorrels, 2019), ought to be over 300 BTU/SCF as a base for safe ignition. Along these lines, the model will recuperate a limit of 70% of flare gas, which is for onshore around 3.5 MMSCFD out of 5 MMSCFD and offshore around 0.045 MMSCFD out of 0.15 MMSCFD. The subsequent warming estimation of SOFC exhaust gas and remaining flare gas would be more than 300 BTU/SCF which is sufficient to support the persistent fire at the highest point of the flare tip and stream rate would be a lot higher than the base flare gas stream required for the flare stack flaring.

These values are given in Table 3 including LEL and UEL values for the new gas blends. LEL value of the blended flares gas (flare remaining gas + SOFC exhaust gas) is close to the fuel gas flare LEL esteem despite having some combination of hydrogen from the SOFC exhaust gas.

Table 3: Heating and LEL, UEL parameters

Parameters	Onshore	Offshore	Units
Remaining flare to Stack	1.5	0.015	MMSCFD
SOFC exhaust gas + Flare gas flow to stack	6.175	0.185	MMSCFD
(SOFC exhaust gas + Flare gas) HV	310	310	Btu/SCF
LEL for blended gas	4.42	4.42	%
UEL for blended gas	24.38	24.38	%

The AC output produced from SOFC would be 20 MW. The details of the inputs and outputs of SOFC are given in Table 4.

Table 4: Fuel rate and power production for onshore and offshore cases

Parameters	Onshore	Offshore	Units
SOFC Fuel rate	3.5	0.105	MMSCFD
AC power output	20	0.6	MW

CO_2 eq. substance releases for the blended flare gas stream (SOFC exhaust gas + Flare gas) to show the discharge as a result of the SOFC flare recovery model. An assessment is made between the flare gas ignition of 5 MMSCFD gas for onshore and for offshore at 0.15 MMSCF, and SOFC exhaust gas + flare gas at a rate of recovering 70% of flare gas in SOFC unit as shown for onshore in Figure 2 and for offshore in Figure 3.

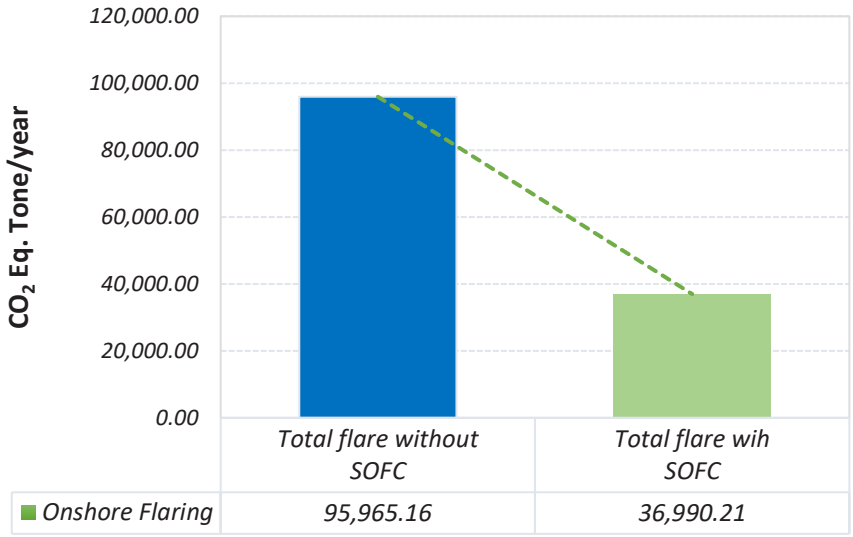

Figure 2: Onshore flaring

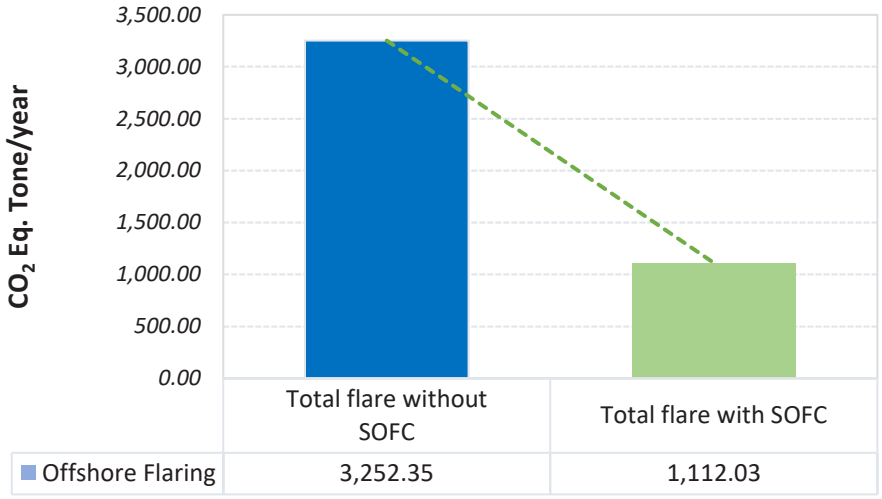

Figure 3: Offshore flaring

It is determined that there would be a decrease in emissions for more than 60% for both locations by recovering 70% of flare gas in the two areas. The diminishing in GHG emissions is observed while blending the exhaust gas from SOFC to the outstanding of the flare gas. The CO_2 savings obtained by using and incorporating SOFC for an aggregate of 25 years is about 1.5 million tons of CO_2 eq.

V. Conclusions

This examination shows a clean transformation of flare gas into power by using SOFC as an incorporated framework with a flare unit in a natural gas plant. The fuel used to produce power is a waste fuel, which is typically emitted to nature with huge destructive impacts on the air contamination and increase the GHG. Also, the power independence can be accomplished without any reliance on the national grid or diesel generator and diesel fuel. This can diminish the issues identified with offshore situations just like any other discharges from diesel consumption. While the extra delivered power from the SOFC in onshore is more than plant demand, and it can be traded to the national grid with decreased releases and expanded power productivity. If such integration of SOFC with the flare is applied in all gas plants, while guaranteeing the safety is met, at that point, the general reserve funds on power bills can be very impressive.

This consideration showed the ecological and mechanical attainability of SOFC integration into petroleum gas process plants through a multi-dimensional and incorporated investigation to react to the need in the oil and gas industry to use the waste gases to create clean power with high efficiencies and low emissions. Eventually, the extensive usage of SOFC innovation for various cases in the oil/gas industry is required to prompt a general framework effectiveness upgrade.

Acknowledgments

The authors express gratitude toward Hamad Bin Khalifa University, Qatar Foundation, and recognize the help of Dolphin Energy Ltd, Qatar.

References

Al-Khori, K., Bicer, Y., Boulfrad, S., Koc, M., 2019. Techno-economic and environmental assessment of integrating SOFC with a conventional steam and power system in a natural gas processing plant. Int. J. Hydrogen Energy 4. https://doi.org/10.1016/j.ijhydene.2019.07.016

Anajafi, E., Sangsaraki, M.E., 2015. Design Criteria and Simulation of Flare Gas Recovery System. Int. Conf. Chem. Food Environ. Eng. 35–39.

Astbury, G.R., 2007. Venting of Low Pressure Hydrogen Gas A Critique of the Literature y. Trans IChemE 85, 289–304. https://doi.org/10.1205/psep06054

Dewar, G., 2013. Employing Micro Gas Chromats for Flare Analysis to meet 1–7.

Emam, E.A., 2015. Gas Flaring in Industry: an Overview. Pet. Coal 57, 532–555.

EPA, 2018. Emission Factors for Greenhouse Gas Inventories. Intergov. Panel Clim. Chang. 2017, 1–5.

EPA, 2016. Direct Emissions from Stationary Combustion Sources.

Masih, A.M.M., Albinali, K., DeMello, L., 2010. Price dynamics of natural gas and the regional methanol markets. Energy Policy 38, 1372–1378. https://doi.org/10.1016/j.enpol.2009.11.018

Oriji, B.A., Moses, D.E., 2017. Optimizing Vertical Gas Fare Stack ' s Sizing Parameters for Flare Efficiency in Niger Delta 8, 175–183.

Sorrels, J.L., 2019. Section 3 VOC Controls, in: Flares.

Yaws, carl l., 2001. Matheson Gas Data Book.

Exergy and CO_2 emissions analysis of an emerging alternative iron and steel making process

[1*]Binay Kumar, [2]Gour Gopal Roy, [3]Prodip Kumar Sen
[1] IIT Kharagpur, Research Scholar, Department of Metallurgical & Materials Engg., Kharagpur, 721302, India
[2,3] IIT Kharagpur, Professor, Department of Metallurgical & Materials Engg., Kharagpur, 721302, India

*E-mail: binay.kumar@iitkgp.ac.in

Abstract
Depletion of coking coal reserves, generation of ore/coal fines and growing environmental concerns motivated researchers to search for coke-free ironmaking processes using ore/coal fines leading to alternative routes of ironmaking. In this way, several alternative routes of ironmaking have evolved. Rotary hearth furnace (RHF) processes are the emerging alternative routes of ironmaking since it is reported that these processes consume lower energy with lesser CO_2 emissions compared to conventional ironmaking process but resource-based energy utilization efficiency has not been reported. Thus, there is a need for exergy analysis beyond emission/energy profiles. The final product of the RHF processes could be either directly reduce iron (DRI) or nugget depending on the process parameters and those are further smelted in electric arc furnace (EAF) to produce steel. Model-based exergy and CO_2 emissions analysis of both variants of RHF-EAF iron and steel making processes are studied. All the thermodynamic data used has been estimated with the help of thermodynamic software FactSage. In the present study, three kinds of exergy indices are measured: total exergy loss, metal-based exergy efficiency and metal+gas-based exergy efficiency based on input exergy. For the nugget based RHF-EAF process, these exergy indices are found as 7992 MJ/tcs, 33% and 67%, respectively; whereas for the DRI based RHF-EAF process, those values are calculated as 9585 MJ/tcs, 31% and 61%, respectively. Results indicate that nugget based RHF-EAF process is superior to DRI based RHF-EAF process. However, exergy indices of RHF-EAF systems are either superior or comparable (depending on RHF product) to conventional iron and steel making process. In order to calculate the CO_2 emissions from the RHF-EAF processes, carbon flows in RHF and EAF; and electricity demand in EAF are investigated. Net total CO_2 emissions through both the RHF-EAF processes are estimated to around 1.92-2.01 ton/tcs which is comparable to conventional iron and steel making process.

Keywords: Iron and steel making, exergy analysis, exergy loss, exergy efficiency, CO_2 emissions

I. Introduction

Steel is the world's most popular construction material due to its durability, processability, and cost. However, producing steel from iron ore creates high energy consumption and CO_2 emissions. Presently, around 70% of world steel is produced through the conventional (BF-BOF) iron and steelmaking route (World Steel Association, 2018), which requires metallurgical coke. Coking coal reserves are decreasing day by day, and also generation of mines byproducts like iron oxide fines and coal fines motivated researchers to search for coke free iron making processes using mines useful byproducts leading to alternative routes of iron and steel making. Rotary hearth furnace-electric arc furnace (RHF-EAF) processes are one of the emerging alternative routes of iron and steel making. Ironmaking using RHF processes like Fastmet, Fastmelt, and ITmk3 has drawn attention of the researchers for the last couple of decades since these processes are coal-based direct reduction process that uses iron ore fines and non-coking coal fines in the form of composite pellets. RHF is a doughnut-shaped moving bed reactor where composite pellets are charged from entry door placed next to the exit door through which DRI or nugget (depending on the operating parameters) is discharged after moving through 360° through the tunnel encompassing various temperature regime, namely preheating, reduction and cooling zone, and those are further melted in either electric arc furnace (EAF) or induction furnace (EIF) to produce steel. Due to heat transfer restrictions in RHF, RHF based processes involve operation on one or two layers only over the hearth, puts limitation on productivity. Figure 1 represents the typical process flow in an RHF-EAF steelmaking system. It is claimed that in RHF-EAF steelmaking processes, the intimacy of iron ore fines and non-coking coal fines (reductant) improves the mass transfer efficacy and efficient carbon utilization in RHF results in lower energy requirements with lesser CO_2 emissions compared to conventional iron and steel making process (Fujita and Harada, 2010).

Since exergy analyses are widely used in evaluation and optimizations of chemical and metallurgical processes and global climate change caused by CO_2 has become a hot issue worldwide, several studies have been reported on the exergy and CO_2 emissions analyses of the conventional iron and steel making process; however, reports on exergy and CO_2 emissions analyses of RHF-EAF steelmaking processes are limited. The present article focuses on the exergy and CO_2 emissions analyses of RHF-EAF steelmaking processes. The detailed exergy calculation methodology of the metallurgical streams could be found elsewhere (Kadrolkar et al., 2012). To estimate total CO_2 emissions from the RHF-EAF processes, carbon flows in RHF and EAF; and carbon equivalent of calculated electricity demand in EAF are analysed. Comparison of exergy indices and CO_2 emission values of RHF-EAF steelmaking systems with conventional iron and steel making process are also presented.

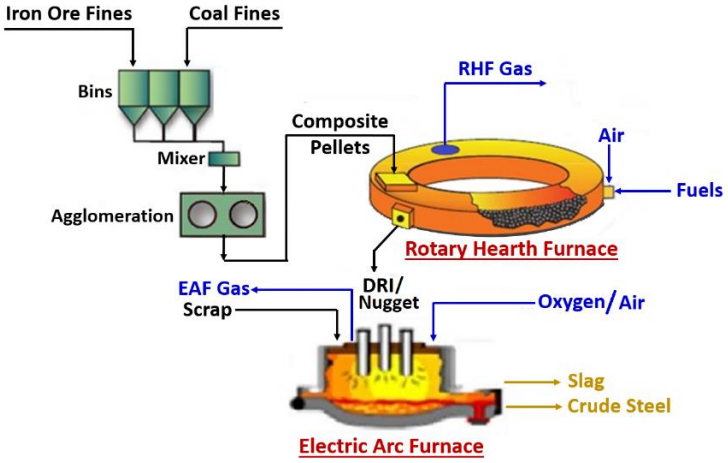

Fig. 1: Schematic representation of process flow in an RHF-EAF steelmaking system

A. Exergy indices

Figure 2 represents a typical exergy flow in any industrial system. Internal exergy loss ($B_{int\ loss}$) in complex metallurgical processes are occurred mainly due to combustion reactions, chemical reactions and heat transfer. It may be noted that $B_{int\ loss}$ is specific to a process chosen and therefore characterized as process system exergy loss. Total exergy loss ($B_{total\ loss}$) is the summation of internal exergy losses and external exergy losses. External exergy losses contribute exergy of lost material, exergy of waste products, exergy loss due to radiation and convection, and thermal exergy losses. External loss is the exergy of all flows that cross the boundaries of the process and have no commercial value. Crude steel (CS), RHF gas and EAF gas are considered as useful products, whereas waste products are EAF slag, RHF gangue and EAF fume.

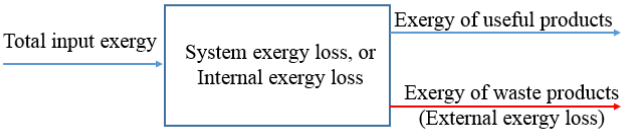

Fig. 2: Schematic representation of exergy flow in a system

In the present study, following exergy indices are measured: internal exergy loss, total exergy loss, metal-based exergy efficiency (when only metal is the useful product) and metal+gas-based exergy efficiency (when metal, as well as gas both, are the valuable product).

Internal/System exergy loss ($B_{int\ loss}$) is estimated by

$$B_{int\ loss} = B_{total\ input} - B_{total\ output} \quad (1)$$

Total exergy loss ($B_{total\ loss}$) is evaluated by

$$B_{total\ loss} = B_{total\ input} - B_{useful\ products} \quad (2)$$

Metal-based exergy efficiency (Ψ_m) is calculated by

$$\psi_m = \frac{B_{metal}}{B_{total\ input}} \quad (3)$$

Metal + Gas-based exergy efficiency ($\Psi_{m\text{-}g}$) is expressed by

$$\psi_{m\text{-}g} = \frac{B_{metal} + B_{gas}}{B_{total\ input}} \quad (4)$$

Where $B_{total\ input}$ is the total input exergy, $B_{total\ output}$ is the total output exergy, and $B_{useful\ products}$ is the summation of exergies of all useful products coming out from the system. B_{metal} is the exergy of DRI/nugget for RHF and exergy of crude steel for EAF, and B_{gas} is the exergy of useful gases coming out from the respective processes.

II. Exergy analysis of RHF-EAF steelmaking process

For analyzing the exergy flow of RHF processes, knowledge of input and output mass streams from RHF in necessary. These input and output mass streams data can be either taken from reported actual plant data or developed from a thermodynamic model. Actual plant data are limited reported in literature and only a few work has been reported on thermodynamic modelling of RHF for arriving at mass and energy requirements of RHF process. Therefore, a thermodynamic model for RHF process is developed and validated with data available in the literature (Kumar et al., 2017). The model is capable of estimating input and output mass streams like iron ore rate, reductant coal rate, external fuel rate, exit gas temperature and composition based on the given composition and operating parameters. For exergy analysis of EAF process, a separate model has been developed based on mass and heat balance. Later both models are coupled together, and exergy flows of combined RHF-EAF iron and steelmaking process are studied. Figure 3 represents the exergy flow in DRI-based and nugget-based RHF-EAF steelmaking systems. System exergy loss in RHF and electricity demand in EAF are higher for DRI-based RHF-EAF steelmaking system since higher amount of DRI is required to melt to produce 1-ton CS than amount of nugget needed in nugget-

based RHF-EAF process. For the nugget-based RHF-EAF process, total exergy indices, Ψ_m and Ψ_{m-g} are found as 7992 MJ/tcs, 33% and 66%, respectively; whereas for the DRI-based RHF-EAF process, those values are calculated as 9585 MJ/tcs, 31% and 61%, respectively. Here total exergy loss composed of system exergy losses, external exergy losses and exergy consumed in power generation. Results indicate that nugget-based RHF-EAF process is superior to DRI-based RHF-EAF steelmaking process.

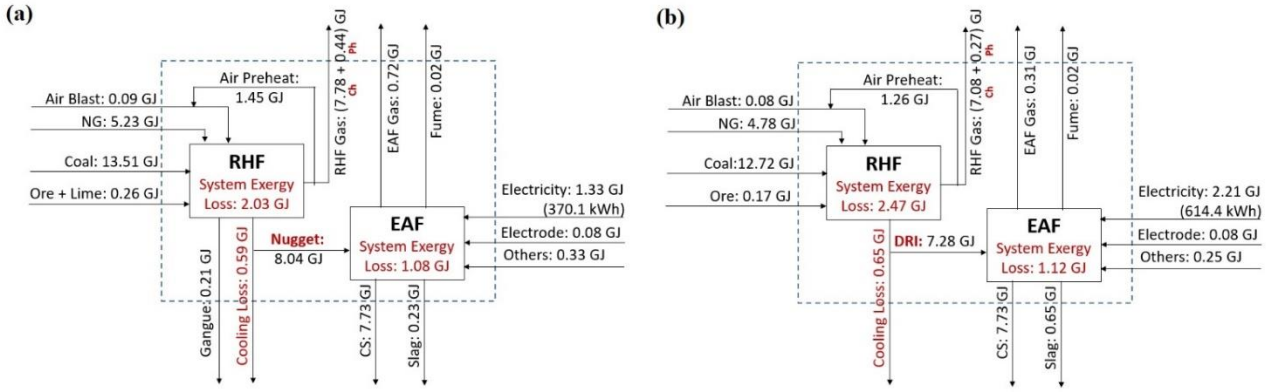

Fig. 3: Schematic representation of exergy flow in RHF-EAF steelmaking systems (per ton crude steel) (a) Nugget-based, and (b) DRI-based

III. Comparison of exergy indices of RHF-EAF systems with BF-BOF process

Comparison of exergy indices between RHF-EAF processes and reported conventional iron and steelmaking process (BF-BOF process) can reveal characteristics and sustainability of the RHF-EAF system. Total exergy losses, metal-based exergy efficiency (Ψ_m) and metal+gas-based exergy efficiency (Ψ_{m-g}) of BF-BOF process taken from literature and RHF-EAF processes studied are shown in Table 1.

Exergy indices indicate that nugget-based RHF-EAF steelmaking process is superior to DRI-based RHF-EAF steelmaking process as well as BF-BOF process. However, exergy efficiencies of integrated BF-BOF process are comparable to DRI-based RHF-EAF steelmaking processes. Even though high exergy components like natural gas (NG) and electricity are used in RHF-EAF systems, exergy indices are either superior or comparable to integrated BF-BOF systems since former systems are two-step steelmaking units whereas integrated BF-BOF systems are four-step iron and steelmaking processes. Controlled hot charging of DRI and nugget, and scrap addition in EAF may further improve exergy indices of RHF-EAF systems.

Table 1. Comparison of total exergy losses in integrated steelmaking systems with previous studies.

		(Michaelis et al., 1998)	(Costa et al., 2001)	(Zhang et al., 2018)	Present study	
Processes		BF-BOF route	BF-BOF route	BF-BOF route	Nugget-based RHF-EAF route	DRI-based RHF-EAF route
Total exergy loss (GJ)*	Pellet plant		0.23			
	Sinter plant	1.51	2.20	1.88		
	Coke oven	2.17	2.64	1.79		
	Hot stove					
	BF	3.87	3.43	4.10		
	BOF/EAF	1.41	1.41	1.27	2.05	2.10
	Power plant				2.47	4.10
	RHF				3.47	3.39
	Total	8.96	9.91	9.04	7.99	9.59
Ψ_m(%)*			30.00	33.51	33.23	31.39
Ψ_{m-g}(%)*			48.00	63.27	65.65	60.72

*Calculations are based on the results of these literatures and method in this study.

IV. CO_2 emissions analysis of RHF-EAF steelmaking process

In order to estimate the net CO_2 emissions from the RHF-EAF iron and steel making processes, net carbon flows in both variants of RHF-EAF system are examined with material flow analysis, obtained through the model developed. Figure 4 shows the carbon flow per ton crude steel in both variants of RHF-EAF Process. Results indicate that the primary carbon sources of CO_2 emissions in RHF are reductant coal and external fuel (NG), and in EAF, main carbon sources of CO_2 emissions is fuel required (India grid factor- 0.218 kg C/kWh (Central Electricity Authority, 2018)) for power generation. The net CO_2 emissions have been estimated by converting net carbon input (net carbon input = total carbon input – carbon in crude steel) into CO_2 completely. Calculated net CO_2 emissions per ton crude steel from the DRI-based and nugget-based RHF-EAF iron and steel making processes are 1922.10 kg and 2014.28 kg, respectively.

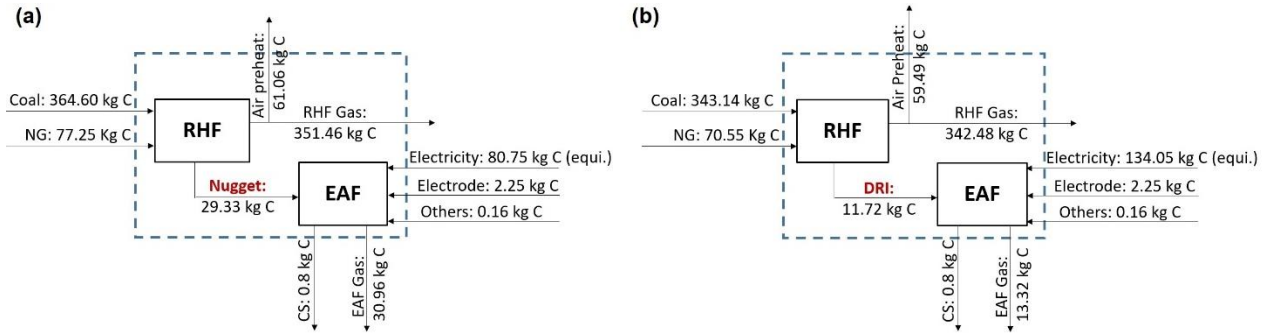

Fig. 4: Carbon flow per ton crude steel in RHF-EAF steelmaking process (a) Nugget-Based, and (b) DRI-based

The net CO_2 emissions value from conventional iron and steel making process (BF-BOF route) is around 2000 kg per ton crude steel (Sahoo et al., 2019; Sarkar et al., 2018; Song et al., 2019). Therefore, net total CO_2 emissions through both variants of RHF-EAF routes may be comparable to conventional iron and steel making process (BF-BOF route).

V. Conclusions

1. For the nugget-based RHF-EAF process, total exergy loss, Ψ_m and $\Psi_{m\text{-}g}$ are found as 7992 MJ/tcs, 33% and 67%, respectively; whereas for the DRI-based RHF-EAF process, those values are calculated as 9585 MJ/tcs, 31% and 61%, respectively.
2. Exergy indices of nugget based RHF-EAF steelmaking process are superior to DRI based RHF-EAF steelmaking system.
3. Exergy indices indicate that exergy efficiencies of RHF-EAF steelmaking systems are either superior or comparable (depending on RHF product) to integrated BF-BOF steelmaking system.
4. Benefits of lesser units in RHF-EAF steelmaking systems (two units compared to four units in integrated BF-BOF system) are nullified by use of high exergy components like NG and electricity, and thermal exergy loss of DRI/nugget during transfer from RHF to EAF.
5. Net CO_2 emissions from the DRI-based and nugget-based RHF-EAF iron and steel making processes are calculated as around 1922 kg and 2014 kg /tcs, respectively which are comparable to conventional iron and steel making process.

References

Ayres, R.U., Ayres, L.W., Masini, A., 2006. Sustainable Metals Management, Eco-Efficiency in Industry and Science. Springer Netherlands, Dordrecht. https://doi.org/10.1007/1-4020-4539-5

Beer, J. de, 2000. Potential for Industrial Energy-Efficiency Improvement in the Long Term, 2000th ed, Eco-Efficiency in Industry and Science. Springer Netherlands, Dordrecht. https://doi.org/10.1007/978-94-017-2728-0

Central Electricity Authority, 2018. CO_2 Baseline Database for the Indian Power Sector. Minist. of Power, Government India.

Costa, M.M., Schaeffer, R., Worrell, E., 2001. Exergy accounting of energy and materials flows in steel production systems. Energy 26, 363–384. https://doi.org/10.1016/s0360-5442(01)00004-4

Fujita K, Harada T, M.S. and T.H., 2010. CO_2 Emission Comparison between Coal-based Direct Reduction Process and Conventional Blast Furnace Process, in: Int. Symposium on Ironmaking for Sustainable Development. Osaka, Japan.

Kadrolkar, A., Roy, S.K., Sen, P.K., 2012. Minimization of exergy losses in the COREX process. Metall. Mater. Trans. B 43, 173–185. https://doi.org/10.1007/s11663-011-9586-2

Kumar, B., Mishra, S., Roy, G.G., Sen, P.K., 2017. Estimation of Carbon Dioxide Emissions in Rotary Hearth Furnace Using a Thermodynamic Model. Steel Res. Int. 88. https://doi.org/10.1002/srin.201600265

Michaelis, P., Jackson, T., Clift, R., 1998. Exergy analysis of the life cycle of steel. Energy 23, 213–220. https://doi.org/10.1016/S0360-5442(97)00081-9

Sahoo, M., Sarkar, S., Das, A.C.R., Roy, G.G., Sen, P.K., 2019. Role of Scrap Recycling for CO_2 Emission Reduction in Steel Plant: A Model Based Approach. Steel Res. Int. https://doi.org/10.1002/srin.201900034

Sarkar, S., Bhattacharya, R., Roy, G.G., Sen, P.K., 2018. Modeling MIDREX Based Process Configurations for Energy and Emission Analysis. Steel Res. Int. https://doi.org/10.1002/srin.201700248

Song, J., Jiang, Z., Bao, C., Xu, A., 2019. Comparison of energy consumption and CO_2 emission for three steel production routes-integrated steel plant equipped with blast furnace, oxygen blast furnace or corex. Metals. https://doi.org/10.3390/met9030364

World Steel Association, 2018, Fact Sheet, Steel Industry Co-Products, https://www.worldsteel.org/en/dam/jcr:1b916a6d-06fd-4e84-b35d-c1d911d18df4/Fact _By-products_2018.pdf (accessed 17 June 2019)

Zhang, Q., Xu, J., Zhao, X., Wang, Y., 2018. Energy and exergy analyses of an integrated iron and steel making process. Int. J. Exergy 26, 454. https://doi.org/10.1504/ijex.2018.10014412

Experimental Investigation of Heat Transfer Characteristics of A Gravitational Water Vortex Flow

[1]Muhammad Tayyab, [1*]Taqi Ahmad Cheema, [1]Ali Ul Atas Khan, [1]Muhammad Talha Riaz
[1]GIK Institute of Engineering Sciences and Technology, Faculty of Mechanical Engineering, Topi, 23460, Pakistan

*E-mails: tacheema@giki.edu.pk, taqi_cheema39@hotmail.com

Abstract
A free vortex is naturally generated under the force of gravity by introducing water in a cylindrical tank with a small hole at the bottom and is called gravitational vortex flow (GVF). To date, only the hydraulic energy of GVF has been converted to mechanical energy despite the fact that a huge potential of thermal energy transfer also exists for such artificially induced vortex flows. For this purpose, another fluid stream may be introduced on the outer periphery of the basin responsible for vortex formation. In the present study, two flow configurations to exchange heat using a GVF are designed and experimentally tested on an in-house built experimental setup. One of the configurations uses spiral flow channels (SFC) built around the basin whereas the other design involves a shell with baffles (SWB) to direct the flow on the outer periphery of the basin. Two sets of experiments each comprising of seven test conditions for each configuration were performed under different inlet conditions on the developed heat exchange setup of GVF. At first, an energy balance between the two fluids was investigated and then the same data was utilized to develop the Nusselt number correlation for the GVF heat transfer. Since the flow volumes of the two streams involved in the heat exchange are vastly different and thus requires more time of contact between the two fluid streams. For this reason, SWB configuration showed better heat transfer and closer energy agreement than SFC design. The present study is expected to act as a benchmark for the new class of heat exchangers based on a new flow configuration, i.e. GVF.

Keywords: energy balance, spiral flow channels, basin, shell with baffles, gravitational vortex flow

I. Introduction
A promising passive technique for heat transfer enhancement is the use of vortex generators (VGs). VGs produce secondary flows by generating vortices in the direction of flow thereby disturbing the thermal boundary layer and enhance bulk mixing. Some commonly used profiles of VGs are cans, ribs, wings and winglets etc. [1-3]. For instance, Fiebig et al. studied the performance of four different kinds of longitudinal vortex generators (delta wing, delta winglet pair, rectangular wing and rectangular winglet pair) in developing laminar rectangular channel flow [4]. The secondary flow may also be generated by using swirl devices in the form of conical ring, helical wire and coil wire to increase the heat transfer [5, 6].
Although the above-mentioned studies claim the use of a vortex flow configuration, but they do not satisfy the actual physics of a vortex flow. Instead they may be termed as a turbulent flow forced to form a spiral, helical or circular pattern with the help of some external devices. In actual, the primary flow of fluid in a circular path must be regarded as a vortex flow. It can be categorized as free or forced vortex flow and can be seen in a real vortex, also termed as Rankine vortex. Free vortex is generated under gravity and a solid body rotation causes the forced vortex [7]. Artificially, a free vortex can be induced in a cylindrical tank (basin) with a small hole (orifice) at the bottom under the force of gravity and this has been extensively used for hydro power production [8-10].
Gravitational vortex flow (GVF) is a class of flow configuration which needs to be explored from the heat exchange point of view. In a preliminary experimental study, the authors found that a large amount of heat exchange between two fluid streams is possible provided a correct structural configuration is employed to tap maximum heat transfer [11]. To date, only one configuration that uses spiral flow channels (SFC) built around the basin, has been used and investigated. The present study proposes another possible configuration incorporating a shell with baffles (SWB) structure around the basin to increase the flow contacting surface area and time of contact between the two fluids through a wall between them. In this way, an enhanced heat transfer to the GVF is expected than SFC structure. A comparison of the energy balance has been made based on the measurements obtained from the experimentation conducted on in-house built experimental setup. A water to water heat exchange has been investigated for the two configurations producing a GVF on the colder side. One of the main advantages of heat exchange process using a GVF is the absence of pumping power requirement in transferring heat since flow is driven with the help of gravity. The discussion after a detailed analysis of the present study will be helpful in further development of the GVF based heat exchangers.

II. Experimental setup and methodology
The schematic of the experimental setup used in the present study is shown in Fig. 1. The test setup consists of an open hot fluid loop whereas the cold fluid loop is an open type to maintain the inlet flow conditions. Cold fluid path contains the basin exposed to atmosphere, to generate a GVF. To ensure a flow under gravity, an overhead tank supplies water to the basin through upstream channel and leaves through the orifice at the bottom. A gate valve controls the flow rate and temperatures are measured using gauges installed at the inlet and outlet of basin. The hot fluid loop consists of hot fluid storage tank, a pump, an overhead tank and a hot fluid path around the basin, i.e. SFC or SWB. A heating element of 6000W is fixed to heat the water in tank to achieve the desired temperature and controlled by a thermostat, installed with the heating element. Flow of water through SFC or SWB is only due to

gravity without a pump. The temperature gauges and ball valves are installed before and after the GWVHE. To find the heat transfer characteristics of a GVF, two configurations on the hot fluid side have been designed and tested. One of the configurations uses spiral flow channels (SFC) built around the basin whereas the other design involves a shell with baffles (SWB) to direct the flow on the outer periphery of the basin as shown in Fig. 2.

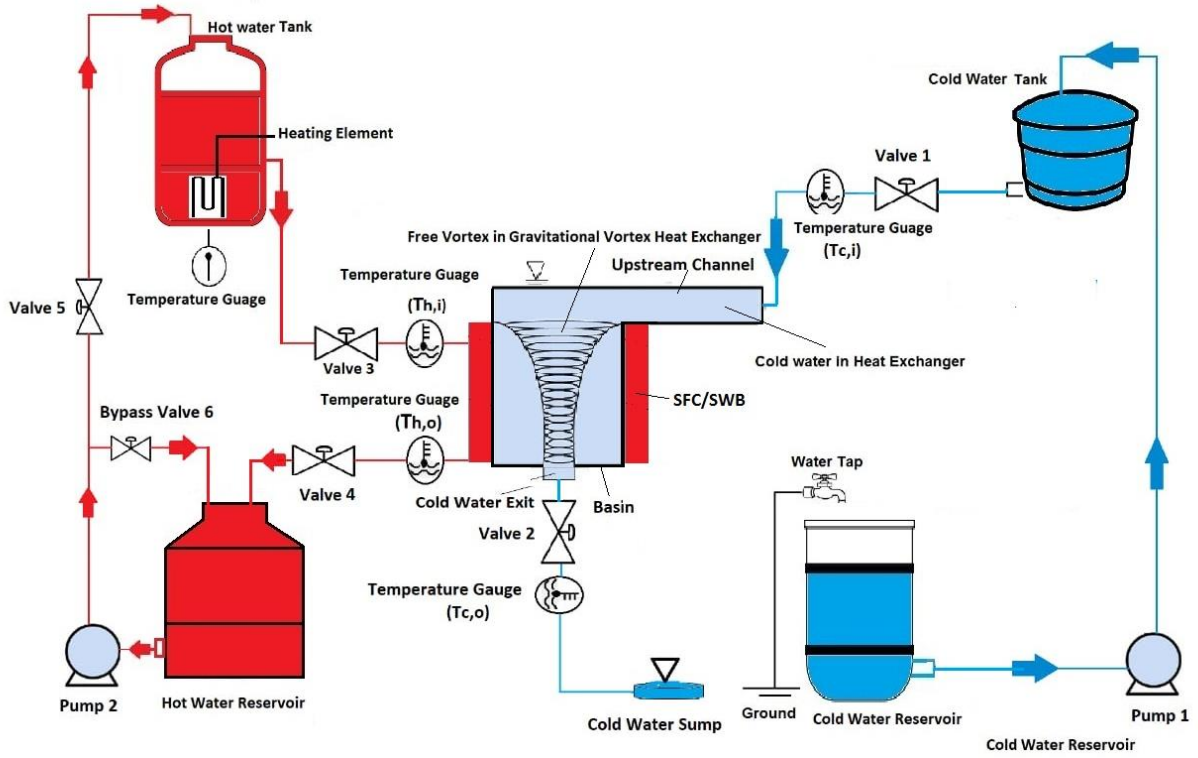

Fig. 1: Schematic of the experimental setup

The flow rate of cold water is calculated by the opening and closing of valve of discharge of cold fluid overhead tank while keeping the discharge valve of basin closed. Once the cold-water flow rate of required is set then the specific height of the vortex is also required in the basin. It is achieved by adjusting the flow rate of cold fluid overhead tank discharge and flow rate of basin discharge valve. The maximum contact of cold water and hot water is required for better heat exchange so for this purpose, both spiral channels and the baffles should be filled completely with hot water. The valve at the discharge of hot fluid overhead tank is open and flow rate of hot water is controlled by the valve present at the discharge of the hot water after GWVHE. The temperature for inlet of cold water $(T_{c,i})$ and hot water $(T_{h,i})$ is fixed and the outlet temperatures of water $(T_{c,o}\text{and } T_{h,o})$ can be measured by the help of temperature gauges installed after the heat exchanger. Number of experiments were carried out, beginning from the minimum flow rate of hot water to the maximum possible flow rate of hot water while keeping the cold-water flow rate fixed. Similarly, number of experiments were carried out by fixing the hot water flow rate fixed and varying the cold-water flow rate from minimum to maximum possible flow rate of cold water. Readings at temperature gauges were recorded when the steady state was achieved. Whole experiment is carried out at two sets of inlet temperatures of 40°C and 50°C.

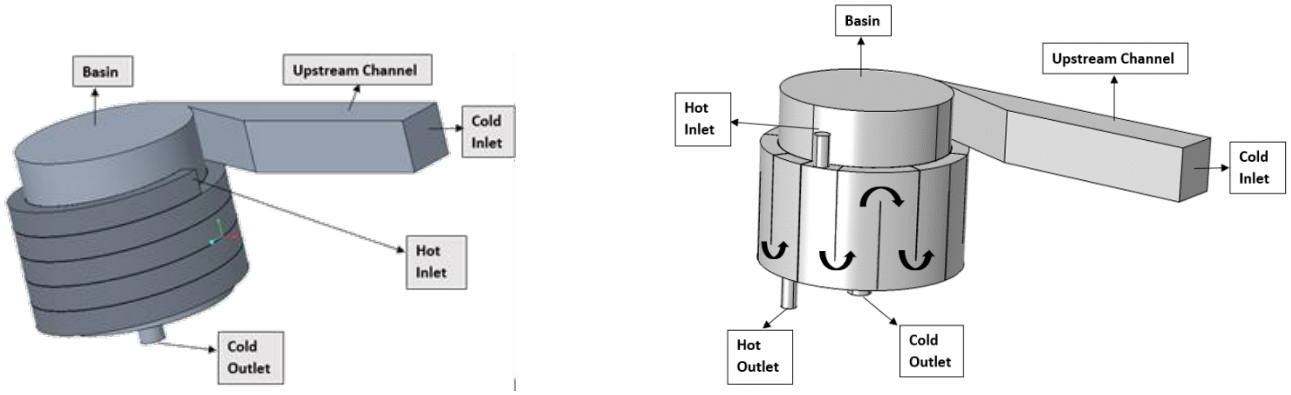

Fig. 2: Schematic of the heat exchanging configurations (a) SFC (b) SWB

III. Results and discussion

Primarily, the main aim and focus of the present work is to investigate the heat transfer characteristics of a GVF. For this purpose, two possible geometric configurations were developed and tested on the experimental setup. The energy balance of the two fluids, exchanging heat between them were investigated for each configuration to validate the experimental conditions. Comparison of energy balance for two different configurations were also carried out

under the same inlet conditions. For each configuration, two sets of experiments were carried out by varying the inlet conditions for each set of experiments. Each set of experiment consists of seven sub-experiments, conducted by varying the cold side flow rates of the fluids. Here they are represented as experimental conditions, i.e. A1, B1, C1, D1, E1, F1 and G1, for the first set of experiments ($T_{h,i}$=323K and $T_{c,i}$=293K) and each condition corresponds to the strength of the vortex formed in the basin for cold side mass flow rates of 0.14, 0.16, 0.2, 0.25, 0.33, 0.5 and 1 kg/s, respectively. Similarly, conditions for the second set of experiments ($T_{h,i}$=313K and $T_{c,i}$=293K) are represented as; A2, B2, C2, D2, E2, F2 and G2, respectively. For each fixed cold side flow rates (experimental condition), the hot fluid mass flow rate was varied in the range of 0.16 to 2.45 kg/s for both configurations. The rate of heat lost by the hot fluid ($\dot{Q}_h$) can be calculated as;

$$\dot{Q}_h = \dot{m}_h c_h (T_{h,i} - T_{h,o}) \quad (1)$$

Similarly, the rate of heat gained by the cold fluid ($\dot{Q}_c$) can be calculated as;

$$\dot{Q}_c = \dot{m}_c c_c (T_{c,o} - T_{c,i}) \quad (2)$$

where $\dot{m}_h$ and $\dot{m}_c$ are the hot and cold fluid mass flow rates, C_h and C_c are the heat capacities of hot and cold fluid respectively.

Fig. 3 and 4 show an energy balance between the two fluids for the two sets of experiment for condition 1 only. These graphs provide a comparison of the two configurations i.e, SFC and SWB used in the experiment. Fig. 3 shows a comparison of the heat lost by hot fluids in the two configurations and an overall analysis suggests that rate of losing heat of SWB configuration is marginally more than that of SFC. In general, it is also observed that the heat transfer rate in each configuration is proportional to the mass flow rate similar to any other heat exchange process. For the same experimental conditions, the colder side of SWB configuration provides more better characteristics of gaining the rate of heat transfer. A similar trend is observed for the second sets of experiments as shown in Fig. 4. Thus, it can be concluded from these results that the SWB configuration performs better than SFC configuration for the same conditions in both losing and gaining the heat transfer rate.

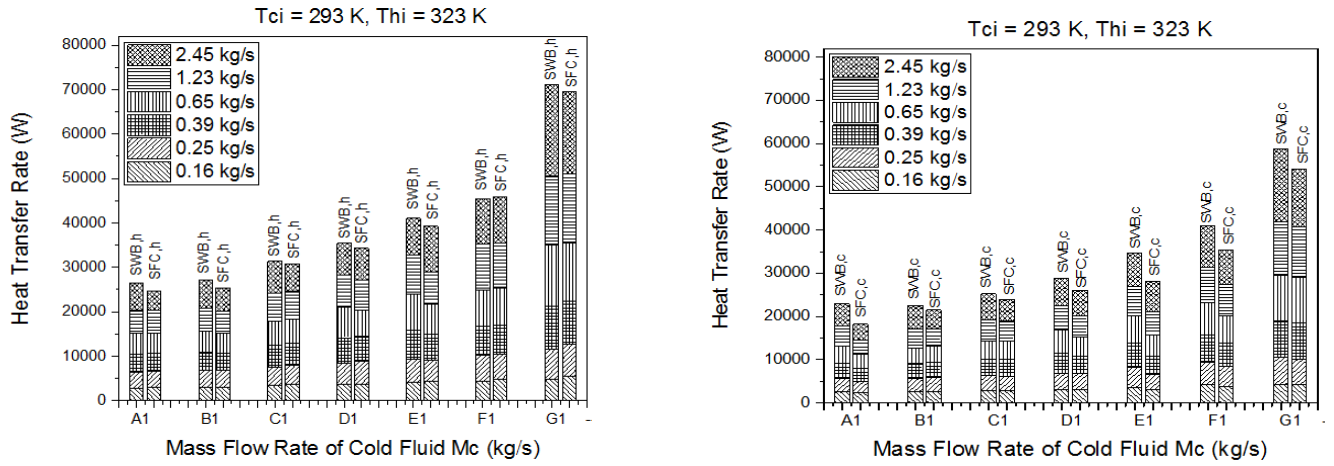

Fig. 3: Comparison of between SFC and SWB configurations for first set of experiments in terms of (a) rate of heat lost (b) rate of heat gain

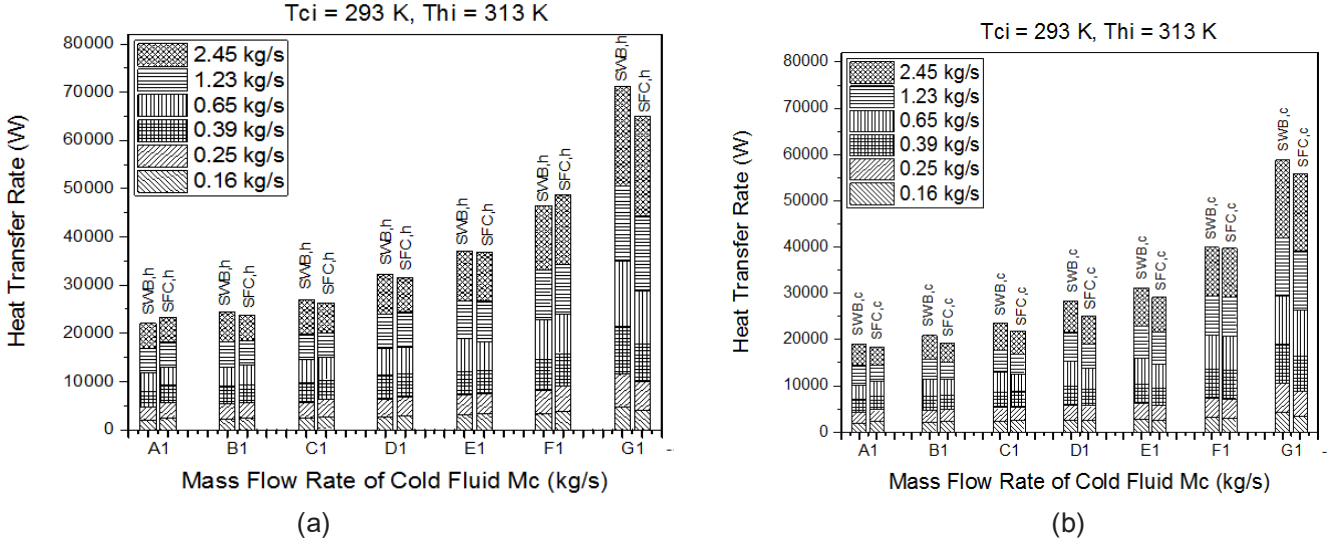

Fig. 4: Comparison of between SFC and SWB configurations for second set of experiments in terms of (a) rate of heat lost (b) rate of heat gain

The energy balance presents a combined effect of the mass flow rates and outlet temperatures of the two fluids. For each configuration, the difference between two points corresponding to same mass flow rate along the heat transfer rate axis may be attributed to the energy loss to the surrounding. In most of the cases studied here, a rational energy agreement exists with the largest loss of 25% which may be attributed to the instrumentation used for the measurement in addition to the evaporative loss of energy to the environment from the open surface at the top of the basin. One of the major findings of the study is critical nature of the role of the hot side flow rate to attain the energy balance. In the second set of experiments, relatively higher heat loss may be a result of smaller temperature difference thereby affecting the presence of thermal inertia. Moreover, the role of analog type of instrumentation and atmospheric boundary conditions at the top of the basin may not be ignored in the energy difference of the two fluid streams.

IV. Conclusions

The present study presents the heat transfer characteristics of two configurations to determine the heat exchange potential of GVF. At first, a spiral flow structure was built around a basin responsible for the generation of gravitational water vortex. Then, 16 baffles were introduced around a similar basin inside a shell to study water to water heat exchange. The two configurations were tested under various flow and thermal conditions when both the flows were flowing under gravity. A comparison of the two configurations based on the energy balance suggests that SWB configuration is better than SFC because of having more surface area available for the heat transfer. More research potential exists with better configurations and improved heat transfer.

Acknowledgements

The authors acknowledge the financial support of the Higher Education Commission of Pakistan and. The authors also acknowledge the technical support provided by GIK Institute of Engineering Sciences and Technology, Topi, 23460, KPK, Pakistan.

References

[1] Joardar, A. and Jacobi, A.M., "Heat transfer enhancement by winglet-type vortex generator arrays in compact plain-fin-and-tube heat exchangers", International journal of refrigeration, vol. 31(1), pp.87-97, 2008.
[2] Habchi, C., Russeil, S., Bougeard, D., Harion, J.L., Lemenand, T., Della Valle, D. and Peerhossaini, H., "Enhancing heat transfer in vortex generator-type multifunctional heat exchangers", Applied Thermal Engineering, vol. 38, pp.14-25, 2012.
[3] Torii, K., Kwak, K.M. and Nishino, K., "Heat transfer enhancement accompanying pressure-loss reduction with winglet-type vortex generators for fin-tube heat exchangers", International Journal of Heat and Mass Transfer, vol. 45(18), pp.3795-3801, 2002.
[4] Fiebig, M., Kallweit, P., Mitra, N. and Tiggelbeck, S., "Heat transfer enhancement and drag by longitudinal vortex generators in channel flow", Experimental Thermal and Fluid Science, vol. 4(1), pp.103-114, 1991.
[5] S. Eiamsa-Ard, K. Wongcharee, P. Eiamsa-Ard, and C. Thianpong, "Thermohydraulic investigation of turbulent flow through a round tube equipped with twisted tapes consisting of centre wings and alternate-axes," Experimental Thermal and Fluid Science, vol. 34, pp. 1151-1161, 2010.
[6] J. Y. San, W.-C. Huang, and C.-A. Chen, "Experimental investigation on heat transfer and fluid friction correlations for circular tubes with coiled-wire inserts," International Communications in Heat and Mass Transfer, vol. 65, pp. 8-14, 2015.
[7] P. K. Kundu, I. M. Cohen, and D. Dowling, "Fluid Mechanics" 4th edition, Elsevier, 2008.
[8] Dhakal, S., Timilsina, A.B., Dhakal, R., Fuyal, D., Bajracharya, T.R., Pandit, H.P., Amatya, N. and Nakarmi, A.M., "Comparison of cylindrical and conical basins with optimum position of runner: Gravitational water vortex power plant", Renewable and Sustainable Energy Reviews, vol. 48, pp.662-669, 2015.
[9] Ullah, R., Cheema, T. A., Saleem, A. S., Ahmad, S. M., Chattha, J. A., & Park, C. W., 2019. Performance analysis of multi-stage gravitational water vortex turbine. Energy Conversion and Management, 198, 111788.
[10] Ullah, R., Cheema, T. A., Saleem, A. S., Ahmad, S. M., Chattha, J. A., & Park, C. W., 2020. Preliminary experimental study on multi-stage gravitational water vortex turbine in a conical basin. Renewable Energy, 145, 2516-2529.
[11] Tayyab, M., 2019. Hydro-thermal investigation of gravitational water vortex heat exchanger: MS Thesis, Ghulam Ishaq Khan Institute of Engineering Sciences and Technology, Topi, Sawabi Pakistan.

Error Correction of Estimation Techniques in a Synchro-Phasor Measurement Unit

[1]Bentarzi Hamid, [1]Mahboubi Meriam, [1]Ouadi Abderrahmane, [2]Abdelmoumene Abdelakder
[1] Laboratory Signals and Systems, University M'Hamed BOUGARA Boumerdes, IGEE, Boumerdes, Algeria
[2] Doha, Qatar

* E-mails: lss@univ-boumerdes.dz

Abstract
More efforts may be needed to develop models of Phasor Measurement Unit (PMU) which may be utilized in smart grid simulation (off line) or real time implementation without the need for spending another efforts to update the model algorithm when the system parameters change. It is necessary to use a method which can somehow estimate the frequency and correct the phasors. The easiest and conventional way to determine frequency is to detect zero crossings per unit time. However, this method may require a very high sampling rate to capture the point of zero crossing along with some form of interpolation which might increase the cost and reduce the accuracy. Also, after determining the frequency, the phasor should be correctly estimated by suitably modifying the algorithm without omitting any data which might be critical.
The approach that has been developed in this research work is to generate a configurable input signal, sample it and use the different estimation techniques such as Discrete Fourier Transform (DFT), Sliding Discrete Fourier Transform (SDFT) to estimate the phasors. These estimated values would be incorrect if the input signals are at an off-nominal frequency and the phase angles would drift away from the true values. To correct this issue, first of all the off-nominal frequency has been estimated using different estimation techniques such as Least Error Squares, Kalman Filters, Demodulation, and Phasor measurement angle changing and then use it to correct the phasors. The developed PMU model has been verified by simulation first using Matlab and then implemented in real time framework using FPGA based NI card and LabVIEW. The obtained results show that the correction has been improved significanty.

Keywords: Discrete Fourier Transform (DFT), Least Error Squares, FPGA, LabVIEW

I. Introduction

Nowadays, the demand for electrical energy has increased remarkably. Power system is now operating in a more complicated situation and is facing more challenges than ever before. The motivation to make the power system Smarter and reliable has attracted many researchers to have further development in this area. Significant efforts have been dedicated to the development of efficient and precise measurement methods. A synchronized phasor measurement is one of those methods that have become very prominent for real time monitoring of power systems. At present PMU is the most sophisticated time-synchronized technology available for power engineers and system operators in wide area of applications. It provides real time monitoring, protection, and control of the system [1]. Several signal processing techniques to estimate phasor have been developed so far. The conventional and the most commonly-used algorithm for amplitude and phase estimations is the discrete Fourier transform (DFT)[3],[8]-[12] introduced in two forms: nonrecursive and recursive.

Using the DFT algorithm, researchers have focused their efforts on studying the gain frequency response in terms of suppressing the effect of harmonics included in the AC voltage on phase detection.[4],[5] However, the absolute phase detected by the DFT, especially recursive DFT, may involve considerable error during input signal dynamics and system disturbances.

In 1998, it has been proved that an accumulated error with small frequency in the estimated phasor quantities is produced when using recursive DFT. This error is further emphasized as the power frequency derivates from 50Hz.[7] And regarding the fact that a deviation in frequency of 1% is tolerated in the power systems, in addition to the results presented in case two of the paper [6].it is clear that the accumulation error results in totally wrong measurements after a certain number of cycles. Analysis of this error with proposal, for effective solution of this disastrous effect on PMUs is detailed in this paper.

In this work, we study, by computer simulation, the performances of the recursive DFT algorithm, which involves fewer calculations than the classical DFT. possible numerical recursive DFT accumulation error is addressed. To solve this problem, a reset of the DFT algorithm at appropriate intervals is proposed and evaluated. This paper offers a method that reduces the calculation load and minimizes the reset error, while resetting the error accumulation at a predefined period; its effectiveness is proved by simulation.

II. DFT Estimator

An AC waveform input signal of frequency fo can be mathematically represented by:

$$x(t)=Xm \cos(2\pi fot+\varphi) \quad (1)$$

Where, Xm : maximum value of the input signal,
f0: the nominal frequency,
φ : the initial phase angle of the input signal

The signal has also a Fourier series:

$$x(t) = ak\cos(2\pi fot) + bk\sin(2\pi fot) \quad (2)$$

$$x(t) = \left\{\sqrt{a_k^2 + b_k^2}\right\}\cos(2\pi fot + \varphi) \text{ where } \varphi = \arctan\left(\frac{-b_k}{a_k}\right) \quad (3)$$

Conventionally, the signal is expressed by a phasor $\bar{X}$ related to the fundamental frequency component of its DFT:

$$\bar{X} = \frac{X_m}{\sqrt{2}}e^{j\varphi} = Xe^{j\varphi} \quad (4)$$

$$\bar{X} = X\cos\varphi + j\,X\sin\varphi \quad (5)$$

Where,

$$X_m = \left\{\sqrt{a_k^2 + b_k^2}\right\} \quad (6)$$

Assuming that the periodic signal x(t) is sampled N times per fundamental period, the phasor representation is given by: $\bar{X} = \frac{\sqrt{2}}{N}(Xc - jXs)$ (7)

Where,

$$X_c = \sum_{k=1}^{N} X_k\cos\left(\frac{2\pi}{N}k\right) \quad (8)$$

$$X_s = \sum_{k=1}^{N} X_k\sin\left(\frac{2\pi}{N}k\right) \quad (9)$$

In some literatures, the definition of DFT with no harmonics is:

$$X = \frac{\sqrt{2}}{N}\sum_{k=1}^{N} X_k e^{\frac{-j2\pi}{N}k} \quad (10)$$

By using this technique, the phasor obtained from a constant sinusoid of nominal power system frequency will have a constant magnitude and will rotate in the counter clockwise direction by angle θ as the data window advances by one sample [2].

Once the first phasor is calculated, its update for successive windows is performed with one of the two different algorithms described in this section. The simplest way is by using non-recursive algorithm which performs calculations freshly each time for the upcoming windows. The other way is by using a recursive algorithm where only phasor updating is needed instead of new phasor estimation for the new window.

For recursive phasor estimation, the phasor is calculated for X_{N-1} only, and then the new phasor X_N (obtained after an elapsed time corresponding to 2π/N radians.) is obtained by making a recursive update on the old phasor. (N – 1) multiplications by the Fourier coefficients are common to the new and old windows, only one sample (x_0) is discarded and one sample (x_N) is added to the data set; making this a very efficient computational algorithm.

Its formula is given as in (11):

$$\hat{X}^N = \frac{\sqrt{2}}{N}\sum_{k=0}^{N-1} X_{k+1}e^{\frac{-j2\pi}{N}(k+1)} = X^{N-1} + \frac{\sqrt{2}}{N}(x_N - x_0)e^{\frac{-j2\pi}{N}0} \quad (11)$$

Where $e^{\frac{-j2\pi}{N}0} = e^{\frac{-j2\pi}{N}N}$, since N samples span exactly one period of the fundamental frequency.

When the last sample in the data window is (N + r), the recursive phasor estimate is given by:

$$\hat{X}^{N+r} = \hat{X}^{N+r-1} + \frac{\sqrt{2}}{N}(x_{N+r} - x_r)\,e^{\frac{-j2\pi}{N}r} \quad (12)$$

Where r represents the present state and (r-1) represents the past state.

In general, the recursive algorithm is faster, yet, numerically unstable. If an error in the estimate occurs from one window, it will be present in all the phasor estimates from then on. In other words, the Input signal dynamics and frequency drifts would produce a pattern of accumulated error in the estimated phase and magnitude during real time operation. Nevertheless, because of the great computational efficiency of the recursive algorithm, it is usually the algorithm of choice in many applications. Unless stated otherwise explicitly [2].

In recursive phasor estimation, the phasor of a constant sinusoid remains stationary. Note that $\hat{X}^{N+r} = \hat{X}^{N+r-1}$ as long as the sample $x_{N+r} = x_r$.

III. Recursive DFT Model

In this section, the recursive DFT algorithm shown in Fig.1 is implemented and tested using computer simulation. Figure 2 shows the developed simulation model using Simulink.

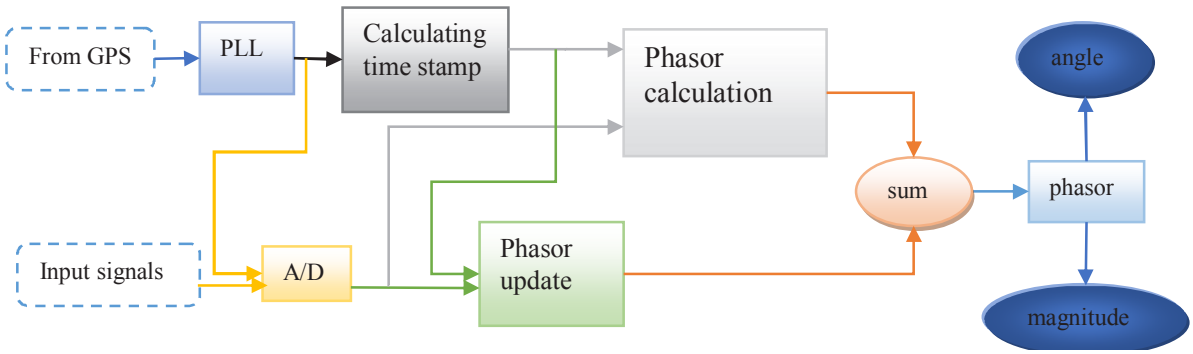

Fig.1. PMU model using recursive algorithm

.

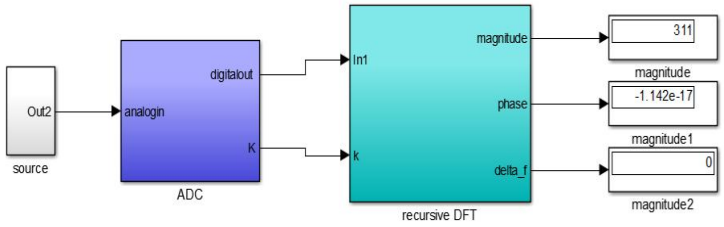

Fig.2.PMU simulink model

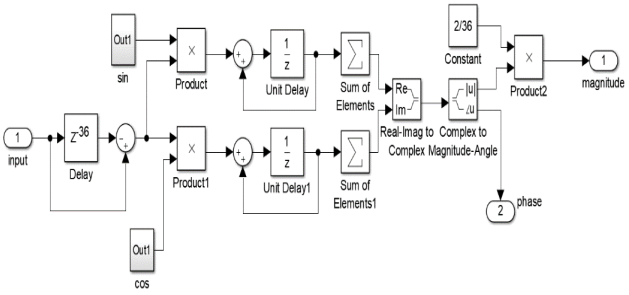

Fig.3. Full-cycle recursive DFT Simulink model

The PMU system, in general, needs two input signals: an analog sinusoidal signal which is the main input and a synchronization signal of 1pps from global positioning system (GPS). In this work, only the phasor calculation part is considered. Hence the sampling frequency is generated using a pulse generator.

First of all, the 50Hz sinusoidal analog input signal is sampled and quantized inside the ADC unit to obtain the samples x0, x1, x2....xN-1. Thereafter, fundamental components of input signal samples are extracted using the recursive DFT algorithm. Figure 2 shows the equivalent recursive DFT model using Simulink.

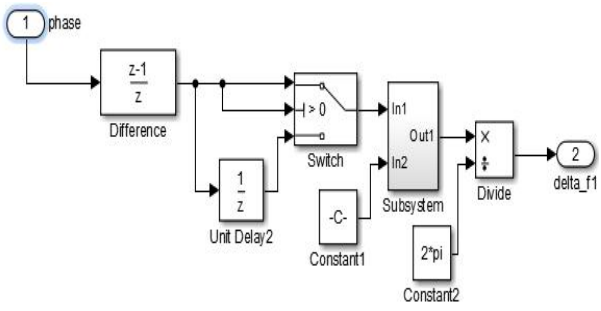

Fig.4. Simulation of the frequency calculation block

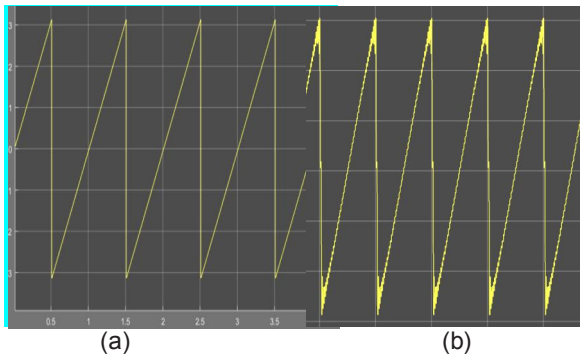

(a) (b)

Fig.5. Output: tracking of phase accumulated errors for f = 51Hz. (a) Just after signal application, (b) 1hour postsignal application

This model represents the implementation of recursive DFT as per equation 12. The block z^{-36} delay time represents the full-cycle sliding window of 36 samples.However,z^{-1}, represents the real time-recursive operation of (11) and (12). Product and Product1 multiply the difference between the new and old samples by the sine and cosine functions, respectively. The Real-Imag to Complex block formulates the phasor which will be then converted into magnitude and phase.

The two summing blocks are used for the purpose of conversion. They convert the fixed-point data into the standard float-point format defined by the IEEE standards, since it is not possible to carry on the fixed-point data directly to Real-Imag to Complex block. The rounding of the mathematical operation at the summing points is set to floor, which is the default option for most available CPUs.

For protection and control purposes, it is necessary to accurately measure and track the fundamental power frequency. In the proposed simulation, a frequency calculation block was constructed, too, as shown in Fig.4.

Figure 5 shows the output of the recursive DFT modeled by Fig. 3, with an input signal having 50 Hz frequency and 311V peak voltage. The recursive plot has only one phasor with amplitude of 311 and angle of 0°.

It should be noted that the limit cycle has never been recorded with this growing magnitude for the non-recursive DFT even with significant frequency deviations in the input signal.

IV. Proposed Method For Error Elimination

In order to eliminate the accumulation of errors, many different concepts can be applied. One of them is the reset of accumulation error at appropriate intervals.

In the proposed method, the reset period can be set arbitrarily, but new Fourier coefficients should be provided when the reset is to be performed. For simplicity, the reset period is synchronized with the DFT processing cycle. Figure 6 shows the Simulink model of DFT processing using the proposed reset algorithm.

In this simulation, a sampling counter, with values from 0 to (i_{N-1}) is used. When the count reaches k = i_{N-1}, reset is performed. The product input and multiplier $e^{j(\frac{2\pi k}{N})}$ is added to the reset phase data X_{res}; the result is then substituted for DFT calculation data X_1, while X_{res} is cleared to 0. Hence, reset processing at each sampling step reduces to calculation of X_{res} = X_{res} + input, which involves only minor additional processing.

The results of this simulation are shown in Fig. 7

The algorithm was proved effective in combination with the error correction. Using the proposed method, high-precision phase detection can be implemented using DFT in high-speed sampling.

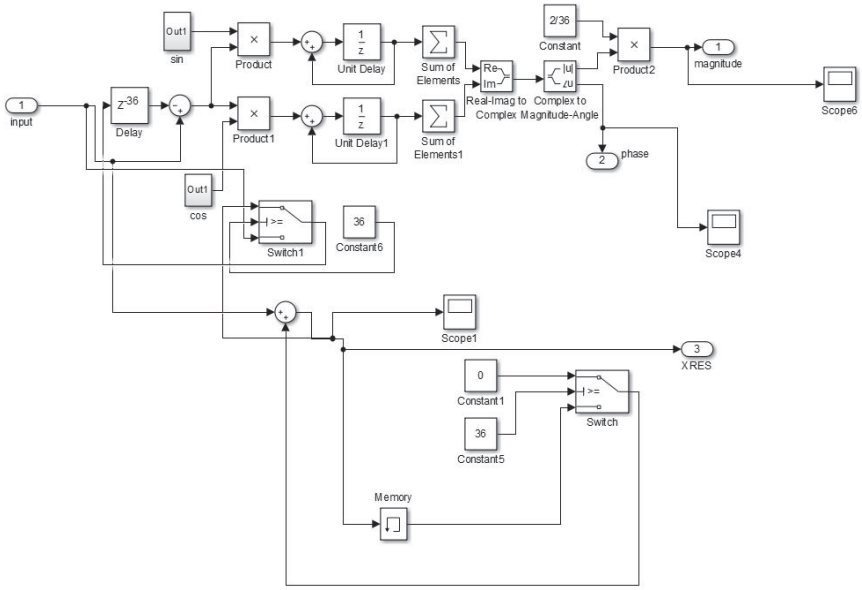

Fig. 6.Simulink model of DFT processing using reset algorithm

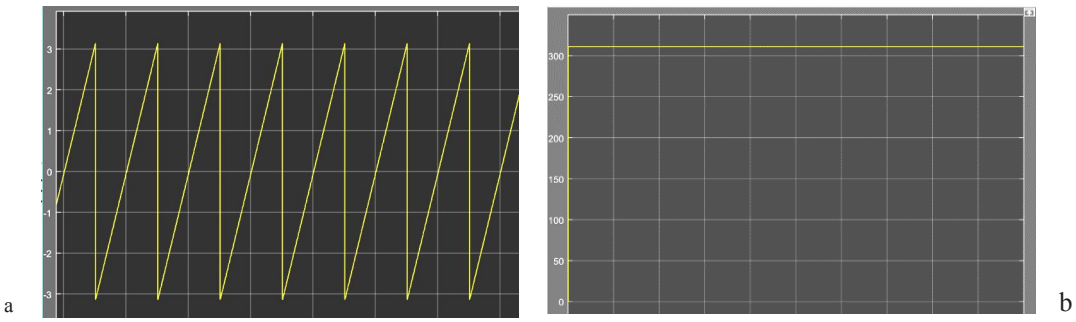

Fig. 7. Experimental tracking. (a) phase, (b) magnitude 1-hour postsignal applicationfor an input signal off = 51Hz using the reset algorithm

V. Conclusions

In this work, a new algorithm for recursive DFT error correction in PMUs is proposed. When using a recursive algorithm, the DFT involves less calculation. On the other hand, the accumulation of numerical error in the Fourier coefficients is an intrinsic problem, which must be solved. This study deals with the phase detection error of the recursive DFT. The proposed solution for eliminating this error was by performing a reset at appropriate intervals with minimal additional DFT calculation.Considering the simulated results, the algorithm was found to be effective and accurate. Using the proposed method, high-precision phase detection can be implemented using a DFT in high-speed sampling.

Acknowledgements

This research was supported by DGRDT/MESRS, Algeria.

References

1. Dhruba Kumar: “Simulation of Phasor measurement unit (PMU) in Matlab”. Space Dept of ECE, K L Univercity,(2015)
2. Phadke Arun G., Thorp S.: Synchronized phasor measurement and their applications. 2nd edn. Springer,Verginia,(2008).
3. M. Wang and Y. Sun, “A practical, precise method for frequency tracking and phasor estimation,” IEEE Trans. Power Del., vol. 4, no. 3, pp. 1547–1552, Jul. 2004.
4. Jose A. de la O et al. A new digital filter for phasor computation part I: Theory. IEEE Trans PS 1998;13;1026-1031.
5. Jose A. de la O et al. A new digital filter for phasor computation part II: Evaluation. IEEE Trans PS 1998;13;1032-1037.
6. Munukutla Naga Chaitanya and G. V. Siva Krishna Rao: “ Performance evaluation of recursive DFT as phasor estimator in PMUs under power quality disturbances”. International journal of engineering research & technology (IJERT). Vol.4 Issue 09, September 2015.
7. H. A. Darwish and I. Hartimo, “A close accord on DFT based frequency and phasor estimators for numerical relays,” Bull. Elect. Res. J., Oct.2001.
8. A. G. Phadke and J. S. Thorp, Computer Relaying for Power System. New York: Wiley, 1988.
9. A. G. Phadke, J. S. Thorp, and M. G. Admiak, “A new measurement technique for tracking voltage phasors, local system frequency, and rate of change of frequency,” IEEE Trans. Power App. Syst., vol. PAS-102, no. 5, May 1983.
10. G. Benmouyal, “An adaptive sampling interval generator for digital relaying,” IEEE Trans. Power Del., vol. 4, no. 3, pp. 1602–1609, Jul. 1989.
11. A. G. Phadke, “Synchronized sampling and phasor measurements for relaying and control,” IEEE Trans. Power Del., vol. 9, no. 1, pp. 442–452, Jan. 1994.

Energy-Efficient Retrofitting Strategies for Hospital Building for Heating Season

[1*]İsmail CANER, [2]Nadir İLTEN
[1,2] Balikesir University, Engineering Faculty Department of Mechanical Engineering,
Cagis Campus, Balikesir, 10145, Turkey

E-mail: * ismail@balikesir.edu.tr

Abstract
In this study, the current energy consumption values of Balikesir University Health Application and Research Hospital were examined and methods for reducing energy consumption during the heating season were determined. The building was modelled using Design Builder simulation program and user density, HVAC system, lighting, insulation and window types were entered into the program and simulated and actual energy consumption were compared. Then, the saving potential for the heating season was determined by the external wall and roof insulation, changing the windows and shading devices. Saving potential was determined between 4.88% to 7.84% by changing the roof and external wall insulation, and 0.56% to 12.59% by changing the window types. However, shading devices increased the energy consumption between 2.04% to 5.09%.

Keywords: Thermal Insulation, Building Energy Savings, Design Builder

I. Introduction

The growing needs on HVAC systems in residential, commercial and industrial environments have an outcome in a huge increase in energy usage, especially in the summer. Developing energy efficient HVAC systems is essential, both to protect consumers from surging power costs and to protect the environment from the adverse impacts of emissions. With rapid changes in science and technology, there are several methods that can be used to achieve energy-efficient HVAC systems (Vakiloroaya et al., 2014). Environmental pollution arising from increasing population, industrialization, urbanization and increased energy consumption has exposed the need for energy saving. One of the most effective ways to provide this is to decrease the energy consumption of buildings that account for about a third of global energy consumption. In many studies, applying heat insulation to the external walls or change the window type of building has been identified as the most effective method of reducing the energy consumption (Kaynakli and Yamankaradeniz, 2007). Simulation tools are helpful for designers or decision makers in order to investigate appropriate and suitable architectural and/or technical solutions to provide comfortable indoor and outdoor built environments. Most of the studies in literature showed that several building simulation softwares are existing and used effectively. They stated that it is important to decide which program to use in terms of margin of error. Thus, the reliability of some softwares were assessed by comparing simulation results with experimental data by researchers (Yildiz et al., 2018).

The aim of this study is to analyze the current energy consumption of Balikesir University hospital building by using energy consumption data and to reveal the energy consumption trends and reasons with the collected information. The energy saving potential of the cooling period is examined by taking into consideration the increasing cooling period due to the effect of global warming. The aim of the course is to determine the strategies aimed at significantly reducing the energy consumption for cooling season and to examine and evaluate the energy saving potentials with the help of simulations. For this reason, the energy consumption trend of the existing building located at the Çağış Campus of Balıkesir University has been examined by taking into consideration the characteristics of usage. In general, this study attempts to analyze potential opportunities for energy savings and effects with the goal of significantly reducing energy consumption for cooling purposes.

II. Experimental Procedure/Methodology/System Description

We selected a Balikesir University Health Application and Research Hospital building (Fig. 1) representing common construction and design features. Balikesir is located at 39.39° N latitude and 27.53° E longitude. Winters usually have cold temperatures and rainy weather; summers are dry and hot. The floor area of the building is approximately 37000 square meter. It is a six-floor building and consists of seven blocks. Its floor height is 3.8m. Electricity is used for cooling. Ventilation is done with a fan coil and controlled by a thermostat. Hospital has 200 beds for patients and also contain a variety of facilities including surgery rooms, laboratories, staff rooms, seminar rooms, computer suites, and cafeteria. The orientations of patient rooms are North-West and North-East and have large windows offering a great amount of daylight. About 93% of this total area is heated and cooled. A 3D model of the building was designed in the DesignBuilder program (Fig. 1).

General view of the Balikesir University hospital building.

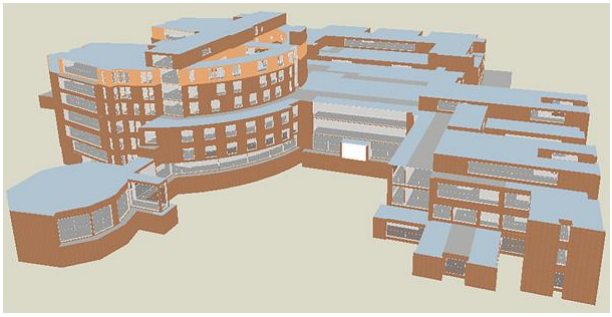

A view of the Balikesir University hospital building model.

Fig. 1. Balikesir University hospital building and model

By entering occupation density, lighting status, HVAC system, indoor temperature values, existing window, and insulation types, a model was tried to be modeled close to the actual consumption values (Fig. 1).

After defining the existing building features in the DesignBuilder program, the energy simulation model is calibrated using the current energy consumption values for testing the reliability and validity of the simulation results. Before implementing any energy efficiency improvement strategy, the results were compared with the actual electricity consumption data of the building. Mean Bias Error (MBE) and CVRMSE (Cumulative Variation of Root Mean Squared Error) were used to test the reliability and validity of the models.

Firstly, MBE was calculated. MBE is related to the average difference between the actual measured energy consumption data obtained for each month and obtained as a result of the simulation (Coakley et al., 2014). It is calculated using the following equation:

$$MBE(\%) = \frac{\sum_{i=1}^{N_p}(m_i - s_i)}{\sum_{i=1}^{N_p}(m_i)} \quad (1)$$

mi: actual measured value
si: simulated value
Np: The number of data in the range “p” (N monthly=12).

Another parameter to be calculated is the Root Mean Squared Error, which represents the root of the mean of the error frames. For this, the differences between the measured and simulated energy consumption values are squared every month. Then, the square root of the mean error squares obtained for each month is calculated and CVRMSE value is found. When this calculated RMSE value is divided by the measured actual energy consumption values, CVRMSE (Cumulative Variation of the Root Mean Squared Error) occurs. CVRMSE is formulated as follows:

$$CVRMSE = \frac{\sqrt{\sum_{i=1}^{N_p}((m_i - s_i)^2/N_P)}}{\overline{M_P}} \quad (2)$$

Mp: is the average of the actual values measured.
Mp is also calculated by the following formula:

$$\overline{M_P} = \frac{\sum_{i=1}^{N_p} m_i}{N_P} \quad (3)$$

The MBE and CVRMSE values calculated for the calibration of building energy simulation models are based on a variety of standard criteria determined according to the monthly or hourly measurement of the data (Jihad and Tahiri, 2018). The building energy simulation model is generally considered “reliable as long as the results meet the criteria shown in Table 1 as defined by the ASHRAE Guide 14, 2002 (Turner et al., 2008)

Table 1. Criteria for the calibration of building energy simulation models (Ashrae, 2002).

Standard	Monthly criteria (%)		Hourly criteria (%)	
	MBE	CVRMSE(monthly)	MBE	CVRMSE (hourly)
ASHRAE	5	15	10	30
IPMVP	20	-	5	20
FEMP	5	15	10	30

For the calibration of the hospital building, 1-year simulation of the model was performed. The cooling season electricity consumption data obtained from the simulation and the actual electricity consumption for 2018 are compared as in Fig. 2.

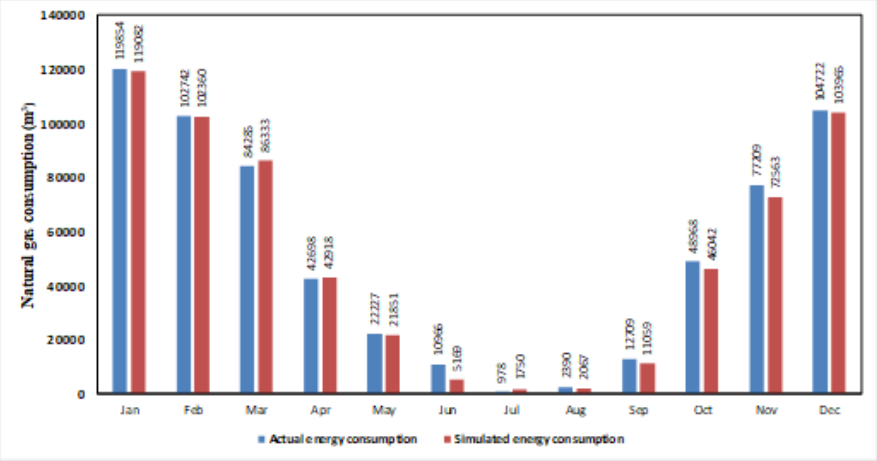

Fig. 2. Comparison of real and simulated energy consumption values.

According to these data, MBE and CVRMSE values were calculated to check the validity of the model (Eq. 1). As a result of calculations for natural gas consumption; MBE value was found as 3.28%; CVRMSE value was found as 4.70%. According to the values obtained from ASHRAE Guideline 14, since MBE monthly is 3.28% <5% and CVRMSE monthly is 4.70% <15%, the model is valid and reliable for natural gas consumption. For each strategy, five different levels were chosen. The levels are the commonly used options and were taken from literature. For EW and Roof, the values belong to optimum insulation thicknesses and calculated via Eq. 4.

$$x_{opt,H} = 293.94.\left(\frac{HDD.C_{fuel}.k.PWF}{H_u.C_{ins}.\eta}\right)^{\frac{1}{2}} - k.R_{t,w} \quad (4)$$

Table 2. Energy efficient retrofitting strategies and levels.

EW (cm)	Roof (cm)	Window U Value (W/m².K)	SHGC value of window	SD (m)	Temperature (°C)
4.78 EPS	3.13 EPS	1.978	0.687	0	24.4
3.17 XPS	1.82 XPS	1.8	0.641	0.5	24
7.48 GW	5.74 GW	1.3	0.47	1	23.5
7.07 RW	5.34 RW	1.1	0.30	0.5	23
2.15 PUR	1.11 PUR	0.7	0.135	1	22

III. Analysis

In this section the effects of strategies were examined (Fig 4.)

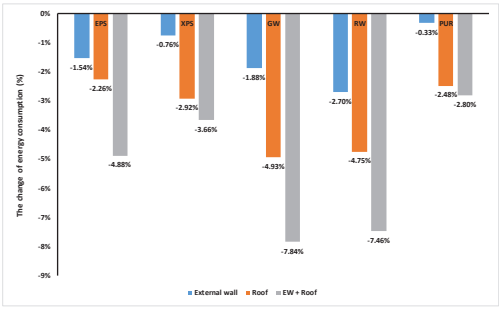

The effect of external wall and roof insulation

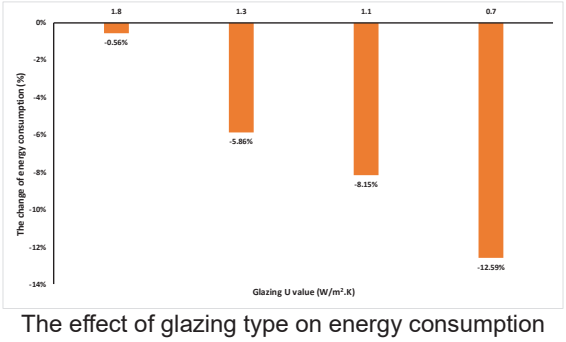

The effect of glazing type on energy consumption

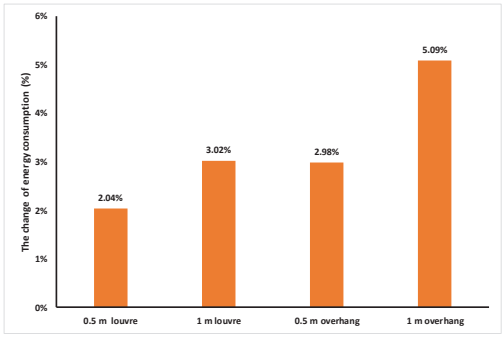

The effect of shading device on energy consumption

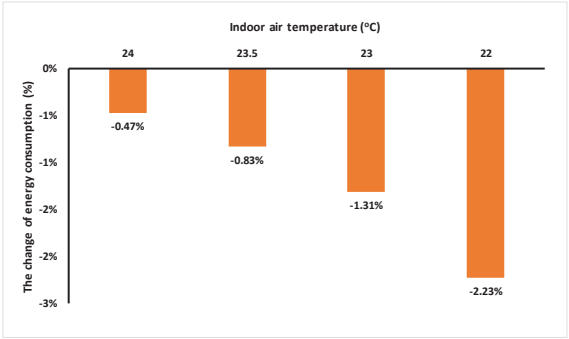

The effect of indoor air temp. on energy consumption

Fig. 4. The effects of strategies on energy consumption

IV. Results and discussions

When the effect of external wall and roof insulation on energy consumption was examined, the highest saving amount was obtained with 7.84% for GW at optimum insulation thickness It was calculated as 7.46% in case of applying optimum insulation with RW, 4.88% in case of appliying EPS, 3.66% in case of appliying XPS and, 2.80% in case of PUR insulation. When the change of glazing type is examined, the maximum energy saving for heating consumption is calculated as 12.59% with the application of glazing with U value of 0.7 W / m^2K. It was calculated that there was 8.15% saving potential with applying glazing with U value is 1.1 W / m^2K, 5.86% with 1.3 W / m^2K U value and 0.56% with 1.8 W / m^2K U value glazing application. Considering the effect of the shading devices, the energy consumption for the heating period increased by 2.04% with the application of 0.5 m louvre. The increase in energy consumption was 3.02% with a 1 m louvre application. The effect of 0.5 m overhang against heating consumption was 2.98% and 5.09% for 1 m overhang application. The average indoor air temperature calculated for the heating period was 24.4°C, while the energy consumption was found as 6381361 kWh. When the indoor temperatures are arranged according to TS 825 (TS 825, 2009), ASHRAE and DIN 1946, the decrease at energy consumption for 24°C is 0.47%, and 22°C is 2.23%.

V. Conclusions

As a result, the optimum values should be selected. However, energy savings, life cycle savings, payback periods and life cycle total costs should have been considered. The standards can change from region to region according to climate of area. Thus, local climate conditions effect the optimum insulation thickness. So, degree-day values that effect the optimum values should be calculate for each area.

Acknowledgements

This research was supported by the Balikesir University Scientific Research Projects Unit with number 2017/043.

References

Coakley, D., Raftery, P., Keane, M., 2014. A review of methods to match building energy simulation models to measured data. Renew. Sustain. Energy Rev. https://doi.org/10.1016/j.rser.2014.05.007

Jihad, A.S., Tahiri, M., 2018. Forecasting the heating and cooling load of residential buildings by using a learning algorithm "gradient descent", Morocco. Case Stud. Therm. Eng. 12, 85–93. https://doi.org/10.1016/j.csite.2018.03.006

Kaynakli, Ö., Yamankaradenİz, R., 2007. Isıtma Süreci ve Optimum Yalıtım Kalınlığı Hesabı. Viii. UlusalTesisMühendisliğiKongresi 187–195.

TS 825, 2013. Turkish Standard. Türk Stand. https://doi.org/10.1063/1.2884688

Turner, S.C., Kwok, A.G., Aynsley, R.M., Brager, G.S., Deringer, J.J., Ferguson, J.M., Filler, J.M., Int-hout, D., Levin, H., Levy, H.F., Rourke, M.P.O., Sekhar, C., Simmonds, P., Sipes, J.M., Sterling, E.M., Stoops, J.L., Sun, B.P., Taylor, S.T., Tinsley, R.W., Kennedy, S.D., Jayaraman, N.R., Myers, F., Cummings, S.D., 2008. ASHRAE STANDARD Thermal Environmental Conditions for Human Occupancy 4723.

Vakiloroaya, V., Samali, B., Fakhar, A., Pishghadam, K., 2014. A review of different strategies for HVAC energy saving. Energy Convers. Manag. https://doi.org/10.1016/j.enconman.2013.10.023

Yildiz, Y., Caner, I., Ilten, N., Karaoglan, A.D., 2018. Field study to analyse luminous comfort in classrooms. Proc. Inst. Civ. Eng. Eng. Sustain. 171, 151–165. https://doi.org/10.1680/jensu.16.00001

The Life Cycle Assessment Related to Insulation Thickness of External Walls of the Hospital Buildings

[1*]İsmail CANER, [2]Nadir İLTEN, [3]Okan KON
[1,2,3] Balikesir University, Engineering Faculty Department of Mechanical Engineering,
Cagis Campus, Balikesir, 10145, Turkey

E-mail: * ismail@balikesir.edu.tr

Abstract
In this study, energy savings to be gained by the insulation of the external walls of hospital buildings are examined according to Turkish Building Insulation standard (TS 825) which is renewed in December 2013. In addition, life cycle total cost (LCT) and life cycle savings (LCS) are calculated. In the literature generally, energy saving, life cycle total cost (LCT) and life cycle saving (LCS) values due to insulation thickness are calculated for the external walls of residences. In this study, these calculations were made for hospital buildings with high usage areas and external surface areas. Unlike the residences, the hospital buildings indoor temperatures should be 22 to 24 °C during the heating period according. According to TS 825, Balikesir University hospital building in Balikesir province stated in 2nd zone. Depending on these, the degree-day values of 2nd zone are calculated for the heating season. The basic temperature for the cooling period degree days is accepted as 22 ^{0}C for TS 825 and 24 ^{0}C for ASHRAE and the cooling degree-day values are calculated. Finally, the optimum insulation thickness was determined for the external walls of the hospitals buildings. The degree-of-day method is used in calculations. Extruded polystyrene (XPS), Expanded polystyrene (XPS), glass wool (GW), rock wool (RW) and polyurethane are used as insulation material. Optimum insulation thickness is the lowest polyurethane insulation material in the highest glass wool insulation material.

Keywords: Life cycle assessment, TS 825, thermal insulation, building energy savings

I. Introduction

The purpose of this work investigates the savings in energy consumption by insulation to be applied to the external walls of the hospital building which be built at five different climate zones according to TS 825. Life cycle assessment calculations are made for long term energy consumption. Optimum insulation thickness was calculated for the external walls of the hospital depending on the life cycle assessment calculations.

II. Methodology and System Description

Table 1 shows that heating and cooling degree-day values. When calculating degree-day values indoor air temperatures were accepted 22°C and 24 °C which recommended by TS 825 and ASHRAE, respectively. Degree-day values calculations are as follows (Kon, 2017),

$$HDD=30\sum_{1}^{12}(T_i-T_o) \quad (1)$$

$$CDD=30\sum_{1}^{12}(T_o-T_i) \quad (2)$$

Calculation of energy consumption

Annual heating load equation is

$$E_H=\frac{0.024.U.HDD}{\eta} \quad (3)$$

Annual cooling load equation is

$$E_C=\frac{0.024.U.CDD}{COP} \quad (4)$$

Calculation of degree-day is

$$DD=\frac{CDD}{COP}+\frac{HDD}{\eta} \quad (5)$$

Where CDD is cooling degree-day, HDD is heating degree-day, COP is cooling performance coefficient and η is heating system efficiency. Optimum insulation thickness equation is (Kurekci, N.A., 2016, Alghoul et al., 2016, Jraida et al., 2017),

$$x_{opt}=\left(\frac{0.024.C_e.PWF.k.DD}{C_i}\right)^{\frac{1}{2}}-k.R_{wt} \quad (6)$$

Where, C_e is cost of electricity, PWF is present value factor, k is heat thermal conductivity of insulation material, C_i cost of insulation material, R_{wt} thermal resistance of uninsulated wall. Optimum insulation thickness is the value that makes the total life cycle cost calculation minimum. Energy saving (ES) and life cycle total cost (LCT) of and life cycle saving (LCS) energy consumption equation is (Alghoul et al., 2016, Jraida et al., 2017, Kaynakli, 2012),

$$ES=C_e\left(\frac{(E_H(noins)-E_H(withins))+}{(E_C(noins)-E_C(withins))}\right) \quad (7)$$

$$LCS=C_e\left(\frac{(E_H(noins)-E_H(withins))+}{(E_C(noins)-E_C(withins))}\right)PWF\text{-}x.C_i \quad (8)$$

$$LCT=C_e(E_H+E_C)PWF+x.C_i \quad (9)$$

If i<g real interest rate is,

$$r=\frac{g-i}{1+i} \quad (10)$$

If g<i real interest rate is,

$$r=\frac{i-g}{1+g} \quad (11)$$

$$\text{Then } PWF=\frac{(1+r)^N-1}{r(1+r)^N} \quad (12)$$

Where i is interest rate and g are inflation rate (Dombayci et al., 2006).

Values used in calculations

Electricity price was taken as 0.107 \$/kW and natural gas price as 0.385 \$/m^3.. Electricity was used as an energy source for the cooling season and the cooling performance coefficient was taken as 2.5 (Čongradac et al., 2012). System efficiency is 0.99 for cooling season and 0.92 for heating season. The interest rate and the inflation rate were taken 7.25%, 11.13% respectively (Kon and Caner, 2019). Accordingly, PWF was found 8.27. Table 1 presents properties of insulation materials. Table 2 shows heating and cooling degree-days. Fig. 1. gives external wall structural components and properties.

Table 1. Properties of insulation materials (Kurekci, 2016)

Insulation Materials	Thermal Conductivity (W/m.K)	Price C_{ins} ($/m^3)
Expanded Polystyrene (EPS)	0.039	120
Extruded Polystyrene (XPS)	0.031	180
Glass Wool (GW)	0.040	75
Rock Wool (RW)	0.040	80
Polyurethane (PU)	0.024	260

Table 2. Heating and cooling degree-days (TS 825, 2013, ASHRAE)

Standard	Heating Degree-Day (HDD)	Cooling Degree-Day (CDD)	Accepted indoor air temp. (°C)	Recommend indoor temp. (°C)
ASHRAE	3277	23	24	22-24
TS 825	2719	194	22	22

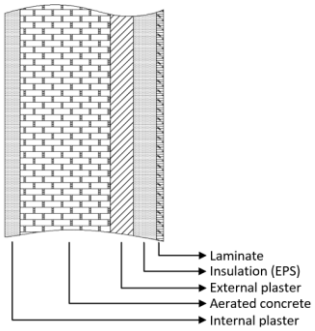

Fig. 1. Structural components of external wall (Kurekci, 2016)

Table 3. Optimum insulation thicknesses for five different insulation materials.

Standard	Optimum EPS (cm)	Optimum XPS (cm)	Optimum GW (cm)	Optimum RW (cm)	Optimum PUR (cm)
TS 825	4.04	2.60	6.48	6.11	1.73
ASHRAE	4.64	3.04	7.25	6.85	2.05

III. Analysis

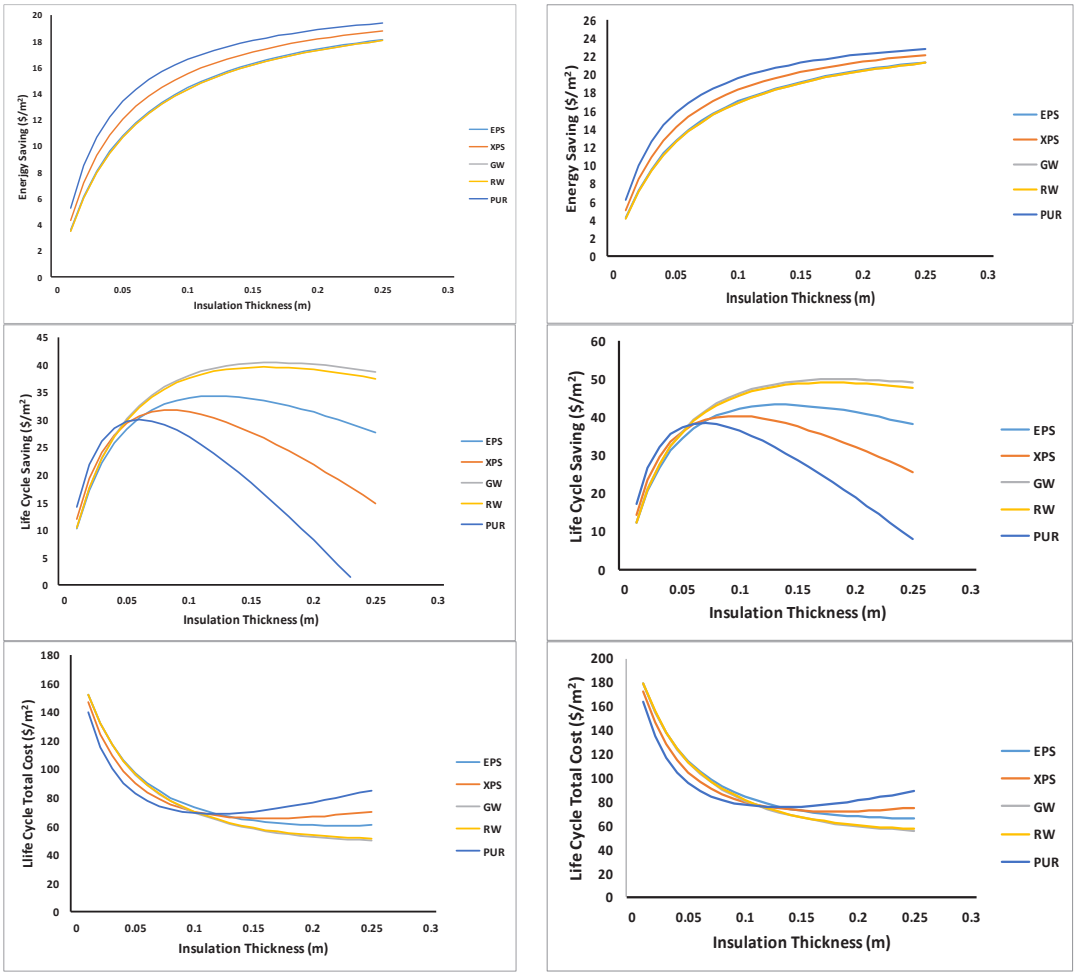

(a) **(b)**

Fig. 2. energy saving chart / life cycle saving chart / life cycle total cost chart according to optimum insulation thickness (a) TS825, (b) ASHRAE

IV. Results and discussions

Table 4. Optimum insulation thickness, energy saving, life cycle saving and life cycle total cost values for five different insulation materials

Standard	EPS	XPS	GW	RW	PUR
Optimum insulation thickness (cm)					
TS 825	4.04	2.60	6.48	6.11	1.73
ASHRAE	4.64	3.04	7.25	6.85	2.05
Energy Saving ($/m^2)					
TS 825	9.6358	7.4328	12.2316	11.8426	7.6741
ASHRAE	13.6741	10.9842	14.9246	14.4312	10.2158

Table 4. Optimum insulation thickness, energy saving, life cycle saving and life cycle total cost values for five different insulation materials (continue)

Life Cycle Saving ($/m^2)					
TS 825	25.8613	21.9416	33.5832	32.4332	20.3124
ASHRAE	33.3846	29.5198	42.0216	40.9614	26.7418
Life Cycle Total Cost ($/m^2)					
TS 825	105.1622	115.4224	85.2718	88.9078	121.7314
ASHRAE	118.4318	127.6814	94.9310	97.0618	134.256

According to TS 825 for Energy Saving, Life Cycle Saving and Life Cycle Cost (Table 4) for 5 different insulation materials used on the wall, energy saving values changes between 7.4328 to 12.2316 ($ / m2). Life cycle savings values changes between 20.3124 to 33.5832 ($ / m2). When the life cycle total cost is examined; it changes between 85.2718 to 121.7314 ($ / m2). According to ASHRAE-55 for 5 different insulation materials used on the wall, energy saving varies between 10.2158 and 14.9246 ($ / m2). Life cycle savings changes between 26.7418 to 42.0216 ($ / m2). When the life cycle cost is examined; it changes between 94.9310 to 164.256 ($ / m2). When the optimum insulation thicknesses are examined, it changes between 2.60 and 6.48 m for TS 825 and 2.05 and 7.25 m for ASHRAE-55.

V. Conclusions

The polyurethane has the lowest thermal conductivity and the lowest insulation thickness. Glass wool insulation material has the highest thermal conductivity and the lowest insulation material price The highest life cycle total cost value is found in polyurethane insulation material and the lowest in glass wool insulation material. Optimum insulation thickness is the lowest polyurethane insulation material in the highest glass wool insulation material.

Acknowledgements

This research was supported by the Balikesir University Scientific Research Projects Unit with number 2017/043.

References

ASHRAE Stand., vol. 2013, no. 55, 2013

Alghoul, S.K., Gwesha, A.O. and Naas, A.M. 2016. 'The effect of electricity price on saving energy transmitted from external building walls', Energy Research Journal, Vol. 7, No. 1, pp.1–9. https://doi.org/10.3844/erjsp.2016

Čongradac, V., Prebiračević, B., Jorgovanović, N., Stanišić, D., 2012. Assessing the energy consumption for heating and cooling in hospitals. Energy Build. https://doi.org/10.1016/j.enbuild.2012.01.022

Dombaycı, Ö.A., Gölcü, M. and Pancar, Y. (2006) 'Optimization of insulation thickness for external walls using different energy-sources', Applied Energy, Vol. 83, No. 9, pp.921–928. https://doi.org/10.1016/j.apenergy.2005.10.006.

Jraida, K., Farchi, A., Mounir, B. and Mounir, İ. (2017) 'A study on the optimum insulation thickness of building walls with respect to different zones in Morocco', İnternational Jounal of Ambient Energy, Vol. 38, No. 6, pp.550–555. https://doi.org/10.1080/01430750.2016.1155490.

Kaynakli, O., 2012. A review of the economical and optimum thermal insulation thickness for building applications. Renew. Sustain. Energy Rev. https://doi.org/10.1016/j.rser.2011.08.006

Kon, O., 2017. Determination of optimum insulation thicknesses using economical analyse for exterior walls of buildings with different masses. An Int. J. Optim. Control Theor. Appl. 7, 149. https://doi.org/10.11121/ijocta.01.2017.00462

Kon, O., Caner, I., 2019. The life cycle assessment related to insulation thickness of external walls of the airport. Int. J. Sustain. Aviat. 5, 158. https://doi.org/10.1504/ijsa.2019.101748

Kurekci, N.A., 2016. Determination of optimum insulation thickness for building walls by using heating and cooling degree-day values of all Turkey's provincial centers. Energy Build. https://doi.org/10.1016/j.enbuild.2016.03.004

TS 825, 2013. Turkish Standard. Türk Stand. https://doi.org/10.1063/1.2884688

Minimum Insulation Thickness to Prevent the Condensation of Building Outdoor Walls in a Different Direction

[1]Okan KON, [2*]İsmail CANER
[1,2] Balikesir University Engineering, Faculty Department of Mechanical Engineering,
Cagis Campus, Balikesir, 10145, Turkey

* ismail@balikesir.edu.tr

Abstract
The minimum insulation thickness should be calculated to prevent condensation on the external walls according to the type and property of the insulation material. This thickness is the thickness at which the saturation pressure in the insulation layer of the external wall is greater than the partial pressure. Both heat and mass transfer equations are used in the calculations. In the study, for minimum insulation thickness calculations, cities in five different climate zones were selected according to Turkish Insulation Standard TS 825. The coldest air temperature was determined from January which was the coldest month according to the average outdoor air temperature, relative humidity and wind speed values. The solar radiations in different directions were taken from TS 825. The outdoor solar-air temperature was calculated based on different directions in outdoor walls depends on the outdoor surface, emissivity and absorbance of solar radiation. The outdoor surface has been accepted as white and black painted. In the literature, generally, solar air temperature is not used for condensation calculations for outdoor walls. Expanded polystyrene (EPS) was chosen as insulation material and horizontally perforated bricks and tile were selected as a wall material.

Keywords: Outdoor wall insulation, condensation on outdoor walls, solar-air temperature

I. Introduction
The purpose of this study is to calculate the minimum insulation thickness to prevent the condensation on the external walls during the lowest outdoor temperature for five different cities selected to represent each climate zone according to TS 825. For January with the lowest temperature of the year, outdoor temperature, relative humidity, solar radiation in different directions and wind speed values were determined. While the outdoor temperature was found, the surface emissivity and absorbance coefficients were determined according to the white (acrylic) and black walls. In the outdoor temperature calculations, the northern direction with the lowest solar radiation is taken into account. Expanded polystyrene (EPS) are accepted as external wall material.

II. Methodology
The structure of the external wall was given in Figure 1. The place where condensation occurs was determined as the place where the external plaster contacts the surface of the insulation material. The values obtained from the Turkey General Directorate of Meteorology were given in Table 1. Table 2 shows the relative humidity and temperature values used for the condensation calculations. Table 4 shows the outdoor temperature values of the white and black painted exterior walls calculated for the cities in different climate zones depending on the directions and solar radiation. As can be seen from Table 4, the lowest temperature value was calculated in the north direction. Thus, the north direction temperatures were taken into consideration. The Solar Radiation Values given in TS 825 are 72 in the south direction, 26 in the north direction and 43 (W/m^2) in the west/east direction. The external wall heat transfer coefficients recommended in TS 825 are 0.660 for Zone 1, 0.570 for the second zone, 0.480 for the third zone, 0.380 for the fourth zone and 0.360 $W/m^2.K$ for the fifth zone (TS 825, 2013).

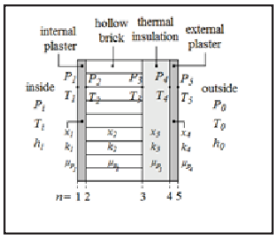

Fig 1. The external wall diagram (Yamankaradeniz, 2015, Kaynaklı, at all. 2018)

Table 1. Climate data for cities in different climate zones for January
(Turkish State Meteorological Service Datas, 2017)

City name	Climate zone	Temperature (^0C)	Relative Hum. (%)	Wind speed (m/s)
İzmir	1st zone	*8.06*	*67*	*3.10*
Balikesir	2nd zone	*3.37*	*83*	*2.41*
Ankara	3rd zone	*-0.01*	*78*	*2.22*
Van	4th zone	*-2.55*	*67*	*1.22*
Kars	5th zone	*-9.60*	*75*	*1.89*

Table 2. The values used in condensation calculations (TS 825, 2013)

Parameter	Value
Indoor Conditions	
Temperature, (°C)	*20*
Relative humidity (%)	*65*
Convective heat transfer coefficient for condensation calc., (W/m^2 K)	*4.0*
Outdoor Conditions	
Convective heat transfer coefficient, (W/m^2 K)	*25*

Table 3. Outdoor wall structural and properties (TS 825, 2013)

External wall construction component	Thickness (m)	Thermal Conductivity λ (W/mK)	Vapor diffusion resistance coefficient (μ)
Lime-cement mortar interior plaster	*0.030*	*1.000*	*15*
Horizontal perforated brick (Wall-1)	*0.190*	*0.330*	*5*
Tile (Wall-2)	*0.190*	*0.920*	*20*
Ekspanded polystrene (EPS)	---	*0.400*	*30*
Cement mortar exterior plaster	*0.040*	*1.600*	*15*

Table 4. Outdoor temperatures of white and black painted external walls with the effect of solar radiation for cities in different climate zones

Direction	1st zone	2nd zone	3rd zone	4th zone	5th zone
			White painted		
South	*7.33*	*3.80*	*1.40*	*-0.07*	*-5.50*
North	*6.54*	*2.93*	*0.50*	*-1.13*	*-6.56*
West / East	*6.83*	*3.25*	*0.83*	*-0.74*	*-6.17*
			Black painted		
South	*10.58*	*7.49*	*5.28*	*4.57*	*-0.40*
North	*7.60*	*4.21*	*1.90*	*0.60*	*-4.37*
West / East	*8.70*	*5.42*	*3.15*	*2.07*	*-2.91*

III. Analysis

III. I. Outdoor temperature calculation depending on solar radiation and external wall surface properties

The outer surface combined heat transfer coefficient (convection and radiation) (Yüksel at all, 2019);

$$h_{out}=8.91+2w \quad (1)$$

sky surrounding surface temperature;

$$T_{sky}=0.0552.(T_{out})^{1.5} \quad (2)$$

Outdoor temperature calculation depending on solar radiation;

$$T(t)=T_{out}(t)+\frac{\propto.I_s}{h_{out}}-\frac{\varepsilon.\sigma.\left(T_{out}^4-T_{sky}^4\right)}{h_{out}} \quad (3)$$

Here, I_s is solar radiation value, $\propto$ (0.26 for white paint and 0.98 for black paint) and ε (0.90 for white paint and 0.98 for black paint) are the solar absorptivity and the emissivity of the external wall face, T_{sky} is sky surrounding surface temperature, σ is the Stefan-Boltzman constant and w is outdoor wind speed (Çengel, 2014, Yüksel at all, 2019).

III. II. The equation of condensation calculations

Steady-state heat flux can be written as;

$$q=h_i\left(T_i-T_1\right)\rightarrow T_1=T_i-\frac{q}{h_i} \quad (4)$$

$$q_n=\frac{k_n}{x_n}\left(T_n-T_{n+1}\right)\rightarrow T_{n+1}=T_n-\frac{q}{\frac{k_n}{x_n}} \quad (5)$$

$$\theta_i=\frac{P_i}{P_{s,i}} \quad (6)$$

$$\theta_0=\frac{P_0}{P_{s,0}} \quad (7)$$

θ indoor and outdoor are relative humidty. $P_{s,i}$ and $P_{s,o}$ are the saturation water vapour pressures are indoor and outdoor air temperatures, respectively (Yamankaradeniz, 2015, Canbolat at all. 2018, Kaynaklı at all, 2018, Kon and Caner, 2019, TS 825, 2013).

$$\delta=\frac{1}{\mu_p} \quad (8)$$

Vapour permeability resistance is given in terms of the vapour diffusion resistance factor of material (μ) and vapour permeability resistance of air (δair) as follows

$$\delta=\mu\delta_{air} \quad (9)$$

in water vapour diffusion processes within the range of −20 °C to +30 °C.

$$\delta_{air}=\frac{D}{RT} \quad (10)$$

where R the gas constant for water vapor (Nm/mg K), T temperature (K) and D water vapor diffusion coefficient (m^2/h).

$$\delta_d=\mu.x \quad (11)$$

δ_d , diffusion of water vapor equivalent air layer thickness (m), μ is vapor diffusion resistance coefficient; x is thickness of building material layer (m) (Kaynaklı, 2018, Kon and Caner, 2019, TS 825, 2013) .In order to prevent condensation on the external wall, the pressure of the partial pressure (Pi) should be smaller than the saturation pressure (Psi). The first insulation thickness with the opposite is the minimum insulation thickness (Yamankaradeniz, 2015; Kon and Caner, 2019).

$$P_{si}-P_i>0 \quad (12)$$

III.III. Minimum insulation thickness calculation depending on the insulation material recommended in TS 825

Total heat transfer coefficient for the wall,

$$U=\frac{1}{(R_i+R_w+\left(\frac{y}{k}\right)_{ins}+R_o)} \quad (13)$$

Total thermal resistance for non-insulated wall according to $R_{t,w}$ is the total heat transfer coefficient of the wall,

$$U=\frac{1}{(R_{t,w}+\left(\frac{y}{k}\right)_{ins})} \quad (14)$$

Here, R_i and R_o are indoor and outdoor heat transfer coefficient. y is insulation thickness; k is insulation materials' heat transfer coefficient. (y/k) is insulation layers' thermal resistance (Bolattürk, 2006; Kaynaklı and Yamankaradeniz, 2007, Kon, 2017).

IV. Results and discussions

In Table 5, the minimum insulation thicknesses that are calculated based on the heat transfer coefficient recommended in TS 825 for different climatic zones are given. Table 6 shows the minimum insulation thicknesses calculated according to the condensation status for the white and black painted outer wall with brick and tile construction material in cities in different climate zones. It is observed that there is not a certain insulation thickness in all areas of the tile wall material in order to avoid condensation in the wall paint. This is because the heat transfer coefficient of the brick wall material is lower and the heat transfer coefficient of the tile wall material is higher. It is calculated that there is no need for insulation for brick wall material in order to avoid condensation in the first climate zone only. In order to avoid condensation on the brick wall material, the minimum insulation thickness required for the white painted wall is higher. This is caused by the difference in the surface absorbance coefficient of the wall surface. It is calculated that the minimum insulation thickness required to prevent condensation from occurring in the brick wall material in the 3rd climate zone is higher than in the 4th climate zone. This is because the relative humidity in the 3rd climate zone is higher. In the fifth climate zone, it is seen that the minimum insulation thickness required to prevent condensation is at a very high value compared to other climate zones. The reason for this is that the outdoor temperature in the fifth climate region is very low compared to other zones.

Tablo 5. Minimum insulation thickness recommended in TS 825 for different climate zones

Structure material	Zones				
	1st zone	2nd zone	3rd zone	4th zone	5th zone
Brick	*0.024*	*0.033*	*0.046*	*0.068*	*0.074*
Tile	*0.039*	*0.049*	*0.060*	*0.083*	*0.089*

Tablo 6. Minimum insulation thicknesses due to Condensation investigation for white and black painted external wall with brick and tile construction material in cities in different climate zones

Structure material	Zones				
	1st zone	*2nd zone*	*3rd zone*	*4th zone*	*5th zone*
			White painted		
Brick	---	*0.048*	*0.059*	*0.058*	*0.194*
Tile	---	---	---	---	---
			Black painted		
Brick	---	*0.028*	*0.038*	*0.021*	*0.135*
Tile	---	---	---	---	---

(a) (b)

Fig. 2. Pressure change depending on the insulation thickness for the a) white b) black painted external wall with brick material for the city of Izmir in the first climate zone

Fig. 3. Pressure change depending on the insulation thickness for the a) white b) black painted external wall with tile material for the city of Kars in the fifth climate zone

V. Conclusions

The insulation thickness recommended in TS 825 due to the expanded polystyrene insulation material is suitable for the minimum insulation thickness required for the condensation investigation for the first climate zone. In the second climate zone, the brick wall material is insufficient for the white painted wall and it is sufficient for the black painted wall. In the third climate zone, brick wall material is insufficient for a white painted wall and it is sufficient for a black painted wall. In the fourth climate zone, it is sufficient for both white painted and black painted walls. In the fifth climate zone, the insulation thickness recommended in TS 825 remains very low compared to the minimum insulation thickness required to prevent the condensation. For tile external wall material, the insulation thickness recommended in TS 825 is suitable for all regions and black and white painted external walls (Table 6).

References

Bolattürk, A., 2006. Determination of optimum insulation thickness for building walls with respect to various fuels and climate zones in Turkey. Applied Thermal Engineering, 26,11-12,1301-1309. https://doi.org/10.1016/j.applthermaleng.2005.10.019

Canbolat, A., S., Bademlioğlu, A., H., Kaynaklı Ö. 2018. Sandviç duvarlar için yalıtım kalınlığının belirlenmesinde yoğuşma faktörünün etkisi, IV. Uluslararası Katılımlı Anadolu Enerji Sempozyumu, 18-20 Nisan, Edirne, Türkiye.

Kaynaklı Ö., Bademlioğlu, A., H., Ufat, H., T., 2018. Determination of optimum insulation thickness for different insulation applications considering condensation, Technical Gazette, 25,1, 32-42. https://doi.org/10.17559/TV-20160402130509

Kaynaklı, Ö.,Yamankaradeniz, R., 2007, Isıtma süreci ve optimum yalıtım kalınlığı hesabı, VII. Tesisat Mühendisliği Kongresi, , İzmir, 25-28 Ekim, 187-195.

Kon, O. 2017. Ekolojik sürdürülebilirlik kapsamında binalarda kullanılan çevre dostu ısı yalıtım malzemeleri ve bunlara bağlı yenilenebilir yakıt tüketimi, Academia Journal of Engineering and Applied Sciences, Vol. 1, Issue 3, 143-155.

Kon, O., Caner, İ., 2019. Investigation of insulation thickness for buildings' external walls according to extreme climate conditions, 22.. Isı Bilimi ve Tekniği Kongresi / 22nd Congress on Thermal Science and Technology 11-14 September, Kocaeli, Turkey.

Türk Standardı, TS 825, Thermal Insulation Regulations in Buildings, December 2013.

Turkish State Meteorological Service Datas, 2017.

Yamankaradeniz, N., 2015. Minimization of thermal insulation thickness taking into account condensation on external walls, Advances in Mechanical Engineering, 7, 9, 1–11. https://doi.org/10.1177/1687814015604803

Yüksel, A., Arıcı, M., Karabay, H., 2019. Tarihi ve modern binalarda duvar yapılarının ısıl performensa etkileri, 22.. Isı Bilimi ve Tekniği Kongresi / 22nd Congress on Thermal Science and Technology 11-14 September, Kocaeli, Turkey.

Cengel, Y., 2014, Heat and mass transfer: fundamentals and applications. McGraw-Hill Higher Education.

Entropy Generation of a FLiBe Molten Salt Modular Nuclear Reactor Cooled by Supercritical Carbondioxide

[1*]Muhammed Emin TOPAL, [2]Adnan MİDİLLİ
[1] Recep Tayyip Erdogan University, Faculty of Engineering, Department of Mechanical Engineering, Rize, 53100, Turkey
[2] Yildiz Technical University, Faculty of Mechanical Engineering, Department of Mechanical Engineering, Besiktas,İstanbul, 34349 , Turkey

* E-mails: muhammedemin.topal@erdogan.edu.tr

Abstract
The main objective of this study is to investigate the entropy generation of cooling a FLiBe modular nuclear reactor with sCO_2 secondary coolant. In this regard, the cooling and power generation cycles of a 200 MW thermal power-modular nuclear reactor with LiF-BeF_2 salt as the main coolant are designed. Consequently, electricity production and energy efficiency are respectively calculated to be 82.9 MW, 41.5 % for the power generation system. The entropy generation of the turbine is calculated as 3.12 kW/K, the entropy generation of the low pressure compressor 0.77 kW/K, the entropy generation of the high pressure compressor 0,68 kW/K and the entropy generation of the reactor vessel 160 kW/K.

Keywords: Nuclear, Supercritical carbondioxide, Molten Salt, Energy, Entropy.

I. Introduction

Fossil fuel reserves, which are widely used in energy consumption today, are expected to decrease significantly in the near future (Kandiyoti et al., 2017; Chiari and Zecca, 2011). In addition, there are many damages of fossil fuels to nature (Cui et al., 2019; Billig et al., 2019). This situation forced scientists to develop different energy technologies and methods. One of these technologies is nuclear energy, which is a clean and sustainable energy source. Nuclear energy, which is a much cleaner type of energy compared to fossil fuel power plants, is becoming more and more secure with the help of developing technology, new technological designs and integrated cooling systems. Today's world, which always has to meet its electricity needs, can also benefit from smaller scale nuclear power plants as an alternative. It can be said that small modular reactors are safer in terms of closed loop and easier cooling than existing nuclear power plants. Such facilities can be installed and operated more easily in a more limited area at a lower cost. This important advantage facilitates easier implementation of such plants, especially in countries with limited space (Black et al., 2019; Devanand et al., 2019; Vegel and Quinn, 2017). Nuclear power plants can be classified in various ways in terms of the installed capacity, the type of coolant, the purpose of use (Bodansky, 2005; Ferguson, 2011). International Atomic Energy Agency defines small-scale modular nuclear reactors as nuclear power plants generating up to 300 MWe of electrical energy (IAEA, 2014; Todreas, 2015). Small modular nuclear reactors can be based on any of the nuclear technologies, including water, gas or salt cooled reactors and next generation (fourth generation) reactors (Breeze, 2019). Small modular nuclear reactors can be used for heat and/or power generation (Breeze, 2019). Their designs are simple, the production of their components can be in one place and build in another. Small modular reactors are systems whose construction costs are much lower than conventional nuclear reactors and can be installed in a shorter time (Ingersoll, 2015). In the establishment of a nuclear power facility, factors such as power requirement, cost, facility life and how long the system will pay for itself are taken into consideration. These calculations are based on the laws of thermodynamics. While the power generated in the system is calculated by the energy analysis of thermodynamics based on the first law, the irreversibilities and related losses in the system are calculated by the entropy analysis performed based on the second law of thermodynamics (Cengel and Boles, 2006).

In light of these considerations, within the scope of the study, the cooling of the LiF-BeF_2 (FLiBe) salt-cooled modular nuclear reactor with supercritical carbondioxide and power generation has been analysed in terms of entropy generation.

2. ANALYSIS

Potential improvements of the system or processes are provided with the energy analysis performed within the scope of the first law of thermodynamics. With the entropy analysis made within the scope of the Second Law of Thermodynamics, solution proposals are put forward for determining and reducing the type, location, size, quality and amount of irreversibilities occurring in systems or processes, and thus how to improve efficiency. Entropy can be defined as the distinction between irreversible and reversible processes. Entropy is also a measure of the amount of molecular disturbance in the system. Entropy generation can occur in systems, but it cannot be destroyed, it can only be increased or decreased (Dincer and Cengel, 2001).
In this study, entropy generation during the cooling and power generation of a modular FLiBe cooled nuclear reactor with supercritical carbondioxide (sCO_2) are investigated.

Assumptions

- A very high level of heat is generated from the fuel rods in the core of the reactor zone.

- It is assumed that the coolant completely receives this fission energy.
- Potential and kinetic energy and exergy values are neglected.
- The system is considered to be stable in continuous open continuous flow.
- Enthalpy and entropy values were obtained from NIST in November/2019 and may change due to changes in NIST.

This study was conducted in accordance with the above assumptions and the following general equations were used.

$$\sum \dot{m}_i - \sum \dot{m}_o = \frac{dm}{dt} = 0 \quad (1)$$

Based on the principle of energy conservation, the energy balance is written as follows.

$$\sum \dot{E}_i - \sum \dot{E}_o = \frac{dE}{dt} = 0 \quad (2)$$

The entropy balance is written as follows;

$$\sum \dot{S}_i - \sum \dot{S}_o + \dot{S}_{generation} = \frac{dS}{dt} = 0 \quad (3)$$

Based on this information and formulas, the thermodynamic analysis of cooling and power generation cycle was carried out.

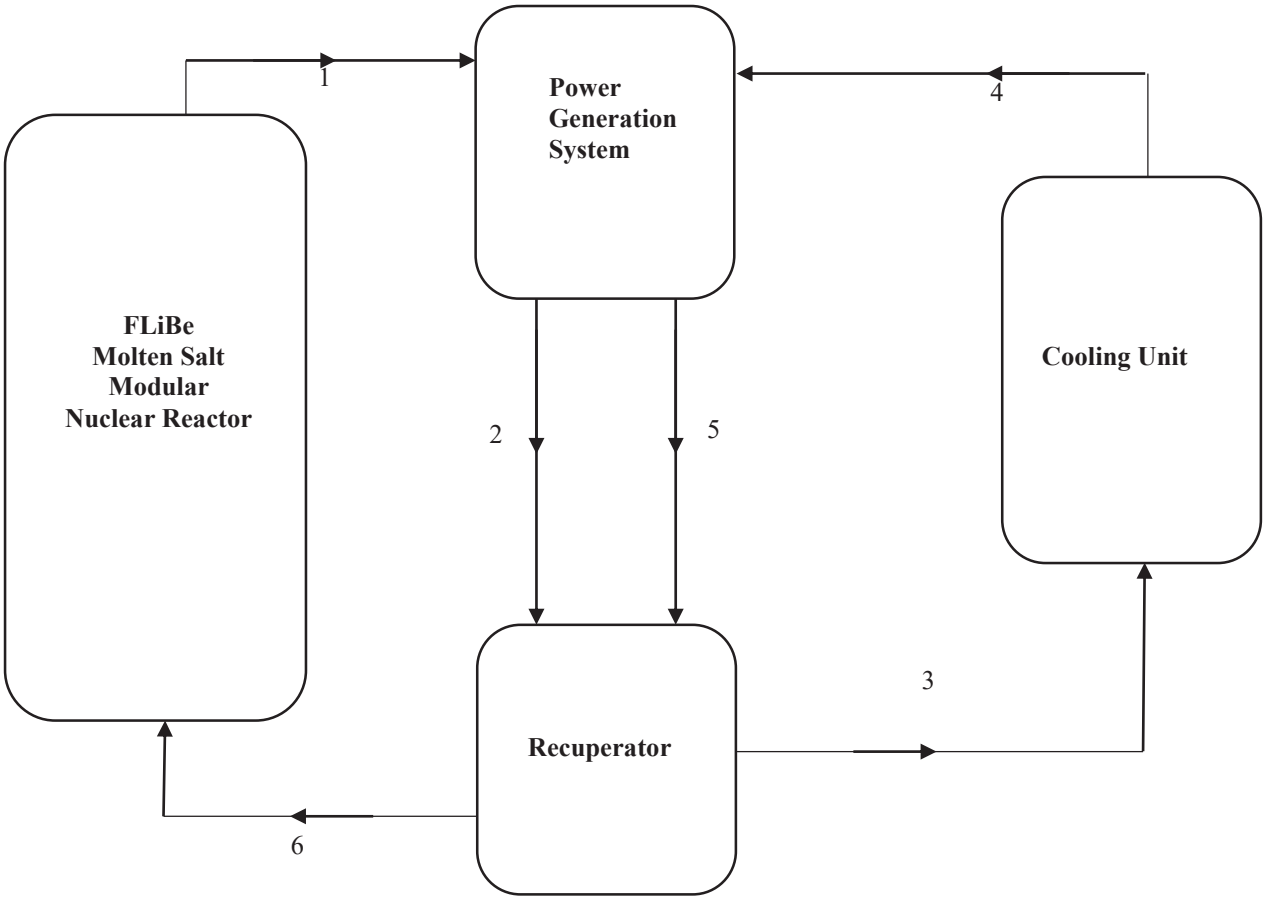

Figure 1. Schematic illustration of the system

The reactor vessel is cooled with 840 kg/s of FLiBe salt as in the first mode. The molten FLiBe salt circulated in the heat exchanger integrated in the reactor is cooled with the aid of sCO_2 at a flow rate of 476 kg/s and is sent back to the system via the circulation pump. The SCO_2, which is heated in the heat exchanger integrated in the reactor, enters the power generation system. Power generation system consists of a turbine and two compressors. The sCO2 cooler from the FLiBe Molten Salt Modular Reactor first enters the turbine. The turbine converts the kinetic and potential energy of sCO2 into mechanical energy. Using a generator, the mechanical energy obtained from the turbine is converted into electrical energy. The fluid whose pressure and temperature decreases in the turbine is cooled in the recuperator and then sent to the cooling unit. The cooling unit consists of two heat exchangers. One of these heat exchangers is located before the high pressure compressor and the other before the low pressure compressor. The role of the cooling unit is to ensure that the SCO2 coolant enters the compressor at the appropriate temperature. After the cooling unit, the coolant returns to the power generation system and enters

the compressor. The task of the compressors is to pressurize the coolant to complete the cooling and power cycle and send it to the recuperator and then to the FLiBe Molten Salt Modular Reactor. The coolant that is pressurized from the compressor to the reactor inlet pressure enters the recuperator. The coolant reaches the reactor inlet temperature by exchanging heat in the recuperator and then sent to the reactor. Thus, the cycle is completed.

Table 1. Entropy balance equations for the system

Unit	Entropy Balance
FliBe Molten Salt Modular Nuclear Reactor	$\dot{m}_1 s_1 + \dot{S}_{gen} = \dot{m}_6 s_6$
Power Generation System	$\dot{m}_1 s_1 + \dot{m}_4 s_4 + \dot{S}_{gen} = \dot{m}_2 s_2 + \dot{m}_5 s_5 + \dot{Q}_k / T_s$
Cooling Unit	$\dot{m}_3 s_3 + \dot{S}_{gen} = \dot{m}_4 s_4 + \dot{Q}_k / T_s$
Recuperator	$\dot{m}_2 s_2 + \dot{m}_5 s_5 + \dot{S}_{gen} = \dot{m}_3 s_3 + \dot{m}_6 s_6 + + \dot{Q}_k / T_s$

IV. Results and discussions

In this study, entropy analysis of cooling and power generation cycle of a modular nuclear reactor were carried out.

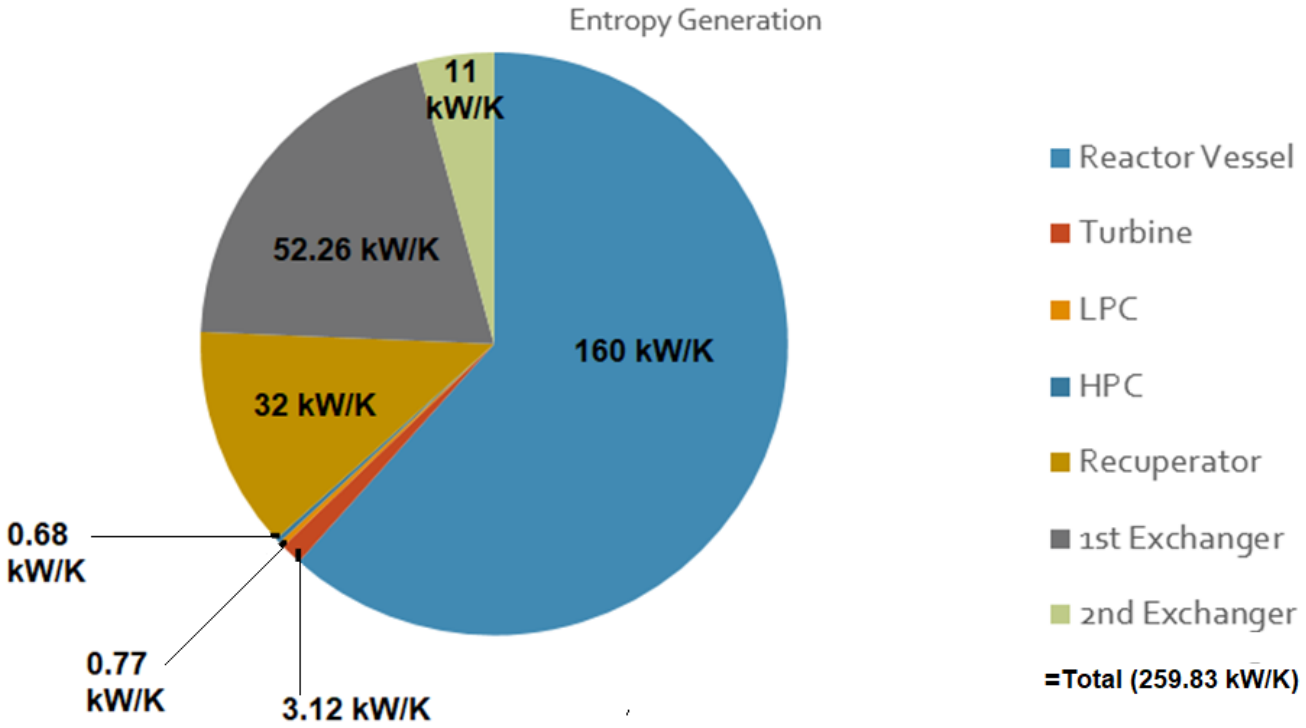

Figure 2. Entropy distribution of the system components

While the entropy generation realized in the turbine is 3.12 kW/K, this generation amount is calculated as 0.77 kW/K in the low pressure compressor, 0.68 kW/K in the high pressure compressor, 32 kW/K in the Recuperator, 52.26 kW/K in the 1st heat exchanger, 11 kW/K in the 2nd heat exchanger and 160 kW/K in the reactor vessel. As it is seen in the calculations, the highest entropy generation was realized in the reactor vessel in accordance with the literature. It is expected that this study will guide the researchers about the sCO_2 cycle for molten salt reactors.

V. Conclusions

At the end of the analysis, the following concluding remarks may be drawn:

- Entropy generation takes place mostly in the core area of the reactor.

- The lowest entropy generation conducts in the high pressure compressor.
- Recuperator is very important component exchanging heat. Therefore, in this equipment, the amount of entropy generation should be taken into consideration and decreased by designing an appropriate system.

References

Billig, E., Decker, M., Benzinger, W., Ketelsen, F., Pfeifer, P., Peters, R., Stoltena, D., Thräna, D. (2019). Non-fossil CO2 Recycling—The Technical Potential for The Present and Future Utilization for Fuels in Germany, Journal of CO2 Utilization, Pages 130-141. https://doi.org/10.1016/j.jcou.2019.01.012

Black, G.A., Aydogan, F., Koerner, C.L. (2019). Economic Viability of Light Water Small Modular Nuclear Reactors: General Methodology and Vendor Data, Renewable and Sustainable Energy Reviews, Volume 103, Pages 248-258. https://doi.org/10.1016/j.rser.2018.12.041

Bodansky, D., 2005. Nuclear Energy Principles, Practices, and Prospects Second Edition. DOI: 10.1007/b138326

Breeze, P. (2019). Nuclear Power. Power Generation Technologies, pages 399–429.

Cengel, Y.A. and Boles, M.A. (2006) Thermodynamics an Engineering Approach. Fifth Edition, McGraw Hill, New York.

Chiari, L., Zecca, A. (2011). Constraints of Fossil Fuels Depletion on Global Warming Projections, Energy Policy, Volume 39, Issue 9, Pages 5026-5034. https://doi.org/10.1016/j.enpol.2011.06.011

Cui, X., Newman, S., Xu, X., Andrews, A.E., Miller, J., Lehman, S., Jeong, S., Zhang, J., Priest, C., Campos-Pineda, M., Gurneyg, K.R., Graven, H., Southon, J., Fischer, M.L. (2019). Atmospheric Observation-Based Estimation of Fossil Fuel Co2 Emissions from Regions of Central and Southern California, Science of The Total Environment, Volume 664, Pages 381-391. https://doi.org/10.1016/j.scitotenv.2019.01.081

Devanand, A., Kraft, M., Karimi, I. (2019). Optimal Site Selection for Modular Nuclear Power Plants, Computers & Chemical Engineering, Volume 125, Pages 339-350. https://doi.org/10.1016/j.compchemeng.2019.03.024

Dincer, I., Cengel, Y.A. (2001). Energy, Entropy and Exergy Concepts and Their Roles in Thermal Engineering. Entropy, 3, 116-149. DOI: 10.3390/e3030116

Ferguson, C., 2011. Nuclear Energy What Everyone Needs to Know, Oxford University Press.

IAEA, 2014. “Advances in Small Modular Reactor Technology Developments,” September, 2014.

Ingersoll, D. T. (2015). Small modular reactors (SMRs) for producing nuclear energy: international developments. Handbook of Small Modular Nuclear Reactors, 27–60.

Kandiyoti, R., Herod, A., Bartle, K., Morgan, T. (2017). Fossil Fuels and Renewables, Solid Fuels and Heavy Hydrocarbon Liquids (Second Edition), Thermal Characterization and Analysis, Pages 1-9.

Todreas, N. (2015). Small modular reactors (SMRs) for producing nuclear energy: an introduction. Handbook of Small Modular Nuclear Reactors, 3–26.

Vegel, B., Quinn, J.C., (2017). Economic Evaluation of Small Modular Nuclear Reactors and The Complications of Regulatory Fee Structures, Energy Policy, Volume 104, Pages 395-403. https://doi.org/10.1016/j.enpol.2017.01.043

Wind Speed Analysis by Using Mixed Extreme Value Distributions

[1]*Hassan Tahir, [2]Arsalan Ahmed, [3]Weidong Zhao
[1] Ocean University of China, Faculty of Science, School of Mathematical Sciences, 238 Songling Road, Qingdao, 266100, China
[2] Dawood University of Engineering and Technology, Faculty of Science, Department of Basic Science and Mathematics, Karachi, 74600, Pakistan
[3] Shandong University, Faculty of Science, School of Mathematics, 27 Shanda Road, Jinan, 250100, China

*Email: hassantahir039@gmail.com

Abstract
The wind speed analysis is mandatory in designing and developing large infrastructure projects, airports, mass transit, and wind energy farms. It helps us understand the geographical distribution, the expected return period of extreme wind events and supports structural engineers to design and plan appropriate reinforcement for a resilient system. Four extreme value distributions, such as Gumbel, Weibull, Frechet, and Generalized Extreme Value, are generally used for probability distributions to model the wind speed data. This study aims to establish a comparison between univariate and mixed distributions (with the combination of two distributions and three distributions models). Due to the complexity associated with the mathematical formulation with the partial derivatives relative to the unknown parameters, the fmincon technique will be used to determine the unknown parameters. The optimum distributed univariate or mixture can be selected based on the minimum standard error of fit (SEF) criteria. We found that mixed distributions with the combination of three distributions are more accurate than univariate and mixed distribution with the combination of two distributions. In the given data set, 80% is fitted better for mixed distributions with a combination of three distributions, while the remaining 20% supports the mixed distributions with a combination of two distributions. Furthermore, the addition of more parameters resulted in improved results. It can be deduced from this statistical study that mixed distributions with the combination of three distributions can be opted as a mathematical tool for investigating extreme wind speeds.

Keyword: Wind speed, mixed extreme value distributions, parameter estimation

I. Introduction
The long-term use of fossil fuel based energy has led to the rise of global temperature near to the critical limit and the probability of risk associated to natural disasters such as floods, glaciers melting and landscape erosion, is increasing (Nemitallah et al., 2020). In order to combat climate change, the clean power generation has become essential with the addition of eliminating emissions from fossil fuel based power plants (Imteyaz et al., 2020; Imteyaz and Tahir, 2019). With the recent developments and the declining tariff in the past decade, solar and wind-based power generation have become the main renewable resources (Ali et al., 2018; Qadir et al., 2020). Wind power is considered the uncontaminated and most sustainable form of electricity generation because it does not produce toxic pollution or global warming emissions. Although it is enormous potential, environmental impacts associated with wind power generation must be recognized and diminished (Sahu, 2018). In order to examine the wind energy potential statistical distributions are used that can predict future wind distributions (Jung and Schindler, 2019). Various probability distributions were used to match the wind results, such as Gumbel, Fréchet, Weibull, and Generalized extreme value (Jung and Schindler, 2019). For wind speed analysis, Carta et al. studied probability distributions (Carta et al., 2009). The statistical analysis was undertaken to see if the collection of wind speed data came from a population with a particular probability distribution. Carlos and Agustin estimated extreme wind speeds by using Mixed Distributions (Carlos Agustín, 2013). It was demonstrated that how the extreme wind speed models could be implemented with mixed distributions and yield stronger results than univariate distributions. Unfortunately, the mixed distribution approach is insufficient, and could be more effective for three populations instead of two, which would refine the data on wind speed and detailed performance.

II. Methodology
The formulation of univariate and mixed distributions for assessing wind speed distributions are as follows:

Univariable Extreme Value Distributions

In general, extreme value distributions have been widely used to fit extreme wind speed distributions (Jung and Schindler, 2019). The probability density functions (PDF) of these extreme value distributions are as follow:

Gumbel distribution

$$f(x) = \frac{1}{\alpha} exp\left[-exp^{\left(-\frac{x-v}{\alpha}\right)}\right] exp^{\left(-\frac{x-v}{\alpha}\right)} \quad (1)$$

where $v\ and\ \alpha$ are the location and scale parameters, and $\alpha > 0$. The shape of the Gumbel model is independent of the distribution parameters.

Fréchet distribution

$$f(x) = \lambda \sigma^{\lambda} x^{-(1+\lambda)} exp^{\{-\left(\frac{\sigma}{x}\right)^{\lambda}\}} \quad (2)$$

Where $\sigma\ and\ \lambda$ are the scale and shape parameters, and $\sigma > 0\ and\ \lambda > 0$.

Weibull distribution

$$f(x) = \frac{k}{\phi}\left(\frac{x}{\phi}\right)^{k-1} exp^{\{-\left[\frac{x}{\phi}\right]^{k}\}} \quad (3)$$

Where $\phi\ and\ k$ are the scale and shape parameters, and$\phi > 0\ and\ k > 0$.

Generalized Extreme Value distribution (GEV)

$$f(x) = \frac{1}{\eta}[1 - \left(\frac{x-\omega}{\eta}\right)\beta]^{\frac{1}{\beta}-1} exp^{\{-[1-\left(\frac{x-\omega}{\eta}\right)\beta]^{\frac{1}{\beta}}\}} \quad (4)$$

where $\omega, \eta\ and\ \beta$ are the location, scale, and shape parameters, with $-\infty \leq \omega \leq \infty, \eta \geq 0\ and\ -\infty \leq \beta \leq \infty$.

Mixed Distributions

In order to produce mixed distributions and simulate wind speed results, this study considered four extreme value distributions, namely Gumbel, Fréchet, Weibull, and Generalized extreme value distributions. In this section, to generate mixed distributions, substitute equations (1 – 4) into the following equations (5) and (6). Long ago, it was proposed to use mixed probability distribution functions to model data samples from two populations (Mood et al., 1974):

$$P_r(X \leq \varepsilon) = F(x) = pF_1(x) + (1-p)F_2(x) \quad (5)$$

Where p is a factor used to weight the relative contribution of each population $(0 < p < 1)$. Carlos and Agustin used this model to mixed the two Extreme values distributions and got a better result rather than univariate distributions (Carlos Agustín, 2013). This study will modify the above equation with one more function and one more relevant parameter.

$$P_r(X \leq \varepsilon) = F(x) = pF_1(x) + rF_3(x) + (1-p-r)F_3(x) \quad (6)$$

Where p and r are associated parameters, $0 < p + r < 1$.

III. Analysis

Extreme value distributions, which are Gumbel, Fréchet, Weibull, Generalized Extreme Value distribution (GEV). Mixed Distributions (with the combination of two distributions) includes mixed Gumbel and Weibull

distributions (GW), Gumbel and Frechet distributions (GF), Gumbel and GEV distributions (GGEV), GEV and Frechet distributions (GEVF), Weibull and Frechet distributions (WF) and Weibull and GEV distributions (WGEV). Mixed Distributions (with the combination of three distributions) includes mixed Gumbel, Frechet and GEV (GFGEV), Gumbel, Weibull, and Frechet (GWF), Gumbel, Weibull, and GEV (GWGEV), and Weibull, Frechet and GEV distributions (WFGEV). The data source for this study is the China Meteorological Data Service Center ("China Meteorological Data Service Center," n.d.). Fourteen univariate and mixed distributions have been used. The fmincon technique is used to determine the unknown parameters. The best-distributed univariate or mixed can be chosen based on the minimum standard error of fit (SEF) criteria, as (W., 1988):$SEF_j = \left[\frac{\sum_{i=1}^{n}(g_i - h_i)^2}{(n-q)}\right]^{\frac{1}{2}}$, where j is the number of stations being analyzed, g_i is the recorded event, h_i is the event magnitude computed from the univariate or mixed distribution of the probabilities obtained from the ranks of g_i, q is the number of parameters estimated for univariate or mixed distributions, and n is the length of the record.

IV. Results and discussion

In this study, comparison is made between univariate and mixed distributions (combining two and three distribution models) as shown in Table 1. The newly proposed mixed distribution model performs well and is better than other distributions compared to wind speed data. The results show that GFGEV is the most suitable distribution. However, this work also showed that it is challenging to determine a single distribution that can be universally applied. Moreover, the results show that mixed distribution with a combination of three distributions fitted better in four wind stations out of five wind stations, and the rest station fitted with mixed distribution with a combination of two distributions.

Table 1. The SEF for univariate or mixed distributions for different wind stations (m/s)

	Huimin	Yanzhou	Beijing	Chongqing	Chengshan
Weibull	10.71	12.46	9.12	4.48	21.48
Gumbel	12.66	17.42	11.06	5.47	21.48
Frechet	13.69	17.37	13.35	11.92	23.35
Gev	10.17	12.13	9.06	4.82	20.26
GW	10.2	11.52	16.09	12.13	20.20
GF	20.84	18.75	17.79	19.08	32.88
GGev	10.56	11.25	9.84	4.68	19.11
GevF	20.88	18.42	15.63	13.11	31.22
WF	20.9	18.21	20.42	10.88	32.83
WGev	11.05	11.52	9.53	4.51	19.56
GFGev	11.14	11.25	9.01	4.41	20.01
GFW	10.1	48.34	9.62	4.47	20.10
GWGev	12.14	43.01	11.59	4.94	21.32
WFGev	10.51	12.6	12.86	4.50	75.36

V. Conclusion

This study's general objective is to establish a comparison between fourteen univariates and mixed distributions (with the combination of two distributions and three distributions models). Direct minimization is used to find the unknown parameters. The minimum standard error of fit (SEF) criteria is used to select the best models. Results have shown that there exists a reduction in the standard error of fit when estimating the parameters with mixed distributions instead of univariate distributions. 80% of samples were fitted better for mixed distributions with a combination of three distributions. Results suggest that it is important to consider the mixed distributions (with a combination of three distributions or more) as an additional mathematical tool when analyzing extreme wind speeds.

References

Ali, H., Tahir, F., Atif, M., AB Baloch, A., 2018. Analysis of steam reforming of methane integrated with solar central receiver system, in: Qatar Foundation Annual Research Conference Proceedings Volume 2018 Issue 1. Hamad bin Khalifa University Press (HBKU Press). https://doi.org/10.5339/qfarc.2018.EEPD969

Carlos Agustín, E.-S., 2013. Estimation of Extreme Wind Speeds by Using Mixed Distributions, Ingeniería, Investigación y Tecnología. Elsevier. https://doi.org/10.1016/s1405-7743(13)72233-9

Carta, J.A., Ramírez, P., Velázquez, S., 2009. A review of wind speed probability distributions used in wind energy analysis. Case studies in the Canary Islands. Renew. Sustain. Energy Rev. https://doi.org/10.1016/j.rser.2008.05.005

China Meteorological Data Service Center [WWW Document], n.d.

Imteyaz, B., Qadir, S.A., Tahir, F., 2020. Prospects of CO2 Utilization after Carbon Capture Process, in: 12th International Exergy, Energy and Environment Symposium (IEEES-12), Doha, Qatar.

Imteyaz, B., Tahir, F., 2019. Thermodynamic analysis of premixed and non-premixed oxy-methane combustion cycle with membrane assisted oxygen separation, in: 8th Global Conference on Global Warming (GCGW), Doha, Qatar. p. 33.

Jung, C., Schindler, D., 2019. Wind speed distribution selection – A review of recent development and progress. Renew. Sustain. Energy Rev. 114, 109290. https://doi.org/10.1016/j.rser.2019.109290

Mood, A., Graybill, F., Boes, D., 1974. Introduction to the Theory of Statistics, 3rd ed. McGraw-Hill, New York.

Nemitallah, M.A., Abdelhafez, A.A., Habib, M.A., 2020. Global Warming and Emission Regulations, in: Approaches for Clean Combustion in Gas Turbines. pp. 1–12. https://doi.org/10.1007/978-3-030-44077-0_1

Qadir, S.A., Tahir, F., Al-Fagih, L., 2020. Impact of Fossil Fuel Subsidies on Renewable Energy Sector, in: 12th International Exergy, Energy and Environment Symposium (IEEES-12), Doha, Qatar.

Sahu, B.K., 2018. Wind energy developments and policies in China: A short review. Renew. Sustain. Energy Rev. 81, 1393–1405. https://doi.org/10.1016/j.rser.2017.05.183

W., K.G., 1988. Frequency and Risk Analysis in Hydrology. Water Resources Publication.

Commodities Relationships Effect on Adopting Pro-environmental Measures

[1*]Reem Mamoon Mohamed, Frank Himpel

[1] Division of Engineering Management and Decision Sciences (EMBS), College of Science and Engineering (CSE), Hamad Bin Khalifa University, Qatar Foundation (QF), Education City, Doha, Qatar

* remohamed@mail.hbku.edu.qa, fhimpel@hbku.edu.qa

Abstract
This Research examines the form of relationship among commodities (either being substitutes or complements) ability to incentivize the adoption of pro-environmental measures. The study concentrates on producers in the manufacturing and food industries in different countries competing in the global market. Therefore, they are faced with different environmental regulations. Understanding the behavior rising from such relations would enhance our estimation of environmental policies' importance with respect to market dynamics. For instance, a firm is taking the lead on adopting pro-environmental technology due to government regulations. The substitute's producer in a country with less regulations would not adopt such technology to keep prices low and gain market share. However, if the follower decides to adopt the same change, it can indicate market preference of green production. This research would be conducted using an econometric model to study survey data of firms' adopting measures to reduce environmental impact. The outcome of the econometric model used will indicate the degree of causality between the market relation and pro-environmental measures through time. The empirical work would be analyzed considering organizational behavior theories and sociocognitive dynamics that could explain firm tendencies to adopt such measures in relation to other firms and consumers.

Keywords: pro-environmental behavior, substitutable products, complementary products, environmental regulations, econometric model

I. Introduction:

Factors that increase or deter a company's adoption of pro-environmental measures have been studied extensively. One framework to serve this purpose is to analyze consumer behavior towards environmentally friendly products. Some research findings have shown there is an increase in customer willingness to pay more due to an environmental aspect of a product or the process of its production (Dosi and Moretto, 2001). The practice of ecolabelling exploits this result, especially due to the policymakers' most agreed-upon view that ecolabelling leads to "spontaneous innovation" and competition among firms (Dosi and Moretto 2001). This view by policymakers could be translated as the following assumption: consumer assurance that a product is environmentally friendly corresponds to favoring the product. However, consumer reaction towards such products could be clouded by mistrust and a lack of understanding of associated terminologies. For instance, (Suku et al. 2006) have shown that consumers in the food industry consider the use of terminology as environmentally friendly "confusing". Moreover, customers do exhibit distrust towards companies' claims and do not perceive the products as beneficial in a manner that explains their higher price.

Consumer behavior could impact the possibility of a competitive advantage owing to environmentally friendly innovations. Our research does not question the idea of innovation firsthand. Yet, it is embedded in it. This is due to our evaluation of measures adoption, regardless if the development of the technology was carried by the same company. Thus, this line of research is studied, as competitiveness is a reflection of product substitutability. The use of green measures for successful product differentiation is still an arguable point. Similar to approaching the question via ecolabeling, it is not clear how customers react to these products due to the significance of other factors that cannot be easily disintegrated. According to (Forsman, 2013) companies that gained a competitive advantage after investing in innovations for greener products, do exhibit other common traits. for example, financial security and longer market presence. This undermines the role of the environmental innovation connection to an increase in sales.

In this context, one can approach this paper asking whether an environmentally friendly product can be substituted or complemented by a product that is not environmentally friendly even if the functionality did not change. This paper is proposing a product categorization theory as one route towards such an analysis because one needs to understand the effect of this new characteristic on the consumer cognitive conceptualization of the product. We are considering a sociocognitive approach regarding product categorization, establishing a model based on empirical results and theory.

Note that this paper is a work in progress, it will only discuss the substitutability aspect of the question.

II.Methodology

Theoretical Framework

This paper proposes that the difference in consumers' reaction to environmentally friendly products stems from their conceptualization of these new characteristics affect on already existing product categories. Consumers do not categorize the environmentally friendly product due to functionality, but it is a category based on representation. It is a category that relates to morality, ethics, and social responsibility. It opposes the more common functional categorization, which "enhance information processing efficiency as well as cognitive stability (Cohen and Basu, 1987). As a result, this paper would adopt a sociocognitive view of the product's market. In this view "products are tangible manifestations of informational cues that attach to definitions and become commonly understood and taken for granted" (Rosa et al., 1999). Thus, the authors argue that products are linked through "mental representations." This concept allows consumer conceptualization of product categories based on a wider range of factors other than functionality. For instance, their awareness of environmental issues or their location in countries threatened by climate change.
In addition, the paper questions market dynamics' significance considering countries' regulations. If such a relationship can be established, this indicates a market multiplier of adoption, which reduces the pressure on regulating all the countries as it can be a complicated political process. Therefore, a handful of countries adopting pro-environmental measures would give rise to a proactive environmental strategy by firms in other, less regulated countries.

Data

This paper aim to establish a cause-effect model to explain two depndendent variable. We utilize data from Enterprise Sureys provided by the World Bank for 17 countries along to data from the Enviornmental Performance Index. There are 6067 observations. Note that all the firms are manufacturing firms for their main product. This is a cross sectional analysis to see the effect on two measures, whether a firm adopted pro-environmental measure at all, and the number of measures adopted. We examine the relationship between products relationship affect on the two measure, taking in consideration a number of other variables. The other varibales are the market of operation, environmental performance index ranking of the firm's country, and whether the consumer require certification to adhere to some environmental regulations in the production.
We will be using two regression models. The variable $env\_measure$ is binary, that takes the value of 1 if at least one pro-environmental measure was adopted in the last three years. Consequantly a logistic regression is appropriate. A linear regression is used to analyse the dependent variable total_measure that calculate the sum of the measures adopted by a firm in the last three years. Note that in this survey, the firm's respondant choose from ten options, where one option reflects the adoption of other forms not stated in the survey.

Logistic regression:

$$env\_measure_i = \beta_0 + \beta_1 international_i + \beta_2 cert_i + \beta_3 prod\_code_i + \beta_4 EPIrank_i + \mu_i$$

Linear Regression:

$$total\_measure_i = \beta_0 + \beta_1 international_i + \beta_2 cert_i + \beta_3 prod\_code_i + \beta_4 EPIrank_i + \mu_i$$

The dependent variable $international_i$ is binary reflecting whether the market for a firm's main product is national or international. $cert_i$ is also binary equal to 1 if customers require of a certifications or adherence to some environmental standards and 0 if not. $prod\_code_i$ is a categorical variable with a code given to categorize the main product for a firm. We will be analyzing the significance of this variable closely, to see whether companies exhibits similar measurement adoptions. The Enterprise Surveys codes are from the International Standard Industrial Classification of All Economic Activities. Finaly, $EPIrank_i$ is the countries rank on the environemntal performance index. The higher the number, the lower a countries environmental performance. All the variables independent or dependent apply for the i-th firm. The use of the EPI ranking is meant to reflect general sentiments towards a country's environmental point of view in a way that is more rigorous than regulations. As regulations are not necessarily implemented for instance. Note that the surveys provide us with levels to a company's view of environmental regulations. For instance, if a company reports that regulations are a very severe obstacle would be given a higher value than others. Table 1 is the result of running a simple linear regression in which we see a statistically significant negative coefficient of the obstacle level. Countries where regulations are considered a bigger obstacle, will have a lower EPI rank.

VARIABLES	(1) Model 1
How much of an obstacle: Environmental Regulations	-6.182***
	(0.505)
Constant	86.63***
	(0.655)
Observations	5,540
R-squared	0.029

Robust standard errors in parentheses
*** p<0.01, ** p<0.05, * p<0.1

Table 1

It is interesting to note though using regulations obstacle variable in the regressions does not yield a statistically significant outcome unlike the EPI ranking.

III. Results and discussions

Table 2 and Table 3 are the results of the logistics and linear regressions respectively. In the case of logistic regressions note that the result is not the coefficient but the odds ratio. This means if the dependent variable increase by 1 for example the odds of the occurance of the event, which is $\frac{probability\ of\ the\ event}{1-probability\ of\ the\ event}$ is multiplied by the odds ratio. If the odds ratio > 1 then it is a positive relationship and if it is < 1 it is a negative one.

VARIABLES	(1) Odds ratio
env_measure	
1.international	1.890***
	(0.210)
2.cert	0.169***
	(0.0250)
Preparation and spinning of textile fibers; weaving of textiles	0.417***
	(0.114)
Manufacture of structural metal products	0.507***
	(0.128)
Manufacturing of steam generators, except central heating hot water boilers	0.0965***
	(0.0693)
Maufacture of machinery for mining, quarrying and construction	0.311***
	(0.121)
EPIrank	1.003***
	(0.000856)
Constant	19.44***
	(5.211)
Observations	5,950

seEform in parentheses
*** p<0.01, ** p<0.05, * p<0.1

Table 2

VARIABLES	(1) Model 1
total_measure	
1.international	1.366***
	(0.126)
2.cert	-2.561***
	(0.113)
Preparation and spinning of textile fibres; weaving of textiles	-1.078***
	(0.316)
Manufacture of structural metal products	-0.798***
	(0.280)
Manufacture of steam generators, except central heating hot water boilers	-3.010***
	(0.878)
Manufacture of machinery for mining, quarrying and construction	-1.119**
	(0.457)
EPIrank	0.00314***
	(0.00104)
Constant	5.543***
	(0.267)
Observations	5,434
R-squared	0.179

Robust standard errors in parentheses
*** p<0.01, ** p<0.05, * p<0.1

Table 3

In the logistic regression, the odds of adopting at least 1 environemntal measure increase if a firm main market is the international market. The interesting result is the negative relationship with customer requirement of a certificate to adhere to some environmental regultions. Both of these variables are statistically significant with a p -value equal to 0.000. A similar result was opbtained in the linear regression as the sign of the coefficient is negative for the variable $cert$ and positive for $international$.
There are 128 product categories, only few categories are exhibited in the tables. Most of the categories are not actually statistically significant in both regressions. Therefore, a closer look would be adequate into the handful industries where their categories is statistically significant. In addition, we would re-examine the data regarding the customer requirement of certification.

IV. Conclusions

This paper examines the effect of product relationship on a manufacturer adoption of pro-environmental measures. The paper considered a sociocognitive view to explain the potential of such an angle to explain consumer behavior and incentivize companies' proactive environmental strategy.
The empirical work showcased that specific product categories have a significant effect on a firm's adoption of a measure and the total number of measures adopted. Moreover, it showcased that firms that are engaged in the international market tend to adopt more environmental measures. The work on this research would proceed to enhance the scope of the data and the variables included. In addition, develop a proxy that captures substitutability and study the complementary products affect.

Acknowledgements

This publication was made possible by an award from Qatar National Research Fund (a member of Qatar Foundation) with scholarship number GSRA6-2-0525-19041. The contents herein are solely the responsibility of the authors. The authors acknowledge the support provided by the Hamad Bin Khalifa University, Qatar Foundation.

References

Cesare, D., Michele, M., 2001. Is Ecolabelling a Reliable Environmental Policy Measure?. Environ. Resour. Econ. 1, 113

Cohen, J.B., Basu, K., 1987. Alternative Models of Categorization: Toward a Contingent Processing Framework. J Consum Res. 4, 455-472

Enterprise Surveys (http://www.enterprisesurveys.org), The World Bank.

Forsman, H., 2013. Environmental Innovations as a Source of Competitive Advantage or Vice Versa?. Business Strategy and the Environment. 5, 306-320

Rosa, J.A., Porac, J.F., Runser-Spanjol, J., Saxon, M.S., 1999. Sociocognitive Dynamics in a Product Market. J. Market. 4, 64-77

Suku, B., Michael, P., John, C., Shadwell, F., 2006. Environmentally sustainable food production and marketing : Opportunity or hype?. Br. Food J. 8, 677-690

Wendling, Z. A., Emerson, J. W., Esty, D. C., Levy, M. A., de Sherbinin, A., *et al*.,2018. 2018 Environmental Performance Index. New Haven, CT: Yale Center for Environmental Law & Policy.

Natural Gas Portfolio Optimization for Thermopower and Petrochemical Feeds

[1] Henrique Plaudio, [2*]Brenno Menezes, [1] Fernando Pessoa
[1] Federal University of Rio de Janeiro, Department of Chemical Engineering, Rio de Janeiro, Brazil
[2] Hamad Bin Khalifa University, College of Science and Engineering, Division of Engineering Management and Decision Sciences, Qatar Foundation, Doha, Qatar

* E-mail: bmenezes@hbku.edu.qa

Abstract
Natural gas (NG) is a clean fuel, highly efficient (highest enthalpy per mass) and lowest carbon intensive amongst fossil fuels. For these reasons, its increasing importance for society related to climate change and industry in terms of energy security and costs push the CH_4 based fuel into the demanded transition to an environment-friendly energy market. The development of infrastructure to produce and process natural gas for exports or utilization in thermopower and petrochemicals will become essential in its value chain. In such context, the installation of thermopower plants (TTPs) and natural gas processing plants (NPPGs), the later associated to transmission pipelines, are considered in the proposed portfolio optimization presented in this paper. The problem considers the NG projections in Brazil, with a potential of 65% increase in its production between 2020 and 2029, to determine business models capable to fulfil expectations of enterpreneurs and stakeholders in this industry. In the example, the main exploration regions found in the Brazilian National Energy Plan are defined as production clusters to properly aggregate the exploration fields. The selection of the production clusters follow the already installed transmission pipelines connecting to the locations of the thermopower plants and processing units to be installed. The net present value (NPV) of the investments are compared to determine the optimal scenarios to be adopted for the set of the GN production nationwide. The methodology is generic enough to the applied in other countries such as Qatar where recent discoveries of new reserves will enlarge its giant production mainly to reach an increase of 64% by 2027 in liquid natural gas (LNG) exports. The new production expansion will allow Qatar to increase its long-distance exports from its current 25% worldwide to the past few years 30% of the LNG market as well as intensify its use in thermopower and petrochemical feeds, opening the possibility for the industrial expansion nationwide and the governmental initiative known as Qatarization that aims to rise the number of nationals in public and private sector with an objective of 50% of the workforce in the industrial and energy sectors.

Keywords: Natural gas, thermopower plants, petrochemical feeds, portfolio optimization, net present value

I. Introduction

Natural gas (NG) is considered the cleanest fossil fuel by its highest release of energy per mass (therefore more efficient) and its reduced carbon intensity (roughly 90% of CH_4 for a light or non-associated NG); therefore reducing the impacts of CO_2 emissions by its utilization as source of energy. The global energy consumption has reached 13,865 billion tones of crude-oil equivalent in 2018, wig NG figuring around 24% after coal (27%) and crude-oil (34%) (BP, 2019). The global NG consumption was responsible for more than 40% of the primary energy consumption increase between 2017 and 2018, which demonstrate the potential of such energy worldwide. The NG production is continually increasing with an evolution from 1.2 trillion of cubic meters in 1973 to 3.8 trillion of cubic meters in 2018 (BP, 2019). In Brazil, the GN market share evolved from 9.69% in 2007 to 12.5% in 2018 highlighting the increasing of such resource (EPE, 2008; EPE, 2019a).

Particularly, in terms of electricity generation worldwide, thermopower plants (TPPs) based on NG represent roughly 23.2% of the total and coal 38.0% (BP, 2019). In Brazil, the major production of electricity comes from hydropower due to the huge national capacity of rivers resulting in 66,6% (Epe, 2019a). Today, the Brazilian energy matrix counts on NG to continually increase its utilization in the electricity production in order to reduce the huge dependence on hydropower generation and as a backup of the other renewables such as wind and solar energy sources since those rely on intermittent conditions. Nevertheless, NG is nowadays the second most utilized source of energy to produce electricity equivalent to 8,6% in Brazil (EPE, 2019a). The utilization of NG is increasing internationally, mainly due to climate change and energy security issues as well as to use cleaner fuels (Zhang et al., 2018). The same scenario occurs in Brazil and can be enlarged by new discoveries of associated gas in the Pre-Salt regions and in the new exploration frontline in the Sergipe-Alagoas Basin (EPE, 2019b; Instituto Acende Brasil, 2016).

To sell NG considering the determinations of regulatory agencies, NG must be processed in complex natural gas processing plants (NGPP) with several fractionation towers to specify the NG using separation processes of the diverse components removing impurities and contaminants and allowing to recover the heavier fractions as ethane, propane, butanes (nC_4 and iC_4), liquefied petroleum gas (LPG), and C_{5+}. These streams can be sold separated to petrochemical plant as feeds. On the other hand, a simplified treatment to remove the heavy components from the NG allows the lighter product stream to be commercialized for specific uses such as in thermopower as energy source to produce electricity from non-specified NG. In this case, there is no possibility of commercialization of the heavy fractions of NG, however the necessity of NGPP and consequently its installation and operational costs are eliminated.

The possibility of utilization of NG as raw or processed streams allows the exploration in regions with or

without NG infrastructure (NGPP, pipelines, consumers), so that guarantee flexibility to capitalize in investment using NG. In such a context, this work aims to determine the best options of the project as a portfolio optimization case to maximize net present value (NPV) of the assets of NG evaluated (TPPs, NPPGs) for Brazil considering the national projections in NG production.

II. Methodology

The first step of this work is to define the regions of the portfolio optimization study. The production regions area aggregated in one single stream to the destination of the project to be evaluated. The groups from A to J are found in Figure 1.

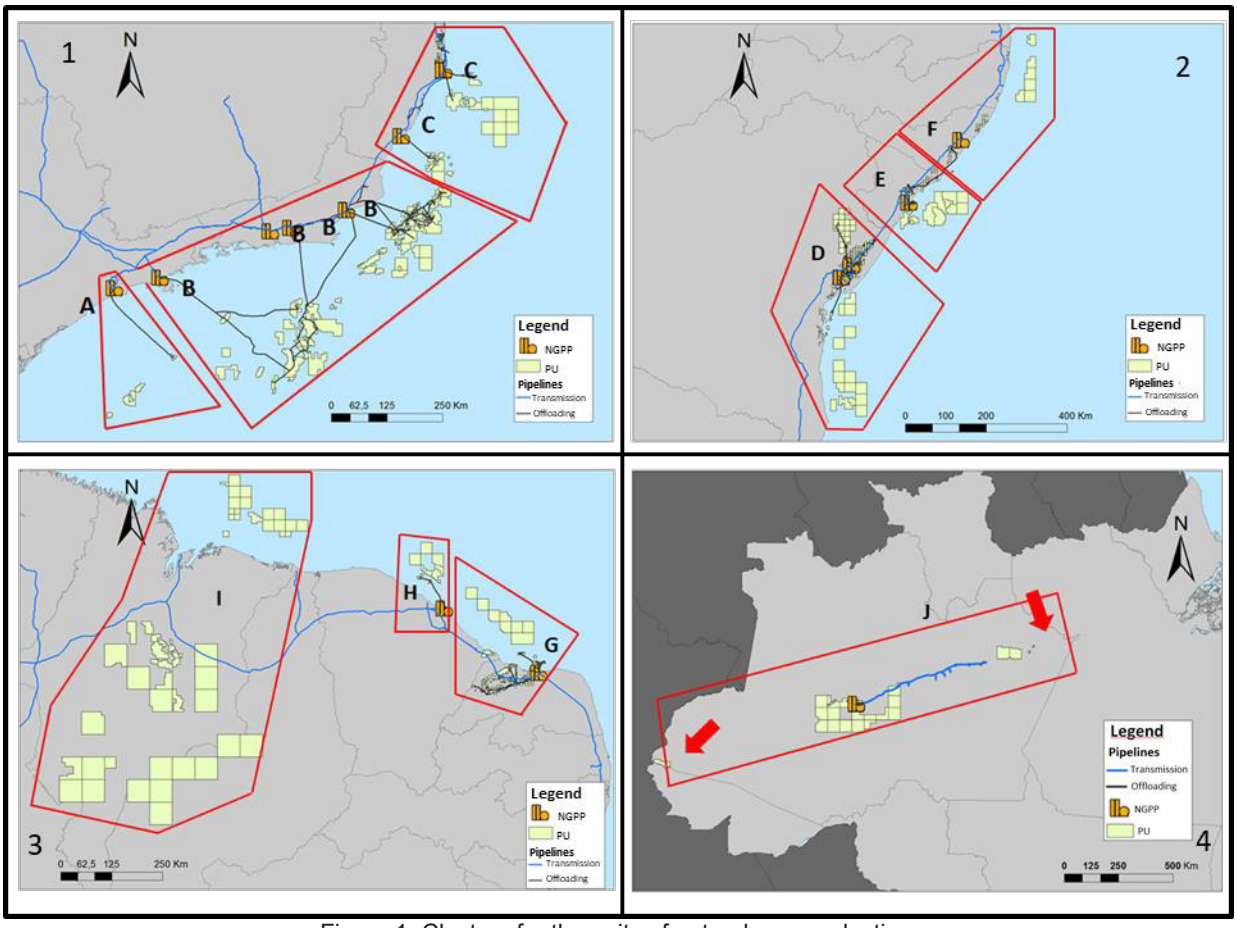

Figure 1: Clusters for the units of natural gas production.

The natural gas production clusters are defined by the proximity to the pipelines, by the presence of other production units and if there is a natural gas processing plant (NPGG) installed. Such premises are defined to reduce in the first moment the costs relative to unify the streams to be sent to the new thermopower plant (TPP) and NGPP installations. Although in Brazil there are other natural gas production clusters, this paper considers the Pre-Sal (B) and Sergipe (E) clusters as seen in Figure 1, since these two are the ones with higher production potential in the following years as described in EPE (2019b) and EPE (2019c) reports.

For the chosen clusters B and E the volumetric composition of each natural gas component is determined. This calculation utilizes reports from the Brazilian Petroleum National Agency (ANP, 2019) for the fields already in production. For the remaining production units without production and described in EPE (2019b), the composition is defined as a function of the natural gas associated or not with crude-oil and with respect to the exploratory environment (onshore, offshore, Pre-Salt, etc.) as presented in Table 1.

Table 1. Average composition per exploratory environment and type of resource (if associated with crude-oil or not)

Environment and resource	C_1	C_2	C_3	C_4	C_{5+}	Outros
Associated (Onshore and Offshore)	*0,77*	*0,09*	*0,05*	*0,03*	*0,02*	*0,04*
Non Associated (Onshore and Offshore)	*0,86*	*0,07*	*0,03*	*0,01*	*0,01*	*0,02*
Pre-Salt Associated (Onshore and Offshore)	*0,65*	*0,11*	*0,08*	*0,01*	*0,01*	*0,12*
Fields in Production	*ANP (2019)*					

In the modeling of the installations is considered the specificities of each type of project and a methodology for the design and evaluation of the CAPEX (Capital Expenditure) for the TPPs and NGPPs. Additionally, for each project is determined the net present value (NPV) considering finantial and economic particularities such as tributes, type of product to be commercialized (energy, NG fractions), etc. The NPGG modeling uses the

methodology presented in EPE (2016) to determine the capacities of the separation units to split the NG components (of fractions when there is more than one component), producing the streams to be commercialized. The separation efficiencies are presented in Rangel et al. (2018) and we select the most efficient process among Joule-Tomson, Simple Refrigeration and Turboexpansion for the NPGG installation. The design of the NPGG unit is determined as a function of the volume of gas to be processed for the Turboexpansion type, as demonstrated as the most efficient NG separation in Rangel et al. (2018). The methodology and indices of the recovery are seen in Figure 2.

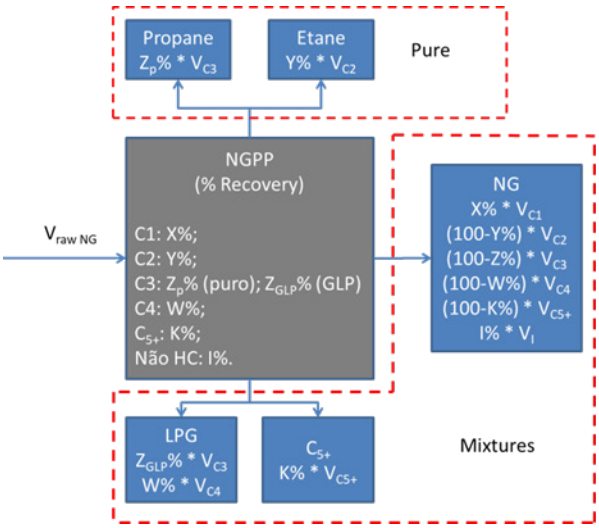

Recovery of components

Type	C_2 (%)	C_3 (%)	C_{4+} (%)
Turboexpansion	85	99	100

Fig. 2: Methodology for a gas processing plant and % of recovery of the components

The TPPs modeling considers selling the available generation capacity in thermoplants with combined cycle (higher efficiency) and with a minimal generation of 50% of the installed capacity (inflexibility of 50%). The design (KW) is calculated as a function of the volume to be consumed in the TPP and the specific consuming (thousand m^3/day/KW), obtained from the average of the Brazilian TPPs and used in Rangel et al. (2018). The CAPEX of this type of project was calculated from the reference cost (US$/KW) and capacity. Financial data for the NPV such as taxes, final price, operation costs, NG purchasing, financing taxes, interest rate and costs related to internalization of items, etc.) can be found in Rangel (2018).

III. Analysis

The production of the NG regions is obtained from EPE (2019c) projections. For the Pre-Salt (region B in Figure 1), the total volume is around 71 MMm^3/day in 2030, although 44 MMm^3/day is already planned for other projects, remaining 27 MMm^3/day for this study. For the Sergipe (region E in Figure 1) the estimated production is around 32 MMm^3/day. In this region, there is already installed an NG processing capacity of 4,8 MMm^3/day with utilization of 50% (ANP, 2019), therefore the extra stream considering in this work is 30 MMm^3/day. With the volumes defined for the study, the CAPEX and NPV of each type of project is calculated to determine the optimal investiment.

IV. Results and discussions

The results obtained for both clusters (B and E) are found in Table 2.

Table 2. CAPEX and NPV for the projects in clusters B and E

		CAPEX (bi US$)	NPV (bi US$)
Pre-Salt	**Gas Power Plant**	*8.7*	*0.9*
	Turboexpansion	*2.6*	*2.9*
Sergipe	**Gas Power Plant**	*10.3*	*1.4*
	Turboexpansion	*2.9*	*3.5*

The results show that the best option for the regions is the investment in NGPP turboexpander. Such results are expected because of the richness of the gases from these two regions therefore the production of high added products such as ethane, propane and LPG is preferred rather than the utilization of the NG as energy source in TPPs.

References

ANP – Agência Nacional do Petróleo, Gás Natural e Biocombustíveis, 2019a. Preço de Referência do Gás Natural – Novembro – 2019. Brazil. http://www.anp.gov.br/arquivos/royalties-outras-participacoes/preco_referencia_gas/memoria_calculo/2019/memoria-calculo-nov-2019.pdf

ANP – Agência Nacional do Petróleo, Gás Natural E Biocombustíveis, 2019b. Anuário Estatístico Brasileiro do Petróleo, Gás Natural e Biocombustíveis 2019. Brazil.
http://www.anp.gov.br/arquivos/central-conteudos/anuario-estatistico/2019/2019-anuario-versao-impressao.pdf

BP – British Petroleum, 2019. BP Statistical Review of World Energy 2019, 68th edition.
https://www.bp.com/content/dam/bp/business-sites/en/global/corporate/pdfs/energy-economics/statistical-review/bp-stats-review-2019-full-report.pdf

EPE – Empresa de Pesquisa Energética, 2008. Balanço Energético Nacional – Ano Base 2007. Brazil.
http://www.epe.gov.br/sites-pt/publicacoes-dados-abertos/publicacoes/PublicacoesArquivos/publicacao-135/topico-110/Relat%C3%B3rio%20Final%202008.pdf

EPE – Empresa de Pesquisa Energética, 2016. Metodologia para Cálculo da Oferta de Gás Natural Seco e Derivados. Brazil
http://www.epe.gov.br/sites-pt/publicacoes-dados-abertos/publicacoes/PublicacoesArquivos/publicacao-250/topico-298/EPE,%202016%20-%20Nota%20T%C3%A9cnica%20Metodologia%20G%C3%A1s%20Natural%20Seco%20e%20Derivados.pdf

EPE – Empresa de Pesquisa Energética, 2019a. Balanço Energético Nacional – Ano Base 2018. Brazil.
http://www.epe.gov.br/sites-pt/publicacoes-dados-abertos/publicacoes/PublicacoesArquivos/publicacao-377/topico-494/BEN%202019%20Completo%20WEB.pdf

EPE – Empresa de Pesquisa Energética, 2019b. Plano Decenal de Expansão de Energia 2029. Brazil.
http://epe.gov.br/sites-pt/publicacoes-dados-abertos/publicacoes/PublicacoesArquivos/publicacao-422/PDE%202029.pdf

EPE – Empresa de Pesquisa Energética, 2019c. Plano Indicativo de Processamento e Escoamento de Gás Natural. Brazil.
http://epe.gov.br/sites-pt/publicacoes-dados-abertos/publicacoes/PublicacoesArquivos/publicacao-434/PIPE%20-%20Plano%20Indicativo%20de%20Processamento%20e%20Escoamento%20de%20G%C3%A1s%20Natural.pdf

IEA – International Energy Agency, 2018. Key world energy statistics. France.
https://webstore.iea.org/download/direct/2291?fileName=Key_World_2018.pdf

Instituto Acende Brasil, 2016. O Mercado de Gás Natural e a Geração Termelétrica.
http://www.acendebrasil.com.br/media/estudos/2016_WhitePaperAcendeBrasil_16_GasNatural_Rev_1.pdf

Rangel, H. P. G, Luz, R., Menezes, B.C., Cavalcante, R.M, Pessoa, F.P., 2018. DESENVOLVIMENTO DE METODOLOGIA PARA SELEÇÃO DE PROJETO PARA APROVEITAMENTO DE GÁS NATURAL. Congresso Brasileiro de Engenharia Química, São Paulo, Brazil.

Zhang, Y., Ji, Q., Fan, Y. 2018. The price and income elasticity of China's natural gas demand: A multi-sectoral perspective. Energy Policy 113, 332-341.

CO_2 Emission using Road Gradient and Real-Time Traffic Monitoring in Vehicle Routing Problems

[1*]Eduardo Bastida-Escamilla, [1*]Marzieh Khakifirooz, [2*]Brenno Menezes, [3*]Mahdi Fathi
[1] Tecnologico de Monterrey, School of Engineering and Science, Department of Industrial Engineering, Monterrey, N.L., Mexico
[2] Hamad Bin Khalifa University, College of Science and Engineering, Division of Engineering Management and Decision Sciences, Qatar Foundation, Doha, Qatar
[3] University of North Texas, Department of Information Technology & Decision Sciences, G. Brint Ryan College of Business, Denton, TX, USA

* E-mails: eduardo.bastida@tec.mx, mkhakifirooz@tec.mx, bmenezes@hbku.edu.qa, mahdi.fathi@unt.edu

Abstract
The upsurge in atmospheric CO_2 levels has come to humankind's attention during the last couple of decades, mainly because of the rise in the global temperature, ice sheets melting, and more frequent and intense natural disasters. Hereby, the focus of this study is to develop a robust routing model that minimizes CO_2 transportation emissions so that this can be used worldwide to minimize global warming issues. The empirical study in this work proves that the advantages of our proposed method for CO_2 reduction in regions with a growing economy, especially in Latin America and the Caribbean, where GDP growth disassociates from fossil fuel consumption and the topography can seriously affect the air pollution generated by vehicles, is an efficient solution as a short-term mitigation strategy. The main contribution of this study is to penalize very steep or slow roads from the fleet route map. The application of this method is vastly relevant in areas where elevation above sea level of towns is very high. Therefore, how the routes are made plays a huge role in the carbon footprint of vehicle fleets. The problem considered in this paper is to produce routes for a fleet of delivery vehicles that minimizes fuel emissions, considering the load of the vehicle, the time traveled, the distance traveled, and the road gradient of a road network using the information extracted from Google Earth. The study investigates a dynamic capacitated vehicle routing problem as an NP-hard problem and generates a linear model that efficiently can capture CO_2 emissions. Numerical results using ant colony optimization (ACO) validate the proposed strategy. Key findings highlight -2.62% of CO_2 emissions changes within a short computational time.

Keywords: CO_2 emission, vehicle routing problems, road gradient, real-time traffic monitoring, ant colony optimization

I. Introduction
Efforts for sustainable urban design based on requirements for developing and managing smart cities, so-called Society 5.0, have been received particular attention in recent years (Velásquez-Bermúdez et al., 2019; Fathi et al., 2019). Research in this domain includes performance development evaluation for green supply chain (Santoso et al., 2019) and eco-efficiency design of vehicle routing problem (VRP) (Fathi et al., 2009). To respond to the increasing social environmental awareness and to decrease the CO_2 emissions that vehicle routing causes, an efficient solution method is required. Our methodology describes the use of the route required information to build delivery sequences using a modified ant colony optimization algorithm. Results of the optimization are compared with to traditional approaches. Finally, the main conclusions and future research work are presented.

II. Methodology
The problem in this paper is considered to recommend routes for a fleet of delivery vehicles that minimizes fuel emissions based on the vehicle load, travel time, travel distance, and road gradient. For measuring the road elevation/gradient, Google Earth information is used every time that the vehicle changes the road or makes a turn. According to the Google Earth information, the gradient is calculated as a difference between altitude at the point i (beginning of a road) and point j (end of the road) and shown by e_{ij}. The travel time (t_{ij}) is obtained by calculating the time of the trip when the vehicle is departed from point i and arrived at point j. A controlled variable is considered as the ratio of general t_{ij} over the travel time when traffic is at its lowest. By measuring the control variable, the extra time in each route caused by the traffic conditions at the desired time can be estimated. The travel distance (d_{ij}) between point i and j is extracted from the Google map API key.

To estimate the CO_2 emissions for a heavy-duty vehicle (HDV) with a range of 32-40 tons capacity for general merchandise, a linear function of d_{ij}, e_{ij}, t_{ij}, and truckload (q) between points i and j is considered as follow:

$$CO_2(q_{ij}, d_{ij}) = d_{ij}\left(\frac{f_1 - f_2}{C} q_{ij} + f_2\right) t_{ij} e_{ij} \quad (1)$$

where f_1 and f_2 are constant values of CO_2 emission when an HDV truck is fully loaded and is empty equal to 1.096 kg/km and 0.772 kg/km, respectively (Olivera and Viera, 2007), and C is the vehicle capacity. This model is inspired by the works of (Ayadi et al., 2014) and (Elbouzekri et al., 2013), where they did not consider the effect of e_{ij} and t_{ij}.

In addition, given the complexity of the problem to estimate the optimal/near-optimal solution, the ant colony optimization (ACO) algorithm is adopted to solve the optimization problem. Following the optimization process by ACO algorithm is described in detail:

Ant: A vehicle that starts at point *a*, and after visiting all clients and returns to point *a*.

Pheromone trail: The history of all the paths made by vehicle k $(k = 1, \dots, m)$ and change/update the intensity of the routes with each new iteration.

Selection of paths: The random variable r is generated form Uniform distribution $[0,1]$ and if $r \geq r0$ the node j is chosen based on:

$$j = argmax\left(\tau_{ij}^{\alpha}\eta_{ij}^{\beta}\right) \qquad \text{if } (i,j) \notin \mathbf{T} \tag{2}$$

where η is the attractiveness of the move and is the inverse of the Equation (1), τ represents the level of pheromone of the move which indicates how good the move was in the past, and $\mathbf{T}$ is a list of forbidden moves (clients that have already been visited by ant k or clients that ant k does not have the capacity to visit them), and α, β are parameters that are used to establish the relative influence of η against τ.

Pheromone update:

Local update: for a given path (i,j) the pheromone trail updates as follow:

$$\tau'_{ij} = (1-\rho)\tau_{ij} + \rho\tau_0 \tag{3}$$

where ρ represents the evaporation rate of the pheromone trail and, τ_0 is a constant value.

Global update: for a given path (i,j) when an iteration has ended for all ants, and the best route achieved, the pheromone trail updates as follow:

$$\tau'_{ij} = \begin{cases} (1-\rho)\tau_{ij} + \rho\left(\dfrac{1}{\text{best solution}}\right) & \text{if } (i,j) \in \text{best solution} \\ (1-\rho)\tau_{ij} & \text{if } (i,j) \notin \text{best solution} \end{cases} \tag{4}$$

Algorithm: for a given number of ants, iterations, and parameters $(\alpha, \beta, \eta, \tau_0, C, f_1, f_2, t_{ij}, e_{ij}, d_{ij})$, first initialize the τ_{ij}, then for each iteration and each ant, randomly choice and unused truck, build the route for this truck using Equation (2), then locally update the τ_{ij} using Equation (3) until the chosen ant complete its solution. Finally, update τ_{ij} using Equation (4).

III. Analysis

For evaluating the proposed model, a real dataset consists of 38 instances of HDVs, including the information of latitude, longitude, and demand of each client of a company in Mexico is used for further investigation. The summary of the data of clients, the vehicles, and the average demand (in unit box) is presented in Table 1.

For running the ACO algorithm, the unit box is considered to 1 kg, such that the capacity of trucks can satisfy the demand of each store in each day without visiting a client more than one time. Therefore, the maximum capacity of trucks should be at least equal to the maximum demand of clients. Consider this fact, the maximum capacity of the trucks is set to 1.7 tons.

The parameter settings of the ACO algorithm is selected based on (Bouyahyiouy and Bellabdaoui, 2017) and are presented in Table 2.

Table 1. Summary of dataset

# of client to visit	5	6	7	8	9	10	11	15	16	17	18	19	20	21	42
# of vehicle	32	5	6	8	4	2	1	1	1	1	1	1	1	1	1
Average demand	2929.33	3303.5	2414.6	3008.17	4259.75	3602.5	3711.5	3110	4256	3583	8063	5184	4502	8374	9058

Table 2. Parameter setting of ACO algorithm

Parameter	α	β	ρ	τ_1	r_0	τ_0	# of iterations
Value	1	2.3	0.1	$\frac{1}{d_{ij}} \forall i,j, i \neq j$	0.9	average of τ_1	500

IV. Results and discussions

For validating the performance of the proposed ACO algorithm, it is compared with the Capacitated VRP (CVRP) with the Miller-Tucker-Zemlin (MTZ) subtour elimination constraint (Desrochers, and Laporte, 1991) where for simplicity, the objective function is set to minimize distance instead of CO_2 emission reduction. The problem is solved with a time limit of 20,000 seconds and 200,000 seconds for the simple and complex objective functions, respectively. ACO algorithm is coded in Python 3.6 and tested on a PC with Intel(R) Core (TM) i5 2.40 GHz, 16 GB of RAM Memory, and Windows 10 OS. The GAMS software version 22.6 is used for running the optimization

algorithm. In addition, the Python PyMathProg (Pyomo) package is utilized for solving linear mathematical problems. The main hypothesis was to test that shorter distance does not necessarily mean fewer emissions produced by the vehicles, and travel time and elevation can lead to different decision making for better solutions.

Table 3 presents a summary of the results. The number of clients to visit is used to express the complexity of the problem. According to the result, the method that performed the worst is the MTZ algorithm solved with GAMS software, and the ACO algorithm with the objective of minimizing CO_2 is the one which performed best. The ACO algorithm is compared to the MTZ has 0.74 % better performance in terms of emission reduction, however, if the complexity of the problem (clients to visit) to be considered as a weighted average, the ACO algorithm performed 2.62 % better than the MTZ algorithm as shown in Table 3.

Table 3. Summary of the results obtained by each method.

		ACO_CO_2		ACO_distance		MTZ (in Pyomo)		MTZ (in GAMS)	
		Result	*Difference to GAMS*	*Result*	*Difference to GAMS*	*Result*	*Difference to GAMS*	*Result*	*Difference to GAMS*
Weighted Average	*CO_2 Emission*	*3091.04*	*-2.62*	*317.13*	*-0.01*	*348.31*	*8.95*	*317.15*	*-*
	Distance	*245.99*	*1.99*	*241.09*	*0.00*	*261.98*	*7.97*	*241.08*	*-*
Average	*CO_2 Emission*	*194.93*	*-0.74*	*199.57*	*1.61*	*202.44*	*3.00*	*196.37*	*-*
	Distance	*163.02*	*2.63*	*160.83*	*1.30*	*162.80*	*2.50*	*158.73*	*-*
	Run time	*34.73*	*-21000*	*28.57*	*-26000*	*17000*	*56.11*	*7400*	*-*
	Trucked used	*2.76*	*-1.9*	*2.79*	*-0.94*	*2.76*	*-1.90*	*2.82*	*-*

Regards the distance performance, the MTZ algorithm performed similarly to other algorithms; however, it runs out of time after 27.7 hours. After that, the ACO algorithm with distance reduction objective has the second-best performance, and the algorithm that performed the worst is the ACO algorithm for the CO_2 reduction objective.

It is worth to point out that, the optimal result for ACO with CO_2 reduction objective is achieved in a fraction of the time (215 times faster on average) and also used the minimum number of trucks unlike the MTZ algorithm solved by GAMS that used one more truck in two instances and the ACO algorithms that minimizes distance that used one more truck in one instance. Overall, the ACO algorithm for minimizing distance performed very good in comparison to the GAMS software and was the fastest amongst all other methods.

The obtained results show that for small and simple instances (less than ten clients to visit), the difference between optimizing the distance and the emissions are almost negligible, however for a more complex system, the deviation is more significant (see Figure 1 and 2). In this situation, a better decision is to control the load of the trucks, the travel time, elevation, and distances between transition points.

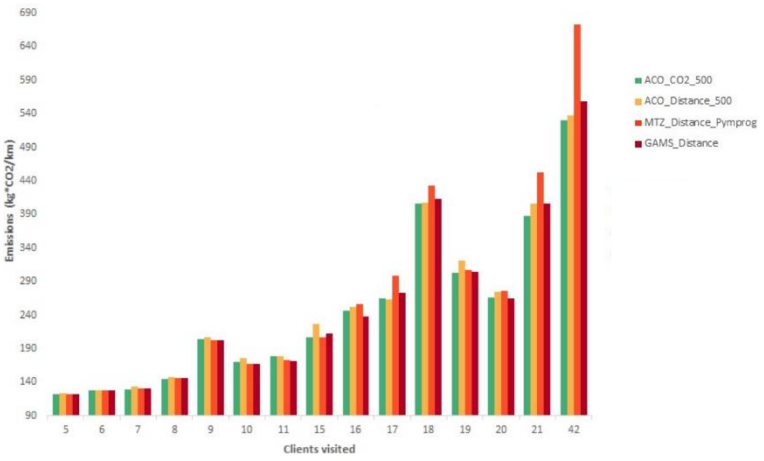

Figure 1. The result of CO_2 emission reduction for each algorithm.

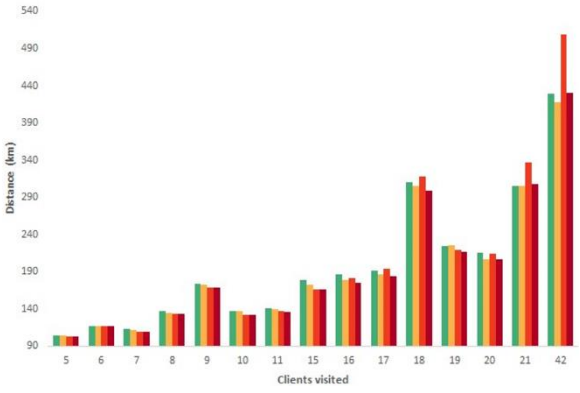

Figure 2. The result of distance reduction for each algorithm.

It is also worth noting that the stopping criteria for ACO algorithms were the number of iterations. We used 500 iterations for the ACO algorithms because we found it to be a good balance between the optimal solution and a decent running time, 100 iterations did not achieve a good result, and 1,000 iterations achieved just a 0.33% improvement by almost doubling the average running time.

V. Conclusions

In this study, an optimization solution to deal with CO_2 emissions produced by heave-duty vehicles (HDVs) considering the travel time and elevation for each path using information from Google Earth are proposed by avoiding or penalizing steep and slow roads. The result is vastly relevant, especially in Latin America where the

population, the topography of big cities, and the height above the sea level is higher than the average of the world (2,400 meters compared with 2,240). Therefore, the way street routes are made play a huge role in the carbon footprint. For the future research, the problem can consider the same issue for the combination of vehicle routing problem (VRP) and location-inventory problem (Fathi et al., 2015; Mousavi et al., 2019), in a team-oriented supply chain (Hu et al., 2018).

References

Ayadi, R., Elldrissi, A.E., Benadada, Y. and Alaoui, A.E.H., 2014, June. Evolutionary algorithm for a green vehicle routing problem with multiple trips. In 2014 International Conference on Logistics Operations Management (pp. 148-154). IEEE.

Desrochers, M. and Laporte, G., 1991. Improvements and extensions to the Miller-Tucker-Zemlin subtour elimination constraints. Operations Research Letters, 10(1), pp.27-36.

El Bouyahyiouy, K. and Bellabdaoui, A., 2017, April. An ant colony optimization algorithm for solving the full truckload vehicle routing problem with profit. In 2017 International Colloquium on Logistics and Supply Chain Management (LOGISTIQUA) (pp. 142-147). IEEE.

Elbouzekri, A., Elhassania, M. and Alaoui, A.E.H., 2013. A hybrid ant colony system for green capacitated vehicle routing problem in sustainable transport. Journal of Theoretical and Applied Information Technology, 54(2).

Fathi, M., Claeys, D. and Bruneel, H., 2015. An integrated inventory-location model for a supply chain under stochastic demand and lead time. In 29th Belgian Conference on Operations Research (ORBEL 29-2015) (pp. 98-98).

Fathi, M., Hasanzadeh, A., Raad, A., Dehghanian, F. and Mansour, S., 2009, December. Using compromised method in design of reverse logistics network with eco-efficiency consideration. In 2009 IEEE International Conference on Industrial Engineering and Engineering Management (pp. 1454-1458). IEEE.

Fathi, M., Khakifirooz, M. and Pardalos, P.M., 2019. Optimization in Large Scale Problems Industry 4.0 and Society 5.0 Applications. Vol. 151. Springer Nature. https://doi.org/10.1007/978-3-030-28565-4.

Hu, W., Fathi, M. and Pardalos, P.M., 2018. A multi-objective evolutionary algorithm based on decomposition and constraint programming for the multi-objective team orienteering problem with time windows. Applied Soft Computing, 73, pp.383-393.

Mousavi, S.M., Pardalos, P.M., Niaki, S.T.A., Fügenschuh, A. and Fathi, M., 2019. Solving a continuous periodic review inventory-location allocation problem in vendor-buyer supply chain under uncertainty. Computers & Industrial Engineering, 128, pp.541-552.

Olivera, A. and Viera, O., 2007. Adaptive memory programming for the vehicle routing problem with multiple trips. Computers & Operations Research, 34(1), pp.28-47.

Santoso, C.H., Khakifirooz, M., Fathi, M. and Wu, J.Z., 2019. Adoption, Implementation, and Performance of Green Supply Chain Management: The Case of Coal Power Generation Industry in Indonesia. In Sustainable Interdependent Networks II (pp. 249-265). Springer, Cham.

Velasquez, J., Khakifirooz, M. and Fathi, M., 2019. Large Scale Optimization in Supply Chains and Smart Manufacturing-Theory and Applications. Vol. 149. Springer Nature. https://10.1007/978-3-030-22788-3.

Vegan Burger Recipe Optimization for Meat Quality Nutrition in the Food Industry

[1*]Brenno Menezes, [1,2]Mohamed Sawaly, [1,3*]Tareq Al-Ansari
[1] Hamad Bin Khalifa University, College of Science and Engineering, Division of Engineering Management and Decision Sciences, Qatar Foundation, Doha, Qatar
[2] Hamad Medical Corporation, Supply Chain Department, Doha, Qatar
[3] Hamad Bin Khalifa University, College of Science and Engineering, Division of Sustainable Development, Qatar Foundation, Doha, Qatar

* E-mails: bmenezes@hbku.edu.qa, talansari@hbku.edu.qa

Abstract
The move to an environmental-friendly lifestyle is modifying the food manufacturing and its respective supply chain, since the agriculture of crops and livestock to the marketing of new products such as the plant-based meat. From this context, for a diet-behavioral change, one can replace meat (like fish, chicken, pork, goat, cattle) by a vegan diet in its variants of pure vegan or the more popular ovo-lacto-vegan diet. Considering the food industry impacts by this moving, we research a vegan burger recipe optimization that meets meat quality nutrition in order to determine the different raw materials from the harvest and upstream chains to be adopted as recipes of transforming vegetables into vegan burgers for the market consumption. The vegan burger to be considered is made of a blend of beans for proteins, leaves (for vitamins and fiber) and other types of vegetables as roots (carrots, beets, etc.) for carbohydrates, where we aim to maintain the protein, lipids, carbohydrates, fiber, etc., contents to match a beef patty nutrition, at a comparable cost and with a desired and similar taste. In the vegan burger recipe optimization problem, a nonlinear programming (NLP) solution determines the amounts of each vegetable inside the main groups to match the ingredient contents found in a beef patty. A linear (LP) approximation using factors for qualities is also calculated to be compared to the NLP approach, where cuts of linear amounts of qualities replace by the NLP formulas. A comparison between both LP and NLP vegan burger recipe approaches are considered for their applicability in the optimization of the processing plants when integrated to a complete supply chain of harvesting farms, burger producers and centers of distribution and commercialization. A broad discussion on the impacts of veganism by replacing meat with vegetables in the daily diet is given.

Keywords: Vegan burger, recipe optimization, food supply chain, nutrition

I. Introduction

The United Nations' Food and Agriculture Organization (FAO) defines sustainable diets as those which are "healthy, have a low environmental impact, affordable and are culturally acceptable". der Weele et al. (2018) argue that while consumers may be aware of the health benefits of vegan and vegetarian diets or of the unsustainability of meat-based diets, the idea of reducing their meat intakes faces resistance. Meat intake is maintained by way of coping strategies such as adapting beliefs, obscuring sources of meat, or just strategic ignorance. According to the authors, addressing supply chain problems associated with meat production should include tradeoffs such as reduced antibiotics use, improved animal welfare, better public health regulations, and better resource utilization. While vegans abstain completely from animal products and byproducts, their impact on the overall dietary patterns (and the supply chain) is insignificant, given the small number of practicing vegans worldwide. (Macdiarmid et al., 2016).

The research into the costs of healthy diets shows that fruits, whole grains, vegetables, and lean meat increase the cost of diets (Monsivais and Drewnowski, 2007; Flynn and Schiff, 2015). Market basket studies show that the food environment can have a considerable impact on the healthier dietary choices of low-income consumers. Market basket samples do not also adjust for behavioral factors, which, given the fact that food choices are a function of consumer preferences, the food environment, and nutrition literacy, should be relevant for vegan and vegetarian diets (Jetter and Cassady, 2006). However, Flynn and Schiff (2015) investigated the cost of a seven-day meal plan for an economic meat-based diet and a plant-based alternative (each giving 2000 calories). Servings of fruits, whole grains, and vegetables were determined. The results showed that the plant-based alternative cost $38.75 while the budget meat-based meal cost $53.11 (with lean animal protein accounting for 21% of the total cost). The former had more servings of vegetables, whole grains, and fruits. To fill the gap on the relative prices of foods, Rao et al. (2013) undertook a systematic review of 27 studies drawn from 10 countries published in MEDLINE between 2001 and 2011 comparing inflation/PPPI-adjusted prices of healthy and unhealthy and healthy foods. The authors used random-effects modeling and the study quantified prices differences in healthier and less healthy options for specific types of food, diets, and units of the price (day, calorie, and serving) (95% CI $0.19 to $0.40). The results reveal that healthier food options cost $0.29 per serving and $0.47/kilocalorie ($0.42 to $0.53) more than healthy options, even though the unit price differences between healthier and healthy foods are fairly less among grains, snacks, dairy, and oils/fats. The price differences are statistically insignificant in juices/soda and with considering the nutritional value of the various diets (Rao et al., 2013). This study is one of the most comprehensive comparisons of prices between healthy and healthier foods and one which incorporated systematic search, adjustments for inflation, and accounted for units of comparison, food type, and intensity of contrast. However, the study was limited because of the less available on prices and restaurant prices from middle and low-income countries.

Other studies show that while the cost of plant-based diets is high, the increasing food price inflation would make them more affordable in the future (Aiking and de Boer, 2018; Cleveland and Gee, 2017). According to the

authors, about half of the global food supply is produced by smallscale farmers, who not only lack market power. Low land ownership and access to capital create bottlenecks that are increasingly driving such farmers out in favor of largescale farmers, to whom animal proteins are economically important. When using intensive production systems, producing plant proteins is wasteful because of the relatively lower returns compared to meat. The economic competition between plant and animal proteins is likely to put pressure on production resources, resulting in the compaction of heavy equipment, worsening soil quality, and erosion. Consequently, KPMG projects price inflation of up to 90% by 2030, with animal products expected to rise faster than plant products (Aiking & de Boer, 2018s.

Even if the transition away from meat is organisationally and technologically possible, there may still be resistance from the high social status of meat (Aiking, 2011; Aiking and de Boer, 2018), inadequate technological know-how on plant substitutes (Goldstein et al., 2017), entrenched interests in meat supply chains, and optimized reuse of by-products in the meat chain (der Weele et al., 2018; Chai et al., 2019; Aiking and de Boer, 2018). Past studies covered production costs (Monsivais and Drewnowski, 2007), technological feasibility (Aiking and de Boer, 2018), effect on societal organization as well as market power, resonance with behavioural and cultural consumption patterns (der Weele et al., 2018). However, there is little research into the integrated evaluation of meat alternatives as production systems including their related economic, social, organizational and ecological implications (der Weele et al., 2018). The authors apply an integrated conceptual framework to comparative measure the nutritional implications, sustainability gains, socio-institutional, and technological change needed for five meat substitutes. The results show that without a high level of societal coordination, it is difficult to generate potentially disruptive levels of organizational, institutional, and technological innovations necessary for novel alternatives to be viable.

In such a context, as an option for the replacement of reat meet patty in the market, a vegan burger recipe optimization is proposed in this work to meet red meat quality nutrition considering the main components as beans, leaves and roots. The approximation of the typical nonlinear (NLP) model considering a recipe optimization of blending of streams as a LP quantity-quality balance from Kelly et al. (2018) allow more complex calculation in mixed-integer linear (MILP) problems to determine the needs of different quality raw materials from the harvest and upstream chains to be processed in manufacturing sites transforming vegetables into vegan burgers for the market distribution and consumption, creating the so-called qualogistics problem instead of considering fixed recipes in pure logistics problems. In such a way, this approximation overcomes the solving bottlenecks of a mixed-integer nonlinear (MINLP) model, which would reduce the size of the supply chain scale and scope for a complete harvest, manufacturing, and distribution optimization for a broad study of the vegan diet impacts in the food industry and supply chains.

II. Methodology

Figures 1 and 2 show the burger recipe optimization flowsheets constructed in the unit-operation-port-state superstructure (UOPSS) (Kelly, 2005; Kelly and Menezes, 2019). The diamond structures, shapes or objects (◇) are the sources (or sinks) known as perimeters representing physical material flows. The rectangular shape BBLENDER with the cross-hairs (⊠) is a continuous-process unit with a blackbox subtype where the circles with (⊗) and without (O) cross-hairs are outlet and inlet port-states respectively. Port-state structures are unambiguous interfaces between up and downstream unit-operations known as internal-streams. The arrows (→) are external-streams or paths, also known as routes, lineups, transfers or movements. All these UOPSS objects and their semantics are built-in in the Industrial Modeling and Programming Language (IMPL) from Industrial Algorithms. The UOPSS optimization found in IMPL is very intuitive and reduces the solution time of industrial-sized problems from quarters of hours to seconds as demonstrated in Brunaud et al. (2020).

In Figure 1 is shown the typical blend-shop, whereby the general in-out (or i - j) material balance in the blender BBLENDER is calculated as $m_{j,t} = \sum_i m_{i,t}$ considering the inlet mass amounts of each component i as $m_{i,t}$ and the outlet mass amounts of the product j as $m_{j,t}$. The main qualities or properties p of the blended materials or products leaving the blender output $w_{j,p,t}$ are determined by the NLP mass-based constraint 1. These complete or proper quality balances of mass-based variables in the blender's outlet j represent nonlinear (bilinear) terms given the product of extensive amounts in mass ($m_{i,t}$) and intensive properties ($w_{i,p,t}$) of inlet stock or material flows as well as by the product of the outlet product $w_{j,p,t}\, m_{j,t}$.

$$w_{j,p,t}\, m_{j,t} = \sum_i w_{i,p,t}\, m_{i,t} \quad \forall\, j,p,t \tag{1}$$

Kelly et al. (2018) proposed the linear (LP) constraint 2 to equalize the extended quality amounts of property p (factors multiplied by flows) around the blender unit-operation (BBLENDER in Figure 2) with respect to its factor-flows $m_{j^F,p,t}$ leaving the slack or surplus outlet j^F. The value of the slack or surplus factor-flows $m_{j^F,p,t}$ represents, respectively, the insufficient or excess amounts of qualities for the LP factor flow of each property p to close the quantity-quality product balance around the blender. In the left side of equation 2, for each property p at time period t, input stream amounts $m_{i,t}$ in mass with constant factors for qualities $f_{i,p,t}$ (that is equal to $w_{i,p,t}$ in equation 1) counterbalance the total amount $m_{j,t}$ of the blended material factor or fixed property specification $f_{j,p,t}$ minus slacks or plus surpluses of the factor-flow variables $m_{j^F,p,t}$, in the right side of equation 2. In such a way, for an

upper bound of property specification of the blended material represented by its factor $f_{j,p,t}$, there can be a slack or negative factor-flow variable $m_{j^F,p,t}$ to complete the balance in equation 2, and hence $m_{j^F,p,t} \leq 0$. For a lower bounded property of the blender's factor $f_{j,p,t}$, a positive factor-flow or surplus is needed for such factor balance ($m_{j^F,p,t} \geq 0$).

$$\sum_i f_{i,p,t}\, m_{i,t} = f_{j,p,t}\, m_{j,t} + m_{j^F,p,t} \quad \forall\, j, j^F, p, t \tag{2}$$

Factors are similar to other quality phenomena variables such as densities, components, conditions and other physical-property coefficients except that, as mentioned, factors are constant. Factors can also be used to model simple enthalpy and entropy balances found in steam utility network optimizations where the factors are interfaced or linked to rigorous process simulators to update the enthalpy and entropy as temperatures and pressures change. In the LP vegan burger blend-shop example in Figure 2, there are six properties: calories (CALOR), fat (FAT), protein (PROT), carbohydrates (CARBO), sodium (SODIUM) and fiber (FIBER).

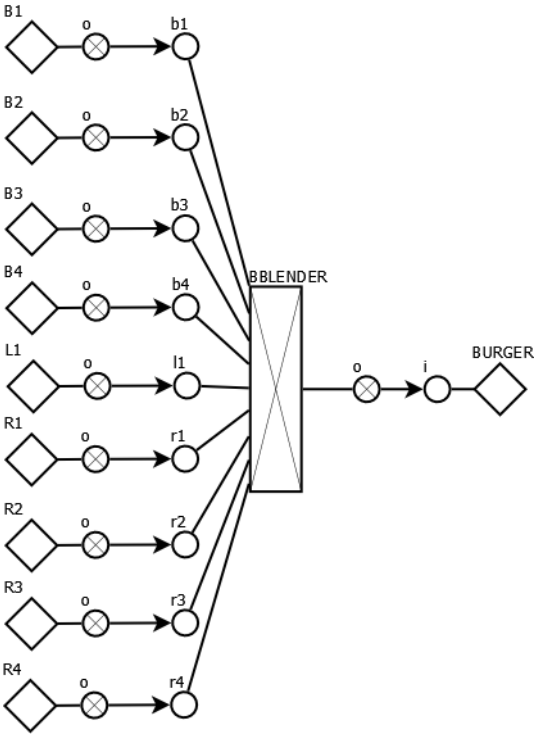

Fig. 1. Nonlinear (NLP) burger recipe optimization.

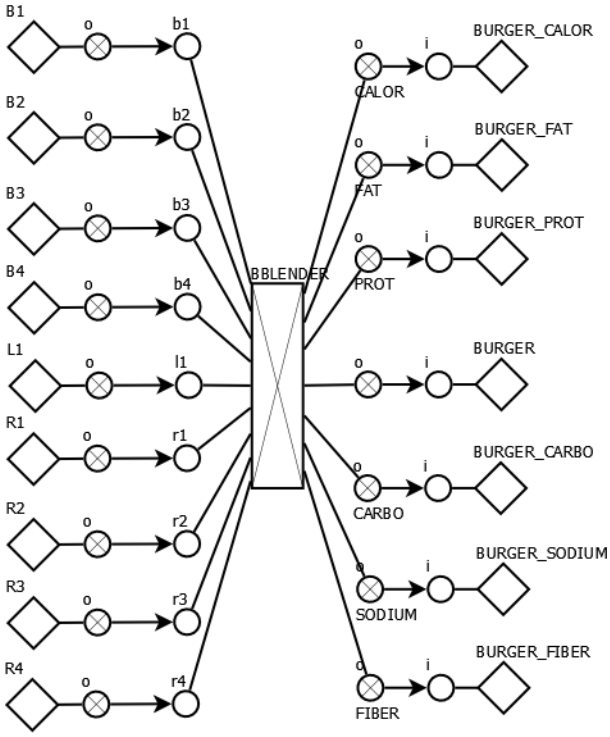

Fig. 2. Linear (LP) burger recipe optimization using factors.

III. Analysis

As shown in Table 1, we have considered the properties of the vegan burger raw materials in beans (B1 to B4), the selected leaf (L1) and roots (R1 to R4). For the examples in Figures 1 and 2, we have fixed content of 10% of leaf to produce 1000 grams of vegan burger which must be blended in its entirety to meet required quality specifications in terms of vitamins and other components not included in the recipe optimization that are only found in the seleted leaf. The lower and upper flow bounds for mixing B1 to B4 and R1 to R4 are 0.0 to 100.0%. The costs of raw materials and prices of the red meat patty burger as well as the nutrion values are easily found in supermarkets.

Table 1. Raw materials (beans, roots and selected leaf) and red met patty burger compositions in grams

	Per 1000 Grams		Calories	Total Fat	Protein	Carbohydrates	Sodium	Fibre
Beans	**Pinto Beans**	B1	3470.0	12.0	214.0	626.0	120.0	155.0
	Black Turtle Beans	B2	3390.0	9.0	212.0	630.0	90.0	249.0
	Kidney Beans	B3	3330.0	8.0	236.0	600.0	240.0	249.0
	Soy Beans	B4	4160.0	199.0	365.0	302.0	20.0	93.0
Roots	**Sweet Potatoes**	R1	859.0	0.5	15.7	201.2	550.0	30.0
	Carrots	R2	410.0	2.4	9.3	95.8	690.0	28.0
	Butternut Squash	R3	450.0	1.0	10.0	116.9	40.0	20.0
	Beets (beetroot)	R4	430.0	2.0	16.0	96.0	780.0	280.0
Leaf	**Arugula**		250.0	6.6	25.8	36.5	270.0	16.0
Red Meat	**Patty**		2255.6	135.6	185.6	75.6	5677.8	5.6

IV. Results and discussions

After the optimization using both the typical blend recipe as an NLP and the LP factor approach with one time-period, the flows of beans and roots for 1000 grams of red meat patty are found in both solutions as follows: 47.89 g of B2, 456.25 g of B4 and 395.85 g of R4 (considering the 100 g of the leaf as fixed). As expected, the solution maximizes the utilization of beans to meet the protein content in the red meat patty. Without considering calories of the patty (2255.6) as an upper bound limiting the recipe, the optimization selected only B4 to meet the protein in the lower bound content (185.6 g). The protein content (PROT) is found at the bound of the patty product, therefore there is no slack or surplus in the LP approach for the property and its factor-flow is zero. For the other properties, they are not at the bounds (given in Table 1) of the red meat patty, therefore there is slack or surplus of specification, well-known in the industry as giveaways.

Considerig the B2, B4, the select Leaf (at fixed 100g) and the R4 amounts found in the optimization, the giveaway of carbohydrates is 134g more than the minimal amount of the read patty (209.6 g considering the lower bound of the patty is 75.6 g). The total fat is content is lower than to the red patty in 42.9 g since the plant-based burger total fat obtained is 92.7 g, which also represents a giveaway. Therefore, both giveaways of the total fat and carbohydrate contents indicates that the vegan burger can meet the protein content of the red meat patty with additional benefits in other nutrition components.

V. Conclusions

We highlighted the application of a vegan burger blending using a typical NLP model as well as the approximation using LP factors. The purpose of such optimization is to determine raw material amounts for the vegan burger product to be included in complete supply chain models connecting the harvesting to the commercialization segments. The recipe optimization as an LP quantity-quality balance, which permits the supply chain calculation in MILP models, resulted in similar solution of the NLP approach. Therefore, by using MILP formulation the diverse raw materials from the harvest and upstream chains to be processed in manufacturing sites for the market distribution and consumption can be determined to evaluate the impacts of the vegan diet in the food industry.

References

Aiking, H. & de Boer, J., 2018. The next protein transition. Trends in Food Science & Technology.. Trends in Food Science & Technology.

Brunaud, B., Perez, H.D., Amaran, S., Bury, S., Grossman. I.E., 2020. Batch scheduling with quality-based changeovers Computers & Chemical Engineering, 132, 106617.

Cleveland, D. & Gee, Q., 2017. Plant-Based Diets for Mitigating Climate Change. In: Vegetarianand Plant-Based Diets in Health and Disease Prevention. Amsterdam, The Netherlands: Elsevier, 135–156.

Goldstein, B., Moses, R., Sammons, N. & Birkved, M., 2017. Potential to curb the environmental burdens of American beef consumption using a novel plant-based beef substitute. PLoS ONE, 12, 12.

der Weele, C. et al., 2018. Meat alternatives: an integrative comparison. Trends in Food Science & Technology, 18, 505-512.

Flynn, M. M. & Schiff, A. R., 2015. Economical Healthy Diets (2012): Including Lean Animal Protein Costs More Than Using Extra Virgin Olive Oil. Journal of Hunger & Environmental Nutrition, 10 (4), 467-482.

Jetter, K. M. & Cassady, D. L., 2006. The availability and cost of healthier food alternatives. Am J Prev Med., 30(1), pp. 38-44.

Kelly, J.D., 2005. The Unit-Operation-Stock Superstructure (UOSS) and the Quantity-Logic-Quality Paradigm (QLQP) for Production Scheduling in The Process Industries, In Multidisciplinary International Scheduling Conference Proceedings: New York, United States, 327-333.

Kelly, J.D., Menezes, B.C., 2019. Industrial Modeling and Programming Language (IMPL) for Off- and On-Line Optimization and Estimation Applications. In: Fathi M., Khakifirooz M., Pardalos P. (eds) Optimization in Large Scale Problems. Springer Optimization and Its Applications, 152, 75-96.

Kelly, J.D., Menezes, B.C., Grossmann, I.E., 2018. Successive LP Approximation for Non-Convex Blending in MILP Scheduling Optimization Using Factors for Qualities in the Process Industry. Ind. Eng. Chem. Res., 57 (32), 11076.

Macdiarmid, J., Douglas, F., Campbell, J., 2016. Eating like there's no tomorrow: Public awareness of the environmental impact of food and reluctance to eat less meat as part of a sustainable diet. Appetite, 19, 487-493

Monsivais, P. & Drewnowski, A., 2007. The rising cost of low-energy-density foods. JAmDiet Assoc., 107, 2071–2076.

Rao, M., Afshin, A., Singh, G. & Mozaffarian, D., 2013. Do healthier foods and diet patterns cost morethan less healthy options? A systematic review and meta-analysis. BMJ Open, 3 (12), e004277.

Moistchar: A Sustainable Approach for Water Stress and Plant Growth

[1]Snigdhendubala Pradhan, [1]Hamish R. Mackey, [1]Tareq Al-Ansari, [1]Gordon McKay
[1] Division of Sustainable Development, College of Science and Engineering, Hamad Bin Khalifa University, Doha, Qatar
[1]spradhan@hbku.edu.qa; hmackey@hbku.edu.qa; talansari@hbku.edu.qa; gmckay@hbku.edu.qa

Presenting author email: spradhan@hbku.edu.qa

Abstract

Food waste is a major issue globally and due to inputs and emissions through the supply chain results in large contributions to greenhouse gas emissions. On the other hand, producing food is a water intensive process, particularly in arid environments which often also have poor soils. Food waste derived biochar is an approach to address both of these issues at once, by turning waste into a soil amendment material that can improve soil productivity and watering efficiency. In this study a biochar was produced from a mixture of vegetable wastes (cauliflower, cabbage, banana peels and corn) at pyrolysis temperatures from 300 to 600 °C and characterized for properties that have a major influence on plant germination, growth and soil water retention. A temperature of 400 °C produced the optimum biochar and was used for pot tests with two ornamental plant seeds (sunflower and capuchina) and one crop seeds, cucumber. Biochar at 2% mass loading in sandy soil was tested against a control without biochar (0%). Biochar addition reduced soil salinity and increased cation exchange capacity, which is related to fertilizer retention. In the 2% biochar pots, after 5 days and 50 mL of water, 28 sunflower seeds germinated out of 30 with height from 1.8 to 4.5 cm. Under the same conditions in the control no germination was observed. Similarly with capuchina, all seeds were germinated in biochar amended soil while only 24 seeds germinated in the control after 5 days. Germination of cucumber occurred for 6 seeds out of 10 in biochar compared with 3 in the control after 5 days and the height of the germinated seeds was approximately 3 times greater in biochar amended soil after 10 days. This study demonstrates the effective application of a circular economy to manage the water-food nexus.

Keywords: Food wastes; Biochar; Water retention; Seeds germination; Water food nexus

Introduction

According to UNFAO (2011), 1.3 billion tonnes of food wastes are generated globally and due to improper food transport and disposal strategies with significant impacts on the world economy, environmental pollution and food security. It is estimated 23 million tons of grains, 12 million tons of fruits and 21 million tons of vegetables are lost through the supply chain with a value of about 4.4 billion USD, where the total value of all food loss is estimated at 10.6 billion USD (UNFAO, 2011). Various approaches exist for managing food waste including composting, landfilling and anaerobic digestion. Conversion to biochar, a carbon rich soil amendment, is another approach, which is produced through pyrolysis and has been proposed as a sustainable approach to reduce food waste and cost for a complete waste management cycle (Zhang et al., 2012). However, production and consideration of effective biochar as an amendment for soil fertility and plant growth depends upon the properties of the biochar, which is substantially dependentent on the food waste feedstock (Lou et al., 2016). Biochar from agricultural wastes have been applied to soil to enhance agricultural yields and increase water retention capacity. These biochars have been an effective amendment for low quality soil. However there is lack of information for the production of biochars from vegetable wastes, which differ significantly in composition, and their application for water retention capacity, plant germination and growth. This study aims to determine the effect of biochar produced from mixtures of vegetable wastes on plant germination, growth and the water retention capacity of soil.

Materials and methods

Biochar was produced from a mixture of vegetable wastes that included cauliflower, cabbage, corn and raw banana peels at different pyrolysis temperatures from 300 to 600 °C in a muffle furnace. Various properties such as pH, electrical conductivity of the extract (ECE), cation exchange capacity (CEC), and carbon to nitrogen ratio (ASTM, 2013, 2010; Lou et al., 2016) were analysed for a char passing through a 75 µm sieve (ASTM, 2007). The optimal biochar, based on the various parameters characterized for the different temperatures of pyrolysis, was

selected to apply in soil for pot testing. The soil biochar mixture was prepared at 0% (control), 2% and 6% (w/w) for two two ornamental plant seeds, capuchina (*Tropaeolum majus*) and sunflower (*Helianthus*), and one crop seed, cucumber (*Cucurbitaceae*). Thirty numbers of capuchina and sunflower seeds and ten cucumber seeds were soaked with water for an hour and planted for germination in individual pots. Pot tests were conducted for the three biochar loadings of 200 g by weight of regional sand for capuchina and sunflower and 400 g for cucumber by using pots with square dimensions of 7.5 cm and a depth (height) of 4.5 cm. A water mass balance was conducted on the various pots, as well as a measurement of the number of seeds germinated, germination period, plant height with time and the number of leaves with time for the pots, over the germination or initial growth phase at the three different biochar loading conditions of 0%, 2% and 6% by weight.

Results and Discussion

Out of four pyrolysis temperatures 300, 400, 500 and 600 °C, the biochar produced at 400°C was selected for pot tests based upon maximum cation exchange capacity (CEC) of 53.2 $cmol_c.kg^{-1}$, a suitable carbon to nitrogen ratio (C/N) of 24.8 (Harvey et al., 2011; Rawat et al., 2019) with pH 8.53 and 475 µS. cm^{-1}. The water balance showing drainage, evapotranspiration and retention over the period of twenty days of observation for the planted pots is shown in Fig. 1 for capuchina, sunflower and cucumber respectively. A small variation was observed upto ten days of water application between the biochar loadings for sunflower seeds, but was significant between the biochar loadings by day 20. In the capuchina and cucumber pots, notable differences were observed from the outset, where water retention was higher for higher biochar loadings.

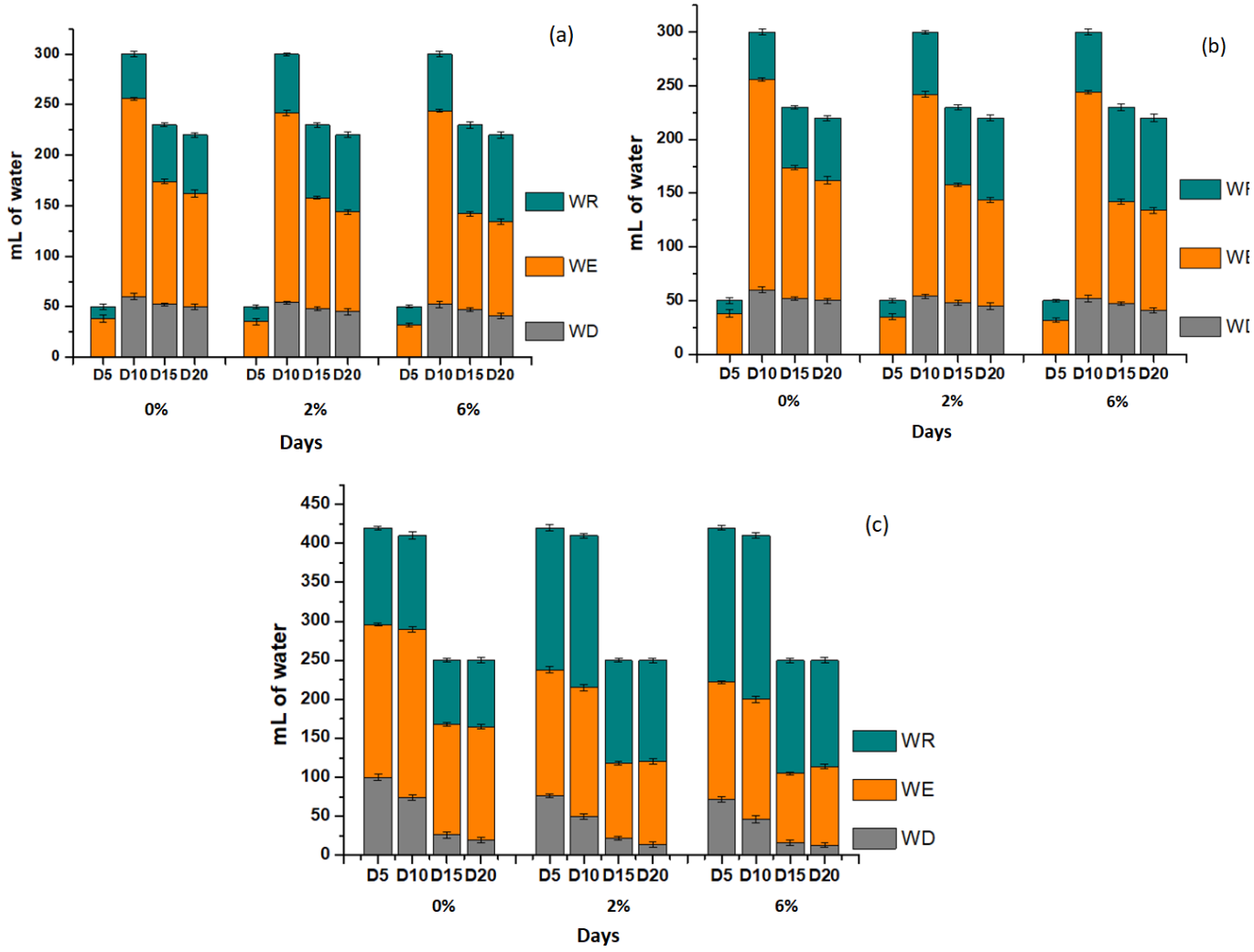

Fig.1: Water mass balance over 20 days in (a) capuchina pot (b) sunflower pot and (c) cucumber pot; *WD: water drained; WE: water evaporated; WR: water retained*

In all test conditions, optimum seeds germination was observed within ten days (Fig. 2 (a)). Increasing height of each plant and number of leaves was observed up to 20 days of operation and shown in Fig. 2 (b, c). Out of 30

seeds, 28 capuchina seeds, 20 sunflower seeds and 3 cucumber seeds were germinated in 0% biochar. The optimum seeds germination was observed in 2% for all cases (30 capuchina seeds, 28 sunflower seeds and 6 cucumber seeds) over ten days. While the differences in germination between 2% biochar and the control were quite small for germination, more noticeable differences were observed for plant height and number of leaves.

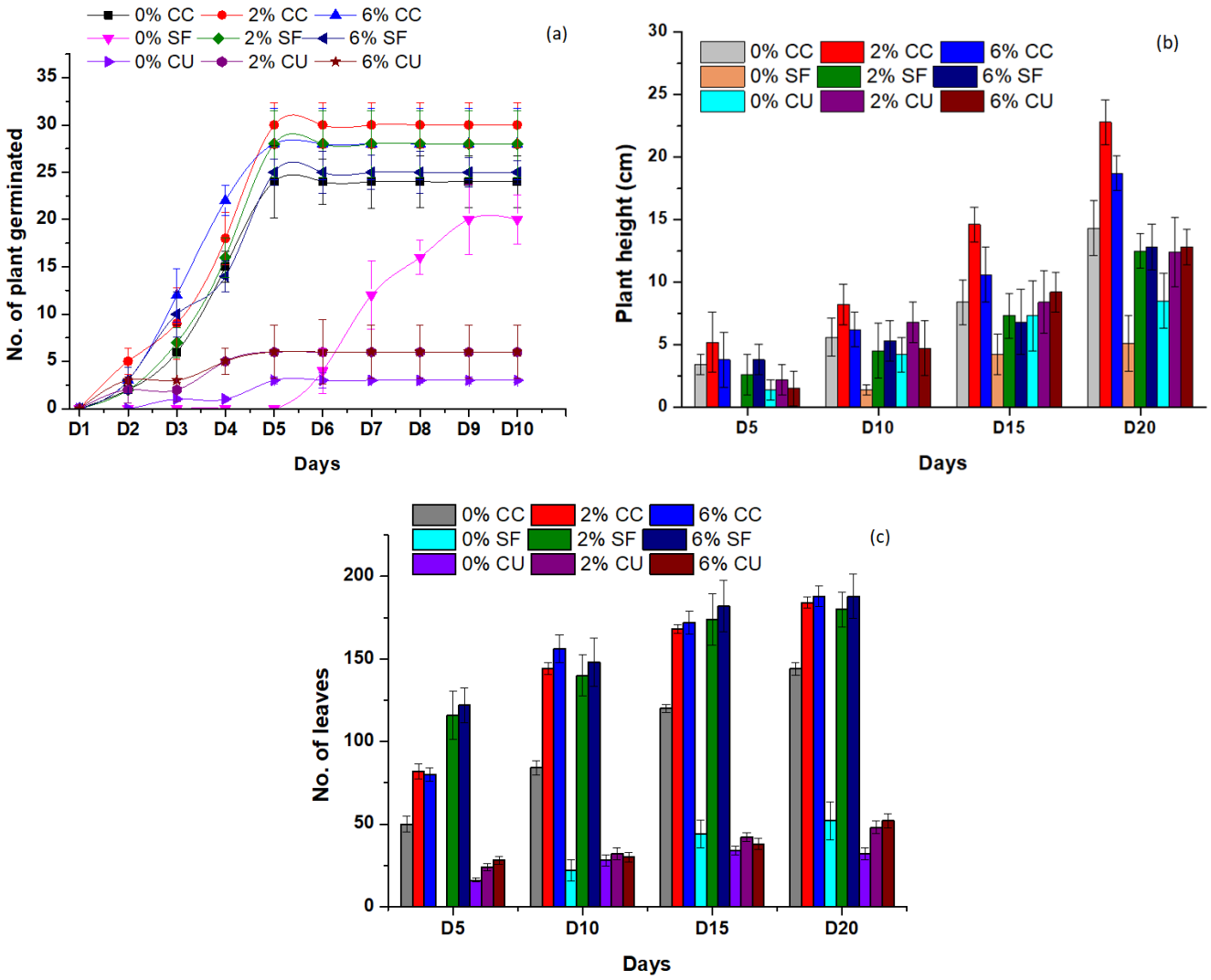

Fig.2: (a) Number of plants germinated out of total seeds (b) increasing rate of plant height and (c) number of leaves. *CC: capuchina; SF: sunflower; CU: cucumber*

For plant height, little difference existed between 2% and 6% loading for sunflower and cucumbers, but both biochar amendments showed significant improvements over the control by day 20. For capuchina, the 2% biochar loading resulted in much greater growth than either the control or the 6% biochar loading. For the number of leaves, the application of biochar was most effective at increasing development for sunflowers, where the number of leaves was more than threefold for both biochar loadings over the control. More modest improvements were seen with capuchina and cucumber.

Conclusion

This study established the efficiency of biochar produced from vegetable wastes for crops and ornamental plant growth using a biochar produced at 400 °C, with overall improvements across multiple water and growth related factors observed. The biochar produced at low pyrolysis temperature and fine particle size demonstrated a promising effect for three plants, resulting in enhanced soil-water retention capacity when using sandy soil and increased success in germination compared with the control. Growth effects on plant height and number of leaves differed based on plant type, but all cases also showed improvement over the control conditions, with typically little difference between 2% and 6% loading. The study demonstrates that recycling of food waste to biochar provides an effective means to reduce the burden from municipal solid waste management and improve agricultural activity.

Acknowledgement

The authors would like to thank Qatar National research Fund for the provision of an award, Number: NPRP11S-0117-180328- to support this project.

References

ASTM, 2013. Standard test methods for proximate analysis of coal and coke by macro thermogravimetric analysis D 7582-15.

ASTM, 2010. Standard test method for measuring the exchange complex and cation exchange capacity of inorganic fine-grained soils D7503-10.

ASTM, 2007. Standard test method for particle-size analysis of soils D 422-63.

Harvey, O.R., Herbert, B.E., Rhue, R.D., Kuo, L.-J., 2011. Metal interactions at the biochar-water interface: energetics and structure-sorption relationships elucidated by flow adsorption microcalorimetry. Environ. Sci. Technol. 45, 5550–5556.

Lou, K., Rajapaksha, A.U., Ok, Y.S., Chang, S.X., 2016. Pyrolysis temperature and steam activation effects on sorption of phosphate on pine sawdust biochars in aqueous solutions. Chemical Speciation & Bioavailability 28, 42–50. https://doi.org/10.1080/09542299.2016.1165080

Rawat, J., Saxena, J., Sanwal, P., 2019. Biochar: A Sustainable approach for improving plant growth and soil properties. In biochar-an imperative amendment for soil and the environment. Fruit and Vegetable Waste: Bioactive Compounds, Their Extraction, and Possible Utilization, IntechOpen.

UNFAO, 2011. Food and Agriculture Organization of the United Nations. http://www.fao.org/news/archive/news-by-date/2011/en/ (accessed 1.24.20).

Zhang, A., Bian, R., Pan, G., Cui, L., Hussain, Q., Li, L., Zheng, Jinwei, Zheng, Jufeng, Zhang, X., Han, X., Yu, X., 2012. Effects of biochar amendment on soil quality, crop yield and greenhouse gas emission in a Chinese rice paddy: A field study of 2 consecutive rice growing cycles. Field Crops Research 127, 153–160. https://doi.org/10.1016/j.fcr.2011.11.020.

Thermo-hydraulic and exergy analysis of parabolic trough collector with wire matrix turbulator: An experimental investigation

[1]K. Varun, [2]U.C. Arunachala*
[1,2] Renewable Energy Center, Department of Mechanical and Manufacturing Engineering, Manipal Institute of Technology, Manipal Academy of Higher Education, Manipal 576 104, Karnataka, India

* Corresponding author (E-mail: arun.chandavar@manipal.edu)

Abstract
The present energy crisis due to exhaustion of fossil fuels, global warming, surging gap between energy supply and demand, high electricity price etc. have paved a path to harness renewable energy resources effectively. Among various sources, due to enormous potential and implicit superiority, solar thermal energy has been proved to be the best solution for the energy crisis. Further, parabolic trough collector (PTC) is the oldest and prevailing solar concentrating technology. As, the receiver of PTC is subjected to highly non-uniform concentrated heat flux (circumferentially), majority of the studies are numerical. Even outdoor testing is a laborious task due to transient operating condition. Hence, an innovative method encompassing analytical model-SOLTRACE®-differential resistance heating is incorporated in the present indoor experimental study to simulate the realistic highly non-uniform solar irradiance over the receiver. In order to effectively utilize the solar energy and to improve the exergetic efficiency of PTC, three variations of wire matrix have been employed and its thermo-hydraulic effect is studied using performance evaluation criterion (*PEC*). Apart from energy analysis, exergy analysis is done to gauge the energy conversion process. In the analysis, DNI of 800 W/m^2 is chosen as the SOLTRACE® input and Therminol VP-1 is the heat transfer fluid with flow range of *Re*=2800-7800. Various energy parameters viz. Nusselt number, friction factor, PEC and exergetic efficiency have been analyzed. *Nu* increment of 2.46 times at the cost of 10.37 times *f* is observed in the best wire matrix case. The PEC analysis yielded best value as 1.14. Eventually, an exergy enhancement ratio of 4.3 is achieved due to wire matrix insert.

Keywords: Parabolic trough collector, SOLTRACE®, Wire matrix, Performance evaluation criterion, Exergetic efficiency.

I. Introduction

Solar thermal energy is the best solution for present day energy crisis as its abundance can meet both the present and future needs. Further, parabolic trough collector (PTC) has proven to be the most prominent and promising solar thermal energy conversion technology having a variety of applications in the temperature range of 150°C to 400°C. In PTC, the receiver is subjected to highly non-uniform concentrated heat flux (circumferentially) which results in high radiation loss and thermal stress. Hence for its retardation, several heat transfer augmentation (HTA) techniques have been introduced which in turn enhances the thermo-hydraulic performance. Out of active and passive techniques, the use of flow inserts/turbulators (passive) have become popular recently as its benefits overrides the intricacy.

A review by (Bellos and Tzivanidis, 2019) enlisted the use of several inserts viz. screw tape, wavy tape, twisted tape, porous disc, metal foam, multi fin, star flow insert and wire coil in PTC and concluded it as superior than nanofluid. (Manikandan et al., 2019) have suggested conical rings, wire coil, wire coil combined with twisted tape and twisted wire brush (similar to the wire matrix). (Sandeep and Arunachala, 2017) have commented turbulators as the best in PTC. Further, (Kumar et al., 2020) compiled the effect of various inserts and suggested its extended studies on exergy. Data compiled by (Bellos et al., 2018) disclosed that inserts-specific studies in PTC has increased by 20 folds between the year 2009 and 2017. Ultimately the appraisal of review articles depicted wire matrix (WM) as the less explored turbulator in PTC as it has already been found in general applications as (Ritchie et al., 2009) have introduced hiTRAN® wire matrix (WM) for mitigating particulate fouling and to enhance the tube side coefficient. Further, (Drögemüller, 2015) incorporated the same WM in tubular heat exchanger and found enhancement in heat transfer coefficient and mass transfer rates.

Apart from the application of turbulators, recent articles have also focused on different heat flux patterns in PTC. Even though the solar flux distribution over the receiver is highly non-uniform, (Ghasemi and Ranjbar, 2017) have employed only two heat flux zones, i.e. normal irradiance at the upper half and concentrated flux at the bottom, in the numerical study. Further, numerical studies also incorporated Monte Carlo ray tracing method (MCRT) to simulate the non-uniform flux (Gong et al., 2017; Zhu et al., 2017). (Chang et al., 2018) have investigated the performance of PTC with concentric and eccentric rod inserts using MCRT with user defined function (UDF) which resulted in eccentric rod insert as the superior. However, a perfect non-uniform flux distribution can be achieved in outdoor testing as depicted by (Jamal-Abad et al., 2017) with copper foam as the insert. SOLTRACE® as a ray tracing software (Wendelin, 2009) has been recently employed in the PTC analysis. As outdoor testing is a laborious task due to transient operating condition, for the first time, (Elton and Arunachala, 2018) have employed SOLTRACE® technique in an indoor test rig to study the influence of twisted tape.

Till date literature survey on PTC included HTA review, recent innovations in turbulators and ray tracing methodology. Appraisal of review articles hinted WM as the least explored turbulator in PTC. Further, since the heat flux pattern is highly non-uniform, majority of the insert-based studies are numerical with an exception of outdoor

(Jamal-Abad et al., 2017) and indoor experimental studies (Elton and Arunachala, 2018). It highlights the lack of realistic non-uniform heat flux based experimental data (including exergy analysis) of WM, intending PTC application. Hence in the present study, SOLTRACE® based non-uniform heat flux is applied to the receiver of PTC (in an indoor set up) and by incorporating WM, performance evaluation criterion (PEC) and exergy enhancement ratio (EER) have been evaluated.

II. Physical and mathematical models

The major components of PTC are reflector, evacuated receiver and HTF as depicted in Fig. 1. The parabolic trough (width W) is having high reflective/low absorptive coating. Generally, stainless-steel receiver of known length (L) with an evacuated glass cover is used. Apart from its geometrical specifications, the optical properties viz. glass cover transmissivity (τ), trough reflectivity (ρ), receiver absorptivity (α) and its emissivity (ε) plays a crucial role in its performance. Hence, all these parameters are incorporated in the mathematical model.

A MATLAB code is written for predicting the total heat loss from the receiver which includes optical efficiency, overall heat transfer coefficient, collector efficiency factor, collector heat removal factor and useful heat gain (Elton and Arunachala, 2018). The input parameters viz. solar irradiance, wind speed and ambient temperature, are acquired from NREL (https://maps.nrel.gov/nsrdb-viewer/). The total heat loss calculated here is incorporated in the heat supply analysis.

III. Heat supply analysis

SOLTRACE® is a general-purpose ray tracing software developed by the National renewable energy laboratory (NREL) for optical modeling and analysis of concentrated solar systems (Wendelin, 2009). In the present indoor experimental analysis, optical properties of LS-II receiver and geometrical dimensions of a lab size reflector (due to practical constraints) are taken (Elton and Arunachala, 2018). The results of SOLTRACE® are extracted, analysed in MS-Excel for grid independence (sensitivity) and further discretized based on the number of segments (bins) around the receiver circumference. The sun rays sensitivity analysis (Fig. 2) yielded 24 bins and 9 E08 rays as the optimum combination. Later, 24x24 bins are averaged to eight bins (due to experimental constraint) and consequently the receiver circumference is split into eight parts (over which non-uniform solar irradiance is incident) for further data processing.

The SOLTRACE® output is taken for defining local concentration ratio (LCR) which is the ratio of concentrated heat flux on specific segment to the incident beam radiation. Due to same LCR value, top-most and bottom-most two bins are seperatley merged which resulted in six segments i.e. six heating strips in the experimental analysis as depicted in Fig. 3.

By referring LCR, the rate of heating to each strip (segment) is computed using Equation 1 which considers the absorptivity (α) of the receiver (no option in SOLTRACE® analysis). Later, the total heat loss from the receiver (MATLAB output) is deducted from the power computed for each strip and the net power supplied (as receiver is adiabatic in the study) to each strip is determined by Equation 2.

$$P_{seg} = [I_b LCR_{seg} W_{seg} L_{seg}]\alpha \quad (1)$$

$$P_e = \left[I_b LCR_{seg} W_{seg} L_{seg}\right]\alpha - \left[\frac{Q_L}{A_r} W_{seg} L_{seg}\right] \quad (2)$$

Where I_b is the solar irradiance (W/m^2), W_{seg} is the width of strip/segment, L_{seg} is the length of strip/segment, A_r is the receiver area (m^2) and Q_L is the heat loss from the receiver (W/m^2)

For example, DNI of 800 W/m^2 results in total heat loss from receiver as 42 W for known operating condition which results in concentrated flux (net heat supplied) distribution as depicted in Fig. 3. Here, maximum flux of 20.01 kW/m^2 is falling at the bottom and a minimum of 0.61 kW/m^2 at the top. It corresponds to 450.1 W and 13.7 W of heating respectively by the strips.

IV. Experimental analysis

The aim of the experiment is to investigate the effect of WM on heat transfer and exergy and, to suggest the best variant based on thermo-hydraulic and exergetic performance. As test section is adiabatic, variation in ΔT of HTF (for the same operating condition) indicates the effect of WM.

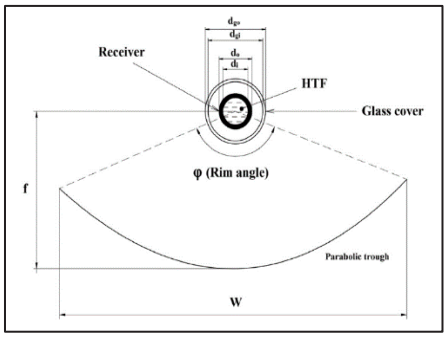

Fig. 1: Schematic of PTC

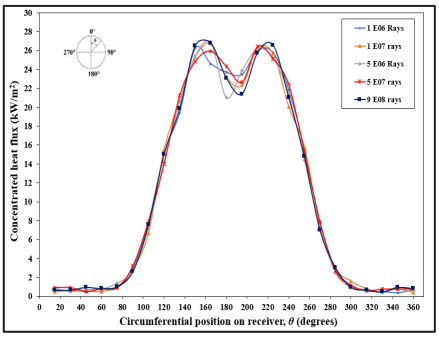

Fig. 2: Sun rays sensitivity analysis

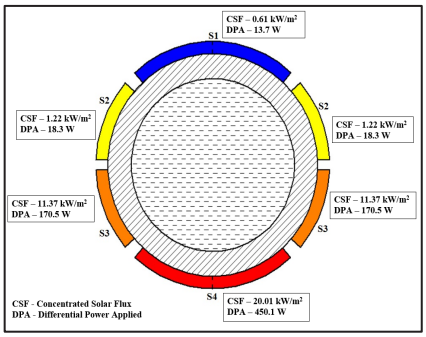

Fig. 3: Differential heating for the receiver

(a) Experimental setup

The schematic of the indoor experimental test rig is depicted in Fig. 4. The setup consists of entry length (EL, 1.5 m SS tube), test section (TL), HTF flow line, control system and instrumentation. The test section is SS 304 L stainless steel pipe (d_i/d_o/L as 26.72/31.45/1550 mm) welded with sixteen K-type (pre-calibrated) thermocouples (T1-T16) at equidistant points (both axially and circumferentially) and then wrapped with flexible mica sheet (0.1 mm thick) for electrical insulation. Four more thermocouples (T17-T20) measures HTF temperature difference, insulated surface and ambient temperature. For pipe surface heating, six nichrome strips of 0.5 mm thick and 1550 mm long (four strips of 10 mm and two strips of 20 mm width) are firmly placed over the pipe using high temperature insulating tape. The test section is made adiabatic with the use of insulating materials, viz. ceramic wool and rockwool.

A thermostatic bath (TB, SISKIN Profi Chill RHC3500-S1, ±0.1°C) with a combination of a gear pump (GP, Hiren Hechdr/04) and variable frequency drive (VFD) (Mitsbushi/FR-D720S-070-EC, ±0.1 Hz) recirculates the HTF at known temperature through the test section. Therminol-VP 1 is the HTF since it has a practical application in solar thermal power plants and thus a realistic approach. For measuring the pumping power, power analyser (PA, Yokogawa WT300E, ±0.1 W) is connected to VFD. Differential pressure transducer (DP, Honeywell/ST700, ±1 Pa) and flow meter (FM, Deshwaan, ±0.1 LPM) are also connected to flow line. Further, each of the nichrome strip is differentially heated by supplying calculated (concentrated heat flux) power with the combination of Dimmerstats (DS) and step-down transformers (TF, 1000/500/300/100 VA) and, power supplied being measured Wattmeter (WM). Data logger (DL, Agilent 34972A) is used to capture real time data.

The WM compactness is represented by number of wire turns per foot length. WM of three variations viz. low dense wire matrix (LDWM - 39 turns per foot length), medium dense wire matrix (MDWM - 44 turns per foot length), high dense wire matrix (HDWM - 48 turns per foot length) have been used as shown in Fig. 5. In both MDWM and LDWM, radial clearance of ≈1 mm is observed whereas the HDWM is having push fit with the receiver. The cross-sectional view of WM (Fig. 5) has 8 rings of 0.6-0.8 mm thick wire wound over a central rod of 3.5 mm diameter in such a way that the diameter of each ring is 13 mm.

(b) Experimental procedure

Here *Re* range is varied (2800-7800) by changing both flow rate and HTF entry temperature. The tests were conducted for both plain receiver and receiver with three variations of WM. Initially the system is started with a precalculated flow rate and entry temperature. In order to circumvent any partial flow in the system, the flow line is gradually pressurized using a gate valve. Then the net differential heat is supplied (calculated from MATLAB and SOLTRACE®) for a solar irradiance of 800 W/m^2 across each strip is supplied through the variac-transformer arrangement. The HTF is allowed to recirculate for sufficient time to attain steady state and thereafter various parameters are recorded using data acquisition unit. The same procedure is repeated in cases of insert and for satisfying the repeatability aspect, the entire experiment was repeated four times.

(c) Data reduction

The important energy parameters are discussed here with the supporting terms from (Elton and Arunachala, 2018). The Nusselt number, friction factor and PEC are calculated as,

$$Nu = \frac{h_f * d_{ri}}{k} \tag{3}$$

$$f = \frac{2 * d_i * \Delta P}{\rho * L * v^2} \tag{4}$$

$$PEC = \frac{Nu_{enhanced}}{Nu_{plain}} \Big/ \left(\frac{f_{enhanced}}{f_{plain}}\right)^{1/3} \tag{5}$$

Further, the exergetic efficicency (η_{ex}) is calculated based on useful exergy output (E_u) (Bellos and Tzivanidis, 2017) and exergy flow of solar radiation (E_s) (Petela, 2003).

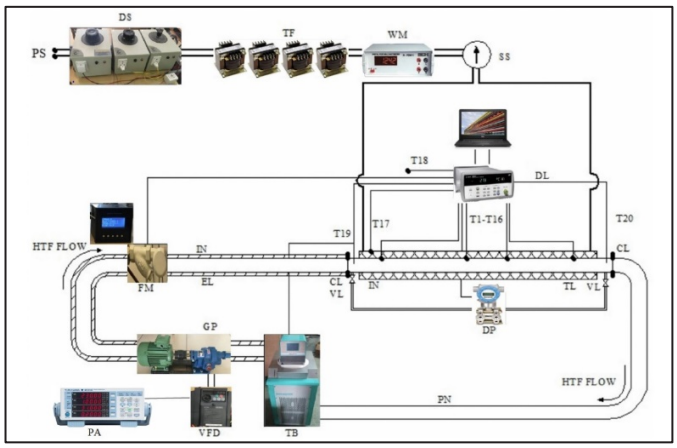

Fig. 4: Schematic of experimental setup

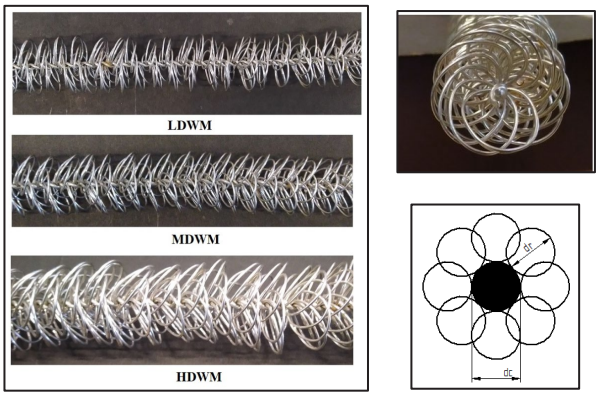

Fig.5: Variations of wire matrix

$$E_u = Q_u - m \cdot C_p \cdot T_{amb} \cdot \ln\left(\frac{T_{out}}{T_{in}}\right) - m \cdot T_{amb} \frac{\Delta P}{\rho_{fluid} \cdot T_{fluid}} \quad (6)$$

$$E_s = A_{aperture} \cdot I_b \cdot \left(1 - \frac{4}{3} \cdot \left(\frac{T_{amb}}{T_{sun}}\right) + \frac{1}{3} \cdot \left(\frac{T_{amb}}{T_{sun}}\right)^4\right) \quad (7)$$

$$\eta_{ex} = E_u / E_s \quad (8)$$

Exergy enhancement ratio (EER) is defined as

$$EER = \eta_{ex-enhanced} / \eta_{ex-plain} \quad (9)$$

(d) Uncertainty analysis

Further, uncertainty analysis is performed by considering the error involved in each measurement which yielded maximum uncertainty of ±0.46 % and ±0.16 % in the calculation of PEC and *EER* respectively.

V. Results and discussions

Different configurations of WMs have been investigated under simulated solar radiation. The major experimental findings are heat transfer enhancement (*Nu*), friction factor (*f*) rise, PEC and *EER*.

The best way to gauge HTA is *Nu*. Fig. 6 portrays the variation in *Nu* with *Re* for different WM variants. As backed by the literature, the *Nu* rise is substantial in laminar and transition flow regimes and, minimal in turbulent region. Compare to plain receiver, in the transition region (Re=2800), the rise for MDWM, HDWM and LDWM case is 146%, 110% and 84% respectively against 64%, 29% and 26% in fully turbulent (Re=7800) condition. The HTA in the receiver with WM is due to high resident time of HTF, highly random flow through WM (enhanced secondary swirls), compactness of wire matrix (number of wire turns adds to local turbulence) and radial clearance (annular flow) between the receiver wall. As cited earlier, both LDWM and MDWM possess a radial clearance of ≈1 mm which leads to narrow annular flow (in contact with receiver inner surface) in addition to the local turbulence and resident time. Hence, MDWM performs better (annular flow is effective) than HDWM (even though closely packed). Further, the cumulative effect of annular flow, lower local turbulence and resident time for LDWM resulted in lower performance than the other two. Hence, MDWM yielded a maximum of 2.46 times rise in *Nu* than HDWM (2.1) and LDWM (1.84).

HTA with inserts are always at the cost of pressure drop/friction factor. The variation of *f* with Re is depicted in Fig. 7 which follows the general trend of lower *f* at higher *Re*. Although the pressure drops associated with WM is too high, due to highly restricted flow area (cross section of WM in Fig. 5), moderate increment in *f* is found. Hence, the maximum rise (compared to plain receiver) in *f* for MDWM, HDWM and LDWM are 10.37, 6.34 and 4.2 times respectively. Radial clearance, thicker wire material and moderate compactness led to higher friction loss in MDWM.

Further, cumulative thermo-hydraulic effect of WM is studied through PEC analysis as illustrated in Fig. 8. The variation of PEC follows the trend LDWM>HDWM>MDWM until the early turbulent regime. Due to lower f_e/f_p and moderate Nu_e/Nu_p, LDWM delivered maximum PEC of 1.14 (at *Re* = 2800) followed by 1.13, 1.12 for HDWM and MDWM respectively. However, in turbulent regime MDWM outclasses HDWM due to higher Nu_e/Nu_p but falls behind LDWM due to high friction loss. As noticed in the literature, PEC values for all the variants of WM are below 1 in turbulent regime due to inherent turbulence. Hence, MDWM can be employed in PTC when thermal enhancement is of concern and LDWM for thermo-hydraulic factor.

Exergetic analysis (stemming from second law of thermodynamics) is a practical approach to gauge the energy conversion process as it identifies the causes and magnitude of process inefficiencies and suggests the areas for heat recovery. In order to effectively utilize the solar energy, the WMs employed results in an improvement of the exergic efficiency which is characterized by a dimensionless term *EER* as shown in Fig. 9. The variation of EER follows the trend of MDWM>HDWM>LDWM, with MDWM resulting in a maximum *EER* of 4.3 at *Re*=2800. The corresponding values for HDWM and LDWM are 4.02 and 3.84 respectively. Further, the increment in exergetic efficiency decreases with Re as process inefficiency increases dramatically in highly turbulent region. The least *EER* observed is 1.82 (MDWM), 1.25 (HDWM) and 1.1 (LDWM) at *Re* = 7800. Thus, it can be inferred that the MDWM variant effectively overrides the inefficiencies and is a potential insert for heat recovery applications.

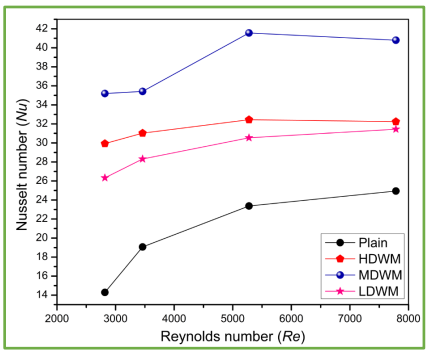

Fig. 6: Variation of *Nu* with Re

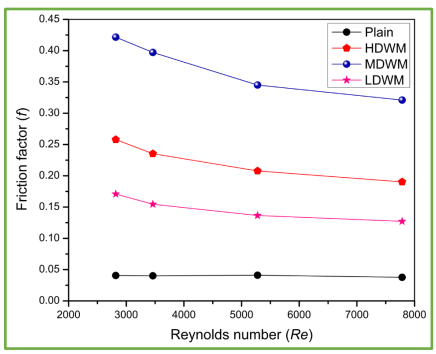

Fig. 7: Variation of *f* with Re

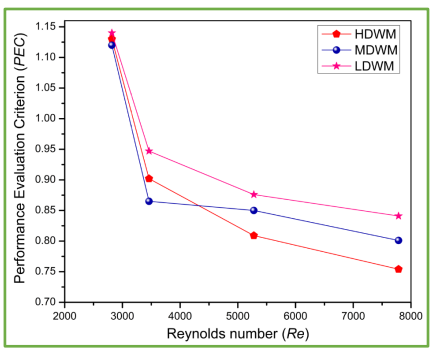

Fig. 8: Influence of WM on *PEC*

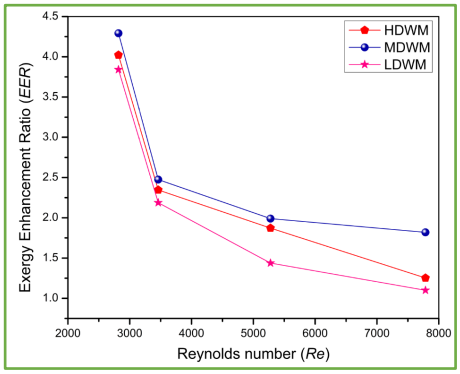

Fig. 9: Exergy enhancement ratios for WM

VI. Conclusions

The SOLTRACE® based indoor experimental investigation of HTA in PTC with WM led to following conclusions.

Annular flow due to radial clearance in WM led to additional local turbulence and resulted MDWM as the best insert. The maximum *Nu* enhancement of 2.46 times at the cost of 10.37 times friction loss emphasized the benefit of MDWM. Thermo-hydraulic analysis depicted LDWM (*PEC*=1.14) as the best due to relatively lower friction loss. Exergetic analysis led MDWM as the potential insert (*EER*=4.3) for overriding the process inefficacy and thus suitable for heat recovery applications.

Hence despite of allied maintenance and operational issues in using WM, MDWM is the best variant when thermal / exergy aspects of PTC are of concern and LDWM when hydraulic aspects play a major role.

References

Bellos, E., & Tzivanidis, C. (2017). A detailed exergetic analysis of parabolic trough collectors. *Energy Conversion and Management*, *149*, 275–292. https://doi.org/10.1016/j.enconman.2017.07.035

Bellos, E., Tzivanidis, C., & Tsimpoukis, D. (2018). Enhancing the performance of parabolic trough collectors using nanofluids and turbulators. *Renewable and Sustainable Energy Reviews*, *91*(March), 358–375. https://doi.org/10.1016/j.rser.2018.03.091

Bellos, E., & Tzivanidis, C. (2019). Alternative designs of parabolic trough solar collectors. *Progress in Energy and Combustion Science*, *71*, 81–117. https://doi.org/10.1016/j.pecs.2018.11.001

Chang, C., Sciacovelli, A., Wu, Z., Li, X., Li, Y., Zhao, M., Ding, Y. (2018). Enhanced heat transfer in a parabolic trough solar receiver by inserting rods and using molten salt as heat transfer fluid. *Applied Energy*, *220*(December 2017), 337–350. https://doi.org/10.1016/j.apenergy.2018.03.091

Drögemüller, P. (2015). The Use of hiTRAN Wire Matrix Elements to Improve the Thermal Efficiency of Tubular Heat Exchangers in Single and Two-Phase Flow. *Chemie-Ingenieur-Technik, 87*(3), 188–202. https://doi.org/10.1002/cite.201400081

Elton, D. N., & Arunachala, U. C. (2018). Parabolic Trough Solar Collector for Medium Temperature Applications: An Experimental Analysis of the Efficiency and Length Optimization by Using Inserts. *Journal of Solar Energy Engineering*, *140*(6), 061012. https://doi.org/10.1115/1.4040583

Ghasemi, E., S., & Ranjbar, A., A. (2017). Numerical thermal study on effect of porous rings on performance of solar parabolic trough collector. *Applied Thermal Engineering*, *118*, 807–816. https://doi.org/10.1016/j.applthermaleng.2017.03.021

Gong, X., Wang, F., Wang, H., Tan, J., Lai, Q., & Han, H. (2017). Heat transfer enhancement analysis of tube receiver for parabolic trough solar collector with pin fin arrays inserting. *Solar Energy*, *144*, 185–202. https://doi.org/10.1016/j.solener.2017.01.020

Jamal-Abad, M. T., Saedodin, S., & Aminy, M. (2017). Experimental investigation on a solar parabolic trough collector for absorber tube filled with porous media. *Renewable Energy*, *107*, 156–163. https://doi.org/10.1016/j.renene.2017.02.004

Kumar, A., Sharma, M., Thakur, P., Thakur, V. K., Rahatekar, S. S., & Kumar, R. (2017). A review on exergy analysis of solar parabolic collectors. *Solar Energy*, *197*, 411–432. https://doi.org/10.1016/j.solener.2017.01.020

Manikandan, G. K., Iniyan, S., & Goic, R. (2019). Enhancing the optical and thermal efficiency of a parabolic trough collector – A review. *Applied Energy*, *235*(August 2018), 1524–1540. https://doi.org/10.1016/j.apenergy.2018.11.048

Ritchie, J. M., Droegemueller, P., & Simmons, M. J. H. (2009). HiTRAN® wire matrix inserts in fouling applications. *Heat Transfer Engineering*, *30*(10–11), 876–884. https://doi.org/10.1080/01457630902753797

Sandeep, H. M., & Arunachala, U. C. (2017). Solar parabolic trough collectors: A review on heat transfer augmentation techniques. *Renewable and Sustainable Energy Reviews*, *69*(August 2015), 1218–1231. https://doi.org/10.1016/j.rser.2016.11.242

Petela, R. (2003). Exergy of undiluted thermal radiation. *Solar Energy*, *74*(6), 469–488. https://doi.org/10.1016/S0038-092X(03)00226-3

Zhu, X., Zhu, L., & Zhao, J. (2017). Wavy-tape insert designed for managing highly concentrated solar energy on absorber tube of parabolic trough receiver. *Energy*, *141*, 1146–1155. https://doi.org/10.1016/j.energy.2017.10.010

Novel passive heat transport device for solar indoor cooking: A numerical study

[1]K. Varun, [2]U. C. Arunachala*, [3]M. S. Manjunath
[1,2,3] Renewable Energy Center, Department of Mechanical and Manufacturing Engineering, Manipal Institute of Technology, Manipal Academy of Higher Education, Manipal 576 104, Karnataka, India

* Corresponding author (E-mail: arun.chandavar@manipal.edu)

Abstract
Thermosyphon heat transport device (THTD) is a fluid-filled unit employed for transporting heat from a source to sink by natural circulation. Both the source and sink are amalgamated within the THTD. Hence, once the geometry, fluid and boundary conditions are defined, its heat transport capability is fixed. THTD can incorporate single-phase, two-phase and/or supercritical fluids. Limitation in heat pipe like slower capillary action is overcome by THTD. It has been attempted in diverse passive fuel cooling system for advanced high temperature nuclear reactors. The present numerical study explores the possibility of employing THTD in solar indoor cooking by utilizing beam down concentrated heat flux. Vertical tube-in-tube design has been incorporated which consists of heat source, adiabatic height and sink. Design and numerical analysis are carried out using ANSYS Fluent module. The parametric study focuses eight variations of adiabatic height and sink length using Therminol VP-1 as heat transfer fluid (HTF) and water circulation chamber as sink. As THTD is meant for transferring heat from source to sink, time based transient analysis is of practical importance. The variation in heat transport time, flow path, flow velocity and HTF temperature are extracted from the simulation. Eventually, the THTD is compared with simple closed loop thermosyphon tube/system (SCLT) for different adiabatic heights. The results portray that the heat of 1 kW can be transferred in 17-42 minutes for the cases of 0.25-2 m adiabatic height. However, the SCLT shows noticeable amount of recirculation zones which results in time as 28-120 mins. In comparison, only 50% of the heat is transported in SCLT at a time when THTD has transported 100% and thus the quality of THTD is proved. Based on the application type, the numerical results suggest the optimum sink length as 0.25 m due to increased recirculation zones in other variants.

Keywords: Thermosyphon heat transport device, Simple closed thermosyphon system, Transient analysis, Natural circulation.

I. Introduction

Ever increasing energy crisis due to surging gap between energy supply and demand, global warming, exhaustion of fossil fuels, high fuel price etc. has led the transition to solar thermal energy due to its boundless potential and inherent superiority. Concentrated solar power (CSP) technologies viz. parabolic trough collector (PTC) and parabolic dish reflector (PDR) are the oldest and prominent techniques for tapping solar power. Its application ranges from power generation to process industry / cooking. Due to depletion of conventional fuel sources, in particular, high temperature PTC / PDR based cooking has become popular.

In conventional way, PTC and PDR systems have been used by the researchers (Al-Soud et al., 2010; Herez et al., 2018; Indora and Kandpal, 2018; Noman et al., 2019 and Onokwai, 2019) in solar cooking. Recently the use of Thermosyphon heat transport device (THTD) with PDR in solar indoor cooking has been suggested by Vijayan et al., 2019.

The origin of THTD is heat pipe. However, due to absence of vacuum region and wick structure, it is simple and works effectively when the source and sink are far away. Hence, Limitation in heat pipe like slower capillary action is overcome by THTD. It is a simple vertical tube-in-tube design fluid-filled unit employed for transporting heat from a source to sink by natural circulation. Its internal tube is made of thermally insulating material (such as ceramics, glass, steel tubes with air gap) so as to ensure a unidirectional flow of heat transfer fluid (HTF) as shown in Fig. 1 (a) (Vijayan et al., 2019). Both the heat source and heat sink are amalgamated within the structure of THTD. One or more THTDs can be incorporated in series and/or parallel to accomplish the required heat transport function. Since the studies pertaining to THTD are scanty, further review focuses on development of THTD concept.

The application of heat pipe since (Grover, 1964) has been extended to solar and nuclear applications recently. (Jouhara et al., 2017) have intensively reviewed different heat pipes and deduced that it works effectively for only small temperature gradient, and thus its potentiality in CSP is limited. To overcome the inherent problems of heat pipe, (Japikse and Winter, 1971) introduced a single-phase open thermosyphon loop (OTL), which led to higher temperature gradient / heat transfer rate. Further, (Japikse et al., 1971) investigated the single-phase closed thermosyphon loop (CTL) under vertical and inclined conditions and, found to be better than OTL. In addition, (Japikse, 1973), consolidated the behavior, operation, stability criteria and applications of open, closed and two-phase thermosyphons. The study defined a closed thermosyphon (CT) as a vertical/inclined closed pipe with heat source at the bottom portion and heat sink at top which is suggested for turbine cooling application due to simple design.

Aforementioned review focuses on the history and development of thermosyphon loops. Since THTD is based on CT systems, further review is aimed at recent developments in OTLs and CTLs. OTLs have been widely employed in solar collectors (Liu et al., 2013). In a CT system, generally the HTF undergoes boiling at heat source and condensation at sink. Hence, they are often referred as two-phase closed thermosyphon (TPCT). (Jafari et al., 2016), have extensively reviewed the flow phenomenon and applications of TPCT. Further (Jafari et al., 2017) have

experimentally investigated the condensation and evaporation heat transfer phenomenon in TPCT. It can be noted that TPCTs have been extensively studied (Noie, 2005; Shabgard et al., 2014 and Gedik, 2016), by varying HTF and its filling ratio, heat input, evaporator length, coolant flow rate and inclination angles.

Although TPCT achieved high temperature gradient heat transfer, it lacked in ability to transfer heat faster. In order to effectively simplify the CT system, (Lingade et al., 2015) introduced a vertical THTD, working on the principle of natural circulation loop, made of borosilicate glass and experimentally investigated its heat transfer capability. It comprises of 3 separate components (viz. heater, fluid unit and sink) joined together with water as both HTF and coolant. Further, flow phenomenon inside the THTD was depicted numerically and found in good agreement with experimental data. In a similar study, (Bobin et al., 2015) incorporated a cross-over device (sleeve) and numerically evaluated the performance of THTD by varying heating section and sleeve length. Both the variations led to a proportional increment in the heat output, since THTD was subjected to isothermal boundary conditions. (Vijayan et al., 2018) have performed theoretical study and suggested THTD (with and without cross-over device) for diverse passive fuel cooling in advanced high temperature nuclear reactors. (Vijayan et al., 2018) have also proposed a conceptual design for a mini solar thermal power plant working on the principle of coupled series natural circulation loop integrated with THTD and beam down solar power.

An extensive review deduced that till date literature pertaining to THTD is scanty. Although THTD with cross-over device has been reported, its simpler version benefits in cost and pressure drop. As THTD is meant for transferring heat from source to sink, time based transient analysis is of practical importance. Finally, the versatility of THTD has to be justified through a parametric study. Hence, the present transient numerical study focuses eight variations of adiabatic height and sink lengths of THTD using Therminol VP-1 as heat transfer fluid (HTF) and water as coolant in the sink. The variation in heat transport time, flow path, flow velocity and HTF temperature are extracted from the simulation. Further, the novelty of THTD has been proved by comparing it with a simple closed loop thermosyphon system (SCLT).

II. Configuration and working of THTD

The geometry of THTD is divided into three sections, viz. heating length (L_h), adiabatic/unheated length (L_a) and sink (L_s) as depicted in Figure 1 (a). The working of THTD is based on temperature/density difference of the HTF between the hot and cold columns/legs. The heating section is subjected to heat flux from outer tube (highly conductive) and gets transferred to HTF (in hot leg) and induces the thermosyphon effect. Here, inner tube (less conductive) acts as a cold leg. In order to transport heat effectively, the cross-sectional areas of inner and annulus column/region must be equal. Water circulation chamber (with 10 mm radial gap) is used as the heat sink (Figure 1 (b)).

III. CFD analysis

Ansys® Fluent is used for modelling and analysis. Water is the sink fluid with constant inlet temperature of 303 K. The performance of THTD (Therminol-VP1 as HTF) is compared by varying its adiabatic height / sink length. Laminar (viscous heating) model is used for transient time step-based analysis. Even the performance of SCLT (with Therminol-VP1) is also studied and compared with THTD for different adiabatic heights. The properties of Therminol-VP1 (http://www.twt.mpei.ac.ru/tthb/hedh/htf-vp1.pdf) are incorporated as equations.

(a) Geometry description

The schematic of THTD with sink is given in Figure 1 (b) and specifications in Table 1. For computational flexibility, the inner tube (which must be of thermal insulating material) is sliced away from the model by treating the section as adiabatic while the outer tube is of copper. The inner and outer tube dimensions are chosen in such a way that in hot and cold leg cross-sectional area is equal. By keeping heating section length constant as 0.5 m (L_h), the

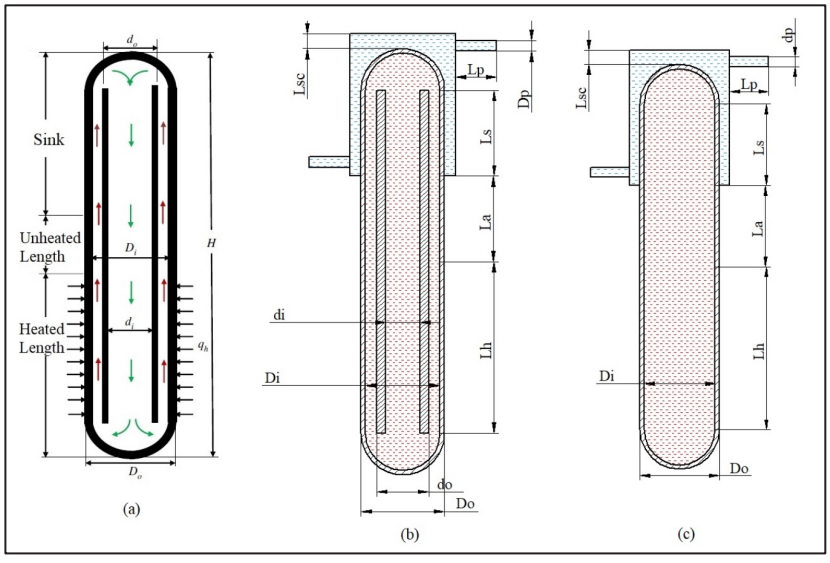

Fig. 1: Geometry: (a) General view of THTD (Vijayan et al., 2019); (b) THTD in present study; (c) SCLT system

adiabatic length (L_a) and sink length (L_s) are varied between 0.25-2 m and 0.05-0.45 m respectively. Water circulation chamber is modelled in contact with THTD as sink section. The geometry of SCLT is same as THTD but it doesn't contain inner tube as shown in Figure 1 (c). In this case, only the adiabatic height is varied between 0.25-2 m keeping other two heights constant.

Table 1: THTD geometrical specifications

Outer diameter of outer tube, D_o	*45 mm*
Inner diameter of outer tube, D_i	*41 mm*
Outer diameter of inner tube, d_o	*21 mm*
Inner diameter of inner tube, d_i	*32 mm*
Heated Length, L_h	*0.5 m*
Adiabatic Length, L_a	*0.25 m*
Sink Length, L_s	*0.25 m*
Sink inlet and outlet pipe length, L_p	*45 mm*
Sink inlet and outlet pipe diameter, D_p	*12.7 mm*
Sink radial clearance, L_{sc}	*10 mm*

(b) Meshing and grid independence

The THTD is modelled and meshed by giving appropriate number of inflation layers at the solid-fluid contact regions, and the accuracy of the mesh is proven by conducting grid independence test. The number of elements was varied from 422077 to 7720043 by changing the body sizing and the transient analysis were performed keeping other boundary conditions and convergence criteria fixed.

The output parameters, T_{out} (water outlet temperature at sink) and the HTF flow velocity (V_{cs}) across a cut-section were used to ascertain the quality of the mesh. The mesh test (Fig. 2) resulted in a random behavior of those parameters till 2785968 elements and flattens thereafter until 7720043 elements (0.03% variation). Hence, 2785968 elements were considered as the grid independent zone for further analysis. As the study is transient analysis, time-step independence also plays a vital role in deciding the optimum size of time-step. To achieve time step independency for the mesh grid independent model, the time steps were varied from 0.4-3 seconds and the results were extracted at a flow time of 8 minutes. The results (Fig. 3) portrayed 0.01-0.02% variation in the band of 0.4-1 sec, which then diverged in the band of 1.5-3 sec. Hence, 2785968 elements (body sizing 2 mm) and time-step size of 1 sec were chosen for further analysis. The cut section of chosen mesh is as depicted in Fig. 4. Tetrahedral elements are used for the entire body mesh and inflation boundary layers (first layer thickness 0.1 mm, growth rate of 1.2 with 15 layers) is applied at various regions (viz. fluid-wall contact in heater region, fluid at sink inlet-outlet and fluid-wall contact at sink).

(c) Boundary conditions

The numerical simulation is accomplished through a double precision based CFD solver with all three basic equations (energy, continuity and momentum) being invoked. The pressure-velocity coupling is induced using SIMPLE algorithm and pressure discretization is subjected to body force weighted scheme (natural circulation).

Second order upwind scheme is used for spatial discretization. Laminar viscous heating turbulence model is considered since THTD based NC loops are subjected to highly laminar flow. The convergence criteria for energy, momentum and continuity equations are kept constant at 10^{-6}. Since the HTF circulates due to density difference, Boussinesq approximation (Vijayan et al., 2019) is invoked in material properties which is presented as,

$$\rho = \rho_0 * [1 - \beta(T - T_0)] \quad (1)$$

Where ρ_0 is the density (kg/m^3) at reference temperature T_0 (K) and β (1/K) is the volumetric coefficient of the HTF for the entire temperature range.

Further, the following boundary conditions are applied for the THTD model:

i. At sink inlet, mass flow rate for the water is kept constant at 0.01 kg/sec (Re=1200) in developed condition.
ii. Outflow condition, at sink outlet.
iii. Heat flux equivalent to 1kW heat is applied at the heating section wall
iv. No slip condition at all other walls.

The convergence of the solution is checked by the plot of sink outlet temperature, as heat output is,

$$Q = \dot{m} * C_p * (T_{out} - T_{in}) \quad (2)$$

Where, $\dot{m}$ is the mass flow rate of the sink fluid (kg/sec), C_p being the specific heat (J/kg-K), T_{out} as sink outlet temperature (K) and T_{in} as sink inlet temperature (K).

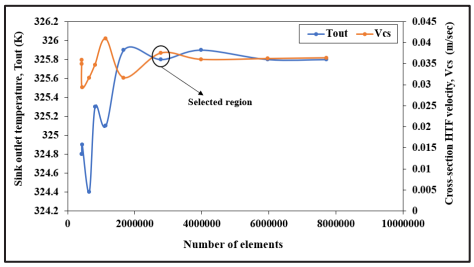

Fig. 2: Mesh grid independence test

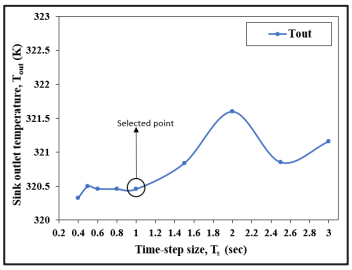

Fig. 3: Time-step independence test

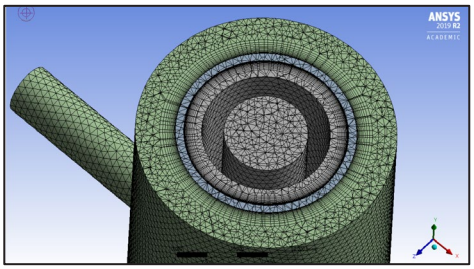

Fig. 4: Cross-section view of mesh

Since, the analysis is based on heat transportation validation doesn't play a crucial role as the system is itself validated by first law of thermodynamics. However, a transient behavior of the model needs validation which will be the future scope.

IV. Results and discussions

As mentioned earlier, change in transient heat output and HTF flow pattern are discussed here by considering variation of adiabatic length in SCLT and, both adiabatic length and sink length in case of THTD

The supremacy of THTD need to be justified by comparing with SCLT (CT system) under same working condition. Out of eight variations in adiabatic height (0.25-2 m) analysed, Fig. 5 shows only three variants (0.25, 1 and 2 m) each for better understanding. The quality check involved here is the rise in HTF temperature with time. Both THTD and SCLT performed effectively for 0.25 m case as THTD obtained 100% heat output at a flow time of 17 minutes against 87% for SCLT. However for 1 m height, the deviation becomes significant (26%) due to increased number of recirculation zones and irregular flow path in SCLT. For example, in 1 m variant, THTD attains 100% heat output at a flow time of 28 minutes whereas SCLT attains only 74%. Further for 2 m height, THTD obtained 100% output at 42 minutes against 62% in SCLT (120 minutes for 100% output), thus resulting in 40% deviation. Further, the performance deterioration in both THTD and SCLT due to rise in adiabatic height (and hence the flow loss) is observed in vector plots.

In order to ascertain the performance of THTD with different adiabatic heights, eight variations (in the range of 0.25-2 m) are considered. It can be observed from Fig. 6 that the transient performance diminishes with adiabatic height. In comparison, THTD of 0.25 m adiabatic height achieves 100% heat output at a flow time of 17 minutes and at the same time THTD of 2 m adiabatic height yields 61%. A detailed analysis depicted that the time-based performance diminishes drastically for adiabatic heights greater than 1 m. The variation in the performance is due to the additional flow length and allied friction loss. To summarize, the flow time taken to achieve 100% heat output is as less as 17 minutes (0.25 m) to 42 minutes (2 m). However as mentioned earlier, in SCLT for 2 m adiabatic height, the time required is 120 minutes which justifies the capability of THTD to transport heat to larger height.

The sink length in THTD is based on the type of application. Fig. 7 illustrates the variation of THTD's performance for eight different cases of sink length in the range of 0.05 m – 0.45 m for heater length of 0.5 m. It can be inferred that the THTD performance enhances with sink length. For comparison, THTD with 0.45 m sink length achieves 100% heat output at a flow time of 14 minutes, whereas at the same time 0.05 m sink length unit yields 70%. However, it should also be noted that for sink lengths greater than 0.25 m (encircled region) there is no noticeable deviation due to increased recirculation zones caused by excess cooling of HTF. For example, the flow time taken to achieve 100% heat output in 0.05, 0.1, 0.15, 0.2, 0.25, 0.3, 0.4 and 0.45 m sink length is 29, 27, 24, 22, 18, 16, 16 and 14 minutes respectively. As there is miniscule variation in transient performance of THTD after 0.25 m variant, the optimum sink length can be 1/4th of the total THTD height.

To complement the above-mentioned effects, the flow pattern vector plots are obtained for 1 m height variant of SCLT and THTD. Fig. 8 compares flow pattern at the heat source end. In case of THTD the flow is unidirectional in both hot and cold passage whereas the flow in SCLT is multi-directional with number of recirculation zones. It can be inferred that in SCLT fluid takes longer time to establish thermosyphon effect. Similar trend of flow path is observed in adiabatic section as shown in Fig. 9. The number of recirculation zones increased drastically in case of SCLT. Whereas due to restricted passage in THTD, the recirculation effect is nullified due to enhanced thermosyphon effect. In sink section (Fig.10), both SCLT and THTD reports recirculation zones / irregular flow due to cooling of the HTF by sink fluid. Due to presence of recirculation zones throughout the length of SCLT, its performance deteriorated as compared to THTD.

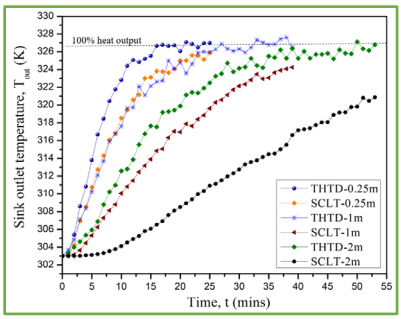

Fig. 5: Variation of T_{out} in THTD and SCLT

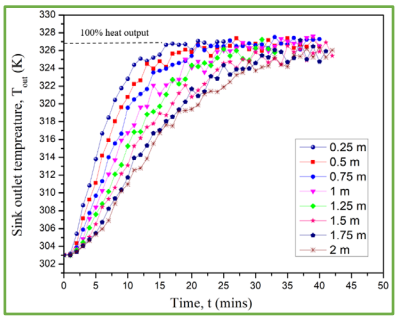

Fig. 6: Variation of T_{out} in THTD for different adiabatic heights

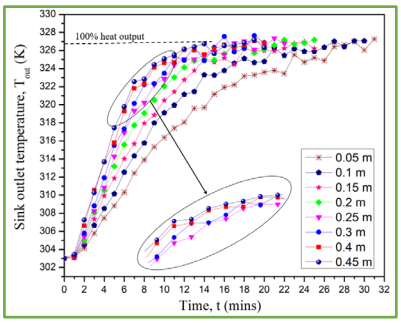

Fig. 7: Variation of T_{out} in THTD for different sink lengths

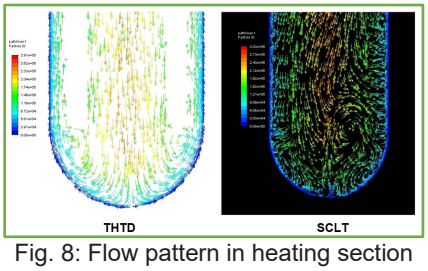

Fig. 8: Flow pattern in heating section

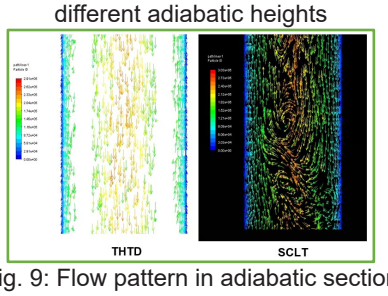

Fig. 9: Flow pattern in adiabatic section

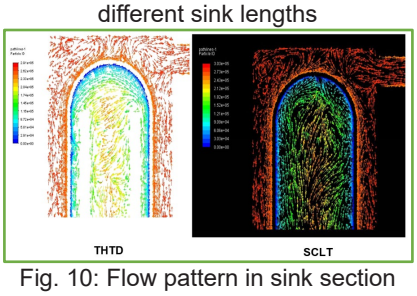

Fig. 10: Flow pattern in sink section

V. Conclusions

The present transient numerical analysis emphasized the performance variation in THTD due to adiabatic height and sink length. Additionally, the performance deterioration of SCLT is also observed which led to the following conclusions

The novelty of THTD is justified as the heat gained is 1.62 times that of SCLT for 2 m adiabatic height configuration and improves further with larger heights. A unidirectional-undisturbed flow pattern in THTD led to better performance over SCLT. The performance of THTD deteriorates with flow length (adiabatic height) as 0.25 m case yields 1.6 times heat gain than 2 m height. But in comparison, the THTD of larger adiabatic heights is effective than existing CT systems. The performance of THTD improves with sink length being 0.25 m as the optimal length. Marginal increase in recirculation zones led to miniscule ehnacement in sink lengths greater than 0.25 m.

Hence, THTDs can be effectively used for large heights in the proposed indoor solar cooking system (Vijayan et al., 2019).

References

Al-Soud, M. S., Abdallah, E., Akayleh, A., Abdallah, S., & Hrayshat, E. S. (2010). A Parabolic solar cooker with automatic two axes sun tracking system. *Applied Energy*, *87*(2), 463–470. https://doi.org/10.1016/j.apenergy.2009.08.035

Bobin, S. G., Bodkha, K., Borgohain, A., Pilkhwal, D. S., Arunachala, U. C., & Vijayan, P. K. (2015). *Performance Evaluation of a Thermosyphon Heat Transport Device Using CFD*. In Proceedings of the international thorium energy conference: gateway to thorium energy.

Gedik, E. (2016). Experimental investigation of the thermal performance of a two-phase closed thermosyphon at different operating conditions. *Energy and Buildings*, *127*, 1096–1107. https://doi.org/10.1016/j.enbuild.2016.06.066

Grover, G. M. (1964). “Evaporation-condensation heat transfer device”. US Patent No. 3229759

Herez, A., Ramadan, M., & Khaled, M. (2018). Review on solar cooker systems: Economic and environmental study for different Lebanese scenarios. *Renewable and Sustainable Energy Reviews*, *81*(May 2017), 421–432. https://doi.org/10.1016/j.rser.2017.08.021

Indora, S., & Kandpal, T. C. (2018). Institutional and community solar cooking in India using SK-23 and Scheffler solar cookers: A financial appraisal. *Renewable Energy*, *120*, 501–511. https://doi.org/10.1016/j.renene.2018.01.004

Jafari, D., Franco, A., Filippeschi, S., & Di Marco, P. (2016). Two-phase closed thermosyphons: A review of studies and solar applications. *Renewable and Sustainable Energy Reviews*, *53*, 575–593. https://doi.org/10.1016/j.rser.2015.09.002

Jafari, D., Di Marco, P., Filippeschi, S., & Franco, A. (2017). An experimental investigation on the evaporation and condensation heat transfer of two-phase closed thermosyphons. *Experimental Thermal and Fluid Science*, *88*, 111–123. https://doi.org/10.1016/j.expthermflusci.2017.05.019

Japikse, D., & Winter, E. R. F. (1971). Single-phase transport processes in the open thermosyphon. *International Journal of Heat and Mass Transfer*, *14*(3). https://doi.org/10.1016/0017-9310(71)90161-X

Japikse, D., Jallouk, P. A., & Winter, E. R. F. (1971). Single-phase transport processes in the closed thermosyphon. *International Journal of Heat and Mass Transfer, 14*(7). https://doi.org/10.1016/0017-9310(71)90115-3

Japikse, D. (1973). Advances in Thermosyphon Technology. *Advances in Heat Transfer*, *9*(C), 1–111. https://doi.org/10.1016/S0065-2717(08)70061-3

Jouhara, H., Chauhan, A., Nannou, T., Almahmoud, S., Delpech, B., & Wrobel, L. C. (2017). Heat pipe based systems - Advances and applications. *Energy*, *128*, 729–754. https://doi.org/10.1016/j.energy.2017.04.028

Lingade, B. M., Raju, E., Borgohain, A., Maheshwari, N. K., & Vijayan, P. K. (2015). Heat transfer capability of a thermosiphon heat transport device with experimental and CFD studies. Thorium Energy Conference, 2–7.

Liu, Z. H., Hu, R. L., Lu, L., Zhao, F., & Xiao, H. S. (2013). Thermal performance of an open thermosyphon using nanofluid for evacuated tubular high temperature air solar collector. *Energy Conversion and Management*, *73*, 135–143. https://doi.org/10.1016/j.enconman.2013.04.010

Noie, S. H. (2005). Heat transfer characteristics of a two-phase closed thermosyphon. *Applied Thermal Engineering*, *25*(4), 495–506. https://doi.org/10.1016/j.applthermaleng.2004.06.019

Noman, M., Wasim, A., Ali, M., Jahanzaib, M., Hussain, S., Ali, H. M. K., & Ali, H. M. (2019). An investigation of a solar cooker with parabolic trough concentrator. *Case Studies in Thermal Engineering*, *14*(February). https://doi.org/10.1016/j.csite.2019.100436

Onokwai, A. O., Okonkwo, U. C., Osueke, C. O., Okafor, C. E., Olayanju, T. M. A., & Dahunsi, S. O. (2019). Design, modelling, energy and exergy analysis of a parabolic cooker. *Renewable Energy*, *142*, 497–510. https://doi.org/10.1016/j.renene.2019.04.028

Shabgard, H., Xiao, B., Faghri, A., Gupta, R., & Weissman, W. (2014). Thermal characteristics of a closed thermosyphon under various filling conditions. *International Journal of Heat and Mass Transfer*, *70*, 91–102. https://doi.org/10.1016/j.ijheatmasstransfer.2013.10.053

Vijayan, P. K., Ramakrishna, T., Lingade, B. M., & Mahender, D. (2018). *A Diverse Passive Fuel Cooling System for Advanced High Temperature Reactors*. In The 6th International Conference on Nuclear and Renewable Energy Resources (NURER2018)

Vijayan, P. K., Sinha, S. K., Singh, R. K., Kumar, A., Vishnoi, A. K., Kaushik, A., Kedare, S. B. (2018). *Conceptual Design of a Mini Solar Thermal Power Plant*. In The 6th International Conference on Nuclear and Renewable Energy Resources (NURER2018)

Vijayan, P. K., Nayak, A. K., & Kumar, N. (2019). Single-phase, Two-phase and Supercritical Natural Circulation Systems. Woodhead Publishing. https://doi.org/10.1016/C2017-0-01142-4

Numerical Analysis of a Hybrid Thermal Energy Storage System Using Thermochemical and Phase Change Material for Constant, Low Temperature Applications

Swaraj Kumar B[1], Stiben Paul[2], James Varghese[1]
[1] CUSAT, Kerala, India
[2] LBS College of Engineering, Kerala, India

Abstract: Thermal energy storage is one of the viable solutions for the existing energy demand and supply mismatch. Among the different types of thermal energy storage systems thermochemical energy storage system is one of the best options for long term and high-density energy storage. These consist in chemical reversible reactions which are able to store solar thermal energy in one direction, and to release it in the reverse. Thermochemical energy storage is an interesting technology for the future seasonal storage of solar heat. This technology gets attention of researchers because of its high energy density and less or no storage losses. The main drawback of this storage technology is the sudden release of energy, which causes high temperature levels at the start of the reaction. Since most of the applications are at constant temperatures, this drawback of the thermochemical energy storage leads this technology unsuitable for such applications. In this paper we suggest a hybrid thermal energy storage system which continuously supplying constant temperature while releasing the energy. It has the advantages of both thermochemical energy storage and a latent heat storage system. In this paper we use MgSO4 (Magnesium sulphate) and paraffin wax pair as our hybrid thermal energy storage materials. The system is anlysed using COMSOL Multiphysics.

Introduction

There is no doubt that the uncontrolled use of conventional energy sources will lead the world to another crisis. While we can hold on to some extent through the prudent use of energy sources, it will not be a long-term alternative. This is where renewable energy sources come into play. Solar energy is a very important renewable energy source. The amount of solar energy that falls on the earth in one day is enough to meet the energy needs of the earth for one year. However, due to geographical features, variations in solar radiation and even local climate change, we have not yet been able to fully utilize the energy available in such abundance. This results in the loss of most of the solar energy reaching the Earth. Solar energy storage is one of the possible solutions to this. There are many types of solar storage methods, but they are all flawed in one way or another. But thermochemical energy storage is a method that can store energy for a long time and has a high energy density. The heat energy stored in this way flows out when the decomposed components combine. With this type of storage, we can store heat energy for a long time and use it when needed. It can be used as a seasonal storage method in areas where solar energy is scarce. There are three main stages in thermochemical energy storage. Charging, Storing and Discharging. Storing is the decomposition of a chemical compound using thermal energy. This is an endothermic reaction and in this process heat energy is stored in thermochemical material (TCM). This TCM is then stored separately so that it does not interact with each other chemically. This process does not cause heat loss as the heat is released only when they interact with each other. In the final stage i.e.; discharge, the decomposed components react together, this reaction is an exothermic reaction and the stored energy is released as heat.

Many authors reviewed thermochemical energy storage and conversion systems. (Abedin, 2011) critically reviewed several papers related to thermochemical energy storage and compared different thermal energy storage systems. He come up with some possible candidates for thermochemical energy storage with their operating temperature range and energy density. He concluded that the cyclic nature, degradation, energy density etc. of the thermochemical material should be studied. (Mette, Kerskes and Drück, 2012) in the paper gives an overview of the research works going on at international institutions in the area of long term thermochemical energy storage for solar applications. After reviewing several thermochemical systems for solar applications the authors concluded that, even though there were significant advances in this area more researches are required to improve the energy density, cyclability and stability of the thermochemical material, and overall system size. (Cot-Gores, Castell and Cabeza, 2012) reviewed the experimental research works done so far in thermochemical energy storage and conversion and they analysed the performance obtained by the prototypes around the globe. The author

summarises that the researches on thermochemical energy storage for heating applications were less compared to cooling applications. They also pointed out some promising experimental results which shows improvements in overall performance of a thermochemical energy storage system. The authors also suggested some critical areas that needs more attention of researchers such as developing advanced cycles for refrigeration systems, study of cyclability, deterioration, and corrosion in the chlorides salt - ammonia systems, testing of large scale prototypes instead of lab scale, intensify the experimental research for heating applications, and the integration of this technology with waste heat recovery system.

Two innovative concepts have been introduced for an efficient regeneration process for thermochemical energy storage by (Mette *et al.*, 2013) and both methods can be used for long term energy storage. Comparative studies show that these concepts are promising. They also did a lab scale experiment on air drying and the results were also confirming the advantages of the new system. Two heat exchangers are numerically studied for charging a thermochemical material by (Lele *et al.*, 2014) using COMSOL software. More papers (De Jong *et al.*, 2014; Solé *et al.*, 2015) discuss the issue of designing a thermochemical energy storage system and corrosion of metals and salt hydrates. The first paper discusses the issue in components and materials level and addresses a key issue in component level that is implementation of a low temperature source. But due to physical and chemical stability issues during the cyclic process the increase in energy storage density is limited. Corrosion is one of the main limitations of thermochemical reactor bed (Solé *et al.*, 2015), this paper discussed the issue of corrosion due to the salt material and experimentally investigated the corrosion takes place in different metals due to various salt materials. From the results stainless steel 316 is the most suitable material for a thermochemical reactor.

Many sensible–latent heat hybrid energy storage systems are studied by various authors numerically and experimentally (Frazzica *et al.*, 2016; Zauner *et al.*, 2017; Ahmed *et al.*, 2019; Abdelsalam *et al.*, 2020) and all the studies highlight the merit of hybrid energy storage. However, studies of hybrid energy storage involving thermochemical energy storage are rare. This underscores the need for more research in this area. A hybrid energy storage system that includes thermochemical energy storage has many advantages. One of them is that as with all hybrid systems, we get the benefits of two storage systems together in a single system. For some reason this technology has not yet been used properly. The reason may be the complexity of the system integration, or corrosive nature of the thermochemical material, or something else. However, there is no doubt that a hybrid energy storage system that incorporates thermochemical energy storage will certainly make a difference in this area.

In this paper we propose a novel concept in hybrid thermal energy storage system for constant low temperature applications.

Design of PCM storage module

The PCM (paraffin wax) is used for storing energy and release it at constant temperature (64ºC) continuously for one full day is calculated. It is found that 810.816 kg of paraffin wax required for one day. The volume of PCM tank is 0.2036 m^3 required for storing this paraffin wax. Instead of putting the PCM in one container we divide the entire volume into 36 cylindrical modules each module having a volume of $5.65 \times 10^{-3} m^3$. This will increase the heat transfer from the reactor bed to the PCM.

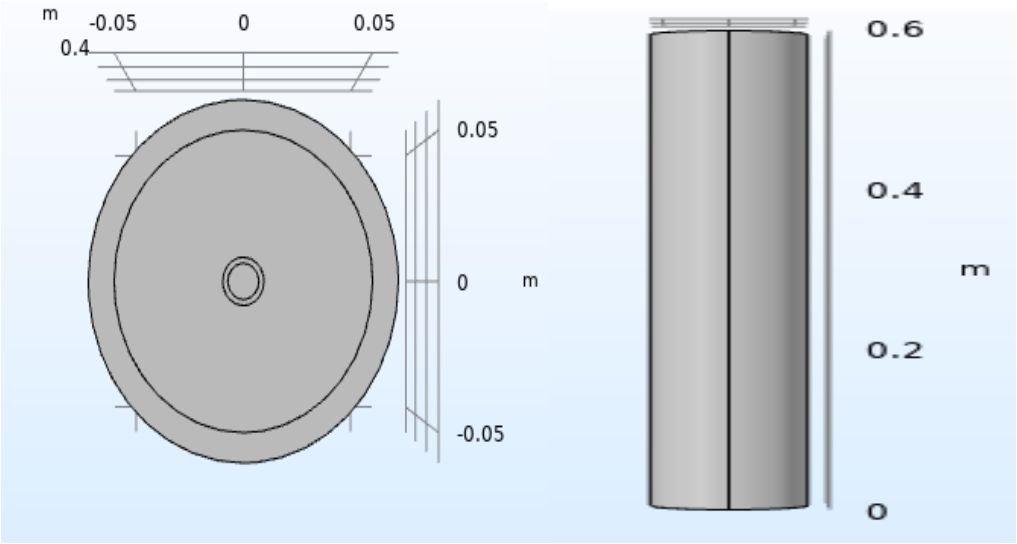

Figure 2. Top and Side view of PCM storage module

Design of Salt storage tank

The estimated amount of salt material required for one day use is 224.64 kg. It requires 0.0846 m^3 volume to occupy. Each module is having volume of 0.00235 m^3. Stainless steel is taken as the material for both salt storage and PCM storage. Figure 3 shows one salt storage module and figure 4 shows the complete assembly of the system.

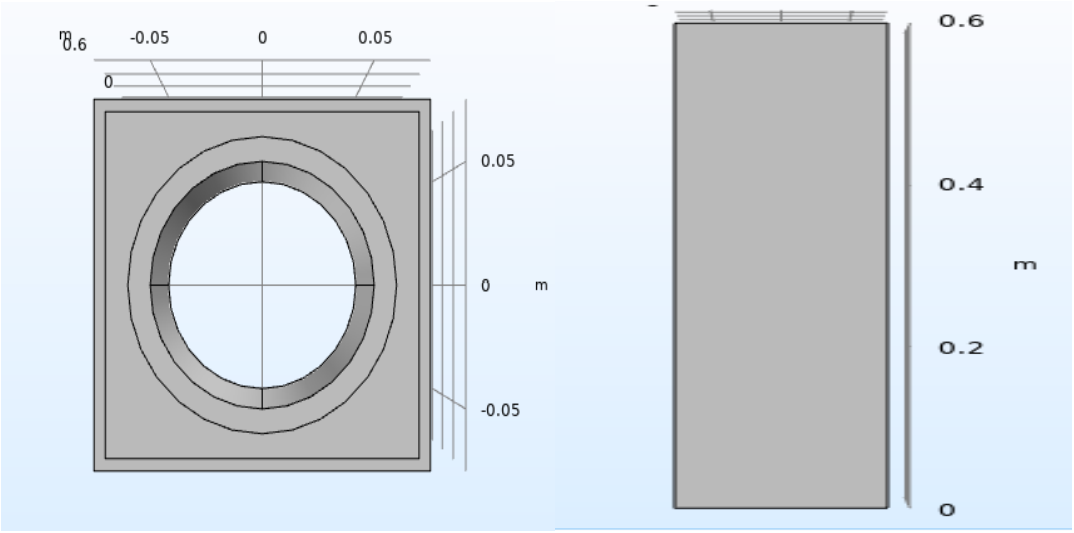

Figure 3. Top and side view of Salt storage tank

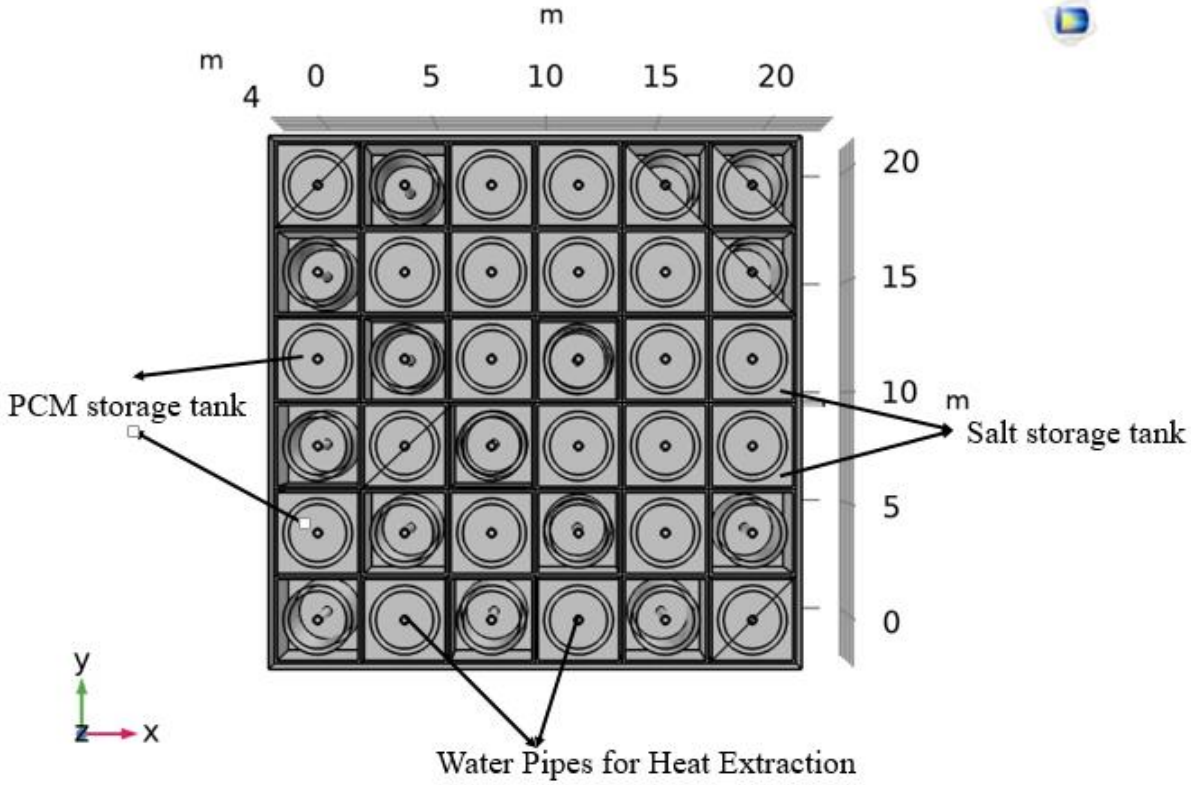

Figure 4. Full assembly of Hybrid Energy Storage system

Results and Discussion

Hydration of $MgSO_4$

Figure 5 shows the Temperature distribution on the reactor bed after the reaction. The temperature rises to 560°K due to the exothermic reaction taking place in the reactor bed. The temperature difference at different points of the bed is due to the hydration kinetics. Water absorption into the bed is not homogeneous. The concentration distribution after reaction the inlet the reaction rate is low and it reaches the maximum while flowing further then the reaction rate reduce slightly, reaches the equilibrium and

continue to flow same concentration.

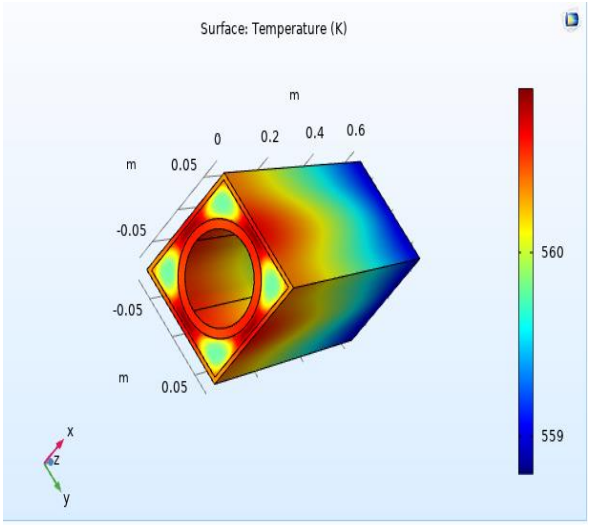

Figure 5. Temperature profile of reactor bed after reaction.

PCM storage modelling

The paraffin wax with heat capacity 2900 J/kg.K, heat of fusion 266 kJ/kg and melting temperature is 64ºC is chosen as the PCM. The water is the heat exchanger fluid with mass flow rate 0.2kg/s. The flow is assumed as laminar flow.

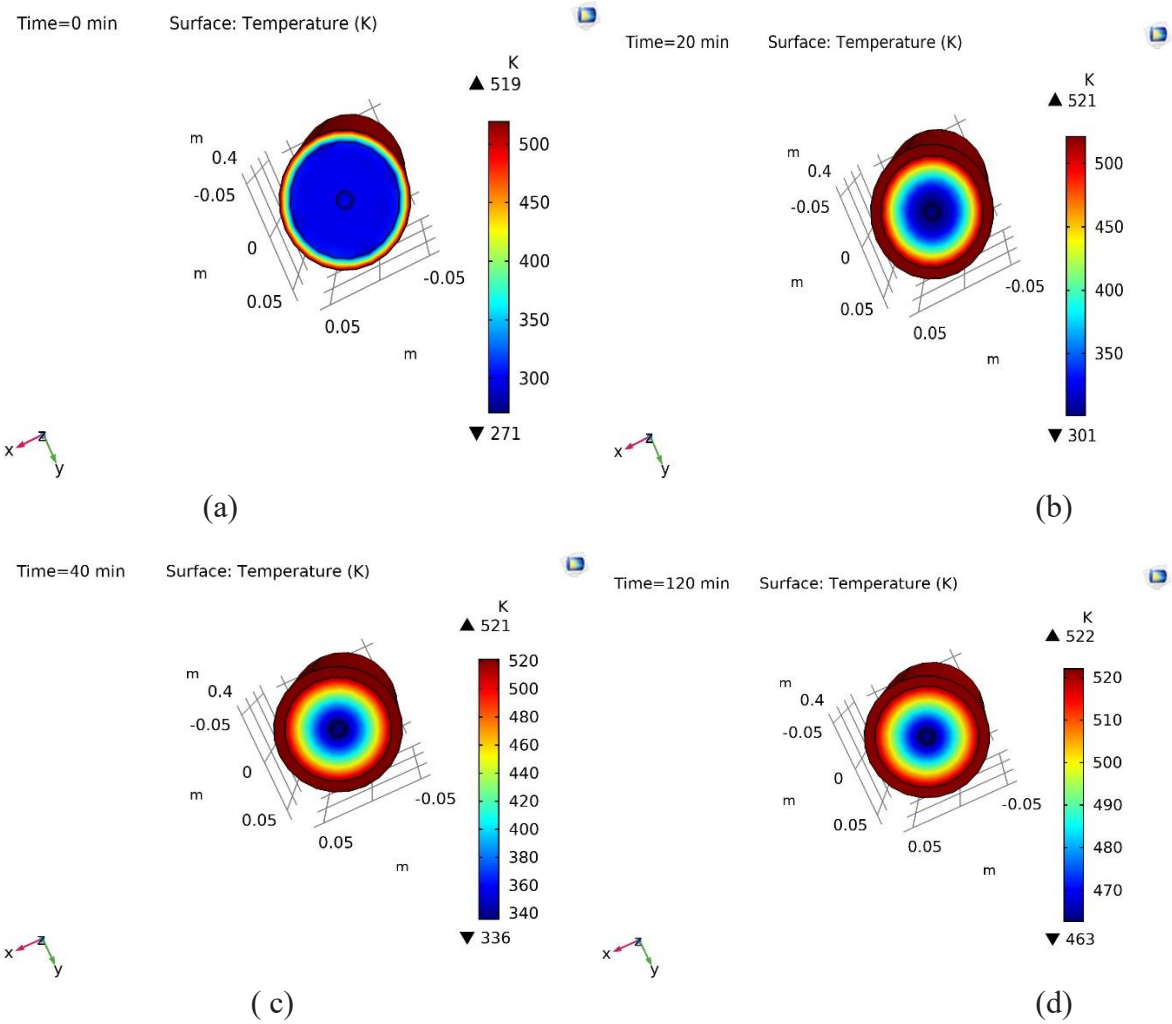

Figure 6. Temperature distribution in the PCM tank, (a) At time= 0 min (b) At time = 20 min (c) At time=40 min (d) At time = 120 min.

Figure 6 shows the temperature distribution in PCM at different time intervals. From this figure we can conclude that it will take approximately 40 minutes to melt the PCM completely with the heat released from the reactor bed. After this the heat is stored in the PCM as sensible heat and the temperature

of PCM increases. This is definitely against our objective to get a constant temperature, so the velocity of heat transfer fluid should be increased accordingly after time = 40 minutes or the reaction must be controlled by controlling the flow of moist air.

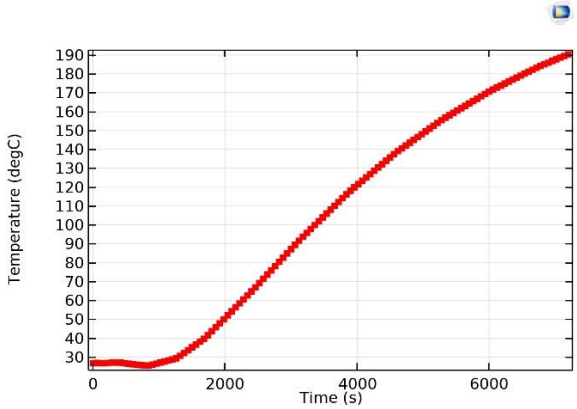

Figure 7. Temperature time plot of PCM

Figure 7 shows the temperature – time plot at the inner core of the PCM. It shows the temperature variation from the start of the experiment. Rise in temperature at the inner core is seen after 16minutes from the start of experiment. Then the temperature rises upto 190°C in 120 minutes.

Temperature profile of heat transfer fluid

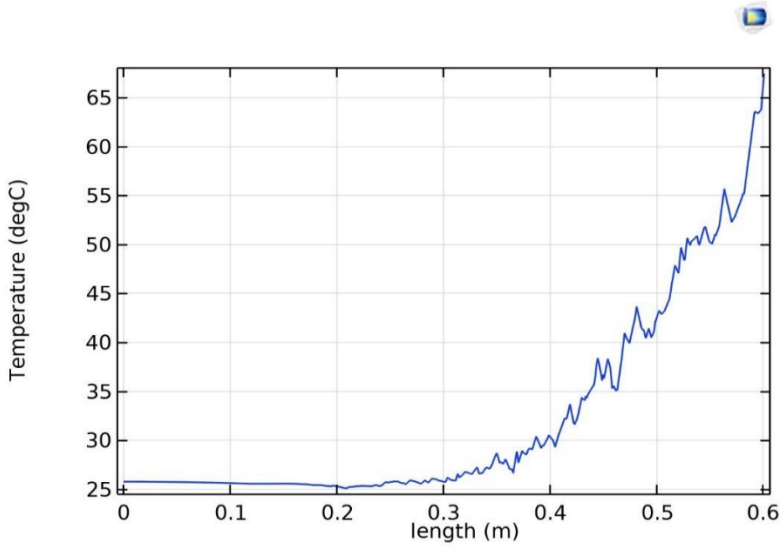

Figure 8. Temperature variation along the pipe.

Water is used as the heat transfer fluid here, figure 8. Shows the temperature variation of flowing water from inlet to outlet of the pipe. It is seen that the temperature of water is reached to 338 K from 298 K with a mass flow of 0.2 kg/s in 40 minutes.

Conclusion

This work is a conceptual design of a hybrid thermal energy storage using a Thermochemical material and Phase change material inorder to exploit the benefits of both. The primary aim of this work was to design a hybrid thermal energy storage system for constant low temperature applications. This study has shown that a hybrid thermal energy storage system using TCM and PCM systems for domestic hot water requirement can be a viable solution. The result of this study shows that the concept is a workable solution to get a constant temperature in the heat transfer fluid.

This paper also proves the ability of $MgSO_4$ salt as a good thermochemical material for low temperature applications. A detailed experimental study has to be performed to validate the results. Since this study is a new start in this area, there have been a number of shortcomings. However, it is certain that these results will be an impetus for further study in the future.

Reference

Abdelsalam, M. Y. *et al.* (2020) 'Hybrid thermal energy storage with phase change materials for solar domestic hot water applications: Direct versus indirect heat exchange systems', *Renewable Energy*. Elsevier Ltd, 147, pp. 77–88. doi: 10.1016/j.renene.2019.08.121.

Abedin, A. H. (2011) 'A Critical Review of Thermochemical Energy Storage Systems', *The Open Renewable Energy Journal*,

4(1), pp. 42–46. doi: 10.2174/1876387101004010042.
Ahmed, N. *et al.* (2019) 'Thermal and economic evaluation of thermocline combined sensible-latent heat thermal energy storage system for medium temperature applications', *Energy Conversion and Management*. Elsevier, 189, pp. 14–23. doi: 10.1016/j.enconman.2019.03.040.
Cot-Gores, J., Castell, A. and Cabeza, L. F. (2012) 'Thermochemical energy storage and conversion: A-state-of-the-art review of the experimental research under practical conditions', *Renewable and Sustainable Energy Reviews*. Elsevier, 16(7), pp. 5207–5224. doi: 10.1016/j.rser.2012.04.007.
Frazzica, A. *et al.* (2016) 'Experimental testing of a hybrid sensible-latent heat storage system for domestic hot water applications', *Applied Energy*. Elsevier Ltd, 183, pp. 1157–1167. doi: 10.1016/j.apenergy.2016.09.076.
De Jong, A. J. *et al.* (2014) 'Thermochemical heat storage - System design issues', *Energy Procedia*. Elsevier B.V., 48, pp. 309–319. doi: 10.1016/j.egypro.2014.02.036.
Lele, A. F. *et al.* (2014) 'Modelling of heat exchangers based on thermochemical material for solar heat storage systems', *Energy Procedia*. Elsevier B.V., 61, pp. 2809–2813. doi: 10.1016/j.egypro.2014.12.284.
Mette, B. *et al.* (2013) 'New highly efficient regeneration process for thermochemical energy storage', *Applied Energy*. Elsevier Ltd, 109, pp. 352–359. doi: 10.1016/j.apenergy.2013.01.087.
Mette, B., Kerskes, H. and Drück, H. (2012) 'Concepts of long-term thermochemical energy storage for solar thermal applications - Selected examples', *Energy Procedia*, 30, pp. 321–330. doi: 10.1016/j.egypro.2012.11.038.
Solé, A. *et al.* (2015) 'Corrosion of metals and salt hydrates used for thermochemical energy storage', *Renewable Energy*, 75, pp. 519–523. doi: 10.1016/j.renene.2014.09.059.
Zauner, C. *et al.* (2017) 'Experimental characterization and simulation of a hybrid sensible-latent heat storage', *Applied Energy*. Elsevier Ltd, 189, pp. 506–519. doi: 10.1016/j.apenergy.2016.12.079.

3-D Computational Study on a Spray Cooled Solar Photovoltaic Panel

[1]Martin Raju, [2*]Abhilash Suryan, [3]Sandro Nizetic,
[1] Graduate Student, Department of Mechanical Engineering,
College of Engineering, Trivandrum, 695016, India.
[2] Assistant Professor, Department of Mechanical Engineering,
College of Engineering, Trivandrum, 695016, India.
[3] Professor, LTEF- Laboratory for Thermodynamics and Energy Efficiency, Faculty of Electrical Engineering, Mechanical Engineering and Naval Architecture, University of Split, RudjeraBoskovica 32, 21000 Split, Croatia

* E-mail: suryan@cet.ac.in

Abstract

A photovoltaic (PV) panel converts a part of solar energy to electrical energy and the rest is reflected and transmitted to the panel causing a rise in panel temperature. The heat generated due to rise in temperature decreases electrical efficiency of the PV panel. Therefore, it is necessary to implement cooling on a PV panel. The advantage of using spray cooling on a PV panel is its self-cleaning effect on the surface of the panel which is an added benefit to the reduction in panel temperature. In this paper a 3-D computational fluid dynamics (CFD) study is done on a water spray cooled PV panel to find the influence of mass flow rate of water ejected from the nozzles on the PV panel temperature profile. Here spray cooling is done on top surface of the PV panel. The gain in electrical efficiency due to reduction in temperature can be found out using a mathematical model. The CFD model is generated for steady state thermal analysis of PV panel. Heat transfer through the PV panel and the intensity of reduction in temperature with water spray cooling method is studied. First, validation of the numerical model is done by comparing the PV panel temperature profile obtained from the computational results to the available experimental results. The mass flow rate of water ejecting from the nozzles is varied and the resulting change in temperature profile on the panel is studied. The change in temperature affects the electrical efficiency of the PV panel resulting in a change in electrical output.

Keywords: Photovoltaic panel, Computational fluid dynamics, Spray cooling.

I. Introduction

The need of cost-effective use of renewable energy resource is of prominence in the present scenario and use of solar energy through PV panel is one such step towards achieving it. In photovoltaic technology, the solar energy is converted to electrical energy. With different panel types and atmospheric conditions, a PV panel converts 6-20% of the incident solar radiation to electric power and rest is converted to heat energy. The heat energy increases the panel temperature due to which substantial drop in voltage occurs causing reduced electrical energy output. It is well known that reduction in PV panel temperature increases its electical efficiency. This issue has been extensively studied in past few years by analyzing different cooling techniques. The electrical efficiency reduction is due to the increase in PV panel temperature which ranges from 0.25% / ºC up to 0.5% / ºC, which depends upon the PV panel technology used. Therefore, with proper cooling technique an improved electrical efficiency of PV panel can be achieved. The accumulation of dust and dirt on the panel blocking the solar radiation is also a challenge as it causes reduced electric output. There are different types of cooling implemented for a PV panel and each has its own advantage which varies with panel types and atmospheric conditions. There are previous studies (Farhana, Irwan, Azimmi, Razliana and Gomesh, 2012) (Tonui and Tripanagnostopoulos, 2007) where air has been used for cooling the panel and also air and water combination (Arcuri, Reda and De Simone, 2014) which shows that when water is used as coolant, the PV panel power output was high compared to cases where air was used as coolant .In the present study water spray cooling was implemented as it also had the additional benefit of cleaning the dust particles accumulated on the surface of the pv panel. (Abdolzadeh and Ameri, 2009) studied water spray cooling over PV panel to understand and enhance the efficiency of water pump PV cooling system. He found that there was 1.8% increase in optical performance of PV panel and a 12.5% increase in average efficiency due to water spray cooling over the PV cells. (Irwan, Leow, Irwanto, Amelia, Gomesh and Safwati, 2015) used a solar simulator to do a comparative study of performance between PV panel with water cooling and without water cooling mechanism. A reduction in operating temperature of 5 - 23°C and an increase in electrical power of 9 - 22 % was inferred from the obtained experimental results.

The present study is a CFD analysis of a part of experimental study done by (Nizetic, Coko, Yadav and Grubisic-Cabo, 2016) which consists of an experimental system to study water spray cooling from top and bottom of the PV panel and its effect on the electric power output. The CFD analysis is done for case with spray cooling from the top of PV panel. The experimental paper (Nizetic, Coko, Yadav and Grubisic-Cabo, 2016) consists of separate data for water spray cooling from top and bottom. The validation of numerical model is done by matching the temperature of the PV panel at a particular flow rate. The static temperature contour is taken to study the effect of spray cooling on the elevated PV panel. The variation of temperature and electric efficiency of the PV panel with different mass flow rates is also studied.

II. Computational Methodology

1) Geometry:

A Three-dimensional computational model in ANSYS design modeler is generated in accordance with the experimental setup (Nizetic, Coko, Yadav and Grubisic-Cabo, 2016) shown in Fig.1. Fig.1 (a) shows a 17° horizontally inclined PV panel with a total number of 10 nozzles on placed top through its perimeter which are inclined 40° into the panel surface for effective wetting of the surface. Fig.1(b) shows the dimension for postion of the nozzle which is at a vertical distance of 150mm from the panel surface. The generated 3-D computational model is shown in Fig.3. The nozzle exit diameter of 2 mm was given.

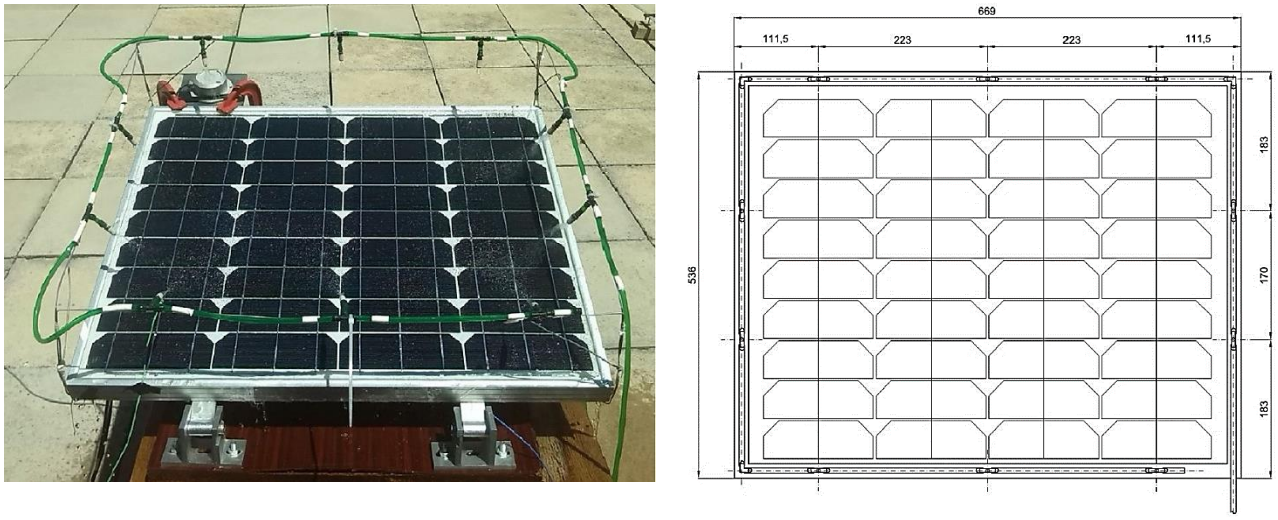

Fig. 1 (a) PV panel with top cooling. (b) Dimensions for position of nozzles around PV panel.

2) Mesh:

Meshing was done using ANSYS ICEM CFD to generate adequate number of elements inorder to produce high quality mesh for fast convergence while solving the fundamental equations using iterative numerical method. Here an unstructured mesh consisting of 1.7×10^6 elements were generated for the 3-D model with an average orthogonal quality of 0.93. The mesh generated is shown in Fig. 2. The element size was smaller near the inlet and slowly progressed by increasing outward as shown in Fig.2 (b).

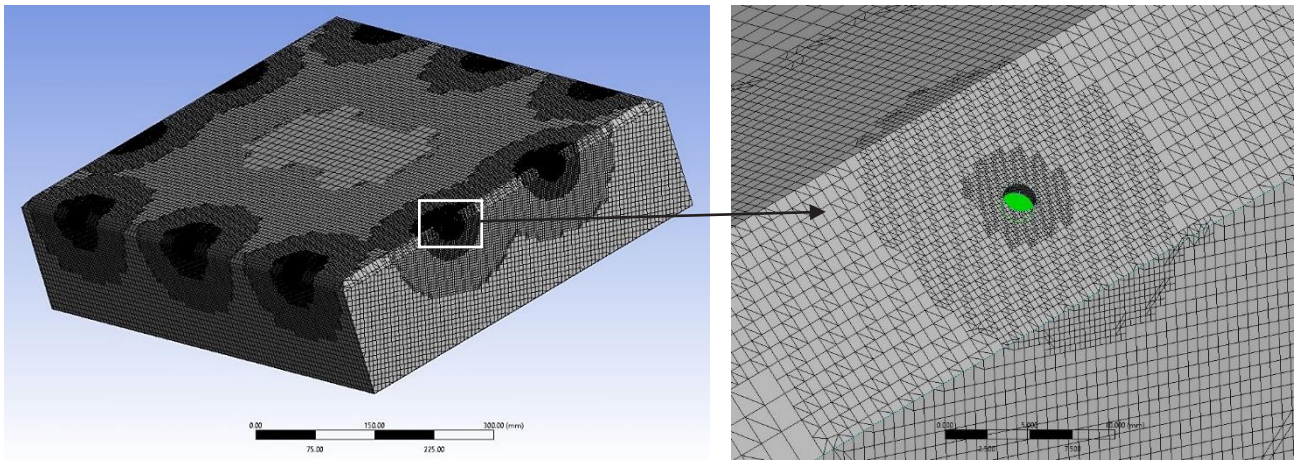

Fig. 2 (a) Generated mesh for 1.7×10^6 elements. (b) Magnified image of the inlet portion.

3) Domain and boundary conditions:

The domain created to solve the computation model consists of velocity inlet which is assigned to all 10 nozzle inlets. The temperature of water is given as 290K (17°C) and the velocity calculated for the mass flow rate of 112.5 L/h from a single nozzle of 1mm radius is 0.74 m/s. The panel surface is assigned as wall with temperature of 327K (54°C). All other parts are given as pressure outlets. Acceleration due to gravity in the negative y direction of $9.81 m/s^2$ and ambient temperature of 300K and 1 atm pressure was given as operating condition. The domain

consisting of different boundary condition is shown in Fig. 3.

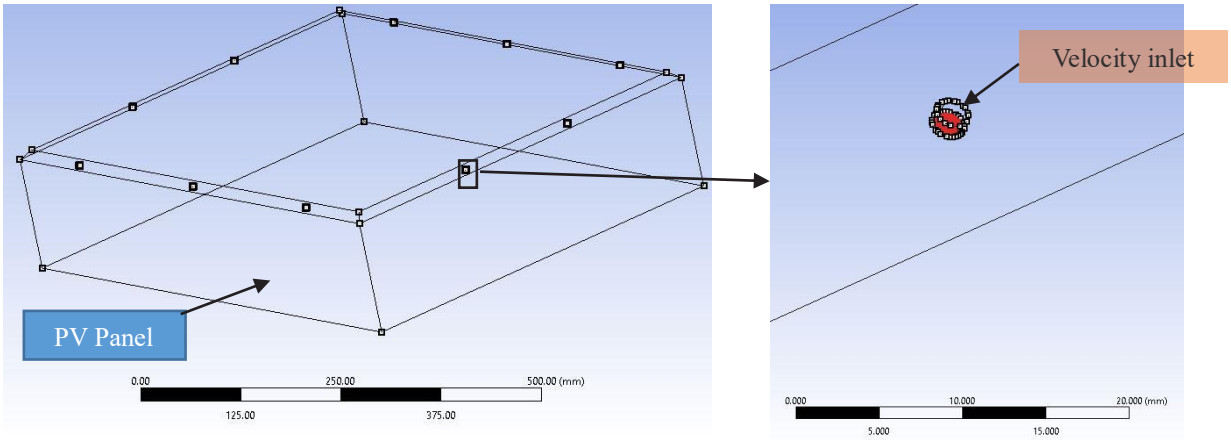

Fig. 3 (a) Domain with PV panel, Pressure oulets and Velocity inlets (b) Velocity inlet

4) Solver

A heat transfer study is performed on the PV panel to study its temperature dependent efficiency degradation. Steady state numerical simulations of 3-D Model were performed on ANSYS FLUENT which employs continuity equation, energy equation and RANS equations. To acquire fast converging solution, a pressure based coupled solver was used. Least Squares Cell-Based method of gradient computation was done where the solution is assumed to vary linearly. A second order upwind interpolation scheme was used to solve the convective terms. Central difference method was used for diffusion term and second-order accuracy was implemented. A multiphase VOF model was chosen where air is primary phase and water is secondary phase and their interaction surface tension was given as 0.072. The turbulence model selected is realizable k-ε model.

IV. Results and discussion

1) Validation:

The average temperature of PV panel surface was found from CFD analysis to be 33°C which matches with the experimental data (Nizetic, Coko, Yadav and Grubisic-Cabo, 2016). Fig. 4 shows the temperature profile of the 17° elevated PV panel and the effect of water cooling on the panel. This study was done for 111.5 L/h mass flow rate case and the temperature profile is not constant throughout the panel as shown in the figure.

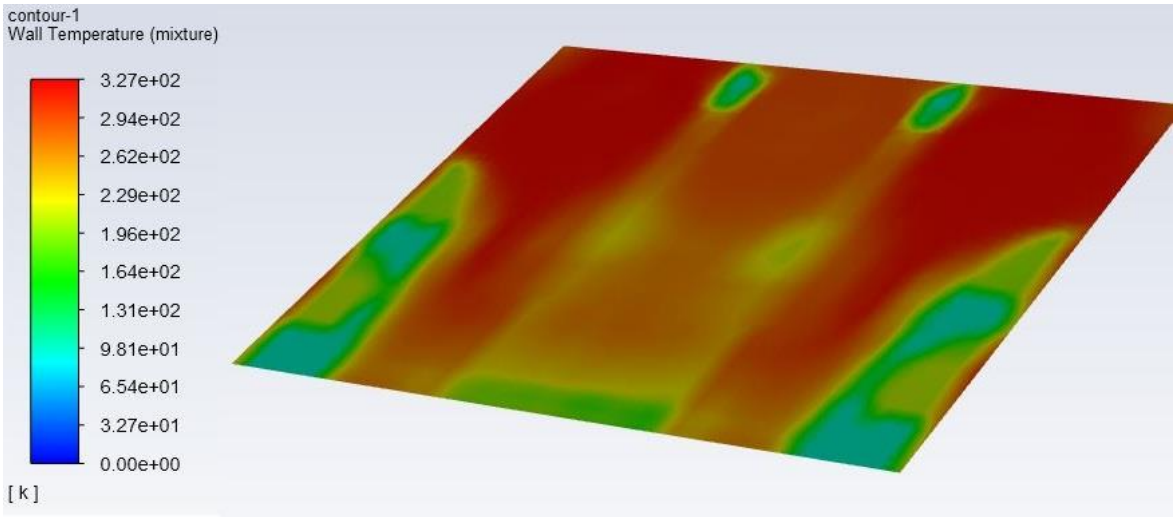

Fig. 4. Static temperature profile at maximum water flow rate of 112.5 L/h.

2) Variation of temperature and electrical efficiency with different water flow rates:

In this study 4 different values of water flow rates are taken to study the change in temperature of panel with for different flow rates and also change in electrical efficiency of the panel with different flow rates. Electrical efficiency ($\eta_{electric}$) can be calculated using the equation discussed in (Corbin and Zhai, 2010) (Sarhaddi, Farahat, Ajam and Behzadmehr, 2010) and is given as equation (1),

$$\eta_{electric} = \eta_{ref}(1 - \beta(T_c - T_{ref})) \quad (1)$$

T_c, is the average PV cell temperature. The nominal cell efficiency η_{ref} is 0.160 and temperature coefficient, β is 0.0032 are supplied by the PV module manufacturer. T_{ref} is the industry standard reference temperature, 25 °C.

Fig. 5 (a) shows how the average surface temperature of PV panel reduces as the water flow rate increase. Fig. 5 (b) shows how the electrical efficiency of the PV panel increases with the flow rate.

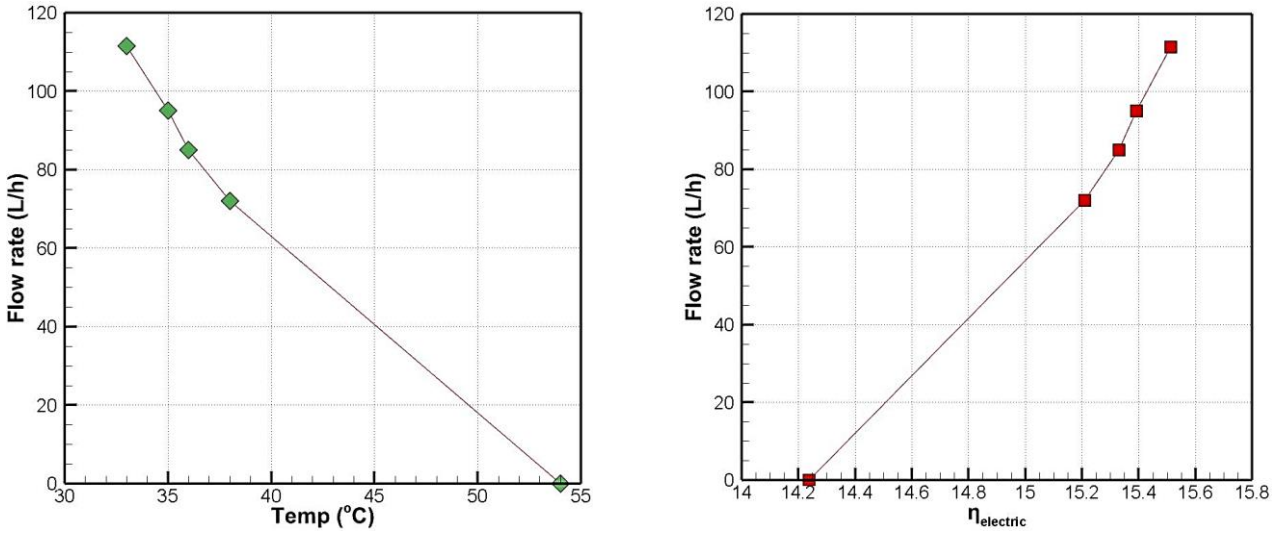

Fig. 5 (a) water flow rate vs Avg panel temperature (b) Flow rate vs Electric efficiency of panel

Table 1 gives the summary of the values calculated and also gives the comparison of the change in electrical efficiency with change in average PV panel temperature.

Table 1. Summary of calculated values

Flow rate (L/h)	Temp (°C)	Electric Efficiency ($\eta_{electric}$)
0	54	14.23
72	38	15.20
85	36	15.33
95	35	15.39
111.5	33	15.51

V. Conclusion

A 3-D steady state CFD analysis was performed for a multiphase problem consisting of a PV panel and nozzle inlet for water spray cooling as computational model. Adequate mesh was developed to solve without divergence issues. Appropriate boundary conditions were given to match the actual experimental condition for cooling the top surface of the PV panel. The validation of the numerical model was done by comparing the computational value of the average temperature achieved on the top surface of the cooled panel to the experimental data. The temperature profile also shows the pattern temperature reduction by water spray mechanism. The decrease in panel temperature and increase in electric efficiency of panel with increase in water flow rate is plotted and also its relationship with each other is studied.

References

Abdolzadeh, M. and Ameri, M., 2009. Improving the effectiveness of a photovoltaic water pumping system by spraying water over the front of photovoltaic cells, Renewable Energy, Vol. 34, No.1, pp. 91-96.

Arcuri, N., Reda, F., De Simone, M., 2014. Energy and thermo-fluid-dynamics evaluations of photovoltaic panels cooled by water and air. Sol Energy. 105, 147–56.

Corbin, C. D. and Zhai, Z. J., 2010. Experimental and numerical investigation on thermal and electrical performance of a building integrated photovoltaic–thermal collector system, Energy and Buildings, Vol. 42, No. 1, pp. 76-82.

Farhana, Z., Irwan, Y.M., Azimmi, R.M.N., Razliana, A.R.N., Gomesh, N., 2012.Experimental investigation of photovoltaic modules cooling system. In: Proc 2012 IEEE symposium on computers & informatics. p. 165–9.

Irwan, Y. M., Leow, W. Z., Irwanto, M., Amelia, A. R., Gomesh, N. and Safwati, I., 2015. Indoor test performance of PV panel through water cooling method, Energy Procedia, Vol. 79, pp. 604-611.

Nizetic, S., Coko, D., Yadav, A. and Grubisic-Cabo, F., 2016. Water spray cooling technique applied on a photovoltaic panel: The performance response, Energy conversion and management, Vol. 108, pp.287-296.

Sarhaddi, F., Farahat, S., Ajam, H., Behzadmehr, A., 2010. Exergetic performance assessment of a solar photovoltaic thermal (PV/T) air collector, Energy and Buildings, Vol. 42, No. 11, pp. 2184-2199.

Tonui, J.K., Tripanagnostopoulos Y., 2007. Improved PV/T solar collectors with heat extraction by forced or natural air circulation. Renewable Energy; 32 (4):623–37.

Strategic and Flexible LNG Production Under Uncertain Future Demand

Noor Yusuf, Rajesh Govindan, Luluwah Al-Fagih, Tareq Al-Ansari*
Division of Engineering Management and Decision Sciences, College of Science and Engineering, Hamad Bin Khalifa University, Doha, P.O. Box: 34110, Qatar

* E-mail: talansari@hbku.edu.qa

Abstract

The LNG supply chain consists of five main sections: upstream, midstream liquefaction process, shipping, regasification, and distribution to the local markets via pipelines. The most capital-intensive part of the LNG chain is the liquefaction process, where the treated gas is liquefied and cooled down to -164 °C. Different LNG liquefaction technologies with different production capacities are adopted in the industry. Small to mid-scale technologies are used for LNG production of up to 5 MTPA, while in mega-scale technologies, the production capacity reaches 7.8 MTPA. Typically, an LNG project investment has two phases: pre-final investment decision (pre-FID) and post-final investment decision (post-FID). The pre-FID activities include project feasibility, market analysis, technology design, location selection, sales and purchase agreements, and project's financing, while the post FID activities focus on the technicality of project's feasibility, construction, utilities, ports and terminals, operations, shipping, regasification, and future build-ups. As such, the business opportunities for LNG production are economically risky. Initial investments are subject to market demand and uncertainties due to competitiveness and prices fluctuations. Moreover, the change in the contracutral structures of the LNG business have impacted the decision-making process in the pre-FID pahase due to the high uncertainties involved. In this study, a strategic flexible approach is proposed for LNG production systems to maximise the expected economic value under uncertanities. First, a baseline fixed design was selected using the analytical herichay process (AHP). The baseline design was then evaluated stochastically under the uncertainties of LNG prices to justify the need of employing a flexible pricing mechanism along with a flexibile production system to capture high demand opportunities and hedge against low market conditions.

Keywords: Liquefied natural gas, flexibile design, jump diffusion processes, long-term contracts.

1. Introduction

In the past decades, the demand for natural gas as an energy source has been growing due to its economical and evinironmental attractiveness. Many countries set regulations to shift from coal and oil to cleaner energy resources after the Paris Agreement in 2015. Amongst the nonconventional fuels, natural gas is the cleanest due to its low C/H density, causing gas molecules to burn completely into carbondioxide and water in the presence of oxygen. Natural gas can be easily transported via pipelines to nearby markets. However, due to the economic constraints, for those markets that are located at distances of more than 2,500 miles, natural gas is liquified and shipped in LNG carriers (Erdos, 2012). Different technologies have been used worldwide to liquefy natural gas by cooling it down to -164 C, reducing its volume to 1/600 of the original volume. The most common mature LNG technologies in the industry are Propane Mixed Refrigerant process (C3MR) and its modification C3MR/Split MR by APCI; Shell Dual Mixed Refirgerant technology (DMR); AP-X technology by APCI; Linde Mixed Fluid Cascade process (MFC); and ConcoPhillips Optimised cascade process (POCP). The liquefaction process is capital intensive where 40-50% of the capital costs are spent on the liquefaction plant in an LNG project. Hence, in order to minimise the risks associated with the investment, signing long-term contracts in the pre-final investment (pre-FID) phase of the project has been essential to secure markets and sales of LNG.

In the recent years, the contractual structure of the LNG business has changed rapidly with the emergence of spot selling, and short/mid term contracts. Different factors were behind this major movement away from relying on long-term contracts (LTCs), such as the huge LNG volumes coming from suppliers in Australia and the US, maturity of natural gas physical and virtual trading hubs like Henry Hub (HH) in the US, and Title Transfer Facility (TTF) in the Netherlands, in addition to the emergence of portfolio players. Furthermore, the huge uncontracted LNG volumes coming into the market lead to high competitiveness wherein some of the suppliers adopted the stretagy of selling LNG with small premiums in order to compete with the major LNG producers like Qatar.

With more uncontracted LNG volumes in the market, LNG buyers are less likely to sign new LTCs, which resulted in increasing complexity in the decision-making process in the pre-FID due to the associated financial risks. Hence, uncertainity analysis is required to convince investors to invest in such capital-Intensive projects by developing new selling strategies. One of the best concepts that can be adopted in LNG systems is the concept of flexibility arising from financial options (Cardin et al., 2015). Saleh et al. (2009) provided a research agenda for designing flexible engineering systems. They reported that a system has to be designed with certain characteristics and design architecture and parameters to allow for flexibility in order to track changes. In LNG production systems, the flexibility approach would give the producer the right but not the obligation to increase LNG production when the

demand is high, maxisiming the possible profits by capturing the high demand opportunities, or producing at a minimum level when the demand in international markets is low, minimising the possible losses from selling LNG at very low prices. Hence, a flexible system minimises possible financial risks by considering uncertainities involved in the project, such as future demand and prices. Previous studies implemented the concept of flexibility to improve the lifecycle of LNG projects by considering local uncertain demand and flexible centralised and decentralised production systems (Cardin et al., 2015; Xia et al., 2016). However, these studies have not considered the technical aspects of flexibility and changing production levels. On the other hand, Hönig et al. (2019) linked the production system with the final uncertain local demand in Europe. The authors analysed both the technological and economic aspects of a C3MR LNG production system under demand and prices uncertainities. However, they did not consider the effect of flexibility in production on improving the economic performance of the project. Thus, implementing flexibility on a certain LNG production technology and linking it to the final uncertain demand and/or prices in the international markets have not reported in earlier studies.

In real-life projects, LNG technologies are selected and evaluated based on average parameters, like expected values for future demand and prices. However, these average parameters do not truly reflect the future scenarios affected by prices fluctuations and demand uncertainities. In the work presented in this paper, an LNG production technology was evaluated under LNG price uncertainities. The LNG prices are volatile and a function of different factors like production disrtuptions due to major events; high demand and seasonality; natural gas spot prices; oil prices; and other competitiveness in the market due to oversupply. Therefore, it is essential to model and evaluate the risks involved in the project arising from prices fluctuations, prior to investment in technologies in order to justify their need for increased flexibility and convince decision-makers to switch to new strategies to counter risks under low market demand conditions.

2. Available Data

Qualitative and quantitative Information about the most common LNG technologies in the industry were used for evaluating and selecting a baseline design (Al-Mutaz et al., 2016; Mokhatab et al., 2013; Pillarella et al., 2007). In order to evaluate the selected AP-X technology under LNG price uncertainties, the following data were used.

The capital and annual operational costs of a brownfield AP-X technology with a production capacity of 7.8 MTPA are $ 5.53 billion in year 2019 and $1.39 billion in year 2025 respectively (Steuer, 2019). The lifetime of the project was considered as 25 years, with 5 years of construction and 20 years of production. The risk-free interest rate was assumed to be 10%, as it is a common case in most oil and gas projects (Cardin et al., 2015). The Capex distribution throughout the construction period was considered as: 6% in year 0 in the pre-FID phase; 5% in year 1; 29% in year 2; 33% in year 3; 25% in year 4; and 3% in year 5 of contrcution (PWC, 2014). The full capacity of LNG was assumed to be sold to high income Asia Pacific markets uncer LTCs with an average forecasted contracted price of $ 8.76/MMBTU in year 2025 (Steuer, 2019). Meanwhile, for the stochastic analysis, a mean-reversion geometric Brownian motion jump diffusion model was implemented to develop a forecasting model for natural gas Henry Hub spot prices with parameters obtained from literature based on historical data from 1990 to 2013 (Lucheroni and Mari, 2015) as indicated in Table 1.

Table 1. Geometric Brownian motion and jump diffusion process model paratmers ((Lucheroni and Mari, 2015)

Parameter	Notation	Value
Mean-Reversion parameters	θ^{gas}	*0.0432*
	α^{gas}	*0.0292*
Jumps intensity	λ^{Jump}	*0.2542*
Standard deviation for passion process	σ^{jump}	*0.1258*
Volatility of gas prices	σ^{gas}	*0.0737*
Mean for passion process	μ^{Jump}	*0.01*

3. Methodology and analysis

Initially, a deterministic analysis was carried out, wherein a baseline technology was selected to estimate the net present value (NPV) under future expectations for LNG prices and demand. The Analytic Hierarchy Process (AHP) was used in selecting a technology amongst all other industrially-matured technologies by considering multiple criteria (Saaty, 1987). The decision criteria include flexibility, ease of operation, economies of scale, and reliability of the process and its equipment. As a result, the AP-X technology scored the highest as the best candidate for this problem.

Subsequently, the project value was evaluated using stochastic modelling. Under fixed capital and operational costs throughout the lifetime of the project, the NPV was simulated using monte carlo simulation (MCS), considering fixed production capacity and stochastic natural gas Henry Hub spot prices. A time series dynamic model, called the mean-reversion Gemotric Brownian motion (GBM) with jumps diffusion (poisson distribution) model, was considered to describe and forecast the stochastic behaviour of Henry Hub natural gas spot prices in order to

evaluate risks arising from prices uncertainities. The simulation was implemented using a large sample size of 10,000 using the Python programming language in Visual Studio Code enabled by the Anaconda software package.

The natural gas spot prices are generally volatile and sensitive to market conditions related to supply and demand, political factors and other shocks in the market. In LNG projects, predicting the profitability of a project under expected future prices and demand does not reflect the real-life scenario of the economic performance of those projects under uncertainities. Mathematically, this is known as Jensen's Law:

$$f(E[x]) \neq E[f(x)] \quad (1)$$

Where $f(E[x])$ is the expected NPV under average demand or prices scenario that does not equal the expected NPV under a distribution of demand or prices $E[f(x)]$ (Cardin et al., 2015). Hence, forecast modelling and evaluating the time-series for natural gas spot prices is essential for estimating the expected NPV of the project $E[f(x)]$ to minimize the investment risks under uncertainities. As such, the mean-reversion GBM stochastic process model describes the normal fluctuations of natural gas prices only. Hence, a jumps diffusion model was additionally introduced to the model to describe the abnormal fluctuations due to shocks (Lucheroni and Mari, 2018), given by:

$$dlog(P_t) = (\theta^{gas} - \alpha^{gas}\log(P_t))dt + \sigma^{gas}dW + JdN \quad (2)$$

Where P_t is the natural gas Henry Hub spot price at time t; θ^{gas} and α^{gas} are the mean-reversion parameters; σ^{gas} is the volatility of gas prices; W is the standard Brownian motion Weiner Process, with zero mean and a standard deviation of 1; and N is the jump-diffffusion process, Poisson process, with a jump amplitude of J and intensity λ^{Jump}. Poisson Process is normally distributed with a mean of zero and a standard deviation σ^{Jump}. Moreover, N and W are considered independent processes.

Finally, the NPV distribution for the project was estimated by considering the simulated LNG prices in equation (3), whilst the ENPV was then calaculated by considering all NPV possibilities after the stochastic analysis using equation (4) given by:

$$NPV = Initial\ investment + \sum_{t=1}^{T} \frac{CF_t}{(1+r)^t} \quad (3)$$

$$ENPV = \frac{1}{N}\sum_{n=1}^{N} NPV_n \quad (4)$$

4. Results and discussions

Amongst the different LNG pricing systems, the forecasts for the U.S Henry Hub natural gas spot prices were considered for estimating the revenues of the proposed LNG project due to its maturity and global acceptance as a pricing system. The data used for estimating the model parameters were from 1990 to 2013, which includes the effects of unexpected events, such as the global economic ressession in 2008; the Arab Spring in 2011; and Hurricane Sandy in 2012.

10,000 simulations using the mean reversion GBM jump diffisuion model resulted in an NPV distribution with different frequencies as shown in fig 1. The histogram of the NPV distribution is a portfolio of selling 7.8 MTPA of LNG to high income Asia Pacific markets under LTCs for 20 years, with 6 years of pre-production expenses. The histogram is positively skewed to the right with a heavy longer right tail. Moreover, the simulation resulted in a median NPV of $7.37 billion. When analysing the NPV distribution, extreme values were not considered due to their rare possibilities of occurance. Instead, indicators such as values at risk and gain, VaR and VaG respectively, were considered to reflect the greatest possible losses or revnues within a certain condifence interval. When considering a confidence interval of 99% in this case, the VaR (1%) is $54.2 million, whilst the VaG (99%) is $24 billion.

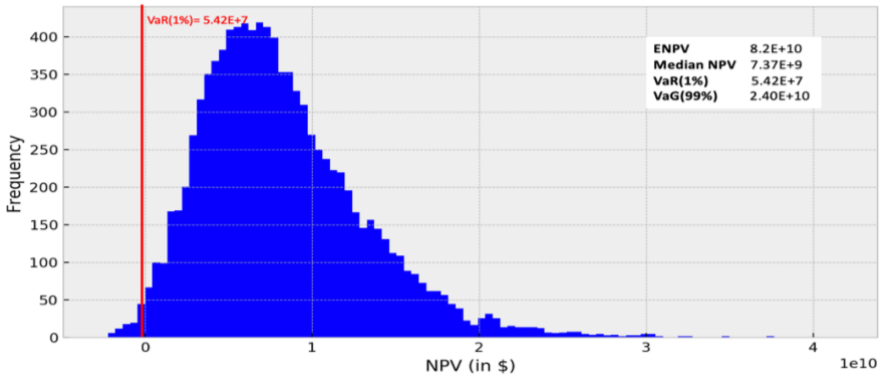

Fig. 1. NPV Histogram for 7.8 MTPA LNG project committed to high income Asia Pacific markets.

On the other hand, the deterministic NPV when considering the average LNG selling price resulted in a value of $5.86 billion, whereas by considering the stochastic behavior of forecasted natural gas spot prices prices, it resulted in an ENPV of $82 billion. An ENPV greater than NPV indicates that dedicating the full capacity of an LNG project to LTCs with a fixed selling price is not the best strategy for selling LNG in international markets. Although LTCs have been used as a hedging strategy against prices fluctuations, they sometimes however restrict the producer from capturing the benefits of volatile market conditions in achieving higher profits, as opposed to selling at contractual prices that are lower than the actual market price, particularly when the demand increases and spot prices spikes.

5. Conclusions

Sales and purchase agreements, and long-term contracts have been used widely prior to starting new LNG projects in order to secure markets and hedge against market fluctuations. However, due to the changes in market and the contractual structures of the LNG business, a strategic flexible approach is now needed to capture those changes in the competitive LNG market. Flexibility in the contractual structures has been adopted by few emerging LNG producers. However, one major aspect that was considered in this study was designing a flexibile LNG production system that is responsive to market fluctuations. The AHP analysis indicated that the AP-X LNG production system is a good candidate for applying flexibility. This technology can produce up to 7.8 MTPA when LNG prices and demand are high, or 5 MTPA when LNG prices and demand are low. Additionally, the technology was also assessed under prices uncertainity. As part of the future work, the design could be further analysed under demand uncertainty where markets are linked to tactical production aspects of the LNG supply chain.

Acknowledgements

This research would not have been possible without the exceptional support of the Dvision of Science and Engineering Management, College of Science and Engineering, Hamad Bin Khalifa University, Qatar Foundation.

References

Al-Mutaz, I.S., Liu, X., Mazza, G., 2016. Natural Gas Liquefaction Technologies-An Overview. OIL GAS-EUROPEAN Mag. 42, 213–218.

Cardin, M., Ranjbar-Bourani, M., De Neufville, R., 2015. Improving the lifecycle performance of engineering projects with flexible strategies: example of on-shore LNG production design. Syst. Eng. 18, 253–268.

Hönig, V., Prochazka, P., Obergruber, M., Smutka, L., Kucerová, V., 2019. Economic and technological analysis of commercial LNG production in the EU. Energies 12, 1–17. https://doi.org/10.3390/en12081565

Lucheroni, C., Mari, C., 2018. Risk shaping of optimal electricity portfolios in the stochastic LCOE theory. Comput. Oper. Res. 96, 374–385. https://doi.org/10.1016/j.cor.2018.02.011

Mokhatab, S., Mak, J.Y., Valappil, J. V, Wood, D.A., 2013. Handbook of liquefied natural gas. Gulf Professional Publishing.

Pillarella, M., Liu, Y.N., Petrowski, J., Bower, R., 2007. The C3MR liquefaction cycle: Versatility for a fast growing, ever changing LNG industry. Gas Technol. Inst. - 15th Int. Conf. Exhib. Liquified Nat. Gas 2007, LNG 15 GNL 15 1, 139–152.

PWC, 2014. The progression of an LNG project.

Saaty, R.W., 1987. The analytic hierarchy process-what it is and how it is used. Math. Model. 9, 161–176. https://doi.org/10.1016/0270-0255(87)90473-8

Saleh, J.H., Mark, G., Jordan, N.C., 2009. Flexibility: A multi-disciplinary literature review and a research agenda for designing flexible engineering systems. J. Eng. Des. 20, 307–323. https://doi.org/10.1080/09544820701870813

Steuer, C., 2019. Outlook for Competitive LNG Supply, Oxford Institute for Energy Studies. https://doi.org/10.26889/9781784671310

Xia, T., Cardin, M.A., Ranjbar-Bourani, M., Caunhye, M.A., 2016. A Decision-Making Tool to Design a Flexible Liquefied Natural Gas System under Uncertainty. Proc. - 2015 IEEE Int. Conf. Syst. Man, Cybern. SMC 2015 789–794. https://doi.org/10.1109/SMC.2015.147

Preliminary Energy Audit of a Residential Engineering University Campus

*Muhammad Sohail Malik, Aleem Ahmed Khan
Ghulam Ishaq Khan Institute of Engineering Sciences and Technology, Pakistan

* E-mails: sohailmalik49@gmail.com

Abstract
Sustainability of our energy resources is becoming of increasing importance to the wellbeing of this and all future generations. To prevent harm to the planet and its living inhabitants' immediate steps are required to be taken towards development of sustainable energy while making the existing infrastructure more efficient to speed up this process. This study focuses on identifying energy consumption patterns of a residential university campus in its current and retrofitted form. This was made possible by collecting loads of individual machines were, power consumption of buildings and analyzing them. Past 4 years of billing data was analyzed for future consumption. Results present in this study suggest significant energy saving can be accomplished by applying different retrofitted techniques.

Keywords: Consumption, Optimization, Retrofitting, GIKI

I. Introduction

Energy has become fundamental to the growth of human species. It has transformed the lives of all humans living on this plant forever and will be a key factor for the future generations. Unfortunately, the need for energy far surpasses any concept of harm being done to the planet. The idea for conservation was not given paramount importance only unit recently when the situation of climate change and carbon level in the earth's atmosphere surpassed dangerous levels. This make sustainability of our sources of energy even more important than ever before. One of the pillars to sustainability is energy audits which show the way forward in improving our system to make them more efficient and have a less carbon foot print. Energy audit in the building sector is Pakistan are of paramount importance as the Pakistan is a country were [45.9%] twice as much energy is consumed by the domestic sector them the industrial sector. This means that a vast amount of energy is being wasted in the domestic sector. This paper will shed light on Ghulam ashiq khan institute energy consumption and the EOQ. Energy audit (EA) is a process designed to identify induvial processes to improve comfort of occupants and to optimize
energy consumption of the building. Important parameters for EA are time of building use, the efficiency of existing equipment and the implementation of new energy conservation ideas. The American Society of Heating, Refrigerating and Air-conditioning Engineers (ASHARE), has introduced a standard that which describes the energy auditing process of a building (ASHRAE, 2006). The process is ensued by the formation of an energy audit team (EAT) which specifies the audit scope. (EA) can be performed in three different levels depending on constraints such as budget, available time and building complexity.
The energy audits levels are defined by the ASHRAE 100-2006 standard as the following: level 1, "walk-through assessment"; level 2, "energy survey and analysis"; and level 3, "detailed analysis

Much research has been conducted in the area of energy audits

and have found that substantial energy saving can be achieved (Anderson and Newell, 2004; Botsaris and Prebezanos, 2004; Butala and Novak, 1999; Chirarattananon and Taweekun, 2003; Deng and Burnett, 2000; Larsen and Jensen, 1999). Many studies have been also been conducted for cooling load in hot and humid climate (Al-Homoud, 1997; Bauer and Scartezzini, 1998; Chirarattananon and Taveekun, 2004; "Daylighting and its implications to overall thermal transfer value (OTTV) determinations," 2003; Laine and Saari, 1994; Leung et al., 2005; Li et al., 2003; Vine et al., 1998; YIK, 2004) On the contrary very few studies have been conducted in the area of office loads in cold climate conditions. A study conducted on the energy loss through windows of specific design and material concluded that by using different window material that do not conduct heat and glazing the windows energy consumption can be reduced by up to 41% (Mehmood and Answar, 2017). A study of 19 Hong Kong government offices clearly stated that by improving energy management practices considerable energy consumption of the building can be reduced (Li, 2008). A study conducted in four different climates shows that by monitoring system operations and other parameters can help in saving energy consumption (Eskin and Türkmen, 2008). A simulation-based study evaluates energy conservation alternatives to prevent the loss of energy (Larsen and Jensen, 1999; Saad Al-Homoud, 2001; Waltz, 2000). A study conducted in a university used the daily load of a group of air-conditioning system to model and control the energy consumption of new and previously built building (Escrivá-Escrivá et al., 2010). A large operating system operating in more than 100 building was examine and was found that by improving operational efficacy energy consumption was reduced by 20% (Mills et al., 2004).

II. Methodology

A. Scope of the evergy audit

In this study, the main objective is to apply energy audit levels for a residential engineering university campus. First, that area to be audited was specified, the level of energy audit and the saving anticipated.

B. Methodology.

This Energy audit was conducted by gathering data by physically going to every building and noting down equipment

usage and power rating. Power of the Equipment that were above 2kw were checked physically by using a clamp meter [Meter number]. Past 5 years of the institutes billing data was calculated and was thoroughly analyzed for pattern as well as future prediction of power consumption. Sub-meter reading was gathered and analyzed for the necessary understating of power consumption distribution among different sectors of the institute.

C. Area to be audited

Table 1. List of building was audited.

NO	Type	Toatal	Description
1	Faculty	5	• Faculty of Electrical Engineering • Faculty of Mechanical Engineering • Faculty of Materiala and Chemical Engineering • Faculty of Engineering Science • Faculty of Management Science
2	HVAC	1	-
3	Hostel	12	1-12
4	Incubation center	1	-
5	Sports complex	1	• Main ground • Swimming pool • Basketball court • Tennis court • Squash court • Table Tennis • Pool
6	Administration	1	-
	Library	1	-

D. % of Energy usage per building

Table 2. Building energy consumption as a % of total energy.

Building type	% of total energy consumption
HVAC	44%
Hostels	17%
FME (Faculty of Mechanical Engineering)	10%
Mess/office	8%
FMCE (Faculty of material and chemical Engineering)	7%
MGS (Faculty of Management Sciences)	6%
Incubation center	4%
FES (Faculty of Science)	3%
FEE (Faculty of Electrical Engineering)	2%
Sports Complex	1%
Administration	1%
Library	1%
Auditorium	1%

E. Description of audit area

The Description of all the building that were audited is provided in table.4 in the appendix section at the end of the paper.

III. Analysis

Level 1 audit: Site inspection and measurement

In this study, the EAT conduced a level 1 audit

A. Walk-through assessment

The EAT carried out a walk-through assessment, which is considered the first step in performing any energy audit. This step although basic requires the most amount of time as it required several visits to the buildings that are to be audited. A checklist of the reading that were to be recorded was prepared before the audit ensued to reduce the required time for level 1 audit. While EAT was performing level 1 audit several issues related were noted. The list of issues violating the energy conservation principle as outline in the ASHRE standard 100-2006 were noted down.

B. HVAC system

When inspecting the HVAC, it was found that HVAC does not have a basic control that automatically start and stop the chiller and the air distribution bases on building demands. It was observed that the indoor temp of some building was lower than expected value and the staff complained the temp was too low. As overserved from the evidence about it is clear that the HVAC is operated manually by an operator working 12-hour shifts. This is because the building is not equipped with Direct Digital Control (DDC). I was also noted that since the HVAC system is very old, so if any part is out of service the mechanic has no choice but to make the part themselves which not a 100%

accurate to the original part and hence the efficiency of the HVAC decreases. Therefore, it is recommended that the HVAC be equipped with Direct Digital Control (DDC) to reduce power consumption. The cheapest way to reduce the energy is to apply temperature sensors in all the building that the HVAC supplies to so that the operator operating the value manually would adjust the value and not wait for the staff of individual building to call the HVAC plant and inform to reduce the flow. Furthermore, it is recommended that the system is regular maintained to keep the system running at peak efficiency.

C. Hostel lighting and equipment

During visits to the hostels it was noted by the EAT that some of the left their room lights on even after they have left the hostels. At EAT asked students about lights not being turned off which they replied by saying the when leaving the room in a hurry for classes the lights may be left switched on. It was also noted that at the time of the survey the summer school session was under way and most of the students choose to spent time in the common room it is equipped with a floor standing air-conditioning unit. It was observed that the A/C was left open even though no one was present in the common room, as well as the windows of the common room are 7feet* 7feet which help in allowing natural light into the space but they have a very poor heat transfer coefficient. Due to this reason the air-conditioning unit which is set to the lowest temperature setting by the students runs constantly without stopping. In Winter times the hostels are heated by using natural gas which is expensive, due to this room heaters run only till 10pm. This makes the room temperature very unpleasant which encourages students to use room heater that are inefficient. Therefore, it is recommended that the window of the common room be replaced by double glazed windows that prevent the loss of energy. Furthermore, it is recommended that the air-conditioning unit be set to a comfortable temperature of 26 degree centigrade to stop it running over time. The cheapest way to save energy is to increase the awareness of the students to turn off the lights when not using the room as well as turn off the bathroom lights when not in use. Geothermal heater should be used to heat the water for the room heater in the winters to reduce the use of natural gas and at the same time keeping the system running longer to prevent the students from using infant tube heaters.

D. Old Air-conditioning technoliogy

During EATs multiple visits to faculty building it was observed that most of the faculty are still equipped with the same air-conditioning unit that were fitted almost 20 years ago. The super computer place in FEE/FCS faculty requires is equipped with four floor standing air-conditioning unit which are required to run 24/7 due to the super computer. All of these 4-air-conditioning unit are almost 20 years old can consume considerably more power than A/C with inverter technology. It was also noted that most of the blinds in every faculty were closed with resulted in very low lux rate. This results in loss of energy as all of the lights in all of the lecture halls and office space are open during day time. Night and weekend visit reviled that some of the equipment mainly PC were left on after working hours. Therefore, it is recommended all the old air-conditioning unit be replaced with new DC inverter technology so save energy. Furthermore, that all the blinds be open so that natural light be used in the day time and energy may not be wasted on lights in the day time. Increasing awareness among the staff member might be the cheapest solution for them to turn off their equipment after working hours.

E. Single glaze windows

One common issue that was raised with every visit by EAT was that all of the building that use the HVAC is that they all are equipped with single pane glad windows with aluminum frame which ae very heat conductive. This means that the heat transfer coefficient of the all the windows is massively affecting the energy consumption of the HVAC. Therefore, it is recommended that the all the windows in the office space be replaced by double glazed window. Which cut down the energy consumption of the HVAC which consumes about 43% of all energy.

IV. Results and discussions

A. Eenergy utilization index (EUI)

The energy utilization index (EUI) is obtained by dividing the annual energy consumed by the total floor area (TFA). This take into account the difference in energy consumption in different buildings due to their floor space. This index is very useful in comparing buildings with similar end use.

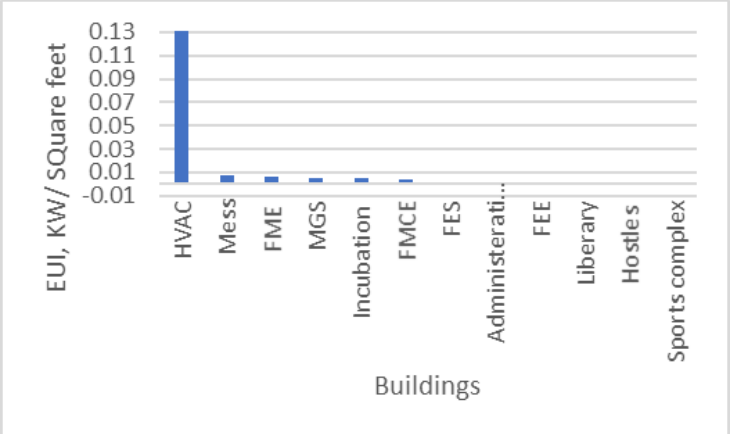

Fig. 1: Energy utilization index graph 1

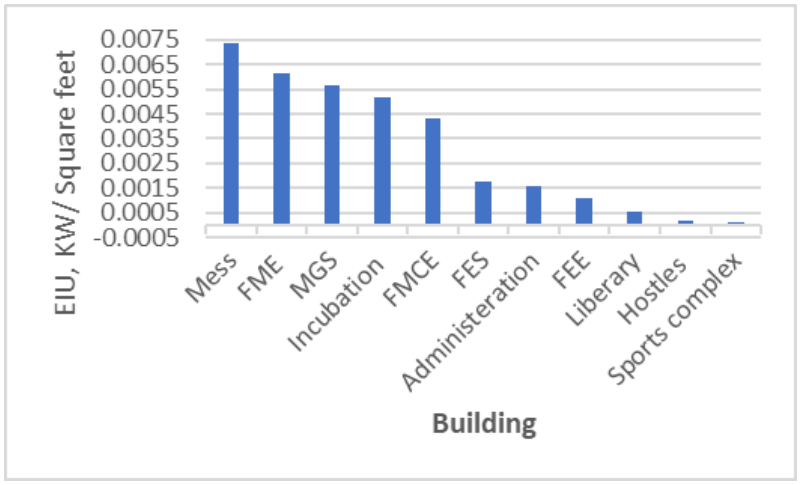

Fig. 2: Energy utilization index graph 2

B. Power consumption analysis

The information of the future prediction of power was concluded by gathering data for the past five years. This data included off peak units, peak units. The general trend as shown in fig.1 show that demand is linearly increasing. This increase in consumption can be directly correlated with the increase in the number of students of new batches. Due to which the two new hostels were built hostel 11 and 12. Demand will likely increase exponentially as a new faculty is being built and will be opened in the start of the semester in September of 2019. And then it will resume the liner increase.

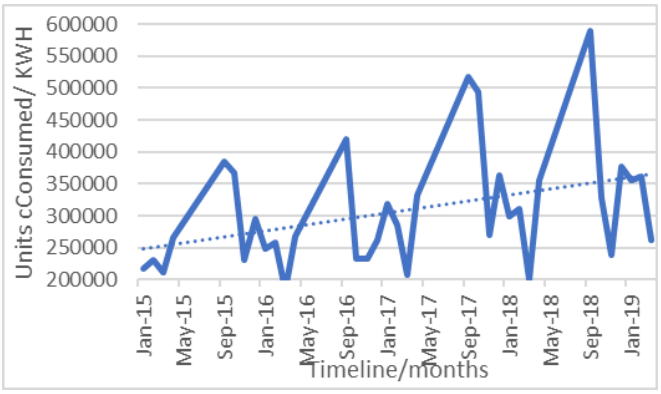

Fig. 3: Total unit conumption of institute trendline

In this institute the new semester stats from September and ends in December. The second semester starts from January and ends in May. This time line is very crucial to understand the consumption of energy as shown in table .1 By far the most energy is consumed in the month of September. This is mainly be attributed to the fact that a new semester has begun and all the students and faculty members are back from holidays. In this month even though the HVAC is turned off the energy consumption is enormous this is because the institute is attached to a residential colony and all the staff members uses air-conditioning unit in the month of September which consumes an enormous amount of energy. The linear increase in energy consumption (discussed in data analysis) can be clearly seen from Fig.4 which shows the energy consumption of September.

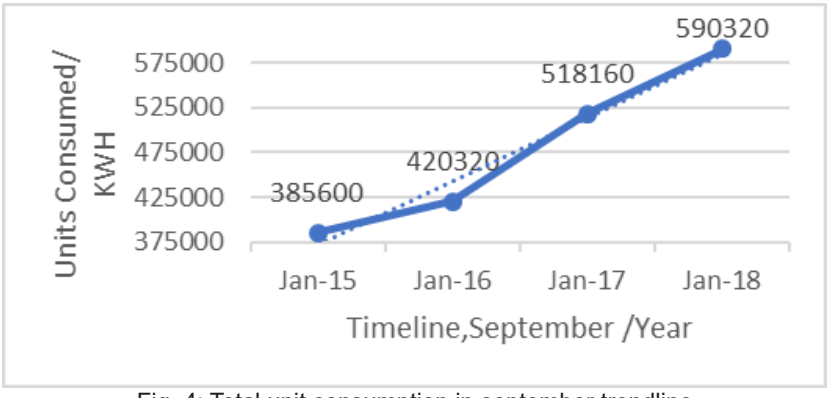

Fig. 4: Total unit consumption in september trendline

The in an exponential increase which can be seen in the year 2016 this is mainly due the opening of hostel 11.

C. Anlaysis of energy consumption

Table.1 has been divided into segment to have a better understanding of the power consumption. The first segment is colored in blue and shows the power consumption in units from the month of January to April (fall Semester). The second is colored in yellow and shows the power consumption from May to august (Summer semester). The third segment is colored in green shows power consumption from September to December. (Winter semester). As seen from table.1 the most amount of energy is consumed in the summer semester is mainly due to the usage of the HVAC. The second most energy is consumed during winter session. This is mail due to heaters being used in hostels and residentials home which use a vast amount of power and are very inefficient. The fall semester is the least energy consumption as winter has passed and but the temperature is such that there is no need for air-conditioning unit or the use of heater. It has to be pointed out that the energy consumed in the month of march and November can be attributed to the holidays after midterm exams, due to which most of the students leave for home and most of the staff also tend to leave for their homes.

D. Speculation

The energy consumption is changing trend. Table.2 shows the accumulated energy used in each semester. It can be clearly seen that winter accumulated energy consumed will soon be surpass summer which is a huge change in energy consumption.

E. Application of solar

The EAT also explored the possibility of using solar power to for the entire institute. To achieve a solar system of 5MW will have to be put in place and will cost depending on the type and company which will be given the task of installing the solar system in place. The cost analysis of the solar system has been shown in table.3. It also shows the amount that will be saved over the years. The EAT estimates that the payback period of the entire solar system will be 10 years. Compared to the average life cycle of solar system which is 20 years, the instate will run for a decade on free and clean energy.

F. Summery of EAT recommendations

A list of recommendations was submitted by the EAT to improve the over all efficiency of the institute. First, all the windows that are in office and laboratories which are cooled by the HVAC must be replaced from single glaze windows to double glaze windows. Second, window blinds should be opened to allow natural light inside to reduce the need to use lights in the day time. Third, all the old technology air conditioners being used in faculties and administration building should be replace with more efficient DC inverter technology air conditioners. Forth, a Digital Direct control (DDC) should be installed for the HVAC to prevent manual inefficient control by the operators. Alternatively, temperature and humidity sensors can be installed in the faculty areas served by the HVAC to provide the operator with more information making the system less energy consuming. Fifth, stop unnecessary energy usage by asking staff member to turn off their equipment when leaving their work place. Alternatively, a person from the sanitation department could be allowed to access the offices after working hours to turn off equipment. Fifth, increasing awareness among the students to switch off lights and other equipment when leaving their rooms. Sixth, the institute electric production should be shifted to solar as it is cheaper in the long run and will end up saving tons of Co2 being put into the atmosphere.

G. Measure amount saved by ECOS

The EAT recommendation were analyzed to calculate the amount of energy saved. The detail of the amount of energy saved has been provided in table.5. The biggest saving of 20.8% is achieved by replacing the old air-condition technology with Dc-inverter technology. Due to lack of equipment the data for window glazing was assumed from (Mehmood and Answar, 2017) and gives an insight into how potentially 10% addition energy can be saved, Further more Improving the HVAC efficiency by proper maintain ace can also beneficial as it can save another 2%.

V. Conclusions

The EAT process concluded that the institutes power consumption can be reduced. In this study a level 1 audit was conducted to a residential engineering university which produced a list of energy saving opportunities. 20.8% of the annual building energy consumption can be saved. Furthermore another 10% of the annual energy consumption can be saved as well as 2% of energy consumption can be reduced.

The EAT process concluded that the institutes power consumption can be reduced. In this study a level 1 audit was conducted to a residential engineering university which produced a list of energy saving opportunities. 20.8% of the annual building energy consumption can be saved. Furthermore another 10% of the annual energy consumption can be saved as well as 2% of energy consumption can be reduced.

Ultimately, 32.8% of the total energy of the energy can be saved if the recommendation by the EAT are implemented. The reduction in CO_2 emission due the recommendation is 719 tons per year. The final decision of implementation of these recommendations is left to the institute

Acknowledgements

The author would like to express his gratuity to Ghulam ashiq khan institute of Engineering and Applied science for funding this research. In particular, all the staff members for providing value information about the institute power usage.

References

Al-Homoud, M.S., 1997. Optimum thermal design of office buildings. Int. J. Energy Res. 21, 941–957. https://doi.org/10.1002/(SICI)1099-114X(199708)21:10<941::AID-ER302>3.0.CO;2-Y

Anderson, S.T., Newell, R.G., 2004. Information programs for technology adoption: The case of energy-efficiency audits. Resour. Energy Econ. 26, 27–50. https://doi.org/10.1016/j.reseneeco.2003.07.001

ASHRAE, 2006. ANSI/ASHRAE Standard 100-2006, Energy Conservation in Existing Building, Atlanta: American Society of Heating. Refrig. Air-Conditioning Eng. Inc., Atlanta, GA.

Bauer, M., Scartezzini, J.L., 1998. A simplified correlation method accounting for heating and cooling loads in energy-efficient buildings. Energy Build. 27, 147–154. https://doi.org/10.1016/s0378-7788(97)00035-2

Botsaris, P.N., Prebezanos, S., 2004. A methodology for a thermal energy building audit. Build. Environ. 39, 195–199. https://doi.org/10.1016/j.buildenv.2003.08.016

Butala, V., Novak, P., 1999. Energy consumption and potential energy savings in old school buildings. Energy Build. 29, 241–246. https://doi.org/10.1016/s0378-7788(98)00062-0

Chirarattananon, S., Taveekun, J., 2004. An OTTV-based energy estimation model for commercial buildings in Thailand. Energy Build. 36, 680–689. https://doi.org/10.1016/j.enbuild.2004.01.035

Chirarattananon, S., Taweekun, J., 2003. A technical review of energy conservation programs for commercial and government buildings in Thailand. Energy Convers. Manag. 44, 743–762. https://doi.org/10.1016/S0196-8904(02)00082-1

Daylighting and its implications to overall thermal transfer value (OTTV) determinations, 2003. . Fuel Energy Abstr. 44, 175. https://doi.org/10.1016/s0140-6701(03)81945-8

Deng, S.M., Burnett, J., 2000. Study of energy performance of hotel buildings in Hong Kong. Energy Build. 31, 7–12. https://doi.org/10.1016/S0378-7788(98)00067-X

Escrivá-Escrivá, G., Álvarez-Bel, C., Valencia-Salazar, I., 2010. Method for modelling space conditioning aggregated daily load curves: Application to a university building. Energy Build. 42, 1275–1282. https://doi.org/10.1016/j.enbuild.2010.02.020

Eskin, N., Türkmen, H., 2008. Analysis of annual heating and cooling energy requirements for office buildings in different climates in Turkey. Energy Build. 40, 763–773. https://doi.org/10.1016/j.enbuild.2007.05.008

Laine, J., Saari, M., 1994. Realization of good indoor climate in low-energy office. Build. Environ. 29, 401–408. https://doi.org/10.1016/0360-1323(94)90041-8

Larsen, A., Jensen, M., 1999. Evaluations of energy audits and the regulator. Energy Policy 27, 557–564. https://doi.org/10.1016/S0301-4215(99)00033-6

Leung, T.M., Chau, C.K., Lee, W.L., Yik, F.W.H., 2005. Willingness to pay for improved environmental performance of the building envelope of office buildings in Hong Kong. Indoor Built Environ. 14, 147–156. https://doi.org/10.1177/1420326X05052562

Li, D.H.W., Wong, S.L., Lam, J.C., 2003. Climatic effects on cooling load determination in subtropical regions. Energy Convers. Manag. 44, 1831–1843. https://doi.org/10.1016/S0196-8904(02)00189-9

Li, J.S.M., 2008. A study of energy performance and efficiency improvement procedures of Government Offices in Hong Kong Special Administrative Region. Energy Build. 40, 1872–1875. https://doi.org/10.1016/j.enbuild.2008.04.011

Mehmood, T., Answar, 2017. Building energy consumption analysis, :Energy saving M.S. Alhomoud, Optimum thermal design of office buildings. Pakistan J. Eng. Appl. Sci. 21, 1–10.

Mills, E., Friedman, H., Powell, T., Bourassa, N., Claridge, D., Haasl, T., Piette, M.A., 2004. THE COST-EFFECTIVENESS OF COMMERCIAL-BUILDINGS COMMISSIONING A Meta-Analysis of Energy and Non-Energy Impacts in Existing Buildings and New Construction in the United States, Lbnl – 56637.

Saad Al-Homoud, M., 2001. Computer-aided building energy analysis techniques. Build. Environ. 36, 421–433.

Vine, E., Lee, E., Clear, R., DiBartolomeo, D., Selkowitz, S., 1998. Office worker response to an automated venetian blind and electric lighting system: A pilot study. Energy Build. 28, 205–218. https://doi.org/10.1016/s0378-7788(98)00023-1

Waltz, J.P., 2000. Computerized building energy simulation handbook.

YIK, F., 2004. An evaluation of the appropriateness of using overall thermal transfer value (OTTV) to regulate envelope energy performance of air-conditioned buildings. Energy. https://doi.org/10.1016/s0360-5442(04)00076-3

Effects and critical analysis for Carbon Emission Estimation in the Transportation Sector

[1]Ruba Al-Foraih, [2]K. J. Sreekanth
Kuwait Institute for Scientific Research, Energy Efficiency Technologies Program, Energy and Building Research Center, Shuwaikh,13109, Kuwait

E-mails:rforaih@kisr.edu.kw[1]
sreekanthkj@kisr.edu.kw[2]

Abstract
Road transportation and the corresponding GHG emissions are one of the major causes of environmental pollution in almost all countries, and Kuwait is not an exception. Emissions of CO2, NOx, CO, and CH4 due to the operation of vehicles lead to environmental pollution and serious health issues. This research focuses on the use of Effects and Criticality Analysis (ECA) which identifies how a product, service, or process can fail –for analyzing the effects and associated risk assessment due to these emissions. A structured approach is made in this study to estimate the risk associated with specific failure causes and prioritize the actions to reduce the risk of failure. ECA requires identifying different possible failure modes of the present road transportation system, their frequency, and potential causes in conjunction with the emission sector. The standard ECA process evaluates failure modes for occurrence, severity, and detection. The focus of this study was mainly on automobiles' fuel consumption, energy consumption, and emissions produced by private vehicles. ECA was made to calculate these measures and predict them for the future. The multiplication of the parameters leads to what is known as the Risk Priority Number (RPN). A rating is assigned for severity, occurrence, and detection to calculate RPN for each failure mode and to select the first five high priority failure modes to be used in the improvement phase, as they are approximately 70% of all RPN. The reason for 70% comes from the Pareto principle. Based on the obtained results, some important recommendations were made such as, service intervals for the optimum time to change the filter, tire pressure check at regular intervals, tire inflation its effect, the effect of carrying excess weight, vehicle idling time and its effect on fuel consumption, and the harmful effect of CO2 into the atmosphere.

Keywords: Fuel consumption, energy consumption, emissions, exhaust gases, ECA.

I. Introduction
Transport represents the major oil consumer sector in the world and therefore one of the main concerns for climate change and energy security of supply policies of any country. Internationally , 98% of the energy consumption from transportation is through oil (Ruamsuke, Dhakal, & Marpaung, 2015)[3]. Road transportation in the Middle East countries is mostly dependent on private vehicles, while the influence of carbon dioxide (CO_2), particulate matter (PM), volatile organic compounds (VOCs), nitrogen oxides (NO_x), carbon monoxide (CO), sulfur dioxide (SO_2) and other green house gases (GHG) are major worries to global warming (Sreekanth et al. 2018)[8]. Kuwait is not different, utilizing nearly 20% of its total energy expenditure on its transportation sector, and this figure is estimated to increase higher in the next decade (Al-Foraih et al. 2018)[7].
This paper will assess the risk associated with specific failure causes and prioritize the actions to reduce the risk of failure. Effects and Criticality Analysis (ECA) will identify various possible failure modes for the current road transportation system in Kuwait and the frequency of their occurrence as well as the potential causes in conjunction with the emission sector.

II. Methodology
Failure Mode Effect Analysis (FMEA) is a tool to recognize the ways in which a product, service, or process can fail. A structured method is to identify the risk associated with specific failure causes and review the actions to lessen risk of failure. FMEA requires recognizing failure mode of a specific product or system, its frequency, and potential causes (Rowlands et al., 2004) [5]. The standard FMEA process

appraises failure modes for occurrence, severity and detection. The multiplication of these values leads to what is known as Risk Priority Number (RPN) (Rana et al., 2018) [4].

$$RPN = Severity * Occurrence * Detection$$

Severity

The measure of severity is a scale to gage how critical the consequence is on the performance of the element under examination. The ranking scale is measured from 1 to 10, where 1-2 indicates the impact to be minimal to the element and 10 to be catastrophic, producing possible destruction to the element. In this paper the severity scale refers to the impact the identified effects will have on the functioning of private vehicles, (Dargahi et al., 2005)[2].

Occurrence

The scale of occurrence is a figure accomplished by evaluating the situation and judging its likelihood of failure. An occurrence rating scale of 1-2 refers to the probability of the failure as unlikely to happen, where a rating scale of 10 suggests it is highly probable the failure will occur, (Dargahi et al., 2005)[2].

Detection

The detection rate scale is created by initially categorizing the control element which will stop the effect from occurring, and prevent it from occurring. This paper will study the detection rate scale for the environmental features concerning private vehicles. A scale of 1-2 shows very high chance that the failure effect will be detected and controlled where a scale of 10 shows that failure effect was not detected and it cannot be controlled, (Dargahi et al., 2005)[2].

III. Results & Recommendations

The likely failure modes and their causes and effects are identified for driving a private vehicle in Kuwait. The scale rating for severity, occurrence and detection are assigned and the RPN is calculated for each failure mode. The RPN is then studied to choose high priority failure modes for Kuwait. Nine potential failure modes are decided for the vehicle, (Keyvanfar, 2018)[3].
The severity, occurrence and detection rating scales for these failure modes are established as shown below in table 1 and the RPN calculated.

Table 1. Risk Priority Number (RPN) for Identified Failure Modes.

Failure Causes	Severity Rating Scale	Occurrence Rating Scale	Detection Rating Scale	Risk Priority Number (RPN)
Clogged air filters	5	8	8	320
Accelerating rapidly	5	5	6	150
High speed driving	5	7	4	140
Idling for long periods of time	5	7	6	210
Dirty carburetors	5	5	5	125
Carrying excess weight in the vehicle	5	8	6	240
Use of incorrect oil for the engine	5	3	6	90
Unbalanced tire pressure.	5	8	7	280
Irregular oil change	5	7	5	175

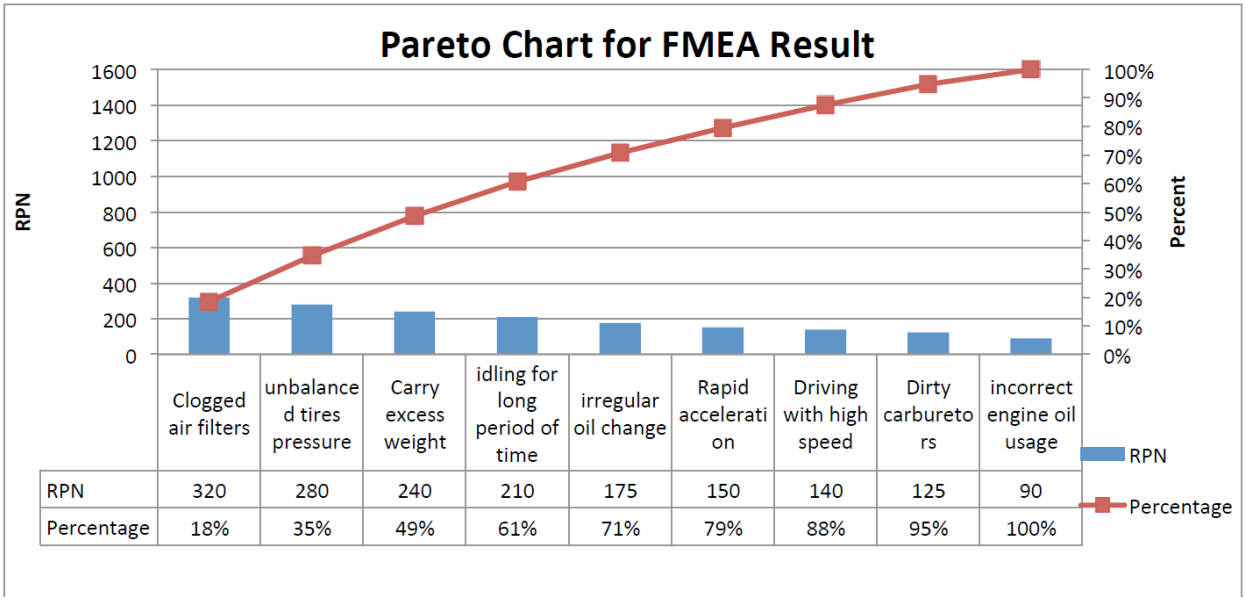

Fig 1: Pareto chart for FMEA result

The potential failure effects for these failure modes are surplus fuel consumption directing to an upsurge of pollutant emissions such as carbon dioxide (CO_2), particulate matter (PM), volatile organic compounds (VOCs), nitrogen oxides (NO_x), carbon monoxide (CO), sulfur dioxide (SO_2) and other greenhouse gases (GHG) resulting in poor air quality which affect human health and lead to climate change. The control elements to avoid the failure effects are systematic vehicle service and maintenance as well as abiding by the legal speed limit.

Private vehicle owners must follow their vehicle's safety strategies and standards to reduce or eliminate the risks allied with high priority failure modes. Some reasons for failure include clogged air filters and unbalanced tire pressure. Below is a list of recommendations the driver should follow to reduce the effect of the failure mode, (Alessandrini, 2009)[1].

1. Regular vehicle examination and stick to the maintenance service schedule.
2. Monthly tires inspection for uneven wear. Check for proper tire inflation as under-inflated tires burn more fuel, hence releasing more harmful gases.
3. Do not let the vehicle idle for more than a minute. As idling consumes half a gallon to one gallon of gas per hour and pumps useless carbon dioxide into the atmosphere.
4. Switch off the vehicle when waiting in spot to prevent discharging harmful emissions to the environment.
5. Avoid uncontrolled driving as it burns more fuel triggering an increase of pollutants.
6. Keep the correct level of your vehicle's engine oil, brake fluid and coolant with regular top-ups and holding the other mechanical parts well lubricated helps smooth functioning of your vehicle and lessens making emissions.
7. Overloading the vehicle with needless weight damages the stability of the vehicle. It has unyielding effects on the suspension, tires and the chassis. Overloading the vehicle causes it unstable, influences acceleration, affects the braking system, and also lead to breakdowns or accidents. It overextends the vehicle, which leads to burning more fuel, which in turn emits pollutants to the environment.
8. Monitor the cooling system as it can produce the vehicle to overheat.
9. Watch for your vehicle's warning lights.
10. Avoid driving at high speeds and accelerating rapidly , especially when it's very hot or very cold outside. This will burn more fuel and emit carbon dioxide and other greenhouse gases to the environment.

11. Avoiding speeding, fast starts, stops, and turns potholes and objects on the road. Do not burn rubber. As this leads to emitting harmful pollutants to the environment.
12. Put less strain on your engine and automatic transmission by shifting to neutral at red lights. Else , the engine is still working to thrust the vehicle even though it has stopped and releases harmful gases.

IV. Conclusions

The potential failure modes for the current road transportation system in Kuwait were recognized and recommendations to prevent them were described above. Following these recommendations will unavoidably lead to a decrease in fuel consumption and decrease harmful emissions. These emissions include carbon dioxide (CO_2), particulate matter (PM), volatile organic compounds (VOCs), nitrogen oxides (NO_x), carbon monoxide (CO), sulfur dioxide (SO_2) and other greenhouse gases (GHG) released from vehicles which are supposed to instigate global warming as well as cancer and noncancerous health effects, such as neurological, cardiovascular, respiratory, and reproductive and immune system injury.

References

[1] Alessandrini, A., Cattivera, A., Filippi, F., & Ortenzi, F., (2009). Driving Style Influence on Car CO2 emissions. Via Eudossiana 18, 00184 Rome, Italy.

[2] Dargahi, M., Naderi, S., Hashemi, S., Aghaiepour, M., Nouri, Z., & Sahneh, S., (2016). Use of FMEA Method for Environmental Risk Assessment in ore Complex on Wildlife Habitats, Human and Ecological Risk Assessment: An International Journal.

[3] Keyvanfar, A., Shafaghat, A., Muhannad, N., & Ferwati M., (2018). Driving Behaviour and Sustainable Mobility- Policies and Approaches Revisited. Open Access Journal, vol. 10(4), pages 1-27.

[4] Rana, M., Zhang, X., & Abdul Akher, S., (2018). Determination of Factors and Quality Control of Car Painting Based on FMEA and SPC.V2. 8,158-177

[5] Rowlands, D., Micheal, G., Maxey, J. & Upton, M. (2004). Failure Mode Effects Anaysis. *The Lean Six Sigma Pocket Toolbook*. 241-244 .

[6] Ruamsuke K, Dhakal S, Marpaung COP. Energy and economic impacts of the global climate change policy on Southeast Asian countries: a general equilibrium analysis. Energy 2015;81:446–61.

[7] R. Al-Foraih, Sreekanth. K. J., A. Al-Mulla, A techno-economic analysis of the integration of energy storage technologies in electric power systems, Journal of Renewable and Sustainable Energy 10, 054102 (2018), doi: 10.1063/1.5024965.

[8] Sreekanth. K. J., R. Al-Foraih, A. Al-Mulla, B. Abdulrahman., “Feasibility analysis of Energy Storage Technologies in Power Systems for Arid Region”. Journal of Energy Resources Technology, ASME, 141(1), 011901 (2018), Paper No: JERT-18-1271; doi: 10.1115/1.4040931.

Development of Virtual Sensors for Prediction of Flue Gas Composition of a Cement Plant using Ensemble Learning Technique

[1]Usman Jadoon, [1*]Iftikhar Ahmad, [1]Arshad Hussain, [2*]Brenno Menezes
[1] Department of Chemical Engineering, National University of Sciences and Technology, Islamabad, Pakistan
[2] Hamad Bin Khalifa University, College of Science and Engineering, Division of Engineering Management and Decision Sciences, Qatar Foundation, Doha, Qatar

* E-mails: iftikhar.salarzai@scme.nust.edu.pk, bmenezes@hbku.edu.qa

Abstract
The cement industry is one of the largest sources of CO_2 emission to the environment. To minimize the pernicious impact of the CO_2 emission on the environment, CO_2 capturing has been the focus of research. Sour compression technique (SCU) is one of the most commonly used techniques for CO_2 capture. For a stable and efficient operation of SCU, a robust sensing and control system is vital. The data-based model also termed as data-based virtual sensors have been attracting attention in the process industry for enhancement and replacement of the conventional hardware sensors such as flow meter, pressure gauge, and composition analyzer. In this study, a data-based virtual sensor is designed to relate process conditions such as temperature, pressure and flow rate to the carbon-capturing capability of SCU. An Aspen Plus based model of the SCU comprising of CO_2 capturing, desulfurization and denitrification processes was developed. To capture the behavior of real-time cement plant operation, the process model was converted to dynamic mode through the interfacing of MATLAB-Excel-Aspen. Four hundred fifty (450) datasets were generated that consisted of process conditions and their corresponding values of the CO_2, SO_2, NO and CO in the process outlet streams. The data was used to develop the virtual sensor using ensemble learning i.e., boosting. Prediction performance of the virtual sensors for CO_2, SO_2, NO, and CO was 98.86%, 99.63%, 99.7%, and 99.9%, respectively. The results demonstrated that the proposed framework can be used effectively for composition monitoring of CO_2, SO_2, NO and CO in the exhaust stream of a cement production plant.

Keywords: Sustainability; soft-sensors; process flow sheeting; greenhouse gases; process industry

I. Introduction:

The cement industry is one of the largest sources of CO_2 emission to the environment. The average emission of 0.9 kg of CO_2/kg of cement produced resulting in a hefty amount of 36 Giga tonnes emissions globally per year (Hills et al., 2015; Salas et al., 2016). To minimize the pernicious impact of the CO_2 emission on the environment, CO_2 capturing has been the focus of research. CO_2 capturing by absorption using chemicals like monoethyl amine or absorption, Sour Compression Unit (SCU), cryogenic distillation, electrochemical pumps, and chemical looping have been used (Songolzadeh et al., 2014; Zheng, 2011). However, SCU has an advantage over other techniques because it uses water for the absorption of NOx and SOx from flue gas (Kühnemuth et al., 2008; White et al., 2013; Yan et al., 2011).

For a stable and efficient operation of SCU, a robust sensing and control system is vital. The data-based model also termed as data-based virtual sensors have been attracting attention in the process industry for enhancement and replacement of the conventional hardware sensors such as flow meter, pressure gauge and composition analyzer (Kano and Ogawa, 2010). Principal component analysis, partial least square, ensemble learning, and artificial neural network are a few methods used for development of database virtual sensors. The ensemble learning works on the idea of developing a robust model by combination of several weak learners/models (Ahmad et al., 2018).

In this study, ensemble learning based virtual sensor is designed to relate process conditions, i.e., temperature, pressure and flow rate, etc., to the carbon-capturing capability of SCU. An Aspen Plus based model of the SCU comprising of CO_2 capturing, desulfurization and denitrification processes was developed. To capture the behavior of real-time cement plant operation, the process model was converted to dynamic mode through the interfacing of MATLAB-Excel-Aspen. The data was used to develop the virtual sensors through ensemble learning i.e., Least-Square Boosting.

Section II of this study is about the detailed description of Process Flow Diagram (PFD) of the purification process of CO2 from typical impurities like SO_2, NO, NO_2, O_2, N_2, and moisture. Whereas section III describes the results and discussion and section IV concludes this study.

II. Process flow sheeting

A process flow diagram (PFD) of SCU developed in Aspen-PLUS is shown in Figure 1 (Meunier et al., 2014) Flue gas containing N_2, CO_2, O_2, NO, SO_2, and moisture are taken from oxyfuel cement plant after de-dusting passed through a two-stage compressor, cooler and flash tank. Then, it enters the first absorber counter currently with water to remove SO_2. Following the process, the gas stream leaves from top of the absorber to the third compressor where compression takes place up to 30 bar. Then, it enters the second absorber where NOx is removed by water. These washed gases are passed for dehydration of any residual moisture. After the treatment process with the flue gas SO_x and NO_x are present in a very minute amount. From Table 2, after the desulfurization and denitrification absorber amount of NO and SO_2 in the gas, they are still presented in traces which shows about the 99% removal of

these two gases.

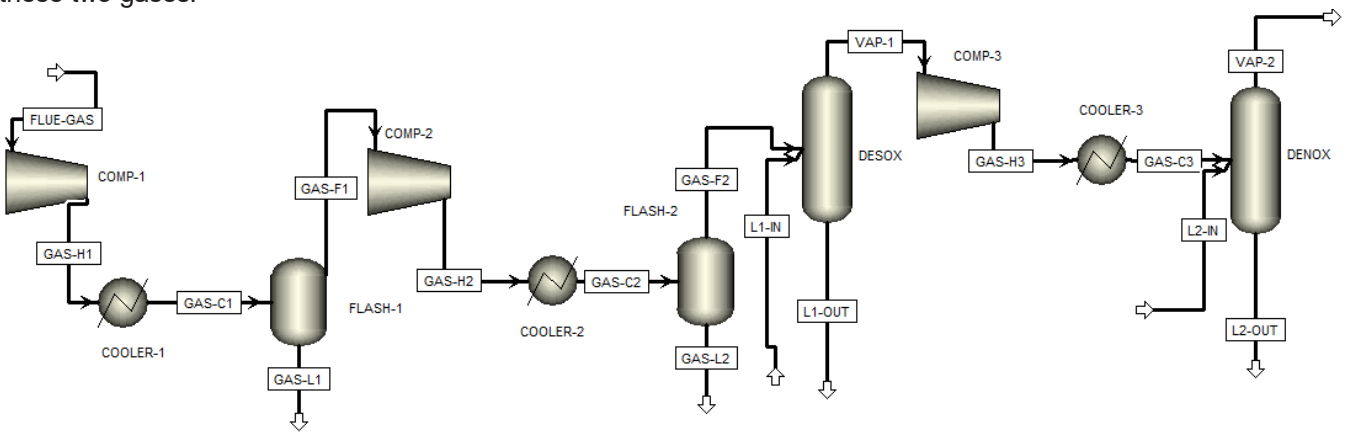

Figure 1: Flow diagram of "Sour Compression Unit"

Two absorption towers work on 15 and 30 bar pressure for the removal of SO_2, NO/NO_2 respectively. Design values of both absorption towers are given in Table 1 with associated flowrates of gases and water used.

Table 1. Design Specification of absorption towers

Design Specification	1st Absorber	2nd Absorber
Calculation type	Equilibrium	Equilibrium
Top stage pressure	16 bar	30 bar
Number of stages	10	10
Flue gas feed stage	10	10
Water feed stage	1 (Top)	1 (Top)
Total liquid flow rate	2339 lbmol/hr	7015 lbmol/hr
Total gases feed rate	7946 cum/h	7873 cum/hr

Data sets are generated through interfacing of Aspen Plus-Excel-MATLAB for creating the possible scenarios of streams condition and their resulting output. A schematic view of data generation and model development is shown in Fig. 2.

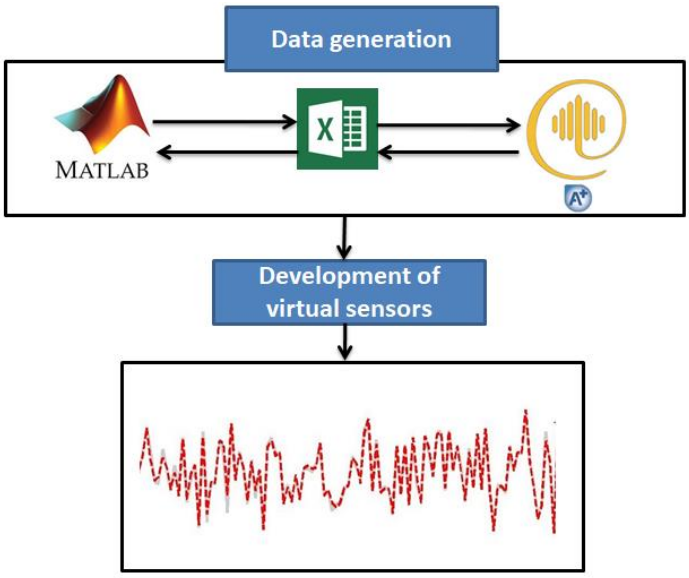

Figure 2: Adopted mechanism of data generation and model developemnt

III. Results and Discussion

This section covers the results by Aspen plus simulation and application of data-based soft sensors to the CO_2 capturing accuracy by SCU. Aspen-Plus based simulation results are given in Table 2 both NO_x and SO_x are presented only in traces after both absorbers. Nine process input variables were selected for ensemble models development by considering flowrate, temperature and pressure of these input variables, see Table 3. In a total of 450 data sets containing input and output were generated, whereby 80% of data generated by interfacing MATLAB-

Excel-Aspen was used for model training while 20% was used for validation. Correlation Coefficient (C-Coeff) among targeted and predicted values of soft sensors was used to analyze prediction accuracy. C-Coeff of soft sensors for CO_2, CO, SO_2 and NO were 0.9965, 0.9975, 0.9906 and 0.9934 respectively.

Table 2. Overall results of the SCU unit

Gas Composition	Flue gas Inlet	DESOx outlet	DENOx outlet
H_2O %	2	1.909	1.169
CO_2 %	24.99	24.788	23.34
N_2 %	58.70	59.461	63.443
O_2 %	7.99	8.081	8.385
CO %	0.29	0.25	0.1
SO_2 %	528ppm	0.241	0.0308 (traces)
NO %	530ppm	3.043	0.330 (traces)
Total cum/hr	7946	7873	7240

Table 3. Process input variables

No	Process Variables	Units	Values
1	Flue Gas Flowrate	Cum/hr	7946
2	Flue Gas Temperature	°C	35
3	Flue gas Pressure	Bar	1
4	L1-IN Flowrate	Lbmol/hr	2339
5	L1-IN Temperature	°C	60
6	L1-IN Pressure	psia	250
7	L2-IN Flowrate	Lbmol/hr	7015
8	L2-IN Temperature	°C	60
9	L2-IN Pressure	psia	1000

Similarly, root mean square error (RMSE) values were evaluated between targeted and predicted values of soft sensors to evaluate standard deviation. RMSE for CO_2, CO, SO_2 and NO were 6.5e-03, 4.07e-06, 9.95e-05 and 1.03e-06, respectively. Figure 3 (a-d), shows the regression analysis along with the results of the LSBoost ensemble in terms of the predicted and targeted values of mass fractions of each gas.

IV. Conclusion

In this study, data based virtual sensors analysis is carried out on the recovery process of CO_2. For soft sensor development, least squares boosting, a kind of ensemble learning technique is used. The sour compression unit was simulated in the Aspen-Plus environment and its data generated by interfacing Excel and MATLAB for soft sensor analysis. The soft sensor incorporation through MATLAB with Aspen-PLUS data indicated the high accuracy of the model developed. Correlation coefficients and root mean square error indicated high prediction accuracy of soft sensors. The accuracy of boosting results of SO_2 and NO removal is 99.6% and 99.7% respectively while CO_2 recovery from SCU unit is 98.9%.

References:

Ahmad, I., Ayub, A., Rashid, M.H., Ansari, F., Mohammad, N., 2018. Sensitivity Analysis of Entrained Flow Coal Gasification Process Through Fourier Amplitude Sensitivity Test (FAST) and Sobol Techniques, 2018 International Conference on Applied and Engineering Mathematics (ICAEM). IEEE, pp. 79-84.

Hills, T., Leeson, D., Florin, N., Fennell, P., 2015. Carbon capture in the cement industry: technologies, progress, and retrofitting. Environmental science & technology 50(1), 368-377.

Kano, M., Ogawa, M., 2010. The state of the art in chemical process control in Japan: Good practice and questionnaire survey. Journal of Process Control 20(9), 969-982.

Kühnemuth, D., Normann, F., Johnsson, F., Andersson, K., 2008. Evaluation of Concepts for secondary SOx and NOx Removal from the Oxy-fuel Process, ICPWS_15, Berlin, Germany.

N. Meunier, S. Laribi, L. Dubois, D. Thomas, and G. De Weireld, "CO_2 capture in cement production and re-use: first step for the optimization of the overall process," *Energy Procedia,* vol. 63, pp. 6492-6503, 2014.

Salas, D.A., Ramirez, A.D., Rodríguez, C.R., Petroche, D.M., Boero, A.J., Duque-Rivera, J., 2016. Environmental impacts, life cycle assessment and potential improvement measures for cement production: a literature review. Journal of Cleaner Production 113, 114-122.

Songolzadeh, M., Soleimani, M., Takht Ravanchi, M., Songolzadeh, R., 2014. Carbon dioxide separation from flue gases: a technological review emphasizing reduction in greenhouse gas emissions. The Scientific World Journal 2014.

White, V., Wright, A., Tappe, S., Yan, J., 2013. The air products Vattenfall oxyfuel CO2 compression and purification pilot plant at Schwarze Pumpe. Energy Procedia 37, 1490-1499.
Yan, J., Anheden, M., Winkler, F., Schoedel, N., Ritter, R., Biele, M., Kaß, H., 2011. CO2 Processing Experiences for Oxyfuel Combustion CO2 Capture-Based on Results from Vattenfall's 30 MWth Oxyfuel Pilot Plant, 2nd Oxyfuel Combustion Conference. pp. 12-16.
Zheng, L., 2011. Oxy-fuel combustion for power generation and carbon dioxide (CO2) capture. Elsevier.

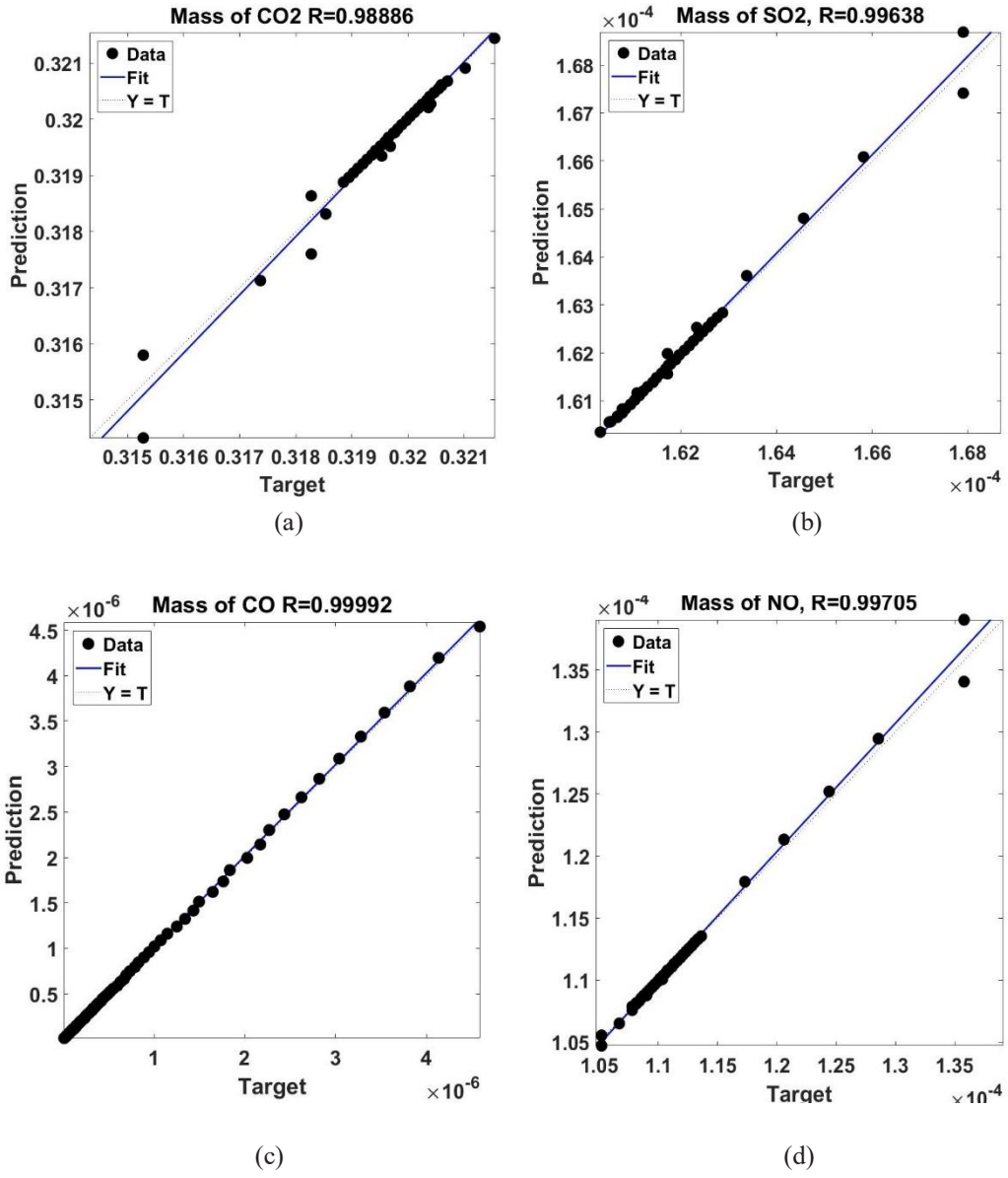

Fig. 3. Regression performance of ensemble model for prediction of mass fractions of (a) CO_2, (b) SO_2, (c) CO and (d) NO

MODEL-BASED QUALITY, EXERGY AND ECONOMIC ANALYSIS OF FLUIDIZED BED MEMBRANE REACTORS

[1]Tabassam Nafees, [1]Adnan Ahmed, [1*]Iftikhar Ahmad, [2]Brenno Menezes, [1]Muhammad Ahsan
[1]Department of Chemical Engineering, National University of Sciences and Technology, H-12 Islamabad, Pakistan
[2]Hamad Bin Khalifa University, College of Science and Engineering, Division of Engineering Management and Decision Sciences, Qatar Foundation, Doha, Qatar
* E-mails: iftikhar.salarzai@scme.nust.edu.pk

Abstract
Naphtha reforming units are of great interest for hydrogen and reformate production in petroleum refineries. Conventionally employed packed bed reactors for naphtha reforming have drawbacks such as a high pressure drop, diffusion limitations in catalyst, and radial and axial gradients of temperature and concentration. A fluidized bed reactor (FBR) attends to some of the draw backs of packed bed reactor. Coupled with the advantages of fluidization, the incorporation of membrane can improve the yield of products by selectively removing hydrogen from the reaction side. In this work, a sequential modular simulation (SMS) approach was adopted to simulate hydrodynamics of a fluidized-bed membrane reactor (FBMR) for catalytic reforming of naphtha in Aspen Plus. Aspen Plus was used for flowsheet development of the FBMR. The hydrodynamic parameters and membrane permeation phenomena were implemented using an interfacing of Excel with the Aspen Plus model of the FBMR. A fluidizedbed reactor without membrane, i.e., FBR, was also modeled for comparison with FBMR. FBMR outperformed the FBR in terms of increase in aromatics in reformate stream, effective separation of hydrogen during the reaction, chemical exergy efficiency, and economic viability. The proposed method can be readily adopted by process engineers for design and optimization decisions.

Keywords: Naphtha catalytic reforming, Aspen Plus, Excel interfacing, Two-phase theory of fluidization, Hydrogen production

I. Introduction

The catalytic reforming of naphtha is a process utilized for conversion of low-octane, straight-run naphtha into high-octane reformates which are then blended in gasoline to boost its octane rating. It is also a source of BTX (benzene, toluene, xylene isomers) which are important precursors for further chemical synthesis. A considerable amount of hydrogen gas is also produced in the process which is utilized in the refinery or other applications (Ancheyta, 2011; Ciapetta and Wallace, 1972) Gasoline is still the fossil fuel of choice in terms of transportation although its combustion products are recognized as a source of global warming. In order to mitigate environmental concerns, various legislations are passed one of which is requirement of high research octane number (RON) (Rahimpour et al., 2013). RON is the quality parameter of gasoline that shows how much compression it can withstand without knocking in a gasoline engine. The octane number of gasoline is conveniently boosted by use of catalytic reforming and it is carried out in three or four radial or axial flow fixed bed reactors. Mode of operation is semi-regenerative, cyclic or the newer continuous regenerative types classified according to their severity, and mode of catalyst regeneration. A packed bed reactor (PBR) is used conventionally for naphtha reforming. It is a fixed bed type of reactor in which the catalyst is placed in a dumped arrangement. Catalyst particle size is kept at a value which is a compromise between pressure drop and increased surface area. Larger particles provide less resistance to gas flow but have low particle effectiveness factor (Patil et al., 2005). Reducing the particle size increases area for mass transfer but the resulting low voidage causes excessive pressure drop. The desired (forward) reaction can be boosted by selective removal of the products from product gases (Barbieri et al., 2001; Lamm and Melin, 2001). In this context, one idea worth exploring is using a fluidized catalyst bed reactor with Pd membrane-based walls for naphtha reforming which is the focus of this work. This mode of reactor configuration enables simultaneous, in situ removal of hydrogen from product gases, which increases the production of aromatics as the reactants pass through the reactor. In membrane reactor, the walls are replaced with a perm-selective membrane material.
Developing membrane reactor technology carries significance because it also increases hydrogen production. In reported studies, palladium and its alloys such as palladium-copper (Howard et al., 2004), palladium-silver (Barbieri and Di Maio, 1997; Shu et al., 1994) and palladium (Keuler and Lorenzen, 2002) have been used inside the membrane reactors. For synthesis of methanol, Rahimpour and Ghader proposed membrane reactors with Pd–Ag membrane and pure Pd membrane (Gobina et al., 1995; Itoh, 1987). (Pasha et al., 2019) developed Excel interfacing with Aspen Plus to simulate FBMR for steam methane reforming. Tosti et al. have experimented with different configurations of palladium-based membrane reactors for extraction of ultra-pure hydrogen (Tosti et al., 2008). (Roy et al., 1998) focused on the simulation of membrane based fluidized bed reformers and its economic aspects. (Khosravanipour Mostafazadeh and Rahimpour, 2009) and (Rahimpour et al., 2011) presented the concept of membrane assisted naphtha reformer and studied the effects of in-situ hydrogen separation in a packed-bed reactor and fluidized bed reactor for naphtha reforming. Results presented showed an enhancement of aromatics along the reactor. In another study, (Sarvar-Amini et al., 2007) studied the effects of combining the endothermic naphtha reforming reaction and hydrogenation of aniline to nitrobenzene in a thermally coupled fluidized-bed reactor. Modeling of a membrane reactor is a challenging task because of simultaneous occurrence of diffusion coupled with mass transfer and chemical reaction inside the reactor (Reactor, 1987). The studies on FBMR in naphtha

reforming used MATLAB or FORTRAN that are not readily accessible to design engineers in the process industry. Other than these theoretical studies not much have been explored and thus very few are available in the literature of fluidized-bed naphtha reformers within situ hydrogen separation via membrane.

In this study, an FBMR for naphtha reforming is developed on the Aspen Plus platform with Excel interfacing. Aspen Plus is a widely employed process simulator for industrial process simulations. The physical phenomena pertaining the FBMR are implemented by utilizing the hydrodynamics theory as an integrated sub-model and chemical reactions are conveniently implemented by built-in power law input panel of Aspen Plus. Ideal reactor models are available as modules in Aspen Plus and are combined in a sequential manner to mimic the behavior inside the fluidized bed membrane reactors (Mazzieri et al., 2009). Excel is used for supplying of hydrodynamic parameters to Aspen for calculation of volumes and voidage in CSTR and PFR blocks of Aspen Plus. Exergy and economic analysis of the FBMR and FBR models are performed to have a comparative view of the exergy efficiency and economic viability.

The reforming process is described in section 2. An industrial setup for a semi-regenerative reformer is taken as an example from literature where three packed bed reformers are used. Section 3 details the model building and flow sheeting process in the Aspen Plus environment with Excel interfacing. Results from the simulation are discussed and compared with FBR in section 4 followed by conclusions in section 5.

II. Process Description

During the naphtha reforming process, the low-octane hydrocarbons are modified to yield high value reformate for addition to the reformate pool. During the reconstruction, the boiling point range of naphtha does not change significantly. Typically, a naphtha reformer feed is a mixture composed of the following: straight–run naphtha: 30 to 90 °C is light naphtha (C5 and C6), 90 to 150 °C is medium–weight naphtha (C7 and C9), and 150 to 200 °C is heavy naphtha (C9 and C12). Straight-run naphtha constitutes typically 15 to 30 wt% of the crude oil. It is obtained directly from the atmospheric crude oil distillation column and is a mixture of paraffin, naphthenes, and aromatics in the C5– C12 range and boiling point between 30 and 200 °C.

Reformer operating conditions require that the feed be heated at high temperature (~770 K, 3.7 MPa). Reactions are carried out under high hydrogen partial pressure to reduce catalyst deactivation due to coking. Typically, 3-4 serially connected fixed-bed reactors are employed for reforming with inter-stage heating. The feed gas is pre-heated with heat exchange from the effluent of the last reactor. Heat exchangers are usually of shell and tube type. As the reforming reactions are endothermic, effluent from each reactor requires reheating to compensate for temperature drop and related rate of reaction decline.

As shown in Figure 1, the feed and recycle hydrogen is mixed in specific proportion to maintain the H2/HC ratio around 4 and preheated by products from the final reactor. The preheated feed is brought to the reaction temperature of 777 K in the feed heater and fed to the first reactor. Reactors are loaded with Pt-Re catalysts on an alumina support. The catalyst is bi-functional, the alumina provides acid function and Pt-Re provides the metal function for dehydrogenation of naphthenes. The partially reacted effluent from reactor 1 is brought up to reaction temperature in heater 2 and becomes feed to reactor 2. With the passage through reactors, rates of reaction drop resulting in increased reactor volume. There is also a notable drop in endothermicity of reactions and consequently the heating requirements also decrease. The product stream from the third reactor is first precooled with incoming feed and is sent to flash separator vessel where the liquid and gaseous components are separated. Cooling of product stream is required due to its high temperature. A drop in temperature affects the separation of lighter gases from reformate liquid. Flashed-gas contains hydrogen along with products of cracking mainly small quantity of light gases namely methane, ethane, propane, and butanes. The hydrogen from flash separator is split into two parts. One part is compressed and added to naphtha feed to maintain inlet H2/HC ratio. Liquid product from the bottom is sent to the fractionation section (stabilizer).

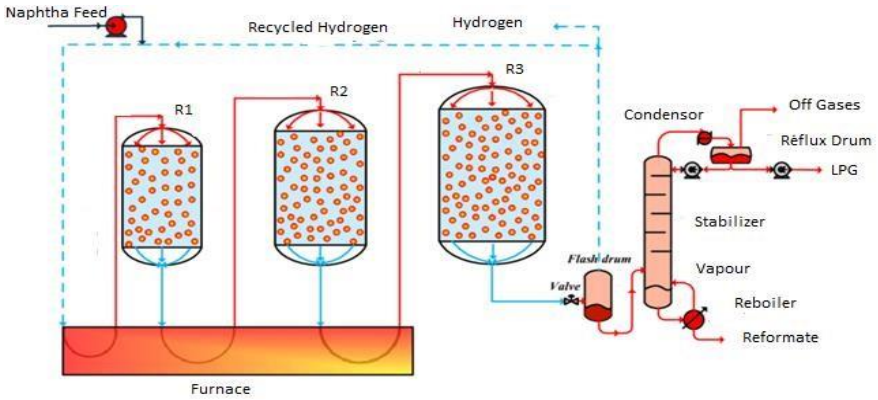

Fig. 1: PFD for Conventional Catalytic Naphtha Reforming Process.

The dehydrogenation reaction is the main reaction responsible for the rise of RON value (Benitez et al., 2007). Temperature drops by almost 50 °C in the first reactor which essentially quenches other reactions and thus requiring reheating of reactants in conventional refinery system. In order to maintain the inlet condition of each reactor for

membrane system, a heat exchanger is used to accommodate the changes in pressure and temperature. A bi-functional catalyst is employed for the reforming process. The two functions are actually metallic and acidic in nature and are needed for different reactions. Hydrogenation and dehydrogenation reactions are catalyzed by the metal function while the acid function promotes the isomerization and cyclization reactions (Froment, 1987; Marin et al., 1983; Smith, 1959) The dehydrogenation reaction which is the dominant reaction has been studied and reported in the literature. The first reported study was from (Ramage et al., 1980) which included dehydrogenation in his 4 lumped model. Other variations of Smith's model have been proposed later with the passage of time. (Ancheyta-Juárez and Villafuerte-Macías, 2000; HOU et al., 2006; Hu et al., 2004; Iranshahi et al., 2013; Padmavathi and Chaudhuri, 1997; Pasha et al., 2019) have performed detailed studies regarding reforming kinetics and have included pertinent reactions. The dehydrogenation reaction scheme is presented in Table 1 (Iranshahi et al., 2013).

III. Analysis

To fluidize a fixed bed, the catalyst particles are crushed to a small size (100 microns). An FBMR scheme for naphtha reforming is depicted in Fig. 2. During the reforming process, heat and mass transfer process occurs within the reactor creating a hydrogen partial pressure gradient which results in a net transfer of hydrogen to the shell side. This transfer of excess hydrogen results in displacing the reaction toward the formation of more product. The fluidization of catalyst particles is carried out by feeding the catalyst filled reactor with gas from bottom through a porous plate distributor. Hydrogen gas is used as sweep gas in the shell compartment where its flow is co-currently with the reactant gas. Fluidization results in a very low pressure drop even using a very small catalyst size which would not be feasible in a fixed bed. The membrane material of choice is a palladium-silver alloy combining the excellent perm selectivity of palladium with silver providing mechanical stability. Hydrogen gas in the product permeates through the membrane surface, which results in displacement of equilibrium in the forward direction and thus both reformate and hydrogen yield is increased but due to the separation of hydrogen from each reactor in the membrane based fluidized bed reactor the hydrogen yields consequently decreases owing to the compositional difference with the fixed bed reactor. The hydrogen permeation process is shown in Figure 3. Inside the shell, set-up of a vacuum or hydrogen as the sweep gas, the pressure of which is a manipulated variable to control the driving force for hydrogen permeation. The membrane simulated is of 20 μm thickness. The Pd–Ag (23% Ag) membrane is on a stainless-steel support. Membrane length is equal to 6.29 m and its area is 30.02 m2.

Table 1. Dehydrogenation reactions with rate constant and heat of reaction data.

$ACH \leftrightarrow A_n + 3H_2$	$r_{1n}=k_{1n}\left(P_{ACHn}-\frac{P_{An}P_{H2}^3}{K_{1n}}\right)$	$k_{1n}=exp\left(a-\frac{E}{RT}\right)$ $(kmol.kg_{cat}^{-1}.h^{-1}.kPa^{-1})$		$K_{1n}=exp\left(A-\frac{B}{T}\right)$ $(kPa)^3$	
	$\triangle H\left(\frac{kJ}{molH_2}\right)$	a	$\frac{E}{R}\times 10^{-3}$	A	B
C_6	68.73	18.75	19.50	59.90	24800
C_7	208.47	20.70	19.50	60.23	25080
C_8					
for A_n = MX*	64.50	17.89	19.50	60.37	23270
for A_n = OX*	65.10	19.15	19.50	60.32	23490
for A_n = PX*	64.74	18.66	19.50	60.13	23360
for A_n = EB*	68.70	18.71	19.50	60.40	24780
C9+	66.05	20.38	19.50	61.05	21330

* improvements made to the Padmavathi et al. model.

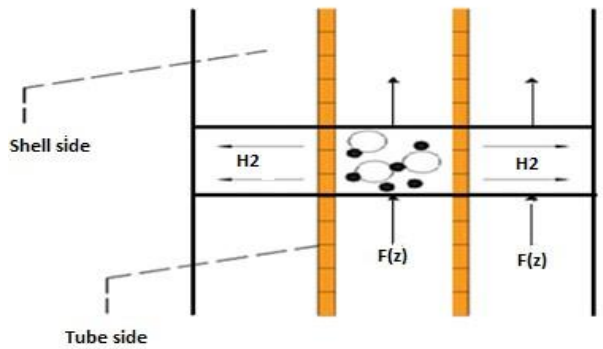

Fig. 2: FBMR Model (Yun and Ted Oyama, 2011)

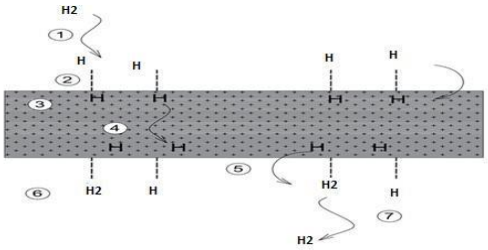

Fig. 3: Hydrogen Permeation from Walls (Yun and Ted Oyama, 2011)

A fluidized bed is not an ideal reactor thus its hydrodynamics cannot be represented simply by a plug flow type or perfectly mixed type model. Two distinct phases can be identified in a fluidized bed: emulsion phase and bubble phase. An excel calculator block is developed for calculation of hydrodynamic parameters using the two-phase theory of fluidization that calculates catalyst weight and distribution and volume of CSTR and PFR combination.

Preliminary Assumptions:

- The dense catalyst bed has two identifiable phases: a bubble phase and an emulsion phase
- Steady-state and pseudo-steady-state operation is assumed
- Much of the reactions occur within the emulsion phase
- Permeation of hydrogen is assumed to occur from the emulsion phase only
- Hydrogen diffuses through the membrane radially
- Assumption of spherical bubbles hold
- Movement of gas in bubbles is assumed to follow plug flow and due to very low quantity of catalyst the reaction rates are very low compared to emulsion gas phase velocity
- Contents of the bed are well mixed and both emulsion and bubble phase are at a uniform temperature
- Adiabatic conditions.
- The membrane is 100% perm-selective for hydrogen.
- Sieverts' law is applicable for hydrogen permeation through the membrane (Sieverts, 1935) Eq (A).

$$Q_{H_2} = \eta k C_{mp}\left[P_{RH_2}^{0.5} - P_{MH_2}^{0.5}\right]e^{\left(-\frac{E_a}{RT}\right)} \qquad Eq\ (A)$$

The following sub-section describes the membrane integration within Aspen Plus and the combination of CSTR and PFR reactor with the membrane module to simulate the overall FBMR process. An Excel calculator block is developed which calculates hydrodynamic parameters of the fluidized bed. The equations used from the literature are presented in Table. 2. The output from this block is transferred to CSTR and PFR units through an internal Excel interface and transfer modules. A fluidized bed exhibits complex hydrodynamics. To model its behavior, the dense bed is divided into bubble phase and an emulsion phase. Membrane permeation occurs simultaneously with reaction. Gas flowing in the form of bubbles is modelled as flowing through a plug flow reactor and the gas flowing though the emulsion phase is modelled as flowing through a mixed flow reactor or CSTR. In this way the fluidized bed reactor is represented by

PFR and CSTR which are available standard modules in Aspen Plus. A separate 'SPLT' Excel file is used to implement equations described in Table 2. After evaluating the hydrodynamic parameters, the data is transferred to Aspen Plus which uses its internal database to calculate thermodynamic properties based on material and energy balance equations. The effluent streams from each section is then transferred to the 'TRF' Excel block where mass transfer equation (in the case of FBR) and additionally Sievert's equation (in the case of FBMR) is implemented. Afterwards the exit streams are transferred to respective PFR and CSTR for the next section (i+1). Calculations then proceed in this manner until they reach the top most section of the bed.The membrane performance is affected by non-uniformity in membrane fabrication, blockage of the membrane surface by catalyst dust etc. The membrane permeation effectiveness factor (η) account for all these negative influences on permeation rate and determined experimentally (Khosravanipour Mostafazadeh and Rahimpour, 2009). To simulate the hydrogen permeation process through the membrane tube, a User Model 2-unit operation block with an Excel spreadsheet was used to perform the calculations. Aspen Plus supplies properties of the feed stream of the user model and some additional parameters (η,k,Cmp,E,R,T,PRH2 and PMH2) to the Excel spreadsheet. The additional parameters are shown in Table 2. Excel organizes this information and calculates product stream properties with hydrogen production rate ($QH2$) based on Sieverts' law. This information is then returned to the Aspen Plus interface and results are displayed. The effect of increasing the number of stages is that there is an increase in the transfer of partially reacted bubble gas to emulsion gas where it will have higher chances for reaction. The right number of stages to model this system is dependent on its kinetics and hydrodynamics. The reformer is divided into 5 sections to simulate the conditions inside a real-world operational unit. Figure 4 shows that as the number of stages are increased the rate of reaction increase for aromatics and of (or decrease in the case of naphthenic) hydrogen. A further increase in subsections alters the hydrodynamics from that of a CSTR to that inside a PFR decreases thus the production (or consumption) becomes steady. For the FBMR, the optimum number of stages was determined to be 5.

Table 2. Parameters for hydrodynamic calculation

Studied Parameter	Model Equation
Superficial velocity at minimum fluidization	$\frac{1.75}{\epsilon_{mf}^3 \varphi_s}\left[\frac{d_p \rho_g u_{mf}}{\mu}\right]^2 + \frac{150(1-\epsilon_{mf})}{\epsilon_{mf}^3 \varphi_s}\left[\frac{d_p \rho_g u_{mf}}{\mu}\right] = Ar$
Archimedes' number	$Ar = \frac{d_p^3 \rho_g (\rho_p - \rho_g) g}{\mu^2}$
Bubble diameter	$d_b = d_{bm}(d_{bm} - d_{b0})exp(-0.3z/D)$ $d_{b0} = 0.376(u_0 - u_{mf})^2$ $d_{bm} = 0.65\left[\frac{\pi}{4}D^2(u_0 - u_{mf})\right]^{0.4}$
Coefficient of mass transfer (bubble to emulsion phase)	$K_{be} = \frac{u_{mf}}{3}\left[\left(4D_{jm}\epsilon_{mf}u_b/(\pi d_b)\right)\right]^{1/2}$
Velocity of bubble rise	$u_b = u - u_{mf} + 0.711\sqrt{g d_b}$
Volume fraction of bubble phase to overall bed	$\delta = (u - u_{mf})/u_b$
Specific surface area for bubble	$a_b = 6\delta/d_b$
Density for emulsion phase	$\rho_e = \rho_p(1 - \epsilon_{mf})$

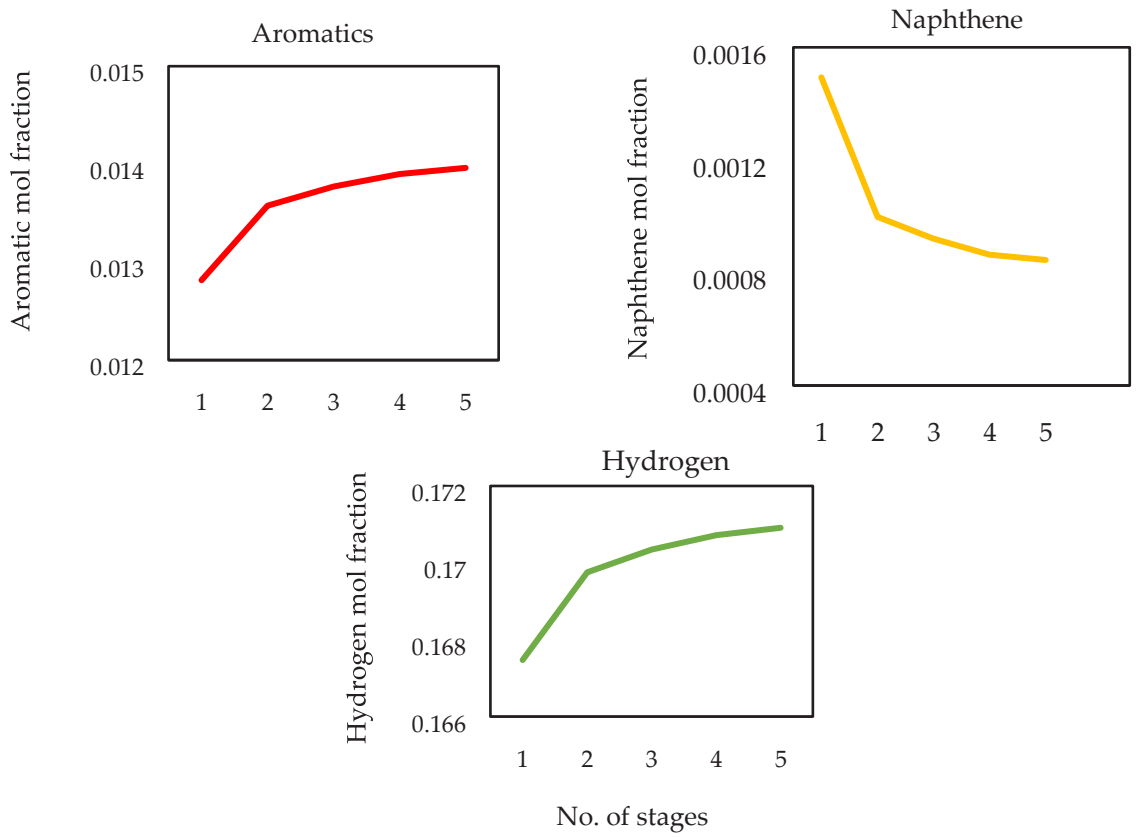

Fig. 4: Effect of number of stages on FMBR.

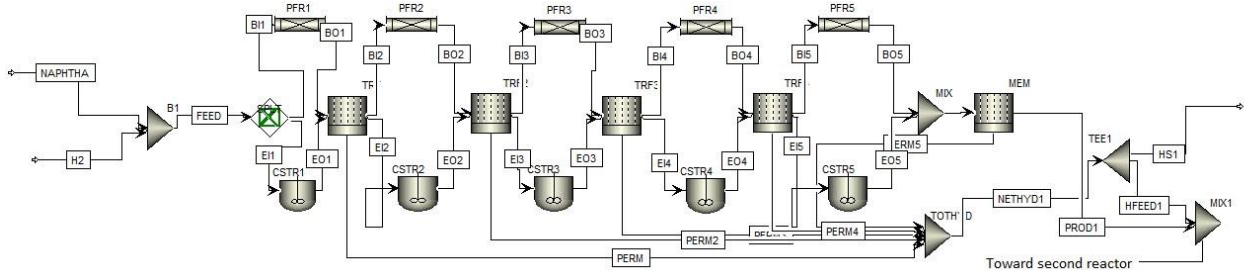

Fig. 5: PFD of FBMR for First Reactors.

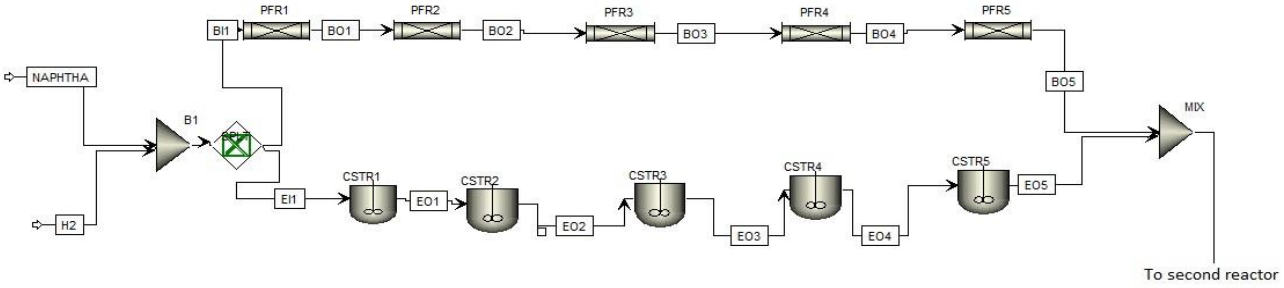

Fig. 6: PFD of FBR for First Reactors

IV. Results and discussions

A number of variables affect the catalyst performance. The more important parameters in the context of FBMR are the temperature at which reaction is carried out, pressure of the shell side, and hydrogen to hydrocarbon molar ratio.

Influence of Reactor Temperature

Endothermic reactions improve in yield as the temperature is raised. The dehydrogenation reaction is highly endothermic and thus high temperature favors it. In Figure 7, it is shown that a rise in temperature has a favorable impact on aromatic mole fraction. As the reaction proceeds inside the reactor due to its endothermic nature, the temperature will drop and reaction rate will decrease. Further contact with catalyst will not produce any further increase in products thus the reaction is carried out in three separate adiabatic reactor vessels with varying catalyst amount and inter stage heaters are provided to reheat the product stream to the reaction temperature.

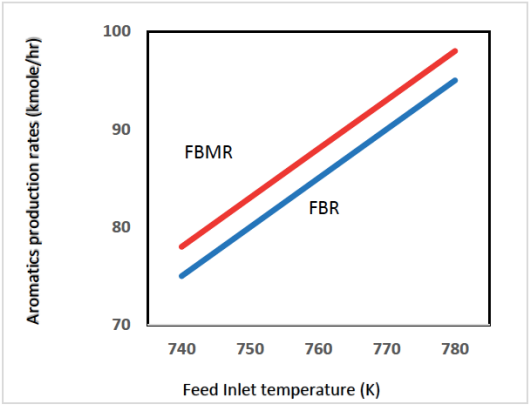

Fig. 7: Effect of temperature on aromatic production

Influence of shell-side pressure

The second parameter to be evaluated is the shell side pressure. The difference between reaction side and permeate side pressure creates a driving force for hydrogen permeation. As the dehydrogenation reaction is hydrogen producer, with the reaction proceeding more hydrogen will be produced. In the case of FBR, this hydrogen accumulates inside the reactor and increases its partial pressure and increase the affinity for products to move towards right side i.e. increasing the moles of reactants. The results are plotted in Figure 8. But in the case of the membrane reactor, the excess hydrogen is removed alongside the wall and thus keeps its partial pressure constant or even decreasing it if the shell side pressure is further reduced. This is the main reason that the FBMR produces more aromatics as compared to a FBR due to increased rate of forward reaction. Also, a good quantity of ultrapure hydrogen is available for fuel cell application from the FBMR. While the pressure inside the reactor is controlled within narrow limits, the pressure inside the shell is varied and as a result, hydrogen and thus aromatic production is controlled.

Influence of membrane thickness

The third parameter to be evaluated is the membrane thickness. The effect of membrane thickness on molar aromatic production was investigated. Result is plotted in Figure 9. It can be clearly seen that when the membrane is very thin around 10 microns, aromatic production shows a sharp increase with further reduction in thickness. Furthermore, it is also observed that when the thickness is about 20 microns, further increase in thickness does not bring any significant reduction in aromatic molar production. Thin membrane requires a support material. Stainless steel and alumina are the more frequently used materials for providing support. Alloying with silver is also a technique to provide mechanical strength.

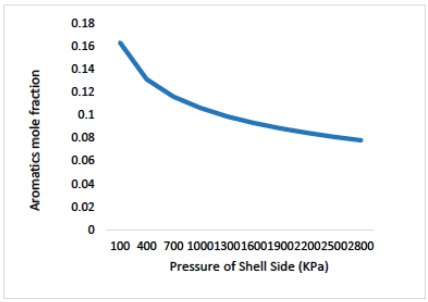

(a)

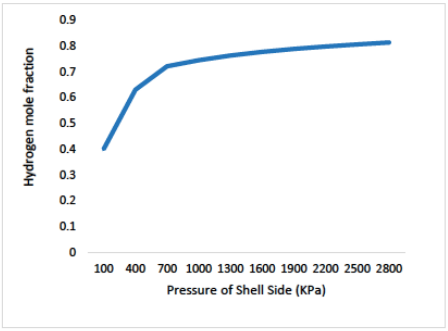

(b)

Figure 8. (a) Mole fraction of aromatic and (b) mole fraction of outlet hydrogen in reaction side as a function of shell side pressure

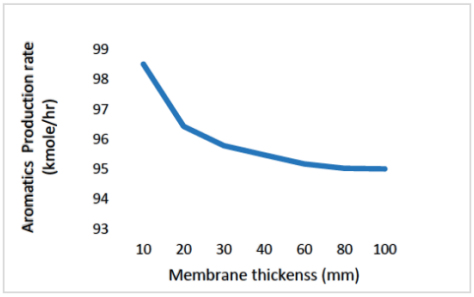

Figure 9. Aromatic production as a function of membrane.

Influence of H2/HC

The naphtha reforming reactions proceed under a hydrogen atmosphere to suppress the cracking reaction and the hydrogen to hydrocarbon molar ratio is an important parameter from an industrial stand point therefore its variation on aromatic production is included in this study. Higher H2/HC ratios result in a milder reaction condition inside the reformer as hydrogen removes coke precursor from the catalyst surface. On the other hand, higher ratios mean lower aromatic molar production which can be seen in Figure 10. Here the advantage of membrane becomes clear. The effect of high H2/HC ratio is more in the case of FBR as compared with an FBMR due to in situ hydrogen removal. It is because the produced hydrogen accumulates in an FBR but it is removed in FBMR keeping the aromatic molar flowrate higher than that from FBR.

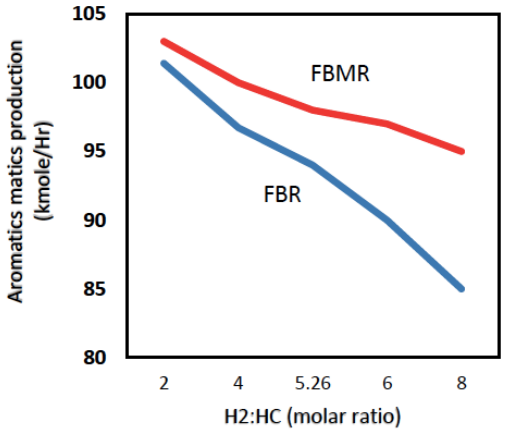

Figure 10. Aromatic production rate vs H2/HC ratio

Aromatics and Hydrogen Yields

In Table 3, component wise yield through the FBR and FBMR are compared. The first column shows the components chosen from the Aspen Plus database to represent the hydrocarbon. The second column gives the composition of the chosen components. The next two columns show the products flow rates from the last reactors of FBR and FBMR respectively. In the case of the FBMR, a part of the hydrogen is continuously removed resulting in higher product of aromatics and simultaneously a portion of the pure hydrogen is recycled back to reactors 2 and reactors 3 to maintain the hydrogen to hydrocarbons ratios (H2: HC = 5.69:1) . The products streams of the FBMR and FBR show a very indicative difference of aromatics and reformates production along with off gases and hydrogen production yields. In Table, 4, the output from the FBMR and the FBR are summarized. The first column shows the quantity of aromatic and hydrogen in the feed. The second and third column shows the production rates of the respective component of FBR and FBMR system. The calculated daily and yearly increase in aromatic and hydrogen is tabulated and is used for the cost estimations of FBR and FBMR configuration.

Table 3. Aromatics production in FBR and FBMR.

Components	FEED	FBR (CPROD3)	FBMR (PROD3)
	Mole Fractions	kmol/hr	kmol/hr
METHA-01	0.0089	17.14	81.04
ETHAN-01	0.0098	18.76	30.37
PROPA-01	0.0085	16.41	16.41
N-BUT-01	0.0045	8.60	8.59
ISOBU-01	0.0031	5.94	5.95
N-PEN-01	0.0015	2.84	2.84
2-MET-01	0.0032	6.18	6.18
N-HEX-01	0.0097	15.04	7.15
2-MET-02	0.0098	15.34	18.89
N-HEP-01	0.0124	19.11	9.05
2-MET-03	0.0133	20.65	25.56
N-OCT-01	0.0101	9.21	4.01
2:2:4-01	0.0143	13.53	27.50
N-NON-01	0.0066	10.01	4.63
2:2:5-01	0.0103	15.90	19.85
CYCLO-01	0.0033	0.91	0.07
METHY-01	0.0036	0.88	0.06
ETHYL-01	0.0049	0.31	0.01
N-PRO-01	0.0008	0.19	0.01
CYCLO-02	0.0000	0.08	0.08
METHY-02	0.0013	2.43	2.41
ETHYL-02	0.0028	5.25	5.19
N-PRO-02	0.0036	6.79	6.71
N-BUT-02	0.0005	0.97	0.96
BENZE-01	0.0036	19.40	75.98
TOLUE-01	0.0046	24.28	4.21

M-XYL-01	0.0006	9.01	6.00
O-XYL-01	0.0007	8.80	8.87
P-XYL-01	0.0015	12.45	1.21
ETHYL-03	0.0009	10.08	1.06
N-PRO-03	0.0011	9.97	1.12
HYDRO-01	0.8403	1866.82	271.21

Table 4. The Net Increment in Aromatics and Hydrogen.

Components		***FBR***	***FBMR***	***Increase by using membrane***	
	Feed kg/hr	*Out kg/hr*	*Out kg/hr*	*Daily increase kg/day*	*Yearly increase kg/Yr.*
Hydrogen	*3250*	*4179*	*4195*	*384*	*140160*
Aromatics	*2374*	*14914*	*15268*	*8496*	*3,101,040*

Exergy and Economic Analysis

For the exergy analysis, reference temperature and pressure were set at 25 oC and 101.3 kPa, respectively. The summary of the exergy analysis is provided in Table. 5. Chemical exergy of FBMR system leaving reactor R-3 is 37642 kW more than that of the FBR having 37515 KW with a difference of 127 KW. However, due to the endothermic nature of reforming reactions, physical exergy of the FBMR stream reactors decreases. This decrease contributes to entropy generation and loss of overall exergy in the reactors.

The Total capital investment and operating cost were calculated using the economic analyzer of Aspen plus version 10.0. Income tax @ 42 % and straight-line method for depreciation at the rate of 10% were assumed. The manpower costs were taken at the rate of 0.03 %. In the model a detail working of the Direct Cost (costs for equipment, piping, civil, structural steel, instrumentation and controls, electrical equipment and materials, insulation and paint), labour cost, chemicals and catalyst etc. was performed. The total cost obtained by Aspen Plus economic module were 250 MM USD and 235 MMUSD for the FBMR and FBR, respectively. Operating costs for FBMR and FBR were 30 and 28 MMUSD USD/year, respectively. The FBMR and FBR gave net annual income of 38 and 31 MMUSD, respectively. The FBMR and FBR had payback period of 6 and 8 years, respectively.

V. Conclusions

A fluidized-bed naphtha reformer with in situ membrane separation model was developed in the Aspen Plus environment. The hydrodynamic parameters and membrane permeation phenomena were implemented using Excel interfacing. The results of the FBMR were compared with a simple fluidized bed reactor (FBR). It was observed that hydrogen removal from the permeate side drove the reaction forward and resulted in an increase of the aromatic yield. In addition, hydrogen production also increased due to its simultaneous separation during the reaction in the two reactors while it decreases in the third reactor. The first possible reason of this less production is mainly lower throughputs in these reactors compare to FBR system. The detail reasoning needs further investigation in the reactors operation of each section of both the systems for future studies. Chemical exergy of FBMR system leaving reactor R-

3 is 37642 kW more than that of the FBR having 37515 KW with a difference of 127 KW. The total cost obtained by Aspen Plus economic module were 250 MM USD and 235 MMUSD for the FBMR and FBR, respectively. Operating costs for FBMR and FBR were 30 and 28 MMUSD USD/year, respectively. The FBMR and FBR gave net annual income of 38 and 31 MMUSD, respectively. The FBMR and FBR had payback period of 6 and 8 years, respectively.

Table 5. Exergy Analysis for FBMR and FBR

		Phy-Exergy (KW)	**Che-Exergy (KW)**	**Mix-Exergy (KW)**	**Total-Exergy (KW)**
Feed	H2	3152	6553	-4268	5437
	Naphtha	1827	30420	-1642	30604

FBMR	Nethyd1	28	69	-41	56
	Nethyd2	2138	5298	-3214	4222
	Nethyd3	1672	4088	-2499	3261
	Prod3	1414	28187	-928	28672
	Total	5252	37642	-6683	36212
FBR	BPROD3	5371	37515	-6650	36235
Difference (FBMR-FBR)		-119	127	-259	-24

Table 6. Payback Period Estimation of FBMR and FBR Reformer System.

	FBMR	***FBR***
Item	$ MM	$ MM
Capital Cost of plant	230	235
Associated Cost (Membrane)	20	0
Total Investment	250	235
Gross Income	204	188
Revenue		
Naphtha Cost	82	82
Operating Cost	30	28
Depreciation	25	23.5
Net Income before Tax	67	54
Tax @ 42.5 %	28	23
Net Income after Tax	38	31
Payback Periods	**6**	**8**

Gross Income Product Slate (FBMR)

Products	**Production rate (tons/ yr.)**	**Rate ($/To ו)**	**$ MM**
*NG (1872450 MMBtu)	25052	2.54	4.8

Gasoline	82881	212	18
Aromatics	145382	900	131
H_2	40536	1260	51
Total Revenue			204
(Feed Cost)		**273**	**80**

Gross Income Product Slate (FBR)

Products	**Production rate (tons/ yr)**	**Rate ($/ ton)**	**$ MM**
*NG (1203393 MMBtu)	15357	2.54	3.1
Gasoline	116103	212	25
Aromatics	123432	900	111
H_2	38959	1260	49
Total Revenue			188
(Feed Cost)	293851	273	80

*Gas Rate is 2.54 $/MMBtu

References

Ancheyta-Juárez, J., Villafuerte-Macías, E., 2000. Kinetic modeling of naphtha catalytic reforming reactions. Energy and Fuels 14, 1032–1037. https://doi.org/10.1021/ef0000274

Ancheyta, J., 2011. Modeling and Simulation of Catalytic Reactors for Petroleum Refining. Model. Simul. Catal. React. Pet. Refin. https://doi.org/10.1002/9780470933565

Barbieri, G., Di Maio, F.P., 1997. Simulation of the methane steam re-forming process in a catalytic Pd-membrane reactor. Ind. Eng. Chem. Res. 36, 2121–2127. https://doi.org/10.1021/ie9601615

Barbieri, G., Marigliano, G., Perri, G., Drioli, E., 2001. Conversion-temperature diagram for a palladium membrane reactor. Analysis of an endothermic reaction: Methane steam reforming. Ind. Eng. Chem. Res. 40, 2017–2026. https://doi.org/10.1021/ie0006211

Benitez, V., Boutzeloit, M., Mazzieri, V.A., Especel, C., Epron, F., Vera, C.R., Marécot, P., Pieck, C.L., 2007. Preparation of trimetallic Pt-Re-Ge/Al2O3 and Pt-Ir-Ge/Al2O3 naphtha reforming catalysts by surface redox reaction. Appl. Catal. A Gen. 319, 210–217. https://doi.org/10.1016/j.apcata.2006.12.006

Ciapetta, F.G., Wallace, D.N., 1972. Catalytic naphtha reforming, Catalysis Reviews. https://doi.org/10.1080/01614947208076866

Froment, G.F., 1987. The kinetics of complex catalytic reactions. Chem. Eng. Sci. 42, 1073–1087. https://doi.org/10.1016/0009-2509(87)80057-X

Gobina, E.N., Oklany, J.S., Hughes, R., 1995. Elimination of Ammonia from Coal Gasification Streams by Using a Catalytic Membrane Reactor. Ind. Eng. Chem. Res. 34, 3777–3783. https://doi.org/10.1021/ie00038a014

HOU, W., SU, H., HU, Y., CHU, J., 2006. Modeling, Simulation and Optimization of a Whole Industrial Catalytic Naphtha Reforming Process on Aspen Plus Platform. Chinese J. Chem. Eng. 14, 584–591. https://doi.org/10.1016/s1004-9541(06)60119-5

Howard, B.H., Killmeyer, R.P., Rothenberger, K.S., Cugini, A. V., Morreale, B.D., Enick, R.M., Bustamante, F., 2004. Hydrogen permeance of palladium-copper alloy membranes over a wide range of temperatures and pressures. J. Memb. Sci. 241, 207–218. https://doi.org/10.1016/j.memsci.2004.04.031

Hu, Y., Xu, W., Su, H., Chu, J., 2004. A dynamic model for naphtha catalytic reformers. Proc. IEEE Int. Conf. Control Appl. 1, 159–164. https://doi.org/10.1109/cca.2004.1387204

Iranshahi, D., Amiri, S., Karimi, M., Rafiei, R., Jafari, M., Rahimpour, M.R., 2013. Modeling and simulation of a novel membrane reactor in a continuous catalytic regenerative naphtha reformer accompanied with a detailed description of kinetics. Energy and Fuels 27, 4048–4070. https://doi.org/10.1021/ef302057k

Itoh, N., 1987. A membrane reactor using palladium. AIChE J. 33, 1576–1578. https://doi.org/10.1002/aic.690330921

Keuler, J.N., Lorenzen, L., 2002. Comparing and modeling the dehydrogenation of ethanol in a plug-flow reactor and a Pd-Ag membrane reactor. Ind. Eng. Chem. Res. 41, 1960–1966. https://doi.org/10.1021/ie010127c

Khosravanipour Mostafazadeh, A., Rahimpour, M.R., 2009. A membrane catalytic bed concept for naphtha reforming in the presence of catalyst deactivation. Chem. Eng. Process. Process Intensif. 48, 683–694. https://doi.org/10.1016/j.cep.2008.08.003

Lamm, A., Melin, T., 2001. Membrane reactors for hydrogen production. Chemie-Ingenieur-Technik 73, 768. https://doi.org/10.1002/1522-2640(200106)73:6<768::AID-CITE7682222>3.0.CO;2-T

Marin, G.B., Froment, G.F., Lerou, J.J., De Backer, W., 1983. Simulation of a Catalytic Naphtha Reforming Unit. EFCE Publ. Ser.

(European Fed. Chem. Eng.
Mazzieri, V.A., Pieck, C.L., Vera, C.R., Yori, J.C., Grau, J.M., 2009. Effect of Ge content on the metal and acid properties of Pt-Re-Ge/Al2O3-Cl catalysts for naphtha reforming. Appl. Catal. A Gen. 353, 93–100. https://doi.org/10.1016/j.apcata.2008.10.024
Padmavathi, G., Chaudhuri, K.K., 1997. Modelling and Simulation of Commercial Catalytic Naphtha Reformers. Can. J. Chem. Eng. 75, 930–937. https://doi.org/10.1002/cjce.5450750513
Pasha, M.K., Ahmad, I., Mustafa, J., Kano, M., 2019. Modeling of a nickel-based fluidized bed membrane reactor for steam methane reforming process. J. Chem. Soc. Pakistan 41, 219–229.
Patil, C.S., Van Sint Annaland, M., Kuipers, J.A.M., 2005. Design of a novel autothermal membrane-assisted fluidized-bed reactor for the production of ultrapure hydrogen from methane. Ind. Eng. Chem. Res. 44, 9502–9512. https://doi.org/10.1021/ie050244y
Rahimpour, M.R., Jafari, M., Iranshahi, D., 2013. Progress in catalytic naphtha reforming process: A review. Appl. Energy 109, 79–93. https://doi.org/10.1016/j.apenergy.2013.03.080
Rahimpour, M.R., Vakili, R., Pourazadi, E., Iranshahi, D., Paymooni, K., 2011. A novel integrated, thermally coupled fluidized bed configuration for catalytic naphtha reforming to enhance aromatic and hydrogen productions in refineries. Int. J. Hydrogen Energy 36, 2979–2991. https://doi.org/10.1016/j.ijhydene.2010.11.112
Ramage, M.P., Graziani, K.R., Krambeck, F.J., 1980. 6 Development of mobil's kinetic reforming model. Chem. Eng. Sci. 35, 41–48. https://doi.org/10.1016/0009-2509(80)80068-6
Reactor, A.M., 1987. A Membrane Reactor using palladium. AIChE J. 33, 9–11.
Roy, S., Cox, B.G., Adris, A.M., Pruden, B.B., 1998. Economics and simulation of fluidized bed membrane reforming. Int. J. Hydrogen Energy 23, 745–752. https://doi.org/10.1016/s0360-3199(97)00136-5
Sarvar-Amini, A., Sotudeh-Gharebagh, R., Bashiri, H., Mostoufi, N., Haghtalab, A., 2007. Sequential simulation of a fluidized bed membrane reactor for the steam methane reforming using ASPEN PLUS. Energy and Fuels 21, 3593–3598. https://doi.org/10.1021/ef7003514
Shu, J., Grandjean, B.P.A., Kaliaguine, S., 1994. Methane steam reforming in asymmetric Pd- and Pd-Ag/porous SS membrane reactors. Appl. Catal. A Gen. 119, 305–325. https://doi.org/10.1016/0926-860X(94)85199-9
Smith, R.B., 1959. Kinetic analysis of naphtha reforming with platinum catalyst. Chem.Eng 76–80.
Tosti, S., Basile, A., Bettinali, L., Borgognoni, F., Gallucci, F., Rizzello, C., 2008. Design and process study of Pd membrane reactors. Int. J. Hydrogen Energy 33, 5098–5105. https://doi.org/10.1016/j.ijhydene.2008.05.031
Yun, S., Ted Oyama, S., 2011. Correlations in palladium membranes for hydrogen separation: A review. J. Memb. Sci. 375, 28–45. https://doi.org/10.1016/j.memsci.2011.03.057

The Advantages of Microwave Technology in Commercially Biodiesel Production

[1*] Veli Gokhan Demir, [2]Nadir İLTEN, [3]Ismail Caner, [4]Hakan Serhad Soyhan
[1,2,3] Balikesir University, Engineering Faculty Department of Mechanical Engineering,
Cagis Campus, Balikesir, 10145, Turkey
[4] Sakarya University, Engineering Faculty Department of Mechanical Engineering,
Esentepe Campus, 54187, 10145, Turkey

* veligokhandemir@balikesir.edu.tr

Abstract
One of the major hurdles of spreading commercial biodiesel is the higher production costs compared to the petroleum based diesel. Transesterification is the most used method to produce biodiesel, and the academic and industrial investigations have been performed for optimizing transesterification reaction parameters to enhance fuel conversion efficiency and properties. Besides, in recent years, using advanced technologies in biodiesel production has increasingly become the focus to decrease production costs by minimizing reaction time and energy consumption in production processes. In this review work, the utilization methods of the alternative energy stimulant, "microwave technology" in biodiesel production are examined, and the alkali-catalyzed transesterification reactions carried out under the microwave irradiation are compared with the similar conditioned ones using conventional heating systems. As a result, it is observed that using the microwave technology can reduce the biodiesel production cost by providing considerable influence on reducing reaction time and increasing biodiesel yield in comparison with similar conventional methods. In biofuel industry, any industrial scale microwave assisted biodiesel reactor has not yet been used. Therefore, to compete with petro-diesel, commercial biodiesel processing cost should be decreased by developing microwave assisted reactors for industrial scale biodiesel productions.

Keywords: Microwave, Biodiesel Production, Transesterification, Methyl Ester, Alkali-catalyzed.

I. Introduction

It is reported that oil, coal and gas reserves will be depleted approximately 35, 107 and 37 years later, respectively (Shafiee and Topal 2009). However, fuel demand for internal combustion engines (ICEs) constitutes the largest part of oil demand, and it will have continued by 2040 with 63.2 millions of barrels per day. Electric vehicles will have only 13% of the total fleet in 2040 (OPEC 2019). Hence, in order to supply diesel ICEs fuel requirement, alternative energy sources are being investigated. Biodiesel, the renewable substitute fuel of petro-diesel, are derived from vegetable oils, animal fats, and used waste cooking oils. Its fuel properties have wide similarities with petro-diesel, thus it can be used in diesel ICEs without any modifications (Demirbaş 2002). Biodiesel has numerous benefits over petro-diesel. For instance, biodiesel is less toxic, more rapidly biodegradable, has a higher flash point and cetane number, has lower sulphur content, also provides sustainable energy diversification (Ajala, Aberuagba et al. 2015). On the other hand, bout 10% of the world's greenhouse gas (GHG) emission is sourced by the exhausts of ICEs consuming fossil fuels (Reitz, Ogawa et al. 2020). Biodiesel known also as a carbon neutral fuel can reduce carbon dioxide, polycyclic aromatic hydrocarbons, and GHG emissions (Nigam and Singh 2011). Besides these facts, the major obstacle for spreading and commercialization of biodiesel is its higher production costs against petro-diesel. One of the reasons influencing fuel cost is the production processes. Conventional biodiesel production methods are not energy-efficient and are expensive and offer scope for further improvements. Therefore, alternative and novel technologies such as radiofrequency and ultrasound waves have become popular in the last decade. In this field, microwave energy has drawn attention because it maintains short reaction time, cleaner reaction products, and reduced separation-purification times (Gude, Patil et al. 2013).
In the present study, it is aimed to display the significant advantages of microwave technology, which could contribute to being widespread of commercial biodiesel. In this context, the biodiesel productions carried out with conventional or microwave heating in the presence of the most used commercial chemicals (catalysts and alcohols) are reviewed, and the comparison of them are made. It is expected that our study will be useful for the researchers interested about this topic.

II. Biodiesel Production

Transesterification

Biodiesel can be obtained by reducing the viscosity and specific gravity values of vegetable oils with various methods. Among these, transesterification is the generally used method because it is reliable, feasible, and could be used to synthesis biodiesel easily (Shahid and Jamal 2011). Transesterification is known as the process in which oils (triglycerides) are chemically reacted with an alcohol, and finally esters and glycerol are obtained as product and by-product, respectively. The stoichiometric relation between alcohol and the oil is 3:1. However, an excess of alcohol is usually more appropriate to improve the reaction towards the desired product (Marchetti, Miguel et al. 2007). In this reaction, methanol and ethanol are the most commonly used alcohols due to their low costs and availability (Baskar, Kalavathy et al. 2019). Catalysts are used to improve the reaction rate and the biodiesel yield. In transesterification, base catalysts are faster than acid catalysis. Moreover, base catalysts are less corrosive than acidic catalysts. For these reasons, base catalysts such as alkaline metal alkoxides and hydroxides, and sodium or

potassium carbonates are generally preferred in industrial biodiesel productions (Schuchardt, Sercheli et al. 1998).

Heating Systems

In the literature, most of the investigations about defining optimum conditions of transesterification parameters have been carried out in laboratory, semi industrial and industrial scale biodiesel synthase units having conventional heating systems. Commonly used biodiesel reactors consist of hotplates, batch reactors, semi-continuous-flow reactors, and continuous-flow reactors using electric heaters located inside, or at the bottom, or covered (silicone band heaters) of the reactor vessel. Microwave heating is proposed as a good alternative to conventional heating. Microwave energy is transported as electromagnetic waves having 0.3 to 300.103 MHz frequencies (Benlloch-Tinoco, Igual et al. 2013). In microwave irradiation, selective heating of the products reduces by-product formation and makes reaction faster due to the fact that polar molecules can absorb microwaves while non-polar molecules treat as inert substances (El Sherbiny, Refaat et al. 2010). In general, when a conventional heating system is used, the reaction mixture is heated by the energy source thorough the wall of the vessel at slow speeds. Firstly, the energy is consumed for heating the vessel wall, then the mixture starts to be heated via convection. However, in microwave systems, the radiations influence directly on the materials to be heated and absorbed by them. In the microwave-assisted reactions, the vessel wall is colder than the material, therefore if the reagents can be mixed effectively, no regional temperature differences occur, so the byproduct production can be almost prevented and a significant part of the heating energy can be saved for heating (Bogdal 2005).

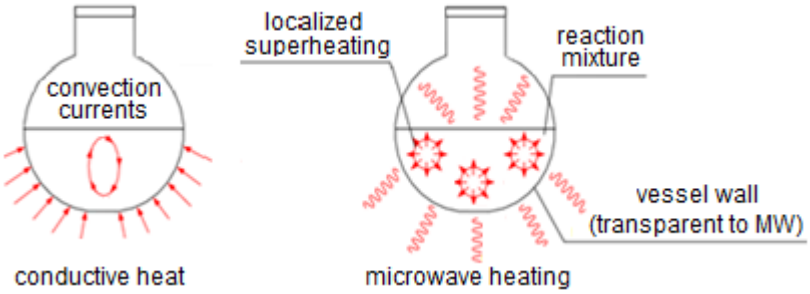

Figure 1. *Conventional and microwave heating (Bogdal 2005).*

III. Comparison of Conventional and Microwave-Assisted Biodiesel Production Methods

In Table 1, biodiesel productions carried out in similar reaction parameters in laboratory scales are presented comparatively according to their heating processes. In order to make a comparison, biodiesel purity (ester content) or yield values, which vary depending on the reaction time and exhibit the completion rate of the transesterification reaction, were taken into account.

As it is seen from the table, the amount of catalyst and methanol used in the reactions are quite close to each other both for conventional and microwave-assisted processes. In conventional productions, in order to achieve the acceptable or desirable results (Yield>90%, Purity>96.5%), the reaction times at the range of 30 to 240 min are required. However, the most preferred reaction duration is 60 min. On the other side, 1 to 9.6 min time range is allowable to complete the conversions of various feedstocks to biodiesel under microwave irradiation. The shortened reaction times are remarkable when they are compared with conventional production methods.

Table 1. *The comparision of conventional and microwave-assisted biodiesel productions*

	References	Feedstock (Oil type)	Catalyst (m_{cat}/m_{oil}%)	Methanol:Oil ratio	Temp. (°C)	Reaction Time (min)	Results(%) Y(Yield) P(Purity)
Conventional Productions	(Vicente, Martınez et al. 2004)	Canola oil	1.0 NaOH	6:1	60	60	>97.5 P
	(Fedai 2006)	Canola oil	1.05 NaOH	25% ($V_{alcohol}$:V_{oil})	55	60	99.2 Y
	(Meher, Dharmagadda et al. 2006)	Pongamia pinnata oil	1.0 KOH	6:1	65	180	96 Y
	(Azcan and Danisman 2007)	Cotton oil	1.5 KOH	6:1	60	60	91.4 Y 99.9 P
	(Özsezen 2007)	Waste cooking oil	1.0 KOH	6:1	60	240	96.5 P
	(Dias, Alvim-Ferraz et al. 2008)	Sunflower oil	0.6 NaOH	6:1	60	60	≈ 97 Y
		Soybean oil	0.8 NaOH				
	(Porwal, Bangwal et al. 2012)	Pongamia pinnata oil	1.0 KOH	4:1	60	60	98.5 Y
	(Alptekin, Canakci et al. 2014)	Corn oil	1.0 KOH	6:1	60	120	91 Y
	(Pullen and Saeed 2015)	Rapeseed oil	1.0 NaOH	6:1	60	60	>97.5 P
	(Keera, El Sabagh et al. 2018)	Castor oil	1 KOH	9:1	60	30	95 Y

Microwave-Assisted Productions	(Azcan and Danisman 2007)	Cotton oil	1.5 KOH	6:1	60	7	92.7 V 99.7 P
	(El Sherbiny, Refaat et al. 2010)	Jatropha oil	1.5 KOH	7.5:1	65	2	97.4 Y
	(Kamath, Regupathi et al. 2011)	Pongamia pinnata oil	1.0 KOH	13.9:1	-	1	99.2 Y
	(Encinar, Gonzalez et al. 2012)	Soybean oil	1.0 KOH	12:1	70	2	99.7 P
	(Lin, Chen et al. 2014)	Jatropha oil	1.0 $NaNH_2$	9:1	65	7	96.2 Y
	(Suryanto, Suprapto et al. 2015)	Coconut oil	1.0 NaOH	6:1	-	5	97.76 Y
	(Lin and Chen 2017)	Jatropha oil	1.0 KOH	6:1	65	0.17	≈ 90 Y
	(Milano, Ong et al. 2018)	Waste cooking oil - Calophyllum inophyllum oil	0.774 KOH	59.6% ($V_{alcohol}$:V_{oil})	100	7.15	97.4 Y
	(Sharma, Kodgire et al. 2019)	Waste cotton-seed oil	0.65 KOH	7:1	50	9.6	96.55 Y
	(Allami, Tabasizadeh et al. 2019)	Palm kernel oil	1.0 NaOH	6:1	-	2.5	97.6 Y

The shorter reaction times can be defined as the expected superiorities of microwave energy but this phenomenon is not fully understood and explained yet (Bogdal 2005). However, the reduction of the reaction time is generally explained by the energy-charged molecules and ions. They make movements and rotations extremely faster and it induces molecular friction occurrences and initiation of chemical reactions (Nüchter, Ondruschka et al. 2000, Lidström, Tierney et al. 2001, Saifuddin 2004). According to the results, it is also seen that microwave technology increases biodiesel efficiency. This is expounded by the superheating effect of microwave, which causes the solvents exposed to the microwave irradiation to boil up to 30°C above their boiling points (Mingos and Baghurst 1991). In addition, microwave-assisted biodiesel production has more various advantages such as lower relative energy consumption, environmental friendliness, controllable processing, quality and properties improvement etc. against conventional biodiesel production (Nomanbhay and Ong 2017). “However, large-scale experiments of microwave-assisted chemistry were demonstrated using laboratory-scale glassware, which has limited volumes due to the strength of glass and the space available in microwave cavities. These glassware-based microwave reactors inside the cavity structure are physically not feasible for scale-up to commercially available levels in tons.” (Kim, Seol et al. 2016), also the reproducibilities of parallel outcomes with laboratory-scale investigations at the biodiesel industry level are still doubtful (Nomanbhay and Ong 2017).

IV. Conclusion

In the present study, the potential advantages of microwave energy in commercial biodiesel production are investigated. It is observed that in the presence of methanol and base catalysts, microwave heating is fairly faster than conventional heating. Desired conversion rates can be obtained in a few minutes with higher product yields. This occasion can be aid to decrease the biodiesel production cost by saving energy and optimizing production time processes. However, microwave energy is not efficiently used in large scale biodiesel production yet. Hereby, microwave technology should be utilized in commercial biodiesel production, and more investigations on scale-up microwave-assisted reactors must be done to demonstrate the industrial feasibility of microwave technology.

References

Ajala, O. E., et al. (2015). "Biodiesel: Sustainable Energy Replacement to Petroleum-Based Diesel Fuel–A Review." ChemBioEng Reviews 2(3): 145-156.

Allami, H. A., et al. (2019). "Precise evaluation the effect of microwave irradiation on the properties of palm kernel oil biodiesel used in a diesel engine." Journal of Cleaner Production 241: 117777.

Alptekin, E., et al. (2014). "Biodiesel production from vegetable oil and waste animal fats in a pilot plant." Waste management 34(11): 2146-2154.

Azcan, N. and A. Danisman (2007). "Alkali catalyzed transesterification of cottonseed oil by microwave irradiation." Fuel 86(17): 2639-2644.

Baskar, G., et al. (2019). Advances in bio-oil extraction from nonedible oil seeds and algal biomass. Advances in Eco-Fuels for a Sustainable Environment, Elsevier: 187-210.

Benlloch-Tinoco, M., et al. (2013). "Comparison of microwaves and conventional thermal treatment on enzymes activity and antioxidant capacity of kiwifruit puree." Innovative Food Science & Emerging Technologies 19: 166-172.

Bogdal, D. (2005). Microwave-assisted organic synthesis: one hundred reaction procedures, Elsevier.

Demirbaş, A. (2002). "Biodiesel from vegetable oils via transesterification in supercritical methanol." Energy conversion and management 43(17): 2349-2356.

Dias, J. M., et al. (2008). "Comparison of the performance of different homogeneous alkali catalysts during transesterification of

waste and virgin oils and evaluation of biodiesel quality." Fuel 87(17): 3572-3578.

El Sherbiny, S. A., et al. (2010). "Production of biodiesel using the microwave technique." J. of Adv. Research 1(4): 309-314.

Encinar, J., et al. (2012). "Soybean oil transesterification by the use of a microwave flow system." Fuel 95: 386-393.

Fedai, Ö. (2006). "The optimization of methyl ester synthesis with canola oil transesterification." Master thesis. Chemical Engineering Dept, Gazi University, Turkey.

Gude, V. G., et al. (2013). "Microwave energy potential for biodiesel production." Sustainable Chemical Processes 1(1): 5.

Kamath, H. V., et al. (2011). "Optimization of two step karanja biodiesel synthesis under microwave irradiation." Fuel processing technology 92(1): 100-105.

Keera, S., et al. (2018). "Castor oil biodiesel production and optimization." Egyptian Journal of Petroleum 27(4): 979-984.

Kim, D., et al. (2016). "Energy efficiency of a scaled-up microwave-assisted transesterification for biodiesel production." Korean Journal of Chemical Engineering 33(2): 527-531.

Lidström, P., et al. (2001). "Microwave assisted organic synthesisÐa review." Tetrahedron 57: 9225-9283.

Lin, J.-J. and Y.-W. Chen (2017). "Production of biodiesel by transesterification of Jatropha oil with microwave heating." Journal of the Taiwan Institute of Chemical Engineers.

Lin, Y.-C., et al. (2014). "Rapid Jatropha-biodiesel production assisted by a microwave system and a sodium amide catalyst." Fuel 135: 435-442.

Marchetti, J. M., et al. (2007). "Possible methods for biodiesel production." Ren. and sus. energy reviews 11(6): 1300-1311.

Meher, L., et al. (2006). "Optimization of alkali-catalyzed transesterification of Pongamia pinnata oil for production of biodiesel." Bioresource technology 97(12): 1392-1397.

Milano, J., et al. (2018). "Optimization of biodiesel production by microwave irradiation-assisted transesterification for waste cooking oil-Calophyllum inophyllum oil via response surface methodology." Energy conversion and management 158: 400-415.

Mingos, D. and D. Baghurst (1991). "Microwaveassisted reactions and processes." Chem. Soc. Rev 20: 1-47.

Nigam, P. S. and A. Singh (2011). "Production of liquid biofuels from renewable resources." Progress in energy and combustion science 37(1): 52-68.

Nomanbhay, S. and M. Y. Ong (2017). "A review of microwave-assisted reactions for biodiesel production." Bioeng. 4(2): 57.

Nüchter, M., et al. (2000). "Organic processes initiated by non-classical energy sources." J. of Phy. Org. Che. 13(10): 579-586.

OPEC (2019). World Oil Outlook 2040 Launch of 2019 edition, OPEC.

Özsezen, A. (2007). " Investigation of the effects of biodiesel produced from waste palm oil on the engine performance and emission characteristics" Phd thesis. Mech Eng Dept, Kocaeli University, Turkey.

Porwal, J., et al. (2012). "Reactive-extraction of pongamia seeds for biodiesel production."

Pullen, J. and K. Saeed (2015). "Investigation of the factors affecting the progress of base-catalyzed transesterification of rapeseed oil to biodiesel FAME." Fuel processing technology 130: 127-135.

Reitz, R., et al. (2020). IJER editorial: the future of the internal combustion engine, SAGE Pub. Sage UK: London, England.

Saifuddin, N. (2004). "Production of ethyl ester (biodiesel) from used frying oil: optimization of transesterification process using microwave irradiation." Malaysian Journal Of Chemistry 6(1): 77-82.

Schuchardt, U., et al. (1998). "Transesterification of vegetable oils: a review." J. of the Brazilian Chemical Society 9(3): 199-210.

Shafiee, S. and E. Topal (2009). "When will fossil fuel reserves be diminished?" Energy policy 37(1): 181-189.

Shahid, E. M. and Y. Jamal (2011). "Production of biodiesel: a technical review." Ren. and sus. energy reviews 15(9): 4732-4745.

Sharma, A., et al. (2019). "Biodiesel production from waste cotton-seed cooking oil using microwave-assisted transesterification: Optimization and kinetic modeling." Renewable and sustainable energy reviews 116: 109394.

Suryanto, A., et al. (2015). "The production of biofuels from coconut oil using microwave." Modern Applied Science 9(7): 93.

Vicente, G., et al. (2004). "Integrated biodiesel production: a comparison of different homogeneous catalysts systems." Bioresource technology 92(3): 297-305.

Flowsheet development for the steam gasification of animal manure with subsequent of CO_2 capturing using CaO: An ASPEN Plus® modelling

[1*]Muhammad Shahbaz, [1]Tareq Al-Ansari, [1]Ahmed AlNous, [1]Gordon Mckay
[1] Division of Sustainable Development, College of Science and Engineering, Hamad Bin Khalifa University (HBKU), Qatar Foundation, P.O. Box 5825, Doha, Qatar

* E-mails: mshahbaz@hbku.ed

Abstract

Animal manure is one of the important wastes present in the state of Qatar. Gasification is a promising technique that could convert that waste into valuable chemicals and gaseous fuels. This can help not only reduce the waste of Qatar as well as make energy mix with renewable fuel. The objective of this study, to develop a process for the steam gasification of animal manure for production of syngas. The most important feature of current study, to investigate the effect of CaO for the reduction of CO_2 and on syngas composition. Aspen plus was utilized for the development of a flow sheet for the steam gasification process using the Gibbs free energy minimization. The effect of three key variables such as the temperature of (600-800 °C), steam/feedstock ratio of (0.5-2), and CaO/feedstock ratio of (0-1.2) on syngas production. The CO_2 reduced from 23 to 1vol % and H_2 increased from 56 to 88 vol% by varying the CaO/feedstock ratio from 0-1.2 at the temperature of 600 °C and steam/biomass production is increased from 64 to 84 vol% with the increase of temperature and steam/feedstock ratio of 0.5. Whereas the CO_2 reduced from 16 to 15 vol% at a elevated temperature of 750 °C by varying CaO/feedstock ratio. The reduction of CO_2 contents by the activation of the carbonation reaction. Steam/feedstock ratio and temperature have a direct impact on hydrogen production which is due to the acceleration of water gas shift reaction. Methane production found suppressed with the increase of steam as well as temperature is due to the activation of steam methane reforming reaction.

Keywords: Animal manure, CO_2 capturing, gasification, Aspen plus, syngas.

I. Introduction:

The prime agenda of the world is to develop a sustainable development that is directly associated with the ever-increasing demand for energy (AlNouss et al., 2019). The current energy demand was fully dominated by fossil fuels in most of the countries. The issues such as the depletion of fossil fuels, un-even sources distribution, politics on energy trade, greenhouse gas emissions, climate changes, and waste accumulation and its effective utilization are the main concerns to attain the sustainable development (Shahbaz et al., 2017). Qatar has made substantial development in the last two decades but like most countries, the main sources for energy are fossil fuel and facing similar issues (AlNouss et al., 2018). In addition, Qatar has also signed the Kyoto protocol and the second round of commitment for (2013-2020) known as the Doha Amendment as held in Qatar in which was decided to reduce the temperature by cutting the greenhouse gas emissions (Gupta, 2016). As Qatar energy demand is also fetched through fossil sources and it is finding the means to make its energy mix with renewables sources such as the use of solar energy and biomass and waste generated (AlNouss et al., 2018).

Biomass is the most important source that is able to produce different forms of energy with carbon neutrality as well as renewable and used in existing infrastructure. Animal manure is one of the important wastes that produced all over the world it has the potential to produced energy through many ways such as bio gas, pyrolysis, combustion, and gasification (AlNouss et al., 2020). The management of animal manure waste and its proper utilization still have many concerns in many countries. Like all other GCC countries, live stocks have been farming widely for many purposes such as milk, food, and other in Qatar. Animals in Qatar are produced a huge amount of manure waste that mostly consists of organic matter such as C and H_2 that are combustion able (AlNouss et al., 2020). Among all thermochemical conversion processes, gasification is one of the best processes to convert the carbonaceous material into gaseous products such as syngas (Shahbaz et al., 2017). The potential of application of gasification for Qatar based biomass is documented in a previous study (AlNouss et al., 2020). Steam gasification has an edge on-air gasification due to H_2 rich syngas production with no dilution of N_2 (Shahbaz et al., 2017). The produced syngas has a high share of CO_2 that is not required. For this purpose, many methods have been applied such as pre and post-combustion CO_2 capturing processes. Dolomite is a mineral compound that is enriched with CaO and has an ability to capture the CO_2 with the process. The use of dolomite for CO_2 capturing in the gasification process experimentally has been but most of the work on forestry and crop residues not on animal manure. In addition, there is very less work have made in thermodynamic modeling using Aspen Plus for use of dolomite and animal manure. The objective of this study, to develop a flowsheet for the steam gasification of animal manure for syngas production

with the uses of Cao for CO_2 capturing. For this purpose, the impact of important parameters such as temperature (600-800 °C), steam/biomass ratio (0.5-2) and CaO/biomass ratio (0-1.2) was also considered to determine to optimum process parameter for maximum H_2-rich syngas production with the minimum CO_2 production.

II. Methodology and Process Description:

Modeling and simulation of solid processing steps are important for many common operations including biofuels, pharmaceuticals, metals, polymers and other specialty chemicals. The advanced process simulation capabilities using Aspen Plus allow for high performance integrated simulation of solids and fluids processing steps with reliable physical properties. In this paper, the gasification of animal manure using steam as gasifying medium is modeled using Aspen Plus®. The model is simulated with the main assumptions of isothermal and steady-state operation, char is carbon, atmospheric operation with no pressure drop and neglected tar formation. The simulation model illustrated in Fig. 1, starts with a biomass decomposition reactor that yields the conventional components from the animal manure biomass attributes presented in Table 1. The reactor operates at 40 °C and 1 bar. The effluent is fed to the gasification unit operated at 700 °C and 1 bar along with steam as a gasifying agent and CaO used to capture formed CO_2. The gasification unit is modeled through the minimization of Gibbs free energy to achieve chemical and phase equilibrium. The reaction between CaO and CO_2 yields solid $CaCO_3$ which is separated along with ash from the rest of the produced gas in the solid separation section. The purified syngas is further cooled and purified from water to yield high-energy gas.

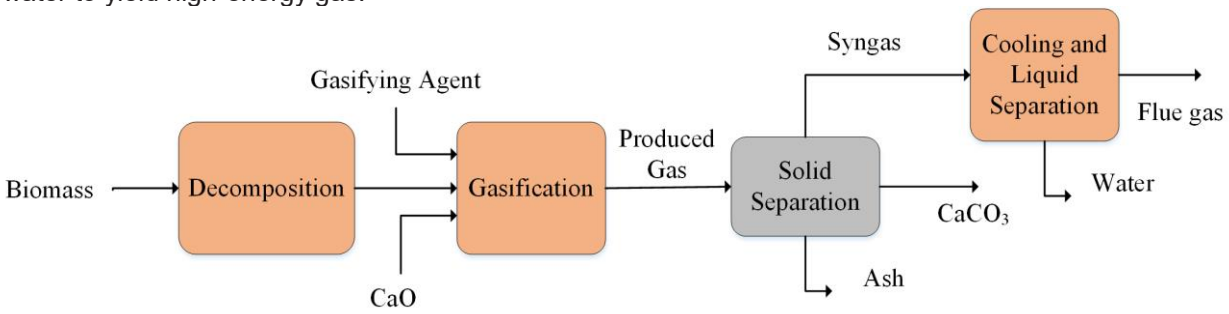

Fig. 1: Process flow diagram for steam gasification of animal manure.

Table1. Proximate and ultimate analysis of animal manure (AlNouss et al., 2019).

Biomass	**Animal Manure**
Mass Flowrate (kg/h)	1000
Moisture (wt %)	27.4
Proximate analyses (dry, wt %)	
Fixed carbon	13.5
Volatile matter	65.3
Ash	21.2
Ultimate analyses (wt %)	
N	3.7
H	5.1
C	37.1
O	31.4
Cl	1.0
S	0.5
Ash	21.2

The model is further used in performing sensitivity cases to analyze the effect of changing three important parameters that include gasification temperature in the range of (600-800 °C), steam to feedstock ratio in the range of (0.5-2), and CaO to feedstock ratio in the range of (0-1.2) on the quality of syngas production

III. Results and discussions:

The results of the simulation model are presented in terms of the different analysis performed on the animal manure gasification system. The effect of changing the temperature between 600 and 800 °C on the quality of the produced syngas is illustrated in Fig. 2. Temperature is one of the important design and operating parameter in biomass gasification. Generally, the biomass components decompose more effectively at higher temperatures leading to more syngas products. This is due to the high influence of higher temperatures on the gasification reactions. In the case of animal manure, it can be noticed that by increasing the temperature from 600 to 800 °C while keeping the steam/feedstock ratio at 0.5 and CaO to biomass ratio at 0.6, the hydrogen content in the produced syngas increases from 70% to approximately 74%. Similarly, the trend of CO increases from 8% to around 16% with an elevation in gasification temperature. Whereas, the trends of CO_2 and CH_4 decreases from 13% and 6% to

approximately 7% and 0.06%, respectively, with the increase in temperature. These trends with respect to temperature could be explained from the fact that at higher temperatures, the reactions of Boudouard, steam-methane reforming and CO shift are favored (Shahbaz et al., 2019).

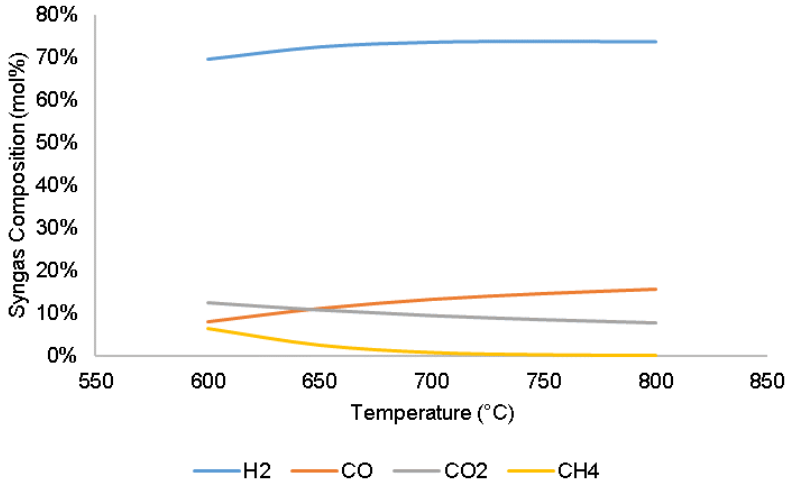

Fig. 2. Impact of temperature on syngas composition

The change in steam/feedstock ratio has a similar impact of temperature on hydrogen formation as illustrated in Fig 3. The increase in steam to biomass ratio at constant temperature of 750 °C and constant CaO to biomass ratio of 0.6, demonstrates an increase in hydrogen production from 74% to 76%. Similarly, the CO_2 trend indicates an increase from 8% to 15% with the increase in Steam/feedstock ratio. Whereas, the CO trend indicate a decrease from 15% to 6% with the increase in S/B ratio. These results indicate the acceleration of gasification reactions; mainly methane reforming reaction and water gas shift reaction.

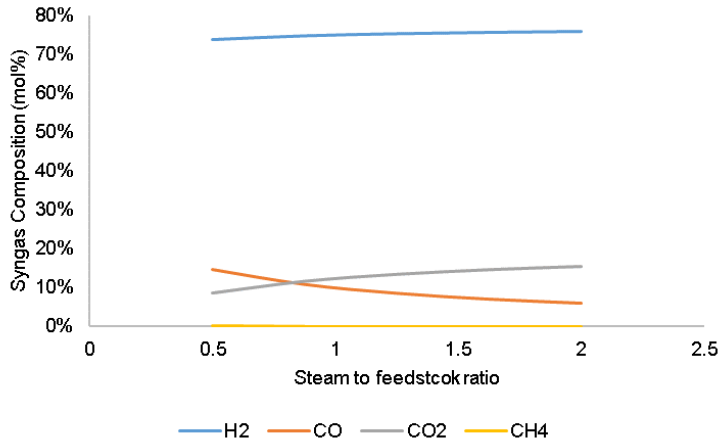

Fig. 3. Impact of steam to feedstock ratio on syngas composition

Finally, the change in CaO to biomass ratio has a similar effect on hydrogen formation as illustrated in Fig. 4. The increase in CaO/biomass ratio at a constant temperature of 750 °C and constant steam to biomass ratio of 0.5, demonstrates an increase in hydrogen production from 60% to 90%. Whereas, the CO_2 and CO trends indicate a decrease from 17% and 21% to 1.5% and 4.5% with the increase in CaO/Biomass ratio. The reduction of CO_2 with the use of CaO was also reported by experimentally in the literature (Yusup et al., 2014).

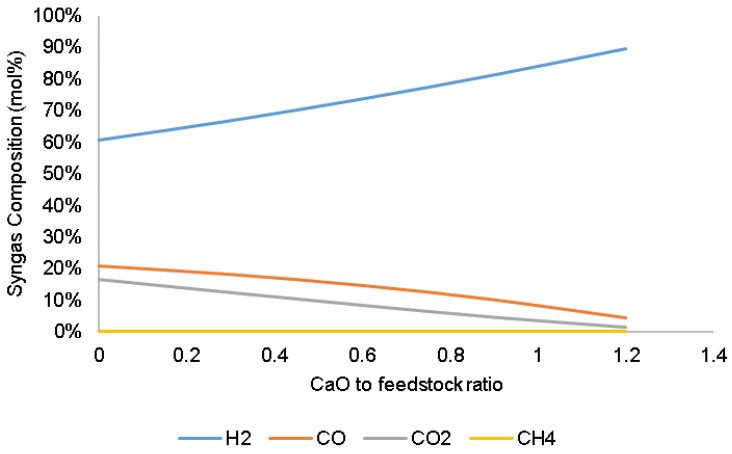

Fig. 4. Impact of CaO to feedstock ratio on syngas composition

IV. Conclusions:

The utilization of animal manure to produce high-energy syngas is highly significant from an environmental perspective, especially when compared to landfilling and incineration alternatives. Gasification is a promising technique used to convert waste into valuable chemicals and gaseous fuels. This paper aims to develop a model for the steam gasification of animal manure for syngas production. The most important feature of this study is to investigate the effect of CaO on the reduction of CO_2 and on syngas composition. Aspen plus was utilized for the development of a flow sheet for the steam gasification process using the Gibbs free energy minimization. The effect of three important parameters that include a temperature in the range of (600-800 °C), steam/feedstock ratio between (0.5-2), and CaO/feedstock ratio in the range of (0-1.2) on syngas production. The results demonstrate that steam to feedstock ratio and temperature have a direct impact on hydrogen production due to the acceleration of water gas shift reaction. Methane production found suppressed with the increase of steam as well as temperature due to the activation of steam methane reforming reaction.

Acknowledgments:

The authors would like to acknowledge the Hamad Bin Khalifa University, Doha, Qatar for support financial and technical support.

References:

AAlNouss, A., McKay, G., Al-Ansari, T., 2018. Optimum utilization of biomass for the production of power and fuels using gasification, Computer Aided Chemical Engineering. Elsevier, pp. 1481-1486.
AlNouss, A., McKay, G., Al-Ansari, T., 2019. A techno-economic-environmental study evaluating the potential of oxygen-steam biomass gasification for the generation of value-added products. Energy Conversion and Management 196, 664-676.
AlNouss, A., McKay, G., Al-Ansari, T., 2020. Production of syngas via gasification using optimum blends of biomass. Journal of Cleaner Production 242, 118499.
Gupta, A., 2016. Chapter 1 - Climate Change and Kyoto Protocol: An Overview, in: Ramiah, V., Gregoriou, G.N. (Eds.), Handbook of Environmental and Sustainable Finance. Academic Press, San Diego, pp. 3-23.
Shahbaz, M., Yusup, S., Al-Ansari, T., Inayat, A., Inayat, M., Zeb, H., Alnarabiji, M.S., 2019. Characterization and Reactivity Study of Coal Bottom Ash for Utilization in Biomass Gasification as an Adsorbent/Catalyst for Cleaner Fuel Production. Energy & Fuels 33(11), 11318-11327.
Shahbaz, M., Yusup, S., Inayat, A., Patrick, D.O., Pratama, A., Ammar, M., 2017. Optimization of hydrogen and syngas production from PKS gasification by using coal bottom ash. Bioresource Technology 241, 284-295.
Yusup, S., Khan, Z., Ahmad, M.M., Rashidi, N.A., 2014. Optimization of hydrogen production in in-situ catalytic adsorption (ICA) steam gasification based on Response Surface Methodology. Biomass and Bioenergy 60, 98-107.

A novel multi-generation system with reverse osmosis for a greenhouse in the Sabkha-Tah region of Western Sahara in Morocco.

Yasser M. ABDULLATIF[1], Eric C. OKONKWO[1*], Yusuf BICER [1], Tareq AL-ANSARI[1]
[1] Division of Sustainable Development, College of Science and Engineering, Hamad Bin Khalifa University, Education City, Qatar Foundation, Doha, Qatar.
[*]Corresponding author's email: eokonkwo@hbku.edu.qa

Abstract

The Sahara region of Africa is characterized by low rainfalls and high temperatures. Such conditions make it difficult to have a natural supply of freshwater for domestic purposes and food production. The Sabkha-Tah region of Western Sahara is one such location were the adverse weather conditions make it difficult for the conventional farming of certain crops to occur. The region is, however, uniquely situated 60 m below sea-level. This study analyzes the deployment of a multi-generation system to produce power, cooling, and freshwater for a 250 km^2 greenhouse situated in the Sabkha-Tah region of Western Sahara. The system is powered by the sun and uses the hydrostatic energy of the Atlantic Ocean to power a reverse osmosis (RO) water desalination system. A solar-powered Rankine cycle is used to meet the energy demands of an RO and vapor compression units. A thermodynamic analysis of the system is performed, and the results show that the use of an energy recovery turbine along with the geographical advantage of the region decreased the power requirement of the RO unit. The energy saved using the static pressure of the water was 3.27 kW. The net power consumption in the RO unit is 102.2 kW and it was able to provide 0.0185 kg/s of freshwater to the greenhouse. The overall energy and exergy efficiencies for the multi-generation system were calculated to be 50% and 35% respectively.

Keywords: multi-generation; reverse osmosis; solar tower; energy; exergy.

I. Introduction

In today's societies, energy has become an essential need as it powers various devices used in our daily life. Most of the world's energy is produced using fossil fuels which have become a finite resource. Moreover, the energy produced from the combustion of these fuels leads to the emission of gases harmful to the environment which causes climate change. These increasing environmental threats have encouraged many governments and international organizations to develop regulation that would help keep the environment safe and support sustainable energy solutions (e.g. United Nations [1]). Some of the sustainable energy sources include solar, wind, ocean, biomass, etc. However, the intermittent nature of many of these sources of renewable energy has posed a limitation to the reliability of these technologies. A lot of research had been conducted to design integrated renewable multi-generation systems that try to maximize the efficiency of these renewable systems and also to make them more reliable.

Extracting energy from water could be achieved by two means; hydrostatic and hydrokinetic. Hydrostatic is the usual way of using the potential energy of water stored on a higher level. The potential energy is converted into electricity by the use of suitable turbomachinery. The hydrokinetic approach doesn't depend on the potential energy of water and it does not need any head height. It converts the flowing water into electricity directly. It uses small scale turbines in this approach[2,3].

Al-Kharabsheh [4] proposed a system that utilizes the hydrostatic pressure of elevated water bodies for reverse osmosis desalination. The energy required to produce a meter cube of freshwater was 0.85 kWh. Their system was more efficient than the conventional reverse osmosis plants which use about 3-10 kWh to produce a one-meter cube of freshwater. Another system proposed by Dashtpour, and Al-Zubaidy [5] for water desalination was investigated. The system takes advantage of a depth of 500 m below sea level. It uses the head pressure obtained from the column of water above it. This head pressure is used to power a reverse osmosis desalination system. From their thermodynamic analysis, the energy required to produces a 1-meter cube of water was 0.7 kwh.

A lot of renewable energy sources are used for reverse osmosis desalination. The most used sources are solar and wind. Not a lot of investigation has focused on the use of the hydrostatic energy of water which only exists at certain heights or depths. One such study gives the hydrostatic pressure for RO plants and the energy required for each plant. The energy required to produce a one-meter cube of water from a submarine underground plant is 2.98 to 3.54 kwh. For a column of water that generates head pressure due to the height difference, the energy required to produce the same amount of water is 1.4 kWh. On the other hand, the required energy for the conventional desalination process is about 3 to 10 kWh for producing the same amount of freshwater [6]. Another research was conducted to use both the gravitational and wind energy to desalinate water using reverse osmosis. Their result shows that the required energy to produce a 1-meter cube of freshwater from this system was 2.811 kW [7].

A lot of non-fossil fuels powered multigeneration systems has been studied, one of those proposed systems utilized an oxyhydrogen combustor and concentrating solar panel to produce 11.4 MW, approximately 828 m^3/day of fresh water, 36 kg/s of hot air for food drying, 31 kg/s of heated domestic water, approximately 920 kg/day of H_2 and 2.26 MW of cooling. The system was thermodynamically analyzed and the energy and exergy efficiency was calculated to be 50% and 34% respectively [8].

The absorption cooling cycle is a popular industrial application driven by heat source from fuel combustion. Solar-based absorption cooling cycle is relatively new, although extensively researched in literature, it is rare to find its application in the industries. The regular compression refrigeration systems are more efficient than the ammonia-water absorption for small scale projects. Aman develops a solar-based ammonia-water absorption system where

the required cooling load using the proposed system was 10 kW. The system was analyzed from the exergy and energy viewpoints. It was found that 63% of losses were in the absorber then 13% in generator and finally 11% from the condenser. One of the important results in this study was that the exergy losses in absorber and generator increase with the increase of temperature. However, losses in the generator decrease with the increase of temperature. However, the evaporator losses did not show a considerable relationship with the temperature [9].

The compressor in the normal refrigeration cycle consumes most of the energy demands of the cycle. Fossil fuel combustion is used to meet the high energy required by the compressor which leads to climate change. The solar-based cooling absorption cycle presents a sustainable alternative to reduce the energy required for cooling as the compressor in this cycle is replaced by a pump. Solar thermal cooling systems are sustainable as they give the most cooling during peak temperatures as the radiation is used to feed the unit will be at its maximum.

The present work aims to thermodynamically analyze a multi-generation system that produces power, freshwater, and cooling for a greenhouse. The system is innovatively designed to satisfy the desired output of a greenhouse situated in the Sabkha-Tah region of Western Sahara situated 60 m below sea level. The system uses the hydrostatic energy of the water for water desalination and a solar-powered Rankine cycle is used to power a vapor compression system for cooling. The objective of the system is to reduce the required energy for the RO desalination process by using the head pressure of water coming from the Atlantic Ocean.

II. System Description

In this section, we look at the energy sources of the various subsystems and their applications. The schematic diagram of the system is shown in Fig.1. The energy sources used are water and solar. The proposed system includes a number of subsystems. There is a tomato greenhouse, vapor compression cycle, solar tower, Rankine cycle, water storage, reverse osmosis unit using gravitational energy which is used to provide fresh water and cooling for tomato greenhouse. This system is proposed to be built in Sabkha Tah, Western Sahara, in Morocco. This region is 60 m below the sea level and 14 km from the Atlantic Ocean.

A tomato greenhouse will be built in an area of 250 km^2 in the mentioned region with a length of 30 km and a width of 10 km. The dimensions of the greenhouse will be 3 km by 0.9 km. the greenhouse needs fresh water and cooling which will be supplied using a reverse osmosis process and vapor compression cycle. A solar power system will be used to supply heat for the Rankine cycle. The heliostats will concentrate solar radiation as shown in Fig. 1 onto a receiver containing the working fluid. The working fluid used is water and it supplies heat to the boiler of the Rankine cycle. Using the heat supplied, the Rankine cycle produces electricity to power the reverse osmosis pump and vapor compression cycle compressor. The reverse osmosis process will provide fresh water by desalinating seawater that comes from the Atlantic Ocean.

The pressure required for the reverse osmosis process will be reduced using the static pressure of water as the region is 60 m below the sea level and a recovery turbine that uses the pressure of the brine rejected from the reverse osmosis unit. The amount of pressure needed after reduction will be achieved using a pump power by electricity produced from the Rankine cycle. The cooling required for the greenhouse will be provided using a vapor compression cycle operating with R-134a as its working fluid. For nighttime, the greenhouse will not need any cooling as the maximum temperature at night in this region is 20°C. However, the greenhouse will need fresh water which will be supplied using a water storage tank that will be located on a higher level from the greenhouse. In the nighttime, the potential energy of the stored water will be used to supply the water to the greenhouse. The amount of water required at night will be supplied into the storage tank during the sunny hours from the reverse osmosis unit.

III. Analysis

The first and second laws of thermodynamics are considered, and properties such as enthalpy, entropy, and specific exergy are determined for each component. Mass, energy, entropy, and exergy balance equations are described accordingly. The analyses are performed using the Engineering Equation Solver (EES) software. The required heliostat areas for the desired amount of heat is determined. The electricity produced from the Rankine cycle along with the cooling required for the greenhouse is calculated. The vapor compression cycle is designed to produce cooling while freshwater is supplied by the reverse osmosis unit. Finally, both exergy and energy efficiencies of the overall system are calculated and assessed.

The following assumptions are made for thermodynamic analysis and evaluation:

- The reference state temperature (T_0) and pressure (P_0) are 25°C and 100 kPa, respectively.
- The temperature of the sun is taken as 6000 K.
- The minimum solar radiation in Sabkha-Tah was considered in the calculation to be 875 W
- The sunny hours per day were taken to be 8 hours.
- Both kinetic and potential energy and exergy changes are negligible.
- The turbine and pumps operate adiabatically with an isentropic efficiency of 80%.
- The working fluid of the solar tower and Rankine cycle is water.
- The working fluid of the vapor compression cycle is R-134a.

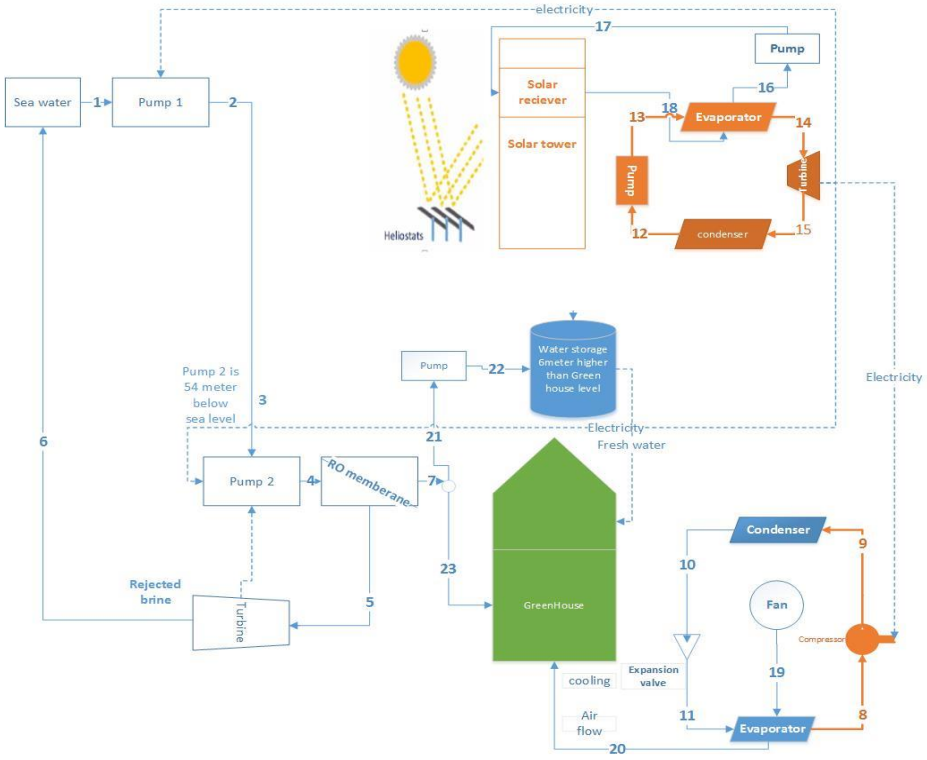

Figure 1: Schematic diagram of the multi-generation system for the Sabhka-Tah region.

3.1 General thermodynamic equations

The general mass balance equation for each component can be described as follows:

$$\dot{m}_{in} = \dot{m}_{out}$$

The first law of thermodynamics is employed to determine the work rates $\dot{W}$ and heat rates $\dot{Q}$ during each process. The general energy balance equation for steady-state can be defined as follows:

$$\dot{m}_{in} * h_{in} + \dot{Q}_{in} + \dot{W}_{in} = \dot{m}_{out} * h_{out} + \dot{Q}_{out} + \dot{W}_{out}$$

Using the second law of thermodynamics the entropy generated can be calculated. The general entropy balance equation is defined as follows

$$\dot{m}_{in} * s_{in} + \dot{s}_{gen} + \frac{\dot{Q}_{in}}{T_s} = \dot{m}_{out} * s_{out} + \frac{\dot{Q}_{out}}{T_b}$$

Using the general exergy balance equation, the exergy destruction in each component will be calculated along with the exergy destruction (Ex_d) in each component due to entropy generation. The general exergy balance equation can be expressed as follows:

$$\dot{m}_{in} ex_{in} + \dot{E}x^{Q_{in}} + \dot{W}_{in} = \dot{m}_{out} ex_{out} + \dot{E}x^{Q_{out}} + \dot{W}_{out} + \dot{E}x_{D.}$$

The general exergy terms (ex_i) at each state point can be defined as follows:

$$ex_i = (h_i - h_0) - T_0(s_i - s_0)$$

where, h_0 and s_0 are enthalpy and entropy values for the dead state conditions (T_0 and P_0).
The general exergy destruction at each state:

$$\dot{E}x_D = T_0 \dot{S}_{gen,}$$

IV. Results and discussions

Table 1: The main calculated values

Electricity consumption in RO	102.2 KW
Freshwater mass flow rate	0.01815 kg/s
Refrigeration cycle cooling	76.25 kW
Refrigeration cycle compressor required power	9.667 kW
Heat input to Rankine cycle	279.3 kW
Rankine cycle for electricity production	119.3 kW
Area of Greenhouse	100 m^2
Number of tomato plants	276 plants
Total electricity consumption for the overall system	112.2 kW

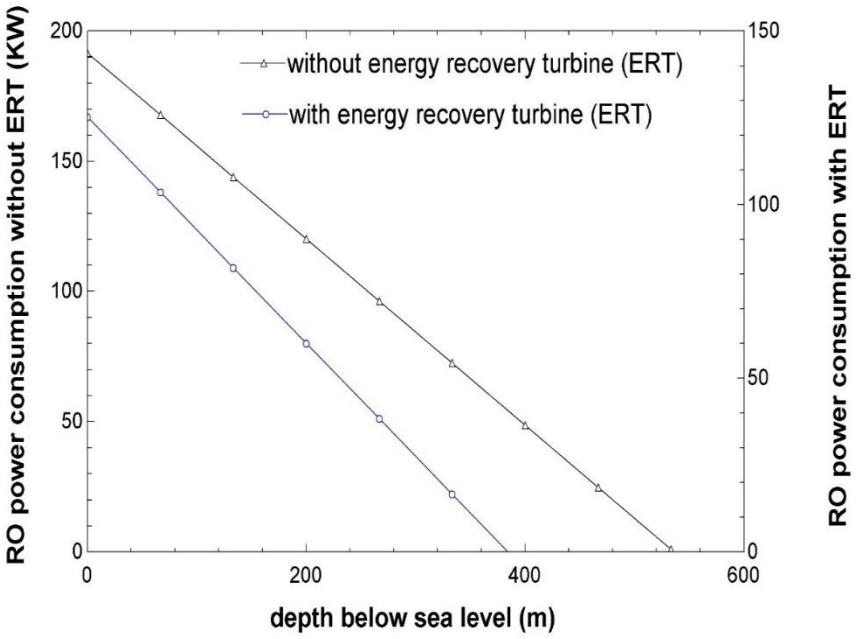

Figure 2: Power for RO unit with and without ERT vs the depth of region below sea level.

Table 1 shows the energy input and output of each of the subsystems. Fig. 2 shows the effect of the depth below the sea level on the energy required for the RO Unit. The RO unit used has a recovery ratio of 0.5. Two types of RO units were investigated. One is a normal reverse osmosis unit and the other is integrated with an energy recovery turbine. The power required for both units decreases with the increase in the region's depth below sea level.

V. Conclusions

In this work, the energy, cooling and water needs of a greenhouse are met using renewable sources of hydro and solar. The freshwater is supplied through the RO system while cooling is obtained from a vapor compression cycle. To meet the electricity required in the RO unit and vapor compression cycle a solar-powered Rankine cycle is used. The main novelty is the reduction in the power consumption of the RO unit. Further decrease in the power required for the RO system was done using an energy recovery turbine. Also, the geography of the location (60 m below the sea level) was used in reducing the energy needs by hydrostatic pressure. The energy saved using hydrostatic pressure was 3.27 kW. The following conclusions are drawn;

- The cooling produced using the vapor compression cycle was designed to meet the greenhouse cooling load which is 76.25 kW
- The Rankine cycle was designed to meet electricity required for the overall system which is 112.2 kW
- A solar tower with the heliostats was used to supply 279.3 kW of heat rate required to power the Rankine cycle.
- The freshwater produced by RO is 0.0185 kg/s and is used to meet the water demands of the greenhouse.
- The energy and exergy efficiency for the overall system was calculated to be 50% and 35% respectively.

References

[1] D. of E. and S. Affairs, Disability, #Envision2030: 17 goals to transform the world for persons with disabilities, (2016).
[2] D. Mugisidi, O. Heriyani, Study of Utilization under Sea-water Hydrostatic Pressure as Hydro Power Generation, E3S Web Conf. 73 (2018) 2–4. https://doi.org/10.1051/e3sconf/20187301020.
[3] S. Dhakal, A.B. Timilsina, R. Dhakal, D. Fuyal, T.R. Bajracharya, H.P. Pandit, N. Amatya, A.M. Nakarmi, Comparison of cylindrical and conical basins with optimum position of runner: Gravitational water vortex power plant, Renew. Sustain. Energy Rev. 48 (2015) 662–669. https://doi.org/10.1016/j.rser.2015.04.030.
[4] S. Al-Kharabsheh, An innovative reverse osmosis desalination system using hydrostatic pressure, Desalination. 196 (2006) 210–214. https://doi.org/10.1016/j.desal.2005.11.023.
[5] R. Dashtpour, S.N. Al-zubaidy, Fig. 2. Comparisons between the submerged reverse osmosis system current schemes, 3 (2012).
[6] C. Charcosset, C. Falconet, M. Combe, Hydrostatic pressure plants for desalination via reverse osmosis, Renew. Energy. 34 (2009) 2878–2882. https://doi.org/10.1016/j.renene.2009.02.026.
[7] E.A.F.A. Fadigas, J.R. Dias, Desalination of water by reverse osmosis using gravitational potential energy and wind energy, Desalination. 237 (2009) 140–146. https://doi.org/10.1016/j.desal.2007.12.029.
[8] M. Luqman, Y. Bicer, T. Al-Ansari, Thermodynamic analysis of an oxy-hydrogen combustor supported solar and wind energy-based sustainable polygeneration system for remote locations, Int. J. Hydrogen Energy. (2019) 2020. https://doi.org/10.1016/j.ijhydene.2018.12.191.
[9] J. Aman, D.S.K. Ting, P. Henshaw, Residential solar air conditioning: Energy and exergy analyses of an ammonia-water absorption cooling system, Appl. Therm. Eng. 62 (2014) 424–432. https://doi.org/10.1016/j.applthermaleng.2013.10.006.

Removal of toxic cadmium from water using a binary site ion exchange resin derived from waste printed circuit board

Meng Xu[2], Haya Alyasi[1*], Junaid Saleem[1], Ning Chao[2], Chi-Wai Hui[2], Hamish Mackey[1], Tareq Al Ansari[1], and Gordon McKay[1]

[1] Division of Sustainable Development, College of Science and Engineering, Hamad Bin Khalifa University, Education City, Qatar Foundation, Doha, Qatar.

[2] Department of Chemical and Biological Engineering, School of Engineering, Hong Kong University of Science and Technology, Kowloon, Hong Kong, SAR China.

*Correspondence: haalyasi@mail.hbku.edu.qa

Abstract

Many industries discharge effluents containing toxic heavy metal ions into receiving waters. These industries include nickel-cadmium batteries, metal plating, microelectronics, mining, metal fabrication etc. It is important to find effective and economic solutions to process these effluents by removing the contaminating metal ions to make the water suitable to meet environmental standards and trying to recover and recycle the metals. Cadmium is known to be toxic and carcinogenic and in water can be absorbed by plants, crops, aquatic species and then enter the food chain by these routes. In humans it can adversely affect the kidneys, cause renal disfunction, bone lesions and cancer.

In this study, an activated alumina-silicate resin (AASR) has been prepared from the waste mother board of printed circuit board e-waste. The preparation and characterisation of this resin is described, then its ability and the mechanisms involved in the removal of cadmium is described and modelled. The mechanism is unique as the AASR contains both potassium and calcium ion exchange sites for the cadmium. The analysis of this type of binary ion exchange waste derived material explains the high capacity of the AASR for cadmium. An outline schematic is provided of the AASR production path route and for the novel dual ion exchange mechanism.

Keywords: Ion exchange, cadmium, activated alumina-silicate resin, waste printed circuit board

I. Introduction

Electronic waste (e-waste), due to its hazardous nature, has been one of the key problems associated with solid waste management. With the ever-increasing demand for new and updated electronic items, the product life cycle has been significantly compromised. Amongst various components of an electronic device, the Printed Circuit Board (PCB) is the most important part and is often considered as the heart of the assembly. It is the platform at which semiconductor chips and capacitors are mounted. Once the PCBs are outdated, they are discarded and piled up into landfill sites. The waste PCB comprises of metallic and non-metallic components. While the metallic part is usually recovered and sold, the non-metallic fraction (NMF), which constitutes more than 70% by mass, is either dumped into landfills or used as a low-value product such as fillers. Previous work reported the production of this material under similar conditions (Hadi et al., 2013) but the mechanism reported previously was based on a single model to correlate the data without the involvement of the individual ion exchange steps. The main novel aspect of this study is the confirmation of a dual ion exchange mechanism with mass balance and equilibrium isotherm analyses providing the supporting evidence.

II. Experimental Procedure/Methodology/System Description

Recently, McKay et al. developed a technique to produce high quality activated alumina-silicate resin (AASR) as shown in Figure 1. In this method, waste PCBs are shredded using a high-impact size reduction technique followed by corona-electrostatic separation (CES). By applying a high voltage electrostatic field using a corona and an electrostatic electrode, metallic and non-metallic components are separated. The metallic portion containing mostly copper, 70 to 90% by weight, can be sold for copper smelting to produce relatively pure highly refined copper metal. The NMF powder is then impregnated with the activating agent, such as KOH, under continuous stirring for 3 hours at room temperature. The resultant slurry is heated to 250 °C at a rate of 5 °C/min for 3 hours in a muffle furnace under an inert atmosphere. It is followed by washing with hot and cold water and dried at 110 °C for 24 hours to produce the adsorbent/ion exchange aluminosilicate powder product, AASR.

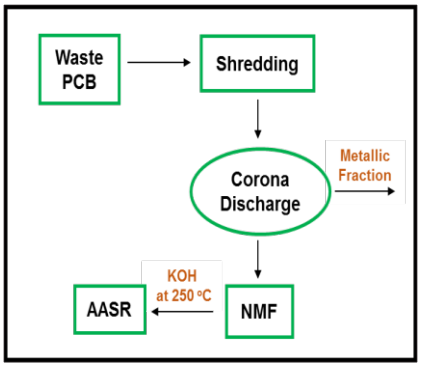

Fig. 1: Process Schematic for the production of AASR from waste PCB,

For ion exchange studies , In the equilibrium studies 50 mg AASR was shaken with 50 ml Cd solutions of varying concentrations at pH = 4.5. All solution ion concentrations, Cd, Ca and K, were measured using inductively coupled plasma-atomic emission spectrophotometer (ICP-AES) (Optima 7300 DV, Perkin-Elmer).

III. Analysis

The equilibrium isotherm for cadmium adsorption was determined experimentally by the method described and are shown in Figure 1 as $q_{e,s}$ versus C_e. The concentrations of potassium and calcium exchanged into the solution were also measured at each concentration and the uptake of these two exchanged metal ions into the solution were also plotted in Figure 1 as q_e values versus C_e.

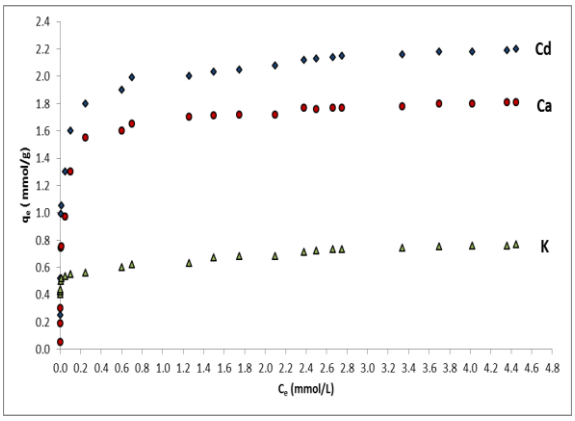

Fig. 2: Uptake of cadmium onto AASR and the discharges of calcium and potassium into solution versus the concentration of cadmium ions in solution at equilibrium

IV. Results and discussions

Table 1. Isotherm constants and error values for the Redlich-Peterson and the Langmuir isotherm

Isotherm	Parameter Values			AIC	SSE
Cadmium	1	2	3		
Langmuir	$q_{m,L}$ (mmol/L)=2.08	K_L(L/mmol)=72.5	-	-23.9	0.336
R-P	$q_{m,RP}$ (mmol/L)=1.98	K_{RP} (L/mmol)=151	$1/n_{RP}$=0.925	-78.7	0.031
Calcium	1	2	3	AIC	SSE
Langmuir	$q_{m,L}$ (mmol/L)=1.75	K_L(L/mmol)=46.2	-	-40.2	0.180
R-P	$q_{m,RP}$ (mmol/L)= 1.67	K_{RP} (L/mmol)=79.9	$1/n_{RP}$=0.938	-63.8	0.059
Potassium	1	2	3	AIC	SSE
Langmuir	$q_{m,L}$ (mmol/L)=0.672	K_L(L/mmol)=776	-	-48.8	0.124

R-P	$q_{m,RP}$ (mmol/L)=0.670	K_{RP} (L/mmol)=1000	$1/n_{RP}$=0.951	-63.8	0.041

The experimental data were analysed using six model isotherm equations, namely, Langmuir, Freundlich, Sips, Redlich-Peterson, Dubinin-Radushkevich and the Temkin isotherms. In terms of error values, the Redlich-Peterson (best) and the Langmuir provided the best correlations with the experimental data as shown in Table 1. The theoretical isotherm model lines for these two best fit isotherms are presented in Figures 2 and 3 and compared with the experimental data points.

Based on the assumptions that the cadmium is only removed from solution by ion exchange with calcium or potassium, then it should be possible to confirm this by a mass balance according to the equation (1):

$$q_{e[Cd]} = q_{e[Ca]} + q_{e0.5\,[K]} \quad (1)$$

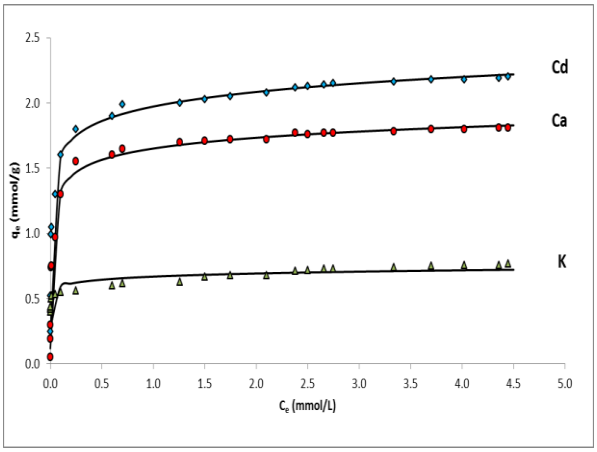

Figure 2. Redlich-Peterson model isotherms(solid lines) compared with the correspondingexperimental data points (symbols).

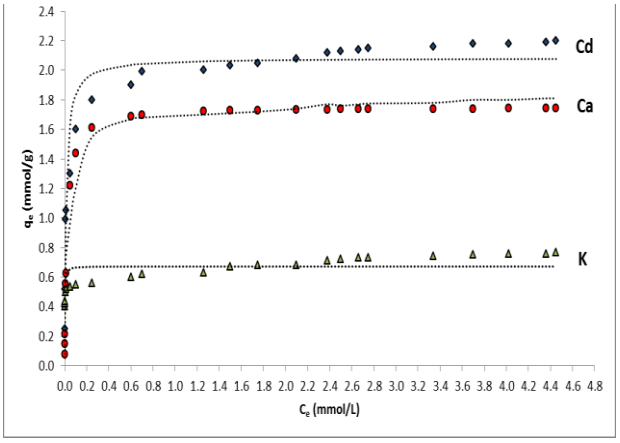

Figure 3. Experimental points (symbols) for thethree metals and using the Langmuir isotherm model correlations (dotted lines).

The result of the mass balance for a few data points are shown in Figure 4 providing excellent correlation of the data and confirmation of the mass balance model.

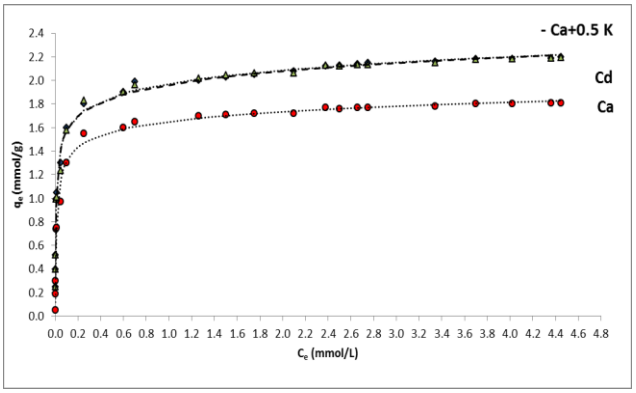

Fig 4. The best fit Cd model (Redlich-Peterson) equation: $q_e = q_e(Ca) + q_e(0.5K)$ versus C_e

The best isotherm correlation is the Redlich-Peterson, which is generally regarded as a modified or pseudo-Langmuir isotherm. For one exchange site, we would expect a good Langmuir fit, but in this case there are two individual sites exchanging justifying a deviation, but only small, from the conventional Langmuir – applicable to homogeneous, constant energy exchange sites.

V. Conclusions

The mechanism of Cd adsorption on novel AASR has been explained by a dual ion exchange process.

Acknowledgements

Author (HA) is grateful to Qatar National Research Foundation for a QNLP Award.

References

“

Hadi, P., Gao, P., Barford, J.P., McKay, G. *J. Hazard. Mater*. **2013,** 252-253, 166-170.

Integration of Kalina Cycle with CPVT for Multi-generation and Hydrogen Production: An Energy, Exergy and Environmental Performance Study

[1*]Olusola Bamisile, [1]Qi Huang, [2]Olamide Olotu, [3]Mustafa Dagbasi, [4]Eric C. Okonkwo, [4]Tareq Al-Ansari, [5]Tahir A.H Ratlamwala
[1] Univeristy of Electronic Science and Technology of China, School of Mechanical and Electrical Engineering, Electronics Science and Technology Department, Chengdu, 611731, China.
[2] Afe Babalola University, Department of Mechanical Engineering, 5454, Ado-Ekiti, Nigeria.
[3] Cyprus International University, Faculty of Engineering, Energy Systems Engineering Department, Haspolat-Lefkosa, Mersin 10, 99010, Turkey.
[4] Hamad Bin Khalifa University, Education City, Division of Sustainable Development, College of Science and Engineering, Qatar Foundation, Doha, Qatar.
[5] Department of Engineering Sciences, National University of Science and Technology, Karachi, Pakistan.
* E-mails: boomfem@gmail.com

Abstract
Electricity is the most convenient and versatile form of energy. Unlike steam and gas cycles, Kalina cycle can utilize low grade heat to produce electricity with ammonia solution as working fluid. Concentrated photovoltaic thermal (CPVT) systems have proven to be a technology that can be used to maximize solar energy. In this research, the integration of a Kalina cycle with a CPVT system for multigeneration and hydrogen production is presented. The aim of this study is to increase the share of electricity produced by the CPVT system. The performance of the multigeneration system with and without a kalina cycle is compared. The multigeneration system is designed to produce electricity, hot water, cooling effect, hot air, and hydrogen. A proton exchange membrane is integrated with the multigeneration system for hydrogen production. The analysis of the system modeled will focus on the energy and exergy performance. The environmental benefit of this configuration in terms of carbon emission reduction and fossil fuel savings is also highlighted. The energy and exergy efficiencies of the heliostat used in concentrating solar radiation onto the CPVT are 90% and 85.53% respectively and the hydrogen production when integrated with a Kalina cycle is 58.39 L/min. The CPVT system has a 74% energy efficiency and 45.75% exergy efficiency while the hot air production chamber has a 95% and 92.12% energy and exergy efficiency. Although the overall energy efficiency of the multigeneration system reduces with the integration of kalina cycle, the increase in electricity production justifies the importance of the configuration.

Keywords: CPVT, Energy, Exergy, Hydrogen Production, Kalina Cycle, Multigeneration.

I. Introduction

Climate change effects due to global warming is promoting the development of more efficienct energy systems. In 2011, About 10 gigatonnes (37%) of the 27 gigatonnes of CO2 emitted globally were from electricity production. This is expected to increase over the next 20 years as electricity demand is projected to increase by 43% over the same time period (World Nuclear Association, 2011). At the end of 2018, the use of renewable energy (RE) had reduced the average carbon intensity from electiricity production to 475 gCO2/kWh although this is still significantly high due increased demands. Also, the emission from the transportation sector was reported as 8 gigatonnes at the end of 2018. The demand for a cleaner environment has increased the share of RE systems for power generation in recent years. At the end of 2018, the share for global electricity generated from RE was reported to be 26.2% (REN21, 2019). The re-introduction and high adoption of electric vehicles (EVs) into the global energy mix in the last decade had significant positive impact on CO2 emission. This has also revived the need for more hydrogen energy in the energy industry.

In recent years, the effective and efficient utilization of RE sources such as: wind, hydro, solar, geothermal, biomass etc. have attracted wide research attention in literature. One the most developed RE technologies is solar photovoltaic (PV), it accounted for 2.4% of global electricity consumption in 2018 (REN21, 2019). The development of (concentrated) solar PV thermal hybrid systems has further increased the efficient utilization of solar energy (Chow, 2010). The use of concentrated solar PVT systems can result in a system system efficiency of 80% (Sezer and Koç, 2019). The use of multigeneration systems instead of traditional electricity generation cycles have proven to be an efficient means of utilizing energy sources. In literature, most studies concentrate on the integration of RE systems for multigeneration. This can result in an energy efficiency ranging from 40% to 90%. Yuksel et al. presented a multigeneration system with 65.71% and 62.35% energy and exergy efficiency respectively (Yuksel et al., 2019). In another study (Siddiqui and Dincer, 2017), it was concluded that multigeneration systems increased energy and exergy efficiencies by 19.3% and 17.8%.

Owing to the fact that electricity is the most versatile form of energy and considering a more environmentally friendly means of producing electricity. In this research, the integration of kalina cycle with CPVT for multi-generation and hydrogen production is presented. Although CPVT have been considered for multigeneration in past literature, this research is novel as it utilizes a kalina cycle to further increase the share of electricity produced by the multigeneration system. The system presented in this study will use a CPVT, single effect absorption cycle, kalina cycle, and hot air/hot water chambers to produce electricity, hot air, cooling effect, hot water and hydrogen from solar energy input. Thermodynamics approach will be used to analyze the performance of the system. The energy efficiency, electricity production, and exergy efficiency of the multigeneration will be considered with and without the use of a kalina cycle. Finally, the environmental benefits of the system will be highlighted.

II. System Description

In this section the modelled systems are described briefly. The performance of a CPVT system with and without a kalina cycle is compared in this research. With respect to Fig. 1, solar radiation (state 1) is concentrated onto PVT panels using heliostats (state 2) and this is used to produce to electricity and thermal energy. A portion (10%) of the electricity produced (state 3) is used to produce hydrogen using a proton exchange membrane (PEM) electrolyzer. The thermal energy from the CPVT system is used to produce cooling effect, hot air and hot water. While 65% of the thermal energy production is used by a single effect absorption cycle to produce cooling effect, 20% fo thermal energy is used for hot air production. The remaining 25% of the thermal energy produced by the CPVT system is used to produce hot water.

In order to produce more electricity with the configuration presented in Fig. 2, 50% of the thermal energy produced by the CPVT is utilized by the kalina cycle for electricity production. The remaining 50% are shared between a single effect absorption system (35%) and the hot water chamber (15%). Also, in order to maximize the energy within the kalina cycle, hot air production is integrated with the condenser of the kalina cycle as presented in Fig. 2. The input parameters for the two systems modelled are presented in Table 1.

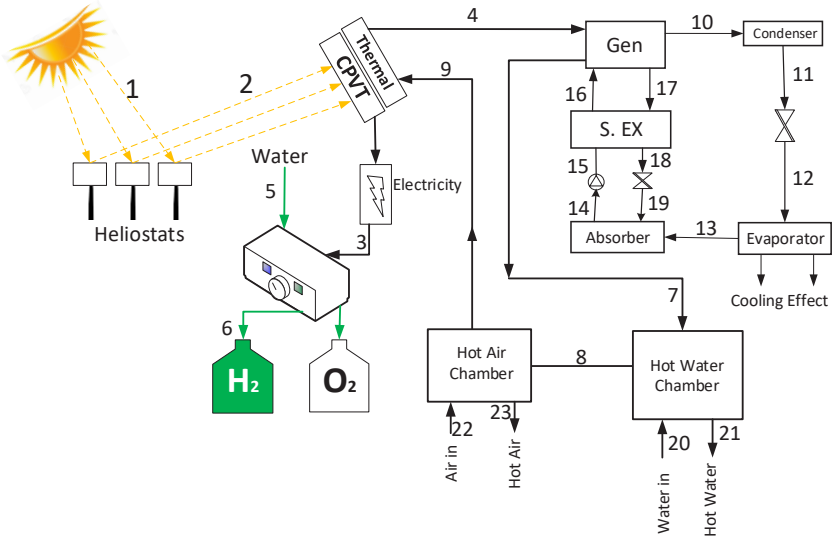

Fig. 1: CPVT powered multigeneration system schematic diagram

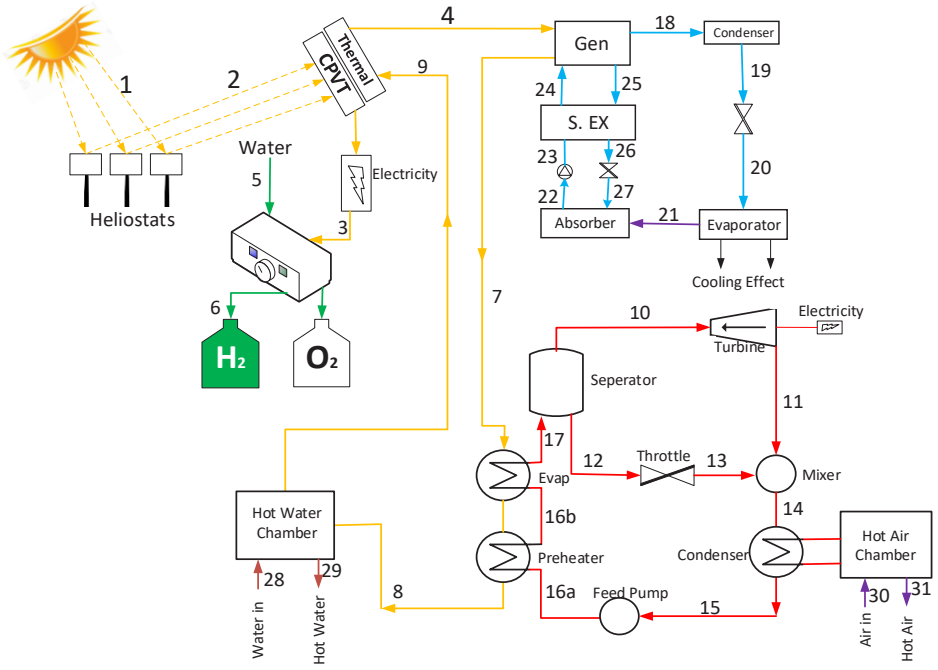

Fig. 2: CPVT integrated with Kanlina cycle multigeneration schematic diagram

III. Mathematical Modeling

In this section the mathematical equations used in the modelling the systems presented in section II are highlighted. This equations are modelled in accordance to literature (Bamisile et al., 2019; Sezer and Koç, 2019; Wakana, 2014). Engineering equation solver (EES) is used to solve the mathematical model presented in this section. The system is modelled based on the following assumptions:

- Air is considered as an ideal gas.
- The solar light spectrum used for solar reference is the ASTM Air Mass 1.5 direct spectra (AM1.5D).
- The pump and turbine are considered to be adiabatic.
- Changes in potential and kinetic energy are considered negligible.
- Capacity factor for the solar field is 0.33.
- Inverter DC/AC conversion efficiency is 0.98.

The overall energy efficiency for the two multigeneration systems can be modelled with Equation 1.

$$\eta_{en,MG} = \frac{W_{Total,MG}}{\dot{Q}_{in,solar}} \quad (1)$$

Where $W_{Total,MG}$ is the total useful outputs by the multigeneration system and this can be modelled with:

$$W_{Total,MG} = W_{net,power} + \dot{Q}_{out,HAC} + \dot{W}_{Evap} + (\dot{m}_{H_2} \times LHV_{H_2}) + \dot{Q}_{out,HWC} \quad (2)$$

Where $\dot{Q}_{out,HAC}$ and $\dot{Q}_{out,HWC}$ are the energy equivalence of hot air and water produced, $\dot{W}_{Evap}$ is the cooling effect production and $(\dot{m}_{H_2} \times LHV_{H_2})$ is the hydrogen production. $W_{net,power}$ is the summation of the electricity produce by the CPVT and kalina cycle. For the multigeneration system presented in Fig. 1, kalina cycle electricity production is taken as zero. The overall exergy efficiency is modelled with Equation 3 and Equation 4.

$$W_{Total,MG} = W_{net,power} + \dot{W}_{out,HAC}\left(1 - \frac{T_0}{T_{out,HAC}}\right) + \dot{W}_{Evap}\left(\frac{T_0}{T_{abs,E}} - 1\right) + \left(\dot{m}_{H_2} \times LHV_{H_2}\right) + \dot{W}_{out,HWC}\left(1 - \frac{T_0}{T_{out,HWC}}\right) \quad (3)$$

$$\eta_{ex,MG} = \frac{W_{ex,Total,MG}}{\dot{Q}_{ex,in,solar}} \quad (4)$$

The environmental analysis of the systems presented in this research is calculated with reference to #5 fuel oil emission properties.

Table 1. Multigeneration input parameters (Ezzat and Dincer, 2016)

Parameters	Inputs
Solar Concentration	500 suns
Global Solar Irradiance	900 W/m^2
Turbine Isentropic efficiency	90%
Collector Area	4000 m^3
Kalina cycle Turbine/Pump Efficiency	85%/80%
Hot Air/Water Chamber Efficiency	95%
Absorption Cycle Minimum Temperature/ Low Side Rated Pressure	279.1 K/4.82 kPa
Hot Water and Hot Air Inlet Temperature/Pressure	298 K/101.3 kPa
Rated Temperature/Pressure for Kalina cycle	

IV. Results and discussions

In this study the integration of Kalina cycle with CPVT systems in order to have a higher electricity production while multigenerating has been compared with the performance a CPVT multigeneration system without Kalina cycle. In order to achieve a high efficiency, 500 suns were concentrated on the PV cells of the CPVT system using a 4000 m^2 heliostat field. This produces an electrical output of 297.4 kW without the integration of a Kalina cycle (Table. 2). The cooling effect, hydrogen, hot water, and hot air production are 331.6 kW, 0.89 L/s, 1.091 L/s, and 12.69 kg/s respectively. The overall energy and exergy effciencies of the system without Kalina cycle integration are 74.64% and 59.46% respectively. The performance of the system without a Kalina cycle is good in comparison to research in literature. Hydrogen production from the multigeneration is crucial as this will cater for excess electricity production and make the environment more sustainable.

Table 2. Summary of multigeneration system performance

Production	Multigeneration system with Kalina cycle	Multigeneration system without Kalina cycle
Electricity	327.2 kW	297.4 kW
Hydrogen	0.9898 L/s	0.89 L/s
Cooling Effect	178.2 kW	331.6 kW
Hot Water	0.653 L/s	1.091 L/s
Hot Air	26.63 kg/s	12.69 kg/s
Energy Efficiency	72.49 %	74.64 %
Exergy Efficiency	54.01 %	59.46 %

Considering the same input conditions for the CPVT system, the integration of Kalina cycle increases the electricity production of the multigeneration system to 327.2 kW. The hydrogen and hot air production also increase to 0.9898 L/s and 26.63 kg/s respectively. The significant increase can be attribute to the integration of a hot air chamber at the condenser stage of the Kalina cycle. The cooling effect, and hot water reduces to 178.2 kW and 0.653 L/s. The overall efficiencies of the multigeneration system integrated with Kalina cycle are 72.49% for energy

and 54.01% for exergy. Although, the Kalina integrated systems' overall efficiencies are slightly lower but the higher electricity production makes it more superior.

The emission savings of the multigeneration system without and with Kalina cycle integration are presented in Fig. 3. The system can save as much as 245.4 kg/hr and 238.3 kg/hr of CO2 with and without the integration of Kalina cycle. This emission reduction adds to sustainability of the system as it is also environmentally friendly and needful for the future.

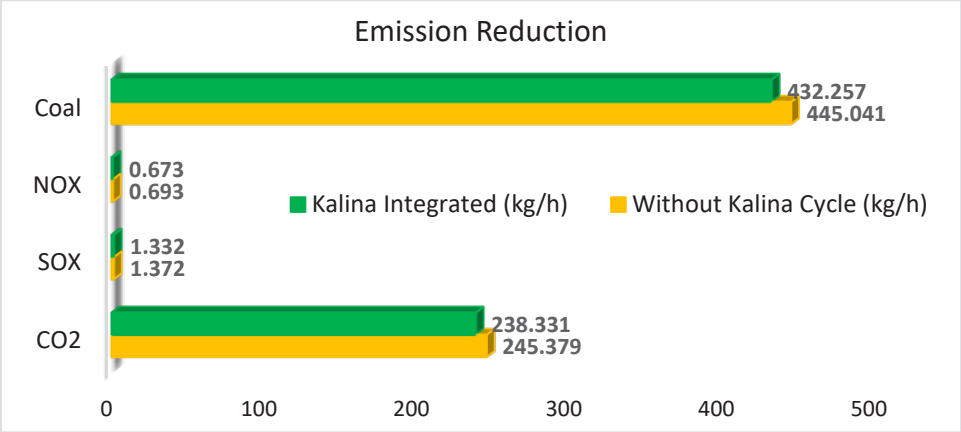

Fig. 3: Emission reduction summary

V. Conclusions

The integration of Kalina cycle with CPVT systems for a higher electricity production while multigenerating has been presented in the study. The performance of the Kalina integrated system is compared with that of a CPVT powered multigeneration system considering same input parameters. The outstanding conclusions from this study are highlighted below:

- The energy and exergy efficieny of the Kalina integrated system are 72.49% and 54.01% respectively.
- The Kalina integrated multigeneration system proves it superiority with a higher electricity, hydrogen and hot air production.
- A parametric study on the effect of ambient temperature shows that the system is adaptable to different atmospheric conditions.
- The environmental analysis indicates that system reduces a significant amount of carbon emission in comparison to its capacity.
- This multigeneration system will be suitable for underdeveloped, developing, and developed countries with good solar potential.

Acknowledgements

This research is supported by Sichuan Youth Science and Technology Innovation Team Fund under Grant No. 2017TD0009.

References

Bamisile, O., DAGBASI, M., ABBASOGLU, S., 2019. Energy and Exergy Analyses of a Novel Solar PTC Assisted Multi-Generation System. Int. J. Exergy 28, 1. https://doi.org/10.1504/ijex.2019.10019028

Chow, T.T., 2010. A review on photovoltaic/thermal hybrid solar technology. Appl. Energy 87, 365–379. https://doi.org/10.1016/j.apenergy.2009.06.037

Ezzat, M.F., Dincer, I., 2016. Energy and exergy analyses of a new geothermal-solar energy based system. Sol. Energy 134, 95–106. https://doi.org/10.1016/j.solener.2016.04.029

REN21, 2019. Ren21: Renewables 2018 global status report. https://doi.org/978-3-9818911-3-3

Sezer, N., Koç, M., 2019. Development and performance assessment of a new integrated solar, wind, and osmotic power system for multigeneration, based on thermodynamic principles. Energy Convers. Manag. 188, 94–111. https://doi.org/10.1016/j.enconman.2019.03.051

Siddiqui, O., Dincer, I., 2017. Analysis and performance assessment of a new solar-based multigeneration system integrated with ammonia fuel cell and solid oxide fuel cell-gas turbine combined cycle. J. Power Sources 370, 138–154. https://doi.org/10.1016/j.jpowsour.2017.10.008

Wakana, F., 2014. Preliminary Study of Binary Power Plant Output Comparing ORC and Kalina for Low-Temperature Resources in Rusizi Valley, Burundi, in: ARGEO-C5 Conference.

World Nuclear Association, 2011. Comparison of Lifecycle Greenhouse Gas Emissions of Various Electricity Generation Sources. WNNA Rep. 10. https://doi.org/10.1002/esp

Yuksel, Y.E., Ozturk, M., Dincer, I., 2019. Energetic and exergetic assessments of a novel solar power tower based multigeneration system with hydrogen production and liquefaction. Int. J. Hydrogen Energy 44, 13071–13084. https://doi.org/10.1016/j.ijhydene.2019.03.263

Study of GaAsPN/GaP Quantum Dots Sturcture for Solar Cell Applications

[1,2*] Abdelkader Aissat, Said Nacer[1], Jean Perre Vilcot[2]
[1] Faculty of Technology University of Blida 1 09000, Blida Algeria
[2] Institut d'Electronique, de Microélectronique et de Nanotechnologie (IEMN), UMR CNRS 8520. Université des Sciences et Technologies de Lille 1 Avenue Poincare´, BP 60069, 59652 Villeneuve d'Ascq, France

* E-mails: sakre23@yahoo.fr

Abstract
This study focuses on the simulation and modeling of GaAsPN/GaP quantum dot solar cell QDSC. This quaternary alloy is one of the III-V semiconductors, which gained importance in the recent years for optoelectronic applications due to its perfect lattice matching to Si and GaP substrates and to its band gap that can be decreases drastically with the incorporation of Nitrogen and Phosphorus on GaP improving consequently the absorption the wavelengths near the red part. These superiorities of GaAsPN make it a good candidate for growth with Si substrate, then a good option to decrease the cost of the solar cell. The heterostructures consist of $GaAs_{0.18}P_{0.814}N_{0.006}$ quantum dots separated by GaP barrier layers. The width and thickness of the quantum dot are 10 nm and 5 nm, respectively. Our results have been shown that 20 $GaAs_{0.18}P_{0.814}N_{0.006}$/GaP QD layers produce a short circuit current and efficiency of about 3.555 mA/cm2 and 7.5 %, respectively. In addition, the same number of QD layers extends the absorption edge of the GaP solar cell from 0.447 µm to 0.5 µm.

Keywords: component; efficiency, QDSC, solar cell, III-V semiconductors.

I. Introduction

The use of cheap Silicon substrates could allow integration of III-V-based devices as photodetectors and single photon sources with Si electronics [Kuyanov,2015]. However, integration of III-V materials on silicon substrate is a technological challenge due to the high density of dislocations and defects caused by the large lattice mismatch between the most III-V materials and Si, and also to the large difference in thermal expansion coefficients leading to stress [Cheng,2010]. One of the promoted new materials systems that attracted the researchers in the recent years is $GaAs_{1-x-y}P_xN_y$, thanks to its lattice matched to Si and their alterable band gap energy. These superiorities make GaAsPN a promising material for quantum wells QWs and quantum dots QDs manufacturing. This paper focuses on the modeling and simulation of GaAsPN/GaP growing on Si substrate, with fixed x and y to 0.814 and 0.006, which corresponding to a band gap energy and lattice parameter of 1.8 eV and 5.473 A, respectively. The electrical properties of QDSC with a variable number of quantum dot layers were compared to a GaP pin solar cell to show the advantages of the QDs insertion. Moreover, the optical properties were analyzed by external quantum efficiency EQE and the absorption coefficient.

Fig.1 shows the structure of $GaAs_{0.18}P_{0.814}N_{0.006}$/GaP QDSC with 10 layers of $GaAs_{0.18}P_{0.814}N_{0.006}$/GaP QD inserted in the intrinsic region of GaP p-i-n solar cell. Two green layers of GaP on bottom and top represent the base n-type and emitter p-type, respectively, with doping concentration of about 1×10^{18} each one. Another green GaP layer in the middle represents the intrinsic region contains the $GaAs_{0.18}P_{0.814}N_{0.006}$/GaP QD periods shown by a yellow color with a high of 5 nm and a width of 10 nm.

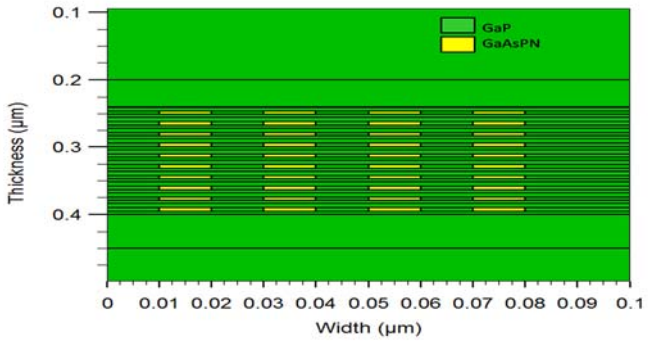

Fig. 1: $GaAs_{0.18}P_{0.814}N_{0.006}$ /GaP QDSC with 10 QD layers embedded in intrinsic region.

II. THEORETICAL MODEL

In this section, we will describe the empirical equations and physical models used in this simulation. The Drift-Diffusion model is used to calculate the current density of holes and electrons in the bulk regions expressed by the continuity equation [Khoie, 2006]:

$$\frac{dn_b}{dt} = G_b - U_b - \frac{n_b}{\tau_{cn}} - \frac{n_{qw}}{\tau_{en}} + \frac{1}{q}\frac{dJ_n}{dx} = 0 \quad (1)$$

$$\frac{dp_b}{dt} = G_b - U_b - \frac{p_b}{\tau_{cp}} + \frac{p_{qw}}{\tau_{ep}} - \frac{1}{q}\frac{dJ_p}{dx} = 0 \quad (2)$$

Where p_b and n_b are the bulk hole and electron densities, symbols τ_{ep} and τ_{en}, are the hole and electron escape times and τ_{cp}, τ_{cn} are the hole and electron capture times, respectively. G_b and U_b are the photogeneration rate and the Shockley–Read–Hall (SRH) of the bulk, respectively. p_{qw} and n_{qw} are the quantum-well hole and electron densities, respectively, and J_p, J_n are the hole and electron current densities, respectively. Current continuity equations for the quantum well systems are expressed as follow [Khoie, 2006]:

$$\frac{dn_{qw}}{dt} = G_{qw} - U_{qw} - \frac{n_b}{\tau_{cn}} - \frac{n_{qw}}{\tau_{en}} = 0 \quad (3)$$

$$\frac{dp_{qw}}{dt} = G_{qw} - U_{qw} - \frac{p_b}{\tau_{cp}} + \frac{p_{qw}}{\tau_{ep}} = 0 \quad (4)$$

Where G_{qw} and U_{qw} are the photogeneration rate and the Shockley–Read–Hall (SRH) recombination rate, respectively. These two equations are solved using the Poisson equation [Khoie, 2003]:

$$\frac{d^2V}{d^2x} = \frac{q}{\varepsilon}\left[N_A^- - N_D^+ + n_b + p_b - n_{qw} - p_{qw}\right] \quad (5)$$

The mobility of carrier's dependent concentration described by Masetti model and the carriers recombination modeled by SRH recombination using concentration dependent lifetimes model is given in detail in [Benyettou, 2015]. Radiative recombination has been neglected due that simulations are done at T=300K. [Gurioli,1991]. The External Quantum Efficiency is calculated using the equation below.

$$J_{ph} = q\int_{\lambda_i}^{\lambda_f} F(\lambda)\cdot EQE(\lambda)\,d\lambda \quad (6)$$

Where J_{ph} is the photocurrent supplied by the solar cell which is calculated using the continuity equations, F(λ) is the spectral solar irradiance, λ_i is initial wavelength and λ_f is the final wavelength. The absorption coefficient can be extracted from the EQE and it is given by [Thériault,2015].

$$EQE(\lambda) = (1 - R(\lambda))\cdot \exp(-\alpha(\lambda)\cdot x_i) \quad (7)$$

Where R(λ) is the spectral reflection, we have taken it 0.1 in our simulation; α(λ) is the absorption coefficient and xi is the total intrinsic region. The band gap of $GaAs_{1-x-y}P_xN_y$ is expressed by [Yu,2011].

$$E_{gGaAs_{1-x-y}P_xN_y} = E_{g_{GaP}}\cdot x + E_{gGaN}\cdot y + E_{gGaAs}\cdot(1-x-y) - (x\cdot(1-x-y)\cdot C_{GaAsP}) - (y\cdot(1-x-y)\cdot C_{GaAsN}) - (xy\cdot C_{GaPN}) \quad (8)$$

Where Eg_{GaP}, Eg_{GaN} and Eg_{GaAs} are the band gap energies of GaP, GaN and GaAs at room temperature, respectively. In our simulation, they have the values of 2.77 eV, 3.18 eV and 1.42 eV [9], respectively. The C symbol represents the bowing parameter and is given for GaAsP, GaAsN and GaPN: 0.19 eV, 119.8 eV, and 3.9 eV, respectively [9].

IV. Results and discussions

Along this work, we have chosen a solar spectrum AM1.5G and a temperature of 300 K as standard conditions for simulation. For each simulation, the important characteristic parameters, the current density-voltage J-V and the EQE curves a solar cell are presented and discussed. The Schrodinger, Poisson and drift-diffusion equations described above are coupled and solved numerically for calculation of EQE and J-V characteristics of the devices. Eq. 9 is used to extract the absorption coefficient from EQE curves. The used material parameters are given by [9]. Fig.2 shows the External Quantum Efficiency EQE of the two structures studied: GaP pin, and $GaAs_{0.18}P_{0.814}N_{0.006}$/GaP QDSC for various QD layers. It was evident that the spectral response of GaP pin extends from 447 nm up to 500 nm when we insert the quantum dot layers. This is due to the absorption of low-energy photons by the QDs. Moreover, at the wavelength 480 nm, the EQE was reached a gain of about ΔEQE= 8.87 % with 20 QD layers. This study allows us to show how the QD layers insertion improves the EQE characteristic of the GaP pin solar cell.

Fig.3 illustrates the calculated curve of the GaP pin absorption coefficient, and $GaAs_{0.18}P_{0.814}N_{0.006}$/GaP QDSC for different number of QD layers. It was evident that the $GaAs_{0.18}P_{0.814}N_{0.006}$/GaP QDSC takes higher values in the range of wavelengths 300 nm-500 nm. For example, at 400 nm, the absorption coefficient was reached a gain of about $\Delta\alpha = 5.24\times10^4$ cm^{-1}. This study allows us to show how the QD layers insertion enhances the absorption of the

GaP pin solar cell. Fig.4 and Fig.5 show the current-voltage J(V) characteristic and the power-voltage P(V) characteristic, of $GaAs_{0.18}P_{0.814}N_{0.006}$/GaP QDSC for 0, 10, and 20 QD layers, respectively. The short-circuit current increases with the number of QD layers integrated inside the i-region due to the additional electron-hole pairs photogenerated.

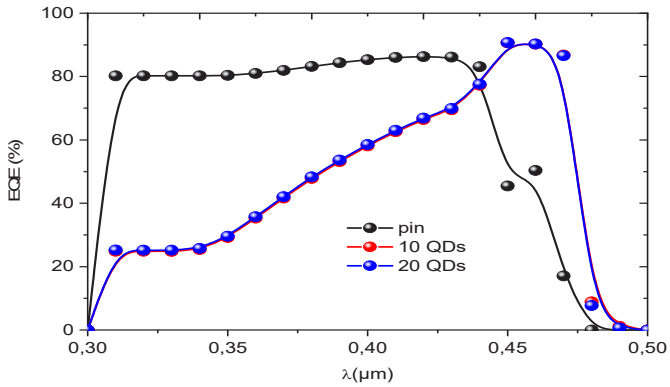

Fig. 2. J(V) of ~~of~~ GaP pin solar cell and $GaAs_{0.18}P_{0.814}N_{0.006}$/GaP QDSC for two numbers of QD layers: 10 and 20.

The open circuit voltage slightly increased because the short circuit increases. Consequently, the efficiency is rising with the increase of the quantum dot number until 20 QDs; after this number, the efficiency and the power generated keep the same value. Comparing a pin solar cell and a 20-layers $GaAs_{0.18}P_{0.814}N_{0.006}$ quantum dot solar cell, allows us to have a relative increase of about 22.26% of efficiency.

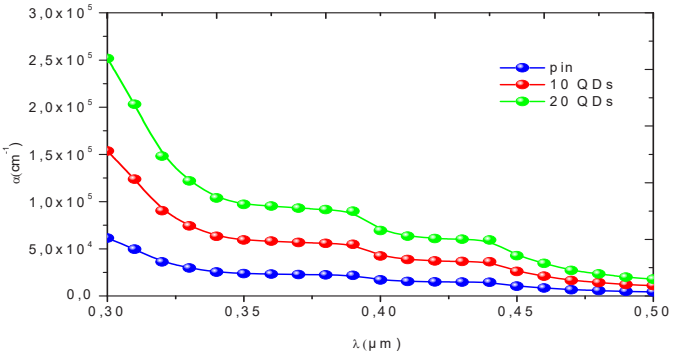

Fig. 3. Absorption coeficient of $GaAs_{0.18}P_{0.814}N_{0.006}$ /GaP QDSC and pin solar cell.

Table 1. The important parameters of p-i-n solar cell and $GaAs_{0.18}P_{0.814}N_{0.006}$/GaP quantum dot solar cell with different number of QD layers.

QDs	J_{sc} (mA/cm²)	V_{oc} (V)	FF (%)	η(%)
0	*3.39*	*2.19*	*78.53*	*5.83*
10	*3.55*	*2.25*	*93.15*	*7.44*
20	*3.55*	*2.25*	*93.76*	*7.50*

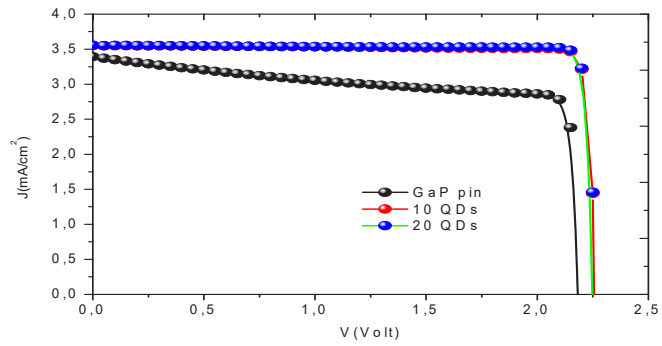

Fig. 4. J(V) of GaP pin and $GaAs_{0.18}P_{0.814}N_{0.006}$ /GaP QDSC for two number of QD layers: 10 and 20 .

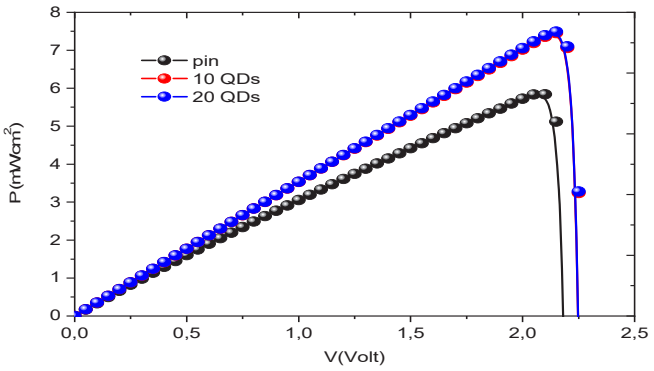

Fig. 5. P(V) of GaP pin and $GaAs_{0.18}P_{0.814}N_{0.006}$/GaP QDSC for two number of QD layers: 10 and 20

V. Conclusion

In this paper, we have studied the insertion effect of quantum dot QD material system $GaAs_{0.18}P_{0.814}N_{0.006}$ in the intrinsic region of a GaP pin solar cells in goal to grow it on silicon substrate. Our results show that insertion of 20-layers of $GaAs_{0.18}P_{0.814}N_{0.006}$/GaP improves relatively the conversion efficiency by 22.30 %. In other hand, the absorption range edge of photons with low energy is widely extended from 447 nm to 500 nm by using the same number of QD layers with a gain of about 8.873 % of EQE. Finally, we hope that this work will be useful for others work in the field of photovoltaic.

References

P. Kuyanov, R.R La Pierre , “Photoluminescence and photocurrent from InP nanowires with InAsP quantum dots grown on Si by molecular beam epitaxy”, IOP Publ Nanotechnol, vol.26, p. 315202, 2015.

J. Cheng1, A. El Akra, C. Bru-Chevallier, G. Patriarche, L. Largeau, P. Regreny, et al, “Optically active defects in an InAsP/InP quantum well monolithically integrated on SrTiO3(001)”, Mater. Res. Soc. Symp. Proc p. 1252, 2010.

R. Khoie and S. M. Ramey, “Self-consistent modeling of escape and capture of carriers in quantum wells”, Phys. E, vol. 34, p. 449, 2006.

R. Khoie and S. M. Ramey, “Modeling of multiple-quantum-well solar cells including capture, escape, and recombination of photoexcited carriers in quantum wells”, IEEE Trans. Electron. Devices, vol. 50, p. 1179, 2003.

F. Benyettou, A. Aissat, M. Benamar, J. Vilcot, “Modeling and simulation of GaSb/GaAs quantum dot solar cell”, Energy Procedia, vol. 74, p. 139, 2015.

M. Gurioli, A. Vinattieri, M. Colocci, C. Deparis, J. Massies, G. Neu, A. Bosacchi, and S. Franchi, “Temperature dependence of the radiative and nonradiative recombination time in GaAs/AlGaAs quantum-well structures”, Phys. Rev. B, Condens. Matter, vol. 44, p. 3115, 1991.

O. Thériault, “Analysis of the external quantum efficiency of quantum dot-enhanced multijunction solar cells”, Phd Thesis. University of Ottawa, 2015.

A. Yu. Egorova, N. V. Kryzhanovskayab, and M. S. Soboleva, “Optical Properties of Quantum Confined Heterostructures Based on GaPxNyAs1–x–y Alloys”, Semiconductors, Vol. 45, pp. 1164–1168, 2011.

Optimal sizing of a residential grid-interactive PV with battery storage using HOMER

[1*]Stephan Marais, [2]Kanzumba Kusakana
[1,2] Central University of Technology South Africa, Faculty of Engineering, Built Environment and Information Technology, 20 President Brand, Bloemfontein, 9300, South Africa

* E-mails: stephen.marais777@gmail.com; kkusakana@cut.ac.za

Abstract
In this paper, the optimal size of a residential grid-interactive photovoltaic system with a battery storage system is computed using HOMER software. The proposed grid interactive system operates under the Time of Use and Feed-in tariff in the South African context. Based on the simulation results, it is found that the optimal configuration is composed of one 2.1 kW PV, with one 2kW converter and four batteries. This system's configuration met the load demand at no shortage and incurred a levelized cost of energy of US$ 0.32 or ZAR 5/kWh. The annual average electricity production from the PV is about 49% of the total generation, while the remainder of the necessary power is purchased from the grid. Therefore, the major share of the power is obtained from the PV to meet the load requirement and to keep zero unmet energy by the system.

Keywords: Time of Use; Feed-in Tariff; Grid interactive; Photovoltaic; Battery; Sizing

I. Introduction

In South Africa, electricity is solely supplied by Eskom, a state-owned enterprise. For the last decade, Eskom have experienced challenges in meeting the national demand. The issue of the supply being less than the demand, has led to the requirement of additional fossil fuel plants, which resulted in financial challenges. These financial challenges have resulted in harsh tariff increases for consumers. With the aim to reduce the load-demand of the grid during peak periods, the electricity supply commission (ESKOM), implemented the time-of-use (TOU) tariff structure, billing consumers at a higher tariff rate during certain periods of the day. These tariff increases are compelling residential consumers to search for alternative ways in meeting their energy demand such as the use of small embedded renewable energy systems (Kusakana; 2017).

As a result of the electricity challenge in South Africa, a few municipalities have begun revising the regulations on small scale embedded generators, permitting consumers, under strict regulations, to feed-back excess energy into the grid (Koko et al; 2018). This study investigates the use of a residential PV system, combined with battery storage operating under the Time of Use and Feed-in tariff in the South African context. Therefore, the system needs to be optimally sized to meet the load demand while minimize the net cost between the energy purchased from the grid and the revenues generated by exporting the energy generated by the PV.

An optimal size (configuration) of the proposed grid-interactive PV with battery storage system is computed using the Hybrid Optimization Model for Electric Renewable HOMER software (Kusakana and Vermaak; 2013). Input dada such as the load, the renewable energy resources, the size and cost of the different components, the TOU structure and other parameters are run through the software where it compares all the possible options and gives the most optimized system configuration that will met the load at the lowest cost of energy produced.

II. System Description and data collection

II.1. System description

Figure 1 presents the schematic diagram for the proposed grid-interactive PV with battery storage system, to be sized using HOMER software. The following constraints where considered in designing the system:

- The funding available to implement the system,
- The space available on site to implement the system,
- The grid requirement, in terms of the mount of power and energy that is permitted to be exported,
- The energy savings target on the consumer's side.

The proposed system consists of a PV array, converter, battery as well as the utility grid supplying the load.

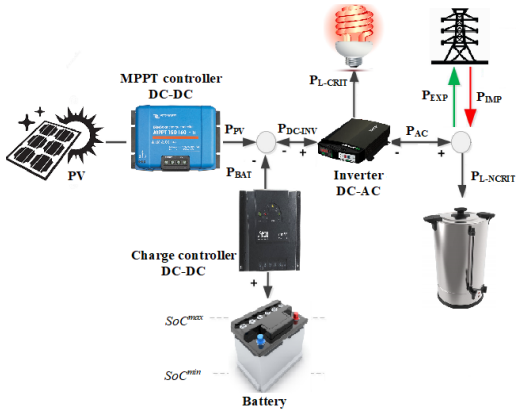

Fig. 1: Design configuration of PV battery-based grid-interactive system

II.2. Load description

The household identified for this case study, is in the City of Cape Town, Western Cape. This is a typical South African household with the yearly demand given on Figure 2. It may be noted that the average peak demand usage during the recorded period was 16.12 kWh/d, with an average peak consumption of 2 kW (Marais et al; 2019a). During the summer months, the load consumption was significantly less than during winter months, due to the use of water and space heaters.

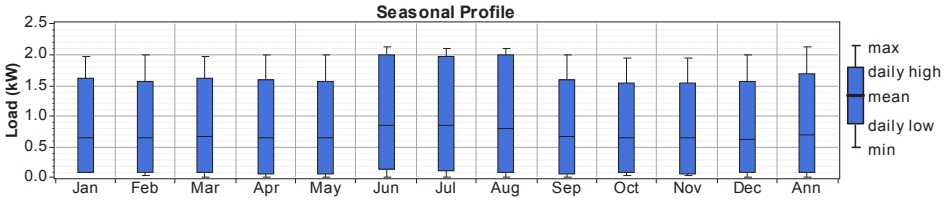

Fig. 2: Acquired annual residential load demand using Efergy monitoring device

II.3. Solar resources

The solar resource profile for this study has been obtained from the Southern African Universities Radiometric Network (SAURAN) database. Figure 3 shows the solar radiation used in this study. The maximum radiation levels take place during November, December and January. Hence, this reveals that the large amount of PV power may be obtained in the study area.

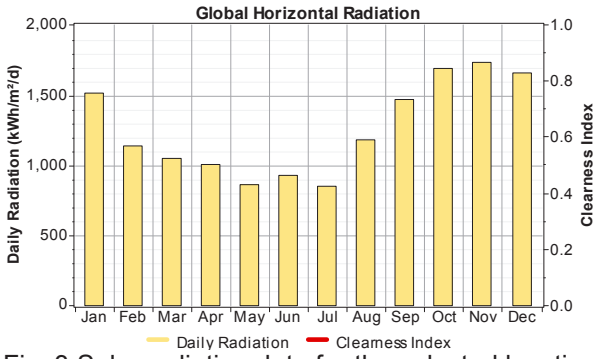

Fig. 3 Solar radiation data for the selected location

II.3. Components cost

The PV panel selected based on market price suitable for this study is Renewsys. The market price of a PV panel is ZAR 2000 for a 440W. Compared to the capital and installation cost, the O&M cost is minimal and is estimated to be 2% of the installation cost/year for each kW considered; the lifetime is set to 20 years.

For this study, the 2 kW Steca single phase grid-interactive inverter is selected. This inverter has a maximum load current of 11.2 A, with an efficiency rate of above 94% for PV to battery and above 93% for battery to the AC system. When the load profile is observed, it is noticed that the load does not exceed 2 kW peak during summer or winter periods. From the inverter's technical specifications, it has a peak output power of 2.5 kW and a rated output power of 2 kW. The price of the PV converter used in this study is ZAR 11495. The converter yearly O&M cost is estimated to be 5% of the total investment.

The battery storage selected for the design was the Trojan T-105 model. The South African market price of purchasing this battery is ZAR 3195, with a lifespan of 5-7 years (Kusakana; 2015).

Eskom Ruraflex Gen tariff will be applied as a case study, since it permits the consumer to inport and export energy at the same point of supply. Eskom Ruraflex Gen TOU tariff for high and low-demand seasons, as applied to consumers are shown of Figure 4 and the corresponding cost can be found in reference. For this study, the FIT incentive for residential embedded generation used in this municipality will be used as 65% (Marais et al; 2019b).

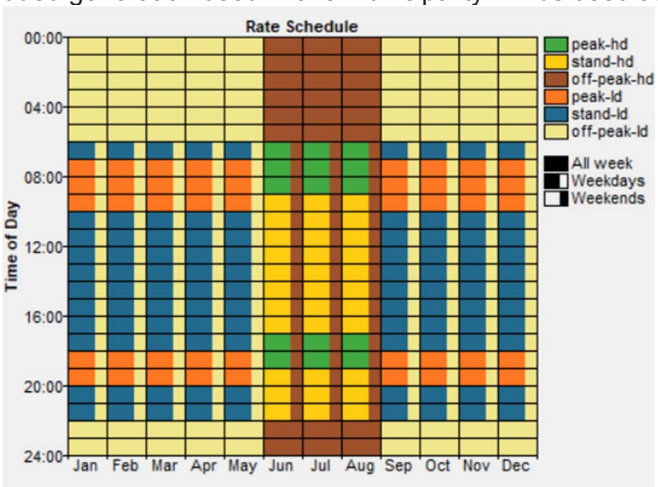

Fig. 4: TOU schedule for low demand and high demand season as applied by the utility

III. Simulation results and discussion

III.1. Sizing result and components operation

HOMER determines the most economical configuration for the proposed grid-interactive system, by using the data mentioned in Section II. Lastly, in order to improve the accuracy of the results, the simulation was performed over a period of 8760 hours to incorporate the effect the seasonal changes might have.

From HOMER optimization results in Figure 5, the chosen optimal configuration is utilizing one 2.1 kW PV, with one 2kW converter and four (TROJAN T-105) batteries.

T-105 Min. Life (yr)					PV (kW)	T-105	Conv. (kW)	Grid (kW)	Initial Capital	Operating Cost ($/yr)	Total NPC	COE ($/kWh)	Ren. Frac.
4.0					2.1	4	2	1000	$ 2,790	1,477	$ 21,673	0.320	0.56
4.5					2.1	4	2	1000	$ 2,790	1,477	$ 21,673	0.320	0.56
6.0					2.1	4	2	1000	$ 2,790	1,477	$ 21,673	0.320	0.56
7.0					2.1	4	2	1000	$ 2,790	1,477	$ 21,673	0.320	0.56

Fig. 5: Overall optimization results with sensitivity analysis

The monthly average of electricity produced by each component of the system is presented in Figure. 6. The monthly and seasonal variations in amount of electricity produced by PV system and contribution from the grid, may be observed from this figure. The maximum average monthly power generated by the solar PV during summer periods, is around 0.45 kW and a maximum of 0.4 kW during winter.

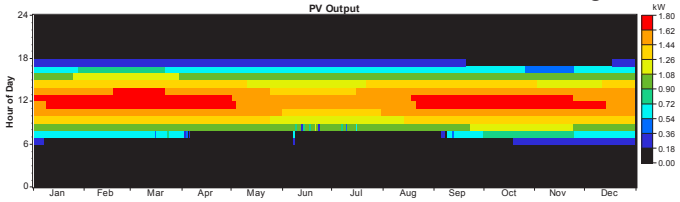

Fig. 6: PV power output

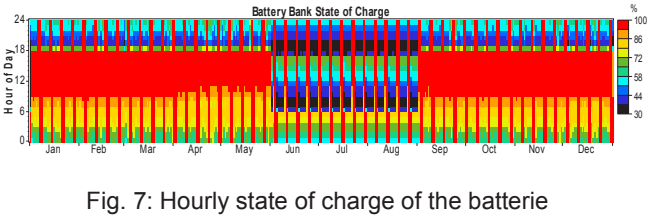

Fig. 7: Hourly state of charge of the batterie

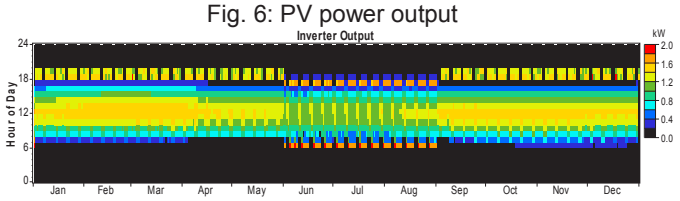

Fig. 8: Inverter output power

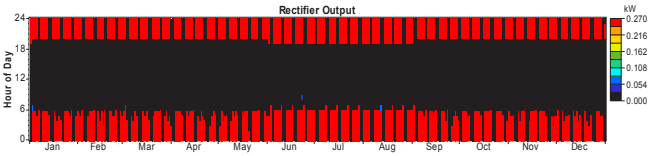

Fig. 9: Rectifier output power

The yearly output PV production based on hourly load for each day of every month, is shown in Figure 6. The results from Figure 6, shows that the PV system starts generating as soon as from 06h00 in the summer, while the generation starts from 07h30. The peak power production is observed to be between 09h00 and 15h00.

Figure 7 presents the hourly state of charge of the batteries for each month during the simulated period. It shows that the battery remains fully charged from 09h00 to 18h00 during summer periods (January to May and September to December), having a minimum state of charge around 18h30. During winter periods (June to August) the batteries are never fully charged, reaching a minimum state of 30% around 07h00 in the morning and 18h30 in the evening.

Figures 8 and 9, represent the inverter output and rectifier output. Figure 8 shows that the majority of the DC to AC power conversion takes place during midday. The opposite may be seen in Figure 9, where the model solely converts AC to DC power in the morning and the evenings.

III.2. Power flow analysis

- *The system behaviour from 00h00 to 06h00*

Figure 10, illustrates the load profile and PV output power for 12 January 2017. During this period, the load profile remains constant for the first 3 hours, then rapidly increases, reaching a maximum of 1.48 kW.

Figure 11 presents the energy sold to the grid, vs the energy purchased from the grid. It is shown that no energy is exported, however, that the consumer imported energy from the grid.

The battery state of charge in Figure 12, shows that the batteries are charged during this period.

- *The system behaviour from 06h00 to 12h00*

Figure 10 shows a rise in solar radiance, as the output power of the PV reaches a peak of 1.7 kW. As the consumer starts preparing for work the load demand reaches a peak of 1.3 kW around 06h00.

During this period Figure 11 shows that the amount of energy imported from the grid starts reducing. It may further also be seen that the consumer starts selling energy to the grid. Figure 12 shows that the batteries continue to charge. The power flow of the inverter which converts electricity from DC to AC is presented in Figure 13 where it is flowing through the inverter; reaching a peak power flow of 1.4 kW.

The challenge with the power flow through the inverter, is that it is not possible to determine from where it originated; it may be supplied from the PV or the battery bank.

- *The system behaviour from 12h00 to 18h00*

Figure 10 shows that during this period, the PV output power starts reducing as the sun sets. Figure 10 further shows that the load remains constant for most of this period and only begins to increase at approximately 17h00.

Figure 11 shows a reduction in the amount of energy exported due to the fact that the power produced by the PV is reduced and is used to supply the load as first priority.

Figure 12 shows that the batteries continue to charge, reaching 100% state of charge before 18h00. Figure 13 shows a reduction in the amount of energy flowing through the inverter to supply the load or to be exported.

- *The system behaviour from 18h00 to 24h00*

Figure 10; shows that during this period, there is no power produced by the PV, while the load demand has a significant increase. During this period, Figure 11 shows that the amount of energy imported is quite important. The state of charge of the batteries in Figure 12 decreases, thereafter it increases reaching a minimum of 60% at the end of the day. Figure 13 shows that the inverter input is decreasing and reaching zero from 20h00 t0 24h00; this means that there is no power from the PV or from the battery, the load entirely relies on the grid during this period.

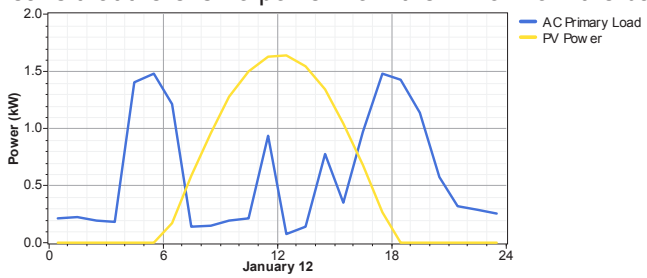

Fig. 10: PV output power and load profile

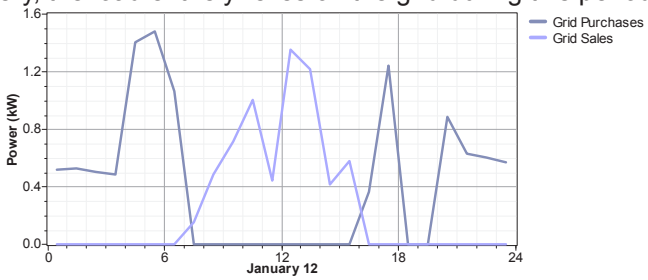

Fig. 11: Grid purchases vs grid sales

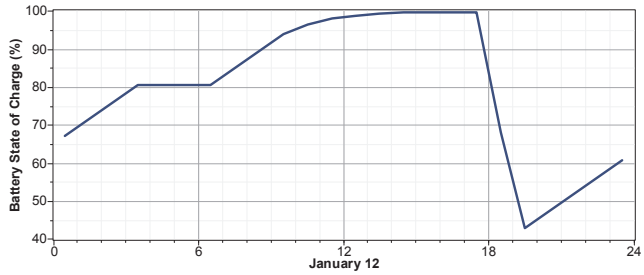

Fig. 12: Battery state of charge

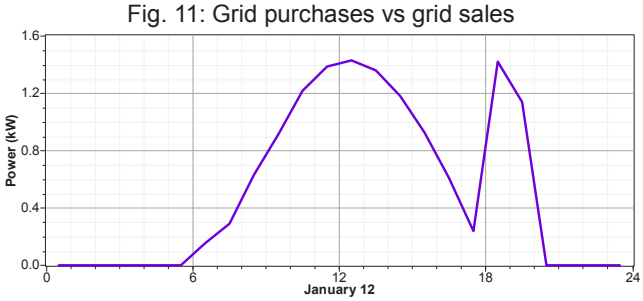

Fig. 13: Inverter input

IV. Conclusion

The main goal of this paper, was to conduct a sizing and techno economic analysis of grid-interactive PV with incorporating a battery system in the South African context. From HOMER optimization results, the chosen optimal configuration is utilizing one 2.1 kW PV, with one 2kW converter and four (TROJAN T-105) batteries. This system's configuration met at no shortage and incurred levelized cost of energy of $ 0.32 or ZAR 5/kWh. The results further highlighted that the reliance on the grid went from 100% to 51%, with the PV producing 49% of the required energy. The results also revealed that HOMER avoided importing energy from the grid during peak billing periods; however, the battery state of charge had a vital impact on the amount of energy imported during peak periods.

In Section III.2, the power flow of each component was presented in the figures. After analyzing these results, it can be seen that it is not possible to further analyze the specific power flow of each component at a specific time frame, as HOMER did not permit to display the following specific power flows from the PV to the load, from the PV to the grid, from the PV to the battery bank, from the battery bank to the load, battery bank to the grid, from the grid to battery bank or from the grid to the load. HOMER solely provides the option of plotting the power flowing through the inverter and rectifier. Hence, this limitation denoted that there is a continuous need to model an optimal energy management scheme, allowing the consumer to analyze the power flow of each component, allowing the consumer to make an optimal decision.

References

Koko, S.P., Kusakana, K. and Vermaak, H.J., 2018. Optimal power dispatch of a grid-interactive micro-hydrokinetic-pumped hydro storage system. Journal of Energy Storage, 17, pp.63-72.

Kusakana, K., 2017. Energy management of a grid-connected hydrokinetic system under Time of Use tariff. Renewable Energy, 101, pp.1325-1333.

Kusakana, K. and Vermaak, H.J., 2013. Hybrid renewable power systems for mobile telephony base stations in developing countries. Renewable Energy, 51, pp.419-425.

Kusakana, K., 2015. Optimal operation control of hybrid renewable energy systems (Doctoral dissertation, Bloemfontein: Central University of Technology, Free State).

Marais, S., Kusakana, K. and Koko, S.P., 2019a, October. Energy Monitoring for Potential Cost Saving in a Typical South African Household. In 2019 Open Innovations (OI) (pp. 122-126). IEEE.

Marais, S., Kusakana, K. and Koko, S.P., 2019b, March. Techno-economic feasibility analysis of a grid-interactive solar PV system for South African residential load. In 2019 International Conference on the Domestic Use of Energy (DUE) (pp. 163-168). IEEE.

Thermal performance evaluation of solar powered quadruple effect absorption refrigeration cycle

[1*]Muhammad Abid, [2]Tahir A. H. Ratlamwala
[1] Cyprus International University, Faculty of Engineering, Department of Mechanical Engineering, Nicosia, North Cyprus via Mersin 10, Turkey
[2] Department of Engineering Sciences, National University of Science and Technology (NUST), Karachi, Pakistan

* E-mails: mabid@ciu.edu.tr

Abstract
Multi-effect absorption refrigeration cycles from single to quadruple effect are examined in this study with the prospective of the first and second laws of thermodynamics. They are designed and simulated to produce the identical cooling load under same operating conditions. The quadruple effect absorption refrigeration cycle (QEARC) is composed of four desorbers and four condensers and is an extended version of the conventional single and double effect absorption refrigeration cycles (DEARC). The higher number of desorbers will separate more vapor from the solution entering the desorbers. The more vapor will help in increasing the cooling capacity which results in increasing the coefficient of performance (COP) of the cycles. It is observed that the QEARC is leading with the highest COP (2.11) followed by TEARC, which has the COP of 1.75. The second law efficiency also shows that the QEARC works better than the respective cycles of single, double and triple effect under the same operative environment. The second law (exergetic) efficiency of the QEARC is witnessed to be 11.7% higher than the SEARC and 6% higher than triple effect absorption cycle. It is found that for a fixed evaporator temperature and for a fixed condenser load, there is an optimal temperature of the generator, where the COP and exergy efficiency are found to be maximum. The results show that the QEARC needs 63% less thermal energy in comparison to SEARC to produce the same cooling load. The mass dissemination among the desorbers too affect the cooling production along with the performance of the absorption refrigeration cycles.

Keywords: Parabolic trough, exergy, comparison, quadruple effect, cooling load

I. Introduction

Absorption refrigeration cycle (ARC) is a device to provide the required refrigeration using thermal energy. The absorption refrigeration cycles are different than the compression refrigeration cycles (CRC) the way they are operated. The ARC's can be operated with low grade heat while electrical energy is needed to drive the CRC. The ARC are capable of providing necessary cooling and heating using inexpensive source of energy such as solar energy. The solar collectors such as parabolic trough solar collectors can easily be integrated to absorption cycles to fulfill their energy requirements (Tahir and Abid, 2018). Studies performed by (Li et al., 1999) and (He et al., 2001) describe a 100 kW absorption system which is designed to deliver heating as well as cooling concurrently. The system was designed to save energy significantly as well as to be environment friendly. A single effect absorption cycle (SEAC) operated on solar collectors was designed and experimented in Malaysia by (Assilzadeh et al., 2005). It was observed that the higher solar irradiation results in producing higher useful energy as well as the higher outlet temperature of the solar collector. On the other hand, increase in inlet temperature of the solar collector decreases the useful energy production and increases cooling load, the higher cooling will have higher COP of the system. Authors believed that countries, such as Malaysia with higher solar radiations, are good for solar assisted absorption cooling systems. A comparative study performed between double effect (DE) parallel and series flow lithium-bromide absorption system by (Arun et al., 2001).The results of their study show that optimal coefficient of performance (COP) attained for first system is greater than the second one. In addition, rate of heat given to the low pressure generator has more effect on parallel system rather than on the series flow system.

(Oouchi et al., 1985) performed analysis of three condenser-three desorbers (3C3D) triple effect (TE) absorption cycles, which is an extended form of traditional DE cycle with an evaporator and an absorber to absorb the refrigerant, 3C3Ds recover heat for the lower temperature desorber from the condenser of high temperature. The application of water and ammonia pair to the several versions of three stage system was examined and presented by (De Vault and Marsala, 1990). They explained that the feasibility of three- condenser system was not justifiable as the ammonia critical point was lower than the condensation temperature. (Gomri R., 2010) carried out simulation analysis for single and multistage absorption cooling systems and concluded to achieve the COP of around 1.62-1.9 for series flow TE cycles. The exergy efficiency was also observed to be higher for triple effect cycles in comparison to single and double effect cycles. Some other researchers (Xu et al., 1997, Arun et al., 2000) performed thermodynamic analysis of triple effect cycles. It is observed in their analysis that these multistage systems can be compared not only for energy efficiency but also for practicality, economics and environmental aspects. The quadruple effect (QE) absorption cycles, which are the extended versions of the triple effect cycles are relatively new and not fully explored. There is not much literature available on quadruple effect cycles. (Ratlamwala et al., 2013) carried out their research on quadruple effect absorption cycles to evaluate their COP along with their exergetic efficiency. The authors used ammonia-water mixture as the working pair and performed energetic and exergetic analysis of the QE cycles. As mentioned earlier that quadruple effect cycle working on LiBr-

H_2O has not been studied in earlier research works. Therefore, the present research focuses on to evaluate the performance of quadruple effect cycle using LiBr-H_2O working pair. The quadruple effect cycle along with other cycles are modelled and analyzed for their energetic and exergetic performance perspective. The mathematical models of the absorptions cycles are being simulated to operate on solar heat. In order to compare the COP of the absorption cycles, the other three (single, double and triple effect) absorption cycles are also being analyzed in the present research.

II. System Description

Fig. 1 represents the schematic illustration of the quadruple effect absorption cycle (QEAC). The rest of the cycles such as single, double and triple effect work the same way as quadruple effect cycle. The higher the number of stages the higher the vapor generation though generators. There are four generators in QEAC namely, low, medium, high and very high temperature generators. The working principle of the cycle can easily be followed using the number scheme provided on the cycle. The detailed working principle of the similar cycle is presented by (Tahir and Abid, 2018). The cycle is assisted on solar parabolic trough collectors to obtain the heat required to drive the cycle. Three different heat transfer fluids are used in solar collector. The absorption cycle comprises of four generators, four heat exchangers, an absorber, an evaporator and a condenser. The system is designed and analyzed based on parallel arrangement using LiBr-H_2O as working pair. The solution gets distributed in different generators with user defined mass ratio. As mentioned earlier the higher number of stages will have higher vapor production which will help in increasing the refrigeration capacity of the cycle.

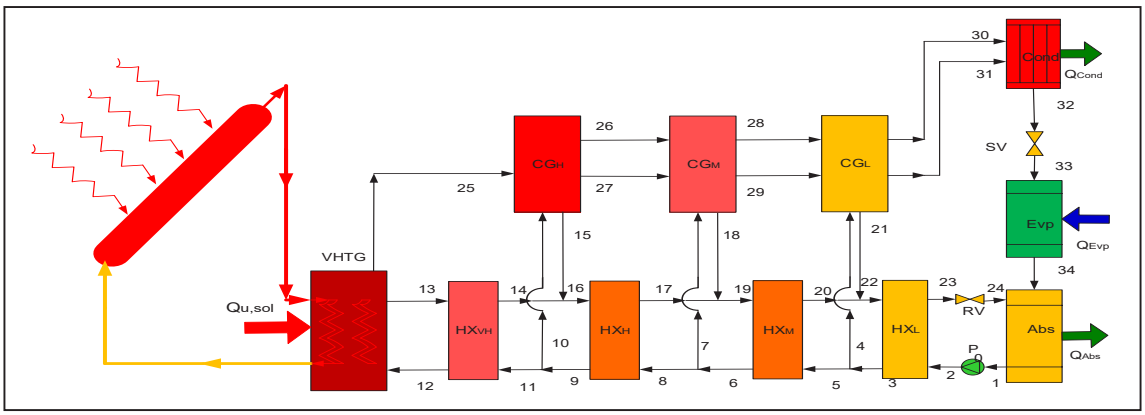

Fig. 1: The schematic illustration of the quadruple effect absorption cycle

The QEAC requires high temperature heat source to work in comparison to other cycles. On the other hand, it produces the maximum refrigeration so it has the highest COP among the rest of the cycles.

III. Methodology

The mathematical modelling of the absorption cycles is done using the engineering equation solver (EES) tool for their energetic and exergetic point of views. The main equations of the integrated system are presented in this section.

III.I: Parabolic trough solar collector

The useful energy produced by solar collector as proposed by (Duffie and Beckman, 2006) can be calculated as

$$\dot{Q}_g = F_r \,.\, [S \,.\, A_{ap} - A_r \,.\, U_L \,.\, (T_{r,i} - T_0)] \quad (1)$$

where A_{ap}, S, are aperture area (m^2) and absorbed solar radiation (W/m^2). The overall heat transfer coefficient is determined as

$$U_0 = \left[\frac{1}{U_L} + \frac{D_{r,0}}{h_{c,r,in} \,.\, D_{r,i}} + \frac{D_{r,0}}{2.\, k_r} \,.\, \ln\left(\frac{D_{r,0}}{D_{r,i}}\right)\right]^{-1} \quad (2)$$

where k_r is the thermal conductivity (W/m.K) of the receiver tube. The energetic efficiency of the solar collector is calculated as

$$\eta_{en,PTSC} = F_r \,.\, \left[\eta_r - U_L \,.\, \left(\frac{T_{r,i} - T_0}{G_b.C}\right)\right] \quad (3)$$

III.II: Absorption cycles

The absorption cycles of single, double, triple and quadruple effect are modelled and the main equations are presented here in this sub-section. The mass and energy balance of the absorption cycles is defined as

$$\sum \dot{m}_i - \sum \dot{m}_o = 0 \quad (4)$$

$$(\sum \dot{m}_i . h_i - \dot{m}_0 . h_0) + (\sum Q_i - \sum Q_o) + W = 0 \quad (5)$$

Furthermore, the enthalpy at each state point is calculated to perform the energy and exergy balance of the systems. The exergy at every point is calculated as:

$$e_x = (h - h_0) - T_0(s - s_0) \quad (6)$$

where ex is the specific exergy (kJ/kg), h is the specific enthalpy (kJ/kg), and s is the specific entropy (kJ/kg K) for the given state point. Finally the COP and exergy efficiency of the absorption cycles are calculated as:

$$COP = \frac{\dot{Q}_{evp}}{\dot{Q}_G + \dot{W}_P} \quad (7)$$

$$\eta_{ex} = \frac{\dot{E}_{th,evp}}{\dot{E}_{th} + \dot{W}_p} \quad (8)$$

IV. Results and discussions

This section presents the simulation results of the proposed models of the absorption cycles. Fig. 2 provides a comparison of the COPs of the simulated models against the increase in the weak solution of the LiBr-H_2O mixture. It can be seen that the COP of the QE cycle is highest among the rest of the analyzed cycles. The increase in the percentage of the weak solution also helps in increasing the COP of all the cycles. The main reason for higher COP is the amount of vapor produced by the respective cycle. The QE cycle having four generators is producing more vapor which results in increasing the refrigeration capacity of the cycle. Secondly, the increase in the percentage of the weak solution will produce more refrigerant, the more the refrigerant the higher the refrigeration capacity.

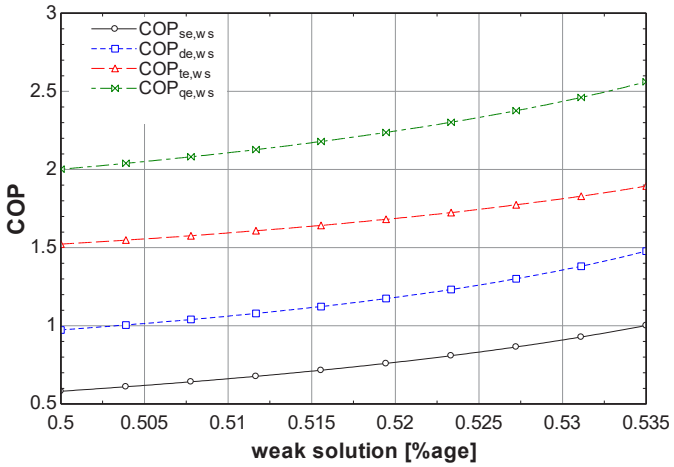

Fig. 2. The effect of weak solution the COP of the absorption cycles

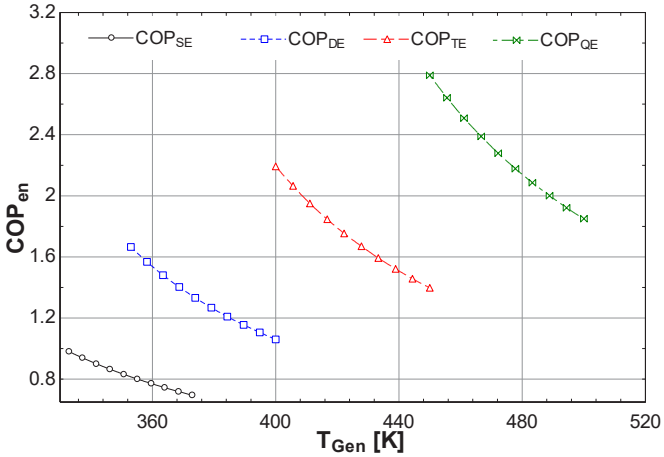

Fig. 3. The influence of generator temperature on the COP of the absorption cycles

Fig. 3 provides an illustration in between the COPs of the absorption cycles and the generator temperature. It is observed that QE cycle has the highest COP among its counterparts. The increase in generator temperature is

witnessed to have adverse effect on the COPs of the cycles. The reason for this decline is the fixed evaporator load. The cycles are designed to have a fixed evaporator load, therefore, increasing the generator temperature will inject more heat into the system which has a negative effect on the system according to the equation 7. On the other hand, injecting more heat into the system should increase the refrigeration capacity, which is actually the case when the evaporator load is variable.

V. Conclusions

The work presents a comparison in between the absorption cycles of single, double, triple and quadruple effet. The cycles are power by solar parabolic trough collectors. The energy and exergy analysis are performed to analyze the cycles. They are being analyzed to have a fixed cooling capacity. Some of the main outcomes of the work are presented below.

- The COP of the absorption cycles is witnessed to increase with distribution of the mass flow rate among the generators. The highest COP (QE cycle) was observed to be at 40% of the total mass provided to the low temperature generator.
- The COP of the QE cycle is observed to be the highest among all the cycles.
- The percentage of the strong and weak solution play an importan role in enhancing the cooling capacities of the cycles.
- The COP of the quadruple effect absorption cycle is 21.36% higher than triple effect absorption cycle and it is 2.55 times higher than SE cycle. It is also noticed to be 1.7 times higher than DE cycle at an evaporator temperature of 286 K.

References

Assilzadeh F., S.A. Kalogirou, Y. Ali, K. 2005. Sopian Simulation and optimization of a LiBr solar absorption cooling system with evacuated tube collectors *Renewable Energy*, 30, pp. 1143–1159.

Arun, M.B.,Maiya, M.P.,Murthy, S.S. 2000. Equilibrium low pressure generator temperatures for double effect series flow absorption refrigeration systems. *Appl. Therm. Eng.* 20, 227-242.

Duffie, J. and Beckman, W. 2006. Solar Engineering of Thermal Processes. *2nd edition*. *John Wiley and Sons.* New Jersey.

Gomri R. 2010. Investigation of the potential of application of single effect and multiple effect absorption cooling system. *Energy Convers. Manage*. 51 1629–1636.

He Zinian, Zhu Ning, Liu Fang, Guo Shuling. 2001. Design and performance of a solar absorption air conditioning and heat supply system *Acta Energiae Solaris Sinica,* 22 (1), pp. 6–1

Li Jianhong, Ma Weibin, Jiang Qing A. 1999. 100 kW solar air-conditioning system *Acta Energiae Solaris Sinica*, 20 (3), pp. 239–243

M.B Arun, M.P Maiya, S.Srinivasa. 2001. Murthy Performance comparison of double-effect parallel-flow and series flow water–lithium bromide absorption systems*, Applied thermal Engineering*, 21, pp. 1273–1279.

Oouchi, T., Usui, S., Fukuda. K., and Nishiguchi, A. 1985. Multi-stage Absorption Refrigeration System. *US Patent* No. 4,520,634.

Ratlamwala A. H. T., Abid M. 2018. Performance analysis of solar assisted multi-effect absorption cooling systems using nanofluids: A comparative analysis. Int. J. Energy. Res. 2901-15

Ratlamwala TAH, Dincer I., Gadalla MA. 2013. Energy and exergy analyses of an integrated solar-based desalination quadruple effect absorption system for freshwater and cooling production. *Int. J. Energy Res*. 37:1569–1579

R. C. DeVault and J. Marsala. 1990. Ammonia-water triple-effect absorption cycle. *ASHRAE Trans*. 96 Part 1.

Xu, G.P., Dai, Y.Q. 1997. Theoretical analysis and optimization of a double-effect parallel flow type absorption chiller. *Appl. Therm. Eng*. 17 (2), 157-170.

Numerical Analysis of 3-D Vanadium Redox Flow Battery with Flow Field

Snigdha Saha, Gajanan Dattarao Surywanshi *Venkata Suresh Patnaikuni
Department of Chemical Engineering, National Institute of Technology Warangal-506004, India

*E-mails: pvsuresh@nitw.ac.in

Abstract
Vanadium redox flow battery (VRFB) is a kind of rechargeable battery with large scale energy storage capacity. It can be used as an intermittent energy storage for the renewable energy sources. The performance of the battery depends on many factors such as mass transfer losses, electrolyte contamination and thermal precipitation of electrolyte. The mass transfer losses can be rectified by employing proper flowfield design. Flow channels are carved on the surface graphite plate to enhance the mass transport of electrolyte. The pressure drop occurred due to the circulation of the electrolytes through the cell can be reduced by flow channels. A 2-D numerical model for VRFB using electrochemistry model is first validated with the available results in the literature using COMSOL (a CFD simulation tool). The model is then further extended to full scale 3-D numerical model for comparative performance analysis of Conventional, Serpentine and Parallel flow fields. This model includes the fluid flow coupled with the electrochemistry. The active area of the VRFB considered is 25 cm^2. A parametric study is performed by varying flow rate of electrolyte and state of charge of battery to analyse the current density, cell voltage, pressure drop and over-potential of cell. From the present study, it can be concluded that, serpentine flow channel layout gives the optimal performance among all the cases considered.
Keywords: Vanadium Redox Flow Batteries, Flow Field Design, 3-D multi physics, COMSOL modeling.

I. Introduction

Increasing demand for renewable energy resources, such as solar, hydral and wind power, has led to the development of storage technologies of large capacity. Intermitent energy production from the renewable sources can be converted into stable power supply with the intergartion of energy storage systems. Some of the large-scale energy storage techniques are hydro-pumping, compressed-air energy storage (CAES), sodium–sulfur battery, sodium–nickel battery etc. All these large scale energy storage techniques generally suffer from restriction by the geographical environment, high operating temperature, poor safety, short life cycle. This leads to the limited utilization of these storage techniques (Zhang et al., 2018). Many advances have been made in electro-chemical battery storage. With flexibility in design of uncoupled power output and energy storage, redox flow batteries (RFBs) are gaining attention. RFBs are the stationary batteries with features like long calendar life, modular design, flexibility, nontoxic to environment and no dependency on appropriate geography (Chen et al., 2017). Some examples of RFB on the basis of different electroactive species are all vanadium, Iron-Chromiun, Zinc- Cerium, all Iron and soluble lead acid battery. Among various flow battery types available, all Vanadium redox flow battery (VRFB) is the most promising one, which utilizes all four oxidation states of vanadium metal VO^{2+}, VO_2^+, V^{2+} and V^{3+} (Zhang 2018).

VRFB cell design basically involves membrane (nafion), grafite felt electrode, grafite plate with flow distributor/channel and current collector. Performance of the battery depends on many factors like material, dimension or design of these battery components. Flow channels grooved on the graphite plate surface reduces the polarization by enhancing the mass transport of the electrolyte. Feeding electrolyte directly to electrode (no flow field) results in excessive pressure drop (Kumar and Jayanti, 2016). Flow field minimizes the pressure drop by maintaining proper distribution of the reactants and also ensures the maximum utilization of the of cell area.

(Xu et al., 2013) proposed 3D numerical model to study conventional, serpentine and parallel flow fields of VRFB. The study calculates power-based efficiency with cell performance and pumping power at various electrolyte flow rates to obtain maximum efficiency. (Canzi et al., 2017) analysed the effect of the flow field design on the electrochemical performance and pressure drop using ANSYS Fluent. Their results showed that interdigitated flow field design gives uniform reactant distribution with low pressure drop. (Yin et al., 2014) numerically analysed a VRFB model with interdigitated flow design using multi-inlet defining electrochemical and fluid flow characteristics. They concluded that for a multi inlet interdigitated design at high flow rates, utilizes the porous electrode more efficiently resulting in uniform potential distribution across the cell. (Messagi et al., 2018) praposed a 3D CFD model for interdigited and serpentine distributor concluding that Serpentine distributor exhibits higher pressure drop. Reaction rate is more uniform in interdigited flow field. (Ma et al., 2011) analysed the performance of the VRFB considereing only negative half cell. Effect of electrolyte velocity distribution on concentration, current density and overpotential was studied. It was concluded that, electrolyte flow rate has significant influence on overpotential of VRFB.

From the above discussion it can be inferred that there are very few comparative studies on numerical characterization of 3D VRFB model on Conventional, Parallel and Serpentine flow field employing coupled fluid flow and electrochemistry. The present model is validated against the 3D model data available on VRFB without flow field in the literature (Ma et al., 2011). In this paper full scale 3D computational model is presented by coupling multiphysics models of hydrodynamics and electrochemical reactions to measure the performance of VRFB for conventional (without flow field), parallel and serpentine flow field design.

II. Model Development

The model consisting of two different cell compartments, with different ion compositions and electrode reactions, separated by anion-exchange membrane has been considered.

II.1. Model Definition

The model contains five domains, a negative porous electrode (3 mm thick), an ion-exchange membrane (0.2 mm thick) and a positive porous electrode (3 mm thick). Flow channel attached to both the electrodes are 2 mm thick. The cell is 50 mm high and 50 mm wide. The cell includes inflow channel and outflow channel in counter-current manner. The geometries modeled along with computational meshes are shown in Fig. 1.

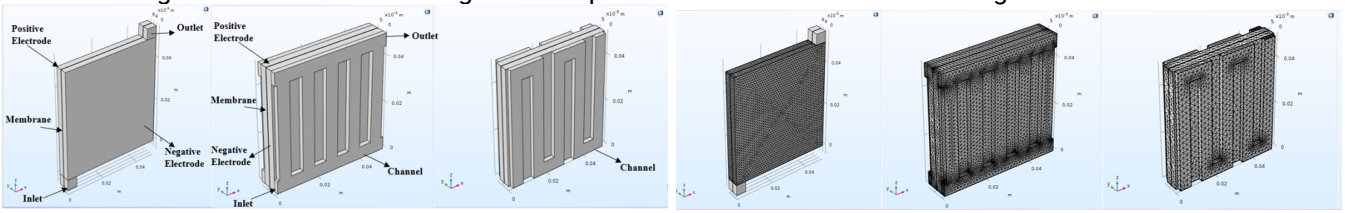

(a) (b)

Fig. 1 (a) Model geometries – without flow field (conventional), with parallel flow field, with serpentine flow field and (b) Computational mesh of the modeled geometries

Each inlet channel of the cell is fed with an electrolyte containing sulfuric acid and a vanadium redox couple, flowing through the porous electrodes. The liquid enters the cell from bottom and top of negative and positive electrodes respectively, at a fixed flow rate of 40 ml/min in the present study, current is with drawn from the positive electrode at a rate of 60 mA/cm^2 and the negative electrode is earthed.

The computational geometery is meshed using COMSOL Multiphysics® package (version 5.3a), physics-controlled meshing. Mesh density is higher close to membrane where reaction occurs.

Model Assumptions

- The dilute-solution is approximated considering concentrated solution theory
- The flow is regarded as laminar and incompressible as the bulk of the liquid is water.
- Electrodes and Membrane are isotropic and homogeneous.
- System is considered as isothermal and side reactions (evolution of O_2 and H_2) are not considered for calculation.
- Charged species are transportd by convection, migration and diffusion.
- There is no leakage of reactant or charge through the cell external surfaces.
- Membrane is impermeable to Vanadium ions.

II.2. Governing equations

Species participating in the electrode reactions, in addition to the four vanadium species and water are H^+, $HSO_4^-$and $SO4_2^-$. The reactions occurring along with the ions participated in the electrodes are given in Table 1. Table 2 lists different governing equations solved for the Multiphysics involved in the system.

Table 1. Reactions and ions involved in the electrodes

Electrode	Reaction	Ions in the electrolyte
Negative electrode	$V^{3+} + e^- \leftrightarrow V^{2+}$	H^+ HSO_4^- SO_4^{2-} V^{3+} V^{2+}
Positive electrode	$VO^{2+} \leftrightarrow VO_2^+ + e^-$	H+ HSO_4^- SO_4^{2-} VO_2^+ VO^{2+}

Table 2. Governing equations solved in the model

Governing Equations		Significance
Reaction Kinetics		
Nernst equation	$E_{eq,neg} = E_{0,neg} + \frac{RT}{F}\ln\left(\frac{a_{V^{3+}}}{a_{V^{2+}}}\right)$	To calculate equilibrium potential for the above reactions
Butler-Volmer equation	$i_{neg} = Ai_{0,neg}\left(\exp\left(\frac{(1-\alpha_{neg})Fn_{neg}}{RT}\right)-\exp\left(\frac{-\alpha_{neg}Fn_{neg}}{RT}\right)\right)$ $i_{neg} = Fk_{neg}\left(a_{V^{2+}}\right)^{1-\alpha_{neg}}\left(a_{V^{3+}}\right)^{\alpha_{neg}}$	To model the rates of electrochemical reactions that take place on the porous carbon electrode surface
overpotential	$\eta = \varphi_s - \varphi_l - E_{eq}$	
Transport through the porous electrode		
Nernst-Planck	$N_i = -D_i\nabla C_i - Z_i u_{mob,i} F C_i \nabla\varphi_l + c_i\mathbf{u}$	To obtain ion flux and charge transport by due to

equations		convection, migration and diffusion.
Total current density in electrolyte by Faraday's law	$i = \sum i = -F\sum Z_i D_i^{eff} \nabla C_i - F^2 \sum Z_i^2 C_i \mu_i \nabla \varphi_s$	To calculate electrolyte current density
Transport through the membrane		
Total current density in Membrane	$i_l = -u_{mi} F^2 C_i \nabla \varphi_l$	Membrane consists of polymer electrolyte, where all the negative ions are fixed in the polymer matrix, implying that the concentration is constant, and the only positive ion present is H+.
Fluid Flow Equations		
Brinkmann Equation	$\frac{\mu}{k} \vec{v} = -p + \mu\left[\nabla \vec{v} + (\nabla \vec{v})^T\right]$ $\nabla . \vec{v} = 0$	Used for coupling of free and porous flow media (here electrode is porous medium and flow field is free medium). (Ma et al,2011)

where, E_0: reference potential for the electrode reaction (V), a_i:chemical activity, R: molar gas constant (8.31 J/(mol·K)), , A:specific surface area (m^3/m^2), α: transfer coefficient, k: rate constant, η: overpotential(V), ϕ_s: electrode potential (V), ϕ_l : electrolyte potential (V), N_i : molar flux of species i, D_i : diffusion coefficient (m^2/s), F: Faraday's constant (96,485 s·A/mol), z_i : migration, u_{mob} : species mobility(s·mol/kg), u: fluid velocity vector (m/s). T: cell temperature (K)

II.3.Boundary conditions

Boundary conditions at the interface for membrane and electrodes are:

Current density in the membrane and electrolyte are equal $n.i_{l,e} = n.i_{l,m}$

From Faraday's law, proton flux is proportional to current. $n.N_{+,e} = n.\frac{i_{l,m}}{F}$

The relation between the potentials and the concentrations is given by: $\varphi_{l,m=} \varphi_{l,m} + \frac{RT}{F} \ln\left(\frac{c_{i,m}}{c_{i,e}}\right)$

Diffusive fluxes are set to be zero near the outlet (fully developed flow) $-D_i \nabla C_i . n = 0$

$c_{i,m}$: permeable ion concentration in the membrane; $c_{i,e}$: permeable ion concentration in the free electrolyte.The potential shift caused by Donnan potential. The flux is zero for the non-permeable ion. Pressure is set to zero at outlet. Electrode walls are set to slip boundry condition and no-slip applies to the membrane.

Numerical details and Parameters

All the model equations are solved by finite-element method using COMSOL Multiphysics®. The relative tolerance was set to 10^{-3}. The electrochemical properties used in present simulations are listed in Table 3. The solution was found with Newton-Raphson algorithm (Iterative Solver).

Table 3. Electrochemical Parameters used in model

Standard potential, negative reaction	-0.255[V]	$V^{(2+)}$ initial concentration	1280[mol/m^3]
Standard potential, positive reaction	1.004[V]	$V^{(3+)}$ initial concentration	320[mol/m^3]
$VO_2^{(+)}$ initial concentration	1280[mol/m^3]	$VO^{(2+)}$ initial concentration	320[mol/m^3]

IV. Results and discussions

Fig. 2 shows contour planes of velocity, pressure and V^{2+} concentration in the electrode and membrane domains. In case of conventional flow field, velocity at inlet and outlet are maximum, while it is less in the rest of the flow domain. The fluid pressure is highest at the inlet and reduces gradually to the atmospheric pressure as it reaches the outlet. Parallel flow field is able to minimize the pressure drop but the distribution of reactant is not uniform. There is more flow in the first and last channels. The central channels have lower velocities. In case of serpentine flow fields, fluid velocity in the channel is high compared to the other two flow fields and gradually decreases towards exit. Because of the pressure difference between the two adjacent channels away from the U-bend (Fig. 2b), there will be convection under the rib through the electrode. Hence, the electrolyte distribution through the rib is more uniform because of both diffusion and convection. However, this convective flow is low near U-bends. Under the rib fluxes are influenced by channel dimension and shape (Canzi et al., 2017).

Fig. 2c shows concentration of V^{2+} ions in the negative cell of conventional, parallel and serpentine flow field. The electrolyte from inlet first flows in channel convectively then enters the electrode by diffusion (Maurya et al., 2018). In conventional flow field, the concentration of V^{2+} is found to be highest at the inlet and lowest at the outlet due to conversion from reaction V^{2+} to V^{3+}. Due to low under the rib convection in parallel flow design reactants are not evenly distributed. For Serpentine flow field, V^{2+} concentration drops from each inlet channel to the adjacent outlet channel. Electrolyte flowpath in channel from inlet to outlet is different from electrode due to

distribution pattern of electrolyte at given flowrate. The concentration of V^{2+} decreases towards the exit because of it getting converted to V^{3+}. This can be observed to be higher in case of serpentine compared to the cases with parallel and conventional flow fields.

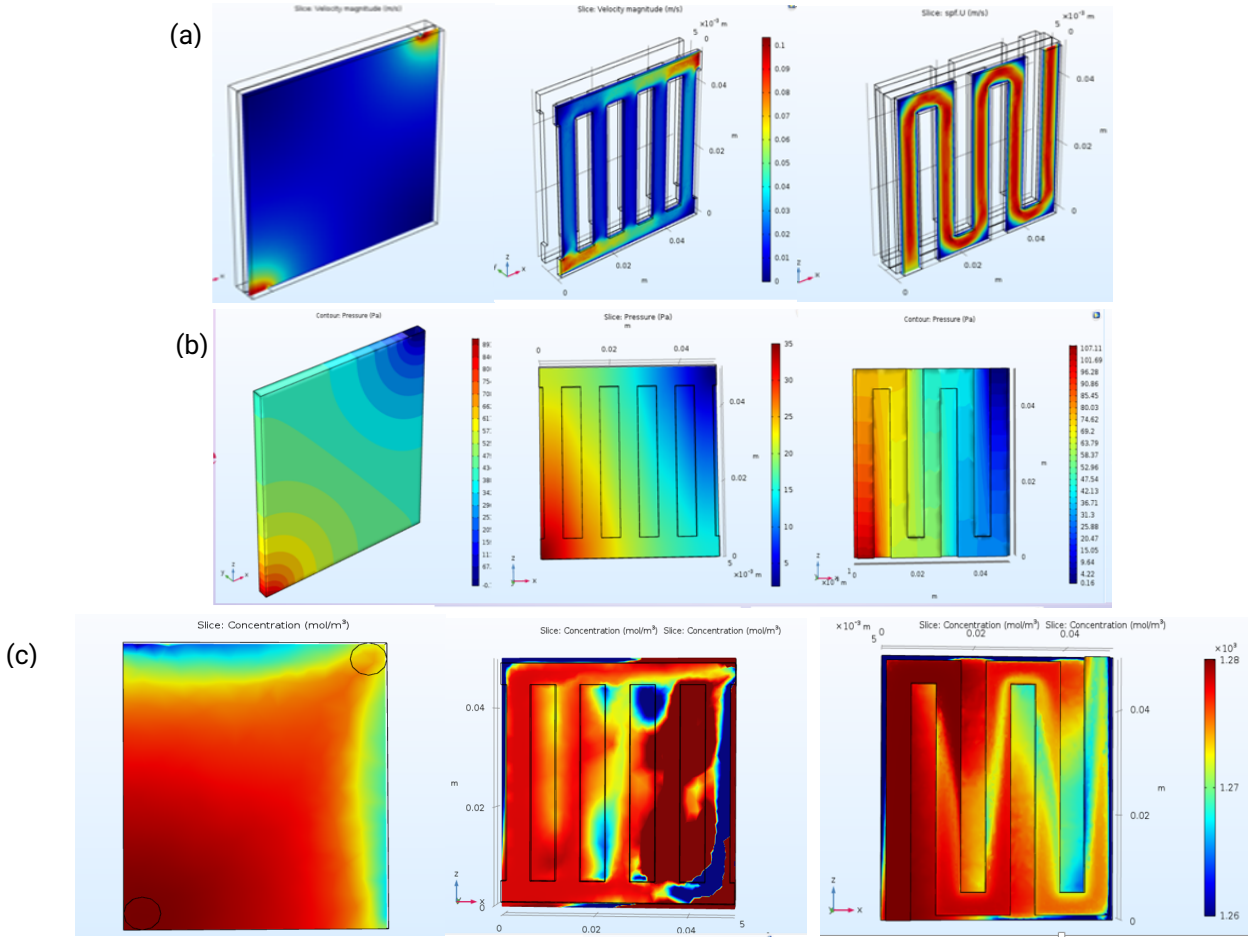

Fig. 2: (a) Velocity, (b) Pressure and (c) Concentration contour plots of Conventional Flow, Parallel Flow and Serpentine Flow electrodes and channel.

Conclusion

In this work, the effect of flow field design such as conventional, parallel and serpentine on the distribution and conversion of the reactants in electrolyte is studied. Distribution of velocity, pressure and reactant concentration in different flow filed designs are reported. From this study, it was concluded that the uniformity of velocity is the major requirement for proper distribution of electrolyte. Out of the all the flow designs considered, serpentine flowfield resulted in the better distribution and conversion of reactants.

References

Canzi, P., 2017. Analysis of Flow Field Design for Vanadium Redox Flow Batteries through the Development and Validation of CFD codes, Ph. D. Thesis, School of Industrial and information engineering, Milano.
Kumar S., Jayanti S., 2016. Effect of flow field on the performance of an all-vanadium redox flow battery, Journal of Power Sources 307, 782-787.
Ma, X., Zhang, H., Xing, F., 2011. A three-dimensional model for negative half cell of the vanadium redox flow battery Electrochimica Acta 58, 238–246
Messaggi, M., Canzi P., Mereu R., Baricci A., Inzoli F., Casalegno A., Zago M., 2018. Analysis of flow field design on vanadium redox flow battery performance: Development of 3D computational fluid dynamic model and experimentalvalidation. Applied Energy 228, 1057–1070
Shah A.A., Watt-Smith M.J., Walsh F.C, 2008. A dynamic performance model for redox-flow batteries involving soluble species, Electrochimica Acta 53, 8087–8100.
Xu, Q., Zhao T. S., Leung P. K., 2013. Numerical investigations of flow field designs for vanadium redox flow batteries Applied Energy 105, 47–56
Yin, C., Gao, Y., Guo S., Tang, H., 2014. A coupled three dimensional model of vanadium redox flow battery
for flow field designs Energy 74, 886-895
Zhang, H., Li, X., Zhang, J., 2018. Redox Flow Battery Fundamentals and Applications, CRC Press, Taylor and Francis group.

Integration of Petroleum Refinery and Petrochemical Plants for Condensate Feedstock: Challenges and Opportunities

Salman Ashkanani, and Dr Brenno Menezes
College of Science and Engineering, Hamad Bin Khalifa University, Doha, State of Qatar
* E-mails: salshkanani@hbku.edu.qa, bmenezes@hbku.edu.qa

Abstract
This paper presents a case study about the global move in liquid hydrocarbon industries on the integration of petrochemical plants into the refinery business to struggle against the decline of profit margins in the petroleum refinery field. Challenges in the petroleum refining business are increasingly growing with new markets, feedstocks and restrictive regulations. The refinery and petrochemical systems discussed here were modelled as a mixed-integer problem with the objective of minimizing the operational cost over a given time horizon and maximizing the added value of the petrochemical network. To maintain sustainable profitability, the refinery of the future must respond quickly to changing market conditions, switching from one stratagem to another as profit margins change. It is known that consistent profitability in the refinery sector is a challenge. In this case study, the Pearl Refinery Company (PR) is discussed, which was built and is operated strategically to meet domestic consumption needs and optimize the profitability. In addition, PR has a critical support role for local LNG plants. As it processes' in continuous operation through relinquishing all condensates produced during LNG production. PR also functions as a swing-producer to buffer low-prices as the condensate market fluctuates. This case study considers how a refinery can make better use of process enhancements to improve profit margins by 20.5%. It is proposed to implement an integrated refinery and petrochemical complex model to sustain profitability through optimization. This paper demonstrates that an appropriate equitable cost allocation mechanism will help withstand overall PR corporate performance and profitability to justify implications of case study results. It is concluded that with proposed enhancements to the refinery and a combination of solutions to improve the current performance through the restructuring of the budgeting process, an update of the organizational model, new ingenuities, and overall cost optimization opportunities.

Keywords: Performance management, profit margin, process enhancements, cost optimization, profitability

I. Introduction

The recent shift from local markets to a large global one increased the competitive pressures on petrochemical industries. Further, because of fluctuations in products' price and high price of feedstocks, economical attractiveness of petrochemical plants can be considered as a main challenge (Nasr, Sahebdelfar, Ravanchi, & Beshelli. 2020).
Pearl Refinery (PR) is a joint venture involving Dock Petroleum (DP) Company, sharing 60%, with four other partners, established in 2000, in the State of Pearl. It is one of the largest condensate refineries in the world. It started its operation in the 3rd quarter of 2007 with a capacity to process 200,000 barrels per stream day (BPSD) of Pearl Field Condensate received from several plants operating near PR. Pearl Operating Company (POPCO), which is not within PR group, operates PR. The plant facilities are worth about one billion US dollars as on Year 2007. PR Project was completed with an excellent safety record. At the time of completion, the Project had achieved 25.4 million man-hours with a single Lost Time Incident (LTI). The Project was completed without any recordable incidents since March 2007. PR has successfully completed the performance test in December 2007 and the Company has accepted the care and custody of the refining plant from the contractors. Since then, the PR runs at maximum capacity and all specified products runs down to storage tanks for further dispatching to local consumption and exports. PR is designed to process a single-quality feedstock as condensate (light to medium hydrocarbons and it has a long-term agreement with condensate suppliers. Products from PR operation are liquefied petroleum gas (LPG), naphtha, kerojet, and gasoil (diesel) yielding 45% of naphtha usually sold at lower price than the feedstock. Facilities to produce gasoline and BTX (benzene, toluene, and xylene) from naphtha are not included in the PR process network. The profitable products kerojet and gasoil (diesel) constitute 50% of the PR output. FG and are roughly 5% of the production and hold lower price than condensate feedstock.
This work considers the Pearl Refinery (PR) company in the State of Pearl. Pearl Operating Company (POPCO) operates PR as well as eight other ventures producing liquefied natural gas (LNG) and natural gas liquids (NGL) in addition to helium and sulphur recovery plants. PR was constructed in two phases; PR1 was commissioned in 2007 and PR2 was commissioned in 2017. PR is a collective reference for PR1 and PR2. Refining capacity of PR is 2 x 200,000 bbl/day (total 400,000 bbl/day). While PR is part of POPCO's integrated operational organization, PR also has its own dedicated operational resources; such resource costs (primarily, manpower) and other directly identifiable costs (chemicals/ catalysts, utilities, spares and consumables, land-leases, and other similar costs) are charged onto PR directly. Common costs such as Managing Director office costs, shared service costs, home office costs, support services, and similar other costs are allocated to PR. POPCO has cost allocation system in which they allocate cost between the LNG, NGL Ventures and PR. The cost allocation comes from the following groups: administration, finance, engineering and projects, safety, environment and quality, plus the top management services such as legal, audit and MD (??) group. Overall, PR's allocated cost from POPCO is more than 7% of its overall costs in 2010. Benchmark study indicated and highlighted that an exceedingly high cost is allocated to PR and the basis was reassessed to bring it down to approximately 4% during the periods 2016 through 2018.

benefit and the main objective of petrochemical producers is to upgrade the feed quality and feed availability, decreasing the operating cost and increasing the benefits (Haelsig, Taubman, Goelzer, Crawford,1997). Cost minimization is a key for profitability while cash shortages may result in the closure of refinery. The following are the structure and maneuverability opportunities towards cost reduction:

- Fixed costs (like salaries and wages of permanent staff, land-lease, utilities for permanent establishments, depreciation on fixed assets etc.) has very limited opportunities to reduce. These costs are mainly allocated in an integrated facility like PR. Allocation basis is a critical item for optimization.
- Variable costs (like utilities cost, chemicals, catalysts and consumables costs, incremental costs for meeting peak-production requirements etc.) has cost minimization opportunities by maintaining low-energy/ and low consumption through efficient management.
- In addition, opportunity for reduction of costs like increasing annual turnaround cycle, enhancing catalyst life-cycle longevity, improving reliability, availability, and maintainability more than 97% by predictive maintenance and reliability centred maintenance (RCM) are few other ways to achieve reduced cost per refined barrel.

II. Petroleum Refined Products: Process and Market Challenges

This work is segmented on four areas as discussed in the following sections:

- **Broad market areas**: crude-oil sourcing and refining centres are widespread across the, having impacts on crude-oils sourced from different places such as: specific gravity, sulphur concentration and chemical compositions. Decisions on the refined feedstock mix involve primarily the refinery process technologies, but also the nature of economies, public awareness and governmental policies (such as subsidies on essential commodities like diesel, LPG for common public, ethanol mix in gasoline, environmental restrictions on GHG emissions, catalyst dispositions etc.) . Current economic models establish the creation of new refining capacities either in crude-producing regions (Middle East) or consuming countries (Asia Pacific regions) as a viable opportunity. A hybrid model of joint-ownership in consuming countries having a long term demand is gaining momentum. This is substantiated by countries like Saudi Arabia, Kuwait and UAE establishing refineries in China and India.
- **Evolving technological and environmental changes:** world crude-oil refining capacity has been relatively flat the past few years, concurrent with increasing conversion capability, measured as the sum of fluid catalytic cracking (FCC), hydrocracking, catalytic reforming, and alkylation capacities. With crude supply becoming heavier and higher in sulphur, the bottom of the barrel, which is deficient in hydrogen, contains increasing amounts of contaminants such as carbon, sulphur, metals, and nitrogen. There are three upgrading routes available for bottoms materials:
  - Hydrogen addition (hydro-treating, hydro-refining, hydrocracking)
  - Carbon rejection (coking, visbreaking, solvent deasphalting, FCC)
  - Gasification (addition of oxygen for burning in power-generation facilities), with value-added production of hydrogen and fuel gas.

  These options are necessary for deep-conversion refineries, planned or existing. But no single optimal configuration exists for the refinery of the future. A technological breakthrough is necessary to continue to operate in the high-cost refining business, where product quality specifications are driven by environmental regulations. Catalyst performance is being scrutinized as refiners require longer run lengths and lower gas makes, and process heavier feedstocks.
- **Matured markets and evolving market energy balances and investment climate:** refinery configurations are driven by regional market demands. For example, in the U.S., FCC units and Coker's often are the refinery centrepiece because of heavier crude slates, high gasoline demand, and low residual fuel oil demand. In Europe, because of available fuel oil outlets, thermal cracking often is substituted for coking. The residual fuel oil market in Europe is shrinking. Refinery upgrade networks are evolving in Asia/Pacific area as well. Economic uplift of emerging nations makes them high energy consumers because of increased standard of living. Lessening of demands in saturated markets becomes compensated by the emerging markets. The increasing net global energy demand ensures sustainability and robust growth for refineries in the near future.
- **Competing technologies and assertive demands for refined products:** wind and solar energy is competing with power utilities. Furthermore, natural gas is becoming preferred fossil fuel in place of crude-oil. Transportation forms the backbone of the world's demand for crude-oil. This segment is challenged by electric vehicle emergence; however, efforts are underway to boost the efficiency of gasoline engines by redesigning them to enhance the efficiency by around 30% ~40%. Furthermore, oil refineries are focusing on petrochemicals to accommodate the volumes shifted from the transportation sector.

Energy demand in emerging countries (such as India and China) is growing at a substantial rate owing to industrialization, growing population, and urbanization. But these countries do not have enough infrastructures for distribution of natural gas and generating renewable energy to meet the growing demands. Therefore, emerging countries are expected to remain heavily dependent on oil to meet the demands. The modern refineries built are highly efficient and are more equipped in producing fuels that meet strict government regulations. Therefore, needed technological advancements are expected to boost the increase of the profit margins for the refinery operators since many companies, particularly in Europe and in US, are shutting down plants due to low profit margins.

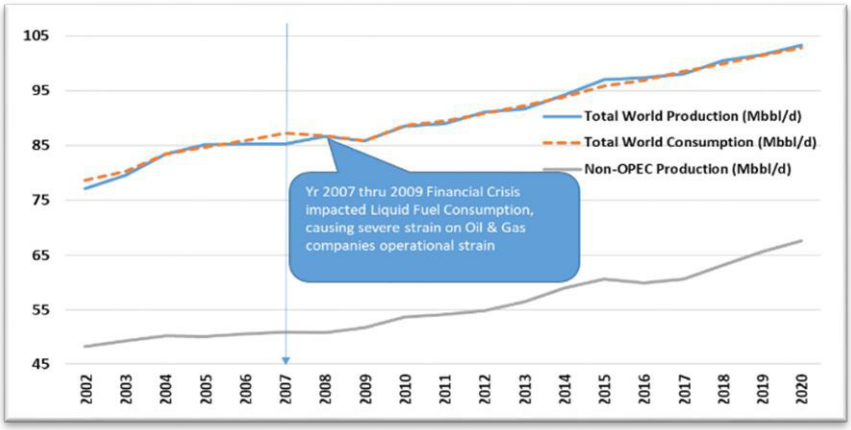

Fig. 1: Liquid fuel production and consumption and forecasts

Considerable downside risks remain in the refinery industry such as: additional project delays, declines in crude-oil drilling activities and unexpected rapid decline rates (resulted from financial crisis) and the current cost of environmentally-friendly measures. The combination of lower oil demand, rising natural gas liquid production, and increases in crude oil production capacity over the next two years will result in an OPEC surplus production capacity averaging 1 to 2 million barrels per day over the period. The financial constraints and prospects of weak demand could lead OPEC members to further delay expansion programs, reducing future surplus capacity and setting the stage for higher prices once the economic recovery catches up.

III. Methodology

Traditionally, refineries have been mostly involved in fractionation, conversion and blending of petroleum cuts. The refining industry has its own challenges. (Ramírez-Corredores, 2000).This paper established that an appropriate equitable cost allocation mechanism (Shared Services Cost) help to sustain PR business performance and profitability. To achieve this, we propose the following:

- Modify the organization structure to centralize the management of the refinery (including off plot assets like tank farm and jetty) under the authority of the asset manager reporting to the chief manager operations (CMO) or to the refinery ventures manager.
- Implement the new proposed PR organization to have clear accountability responsibilities.
- Focus on the following improvements:
  - Optimize the valorization of condensate, which is a feedstock for the refinery.
  - Incorporate adequate flexibility to enhance efficient and quick decision-making ability to successfully manage the refining business.
  - Optimize the overall supply chain for condensate and products.
  - Maximize the profitability of the commercial activity.
  - Evaluate the feasibility of implementing one of the options, listed in the following, to mitigate the impact of high allocated cost from the PR operator, POPCO.

The strategies options considered are:

Option 1:

a. Create a dedicated management position to own/ steward and control all aspects cost of management (ownership, responsibility, and accountabilities).
b. Execute “service contracts” for availing support services from PG (Pearl Gas) OPCO, thus enforcing a planned basis for optimization.
c. Budget, track, identify and close cost gaps between PR and worldwide benchmarks.

Option 2:

a. Independent PR: free to contract for support service outside of PG OPCO or build a self-contained support organization within PR.

IV. Results and Analysis

The PR Company went through benchmarking study to identify the gaps and opportunities for improvements. The benchmark study indicated that further improvement is required in order to stay competitive in the market. The identified options for improvement are: feedstock management, feedstock quality, direct cost minimization, marketing strategy, downstream business, allocation principle review.

Impact of Changes in Allocation Methods: primary allocation driver has changed from modified equipment count to Headcount effective April 2010, resulting in allocation percentage changes as follows. The allocation charge to PR has been significantly increased by changing the allocation methodology. Nevertheless, such an increase is not justified. Considering the impact on PR2 refining margin, various alternative methods of cost allocation were studied, befitting the effort/ resource spending, services received and an equitable method of cost allocation for the shared services. POPCO applied a hybrid cost allocation methodology for PR support.

Results of Product Optimization: as an important and long-term solution for the optimization of performance, PR shall pay more attention for new opportunities for its products. For example, by using naphtha (which is roughly 50% of PR production) as feedstock to produce value added products, such as Para-Xylene, Benzene, and Toluene. This helps PR to significantly improve the economics of the refinery.

SWOT: SWOT has been conducted for the PR, to evaluate the strengths, weaknesses or limitations, opportunities, and threats involved in the refinery. Based on the identification of the relevant factors, we could formulate the strategies to be followed by PR.

The important factors considered comes under cost saving activities in short period operations are: throughput capacity, technological efforts, feed/product optimization, maintenance cost minimization, and green save environment.

V. Recommendations

Through the thorough analysis, the following recommendations have been formed for Pearl Refinery to focus on its performance improvement:

- Maximize feed condensate at the refinery through: (a) increase the throughput of the units within safe operating envelops when the margin exists, (b) expedite the debottlenecking study, (c) reduce the giveaway (over specification) of the products (d) enlarge the yields, and (e) match in mass balance to meet current market demand and maximum revenue.
- Optimize the overall supply chain for condensate and products: (a) adjust the ships lifting plan to the refinery production and not the production to the shift lifting plan, (b) manage the inventory at a minimum level, and (c) increase the parcel-size in the ships.
- Consider feasibility of implementation of the following options to mitigate the issue related to cost allocation by POPCO.
    - Option 1: Focus on cost management by: (a) creating management position to own all aspects (ownership, responsibility, and accountabilities), (b) establishing " service contracts" for support services between PR and POPCO, and (c) beginning initiative to identify and close cost gaps between PR and worldwide benchmarks.
    - Option 2: Independent PR: free to contract for support service outside of POPCO or build support organization within PR.
- Maximize the profitability of the commercial activity through: (a) creating a real incentive for better sales of PR products on the International market, (b) finding a valorization to the quality of naphtha, and (c) getting more flexibility with condensate and product programs.

VI. Conclusions

The maximization of the feedstock condensate and product sales considering the opportunity for mass balance optimization, including naphtha to FEED proposal should be the main focus since they have the largest potential for improvements in gains. The profitability of commercial activities is a permanent challenge for PR as any other petroleum processer, because of short refining margins inherent to the field. Re-structure and modify the organization to centralize the management of the Refinery (inclusive Tank Farm and jetty) under the authority of the Refinery Asset Manager to get ownership of all activities.

Acknowledgements: My colleagues and peers have been provided significant support to finalize this case study in a professional manner which I thankfully acknowledged here.

References

1. C. Haelsig, J. Taubman, A. Goelzer, C. Crawford, "Added Value by Integrating Refining and Petrochemicals Operations", European Refining Technology Conference, London, United Kingdom, 1997.
2. Gary, J.H. & Handwerk, G.E. (1984). Petroleum Refining Technology and Economics (2nd ed.). Marcel Dekker, Inc. ISBN 0-8247-7150-8.
3. Gudde, Nicholas J (2017-02-20). "Adaptation of oil refineries to make modern fuels". Proceedings of the Institution of Mechanical Engineers, Part D: Journal of Automobile Engineering. 232 (1): 5–21. doi:10.1177/0954407016680522. ISSN 0954-4070.
4. Gunter Alfke, Walther W. Irion & Otto S. Neuwirth (2007). "Oil Refining". Ullmann's Encyclopedia of Industrial Chemistry. doi:10.1002/14356007.a18_051.pub2.
5. M. M. Ramírez-Corredores, Catalysis: New Concepts and New Materials, 16th World Petroleum Congress, Calgary, Canada, 2000.
6. Nasr, M. & Sahebdelfar, Saeed & Takht Ravanchi, Maryam & Beshelli, Majid. (2020). "*Integration of Petrochemical and Refinery Plants as an Approach to Compete in Hydrocarbon Market*".

A sustainable PV-powered energy retrofit modeling to achieve net ZEB in churches: A simulation study for San Marcello Al Corso

[1*]Mohammad Mohammadzadeh, [2]Navid Hadifar, [3]Bahareh Mohammadzadeh
[1*] Department of Mechanical Engineering, University of Kentucky, Lexington, KY, USA,40506-0503
Email: mmo231@g.uky.edu
[2] University of Rome "La Sapienza", Department of Astronautical, Electrical and Energy Engineering (DIAEE) Sapienza University of Rome, Via delle Sette Sale, 00184, Rome, Italy
[3]School of Architecture, Louisiana State University, Baton Rouge, LA,USA 70803

Abstract

This study proposes practical modifications for achieving net zero energy building (net ZEB) in historical churches while all the values of the church have been recognized and preserved. The church studied from three perspectives; 1) structural: horizontal air curtains used with the aim of decreasing ample space to decrease energy loss and conserving artworks and masonry in the facade 2) Mechanical: a heat pump has been installed to provide HVAC and utilities of the church. Phase change materials have been used in underfloor heating and cooling system to minimize temperature fluctuations in the church. 3) Electrical: A grid-connected PV system has been set up and a net metering scheme implemented using a grid-tie inverter to achieve net ZEB in the church. Energy analysis is carried out for the church before and after applying modifications. It is concluded that proposed modifications have positive effects on increasing the first and second law efficiency of the church. In heating mode, energy and exergy efficiency increased to 58.3% and 18.2%, respectively. Therefore, a 25.9% rise in energy efficiency and an 8.1% rise in exergy efficiency are observed. Also, a 98% match in annual energy exchange has been reached between the power generated on-site and the utility grid.

Keywords: energy retrofit, PV system, net zero energy building (net ZEB), net metering, sustainability, horizontal air curtain; exergy analysis.

I. Introduction

There are numerous historical churches and basilicas across Europe; these ancient buildings are lacking efficient heating, ventilation, and air conditioning (HVAC) as they were built years ago. Nowadays, many international treaties and agreements have been passed by the governments, the EU Parliament, and the UN for decreasing the amount of emitted greenhouse gases (GHG) in the atmosphere and increasing systems' efficiency[1] . Therefore, historical buildings need modifications to enhance their energy efficiency and to become compatible with new environmental laws. Any modification in these buildings needs to be investigated from different perspectives i.e. social values and community expectations, economic viability, and environmental sustainability.

Known to be one of its most famous churches in Rome, San Marcello Al Corso church is similarly quite high in altitude, making it an elegant structure built in 309 a.d. The church has a dimension of 60mx26mx10m. The tall vault of the church creates a large ample space. Providing HVAC for the upper ample space of the church causes considerable energy demand. On the other hand, hot air tends to rise due to lower density. Therefore, precious artworks face with hot air from the central heating system. The system shutdown in non-working hours causes an intense fluctuation in temperature. Consequently, dissolution-re crystallization cycles of soluble salts happen in artworks and stone works [2].

For reducing this adverse effect, the temperature of the church need to be stabilized. Two approaches are adopted to impede temperature fluctuations in the church, the upper section of the church where the ceiling and windows are located is separated via horizontal air curtains so the HVAC load for this section will cut off and the upper section environmental condition will be closer to the outside environment. For the lower section, Phase change materials (PCMs) are used to stabilize the temperature during non-operating hours of the church when the HVAC system is turned off. Therefore, masonry and paintings of the lateral walls will not be affected. Furthermore, the underfloor heating and cooling (UFHC) system uses natural convection heat transfer to eliminate noises and maintain silence in the church.

For supplying the energy demand of the proposed HVAC system, The RE systems have been designed in a way to satisfy the aims of net zero energy buildings (net ZEB). To achieve net ZEB in the church, the Photovoltaic (PV) system with the scheme of net metering method has been proposed to supply electricity for the HVAC and utilities.

Current interdisciplinary research studies energy retrofit modeling of a church from three perspectives (mechanical, electrical and architectural) covering environmental, social and cultural aspects. Numerous studies have been conducted in the field to discuss diverse methods according to the environment and social impacts. This study uses state of the art methods to renovate a historic church to make it cost and energy efficient.

II. Structural Modifications

The proposed design concept is based on lowering the ceiling and segregating upper and lower spaces. In this framework, energy is consumed only to keep the latter space warm/cold and to isolate artworks in a preservation environment.

The main hall is traditionally divided into two sections. A horizontal air curtain has been proposed to segregate

spaces and decrease cooling and heating height to 5 meters above the floor by creating an artificial ceiling made out of air. This keeps the upper sections separated from the HVAC space. Air curtain's piping and connections have the least visual impact on the existing setting as it is located underneath windows on a preexisting platform. The proposed system is promising in restricting circulating air from the HVAC system to the accommodation area. Air curtain efficiency is considered 80 percent in calculations [3]. Figure 1 shows the effect of adding horizontal air curtains on the segregation of internal spaces.

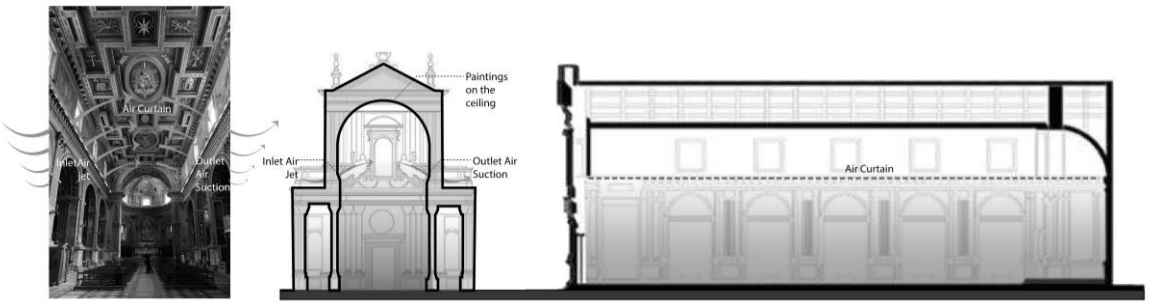

Figure 1 Horizontal air cuirtain design for internal space segregation

III. Mechanical Modifications

UFHC system has been proposed for the church. UFHC consists of several layers including PCMs, insulation, and underfloor piping to decrease losses and to conserve energy. UFHC utilizes natural convection heat transfer so it has a great advantage compared to forced convection methods where high-speed fans and ventilation noises become a serious source of inconvenience for worshipers [4].

Floorings consist of the following layers: 1) a layer of insulation is placed on the floor to minimize heat transfer between the ground and pipes, 2) a layer of environmentally-friendly biodegradable BioPCM® Q23 has been placed on the top of the insulation. The Q23's melting point of 23_ perfectly suits the ASHRAE 62 ventilation standard temperature for the current usage. Piping have been done on the top of the PCM layer for circulating heat transfer fluid (HTF) in the church; water has been used as HTF in the system.

In the current study, the system consists of a fluid-to-fluid heat pump for supplying required cooling and heating to the church. Energy analysis of the system is conducted for finding maximum cooling/heating load in the church. Calculations have been done based on a fixed temperature difference of 20 Celsius between inside and outside environments. A dynamic load management scheme has been implemented for calculating the system's load for different months of the year.

III.I. First and second law of thermodynamics analysis for the church

The first law of thermodynamic is a useful tool for finding the church's thermal energy demand and evaluating the performance of heating and cooling devices. The first law analysis of buildings and energy conversion systems do not consider the quality of exploited or conserved energy. Therefore, second law analysis has been applied to the church to find how the church's " low-quality" (low temperature) thermal energy demand provided from a "high-quality" source (electrical).

IV. Electrical Modifications

To achieve net ZEB in the church a microgrid has been designed where the PV system is used to supply the demanded load. The feasibility of this scheme has been investigated by Bandeiras et al [5]. It was found that PV systems could rise energy efficiency while decreases the energy cost of buildings. In this study Due to proximity to the utility grid, the net metering method has been proposed for this study. Thus, energy storage systems are neglected. Net metering is a billing scheme that motivates the consumers to sell their excess electricity generation by PV panels to the grid during the sunny days when the solar irradiation is available and inversely, buy electricity from the grid when the PV system fails to supply the church's load due to the lack of solar irradiation.

A unique type of power inverter namely grid-tie inverter utilized in the system. In this study a grid-tie inverter is used to reach a relative balance between imported and exported electricity. In this scheme the system exports electricity to the utility grid when there is a surplus in the generated electricity and imports electricity when the PV system is not operating. The cost of electricity for commercial customers in Italy is considered $0.18 per kWh in calculations [6].The system has been simulated in HOMER® and the lifetime of the project has been taken 25 years. Optimal solutions in terms of the technical and financial aspects have been found.

IV.I. Configuration and simulation of the PV system

The amount of electricity that can be exploited from the PV panels depends on the solar irradiation of the chosen site, the types and, the cell temperature of PV panels [7]. The latitude and longitude of the church in Rome is 41°53.9'N, 12°28.9'E. The daily average solar radiation in each month and clearness index in Rome have been collected from NASA surface meteorology [8]. The clearness index is a fraction of solar radiation from the atmosphere which reaches to a certain point on the earth. It is an indicator of clearness of the atmosphere.

IV.II. Sizing and simulation of the PV system

For sizing the optimal PV system, HOMER optimizer has been used where multiple parameters such as solar radiation of the site, load profile, system components, and grid scheme have been considered to calculate the optimal PV system. The optimized PV system has been selected from local solutions considering the technical and economic aspects. The PV system consist of fixed mono-crystalline PV panels (no tracking system), a grid-tie inverter, and a generation meter. PV panels have a tilt angle of 34°, an efficiency of 18% and a lifetime of 25 years. The capital cost of PV panel for 1 kW has been taken $1500 with operation and maintenance cost of 10 ($/year). For the inverter, the cost of 1kW is $400 with an efficiency of 95% and a lifetime of about 15 years.

V. Results and discussions

V.I. Heating System

Ambient air provides the hot source for the heat pump. The heat is transferred from the refrigerant to the circulating water using a fluid to fluid heat exchanger. Circulating water enters the church at 44 °C and leaves it at 37 °C. Table 1 shows the system specifications in the cold seasons before and after applying modifications.

Table 1. Heat pump Heating specifications

Status	Electric input (kW)	Cooling power (kW)	Dry Bulb (°C)	Wet Bulb (°C)	Relative Humidity (%)	T Inlet (°C)	T Outlet (°C)	flow rate (kg/s)
Before	153.5	537.25	23	15.6	50	44	37	24.3
After	82.5	288.75	23	15.6	50	44	37	13.2

V.II. Cooling system

In this mode, the water enters the church at 8 °C and leaves it at 13 °C. A portion of the generated heat at the other side of the heat pump is sent through a heat exchanger to supply hot water for the church. Also, a cooling system is designed for the time more cooling power is required. Table 2 shows the system specifications in hot seasons before and after applying modifications.

Table 2. Heat pump Heating specifications

Status	Electric input (kW)	Heat rejection (kW)	Dry Bulb (°C)	Wet Bulb (°C)	Relative Humidity (%)	T Inlet (°C)	T Outlet (°C)	flow rate (kg/s)
Before	132.46	463.4	23	15.6	50	8	13	27.8
After	91.81	318.5	23	15.6	50	8	13	17.7

V.III. First and Second law analysis

The first and second law analysis of the church has been conducted and results are tabulated in table 3 and table 4.

Table 3. First and second law analysis of the church before applying modifications.

Operation Mode	Heat input Q (kW)	heat loss (kW)	Q_use (kW)	Ex_use (kW)	Ex_in (kW)	exergy efficiency(%)	energy efficiency (%)
Heating	537	-363	174	2.96	29.2	10.1	32.4
Cooling	-463	363	-100	1.705	26.62	6.4	21.5

Table 4. First and second law analysis of the church after applying modifications.

Operation Mode	Heat input Q (kW)	heat loss (kW)	Q_use (kW)	Ex_use (kW)	Ex_in (kW)	exergy efficiency(%)	energy efficiency (%)
Heating	288	-120	168	2.865	15.71	18.2	58.3
Cooling	-318	120	-198	3.377	18.34	18.4	62.2

V.IV. Analysis of cost summary

The optimal system is achieved where a cost minimization approach has been adopted to develop a system with minimum net present cost (NPC), cost of energy (COE), and capital costs [9]. Table 5 shows the economic data of the system after optimization. Moreover, the cost summary of the proposed system has been given in table 6.

Table 5. Optimized grid-connected PV system economic data

PV (kW)	Grid (kW)	Converter (kW)	NPC ($)	COE($/kWh)	Operating cost ($)	Initial capital ($)	Capital cost ($)	Production (kWh/yr)
40	23	40	87,869	0.0756	918.11	76,000	60,000	63,025

Table 6. The cost summary of system

Component	Capital cost ($)	Replacement cost ($)	O &M cost ($)	Total cost ($)
Grid	0	0	1,187,16	1,187.16
PV panel	60,000	0	5,171.01	65,171.01
Converter	16,000	6,788.38	0	21,510.74
System	76,000	6,788.38	6,358.17	87,868.91

V.V. Electrical result analysis

The final results have been shown in table 7, a relative balance (98% match) is reached in terms of exporting and importing energy between the PV system and the utility grid. There is no unmet electric load and excess electricity and the capacity shortage is almost zero.

Table 7. Electrical specification for PV system

Production	Unit (kWh/year)	Percent (%)	Consumption	Unit (kWh/year)	Percent (%)
PV generated	63,025	67.7	Church load	60,384	67.1
Grid imported	30,079	32.3	Grid exported	29,569	32.9
Total	93,104	100	Total	89,953	100

VI. Conclusion

In this study, new methods have been proposed for modifying old churches to achieve net ZEB. San Marcello Al Corso, a historic church in Rome, has chosen for performing the analysis.

The energy assessment was conducted for the system, a 248.5 kW decrease in heating load and a 144.9kW decrease in cooling load were observed after applying modifications to the church. The proposed modifications offer 46.2% and 31.2% reductions in energy consumption for heating and cooling, respectively.

Furthermore, applying modifications have positive effects on increasing the first and second law efficiency of the church. In Heating mode, energy and exergy efficiency increased to 58.3% and 18.2%, respectively. Therefore, a 25.9% rise in energy efficiency and an 8.1% rise in exergy efficiency are observed. In cooling mode energy and exergy efficiency increased to 62.2% and 18.4%, respectively. Therefore, a 40.7% rise in energy efficiency and a 12% rise in exergy efficiency are observed.

The electrical analysis has shown that 29,569 kWh/year power surplus has been exported to the utility grid while 30,079 kWh/year power has been imported to supply the church's load when solar irradiation is not enough. Consequently, the concept of net ZEB has been accomplished in the church and a relative balance in annual energy exchange between the on-site generation and the utility grid has been reached.

References

[1] S. Ruester, S. Schwenen, M. Finger, and J. M. Glachant, "A post-2020 EU energy technology policy: Revisiting the strategic energy technology plan," *Energy Policy*, vol. 66, pp. 209–217, Mar. 2014.

[2] C. Bläuer Böhm, K. Zehnder, H. Domeisen, and A. Arnold, "Climate control for the passive conservation of the romanesque painted wooden ceiling in the church of Zillis (Switzerland)," *Stud. Conserv.*, vol. 46, no. 4, pp. 251–268, Dec. 2001.

[3] X. Luo, S. Lei, W. Tian, and Z. Gu, "Evaluation of air curtain system orientated to local environmental control of archaeological museum: A case study for the stone armor pit of Emperor Qin's Mausoleum Museum," *Sustain. Cities Soc.*, vol. 57, p. 102121, Jun. 2020.

[4] U. Berardi, E. Cirillo, and F. Martellotta, "A comparative analysis of acoustic energy models for churches," *J. Acoust. Soc. Am.*, vol. 126, no. 4, p. 1838, 2009.

[5] F. Bandeiras, M. Gomes, P. Coelho, and J. Fernandes, "Towards net zero energy in industrial and commercial buildings in Portugal," *Renew. Sustain. Energy Rev.*, vol. 119, p. 109580, Mar. 2020.

[6] A. M. Pavan and V. Lughi, "Grid parity in the Italian commercial and industrial electricity market," in *4th International Conference on Clean Electrical Power: Renewable Energy Resources Impact, ICCEP 2013*, 2013, pp. 332–335.

[7] C. Lupangu and R. C. Bansal, "A review of technical issues on the development of solar photovoltaic systems," *Renewable and Sustainable Energy Reviews*, vol. 73. Elsevier Ltd, pp. 950–965, 01-Jun-2017.

[8] Stackhouse and P. W., "Surface Meteorology and Solar Energy (SSE) Data Release 5.1."

[9] K. Branker, M. J. M. Pathak, and J. M. Pearce, "A review of solar photovoltaic levelized cost of electricity," *Renewable and Sustainable Energy Reviews*, vol. 15, no. 9. Pergamon, pp. 4470–4482, 01-Dec-2011.

Removal of crystal Violet dye from water by Sand of Algerian Sahara

[1*]ARRIS Sihem, [2]NDermouchi Aida, [3]Bencheikh Lehocine Mossaab,[4] Meniai H-A
[1]University Salah Boubnider Constantine 3, department Environmental Enginnering, Constantine, 25000, Algeria
[2]University Salah Boubnider Constantine 3, department Environmental Enginnering, Constantine, 25000, Algeria
[3]University Salah Boubnider Constantine 3, department Environmental Enginnering, Constantine, 25000, Algeria

* E-mails: arris_s@yahoo.fr

Abstract
Dye-based industries, particularly small and medium scale, discharge their effluents into waterways without treatment due to cost considerations. In this study, sand from the ELOUED region in Sahara of Algeria was evaluated for his ability to remove crystal violet (CV) dye from aqueous solutions
Adsorption studies were carried out at different initial dye concentrations (20, 40, 80 and 100 mg/L), contact time (5, 10, 15, 20, 30, 60, 90 and 120 min). Sorption equilibrium reached rapidly with 99.99% CV removal in 15 min. Fit of the sorption experimental data was tested on the pseudo-first, pseudo-second-order, intraparticular diffusion and Temkin kinetics mathematical equations.
Kinetic data followed the pseudo-second-order model, with coefficient of correlation R^2=1, suggesting that the sorption process is more inclined toward the chemisorption mechanism We found a maximum sorption capacity of 4.99 mg/g (R=99.99%) for the CV with stirring speed of 100tr/min, concentration of 50mg/L, temperature of 20°C, particle size less than 0.375mm, ratio of 10mg/L, and natural pH = 9.87. Sand was also shown to be highly effective in removing CV from aqueous solution in continuous-flow fixed-bed column with efficiency of 99.99% after 15 minutes of reaction. The study shows Saharian Sand has the potential of application as an efficient sorbent for the removal of CV from aqueous solutions.

Keywords: "Sorption, crystal violet, tannery, wastewater treatment, Sand"

I. Introduction

The dye wastewater has long been a major environmental problem all over the world. The problem is further aggravated by rapid industrialization, population growth and unskilled utilization of natural water resources [1]. The discharge of effluent containing synthetic dyes from several industries like textile, printing, leather and cosmetics into the hydrosphere have adverse effect in environment. The presence of very small amounts of dyes in water (less than 1 ppm for some dyes) is highly visible and undesirable [2]. It is already demonstrated that dyes damage the aquatic ecosystem by varying the path of sunlight which largely affect the photosynthetic activity (lowers down the dissolve oxygen) [3]. Moreover, many dyes are toxic and even carcinogenic thus affecting the human health [4]. As a representative of synthetic dyes, Crystal violet (CV) is a cationic dye that can easily interact with negatively charged cells membrane surfaces, enter into cells and can concentrate in cytoplasm [5]. CV is a member of triphenylmethane group. Even though the dye is carcinogenic it is still extensively used as a biological stain for identifying the bloody fingerprints being a protein dye, as a dermatological agent and is used in various commercial textile operations [6]. It is also used in Gram's stain for the demonstration and primary classification of dyes [7]. Many researchers have reported that Crystal violet could induce carcinogenic effects, is toxic to mammalian cells and also a mutagen, mitotic poison [8]. It can cause skin and digestive tract irritation. It is responsible for moderate eye irritation, causing painful sensitization to light. It can cause permanent injury to the cornea and conjunctiva [9], which is also non-biodegradable and persists in the environment for longer time [10]. Therefore, wastewater containing CV must be purified before release in the environment to protect the ecosystem and human health. For this purpose, various methods of treatment exploited through the years by industries for removing colorants include physicochemical, chemical, and biological methods, such as flocculation, coagulation, precipitation, adsorption, membrane filtration, electrochemical techniques, ozonation, and fungal decolorization [7]. However, due to the fact that effluents contain different dyes, and these dyes contain complex structures, is very difficult to treat using conventional methods [8].

II. Experimental Procedure

Adsorbent and adsorbate:

Our material is a sand from the south of Algeria in the El Wed region, its shown in Fig 2. We tried to characterize experimentally, test and improve performance. And the adsorbate tested in this study is crystal violet (CI 42555, Class: basic dye 3) having chemical formula: $C_{23}H_{30}ClN_3$ and molecular mass: 407.97 g/mol, fusion temperature:215°C , and solubility in water at 25°C: 4g/L . Structure of crystal violet molecule is shown in Figure 1..

III. Adsorption study

The adsorption was performed using the batch procedure and effect of parameters such as time of contact, pH, initial concentration, was studied. Kinetic experiments were carried out by agitating 2 g of adsorbent with 200 mL of dye solution with initial concentration of 50 mg L-1 at room temperature (25 ± 2 °C) at 300 rpm. The collected samples were then filtrated (0,4mm) and the concentration in the supernatant solution was analyzed using a UV spectrophotometer (UV-Visible Spectrophotometer UV 1601.Shimadzu) by measuring absorbance at λ = 591 nm and pH = 5 [11]. The adsorption capacity (mg/g) of adsorbents was calculated using Eq. 1:

$$q_t = \frac{(C_0 - C_t)\cdot V}{m} \quad (1)$$

q_t:sorption capacity at time t (mg/g), C_t is concentration of MR at time t (mg/L), C_0 is initial concentration (mg/g), V is solution volume (L) and m is sorbent mass (g).

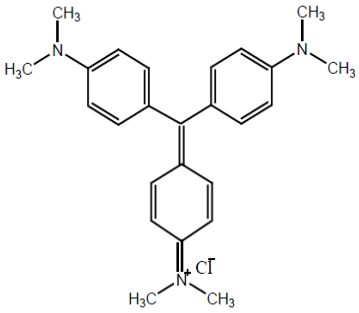

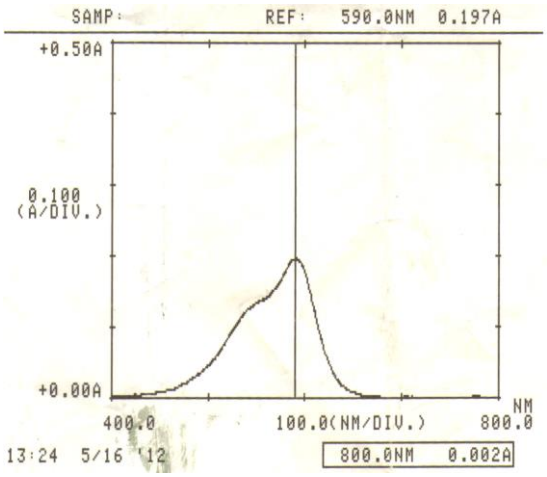

Fig 1. chemical structure of CV **Fig 2. Spectrum of CV** **Fig 3. Sand of El Wed in Algeria**

IV. Results and discussions

Effect on contacting time and kinetic study:

Fig. 1 presents the effect of contact time on the CV removal. As shown, from the previous results we notice that equilibrium is reached very quickly (15 minutes) with important adsorption capacity.

However, from the shape of the curve, we notice the existence of three phases. The first: almost linear with a yield of 99.99 after 15 minutes. The second: a plateau indicating stabilization, which may be due to the exhaustion of active sites. A third: showing a linear decrease in yield after 90 minutes of contact. This indicates an increase in the molecules of the violet crystal in solution, which lets us predict a possible desorption or an exchange of ions.

Table 1: Yiel retention of CV by Saharian Sand

t (min)	5	10	15	30	60	90	120	180
R(%)	99.9600	99.9856	99.9946	99.9946	99.9040	99.9946	99.9280	99.8790

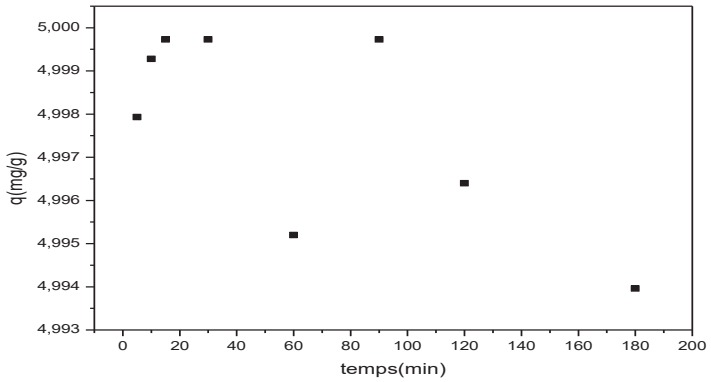

Fig.**2**. Effect of contact time on sorption of CV onto Saharian Sand
Conditions : C0=50mg/l, pH_0=9.87, T= 20°C, r=10g/l, v=100tr/min, d<0.315.

In order to investigate the adsorption processes of CV onto adsorbents, pseudo-first order and pseudo second order kinetic models were applied to the experimental data. The pseudo-first-order kinetic model, proposed by Lagergren, has been widely used to predict the dye adsorption kinetics. The dye adsorption kinetics following the pseudo-first-order model is given by [12]:

$$\frac{dq_t}{dt} = k_1(q_e - q_t) \quad (2)$$

where *q* and *qe* represent the amount of dye adsorbed (mg g-1) at any time t and at equilibrium time, respectively, and *k*1 represents the adsorption rate constant (min-1). Integrating Eq. (3) with respect to boundary conditions *q* = 0 at *t* = 0 and *q* = *q* at *t* = *t*,

then Eq. (2) becomes:

$$\log(q_e - q_t) = log q_e - \frac{k_1}{2.303}t \quad (3)$$

Thus the rate constant *k*1 (min-1) can be calculated from the plot of log (*qe-q*) *vs.* time *t.*
The kinetic data were further analyzed using a pseudo second- order relation proposed by [13] which is represented by:

$$\frac{dq_t}{dt} = k_2 \,.\, (q_e - q_t)^2 \qquad (5)$$

where *k*2 is the pseudo-second-order rate constant (gmg-1 min-1) and *qe* and *q* represent the amount of dye adsorbed (mg g-1) at equilibrium and at any time *t*. Integrating Eq. (5) for the boundary conditions *t* = 0 to *t* = *t* and *q* = 0 to *q* = *q* gives: $\frac{t}{q_t} = \left(1/k_2 \,.\, q_{eq}^2\right) + \left(1/q_{eq}^2\right).t$ (6)

A plot *of t/q vs*. *t* gives the value of the constants *k*2 (g mg-1 min-1), and also *qe* (mg g-1) can be calculated.
Because the above two equations cannot give definite mechanisms, the intraparticle diffusion model was tested. According to Weber and Morris [14], an intraparticle diffusion coefficient kdif is defined by the equation:

$q_t = k_{int}\, t_{1/2}$ (7) $\qquad t_{1/2} = \frac{0.03 r_0^2}{D}$ (8)

where *k*dif is the intraparticle diffusion rate constant (mg g-1 min-1/2), and *C* is the intraparticle diffusion constant (mg g-1). The constants *k*dif and *C* can be obtained, respectively, from the slope and intercept of the plot of qt versus *t*1/2. r0: the grain diameter of the adsorbent in cm and D is the intraparticle diffusion coefficient (cm2 s-1).
The relative values of *C* give an idea about the boundary layer thickness, i.e., the larger the intercept value, the greater the boundary layer effect [14-15].
The Elovich equation is also used successfully to describe second order kinetics by assuming that real solid surfaces are energetically heterogeneous. This model is represented by the following equation [16]:

$$q_t = \frac{1}{\beta}\ln(\alpha\beta) + \frac{1}{\beta} lnt \qquad (10)$$

Where: α is the initial adsorption rate in (mg / g min) t0 = 1 / (α + β); β is constant linked to the external surface and to the activation energy of chemisorption in (g / mg). α and β, which are the Elovich coefficients, and which respectively represent the initial sorption rate (mg.g-1.min-1) and the desorption constant.
From the results of the table, we can conclude that the kinetics of retention of the CV by the Saharan sand is pseudo second order with a regression factor equal to 1. Also it is controlled by an intraparticle diffusion, but this cannot exclude other phenomena involved.
The best correlation for the system provided by the pseudo-second-order model suggests that chemical adsorption involving valency forces through sharing or exchange of electrons between adsorbent and adsorbate might be significant [10]. Saeed et al. [18], El Sayed [14], Ahmad [16] reported that CV dye adsorption on grapefruit peel, palm kernel fiber and coniferous pinus bark powder fitted well to pseudo-second order kinetic model, and the process was thought to be chemisorption controlled. Table 2: Kinetics constants

Table 2: Constant Kinetics

Model	Correlation facteur R^2	Kinetics constants	
Pseudo first order model	0.7866399	q_e (mg/g)	K_1(min-1)
		0.00096908	0.0110834
Seudo second order model	1	q_e (mg/g)	K_2 (g mg^{-1} min^{-1})
		4.994506	-8.658325939
diffusion intraparticular model	0.814275	k_{int}	D (cm^2 /s)
		1.1173E-3	≤3.969E-8
diffusion im liquid film model	-0.740945	K_{fd}	
		1.00996E-2	
Elovich model	-0.565401	α	β
		0	-987.4105

From the results of the table, we can conclude that the kinetics of retention of the CV by the Saharan sand is pseudo second order with a regression factor equal to 1. Also it is controlled by an intraparticle diffusion, but this cannot exclude other phenomena involved.
The best correlation for the system provided by the pseudo-second-order model suggests that chemical adsorption involving valency forces through sharing or exchange of electrons between adsorbent and adsorbate might be significant [10]. Saeed et al. [28], El Sayed [44], Ahmad [26] reported that CV dye adsorption on grapefruit peel, palm kernel fiber and coniferous pinus bark powder fitted well to pseudo-second order kinetic model, and the process was thought to be chemisorption controlled.

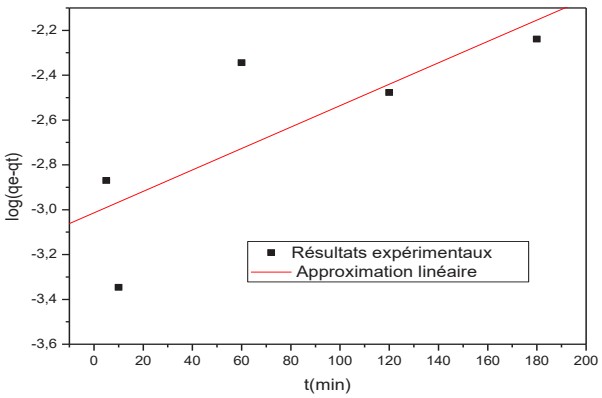

Fig 3: Pseudo first order model

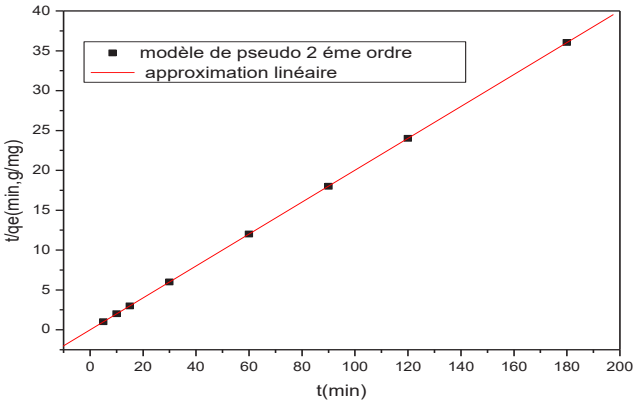

Fig.4 : Pseudo second order model

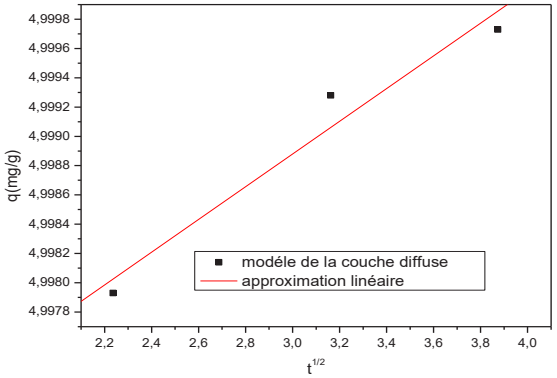

Fig 5 Kinetic model of the diffuse layer

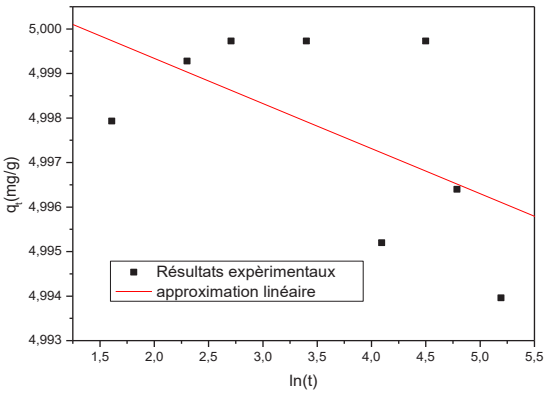

Fig 6: Elovich Kinetic model

V. Conclusions

The present study showed that is possible to use Algerian sand in sorption process. The sand from el wed region in the sahara of Algeria is effective adsorbent for removal the cationic dye crystal violet from aqueous solution. The pseudo-second order model provides the best correlation of the experimental data for both adsorbents and intraparticle diffusion is involved in the adsorption process, but it is not the only ratelimiting step. We found a maximum sorption capacity of 4.99 mg/g (R=99.99%) for the CV with stirring speed of 100tr/min, concentration of 50mg/L, temperature of 20°C, particle size less than 0.375mm, ratio of 10mg/L, and natural pH = 9.87. Sand was also shown to be highly effective in removing CV from aqueous solution in continuous-flow fixed-bed column with efficiency of 99.99% after 15 minutes of reaction. The study shows Saharian Sand has the potential of application as an efficient sorbent for the removal of CV from aqueous solutions.

References

[1] Hayzoun H., Ouammou A., Saidi O., Khalil F., Bouayyadi L., J. Mater. Environ. Sci. 5 (S2) (2014) 2438.
[2] Miyah Y., Lahrichi A., Idrissi M., Boujraf S., Taouda H., Zerrouq F., Journal of the Association of Arab Universities for Basic [and Applied Sciences. 23 (2017) 20.
[3] Yagub M. T., Sen T. K., Afroze S., Ang H. M., Advances in colloid and interface science. 209 (2014) 172.
[4] Miyah Y., Idrissi M., Zerrouq F., Journal of Materials and Environmental Science. 6 (3) (2015) 699.
[5] Rajeswari Kulkarni M., Revanth T., Acharya A., Bhat P., Resource-Efficient Technologies. 3 (1) (2017) 71.
[6] Idrissi M., Miyah Y., Benjelloun Y., Chaouch M., J. Mater. Environ. Sci. 7 (1) (2016) 50.
[7] Bennani Karim A., Mounir B., Hachkar M., Bakasse M., Yaacoubi A., J. Mater. Environ. Sci. 8 (3) (2017) 1082.
[8] Jayganesh D., Tamilarasan R., Kumar M., Murugavelu M., Sivakumar V., J. Mater. Environ. Sci. 8 (4) (2017)1508.
[9] Güzel F., Sayğılı H., Sayğılı G.A., Koyuncu F., Journal of Molecular Liquids, 206 (2015) 244.
[1] Benjelloun Y., Lahrichi A., Boumchita S., Idrissi M., Miy https://doi.org/10.1109/TNSRE.2003.814453
[11] Dabrowski, A. *Adv. Coll. Interface Sci.* **2001**, *93*,135.*Bertolini et al. Orbital: Electron. J. Chem. 5 (3):179-191, 2013*
[12] Orthman, J.; Zhu, H. Y.; Lu, G. Q. *Sep. Purif. Technol.***2003**, *31*, 53.
[13] Fungaro, D. A.; Izidoro, J. C.; Almeida, R. S.; *Eclética Quim.* **2005**, *30*, 31.
[14] Y. Gao, Y. Guo and H. Zhang, J. Hazard. Mater., 302, 105 (2016)
[15] C. Leodopoulos, D. Doulia and K. Gimouhopoulos, Sep. Purif. Revs.,44, 74 (2015)
[16] A.M. Aljeboree, N. Abbas, A.N. Alshirifi, A.F. Alkaim**Kinetics and equilibrium study for the adsorption of textile dyes on coconut shell activated carbon** Arab. J. Chem., 10 (2017), pp. S3381-S3393
[17] Z. Chennouf-Abdellatif, B. Cheknane, F. Zermane, E.M. Gaigneaux, O. Mohammedi, N. Bouchenafa-Saib**Equilibrium and kinetic studies of methyl orange and Rhodamine B adsorption onto prepared activated carbon based on synthetic and agricultural wastes**
Desalination Water Treat., 67 (2017), pp. 284-291
[18] Z. Guo, X. Liu, H. Huang**Kinetics and thermodynamics of reserpine adsorption onto strong acidic cationic exchange fiber** PloS One, 10 (9) (2015), Article 0138619.

Characterization of natural carob used for removal of crystal Violet dye from wastewater

[1*]ARRIS Sihem, [2]BENCHEIKH Lehocine Mossaab, [3]MENIAI H-A
[1,2,3]University Salah Boubnider Constantine 3, Faculty of Engineering Process, Environmental Engineering Department, Ali Manjeli Nouvelle ville, Constantine, 25000, Algeria

* E-mails: arris_s@yahoo.fr

Abstract
The objective of this work is to test a natural biosorbent: carob in the depollution of effluents loaded with violet crystal (CV). We have characterized our sorbent by some methods such as: Spectrophotometric analysis, determination of surface functions by the Boehm method, contact pH, zero point of charge pH, iodine index, phenol index, methylene blue index and infrared. The boehm values and the pH_{PZC} value show that the biosorbent pH is slightly acidic. The measurement of the iodine index shows that the carob is a microporous biosorbent Id = 437.80 mg/g, the maximum retention capacity of the BM is 24.75 mg/g mg/g with a yield of 97.16%. The phenolic character of the carob appears during the measurement of the phenol index, where the release of phenol in water was confirmed with a rate of 3%. The results of the characterization of the raw carob and carob saturated in violet crystal showed the appearance of phenolic groups in the raw carob, and of the nitro aromatic and chloro alkane groups in the saturated carob confirming the presence of CV.
This work examines also the study of the sorption of a violet crystal dye by carob to decontaminate waste water. We found a maximum sorption capacity of 24.29 mg/g (R=97.16%) for CV with stirring speed of 300tr/min, concentration of 50mg/L, temperature of 20°C, particle size less than 0.375mm, ratio of 10mg/L, natural pH = 6.8 and during 30 minutes of reaction

Keywords: Sorption, crystal violet, tannery, wastewater treatment, biomaterial, characterization, carob by-product

I.Introduction

Environmental pollution due to industrial effluents is of major concern because of their toxicity and threat for human life and the environment. The discharge of textile effluents to the water bodies has raised much concern because of potential health hazards associated with the entry of toxic components into the food chains of humans and animals. Chemical synthetic dyes are widely used in many industrial processes for various purposes such as textile dyeing, paper, and plastic, leather tanning. These dyes are also used in food, pharmaceutical or cosmetic [1,2]. Over 10, 000 dyes with an annual production over $7x10^5$ metric tones world wide are commercially available and 5-10% of the dye stuff is lost in the industrial effluents However, most of the solutions used containing these dyes are discarded as effluents. It has been observed that some of these dyes have toxic and carcinogenic effects [3-5] on aquatic life and on human's health. Thus, for reasons related to human health and to protect the environment, the removal of synthetic dyes from aqueous effluents is of great importance. Therefore there is a need to remove dyes before effluent is discharged into receiving water bodies.

The most popular treatment methods for textile wastewater are combinations of biological treatment, chemical coagulation and activated carbon adsorption [2-4]. Adsorption onto activated carbon is proven to be very effective in treating textile wastes. However, in view of the high cost and associated problems of regeneration, there is a constant search for alternate low cost adsorbents. Such types of adsorbents include coir pith [5], parthenium [6], coconut shell [7], peanuthull [8] and rice husk [9]. In the present study removal of crystal violet from aqueous solution using carob as an adsorbent was investigated

II. Experimental Procedure

The carob was washed, crushed in a crusher (FRITSCH industry.8 6580 Idar Oberstein), sifted using a sifter (Analysensieb-retsch-5657 HAAN W). Finally, the solid material obtained is stored in a desiccator for use.

Fig.1 The Carob

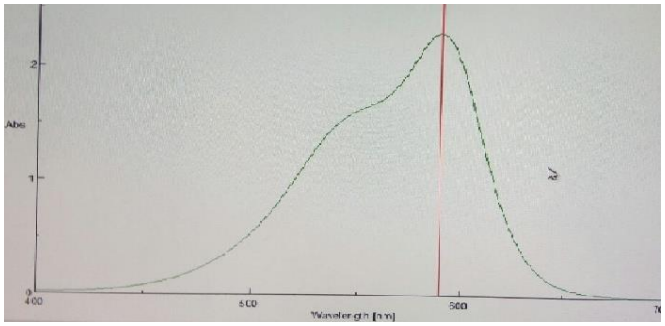

Fig.2 Cristal Violet Spectrum

III. Results ans discussion of characterization of carob:

III.1.Identification and determination of surface functions by the Boehm method:

The dosage of the surface functions was carried out according to the Boehm method which corresponds to the acid-base titration of the functional surface groups. For this 1g carob samples brought into contact with four solutions of

Na_2CO_3, $NaHCO_3$, NaOH and HCl with a concentration equal to 0.1 M. We put these solutions under stirring for 72 hours at a speed of 300 rpm. After shaking we centrifuged them. 10 ml of the filtrate was titrated with a strong base or strong acid (HCl or NaOH) with the addition of a few drops of phenolphthalein or methyl orange (in order to measure the excess base or acid).

This method makes it possible to calculate the total acidity or alkalinity of an adsorbent material, by making the respective sum of the acid and basic functional groups. The number of sites of the various acid functons is calculated by considering that [1]:

- ✓ $NaHCO_3$ neutralizes the carboxylic group
- ✓ Na_2CO_3 neutralizes the carboxylic and lactone groups
- ✓ NaOH neutralizes the carboxylic, lactone and phenolic groups

The results of the two experiments are shown in the following tables:

Table.1: determination of the number of moles of the surface functions (MA and OA)

Solution	NaOH	HCl	$NaHCO_3$	Na_2CO_3
n_{csf} (mol) (MA)	0.001	0	0.00075	0
n_{csf} (mol) (OA)	0.00125	0.00015	0.00065	0

The results of the assay of the carob surface functions show that this material has a concentration of acid functions slightly higher than the basic functions and therefore the activated carbon has an acidic surface (total acid = 0.001mol/L) of which the majority are phenolic. From the results shown in the table 3, it can be seen that our adsorbent has an acid and phenolic character.

Table 2 : determination of surface function ((MA and OA))

Parameter	agitation	oscillation
Basic groupements	0	0.00015
Acid groupements	0.001	0.00125
Carboxylic groupements	0.00075	0.00065
Phenolic groupements	0.001	0.00125
Lactonic groupements	-0.00075	-0.00065

III.2.Contact pH:

The contact pH measurement makes it possible to determine the acidity or basicity of an adsorbent. For this we used two methods found in the bibliography.

a) 1st method: 100 mg of adsorbent were placed in 10 ml of a 0.1 M NaCl solution for. NaCl is a support electrolyte making it possible to make the migration current of species negligible before diffusion. It makes the pH measurement more stable [3].

b) 2nd method: 0.5 g of carob in 10 ml of distilled water.

In both cases the suspension is left under stirring for 3 days, then centrifuged and finally dosed in order to determine the contact pH.

The results of the two tests considered are shown in the following table.

Table.3 : Experimental results of contact

method	Contact pH
Filtrate of NaCl	4.92
distilled water filtrate	5.52

III.3.The zero load point pH (pHpzc):

The pHpzc or pH of the zero load point, corresponds to the pH value for which, the net load of the adsorbent surface is zero. This parameter is very important in adsorption phenomena, especially when electrostatic forces are involved in the mechanisms.

The 1st method:

This method consists in fixing the pHi of the solution close to the value of the contact pH which has been found (4.92) by adding NaOH or HCl. Then, a mass of 1 g of the solid is brought into contact with 20 ml of NaCl solution (0.1 M) with stirring for 48 hours. The final pH is measured. It has been found that:

$$\mathbf{pHp_{ZC} = 4.92}$$

The 2nd method:

50 ml of 0.1 N NaCl solutions are prepared at different pHi varying from 2 to 12 adjusted by NaOH or HCl. We put a mass of 0.5 g in each solution. After stirring for 24 hours, the solutions are centrifuged and the final pH is measured. We carry on a graph $\Delta pH = f(pHi)$ or $\Delta pH = (pHf-pHi)$, the intersection of the curve with the axis which passes through the zero gives us the isoelectric point [4]. (the point where pHf - pH i = 0 is taken as pH pzc)

Table.4 : determination of pH_{PZC} (2nd method)

pH_i	2.03	3.90	6.04	8	10.23	12
pH_{final}	2.06	5.55	5.51	5.87	5.82	8.36
pH_{fina}-pH_i	0.03	1.65	-0.53	-2.13	-4.41	-3.64

According to this figure, the point where pHf - pH i = 0 is almost equal to 5.80 so pHPZC = 5.8. At pH <pH PZC, the

surface becomes positively charged, the concentration of H + ions is high and they compete with the cations of Crystal violet for vacant adsorption sites resulting in a decrease in adsorption. At pH> pHPZC, the surface of the adsorbent is negatively charged and promotes the adsorption of violet crystal (cationic dye) due to the increased electrostatic force of attraction [5].

III.4. Absorbability of Iodine:

The iodine index (iodine nember) is used to measure the micropore content of an adsorbent. This retention index characterizes the areas accessible to any particle of size less than or equal to that of the iodine molecule, in particular the mini-micropores accessible to small particles responsible for tastes and odors [9]

An amount of 2 g carob together with 50 ml of 0.1 N iodine solvents was inserted into a dark and closed bottle, then shaken for 15 minutes. The solution was separated using a centrifuge and a 10 ml of filtrate that was then titrated with 0.1 N sodium thiosulfate solutions. If the yellow color of solvent is close to disappearing, an indicator of 1% amilum was added. The titration was continued until the right blue color disappeared. The capability of the biosorbent to adsorb Iodine is given by Equation

$$Adsorbability\ lod\left(\frac{mg}{g}\right) = \frac{[10-(N\times V)]}{S} \times 12{,}69 \times 5 \quad (3)$$

Id = q_{I2}= 437.80 mg/g

where: V = required sodium thiosulfate solvent, N = normality of sodium thiosulfate solvent, S = weight of carob (g), 12.69 = the amount of Iodine needed for a 1 mL sodium thiosulphate 0.1 N

We can notice that our adsorbent gives a very significant maximum iodine retention capacity which lets us say that the carob is a microporous biosorbent.

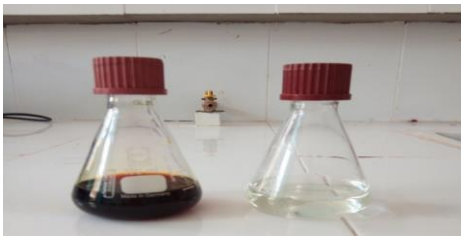

Fig.3: decoloration of iode by carob

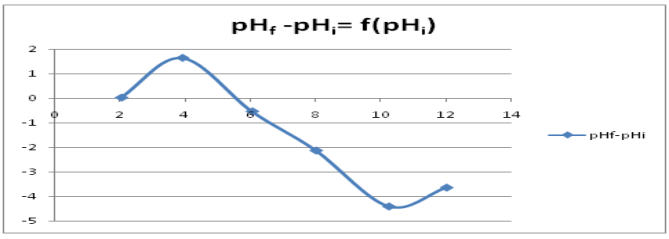

Fig.4 : pH_{PZC} of Carob

III.5.Structural analysis by infrared spectroscopy:

The infrared analysis spectra of adsorbent (carob) before and after retention are shown in Fig.5 and Fig.6 respectively. The most intense bands are reported in the Table.10 :

Table.10: IR absorption band of carob **[19] [20]**:

Wave number (cm^{-1})		groupement	Vibration and bond
Raw carob	Saturated carob		
32.8611	3391.21	**Alcohols and phenol**	Elongation O-H
2933.2	-	**Acid**	Elongation O-H
-	2856.06 - 2922.59	Alkanes	Elongation symétrique C-H
-	1698.98	Aromatics ketones	Elongation C=O
1606.41	1591.34	Aromatics	Elongation C=C
-	1523.49	**Nitro (aromatics)**	Elongation C-NO_2
-	1448.28	**Aromatics**	Elongation C=C
1436.71	-	Alkanes	asymmetric
1340.28	1355.71	Nitro (aromatics)	Elongation C-NO_2
1233.25	-	**Acid**	Elongation C-O
-	1169.62	**Tertiary Alcohols**	Elongation C-O
1106.94	-	secondaryAlcohols	Elongation C-O
1039.44	-	Ethers	Elongation C-O
-	1008.59	**Chloro alkanes**	C-X
989.304	-	Alkenes	Deformation out of plan =C-H
912.165	-	Alkenes	Deformation out of plan =C-H
858.168	-	aromatics	Deformation out of plan =C-H
-	723.175	**aromatics**	Deformation out of plan C-H
-	539.971 - 585.29	**halogen**	Elongation C-Br

The wide absorption band of 32.8611 for the raw locust bean and 3391.2cm-1 for the saturated locust bean corresponds to the vibrations of elongation of the hydrogen of the hydroxyl groups OH (of carboxyls, phenols or alcohols) and of water adsorbed. This confirms the phenolic character previously found in the study of the phenol index. It also corresponds to the elongation vibration of O-H from cellulose, pectin and lignin [15].

IRTF spectra also show absorption bands between 2930 and 2850cm-1 resulting mainly from the C – H stretching vibrations of aliphatic molecules.

The presence of the groups: chloro alkanes at 1008.59 cm-1, aromatic nitro at 1523.49 cm-1 and the aromatic at

723.175 cm-1 which were almost absent for the raw locust bean, and which appear for the saturated locust berry confirms the presence of the purple crystal on the surface of the solid because they exist in its structure.

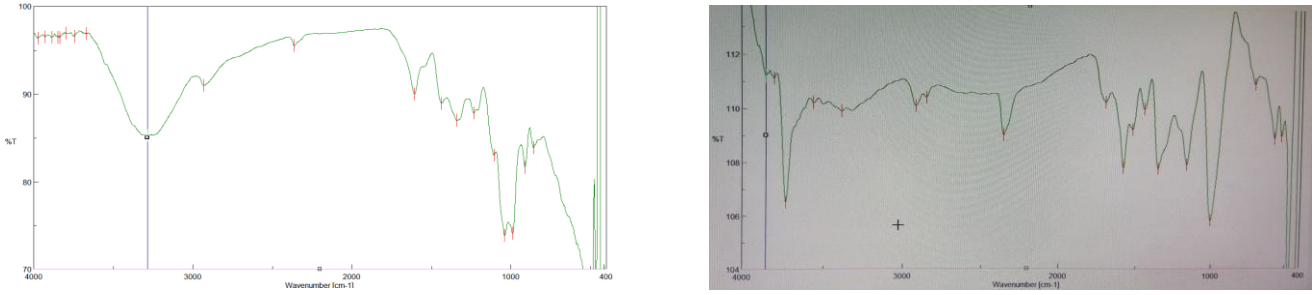

(A) **(B)**

Fig.5 : IR spectrum of raw carob (A) and carob saturated and dried at 110°C (B)

VI. Conclusions

The objective of this work is to test a natural biosorbent: carob in the depollution of effluents loaded with violet crystal. We have characterized our sorbent by some methods such as: Spectrophotometric analysis, determination of surface functions by the Boehm method, contact pH, zero point of charge pH, iodine index, phenol index, methylene blue index and infrared. The boehm values and the pHPZC value show that the biosorbent pH is almost neutral. The measurement of the iodine index shows that the carob is a microporous biosorbent Id = 437.80 mg / g, the maximum retention capacity of the BM is 24.75 mg / g mg / g with a yield of 97.16%. The phenolic character of the carob appears during the measurement of the phenol index, where the release of phenol in water was confirmed with a rate of 3%. The results of the characterization of the raw carob and carob saturated in CV showed the appearance of phenolic groups in the raw carob, and of the nitro aromatic and chloro alkane groups in the saturated carob confirming the presence of CV.

The study of the effect of certain experimental parameters, namely; the contact time, the dose of the solid, initial pH, initial concentration of the dye and the temperature, is considered in batch mode in another work.

This study is only one attempt which had like objective; to test the carob as an adsorbent using for the depollution of water. The carob used in this study has not any treatment of preliminary activation. In the future we propose an experimental study of physical and chemical activation of the carob with an aim of improving his effectiveness.

References:

[1] Y. Miyah, A. Lahrichi, and M. Idrissi, “Assessment of adsorption kinetics for removal potential of Crystal Violet dye from aqueous solutions using Moroccan pyrophyllite,” 2016.

[2] A. K. Kushwaha, N. Gupta, and M. C. Chattopadhyaya, “Removal of cationic methylene blue and malachite green dyes from aqueous solution by waste materials of Daucus carota,” *J. SAUDI Chem. Soc.*, 2011.

[3] Kinetics of Color Removal by Adsorption from Water Using Activated Clay,” no. August 2013, pp. 37–41, 2010. refer 30.pdf.” .

[5] Zhang, B., Xiong, S., Xiao, B., Yu, D., & Jia, X. (2011). Mechanism of wet sewage sludge pyrolysis in a tubular furnace. International jouranl of hydrogen energy, 36(1), 355-363.

[6] Weber, W . J., & Morris, J. C. (1963). Kinetics of adsorption on carbon from solution. J. Sanit. Eng. Div. Am. Soc. Civ. Eng, 89(17), 31-60.

[7] Y. Ho, “Removal of copper ions from aqueous solution by tree fern,” vol. 37, no. 250, pp. 2323–2330, 2003.

[8] Ko D.C.K., Tsang D.H.K., Porter F.J., McKay G., Applications of multipore model for mechanism identification during the adsorption of dye on activated carbon and bagasse pith, *Langmuir*, 19, 722–730, (2003).

[9] M. J. Ahmed and S. K. Dhedan, “Fluid Phase Equilibria Equilibrium isotherms and kinetics modeling of methylene blue adsorption on agricultural wastes-based activated carbons,” *Fluid Phase Equilib.*, vol. 317, pp. 9–14, 2012.

[10] Langmuir, I. (1918). The adsorption of gases on plane surfaces of glass, mica and platinium. Journal of the American Chemical society, 40(9), 1361-1403

[11] C .AYRAL, "Elimination de polluants aromatiques par oxydation catalytique sur charbon actif" these de doctorat (2009).

[12] M. A. Al-ghouti and Y. S. Al-degs, “New adsorbents based on microemulsion modified diatomite and activated carbon for removing organic and inorganic pollutants from waste lubricants,” *Chem. Eng. J.*, vol. 173, no. 1, pp. 115–128, 2011.

[13] M.A.M. Salleh, D.K. Mahmoud, W.A. Karim, A. Idris. Cationic and anionic dye adsorption by agricultural solid wastes: a comprehensive review, Desalin. 280 (2011) 1-13.

[14] C.K. Jain, D.C. Singhal, M.K. sharma, «Adsorption of zink on bed sediment of River London: adsorption model and kinetics», J. Hazard. Mater. B114 (2004) 231-239

[16] M. Farahani, S. Rozaimah, and S. Abdullah, “Adsorption-based Cationic Dyes using the Carbon Active Sugarcane Bagasse,” vol. 10, no. Esiat, pp. 203–208, 2011.

[18] G. L. Nombre, A. Amines, A. Hc, and N. A. Ald, “Tables de fréquence des vibrations de valence pp. 1–4.

Performance Evaluation of Machined and Powder Metallurgically Fabricated Crofer®22 APU Interconnects for SOFC Applications

[1]Alparslan Topcu, [2]Bülent Öztürk, [3*]Ömer Necati Cora
[1] Adana Alparslan Türkeş Science and Technology University, Department of Mechanical Engineering, Adana, 01250, Turkey
[2] Karadeniz Technical University, Department of Metallurgical and Materials Engineering, Trabzon, 61080, Turkey
[3] Karadeniz Technical University, Department of Mechanical Engineering, Trabzon, 61080, Turkey

* E-mails: atopcu@atu.edu.tr, bozturk@ktu.edu.tr, oncora@ktu.edu.tr

Abstract

This study aimed to evaluate the performances of solid oxide fuel cell (SOFC) interconnects made of commercially available bulk Crofer®22 APU alloy through machining as well as powder metallurgy approach (P/M) from Crofer®22 APU powders. To this goal, interconnects with 40x40 mm^2 active area were fabricated via both methods. Porosity, coefficient of thermal expansion measurements and single-cell performance tests were carried out. The P/M sample was found to have 9% porosity and comparable CTE value when compared with the machined from bulk Crofer®22 APU sample. In single performance tests, power values of 3.12 and 2.97 W were obtained at 800 °C operating temperature for the machined and P/M interconnects, respectively. The performance tests were also conducted at 700 °C operating temperature for both interconnects, and a similar trend was observed.

Keywords: Solid oxide fuel cell, metallic interconnect, machining, powder metallurgy, Crofer®22 APU, single cell performance test.

I. Introduction

Solid oxide fuel cells (SOFCs) have great potentials for energy applications, including combined heat and power generation, stationary power units, and transportation due to the advantages of high efficiency and fuel flexibility (Rong et al, 2018). SOFCs operate at relatively high temperatures compared with other fuel cell types (Mahmud et al., 2017). Interconnect is one of the key components of SOFCs stack through which multiple cells that are connected in series (Swaminathan et al., 2017). Interconnects provide electrical contacts between cells, distribute reactive gases on both sides of the cell (anode and cathode) and separate the anodes and cathodes of adjacent cells in the stack (Swaminathan et al., 2017; Mah et al., 2017). Those should exhibit excellent thermal and electrical conductivity, chemical and physical compatibility with the other SOFC components. The coefficient of thermal expansion (CTE) of an interconnect must match with that of the ceramic components. In addition, it should have low-cost and ease of manufacturing (Rubio et al., 2017).

In interconnect manufacturing, usually the machining from bulk process is preferred along with its subsequent finishing operations to obtain desired dimensions (flow channels, gas inlet, and outlet points, etc.) (Tietz et al., 2002). Recently, interconnects are also manufactured by means of powder metallurgy (P/M) approach as it can be seen in Fig.1 (Plansee, 2017). Near-net shape, faster production, and almost no scrap material are the main advantages of the P/M method over machining route (Fergus, 2005; Venskutonis et al., 2005).

Fig. 1. Interconnect plates fabricated with P/M approach by Plansee (Plansee, 2017)

To evaluate the overall SOFC performance, electrochemical tests are carried out per SOFC working conditions. De Marco et al. (2016), manufactured a copper-based anode supported cell which was then sintered at 950 °C, and performed electrochemical performance tests at 500, 600, and 650 °C temperatures. It was noted that the cell performance increased with increasing operating temperature. The power density of 0.26 W/cm^2 was obtained at 0.8 V operating voltage, 471 ml/min air, and 200 ml/min H_2 flow rates and at 650 °C operating temperature conditions. Celik et al. (2013), investigated the effects of cell size, operating current, and flow conditions on temperature distribution of SOFC short stack experimentally. Experimental parameters of 0.5 NL/min H_2, 1 NL/min air flow rates, electrolyte supported cells which have 16 cm^2 and 81 cm^2 active areas, serpentine flow field interconnects were chosen and tested. They indicated that the power density of 305 mW/cm^2 was obtained at 700 °C operating temperature with the co-flow type channel. It was also found that the power density of the co-flow type cell is higher than that of the counter-flow. Canavar et al. (2017) investigated the performance of nickel-based three different woven meshes as an anode flow-field for SOFC using Crofer 22 APU interconnect with 81 cm^2

active area MEA at 800 °C operating conditions.

This study aimed to reveal and compare the performances of interconnects manufactured through machining from bulk Crofer®22 APU and Crofer®22 APU powders via the P/M approach. The performance values of the interconnects were determined at operating temperatures of 700 and 800 °C.

II. Experimental

In interconnect manufacturing via the P/M approach, spherical Crofer®22 APU powders (63 µm in diameter max.) were acquired from ThyssenKrupp VDM Starck GmbH, Germany. The chemical composition of powders is given in Table 1. In compaction trials, insufficient bonding of powders was observed. For this reason, the ball-milling process was applied to the spherical powders using a planetary ball mill (Fritsch Pulverisette 6, FRITSCH GmbH, Germany) for 120 mins. It was then noted that the shape of powders changed from spherical to flaky which leads to increased surface area and contact points. SEM images of initial and ball-milled Crofer®22 APU powders are given in Fig. 2a and 2b. Powders were then compacted at 600 MPa in a rigid die having dimensions of 54x54 mm^2 at room temperature. Subsequently, the sintering process was performed at 1200 °C for 1 h in a rectangular tube furnace, and in a dry hydrogen atmosphere. Prior to sintering the furnace was flushed with nitrogen to remove residual oxygen in it. The porosity and CTE values of samples were measured to characterize the fabricated P/M interconnects. Details on the manufacturing of the interconnects can be found in Öztürk et al. (2018).

Table 1. Chemical composition of Crofer®22 APU powder

Element	Fe	Cr	Mn	Mo	Ni	Si	Ti	Nb	La
% (wt)	*Bal.*	*22.8*	*0.44*	*0.1*	*0.03*	*0.5*	*0.2*	*0.1*	*0.1*

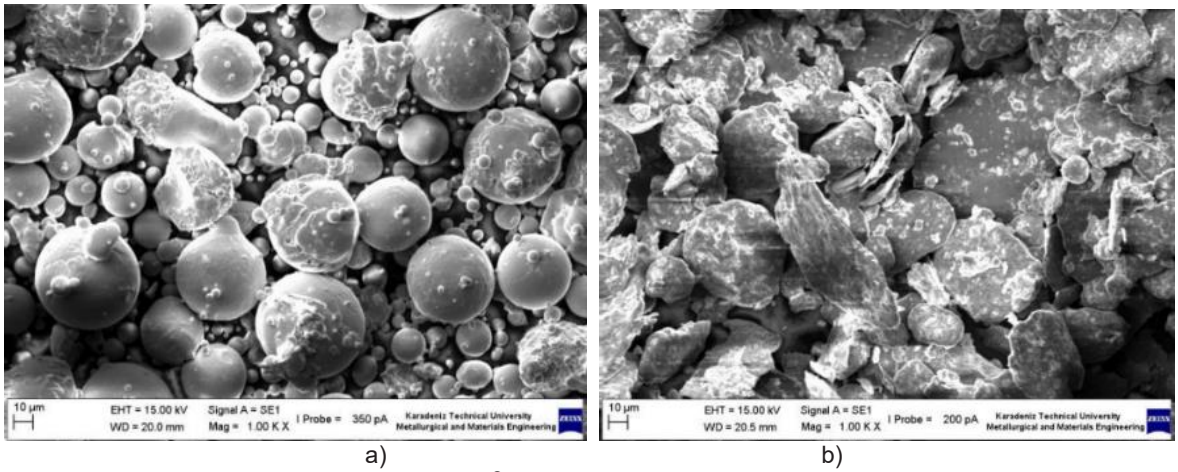

a) b)

Fig. 2. a) SEM image of Crofer®22 APU powders (as received), b) ball-milled powders

Performances of interconnects manufactured through P/M and machining were investigated with single-cell stack tests. Electrolyte supported MEAs (scandium stabilized zirconia electrolyte) with an active cell area of 40x40 mm^2 were used in tests. The MEA (membrane electrode assembly) has NiO-GDC (nickel oxide – gadolinium-doped ceria) based anode and LSM-GDC (lanthanum-strontium-manganite–gadolinium-doped ceria) cathode specifications. The ScSZ-based electrolyte is 150 µm in thickness and anode and cathode electrodes are ~50 µm in thicknesses. The interconnect manufacturing processes by P/M and machining methods were illustrated in Fig. 3. As it can be noted from the figure, the P/M approach offers relatively less number of production steps.

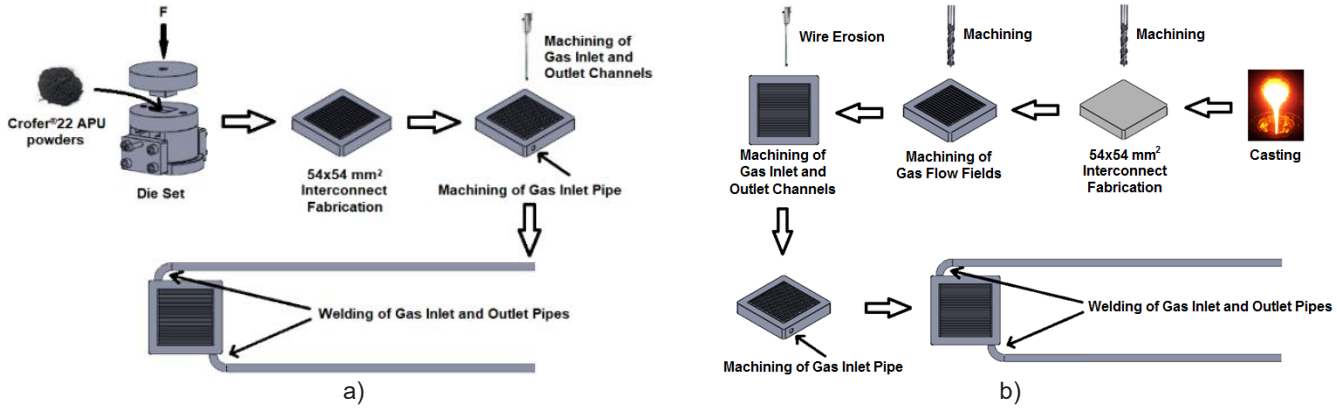

a) b)

Fig. 3. a) Interconnect fabrication process schematics; a) with P/M method b) with machining approach

The representative single stack and test setup schematics are provided in Fig. 4. The stack consists of channeled (flow fields) interconnects with air and hydrogen inlet and outlet, MEA which is sandwiched between sealants. The stack was then placed into a furnace and heated up to the predetermined test temperatures. During the tests, hydrogen and air were used as a reactant and an oxidant with mass flow rates of 0.9 l/min and 1.8 l/min, respectively. The performance values of P/M Crofer®22 APU interconnect and machined Crofer®22 APU interconnect were obtained at 700 and 800°C.

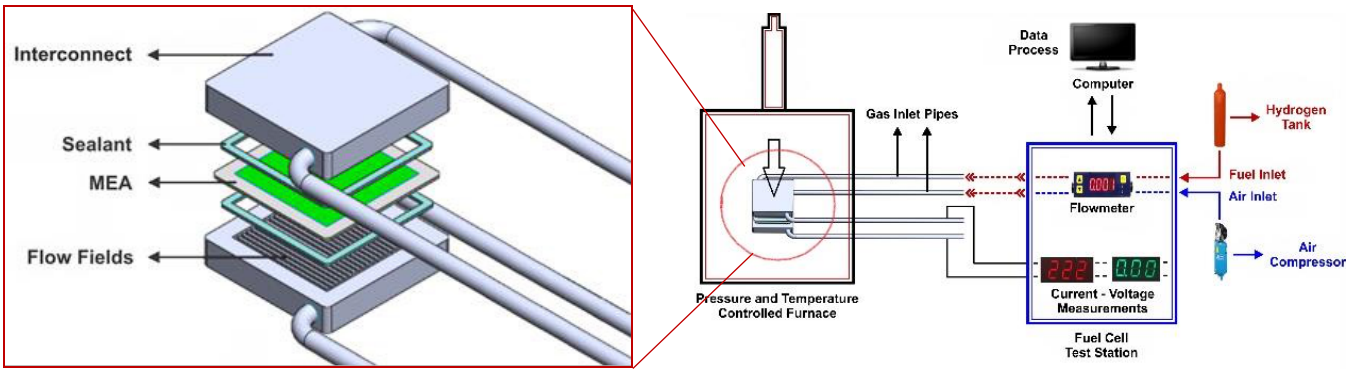

a) b)

Figure 4. Schematic representation of; a) single cell stack, b) test setup

IV. Results and Discussions

The porosity value of the P/M sample was determined as 9.1% while no porosity was obtained for the bulk sample, as expected. The CTE value of P/M Crofer®22 APU was determined as 11.90x10^{-6}/°C while the CTE of interconnect machined from commercial Crofer®22 APU was reported as 11.89x10^{-6}/°C by ThyssenKrupp VDM® GmbH (Crofer®22 APU VDM, 2020).

Open circuit voltage (OCV) value, as an important performance parameter, indicates potential change against current drawn. The OCV should be around ~1.0 V before draw current from the cell during the performance tests. This OCV value indicates that the stack is working properly. The OCV values were determined at 1.0 Volt for both interconnects and the power output of machined interconnect (commercial) was found higher compared to that of P/M interconnect, as seen in Fig. 5-a.

The performance tests for the fabricated interconnects were carried out under same operating conditions. Current-voltage (I-V) and current-power (I-P) curves are plotted. Test results at the operating temperature of 700 °C for both interconnects are presented in Fig. 5-a. It can be noted that the maximum power values were obtained as 2.29 and 2.23 volt for the machined and P/M interconnects, respectively.

The performance test results at 800 °C operating temperature of both interconnects are illustrated in Fig. 5-b. As the test temperature was increased, the OCV value increased to about 1.2 V. The maximum power values of the machined and P/M interconnects were determined as 3.12 and 2.97 Watt at 800 °C operating temperature, respectively (Fig. 5-b). It was concluded that the maximum power values increased with the increasing operating temperature. It is known that various parameters affect the fuel cell performance including material parameters (MEA, glass-ceramic sealant, interconnect type, mesh type, current collect paste, etc.) and operating conditions (operating temperature, operating pressure, gas inlet mass, oxidant or reactant gases types). During the physical examination of interconnect surfaces, corrosion was more visible on the P/M interconnect after performance tests in contrast to the machined interconnect surface.

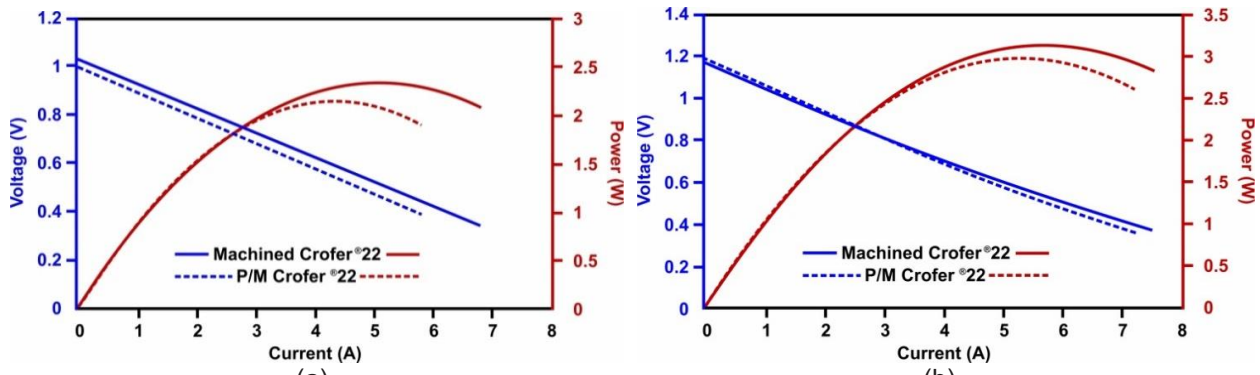

(a) (b)

Fig. 5. The Current-Voltage (I-V), Current-Power (I-P) curves for both interconnects; (a) at 700 °C, (b) at 800 °C

Even though both interconnects have the same chemical composition, the P/M interconnect was considered to be exposed to more corrosion along its grain boundaries and this led to performance decrease at operating conditions. Considering the performance test results, the power values were found in close proximity for both interconnects yet the maximum power values for machined interconnect were determined slightly higher than those for the P/M interconnect.

V. Conclusions

The performance evaluation of solid oxide fuel cell (SOFC) interconnects made of commercially available bulk Crofer®22 APU alloy through machining as well as through the powder metallurgy approach investigated. The performance tests were carried out at 700 and 800 °C operating temperatures and obtained results were evaluated. The maximum power values were increased with increasing operating temperatures and determined as 2.97, and 3.12 Watt for P/M and machined interconnects, respectively. Within the limitation of the current study, it is noted that the performances of machined from bulk and P/M interconnects are comparable yet preferring P/M route in internconnect manufacturing provide ease of manufacturing and cost-effectiveness.

Acknowledgments

The authors acknowledge the partial support provided by the Scientific and Technological Research Council of Turkey (TUBITAK) through project #114M502.

References

Canavar, M., Timurkutluk, B. 2017. Design and fabrication of novel anode flow-field for commercial size solid oxide fuel cells, J. Power Sources. 346, 49-55.

Celik, S., Timurkutluk, B., Mat, M.D., 2013. Measurement of the temperature distribution in a large solid oxide fuel cell short stack, Int. J. Hydrogen Energ. 38, 10534-10541.

Crofer®22 APU Datasheet VDM, https://www.vdm-metals.com/fileadmin/user_upload/Downloads/Data_Sheets/Data_Sheet_VDM_Crofer_22_APU.pdf/. [Accessed 02.01.2020].

De Marco, V., Grazioli, A., Sglavo, V.M., 2016. Production of planar copper-based anode supported intermediate temperature solid oxide fuel cells cosintered at 950 °C, J. Power Sources. 328, 235-240.

Fergus, W.J., 2005. Metallic interconnects for solid oxide fuel cells, Mater. Sci. Eng. A. 397, 271-283.

Mah, J.C.W., Muchtar, A., Somalu, M.R., Ghazali, M.J., 2017. Metallic interconnects for solid oxide fuel cell: A review on protective coating and deposition techniques, Int. J. Hydrogen Energ. 42, 9219-9229.

Mahmud, L.S., Muchtar, A., Somalu, M.R., 2017. Challenges in fabricating planar solid oxide fuel cells: A review. Renew. Sustain. Energ. Rev. 72, 105-116.

Öztürk, B., Topcu, A., Öztürk, S., Cora, Ö.N., 2018. Oxidation, electrical and mechanical properties of Crofer®22 solid oxide fuel cell metallic interconnects manufactured through powder metallurgy. Int. J. Hydrogen Energ. 43, 10822-10833.

Rubio, D., Suciu, C., Waernhus, I., Vik, A., Hoffman, A.C., 2017. Tape casting of lanthanum chromite for solid oxide fuel cell interconnects. J. Mater. Proces. Technol. 250, 270-279.

Swaminathan, S., Ko, Y.S., Lee, Y-S., Kim, D-I., 2017. Oxidation behavior and area specific resistance of La, Cu and B alloyed Fe-22Cr ferritic steels for solid oxide fuel cell interconnects, J. Power Sources. 369, 13-26.

The Plansee Group, https://www.plansee.com/en/news-archive.html. [Accessed 17.02.2020].

Tietz, F., Buchkremer, H-P., Stöver, D., 2002. Components manufacturing for solid oxide fuel cells, Solid State Ion. 152, 373-381.

Venskutonis, A., Glatz, W., Kunschert, G. 2005. P/M processing of ODS Cr-and FeCr-based alloys for solid oxide fuel cell applications, Reutte, Austria, 56, 534-544.

Yu, R., Guan, W., Wang, F., Han, F., 2018. Quantitative assessment of anode contribution to cell degradation under various polarization conditions using industrial size planar solid oxide fuel cells. Int. J. Hydrogen Energ. 43, 2429-2435.

Investigation of Performance Improvement of Geothermal Energy Assisted Power, Heating and Hydrogen Generation Plants with Thermoelectric Generator.

[1]*Nejat TUKENMEZ, [1]Fatih YILMAZ, [1]Murat OZTURK

[1]Department of Mechatronics Engineering, Faculty of Technology, Isparta University of Applied Science, Isparta, Turkey

Email: nejattukenmez@isparta.edu.tr, fatiyilmaz7@gmail.com, muratozturk@isparta.edu.tr

Abstract

Renewable energy, which is generally composed of solar, hydroelectric, wind and geothermal energy sources, is very important in the combat against environmental problems. Geothermal energy is a power source that produces clean, reliable and minimal environmental impacts. In this paper, a geothermal energy supported hydrogen, power and heating generation plant are investigated in terms thermodynamic approach. In addition, in the proposed study, if the thermoelectric generator is used instead of the condenser sub-component, its effect on the plant's performance and hydrogen production rate is researched extensively. This plant consists of an ORC with transcritical CO_2 (t-CO_2) working fluid, a heat pump with R134a, a thermoelectric generator and a PEM electrolyzer for hydrogen generation. The effects of parameters such as reference and geothermal temperature, ORC component pressure, PEM efficiency on the performance of the proposed plant and hydrogen production rate are computed utilizing Engineering Equation Solver (EES). Finally, the energetic and exergetic performance of the examined plant are computed as 28,01%, 24,13%, respectively. Also, the total hydrogen production rate is 0.0004502 kgs^{-1}.

Keywords: Energy, exergy, geothermal, hydrogen, renewable energy.

I. Introduction

Nowadays, since hydrogen is more efficient than other fuels, the number of hydrogen based plants is becoming popular. Therefore, hydrogen production plants are increasingly important. Especially in the academic community and industry, the increase in the studies about hydrogen shows the popularity of hydrogen. Hydrogen production should be carried out with energy plants that are environmentally friendly and support environmental policies. Therefore, many renewable energy based energy generation plants have been designed in the literature. The large-scale hydrogen liquefaction method has been studied by (Seyam et al., 2020). This approach is tried to be realized with geothermal and isobutane power plant. proposed a new energy generation plant that uses hydrogen from geothermal and solar energy by (Bicer and Dincer, 2016). From this combined energy plant, many useful outputs such as hydrogen, heating and cooling are obtained. A new renewable energy based energy generation plant utilizing solar and geothermal energy is designed by (Siddiqui and Dincer,2019). Various useful outputs, especially hydrogen, have been obtained from this system. By conducting a parametric study, the behavior of the parameters affecting the system performance on the system is examined. The production of hydrogen by using geothermal energy as renewable energy and the liquefaction of this produced hydrogen have been studied by (Yuksel et al., 2018). Also, thermodynamic assessment and performance analysis of the plant were carried out. A novel combined energy plant using geothermal energy capable of generating hydrogen and many useful outputs has been proposed by (Yuksel et al., 2018). A parametric examination was performed to find the optimum values of the operating indicators in the cycle in terms of plant performance. Seyam et al., 2019 have performed optimization of the plant for hydrogen energy producing hybrid energy plants. In addition, a thermodynamic analysis study was conducted to examine plant performance. Thermodynamic analysis of an energy production plant designed by utilizing solar energy in a crude oil refinery is conducted by (Altayib and Dincer, 2019). Thermal energy storage sub-plants are integrated into the system to obtain continuous output from the integrated plant. Some improvements have been proposed for the plant designed with the thermodynamic analysis performed.

II. System Description

In this study, the design of an integrated energy cycle using geothermal energy and also the parametric analysis of this cycle and thermodynamic analysis were performed. In addition to being environmentally friendly, this system provides multiple useful outputs and contributes to the efficiency of this system. The designed system is clearly understood in Figure 1. As shown in Figure 1, different outputs are obtained from the integrated system by an environmentally friendly method. The integrated energy system consists of an ORC with transcritical CO_2 (t-CO_2) working fluid, a heat pump with R134a, a thermoelectric generator and a PEM electrolyzer.

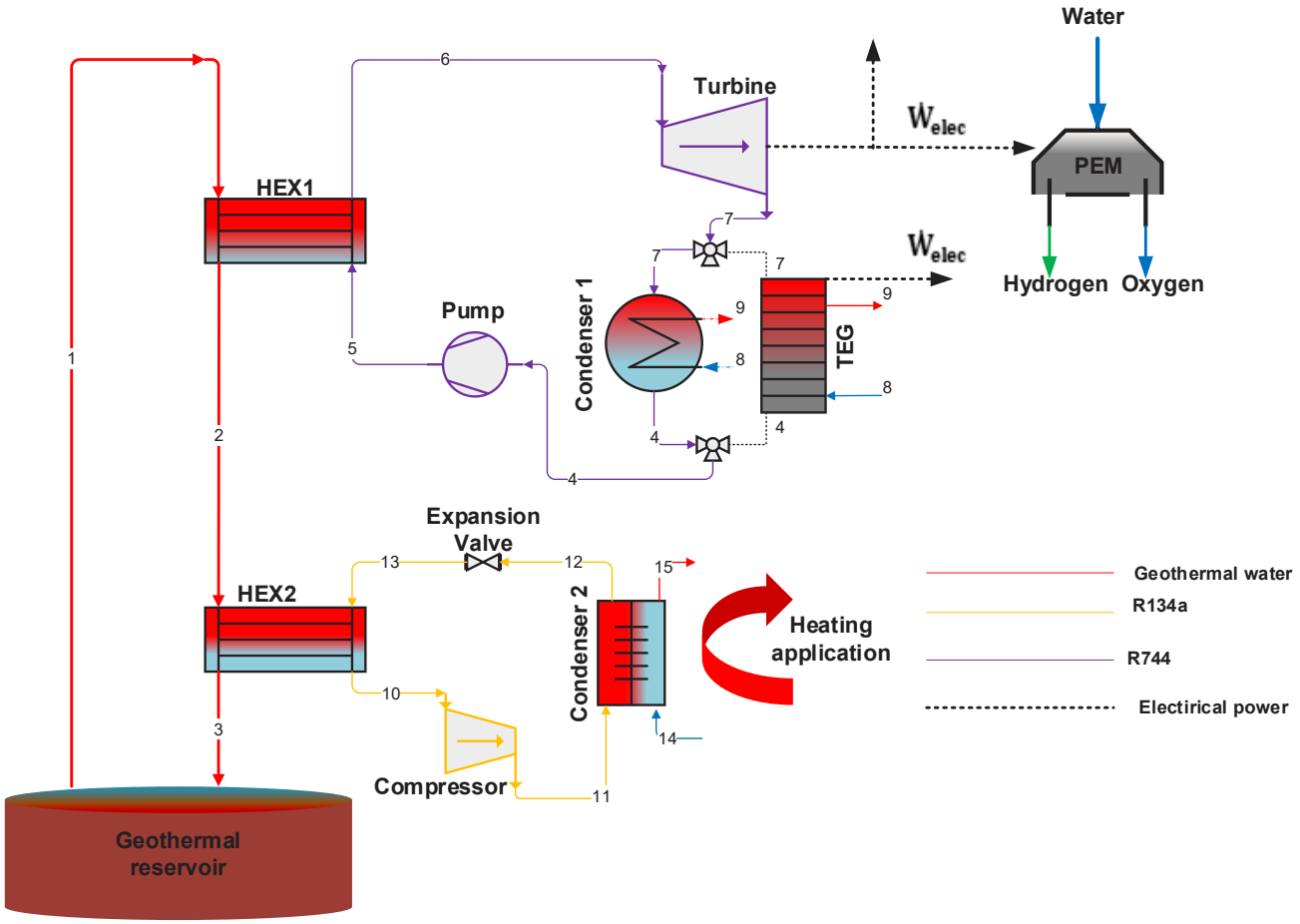

Fig.1. Geothermal Energy Assisted Integrated Plant

III. Analysis

Performance assessment of combined cycle is important in terms of the efficiency of the plant and the outputs obtained from the cycle. Therefore, the mathematical model of the integrated energy system should be prepared in accordance with the thermodynamic equilibrium equations. In particular, if an optimization of the any plant is to be performed, the mathematical model of the system must be carefully created in order for the optimization study to be made to give meaningful results.

The mathematical model of the system is basically determined by formulating mass, energy, exergy and entropy equilibrium equations. For any energy plan, mass, energy, exergy and entropy equilibrium equations are (Dincer and Rosen, 2013):

$$\sum \dot{m}_{in} = \sum \dot{m}_{out} \tag{1}$$

$$\sum \dot{m}_{in} h_{in} + \sum \dot{Q}_{in} + \sum \dot{W}_{in} = \sum \dot{m}_{out}\, h_{out} + \sum \dot{Q}_{out} + \sum \dot{W}_{out} \tag{2}$$

$$\sum \dot{m}_{in}\, s_{in} + \sum \frac{\dot{Q}_{cv}}{T} + \dot{S}_{gen} = \sum \dot{m}_{out}\, s_{out} \tag{3}$$

$$\sum \dot{m}_{in} \dot{e}x_{flow} + \sum \dot{E}x_{in}^{Q} + \sum \dot{E}x_{in}^{W} = \sum \dot{m}_{out} \dot{e}x_{flow} + \sum \dot{E}x_{out}^{Q} + \sum \dot{E}x_{out}^{W} + \dot{E}x_{d} \tag{4}$$

where $\dot{m}_{in}$ is the inlet mass flow rate, $\dot{m}_{out}$ is the outlet mass flow rate. $\dot{Q}$ and $\dot{W}$ shows the heat power, power transfer rate, respectively. h indicates the specific enthalpy of the any process. s and $\dot{S}_{gen}$ are the specific entropy, entropy generation rate, respectively.

IV. Results and discussions

In the proposed study, is performed a thermodynamic evaluation for the production of the power, hydrogen and heating application with using EES software. In addition, the use of TEG instead of the condenser, which is the subcomponent of the ORC cycle for power and hydrogen production, the proposed system performance and its effect on hydrogen production are investigated. Table 1 provides the proposed system design parameters and assessment results. The general energetic and exergetic efficiencies of the designed plant no TEG are calculated as 27.25%, 29.11%, respectively. Furthermore, the general energetic and exergetic performance of the suggested plant with TEG as 36.25% 35.64%, respectively.

Table 1. Plant operating parameters and results values

Parameters	Values
Geothermal water temperature (°C)	180
ORC working fluid	R744
Heat pump working fluid	R134a
Isentropic performance of the pump	0.8
Isentropic performance of the ORC turbine	0.9
Total heat loss from the components (%)	20
Reference temperature (°C)	21
Reference pressure (kPa)	101.325
ORC's energy efficiency (%)	11.25
ORC's exergy efficiency	13.23
Whole plant's energy efficiency (%)	27.25
Whole plant's exergy efficiency (%)	29.11
Overall system's energy efficiency with TEG (%)	36.25
Overall plant's exergy efficiency with TEG (%)	35.64
Hydrogen production rate, per 1 kg/s water (kg/s)	0.0005982
Hydrogen production rate with TEG, per 1 kg/s water (kg/s)	0.002179

Fig.2 illustrates the proposed plant's outputs which heating, hydrogen, and power, versus the geothermal mass flow rate. The proposed plant outputs clearly increase by rising the geothermal mass flow rate from 20 to 40 kg/s. The use of TEG in the proposed plant is clearly seen to have a positive impact on the output of the plant and the hydrogen production rate.

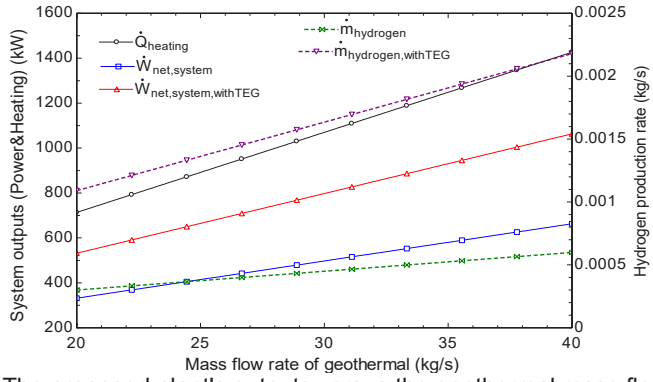

Fig.2 The proposed plant's outputs versus the geothermal mass flow rate

Fig.3 exemplifies the proposed plant's outputs that heating, hydrogen, and power, versus the geothermal water temperature. In addition, the energy and exergy efficiency of the ORC and overall plant with geothermal water temperature is given in Fig.4. it can be clearly stated in both figures that using the TEG instead of the condenser increases the exergy efficiency and hydrogen production of the proposed plant.

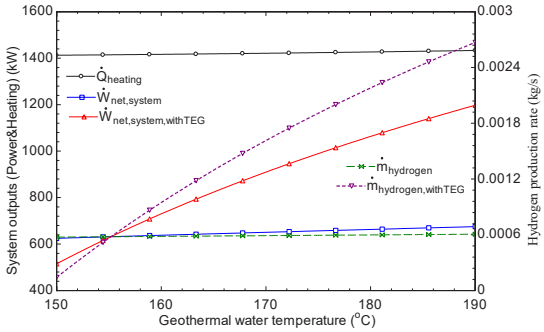

Fig.3 he proposed plant's outputs versus the geothermal water temperature

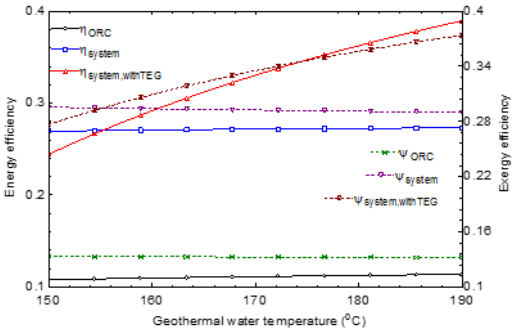

Fig.4 Energy and exergy efficiency of the ORC and overall plant versus the geothermal water temperature

The changing ambient temperature is a significant indicator for the thermal plant design, and thus exergetic and energetic behavior of the whole plant versus the various dead state temperature is presented in Fig.5. as expected, the increasing reference temperature has no influence on the cycle energetic performance. Otherwise, the exergy efficiency of the overall system increases with the same parameters. Also, the use of the TEG increases the exergy efficiency from about to 31% to 37%, at 10 °C reference temperature.

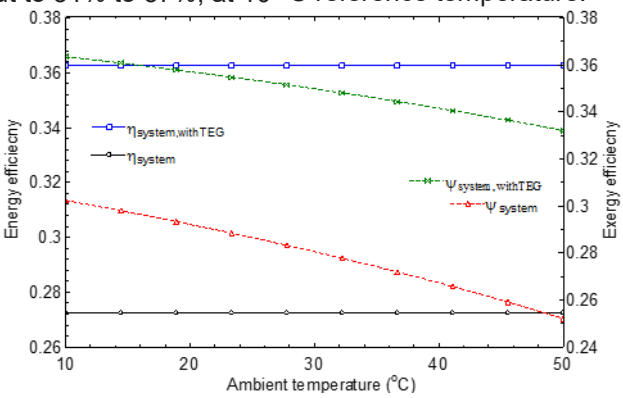

Fig.5 Energetic and exergetic behavior of the whole plant versus the various ambient temperature

V. Conclusions

The goal of this work is to obtain different beneficial products with hydrogen by making use of geothermal energy. Production of hydrogen from the integrated system makes the system privileged. Because it will be possible to use hydrogen produced as fuel for different applications requiring energy. The environmental friendliness of the designed system makes this system support the environmental policies. In this system, two different working fluids were used to generate energy. This contributes to the literature for integrated system design. When the system's performance analysis is performed, the energetic and exergetic performance of the overall plant are computed as 28,01%, 24,13%, respectively.

References

Altayib, K., & Dincer, I. (2019). Analysis and assessment of using an integrated solar energy based system in crude oil refinery. Applied Thermal Engineering, 113799.

Bicer, Y., & Dincer, I. (2016). Development of a new solar and geothermal based combined system for hydrogen production. Solar Energy, 127, 269-284.

Dincer I, Rosen MA. “Energy, Environment, and Sustainable Development”. Elsevier: 2nd ed., Oxford, 2013.

Seyam, S., Al-Hamed, K. H., Qureshy, A. M., Dincer, I., Agelin-Chaab, M., & Rahnamayan, S. (2019, June). Multi-objective Optimization of Hydrogen Production in Hybrid Renewable Energy Systems. In 2019 IEEE Congress on Evolutionary Computation (CEC) (pp. 850-857). IEEE.

Seyam, S., Dincer, I., & Agelin-Chaab, M. (2020). Analysis of a clean hydrogen liquefaction plant integrated with a geothermal system. Journal of Cleaner Production, 243, 118562.

Siddiqui, O., Ishaq, H., & Dincer, I. (2019). A novel solar and geothermal-based trigeneration system for electricity generation, hydrogen production and cooling. Energy Conversion and Management, 198, 111812.

Yuksel, Y. E., Ozturk, M., & Dincer, I. (2018). Analysis and performance assessment of a combined geothermal power-based hydrogen production and liquefaction system. International Journal of Hydrogen Energy, 43(22), 10268-10280.

Yuksel, Y. E., Ozturk, M., & Dincer, I. (2018). Thermodynamic analysis and assessment of a novel integrated geothermal energy-based system for hydrogen production and storage. International Journal of Hydrogen Energy, 43(9), 4233-4243.

Development of a Solar Energy Based Multigeneration System with SOFC for Hydrogen Production

[1]*Nejat TUKENMEZ, [1]Fatih YILMAZ, [1]Murat OZTURK

[1]Department of Mechatronics Engineering, Faculty of Technology, Isparta University of Applied Science, Isparta, Turkey

Email: nejattukenmez@isparta.edu.tr, fatiyilmaz7@gmail.com, muratozturk@isparta.edu.tr

Abstract:

The key purpose of this paper is to design a new multi-generation plant, based on a solar energy source, and to investigate its performance using the thermodynamic approach. The most important outputs of this work, hydrogen generation, along with the power, cooling, heating and hot water. The modeled plant contains a solar parabolic dish collector cycle, a Solid Oxide Fuel Cell (SOFC) plant, a gas turbine (GT) cycle, a supercritical CO_2 reheat power cycle, cooling cycle with ejector, organic Rankine cycle (ORC) plant, a PEM electrolyzer, hot water generation process and hydrogen liquefaction process. Energetic and exergetic performance assessment and also irreversibility rates of the whole system and sub-plants are studied in detail, according to under the various system and environment conditions. Also, the effects of changes in parameters such as dead state temperature and solar radiation on system performance were investigated in terms of thermodynamics. According to analysis results, the top irreversibility is determined in the solar power sub-system whereas the minimum irreversibility is calculated in the cooling plant. Furthermore, the energetic and exergetic behavior of the total system are determined as 56.48%, 54.06%, respectively.

Keywords: Hydrogen, solar energy, thermodynamic analysis, multi-generation

I. Introduction

Nowadays, renewable energy sources are becoming increasingly important both in order to reduce the increasing global warming rate and to design environmentally friendly energy production systems. The fact that renewable energy based systems support environmental policies also increases its popularity in the academic community. The realization of the systems designed theoretically in academic studies with experimental studies shows that these systems provide both cost and environmental impact when used in real life. In particular, obtaining multiple beneficial outputs from these systems also increases system efficiency. In order to examine the performance of these systems, various equations are tried to be derived.

An integrated power generation system was designed with multiple beneficial outputs in addition to hydrogen generation by (Ishaq and Dincer, 2019). This multi-generation system is both solar and biomass based. Performance analysis of this system under different working conditions was performed. Also, a comparative analysis with different operating parameters was performed to examine the effects on system performance. Exergy and energy efficiency equations were utilized in the modeling stage of the system. Useful outputs and performance curves of the system are presented. A new integrated system that utilizes solar energy and also produces hydrogen has been proposed by (Yılmaz et al., 2019). In addition to hydrogen production, this system produces many useful outputs such as heating and cooling. The effect of various parameters on system performance has been examined. In this study, the total energy efficiency of the system is computed as 48.19%, while the whole exergy efficiency of the system is calculated as 43.57%. When the performance outputs are examined, it is stated in this study that the system has a good potential. Optimization study of the hybrid-designed renewable energy system was carried out by (Tang et al., 2020). Exergy equations were used in this optimization study. The system used here is designed for active cooling. It was stated in this study that active cooling increases the cost and effective solutions have been tried to be emphasized. A machine learning based optimization algorithm has been proposed and used to maximize the exergetic performance of the cycle. Energy and exergy-based thermodynamic analysis of a system using solar energy was performed by (Ozturk et al.,in Press). In order to ensure continuity in energy production, this system is supported with a rock bed thermal energy storage plant. At the same time, a parametric study was performed to show system performance. The indicators that have a significant impact on the integrated plant performance are shown in this work. Thermodynamic analysis of a newly designed and proposed plant was performed by (Yuksel et al.,2019). A comprehensive parametric study was conducted to determine the parameters that had the most effect on the system. An environmental impact and performance analysis of a cycle using solar energy was conducted to support the preference of biomass to fossil fuels in terms of environmental impact and performance by (Karapekmez and Dincer, 2020). An analysis of the performance of an offshore wind power plant producing methanol was conducted by (Crivallari et al.,2019).

II. System Description

In this work, a combined energy generation system is planned which utilizes solar energy, which is an edible energy source, and can produce many useful outputs besides hydrogen production. Useful outputs from the system can be expressed as heating-cooling, power, hydrogen, hot-cold water. Comprehensive thermodynamic examination of this designed combined energy system has been done. As indicated in Fig. 1, the combined system comprises of nine sub-plants. These are Solar Power Plant, Solar Tower Cycle, SOFC Plant, Gas Turbine Cycle, Supercritical Carbon dioxide Reheat Power Cycle, Cooling Cycle, ORC, Hot Water Production Cycle and Hydrogen Production and Liquefaction Process.

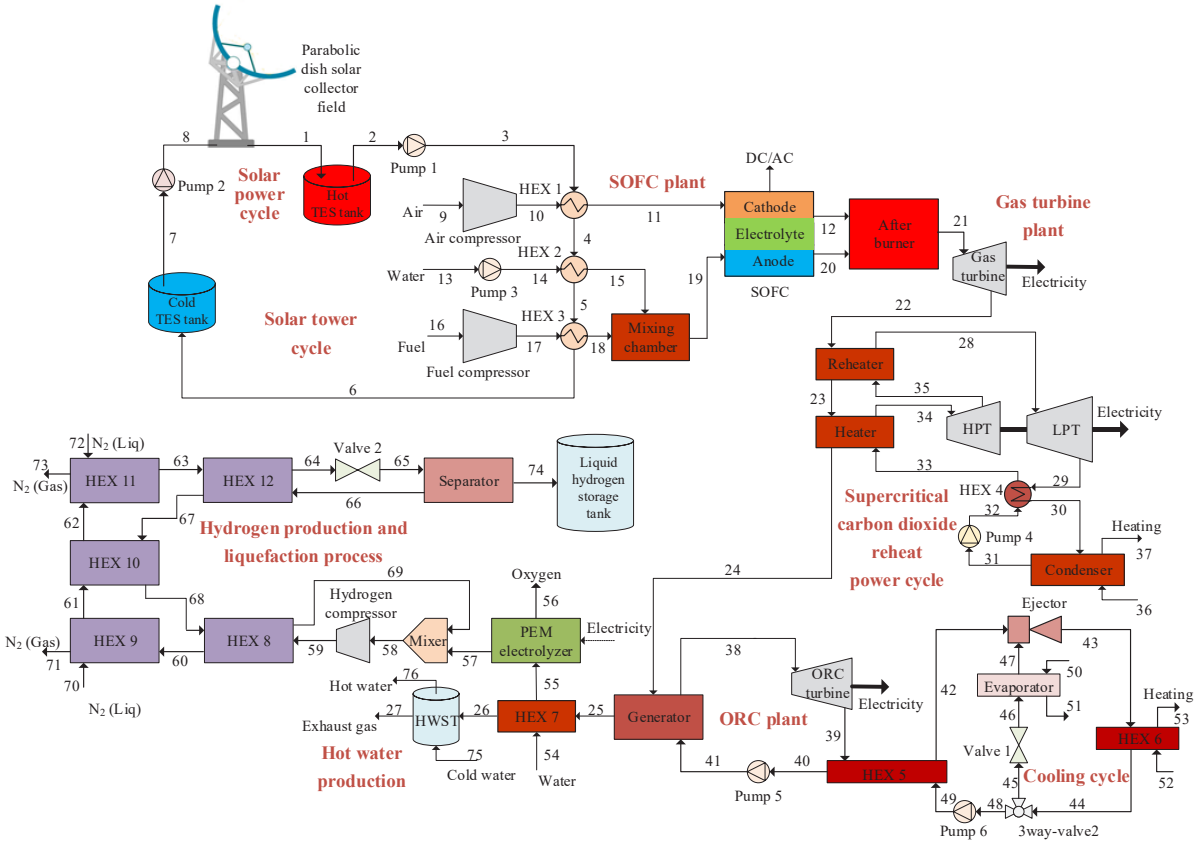

Fig. 1. Schematic diagram of the designed multigeneration plant

III. Analysis

In this part, the equilibrium equations used for the analysis and modeling of the integrated plant are defined. The performance evaluation of the proposed energy system is based on the thermodynamic equilibrium equations. The mathematical model of the system needs to be precisely constructed for useful outputs and system performance.

Thermodynamic evaluation of the integrated plant was done by utilizing the equations of mass, entropy, energy and exergy equilibrium. For any integrated plant, a mass equilibrium equation can be defined as:

$$\sum \dot{m}_{in} = \sum \dot{m}_{out} \tag{1}$$

where $\dot{m}$ is the mass flow rate, subscripts in and out shows the input and output conditions. Also, the general energy and entropy balance equations can be given as (Dincer and Rosen, 2013):

$$\sum \dot{m}_{in} h_{in} + \sum \dot{Q}_{in} + \sum \dot{W}_{in} = \sum \dot{m}_{out}\, h_{out} + \sum \dot{Q}_{out} + \sum \dot{W}_{out} \tag{2}$$

$$\sum \dot{m}_{in}\, s_{in} + \sum \frac{\dot{Q}_{cv}}{T} + \dot{S}_{gen} = \sum \dot{m}_{out}\, s_{out} \tag{3}$$

where, $\dot{Q}$,$\dot{W}$ displays the heat energy and power transfer rate. Furthermore, in Eq.(3), s is the specific entropy. The general exergy equilibrium equation could be written as below;

$$\sum \dot{m}_{in} \dot{e}x_{flow} + \sum \dot{E}x^{Q}_{in} + \sum \dot{E}x^{W}_{in} = \sum \dot{m}_{out} \dot{e}x_{flow} + \sum \dot{E}x^{Q}_{out} + \sum \dot{E}x^{W}_{out} + \dot{E}x_{d} \tag{4}$$

The values of the operating parameters accepted for the combined plant are specified in Table 1.

Table 1. Design condition of the modeled system

Parameters	Values	Parameters	Values
Reference temperature, T_o (°C)	25	Exit pressure from solar tower, P_1 (kPa)	1345
Reference pressure, P_o (kPa)	101.3	Inlet temperature of solar tower, T_8 (°C)	347
Solar irradiance, I_s (W/m^2)	700	SOFC working temperature, T_{SOFC} (°C)	824.3
Solar cycle working fluid	Molten salt (60% $NaNO_3$ and 40% KNO_3)	SOFC working pressure, P_{SOFC} (kPa)	775.6
Rankine cycle working fluid	CO_2	Fuel mass flow rate, $\dot{m}_{16}$ (kg/s)	0.72
ORC working fluid	R113	HP turbine inlet temperature, T_{34} (°C)	380
Cooling plant working fluid	Isobutane	HP turbine inlet pressure, P_{34} (kPa)	15000
Compressor pressure ratio, r_{AC}	8	LP turbine inlet temperature, T_{28} (°C)	219
Compressor isentropic efficiency, η_{AC} (%)	83	LP turbine inlet pressure, P_{28} (kPa)	7750
Gas turbine inlet temperature, T_{21} (°C)	892.3	PEM temperature, T_{PEM} (°C)	80
Gas turbine inlet pressure, P_{21} (kPa)	738.2	PEM electrolyzer thickness, D_{PEM} (μm)	100
Isentropic efficiencies of gas turbine, $\eta_{is,GT}$ (%)	85	ORC turbine inlet temperature, T_{38} (°C)	169.2
Isentropic efficiencies of HP turbine, $\eta_{is,HP}$ (%)	90	ORC turbine inlet pressure, P_{38} (kPa)	1990
Isentropic efficiencies of LP turbine, $\eta_{is,LP}$ (%)	93	Energetic coefficient of performance, COP_{en}	1.783
Isentropic efficiencies of ORC turbine, $\eta_{is,ORC}$ (%)	75	Exergetic coefficient of performance, COP_{ex}	0.637
Isentropic efficiencies of pumps, $\eta_{is,P}$ (%)	80	Hydrogen compressor working pressure, P_{hc} (kPa)	8178
Exit temperature from solar tower, T_1 (°C)	896	Exhaust gaseous temperature, T_{27} (°C)	54

IV. Results and discussions

The mathematical model and the thermodynamic assessment of the plant were examined by utilizing EES program. A detailed thermodynamic study was performed to show the impact of the working indicators having different effects on the plant under different operating situations. The performance evaluation results of the suggested plant are presented in Table 2. The outputs obtained from the united energy system are summarized in Table 3.

Table 2. Thermodynamic analysis results.

Sub-plants/whole plant	Energy efficiency (%)	Exergy efficiency (%)	Exergy destruction rate (kW)
Solar power cycle	54.83	51.21	8,279
SOFC plant	47.12	44.37	5,346
Gas turbine plant	49.51	46.07	6,258
Supercritical CO_2 reheat power cycle	33.24	81.05	4,123
ORC plant	18.76	14.08	1,205
Cooling plant	19.93	16.27	1,098
Hydrogen production and liquefaction process	52.67	48.53	1,652
Hot water production	76.34	72.53	1,157
Combined plant	56.48	54.06	29,118

Table 3. Calculated useful outputs from the combined plant

Parameters	Values	Parameters	Values
$\dot{W}_{SOFC}$ (kW)	6482	$\dot{Q}_{Cooling}$ (kW)	1162
$\dot{W}_{GT}$ (kW)	7053	$\dot{Q}_{Heating}$ (kW)	1824
$\dot{W}_{HPT}$ (kW)	3147	$\dot{Q}_{Hot\_water}$ (kW)	2017
$\dot{W}_{LPT}$ (kW)	1653	$\dot{m}_{Hydrogen}$ (kg/s)	0.0642
$\dot{W}_{ORC}$ (kW)	1021		

A parametric work was made to see the influence of reference temperature and solar radiation on the integrated cycle. The influence of changing reference temperature on the energetic behavior of the combined cycle and subsystems is given in Figure 2 and Figure 3, respectively. The influence of the various dead state temperature on hydrogen production and the beneficial products from the system is shown in Figure 4. The influence of the varying solar irradiation on the performance of the integrated cycle and sup-plants is shown in Figure 5 and Figure 6, respectively. The influence of the varying solar flux on the beneficial outputs from the cycle and on hydrogen production is shown in Figure 7.

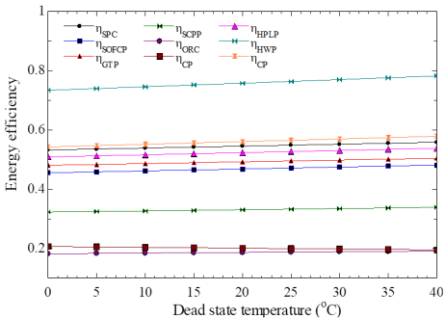

Fig. 2. Variation of plant energetic performance with changing reference temperature

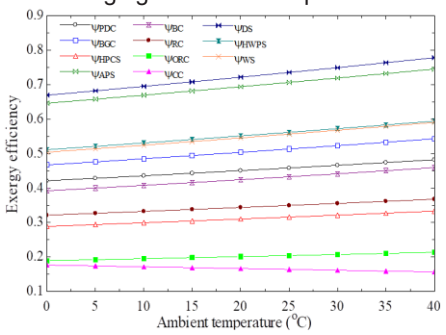

Fig. 3. Variation of plant exergetic performance with changing dead state temperature

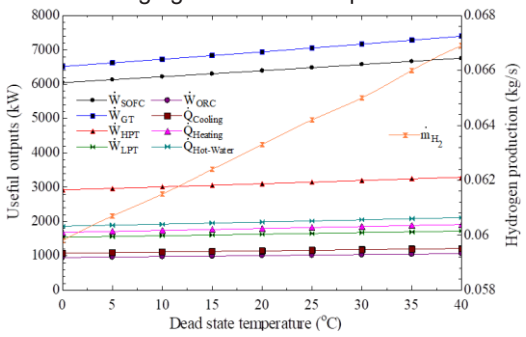

Fig. 4. Variation of plant useful outputs and hydrogen production with changing dead state temperature

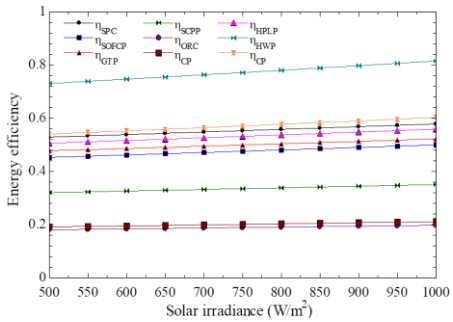

Fig. 5. Impact of solar irradiance on the energetic behavior

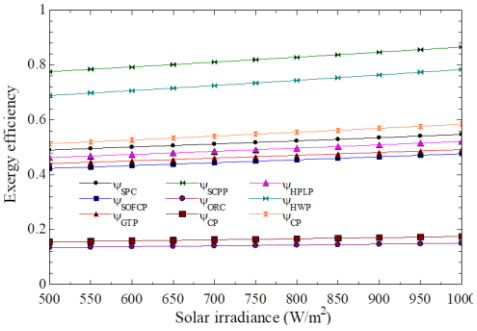

Fig. 6. Influence of solar irradiance on exergetic behavior

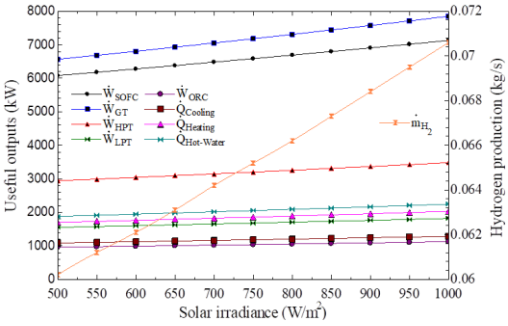

Fig. 7. Impact of solar irradiance on plant beneficial products and hydrogen generation

V. Conclusions

In this paper, a study has been carried out to obtain useful outputs especially with hydrogen production with an environmentally friendly integrated system. Besides hydrogen production, the storage of the produced hydrogen shows that the integrated system has a functionally good potential. When the thermodynamic analysis results are examined, it is seen that the increasing environmental temperature and solar radiation contribute positively to the energetic and exergetic behavior of the overall system.

References

Crivellari, A., Cozzani, V., & Dincer, I. (2019). Exergetic and exergoeconomic analyses of novel methanol synthesis processes driven by offshore renewable energies. Energy, 187, 115947.

Ishaq, H., & Dincer, I. (2019). Design and performance evaluation of a new biomass and solar based combined system with thermochemical hydrogen production. Energy Conversion and Management, 196, 395-409.

Karapekmez, A., & Dincer, I. (2020). Comparative efficiency and environmental impact assessments of a solar-assisted combined cycle with various fuels. Applied Thermal Engineering, 164, 114409.

Ozturk, M., Dincer, I., & Javani, N. (2019). Thermodynamic modeling of a solar energy based combined cycle with rock bed heat storage system. Solar Energy.

Tang, L., Zhou, Y., Zheng, S., & Zhang, G. (2020). Exergy-based optimisation of a phase change materials integrated hybrid renewable system for active cooling applications using supervised machine learning method. Solar Energy, 195, 514-526.

Yilmaz, F., Ozturk, M., & Selbas, R. (2019). Energy and exergy performance assessment of a novel solar-based integrated system with hydrogen production. international journal of hydrogen energy, 44(34), 18732-18743.

Yuksel, Y. E., Ozturk, M., & Dincer, I. (2019). Performance assessment of a solar tower-based multigeneration system with thermal energy storage. Energy Storage, 1(4), e71.

Potential energy optimisation of the coefficient of performance of a residential air source heat pump water heater

[1*]Stephen Tangwe, [2]Kanzumba Kusakana
[1] Central University of Technology, Faculty of Engineering, Built Environment and Information Technology, Department of Electrical, Electronic and Computer Engineering, Private Bag X20539, Bloemfontein, 9300, South Africa
[2] Central University of Technology, Faculty of Engineering, Built Environment and Information Technology, Department of Electrical, Electronic and Computer Engineering, Private Bag X20539, Bloemfontein, 9300, South Africa

* E-mails: lstephen@cut.ac.za

Abstract

Air source heat pump (ASHP) water heaters are very efficient devices for sanitary hot water heating. The study focused on the determination of the coefficient of performance (COP) of a 1.2 kW, 150 L split type ASHP water heater in terms of enthalpy and energy factor, and the potential opportunity to optimise the COP. The COP was based on the changes in enthalpy of the refrigerant of the ASHP unit and the input and output energies of the ASHP water heater. A power meter, flow meters, temperature sensors, pressure sensors, ambient temperature and relative humidity sensor were installed at precise locations of the ASHP water heater. Specific controlled volume of 150, 50 and 100 L were drawn off from the tank of the ASHP water heater during the morning, afternoon and evening for a full year. The results depicted that during the summer periods, the average COP in terms of the input electrical consumed and output thermal energies gained by the ASHP water heater was 3.04. The COP in terms of the change in the enthalpy of the refrigerant at the inlet and the outlet of the condenser and the evaporator of the ASHP unit was 3.53. It can be concluded that the derived COPs of the ASHP unit was higher than that of the ASHP water heater. The difference in the two COPs could be ascribed to the electrical energy consumed by the fan and the water circulation pump. The input power consumed by the ASHP unit was 12.8% lower to that of the ASHP water heater. The corresponding change in enthalpy of the refrigerant in the condenser was greater than that at the evaporator throughout the different volumes of hot water drawn off. A potential replacement of the existing electric motors in the prime movers with energy efficient types, will enhanced the COP.

Keywords: Air source heat pump (ASHP) water heater, Coefficient of performance (COP), COP of ASHP unit, COP of ASHP water heater, Change in enthalpy of refrigerant, Input electrical energy, Useful output thermal energy.

Abbreviations

ASHP = Air source heat pump
COP = Coefficient of performance
COPe = COP of ASHP water heater
COPt = COP of ASHP unit
EE = Electrical energy consumed in kWh
TE = Thermal energy gained in kWh
p = Average power consumed in kW
Pevpi = Refrigerant pressure at inlet of evaporator in MPa
Pevpo = Refrigerant pressure at outlet of evaporator in MPa
Pconi = Refrigerant pressure at inlet of condenser in MPa
Pcono = Refrigerant pressure at outlet of condenser in MPa
Tevpi = Refrigerant temperature at inlet of evaporator in °C
Tevpo = Refrigerant temperature at outlet of evaporator in °C
Tconi = Refrigerant temperature at inlet of condenser in °C
Tcono = Refrigerant temperature at outlet of condenser in °C
m = Mass of water heated in kg
c = Specific heat capacity of water in kJ/kg°C
Ti = Water temperature at inlet of ASHP
To = Water temperature at outlet of ASHP
VCRC = Vapour compression refrigeration cycle

1. Introduction

Sanitary hot water heating is among the residential energy users that are contributing to large electrical energy consumption [1]. Sanitary hot water heating in South Africa account for up to 30-50% of the monthly electrical energy cost and most of the hot water heating is via the implementation of inefficient geysers [2]. Geysers can be retrofitted with ASHP units and the resultant device is known as ASHP water heaters. The trivail attributes that provides the ASHP water heaters with exceptional performance is referred as the COP. ASHP water heater is classified as a renewable and an energy efficient device [3]. The COP of the ASHP water heater ranges from 2 to 4 and is influence by the ambient temperature, the system design of the close loop circuit of the vapour compression refrigeration cycle and the hot water heating loads [4]. The operational performance of the ASHP water heaters has been reported to be better in the summer than in the winter periods. This can be substantiated by the favourable ambient temperature experienced during the summer [4]. The ASHP water heaters are commonly divided into the split and integrated types. In the split type ASHP water heater, the ASHP unit and the hot water storage tank are connected by copper pipes with the ASHP unit situated below the tank [5]. Conversely, the integrated type ASHP water heater is a compact design with the ASHP unit located above the tank while the condenser is immersed into the tank [5]. The prime movers of a typical ASHP water heater includes the compressor, the fan and the water circulation pump. Although, the ASHP water heaters are efficient hot water heating devices, the COP can further be improved, if the ASHP water heater is forced to operate within the range of the Carnot's COP of an ASHP unit [6]. The study focused on the investigation and analyses of the input electrical energy consumed and the useful output thermal energy gained by the ASHP water heater. It also deal with the determination of the change in enthalpy of the refrigerant at the inlet and outlet of the heat exchangers (evaporator and condenser) of the ASHP unit, due to 50, 100 and 150 L of hot water drawn off.

2. Materials and methods

2.1 Materials

Table 1 present the materials used for the purpose of achieving the objectives of the study.

Table 1: List of materials employed in the study

Item	Material	Quantity
1	1.2 kW split type ASHP unit	1
2	150 L , 3 kW high pressure geyser	1
3	Hot water volume control valve	1
4	Ambient temperature and relative humidity sensor	1
5	Power meter	1
6	Temperature sensors	11
7	Pressure sensors	4
8	Flow meters	2
9	Hot water collecting drum	1
10	Data loggers	2
11	REFPROP software	1
12	Hoboware pro software	1
13	Weather and waterproof enclosure	1

2.2 Methods

The methods implemented for the study were divided into three procedures as follows;

i. The design and installation of the split type ASHP water heater and the configuration and installation of the sensors.
ii. Analysis of the COP of the ASHP water heater during the summer period (October-December 2018) in terms of the input electric energy consumed and the useful output thermal energy gained due to the specific volumes (50, 100 and 150 L) of hot water drawn off.
iii. Analysis of the COP of the ASHP unit during the summer period (October-December 2018) pertaining to the enthalpy change of the refrigerant between the inlet and outlet of the evaporator and the condenser as a result of the specific volumes (50, 100 and 150 L) of hot water drawn off.

2.3 Experimental setup

Figure 1 shows the schematic diagram of the installed split type ASHP water heater at the outdoor space of the renewable energy laboratory, in the Central University of Technology, Free State Province, South Africa. The split type ASHP water heater comprised of a 1.2 kW input ASHP unit with a 150 L, 3 kW geyser. The geyser served as a storage tank with its 3 kW heating element disabled and retrofitted by the ASHP unit. The ASHP unit was embedded with a 90 W water circulation pump that provided the require water pressure. The pressure exerted by the water circulation pump allow for the circulation of water between the geyser and the ASHP's condenser during the VCRC. The ASHP unit contained a propeller axial fan of 70 W, at the rear end of the evaporator. Figure 1 also, shows the installed sensors on the ASHP water heater. An ambient temperature and relative humidity sensor (Ta/RH) was installed in the vicinity of the ASHP water heater and measured both the ambient temperature and relative humidity. A power meter with an inbuilt logging capability was installed on the power line supplying electricity to the split type ASHP unit and measured the input electrical power consumed by the ASHP water heater. Two flow meters (V and Vd) were installed closed to the inlet of the ASHP unit and at a position on the copper pipe, in proximity to the hot water discharge end of the geyser. These flow meters measured the volume of hot water heated by the ASHP unit and the volume of hot water drawn off from the storage tank, respectively. Eleven temperature sensors were installed at different locations on the installed ASHP water heater. Temperature sensor (T1) measured the temperature of the incoming cold water from the mains into the storage tank of the ASHP water heater. Temperature sensor (T2) measured the temperature of the air in the vicinity of the ASHP's evaporator. Temperature sensor (T3) measured the temperature of the hot water discharged from the storage tank into the collecting drum. Temperature sensors (T4 and T5) measured the temperature of the water at the inlet and the outlet of the ASHP unit. Temperature sensors (T6 and T7) measured the temperature of the refrigerant at the suction and discharge ends of the ASHP's compressor. Temperature sensors (T8 and T9) recorded the temperature of the refrigerant at the inlet and the outlet of the ASHP's condenser. The temperature sensors (T10 and T11) measured the temperature of the refrigerant at the outlet and the inlet of the ASHP's evaporator. The pressure transducers (P1 and P2) recorded the pressure of the refrigerant at the inlet and the outlet of the ASHP's evaporator. The pressure transducers (P3 and P4), measured the pressure of the refrigerant at the inlet and the outlet of the ASHP's condenser. All the sensors and the transducers were accommodated in two U30 no remote communication data loggers and each comprised of 15 logging channels. All the sensors and the transducers were products of the Hobo Corporation and were compatible with the U30 no remote communication data loggers. The sensors and transducers were configured by the hoboware Pro software to log in 5-minute interval throughout the experiment. The data acquisition system was accomodated in a waterproof enclosure to prevent it from being damaged by interference from solar radiations and other unfavourable ambient conditions. The enthalpy measurements of the primary refrigerant were obtained from the REFPROP software. The REFPROP software was programme and simulated to generate the saturated liquid and vapour table for the refrigerant R417A (the refrigerant contained in the experimental ASHP unit).The generated liquid-vapour saturated refrigerant table was based on the measured temperatures and pressures of the refrigerant (R417A) at the inlet and the outlet of the evaporator and condenser during the VCRC [7].

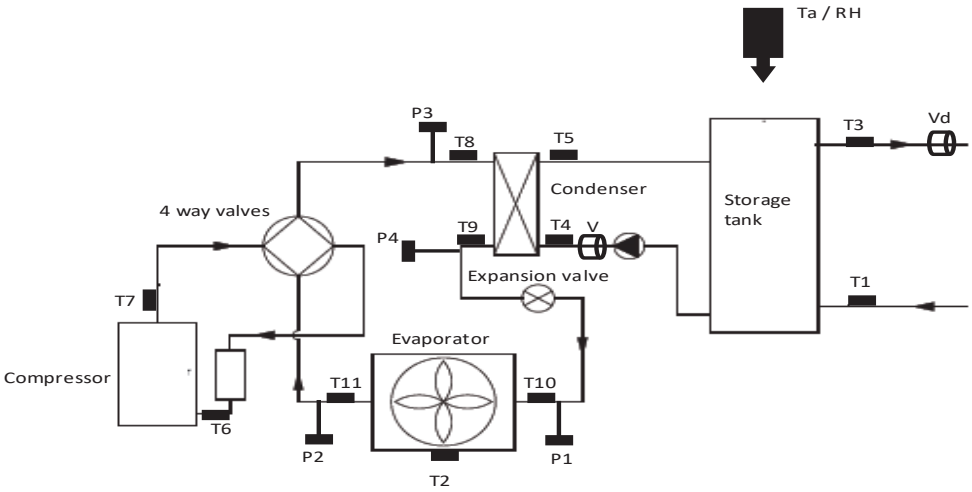

Figure 1: Schematic layout of the installed split type ASHP water heater and the metering sensors

3. Calculation and theory

The input electrical energy consumed by the ASHP water heater during a VCRC is the product of the average electrical power consumed and the time taken for the completion of the heating cycle, as shown in Equation 1.

$$EE = pt \quad (1)$$

The useful output thermal energy gained by the stored hot water is the product of the mass of water heated by the ASHP unit, the specific heat capacity of water and the difference in the water temperature between the outlet and inlet of the ASHP unit during the VCRC and is given in Equation 2.

$$TE = mc(To - Ti) \quad (2)$$

The COP of the ASHP water heater is the ratio of the useful output thermal energy gained by the stored water and the input electrical energy consumed during the VCRC and is given in Equation 3.

$$COPe = \frac{TE}{EE} \quad (3)$$

The COP of the ASHP unit is the ratio of the change in the enthalpy of the refrigerant at the inlet and the outlet of the condenser to the difference between the change in the enthalpy of the refrigerant at the inlet and outlet of the condenser and the evaporator. The relationship is explicitly expressed in Equation 4.

$$COPt = \frac{hconi - hcono}{(hconi - hcono) - (hevpo - hevpi)} \quad (4)$$

4. Results and discussion

4.1 Summer performance of the COPe and the impact of the refrigerant temperatures

Table 2 shows the minimum, the maximum and the average temperatures of the refrigerant at the inlet and the outlet of the evaporator and the condenser, the electrical power consumed, the electrical energy consumed, the thermal energy gained and the derived COPe during the VCRC, due to 50, 100 and 150 L of hot water drawn off. It can be depicted from Table 2 that the temperature of the refrigerant at the inlet of the evaporator was lower (with an average of 4 °C) compared to the temperature of the refrigerant at the outlet of the evaporator (with an average of 27 °C) in all the drawn off scenarios. The difference between the temperature of the refrigerant at the outlet and the inlet of the evaporator confirmed that both sensible and latent heat were gained by the refrigerant at the evaporator during the VCRC. The temperature of the refrigerant at the inlet of the condenser was higher (average of 79 °C) than the temperature of the refrigerant at the outlet of the condenser (average of 39 °C). The difference in the temperature of the refrigerant between the inlet and the outlet of the condenser depicted that thermal energy was dissipated from the refrigerant at the condenser during the VCRC. The useful output thermal energy was the portion of the dissipated energy that was absorbed by the stored water, enabling it to attain the set point temperature during the VCRC. The power consumed throughout the heating cycle, showed no significant difference over the different volumes of hot water drawn off and the average was 1.27 kW. However, both the electrical energy consumed and the useful thermal energy gained demonstrated a significant difference between the 50 L of hot water drawn off (1.01 and 3.03 kWh) to either the 100 or 150 L drawn off (1.55 and 4.66 kWh; 1.51 and 4.61 kWh), respectively. The average COPe for the different volumes of hot water drawn off was 3.04.

4.2 Summer performance of the COPt and the variation of the refrigerant pressures and enthalpies

Table 3 shows the least, the highest and the average pressures and the enthalpies of the refrigerant at the inlet and the outlet of the evaporator and the condenser of the ASHP unit, along side the derived COPt during the VCRC, due to 50, 100 and 150

L of hot water drawn off. Table 3 affirms that, the average pressure of the refrigerant at the inlet of the evaporator was 0.53 MPa and was practically equal to the average pressure of the refrigerant at the outlet of the evaporator (with an average of 0.52 MPa) in all the drawn off scenarios. The difference between the average enthalpy of the refrigerant at the outlet of the evaporator (395.33 kJ/kg) and at the inlet of the evaporator (285.71 kJ/kg) was 109.62 kJ/kg. Therefore, it can be alluded that thermal energy was extracted by the refrigerant at the evaporator during the VCRC from the ambient air. The average pressure of the refrigerant at the inlet and at the outlet of the condenser was the same (2.68 MPa). In addition, the enthalpy of the refrigerant at the inlet of the condenser (409.33 kJ/kg) was higher compared to that at the outlet of the condenser (259.33 kJ/kg) by 150 kJ/kg. Hence, without any loss of generality, thermal energy is dissapated at the condenser during VCRC. The average COPt for the different volumes of hot water drawn off was 3.52 and was greater than the corresponding COPe (3.04).

Table 2: Summer power, temperatures and COPe with respect to specific volumes of drawn off

	50 L drawn off recorded parameter values			100 L drawn off recorded parameter values			150 L drawn off recorded parameter values		
Parameters	Min	Max	Average	Min	Max	Average	Min	Max	Average
Tevpi / ºC	4.02	7.03	4.93	4.94	3.93	3.82	2.81	5.11	4.07
Tevpo / ºC	22.83	36.56	27.47	22.31	27.26	24.90	21.32	34.29	27.76
Tconi / ºC	65.50	82.50	74.72	74.54	78.84	76.42	73.77	84.03	79.54
Tcono / ºC	38.16	45.22	42.05	38.43	39.69	39.00	36.95	42.51	39.97
p / kW	1.12	1.30	1.21	1.24	1.29	1.27	1.25	1.32	1.29
EE / kWh	0.98	1.03	1.01	1.51	1.55	1.55	1.43	1.67	1.51
TE /kWh	2.94	3.20	3.03	4.75	4.54	4.65	4.28	5.16	4.61
COPe	3.01	3.12	3.00	3.02	3.07	3.00	2.99	3.10	3.07

Tevpi = Refrigerant temperature at inlet of evaporator, Tevpo = Refrigerant temperature at outlet of evaporator, Tconi = Refrigerant temperature at inlet of condenser, Tcono = Refrigerant temperature at outlet of condenser, P = average power consumed, EE = Electrical energy consumed, TE = Thermal energy consumed, COPe = Energy dependent COP

Table 3: Summer pressure, enthalpy and COPt with respect to specific volumes drawn off

	50 L drawn off recorded parameter values			100 L drawn off recorded parameter values			150 L drawn off recorded parameter values		
Parameters	Min	Max	Average	Min	Max	Average	Min	Max	Average
Pevpi / MPa	0.53	0.58	0.53	0.52	0.51	0.51	0.49	0.54	0.53
Pevpo / MPa	0.50	0.55	0.52	0.51	0.50	0.52	0.45	0.52	0.52
Pconi / MPa	2.06	2.98	2.68	2.68	2.74	2.68	2.46	3.10	2.76
Pcono / MPa	1.95	2.87	2.57	2.57	2.63	2.57	2.35	3.00	2.69
hevpi / kJ/kg	277.85	291.66	289.36	287.78	288.86	288.16	277.37	292.27	278.90
hevpo / kJ/kg	390.00	400.00	395.00	392.00	401.00	395.00	390.00	400.00	396.00
hconi / kJ/kg	405.00	420.00	410.00	405.00	415.00	410.00	400.00	420.00	408.00
hcono / kJ/kg	250.00	265.00	265.00	258.00	260.00	260.00	250.00	261.28	253.40
COPt	3.49	3.62	3.48	3.50	3.56	3.52	3.47	3.59	3.55

Pevpi = Refrigerant pressure at inlet of evaporator, Pevpo = Refrigerant pressure at outlet of evaporator, Pconi = Refrigerant pressure at inlet of condenser, Pcono = Refrigerant pressure at outlet of condenser, hevpi = Refrigerant enthalpy at inlet of evaporator, hevpo = Refrigerant enthalpy at outlet of evaporator, hconi = Refrigerant enthalpy at inlet of condenser, hcono = Refrigerant enthalpy at outlet of condenser, COPt = Thermodynamic COP, Min = minimum, Max = maxi

6. Conclusions

Although, the performance of the ASHP water heater depends on the ambient temperature, the COPt will increase, if the enthalpy change of the refrigerant between the outlet and the inlet of the evaporator increases during the VCRC while the changed in enthalpy of the refrigerant between the inlet and the outlet of the condenser remain the same. It can be affirmed that there was a significant difference between the COPt and the COPe due to additional increase in the input electrical energy consumed (from fan and water pump) with reference to the COPe as compared to the COPt during VCRC. The corresponding change in enthalpy of the refrigerant at the condenser was greater than that at the evaporator throughout the different volumes of hot water drawers.

7. Acknowledgments

We acknowledge Central University of Technology for their financial assistance towards the research equipment.

8. References

[1] Swan, L.G. and Ugursal, V.I., 2009. Modeling of end-use energy consumption in the residential sector: A review of modeling techniques. Renewable and sustainable energy reviews, 13(8), pp.1819-1835.

[2] Rousseau, P.G. and Greyvenstein, G.P., 2000. Enhancing the impact of heat pump water heaters in the South African commercial sector. Energy, 25(1), pp.51-70.

[3]Tangwe, S., Simon, M. and Meyer, E., 2014. Mathematical modeling and simulation application to visualize the performance of retrofit heat pump water heater under first hour heating rating. Renewable energy, 72, pp.203-211.

[4] Morrison, G.L., Anderson, T. and Behnia, M., 2004. Seasonal performance rating of heat pump water heaters. Solar Energy, 76(1-3), pp.147-152.

[5] Hepbasli, A. and Kalinci, Y., 2009. A review of heat pump water heating systems. Renewable and Sustainable Energy Reviews, 13(6-7), pp.1211-1229.

[6]De Swardt, C.A. and Meyer, J.P., 2001. A performance comparison between an air‐source and a ground‐source reversible heat pump. International Journal of Energy Research, 25(10), pp.899-910.

[7] Lemmon, E.W., Huber, M.L. and McLinden, M.O., 2010. NIST Standard Reference Database 23, Reference Fluid Thermodynamic and Transport Properties (REFPROP), version 9.0, National Institute of Standards and Technology. R1234yf. fld file dated December, 22, p.2010.

Formulation of Indicators for Sustainable Groundwater Development in Qatar

Salah Basem Ajjur[1] and Husam Musa Baalousha[1,2]
College of Science and Engineering, Hamad Bin Khalifa University, Qatar Foundation, Doha, Qatar
Qatar Environment and Energy Research Institute (QEERI), Hamad Bin Khalifa University (HBKU), PO Box: 34110, Doha, Qatar
Corresponding authors: saajjur@mail.hbku.edu.qa (S. B. Ajjur), baalousha@web.de (H. M. Baalousha)

Abstract

Effective water resources management is very essential to cope with the limited resources, especially in arid countries. Qatar is one of the most arid countries in the world with a very limited rainfall. Over the last few decades, the stresses on water resources have been intensified due to the sharp increase in population and the very high per-capita water consumption. Domestic and industrial water demands are met totally by desalination, while groundwater is used for agriculture, which overexploited the aquifer. Many studies recommended Managed Aquifer Recharge (MAR) as a means to increase water security and to improve the groundwater quality, especially in arid areas. The literature documents various methods for MAR implementation, however the appropriate method and its feasibility in Qatar remains unexplored.

This paper establishes key indicators to develop MAR in Qatar, in the light of successful implementation of MAR in arid regions and taking into consideration the current technical and socio-economic factors. The four MAR methods considered are: (1) aquifer storage and recovery, (2) in-channel modification, (3) rainwater harvesting, and (4) spreading methods. Results show that using the harvested rainfall and desalinated water to feed MAR is the optimum scenario to increase water security and sustainability in Qatar. In addition, rainfall harvesting will contribute to flash flood protection, which adversely impacts the environment. Specific recommendations are emparking on field-scale tests and theoretical models for subsurface dams and rainwater harvesting methods.

Keywords: Qatar; managed aquifer recharge; water resources management; desalinated water

I. Introduction

Qatar is one of the most arid countries in the world with a very limited rainfall (< 80 mm/year on average) (Baalousha, 2016b). Aquifer is the only natural source of water in Qatar, which is heavily over-exploited and deteriorated (Baalousha, 2016b). Agriculturural sector, the most consumer of water, is totally depending on groundwater. Also, the population in Qatar has risen five fold over the last two decades (World Bank, 2018). The annual per-capita water consumption is very high. It increased from 500 l in 2011 (Qatar General Secretariat for Development Planning, 2011) to 613 l in 2017 (Qatar General Electricity and Water Corporation (Kahramaa), 2017). The combined effect of these factors increased the stresses on the already over-exploited aquifer.

As such, there is a need for a policy framework to protect the groundwater resources and mitigate the over-exploitation impact. This requires detecting the relevant knowledge and evaluating the impact of several policy options. Consequently, policymakers can determine the optimum solution of such a problem. The focus of this study is on how to develop groundwater resources in a sustainable way and in the same time to meet the increasing demand. Several methods of Managed Aquifer Recharge (MAR) have been widely used in arid areas as a promising solution. MAR, or artificial recharge, is defined as the storing/injecting of water in the aquifer to further recover it and/or get other environmental benefits (Dillon, 2005). Source water can be rainfall, treated wastewater, desalinated water or surface water such as lakes or rivers. MAR objectives include maximizing water storage, managing the aquifer and improving groundwater quality. Other benefits are reducing seawater intrusion in coastal areas and preventing land subsidence (Dillon, 2005). There are five methods of MAR in arid areas (IGRAC, 2019). As shown in Figure 1, these methods are: Aquifer Storage and Recovery (ASR); spreading methods; bank filtration; in-channel modification and rainwater harvesting. Little work has been done to identify the optimum way for MAR and its feasibility in Qatar.

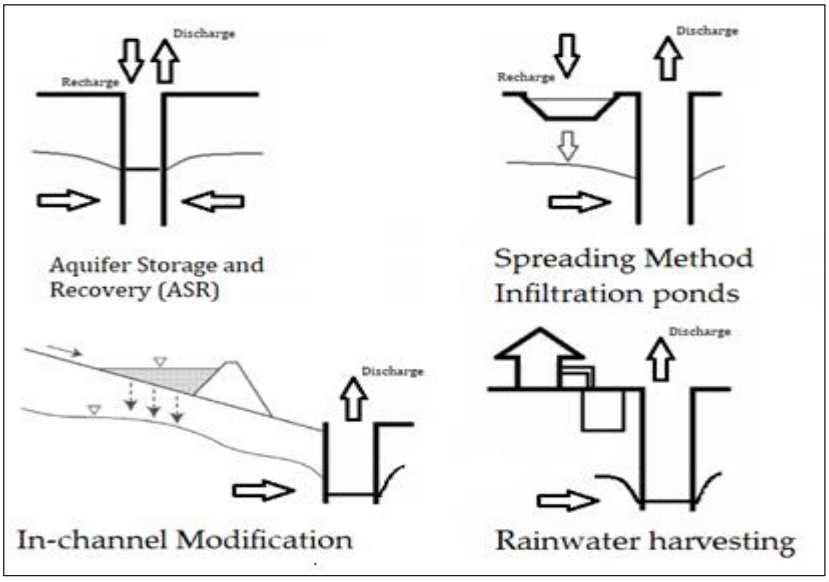

Figure 1. Schematic view of the four methods of MAR (adopted from Dillon 2005)

This study aims at formulating key factors for sustainable groundwater development in Qatar, considering current technical constraints and socio-economic aspects. Advantages and disadvantages of four methods were studied in the lights of successful implementation of arid regions e.g. United Arab Emirates (UAE), Tunisia and Iraq. Such study will be a good start for improving the decision-making process regarding sustainable groundwater development in Qatar.

II. Managed Aquifer Recharge (MAR) Methods

Aquifer storage and recovery (ASR) method

In ASR method, water is injected into the aquifer using wells, shafts and boreholes, especially in low permeable surfaces (Hannappel et al., 2014). The water is abstracted during drought or emergency periods. Identifying water quantity and pumping rates are important for ASR (Herrmann, 2006). Adjustment of the layout and a separation distance are also recommended between wells, which becomes essential to achieve more efficient use of water resources (Gastélum et al., 2009). A good example is LIWA project in UAE where 315 wells were constructed in Liwa desert. The project aims to recover more than 170,000 m^3 daily for three months to fulfill the water needs during emergency periods. A desalination plant (i.e. Shuweihat) is the source of water at a rate of 26,500 m^3/day.
The effectiveness of ASR method in Qatar is questionable. Many factors affect the recovery efficiency of ASR wells such as native water quality, hydraulic conductivity and aquifer transmissivity (Guo et al., 2009). Due to the poor quality of most of the native groundwater in Qatar, it may mix with and deteriorate the injected water, resulting in a low recovery rate. In addition, the aquifer is highly heterogeneous, with transmissivity varies between 20-1000 m^2/day in is the north to less than 2.6 m^2/day in the south (Schlumberger Water Services, 2009). Estimation of the aquifer recharge capacity in the area surrounding the ASR wells is difficult.

In-channel modification method – subsurface dams

This method aims primary to intercept water by building dams in rivers beds or wadis. The water is stored temporary to be infiltrated into the aquifer. Pumping wells are used later to extract water during drought months. In-channel modification process is common for aquifer management purposes in arid areas i.e., preventing floods, increasing storage in unconfined aquifers and controlling seawater intrusion in coastal areas (Zeelie, 2002).
In Qatar, the evapotranspiration rate is high, with daily potential varies between 2.74 mm in January and 8.29 mm in June (Baalousha et al., 2018). Also, the constructed dams are vulnerable to failure due to heavy floods, especially in karst aquifers. To ensure the effectiveness of this method, a proper design of subsurface dams is required based on geological and hydrogeological investigations (Salameh et al., 2019). A subsurface dam (i.e. Gali Basera), was constructed in Northern Iraq. MAR wells around the dam were able to meet water needs during summer periods (Stevanovic and Iurkiewicz, 2008) without deteriorating the aquifer water quality.

Rainwater harvesting (RWH) method

RWH method refers to gathering of rainwater from the roofs of buildings and surfaces to infiltrate into the aquifer using barriers, bonds and trenches. RWH is a cost-effective method (Perrin et al., 2012) to prevent flooding in urban areas. However, the high-water loss due to evaporation and the degradation of water quality, especially in the case of low rainfall, are big disadvantages in RWH method. The percentage of RWH contribution to the total groundwater storage varies between regions, and depends on rainfall (intensity, frequency and duration) and physical and hydrogeological characteristics of the aquifer. In Tunisia, for example, the percentage of the harvested rainfall was estimated at 13% in the central basin (Bel Hadj Salem et al., 2011), whereas it is around 86% in the northwestern

Basin (Kacem, 2008). In the central basin study, 39% of the released water percolates the aquifer. In Qatar, RWH can primarily be used to prevent flooding.

Spreading method

In spreading method, impaired quality water such as urban runoff or reclaimed wastewater is diverted into a basin or a channel that allows water to infiltrate to the aquifer. It is highly recommended to study aquifer conditions and the suitable sites for spreading projects (Ajjur and Mogheir, 2019). This method helps mitigate flooding and takes advantage of rainwater in arid areas. Spreading is a cost-effective method. This method also enhances soil conditions in arid areas via reducing soil erosion and soil removal (Gale et al., 2002). MAR spreading method can increase groundwater storage significantly in any arid country. The main disadvantage of this method is that evaporation rate is high in Qatar. Evaporation may reduce one-third of the water available for recharge (Batchelor et al., 2000).

III. Analysis and Results

Public awareness of the advantages of MAR methods, both to the people and environment, is the success key to define its feasibility. To achieve this purpose in Qatar, current technical constraints and socio-economic aspects should be studied. Prior to that, policymakers should identify the primary objective of MAR. During the last two decades, continuous imprudent abstraction disturbed the hydrologic balance of the aquifer in Qatar. The influent source and the final use of water should be carefully defined. The source could be rainfall, desalinated water or treated wastewater. Socio-economic aspects are very important in this regard. Many people have a negative perception about the use of the treated wastewater in MAR projects. Gaining the social acceptance for this purpose is questionable. At present, the treated wastewater is only be used for landscape irrigation despite the high cost associated with its treatment. Thus, economic analysis is essential to evade substantial losses of water and expenses.

It is documented that ASR is feasible to store water in confined aquifer if the top soil layers are impermeable (Yuan et al., 2016). Spreading methods will not be practical as clogging is popular in impermeable soil conditions. On the other hand, ASR method are costly in comparison with other methods in arid areas (Ross and Hasnain, 2018). Considering that Qatar has a karst limestone aquifer with high heterogeneity (Baalousha, 2016a), MAR choices are limited. One should also consider the physical processes limiting recovery efficiency: stratification; permeability differences and downgradient displacement by the local background flow system (Kimrey, 1985). To illustrate, although ASR-LIWA project was implemented in similar climatic and environmental conditions, hydrogeological situations are different. LIWA has a sandy soil whereas it is limestone and dolomite in Qatar. Sandy soil aquifers are ideal for ASR projects. Generally, economic analysis of MAR with different approaches and sources of water needs to be explored in Qatar.

IV. Conclusions

Given the harsh environment in Qatar, low rainfall and high development rate, one realizes the urgent need for effective water resources management. MAR seems to be a promising solution to sooth water resources problem in the country. This study critically evaluates four MAR methods in similar arid areas. These methods are: (1) aquifer storage and recovery, (2) in-channel modification, (3) rainwater harvesting, and (4) spreading methods. Specific recommendations for policymakers in Qatar are:

- Findings from other projects cannot easily be transferred and adopted in Qatar. Qatar has a karst non-homogeneous aquifer. Researchers should use numerical models to test various possible scenarios and mitigate failure risks. While models are powerful tools, errors and uncertainty are inevitable in arid areas (Ringleb et al., 2016). As such, field tests are necessary to validate the models and document MAR feasibility.
- Studying the prospective challenge of MAR implementation in Qatar should include economic analysis. Aquifer stratification and homogeneity are big concerns, which may reduce recovery rate. Researchers should present cost-benefit analysis for different MAR methods using alternative water sources (desalinated water, rainfall). This might help identify the suitable (effective) method.
- Due to the continuous increase in the socio-economic level in Qatar, water consumption is very high with a rising trend. Water polices ignore the importance of efficient use of water resources, however Islamic rules place a high emphasis on the water use and prohibit the exploitation of resources. MAR cannot be a solution for over-abstraction. This should be addressed, and MAR should be coupled with wise abstraction to achieve groundwater supplies without disturbing the hydrologic equilibrium. Meanwhile, decision-makers should consider alternate water resources for agricultural use e.g. wastewater treatment.

V. Acknowledgements

This research was supported by Hamad Bin Khalifa University (HBKU), under Qatar Foundation (QF). The findings achieved herein are solely those of the authors.

VI. References

AJJUR, S. & MOGHEIR, Y. 2019. Identification of Intrinsic Suitable Sites in Gaza Strip for the Application of Artificial Groundwater Recharge using a GIS Multi-Criteria Decision Analysis. *Journal of Multi-Criteria Decision Analysis*.

BAALOUSHA, H., BARTH, N., RAMASOMANANA, F. & AHZI, S. 2018. Groundwater recharge estimation and its spatial

distribution in arid regions using GIS: a case study from Qatar karst aquifer. *Modeling Earth Systems and Environment,* 4**,** 1319-1329.
BAALOUSHA, H. M. 2016a. Development of a groundwater flow model for the highly parameterized Qatar aquifers. *Modeling Earth Systems and Environment,* 2**,** 67.
BAALOUSHA, H. M. 2016b. The potential of using beach wells for reverse osmosis desalination in Qatar. *Modeling Earth Systems and Environment,* 2, 97.
BATCHELOR, C. H., RAMA, M. R. & JAMES, A. J. 2000. Karnataka Watershed Development Project: Water Resources Audit. 17 ed.
BEL HADJ SALEM, S., CHKIR, N., ZOUARI, K., COGNARD-PLANCQ, A. L., VALLES, V. & MARC, V. 2011. Natural and artificial recharge investigation in the Zéroud Basin, Central Tunisia: impact of Sidi Saad Dam storage. *Environmental Earth Sciences,* 66**,** 1099-1110.
DILLON, P. 2005. Future management of aquifer recharge. *Hydrogeology Journal,* 13**,** 313-316.
GALE, I., NEUMANN, I., CALOW, R. & MOENCH, M. 2002. The Effectiveness of Artificial Recharge of Groundwater: a Review. British Geological Survey Commissioned Report, CR/02/108N.
GASTÉLUM, J. R., SMALL, G. G. & SHENG, Z. Application of the drop pipe hydraulic and aquifer hydraulic equations in design and operation of artificial recharge wells. the 7th International Symposium on Managed Aquifer Recharge, ISMAR7, 2009 Abu Dhabi, UAE. 453-460.
GUO, W., MALIVA, R. & MISSIMER, T. T. Recovery Efficiency Assessment of an ASR Well Using Groundwater Models. the 7th International Symposium on Managed Aquifer Recharge, ISMAR7, 2009 Abu Dhabi, UAE. 414-421.
HANNAPPEL, S., SCHEIBLER, F., HUBER, A., SPRENGER, C. & M., D. 2014. Characterization of European Managed Aquifer Recharge (MAR) Sites-Analysis. *In:* 141 (ed.).
HERRMANN, R. ASR Well Field Optimization in Unconfined Aquifers in the Middle East, In Recharge Systems for Protecting and Enhancing Groundwater Resources. The 5th International Symposium on Management of Aquifer Recharge, 2006 Berlin, Germany. UNESCO: Paris, France, 109-114.
IGRAC 2019. International Groundwater Resource Assessment Centre, Artificial Recharge of Groundwater in the World.
KACEM, A. 2008. *Management of water resources of Sisseb Elam basin: impact of hydraulic installations on water table recharge.* PhD Thesis.
KIMREY, J. 1985. Proposed Artificial Recharge Studies in Northern Qatar. Orlando, Florida.
PERRIN, J., MASSUEL, S. & AHMED, S. Contribution of percolation tanks to total aquifer recharge: The example of Gajwel watershed, southern India. In Achieving Groundwater Supply Sustainability & Reliability through Managed Aquifer Recharge. *In:* DRAEGER, M., ed. the 7th International Symposium on Managed Aquifer Recharge, ISMAR-7, 2012 Abu Dhabi, UAE, 9-13 October 2009. 251-258.
QATAR GENERAL ELECTRICITY AND WATER CORPORATION (KAHRAMAA) 2017. Statistics Report 2017.
QATAR GENERAL SECRETARIAT FOR DEVELOPMENT PLANNING 2011. Qatar National Development Strategy 2011-2016. Towards Qatar National Vision 2030.
RINGLEB, J., SALLWEY, J. & STEFAN, C. 2016. Assessment of Managed Aquifer Recharge through Modeling—A Review. *Water,* 8**,** 579.
ROSS, A. & HASNAIN, S. 2018. Factors affecting the cost of managed aquifer recharge (MAR) schemes. *Sustainable Water Resources Management,* 4**,** 179-190.
SALAMEH, E., ABDALLAT, G. & VAN DER VALK, M. 2019. Planning Considerations of Managed Aquifer Recharge (MAR) Projects in Jordan. *Water,* 11**,** 182.
SCHLUMBERGER WATER SERVICES 2009. Studying and developing the natural and artificial recharge of the groundwater in aquifer in the State of Qatar. Project final report.
STEVANOVIC, Z. & IURKIEWICZ, A. 2008. Groundwater management in northern Iraq. *Hydrogeology Journal,* 17**,** 367-378.
WORLD BANK. 2018. *World Development Indicators database* [Online]. Available: https://data.worldbank.org/country/qatar https://databank.worldbank.org/views/reports/reportwidget.aspx?Report_Name=CountryProfile&Id=b450fd57&tbar=y&dd=y&inf=n&zm=n&country=QAT [Accessed 22/01/2020].
YUAN, J., VAN DYKE, M. I. & HUCK, P. M. 2016. Water reuse through managed aquifer recharge (MAR): assessment of regulations/guidelines and case studies. *Water Quality Research Journal,* 51**,** 357-376.
ZEELIE, S. OMDEL dam and recharge ponds to enhance recharge in the Namib Desert. Management of Aquifer Recharge for Sustainability *In:* DILLON, P., ed. the 4th International Symposium on Artificial Recharge of Groundwater, ISAR-4, Adelaide, Australia, 2002. 22-26.

Microwave Melting Salt Slurries by Serpentinite Granule for Thermal Energy Storage

[1*]Yıldırım Tosun,
[1] Şırnak University, Engineering Faculty, Mining Engineering Department, Şırnak, 73000, Turkey

* E-mails: yildirimismailtosun@gmail.com

Abstract
Heated Ca-ferrite pellets in microwave radiated molten slurries are one of the most promising technologies for advanced fuel energy storage with favorable economic potential and intrinsic properties. The development of solid pellet technology for molten salt is a key issue in the heat transport processing. As for pure molten $MgCl_2$-$CaCl_2$-NaCl eutectic salt at approximately 473-500°C, we have already reported the successful results of transport using gravity and a centrifugal pump. However, molten salt in the carbon pellet/ metal-salt mixes with insoluble fines dissolved in porous basket. The insoluble consists of noble metal fission products, such as Pb, Zn, Cu. In this study, there have been very few transport studies of molten salt slurry (metal fines-molten salt mixture).

Keywords: Microwave Melting, pellets, Heat Storage, Molten Salts, Pellet Granules, Active Carbon

1. INTRODUCTION

There are lots of fluidas for hot thermal storage in ORC systems. However, the higher performance can be achieved by a certain mixture of solid pellet additives in molten salt storage. A preferable advanced design in molten salt in Solar energy storage could produce clean Ca ferrites in the local container of the power station so significant that needs to obtain the highest quality salt fluids melted.
Combustible waste amount could also be evaluated in energy need. Processing technologies using animal manure and combustible municipal waste should be under contribution to the fuel side and natural gas storage (Figure 1)

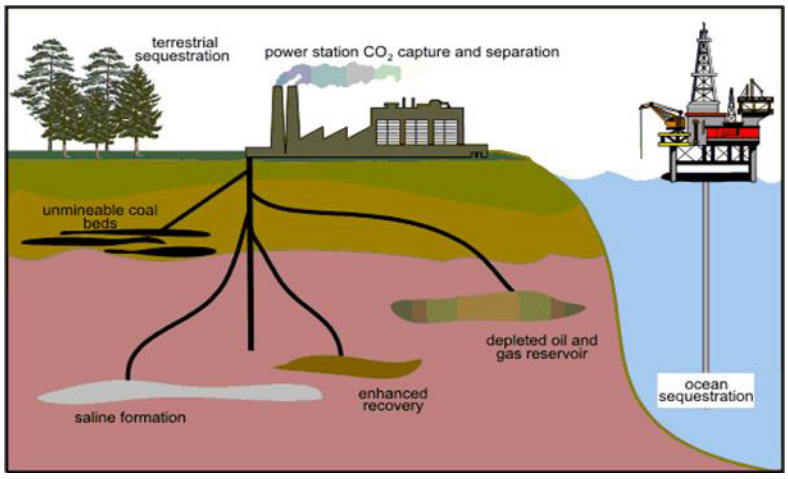

Figure 1. Primary Energy Gas Storage, in Turkey; Natural Gas, Salt Cave Storage, Biomass Combustion CO2 Storage [1,2] .

The possibility to use heat as a by-product is an important asset of biomass ORCs, highlighting the importance of a local heat demand, which can be fulfilled e.g. by industrial processes (such as wood drying) or space heating (usually district heating). Since heat is relatively difficult to transport across long distances, biomass CHP plants are most of the time limited to 6–10MW thermal power, corresponding to 1–2MW electrical power. This excludes traditional steam cycles that are not cost-effective in this power range.
Simplified diagrams of such cogeneration systems are proposed in Figure 2 and Figure 3: heat from the combustion is transferred from the flue gases to the heat transfer fluid (thermal oil) in two heat exchangers, at a temperature varying between 150 and 320°C. The heat transfer fluid is evaporating the working fluid, at a temperature slightly lower than 300°C. Next, the evaporated fluid is expanded, passes through a recuperator to preheat the liquid and is finally condensed at a temperature around 90°C. The condenser is used for hot water generation.

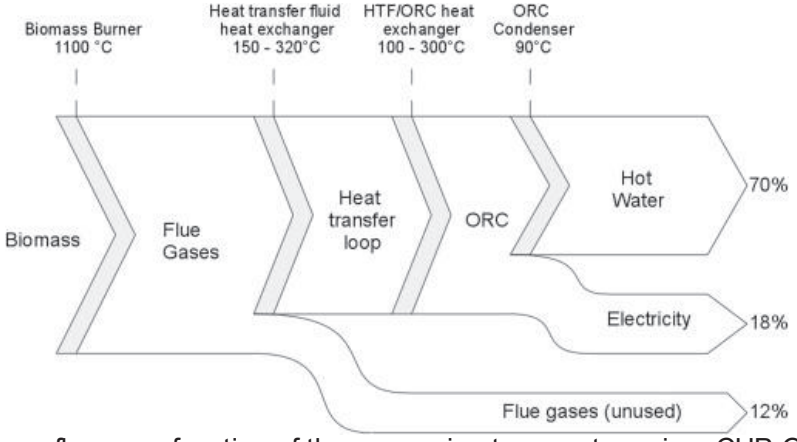

Figure 2. Energy flow as a function of the conversion temperatures in a CHP ORC system.

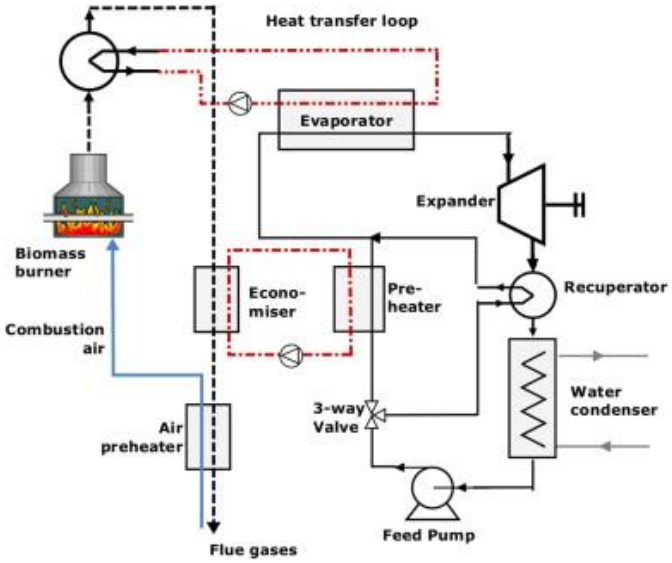

Fig. 3. Working principle of a biomass CHP ORC system.

Relying on advanced technological developments in energy production, the low quality municipal wastes needed the most economical technologies and even in order to make it possible to produce waste-derived fuel products as diverted source in USA (U.S. Environmental Protection Agency 2015) [16]. Combustible municipal waste rate was reached 27,0% as paper and cardboards, additionally dried food waste was 14,6% and the yard waste was 13,5% after suitable segregation of the total collected waste in USA in 2015. Municipal waste conversion for energy production in China as shown in Figure 4 In the view energy storage high value fluids, solid pellets are used for this thermal high conductivity in the recuperators and storage purpose.

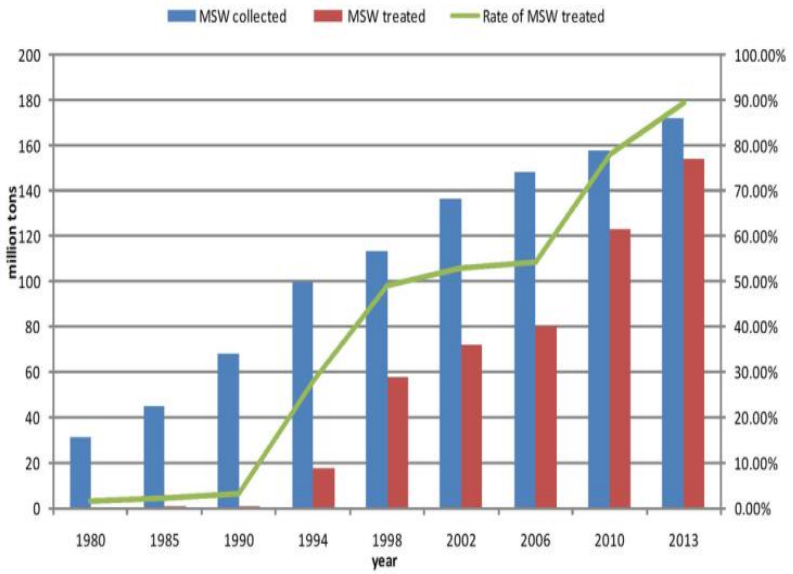

Figure 4. Municipal solid waste (MSW) management in China from 1980 to 2013 [14,15]

2. CALCIUM FERRİTE

The calcium ferrite pellet is all melted and liquid at 1300°C and 1350°C. However the calcium ferrite pellet is in melting state at 1250°C, which shows that the melting point is lower than 1250°C. The results of the x-ray diffraction analysis of molten sample as seen from Figure 5 at 1250°C and 1350°C show that the composition of the calcium ferrite pellet mineral phase is mainly CaO•Fe2O3 and 2CaO•Fe2O3.

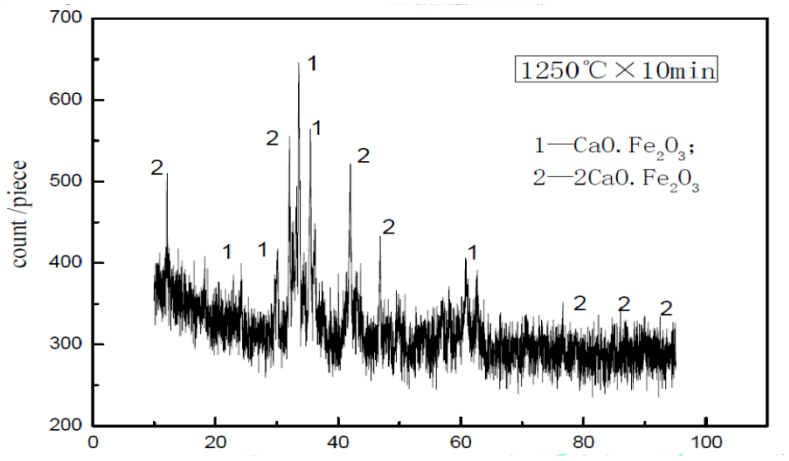

Figure 5. X ray diffractometer diagramme of Ca ferrite components

The chemical composition and physical properties of slag formation material in BOF steelmaking are showed as Table 1. The bulk density average value of the calcium ferrite pellet is 3.02 g/cm3 by drainage. In order to better application of the calcium ferrite pellet the melting point of the calcium ferrite pellet and slag formation material of converter is compared. The concrete method is that firstly the crucible is put into resistance furnace at 1280°C~1320°C and preheating 15 minutes, then the crucible is taken out from resistant furnace and the sample is put into the crucible, finally the sample and crucible is put into resistance furnace at the temperature of 1350°C and time of holding temperature is 10 minutes. The melting state of sample is immediately observed after cooling.

Table 1. The chemical composition and physical properties of materials in experiment

Material name	The chemical composition and the bulk density of materials
The calcium ferrite pellet	CaO:21-28%; SiO2≤10%;Fe2O3:35~45%;Al2O3≤6%;MgO≤4%; P≤0.1%;S≤0.1%, the bulk density:2.8~3.2g/cm3
The sintered ore	CaO:9.16%; SiO2:5.18%;TFe:54.3%;P:0.05%; S:0.02%
Iron oxide powder（cold rolling iron skin）	The content of total iron is 55%
The iron scale	The content of total iron, silica and water is respectively 70.02%, 1.55% and 8.5%.
Lime powder	CaO≥90%

3. MOLTEN SALTS FOR ORC POWER GENERATION

For molten salt fluids used as storageand heat conduction systems, where colloidal suspensions are needed, a careful balance between the colloidal ferrite suspension and shape anisotropy and particle size must be improved. If the anisotropy is too low, then to avoid para magnetism the particles would have to be too big to achieve a colloidal suspension. If the anisotropy is too high, then it might be impossible to produce particles small enough so that the magnetization could be switched in a low-field value. Results of our investigation on cobalt ferrite are used magnetic fluids.

A new design of measurement cell has been made which has the advantages of reducing or eliminating the effects of convection, ensuring the measurement is made in a magnetic field of known uniformity and that the heat losses in the system are constant and minimized under both magnetic and Joule heating.

There is a search for alternative materials. In this paper we report on a study of the compound in terms of its thermal stability. We have produced polycrystalline films of this compound with sub 10 nm grains and examined the thermal stability in layers of thicknesses of up to 30 nm. Using thermal activation studies we have determined a room temperature value of the anisotropy constant of this compound in a tetragonal structure of up to (6.3±0.3) $x10^6$ erg/cm^3. The anti ferromagnetic grains can be aligned by thermal annealing at an optimum temperature of 380K. Above this temperature the magnetic properties deteriorate possibly due to nitrogen desorption.

4. METHODS

The experimental data obtained by for the Ca ferrites with extruded bore form in fixed salt bed columns were used to evaluate the accuracy of the model developed in this work. The characteristic parameters of the column are listed in Table 2. The equilibrium parameters for N_2 adsorption onto Ca ferrites are given and were kept constant in the simulations (a = 0.5 L mg^{-1} and q_m = 10. mg g^{-1}). Ca ferrite image used in experimentation is shown in Figure 6.

Table 2. The Parameters of the fixed bed column used.

Salt Bed porosity (-)	Bed density (g L^{-1})	Diameter of column (cm)	Average diameter of particles(μm)
20.9	2150	5	200

Figure 6. Example of Ca-ferrite image

5. RESULTS AND DISCUSSION

The Ca-ferrite/ Zn-ferrite produced from different calcined temperatures at 700-900 ºC were tested for gas sorption in three column series. The high porous suitable ferrite was obtained for salt melting and conductivity at 4W/m. Test results were determined as sorbed gas weight in TGA. Experimental results showed that high porous ferrite provided high conductivity and contact with melted salt in the hot salt container as shown in Figure 7.

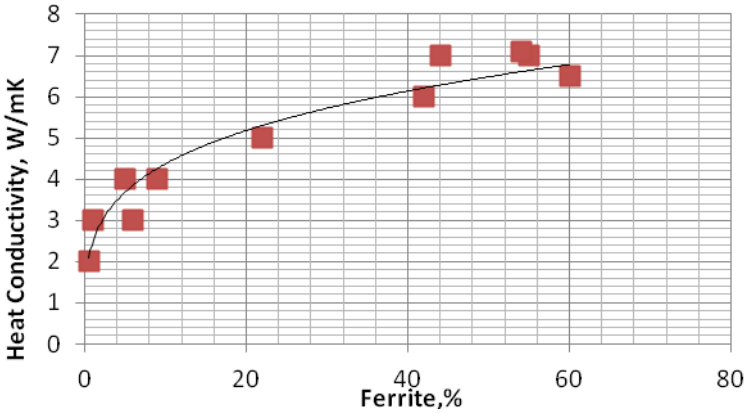

Figure 7 The Ferrire amount parameter of the fixed salt bed column used.

6. CONCLUSION

The results showed that high weight rate of Ca-ferrite on Zn-ferrite managed high gas sorption in three column series. The high porous suitable ferrite was obtained for 90% Ca ferrite pellets in salt melting and conductivity at 3,7W/m. Experimental results showed that high porous ferrite provided high conductivity at higher molten salt temperatures at over 500ºC and suspended well in the hot salt container.

The study of ferrite extruding control at sustainable development from many aspects in storage was compulsory, and then advanced materials and technologies should be used to prevent corroding recuperator material used. In this study it was finally concluded that Ca ferrite was solid matter as efficient and high performance.

References

Akpınar, N and Şen, M,1987, Kentsel katı atıklardan enerji üretimi, Enerji Enstitüsü
Al-Jabari, M., Modeling analytical tests of supercritical fluid extraction from solids with Langmuir kinetics. Chemical Engineering Communications, 190, 1620-1640 (2003).
Anonymous b, 2015, Yakma Kazanları, http://**www.alfakazan.com.tr**, Alfa Kazan ve Makine AŞ,Ankara
Anonymous c, 2015, Kalina Cycle, http://**www.imparatorenerji.com.tr**, İmparator Enerji, GeoPower, İstanbul
Anonymous d, 2015, Akışkan Yataklı Yakma Kazanı, http://**www.mimsan.com.tr**, Mimsan A.Ş. , İstanbul
Anonymous e, 2015,http://www.atlasinc.dk/
Anonymous f, 2015,http://www.santes.com.tr/
Anonymous g, 2015, http://www.ottusa.com/mobile_systems/ mobile_systems.htm
Anonymous, 2017 SEPURAN membrane fibers: http://www.sepuran.com/product/ sepuran/en/ Pages/ selective-permeation.aspx
Bell D.A. Towler B.F., Fan M., 2011, Coal Gasification and Applications, ISBN: 978-0-8155-2049-8, Elsevier Inc., Oxford
Donskoi, E.& McElwain, D.L.S., 1999, Approximate modelling of coal pyrolysis, Fuel, 78 , pp. 825–835 https://doi.org/10.1016/j.apm.2017.01.069
IEA, 2007, IEA Coal Research Ltd, Clean Coal Technology Report, (A.J. Minchener and J.T. McMullan)

Production of Zeolite/ Biochar Active Carbon Composite Pellets for Hydrogen Sorption

[1*]Yıldırım Tosun,
[1] Şırnak University, Engineering Faculty, Mining Engineering Department, Şırnak, 73000, Turkey

* E-mails: yildirimismailtosun@gmail.com

Abstract
The packed bed sorption of Hydrogen gas was carried out over 100 microns on active carbon char and activated zeolite clay pellets. Microwave leached char was activated and in order to enhance this packed flow manner of that compost, clay pellets were put in barrel chamber and leached by 0.1 M HCl solution for 20 min. Extruded biochar pellets pressed with 40%,60% and 80% bio-active carbon, active clay mixtures and microwave leached activated forms were used in our absorption experiments at 1- 2rnrn sized pellets. The cycles of gas transport was managed till saturation of carbon pellets. The simulated sorption on solid carbon porous structure and capturing for Hydrogen gas on active carbon or char developed mechanical separation used. The pellets size-sorption simulation was provided a 7-8% Hydrogen gas sorption and also 14-15% soot addition provided highly developed compressibility. The waste organic oil and soot improved briquetting quality at coarse-grained structure extruding. The clay samples were thought to be subjected to homogenization in microwave leaching and acid treatment.

Keywords: Microwave Activation, Active Carbon, Hydrogen Sorption, Hydrogen ,Storage

1. Introduction

The effects of electromagnetic waves in the microwave heater provide a very rapid movement generated with emitting (2.4 x 10^9 times per second) lead to particle heating [1-3]. There is a very quick response to this mobilization by a combination of molecules constituting particles. Because of this delay movement will consist of a force opposing blocker and the friction which occurs in the particles results will occur at a certain temperature. This event in microwave is based on dielectric heating pass through the particles. Electric field of the microwave, Located in force on charged particle compounds applies. If charged particles are free can move toward the electric field, and heat flow occurs with depending on the compound of charged particles [4].

1.1.Microwave permittivity and Dielectric constant

There is only limited movement and phase movement of the orientation of the electric field in the microwave. It is expressed as dielectric polarization.
Dielectric polarization is installed in substance depending on four different types of particles. It consists of components: electron, nucleus, continuous dipoles and interface loads [5],

$$\alpha t = \alpha e + \alpha a + \alpha d + \alpha i \quad (1)$$

A ferrite or iron ore specimen located within the microwave field will warm dielectric material to a certain extent regarding the dielectric characteristics of iron oxide or ferrite content and type, ε^*, ε^1 and ε^{11} to decide.

$$\varepsilon^* = \varepsilon^1 + j\,\varepsilon^{11} \quad (2)$$

At the very high and very low frequency conditions as happen in the microwave, ε^1 is equal to the total dielectric constant of the material. Electromagnetic energy materials ε^{11} where the value is converted into heat by the amount of electromagnetic energy converted to heat related. Warming the dielectric field presence with the equation below (3) [4], the expressions given by the equation indicated.

$$\tan\delta = \varepsilon^{11} / \varepsilon^1 \quad (3)$$

When microwaves are directed towards a material, part of the energy is reflected, part is transmitted through the surface, and of this latter quantity, part of it is absorbed. The proportions of energy, which fall into these three categories, have been defined in terms of the dielectric properties. The fundamental electrical property through which the interactions are described is the complex relative permittivity of the material ε^*. It is expressed as in Equation 2[5-9]:
The absolute permittivity of a vacuum is ε_o and it is determined by the speed of light C_o and the magnetic constant μ_o, which are linked together by equation below:

$$C_o \mu_o \varepsilon_o = 1 \quad (4)$$

The numerical value for ε_0 is about 8.854 pF/m and for μ_o is 1.26 H/m. In other media (solid, liquid and gaseous), the permittivity has higher values and it is usually expressed relative to the value in vacuum [1]. The relative permittivity ε_r of a material is equal to $\varepsilon_{abs}=\varepsilon_o$, where ε_{abs} is the absolute permittivity of material. Materials which do not contain magnetic components respond only to the electric field.

$$P_{abs}=5.56x10^{-4} f \varepsilon^{11} E^2 \quad (5)$$

The dielectric properties of materials dictate, to a large extent, the behavior of the materials when subjected to radio-frequency (RF) or microwave field for the purposes of heating, drying or processing the materials. The characterization of dielectric properties is vital for understanding the response of a material to microwaves, since most useful quantities needed in the design of microwave thermal processes can be described in terms of them. The equations relating dielectric properties to thermal processing parameters are presented in the following section.

The power dissipated inside a material is proportional to $\varepsilon^{11}/\varepsilon^{1}$. The ratio, $\varepsilon^{11}/\varepsilon^{1}$, called the loss tangent or dissipation factor, a descriptive dielectric parameter, is also used as an index of the material's ability to generate heat [10-12];
Sometimes, d_p is defined as the distance at which the microwave power has been attenuated to 50% of P_{trans}. The penetration depth is a function of ε^{11} and ε^{1} [5,6]:

$$d_p = c\lambda_0{}^2 Pf \frac{\sqrt{\varepsilon^1}}{2\pi\varepsilon^{11}} \quad (6)$$

Where λ_o is the free space microwave wavelength (for 2.45 GHz, λ_o=12.2 cm).
As the wave travels through a material that has significant dielectric loss, its energy will be attenuated. If the attenuation is high in the material, the dielectric heating will taper off quickly as the wave penetrates the material. Attenuation is often expressed in decibels per unit length in meters (dB/m). In terms of power densities and electric field intensity values, The rate of heating can be expressed by the power equation [1]:

$$Pv = 2\pi f \varepsilon_o \varepsilon^{11} E^2 \quad (7)$$

where P_v is the energy developed per unit volume in Wm^3, *f* is the frequency in Hz; and E is the electric field strength inside the load in V/m
The electric field inside the load is determined by the dielectric properties and the geometry of the load, and by the oven configuration. Therefore, this equation is generally impractical since the determination of the electric field distribution is very complex.

2. THERMAL ENERGY STORAGE

The energy storage provide the main support to the renewable energy production. The commercial successes in electric power storage Technologies mentioned and its ability were described some of the emerging applications in power storage like wind farm power stabilization, steam, hydro, wind, etc. (Anonymous a,b, 2013, Dincer et al 2007) Some cost evaluations covering security of supply and environmental impacts, climate change evaluations, and technical and economic analysis, may be disussed in energy planning and activities.

2.1. ORC Technology and Storage Applications

The layout of the Organic Rankine Cycle is somewhat simpler than that of the steam Rankine cycle: there is no water–steam drum connected to the boiler, and one single heat exchanger can be used to perform the three evaporation phases: preheating, vaporization and superheating. The variations of the cycle architecture are also more limited: reheating and turbine bleeding are generally not suitable for the ORC cycle, but a recuperator can be installed as liquid preheater between the pump outlet and the expander outlet, as illustrated in Figure 1. This allows reducing the amount of heat needed to vaporize the fluid in the evaporator.

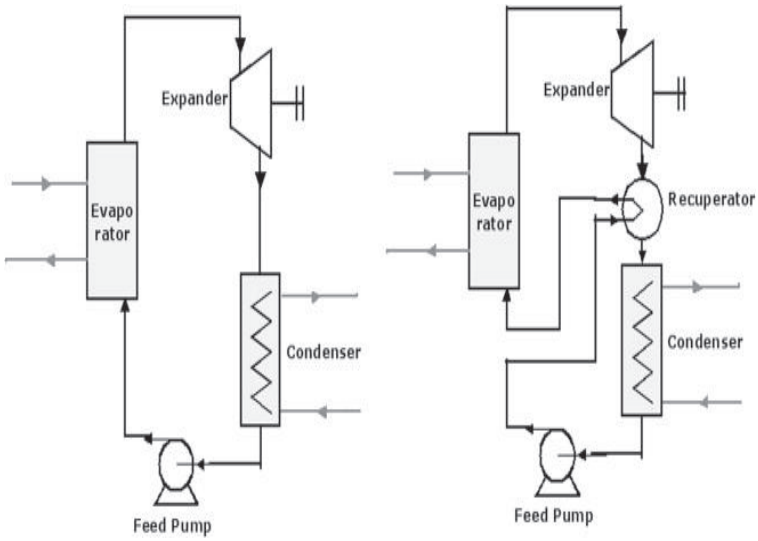

Figure 1. Schematic view of an ORC with (right) and without (left) recuperator.

The simple architecture presented in Figure 1 can be adapted and optimized depending on the target application. The main applications are briefly described in the following sections. Although this review only focuses on state-of-the art commercially available ORC plants, it should be noted that some prospective advanced applications for Organic Rankine Cycles are currently being studied, mainly in the form of prototypes or proof-of-concepts. These innovative applications include:
• Solar pond power systems, in which the ORC system takes advantage of temperature gradients in salt-gradient solar ponds.
• Solar ORC-RO desalination systems, where the ORC is used to drive the pump of a reverse-osmosis desalination plant .
• Ocean thermal energy conversion systems, utilizing the temperature gradients (of at least 20°C) in oceans to

drive a binary cycle.
• Cold production, where the shaft power of the ORC system is used to drive the compressor of a refrigeration system. Note that this layout can also be used to produce heat with a COP>1 if the ORC is coupled to a heat pump.

2.2. Biomass Combined Storage Heat and Power

Biomass is widely available in a number of agricultural or industrial processes such as wood industry or agricultural waste. Among other means, it can be converted into electricity by combustion to obtain heat, which is in turn converted into electricity through a thermodynamic cycle. The cost of biomass is significantly lower than that of fossil fuels. Yet, the investment necessary to achieve clean biomass combustion is more important than for classic boilers. For small decentralized units, the generation cost of electricity is not competitive and combined heat and power generation is required to ensure the profitability of the investment. Therefore, in order to achieve high energy conversion efficiency, biomass CHP plants are usually driven by the heat demand rather than by the electricity demand.

3. Hybrid Power and Design Model for Molten Energy Storage

A fluidized bed reactor was used in coal combustion heated till 600 ºC with a rate 7-10ºC/min by fuel. The process was tested at a scale of 2–3 kg/h; collecting operational and design data to build an industrial installation. A technological diagram of the coal gasification-pyrolysis process developed unit is made. Thermal destruction almost observed at temperature Heat exchanger oil temperature increase from 350 °C to 400°C with storage and performance of 60-70% and also simultaneous dilution of waste oil products by condenser distillate may be used. it is necessary to optimize the storage conditions of oil circulation without the heat loss transported to heat exchanger, where the average heat conductivity per oil amounts changes 20 - 30 kW/m^3, so enhancing ORC heat transfers.

3.1. Solid Salt Matter for Molten Energy Storage

- Phase diagrams of salt matters are shown in Figure 2. The main use was depended on availability, conductive properties of solid to melted salt of NaCl and KCl such as given in Table 1. The ferrite matters were related with the equipment used in pelletizing solid matters during extruders compressing as below;
- Die temperature control units
- Easy on quick-connects
- Safe, easy disposal

Table 1. Pure salts obtained from preliminary screening process.

Alkali metal	T_m (°C)	ΔH_{fus} (kJ/kg)	Cost (USD/kg)	Cost (USD/kJ)
LiCl	610	467	$34	$0.07
KCl	771	353	$9.80	$0.03
NaCl	800.7	482	$4.76	$0.01
CsCl	646	121	$145	$1.20
Alkaline earth metal				
$MgCl_2$	714	453	$8.00	$0.02
$CaCl_2$	775	253	$12.38	$0.05
$SrCl_2$	874	102	$55.65	$0.54
$BaCl_2$	961	76	$12.00	$0.16

Extrusion was managed under homogeneous binding control and process parameters for fine size powders agglomeration.

3.2. Oxidation

Heavy fluid oxidation occurs when supplies of fresh air come into intimate contact with hot heat transfer fluid (during frequent tool change out, for example). The resulting reaction converts fluid molecules to organic acids. Soon the acids themselves begin to degrade thermally. The fluid becomes thicker, darker and more odorous, and its heat transfer capabilities drop dramatically.

3.3.Fouling

As an oxidized fluid becomes more viscous, it becomes more difficult to pump and more susceptible to overheating. Remaining in contact with the heated surfaces too long, the fluid picks up more heat than its chemical bonds can stand. As they break down, the fluid's molecules release their carbon forming an acidic, carbonaceous sludge that precipitates out and adheres to the system's interior surfaces. Much of this sooty, sticky carbon bakes on to the heated surfaces where it was produced. The ORC fluid contains an additive system that inhibits sludge and carbon formation. Even under prolonged exposure to air, the fluid won't foul heated surfaces.

3.4. Efficiency

Due to its low viscosity, the ORC fluid provides unusually high thermal efficiencies and higher than most synthetics. The lower in viscosity (the thinner) a heat transfer fluid is, the less energy is required to pump it through the system. In addition a smaller pump and motor can be specified, and the lower power consumption will provide low costs.

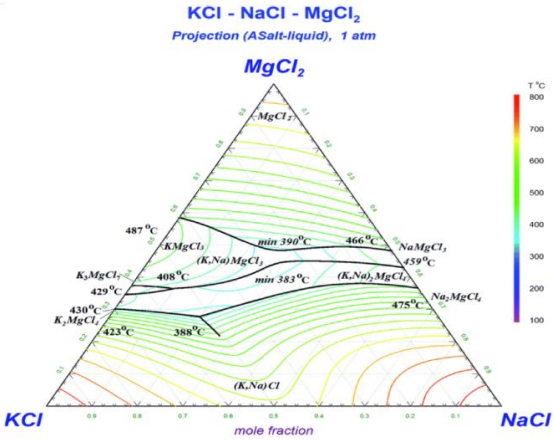

Figure 2. KCl and NaCl, $MgCl_2$ eutectic phase diagramme

4. MATERIALS AND METHOD

The produced high frequency (2.45 GHz) microwaves and the incident power could be varied continuously from 0 to 1000 W. A quartz crucible (about 120 g) containing the pyrite was placed on an alumina platform. The power was varied from 600W to 1000 W. The sample mass ranged from 5 to 50 g. In all experiments, the temperature was measured at the base of the sample, and this is referred to as the sample temperature. A type K thermocouple (wire diameter of 0.20 mm) was employed and the temperature was measured immediately after turning the power off. The variables studied were: incident microwave power, processing time and sample mass. For the microwave roasting tests, samples weighing about 15–20 g, were placed in fireclay salt melting boats and heated. (Figure 3)

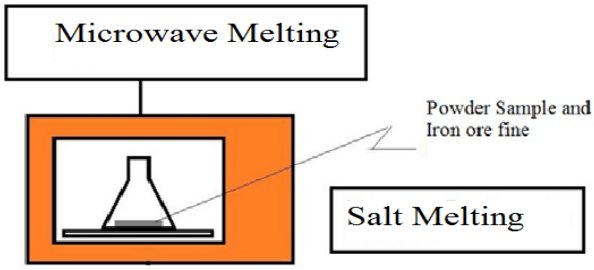

Figure 3. Microwave Experimentation Flowsheet

5. RESULTS AND DISCUSSION

Microwave melting treatment could find application in the minerals industry as a pretreatment method for sintering iron ores. Many drying plants treated the bio-wastes by microwave heating for even torrefaction. Microwave salt melting could be integrated into such a heat storage isolated system in order to make liquid eutectic salt phase faster and more economical. The proposed process that included even microwave melting using Ca ferrite pellets in the calorimeter circuit was investigated and temperature was determined in heating by microwave oven. The test results in this method were shown as permittivity loss and heat increase as temperature change as seen in Figure 4.

Ferrite Type

The advantages of such a procedure are that coarse coal particles have a lower heating rate than fines, thus, temperature control during melting would be enhanced. Additionally, there will be improved coal dust control during melting and the specific energy consumptions required for complete salt melting by microwave heating and conventional melting were about 0,48 and 6,4 kW h/kg, respectively. Typically, the conventional energy consumption in melting was about 9,1 kWh/kg with ferrite pellets. Therefore, the combined energy consumption for microwave salt melting with Ca-ferrite pellets would still be lower with 1,2 kWh/kg than conventional. However salt melting in microwave was time consuming due to viscosity and bubling effect.

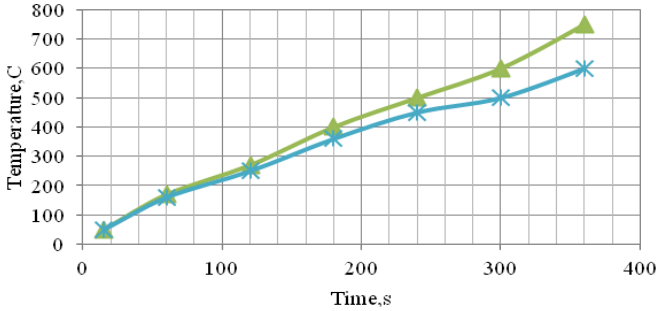

Figure 4. Time effect on temperature in Microwave Salt Melting

6. CONCLUSION

Such eutectic salt mixtures require pretreatment to avoid salt from moisture and impurities. the mixtures of the chlorides and sulphates may be oxidize metal solid content. For this reason oxidized ferrites may show passivity by not fouling. Oxidation of carbonaceous matter before salt melting was also critical. The microwave salt melting method includes low storage cost. The melted liquid could have high fluidity and lower viscosity below 10-25 P. The exchanger silica tubes may avoid corrosion, chlorination, pressure oxidation. Cold wall fouling may avoid fluidity in tubes and digestion and gasification of impurities from ferrites may deteriorate homogeneity in salt mixture. The microwaves could be banned by solid and viscous source of settled salty shield matter. Carbon and metal sulphide impurities as microwave absorbers were oxidized. Some heat was directly lost in isolated oven by corner microwaves. In the present study, the microwave melting of 120 gr salt samples with ferrite at 10 gr was successful. The ferrite was very responsive to microwave heating and this resulted in almost complete melting and in some cases fouling of the material as seen in the corners of oven.

References

Anonymous b, 2015, Yakma Kazanları, http://**www.alfakazan.com.tr**, Alfa Kazan ve Makine AŞ,Ankara

Anonymous c, 2015, Akışkan Yataklı Yakma Kazanı, http://**www.mimsan.com.tr**, Mimsan A.Ş. , İstanbul

Anonymous f, 2015, http://www.ottusa.com/mobile_systems/mobile_systems.htm

Anonymous f, 2013, http://www.electricitystorage.org.

Anonymous h, 2013, http://www.enercon.com.

Akpınar, N , Şen, M, 1987, Kentsel katı atıklardan enerji üretimi**,** Enerji Enstitüsü

Bell D.A. Towler B.F., Fan M., 2011, Coal Gasification and Applications, ISBN: 978-0-8155-2049-8, Elsevier Inc., Oxford

Cabeza, L. F. (Ed)2015, *Advances in thermal energy storage systems* , Elsevier, Woodhead Publishing Series in Energy ISBN: 978-1-78242-088-0

Çakal, GÖ. H. Yücel, A.G Gürüz, 2007, Physical and chemical properties of selected Turkish lignites and their pyrolysis and gasification rates determined by thermogravimetric analysis, Journal of Analytical and Applied Pyrolysis, Volume 80, Issue 1, 262–268

Cherubini, F. Bargigli, S. Ulgiati, S. 2009, Life cycle assessment (LCA) of waste management strategies: landfilling, sorting plant and incineration, Energy, 34, pp. 2116–2123

Dinçer, İ. Rosen. M. A., 2011, Thermal energy storage: systems and applications, second edition, John Wiley & Sons, Ltd ,ISBN: 9780470747063 Online ISBN: 9780470970751, DOI: 10.1002/9780470970751

Donskoi, E.& McElwain, D.L.S., 1999, Approximate modelling of coal pyrolysis, Fuel, 78 , pp. 825–835

Ibrahim H, Ilinca A, Perron J. Energy storage systems—characteristics and comparisons. Renewable and Sustainable Energy Reviews 2007;12: 1221–50.

IEA, 2007,,A.J. Minchener and J.T. McMullan IEA Coal Research Ltd, Clean Coal Technology

IEA, 2013, World Energy Outlook

Bauer, T., Breidenbach, N., Pfleger, N., Laing, D., Eckand, M., 2012. Overview of molten salt storage systems and material development for solar thermal power plants. In: Proceedings of the 2012 National Solar Conference for (SOLAR 2012), Denver.

Brosseau, D., Kelton, J.W., Ray, D., Edgar, M., Chisman, K., Emms, B., 2005. Testing of thermocline filler materials and molten-salt heat transfer fluids for thermal energy storage systems in parabolic trough power plants. J. Sol. Energy Eng. 127 (1), 109–116.

Casati, E., Galli, A., Colonna, P., 2013. Thermal energy storage for solar-powered organic Rankine cycle engines. Sol. Energy 96, 205–219.

Potrovitza, N., Blake, D., Price, H., 2003. Assessment of a molten salt heat transfer fluid in a parabolic trough solar field. J. Sol. Energy Eng. 125 (2), 170–176.

Khokhlov, V., Ignatiev, V., Afonichkin, V., 2009. Evaluating physical properties of molten salt reactor fluoride mixtures. J. Fluorine Chem. 130 (1), 30–37.

Comparative Study for Solar Powered Systems in Pakistan

[1*]Tahir A.H Ratlamwala, [1]Sohaib Ahmed, [1]Moiz Ahmed, [1]Muhammad Umer Khan, [1]Ossama Tahir
[1] National University of Sciences & Technology, Engineering Sciences, Islamabad, 44000, Pakistan

E-mails: tahir.ratlamwala@pnec.nust.edu.pk, sohaib38@gmail.com, amoiz1408@gmail.com, muhammadumerkhankhan@gmail.com, ossamatahir94@gmail.com

Abstract
Pakistan receives ample amount of solar radiation, this potential can be harnessed to produce off-grid electricity to power remote rural areas in the western, northern regions and urban city centers in order to meet the power shortfall. This paper presents the performance of various solar powered electricity generation systems. The solar systems considered are; Heliostat Solar Tower Plants, Parabolic Trough Collector Plants, Photo Voltaic Plants. The cumulative yearly electrical output affiliated with each type of plant, for a solar field size of 10,000m^2, is evaluated for 10 major cities and a comparative analysis is performed. Apart from the thermal and electrical performance of each type of solar system, effect of parameters like Direct Normal Irradiation (DNI) that varies for each city, is analyzed. The electrical output increases as the DNI increases. For all systems, heliostat, parabola and PV systems, the max output power is available during the summer season, i.e. June, July, and August. The output of heliostat exceeds the output of Parabolic Trough by 24% and PV system by 42% due to higher attainable steam temperature, which results in a more efficient power cycle. The solar power output in western areas and northern regions, typically in Quetta, Skardu, Peshawar and Islamabad is comparatively less than areas situated in Sindh and Punjab. Karachi has the highest solar potential for all Solar based systems. The Heliostat integrated Rankine cycle's cost analysis presents the least payback period of 4.4 years, while that of Parabolic Trough collector and Photo Voltaic is of 6 years and 7 years respectively.

I. Introduction

Energy generation and consumption is the key to a prosperous economy because it directly influences human activities and developments. Unfortunately, the usage of fossil fuels in power generation has devastating effects on the environment. According to Pakistan Economic Survey 2019, the installed capacity in 2017-18 was 33,433 MW, which increased to 34,282 MW in 2018-19 and the Electricity generation share is as follows [1]:

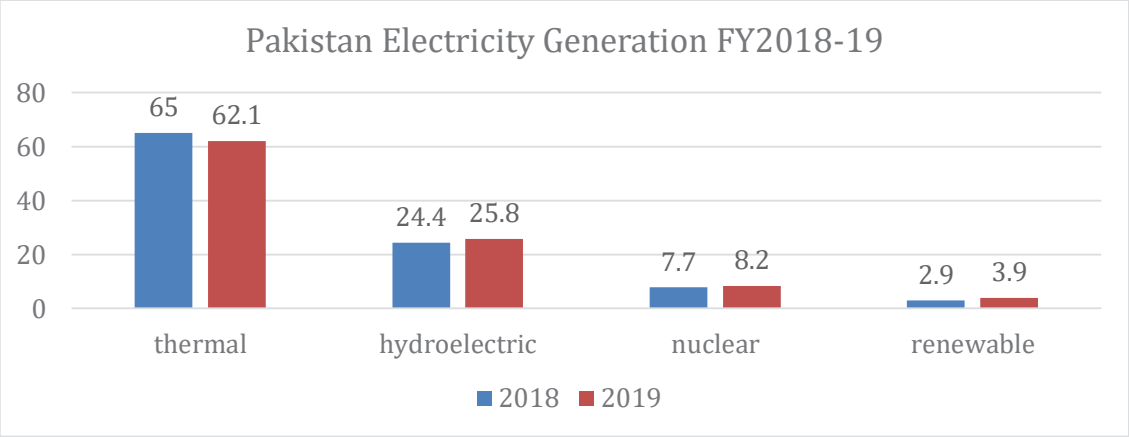

Figure 1: Pakistan Electricity Generation FY2018-19, modified from [1]

However, despite all the efforts the electricity shortfall remains a major problem for Pakistani citizens and hampers growth of industrial sector. In June 2018, the power shortfall reached 9000 MW [2]. Pakistan needs to invest in renewable energy sources to provide clean power for its citizens. According to [3]. Pakistan receives 1KW of solar energy per square meter of its land for 6-7 hours a day, with 3000-3300 hours of average sunshine hours in the country. This potential can be harnessed to produce off-grid electricity to power remote rural areas in the western, northern regions and urban city centers. A comparative study is performed for: 1.) Heliostat Solar Tower Plants 2.) Parabolic Trough Collector Plants 3.) Photo Voltaic Power Plants

II. System Description

Heliostat Power Plants or solar tower power plants is a solar furnace where a tower is installed to receive concentrated solar radiation. A large array of flat mirrors is used to focus sun's radiation upon the central tower where steam is heated up to 550 **°C. This superheated steam is used to drive a Rankine cycle and generate electricity.** Li et al. [4] developed a molten salt system, which was further analyzed by [5]. This consists of four major systems: 1.) Heliostat field system 2.) Central receiver system 3.) Steam generator system 4.) Conventional Ranking based power system. This system uses a field of mirrors (also known as heliostats) with solar tracking system, to reflect sun's rays to a central receiver system where molten salt is heated to high temperature. The salt

flows inside the steam generator system where it exchanges heat with high-pressure steam. This superheated steam is expanded in the turbine to generate power.

Parabolic trough thermal solar power plant is by far the most developed CSP technology operating commercially. The parabolic trough is a type of a solar thermal collector that is straight in one dimension and curved in the other direction like a parabola. The collector reflect the incident solar radiation towards a receiver that absorbs the concentrated solar energy to raise the temperature of the heat transfer fluid i.e. Therminol VP-1 [6], flowing inside it. Parabolic trough power plants consist of a solar field occupied with hundreds and thousands of solar collector assemblies. Each solar collector assembly is an independent solar collector consisting of following major sub systems: 1.) Parabolic reflectors 2.) Receiver tube 3.) Metal support structure 4.) Tracking system
The sun's energy heats up the fluid, which carries the energy to the water in a boiler heat exchanger, reaching a temperature of about 650K. The heat is transferred into the water, producing steam to drive turbine. One such system was also studied by Fahad A. Al-Sulaiman [6].

Photovoltaic uses solar cells to convert sunlight into electricity. It produces direct current that fluctuates with sunlight's intensity. Multiple solar cells are connected in series or parallel to form array and tied to inverter which produces power at desired voltage or frequency. This paper uses Mono-Crystalline Photo Voltaic Panel having efficiency of 15-18% and 350 Watt peak power for the comparative energy analysis.

III. Analysis:

For the calculation of energy and exergy for three different systems we have used the following equations:

Equations for PV:	Equation for Heliostat:	Equation for Parabolic Through collector:
$Energy = p_{dcstc} \times DNI$ $\eta_{energy} = \frac{energy \times \eta_{conv}}{DNI \times area}$	$Q_{absorbed} = Q_{received} \times \eta_{receiver}$ $Q_{incident} = DNI \times Receiver_{area}$ $\eta_{overall} = \frac{W_{net}}{Q_{incident}}$ $\eta_{exergy,overall} = \frac{Wnet}{\Psi_{incident}}$	$Q_u = A_{ap} \times F_R \times (S - \frac{A_r}{A_{ap}} \times U_L \times (T_{fi} - T_a))$ $\eta_{el} = \frac{W_{scyc}}{Q_{incident}}$

Where p_{dcstc} = Dc power at STC(kW) , η_{energy} = Efficiency of PV, $Q_{absorbed}$ and Q_u is useful energy(kWh), $Q_{incident}$ is incident energy of sun(kWh), DNI=Direct Normal Insulation(kWh/m^2), $\Psi_{incident}$ is the exergy incident(kWh), A_r = receiver area(m^2), W_{net} = Total energy(kWh), T_a= Ambient temperature(K), A_{ap}=Aperture area(m^2), F_R=heat removal factor, U_L is the solar collector overall heat loss coefficient(kW/K). W_{stcyc} =net power from the steam Rankine cycle (kW).

IV. Results and discussions:

The average monthly DNI values of 10 cities is presented below in graphical and tabular form. A 35-year data set (1984-2018) was obtained from NASA [7] and then average values were used in the calculations.

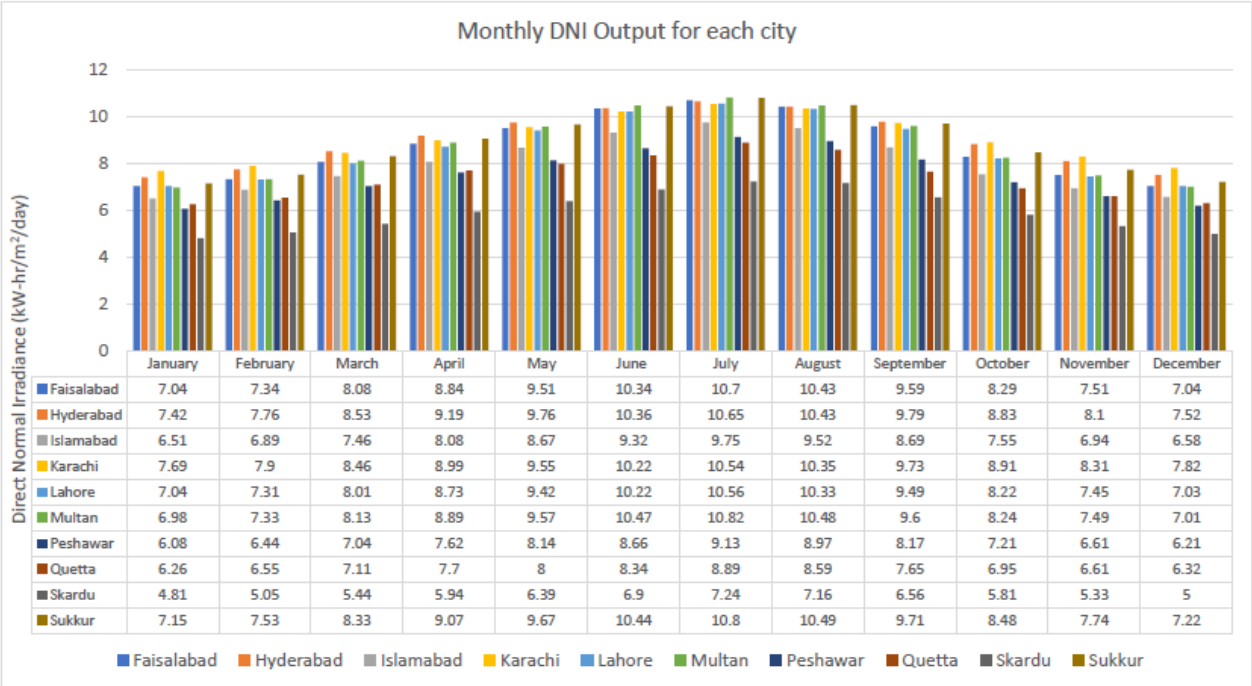

	January	February	March	April	May	June	July	August	September	October	November	December
Faisalabad	7.04	7.34	8.08	8.84	9.51	10.34	10.7	10.43	9.59	8.29	7.51	7.04
Hyderabad	7.42	7.76	8.53	9.19	9.76	10.36	10.65	10.43	9.79	8.83	8.1	7.52
Islamabad	6.51	6.89	7.46	8.08	8.67	9.32	9.75	9.52	8.69	7.55	6.94	6.58
Karachi	7.69	7.9	8.46	8.99	9.55	10.22	10.54	10.35	9.73	8.91	8.31	7.82
Lahore	7.04	7.31	8.01	8.73	9.42	10.22	10.56	10.33	9.49	8.22	7.45	7.03
Multan	6.98	7.33	8.13	8.89	9.57	10.47	10.82	10.48	9.6	8.24	7.49	7.01
Peshawar	6.08	6.44	7.04	7.62	8.14	8.66	9.13	8.97	8.17	7.21	6.61	6.21
Quetta	6.26	6.55	7.11	7.7	8	8.34	8.89	8.59	7.65	6.95	6.61	6.32
Skardu	4.81	5.05	5.44	5.94	6.39	6.9	7.24	7.16	6.56	5.81	5.33	5
Sukkur	7.15	7.53	8.33	9.07	9.67	10.44	10.8	10.49	9.71	8.48	7.74	7.22

Figure 2: Monthly DNI Output for each city obtained from [7]

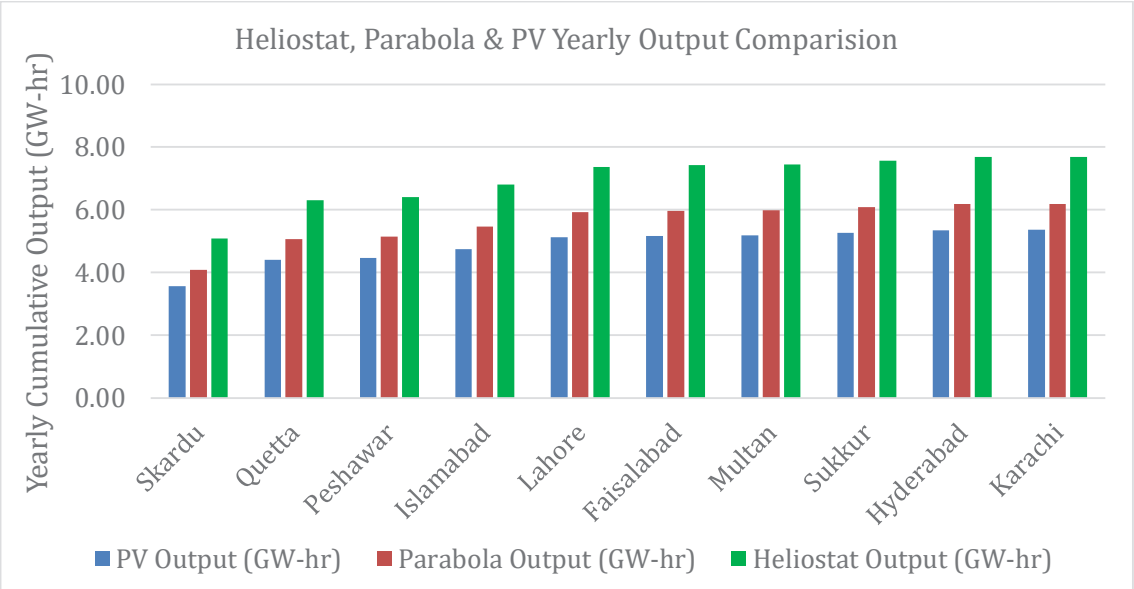

Figure 3: Yearly Cumulative Output Comparison of all solar systems for each city

Figure 2 present the output power of heliostat, parabolic trough, and photovoltaic systems for all ten cities. The heliostat system has the highest output power among all three systems, followed by parabolic trough system and photovoltaic system. In comparison the parabolic trough system produced 15% more output when compared with the photovoltaic system, and heliostat system produced 42% more output when compared with photovoltaic system. The steam temperature in heliostat power cycle is highest which results in a more efficient power cycle. The solar power output in western areas and norther regions, typically in Quetta, Skardu, Peshawar and Islamabad are comparatively less than areas situated in Sindh and Punjab. Karachi has the highest solar potential for all three solar systems. The highest power output for all three systems was in summer season i.e. June, July, & August.

Cost Analysis:

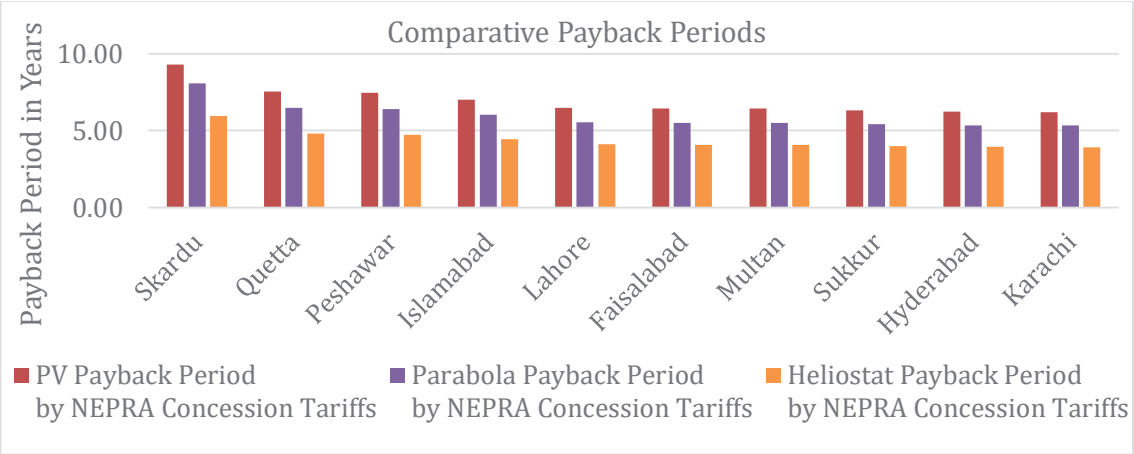

Figure 4: Comparative Payback Period according to NEPRA's concessional Tariffs.

In areas of high solar radiation such as Sindh & Punjab the heliostat system has the smallest payback period of about 4.4 years based on NEPRA's concessional tariff [8], followed by parabolic trough system which has a payback period of 6 years. The PV system has the highest payback period of 7 years due to low output power. The US department of energy aims to achieve 5c/kWh LCOE for CSP systems by 2030 [9].

V. Conclusions

Pakistan faces an acute power shortfall, which can be met by clean power such as CSP (concentrated solar power), and photovoltaic systems. The output power and financial payback suggests that the concentrated solar power is the future of solar power generation. The high efficiency of heliostat power systems (23.3%) and payback of only 4.4 years based on concessional tariff shows that it is a very attractive business opportunity for power companies looking to invest in renewable power sector of Pakistan. The parabolic systems have a higher payback period of

about 6 years due to higher installation cost and lower output efficiency (18%) compared to heliostat systems. The photovoltaic systems are easy to install and maintain but due to low output efficiency (16.5%) and high payback cost it lags behind both heliostat and parabolic trough power systems.

References

[1] "Pakistan Economic Survey," Ministry of Energy, Hydrocarbon Development Institute of Pakistan (HDIP), 2019.

[2] "Power shortfall hits record peak," The Express Tribune PK, 26 June 2018. [Online].

[3] "An assessment of renewable energy potential for electricity generation in Pakistan," *Renew Sustain Energy ,* Vols. 20:240-54, 2013.

[4] W. K. Z. W. C. C. F. B. X. Li, "Thermal model and thermodynamic performance of molten salt cavity receiver," *Renewable Energy 35,* pp. 981-988, 2010.

[5] Z. W. X. L. F. S. Chao Xu*, "Energy and exergy analysis of solar power tower plants," *Applied Thermal Engineering 31,* pp. 3904-3913, 2011.

[6] F. A. Al-Sulaiman, "Energy and sizing analyses of parabolic trough solar collector integrated with steam and binary vapor cycles," *Energy,* pp. 1-10, 2013.

[7] "Power Data Access Viewer," NASA, [Online]. Available: https://power.larc.nasa.gov/data-access-viewer/.

[8] N. E. P. R. A. (NEPRA), "SOLAR TARIFF - INDEPENDENT POWER PRODUCERS (IPPS)," [Online]. Available: https://nepra.org.pk/tariff/gen_ipps-solar.php.

[9] "Goals of the Solar Energy Technologies Office," U.S. Department of Energy Efficiency and Renewable Energy, [Online]. Available: www.energy.gov/eere/solar/goals-solar-energy-technologies-office.

Assessing the environmental impact of grocery bags

[1*]Tahir A.H. Ratlamwala, Adeel Asghar, Hammad Pervez, ShoaibShahbaz, Abeer Farooq
[1]National University of Science and Technology, Department of Engineering Sciences, Islambad, Pakistan
*E-mails:tahir.ratlamwala@pnec.nust.edu.pk, adeel_aryan@hotmail.com, hammadpervez@hotmail.com

Abstract
This paper asseses the environmental feasibility of 3 most commonly used types grocery bags. All relevant data was extracted from the local demographic and trends were subsequently analyzed. Then, using the same data, a cradle to grave life cycle assessment analyses (LCA) was carried out. Considering energy and water consumption along with carbon dioxide (CO_2) emissions, we had derived the conclusion based on 2 factorswhich were environmental impact index (EI) and Ecological sustainable index (ESI). The results obtained depict that Low-density polyethylene (LDPE) bags have a 300% and 400% greater environmental impact index as compared to paper and cotton bags, respectively. However, the ecological sustainability index (ESI) showed that paper and cotton bags exihibted 67 and 75 times more adversity than LDPE bag, respectively. Furthermore, considering the resources in Pakistan are already struggling to meet the growing demands of increasing population, our recommendation is to continue using LDPE bags until a more viable and resource efficient alternative is available for mass market.
Keywords: Life cycle assesment, Grocery bags, Sustainability, Global warming, Plastic, Paper, Cotton

I. Introduction

Given the modern-day premise of unlimited wants and limited resources, it was imperative for us to analyse the various manufacturing processes that go into making a variety of grocery bags. For the brevity of this paper, we will carry out LCA on paper, cotton and LDPE bags, which are the most commonly used grocery bags. Firstly, paper bags constitute approximately 58 kg of water per kg of kraft paper((S.A) 2012). Those values can change pending efficiency of the processes involved. Added to that the energy consumed during manufacturing of paper bags varies from 298to 638 kWh per 1000 kg of pulp, which in return produces 0.522 kg of carbon dioxide per kWh of electricity consumed (Laurijssen 2013).
While in comparison, LDPE bags use energy between 28 to 32 MJ per kg of polyethylene and its CO_2 footprint varies from 2.1 to 2.5 kg per kg of polyethylene. Moreover, the water consumption of LDPE varies from 38 to 114 L of water per kg of polyethylene (Di Donato 2013). Finally, for cotton bag, 60 MJ of energy is consumed pr kg of cotton. The water requirement is a substantial 10,000 L per kg of cotton and its carbon dioxide emission comes out to be 6 kg per kg of cotton (Report 2019). The Figure 1 outlines our approach, which is the standard method of carrying out LCA as per the ISO 14040.

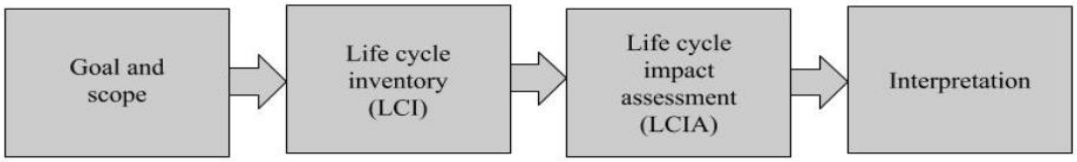

Figure 1: LCA method as per ISO 14040

A recent study carried out in Denmark (Muthu and Li 2014)aimed to correct a common misconception that LDPE bag alternatives such as paper and cotton are far less adverse for the environment which is true but it doesnot portray the complete picture. Infact, the study showed that cotton and paper bags are extremely resource intensive during their manufacturing stage that during its use stage, it turned out to be less efficient than LDPE bags (valenb and envdtudk 2018).

II. Experimental Procedure/Methodology/System Description

Paper bags are made from unbleached kraft paper, which is made from kraftsulphate pulp. The manufacturing of kraft paper uses cellulose fibres, dissolved lignin and black liquor; from which the cellulose fibres are further processed and purified to obtain an impurity free kraft pulp, called the unbleached kraft paper which is then used for making the paper bags. Pakistan imports both – kraft paper and kraftsulphate pulp for making paper bags.

Cotton bags undergo different manufacturing stages – ginning, spinning where, the sliver (soft twisted fiber rope) formed, is rotated upto 2500 revolutions per second to make yarn, which is then processed into the required cloth form, through weaving and dyeing processes. These fabrics are then stitched and sewed together in textile industries to make cotton bags.

Plastic is a by-product of oil refining process. Ethane and natural gas obtained during the process are used to get polyethylene, which is used for plastic formation. However, for the plastic bags, this polyethylene is treated as a resin and passed through the extrusion process along with the addition of different additives, to form the bag.

From Figure 2 we can observe the typical use case scenario of a shopping bag. This is how we shall outline the steps required to perform a life cycle assessment.

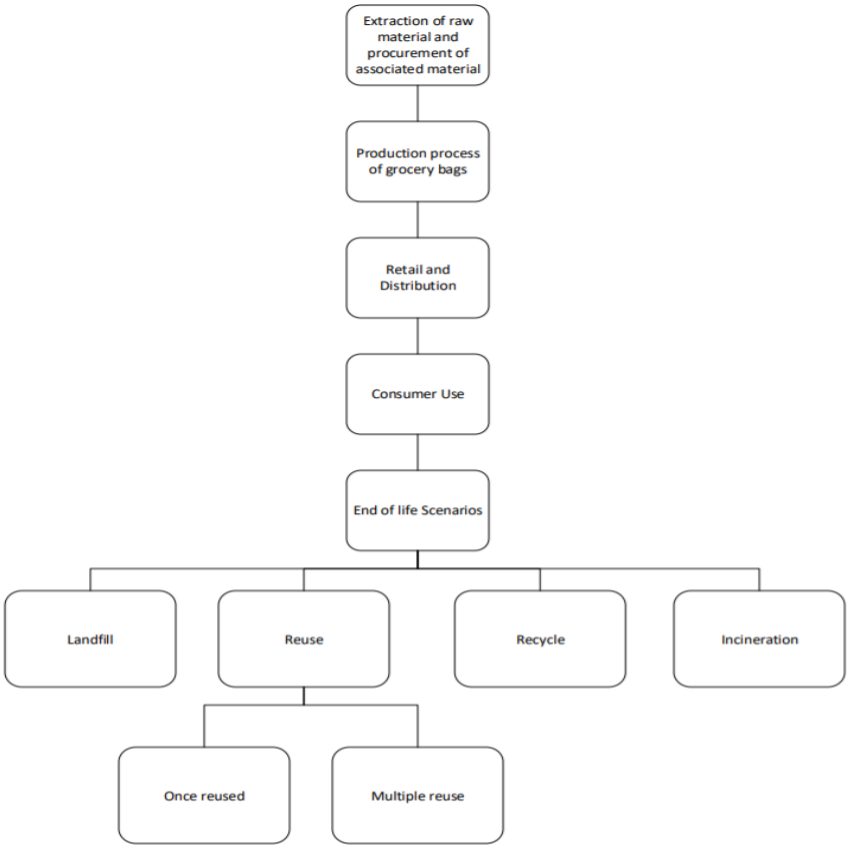

Figure 2: Lifecycle of a typical grocery bag

III. Analysis

The first stage shown in Figure 3 encompasses the following factors:

- The required amount of Oxygen produced or conversely the CO2 absorbed to reduce the global warming impact during production phase of the fiber used in grocery bags sans for LDPE which is a derivative product of crude oil.
- Whether resources utilized during the lifecycle of the grocery bag were of the renewable variety
- The amount of land covered for cultivation, production and distribution during the entire cradle to grave lifecycle of the particular grocery bag.
- Use of chemicals to produce fertilizers, pesticides, insecticides, herbicides etc.
- The recyclable potential of the material used in grocery bags
- The biodegradable nature of the material (Muthu and Li 2014)

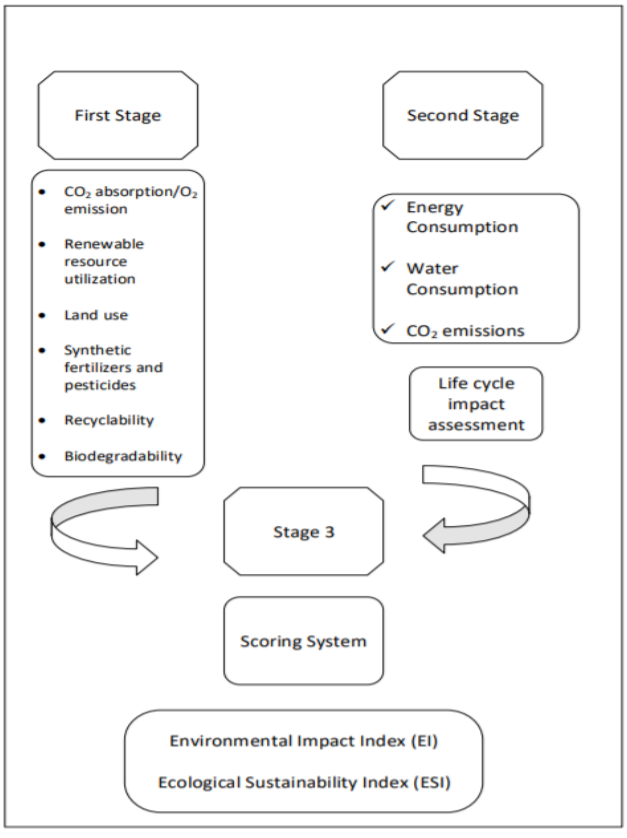

Figure 3:EI and ESI derivation model for grocery bag

Now, we know that among the issues that are needed to be tackled for sustainable development of human life, Energy consumption, Water consumption and Greenhouse gas emissions rank among the very top. The efficient use of these parameters will help to mitigate many of the adverse after effects that are influencing are our daily lives. Thus, we needed to study these very parameters in the lifecycle assessment of grocery bags, by delving deep into their Lifecycle Inventory. And hence, deriving multiple life cycle impact assessment categories in order to ascertain which of them are viable for ecological sustainability.

In the third and final stage, based on the scoring system associated with the factors in Figure 4, we calculated values for the Environmental impact index and Ecological Sustainability Index for the chosen materials. The mathematical expression for the same is as follows

$$EI = \sum \alpha j Yj \quad (1)$$

$$EI = \alpha 1Y1 + \alpha 2Y2 + \alpha 3Y3 + \alpha 4Y4 + \alpha 5Y5 + \alpha 6Y6 \quad (2)$$

$$ESI_k = \left(1 - \frac{EI_k}{EI_{max}}\right) \times 100 \quad (3)$$

Where,

EI = Environmental Impact index

EI_k= Environmental impact index of the kth fiber under consideration

EI_{max} = The gained maximum scores of Environmental impact index among the selected fibers

ESI = Ecological Sustainability Index

ESI_k = Ecological Sustainability Index of the kth fiber under consideration

α_j = Weighting coefficient for the jth factor(Which we consider one)

Y_1 = CO2 absorption/ O2 emission in fiber production ready for textile processing

Y_2 = Use of renewable resources in fiber production

Y_3=Land use in fiber production ready for textile processing

Y_4 = Usage of fertilizers and pesticides in fiber production

Y_5 = Fiber recyclability

Y_6 = Fiber biodegradability

Table 1: Scores allotted according to the scoring system

Fibre	Energy use in MJ per kg of material	Water requirement in liter per kg of material	Carbon Emission kg per kg of material
LDPE	80	58	1.9
Cotton	60	10000	6
Paper	10.83	116.25	2.4

Table 2: Energy, water consumption and carbon emissions per kg of material

Fibre	Value of Y1	Value of Y2	Value of Y3	Value of Y4	Value of Y5	Value of Y6
LDPE	5	5	3	1	5	5
Cotton	-5	-5	5	5	5	1
Paper	-2	0	5	0	5	0

Table 3: Calculated EI and ESI Scores

Fibre	EI	ESI
LDPE	24	0
Cotton	6	75
Paper	8	66.66

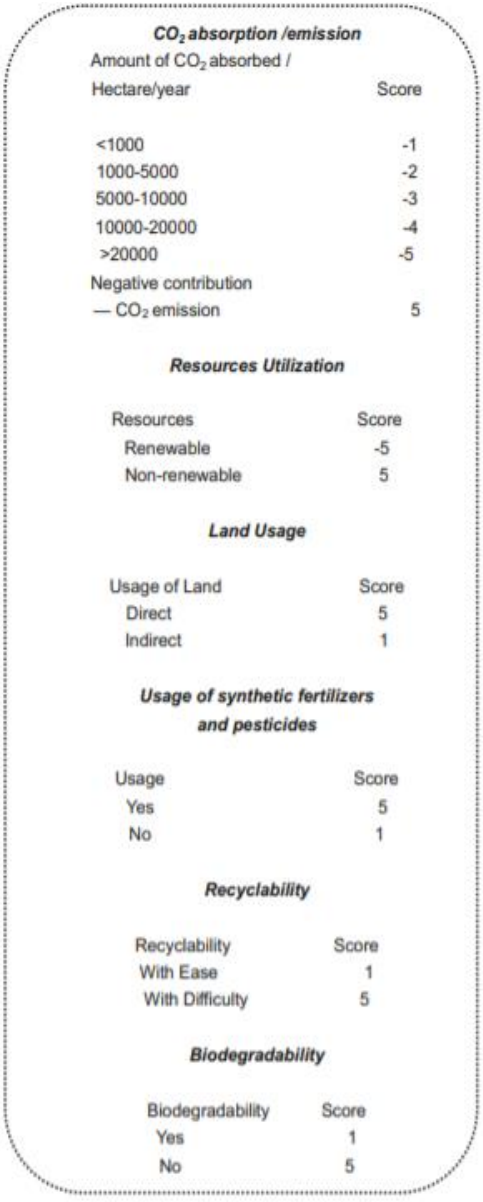

Figure 4: Scoring System

We can concur from the result in Table 3 that the lower Environmental Impact Index favors cotton bag owing to its biodegradability whilst LDPE has the highest for obvious reasons related to its end of life scenario. In contrast however, the Ecological Sustainability Index indicates a stark difference this is because of the resource intensive nature of the production stage of paper and cotton bags which does not hold true for plastic bags since its derived from crude oil and does not require as many resources.

The results of the survey, we conducted, showed that more than 80% of people are using LDPE bags as compared to Paper and Cotton bags. This is mainly down to the lack of availability of feasible alternatives, as quoted by 75% of the participants. If given a choice, more than 60% of the participants would choose Cotton bags and 20% would choose Paper bags while the remainder would still opt for LDPE bags. However, when questioned on how many times are participants likely to reuse each type of bag, their responses were not reasonable given the strength and durability of each type of bag. Figure 5 shows that a participant, on average, is willing to reuse a LDPE bag 37 times, Cotton bag 41 times and Paper bag 30 times. Since the Paper bag is vulnerable to water and LDPE bag lacks durability, it is highly unlikely they can be reused for the given number of times.

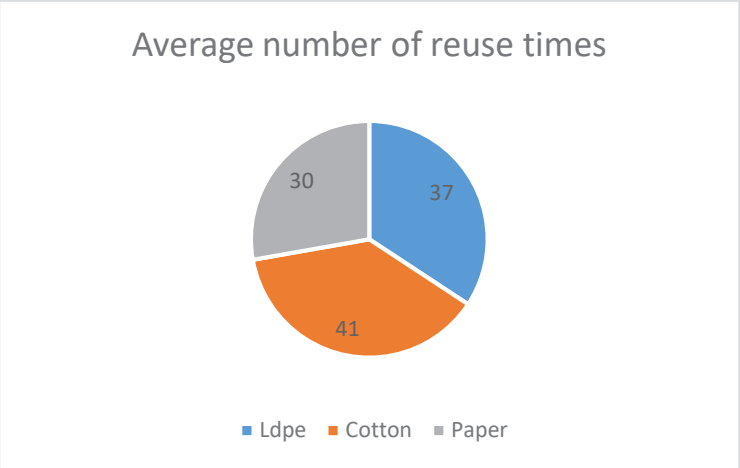

Figure 5: Average number of reuse times

IV. Results and discussion

Pakistan ranks 5th on the Global Climate Risk Index and so stands to face the severe effect of Climate change more than other countries. So, it is not an option anymore to consider alternative ways to reduce the Green House gas emissions but a necessity if we are to survive and prosper. Recently, the ban of single use plastic bag has been the highlight of the news and the use of Cotton and Paper bags have been recommended but few have actually considered the adverse effect Pakistan would face with the production and usage of these alternatives.

Some of the few major issues our society in Pakistan is facing are Energy and water shortages. Our LCA results have clearly indicated that Paper and Cotton bags utilize far more water and Energy than its competitor, LDPE bags. Furthermore, it needs to be considered that Cotton and Paper bags would require excess land to grow the raw material which in itself possess new problems for us as they would directly lead to food shortages and lack of Carbon Dioxide removal from atmosphere.

Given all the results of the LCA and the facts mentioned above, we recommend to lift the ban on single use LDPE bags. This recommendation is entirely dependent on the current issues Pakistan is facing which would make using Cotton and Paper bag far inferior alternative. At the same time, we also encourage concerned authorities to come up with a viable option to replace LDPE bags in near future since LDPE bags takes years to biodegrade and contributes to littering and harm marine life. But until a viable solution is not available, LDPE bags are the only option Pakistan has.

V. Conclusions

After a thorough study of the environmental impacts of paper bags, LDPE bags and cotton bags, the following results were deduced:

- Cotton production is a land and water intensive process. Keeping in view, the current issue of water shortage and that the land for it may be acquired through deforestation, makes the choice of cotton bags unfavorable. Also, cotton production has a greater GWP, followed by LDPE and then paper having the least impact.

- Production of paper requires the cutting down of trees hence, making paper bags a less suitable choice. Also, paper bags have less weight holding capacity.

Therefore, LDPE grocery bags remain the only viable choice since it can be made economically and be recycled into other products or even other reusable non-woven PP bags which itself makes a good argument for being more viable than LDPE.

.

References

(S.A), Wires & Fabriks. 2012. “Water-Meeting Paper’s Need.” www.wirefabrik.com.

Donato, Attilio Di. 2013. “Materials.” Manual of Spinal Endoscopy: A New Method for the Diagnosis and Therapy of Chronic Spinal Pain. 2013.

Laurijssen, Jobien. 2013. *Energy Use in the Paper Industry An Assessment of Improvement Potentials at Different Levels*.

Muthu, Subramanian Senthilkannan, and Yi Li. 2014. *Assessment of Environmental Impact by Grocery Shopping Bags*. EcoProduction. Singapore: Springer Singapore. https://doi.org/10.1007/978-981-4560-20-7.

Report, Pkistan Finance. 2019. “Pakistan Economic Survey.” www.finance.gov.pk.

valenb, and envdtudk. 2018. “Life Cycle Assessment of Grocery Carrier Bags.”

Comparative economic and exergoeconomic analysis of a hybrid cascade refrigeration system using ammonia-propane, propane-propylene and isobutane-propane refrigerant pairs

Kaushalendra Kumar Singh[a,b], Rajesh Kumar[b]*, Anjana Gupta[c]
[a]Department of Mechanical Engineering, Delhi Technological University, Delhi, India
[b]Department of Mechanical Engineering, G L Bajaj Institute of Technology and Management, Greater Noida, India
[c]Department of Applied Mathematics, Delhi Technological University, Delhi, India
E - mail: dr.rajeshmits@gmail.com

Abstract

In this paper, a comparative economic and exergoeconomic analysis of a cascade refrigeration system incorporated with a flash tank in its higher temperature cycle and a flash intercooler with indirect subcooler in its lower temperature cycle is done using ammonia-propane, propane-propylene and isobutane-propane refrigerant pairs. System is modelled on EES software and the analysis of total system cost rate is done followed by evaluation of exergoeconomic factors for different system components for the three natural refrigerant pairs. The results show that Ammonia-Propane is the most economical refrigerant pair while Isobutane-Propane possesses the maximum system cost rate.

Keywords: Cascade Refrigeration System, Flash Tank, Economical Analysis, Exergoeconomic factor Natural Refrigerant Pairs.

I. Introduction:

In recent decades, natural refrigerants have gained notable importance in the area of low temperature refrigeration applications because of their inherent properties of possessing negligible GWP and zero ODP. Although these refrigerants are eco-friendly in nature but their cooling potentials are not as good as synthetic refrigerants. 1 kg of R404A deliver 50% more cooling than that of 1 kg of ammonia (Froid, 2019). Therefore the performance of natural refrigerants should be worked upon in order to improve their cooling potential. Sarkar et al. (2013) worked on natural refrigerant couples by employing them on a cascade refrigeration system and they found that ammonia-propylene is the best pair for COP and propylene-carbondioxide is best for volumetric efficiency. Bakeem et al. (2018) investigated eight refrigerants in a two stage refrigeration system and results revealed that ammonia is the most favourable refrigerant for the system's thermodynamic performance. Sun et al. (2019) worked on a three stage cascade refrigeration system with different low GWP refrigerants and they suggested to use ethylene, ethane and ammonia in low, medium and high temperature cycles respectively. Sarbu et al. (2016) tried and tested various natural refrigerants in different refrigeration systems and stated that carbondioxide is the most promising natural refrigerant to be used for heat pump applications. Mosaffa et al.[6] compared the performance of two different flash tank configurations employed in a cascade system using ammonia-carbondioxide refrigerant couple and concluded that a cascade system incorporated with flash tank in HTC and flash intercooler in LTC is more efficient than that of the cascade system with flash tanks in both LTC as well HTC.

Above studies are based on comparative thermodynamic analysis of a system using different refrigerants or different systems using same refrigerant which give results that favour the system's thermodynamic performances. But these solutions may lead to excessive costs. The properties of refrigerants not only affect the system performance but also the size of system components and hence the overall system cost, therefore it is important to perform a comparative economic and exergoeconomic analysis in order to identify the refrigerants which are thermodynamically efficient and economical. Present work is focussed on identifying such natural refrigerant pair by performing a comparative economic and exergoeconomic analysis on a cascade refrigeration system employed with a flash tank in its higher temperature cycle and a flash intercooler with indirect subcooler in its lower temperature cycle which is a hybrid system that consists of a two stage refrigeration system with flash intercooler and a cascade refrigeration system. Therefore this system will be called hybrid cascade refrigeration system (HCRS) hereafter.

II. System description:

Figure 1(a) shows the schematic diagram of the HCRS. The evaporator (E) extracts heat from cold air by evaporating the LTC refrigerant which after getting compressed in LTC compressor I (L_1) gets intercooled in flash intercooler (FI) and gets subcooled after second compression in LTC compressor II (L_2) followed by condensation in cascade condenser (CC) and expansion in expansion valve I (EV I). The HTC refrigerant takes heat of LTC refrigerant in cascade condenser and rejects to the environmental air in the condenser (C) after being compressed in HTC compressor (H) and then comes back to the CC after passing through the expansion valve III (EV III) and flash tank (FT). Flash tank separates the flashes generated while expansion in EV III. Figure 1(b) shows the thermodynamic cycle on p-h diagram.

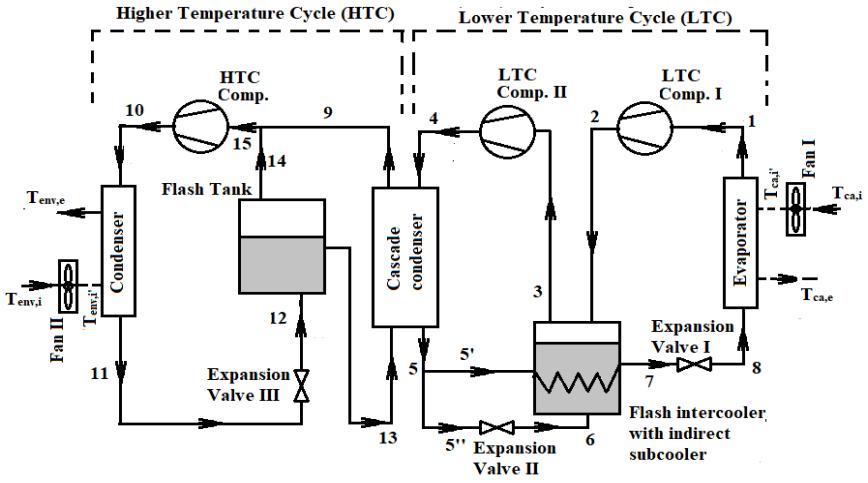

Fig. 1: (a) Schematic Diagram of HCRS, **(b)** Thermodynamic cycle on p-h diagram

Evaporator temperature (T_E), Condenser temperature (T_C), Cascade Condenser temperature (T_{CC}) and Cascade temperature difference (ΔT_{CAS}) are taken as -35 ^{0}C, 35 ^{0}C, 0 ^{0}C and 2 ^{0}C respectively and other system specifications are as taken in Mosaffa et al. (2016).

III. Mathematical Modelling:

Economic Model: Total system cost rate ($/yr) may be written as a sum of annual operational cost ($\dot{Z}_{op}$) and sum of annualized capital and maintenance cost of components ($\sum_k \dot{Z}_k$):

$$\dot{C}_{total} = \dot{Z}_{op} + \sum_k \dot{Z}_k \quad (1)$$

Where $\dot{Z}_{op}$ is :

$$\dot{Z}_{op} = N \times \dot{W}_{TOTAL} \times \alpha_{el} \quad (2)$$

Where *N* is the number of operational hours and α_{el} is cost of electricity in $/kWh. The capital and maintenance cost of k^{th} component can be annualized by following relation (Bejan et al., 1996):

$$\dot{Z}_k = Z_k \times \emptyset \times CRF \quad (3)$$

Where $\emptyset$ is the maintenance factor, The capital cost of k^{th} component (Z_k) can be calculated by the relations given in Table 3 and capital recovery factor (CRF) is expressed as (Bejan et al., 1996):

$$CRF = \frac{i(1+i)^n}{(1+i)^n - 1} \quad (4)$$

Where *i* and *n* are annual cost rate and system life time respectively.

Table 1: Capital Cost functions of different components (Mosaffa et al., 2016).

Component	Capital cost function (Z_k)
Evaporator and Condenser	$1397 \times A_{E\ or\ C}^{0.89}$
Cascade Condenser	$383.5 \times A_{CC}^{0.65}$
LTC compressors	$10167.5 \times \dot{W}_{L_1\ or\ L_2}^{0.46}$

HTC compressor	$9624.2 \times \dot{W}_H^{0.46}$
Flash Tank	$280.3 \times \dot{m}_i^{0.67}$
Flash intercooler	$1438.1 \times A_{FI}^{0.65}$
Expansion valves	$114.5 \times \dot{m}$
Fans	$155 \times (\dot{V} + 1.43)$
Installation charges	$150.2 \times \dot{Q}_E$

Where A is heat exchanger's surface area (Fettaka, 2013):

$$A = \frac{\dot{Q}}{UF\overline{\Delta T}} \quad (5)$$

Where $\dot{Q}$ is the heat transferred, U and $\overline{\Delta T}$ are the overall heat transfer coefficient and logarithmic mean temperature difference (*LMTD*) of the heat exchangers respectively. Other parameters shown in Table: 3 are same as that of ref. [6]. *F* is the correction factor of *LMTD* which has been determined by the expressions given by Fettaka et al. (2013)

Exergoeconomic Model: In exergoeconomic analysis exergy is considered to have some economic value. Each component of the system possesses some value of exergoeconomic factor which signifies the economic importance of that particular component in improving the overall performance of the system (Bejan et al., 1996):

$$f_k = \frac{\dot{Z}_k}{\dot{Z}_k + c_{f,k}(\dot{\chi}_{d,k})} \quad (6)$$

Where $\dot{\chi}_{d,k}$ is the exergy destructed and $c_{f,k}$ is the unit cost of fuel exergy for the k^{th} component and can be calculated by solving the exergy cost rate balance for k^{th} component, which can be expressed in general form as (Mosaffa et al., 2016).

$$\sum_e (c\dot{\chi})_k = \sum_i (c\dot{\chi})_k + \dot{Z}_k + \dot{Z}_{op_k} \quad (7)$$

Where c and $\dot{\chi}$ are the unit cost of exergy and exergy flow rate associated with the exergy stream at inlet and exit of k^{th} component (Mosaffa et al., 2016).

IV. Results and Discussions:

Model Validation: System is modelled on EES software and the model is validated from the data published in Ref.[6]

Table 2: Model validation from results of Mosaffa et al. (2016).

Parameters	Present Model	Mosaffa et al., 2016	% deviation
$\dot{C}_{total}$ $(M\$/Yr)$	0.554	0.675	17.94

The difference of 17.94% is due to the exclusion of environmental cost due to CO_2 leakage in the present analysis.

Economic Analysis: Figure 2(a) shows the variation of total cost rate with the evaporator temperature (T_E). It can be seen that the total annual cost initially decreases and after a certain value of T_E it starts to increase. This is because, as T_E is increased, keeping the other parameters constant, the difference between evaporator temperature and cascade condenser temperature reduces which leads to a reduction in pressure ratio of LTC compressors which further causes a reduction in LTC compressor's power demand and the system operational cost reduces. On the other hand, with the increase in T_E, the required evaporator surface area increases which increases the capital cost of evaporator. Initially the first factor dominates over the second and the overall cost rate decreases but after a certain value of T_E, second factor dominates the first one which results in a continuous increase in overall system cost.

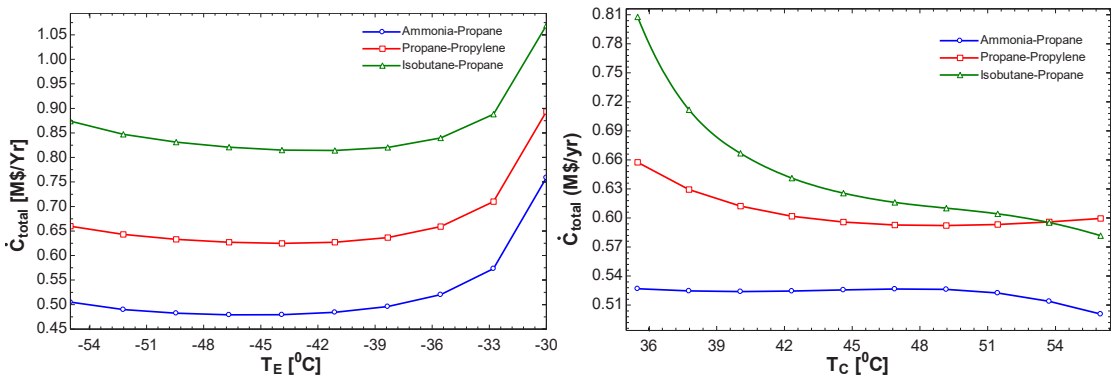

(a) **(b)**

Fig. 2: Variation of total system cost with- **(a)** Evaporator Temperature (T_E), **(b)** Condenser Temperature (T_C)

Figure 2(b) shows the variation of overall system cost rate with condenser temperature (T_C). As can be seen that the trends of variation of $\dot{C}_{total}$ with T_C is different for the three refrigerant pairs. There are two conflicting events which occur simultaneously with the increase in T_C. First is the increase in pressure ratio of HTC compressor caused by increase in temperature difference between HTC evaporator and condenser temperature which leads to an increase in power demand and hence the operational cost of the HTC compressor. Second event is the reduction in condenser surface area with increase in T_C, which leads to the reduction in capital and maintenance cost of condenser and overall system cost rate. These two conflicting facts dominate over each other in different ways in different refrigerant couples due to difference in thermophysical properties of refrigerants and results are as shown in Figure 2(b)

Exergoeconomic Analysis: The exergoeconomic analysis reveals that the value of exergoeconomic factor is 100% for flash tank. This is because flash tank operates on zero temperature difference resulting in zero exergy destruction. While it is minimum in expansion valves because of exergy destructions occurring due the irreversibilities involved in throttling process. A less amount of exergoeconomic factor for a component indicates that investing money to that particular component for its performance improvement is reasonable for the performance improvement of the overall system.

Table 3: Results of Exergoeconomic analysis of components for the three refrigerant couples:

Component	f_k (%)		
	Ammonia- Propane	Propane-Propylene	Isobutane-Propane
Evaporator	81.08	80.52	80.52
Condenser	81.68	94.67	97.29
Cascade Condenser	20.43	15.7	18.45
Flash Tank	100	100	100
Flash Intercooler	92.06	91.06	91.79
LTC comp. I	55.48	55.72	50.03
LTC comp. II	67.71	68.09	49.06
HTC comp.	120.8	128.8	57.53
Fan I	0.48	0.45	0.46
Fan II	0.55	0.52	0.53
Expansion Valve I	0.19	0.30	0.37
Expansion Valve II	37.5	37.5	4.14
Expansion Valve III	20.09	20.32	14.06

V. Conclusion:

After performing a comparative economic analysis of the three refrigerant couples following conclusions can be derived:

- The overall system cost rate of the system initially decrease and then increases with the increase in evaporator temperature.
- The exergoeconomic factor is maximum for flash tank and minimum for the expansion valves for all the three refrigerant couples.
- Ammonia-propane is the most economical refrigerant pair while propane-propylene is moderate and isobutane-propane possesses maximum overall system cost rate.

VI. References:

Baakeem, S.S., Orfi, J., Alabdulkarem, A., 2018. Optimization of a multistage vapor-compression refrigeration system for various refrigerants, Appl Therm Eng, 136, 84-96.
Bejan, A., Tsatsaronis, G., Moran, M.J., 1996. Thermal design and optimization. Wiley.
Fettaka, S., Thibault, J., Gupta, Y., 2013. Design of shell-and-tube heat exchangers using multiobjective optimization, Int J Heat Mass Transfer, 60, 343–354.
Froid, D.U., Selection of refrigerants according to applications: trends http://www.iifiir.org/userfiles/file/webfiles/indepth_files/Selection_refrigerants_Billiard_EN.pdf&ved=2ahUKEwi2tu_x18fmAhVPwTgGHSkKC5oQFjAAkEVyG4
Mosaffa, A.H., Farshi, L.G., Infante, Ferreira, C.A., Rosen, M.A., 2016. Exergoeconomic and environmental analyses of CO2/NH3 cascade refrigeration systems equipped with different types of flash tank intercoolers. Energ Convers Manage, 117, 442-453.
Sarbu, I. Sebarchievici, C., 2016. Substitution strategy of non-ecological refrigerants In: Zanol R, editor. Ground-Source Heat Pumps, Oxford: Academic press, 27-45.
Sarkar, J., Bhattacharyya, S., Lal, A., 2013. Selection of suitable natural refrigerants pairs for cascade refrigeration system, Proc IMechE Part A: J Power and energy, 227(5), 612-622.
Sun, Z., Wang, Q., Dai, B., Wang, M., Xie, Z., 2019. Options of low global warming potential refrigerant group for a three stage cascade refrigeration system, Int J Refrig, 100, 471-483.

Exergoeconomic Performance Evaluation of A PV/T Assisted Wastewater Source Heat Pump System

[1*]Mustafa Araz, [1]Arif Hepbasli, [2]Huseyin Gunerhan,
[1] Yasar University, Faculty of Engineering, Energy Systems Engineering Department, Bornova, İzmir, 35100, Turkey
[2] Ege University, Faculty of Engineering, Mechanical Engineering Department, Bornova, İzmir, 35100, Turkey

* E-mails: mustafa.araz@yasar.edu.tr, arif.hepbasli@yasar.edu.tr, huseyin.gunerhan@ege.edu.tr

Abstract
"In this study, the exergetic and exergoeconomical performance of a PV/T assisted wastewater source heat pump (WWSHP) system has been investigated. The system has been installed at Yasar University, Izmir, Turkey and the experiment was conducted in heating mode. In the first part of the study, conventional exergy analysis was employed using the gathered experimental results, where exergy destructions, efficiencies, relative irreversibilities and improvement potentials are obtained. After that, economic analysis was conducted to get the economic data related to each component of the system. Finally, the results of exergy and economic analysis were combined by using exergoeconomic methods. The highest relative irreversibility among all components occurred in the PV/T unit and is followed by the compressor. The functional exergy efficiencies of the WWSHP and whole system were found to be 0.10 and 0.15, respectively. The exergoeconomic factors of the condenser and WWHE were found to be considerably high among all components, which shows that the main driver of the cost associated with them are related to investment costs. On the other hand, the highest exergy loss per unit price is obtained in the PV/T system.

Keywords: wastewater, wastewater source heat pump, waste heat recovery, exergoeconomic analysis.

I. Introduction

Buildings have a pretty high share with 30% among the global energy consumption (IEA Buildings, 2018). Their share in the EU's total energy consumption is even higher (40%) where the buildings-related CO2 emissions are around 36%. (EU Buildings, 2018). As a consequence, some legislations had been implemented by the EU in recent years. One of these legislations is the Building Energy Directive, according to which all new buildings must be nearly zero energy buildings (nZEB) by December 31, 2020 (EU Buildings, 2018). To reach target, it is important to employ renewable energy applications to cover this energy consumption. Among the renewable energy sources, solar energy is one of the most promising solutions due to its availability and abundancy. Photovoltaic-thermal (PV/T) systems are one of the promising options among different solar energy technologies since they produce hot water and electricity at the same time and can serve to the thermal and electrical demand of the building at the same time. Many studies are available in the literature regarding the performance of PV/T systems.

Even covering some part of energy consumption is not solely enough to reach this target. Therefore, it is important to decrease the energy use of buildings of which the main share is related to the operation of HVAC-R equipment and energy losses from the buildings. According to a study in Switzerland (Schmid, 2009), 6000 GWh of energy is lost via WW every year and the heat loss with WW accounts to 15 % of the total demand of a traditional building. That shows us that any attempt to recover the heat available in WW is important. As a fact, the main characteristics of WW, having lower temperatures in summer and higher temperatures in summer compared to air, having less temperature fluctuations during the day and within the seasons, makes it a very suitable heat source for HPs (Zhou and Li, 2004). Many studies are available in the literature regarding PV/Ts and WWSHP systems. Review studies made by Yazdanifard and Ameri (2018) and Hepbasli et al. (2014) can be addressed for further information related to these topics.

In the present study, a PV/T assisted WWSHP system installed at Yasar University, Izmir, Turkey has been experimentally evaluated using exergoeconomical analysis method. Within this context, first, conventional exergy analysis has been adopted and exergy destructions, exergetic efficiencies, relative irreversibilities and improvement potentials of each system component is calculated. After that, economical analysis were conducted, where the cost rate for each component are calculated taking the time value of money into account. Lastly, these two (conventional exergy and economic analyses) are combined using the so called specific exergy costing (SPECO) and exergoeconomical factors for each component are obtained. The EXCEM (Exergy, cost and energy and mass) method is also applied to the system to see the exergy losses that occur in each equipment per unit price. Considering the literature survey and to the best of the authors' knowledge, this contribution was the first attempt towards applying the SPECO and EXCEM methods to a PV/T assisted WWSHP system based on actual operational data in the open literature.

II. Experimental Procedure/Methodology/System Description

The schematic and pictures of the WWSHP system are given in Fig. 1. As it can be seen from the figure, there are multiple heat exchangers and compressors in the system and they are put in operation depending on the operation mode. In the present study, heating mode was selected and therefore valves 1, 3, 6, 8, 10-13 and 16 were open while the rest were closed. The AC type compressor and plate type WWHE were used during the experiment, while water source HE, which is connected to the fan-coil unit, is used as the condenser. In the WW sub-system two 500-L WW tanks are employed to since there was no access to local sewage system. WW is circulated from one to the

other and during this circulation it passes through a WWHE where it absorbs/rejects heat from/to the intermedium cycle. The temperature of WW is kept constant during the whole experiment using an electrical heater and a cooling coil.There were also five serial-connected PV/T units which are used to heat the water in the intermedium cycle and generate some amount of electricity and cover some part of system's electricity consumption. During the operation, the refrigerant (R-134a) is first compressed by the compressor and sent to the condenser to heat the water in the end-user cycle. The heated water is then sent to the fan-coil unit using a circulation pump and release its heat content to the indoor environment. After the condenser, the refrigerant enters to the expansion valve where it is expanded to the evaporation pressure. The electronic expansion valve has a pressure and a temperature sensor, which are used to determine the superheating degree and regulate the valve. After the expansion valve the refrigerant enters the evaporator to absorb heat from the intermedium cycle water and evaporate with some superheating. As a consequence the temperature of the intermedium cycle water decreases and enters the WWHE to absorb heat from WW. All the necessary data including temperatures and pressures of the fluids and their flow rates, power consumptions of all equipment with a motor and meteorological data were measured continuously and recorded in the data loggers during the experiment.

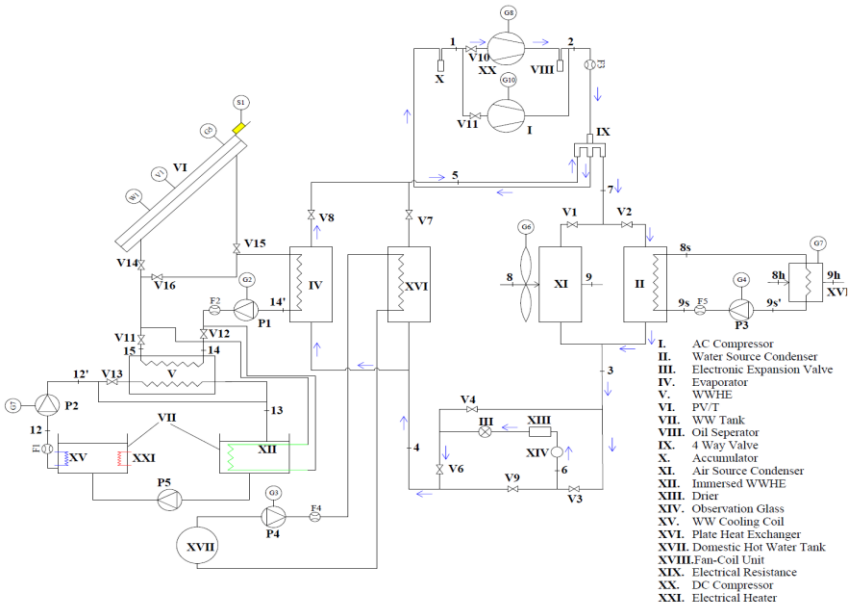

Fig. 1: Schematic of the WWSHP system.

III. Analysis

The assumptions used in the analyses are as follows:
(a) All processes are at steady state and potential and kinetic energy changes are negligible with no chemical interactions, (b) Air is an ideal gas at the given conditions, (c) The pressure losses in the evaporator, WWHE, kondenser and PV/T are taken as 10, 10, 20 and 30 kPa, respectively, (d) Heat losses in the heat exchangers are considered to be negligible, (e) Compressor, fan and pumps are taken along with their motors in exergy analyses, (f) Electrical and mechanical efficiencies of the pumps are taken as 0.88 and 0.82, respectively. (g) The electrical and mechanical efficiency of the fan is taken as 0.80 and 0.40, respectively, (h) The interest rate, salvage value, lifetime of the WWSHP system and operation hours are assumed as 0.01, 0.15, 20 years and 3000 h/year, respectively, while the operation and maintenance costs are taken was 3% of the total capital investment, (i) The unit cost of electricity is taken as 0.1 €/kWh and costs of auxiliary equipment are distributed to other main components, (j) The dead state temperature and pressure are taken as 9 °C and 101.325 kPa, respectively.

General mass, energy and exergy balance equations, which can be found in Cengel and Boles (2008), are applied to all system components. T the so-called product/fuel based exergy efficiency is used for the evaluations(Dincer and Rosen, 2013).

$$\psi = \frac{\sum \dot{Exergetic\ Product}}{\sum \dot{Exergetic\ Fuel}} = \frac{\sum \dot{P}}{\sum \dot{F}} \tag{1}$$

On the other hand for the general system (WWSHP and the whole system) assessment functional exergy efficiencies are used.

$$\psi_{WWSHP} = \frac{\dot{E}x_8 - \dot{E}x_9}{\dot{W}_{comp,elec}} \quad and \quad \psi_{sys} = \frac{\dot{E}x_{9h} - \dot{E}x_{8h} + \dot{W}_{PV/T}}{\dot{W}_{total} + \dot{E}x_{sol}A_{PV/T}} \tag{2}$$

Other exergetic performance indicators such as the relative irreversibility (RI), improvement potential (IP) and sustainability index (SI), which can be found elsewehere (Dincer and Rosen, 2013), are also used for the analysis. For the exergoeconomic analysis, specific exergy costing (SPECO) and exergy, cost, energy and mass (EXCEM) methods are employed. By the SPECO method, first an economic analysis is made taking into account the time value of the money. The equations used for that can be found in (Balli and Hepbasli, 2014) and will not be given here. After that general exergoeconomic balance equation given in Eq. 4 is applied to all components (Bejan et al.,

1996; Lazzaretto and Tsatsaronis, 2006):

$$\sum_e \left(c_e \ . \dot{E}x_e\right)_k + c_{w,k} \ \dot{W}_k = c_{q,k} \ . \dot{E}x_{q,k} + \sum_i \left(c_i \ . \dot{E}x_i\right)_k + \dot{Z}_k \quad (3)$$

where c_i, c_e, c_w, and c_q denote average costs per unit of exergy. This general balance equation is used to find unit cost of fuel and product and exergy destruction costs for each equipment. The equations for these parameters can be found in Bejan et al., 1996 and will not be repeated here. The main indicator used in the SPECO method is the exergoeconomic factor and can be calculated as follows (Bejan et al., 1996; Lazzaretto and Tsatsaronis, 2006):

$$f_k = \frac{\dot{Z}_k}{\dot{Z}_k + c_{F,k}\left(\dot{E}x_{dest,k} + \dot{E}x_{loss,k}\right)} \quad (4)$$

For the EXCEM method, the indicator that was used is the ratio of the thermodynamic loss divided by the the capital cost and expressed as follows (Dincer and Rosen, 2013):

$$\dot{R}_{ex,k} = \frac{\dot{L}_{ex,k}}{K} \quad (5)$$

IV. Results and discussions

In the first part of the study, standard exergy analysis have been implemented to the system, the results of which are listed in Table 1. According to these results, the lowest exergy efficiency is occurred in the PV/T, while the highest among all was the expansion valve. When we compare the relative irreversibilities we see that the WWHE has the lowest RI value, followed by the expansion valve, fan-coil pump and the condenser, while the highest RI occurred in the PV/T system. The compressor is found to be the main component that causes irreversibilities in the heat pump unit, which is mainly related to the electrical and mechanical losses that happen in it. The product/fuel based exergy efficiencies of the WWSHP and the entire system were 0.66 and 0.49, while their functional exergetic efficiencies were obtained as 0.15 and 0.10, respectively. On the other hand, according to the sustainability index results, the expansion valve and condenser were the most sustainable components regarding their exergetic performance.

Table 1. Results of the exergy analysis.

Component	$\dot{P}$ (kW)	$\dot{F}$ (kW)	$\dot{E}x_{dest}$ (kW)	$\dot{I}P$ (kW)	RI_{WWSHP} (%)	$RI_{overall}$ (%)	φ	φ (Eq.2)	SI
Compressor	0.778	1.687	0.909	0.490	77.87	32.17	0.46	-	1.86
Evaporator	0.400	0.490	0.090	0.017	7.75	3.20	0.82	-	5.34
Expansion Valve	0.591	0.673	0.082	0.010	7.01	2.90	0.88	-	8.22
Condenser	0.536	0.622	0.086	0.012	7.37	3.05	0.86	-	7.81
WWHE	0.009	0.025	0.016	0.010	-	0.56	0.36	-	1.37
Fan-coil unit	0.254	0.611	0.357	0.208	-	12.63	0.42	-	1.67
WW pump	0.012	0.141	0.129	0.118	-	4.56	0.09	-	1.10
Intermedium Water pump	0.014	0.167	0.153	0.140	-	5.41	0.08	-	1.09
Fan-coil Pump	0.017	0.095	0.079	0.065	-	2.79	0.17	-	1.19
PV/T	0.097	1.022	0.924	0.836	-	32.73	0.10	-	1.10
Heat pump unit	2.305	3.472	1.167	0.528	100.0	41.31	0.66	0.15	2.98
Overall system	2.708	5.533	2.824	1.906	-	100.0	0.49	0.10	1.95

In the second part of the study, hourly levelized equipment costs and exergy destruction cost rates are calculated using the fuel and product definitions. The results are shown in Fig.2 where one can observe that the widths in the WW sub-system are very narrow compared to that of the end user sub-system. This happens because the temperatures in the WW cycle are very close to the dead state temperature and as a consequence their exergy rates are very small.

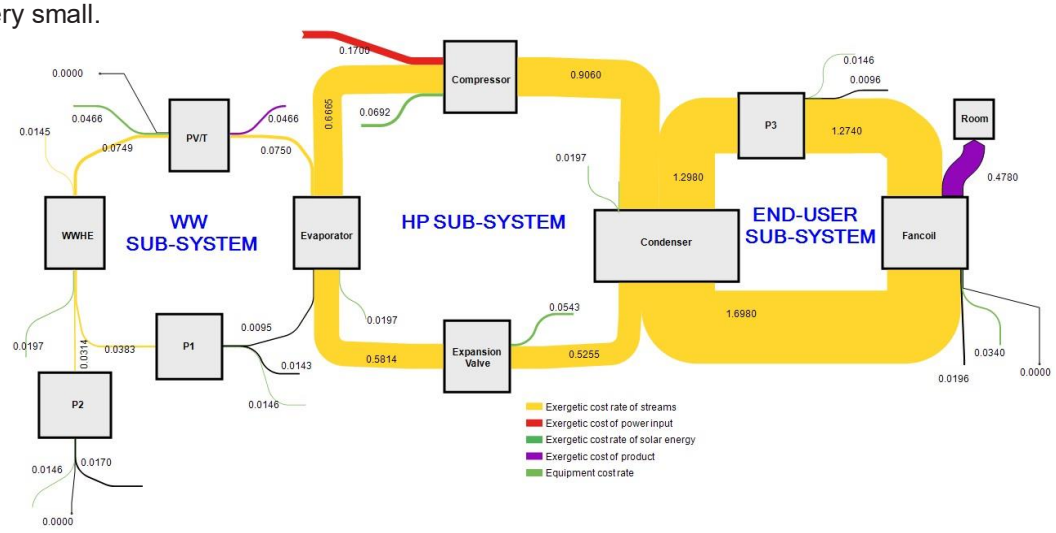

Fig. 2. Cost flow diagram of the WWSHP system.

Exergoeconomic factor (f_c) and R_{ex} values are then calculated for all components and the entire system, the results of which are given in Table 2. As it can be seen the highest exergoecomic factor occurred in the condenser, while the fan-coil unit had the lowest value. In general it can be said that for components with low f_c values, such as the evaporator and fan-coil unit, the exergy efficiency of them can be increased by selecting better components at the expense of the investment cost. For the components with high f_c values it might be meaningful to choose cheaper components, although it would probably result in an increase in the exergy destruction of those components. The fc value for the PV/T unit was found as 1. This is an expected result since the only fuel of the PV/T system is the sun and it costs nothing (c_{sol}=0). Therefore it can be said that exergoeconomic factor for the PV/T is not a valid indicator. To understand the effect of the PV/T technology and efficiency on the exergoeconomics, R_{ex} term can be used. When we compare the results of each component we directly see that that of the PV/T unit is the highest. This means the exergy losses of the PV/T unit is really high with respect to its capital cost. The WWHE had the lowest R_{ex} value and it is followed by the electronic expansion valve with 0.49 W/€ . The compressor and fan-coil unit were the components with the highest Rex values after the PV/T.

Table 2. Exergoeconomic factor and EXCEM results.

Component	Comp.	Evap.	Exp. Valve	Cond.	WWHE	Fan-coil	PV/T	P1	P2	P3	Entire System
f_c (-)	0.43	0.22	0.47	0.70	0.61	0.11	1.00	0.53	0.49	0.64	0.36
R_{ex} (W/€)	4.37	1.55	0.49	1.33	0.33	3.56	6.65	2.94	3.49	1.84	3.06

V. Conclusions

High amounts of thermal energy is lost from buildings and industry to sewerage system through WW, which presents proper characteristics for the use in heat pumps. There are numerous applications with different capacities, from 10 kW to 20 MW, all around the World. In the present study, an attempt has been made to understand the exergoeconomic analysis of WWSHP systems. Within this context, a PV/T assisted WWSHP system was analyzed using experimental data and exergy and exergoeconomic analysis methods. The results revealed that the functional and product/fuel based exergy efficiencies of the WWSHP were found to 0.15 and 0.66, while that of the entire system were 0.15 and 0.49, respectively. The exergoeconomic factor values of the condenser and WWHE were found to be considerably higher, meaning that an attempt can be made to replace them with cheaper products at the expense of higher exergy destruction rates. The PV/T unit had the highest exergy destruction rate per unit price. For further studies, the effect of regional parameters, such as the yearly working period and interest rate, on the exergoeconomic factors and specific exergy cost of the product will be studied parametrically. Also, environmental effect of the system will be estimated using exergoenvironmental analysis.

Acknowledgements

The authors would like to thank The Scientific and Technological Research Council of Turkey (TUBITAK) for financial support given to the project entitled “Design, Construction and Experimental Investigation of a Novel Solar Photovoltaic/Thermal (PV/T)-Assisted Wastewater Heat Pump System (113M532)”.

References

Balli, O., Hepbasli, A., 2014. Exergoeconomic, sustainability and environmental damage cost analyses of T56 turboprop engine, Energy, 64, 582-600.
Bejan, A., Tsatsaronis, G., Moran, M., 1996. Thermal Design and Optimization, New York: John Wiley & Sons, Inc.
Cengel, A.Y., Boles M A., 2008. Thermodynamics: an engineering approach, New Media Version, 6th edition. McGraw Hill, Inc., New York.
Dincer, I., Rosen, M.A., 2013. Exergy, Energy, Environment and Sustainable Development, 2. Edition. Elsevier, United Kingdom.
EU Buildings, https://ec.europa.eu/energy/en/topics/energy-efficiency/buildings (Access Date: 10 March 2018).
Hepbasli, A., Biyik, E., Ekren, O., Gunerhan, H., Araz, M., 2014. A key review of wastewater source heat pump (WWSHP) system, Energy Convers. Manag., 88, 700-722.
IEA Buildings, https://www.iea.org/buildings/ (Access Date: 2 October 2018).
Lazzaretto, A., Tsatsaronis, G., 2006. SPECO: A systematic and general methodology for calculating efficiencies and costs in thermal systems, Energy, 31, 1257-1289.
Schmid, F., 2009. Sewage water: Interesting heat source for heat pumps and chillers, Swiss Energy Agency for Infrastructure Plants, Zürich, Switzerland.
Yazdanifard, F., Ameri, M., 2018. Exergetic advancement of photovoltaic/thermal systems (PV/T): A review, Renew. Sustain. Energy Rev., 97, 529-553.
Zhou, W.Z., Li, J.X., 2004. Sewage heat source pump system’s application examples and prospect analysis in China, International Refrigeration and Air Conditioning Conference, Purdue, USA.

Experimental Study on a Thermoacoustic-Stirling Engine with Acoustic Field Adjustment

[1]Patcharin Saechan, [2*]Isares Dhuchakallaya
[1] Department of Mechanical and Aerospace Engineering, Faculty of Engineering,
King Mongkut's University of Technology North Bangkok, Bangsue, Bangkok, 10800, THAILAND
[2] Department of Mechanical Engineering, Faculty of Engineering,
Thammasat University, Klong-Luang, Pathumthani, 12120, THAILAND

* E-mails: disares@engr.tu.ac.th

Abstract

The simulation and experiment of a thermoacoustic Stirling heat engine (TASHE) with a phase-adjuster are the main scope of this study. The acoustic field can be adjusted by using the phase-adjuster, therefore the thermoacoustic engine could maintain a good performance. The core components of prototype comprising of an ambient heat exchanger, regenerator, hot heat exchanger and feedback pipe, were located in the torus section. Besides, there was a resonator pipe, connecting to the torus, which acts as compliance to maintain the system stability. The phase-adjuster was installed at the end of the resonator. Firstly, the TASHE was modelled by DeltaEC to search the optimal configurations of the prototype. Due to the variations of acoustic load or operating condition from the design criteria, the engine absolutely cannot provide maximum output power. The proposed phase-adjuster could bring back its maximum efficiency by re-matching the frequency. In the experiments, the self-excited temperature of the TASHE was around 482°C, and the steady-state temperature is 397°C. The TASHE can provide an acoustic power up to 40 W. The thermo-to-acoustic efficiency of 12.03%, corresponding to the relative Carnot's efficiency of 22.56% was achieved. There was a fairly good agreement between the measured results and the DeltaEC simulated results. This can reflect on the preciseness of the proposed model. Furthermore, the function of phase-adjuster in tuning the resonance frequency is also demonstrated. In case of the TASHE being operated under the undesired conditions, i.e. due to pressure leak or heat loss, these scenarios would drop the efficiency of the system. Phase-adjuster can improve the efficiency of such consequences.

Keywords: "Heat engine, Oscillating flow, Phase-adjuster, Stirling, Thermoacoustic"

I. Introduction

Thermoacoustic engine is one of the novel heat engines. It has the potential to utilise renewable energy or low-grade thermal energy in a power generation. Thermoacoustic effect is the thermodynamic interactions between working fluid and adjacent solid in the presence of temperature gradient. Under an appropriate phase of acoustic impedance, thermal energy can be converted to acoustic energy or vice versa. The working fluids can be inert gases. These gases are eco-friendly that are non-toxic, non-flammable, non-ozone depleting.

Thermoacoustic engine can be divided into standing-wave and travelling-wave engines based on the phase shift of oscillated pressure and velocity. The standing-wave engine has 90° out-of-phase, and the latter is in-phase manner. The concept of the travelling-wave engine is that the gas-solid interaction resembles a Stirling cycle. The isothermal heat transfer occurred within the regenerator is a reversible process which leads to higher efficiency.

A thermoacoustic-Stirling heat engine (TASHE) proposed by Backhaus and Swift (2000) was claimed as the most efficient thermoacoustic engine. It was designed to improve the drawback of a looped-tube travelling-wave engine of Yazaki *et al*. (1998) by adding a tail resonator to a loop section. This topology can provide a relative Carnot's efficiency up to 41%. For the extended research, many scientists focus on the practical implementation with various geometrical configurations of such engines, for example, a hot air driven TASHE (Tijani and Spoelstra, 2013), two-stage thermoacoustic electricity (Hamood *et al.*, 2018), multi-stage TASHE (Hu *et al*., 2018), travelling-wave refrigerator driven by multi-stage thermoacoustic engine (Sharify and Hasegawa, 2017), etc.

Generally, thermoacoustic engines have been designed with maximum efficiency. It must be understood that the systems might be operated at lower performance subject to the change of operating conditions or acoustic loads throughout the operation periods. These variations certainly disturb the acoustic field of the system, i.e. acoustic pressure, velocity, or the phase difference between them. In past research, these issues have not been taken into account. Therefore, this study attempts to explore a prototype of TASHE which can adjust the acoustic field of the system. The acoustic impedance can be controlled by adjusting the volume of the resonator tube. An in-line phase-adjuster is then invented for such a purpose. This concept would significantly improve the system performance and beneficially maintain the system at a high-efficiency level. Here, the capability of phase-adjuster is demonstrated through the simulation and experiment.

II. Conceptual design

The schematic diagram of the TASHE with the phase adjuster is shown in Fig. 1. The core components were located in the torus section. It built up from a regenerator (REG) sandwiched by a hot heat exchanger (HHX) and an ambient heat exchanger (AHX). Thermoacoustic conversion process takes place in the REG. The HHX and AHX act as the heat source and heat sink, respectively, to induce a temperature gradient along the REG for generating a spontaneously acoustic wave. The acoustic wave is amplified by forcing the working gas in the REG to accomplish a Stirling-like thermodynamic cycle. To keep the thermoacoustic effect continuing, some amount of acoustic power was then fed back via the "feedback pipe" to the thermoacoustic core. A secondary ambient heat exchanger (2nd AHX) was included in the system to remove the surplus heat from hot gas leaving the HHX. A thermal buffer tube (TBT) was located between the HHX and 2nd AHX and used as a thermal cushion. Besides, there was a T-junction applied to connect the torus section and a quarter-wavelength acoustic resonator. The resonator tube consisted of two sections of pipes with different diameters: DN 100 (4 inches) and DN 150 (6 inches), and there was a transitional cone between them.

Theoretically, the REG should be located close to the velocity node, in which the impedance phase shifts from +90° to −90° or vice versa. The impedance phase being zero at the REG is called the "sweet spot" (Gardner and Swift, 2003). Thus, the thermoacoustic core is necessary to be fitted within the sweet spot zone in which $\phi_z \approx \pm 45°$. It provides high energy conversion because of the travelling-wave phasing and high acoustic impedance. However, the sweet spot might be moved out the thermoacoustic core, as the operating conditions e.g. pressure, temperature, and acoustic load are changed on purpose or by chance which differs from the design. These off-design operations definitely deliver a lower efficiency. Therefore, to adjust the sweet spot region is necessary to improve the efficiency of the system.

Firstly, the prototype of the TASHE with phase-adjuster was modelled and optimised by DeltaEC program (Ward *et al.*, 2008). The calculation was executed under the operating conditions as follows: working gas was compressed air at 8 barg, the heat source and heat sink temperatures were set at 425°C and 27°C, respectively. With the designed length, the operating frequency was about 44 Hz. The phase-adjuster was mounted at the end of the resonator as shown in Fig. 1. By changing its length, the volume of the resonator can be adjusted manually. This was used to fine-tune the acoustic field in the REG, resulting to improve the thermo-to-acoustic efficiency of the TASHE. As the operating frequency was changed, the sweet spot was then shifted.

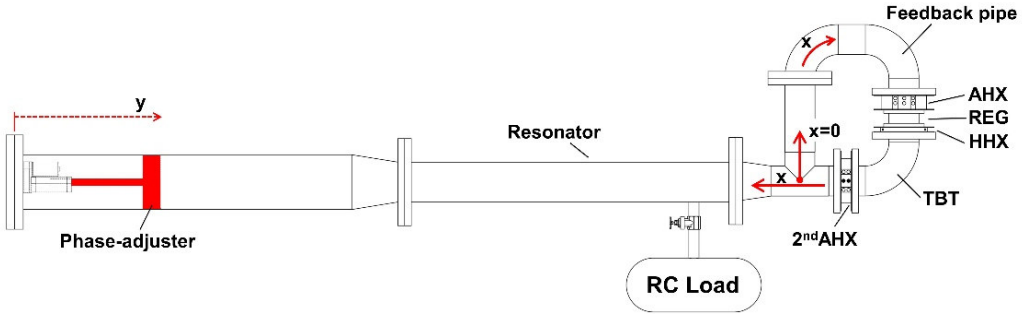

Fig. 1: Schematic diagram of the TASHE with phase-adjuster.

III. Experimental Apparatus and Measurement Setup

The prototype of the TASHE with the phase adjuster was assembled as designed by DeltaEC. The feature of this apparatus is shown in Fig. 2, and the specifications of each component are presented in Table 1. The REG was made out of stainless mesh screen which had 120 mesh with 0.081 mm wire diameter. The HHX contained three, 220 V heat cartridges inserted in; each heat cartridge was 6.35 mm in diameter, 140 mm in length and capable of producing up to 450 W of heat. The hot part of the engine, including the REG and HHX, were covered by thermal insulation materials to reduce the thermal losses.

Type-K thermocouples were probed in the hot part and along the two AHXs to monitor the temperature distribution. As shown in Fig. 2, seven high accuracy piezoelectric pressure transducers (PCB Piezotronics, PCB113B28), labelled P1–P7, were installed along the system to measure the pressure amplitude, frequency, and phase. This measured data delivers the details of acoustic field flowing in the system.

The acoustic power flowed through the resonator was determined by the two-microphone technique (Fusco *et al.*, 1992). The acoustic power can be approximated from:

$$\dot{E}_2 = \frac{A}{2a\rho_m \sin(\omega\Delta x/a)}\left(Im\left(p_A \tilde{p}_B\right)\left\{1-\frac{\delta_v}{2r_0}\left[1-\frac{\gamma-1}{\sqrt{\sigma}}+\left(1+\frac{\gamma-1}{\sqrt{\sigma}}\right)\frac{\omega\Delta x}{a}\cot\left(\frac{\omega\Delta x}{a}\right)\right]\right\}\right.$$
$$\left. +\frac{\delta_v}{4r_0}\left(|p_A|^2-|p_B|^2\right)\left[1-\frac{\gamma-1}{\sqrt{\sigma}}+\left(1+\frac{\gamma-1}{\sqrt{\sigma}}\right)\frac{\omega\Delta x}{a}\csc\left(\frac{\omega\Delta x}{a}\right)\right]\right) \quad (1)$$

where Δx is the distance between transducers, A is the cross-sectional area, r_0 is duct radius, and δ_v is viscous penetration depth. To assess the TASHE performance, the relative Carnot's efficiency is defined as:

$$\eta_{Rel} = \frac{\eta_{th}}{\eta_C}. \quad (2)$$

where η_{th} is the thermo-to-acoustic efficiency, given as the fraction of the acoustic power generated by the TASHE to the thermal power supplied to the HHX, and η_C is the Carnot's efficiency.

Table 1. Specifications of the TASHE with the phase adjuster.

Parts name	Design features	Diameter (mm)	Length (cm)	Porosity
AHX	Aluminium cross-flow HX	83	4	27%
REG	Stainless steel mesh screens	83	5	66%
HHX	Stainless steel cross-flow HX	83	1.2	37%
2nd AHX	Aluminium cross-flow HX	83	3	41%
Main resonator	4 inch steel pipe	108	150	-
2nd resonator	6 inch steel pipe	154	250	-
Phase-adjuster	Linear actuator with piston	154	0-100	-

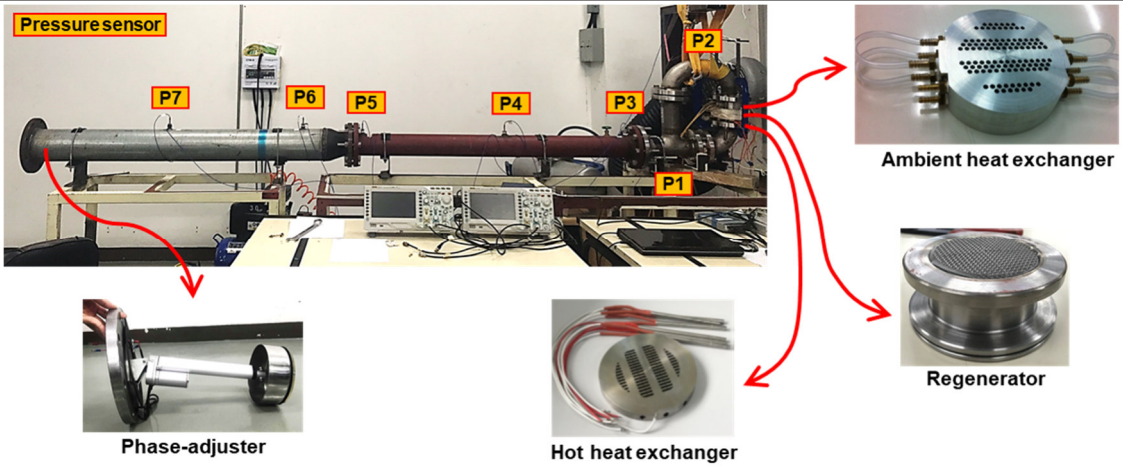

Fig. 2: As-built Stirling thermoacoustic engine and its components.

III. Results and discussions

Fig. 3 shows the development of pressure and temperature during the onset process. Compressed air at 8 barg was used as working fluid, and heating power was set at 1.7 kW. The acoustic oscillations started after the temperature difference between two ends of the REG exceeded the onset temperature gradient. Here, a self-excited oscillation was detected at the onset temperature of 481.6°C, and a large pressure oscillation was generated promptly. This oscillation encouraged the forced convection from hot to cold sides of the REG, resulting in a drop in the slope of the hot end temperature. After reaching a steady state at a temperature of 397.3°C, the resonance frequency of 37.40 Hz was measured.

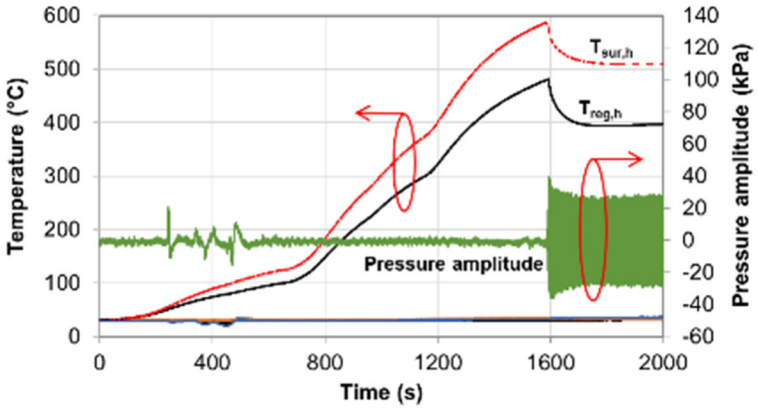

Fig. 3: The time history of measured pressure and temperature of the system during the onset process.

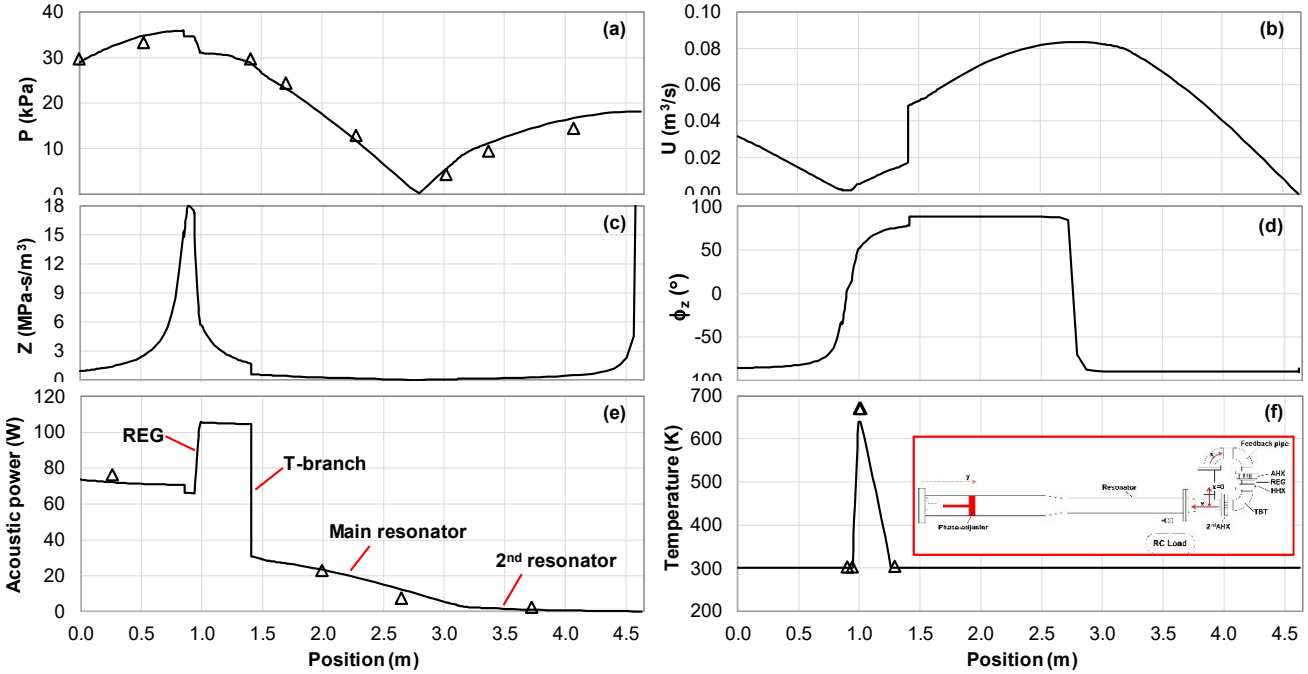

Fig. 4: Acoustic field distribution along the system: **(a)** pressure amplitude; **(b)** volumetric velocity amplitude; **(c)** acoustic impedance; **(d)** phase of acoustic impedance; **(e)** acoustic power; and **(f)** gas temperature.

Fig. 4 shows the simulation and experimental results of the acoustic field flowing along the system. The coordinate *x* started from the T-branch junction as shown in Fig. 1. The REG was located in the high impedance zone, and the phase of impedance was 18.8°, which was in the range of the sweet spot region, where $\phi_z \approx \pm 45°$. A steep rise of velocity amplitude occurred at the T-junction due to the separation flow to the torus and resonator. The acoustic power generated in the REG was 39.8 W, corresponded to the energy conversion efficiency of 12.03%, or relative Carnot's efficiency of 22.56%.

The comparisons of the prediction and measured results are also shown in Fig. 4. The measurement of pressure amplitude, acoustic power and temperature in each location were in good agreement with the predicted results, except the hot-end temperature in the thermoacoustic core. This might be because the heat losses were not taken into account in the DeltaEC. However, the proposed model can predict the crucial features of the TASHE. Thus, this simulation can boost confidence for further improvement of the prototype.

In order to assess the effect of phase-adjuster, the as-built TASHE was further investigated in the off-design operating conditions. In Fig. 5, when the gas pressure of system decreased or the heating temperature of the HHX decreased, the optimal length of phase-adjuster at *y*=0.5 m could no longer provide the maximum efficiency. The increase of phase-adjuster length was required to improve the energy conversion efficiency in case of decreasing the pressure, or vice versa in case of temperature. This might be that the sweet spot was shifted to the AHX side, when the mean pressure increased, and it was moved to the HHX side, when the heating temperature increased. The illustrated results clearly show that the proposed phase-adjuster can effectively tune the phase difference in the REG, leading to recover the efficiency of the TASHE being operated in the off-design conditions.

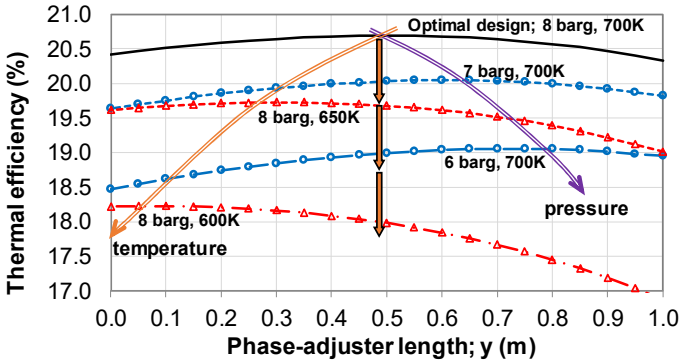

Fig. 5: The effect of phase-adjuster on the relative Carnot's efficiency as the operating conditions changed.

V. Conclusions

The numerical and experimental analysis of the TASHE with in-line phase-adjuster was presented. The new concept of the thermoacoustic engine proposed is that the acoustic network in the REG can be adjusted to respond to the variation of external loads and operating conditions. The optimum length of phase-adjuster could improve the efficiency of the system, which the high impedance and travelling wave phasing zone are found in the REG.

According to the comparison results, the experimental results, i.e. pressure amplitude, acoustic power and temperature, agreed with the prediction results. The REG was located in the sweet spot zone, in which the engine offers a high energy conversion efficiency. The acoustic power of 39.8 W was produced, corresponding to the relative Carnot's efficiency of 22.56%. Furthermore, the performance improvement of the TASHE operated in the off-design conditions was discussed. When the operating pressure or temperature is changed from the design, the acoustic field in the REG is also changed, resulting in lower efficiency. The phase-adjuster can practically shift the sweet spot in the REG to improve the efficiency of the system.

Acknowledgements

The authors gratefully acknowledge the financial support provided by Thammasat University Research Fund under the TU Innovative Scholar, Contract No. 4/2560.

References

Backhaus, S., Swift, G.W., 2000. A thermoacoustic-Stirling heat engine: detailed study. J. Acoust. Soc. Am. 107(6), 3148-3166.

Fusco, A.M., Ward, W.C., Swift, G.W., 1992. Two-sensor power measurements in lossy ducts. J. Acoust. Soc. Am. 91, 2229-2235.

Gardner, D.L., Swift, G.W., 2003. A cascade thermoacoustic engine. J. Acoust. Soc. Am. 114, 1905-1919.

Hamood, A., Jaworski, A.J., Mao, X., Simpson, K., 2018. Design and construction of a two-stage thermoacoustic electricity generator with push-pull linear alternator. Energy 144, 61-72.

Hu, J.Y., Luo, E.C., Zhang, L.M., Chen, Y.Y., Wu, Z.H., Gao, B., 2018. Analysis of a displacer-coupled multi-stage thermoacoustic-Stirling engine. Energy 145, 507-514.

Sharify, E.M., Hasegawa, S., 2017. Traveling-wave thermoacoustic refrigerator driven by a multistage traveling-wave thermoacoustic engine. Appl. Therm. Eng. 113, 791-795.

Swift, G.W., 1992. Analysis and performance of a large thermoacoustic engine. J. Acoust. Soc. Am. 92(3), 1551-1563.

Tijani, M.E.H., Spoelstra, S., 2013. A hot air driven thermoacoustic-Stirling engine. Appl. Therm. Eng. 61, 866-870.

Ward, B., Clark, J., Swift, G.W., 2008. Design Environment for Low-Amplitude ThermoAcoustic Energy Conversion (DELTAEC) program. Los Alamos National Laboratory, New Mexico, USA.

Yazaki, T., Iwata, A., Maekawa, T., Tominaga, A., 1998. Traveling wave thermoacoustic engine in a looped tube. Phys. Rev. Lett. 81(15), 3128-3131.

Exergy analysis of MgO-water nanofluid as a coolant for sinusoidal mini-channel heat sink

[1*]Muhammad Usman Sajid, [1]Yusuf Bicer, [2]Hafiz Muhammad Ali
[1] Division of Sustainable Development (DSD), College of Science and Engineering (CSE), Hamad Bin Khalifa University (HBKU), Qatar Foundation (QF), Education City, Doha, Qatar
[2] Mechanical Engineering Department, King Fahd University of Petroleum & Minerals (KFUPM), Dhahran 31261, Saudi Arabia

* E-mails: musajid@mail.hbku.edu.qa

Abstract
The cooling of mini-channel heat sink via nanofluid has been anticipated to be an effective technique for heat dissipation from contemporary electronic devices. The evaluation of exergetic performance of mini-channel heat sink can play an important role in the evolution of improved heat sink with better cooling characteristics. The main aim of the present study is to experimentally analyze the exergy of distilled water and MgO-water nanofluid as a coolant in a sinusoidal mini-channel heat sink. The MgO-water nanofluid having a concentration of 0.01 vol.% was prepared using two-step method. The coolants (distilled water and nanofluid) were passed through the mini-channel heat sink under heating power of 45W and Reynolds number ranging from 517 to 914. From the results, it can be inferred that the exergy gain for nanofluid was higher than the base fluid (distilled water). This gain in exergy deteriorated with the rise in flow rate for both water and nanofluid. The outlet exergy was found to be enhanced with increase in Reynolds number for coolants. The augmentation in outlet exergy of 44.51% was obtained for nanofluid at the highest Reynolds number as compared to distilled water. The exergy efficiency showed increasing trend with increase in Reynolds number for coolants. The maximum 2nd law efficiency of 35.01% and 26.65% were attained for 0.01 vol.% concentration of MgO-water nanofluid and distilled water respectively, at Reynolds number of 914.

Keywords: Nanofluid, mini-channel heat sink, exergy efficiency, exergy gain

I. Introduction

Due to compactness in electronic equipment and a substantial increase in transistor density, thermal management of electronics has captured the attention of many researchers. The coolants like nanofluid with superior thermal properties can lead to a better thermal performance of the system. A rigorous amount of research work is being carried out to investigate the heat transfer characteristics of systems using nanofluid as coolant. Contrarily, few studies have been conducted to evaluate exergy the performance of equipment using nanofluid as a cooling medium. (Khaleduzzaman et al., 2016) investigated entropy generation and exergy of TiO_2/water nanofluid flowing through water block heat sink. The nanofluid with the nanoparticles volume fraction of 0.1% showed outlet exergy of 206 W and second law efficiency of 39.63% at a flow rate of 1.5 l/min. (Zhao et al., 2019) analyzed the effect of cylindrical grooves on energy, exergy efficiency and entropy generation of CPU using TiO_2-water nanofluid as coolant. The entropy generation for the staggered arrangement of grooves was nearly twice than aligned arrangement. (Narendran et al., 2018) evaluated the effect of nanoparticle concentration and flow rate of nanofluid flowing through mini-channel heat sink on exergy efficiency. The outlet exergy enhanced with an increase in flow rate and the maximum value of 147.52 W for obtained for 0.360 l/min. The energy and exergy analyses of Al_2O_3/water nanofluid for an electronic cooling system were performed by (Khaleduzzaman et al., 2014). For 0.25 vol.% nanofluid, maximum energy and exergy efficiencies of 94.68% and 36.05% were found, respectively. The outlet exergy of TiO_2/water nanofluid with 0.25 vol.% volume fraction was 60% more than pure water (Kumar et al., 2018).
Based on the literature review, it can be inferred that a limited number of studies are available on energy and exergy analysis for heat sink cooling using nanofluids as coolant. The present work investigates the second law efficiency of distilled water and MgO-water nanofluid being used as a coolant in a sinusoidal mini-channel heat sink. The effects of coolant flow rate on outlet exergy, exergy gain and exergy efficiency are analyzed experimentally.

II. Methodology

The schematic diagram of the experimental setup and top view of the heat sink used during experimentation is shown in Figure 1 (a) and (b), respectively. The coolant form storage tank is pumped to the heat sink through a needle valve. A flow meter is installed before the heat sink assembly to measure the flow rate of coolant.
The high-temperature coolant after heat sink was passed through the radiator to dissipate the gained heat and thus completing the cycle. Six K-type thermocouples were employed to measure the temperature of the coolant and heat sink. For the heating purpose, cartage heaters were installed in the heat sink and DC supply was provided to heaters from DC power source. The heat sink is made of aluminum and manufactured by CNC. The dimensions of the heat sink are presented in Table 1.

Table 1: Dimensions of the heat sink

Length of sink (mm)	Width of sink (mm)	Height of sink (mm)	Length of channel (mm)	Width of channel (mm)	Height of fin (mm)	Amplitude (mm)	Wavelength (mm)	Number of channels
75	28	50	79	1	1	1	15	13

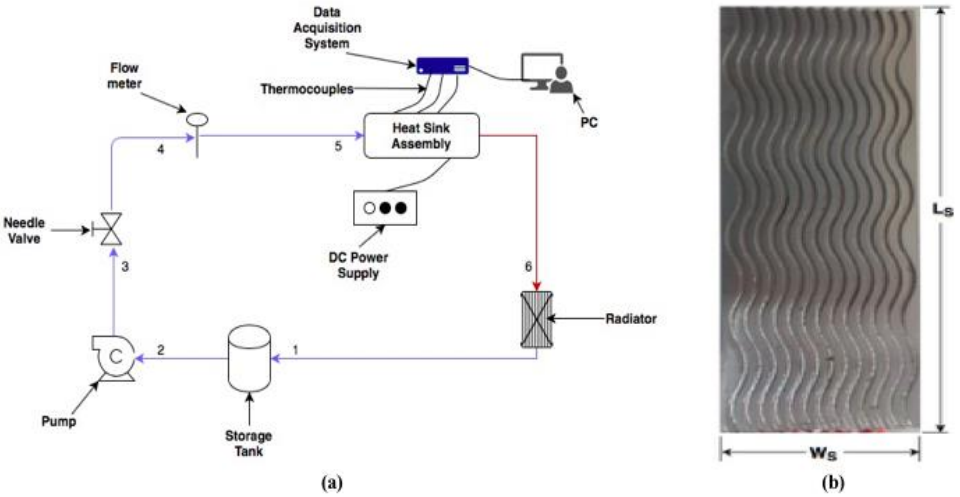

Figure 1: (a) Schematic diagram of the experimental setup (b) Heat sink

Two-step method was adopted to prepare nanofluid having a volume fraction of 0.01%. Initially, MgO nanoparticles were mixed in distilled water and then pH was maintained near 2. For pH of 2.2, MgO nanofluid was transparent and remained stable for a duration of one week (Ali et al., 2015). The magnetic stirring was performed for 2 hours accompanied by 3 hours of sonication in an ultra-sonic cleaner to prevent any agglomeration. The concentration of nanofluid selected for experimentation is small because low concentrated nanofluid is less prone to settlement and agglomeration (Sajid et al., 2019). The properties of MgO nanoparticles are presented in Table 2.

Table 2: Properties of MgO nanoparticles

Purity	Size (nm)	Morphology	Color	Density (kg/m3)
99%	20	Spherical	White	3580

III. Analysis

(Sajid et al., 2019) computed volume fraction of nanoparticles using Eq (1)

$$\emptyset = \left(\frac{\frac{m_p}{\rho_p}}{\frac{m_p}{\rho_p} + \frac{m_{bf}}{\rho_{bf}}} \right) \quad (1)$$

where m_p is the mass of nanoparticles (kg), m_{bf} is mass of base fluid (kg), ρ_p is the density of nanoparticles (kg/m3) and ρ_{bf} is the density of the base fluid (kg/m3).

The outlet exergy is defined by (Khaleduzzaman et al., 2016) and can be computed by Eq (2)

$$Ex_{out} = \dot{m}[h_{out} - h_e - T_e(S_{out} - S_e)] \quad (2)$$

where $\dot{m}$ is the mass flow rate of coolant (kg/s), h_{out} is specific enthalpy of coolant at the outlet of the heat sink (kJ/kg), h_e

is specific enthalpy at ambient temperature (kJ/kg), T_e is environment temperature (K), S_{out} is specific entropy of coolant at the outlet (kJ/kg.K) and S_e is the specific entropy of coolant at environment temperature (K).

For the case of nanofluid, Eq (2) can be rewritten as given by Eq (3)

$$Ex_{out} = \dot{m}C_{p,nf}\left[(T_{nf,out} - T_e) - T_e ln\left(\frac{T_{nf,out}}{T_e}\right)\right] \quad (3)$$

$\dot{m}$ is the mass flow rate of coolant (kg/s), $C_{p,nf}$ is the specific heat of nanofluid (J/kg.K), $T_{nf,out}$ is the temperature of nanofluid at the outlet of the heat sink (K) and T_e is environmental temperature.

The exergy gain can be calculated from Eq (4) (Gupta and Kaushik, 2008)

$$Ex_{gain} = Ex_{out} - Ex_{in} - P_p \quad (4)$$

where Ex_{in} is inlet exergy of coolant (W) and P_p is pumping power (W).

The pumping power can be calculated from Eq (5)

$$P_p = \frac{\dot{m}}{\rho}\Delta P \quad (5)$$

where ΔP is pressure drop (Pa) and ρ is the density of coolant (kg/m3).

The second law efficiency (exergy efficiency) is given by Eq (6)

$$\eta_{exergy} = \frac{Ex_{out}}{Ex_{in} + Ex_{electrical} + P_p} \quad (6)$$

where $Ex_{electrical}$ is electrical power (W) supplied through heaters to the heat sink.

Reynolds number can be estimated by Eq (7)

$$Re = \frac{\rho v d_h}{\mu} \quad (7)$$

where ρ is the density of coolant (kg/m3), v is the velocity of coolant (m/s), d_h is the hydraulic diameter of the channel (m) and μ is viscosity (kg/m.s).
The velocity is calculated using Eq (8)

$$v = \frac{\dot{m}}{\rho A_c} \quad (8)$$

where A_c is cross-sectional area of channel (m2).
The cross-sectional area of the channel can be defined as Eq (9)

$$A_c = W_c h_f \quad (9)$$

where W_c is the width of channel (m) and h_f is the height of fin (m).
The hydraulic diameter is given by Eq (10)

$$d_h = \frac{4A_c}{P_c} \quad (10)$$

where P_c is the perimeter of channel (m).
The specific heat of nanofluid ($C_{p,nf}$) is predicted using Xuan and Roetzel model (Xuan and Roetzel, 2000) given by Eq (11)

$$C_{p,nf} = \frac{\emptyset \rho_P C_{P,np} + (1-\emptyset)\rho_{bf} C_{P,bf}}{\rho_{nf}} \quad (11)$$

where $C_{P,np}$ is the specific heat of nanoparticle (J/kg.K) and $C_{P,bf}$ is the specific heat of the base fluid.
The viscosity of nanofluid is estimated using Corcione model (M. Corcione, 2011) given by Eq (12)

$$\mu_{nf} = \mu_{bf}\left[\frac{1}{1 - 34.87\emptyset^{1.03}\left(\frac{d_p}{d_{bf}}\right)^{-0.3}}\right] \quad (12)$$

where d_p is the diameter of the nanoparticle. The d_{bf} is calculated from Eq (13)

$$d_{bf} = 0.1\left[\frac{6M}{N\pi\rho_{bf}}\right]^{0.33} \quad (13)$$

where M is the molar weight of water and N is Avogadro number.
The density of nanofluid is determined from Pak and Cho correlation (Pak and Cho, 1998) and given by Eq (14)

$$\rho_{nf} = \emptyset\rho_P + (1-\emptyset)\rho_{bf} \quad (14)$$

The experimental setup has been validated in a previous study (Sajid et al., 2019).

IV. Results and discussions

The outlet exergy and exergy gain as a function of Reynolds number are depicted in Figure 2. The outlet exergy enhanced with an increase in flow rate and nanofluid showed about 44.51% more outlet exergy than distilled water for the same flow rate. The maximum value of outlet exergy attained by nanofluid was 22.92 W. The higher value of outlet exergy of nanofluid than distilled water can be attributed to the enhanced thermal conductivity of nanofluid. The exergy gain deteriorated with an increase in the flow rate for both nanofluid and distilled water. The nanofluid obtained 22.65% higher exergy gain than distilled water.

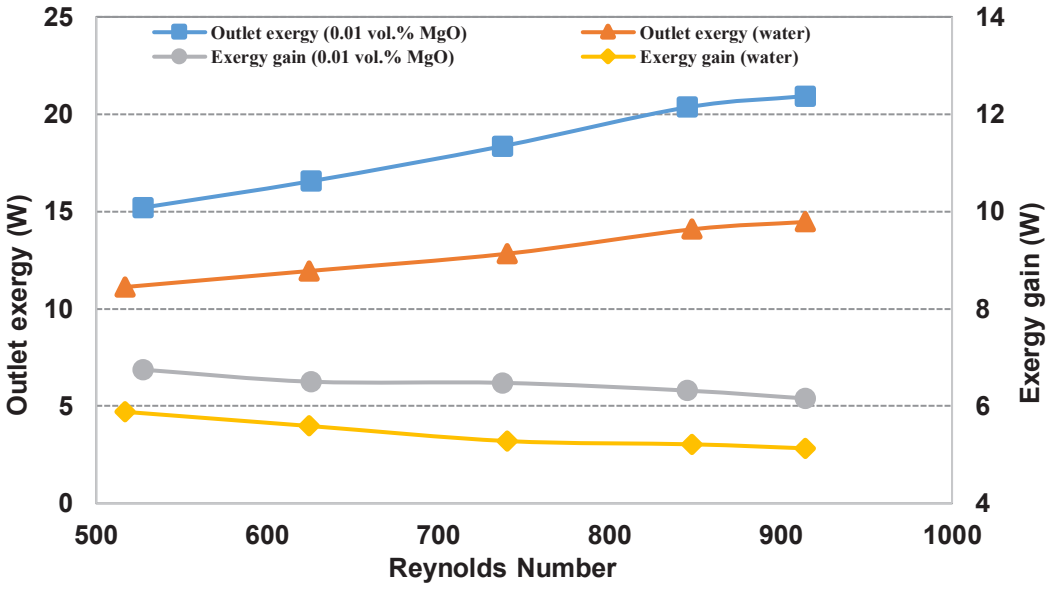

Figure 2: Outlet exergy and exergy gain as a function of Reynolds number

The exergy efficiency of coolants (water and nanofluid) as a function of Reynolds number is presented in Figure 3. The exergy efficiency of both coolants was improved with an increase in flow rate. The nanofluid showed higher exergy efficiency than distilled water. The exergy efficiencies of 0.1 vol.% MgO nanofluid and distilled water were 35.01% and 26.64% respectively, at maximum Reynolds number of 914.

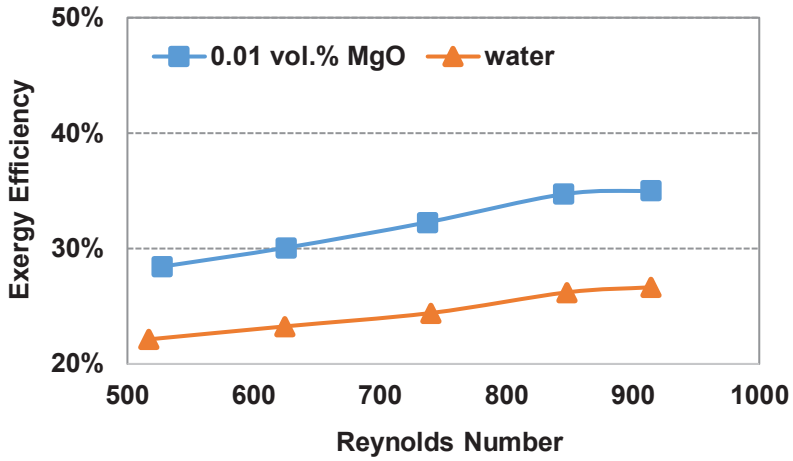

Figure 3: Exergy efficiency of coolants as a function of Reynolds number

V. Conclusions

The second law efficiency of distilled water and MgO-water nanofluid being used as a coolant in sinusoidal mini-channel heat sink as a function of Reynolds number is investigated. The outcome of this study can be beneficial in the development of a better mini-channel heat sink for electronic cooling applications. Based on the experimental investigation, the following results are drawn:

- The outlet exergy enhanced with an increase in flow rate and nanofluid obtained 44.71% higher outlet exergy than water.
- The nanofluid achieved 22.65% higher exergy gain than distilled water.
- The maximum exergy efficiency of 35.01% was obtained for nanofluid.

References

Ali, H.M., Azhar, M.D., Saleem, M., Saeed, Q.S., Saieed, A., 2015. Heat transfer enhancement of car radiator using aqua based magnesium oxide nanofluids. Therm. Sci. 19, 2039–2048. https://doi.org/10.2298/TSCI150526130A

Gupta, M.K., Kaushik, S.C., 2008. Exergetic performance evaluation and parametric studies of solar air heater. Energy 33, 1691–1702. https://doi.org/10.1016/j.energy.2008.05.010

Khaleduzzaman, S.S., Sohel, M.R., Mahbubul, I.M., Saidur, R., Selvaraj, J., 2016. Exergy and entropy generation analysis of TiO2-water nanofluid flow through the water block as an electronics device. Int. J. Heat Mass Transf. 101, 104–111. https://doi.org/10.1016/j.ijheatmasstransfer.2016.05.026

Khaleduzzaman, S.S., Sohel, M.R., Saidur, R., Mahbubul, I.M., Shahrul, I.M., Akash, B.A., Selvaraj, J., 2014. Energy and exergy analysis of alumina-water nanofluid for an electronic liquid cooling system. Int. Commun. Heat Mass Transf. 57, 118–127. https://doi.org/10.1016/j.icheatmasstransfer.2014.07.015

Kumar, A., Narendran, G., Perumal, D.A., 2018. Entropy generation study of TiO2 nanofluid in microchannel heat sink for Electronic cooling application. IOP Conf. Ser. Mater. Sci. Eng. 376. https://doi.org/10.1088/1757-899X/376/1/012013

M. Corcione, R.-B., 2011. Convection heat transfer in nanoparticle suspensions. Int. J. Heat Fluid Flow. 32, 65–77.

Narendran, G., Bhat, M.M., Akshay, L., Arumuga Perumal, D., 2018. Experimental analysis on exergy studies of flow through a minichannel using Tio2/Water nanofluids. Therm. Sci. Eng. Prog. 8, 93–104. https://doi.org/10.1016/j.tsep.2018.08.007

Pak, B.C., Cho, Y.I., 1998. Hydrodynamic and heat transfer study of dispersed fluids with submicron metallic oxide particles. Exp. Heat Transf. 11, 151–170. https://doi.org/10.1080/08916159808946559

Sajid, M.U., Ali, H.M., Sufyan, A., Rashid, D., Rehman, W.U., Zahid, S.U., 2019. Experimental investigation of TiO2–water nanofluid flow and heat transfer inside wavy mini-channel heat sinks. J. Therm. Anal. Calorim. 137, 1279–1294. https://doi.org/10.1007/s10973-019-08043-9

Xuan, Y., Roetzel, W., 2000. Conceptions for heat transfer correlation of nanofluids. Int. J. Heat Mass Transf. 43, 3701–3707. https://doi.org/10.1016/S0017-9310(99)00369-5

Zhao, N., Qi, C., Chen, T., Tang, J., Cui, X., 2019. Experimental study on influences of cylindrical grooves on thermal efficiency, exergy efficiency and entropy generation of CPU cooled by nanofluids. Int. J. Heat Mass Transf. 135, 16–32. https://doi.org/10.1016/j.ijheatmasstransfer.2019.01.106

A predictive model for the thermal conductivity of nanofluids using machine learning algorithms

[1*]Humphrey Adun, [1]ifeoluwa Wole-osho, [2]Eric Okonkwo, [1]Mustafa Dagbasi
[1] Department of Energy Systems Engineering, Cyprus International University, North Cyprus, via Mersin-10, Turkey.
[2] Division of Sustainable Development, College of Science and Engineering, Hamad Bin Khalifa University, Education City, Qatar Foundation, Doha, Qatar.
* E-mails: erykado@gmail.com

Abstract

Nanofluids are novel fluids that are obtained from the colloidal suspension of nanoparticles in base fluids. They are experimentally known to have vast potential in heat transfer applications due to their unique thermophysical properties. The determination of the thermal conductivity of nanofluids is important for analyzing the convective heat transfer of nanofluids. However, experimental methods to determine thermal conductivity are both time-consuming and expensive. Theoretical models have been used to resolve this limitation, however, form literature we observe that due to the numerous varriables that affect thermal conductivity of nanofluids most of the classical and empirical models have discrepancies in making accurate predictions. In this study, intelligent techniques have been proposed to make more precise predictive analysis. The thermal conductivity of hybrid nanofluids is predicted using eleven different input variables, this include: volume concentration, temperature, the acentric factor of the base fluid, nanoparticle bulk density, mixture ratio of particles and particle size. 600 experimental data points from studies using different nanoparticles and base fluids are used in developing an artificial neural network (ANN) model. A feed-forward backward propagation is developed with different hidden layers and neurons in computing the training algorithm for predicting the output parameter (thermal conductivity). The performance validation of the models is computed using the mean square error (RMSE) and the mean absolute percentage error (MAPE). The performance result showed an R-square vale of 0.9999 and 0.9998 in the training and testing phase of the model, which shows that the model is capable of predicting the thermal conductivity of hybrid nanofluids over a wide range of data.

Keywords: Nanofluid, prediction, thermal conductivity, artificial neural networks, nanoparticle.

I. Introduction

The growing interest and research activity in nanotechnology and nanofluids is majorly due to its numerous applications in diverse industries such as automobile, nuclear power industries, food industries, manufacturing processes and thermal industries [1]. The comparative advantage of nanofluids over conventional fluids like water and thermal oil is its superior thermal properties. Several studies have shown that the nanofluids which are suspension of nanoparticles in conventional fluids have higher thermal conductivity, which improves the heat transfer properties of the fluid. The thermal conductivity of nanofluids improves the heat transfer process. Studies have shown that the thermal conductivity of nanofluids is enhanced at higher temperature and concentration.

Sundar et al. [2] investigated the thermal conductivity of magnetic Fe_3O_4/water nanofluid conducted in volume concentration and temperature between 0%-2% and 20°C-60°C respectively. The result showed that a 48% thermal conductivity enhancement was recorded at 2% volume concentration and 60°C temperature as compared to base fluid. [3] measured the thermal conductivity improvement of CuO nanofluid to base fluid. A 23.8% improvement was recorded at volume concentration of 0.1%. Yu et al. [4] investigated the thermal conductivity improvement of multi-walled carbon nanotubes in ethylene glycol and synthetic engine oil base fluid. The result showed that for the CNT-ethylene glycol nanofluid, there was a 12.4% thermal conductivity improvement 1% volume concentration, while there was a 30% thermal conductivity enhancement using the CNT-engine oil nanofluid at 2% volume concentration.

Due to the complexity in measurement and the time it consumes to measure the thermal conductivity of nanofluids, theoretical/process models are important [5]. Process models enable efficient generalization of experimental results and data and gives concise knowledge about the process behavior [6]. There have been traditional propounded which correlate the thermal conductivity of nanofluids in literature. The most common theoretical prediction model for estimation of thermal conductivity of solid-liquid mixture is the Maxwell model [7]. This model is efficient for low volume fraction solid-liquid suspension with randomly dispersed, uniformly sized and non-interacting spherical particles. Other common ones are Hamilton-Crosser, Bruggeman, Jefferey, and Davise [5]. The errors of these models in effectively predicting a wide range of experimental data has given rise to development of computational models of prediction. Recently several studies have utilized heuristic models based on experimental data for prediction of thermal conductivity. Some of these models are artificial neural networks (ANN) [8], Radial basis function (RBF), fuzzy logic (ANFIS) [9], genetic algoritms (GA), and other hybrid models like ANN-GA, ANFIS-ANN [10].

The aim of this study is to develop a general model for prediction of thermal conducitivity of hybrid nanofluid. In developing this model, an extensive literure survey is carried out, to retrieve a wide range of different conditions

of experimental analysis of hybrid nanofluids. The model input parameters used in the ANN model are temperature, volume concentration, accentric factor of base fluid, nanoparticle size, nanoparticle heat capacity, and nanoparticle bulk density. Several configurations of the ANN models were evaluated by changing the the number of layers, number of hidden neurons and network training algorithm. The model is checked for accuracy by evaluating the performance using mean square error and R- square value. The predictive accuracy of the developed models was compared with other theoretical models.

II. Dataset

The studies that have investigated the thermal conductivity of hybrid nanofluid were reviewed. The results of these studies indicate the factors that affect the thermal conductivity of the nanofluids. These factors are temperature, particle size, surfactants, volume concentration, nanoparticle's shape, size, interfacial layers, mixture ratio, inter-particle spacing, nanoparticle's thermal conductivity. Also, the thermal conductivity of hybrid nanofluid is influenced by each nanoparticle in the mixture and the base fluid. In order to make a comprehensive model covering different hybrid nanofluids, the most significant factors that influence thermal conducitivity must be recognized. In previous studies of measuring the thermal conductivity enhancement of nanofluids, the most common parameters measured are temperature, volume concentration and particle size. Recent studies have also considered the effect of mixture ratio on thermal conducitivity of hybrid nanofluid. In the present study, temperature, volume concentration, particle size, mixture ratio, accentric factor of base fluid were selected as input parameters. Table 1 shows the general specicifcation of the data set used in the ANN model development. The thermal conductivity values are computed from the correlation equation developed in the studies from which the parameters are retrieved.

Table 1. Data set used for model development

Parameters	Range
Temperature	*20 - 70*
Volume concentration	*0.1-2%*
Particle size	*7-100 nm*
Mixture ratio	*0.1-1*
Accentric factor of base fluid	

The dataset is culled from studies, and contains 700 data points on thermal conductivity of different hybrid nanofluid (with different base fluids) having diverse wide range of parameters.

III. ANN modelling and Implementation

The neural network is designed to perform a specific taske by adjusting the weights and bias between elements. The weights and bias of the ANN model are characterized with the learning algorithm. The learning algorithm used in this study is the back-propagation. Considering that there are different types of back propagation training algorithms (scaled conjugate gradient (SCG), Levenberg-Marquardt (LM), gradient descent with variable learning rate back propagation (GDX), and Resilient back propagation (RP), it is important to use trail and errors in the training of the dataset in order to get better accurate prediction performance. Adjusting the neural network architecture and traning the data sets enable the model to find accurate output for a given input and targets. Iterative processes occur in the training of the dataset until the target value and the output have a fitting match. The dataset used in this present study is divided into 70% training (490 datapoints) and 30% testing (210 datapoints). The testing data is not used in the training process. The figure 1 and 2 shows the ANN selected structure.

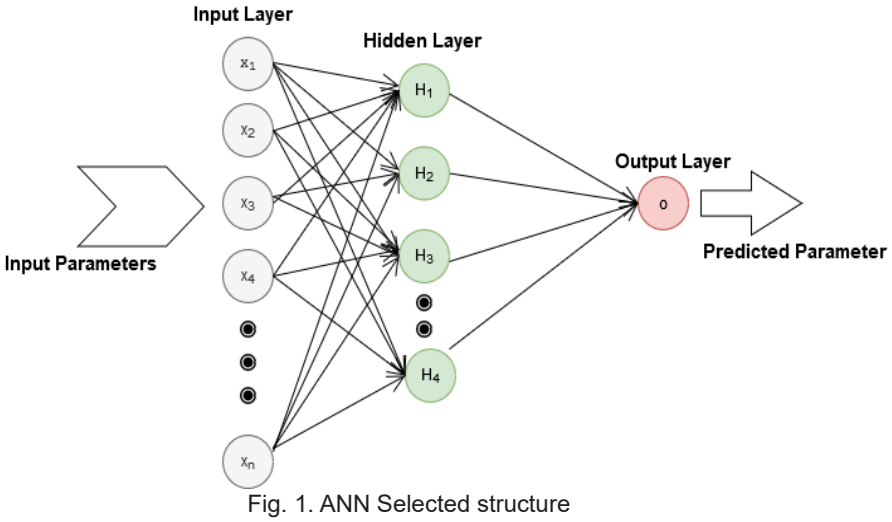

Fig. 1. ANN Selected structure

The dataset were normalized according to equation 1 before used in training and tesing. The data set were then randomly divided into 70% data points for training sub data (for training and testing) and 30% test data set (for prediction of the target data set)

$$X_{norm} = \frac{X - X_{min}}{X_{max} - X_{min}} \quad (1)$$

Where X_{norm} is the normalized dataset, X_{min} is 0 and X_{max} is 1 and X is the variable data set. The performance criteria used in assessing the accuracy of the different model architecture are mean square error (MSE), R square value (R^2), and mean absolute percentage error (MAPE).

$$MSE = \frac{1}{N}\sum_{I=1}^{N}(y_i - \hat{y}_i)^2 \quad (2)$$

$$MAPE = \frac{100\%}{N}\sum_{i=1}^{N}\left|\frac{y_i - \hat{y}_i}{y_i}\right| \quad (3)$$

$$R^2 = 1 - \frac{\frac{1}{N}\sum_{I=1}^{N}(y_i - \hat{y}_i)^2}{\frac{1}{N}\sum_{I=1}^{N}(y_i - \bar{y}_i)^2} \quad (4)$$

Where $y_i, \hat{y}_i, \bar{y}_i$, and n are experimental data, predicted data, average value of experimental data and number of data points respectively. The table 2 shows the performance parameters used for learning in the ANN model. In this study, the logistic sigmoid is used as the neuron activation function as shown in equation 5 and the hidden and output layer is activated by the Purelin function as shown in equation 6. The Purelin function is chosen as the activation function for the output neuron because it is ideal for continuous valued targets.

$$f(x) = \left({}^{1}/_{1 + e^{-cx}}\right) \quad (5)$$

$$f(x) = x \quad (6)$$

Table 2: Performance parameters for learning algorithm

Parameters	Values
Maximum iteration	1000
Minimum gradient	1e-07
Mu, mu-inc, mu-dec, max-fail	0.001, 10, 0.1, 6

Where mu is the momentum update, mu-dec is the mu decrease, mu-inc is the mu increase and max-fail is the maximum validation fails.

IV. Results and discussions

The ANN final configuration is gotten from the trial and errors of different hidden layers and neurons in the layers. Different training algoritms is also utilized in developing the different ANN models. The table 3 shows the examined ANN architecture and the performance of the models. The training is done using the LM algorithm to get the optimum hidden layers and neurons. The optimum layers is then analysed with other training algorithms to ascertain the best algorithm for prediction. The LM algorithm is used because it is the fastest method for training moderate neural networks.

Table 3: ANN Architecture

Hidden layers		Training		Testing
	Neurons	MSE	R^2	R^2
1	10	4.63882e-07	0.9867	0.9876
1	15	6.06971e-07	0.9888	0.9767
1	20	1.70422e-06	0.9978	0.9776
1	25	4.37684e-07	0.9987	0.9886
2	5-10	1.0581e-05	0.9997	0.8977
2	10-10	1.3648e-05	0.9996	0.8788
2	10-15	2.6560e-06	0.9988	0.9788
2	20-20	1.7942e-08	0.9999	0.9998

As it can be observed, the performance result show acceptable ranges. The mot accurate model is seen to be the 2 hidden layers with 20 neurons in each of the layer.

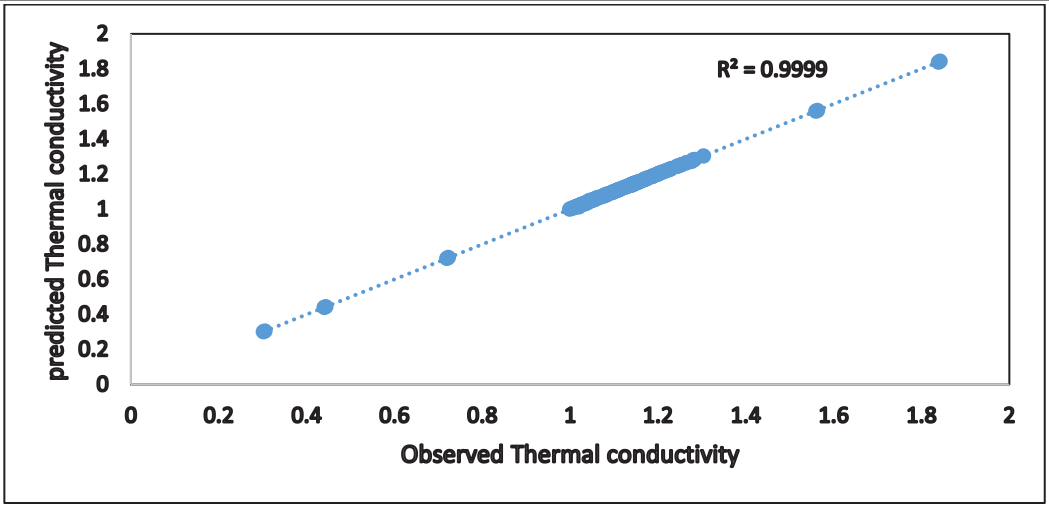

Fig.1. Experimental Thermal conductivity vs ANN predicted Thermal conductivity

The universal prediction formular for thermal conductivity of hybrid nanofluid is computed using the equation 5 and 6 defined in this study. The weights and bias of the formular are gotten from the optimum ANN architecture.

$$\sum_{i=1}^{20} w_{i1}^{3} \left(1 \Big/ \left(1+\exp\left(-\left(\sum_{j=1}^{20} w_{ji}^{2}\left(1 \Big/ 1+\exp\left(-\left(\sum_{k=1}^{5} w_{kj}^{1} u_k + \beta_j^{1}\right)\right)\right) + \beta_i^{2}\right)\right)\right)\right) + \beta_1^{3}$$

Where the bias weight is given as β_j^k and w_{ji}^k is the link weights for the neuron j in layer k. u_k is the input variable matrix for for the eleven model input parameters.

V. Conclusions

This study presented a methodology for predicting the thermal conductivity of hybrid nanofluid using ANN. The model input parameters chosen are the particle size of individual nanoparticles, temperature, volume concentration, base fluid accentric factor, nanoparticle bulk density, nanoparticle thermal conductivity and nanoparticle specific heat capacity. The number of input parameter in the model was eleven, as the bulk density, nanoparticle specific heat capacity, nanoparticle thermal conductivity and nanoparticle size are taken for each of the nanoparticle in the nanocomposite mixture. The data set used for the analysis was culled from researches carried out on thermal conductivity of different hybrid nanofluid. Different ANN architecture was used in training the dataset, and the optimum architecture for the most accurate prediction gotten was two hidden layers with twenty neurons each in each layer. The performance result showed an R-square vale of 0.9999 and 0.9998 in the training and testing phase of the model, which shows that the model is capable of predicting the thermal conductivity of hybrid nanofluids over a wide range of data.

References

[1] Ç. Yıldız, M. Arıcı, and H. Karabay, “Comparison of a theoretical and experimental thermal conductivity model on the heat transfer performance of Al2O3-SiO2/water hybrid-nanofluid,” *Int. J. Heat Mass Transf.*, vol. 140, pp. 598–605, 2019.

[2] L. Syam Sundar, M. K. Singh, and A. C. M. Sousa, “Investigation of thermal conductivity and viscosity of Fe3O4 nanofluid for heat transfer applications,” *Int. Commun. Heat Mass Transf.*, vol. 44, pp. 7–14, 2013.

[3] M. S. Liu, M. C. C. Lin, C. Y. Tsai, and C. C. Wang, “Enhancement of thermal conductivity with Cu for nanofluids using chemical reduction method,” *Int. J. Heat Mass Transf.*, vol. 49, no. 17–18, pp. 3028–3033, 2006.

[4] W. Yu, H. Xie, L. Chen, and Y. Li, “Enhancement of thermal conductivity of kerosene-based Fe3O4 nanofluids prepared via phase-transfer method,” *Colloids Surfaces A Physicochem. Eng. Asp.*, vol. 355, no. 1–3, pp. 109–113, 2010.

[5] M. Moosavi, K. Firoozi Rad, and A. Daneshvar, “A comparative study in the prediction of thermal conductivity enhancement of nanofluids using ANN-MLP, ANN-RBF, ANFIS, and GMDH methods,” *J. Iran. Chem. Soc.*, vol. 16, no. 2019, pp. 2629–2637, 2019.

[6] A. Shahsavar, S. Khanmohammadi, D. Toghraie, and H. Salihepour, “Experimental investigation and develop ANNs by introducing the suitable architectures and training algorithms supported by sensitivity analysis: Measure thermal conductivity and viscosity for liquid paraffin based nanofluid containing Al 2 O 3 nanoparticl,” *J. Mol. Liq.*, vol. 279, no. 2019, pp. 850–860, 2019.

[7] J. C. Maxwell, “On Electricity and Magnetism,” 1881.

[8] A. H. Elsheikh *et al.*, “An artificial neural network based approach for prediction the thermal conductivity of nanofluids,” *SN Appl. Sci.*, vol. 2, no. 2, p. 235, 2020.

[9] N. Zhao and Z. Li, “Experiment and artificial neural network prediction of thermal conductivity and viscosity for alumina-water nanofluids,” *Materials (Basel).*, vol. 10, no. 5, 2017.

[10] H. Karimi, F. Yousefi, and M. R. Rahimi, “Correlation of viscosity in nanofluids using genetic algorithm-neural network (GA-NN),” *Heat Mass Transf. und Stoffuebertragung*, 2011.

Turkeys Industrial waste energy recovery potential via power and hydrogen conversion technologies

[1]Funda Ates, [2*]Hasan Ozcan
[1] Karabuk University, Engineering Faculty, Mechanical Engineering Department, Demir Celik Kampusu, Karabuk, 78050, Turkey
[2] Ankara Yildirim Beyazit University, Faculty of Engineering and Natural Sciences, Mechanical Engineering Department, Etlik Kecioren, Ankara, 06220, Turkey

* E-mails: hozcan@ybu.edu.tr

Abstract
The need for energy in the world is increasing day by day. In particular, this situation will increase the demand for energy in developing countries with population growth, industrialization and technological developments. Turkey is a country dependent on foreign energy by 70%. Fossil energy sources are being depleted day by day and they cause irreversible damages to our world and threaten the life areas of future generations. The industrial sector affects the amount of energy used in Turkey considerably. Given that energy resources are limited and demand for industrial products continues to increase, meeting the industrial energy demand and minimizing the economic impact in the future will be a major challenge. In this study, the energy consumption potential of Turkısh low to high grade industrial waste energy over the years have been calculated and projected. Based on the grade of the heat some selected power systems are adapted to evaluate the potential available energy production. In addition, electrochemical and thermochemical hydrogen generation technologies are considered for hydrogen production from waste heat. Many case studies are performed based on the temperature range of the waste heat. The annual waste energy amount is around 974 PJ and between 9-18% of this energy is recoverable with selected power and hydrogen technologies. Highest amount of power recovery is possible with Gas Turbine while HyS is eligible to recover the highest amount of hydrogen.

KeywordsIndustrial waste heat, cement industry, glass industry, iron-steel industry, power, hydrogen

I. Introduction
World presently suffers from overuse of fossil fuels that result in emissions leading to rapid and unexpected changes in climate that jeopardize all the living on earth. There have been many several intergovernmental attempts do decrease emissions from industrial, residential and mobile applications. Most of these attempts are based on public awareness and extra taxing to discourage wasting. However, most plans are hypothetical and could not act well so far [1]. Recently, a coal-based power plant has been shut down by the Turkish government due to faiure of renewing their filters [2]. This might seem as a temporary solution, however, its economics and amount of grid power contribution can not be sacrificed in near terms. Energy recovery is one of the most promising ideas that contributes sustainable energy production that enhances efficiency and economics of the studied plant. It is based on use of exhaust energy of the conventional plant by either processing the exhaust content or use its extra heat [3]. There are several applications for energy recovery in Turkey that utilizes waste energy for useful products [4] [5] [6]. For example, the cement factory in İzmir creates a new area (Recydia) and recycles 15% of Istanbul's domestic waste and uses it as fuel. Electricity and fertilizers are produced by solid waste separation and processing facility provided by Düzce municipality. With the biogas plant in Ankara almost 12 thousand homes are electrified.

Waste heat recovery is based on use of high temperature exhaust gases as input for an energy conversion system. Therefore, grade of the waste energy is crucial for selection of the right energy conversion technology. According to TUIK (Turkish Statistical Institute) annual amount of energy consumption by industry is around 1983 PJ [7]. There are many major energy intensive industrial sectors in Turkey that utilize high amount of energy. These sectors can be sorted by their energy consumption as follows: iron-steel, nonferrous, nonmetals, petrochemical, food-bevarage, paper-pulp, and others [8]. Ratio of wasted energy to consumed energy for various industrial sectors are provided by [9]. Iron-steel sector has the highest ratio of waste/consumed energy by around 14% and it is followed by nonmetals and nonferrous industry. It is also crucial to know the grade of the wasted heat to utilize it with the right energy conversion technology as represented in Figure 1.

Conventional Steam and gas turbines require temperatures above 500°C while some novel power generation systems such as Organic rankine cycles, Kalina cycle and Absorption power cycles can work at lower source temperatures [10]. In addition hydrogen generation technologies require different temperature ranges. Pure thermochemical cycles require temperatures above 800°C, while hybrid themochemical cycles work at a range of 450-600°C. Electrochemical conversion of water to hydrogen may require high temperatures based on the technology. If a solid oxide electrolysis cell (SOEC) is used, required temperature must be above 800°C while Polymer Exchange Mebrane (PEM) technology works at 80°C by sacrificing from low electricity consumption [1]. Thermochemical cycles decompose water into hydrogen and oxygen using heat and chemical reaction in a closed cycle. In thermochemical cycles, high temperatures are generally required for decomposition [11]. In this study, calcium-bromine (Ca-Br); magnesium-chlorine (Mg-Cl); hybrid sulfur-iodine (HySI) thermochemical cycles and PEM, SOEC electrochemical methods are included for hydrogen production [12].

It is expected that the amount of industrial waste is going to increase by almost 100% by 2050 based on the

projections from the waste heat increase in the last 20 years. Therefore, it is crucial to utilize selected energy conversion technologies to provide useful energy from industrial waste heat. Using the 2017 data on the waste energy and considering only 20% of this waste is converted into useful energy, almost 5.7 GWh of conversion is possible. Figure 2 shows the projection in the increase of waste heat from 2017 to 2050 correlated to number of years. In this study, amount of waste heat is assumed to be utilized via power and hydrogen conversion systems and energy conversion potential is investigated.

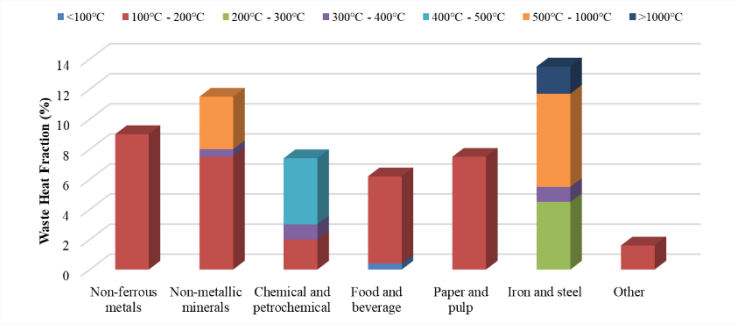

Fig. 1: Waste heat fraction per industrial sector and temperature level.

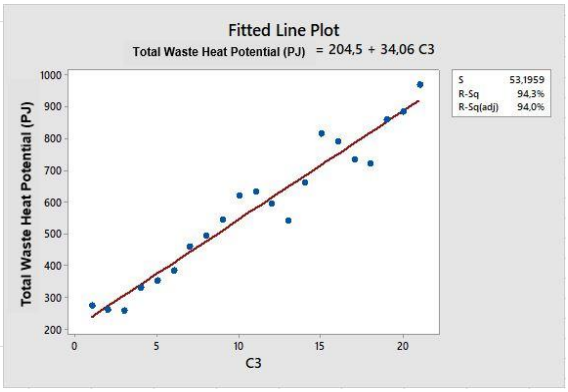

Fig. 2: Waste heat potential estimation by 2050.

II. Methodology and Energy Conversion Systems

All considered power conversion systems are based on the simple idea of a heat engine with a cyclic process that consists of a turbine system. The net power produced from a steam or gas turbine can be written as follows:

$$W_{net} = W_{ext} - W_{con}$$

Here subscripts *ext* and *con* refer to extracted and consumed. Plant efficiencies than can be defined as:

$$\eta_{PW} = \frac{W_{net}}{\dot{Q}_{in}}$$

Where $\dot{Q}_{in}$ is the fuel for the power cycle harvested from waste heat. Power plant analysis is a well known method and can be found elsewhere. For hydrogen production pure cycles do not require additional electricity consumption while hybrid cycles require both electricity and heat. Endothermy and exothermy of a reactor can be found by writing a general energy balance in molara basis as follows [13]:

$$\dot{Q} - \dot{W} = \sum n_{out}\left(\bar{h}_f^0 + \bar{h} - \bar{h}_o\right)_{out} - \sum n_{in}\left(\bar{h}_f^0 + \bar{h} - \bar{h}_o\right)_{in}$$

Where, $\bar{h}_f^0$, is the standard formation enthalpy in the reference state; $\bar{h}$ is the enthalpy in a particular state; $\bar{h}_o$ is the reference enthalpy at 1 atm and 25°C. After writing the general mass and energy equations for chemical reactions, enthalpy and entropy values of the products entering and leaving the system are used, which are referred to as Shomate equation.

$$\bar{h} - \bar{h}_o = AT + B\frac{T^2}{2} + C\frac{T^3}{3} + D\frac{T^4}{4} - E\frac{1}{T} + F - H$$

$$\bar{s} = A\ln(T) + BT + C\frac{T^2}{2} + D\frac{T^3}{3} - E\frac{1}{2T^2} + G$$

Above simple definitions lead to calculation of the required heat of the thermochemicall reactions and heat exchange processes of the thermochemical cycles. For electrolysis step and pure electrochemical conversion systems, the total cell potential is given as follows:

$$E = E_{rev} + E_{act} + E_{ohm} + E_{conc}$$

Where, E_{rev}, E_{act}, E_{ohm}, E_{conc} expressions are defined as reversible cell voltage, activation cell voltage, ohmic cell voltage and concentration cell voltage, respectively. Total voltage of the cell can be used to find the required power of the system with the Gibbs free energy change:

$$E = \frac{\Delta G}{zF}$$

Where, ΔG is change in Gibb's free energy, z is number of transferred electrons, F is defined Faraday's constant [14]. Based on the heat grade requirements various power and hydrogen systems are integrated to harvest energy from waste heat. Since 100-200°C ranged waste heat amount is too high, ORC based power production is considered for power production only, while PEM is adapted for hydrogen generation. Temperature ranges between 200-500 are utilized for running ORC and STC cycles. Temperatures above 500C are used for running GT and STC systems that are adapted to hybrid thermochemical cycles and SOEC. Table 1 represents

amount of heat from total industrial waste for the given temperature range and the selected technology couple. Thermal efficiencies of the power and hydrogen production systems are also provided.

Table 1. Power and hydrogen production cases based on the temperature range of the waste heat [15].

Temperature Range (°C)	Power System	Hydrogen System	Efficiency range of Power System (%)	Heat/work ratio (-)	Efficiency of Hydrogen System (%)	Case #
100-200	ORC/KL/APC	-	8-14	-		1
	ORC/KL/APC	PEM	8-14	0.017	75-85	2
	ORC/KL/APC	Alkaline	8-14	0.210	60-90	3
200-300	ORC	-	18-25	-		4
	ORC	PEM	18-25	0.017	75-85	5
	ORC	Alkaline	18-25	0.210	60-90	6
300-400	ST	-	24-30	-		7
	ST	PEM	24-30	0.017	75-85	8
	ST	Alkaline	24-30	0.210	60-90	9
400-500	ST	-	26-34	-		10
	ST	PEM	26-34	0.017	75-85	11
	ST	Alkaline	26-34	0.210	60-90	12
	ST	MgCl	26-34	0.793	42-51	13
500-1000	GT/ST	-	33-45	-		14
	GT/ST	PEM	33-45	0.017	75-85	15
	GT/ST	SOEC	33-45	0.393	52-75	16
	GT/ST	MgCl	33-45	0.793	42-51	17
	GT/ST	CuCl	33-45	2.313	37-54	18
	GT/ST	CaBr	33-45	2.435	33-46	19
	GT/ST	HyS	33-45	10.49	35-55	20

III. Results and Discussion

In this work, 20 cases are considered to find out the highest efficienct binary couples for power and hydrogen production. According to Table 2, there is a noticeable difference when electrochemical systems and thermochemical systems are compared. Considering the power provided to the system, the amount of daily hydrogen production in hybrid systems is higher than the ones that use the most power. The reason is the power and hydrogen efficiency of the system. However, the operating temperatures of the systems are also important. According to the 20th case, the daily hydrogen production amount was obtained from the thermochemical cycle of hybrid sulfur iodine with approximately 191 tons. HyS is more advantageous due to low cell potential and high efficiency, although operating temperatures are the same compared to SOEC. The maximum daily amount of hydrogen production was obtained from the HyS cycle with approximately 191 tons. Hybrid systems have a very high operating temperature. While making calculations, reaction temperature was added to water heat value in thermochemical cycles. These values are examined from the literature.

Case	Amount of source (MW)	Cycle	Temperature range(ºC)	Cell potential (V)	ΔG (kJ/kmol)	ΔH (kJ/kmol)	Daily H_2 amount (tons)	Product energy (MW)	Daily H_2 amount (tons)	Product energy (MW)	Efficiency Best Case (%)
1	900	Power	-	-	-	-	-	72	-	126	-
2		PEM	80	1.23	237.4	4.146	33.09	54	65.63	107.1	11.8
3		Alkaline	200	1.23	237.4	49.907	26.47	43.20	69.49	113.4	12.6
4	310	Power	-	-	-	-	-	55.80	-	77.5	-
5		PEM	80	1.23	237.4	4.146	25.64	41.85	40.37	65.88	20.9
6		Alkaline	200	1.23	237.4	49.907	20.52	33.48	42.74	69.75	22.6
7	140	Power	-	-	-	-	-	33.60	-	42	-
8		PEM	80	1.23	237.4	4.146	15.44	25.20	21.88	35.70	25.5
9		Alkaline	200	1.23	237.4	49.907	12.35	20.16	23.16	37.80	27.0
10	189	Power	-	-	-	-	-	49.14	-	64.26	-
11		PEM	80	1.23	237.4	4.146	22.58	36.86	33.47	54.62	29.3
12		Alkaline	200	1.23	237.4	49.907	18.07	29.48	35.44	57.83	30.6
13		MgCl	450	0.99	191	151.5	48.64	79.83	59.06	96.39	51.0
14	568	Power	-	-	-	-	-	187.44	-	255.60	-
15		PEM	80	1.23	237.4	4.146	87.14	140.60	133.10	217.30	38.2
16		SOEC	850	1.01	191.04	75.18	59.73	97.47	117.50	191.70	33.7
17		MgCl	450	0.99	191	151.5	146.20	238.60	177.50	289.70	51.0
18		CuCl	500	0.69	133.1	308	128.8	210.20	187.90	306.70	54.0
19		CaBr	750	0.6	115.8	282	114.9	187.40	160.10	261.30	46.0
20		HyS	850	0.16	30.88	323.8	121.80	198.80	191.40	312.40	55.0

Table 2. The amount of energy and hydrogen produced from the system for the worst- and best-case values conditions based on performances (Red: worst case, Green: best case).

Figure 3: Daily hydrogen production comparison (worst-best).

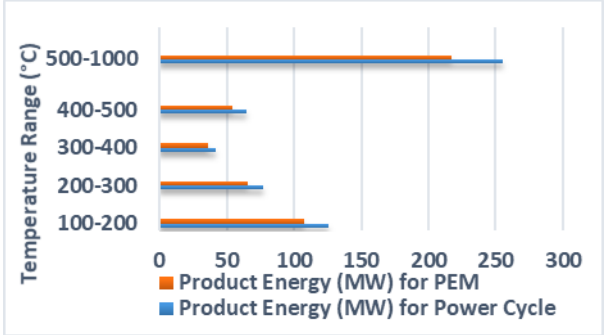

Figure 4. Product energy based on power and H_2.

In Figure 3, daily hydrogen production amounts are compared for the worst and best efficiency values of the cases. Due to the high temperature in power systems, the best efficiency comes from the GT. Considering the 18th and 20th cases, daily hydrogen production amounts are very close to each other for best efficiency. In Figure 4, product energy values were compared from a cycle using an energy cycle and PEM according to the temperature ranges of the sectors. The maximum product energy value was obtained from a power cycle of approximately 255 MW. This value depends on the power and efficiency produced by the sectors in the range of 500-1000 degrees from waste heat. The total produced hydrogen has the potential to compensate up to 5.8% of annual residential natural gas consumption of Turkey with a natural gas equivalent of 512 million m^3.

Conclusions

In this study, power and hydrogen recovery potential from industrial waste heat in Turkey is investigated. Many case studies are performed based on the temperature range of the waste heat. The annual waste energy amount is around 974 PJ and between 9-18% of this energy is recoverable with selected power and hydrogen technologies. Highest amount of power recovery is possible with Gas Turbine while HyS is eligible to recover the highest amount of hydrogen with its low cell potential leading to lower electricity requirement. Cost assessments should be conducted to investigate economically and to compare feasibility of selected hydrogen production technologies.

References

[1] H. Ö. Rami S.El-Emam, "Comprehensive review on the techno-economics of sustainable large-scale clean hydrogen production," *Journal of Cleaner Production,* pp. 593-609, 2019.

[2] AA, "CNN Turk," 1 January 2020. [Online]. Available: https://www.cnnturk.com/turkiye/bakan-kurum-5-termik-santral-tamamen-kapatildi.

[3] I. K. M. R. P. B. M. Clemens Formann, "Estimating the global waste heat potential," *Renewable and Sustainable Energy Reviews,* p. 1568–1579, 2016.

[4] G.Tekiner,"Recydia,"22July2016.[Online].Available: http://www.recydia.com/detaylar/2/basinda_recydia/1050/atiga_deger_katacak.aspx.

[5] İHA, 5 June 2019. [Online]. Available: https://www.haberler.com/baskan-ozlu-kati-atik-tesisi-bir-fabrika-gibi-12051261-haberi/.

[6] "Mamak Çöplüğü Biyogaz Tesisi," 2016. [Online]. Available: https://www.enerjiatlasi.com/biyogaz/mamak-coplugu-biyogaz.html.

[7] 2020. [Online]. Available: http://www.resmiistatistik.gov.tr/.

[8] E. İ. G. M. Enerji ve Tabii Kaynaklar Bakanlığı, "Türkiye Enerji Denge Tabloları," 21 January 2018. [Online]. Available: https://www.dunyaenerji.org.tr/turkiye-enerji-denge-tablolari/.

[9] G. K. A. C. U. L. C. G. M. Michael Papapetrou, "Industrial waste heat: Estimation of the technically available resource in the EU per industrial sector, temperature level and country," *Applied Thermal Engineering,* pp. 207-216, 2018.

[10] I. BCS, "Waste Heat Recovery: Technology and Opportunities in U.S. Industry," U.S Department of Energy: Industrial Technologies Program, U.S, 2008.

[11] G. M. O.A.Jianu, "Hydrogen cogeneration with Generation IV nuclear power plants," *Sustainable Power Technologies and Infrastructure,* 2016.

[12] R. H. Xing L. Yan, Nuclear Hydrogen Production Handbook, 2011.

[13] M. A. B. Yunus A. Cengel, Thermodynamics: An Engineering Approach, New York: McGraw -Hill Companies , 2011.

[14] I. D. Abdullah A. AlZahrani, "Modeling and performance optimization of a solid oxide electrolysis system for hydrogen production," *Applied Energy,* vol. 225, pp. 471-485, 2018.

[15] I. D. C. Z. Greg F. Naterer, Hydrogen Production from Nuclear Energy, London : Springer-Verlag , 2013.

Energy-enviro investigation of solar powered self-sustainable minimal liquid-solid discharge toilet

[1]P. Venkata sai, [2*]K. S. Reddy
[1,2] Institute of Technology Madras, Department of Mechanical Engineering, Chennai, 600 036, India

* E-mail: ksreddy@iitm.ac.in

Abstract
The sewage waste treatment is essential to reduce the concentration of pollutants which can pose a severe threat to the environment. In the present energy-environmental study, the sewage waste is treated in small scales at their source for minimal waste discharges. The proposed system is designed for treatment capacity of 2.4 kg solid waste and 55 liters of black water which is an average discharge from a family of 5 persons (2 adults and 3 children). This system operates under varying solar irradiation during the month of March in the location of Chennai, India. This treatment process consists of the separation of black water from solid waste and their treatment in a multi-stage distillation unit (MSD) and solar dryer. This is a completely self-sustainable process powered by solar renewable thermal and PV technologies. For equal flow distributions in MSD, the maximum distillate yield of 12.27 liters when operated under ambient pressure. The overall energy efficiency of the system is calculated as 29.58%. For a lifetime of 25 years and 300 clear days of operation, the energy payback time of the system is found as 3.19 years. Net CO_2 emissions mitigated over plant life time is calculated as 103.75 tons. The distilled water obtained from multi-stage distillation is used for the non-contact human requirements whereas the dried biomass from the solar dryer can be used either for power generation or as a natural fertilizer.

Keywords: Solar Energy, Black water treatment, Sewage treatment, Solid waste, Multi-stage distillation, Active solar dryer

I. Introduction:

Water pollution due to disposal of untreated sewage, percolation of pollutants from pit toilets into ground water, sewage water leak into potable water due to damaged pipelines are mainly caused due to improper sewage control techniques followed in developing nations (Sharma et.al., 2017). Generally, sewage consists of faeces, urine and laundry waste. As there are billions of human beings on earth, there is a huge discharge of sewage every day. Untreated sewage water contaminates water bodies upon their discharge and pose a severe threat to environment. This sewage often carries harmful bacteria, viruses and toxic chemicals which causes health issues when exposed to environment (Murphy and Morrison, 2006). As the reuse of waste water is highly necessary in regions of high water scarcity, many conventional treatment technologies such as activated sludge-extended aeration plants and biological stabilization ponds are currently in use. These conventional methods consume huge energy for operation, produces large amounts of sludge and treatment process happens in multiple stages (Sikosana, 2019). If the energy required is supplied from non-renewable sources, then the process leads to emission of CO_2 and other harmful gases into environment. There are distillation technologies which operates with solar renewable energy source such as inclined still, multi-stage distillation, multi-effect distillation (Sharon and Reddy, 2015). From above literature, it can be inferred that solar powered distillation and drying are effective methods for sewage treatment. And the treatment of sewage much closer to its source is a viable option to overcome above mentioned problems. Therefore, the present study deals with separate treatment of the black water and faeces mixture using solar multi-stage distillation and active solar drying units.

II. System Description and working principle:

The schematic representation of self-sustainable minimal liquid-solid discharge toilet along with its necessary components is shown in fig.1. This system is designed to treat sewage waste from a single family of 5 people (2 adults and 3 children) producing a load of 2.4 kg semi-solid waste and 55 litres of black water per day. To treat the waste in a sustainable way, the system is designed with liquid-solid separator, multi-stage distillation system, solar flat plate collectors (each 1.3 m^2 area), active solar dryer, solar air heater (2 m^2 area) and necessary auxiliary components for operation. The liquid-solid separator is made of strainer to separate black water and screw conveyor unit to transport semi-solid faeces. A multi-stage distillation system consists of evaporator-condenser unit with 150 litre feed water storage over last stage. Each evaporator-condenser unit consists of bottom tray whose upper surface acts as evaporator and a top tray whose bottom surface acts as condenser. These trays are tilted at an

angle with horizontal surface. Faeces dryer has a tray surface of 1 m^2 area and tilted from horizontal surface to spread faeces uniformly along its surface.

The mixture of black water and faeces from the toilet is separated in liquid solid separator. The separated black water is supplied to feed water reservoir of MSD and semi-solid faeces is fed into faeces dryer. Black water from reservoir is passed through solar flat plate collector where incident solar flux is utilized to raise the temperature of black water. This high temperature black water is fed into four stages of multi-stage distillation unit. When there is a difference in pressure and temperature between black water and stage, the process of flashing occurs releasing certain amount of water vapour and reduces remaining liquid to boiling point of stage. In the first stage of MSD, the high temperature liquid undergoes evaporation and the vapours rises to the upper region of stage. Due to the ambient temperature feed water reservoir over the top stage of MSD, there is a temperature difference created between stages of MSD. This temperature difference leads to convective, radiative heat transfer between stages and condensation of vapours over the condensing surface. The latent heat of condensation released from lower stage is used for enhancing evaporation of next stages which leads to higher yield in further stages. The condensed liquid is called distillate and is used for flushing and other essential requirements in toilet. In case of faeces drying, unsaturated cold ambient air is supplied into solar air heater with the help of centrifugal fan. In the solar air heater, the solar flux falling on the collector area is used to rise the temperature of cold air. This high temperature air is passed through the dryer which increases the temperature of faeces and increases the rate of evaporation. The moisture evaporated from faeces will be carried away by the unsaturated air. The dried semi-solid waste is a form of biomass which can be used either for combustion or manure for agriculture. The mathematical modelling of the complete system is carried out using MATLAB R2018a.

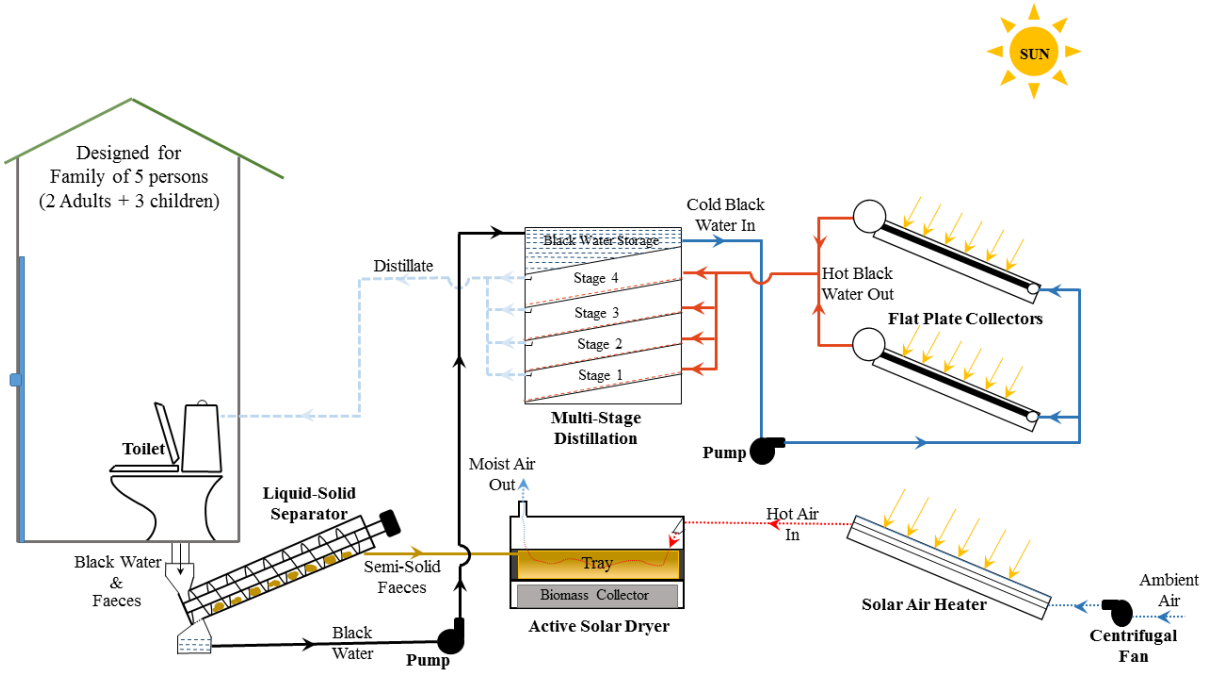

Fig.1. Solar powered self-sustainable minimal liquid-solid discharge toilet.

III. Energy Analysis:

In black water treatment process, the distillate yield produced from MSD and the energy required and lost during operation are calculated using following relations.

Rate of useful heat gain from the solar flat plate collector is given by (Sukhatme, 2008)

$$Q_{useful}=F_r*A_{fpc}*[S-(U_l*(T_{fi}-T_{amb}))] \quad (1)$$

Energy balance for first stage of multi-stage distillation unit can be written as

$$Q_{in1}=Q_{e1}+Q_{c1}+Q_{r1}+Q_{bw1}+Q_{fw1} \quad (2)$$

Energy balance from second to final stages (i-stage) of multi-stage distillation unit can be written as

$$Q_{in\,i}+Q_{e\,i-1}+Q_{c\,i-1}+Q_{r\,i-1}=Q_{e\,i}+Q_{c\,i}+Q_{r\,i}+Q_{bw\,i}+Q_{fw\,i} \quad (3)$$

Rate of distillate mass outflow from each stage of multi-stage distillation unit can be determined by

(Reddy et.al., 2012)

$$\dot{m}_{e\,i} = \frac{h_{cv\,i}}{\rho_{m\,i} * C_{pm\,i}} \frac{P_o}{P_{AM\,i}} \frac{M_v}{R} \left(\frac{P_{v\,i}}{T_i} - \frac{P_{v\,i+1}}{T_{i+1}}\right) Le_i^{-2/3} \quad (4)$$

Considering drying process undergoes constant drying rate until critical moisture of faeces (50% wet basis) after which falling rate drying is followed. The energy required along with duration of drying and the moisture content of faeces at any instant are calculated using following relations.

Rate of useful heat gain from the solar air heater is given by (Sukhatme, 2008)

$$Q_{useful} = F_r * A_{sah} * [S - (U_l * (T_{ai} - T_{amb}))] \quad (5)$$

Moisture content of faeces at the end of each time step under constant drying rate period is calculated using (Prakash and Kumar, 2017)

$$M_{t+1} = M_t - \frac{A*hc*(T_\infty - T_{wb})*\Delta t}{LH} \quad (6)$$

Moisture content of faeces at the end of each time step under falling rate drying period is calculated using Newton's or Lewis model (Koua et.al., 2009)

$$M_{t+1} = M_e + (M_t - M_e) * e^{-Deff*\left(\frac{\Pi}{b}\right)^2 * \Delta t} \quad (7)$$

$$Moisture\ ratio,\ MR = \frac{Mt - Me}{Mi - Me} \quad (8)$$

From this energy analysis, based on eqns.(1-8) the amount of distillate yield produced from MSD is calculated to be 12.27 liters shown in fig.2a when operated under ambient pressure. The rate of change in moisture ratio with respect to time for faeces moisture content ranging from 50-90% is shown in fig.2b Considering complete faeces separation occurring in liquid-solid separator and also losses in pump, centrifugal fan and motor are neglected. The total useful energy required for operation of the system is calculated as 32.6 MJ and total energy supplied to the system is 110.5 MJ. Hence the overall energy efficiency of the system is 29.58%.

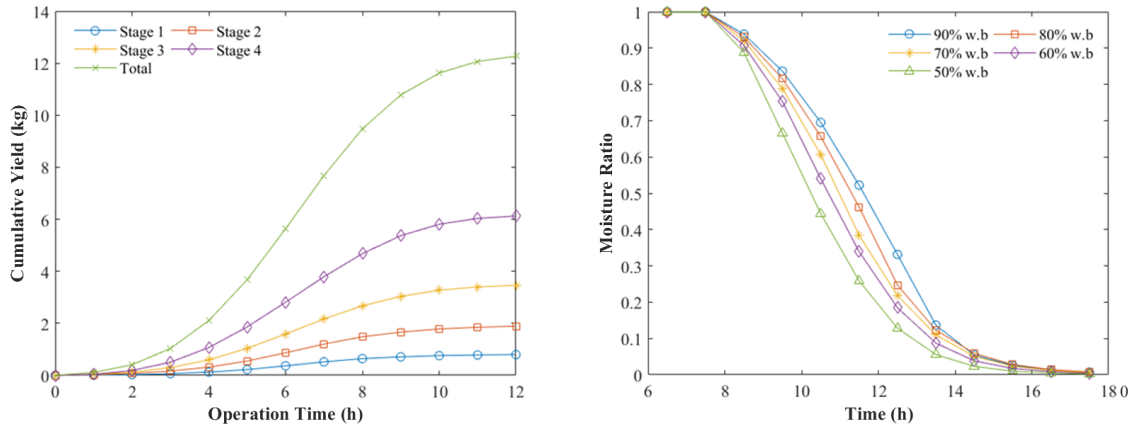

Fig.2. (a) Cumulative distillate yield from MSD, (b) Variation of MR w.r.t time for various moistures of faeces

IV. Environmental Analysis:

In the present study, it is considered that the components used in the system are made using non-renewable energy sources which caused environmental degradation by the emission of pollutants. For every 1 kWh of energy produced from these sources 1.58 kg of CO_2 is emitted. The embodied energy of the complete system is calculated as 30202.9 MJ which is equivalent to 8389.7 kWh. The net CO_2 emissions mitigated during plant life is analyzed as follows (Sharon and Reddy, 2015).

$$CO_2\ emissions\ for\ complete\ life\ time\ (kg) = Embodied\ Energy * 1.58 \quad (9)$$

$$Annual\ CO_2\ emissions\ (kg/yr) = \frac{Embodied\ Energy * 1.58}{LT} \quad (10)$$

$$Annual\ energy\ output\ from\ the\ system\ (kWh), E_{out} = \frac{(M_{Yield} + M_{DriedMoist}) * LH}{3600} \quad (11)$$

$$Energy\ payback\ time\ for\ the\ system\ (yrs), EPBT = \frac{Embodied\ Energy}{E_{out}} \quad (12)$$

$$Net\ CO_2\ emission\ mitigated\ over\ LT\ (kg), NCEM = \frac{((E_{out} * LT) - Embodied\ Energy) * 1.58}{1000} \quad (13)$$

Based on eqns.(9-13) for 300 clear days of operation per year, annual energy output from the system is calculated as 2630 kWh (salinity of 500ppm and 70% (wet basis) initial moisture of faeces). Annual distillate yield of MSD unit is calculated as 3681 liters. Energy payback time for the system is found to be 3.19 years. In a life time of 25 years, it is found that the system mitigates 103.75 tons of CO_2 emission.

V. Conclusion:

In this article, multi-stage distillation process and active solar drying process are proposed for treatment of black water and faeces separately. Energy-enviro analyses of proposed system have been successfully carried out to assess performance and environmental benefits using developed mathematical model. Under ambient operating pressure a mass flow rate of 13.75 LPD black water is supplied to all four stages of MSD which produces a maximum distillate yield 12.27 liters in the month of March. At the same point of time, faeces with 70% (wet basis) is treated in active solar still and reduced its moisture ratio to 0.1 in a span of around 6 hours. The effect of change in moisture ratios for different moistures of faeces is studied. In environmental analysis, embodied energy of whole system is determined as 8389.7 kWh and annual energy output of 2630 kWh from system. From the results, the system has an energy payback of 3.19 years and mitigates 103.75 tons of CO_2 during its life time.

Reference:

Sharma, R.K., Yadav, M. and Gupta, R., 2017. Water quality and sustainability in India: challenges and opportunities. In Chemistry and Water (pp. 183-205). https://doi.org/10.1016/B978-0-12-809330-6.00005-2

Murphy, B. and Morrison, R.D., 2006. Environmental forensics: contaminant specific guide. Academic Press. https://doi.org/10.1016/B978-0-12-507751-4.X5021-6

Sikosana, M.L., Sikhwivhilu, K., Moutloali, R. and Madyira, D.M., 2019. Municipal wastewater treatment technologies: A review. Procedia Manufacturing, 35, pp.1018-1024. https://doi.org/10.1016/j.promfg.2019.06.051

Sharon, H. and Reddy, K.S., 2015. A review of solar energy driven desalination technologies. Renewable and Sustainable Energy Reviews, 41, pp.1080-1118. https://doi.org/10.1016/j.rser.2014.09.002

Sukhatme, S.P. and Nayak, J.K., 2008. Principles of thermal collection and storage. Solar Energy, 3rd Edition, Tata McGraw Hill Publishing company, New Delhi.

Reddy, K.S., Kumar, K.R., O'Donovan, T.S. and Mallick, T.K., 2012. Performance analysis of an evacuated multi-stage solar water desalination system. Desalination, 288, pp.80-92. https://doi.org/10.1016/j.desal.2011.12.016

Prakash, O. and Kumar, A. eds., 2017. Solar drying technology: concept, design, testing, modeling, economics, and environment. Springer. https://doi.org/10.1007/978-981-10-3833-4

Koua, K.B., Fassinou, W.F., Gbaha, P. and Toure, S., 2009. Mathematical modelling of the thin layer solar drying of banana, mango and cassava. Energy, 34(10), pp.1594-1602. https://doi.org/10.1016/j.energy.2009.07.005

Sharon, H. and Reddy, K.S., 2015. Performance investigation and enviro-economic analysis of active vertical solar distillation units. Energy, 84, pp.794-807. https://doi.org/10.1016/j.energy.2015.03.045

Supply Security in Critical Energy Infrastructures for Reliable Energy Grids

[1*]İsa Avcı, [2]Cevat Özarpa, [3]Yusuf Bicer
[1] Istanbul University-Cerrahpasa, Engineering Faculty, Department of Computer Engineering, Avcılar, 34315, Istanbul, Turkey.
[2] Karabuk University, Engineering Faculty, Mechanical Engineering, Balıklarkayası Mevkii, 78050, Karabuk, Turkey.
[3] Hamad Bin Khalifa University (HBKU), Division of Sustainable Development (DSD), College of Science and Engineering (CSE), Qatar Foundation (QF), Education City, Doha, Qatar.

* E-mails: *isaavci@ogr.iu.edu.tr, cevatozarpa@karabuk.edu.tr, ybicer@hbku.edu.qa

Abstract
Energy is an indispensable building block of all countries and has an impact on the entire economy. Disruptions in the energy supply chain threaten health and welfare and directly affect the economy, which prevents continuous and regular energy distribution to consumers. Smart grids and cities in critical energy infrastructures have become one of the most important topics researched around the world in recent years. In this study, we aim to show the increase in the amount of energy supply from the past to the present and draw attention to the importance of this increasing energy supply in terms of security in critical infrastructure. Energy supply security has now become a priority for many critical infrastructure institutions. The consumption of energy supplies is expected to increase more in the coming years due to the increasing population. Renewable energy resources consumption is estimated to be 100 quadrillions in 2020, while consumption in 2050 is 250 quadrillions, and consumption in natural gas resources is estimated to be 200 quadrillions in 2050. Key factors of energy supply security are investigated in electricity, natural gas, coal, oil, renewable energy, nuclear energy. In this study, cyber security, which is one of the high risks, has been drawn attention to its importance due to the increase in attacks on energy resources in recent years. Especially in this study, an energy supply security framework is proposed for energy supply security, and shows the importance and reliability of renewable energies in energy supply security in critical infrastructures.

Keywords: Energy Supply Security, Smart Grid, Critical Energy Infrastructures, Renewable Energy Reliability

I. Introduction

Energy is one of the most important needs of human lives and to secure life in the world. Energy infrastructures in countries can be divided into three main segments: electricity, oil and natural gas. Electricity is obtained from very diverse sources such as coal, natural gas, nuclear, hydro, oil, solar, geothermal and wind, although each country has different source reserves. Due to the nature of the energy sector, the weaknesses are at the top of the issues that must be taken into account by policy makers. In addition, the dependence of all sectors on electricity and fuel brings the obligation and responsibility to increase the resistance of energy infrastructures to possible attacks.

When the practices in developed countries aiming at protection of critical infrastructures are examined, it has been determined that in addition to taking measures against physical and cyber attacks, sharing the experience among sector employees is one of the effective methods. A special program for the energy sector should be developed by integrating the state and private sector with regard to security of energy infrastructures. The specific threats and political position of each country should be assessed and implemented accordingly. According to the primary energy consumption in the world, renewable energy consumption has witnessed a substantial increase over the years as shown in Fig. 1.

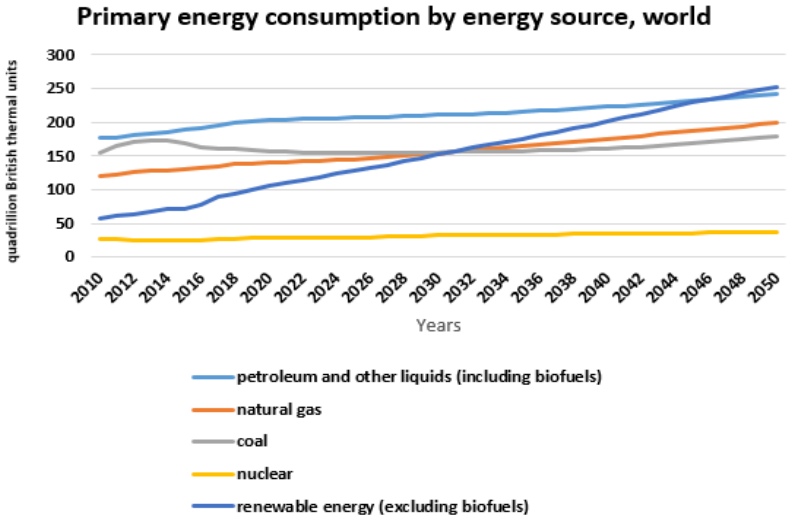

Fig.1. Primary energy consumption by energy source in the world (EIA, 2020).

In this study, firstly critical energy infrastructure for smart cities and grids are determined, and securing primary energy supply within the critical energy infrastructures for reliable energy grids is emphasized by addressing mainly cyber security. Cyber attacks have been increasing day by day for critical energy infrastructures and threaten

energy supply. Hence, a framework for energy supply security is also proposed considering economic, environmental, physical, technological and national security.

II. Critical Energy Infrastructures

The critical energy infrastructure includes all energy-related generation and storage facilities, transmission lines and routes, and consumption facilities and systems. Platforms and natural gas wells used in the production of energy sources such as oil and natural gas, all pipelines and LNG terminals from the main transmission lines that play a role in the transportation of these resources to the secondary transmission lines reaching the homes, tankers, refineries, pump stations, renewable energy facilities, dams and power control and protection systems, nuclear power plants, and all kinds of power generation systems, including power plants are considered within scope of critical infrasructure (Özertem, 2012). These are the basic vital elements of world society and the needs for these elements for the future should be taken into consideration. It is essential to implement a sustainable, environmentally compatible safety rule and policy based on uninterrupted flow and supply security and non-leakage in oil and gas pipeline facilities (The White House, 2003).

The economic welfare and development of the modern state, the use of advanced technology and the development of the level of production and development to ensure the effective use of energy resources and infrastructure security is an indispensable element of national security policies (Caşın, 2014). In addition to coal, oil and natural gas, the widespread use of nuclear energy, the information technologies that ensure the use of energy and the critical infrastructures that make up the distribution systems, ensure the safety and security of the critical infrastructures, making the continuous flow of fuel, gas and electricity used in daily life. The International Energy Agency (IEA) redefines the three vital elements of balanced energy policies as energy security, economic development and environmental protection (CRS Report, 2005).

III. Smart Cities

Smart cities are based on the idea of restructuring cities to maximize human and nature efficiency by reducing their complexity. Furthermore, smart cities have a management approach that creates and supports people-oriented, strategic, development, change, and environment. For these reasons, these cities are urban structures with improved service areas and living standards. These structures are based on the creation of comfortable, healthy, people-oriented, self-sufficient living spaces where innovative and sustainable methods are implemented efficiently and intelligently, respecting the nature, minimizing environmental problems (Nam & Pardo, 2011).

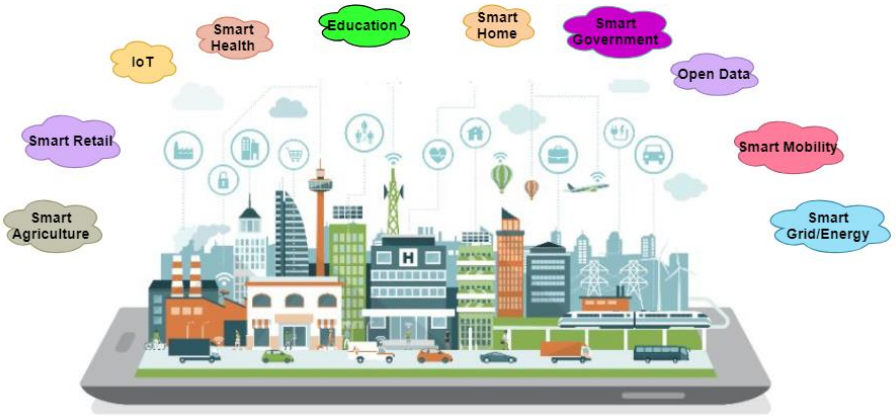

Fig. 2.Smart city overview (Channelpostmea, 2017)

IV. Smart Grids

Infrastructure services have an important position as an indispensable element for city life. Control of these infrastructure services has gained vital importance due to the increase in the urban population. The growing population has made it impossible to use and control infrastructure without Information Technology (IT) applications.

ISO (International Organization for Standardization), which is concerned with optimal management of physical assets, indicates that infrastructure management should be holistic, systematic, risk-based, optimum and sustainable. Organizational life plans are required through a foundation that manages systematized and interconnected movements and assets and institutions systems and controls the execution, risk, and expenditures over the period of success (Minnaar and Basson, 2013). This requires smart grids for systematic control.

The smart grid field communication is based on the IEC 61850 standard. The IEC 61850 protocol standard for the sub-station allows all protection, calculation, testing and monitoring to be combined with a single standard protocol (Baigent and Adamiak, 2004). Otherwise, devices of different manufacturers will not be able to use a large number of protocols and interfaces that do not mutually fit or are not parallel to each other. In the technical field, equipment standardization and interoperability have been implemented for a long time (Dönmez, 2013).

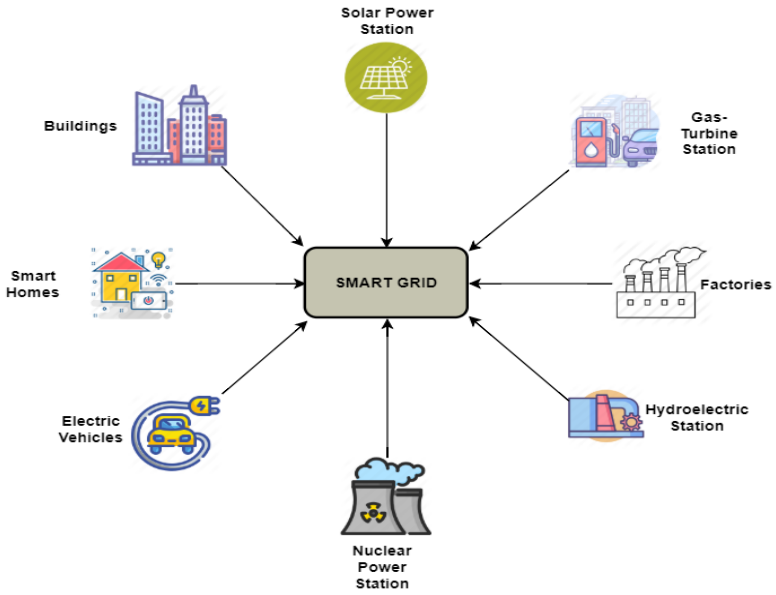

Fig. 3.Smart grid overview (Feroze and Javaid, 2017).

V. Energy Supply Security

Energy supply security is defined as the realization of energy supply, transportation and demand within the scope of production, transmission and consumption of energy in sufficient quantity and quality, at reasonable cost / prices, in an uninterrupted and environmentally sensitive manner" (Stiller vd., 2008). The International Energy Agency (IEA) defines energy supply security as "uninterrupted accessibility of energy resources at an affordable price". Enegy supply security includes security of gas, electricity, oil, coal, nuclear and renewable energy and other vital sources. Energy supply security consists of four main important elements, namely; availability, accessibility, reasonable Price and acceptability. The existence of these four basic elements ensures energy supply security (Kruyt etc., 2009:2165; Jansen etc., 2004:3; Elkind, 2010: 114). The energy supply security framework is proposed as a result of researches to make the energy supply security safer, as shown in Figure 4.

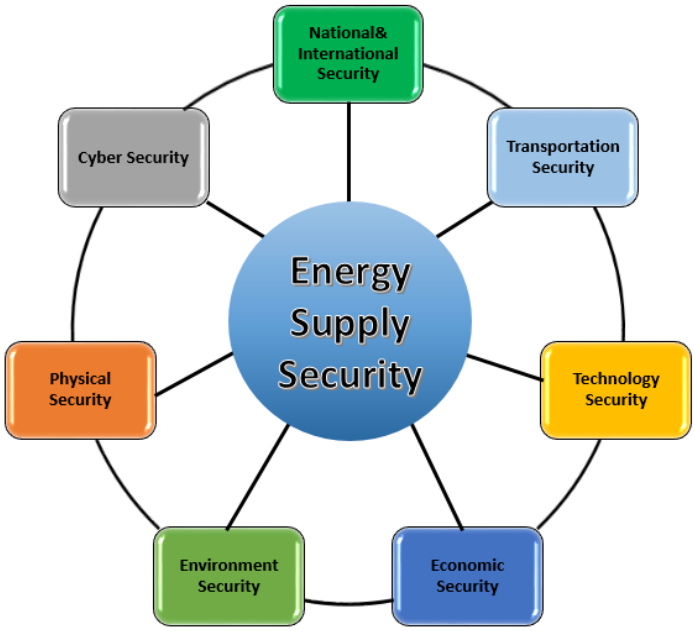

Fig. 4. Proposed energy supply security framework

VI. Investigation Key Factors of Energy Supply Security

The key factors of energy supply security vary depending on many risks. In Table 1, it is attempted to determine the risk types based on six main energy sources. It was determined by asking academicians who are experts on the types of risks identified and the effects of energy sources. The factors affecting energy supply security are given in detailed below in Table 1.

Table 1. Key factors influencing energy supply security

	Types of Risks	Reasons	Gas	Electricity	Coal	Oil	Nucleer Energy	Renewable Energy
1	Geological Risk	Resource Depletion/Shortage	√	√	√	√	X	X
2	Geopolitical Risk	War, Terrorism, Political Instability, Change Energy Policies, Taxation, Energy Management, Location	√	√	√	√	√	X
3	Economical Risk	Lack of Investment, Crisis, Energy Prices, Lack of State Support, Energy Management	√	√	√	√	√	√
4	Technical Risk	Plant Equipment Mulfunctioning/Failure	√	√	√	√	√	√
5	Climatic Risk	Natural Disasters, Extreme Weather Conditions, Higher Prices for Energy Crops	√	√	√	√	√	√
6	Cyber Attack Risk	Cyber Threats, Sabotage, Ransomware	√	√	√	√	√	√
7	Technological Risk	Embargo, Cyber Threats, Lack of Investment, Lack of Equipment, Higher Maintenance Costs	√	√	√	√	√	√
8	Personnel Risk	Cyber Attacks, Sabotage, Vandalism, Malevolence	√	√	√	√	√	√
9	National Risk	Sabotage, Vandalism, Politics	√	√	√	√	√	√
10	International Risk	Embargo, Cyber War, Sabotage	√	√	√	√	√	√
11	Operational Risk	Operational and Maintenance Costs, Accident,	√	√	√	√	√	√
12	Construction Risk	First Construction Costs, Energy Supply, Transportation Problem, Loss or Damage	√	√	√	√	√	√
13	Market Risk	Low Energy Demands, Lower Prices, Imports and Exports	√	√	√	√	√	√
14	Transportation Risk	Access to Resource, Extreme Weather Conditions, Transportation Costs	√	√	√	√	√	√
15	Security Risk	Natioanal and International Security, Physical Security, Information Security, Cyber Security	√	√	√	√	√	√
16	Environmental Risk	Pollution, Wates,	X	X	√	√	X	√
17	Accident Risk	Pollution, Harmful Spread to Health, Fatal	√	√	X	√	X	√

V. Conclusions

In this study, it is emphasized that energy supply security is a very important issue in terms of a vital need with the increase in the population worldwide. Energy is an indispensable building block of all countries and has an impact on the entire economy. Interruptions in the energy supply chain threaten health and welfare and directly affect the economy, preventing continuous and regular energy distribution to consumers. Smart grids and cities in critical energy infrastructures have become one of the most important topics researched in the world in recent years. We tried to describe critical energy infrastructures, smart cities, smart grids and energy supply security briefly. Also in this study, an energy supply security framework is proposed as a result of researches. Energy supply security is generally recommended to be evaluated on this framework. This proposed framework will contribute to the next studies for researchers and institutions doing scientific studies. In these critical infrastructures, key factors affecting energy supply security are evaluated in terms of risks and presented in a tabular form. In this table, key factors affecting energy supply security according to the types of risks are analyzed and specified. In addition, the given in the table the key factors affecting the risks will be developed in future studies and contribute to researchers and institutions.

References

Aminu Bature, A., Melville, L. and etc. 2018, An Investigation into the Effects of Risks and Risk Management of Bioenergy Projects, ICREN.

Baigent, D., Adamiak, M. and Mackiewicz, R., 2004, IEC 61850 communication networks and systems in substations: an overview for users.

Caşın, M.H.,2014, 'Kritik Enerji Altyapı Güvenliğinin Kurumsal Çerçevesi-Kritik Enerji Altyapı Güvenliği', Hazar Strateji Enstitüsü, İstanbul,ss. 5-6.

Channelpostmea, 2017, http://www.channelpostmea.com/2017/03/02/dubai-wants-to-become-a-global-benchmark-for-smart-cities, (ET: 02.03.2017).

CRS Report for Congress, 'Risk Management and Critical Infrastructure Protection: Assessing, Integrating, and Managing Threats, Vulnerabilities and Consequences', Şubat 2005, ss. 5.

Dönmez, M., 2013, Smart grids, and integration, BTC Business Technology.

Eia, 2020, https://www.eia.gov/outlooks/ieo/.

Elkind, J., 2010, "Energy Security, Call for a Broader Agenda", Energy Security, Economics, Politics, Stategies and Implications (Derl: Carlos Pascual ve Jonathan Elkind), Bölüm 6, ss. 119-149, Brookings Institution Press, Washington, D.C.

Erdal, L. and Karakaya, E., 2012, ENERJİ ARZ GÜVENLİĞİNİ ETKİLEYEN EKONOMİK,SİYASÎ VE COĞRAFÎ FAKTÖRLER, Uludağ Journal of Economy and Society.

Feroze, F. and Javaid, N., 2017, Towards Enhancing Demand Side Management using Evolutionary Techniques in Smart Grid, ResearchGate.

Iea, 2020, https://www.iea.org/.

Kruyt B., Vuuren D.P.,Van de Vries H.J.M. and Groenenberg H., 2009, "Indicators for energy security", Energy Policy, c. 37, ss. 2166–2181.

Minnaar, J. R., Basson, W., and Vlok, P. J., 2013, Quantitative methods required for implementing pas 55 or the ISO 55000 series for asset management. South African Journal of Industrial Engineering, 24(3):98-111.

Mutasim, M. and etc., 2019, Novel Approach of Quantifying Energy Security in terms of Economic, Environmental and Supply Risk Factors, Journal of Advanced Research in Fluid Mechanics and Thermal Sciences 57, Issue 1 (2019) 100-109.

Nam, T., & Pardo, T. A., 2011, Conceptualizing smart city with dimensions of technology, people, and institutions. In Proceedings of the 12th Annual International Digital Government Research Conference: Digital Government Innovation in Challenging Times (pp. 282–291). ACM.

Özertem,H.S.,2012,https://www.academia.edu/2449511/Critical_Energy_Insrastructure_Project_Final_Report_Kritik_Enerji_Altyap%C4%B1_G%C3%BCvenli%C4%9Fi_No_3.

Stiller, C., Seydel, P., Bunger, U. and Wietschel, M. (2008) "Early Hydrogen User Centres and Corridors As Part Of The European Hydrogen Energy Roadmap (Hyways)", International Journal Of Hydrogen Energy, c.33, s.41, ss. 4193- 4208.

The White House, 2003,'Risk Management and Critical Infrastructure Protection: Assessing, Integrating, and Managing Threats, Vulnerabilities and Consequences', ss. 5-6.

Life Cycle Assessment of Ammonia Synthesis from Thermo-Catalytic Solar Cracking of Liquefied Natural Gas (LNG)

[1*]Amro M. O. Mohamed, [1]Sami G. Al-Ghamdi, [1]Yusuf Bicer
[1] Division of Sustainable Development (DSD), College of Science and Engineering (CSE), Hamad Bin Khalifa University (HBKU), Qatar Foundation (QF), Education City, Doha, Qatar

* E-mail: ammohamed@mail.hbku.edu.qa

Abstract
Ammonia is considered as a sustainable energy storage medium. It is regarded as one of the critical and green energy storage fuels with zero carbon content. In this work, thermal catalytic cracking of liquefied natural gas (LNG) at elevated temperatures employing concentrated solar tower is considered to produce clean hydrogen (CO_2-free) and studied in terms of life cycle emissions. Then, the generated hydrogen is utilized for ammonia synthesis in a Haber-Bosch reactor. The proposed system is initially assessed from a thermodynamic point of view, considering energy and exergy analyses with emphasis on the optimization of operating conditions. Then, life cycle assessment (LCA) of the proposed system is performed to analyze the environmental impacts of ammonia synthesis. Aggregate environmental impact of the proposed system is quantified and compared with conventional hydrogen and ammonia production processes. Through the utilization of renewable energy resources, the production of ammonia can be attained, avoiding high harmful emissions. The LCA study is carried out in GaBi software, and the selected impact assessment methodology is ReCiPe. The impact categories studied in this work are global warming potential (GWP), acidification, human toxicity, and particulate matter formation potential. The predicted GWP, considering 30 years of use phase, is approximately 1.04 kg CO_2 eq. /kg NH_3. This shows the potential to reduce up to 50% of the GWP compared to the global average value. Concerning human toxicity and particulate matter formation impact categories, the system produces about 0.051 kg 1,4-DB eq. and 9.86e-4 kg PM10 eq., respectively, per kg NH_3.The results are analyzed by dominance, break-even and variation analyses.

Keywords: Methane decomposition, life cycle assessment, solar energy, solar hydrogen, ammonia

I. Introduction

Immense use of energy (1.2% of the primary energy consumption) and extreme emissions of pollutants (0.93% of global greenhouse gas emissions) (Gilbert and Thornley, 2010) are associated with the production of the raw materials necessary for commercial ammonia production. The ammonia synthesis reaction from dinitrogen and dihydrogen is an exothermic reaction which favors low-temperature condition and high pressures to optimize the ammonia yield. The typical operating conditions for the reaction are a temperature of 400-500 ^oC and a pressure of 150-300 bar (Bartholomew and Farrauto, 2010; Bencic, 2001). Nitrogen, which comprises 78% of the atmosphere, is separated from the air mixture through a cryogenic separation which is an energy-intensive process (Smith and Klosek, 2001). On the other side, hydrogen is mainly produced through the reforming process, in which carbon-based fuel (i.e. Natural gas, coal, and petroleum) is combusted in the presence or absence of water vapor to produce synthesis gas and hydrogen. A substantial amount of greenhouse gases are emitted in this process. Several studies reported GHG emissions in the ammonia synthesis plant. A compiled list of these studies is provided in (Makhlouf et al., 2015). The values range from 1.25-2.16 kg CO_2 eq/ kg NH_3, where the global average and European average are estimated to be 2.07 (Williams, G and Al-Ansari, 2007) and (1.91 (Wood and Cowie, 2004) and 1.94 (De Haas, M J.G.; Van Dijk, 2010)). Besides steam reforming, there are other processes such as CO_2 reforming, autothermal reforming, and partial catalytic oxidation.

Production of hydrogen utilizing solar energy and other renewable energies forms can result in a decrease in the environmental impact of producing ammonia. Concentrating solar thermal energy can be a viable solution to achieve high temperatures required to crack hydrocarbon. (Steinberg, 1998) concluded that hydrogen production through methane cracking requires the least process energy and offers the lowest CO_2 emissions. Under 900 ^oC and 56.1 atm, the conversion increases with residence time and approaches equilibrium value without the use of catalytic material. Methane decomposition is favored at low pressures, but the reaction rate is favored by high pressure. The design of methane cracking can be accomplished in a packed or fluidized bed reactor (Abbas and Wan Daud, 2010). Problems associated with methane cracking that have to be resolved before commercialization consideration are carbon management, deactivation, and continuous withdrawal of carbon. Other methods developed to make the process continuous and to overcome the deactivation problem are molten metal and plasma dissociation (Abbas and Wan Daud, 2010). It was argued that burning the accumulated carbon inside the porous structure is the only way to remove carbon, stressing on the absence of other viable methods (Serban et al., 2003).

Dufour et al. used LCA methodology to study the environmental load associated with methane cracking. The decomposition of methane was considered to take place in the presence and absence of catalytic material and compared with conventional steam reforming (Dufour et al., 2009). The functional unit used was 1 Nm^3 of hydrogen. LCA evaluated the material (raw material) acquisition and manufacturing stages. One of the main conclusions was the autocatalytic decomposition presented the lowest total impact and CO_2 emissions. Typically, this is a result of lower temperature operations. Catalytic materials are used to reduce the intensity of the process (lower temperatures are needed for certain conversion). However, in their study, the conversion in the reactor did not rely on a thermodynamic or kinetic model to support it.

A life cycle assessment was accomplished to quantify the environmental impact of hydrogen production following the thermal cracking liquid metal route (Postels et al., 2016). The liquid-metal technology was proposed to eliminate the catalysts requirement. Thus, the cracking is not facilitated by a catalyst and solely dependent on elevated temperatures. It was determined that a 64% reduction in global warming potential (GWP) could be reduced when compared with steam reforming. Carbon produced can be used, with 80% efficiency, in a carbon fuel cell to produce electricity. In addition, carbon can be sold and utilized for the production of inks, paints, tires and batteries (Dincer and Bicer, 2018). Carbon is considered as non-usable co-product (waste) as the other LCA study. Process data were obtained from experiments, simulations and assumptions from literature.

There are four main methods to concentrate solar energy; these are, solar tower, troughs, Fresnel and parabolic dish. Solar power tower or central receiver systems use a circular field array of adequately large sun-tracking mirrors, named heliostats, focus sunlight onto a central receiver. A temperature between 800 and 900 ^{o}C is achievable. Usually, the production of such systems targets the production of a clean and reliable source of electrical power.

Lechon et al. (Lechón et al., 2008) conducted an LCA based analysis focused on determining the environmental impact of electricity produced from 17 MW solar thermal plant with central tower technology. The system utilized 2750 heliostats, and molten salt was used as a heat transfer fluid. The majority of greenhouse gas emissions was attributed to the operational stage, with 91.6% of the total life cycle. Solar field and storage systems combine for 7% of the life cycle emissions. Global warming emissions are mainly due to the consumption of natural gas and external electricity consumption. Besides GWP, other impact categories considered were ozone layer depletion, abiotic depletion, human toxicity, and marine aquatic eco-toxicity.

Kuenlin et al. carried out a comparative LCA study for four different CSP plants; parabolic, central tower, Fresnel and dish (Kuenlin et al., 2013). The LCA modelling was made possible by using data from plant recently built. The Gemasolar plant, located in Spain, was used to model the solar tower case. The Gemasolar plant is constructed in 210 ha with 2650 heliostats. The capacity factor is 63% and the annual net output of 110 GWh. A new power plant (Hysol) was analyzed environmentally using LCA (Corona et al., 2016) for 25 years of lifetime. This study demonstrated the effect of the location on performance. The performance of the plant is a function of location due to natural resources and solar energy.

The objective of this study is to demonstrate the potential of solar cracking of methane, employing a solar tower system, to minimize the environmental load in the ammonia production. This paper focuses on providing a solution for catalytic deactivation by demonstrating a route for carbon management. Energy requirements and design parameters for solar collectors have been defined and estimated previously from thermodynamic calculations. Environmental impacts associated with liquefaction, shipping and cracking of methane to produce ammonia are assessed and quantified in certain impact categories. The chemical plant is designed to fulfill its energy requirement solely from the solar tower concentrated solar energy and LNG feedstock (source of hydrogen). A break-even analysis alongside dominance and contribution analysis are prepared to analyze the overall system.

II. Material and Methods

LCA is a powerful tool to quantify elementary inputs and outputs from a specific product system. It assesses the footprint associated with a particular product and allows for meaningful comparisons. LCA consists of four core phases. First, goal and scope are clearly defined. Second, Inventory analysis is made, which involves data preparation and calculation procedures. Third, emissions and resources depletion is quantified and grouped in categories in impact assessment step. The last step involves reporting and further analysis of the result (Result Interpretation). GaBi software (Thinkstep AG, 2014) is used in the study to model the LCA, most of the material and energy flows are determined from the Ecoinvent database (Swiss Centre for Life Cycle Inventories, 2011).

II.I. Goal and Scope

In this study, catalytic cracking of methane is accomplished at elevated temperatures by means of a solar collector system. A solar field is employed to drive the solar cracking of methane. The deposited carbon on the catalytic material is burned using pure oxygen from an air separation unit (ASU) in a regenerative reactor where carbon dioxide is produced. Carbon dioxide is recycled into the regenerator for temperature moderation. It was shown that the temperature profile of oxy-CO_2 is consistent with air—fired conditions when the molar fraction of CO_2 is set at 66% (Zhong et al., 2018). The produced amount of carbon dioxide is being collected and send to the urea production reaction through an intermediate compression stage. The regeneration and process reactors act as a separation process in the case of steam reformers and so on. A descriptive process flow diagram is shown in Figure (a).
The functional unit is 1 kg of ammonia. System boundaries can be seen in **Error! Reference source not found.**(b). Life stages that are being considered are (1) methane extraction, purification, liquefaction, transportation. (2) Manufacturing of solar-based plant (solar tower, reactor, air separation, etc.). (3) Maintenance and operational impact (use phase of the LCA). Several impact assessment methods are used but primarily GWP, human toxicity, and particulate matter formation potential and fossil depletion. Contribution, dominance and break-even analysis are considered to improve the results of the LCA. Limitations include detailed catalysts design and preparation data. The main assumptions are written as follows:

- Chemical equilibrium and conversions of the reactors are studied.
- Civil work in pipes, storage tanks are not included. Also, fittings, flanges and safety systems are excluded from the inventory analysis.

- Sizing and materials required are scalable.
- Pumps and compressors life spans are set at 10 years with constant efficiency (isentropic 80% efficiency) (Beebe, 2004), so the number of used rotary equipment is calculated taking into consideration by the lifetime of the chemical plant.
- The plant is initially designed to run for 30 years.

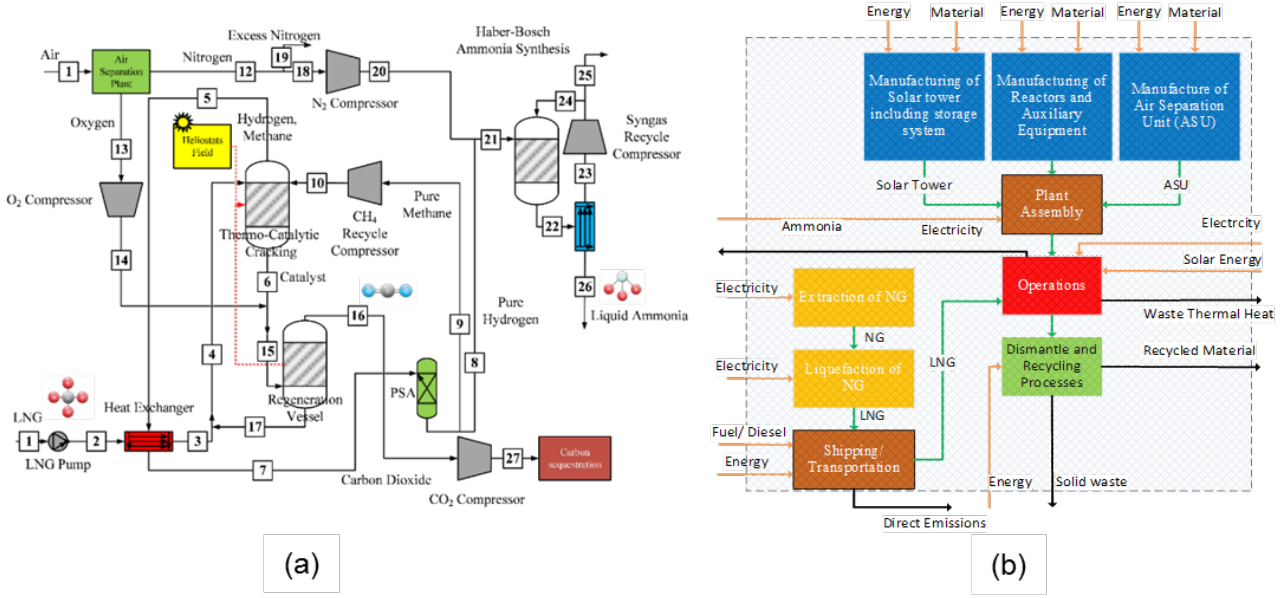

Figure 1: (a) Process flow diagram of the thermo-catalytic synthesis of hydrogen, (b) The system boundaries for the ammonia synthesis from LNG solar-driven decomposition

II.II. Inventory Analysis

Kuenlin et al. studied the LCA of three different sizes of the power plant at (50, 100, 200 MW) utilizing solar tower setup, the extraction and manufacturing, construction, operation and maintenance and dismantling of the solar tower collector was considered in their study (Kuenlin et al., 2013). Direct emissions of some chemicals to the atmosphere were 9.39E-3 and 5.52E-3 kg CO_2 /kWh for the 100 and 200 MW plants, respectively. Another set of inventory data for a solar power plant is the Gemasolar power plant data (Kuenlin et al., 2013). Buildings and other materials regarding insulation and so are gathered from (Viebahn et al., 2008).

Several assumptions have been taken in the inventory analysis to quantify flows of materials:

- High Pressure (HP) stream is at 150 bar and steam condensate are fully recycled
- Japan, natural gas mixture process, was selected from Gabi database to represent the LNG in the modelled operational part of the LCA.
- The pressure swing adsorption (PSA) system was designed to have 10 columns, 5 in operations.
- It was assumed that the recovery of hydrogen is complete to simplify the recycle and cracking modelling.
- The parameters used to assess the catalytic material and adsorbent contributions in the LCA study included the manufacturing of a given amount of these materials. The amount was specified through the determination of the required amount with an additional amount to recover the deactivation and attrition losses in the regeneration/reactor system, ammonia converter and PSA separation system.
- The storage system uses sensible thermal energy storage using a eutectic mixture of Li/K/Na carbonate and amount is quantified to allow for 12 hours of operations using the storage system.
- The catalysts used in the heat-balance reactors is the 7% Ni/Al_2O_3 catalyst was selected in this work as the conditions are similar in terms of the reactor configuration adopted and temperature of the regeneration reaction (Williamson, 1977).
- In order to estimate the amount of material required in building reactors, gas-gas separators, and gas-liquid separations vessels, it was assumed that these vessels are cylindrically shaped. The shell thickness is also calculated based on the material of construction and designed pressure. Separators were designed taking a pre-defined L(H)/D ratio based on the operating pressure.
- The ammonia synthesis converter was designed as steel cylinders of 80-140 cm internal diameter and 10-18 m height.

II.III. Impact Assessment

The selection of the LCIA method, whether it is ReCiPe or another and supports the selection based on literature (Postels et al., 2016) or the specific application and location of the study. The ReCiPe method is considered the most recent and harmonized indicator approach. It does not include potential impacts from future extractions in the impact assessment calculations. The most relevant and important impact assessment is the GWP as this directs the comparison with benchmark processes such as methane steam reforming and has the largest contribution. Fossil depletion has been studied in previous LCA publications, and the importance of this category lies in the

continuous methane depletion (Postels et al., 2016). Other impact categories have included in previous LCA studies on hydrocarbon cracking; these include, ozone layer depletion, acidification, eutrophication, heavy metals, summer and winter smog. (Dufour et al., 2009) showed that acidification and heavy metals depletion are significant in the thermal and catalytic based decomposition of methane.

III. Results and Discussion

Several interpretation techniques are used to report LCA results. The primary focus will be on the integration of impact assessment at the characterization level. The first significant analysis is the dominance analysis, which demonstrates the most pollutant part of the life cycle and is used to reflect on the significance of the solar reactors construction phase. Sensitivity analysis is also adapted to detect changes in process modeling data; this is mainly focusing on inventory data input from the thermodynamic analysis. The proposed system is then compared comprehensively against conventional hydrogen and ammonia production routes.

Results related four selected impact categories are reported here. At the operating temperature of 900 °C, optimum pressure was found, and consequently, amounts of oxygen, nitrogen and LNG are determined. It is worth mentioning that the construction and extraction steps constituted around 10% of the GWP in previous studies. The results, depicted in Figure 2(a), from LCA modeling, show the contribution of the extraction of materials and building of the solar field, receiver and operating system. The extraction and manufacturing processes contribute to 1.45e+7 kg CO_2 eq., which corresponds to approximately 1 kg CO_2 eq. / kg NH_3. This value is relatively higher than the expected value for the construction phase, which may allude to more prolonged services for better offsetting the extraction and construction impact.

On the other hand, the production of nitrogen and oxygen in the ASU contributes to approximately a quarter of the GWP; whereas, LNG contributes to around 64% of the total GWP, as shown in Figure 2(b). The water system used for cleaning purposes and others contributes to about 4%. The major contributor to human toxicity is steel (stainless and reinforcing steel), followed by oxygen and LNG requirements. Three-quarters of the particulate matter formation is demonstrated by LNG. Considering 30 years of operations, the chemical plant would result in a 50% reduction in GWP, relative to the global average (absolute value=1.04 kg CO_2 eq/ kg NH_3). It is important to note that the impact is quantified without allocation. An extended allocation can be considered based on the product's economic value. In some cases, 85% of the share of environmental impact is allocated to ammonia, while the balance 15% is assigned to carbon dioxide.

The particulate matter formation from the construction phase is approximately 0.001 kg PM10 eq. per kg NH_3. LNG is considered the dominating factor in terrestrial acidification. Its impact reaches 50% of the total impact, whereas ASU is responsible for approximately 36% of the acidification. Moreover, Human toxicity and particulate matter formation recorded 0.051 kg 1,4-DB eq. and 9.86e-4 PM10 eq., respectively.

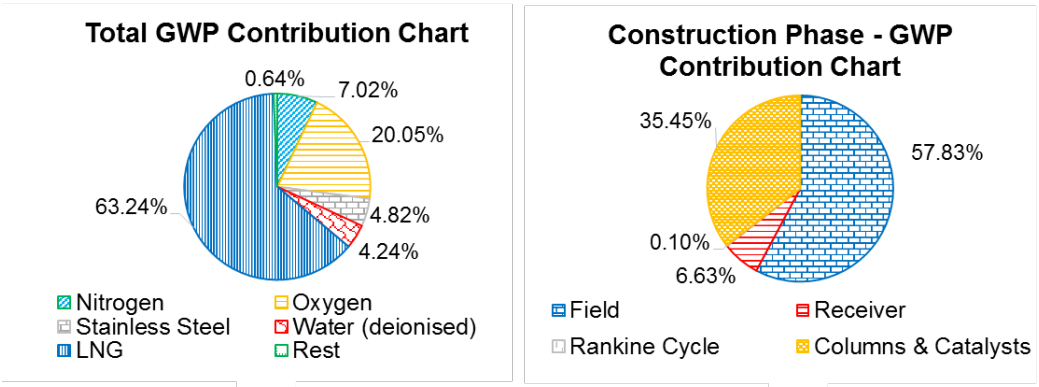

Figure 2: Contribution charts of (a) total GWP and (b) construction phase GWP

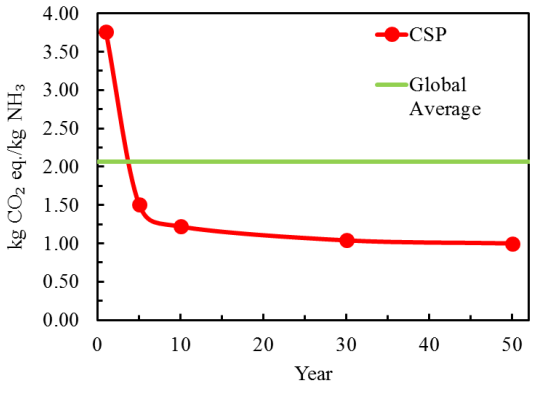

Figure 3: The effects of years of operation on the aggregate GWP of the system

A sensitivity analysis was conducted to demonstrate the effect of the number of years of activity on the three impact categories. The purpose is to capture and isolate the effect of the construction and extraction phase. As demonstrated by Figure 3, the GWP of the system reduces from 1.51 to 1 kg CO_2 eq. (34% reduction), without allocation, starting from 5 to 50 years of operations, respectively. A power law can be used to model the reduction of relative impact per operational year. In addition, the solar field is the main contributor to the construction phase, which comprises 58%, 56% and 95%, of GWP, particulate matter formation and human toxicity, respectively.

From preliminary results, it can be concluded that the solar tower system will significantly reduce the operational phase's environmental impact, while slightly contribute more in the load related to construction and extraction phases. Therefore, the system served the purpose of reducing the impact and produce ready-to-use and potentially sequestrated CO_2 stream.

IV. Conclusions

The process of hydrogen production employer solar methane decomposition was assessed from an environmental standpoint using LCA. A cradle-to-grave LCA was carried to estimate the environmental load. Impact assessment categories discussed in this work varied from local to global scales. The ReCiPe method was selected for classification and characterization of environmental impact. GWP of producing 1 kg of ammonia using the proposed system is estimated to be 1.04 kg CO_2 (eq.)/kg H_2, considering 30 years of continuous operations. This demonstrates the potential of the system to cut emissions to half its global average. The dominance analysis showed that the operational stage is the most pollutant step in this process, considering the amount required of LNG (source of H_2) and energy-intensive ASU. The solar tower system has an environmental break-even point at 3.5 years.

Acknowledgements

This publication was made possible by an award from Qatar National Research Fund (a member of Qatar Foundation) with scholarship number GSRA5-1-0513-18051. The contents herein are solely the responsibility of the authors. The authors acknowledge the support provided by the Hamad Bin Khalifa University, Qatar Foundation.

References

Abbas, H.F., Wan Daud, W.M.A., 2010. Hydrogen production by methane decomposition: A review. Int. J. Hydrogen Energy 35, 1160–1190. https://doi.org/10.1016/j.ijhydene.2009.11.036

Bartholomew, C.H., Farrauto, R.J., 2010. Fundamentals of Industrial Catalytic Processes: Second Edition, 2nd ed, Fundamentals of Industrial Catalytic Processes: Second Edition. Wiley-AIChE. https://doi.org/10.1002/9780471730071

Beebe, R.S., 2004. Predictive Maintenance of Pumps Using Condition Monitoring, Predictive Maintenance of Pumps Using Condition Monitoring. https://doi.org/10.1016/B978-1-85617-408-4.X5000-1

Bencic, S., 2001. Ammonia Synthesis Promoted by Iron Catalysts Literature Report.

Corona, B., Ruiz, D., San Miguel, G., 2016. Life cycle assessment of a HYSOL concentrated solar power plant: Analyzing the effect of geographic location. Energies. https://doi.org/10.3390/en9060413

De Haas, M J.G.; Van Dijk, T.A., 2010. Inventarisatie klimaatvriendelijke kunstmest. Wageningen (Netherlands).

Dincer, I., Bicer, Y., 2018. Ammonia Production, in: Comprehensive Energy Systems. https://doi.org/10.1016/B978-0-12-809597-3.00201-7

Dufour, J., Serrano, D.P., Gálvez, J.L., Moreno, J., García, C., 2009. Life cycle assessment of processes for hydrogen production. Environmental feasibility and reduction of greenhouse gases emissions. Int. J. Hydrogen Energy 34, 1370–1376. https://doi.org/10.1016/j.ijhydene.2008.11.053

Gilbert, P., Thornley, P., 2010. Energy and carbon balance of ammonia production from biomass gasification, in: Bio-Ten Conference.

Kuenlin, A., Augsburger, G., Gerber, L., Maréchal, F., 2013. Life Cycle Assessment and Environomic Optimization of Concentrating Solar Thermal Power Plants, in: 26th International Conference on Efficiency, Cost, Optimization, Simulation and Environmental Impact of Energy Systems (ECOS2013).

Lechón, Y., de la Rúa, C., Sáez, R., 2008. Life Cycle Environmental Impacts of Electricity Production by Solarthermal Power Plants in Spain. J. Sol. Energy Eng. https://doi.org/10.1115/1.2888754

Makhlouf, A., Serradj, T., Cheniti, H., 2015. Life cycle impact assessment of ammonia production in Algeria: A comparison with previous studies. Environ. Impact Assess. Rev. 50, 35–41. https://doi.org/https://doi.org/10.1016/j.eiar.2014.08.003

Postels, S., Abánades, A., von der Assen, N., Rathnam, R.K., Stückrad, S., Bardow, A., 2016. Life cycle assessment of hydrogen production by thermal cracking of methane based on liquid-metal technology. Int. J. Hydrogen Energy 41, 23204–23212. https://doi.org/10.1016/j.ijhydene.2016.09.167

Serban, M., Lewis, M.A., Marshall, C.L., Doctor, R.D., 2003. Hydrogen production by direct contact pyrolysis of natural gas. Energy and Fuels. https://doi.org/10.1021/ef020271q

Smith, A.R., Klosek, J., 2001. A review of air separation technologies and their integration with energy conversion processes. Fuel Process. Technol. https://doi.org/10.1016/S0378-3820(01)00131-X

Steinberg, M., 1998. Production of hydrogen and methanol from natural gas with reduced CO2 emission. Int. J. Hydrogen Energy 23, 419–425. https://doi.org/https://doi.org/10.1016/S0360-3199(97)00092-X

Swiss Centre for Life Cycle Inventories, 2011. Ecoinvent database v2.2.

Thinkstep AG, 2014. GaBi 6 software and databases.

Viebahn, P., Kronshage, S., Trieb, F., Lechon, Y., 2008. Deliverable n 12.2-RS Ia: Final report on technical data , costs , and life cycle inventories of solar thermal power plants, Energy. Brussels.

Williams, G and Al-Ansari, F., 2007. IFA benchmarking of global energy efficiency in ammonia production, Workshop on Energy Efficiency and CO2 Reduction Prospects in Ammonia Production, IFA Technical Committee Meeting, Ho Chi Minh City, Vietnam.

Williamson, K.C. and K., 1977. Hydrogen: Its technology and implications. CRC Press, Boca Raton, FL,.

Wood, S., Cowie, A., 2004. A Review of Greenhouse Gas Emission Factors for Fertiliser Production. Research and Development Division, State Forests of New South Wales, Cooperative Research Centre for Greenhouse Accounting.

Zhong, S., Zhang, F., Peng, Z., Bai, F., Du, Q., 2018. Roles of CO2 and H2O in premixed turbulent oxy-fuel combustion. Fuel 234, 1044–1054. https://doi.org/https://doi.org/10.1016/j.fuel.2018.07.135

Synthetic Natural Gas Production in Power-to-Gas Approaches Involving Biomass Gasification and Anaerobic Digestion

[1*]Anna Skorek-Osikowska, [2]José Luis Gálvez-Martos
[1] Silesian University of Technology, Faculty of Energy and Environmental Engineering, Department of Power Engineering and Tubomachinery, ul. Konarskiego 18, 44-100 Gliwice, Poland
[2] IMDEA Energy, Systems Analysis Unit, Avda. Ramón de la Sagra, 3 Parque Tecnológico de Móstoles, 28935 Móstoles, Madrid, Spain

*E-mail: anna.skorek@polsl.pl

Abstract
Power to gas (PtG) technology allows obtaining liquid and gaseous fuels, such as hydrogen, synthetic natural gas (SNG), methanol, etc. The main goal of this paper is to assess and compare two hybrid systems for the production of synthetic natural gas from electrolytic hydrogen through a methanation processes. First case is a technology consisting of a source of renewable energy (wind or solar), electrolyzers for the production of hydrogen (and oxygen), oxy-gasification unit as a source of carbon monoxide and dioxide for the methanation reactor, which can optionally be equipped with tanks for hydrogen, oxygen and SNG storage. Second case differs from the first one in the source of carbon for methanation, which in this solution comes from an anaerobic digestion process. Thus, the main difference between the two proposed cases is the type of biomass used and its thermal conversion technology, resulting in significantly different composition of the raw gas bearing the source of carbon for methanation. It was assumed that in both cases 1 MW of SNG is produced. To make the assessment of the proposed solutions mathematical models were built and a parametric analysis was made. It allowed determining the main performance indicators of the proposed solutions, such as mass and energy flows, and gas composition in characteristic points of the systems as well as the efficiencies of the full chains. The results show that both cases may be an interesting option for SNG production and energy storage. The energy efficiency of the solutions reaches a value of 84% and 90% for Case 1 and 2, respectively.

Keywords: Electrolysis, methanation, SNG production, thermodynamic assessment

I. Introduction
The increasing share of intermittent and non-programable renewable energy sources in electricity generation systems causes the need for large scale energy storage. This is reflected, among others, in the European Union energy policy (e.g., COM(2018) 773; EASE 2019). One solution for energy storage, characterized by high flexibility and high potential of integration with electricity grid, is power to gas (PtG) technology (Götz et al., 2016). It allows obtaining liquid and gaseous fuels, such as hydrogen, synthetic natural gas (SNG), methanol, etc., that might be stored, used locally for the purpose of energy generation or chemical industry needs, or injected to the natural gas grid (Kopyscinski et al., 2010; Schiebahn et al., 2015). Power to gas systems are gaining increased attention which is reflected in increasing number of projects being implemented in Europe (e.g., Grond et al., 2013; Naturgy 2018; Rönsch et al., 2015). This paper focuses on one of the options of PtG solution, in which SNG, thus a gas with methane content similar to natural gas, is produced based on renewable hydrogen and biomass (converted into gas in gasification and fermentation process) bearing a source of carbon dioxide for methanation. Thus, the main goal of the paper is to assess and compare two systems for the production of synthetic natural gas from the process gas and biogas through a methanation processes.

II. Methodology/System Description
In this paper two hybrid systems allowing for production of SNG are analysed, according to the scheme presented in Figure 1. The models of these systems were built in Aspen Plus and Gate Cycle software. In general, both systems consist of basic technological installations in the form of a renewable energy sources (wind or solar), electrolyzers for the production of hydrogen and oxygen, synthesis reactor (methanation), a source of carbon for methanation and all the necessary equipment (compressors, heat exchangers, tanks, etc.). However, to simplify the calculations, gasification and anaerobic digestion processes were not modelled in detail, but the gases that results from these processes served as an input for the simulation models. The main difference between the two considered solutions lies in the source of carbon dioxide, which in Case 1 is biomass gasification and in Case 2 is anaerobic digestion.

The analysis assumes steady-state conditions and do not consider such factors as potential discontinuous supply of hydrogen (resulting from intermittent operation of a renewable source supplying electrolyzer with electricity), necessity of the use of storage tanks (for gases) or fluctuations of mass/energy streams.

Case 1 assumes that gasification proceeds in the atmosphere of oxygen and steam which allows to (i) partially use oxygen from electrolysis (being a by-product) and (ii) avoid nitrogen ballast in the resulting gas. Conditions and parameters of the process, as well as process gas composition were adopted from the literature (e.g., Lv et al., 2007). Case 1 requires the use of a Shift reactor in which conversion of carbon monoxide to carbon dioxide occurs in the presence of steam. Case 2 involves the use of biogas that is produced in the anaerobic digestion. Similarly

as for Case 1, conditions and parameters of the process as well as composition of the biogas were assumed based on the literature data and previous works of the authors (e.g. Skorek-Osikowska et al., 2019). In both cases the stream of gas (process gas or biogas) is mixed with hydrogen and enters the methanation reactor in which the Sabatier reaction proceeds:

$$CO_2 + 4H_2 \rightarrow CH_4 + 2H_2O \quad \Delta H = -165 \text{ kJ/mol.} \tag{1}$$

Methanation is assumed to be an isothermal process and the heat from cooling of the reactor is used for the production of steam. After methanation the produced synthetic natural gas is cooled and dried. Both considered systems are dimensioned to produce 1 MW of SNG (taking into account composition of the resulting gas). Thus, the stream of hydrogen and biogas/process gas are calculated to fulfil this condition, considering stoichiometric need for the substrates and products according to the reaction (1).

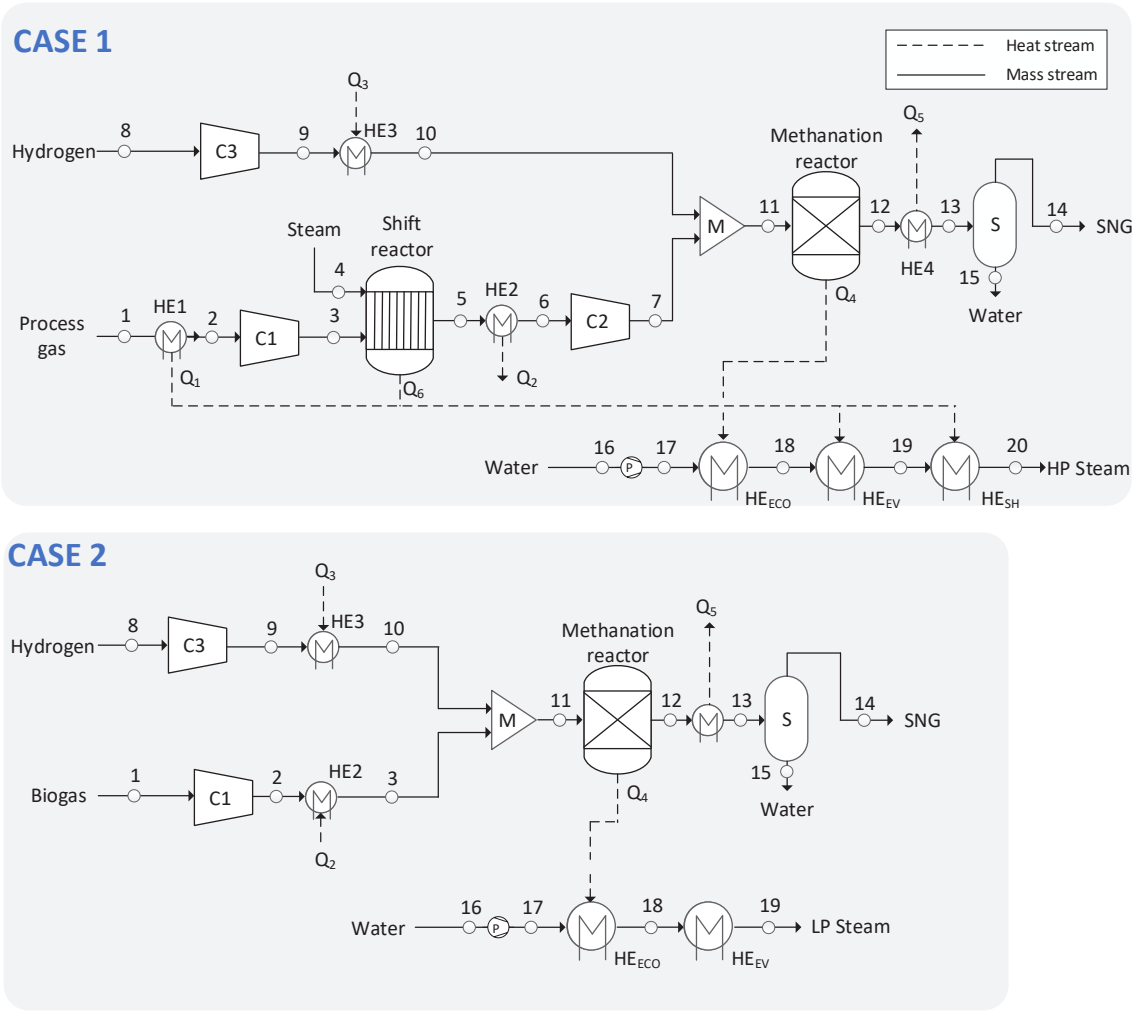

Fig. 1. Schematic diagram of the two analysed systems; denotations: C – compressor, HE – heat exchanger, S – separator; P – pump; M – mixer

The main assumptions for the calculations adopted to the models are presented in Table 1.

Table 1. Main assumptions for the analysis

Parameter	Case 1	Case 2	Unit
Chemical energy of produced SNG, LHV basis	1	1	MW
Temperature in methanation reactor	250	250	°C
Pressure in methanation reactor	10	10	bar
Pressure in shift reactor	10	-	bar
Isentropic efficiency of compressors	0.8	0.8	-
Cooling water temperature (p. 16)	90	90	°C
Hydrogen purity	1	1	-
Hydrogen pressure	5	5	bar

To compare the technologies mass streams and the most important thermodynamic parameters in characteristic points of the systems were calculated. Also, the efficiencies of the considered technologies were

determined. Usually, the energy efficiency (η_E) which considers the chemical energy of streams entering and leaving the system boundaries, is calculated from the following formula:

$$\eta_E = \frac{\dot{E}_{ch,SNG}}{\dot{E}_{ch,Gas}+\dot{E}_{ch,H2}}, \quad (2)$$

where $\dot{E}_{ch}$ is chemical energy of gas (SNG – synthetic natural has, H_2 – hydrogen, Gas – biogas or process gas).

However, the streams entering and leaving the system boundaries are characterized by different enthalpies (particularly in Case 1 the process gas stream is supplied at high temperature) which should be reflected in the above-mentioned definition. Thus, the overall efficiency (η_T) is determined according to the following equation:

$$\eta_T = \frac{\dot{m}_{SNG}(LHV_{SNG}+h_{SNG})}{\dot{m}_{Gas}(LHV_{Gas}+h_{Gas})+\dot{m}_{H2}(LHV_{H2}+h_{H2})}, \quad (3)$$

where $\dot{m}$ is a mass stream expressed in kg/s, *h* is enthalpy in kJ/kg, LHV is lower heating value in kJ/kg.

IV. Results and discussions

Based on the models that were built it was possible to determine basic parameters in the characteristic points of the systems, i.e. flows and thermodynamic parameters of particular streams. Within the system boundaries, heat flows are also generated which, because of the high temperature of the medium, may be usefully utilized for hot water or steam generation. The main sources of heat are cooling of the process gas after gas generator (Case 1), cooling of the Shift reactor (Case 1), cooling of methanation reactor (Case 1 and 2) and cooling of the gas after methanation reactor (Case 1 and 2). Some heat can also be produced from intersectional cooling of the compressors; however, it was not considered useful here. Part of heat generated within the system with the highest parameters is used for production of steam. In Case 1 the quality of heat that is generated allows to produce high pressure steam (HP steam). For that three heat exchangers are present: economizer (increasing water temperature to the saturation temperature, here 224 °C), evaporator and superheater (steam is superheated to 417°C). In Case 2 saturated steam can be produced (LP steam) which involves the presence of only the economizer and the evaporator. In both cases, the stream of water entering these heat exchangers is calculated in order to fulfil the assumptions concerning temperatures of steam that is generated.

The most important results, including values of the streams of energy produced or supplied to the system are shown in Table 2.

Table 2. Selected results from modelling (denotations according to Fig. 1)

Quantity	Value		Unit
	Case 1	Case 2	
Process gas/biogas stream	*257.13*	*138.83*	*kg/h*
Hydrogen stream	*23.11*	*18.69*	*kg/h*
SNG stream	*78.55*	*73.22*	*kg/h*
Water stream (p. 16, Fig. 1)	*310.00*	*153.00*	*kg/h*
Work:			
C1	*39.393*	*9.759*	*kW*
C2	*0.879*	*-*	*kW*
C3	*7.545*	*6.099*	*kW*
P	*0.749*	*0.370*	*kW*
Heat:			
Q_1	*-79.259*	*-*	*kW*
Q_2	*0.022*	*0*	*kW*
Q_3	*11.312*	*9.401*	*kW*
Q_4	*-176.867*	*-108.664*	*kW*
Q_5	*-178.658*	*-81.374*	*kW*
Q_6	*-55.347*	*-*	*kW*
Conversion rate (methanation process)	*0.9880*	*0.9869*	*-*
Energetic efficiency	*0.8406*	*0.9051*	*-*
Overall efficiency	*0.7750*	*0.9037*	*-*

Table 3 shows main parameters and compositions of streams in selected characteristic points of the systems, including process gas/biogas at the inlet (point 1), hydrogen stream (point 8), resulted SNG (point 14) and gas before and after methanation process (point 11 and 12, respectively). For Case 1 gas parameters after Shift reactor (point 5) are additionally presented.

Table 3. Main components and gas parameters in the selected points of the system (see Fig. 1); C1 – Case 1, C2 – Case 2

Quantity	Characteristic point number											
	1		5		8		11		12		14	
	C1	C2	C1	C2	C1	C2	C1	C2	C1	C2	C1	C2
Temp, °C	800	40	214.9	-	20	20	221.2	224.8	250	250	25	25
Pressure, bar	1.5	1.5	10	-	5.0	5.0	10.0	10.0	10.0	10.0	10.0	10.0
LHV, MJ/kg	5.837	12.440	5.580	-	119.958	119.958	15.014	25.195	12.819	22.804	45.734	49.055
Stream, kg/h	257.13	138.83	257.13		23.11	18.69	280.24	157.52	280.24	157.52	78.55	73.22
Enthalpy, kJ/kg	1403.4	29.51	327.1	-	63.61	63.61	555.74	606.01	486.05	519.89	0	0
Composition												
CO_2	0.18	0.5043	0.3132	-	0.0000	0.0000	0.1605	0.1672	0.0041	0.00327	0.0137	0.0066
H_2O	0.45	0.0277	0.3168	-	0.0000	0.0000	0.1623	0.0092	0.7009	0.5061	0.0116	0.0051
N_2	0.01	0.000	0.0100	-	0.0000	0.0000	0.0051	0.0000	0.0074	0.0000	0.0244	0.0000
H_2	0.168	0.000	0.3012	-	1.0000	1.0000	0.6420	0.6685	0.0123	0.0128	0.0405	0.0257
CO	0.135	0.000	0.0018	-	0.0000	0.0000	0.0009	0.0000	0.0000	0.0000	0.0000	0.0000
CH_4	0.057	0.4681	0.0570	-	0.0000	0.0000	0.0292	0.1552	0.2750	0.4778	0.9090	0.9626

V. Conclusions

As it results from the analysis both systems have the potential to generate SNG with the composition similar to natural gas, thus, can potentially substitute fossil natural gas in energy generation systems. Case 2 compared to Case 1 is characterized by higher energy efficiency (90.51% vs 84.06%), however, in Case 1 significantly higher amount of high-quality heat is produced that can be usefully utilized. Total net heat production (production reduced by own consumption) in Case 1 is equal to 490 kW while in Case 2 to 190 kW.

The analysis presented in this paper is based on simplified calculations and general assumptions. In further work the detailed analysis, including detailed modelling of individual technological installations will be made. For a full evaluation of the analysed solution it is necessary to carry out economic and environmental analysis. The key issue here will be the adoption of appropriate assumptions for calculations that can prejudge the profitability of the project in consideration. Such analysis will also be conducted by the authors in the future.

Acknowledgements

The scientific work was funded by the Polish National Science Centre within the framework of the research project entitled *Utilization of electrolysis and oxygen gasification processes for the production of synthetic natural gas in a polygeneration system*, no. 2017/27/B/ST8/02270.

References

COM (2018) 773 final. A Clean Planet for all. A European strategic long-term vision for a prosperous, modern, competitive and climate neutral economy. Brussels, 28.11.2018.

EASE. Energy Storage for a Decarbonised Europe by 2050. European Association for Storage of Energy. Brussels, 11.2019.

Götz M., Lefebvre J., Mörs F., et al. Renewable Power-to-Gas: A technological and economic review. Renewable Energy 85, 2016, 1371–1390.

Grond L., Schulze P., Holstein J. 2013. Systems analyses Power to Gas: Technology review. TKI Gas project TKIG01038, DNV KEMA, Groningen 2013.

Kopyscinski J., Schildhauer T. J., Biollaz S.M.A. 2010. Production of synthetic natural gas (SNG) from coal and dry biomass – A technology review from 1950 to 2009. Fuel 89, 1763–1783.

Lv P., Zhenhong Y., Ma L., Wu Ch., Chen Y., Zhu J., Hydrogen-rich gas production from biomass air and oxygen steam gasification in a downdraft gasifier. Renewable Energy 32, 2007, 2173-2185.

Naturgy, 2018. Gas Natural Fenosa launches pilot project to produce renewable gas in Catalonia. Press Release, https://prensa.naturgy.com/en/gas-natural-fenosa-launches-pilot-project-to-produce-renewable-gas-in-catalonia/.

Rönsch S., Schneider J., Matthischke S., et al. Review on methanation – From fundamentals to current projects. Fuel 166, 2015, 276-296.

Schiebahn S., Grube T., Robinius M., Tietze V., et al. Power to gas: Technological overview, systems analysis and economic assessment for a case study in Germany. International Journal of Hydrogen Energy 40(12), 2015, 4285–4294.

Skorek-Osikowska A., Gálvez-Martos José-Luis, García-Gusano D., Martin-Gamboa M., et at. Thermodynamic and environmental assessment of systems including the use of gas from manure fermentation in the context of the Spanish potential. Proceedings of the 32nd International ECOS Conference, Wrocław, Poland, 23-28 June 2019, 2115-2124.

CFD Investigation of Falling Film Flow over Horizontal Tube

[1*]Furqan Tahir, [1,2]Abdelnasser Mabrouk, [1]Muammer Koç
[1] Division of Sustainable Development (DSD), College of Science & Engineering (CSE), Hamad Bin Khalifa University (HBKU), Education City, P.O. Box 34110, Qatar
[2] Qatar Environment and Energy Research Institute (QEERI), Hamad Bin Khalifa University (HBKU), Education City, P.O. Box 34110, Qatar

* E-mails: futahir@hbku.edu.qa

Abstract
The heat exchangers employed in multi-effect desalination (MED) and ammonia/lithium bromide refrigeration systems are usually of falling film types. In horizontal falling film exchangers, liquid is sprayed on the top of bundle, which forms thin film around the tube that makes these exchangers to operate at low temperature difference and spray density. The film hydrodynamics around the tube affects the heat and mass transfer mechanisms, which causes heat exchanger performance to change. In this work, a 2D computational fluid dynamics (CFD) model has been developed in Ansys fluent v18.0, to understand falling film dynamics around the tube of 25.4 mm diameter. The physical domain consists of two tubes with an impingement height of 15.9 mm and inter-tube spacing of 31.8 mm. For water entrance, 2 mm orifice is selected at the top of first tube. The spray density is varied from 0.02-0.05 kg/(m·s) to examine film thickness and residence time for first and second tube. The CFD results shows that the film thickness increases with the increasing spray density, the average film thickness rises by 56% and time for complete wetting decreases by 48.6% ,when the spray density increases from 0.02 to 0.05 kg/(m·s). In addition, the average film thickness reduces by around 13.7% for second tube as compared to that of first tube because of impingement height difference.

Keywords: CFD, Falling Film, Horizontal Tube, Hydrodynamics

I. Introduction

The horizontal tube falling film evaporators are commonly used in multi-effect desalination (MED) plants as these evaporators exhibit high heat transfer coefficient as compared to flooded exchangers (Mabrouk et al., 2017b; Tahir et al., 2018b, 2019a). The heat transfer coefficient of falling film evaporators strongly affects by film distribution and hydrodynamics (Karmakar and Acharya, 2020, 2019; Narváez-Romo and Simões-Moreira, 2017; Ribatski and Jacobi, 2005; Tahir et al., 2019b). The film thickness around the tube is studied experimentally and numerically by many researchers (Chen et al., 2015; Qiu et al., 2015) and the film distribution is influenced by many factors such as thermophysical properties, wall adhesion, tube layout and operating conditions (Mabrouk et al., 2017a; Tahir, 2020; Tahir et al., 2018a). In 1916, Nusselt (Nusselt, 1916) proposed a film thickness δ correlation as shown in Eq. (1) by assuming negligible inertial effects.

$$\delta = \sqrt[3]{\frac{3\mu_l \Gamma_{1/2}}{\rho_l(\rho_l-\rho_g)g\sin\theta}} \quad (1)$$

where $\Gamma_{1/2}$ is spray density, θ is inclination angle, μ_l is liquid viscosity, ρ_l is liquid density, ρ_g is gaseous phase density and g is acceleration due to gravity. From Eq. (1), it is clear that film distribution is symmetric across the upper and lower half of tube surface. Hou et al. (Hou et al., 2012) performed experiments and observed that the film distribution is asymmetric and also it is affected by tube diameter d and inter-tube spacing s. They modified the Eq. (1) as shown in Eq. (2), by introducing s/d factor and constant C and n for asymmetric profile fit, which are different for upper and lower half of tube.

$$\delta = C \cdot \sqrt[3]{\frac{3\mu_l \Gamma_{1/2}}{\rho_l(\rho_l-\rho_g)g\sin\theta}} \left(\frac{s}{d}\right)^n \quad (2)$$

Ji et al. (Ji et al., 2017) conducted numerical experiments and found the minimum thickness at θ=120° and they proposed modification in Eq. (1) by replacing θ by 0.75θ for better film thickness prediction. Tahir et al. (Tahir et al., 2020a, 2020b) analyzed the effect of thermophysical properties on film distribution and they concluded that the fluid with surface tension and viscosity results in increased conductive thermal resistance which may deteriorate heat transfer performance. In the literature, the influence of inter-tube spacing has been reported however, its effect on residence time is lacking. In the present work, impact of impingement height (15.9 mm for first tube and 31.8 mm for second tube) on film distribution has been analyzed. The film distribution and residence time for first and second tube with respect to spray density has been quantified and discussed.

II. Computational Fluid Dynamics (CFD) model

Fig. 1a shows the CFD domain and boundary conditions, consisting of two tubes of 25.4 mm with 2 mm orifice for water entrance. The thermophysical properties of water and air are computed at 20 °C. As the nature of the problem is symmetric, therefore only half of the domain is selected for computation. It is assumed that the flow is laminar

and adiabatic, there is no vapor flow and tube wall is super hydrophilic to ensure complete wetting of tubes (Khan et al., 2019). The domain is meshed with quad dominant elements with fine boundary layers on the tube wall as shown in Fig.1b, for accurate capturing of liquid-gas interface.

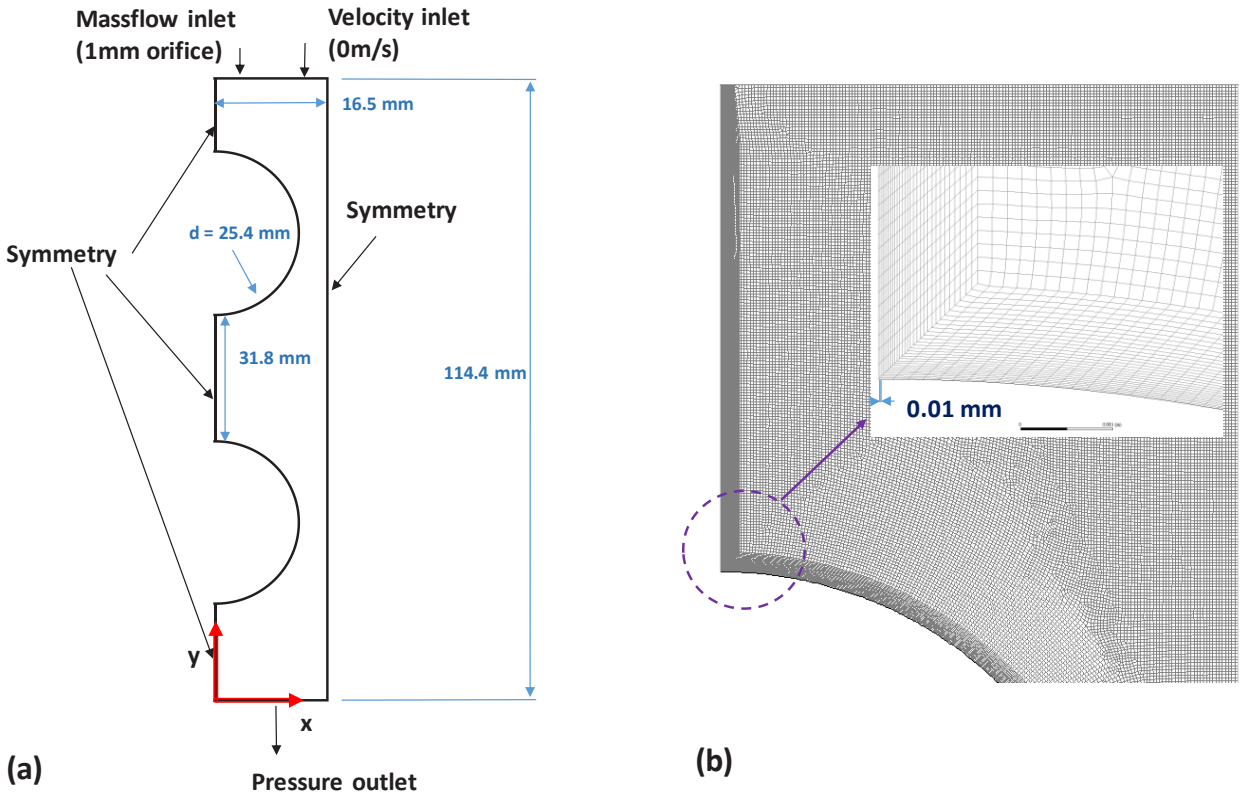

Fig. 1: (a) CFD domain with boundary conditions and (b) Mesh with fine boundary layers near to tube wall

The conservation of mass and momentum are discretized and solved for each phase, as per volume of fluid (VOF) model shown in Eq. 3. The VOF model is widely used where liquid-gas interfaces are distinct (Baloch et al., 2018).

$$\frac{\partial(\alpha_i \rho_i)}{\partial t} + \nabla \cdot \left(\alpha_i \rho_i \overrightarrow{V_i}\right) = 0 \qquad (i = g \ \ or \ \ l) \tag{3}$$

where V is velocity, α is void fraction and g/l denotes gas/liquid phases. The thermophysical property is computed by:

$$\beta = \alpha_l \beta_l + (1 - \alpha_l)\beta_g \tag{4}$$

where β is any thermophysical property. The spray density $\Gamma_{1/2}$ has been varied from 0.02-0.05 kg/(m·s), which corresponds to droplet to jet mode. The detailed methodology, solver settings and validation details can be found in (Tahir et al., 2020a).

III. Results and discussion

Fig.2a shows water film thickness around the tube surface and it can be seen that the film thickness in the impingement and detachment region is higher than other region. As the liquid hits the surface at top, it disperses in to circumferential direction, and with the continuous influx, a thicker region is formed. In addition, as the liquid reaches at the bottom, it starts to compile due to surface tension and viscous force and detaches when it overcomes the gravitational force. The accumulation of liquid phase at the bottom results in higher time-averaged thickness. Due to higher thickness at the top and bottom, average film thickness has been computed from θ = 20°-160° for comparison purpose as shown in Fig. 2b. With the rise in spray density from 0.02 to 0.05 kg/(m·s), the average film thickness increases by 56% and 61% for the first and second tube respectively. At 0.02 and 0.05 kg/(m·s), the average film thickness for the second tube is 14.4% and 11.5% less than that of first tube, respectively.

Fig 3a and b shows the volume fraction contours for top and bottom tubes at t = 0.9 s and $\Gamma_{1/2}$ = 0.05 kg/(m·s). As the spray density of 0.05 kg/(m·s) corresponds to jet-mode, the continuous liquid stream can be observed after the first tube. At t = 0.9 s, the second tube is completely wet and liquid gathers at the bottom of tube which forms

continuous stream after detachment. The residence time, which can be deduced from time for complete wetting of tubes, is shown in Fig 3c, for different operating conditions. The time required to cover the first tube at $\Gamma_{1/2}$ = 0.02 kg/(m·s) is 0.66 s, which decreases as the film average velocity increases because of rise in spray density. The time to cover tube decreases by 48.6% when the spray density rises from 0.02 to 0.05 kg/(m·s). Similarly, the time for complete wetting of second tube at 0.02 kg/(m·s) is 1.62 s, which reduces to 0.87 s at 0.05 kg/(m·s). This trend implies that at higher spray densities, the contact time for heat transfer with the tube surface is lowered, which may results in reduced heat transfer coefficient. This is one of the reason that heat transfer coefficient for droplet mode (low spray density) is higher the jet mode (high spray density) (Hosseinnia et al., 2017).

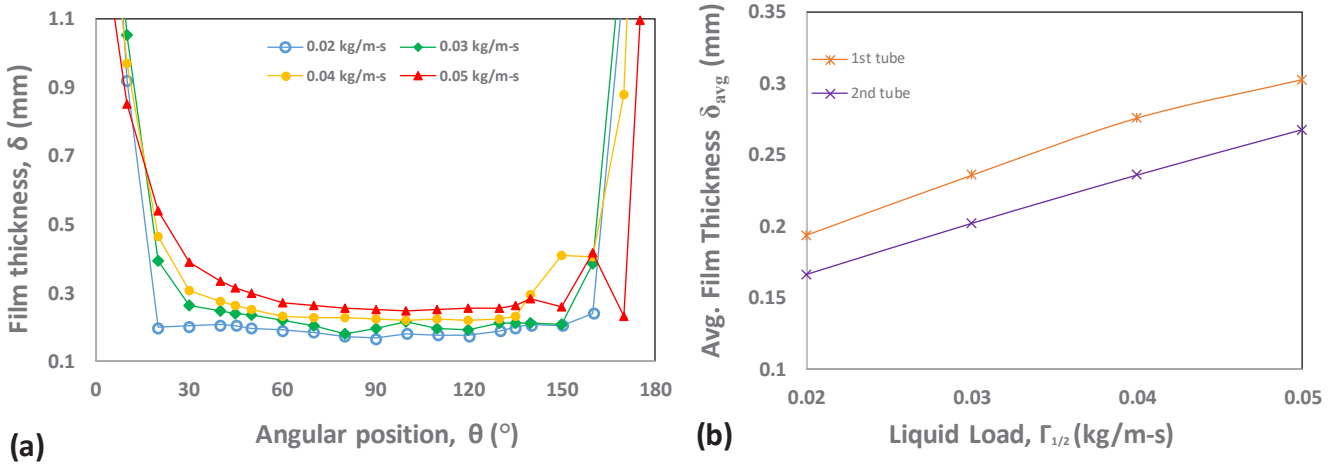

Fig. 2: (a) Film thickness distribution around first tube surface for different spray densities and (b) average film thickness (from θ = 20°-160°) with respect to spray densities

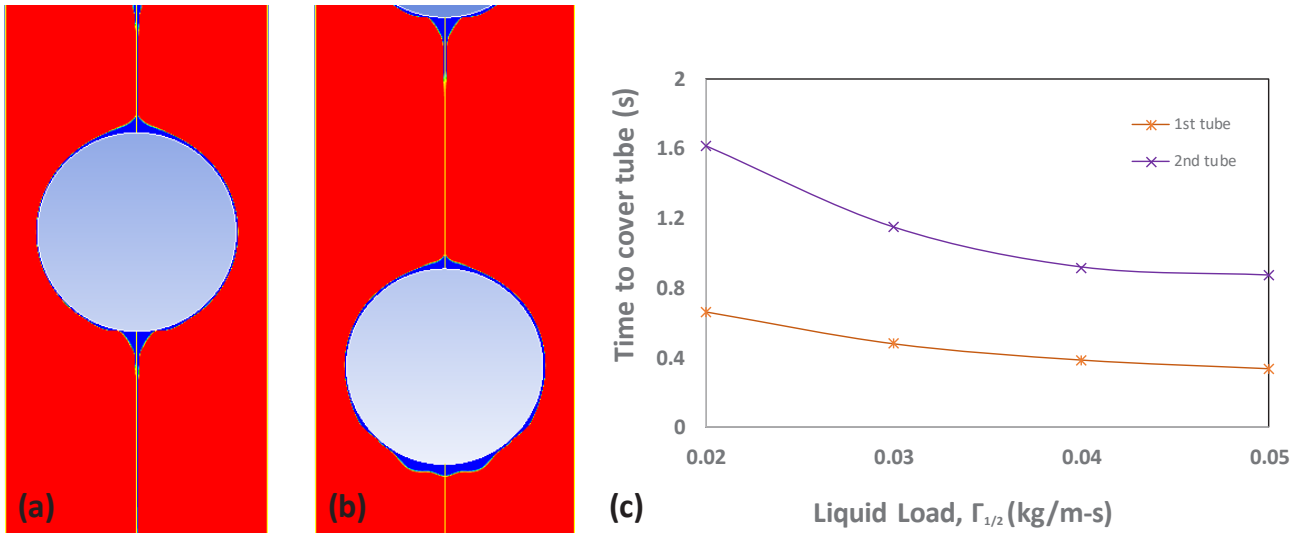

Fig. 3: Wetting of (a) first and (b) second tube at $\Gamma_{1/2}$ = 0.05 kg/(m·s) and t = 0.9 s, and (b) time to complete wetting of first and second tubes with respect to spray densities

IV. Conclusions

A two-dimensional computational fluid dynamics (CFD) model for analyzing falling film hydrodynamics has been presented. Two tubes of 25.4 mm diameter with an impingement height of 15.9 mm and tube-to-tube spacing of 31.8 mm has been selected, to examine the effect of spray density and impingement height on the falling film thickness and the time for the complete wetting of first and second tube. The numerical results shows that the falling film thickness at the impingement and detachment regions, is very high as compared to the other region (θ = 20° - 160°). The average film thickness grows by 56 % and 61 % for the first and second tube, respectively, when the spray density is changed from 0.02 to 0.05 kg/(m·s). The average film thickness decreases by 13.7% for the second tube as that of the first tube due to the impingement height difference. Furthermore, the time for complete wetting of tubes decreases by 48 % for the first tube due to the increased average velocity and the higher spray density. At low spray density (droplet mode), the lower average film thickness that reflects lower conduction thermal resistance and higher residence time, may lead to better heat transfer performance when compared to that of higher spray density (jet mode).

References

Baloch, A., Ali, H., Tahir, F., 2018. Transient Analysis of Air Bubble Rise in Stagnant Water Column Using CFD, in: ICTEA: International Conference on Thermal Engineering.

Chen, X., Shen, S., Wang, Y., Chen, J., Zhang, J., 2015. Measurement on falling film thickness distribution around horizontal tube with laser-induced fluorescence technology. Int. J. Heat Mass Transf. 89, 707–713. https://doi.org/10.1016/j.ijheatmasstransfer.2015.05.016

Hosseinnia, S.M., Naghashzadegan, M., Kouhikamali, R., 2017. CFD simulation of water vapor absorption in laminar falling film solution of water-LiBr — Drop and jet modes. Appl. Therm. Eng. 115, 860–873. https://doi.org/10.1016/j.applthermaleng.2017.01.022

Hou, H., Bi, Q., Ma, H., Wu, G., 2012. Distribution characteristics of falling film thickness around a horizontal tube. Desalination 285, 393–398. https://doi.org/10.1016/j.desal.2011.10.020

Ji, Ge, Wu, J., Chen, Y., Ji, Guangju, 2017. Asymmetric distribution of falling film solution flowing on hydrophilic horizontal round tube. Int. J. Refrig. 78, 83–92. https://doi.org/10.1016/j.ijrefrig.2017.03.022

Karmakar, A., Acharya, S., 2020. Wettability Effects on Falling Film Flow and Heat Transfer Over Horizontal Tubes in Jet Flow Mode. J. Heat Transfer 142. https://doi.org/10.1115/1.4048088

Karmakar, A., Acharya, S., 2019. Wettability Effects on Falling Film Heat Transfer Over Horizontal Tubes in Jet Flow Mode, in: ASME 2019 Heat Transfer Summer Conference. American Society of Mechanical Engineers. https://doi.org/10.1115/HT2019-3532

Khan, S.A., Tahir, F., Baloch, A.A.B., Koc, M., 2019. Review of Micro–Nanoscale Surface Coatings Application for Sustaining Dropwise Condensation. Coatings 9, 117. https://doi.org/10.3390/coatings9020117

Mabrouk, A., Abotaleb, A., Abdelrehim, H., Tahir, F., Koc, M., Abdelrashid, A., Nasralla, A., 2017a. HP MED Plants, Part II: Novel Integration MED-Absorption Vapor Compression, in: IDA 2017 World Congress on Water Reuse and Desalination. Sao Paulo, Brazil.

Mabrouk, A., Abotaleb, A., Tahir, F., Darwish, M., Aini, R., Koc, M., Abdelrashid, A., 2017b. High Performance MED Desalination Plants Part I: Novel Design MED Evaporator, in: IDA 2017 World Congress on Water Reuse and Desalination. Sao Paulo, Brazil.

Narváez-Romo, B., Simões-Moreira, J.R., 2017. Falling Liquid Film Evaporation in Subcooled and Saturated Water Over Horizontal Heated Tubes. Heat Transf. Eng. 38, 361–376. https://doi.org/10.1080/01457632.2016.1189275

Nusselt, W., 1916. Die oberflachenkondensation des wasserdamphes. VDI-Zs 60, 541–546.

Qiu, Q., Zhu, X., Mu, L., Shen, S., 2015. Numerical study of falling film thickness over fully wetted horizontal round tube. Int. J. Heat Mass Transf. 84, 893–897. https://doi.org/10.1016/j.ijheatmasstransfer.2015.01.024

Ribatski, G., Jacobi, A.M., 2005. Falling-film evaporation on horizontal tubes—a critical review. Int. J. Refrig. 28, 635–653. https://doi.org/10.1016/j.ijrefrig.2004.12.002

Tahir, F., 2020. Computational Fluid Dynamics (CFD) Analysis of Horizontal Tube Falling Film Evaporators Used in Multi Effect Desalination (MED) Plant. Hamad Bin Khalifa University.

Tahir, F., Mabrouk, A., Koc, M., 2019a. Review on CFD analysis of horizontal falling film evaporators in multi effect desalination plants. Desalin. Water Treat. 166, 296–320. https://doi.org/10.5004/dwt.2019.24487

Tahir, F., Mabrouk, A., Koc, M., 2019b. Heat Transfer Performance of Falling Film Evaporators Used in Multi Effect Desalination (MED) Plants, in: 1st International Conference on Sustainable Energy-Water-Environment Nexus In Desert Climate, Doha, Qatar.

Tahir, F., Mabrouk, A., Koc, M., 2018a. CFD Analysis of Falling Film Wettability in MED Desalination plants, in: Qatar Foundation Annual Research Conference Proceedings. p. EEPD650. https://doi.org/10.5339/qfarc.2018.EEPD650

Tahir, F., Mabrouk, A., Koç, M., 2020a. Impact of surface tension and viscosity on falling film thickness in multi-effect desalination (MED) horizontal tube evaporator. Int. J. Therm. Sci. 150, 106235. https://doi.org/10.1016/j.ijthermalsci.2019.106235

Tahir, F., Mabrouk, A., Koç, M., 2020b. CFD Analysis of Falling Film Hydrodynamics for a Lithium Bromide (LiBr) Solution over a Horizontal Tube. Energies 13, 307. https://doi.org/10.3390/en13020307

Tahir, F., Mabrouk, A.A., Koc, M., 2018b. CFD analysis of spray nozzle arrangements for multi effect desalination evaporator. Proceeding 3rd Therm. Fluids Eng. Conf. 935–941. https://doi.org/10.1615/TFEC2018.fip.021685

3D Analysis of Film Thickness Distribution in a Horizontal Type Falling Film Evaporator

[1*]Furqan Tahir, [1,2]Abdelnasser Mabrouk, [1]Muammer Koç
[1] Division of Sustainable Development (DSD), College of Science & Engineering (CSE), Hamad Bin Khalifa University (HBKU), Education City, P.O. Box 34110, Qatar
[2] Qatar Environment and Energy Research Institute (QEERI), Hamad Bin Khalifa University (HBKU), Education City, P.O. Box 34110, Qatar

* E-mails: futahir@hbku.edu.qa

Abstract
The film thickness characterization in the horizontal type falling film evaporators have been the primary focus of research in the past decade. Several experimental and numerical studies have been carried out to analyze film thickness distribution around horizontal tube. Because of experimental setup limitations, thickness measurements on complete tube area are not conceivable. However, numerical studies allow researchers to characterize falling film under flexible operating conditions. Present study focuses on quantification of film thickness distribution around horizontal tube in a three dimensional domain. Two tubes of 25.4 mm diameter have been selected for the computational fluid dynamics (CFD) simulations, with an orifice of 2x1 mm^2, an impingement height of 2 mm and an inter-tube spacing of 7.6 mm. The tube section of 22 mm has been opted as per critical wavelength formulation/distance between droplet sites. In order to reduce computational efforts, only quarter of the domain is considered for numerical calculations. The CFD model has been established in Ansys fluent v18.0 and has been validated quantitatively against Nusselt correlation and qualitatively with the experimental data available in the literature. The film thicknesses at different axial positions z = 0, 5.5 and 11 mm have been computed and compared and results show higher film thickness distribution at z = 0 mm (in line with droplet formation site) as compared to that of z = 11 mm (halfway between two droplet formation sites). The film thickness at θ = 90° is found to be 0.195 mm at z = 0 mm which is 21.1% higher than that of z = 11 mm.

Keywords: 3D, CFD, Falling Film, Film thickness, Horizontal Tube, Numerical Model

I. Introduction

The film thickness of the falling film exchangers have been studied experimentally by many researchers (Chen et al., 2015; Gstoehl et al., 2004; Hou et al., 2012). However, because of experimental limitations, thickness measurement at all locations is not possible. Therefore, employing numerical techniques to characterize film thickness distribution and hydrodynamics has been the primary focus in the past decade (Tahir et al., 2019a, 2019b, 2019c). Understanding falling film hydrodynamics would help in improving wettability, heat transfer coefficient and reducing scaling problems as these exchangers are commonly used in desalination and refrigeration industries (Mabrouk et al., 2017b, 2017a; Tahir et al., 2019d). In 1916, Nusselt (Nusselt, 1916) presented film thickness δ correlation, which is widely used till date and is expressed as:

$$\delta = \sqrt[3]{\frac{3\mu_l \Gamma_{1/2}}{\rho_l(\rho_l - \rho_g)g\sin\theta}} \quad (1)$$

where ρ is density, $\Gamma_{1/2}$ is liquid load (mass flow rate on one side of tube per unit tube length), μ is viscosity, θ is inclination angle, and g/l represents gas and liquid phases, respectively. Qiu et al. (Qiu et al., 2018) numerically studied the development of in-line and staggered jet mode. They found that trough is formed between the upstream jets in case of in-line mode and crest is formed in case of staggered mode. Tahir et al. (Tahir et al., 2021, 2020a, 2020b) investigated the effect of thermophysical properties on falling film hydrodynamics. They concluded that the higher surface tension and viscosity lead to higher film thickness that result in increased conduction thermal resistance that reduces the heat and mass transfer and hence the performance. Ding et al. (Ding et al., 2018) numerically examined the effect of wall adhesion on wettability and they noticed that the initial conditions significantly affects the wetted area. Furthermore, lower receding angle lead to improved wetting. Present work focuses on analyzing film thickness distribution in three-dimensional model. The computational fluid dynamics (CFD) model has been developed by discretizing conservation of mass and momentum equations for each phase, using volume of fluid (VOF) model (Tahir et al., 2018). A liquid load of 0.02 kg/(m·s) is considered for film thickness calculations, the results are compared with Nusselt solution and then film thickness distribution is analyzed and discussed.

II. Numerical model

Two tubes of 25.4 mm are selected for numerical calculations as shown in Fig.1a. The liquid enters from the 2x1 mm^2 with mass flow rate as boundary condition. The length of the section is chosen as 22 mm as per critical wavelength (Tahir et al., 2019a). In order to reduce computational efforts, only quarter of the geometry is considered due to symmetric nature. The liquid load $\Gamma_{1/2}$ is 0.02 kg/(m·s) that corresponds to the droplet mode. The thermophysical properties of water and water vapors are calculated at 20 °C. The liquid film falls under the action of gravity and without any vapor flow. The wall-adhesion contact angle is zero to ensure complete wetting (Khan et

al., 2019). The domain is meshed with hexahedral dominant elements as shown in Fig.1b. Fine boundary layers are provided adjacent to tube wall to capture liquid film accurately. The mass and momentum conservation equations for each phase are discretized using volume of fluid (VOF) model as shown in Eq. 2. The VOF model is widely used for multiphase flow problems that require distinct liquid phase interfaces (Baloch et al., 2018; Karmakar and Acharya, 2020).

$$\frac{\partial(\alpha_i \rho_i)}{\partial t} + \nabla \cdot \left(\alpha_i \rho_i \overrightarrow{V_i}\right) = 0 \qquad (i = g \ \ or \ \ l) \tag{2}$$

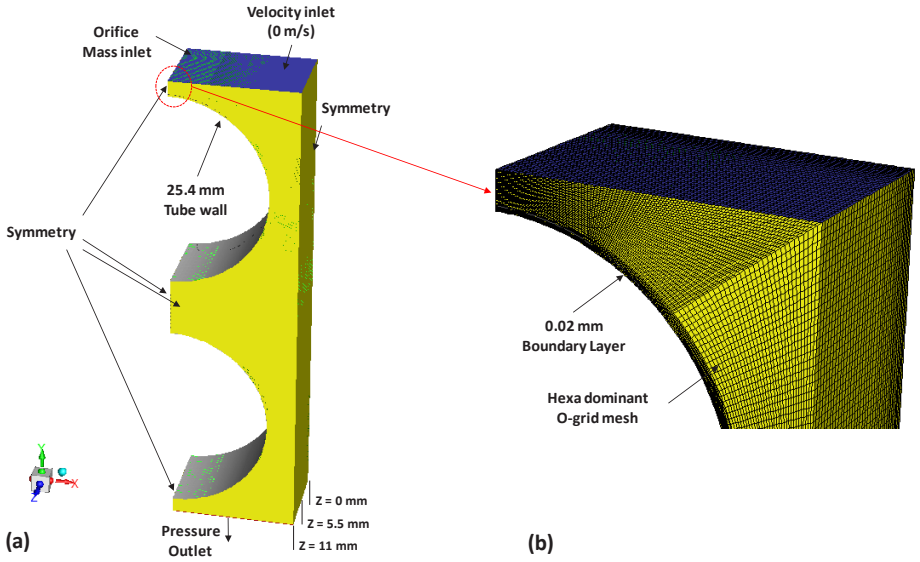

Fig. 1: (a) Domain with boundary conditions and (b) Hexahedral dominant mesh with fine boundary layers near to tube wall

where V represents velocity, α is volume fraction and g/l means gas/liquid phases. The surface tension and viscosity are computed by:

$$\beta = \alpha_l \beta_l + (1 - \alpha_l)\beta_g \tag{3}$$

where β represents any thermophysical property. The total number of elements are 562,575 and time step is 2 x 10^{-5} s after mesh and time dependency check, respectively.

III. Results and discussion

Fig.2 shows the comparison of CFD results and Nusselt solution (Eq.1), the CFD model agrees well in the range of θ = 30° - 150°. The film thickness from CFD deviates from Eq.1, in impingement and detachment regions because of inertial effects that are unaccounted in Eq.1. The water spreading on the tube at different time steps is shown in Fig.3. At t = 0.1 s, the water hits the tube surface and disperse in circumferential and axial direction under the action of gravity. The dispersion of water forms a thin liquid film on the tube surface. From t = 0.15 s to 0.25, it can be seen that the water moves faster at z = 0 mm plane as compared to other axial positions, which is in the same plane of orifice center. At t = 0.3 s, the water film reaches the tube bottom and starts compiling, the viscous and surface tension forces prevent it from falling. At the this moment, the tube is not fully wet and the liquid spreads in the axial direction from t = 0.3 s to 0.5 s. At t = 0.6 s, the tube is completely covered by liquid and the liquid keeps on gathering at the bottom forming departure sites. The liquid detaches as the gravitational force overcomes other forces.

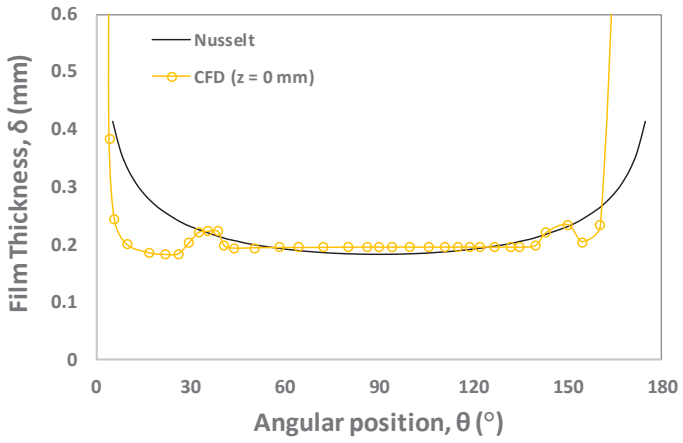

Fig. 2: Comparison between film thickness from CFD and Nusselt (Nusselt, 1916) solution for $\Gamma_{1/2}$ = 0.02 kg/(m·s)

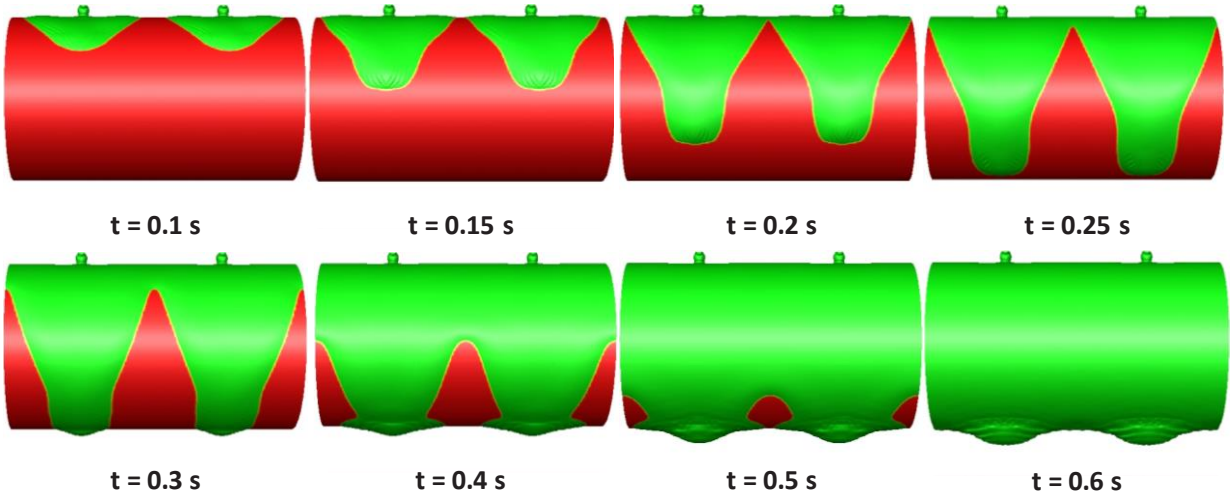

Fig. 3: Tube wetting at different time steps

Fig 4a shows the film thickness distribution around the tube circumference at different planes on axial direction. Three planes at z = 0 mm, 5.5 mm and 11 mm are selected for comparison purposes. The z = 0 mm plane lie in the center of orifice, whereas the z = 11 mm lie halfway between two droplet formation sites. At z = 0, the film thickness is found to be high as the continuous stream from orifice hits the tube surface, however far the impingement zone (z = 5.5 mm and 11 mm), the film thicknesses are low and found to be comparable. In most of the region, the film thickness is in the range of 0.15 – 0.3 mm. The minimum thickness is found at θ = 90° at z = 11 mm. Furthermore, the film thicknesses at different planes are found to be higher at the bottom region of the tube because of liquid accumulation. Fig 4b shows the film thickness variation in the axial direction form z = 0 mm to z = 11 mm at θ = 90°. It can be observed that the film thickness remains unchanged until z = 6 mm and after that it decreases as it is far from the droplet site plane. The film thickness is found to be 0.195 mm at z = 0 mm which is 21.1% higher than that of z = 11 mm.

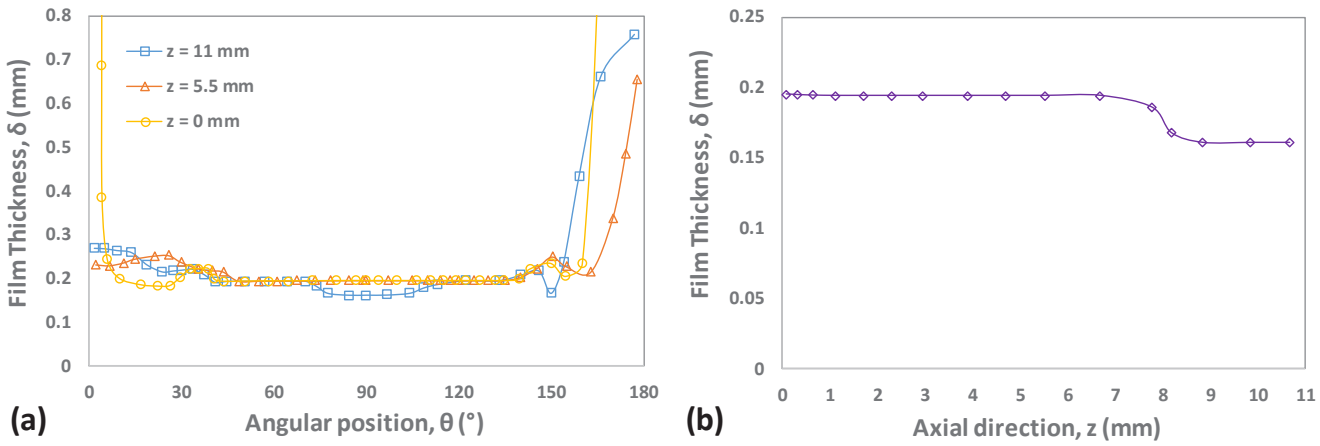

Fig. 4: (a) Film thickness distribution around the tube at different axial positions and (b) film thickness variation in the axial direction at an angular position of θ = 90°

IV. Conclusions

A three dimensional CFD model has been developed in Ansys fluent v18.0. The volume of fluid (VOF) model has been opted for liquid-gas interface tracking. The CFD model has been validated with the Nusselt solution, which is found in good agreement. The Nusslet solution does not accommodate inertial effects and because of this, variation in film thickness has been found in the top and bottom region of tube. As the liquid falls over the tube it moves quickly in the downward direction as compared to axial direction. The liquid film reaches the bottom at t = 0.3 s, however the complete wetting is achieved at t = 0.6 s. The film thickness is found between 0.15 – 0.3 mm, in most of the region and the minimum thickness is found at θ = 90°. In addition, the film thickness at the bottom is found to higher because of water accumulation. As the liquid moves farther from droplet site plane at θ = 90°, the film thickness gets thin. The film thickness and hydrodynamics study can be useful in evaluating conduction thermal resistance (film thickness/thermal conductivity) of liquid film, which can be used in predicting heat and mass transfer.

References

Baloch, A., Ali, H., Tahir, F., 2018. Transient Analysis of Air Bubble Rise in Stagnant Water Column Using CFD, in: ICTEA: International Conference on Thermal Engineering.

Chen, X., Shen, S., Wang, Y., Chen, J., Zhang, J., 2015. Measurement on falling film thickness distribution around horizontal tube with laser-induced fluorescence technology. Int. J. Heat Mass Transf. 89, 707–713. https://doi.org/10.1016/j.ijheatmasstransfer.2015.05.016

Ding, H., Xie, P., Ingham, D., Ma, L., Pourkashanian, M., 2018. Flow behaviour of drop and jet modes of a laminar falling film on horizontal tubes. Int. J. Heat Mass Transf. 124, 929–942. https://doi.org/10.1016/j.ijheatmasstransfer.2018.03.111

Gstoehl, D., Roques, J.F., Crisnel, P., Thome J. R., 2004. Measurement of Falling Film Thickness Around a Horizontal Tube Using a Laser Measurement Technique. Heat Transf. Eng. 25, 28–34. https://doi.org/10.1080/01457630490519899

Hou, H., Bi, Q., Ma, H., Wu, G., 2012. Distribution characteristics of falling film thickness around a horizontal tube. Desalination 285, 393–398. https://doi.org/10.1016/j.desal.2011.10.020

Karmakar, A., Acharya, S., 2020. Wettability Effects on Falling Film Flow and Heat Transfer Over Horizontal Tubes in Jet Flow Mode. J. Heat Transfer 142. https://doi.org/10.1115/1.4048088

Khan, S.A., Tahir, F., Baloch, A.A.B., Koc, M., 2019. Review of Micro–Nanoscale Surface Coatings Application for Sustaining Dropwise Condensation. Coatings 9, 117. https://doi.org/10.3390/coatings9020117

Mabrouk, A., Abotaleb, A., Abdelrehim, H., Tahir, F., Koc, M., Abdelrashid, A., Nasralla, A., 2017a. HP MED Plants, Part II: Novel Integration MED-Absorption Vapor Compression, in: IDA 2017 World Congress on Water Reuse and Desalination. Sao Paulo, Brazil.

Mabrouk, A., Abotaleb, A., Tahir, F., Darwish, M., Aini, R., Koc, M., Abdelrashid, A., 2017b. High Performance MED Desalination Plants Part I: Novel Design MED Evaporator, in: IDA 2017 World Congress on Water Reuse and Desalination. Sao Paulo, Brazil.

Nusselt, W., 1916. Die oberflachenkondensation des wasserdamphes. VDI-Zs 60, 541–546.

Qiu, Q., Zhang, X., Quan, S., Zhu, X., Shen, S., 2018. 3D numerical study of the liquid film distribution on the surface of a horizontal-tube falling-film evaporator. Int. J. Heat Mass Transf. 124, 943–952. https://doi.org/10.1016/j.ijheatmasstransfer.2018.04.020

Tahir, F., Mabrouk, A., Koc, M., 2019a. Review on CFD analysis of horizontal falling film evaporators in multi effect desalination plants. Desalin. Water Treat. 166, 296–320. https://doi.org/10.5004/dwt.2019.24487

Tahir, F., Mabrouk, A., Koc, M., 2019b. CFD Modeling of Falling Film Heat Transfer Over Horizontal Tube for Multi-Effect Desalination (MED) Evaporator, in: 1st International Conference on Sustainable Energy-Water-Environment Nexus In Desert Climate, Doha, Qatar.

Tahir, F., Mabrouk, A., Koc, M., 2019c. Heat Transfer Performance of Falling Film Evaporators Used in Multi Effect Desalination (MED) Plants, in: 1st International Conference on Sustainable Energy-Water-Environment Nexus In Desert Climate, Doha, Qatar.

Tahir, F., Mabrouk, A., Koc, M., 2019d. Energy and exergy analysis of thermal vapor compression (TVC) and absorption vapor compression (AVC) for multi effect desalination (MED) plants, in: 8th Global Conference on Global Warming (GCGW), Doha, Qatar. p. 25.

Tahir, F., Mabrouk, A., Koc, M., 2018. CFD Analysis of Falling Film Wettability in MED Desalination plants, in: Qatar Foundation Annual Research Conference Proceedings. p. EEPD650. https://doi.org/10.5339/qfarc.2018.EEPD650

Tahir, F., Mabrouk, A., Koç, M., 2021. Influence of co-current vapor flow on falling film over horizontal tube. Int. J. Therm. Sci. 159, 106614. https://doi.org/10.1016/j.ijthermalsci.2020.106614

Tahir, F., Mabrouk, A., Koç, M., 2020a. CFD Analysis of Falling Film Hydrodynamics for a Lithium Bromide (LiBr) Solution over a Horizontal Tube. Energies 13, 307. https://doi.org/10.3390/en13020307

Tahir, F., Mabrouk, A., Koç, M., 2020b. Impact of surface tension and viscosity on falling film thickness in multi-effect desalination (MED) horizontal tube evaporator. Int. J. Therm. Sci. 150, 106235. https://doi.org/10.1016/j.ijthermalsci.2019.106235

Experimental study on use of carbon free gaseous fuel (hydrogen) with biodiesel and carbon capture system in CI engine to reduce CO_2 emission

V. EdwinGeo*[a], Guillaume FOL[b], S. Thiyagarajan[a], M Jerome Stanley[a] and Fethi Aloui[b]

[a]Green Vehicle Technology Research Centre, Department of Automobile Engineering, SRM Institute of Science and Technology, Kattankulathur-603203, India
[b]Campus Mont Houy, F-5931 LAMIH UMR CNRS 8201, Department of Mechanical Engineering, Polytechnic University Hauts-de-France, Campus Mont-Houy, F-59313 ValenciennesCedex 9, France

* E-mail: edwingev@srmist.edu.in

Abstract

This research has been focused to quells the colossal demand of fossil fuels by extending the horizon towards the low carbon biofuels. This research uncovers the diesel engine performance, in-cylinder behaviour and emission aspects, when operated with four different low carbon biofuels, viz camphor oil (CMO), cedar wood oil (CWO), wintergreen oil (WGO) and lemon peel oil (LPO). These fuels are blended with diesel oil by 20% in volume and the respective blends are compared with the diesel oil's qualities. The test engine is enabled with common rail direct injection (CRDi) system, allowing it to control the injection timing and the quantity of the fuel to be injected. The study unveils that low carbon biofuels blended with the diesel oil forms an efficient substitute fuel; starting with the improvement in the brake thermal efficiency, reduced CO_2 emissions and reduction in other emissions. The NO_x emission of the low carbon fuels seems predominately higher. Wintergreen oil as the one of the dense and comparatively less viscousfuel among the other chosen biofuels; exhibits 6% improvement in brake thermal efficiency, 3% hike in brake specific energy consumption,7% increase in peak pressure of 59 bar at 7˚ATDC, 20% reduction in CO_2 emissions, 17% in HC and 20% decrement in smoke has been observed in WGO20. Based on the experimental study in phase I, it is observed that among the low carbon biofuel blends tested, WGO20 blend emitted minimum CO_2 and hence taken for the next phase of work. Hydrogen was inducted until the knock limit with WGO20 blend. Hydrogen is a carbon free fuel and hence will aid in mitigation of CO_2 emission. Along with hydrogen induction, zeolite based after treatment system was designed and placed in the exhaust. This will aid in further adsorption of engine-out CO_2 emission.

Keywords: Biofuels, hydrogen, CO2 emission, low carbon fuels

Introduction

Air pollution is among the critical environmental concern in India, which causes health damage and economic losses. The rapid urbanization in India resulted in an increase in motor vehicles, which are doubled in the last decade. The increase in vehicles makes it one of the major contributors of pollution in India. In India, diesel-fueled vehicle population is higher compared to gasoline-fuelled vehicles due to subsidized diesel fuel price and better torque characteristics of diesel-fueled vehicles. Major emissions from diesel-fuelled vehicles include nitrogen oxides, particulate matter, and carbon dioxide. Nitrogen oxide emissions and particulate matter emissions affect the human respiratory system and affecting the lung function. Carbon dioxide (CO2) is unregulated emission indirectly affecting the ecosystem by causing 'global warming.' In India, owing to increased population of diesel-fuelled vehicles, CO_2 emission is five times higher compared to gasoline-fuelled vehicles. The adverse effects of these pollutants include severe health issues on human and atmosphere like acid rain, global warming, ozone depletion, and nutrition enrichment [1]. An average of 0.55°C rise in global temperature was recorded from 1970 till date, which makes it the warmest time compared to the past [2]. According to the Intergovernmental Panel on Climate Change (IPCC), increasing emissions of greenhouse gasses (GHG) will rise the average global temperature by 1.1°C –6.4°C by the end of the 21st century. They have also stated that Earth will face more consequences if the temperature rises above 2°C [3]. IPCC also said that by 2050, GHG emissions need to be reduced by 50 %-70% [4].

With the increase in global warming, India is predicted to face severe climatic events like increase in precipitation, the melting of glaciers and expanding seas are projected to influence the Indian climate severely, with an increase in the incidence of floods, hurricanes, and storms. Global warming also affects the food security situation in India. India's GDP will decline by about 9% with a decrease in 40% of primary crop production [5].

In India, CI engine is preferred over SI engine in heavy-duty vehicles, generators, and power plants and attractive in light load vehicles due to its higher thermal efficiency and higher torque. High compression ratios of CI engine with lean combustion lead to better fuel efficiency and reduced CO and HC emissions compared to SI engine. However, CI engine contributes to increasing NO_x and PM emissions and controlled with stringent emission norms [6]. Complete combustion of diesel emits CO_2 and H_2O. CO_2emission is unregulated, which is a major contributor to global warming. Stoichiometrically, 1 kg of diesel combustion emits about 2.7 kg of CO_2. CO_2 emission from diesel combustion is directly proportional to the number of carbon atoms present in the fuel structure.

The literature lacks an in-depth study on CO_2 mitigation strategies from CI engine. The few mitigation strategies proposed from the previous research works are Low carbon/carbon free fuel, Engine downsizing, Use of carbon capture and storage (CCS) and Use of biofuels. Low carbon/carbon free fuel: CO_2 emission from CI engine depends mainly on the carbon content of the fuel. Many researchers have utilized carbon-free gaseous fuels like hydrogen and ammonia in CI engine and achieved a significant reduction in CO_2 emission. De Morais et al. [7] conducted experiments by injecting gaseous hydrogen in inlet manifold in a multi-cylinder CI engine. Hydrogen injection was limited to 20 % on energy basis to avoid knocking. They achieved a 15 % reduction in CO_2 emission with 20 % hydrogen energy share with diesel. They have concluded that lack of carbon atoms in hydrogen aided in the reduction of CO_2 emission. Gill et al. [8] attempted to decarbonize diesel engine by co-fuelling with ammonia. They inducted 3 % ammonia along with intake air and diesel as base fuel. They have achieved 15 % reduction in CO_2 emission at maximum load condition.Coronado et al. [9] analyzed various fuels like gasoline, diesel ethanol, soybean biodiesel and used frying oil to calculate CO_2 emissions per cubic meter of fuel based on fuel structure at the stoichiometric ratio. They concluded that 1 m^3 of gasoline emits 2.316 ton of CO_2, 1 m^3 of diesel emits 2.683 tons of CO_2, 1 m^3 of ethanol emits 1.511 tons of CO_2, 1 m^3 of soybean biodiesel emits 2.48 ton CO_2 and 1 m^3 of used frying oil emits 2.492 ton CO_2. Among the various fuels analyzed, ethanol emits less CO_2 emission due to low carbon content in the fuel.

Engine Downsizing: Engine downsizing is one of a proven technique to reduce fuel consumption, which in turn reduces CO_2 emission from the engine. Downsizing typically means to lessen the displacement by reducing cylinder size or reducing the number of cylinders. The downsized engine has low frictional and thermal losses compared to the conventional engine. The maximum power produced is less for downsized engine and compensated through advancement in air intake system and fuel intake system. Koerfer et al. [10] attempted to downsize 2.0 liters Euro 4 baseline engine to 1.6 liters by adopting integrated engine design concepts like advanced swirl concepts, exhaust gas recirculation (EGR) control, high-pressure flexible injection with sophisticated combustion chamber design. They have concluded that the proposed concept of downsizing reduced CO_2 emission by 17 %, NO emissions by 50 % and particulate emissions by 10 %.

Use of carbon capture and storage (CCS): CCS is the process of capturing CO_2 emissions from fossil fuel combustion from industries and transportation and storing it without harming the atmosphere. CCS is the best method to reduce CO_2 emissions from industries and transportation with the use of fossil fuel usage and retaining existing energy infrastructure. CCS is done in three methods in industries: 1. Pre-combustion 2. Oxyfuel combustion 3. Post-combustion. Pre-combustion is partially oxidizing hydrocarbon fuel to syngas (CO and H_2O) and then converted to CO_2 and H_2. CO_2 is captured before combustion process, and hydrogen alone is sent for combustion. CO_2 is captured using 'Scrubbing' method and the aqueous solution is recovered and recycled. Oxyfuel combustion is replacing the air with pure oxygen and thereby reducing the fuel consumption, which reduces the CO_2 emission. Post-combustion capture system is done using absorption and adsorption method. Absorption uses an aqueous solution, which reacts with CO_2 in the exhaust, and the CO_2 thus captured can be recovered. Adsorption is using solid based adsorbents like zeolite, activated carbon and captured CO_2 can be regenerated by suitable methods [11].

Use of biofuels: One of the major cornerstones in mitigation of CO_2 emission and reducing the energy dependence is the use of biofuels in engines replacing the conventional fossil fuels. Many technological improvements in the use of biofuels are evolved from the use of first generation biofuels (Vegetable oils) to second generation biofuels like Jatropha and Karanja oil to third generation fuels like algae-based oils. India being an agricultural country has a variety of vegetable oil sources, and many types of research have been carried out in effective utilization of these fuels in CI engine. Biofuels are renewable and can mitigate carbon emissions by ways of 'Eco recycling.' Eco recycling means the plantation producing biofuel acts as a carbon sink and absorbs CO_2 from the atmosphere for the growth which is much higher compared to the emitted CO_2 from engines causing a 'net negative CO_2 emission'.

Results and Discussion

Hydrogen induction and after treatment system

Hydrogen was inducted until the knock limit with WGO20 blend. Hydrogen is a carbon free fuel and hence will aid in mitigation of CO_2 emission. Along with hydrogen induction, zeolite based after treatment system was designed and placed in the exhaust. This will aid in further adsorption of engine-out CO_2 emission

CO_2 emission

Figure 1 shows the variation of CO_2 emission for hydrogen induction and after-treatment system with WGO20 at various load conditions. At maximum load, CO_2 emission for diesel, WGO20 and WGO20 + Hydrogen is 7.9 %, 6.3 % and 4.9 % respectively. CO_2 emission is reduced by 38 % and 22 % in comparison to diesel and WGO20 at maximum load. The absence of carbon atoms in hydrogen resulted in reduction of CO_2 emission in comparison to diesel and WGO20. CO_2 emission is further reduced to 3.6 % for WGO20 + Hydrogen + Zeolite about 54 % and 43 % less comparison to diesel and WGO20 at maximum load. Zeolite has better adsorption capability which results in adsorption of engine-out CO_2 emission.

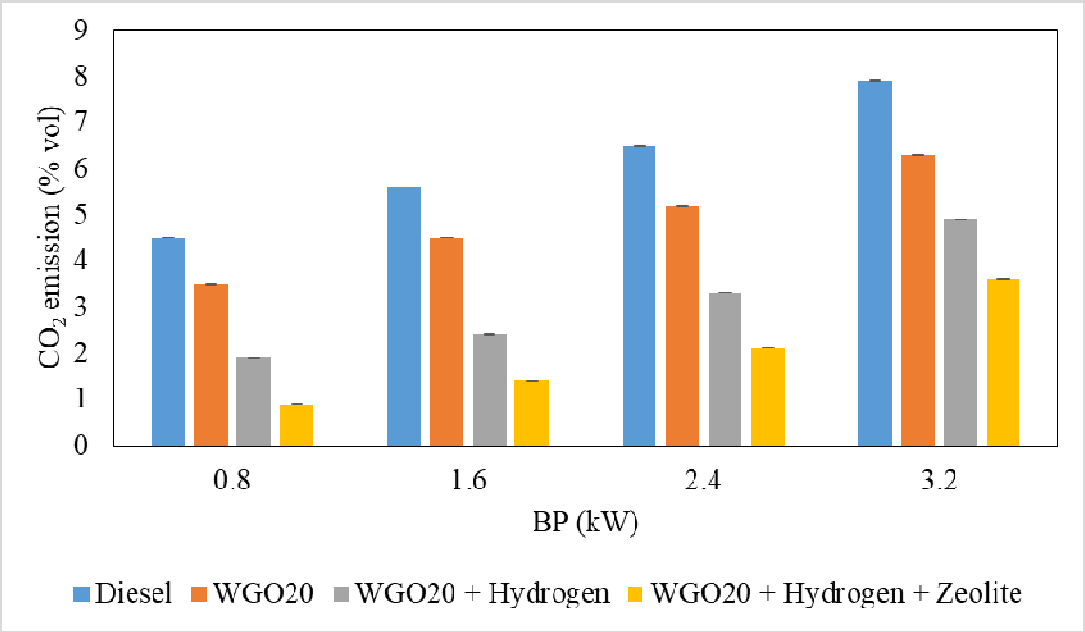

Figure 1 Variation of CO_2 emission for hydrogen induction and after treatment system

NOx emissions

Figure 2 shows the variation of NOx emissions for hydrogen induction and after-treatment system with WGO20 at various load conditions. NOx emissions for diesel, WGO20 and WGO20 + Hydrogen are 679 ppm, 1037 ppm and 1258 ppm respectively at maximum load. Increase in NOx emissions with hydrogen addition are due to improved combustion which increased the in-cylinder temperature leading to more NOx formation. Also, the higher self-ignition temperature of hydrogen leads to increase in ignition delay leading to more fuel accumulation during the delay period and a sudden increase in temperature in pre-mixed combustion phase leads to higher NOx emissions formation. Similar trends were observed at all the load conditions. NOx emissions were reduced to 815 ppm at maximum load with zeolite after treatment system. NOx emissions were reduced by 35.2 % with zeolite based after treatment system in comparison to WGO20 + hydrogen. The adsorption capability of zeolite makes it suitable catalyst for SCR technology which aids in reduction of NOx emissions.

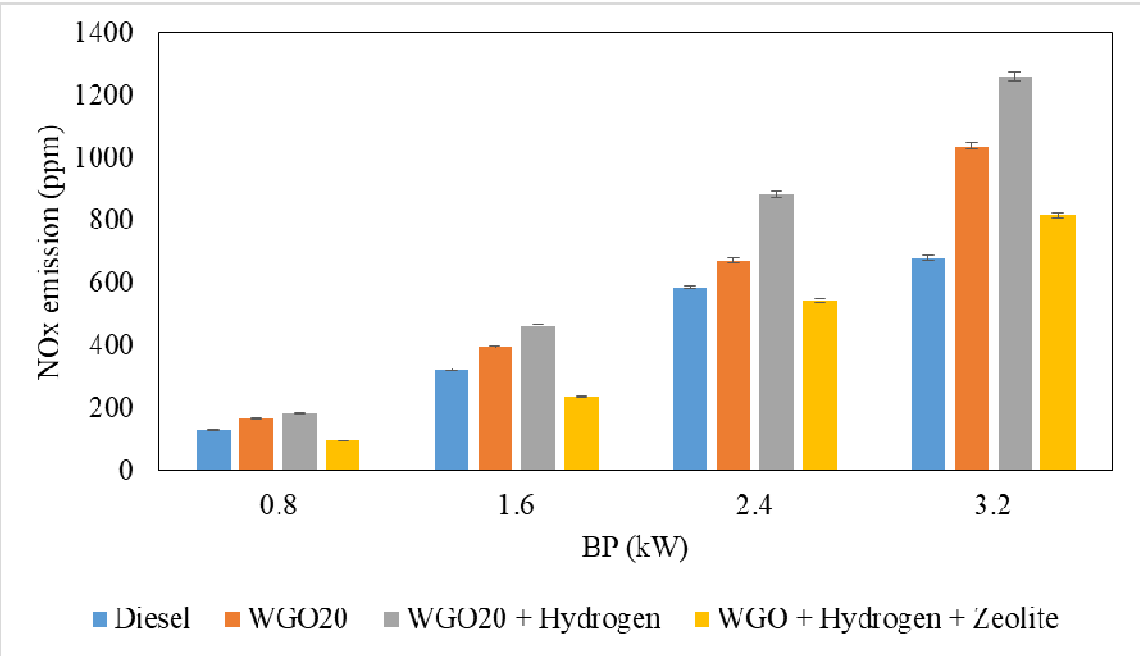

Figure 2 Variation of NOx emissions for hydrogen induction and after treatment system

Smoke emission

Figure 3 shows the variation of smoke emission for hydrogen induction and after-treatment system with WGO20 at various load conditions. At maximum load, smoke emission for diesel, WGO20 and WGO20 + Hydrogen is 79.5 %, 62.9 % and 47 % respectively. Smoke emission is reduced with WGO20 due to improved physical properties in comparison to diesel. With hydrogen induction, smoke opacity was reduced by 25.2 % in comparison to WGO20 at maximum load. The reduction in smoke opacity is due to absence of carbon atoms in hydrogen which reduces the soot particles. Also, the enhanced combustion improves the oxidation of soot particles which also aids in reduction of smoke emissions. With use of zeolite based after treatment system, smoke emission was reduced further to 31.6 % at maximum load. This is due to high adsorption capability of zeolite which adsorbs the carbon particles. The combination of hydrogen induction and zeolite based after treatment system, smoke emission was reduced by 49.7 % and 60.2 % in comparison to WGO20 and diesel respectively at maximum load.

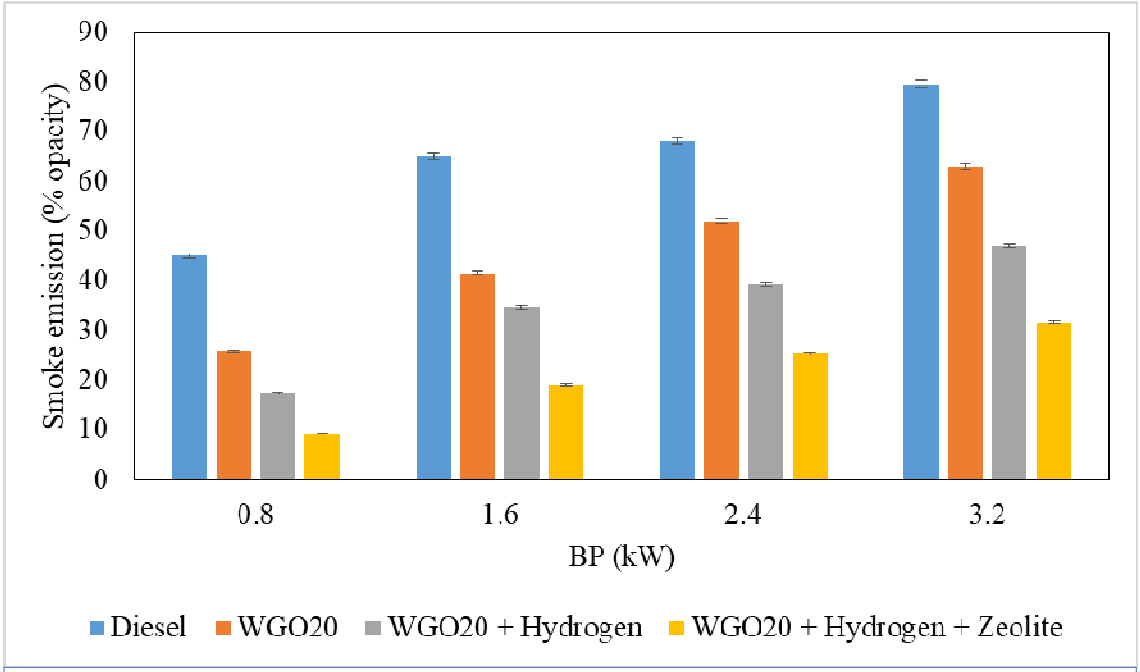

Figure 3 Variation of smoke emission for hydrogen induction and after treatment system

HC Emissions

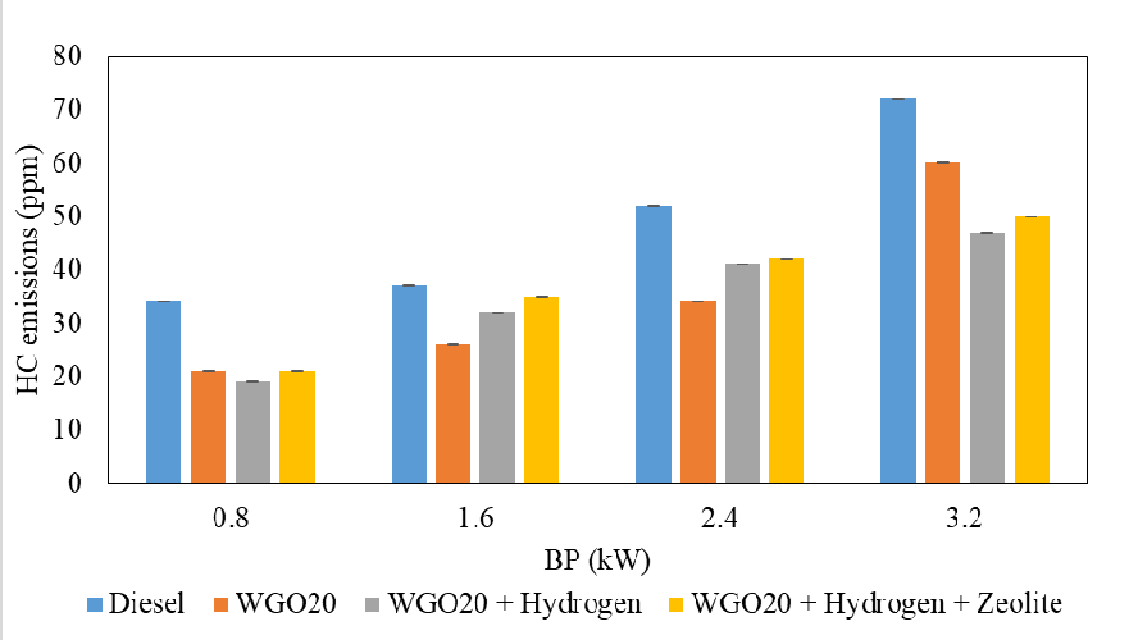

Figure 4 Variation of HC emissions for hydrogen induction and after treatment system

Figure 4 shows the variation of HC emissions for hydrogen induction and after-treatment system with WGO20 at various load conditions. At maximum load, HC emissions for diesel, WGO20 and WGO20 + Hydrogen is 72 ppm, 60 ppm and 47 ppm respectively. Lower carbon-hydrogen ratio with WGO20 aided in reduction of HC emissions in comparison to diesel. With hydrogen induction, HC emissions were further reduced by 34.7 %. This is due to absence of carbon atoms in hydrogen and also improved combustion aided in higher combustion temperature favoring unburnt HC emission oxidation process. With zeolite based after-treatment system, HC emissions were slightly higher due to backpressure effects which led to more fuel consumption which rises HC emissions formation.

Brake thermal efficiency

Figure 4 shows the variation of BTE for hydrogen induction and after-treatment system with WGO20 at various load conditions. At maximum load, BTE for diesel, WGO20 and WGO20 + Hydrogen is 29.9 %, 31.4 % and 35.2 % respectively. BTE was improved with WGO20 due to improved physical properties which aided in enhanced combustion. With hydrogen induction, a significant improvement in BTE was observed. BTE was improved by 12.2 % with hydrogen induction at maximum load in comparison to WGO20. The improvement in BTE was attributed to higher flame speed of hydrogen and higher calorific value of hydrogen which enhanced the combustion process. With use of zeolite based after treatment system, BTE was reduced to 33.8 % with WGO20 and hydrogen. The reduction in BTE with after treatment system is due to backpressure effect which reduces the BP and to compensate for the loss in power more fuel is injected which reduces BTE.

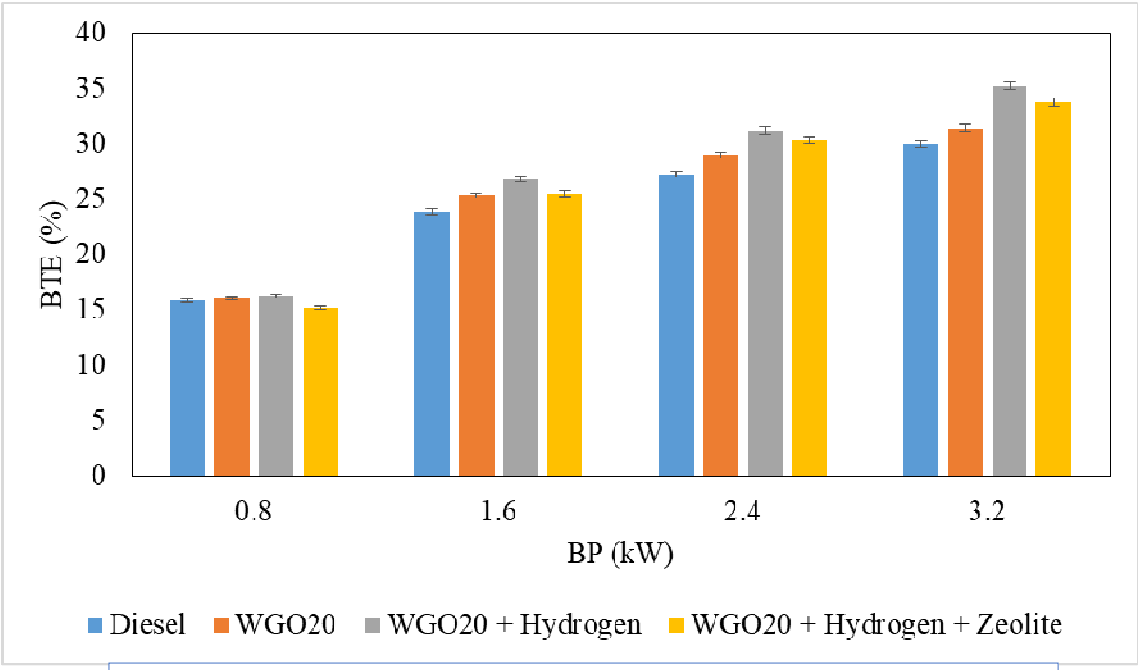

Figure 5 Brake thermal efficiency for hydrogen induction and after treatment system

Combustion Characteristics

Figure 6 shows the variation of in-cylinder pressure versus crank angle for diesel, WGO20, WGO20 + Hydrogen and WGO20 + Hydrogen + Zeolite at maximum load. It is observed that compared to diesel, peak pressure for WGO20 is higher and also occurs late. Peak pressure for diesel and WGO20 is 52 bar and 54 bar respectively. Improved combustion with WGO20 is due to lower viscosity and improved volatility in comparison to diesel. Also, the low cetane number of WGO20 leads to delayed start of combustion leading to delayed occurrence of peak pressure. With hydrogen induction, peak pressure is further improved to 56 bar and occurred further late. This is due to higher self-ignition temperature and also higher flame speed which improved the combustion. It is also observed that use of after treatment system has minimal effect on combustion.

Figure 7 shows the variation of HRR versus crank angle for diesel, WGO20, WGO20 + Hydrogen and WGO20 + Hydrogen + Zeolite at maximum load. It is observed that compared to diesel, peak heat release for WGO20 is higher and occurs late. This is due to reduced viscosity and improved volatility leading to enhanced combustion. With hydrogen induction, due to higher flame speed, combustion is enhanced in addition to higher heating value which improves the combustion further. Hydrogen induction delayed the start of combustion due to higher self-ignition temperature. It is also observed that after

treatment system has minimal effect on HRR and hence no significant changes as observed.

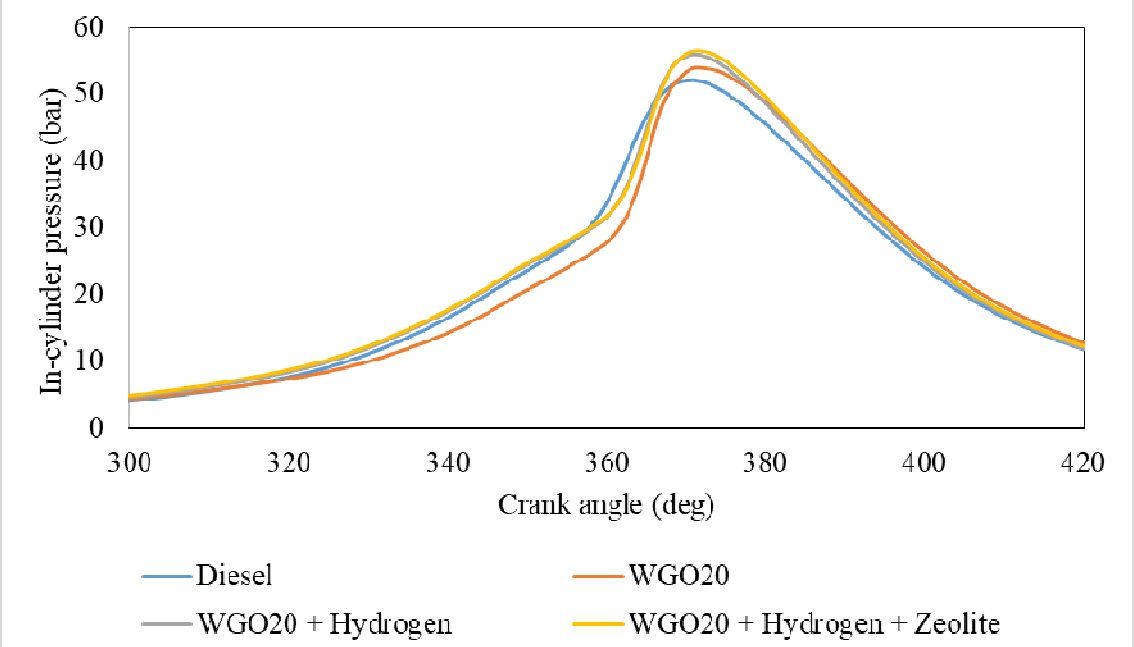

Figure 6 Variation of In-cylinder pressure versus crank angle at maximum load

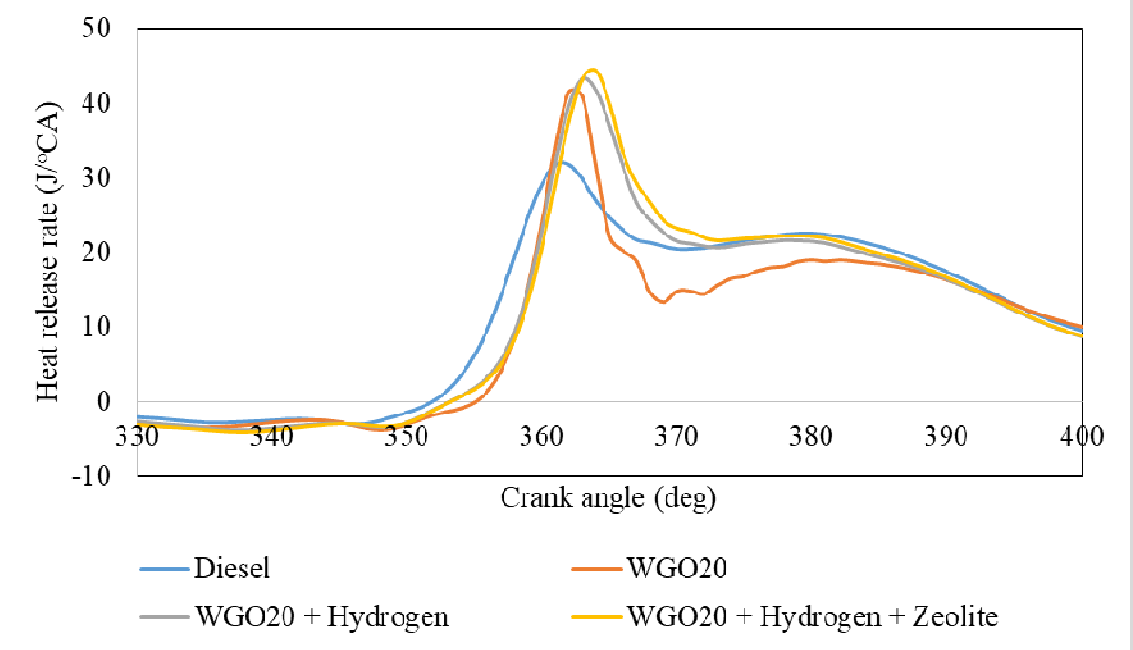

Figure 7 Variation of heat release rate versus crank angle at maximum load

Conclusions

The performance and emission characteristics of the four winter green oil (WGO) with hydrogen induction and zeoliter carbon capture system has been investigated experimentally in a diesel engine; retrofitted with CRDi, enable to modify the injection duration and quantity of the fuel being injected. The experimental results showed that there is a drastic reduction in CO_2 emission low carbon biofuel (WGO). Further reduction is noticed with hydrogen induction and carbon capture system. NOx emissions increases with hydrogen induction but thers is a reduction with zeolite carbon capture system. Smoke emission reduces with hydrogen and further reduction with CCS. HC emissions decreases with hydrogen and there is slight increase with CCS. Brake thermal efficiency increases marginally with hydrogen and slight drop with CCS due to back pressure. Combustion paramters like cylinder pressure and heat release rate increases with hydrogen induction and CCS. Finally it is concluded that WGO20 with hrdoegen addition and CCS decreases the CO2 emission and increases the brake thermal efficiency with slight increase in NOx emissions.

References

[1] Chandrappa, R., & Chandra Kulshrestha, U. (2015). Sustainable Air Pollution Management in Transportation Sector. Environmental Science and Engineering, 291–303.
[2] Scafetta, N. (2013). Solar and Planetary Oscillation Control on Climate Change: Hind-Cast, Forecast and a Comparison with the CMIP5 GCMS. Energy & Environment, 24(3-4), 455–496.
[3] The Intergovernmental Panel on Climate Change (IPCC), 2007a. Climate Change 2007: The Physical Science Basis. Cambridge University Press, Cambridge, UK.
[4] The Intergovernmental Panel on Climate Change (IPCC), 2001. IPCC Third Assessment Report—Climate Change 2001. Cambridge University Press, Cambridge, UK.
[5] Chattopadhyay, N. (2010). Climate Change and Food Security in India. Climate Change and Food Security in South Asia, 229–250.
[6] Tsolakis, A., &Megaritis, A. (2004). Exhaust Gas Fuel Reforming for Diesel Engines - A Way to Reduce Smoke and NOX Emissions Simultaneously. SAE Technical Paper Series.
[7] De Morais, A. M., Mendes Justino, M. A., Valente, O. S., Hanriot, S. de M., &Sodré, J. R. (2013). Hydrogen impacts on performance and CO2 emissions from a diesel power generator. International Journal of Hydrogen Energy, 38(16), 6857–6864.
[8] Gill, S. S., Chatha, G. S., Tsolakis, A., Golunski, S. E., & York, A. P. E. (2012). Assessing the effects of partially decarbonising a diesel engine by co-fuelling with dissociated ammonia. International Journal of Hydrogen Energy, 37(7), 6074–6083.
[9] Coronado, C. R., de Carvalho, J. A., &Silveira, J. L. (2009). Biodiesel CO2 emissions: A comparison with the main fuels in the Brazilian market. Fuel Processing Technology, 90(2), 204–211.
[10] Körfer, T., Lamping, M., Kolbeck, A., Pischinger, S., Adolph, D., & Busch, H. (2009). Potential of Modern Diesel Engines with Lowest Raw Emissions - a Key Factor for Future CO2 Reduction . SAE Technical Paper Series.
[11] Sreenivasulu, B., Gayatri, D. V., Sreedhar, I., &Raghavan, K. V. (2015). A journey into the process and engineering aspects of carbon capture technologies. Renewable and Sustainable Energy Reviews, 41, 1324–1350.

Study on Nitrogen doped Carbon paper electrodes for vanadium Redox Flow Battery Applications.

Muthumeenal Arunachalam[1], Ahmed Sodiq[2], Farida Aidoudi[1] and Belabbes. A. Merzougui[1, 2]

[1]Qatar Environment and Energy Research Institute, [2]College of Science and Engineering, Hamad Bin Khalifa University, Doha, Qatar.

E.mail: msundarapandian@hbku.edu.qa

Abstract

In recent years, vanadium redox flow batteries (VRFBs) have attracted significant attention as a promising large-scale system for storing excess energy from renewable sources like wind or solar energy. The energy is stored in the form of vanadium containing electrolytes, which consist of $V^{2+}/^{3+}$ at the negative and $V^{4+}/^{5+}$ at the positive side. These are flowed through carbon materials, which are usually porous felts or carbon paper electrodes. Carbon electrodes exhibit good stability and electrochemical conductivity in the acidic and corrosive electrochemical environment of the battery system. One disadvantage is their poor kinetic reversibility and electrochemical activity, which makes an activation step necessary. To address this issue, various approaches including heat treatment and acid oxidation have been pursued by several groups to obtain enhanced activity. Several works described heteroatom doping that should provide more active centers for the vanadium redox reactions, and hence lead to a higher electrochemical activity. However, most of these procedures are high energy/time consuming and require the use of environmentally unfriendly and expensive chemical reagents but, more importantly, they appear to be unsuitable for synthesizing large-area electrodes. Herein, we present a new method for the direct fabrication of nitrogen-doped carbon paper electrode for VRFBs. We developed the electrodes by controlled deposition of a thin layer of conducting polymer on the surface of carbon electrode followed by pyrolysis in an inert atmosphere. The study proves that the conducting polymer is an effective precursor for the preparation of nitrogen-doped carbon electrodes and the adopted method for its preparation is convenient and scalable. After doping with nitrogen, it is possible to achieve very less peak separation, ΔE values. The electrode structure and morphology will be investigated by X-ray photoelectron spectroscopy, scanning electron microscopy and the electrochemical performance of the N-doped carbon electrodes will be evaluated by cyclic voltammetry and real cell configuration.

Keywords: Vanadium Redox Flow Battery, Nitrogen doped Carbon electrodes, Electrochemical Energy conversion systems.

1. Introduction

The energy production market must change its output to match real time demand; making production very inefficient and restricting the grid's ability to rely upon intermittent renewable sources, i.e. solar and wind. Both of these issues can be alleviated by grid scale energy storage for eg. Redox flow batteries (RFB), that could store energy when it is available and distribute energy as needed. Carbon based electrodes has been most widely used as electrode for VRFBs due to its wide operating potential range, satisfactory chemical and mechanical stability, high electrical conductivity and low cost **[1]**. However, the pristine carbon based electrodes is plagued by its poor electrochemical activity towards vanadium redox reactions. In an effort to address this issue, a variety of electrode treatment methods, including acid treatment, thermal treatment and nitrogen doping have been investigated **[2, 3]**. To further make the flow battery more attractive from performance and cost perspectives, it is essential to develop advanced catalysts with superior catalytic activity as well as low cost **[4]**. Nitrogen doping, as one of carbon treatment methods, has been reported for many applications involving methanol electro-oxidation **[5]**, biosensor **[6]**, and lithium-ion batteries **[7]**. Moreover, this carbon treatment method has equally been reported as efficient electrocatalyst for all-vanadium redox flow battery, especially when applied to graphite carbon felts **[8, 9]**. Herein, we report on the first time the use of inexpensive and highly conductive Nitrogen doped carbon electrodes as catalysts to enhance the Vanadium redox reaction. Electrode surfaces have been widely modified with electrically conductive polymers, including Polyprrole (PPY), to improve the performance of electrodes. In this study, PPY films were polymerized on electrodes by in-situ polymerization followed by pyrolysis which could dope Nitrogen on the carbon substrate. In-situ polymerization on a carbon paper has the advantages of scalability, time-saving, morphology controllability, easy operation and it can be directly used as electrode in the real cell configuration. The preliminary results suggest that Nitrogen doped carbon electrodes are

effective in improving the electrochemical activity of vanadium redox reactions and have great potential application as high-performance electrodes for VRFBs.

2. Experimental Methods and Characterization

2.1 Materials preparation and characterization

The Nitrogen doped carbon paper (Toray carbon, 200 µm thickness) was prepared by in-situ polymerization of pyrrole, followed by pyrolysis in an inert atmosphere. The electrode structure and morphology were investigated by X-ray photoelectron spectroscopy, scanning electron microscopy and the electrochemical performance of the N-doped carbon electrodes was evaluated by cyclic voltammetry.

2.2 Electrochemical Characterization

Cyclic voltammogram **[Fig 1**] were obtained a traditional three electrode electrochemical cell was set up with a Nitrogen doped electrode (0.35 cm^2) as the working electrode. From the voltammogram, it is inferred that Nitrogen doped Toray carbon paper showed good reversibility for both anodic and reaction of vanadium redox reaction. The electrochemical activities of as an electrode for all-vanadium redox reactions are; on the cathode side, the oxidation peak occurs at potential of +0.947 V and the reduction peak at +0.76 V resulting in peak separation, ΔE, of 0.187 V for the couple V^{4+}/V^{5+}, on the cathode side, the oxidation peak occurs at potential of -0.46 V and the reduction peak at -0.621 V resulting in peak separation, ΔE, of 0.161 V for the V^{2+}/V^{3+} redox couple. The small values of the peak separations (ΔE) of N-doped carbon paper in vanadium for both negative and positive electrode reactions confirm the low activation energy introduced by the hetero atom Nitrogen on the carbon surface. These ΔE values are far smaller than the already reported value **[10].**

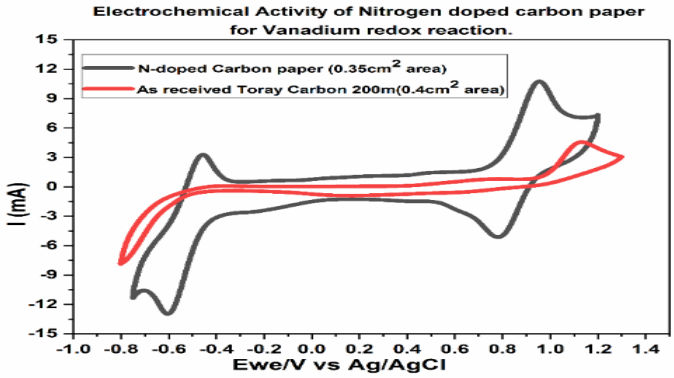

Figure: 1 cyclic voltammogram modified and unmodified of Toray Carbon paper

2.3 Scanning Electron Microscope

From the SEM images shown in the **Fig [2 a, b],** it is inferred that the surface modification followed by pyrolysis formed a uniform globular like morphology (carbon nanobeads) with the particle size of about 0.20µm. After pyrolysis carbon nano beads were formed which is confirmed by SEM studies.

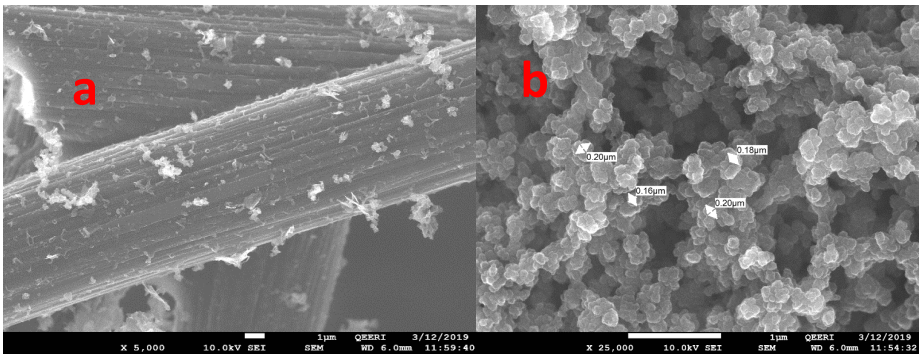

Figure [2a, b] SEM images of Nitrogen doped Toray carbon paper

2.4 XPS measurements

The XPS spectra of unmodified Toray carbon and Nitrogen doped carbon paper are shown in **Fig 3a**, and the major elements present on the surface of carbon paper are presented in the **Table. 1**. As observed, the N1s signal of N-doped carbon paper is quite clear while there is almost no N1s signal in as-received Toray carbon paper. This indicates that the nitrogenous groups are introduced on the surface of carbon paper by the approach we have adopted. Peak fitting of N1s for Nitrogen doped carbon paper was carried out, and the results are shown in **Fig 3b**. The N1s high-resolution spectra of modified carbon paper mainly reveal several nitrogen functional groups: pyridinic nitrogen (N1, binding energy (BE) = 398.4 ± 0.2 eV), quaternary nitrogen (N2, BE = 401.2 ± 0.2 eV), and N-oxides of pyridinic nitrogen (N3, BE = 402.8 ± 0.4 eV). The molecular structures of these nitrogenous functional groups can be described as follows: pyridinic nitrogen (N1) refers to the nitrogen atom on the edge of graphene planes, which is bonded to two carbon atoms and contributes to the aromatic π system with one p-electron; quaternary nitrogen (N2) can be described as 'graphitic nitrogen', in which the nitrogen atom is incorporated into the graphene layer and bonded to three carbon atoms. N-oxides of pyridinic nitrogen (N3) are bonded to two carbon atoms and one oxygen atom, which can be termed as pyridinic – (N^+–O^-). The relative content of N2 is higher than N1 and N3. This could be attributed to that the enhanced reaction at during pyrolysis causes more substitution of N to C in deeper level. It was reported that these nitrogenous groups could facilitate the electron transfer between vanadium ions and electrodes.

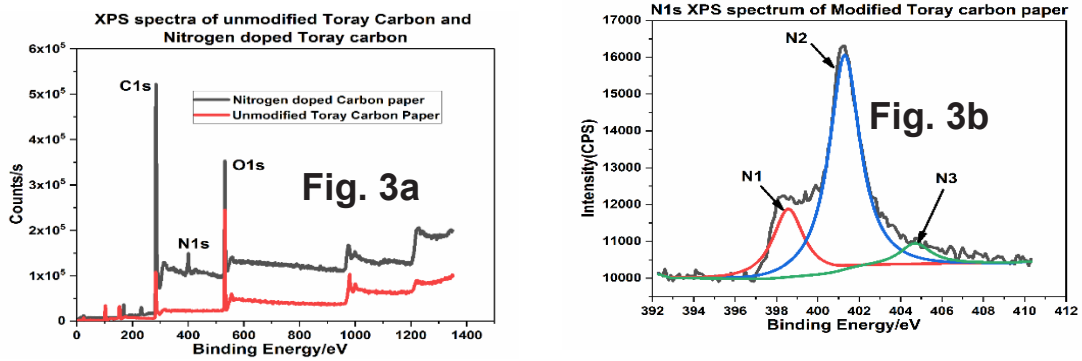

Figure [3a, 3b] XPS of Nitrogen doped Toray carbon paper

Table 1. XPS analyses of the major elements on the surface of carbon paper.

Elements	Peak BE(eV)	Contents (at. %)	
		Unmodified Toray Carbon paper	Nitrogen-doped Toray carbon paper
C1s	284.84	51.86	76.44
O1s	531.87	32.06	14.70
N1s	400.81	-	5.57
Si 2p	103.02	16.07	1.22

3. Conclusions

The electrochemical activity and reversibility of modified Nitrogen doped carbon showed superior electrochemical performance compared with the pristine carbon paper. The excellent electrochemical properties of the modified carbon paper are attributed to the enhanced electrical conductivity, more active sites, and better wettability provided by the introduction of the nitrogenous groups on the surface of carbon paper. This work contributes to a better understanding of the role of the precursor material for Nitrogen doping and the heat treatment (carbonization) and how they affect the properties of electrode materials in a VRFB.

Acknowledgement: This work was made by the support of the Qatar Environment and Energy Research Institute, QEERI, and the National Research Fund (QNRF), through the project # NPRP-10-0126-170254.

References

[1] Mohamed MR, Leung PK, Sulaiman MH. Performance characterization of a vanadium redox flow battery at different operating parameters under a standardized test-bed system. Appl Energy 2015; 137:402–12.

[2] Di Blasi O, Briguglio N, Busacca C, Ferraro M, Antonucci V, Di Blasi A.Electrochemical investigation of thermally treated graphene oxides as electrode materials for vanadium redox flow battery. Appl Energy 2015; 147:74–81.

[3] Ahmed Sodiq, Fathima Fasmin, Lagnamayee Mohapatra, Sabah Mariyam, Muthumeenal Arunachalam, Hicham Hamoudi, Rachid Zaffou, Belabbes Merzougui "Enhanced electrochemical performance of modified thin carbon electrodes for all-vanadium redox flow batteries," Materials Advances, 2020.

[4] Ahmed Sodiq, Lagnamayee Mohapatra, Fathima Fasmin, Sabah Mariyam, Muthumeenal Arunachalam, Aziz Kheireddine, Rachid Zaffou, Belabbes Merzougui, "Black pearl carbon as a catalyst for all-vanadium redox flow batteries," Chemical Communications, vol. 55, no. 69, pp. 10249-10252, 2019.

[5] Wang CH , Chen CC , Hsu HC , Du HY , Chen CR , Hwang JY , Chen LC , Shih HC , Stejskal J , Chen KH, "Low methanol-permeable polyaniline/Nafion composite membrane for direct methanol fuel cells," Journal of Power Sources, vol. 190, no. 2, pp. 279-284, 2009.

[6] Y. Wang, Y. Shao, D. W. Matson, J. Li, and Y. Lin, "Nitrogen-doped graphene and its application in electrochemical bio sensing," ACS nano, vol. 4, no. 4, pp. 1790-1798, 2010.

[7] A. L. M. Reddy, A. Srivastava, S. R. Gowda, H. Gullapalli, M. Dubey, and P. M. Ajayan, "Synthesis of nitrogen-doped graphene films for lithium battery application," ACS nano, vol. 4, no. 11, pp. 6337-6342, 2010.

[8] Y.-C. Chang et al., "High efficiency of bamboo-like carbon nanotubes on functionalized graphite felt as electrode in vanadium redox flow battery," RSC advances, vol. 6, no. 104, pp. 102068-102075, 2016.

[9] Z. He, L. Shi, J. Shen, Z. He, and S. Liu, "Effects of nitrogen doping on the electrochemical performance of graphite felts for vanadium redox flow batteries," International Journal of Energy Research, vol. 39, no. 5, pp. 709-716, 2015.

[10] M. Park, J. Ryu, Y. Kim and J. Cho, Energy Environ. Sci., 2014, 7, 3727–3735.

Al Rayyan's Wind Energy Potential to Satisfy Ahmed Bin Ali Stadium's Energy Demand During the 2022 FIFA World Cup in Qatar

Carlos Méndez* and Yusuf Bicer

Division of Sustainable Development (DSD), College of Science and Engineering (CSE), Hamad Bin Khalifa University (HBKU), Qatar Foundation, Education City, Doha, Qatar

Emails: *cdelgado@mail.hbku.edu.qa; ybicer@hbku.edu.qa

Abstract

Considering the 2022 FIFA World Cup, and the Qatar National Vision 2030, this study analyzes the possibility to use the wind's kinetic energy to produce electricity to satisfy the demand of the Ahmed Bin Ali Stadium located in Al Rayyan, Qatar. An evaluation of the wind potentiality is performed, based on a thorough analysis of environmental parameters and further computation of the wind power density of the district. Furthermore, a commercial wind turbine is chosen, and a case study is carried out to quantify the capacity that wind energy offers to satisfy the maximum energy demand of the stadium. The results indicate that the environmental conditions of Al Rayyan enable energy production implementing wind turbines, based on a 4.63 m/s wind speed mean and a wind power density of 150.96 W/m^2. In addition, a single wind turbine with 3.4 MW of nominal capacity and 130 m hub height is capable of generating an average of 5955.02 MWh of energy in a year while a wind farm composed by ten turbines could produce 59550.19 MWh/year. From the demand point of view, the maximum energy consumption of the stadium during a football match is in the range of 28-30 MWh which means that, in order to satisfy this demand, a single wind turbine should generate electricity for a period of 44.1 hours, while the wind farm requires 4.41 hours to provide the energy needed. Moreover, to prevent the use of a storage system, the electricity generated by the wind turbines will be tied to the grid, lowering the energy production quota of fossil fuel power plants. By applying this approach, Qatar could reduce its environmental footprint by saving about 5.84 tons of CO_2 per match compared to conventional grid supply during the FIFA World Cup 2022.

Keywords: Wind energy, carbon footprint, wind turbine, supply, demand

I. Introduction

Environmental conservation has been rising in recent years, due to the negative impact that humanity has had to his natural surroundings. With this motivation, several attempts have been made to find viable solutions to reduce pollution around the world. One method is related with electricity generation, since most of it is produced by implementing traditional fossil fuel-based power plants, which emits a large amount of greenhouse gases (GHG).

In order to contribute to global warming reduction, Qatar has developed a pillar dedicated to environmental development to address the negative impact that the local industry has within 2030 Qatar National Vision (General Secretariat for Development Planning, 2008). For this reason, the present study investigates the possibility of implementing wind energy to generate electricity in an environmentally friendly way. Also, with the current sector growth, the cost of wind turbines has decreased, making this technology economically appealing (IRENA International Renewable Energy Agency, 2018). Furthermore, Qatar will be hosting the 2022 FIFA World Cup, which implies an exponential increase in electricity demand. In order to lower the GHG emissions during this period, this study determines the wind potential that Al Rayyan has; to propose a wind farm that satisfies the energy demand of the Ahmed Bin Ali Stadium.

Couple of studies of the wind energy potential of Qatar in general have been performed previously. One case indicated that small to medium-size wind turbines could effectively be used based on the country's potential; also, it is economically viable since the cost per unit of energy produced from a wind farm could be up to 15% lower than a gas-based power plant (Marafia and Ashour, 2003). From an energy perspective, one study highlighted that the maximum value of energy that could be harnessed from wind is 306 kWh/m^2/year (Alnaser and Almohanadi, 1990). However, this analysis can be used only for wind turbines with a hub located 25 m above ground. Recently, a study concluded that the Wind Power Density (WPD) of northern Qatar is 187.5 W/m^2 based on a 5.06 m/s wind speed at 130 m, confirming the viability of implementing small to medium turbines; it also indicated that a 5 x 3.4 MW wind farm could produce energy 50% of the time, saving about 6.813 tons of CO_2 emissions in the process (Méndez and Bicer, 2019). In addition, the capacity factor of the wind power plants are commonly higher than solar power plants.

This paper studies the viability of using wind energy to power a football stadium; lowering the GHG emissions during this global event, and showing that one of the largest producers of CO_2/capita in the world (Ferroukhi et al., 2013; Munawwar and Ghedira, 2014), is taking actions to lower its carbon footprint. This research targets the following objectives:

- Determine the wind energy potential of Al Rayyan to power Ahmed Bin Ali Stadium.
- Calculate the amount of energy that could be obtained from a single wind turbine and from a wind farm in Al Rayyan.
- Determine the time needed by a single wind turbine and by a wind farm, to generate the amount of energy required to satisfy the stadium's demand during a football match.
- Calculate the environmental impact reduction achieved through wind energy production.

II. System Description

The present study examines two scenarios to determine the amount of energy that could be harnessed from the wind's kinetic energy. The first scenario considers a single 3.4 MW wind turbine with a 130 m hub height; the second case is a 10 x 3.4 MW wind farm. For the wind farm scenario, the wake effect is neglected; to do so, the turbines are distributed one beside the other, eliminating the influence that an upstream turbine could have on the rest. Furthermore, due to the inconsistent nature of wind energy, a storage system is usually implemented; however, in this study, to prevent the use of batteries, the energy produced in both scenarios will be supplied directly to the power grid knowing that the grid is already available in the stadium. Reducing the share of electricity production from the fossil fuel power plants during this period, this substituted quota will be relocated to the stadium during the football matches assuring the energy supply. By implementing this approach, the overall GHG emissions will be lowered since the wind farm will produce more energy than the one required by the stadium. Meaning that the additional energy will be used to lower the traditional power plants electricity production.

Al Rayyan is the selected location for one main reason. The energy demand is originated in this sector, hence by supplying electricity in this area, the energy production by traditional power plants intended to this region will be replaced. Also, every environmental parameter required to carry out this study (wind speed and direction, temperature, etc.) was measured at this site by the Supreme Committee for Delivery & Legacy in Qatar.

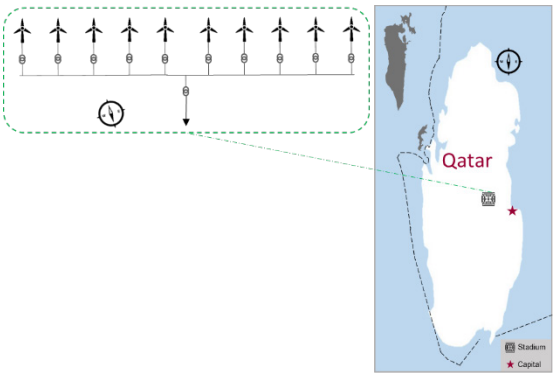

Figure 1. Wind farm distribution and the proposed location

III. Analysis

Three main steps were followed to calculate the energy production for both scenarios. First, the wind characteristics and other environmental parameters (temperature, atmospheric pressure, and air density) were studied. Then, the WPD was determined; finally, based on these calculations and the turbine specifications, the energy production was obtained.

III.I. Wind Speed

Two main aspects affect wind speed. The first one is terrain roughness; this element considers the influence of any obstacles (natural or man-made) that may present resistance. The other aspect is height, from which it can be said that with more elevation, higher the wind speed. In this study, the measurements were obtained at 10 m, hence, to calculate the energy production of the selected turbine, these measurements must be extrapolated to its hub height using equation (1) (Hernández and Ortega, 2014).

$$V = V_0 \left(\frac{H}{H_o}\right)^{\alpha} \quad (1)$$

where: V is the wind speed at height H (m); V_0 is the wind speed at height H_0 (m); α is the friction coefficient or Hellmann Index.

In this study, the values of H_0 and H are 10 m and 130 m, respectively. Also, since the terrain in Al Rayyan lacks a large number of man-made obstacles, and the terrain is flat, the friction coefficient selected is 0.143, which corresponds to the described area. Applying equation (1) in with a selected value of α, the data collected were extrapolated from 10 m to 130 m. The columns of Figure 2**Error! Reference source not found.** highlight that wind speeds between 2 and 5 m/s are those with a higher recurrence. Furthermore, the average speed is 4.63 m/s, the median value is 3.95 m/s, and the maximum recorded speed was 28.31 m/s. To verify this information, a statistical tool known as the Weibull distribution was implemented. This approach analyzes the wind's behavior considering shape and scale parameters; several methods could be implemented, however in this study, these parameters were calculated based on the median as indicated in equations (2) and (3) (El Khchine et al., 2019; Justus et al., 1978).

$$c = \frac{V_m}{ln(2)^{1/k}} \quad (2)$$

$$k = \frac{1.573}{ln(V_{0.75}/V_{0.25})} \quad (3)$$

where: V_m is the median speed; $V_{0.25}$ is the first quartile, also known as Q1; $V_{0.75}$ is the third quartile, also known as Q3; c and k are the shape and scale parameters.

Applying the information above to the recollected data, the Weibull distribution is obtained as a sloped line (see Figure 2**Error! Reference source not found.**). The results concur with the recurrence study, meaning that the range of wind speed that presents the higher probability of occurrence is between 2 and 5 m/s, since approximately 60% of the recorded wind speed is located within this range.

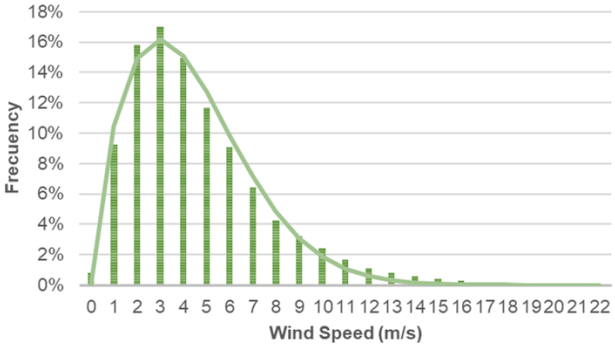

Figure 2. Wind speed recurrence and Weibull distribution

III.II. Wind Power Density

Once the air density value was obtained along with the wind speed, the wind power potential per swept area can be calculated in W/m^2. Hence, by implementing equation (4) (Hernández and Ortega, 2014), considering the information obtained in section III.I, a value of 150.96 W/m^2 of WPD, was found:

$$WPD = \frac{1}{2n}\sum_{i=1}^{n}\rho V_i^3 \quad (4)$$

where: ρ is the air density (kg/m^3); V is the wind speed (m/s); n is the number measurements.

III.III. Energy Production Calculation

The potential energy production of a wind turbine must be calculated considering the wind speed, since a wind turbine power output changes with this variable. So, by calculating the power generation at a specific speed and multiplying it by the recurrence of this velocity, the energy output is obtained. There are two ways to determine the power output of a wind turbine; the first one is to cross-reference the wind speed with the power curve generated by the manufacturer. However, this plot is given under specific climate conditions that could differ from the place in which the turbine will be located. The second method is more independent and accurate since it relies on the turbine's power coefficient (*CP*), the diameter of the rotor, and the ambient parameters of the location where the turbine will be located (Sedaghat et al., 2016):

$$P = \frac{1}{2}\rho A V^3 Cp \quad (5)$$

where: ρ is the air density (kg/m^3); V is the wind speed (m/s); A is the turbine's rotor area (m^2); Cp is the turbine's power coefficient.

In this study, the Senvion 3.44M140 wind turbine with a nominal capacity of 3.4 MW was selected having a swept area of 15393.80 m^2 based on a rotor diameter of 140 m and a hub height of 130 m. This turbine was chosen because it has a 3 m/s cut-in speed, which enables to produce energy regularly at lower wind speeds despite the below-average wind speed that Al Rayyan. In addition, the *Cp* values of the turbine are located between 3 m/s and 10 m/s, which are ideal for the selected location.

IV. Results and discussions

Once the environmental parameters were studied and the wind turbine was selected, using the Equation (5) and Figure 2 data, the energy production was obtained for both, a single wind turbine and a wind farm (consisting of 10 x 3.4 MW). For the first scenario, an average of 12406.29 MWh of energy was produced during the studied period, meaning that a single turbine could generate 5955.02 MWh/year. Also, Figure 3**Error! Reference source not found.** highlights that the energy production trend is similar through the years, showing its highest potential in June. The same calculation was employed for the wind farm, disregarding the wind reduction and the turbulence generation

that the wake effect has in this type of study (Burton et al., 2001). As expected, the energy production for the 10 x 3.4 MW wind farm is 124062.89 MWh, with an average yearly output of 59550.19 MWh, which is ten times the output of a single turbine. Furthermore, since the wind behavior is the same for both scenarios and the change in its direction does not affect the wind farm, due to the absence of wake effect, Figure 3 shows that the energy generation tendency is the same as a single turbine.

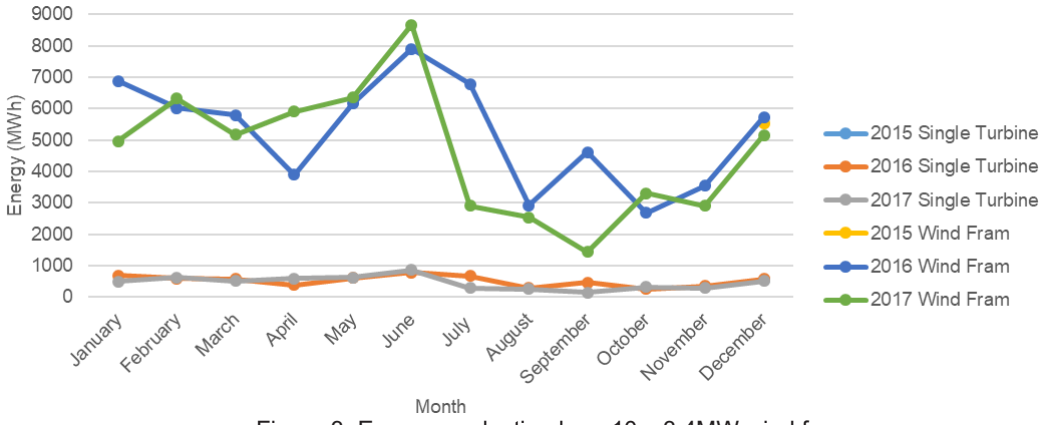

Figure 3. Energy production by a 10 x 3.4MW wind farm

With these results, it is possible to calculate the time that both scenarios need to satisfy the demand of the Ahmed Bin Ali Stadium. This pitch has a maximum load capacity of 10 MW and assuming that a football match requires three hours at full capacity, the highest energy demand during the event is 30 MWh. Therefore, to determine this timeline, the average yearly energy production for both scenarios were used to calculate its typical average power output obtaining 0.68 MW and 6.8 MW for a single turbine and a wind farm, respectively. Based on the power generation, the time required to generate the equivalent of the energy demanded per match is calculated by dividing 30 MWh with the average power generation, which yields 44.1 h and 4.41 h for a single wind turbine and wind farm, respectively.

Since the energy demand of the stadium is supplied by green technology, the amount of CO_2 associated with electricity production is also lowered. For this study, this sustainable source of energy will substitute electricity generated by the combustion of natural gas and diesel, which in Qatar are the dominant form of electricity production. Assuming that the ignition of diesel fuel and natural gas emits 0.250 kg CO_2/kWh and 0.181 kg CO_2/kWh, respectively (US Energy Inf, 2018), Table 1 shows the expected emissions from a single football match. This computation indicates that 5.844 of CO_2 production will be saved since wind turbines do not emit any GHG emissions during operation.

Table 1. CO_2 emissions from diesel and natural gas for 30 MWh electricity generation

Energy Source	Share	Electricity Production	CO_2 Emissions per match (Ton CO_2)
Diesel fuel	20%	6 MWh	1.5
Natural gas	80%	24 MWh	4.344
Total	**100%**	**30 MWh**	**5.844**

V. Conclusions

This study analyzes the possibility to meet the energy demand that Ahmed Bin Ali Stadium has during a football match implementing wind energy. In addition, a single 3.4 MW wind turbine and a 10 x 3.4MW wind farm were evaluated to determine the energy production for each scenario. Furthermore, the required time to produce the energy demanded by the stadium and the CO_2 saved per match were also estimated for both scenarios. After implementing this study, the following main results were obtained:

- Al Rayyan's wind speed mean is 4.63 m/s, and approximately 74% of the available wind flows between 3 m/s and 22 m/s. This result indicates that energy production implementing a proper wind turbine is possible. Furthermore, since the selected turbine has 3 m/s and 22 m/s as its cut-in and cut-out speeds, energy will be produced 74% of the time in a year. Wind farm (10 x 3.4 MW) is capable of generating an average of 59550.19 MWh/year
- The wind power density in Al Rayyan is about 150.96 W/m^2. This value indicated the viability of implementing wind energy at a small to medium scale.
- A single wind turbine will take on average 44.12 h to generate the demanded energy of the Ahmed Bin Ali Stadium for a single match. On the other hand, the proposed wind farm will satisfy the demand ten times faster, needing 4.41 h considering the average wind speed and capacity factor of the wind turbines.
- By utilizing the wind's potential to satisfy the energy demand of the football stadium, 5.844 tons of CO_2 will be reduced per match. This emission reduction is originated by replacing 30 MWh of energy in the power grid, which formerly was generated by hydrocarbon-based power plants.

Acknowledgements

The authors recognize the support provided by the Hamad Bin Khalifa University, Qatar Foundation (210008390). Also, the authors would like to thank the Supreme Committee for Delivery & Legacy and Marco Frioni for providing the wind measurement data and all the assistance.

References

Alnaser, W.E., Almohanadi, A.H., 1990. Wind and solar energy in Qatar. Energy 15, 931–934. https://doi.org/10.1016/0360-5442(90)90075-D

Burton, T., Sharpe, D., Jenkins, N., Bossanyi, E., 2001. Wind Energy Handbook. John Wiley and Sons Ltd.

El Khchine, Y., Sriti, M., El Kadri Elyamani, N.E., 2019. Evaluation of wind energy potential and trends in Morocco. Heliyon 5. https://doi.org/10.1016/j.heliyon.2019.e01830

Ferroukhi, R., Ghazal-Aswad, N., Androulaki, S., Hawila, D., Mezher, T., 2013. Renewable energy in the GCC: Status and challenges. Int. J. Energy Sect. Manag. https://doi.org/10.1108/17506221311316498

General Secretariat for Development Planning, 2008. Qatar National Vision 2030. Doha.

Hernández, A., Ortega, O., 2014. Análisis estadístico del viento como recurso energético I, 3–4.

IRENA International Renewable Energy Agency, 2018. Renewable Power Generation Costs in 2017, International Renewable Energy Agency. https://doi.org/10.1007/SpringerReference_7300

Justus, C.G., Hargraves, W.R., Mikhail, A., Graber, D., 1978. Methods for estimating wind speed frequency distributions. J. Appl. Meteorol. 17, 350–353. https://doi.org/10.1175/1520-0450(1978)017<0350:mfewsf>2.0.co;2

Marafia, A.H., Ashour, H.A., 2003. Economics of off-shore/on-shore wind energy systems in Qatar. Renew. Energy 28, 1953–1963. https://doi.org/10.1016/S0960-1481(03)00060-0

Méndez, C., Bicer, Y., 2019. Qatar's Wind Energy Potential with Associated Financial and Environmental Benefits for the Natural Gas Industry. Energies 12, 3329. https://doi.org/10.3390/en12173329

Munawwar, S., Ghedira, H., 2014. A review of renewable energy and solar industry growth in the GCC region, in: Energy Procedia. Elsevier Ltd, pp. 3191–3202. https://doi.org/10.1016/j.egypro.2015.06.069

Sedaghat, A., Gaith, M., Khanafer, K., Bani-Hani, E., 2016. Rated wind speed reality or myth for optimization in design of wind turbines, in: 2016 11th International Conference on Ecological Vehicles and Renewable Energies, EVER 2016. https://doi.org/10.1109/EVER.2016.7476402

US Energy Inf, 2018. Energy Information Administration (EIA) [WWW Document].

Calculation of Exergy Destruction Cost Rate of a Combined Cycle Power Plant Using SPECO and MOPSA methods

[1*]Cuneyt Uysal, [2]Hasan Ozcan
[1] Karabuk University, TOBB Vocational School of Technical Sciences, Automotive Technologies Program, Karabuk, 78050, Turkey.
[2] Ankara Yildirim Beyazit University, Faculty of Engineering and Natural Sciences, Mechanical Enginering Department, Ankara, 06010, Turkey.

* E-mails: cuneytuysal@karabuk.edu.tr; hozcan@ybu.edu.tr

Abstract
A combined cycle power plant is theoretically modelled. Specific Exergy Costing (SPECO) and Modified Productive Structure Analysis (MOPSA) methods are individually applied to the system. The unit cost of electricity generated by gas turbine is calculated to be 45.36 $/GJ with SPECO method and 58.52 $/GJ with MOPSA method. The exergy destruction cost rate of overall system is determined to be 454.0092 $/h with MOPSA method and 4707.93 $/h with SPECO method. According to the MOPSA method, the combustion chamber is the most responsible equipment for exergy destruction cost rate. However, in SPECO method, the gas turbine is the most responsible for exergy destruction cost rate. Exergy destruction cost rates of system equipment are not proportional with their exergy destruction rates in SPECO method.

Keywords: Combined cycle power plant; Exergy destruction; MOPSA; SPECO; Thermoeconomics.

I. Introduction

Thermoeconomics is an engineering branch that combines thermodynamics and economics. It provides information about the cost structure of system and the costs of intermediate and final products and it allows the cost allocation for multiproduct systems. There are several thermoeconomics method in the literature and are based on different fundamentals and assumptions. Specific Exergy Costing (SPECO) is the most commonly used thermoeconomics method. SPECO method is based on the following equation (Bejan et al., 1996):

$$c_F \dot{E}x_F + \dot{Z} = c_P \dot{E}x_P \quad (1)$$

where c is the unit cost, $\dot{E}x$ is the exergy rate, $\dot{Z}$ is the capital investment cost rate. The F and P subscripts denote fuel and product, respectively. Equation 1 is not including for exergy destruction cost rate. For this reason, the exergy balance equation is used. The exergy balance equation for any thermal system can be given as follows:

$$\dot{E}x_F = \dot{E}x_P + \dot{E}x_D \quad (2)$$

where the D subscript denote destruction. With substituting Equation 2 into Equation 1, the following equation can be obtained:

$$c_F \dot{E}x_P + c_F \dot{E}x_D + \dot{Z} = c_P \dot{E}x_P \quad (3)$$

By this way, the $c_F \dot{E}x_D$ term is used on the costing of exergy destruction rate in SPECO method. However, Uysal (2020) reported that the usage of this term leads to some contradictory results and it was claimed that Modified Productive Structure Analysis (MOPSA) method is more effective method on the costing of exergy destruction. MOPSA method is based on the following equation (Yoo et al., 2018):

$$c_F \dot{E}x_F + c_S \dot{E}x_D + \dot{Z} = c_P \dot{E}x_P \quad (4)$$

where c_S is the unit cost of negentropy. In MOPSA method, the $c_S \dot{E}x_D$ term is used on the costing of exergy destruction rate.

In this study, a combined cycle power plant is theoretically modelled. SPECO and MOPSA methods are individually applied to the system. The unit costs of shaftwork generated by gas turbine and by steam turbine are calculated with both methods. In addition, the exergy destruction cost rates are determined with using SPECO and MOPSA methods. The obtained results are presented and compared.

II. System Description

Figure 1 shows the schematic diagram of combined cycle power plant considered in this study.

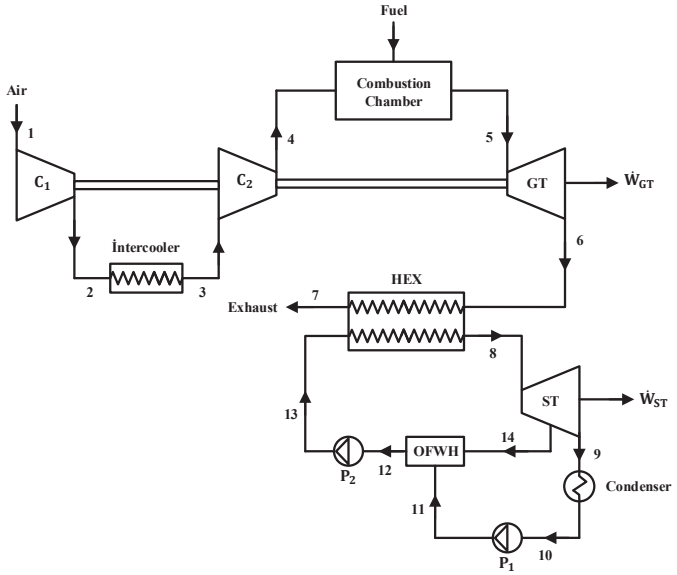

Fig. 1: The schematic diagram of combined cycle power plant

Methane with mass flow rate of 2.172 kg/s is supplied to the system as fuel. The shaftwork generated by the gas turbine (GT) is 52612 kW. A part of shaftwork generated by the gas turbine is used to drive the compressors (C1 and C2). The C1 and C2 consume shaftwork of 10619kW and 10150kW, respectively. Similarly, the shaftwork generated by the steam turbine (ST) is 11191 kW and a part of this shaftwork is used to drive the pumps (P1 and P2). The shaftworks used to drive the P1 and P2 are 22.7 kW and 50.12 kW, respectively.

III. Methodology

In Specific Exergy Costing (SPECO) method, the unit exergy cost of each state located in the system is determined with applying the basic principles from business administration. The general cost balance of SPECO method can be given as follows:

$$\sum\left(c_{in}\dot{Ex}_{in}\right)_k + c_{q,k}\dot{Ex}_{q,k} + \dot{Z}_k = \sum\left(c_{out}\dot{Ex}_{out}\right)_k + c_{W,k}\dot{W}_k \tag{5}$$

where the in, out, q and W subscripts denote inlet, outlet, heat and work, respectively. With applying Equation 5 to each system equipment, an equation set including the number of equations equal to the number of system equipment is obtained. However, to be able to solve equations, the number of equations equal to the number of system states are required in SPECO method. For this purpose, auxiliary equations are required. The auxiliary equations are obtained with applying Fuel-Product (F-P) Rule.

Unlike SPECO method, Modified Productive Structure Analysis (MOPSA) method is based on exergy costing without flow-stream cost calculations. In MOPSA method, the termomechanical exergy is divided into its thermal and mechanical components. In addition, it allows assigning a unit cost term, which is called as the unit cost of negentropy, to exergy destruction terms. The general cost balance of MOPSA can be written as follows:

$$\dot{Ex}^{CHE}c_0 + \dot{Ex}^{BQ}c_{BQ} + \left(\sum\dot{Ex}^{T}_{in} - \sum\dot{Ex}^{T}_{out}\right)c_T + \left(\sum\dot{Ex}^{M}_{in} - \sum\dot{Ex}^{M}_{out}\right)c_M + T_0\left(\sum\dot{S}_{in} - \sum\dot{S}_{out}\right)c_S + \dot{Z}_k = \dot{Ex}^{W}c_W \tag{6}$$

where T_0 is the temperature of dead state and $\dot{S}$ is the entropy rate. The $\dot{Ex}^{CHE}c_0$ term is the cost flow rate of fuel supplied to the system. The T, M, S, W and BQ subscripts and superscripts denote thermal, mechanical, entropy, work and external streams, respectively. An equation set including the number of equations equal to the number of system equipment is obtained with applying Equation 6 to each system equipment. To be able solve this equation set, the number of equations should be equal to the number of unknowns. In MOPSA method, junctions are used to obtain auxiliary equations. Junctions are fictitious equipment where homogenous productions of two or more components merge. Moreover, boundary definition is used in MOPSA method. Boundary is responsible for all exergy destruction rate.

The cost balance equations obtained with applying SPECO and MOPSA to the system considered in this study are tabulated in Table 1 and 2, respectively.

Table 1. Cost balance equations obtained with SPECO method.

Equipment	Cost balance	Auxiliary equation
Compressor-I	$\dot{C}_1 + \dot{C}_{W,C1} + \dot{Z}_{C1} = \dot{C}_2$	$c_1 = 0$
Intercooler	$\dot{C}_2 + \dot{Z}_{int\,cool} = \dot{C}_3$	-
Compressor-II	$\dot{C}_3 + \dot{C}_{W,C2} + \dot{Z}_{C2} = \dot{C}_4$	-
Combustion chamber	$\dot{C}_4 + \dot{C}_{Fuel} + \dot{Z}_{CC} = \dot{C}_5$	$c_{Fuel} = 20\$ / GJ$
Gas turbine	$\dot{C}_5 + \dot{Z}_{GT} = \dot{C}_6 + \dot{C}_{W,GT}$	$c_{W,GT} = c_{W,C1} = c_{W,C2}$
Heat exchanger	$\dot{C}_6 + \dot{C}_{13} + \dot{Z}_{HEX} = \dot{C}_7 + \dot{C}_8$	$c_6 = c_7$
Pump-I	$\dot{C}_{10} + \dot{C}_{W,P1} + \dot{Z}_{P1} = \dot{C}_{11}$	-
Pump-II	$\dot{C}_{12} + \dot{C}_{W,P2} + \dot{Z}_{P2} = \dot{C}_{13}$	-
OFWH	$\dot{C}_{11} + \dot{C}_{14} + \dot{Z}_{OFWH} = \dot{C}_{12}$	-
Condenser	$\dot{C}_9 + \dot{Z}_{cond} = \dot{C}_{10}$	-
Steam turbine	$\dot{C}_8 + \dot{Z}_{ST} = \dot{C}_9 + \dot{C}_{14} + \dot{C}_{W,ST}$	$c_8 = c_9 = c_{14}$ $c_{W,GT} = c_{W,P1} = c_{W,P2}$

Table 2. Cost balance equations obtained with MOPSA method.

Equipment	Cost balance
Compressor-I	$\left(E\dot{x}_1^T - E\dot{x}_2^T\right)c_T + \left(E\dot{x}_1^M - E\dot{x}_2^M\right)\mathbf{c_{1M}} + \left(E\dot{x}_{D,C1}\right)c_S + \dot{Z}_{C1} = \left(-E\dot{x}_{C1}^W\right)c_{W,GT}$
Intercooler	$\left(E\dot{x}_2^T - E\dot{x}_3^T\right)\mathbf{c_{2T}} + \left(E\dot{x}_2^M - E\dot{x}_3^M\right)c_M + \left(E\dot{x}_{D,int\,cool}\right)c_S + \dot{Z}_{int\,cool} = 0$
Compressor-II	$\left(E\dot{x}_3^T - E\dot{x}_4^T\right)c_T + \left(E\dot{x}_3^M - E\dot{x}_4^M\right)\mathbf{c_{3M}} + \left(E\dot{x}_{D,C2}\right)c_S + \dot{Z}_{C2} = \left(-E\dot{x}_{C2}^W\right)c_{W,GT}$
Combustion chamber	$E\dot{x}^{CHE}c_0 + \left(E\dot{x}_4^T - E\dot{x}_5^T\right)\mathbf{c_{4T}} + \left(E\dot{x}_4^M - E\dot{x}_5^M\right)c_M + \left(E\dot{x}_{D,CC}\right)c_S + \dot{Z}_{CC} = 0$
Gas turbine	$\left(E\dot{x}_5^T - E\dot{x}_6^T\right)c_T + \left(E\dot{x}_5^M - E\dot{x}_6^M\right)c_M + \left(E\dot{x}_{D,GT}\right)c_S + \dot{Z}_{GT} = \left(E\dot{x}_{GT}^W\right)\mathbf{c_{W,GT}}$
Heat exchanger	$\left(E\dot{x}_6^T + E\dot{x}_{13}^T - E\dot{x}_7^T - E\dot{x}_8^T\right)\mathbf{c_{6T}} + \left(E\dot{x}_6^M + E\dot{x}_{13}^M - E\dot{x}_7^M - E\dot{x}_8^M\right)c_M + \left(E\dot{x}_{D,HEX}\right)c_S + \dot{Z}_{HEX} = 0$
Pump-I	$\left(E\dot{x}_{10}^T - E\dot{x}_{11}^T\right)c_T + \left(E\dot{x}_{10}^M - E\dot{x}_{11}^M\right)\mathbf{c_{7M}} + \left(E\dot{x}_{D,P1}\right)c_S + \dot{Z}_{P1} = \left(-E\dot{x}_{P1}^W\right)c_{W,ST}$
Pump-II	$\left(E\dot{x}_{12}^T - E\dot{x}_{13}^T\right)c_T + \left(E\dot{x}_{12}^M - E\dot{x}_{13}^M\right)\mathbf{c_{8M}} + \left(E\dot{x}_{D,P2}\right)c_S + \dot{Z}_{P2} = \left(-E\dot{x}_{P2}^W\right)c_{W,ST}$
OFWH	$\left(E\dot{x}_{11}^T + E\dot{x}_{14}^T - E\dot{x}_{12}^T\right)\mathbf{c_{9T}} + \left(E\dot{x}_{11}^M + E\dot{x}_{14}^M - E\dot{x}_{12}^M\right)c_M + \left(E\dot{x}_{D,OFWH}\right)c_S + \dot{Z}_{OFWH} = 0$
Condenser	$\left(E\dot{x}_9^T - E\dot{x}_{10}^T\right)\mathbf{c_{10T}} + \left(E\dot{x}_9^M - E\dot{x}_{10}^M\right)c_M + \left(E\dot{x}_{D,cond}\right)c_S + \dot{Z}_{cond} = 0$
Steam turbine	$\left(E\dot{x}_8^T - E\dot{x}_9^T - E\dot{x}_{14}^T\right)c_T + \left(E\dot{x}_8^M - E\dot{x}_9^M - E\dot{x}_{14}^M\right)c_M + \left(E\dot{x}_{D,ST}\right)c_S + \dot{Z}_{ST} = \left(E\dot{x}_{ST}^W\right)\mathbf{c_{W,ST}}$
T-Junction	$\left(E\dot{x}_2^T - E\dot{x}_3^T + E\dot{x}_4^T - E\dot{x}_5^T + E\dot{x}_6^T + E\dot{x}_{13}^T - E\dot{x}_7^T - E\dot{x}_8^T + E\dot{x}_{11}^T + E\dot{x}_{14}^T - E\dot{x}_{12}^T + E\dot{x}_9^T - E\dot{x}_{10}^T\right)\mathbf{c_T} - \left(E\dot{x}_2^T - E\dot{x}_3^T\right)c_{2T} - \left(E\dot{x}_4^T - E\dot{x}_5^T\right)c_{4T} - \left(E\dot{x}_6^T + E\dot{x}_{13}^T - E\dot{x}_7^T - E\dot{x}_8^T\right)c_{6T} - \left(E\dot{x}_{11}^T + E\dot{x}_{14}^T - E\dot{x}_{12}^T\right)c_{9T} - \left(E\dot{x}_9^T - E\dot{x}_{10}^T\right)c_{10T} = 0$
M-Junction	$\left(E\dot{x}_1^M - E\dot{x}_2^M + E\dot{x}_3^M - E\dot{x}_4^M + E\dot{x}_{10}^M - E\dot{x}_{11}^M + E\dot{x}_{12}^M - E\dot{x}_{13}^M\right)\mathbf{c}_M - \left(E\dot{x}_1^M - E\dot{x}_2^M\right)c_{1M} - \left(E\dot{x}_3^M - E\dot{x}_4^M\right)c_{3M} - \left(E\dot{x}_{10}^M - E\dot{x}_{11}^M\right)c_{7M} - \left(E\dot{x}_{12}^M - E\dot{x}_{13}^M\right)c_{8M} = 0$
Boundary	$\left(E\dot{x}_7^T - E\dot{x}_1^T\right)c_T + \left(E\dot{x}_7^M - E\dot{x}_1^M\right)c_M + \left(E\dot{x}_{D,boun}\right)c_S + \dot{Z}_{boun} = 0$

IV. Results and discussions

The thermodynamic data obtained for the combined cycle power plant are tabulated in Table 3.

When the equations given in Table 1 are solved, the unit cost of electricity generated by gas turbine is calculated to be $c_{W,GT}$ = 45.36 \$/GJ. In addition, the unit cost of electricity generated by steam turbine is determined to be $c_{W,ST}$ = 60.11 \$/GJ. However, the unit costs of electricity generated by gas turbine and steam turbine are calculated to be $c_{W,GT}$ = 58.52 \$/GJ and $c_{W,ST}$ = 35.58 \$/GJ, respectively, when the equations given in Table 2 are solved. According to MOPSA method, the unit cost of negentropy is determined to be c_S = -1.9287 \$/GJ.

The exergy destruction rates and exergy destruction cost rates of system equipment are given in Table 4.

Table 3. The thermodynamic data for the combined cycle power plant

State	$\dot{m}$ (kg/s)	T (K)	P (kPa)	$\dot{E}x^{T}$ (kW)	$\dot{E}x^{M}$ (kW)	$\dot{E}x^{TM}$ (kW)
1	74.71	300	101	0	0	0
2	74.71	403.8	285.7	1110.03	6688.69	7798.72
3	74.71	300	285.7	0	6688.69	6688.69
4	74.71	403.8	808	1110.03	13376.07	14486.10
5	76.88	1637	808	85667.03	14133.88	99800.91
6	76.88	903.6	101	25318	0	25318
7	76.88	506.3	101	4201.07	0	4201.07
8	12.08	883.6	5000	18180.64	59.41	18240.05
9	9.574	333.2	20	2304..02	-0.73	2303.29
10	9.574	333.2	20	68.53	-0.73	67.80
11	9.574	333.4	2000	69.30	18.25	87.55
12	12.08	485.6	2000	2149.90	23.02	2172.92
13	12.08	486.3	5000	2158.94	59.41	2218.35
14	2.508	746.3	2000	3023.88	4.78	3028.66

Table 4. The results obtained with thermoeconomic analysis data.

Equipment	$\dot{E}x_{dest,k}$ (GJ/h)	$\dot{Z}_k$ ($/h)	SPECO		MOPSA	
			$c_{F,k}$ ($/GJ)	$\dot{C}_{D,k}$ ($/GJ)	c_S ($/GJ)	$\dot{C}_{D,k}$ ($/GJ)
Compressor-I	10.1530	0.9281	45.3557	460.4964	1.9287	19.5821
Intercooler	3.9961	0.2244	61.7909	246.9227	1.9287	7.7073
Compressor-II	8.4693	0.9281	45.3557	384.1310	1.9287	16.3347
Combustion chamber	98.0466	0.6825	20	1960.9320	1.9287	189.1025
Gas turbine	78.7353	9.676	32.0015	2519.6455	1.9287	151.8568
Heat exchanger	18.3428	0.8153	32.0015	586.9971	1.9287	35.3778
Pump-I	0.0106	0.0087	60.1144	0.6372	1.9287	0.0204
Pump-II	0.0169	0.011	60.1144	1.0159	1.9287	0.0326
OFWH	3.3958	0.2164	89.0672	302.4544	1.9287	6.5495
Condenser	8.0478	0.1714	51.7896	416.7923	1.9287	15.5218
Steam turbine	6.1823	15.24	51.7896	320.1788	1.9287	11.9238
Overall system	235.3965	28.9019	20	4707.93 (7200.2033)*	1.9287	454.0092

* The value given inside parenthesis is the sum of column.

According to MOPSA method, the exergy destruction cost rate of overall system is calculated to be 454.0092 $/h. The exergy destruction cost rates of system equipment are proportional with their exergy destruction rates in MOPSA method. The highest exergy destruction cost rate is determined to be 189.1025 $/h for combustion chamber and it is followed by gas turbine with 151.8568 $/h. In SPECO method, the exergy destruction cost rate of overall system is calculated to be 4707.93 $/h, when the $c_F \dot{E}x_D$ term is used. However, the sum of exergy destruction cost rate of system equipment is equal to 7200.2033 $/h. The exergy destruction cost rates of system equipment are not proportional with their exergy destruction rate in SPECO method. According to SPECO method, the highest exergy destruction cost rate is determined to be 2519.6455 $/h for gas turbine and it is followed by combustion chamber with 1960.9320 $/h.

V. Conclusions

This study represents a comparison of SPECO and MOPSA methods with applying to a combined cycle power plant. Both methods provide exactly different results for the unit cost of electricity generated by gas and steam turbines. When the exergy destruction cost rate is considered, the results obtained by SPECO method are higher than the results obtained by MOPSA method. The exergy destruction cost rates of system equipment are proportional with their exergy destruction rate in MOPSA method.

References

Bejan, A., Tsatsaronis, G., Moran. M., 1996. Thermal design and optimization, John Wiley and Sons, Inc., New York.

Uysal, C., 2020. A new approach to advanced exergoeconomic analysis: the unit cost of entropy generation, Environmental Progress and Sustainable Energy 39, 13297. https://doi.org/10.1002/ep.13297.

Yoo, Y., Oh, H.S., Uysal, C., Kwak, H.Y., 2018. Thermoeconomic diagnosis of an air-cooled air conditioning system. International Journal of Exergy 26, 393-417. 10.1504/IJEX.2018.093185.

Research on spatial non-uniformity of power distribution for solar radiation simulation

[1*]Bartosz Stanek, [2]Łukasz Bartela, [3]Daniel Węcel, [4]Anna Skorek-Osikowska
[1,2,3,4] Silesian University of Technology, Faculty of Energy and Environmental Engineering,
Department of Power Engineering and Turbomachinery, Akademicka 2a, Gliwice, 44-100, Poland

* E-mail: bartosz.stanek@polsl.pl

Abstract
The worldwide rapid development of renewable energy sources, primarily solar technologies, forces scientists to develop testing devices enabling a meaningful comparison of their work. Solar radiation simulators are used for studing solar technologies in fixed, predetermined conditions. The distribution of energy on the tested surface is an important factor in the case of solar cells and radiation concentrators of various types. Compared to natural solar radiation, simulators are characterized by a heterogeneous distribution of energy due to the use of many sources. The article presents the results of modelling, using a numerical optical-engineering software, aimed at comparing the spatial non-uniformity of the total energy distribution on a given surface using parabolic floodlights of different distribution, size and estimation of the optimal solution. In addition to the indicators contained in the radiation simulation standards, an own factor has also been defined, based on the method of least squares. A 1x1 m illuminated surface, with a minimum of 4 and a maximum of 22 parabolic reflectors was considered. The modelling results are to be used as a guide to the optimal selection of the number, arrangement and size of the reflectors for simulating solar radiation.

Keywords: Solar simulation, solar energy, power distribution

I. Introduction
Solar radiation simulators are devices that enable testing solar technologies under strictly established and repeatable conditions (Sabahi et al., 2016). They consist from a few to several light sources. They allow the simulation of near-natural or multiple concentrated radiation according to the needs. The most commonly used sources for simulation are tungsten halogen, metal-hallides, xenon and, recently, even LEDs (Li et al., 2019). The selection of appropriate sources strictly depends on the purpose of the simulation and the expected effect. The quality of the simulated radiation is determined by standards IEC 60904-9 and ASTM-E927-10, using 3 factors: spectral mismatch to all intervals, spatial non-uniformity and short and long term temporal instability. In this work simulators were tested for power distribution, i.e. heterogeneity of the illuminated field.

II. Methodology
The analysis considered the use of the Arri headlamps with metal-halides sources of 575 W (Osram) nominal power and possible dimming up to 60% of the nominal value. Nominal electric power could be regulated from 345 W to 575 W. Electrical to light efficiency was assumed at 23% (Boubalt et al., 2015). ArriSun headlamps are equipped with parabolic reflectors, where, for calculations, a reflectivity of 90% has been assumed. Also, the position of the discharge lamp with the reflector can be changed, but when modelling, it is assumed that the illuminating gas bubble is exactly in the focal length of the reflector. Additionally, the analysed headlamps can be used together with different types of lenses, however, in this analysis such cases have not been presented. It should be remembered that radiation collimation is important in the examination of radiation concentrators (Meng, 2011).

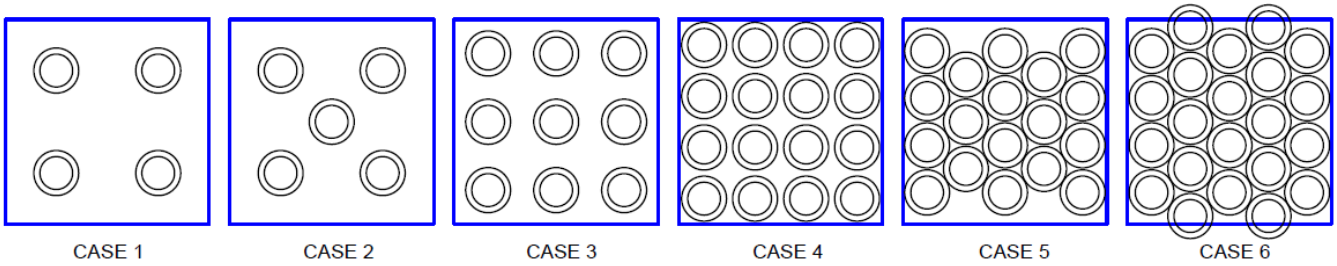

Fig. 1. Reflectors arrangement cases

For each case, a 1x1 m illuminated surface was tested. The surface was placed 1 meter away from the reflectors set. The study was performed for 6 cases (4, 5, 9, 16, 18, 22 reflectors) and the distribution is presented in Fig. 1. The proposed arrangement of the headlights is exemplary, analyses can be carried out for every possible combination. In the tests, the location of the headlights for cases 1, 3, 4 results from dividing the surface area into the appropriate number of fields and then placing the headlight in the centre of this field. Case 2 is a comprehensive case 1, aimed at checking the operation of the simulator with an additional reflector in the centre of the surface. Case 6 involves minimizing the distance between the spotlights and case 5 is the removal of 4 spotlights partially protruding beyond the surface. The diameter of the parabolic reflector is 16 cm. In Fig. 1, the outer circle indicates the geometric dimension of the entire lamp for correct placement. The distribution of radiation was analyzed with

the use of optical-engineering add-in SolidWorks software APEX®, which allows, among others, to study power distribution on the illuminated surface. The field has been divided into 40,000 measuring points, each with dimensions of 5x5 mm. The work did not consider the angle of incidence of rays on the surface but the value of total radiation was measured.

III. Analysis

The energy distribution in solar radiation simulators is defined according to standards IEC 60904-9 and ASTM-E927-10 as (1) the quotient of the difference of the largest and smallest values measured on the surface and the sum of these values:

$$non-uniformity = S_{\mathrm{NE}} = 100\% \frac{E_{\mathrm{maximum}} - E_{\mathrm{minimum}}}{E_{\mathrm{maximum}} + E_{\mathrm{minimum}}}) \quad (1)$$

where E_{maximum} is the highest value of irradiance (W/m^2), E_{minimum} is the lowest value of irradiance (W/m^2).

Spatial non-uniformity is determined using 3 classes: A for S_{NE} <2, B for S_{NE}<5, C for S_{NE}<10. The highest class simulators are characterized by this coefficient at level A. If S_{NE} factor >10 the simulator does not receive a class.

Since the radiation simulator under test is a low-budget device that does not use lenses, it can be expected that the factor shown above will not be valid for use to compare the energy distribution on the surface. For this reason, a different factor has been defined for own needs. The Δ coefficient (2) is defined as the sum of squares of differences in the expected value (average value on the surface) and the measured value at a given point divided by the sum of the average values:

$$\Delta = \frac{\sum_{i=1}^{n} (E_{av} - E_i)^2}{\sum_{i=1}^{n} E_{av}} \quad (2)$$

The coefficients were determined for relative values to compare all cases. Assuming the least-squares method, the value of Δ should go to zero.

IV. Results and discussions

Graphic visualization of the radiation intensity on the examined surface for different cases is presented in Fig. 2. A coloured scale indicates the value of radiation intensity at different points. The presented graphs are intended to illustrate the energy distribution on the analyzed surfaces and are the result of numerical calculations carried out in the aforementioned APEX software. Table 1 provides a summary of the results of modelling and calculations. For each case, the minimum and maximum power per illuminated surface resulting from dimming of metal-halides sources were determined. When testing solar devices in STC-like conditions, we should consider using a minimum of 16 reflectors (case 4), because for this case the power value according to modelling should reach 1000 W.

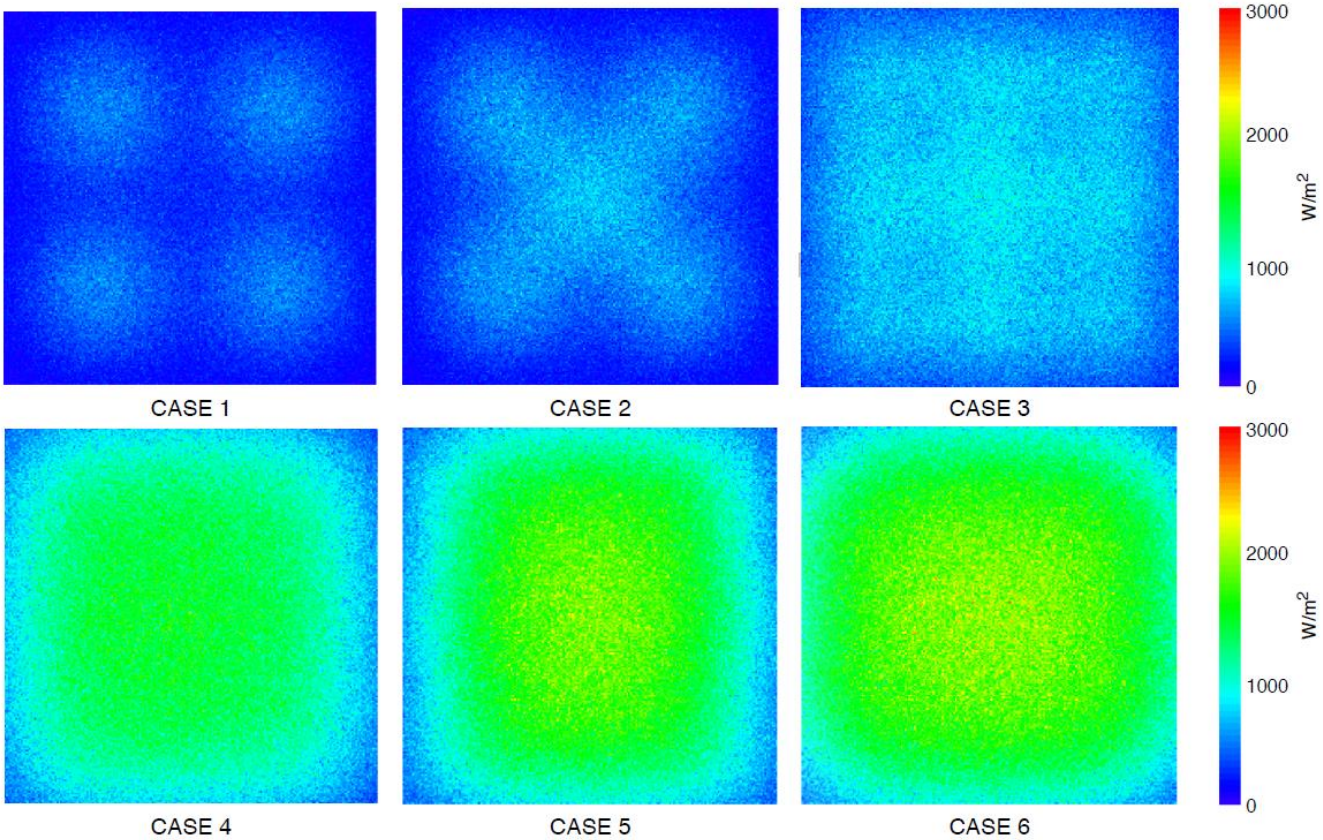

Fig. 2. Irradiance distribution on the tested surfaces

Other cases with fewer headlights have insufficient light output. To determine S_{NE} and Δ coefficients, additional measurements were made for the maximum power of light sources (each 575 W). The maximum and minimum surface intensities were determined. According to the modelling for case 1 and 2, the illuminated surface was covered with unlit fields with an intensity value of 0 W/m^2, hence the normative coefficient S_{NE} reached 100%. The value of the coefficient for the rest of the cases was about 80%, which disqualifies the simulator to determine the class according to standards.

The Δ factor takes into account all measurements made, not only the extremely measured values, and its results in the case of numerical modeling give the opportunity to unambiguously determine the quality of the simulated field. The field appears to be most homogeneous for case 6, 4 and 3. The least homogeneous field appears for case 5. Both coefficients for the reference value, i.e. natural solar radiation, should be 0.

Table 1. Summary of the results

Case	Total power on surface, W		Median value	Max irradiance, W/m²	Min irradiance, W/m²	S_{NE}, %	Δ, -
	From	To					
Case 1 / 4 Reflectors	171.70	286.12	283.46	853.17	0.00	100.00	0.189
Case 2 / 5 Reflectors	221.70	369.54	364.45	1016.99	0.00	100.00	0.227
Case 3 / 9 Reflectors	361.40	602.41	609.25	1277.50	81.90	87.95	0.077
Case 4 / 16 Reflectors	854.24	1065.20	1078.59	2115.76	205.21	82.32	0.080
Case 5 / 18 Reflectors	988.43	1232.91	1239.64	2522.63	202.46	85.14	0.115
Case 6 / 22 Reflectors	1038.13	1431.29	1463.31	2682.73	225.46	84.49	0.071
Reference Case 7 / SUN	-	-	-	-	-	0.00	0.000

Figure 3 compares the delta factor with the total price of the set of reflectors. Additionally, the unit price per 1 radiative watt is presented. In existing radiation simulators this price is about $2.38 (Boubalt et al., 2015). The price of a solar simulator depends largely on its total power. This is due to the need to use specialized power supplies and ignitor systems for arc lamps, the price of which is quite high. From the perspective of financial outlays and the value of the delta coefficient, the most favorable case 3.

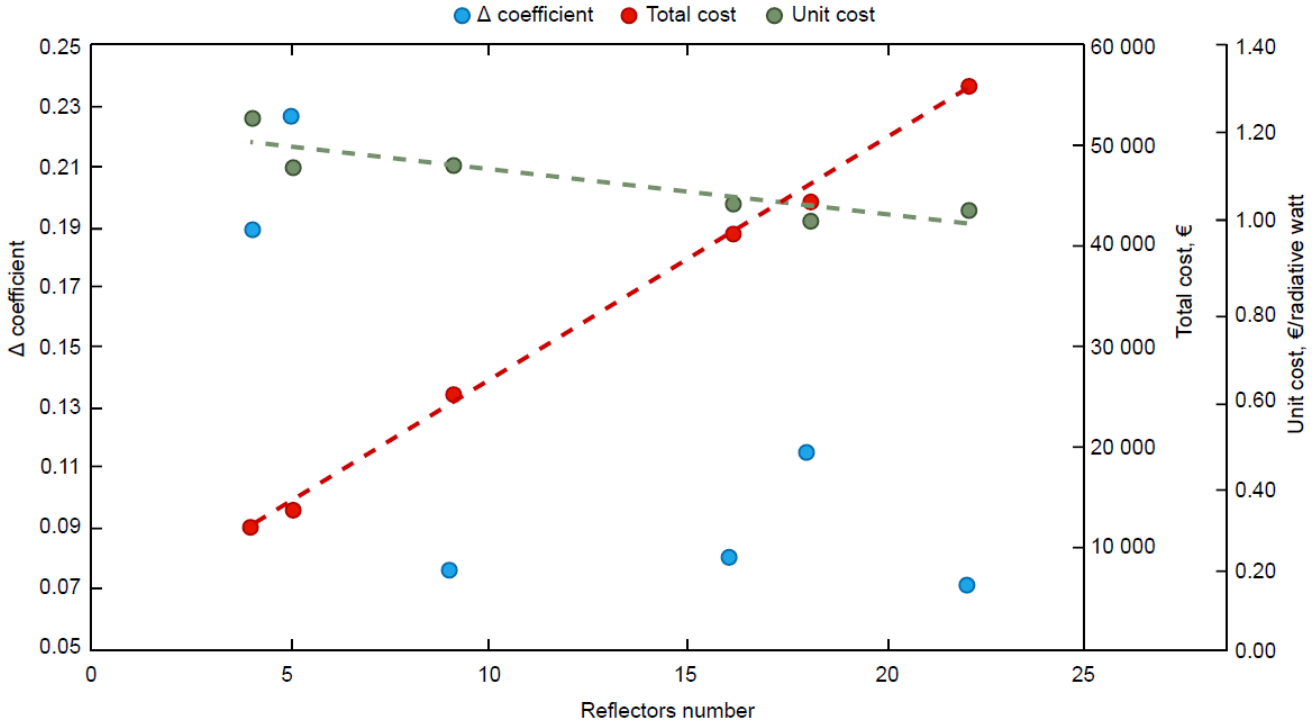

Fig. 3: Comparison of the delta coefficient with the costs of reflectors

V. Conclusions

The paper analyzes the energy distribution on the illuminated surface for simulation of solar radiation. The analyses were performed for 6 cases and referred to the reference forfeiture which is solar radiation. The results were presented using two coefficients, normative and defined for own purposes.

By comparing the two coefficients, it can be concluded that the one defined for own needs better reflects the heterogeneity of the energy field. This is because the analysis was conducted using numerical software. In real-life measurements, it is unlikely that 0 W/m^2 will be measured. In addition, the proposed factor uses all measurement

points, not just extremes, so the quality of this factor seems to be better.

Based on the coefficient Δ, it can be concluded that the best field in terms of homogeneity of energy distribution is case 22, but it requires the use of a large number of reflectors which affects the high price of the installation and a relatively large amount of power supplied. A sensible case for testing solar installations in near-natural conditions is the use of 16 reflectors, where the power on the illuminated surface is about 1000W/m^2 and can be adjusted accordingly. If we are satisfied with a lower power value, the solution may be case 9, due to the good level of heterogeneity. In the case of solar radiation concentrator tests, it is necessary to perform additional analyzes determining the angle of incidence of radiation on the surface. The angle of incidence has a significant impact on the amount of energy supplied to the absorber (e.g. pipe in PTC or photovoltaic cell with CPV) because concentrators use only direct radiation, i.e. radiation that falls at right angles to the surface of the reflector (Kalogirou, 2014)

A solar radiation simulation installation is currently under construction at the Department of Power Engineering and Turbomachinery, SUT (Bartela et al., 2019). It will allow further analysis and comparison of the results of the proposed model and obtained from laboratory measurements. In addition to the test configurations proposed above, analyzes using lenses will be carried out.

Acknowledgements

The scientific work is funded by the National Science Centre within the framework of the research project No. 2018/29/B/ST8/02406.

References

APEX 2019, Breault Research Organization, Inc http://www.breault.com/

ASTM E927-19, Standard Classification for Solar Simulators for Electrical Performance Testing of Photovoltaic Devices, ASTM International, West Conshohocken, PA, 2019, www.astm.org

Bartela Ł., Stanek B., Węcel D., Analysis of production of useful forms of Energy using a solar parabolic trough collectors. Proceedings of the 32nd International Conference on Efficiency, Cost, Optimization, Simulation and Environmental Impact of Energy Systems. Wrocław, Poland, 23-28 June 2019, 3557-3567, ISBN 978-83-61506-51-5

Boubault A., Yellowhair J., Ho C. K., Design and characterization of a 7.2 kW solar simulator. Proceedings of the ASME 2015 Power and Energy Conversion Conference Power Energy 2015 June 28 - July 2, 2015, San Diego, California Power Energy; 2015-49472

Osram. Metal Halide Lamps HMI Digital. Osram Sylvania Inc., https://www.osram.com/

IEC 60904-9 Standard:2007 Photovoltaics devices – Part 9: Solar simulator performance requirements

Li L., Wang B., Pottas J., Lipiński W., Design of a compound parabolic concentrator for a multi-source high-flux solar simulator. Solar Energy 2019;183: 805–811

Meng Q., Wang Y., Zhang L., Irradiance characteristics and optimization design of a large-scale solar simulator. Solar Energy 2011;85:1758–1767

Sabahi H., Tofigh A. A. Kakhki I. M., Bungypoor-Fard H., Design, construction and performance test of an efficient large-scale solar simulator for investigation of solar thermal collectors. Sustainable Energy Technologies and Assessments 2016;15:35–41

Soteris A. Kalogirou, Chapter 10 - Solar Thermal Power Systems, Editor(s): Soteris A. Kalogirou, Solar Energy Engineering (Second Edition), Academic Press, 2014, Pages 541-551, ISBN 9780123972705, https://doi.org/10.1016/B978-0-12-397270-5.00010-8.

EXERGY ANALYSIS OF TUNNEL FURNACE AND TUNNEL DRYER

[1]Gürhan Tahtalı, [2]Hayati Olgun, [3]Mustafa Gunes, [4]Arif Hepbasli

[1]Dev Blok Brick Factory, Ege University, Solar Energy Institute, Bornova, Izmir, 35100, Turkey
[2]Ege University, Solar Energy Institute, Bornova, Izmir, 35100, Turkey,
[3]Ege University, Solar Energy Institute, Bornova, Izmir, 35100, Turkey,
[4]Yasar University, Faculty of Engineering, Dept. of Energy Systems Engineering, Bornova, Izmir, 35100, Turkey

[1]gurhantahtali@devblok.com, [2]hayatiolgun1958@gmail.com, [3]mustafa.gunes@ege.edu.tr, [4]arif.hepbasli@yasar.edu.tr

Abstract
With an average Specific Heat Energy consumption (SEC) of 1.463 kJ/kg, 90 % of total power need of the sample brick factory is consumed at the tunnel furnace. Being the energy dense production systems, the tunnel furnace and the tunnel dryer are chosen as the control volume of the exergy analysis. This is the first time of an exergy analysis on a control volume including the tunnel furnace and the tunnel dryer. Lignite coal with an HHV of 20591 kJ/kg is used as the fuel of the control volume. The waste energy of the tunnel kiln with 116 meters in length is recovered and sent to tunnel dryer with 80 meters in length to dry the wet bricks. The real data are measured at a working brick factory with a daily production of 392 tons fired bricks with an installed heat power of 6,7MW. The production data for a whole year are used in the analysis. The flue gas composition of the coal combustion is determined by making measurements with a flue gas analyser. Differential-Thermo- Analysis (DTA) analysis is performed to understand the firing process of bricks. After making a mass balance with a deficiency of 0.05%, heat energy efficiency of the control volume is calculated as 82.56%. With the input of 372 kW electric power for running the fans in the control volume, the exergy efficiency of the control volume is found out to be 20.49%.

Keywords: "brick factory, tunnel furnace, tunnel dryer, energy analysis, energy efficiency, exergy analysis, exergy efficiency"

I. Introduction
It is found out that the 90 % of the total energy need in brick production is consumed in firing process. Tunnel furnace is reported as the most energy efficient furnace among the furnaces used in brick production (EELA, 2015). Japan International Cooperation Agency made an energy analysis on a tunnel furnace in Turkey and found its thermal efficiency as 56% (JICA, 1997). Energy analysis which incorporates first law of thermodynamics is insufficient in determining the maximum useful work regarding the environmental conditions. Exergy analysisAn nHasanuzzaman et al studied the exergy analysis of annealing furnace, Caliskan and Hepbasli worked on exergetic analysis of tube-heating furnace. The exergetic efficiencies of those furnaces were reported as 7.3% and 9.6 % respectively. Exergy analysis of a tunnel furnace has not been studied up to now. Therefore, tunnel furnace and the dryer are chosen as the control volume for the exergy analysis to make a contribution to the literature.

The furnace of the inspected brick factory is tunnel type with a length of 116 meters, a width of 4.6meters, and a height of 3 meters with a suspended ceiling of 1 meter. Its tunnel dryer is in 80 meters long, 12.4 meters wide and 4.5 meters high. The dryer has 4 input channels and 1 return channel. The dryer car operation is handled in FIFO basis. The dryer uses the waste heat recovered from the tunnel furnace which uses lignite coal as its fuel. The firing capacity determines the production capacity of the brick factory which is 392 tons fired bricks per day. 276 tons of those are dried in the tunnel dryer; the rest is dried under natural sunshine. The wet bricks are loaded onto metal dryer cars with metal palettes. The kiln cars are made of iron and the inside of the kiln cars are filled with fired bricks.

The coal is injected from the top of the furnace in 108 points. The tunnel furnace has preheating, heating and cooling zones. The air and the bricks move in reverse direction in the tunnel furnace which enables the heat transfer between the fired bricks and the air sucked from the furnace exit. The recovered heat is sent to the dryer via two isolated hot air lines. The low temperature of the flue gas at the furnace chimney enables more heat recovery. The dryer has two chimneys to exhaust the moisture in the bricks. The dryer has 96 acceleration fans for a homogenous heat distribution inside the dryer. The architecture of the control volume is shown in Fig. 1.

II. Experimental Procedure
The inputs of the control volume are determined as wet brick bodies, metal palettes on which the wet brick bodies are placed, dryer cars, dried brick bodies, kiln cars, coal fuel, and inlet am tunbient air. The outputs of the control volume are listed as dried brick bodies, metal palettes, dryer cars, kiln cars, fired bricks, ash, flue gas from the furnace chimney and air outlets from the moisture exhaust chimneys of the dryer. The dryer cars, the metal palettes are all made of iron. The chasis and the frame of the kiln cars are made of iron, the inside of the kiln cars are filled with fired bricks.

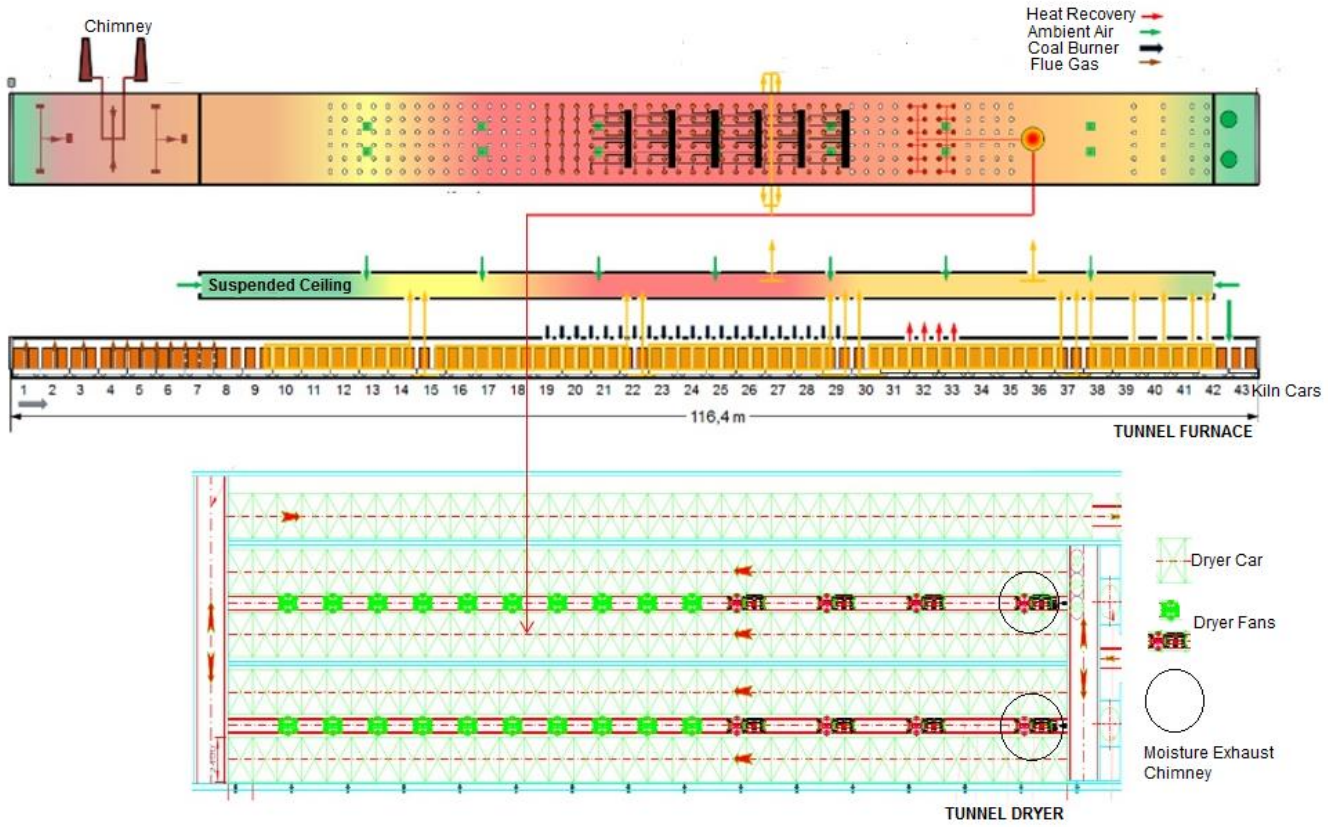

Fig. 1: Control Volume

The temperature measurements on the control volume border of the tunnel furnace and the tunnel dryer are made with K type thermocouples and Pt100 resistance type sensors. Pyrometer is used to measure the temperature of the solid inputs and outputs of the control volume. The weight of the metal palette of the dryer cars is measured with electronic precision scale. The weights of the brick at the dryer input, dryer output, furnace input and furnace output are taken from the measurements made by the factory laboratory through out the whole year. The weights of the dryer cars and kiln cars are calculated from their volume and the iron density. The temperature and flows of flue gas outlet from the furnace chimney and the air outlet from the exhaust chimneys of the tunnel dryer and their composition are measured with a flue gas analyser. The coal and the ash are sent to an acredited lab for ultimate analysis. The coal consumed daily is measured with a truck weigher. The daily production data of the brick factory are taken from the factory administration. The DTA analysis of the clay is taken to investigate the burning process. The voltages and the currents of the electric motors are measured by a multimeter. The on duty ratio of the electric motors is considered in the power calculation.

III. Analysis

The exergy balance and and exergetic efficiency of a control volume can be expressed with (1-7) and (8) (Bejan, Tsatsaronis, Moran, 1996) respectively.

$$\frac{dEx_{cv}}{dt} = \sum_j (1 - \frac{T_0}{T_j})\dot{Q}_j - \left(\dot{W}_{cv} - P_0 \frac{dV_{cv}}{dt}\right) + \sum_i \dot{m}_i e_i - \sum_e \dot{m}_e e_e - \dot{E}_D \quad (1)$$

In (1),T_0 and P_0shows the temperature and pressure of the environment which are defined 25˚C and 1,013 atm. In steady state, this expression can be written as;

$$0 = \sum_j (1 - \frac{T_0}{T_j})\dot{Q}_j - \dot{W}_{cv} + \sum_i \dot{m}_i e_i - \sum_e \dot{m}_e e_e - \dot{E}_D \quad (2)$$

In the right hand side of (2), the first four terms show the rates of exergy transfer into or out of the control volume (cv), in terms of heat, work, material input and material output, the last term indicates the rate of exergy destruction. The exergy of a material consists of physical, kinetic, potential and chemical exergy components:

$$e = e^{PH} + e^{KN} + e^{PT} + e^{CH} \quad (3)$$

$$e^{PH} = h - h_0 - T_0(s - s_0) \quad (4)$$

$$e^{KN} = \frac{1}{2}V^2 \quad (5)$$

$$e^{PT} = \frac{1}{2}gz \quad (6)$$

Where;

h, s,V and z denote the enthalpy, entropy, velocity and elevation of the material at the worked state,

h_0 and s_0 , denote the enthalpy and entropy of the material at the dead state and g is the gravitational acceleration.

In the exergy balance, kinetic and potential exergy components are ignored and just the chemical exergy of the

coal fule is taken into consideration as,

$$e^{CH}=-\Delta G \quad (7)$$

Where, ΔG denotes the formation of enthalpy.

The exergetic efficiency efficiency ε of the control volume can be expressed as the ratio of the exergy of the products and the exergy of the fuel. In this sense, the products will be the sum of exergies of the outputs and the fuel will be the sum of the exergies of the input and the work transfer into the control volume.

$$\varepsilon=\frac{\dot{E}x_p}{\dot{E}x_f}=\frac{\sum_e \dot{m}_e e_e}{\sum_i \dot{m}_i e_i+\dot{W}_{cv}} \quad (8)$$

IV. Results and Discussions

The control volume's input and output mass flows are balanced with a mass defiency of 0.05 %. The measured mass flows of the control volume are shown in Table 1.

Table1. Control Volume Mass Balance (W.V.: Water Vapour)

No	Input	Phase	kg/h	No	Output	Phase	kg/h
1	Wet Brick Clay	Solid	19536.01	1	Dry Brick Clay	Solid	19536.45
2	Wet Brick Moisture	Liquid	3704.55	2	Dry Brick Moisture	Liquid	58.79
3	Iron Palette	Solid	5264.00	3	Iron Palette	Solid	5264.00
4	Iron Dryer Car	Solid	2820.00	4	Iron Dryer Car	Solid	2820.00
5	Kiln Car Refractory	Solid	7280.00	5	Kiln Car Refractory	Solid	7280.00
6	Kiln Car Iron	Solid	8720.00	6	Kiln Car Iron	Solid	8720.00
7	Dry Brick Clay	Solid	17339.35	7	Fired Brick	Solid	16503.84
8	Dry Brick Moisture	Liquid	52.17	8	Kiln Chimney O_2	Gas	10786.97
9	Dry Air	Gas	220388.90	9	Kiln Chimney CO_2	Gas	1273.43
10	W.V.	Gas	1785.71	10	Kiln Chimney CO	Gas	36.75
11	Coal Moisture	Liquid	206.02	11	Kiln Chimney SO_2	Gas	6.43
12	Dry Coal	Solid	1074.40	12	Kiln Chimney NO	Gas	0.76
				13	Kiln Chimney N_2	Gas	38783.86
				14	Kiln Chimney Dust	Solid	1.80
				15	Kiln Chimney W.V.	Gas	1558.96
				16	Dryer Chimney1 O_2	Gas	23858.19
				17	Dryer Chimney1 CO_2	Gas	0.00
				18	Dryer Chimney1 CO	Gas	1.33
				19	Dryer Chimney1 SO_2	Gas	0.55
				20	Dryer Chimney1 NO	Gas	0.07
				21	Dryer Chimney1 N_2	Gas	78803.82
				22	Dryer Chimney1 Dust	Solid	2.34
				23	Dryer Chimney1 W.V.	Gas	2781.27
				24	Dryer Chimney2 O_2	Gas	15617.22
				25	Dryer Chimney2 CO_2	Gas	0.00
				26	Dryer Chimney2 CO	Gas	0.83
				27	Dryer Chimney2 SO_2	Gas	0.55
				28	Dryer Chimney2 NO	Gas	0.02
				29	Dryer Chimney2 N_2	Gas	51583.83
				30	Dryer Chimney2 Dust	Solid	1.31
				31	Dryer Chimney2 W.V.	Gas	2464.51
				32	Ash Moisture	Liquid	8.55
				33	Dry Ash	Solid	270.90
				34	Mass Deficiencies		143.79
	Total		288171.11		Total		288171.11

The potential and kinetic exergies for all flow are omitted. The physical exergies for all the flows are calculated. The chemical exergies of all the flows except the coal and the ash are not considered. The chemical exergy of the coal fuel is calculated according to the ultimate lab analysis of the coal but the HHV is used in the tables which is common in literature. The calculated exergies of the input and output flows are listed in Table 2 and Table 3 respectively.

Table 2.Control Volume Input Exergy Flows

No	Input	$\dot{m}$		T ˚C	C_p		$\dot{H}$ kW	$T_0\Delta\dot{s}$ kW	$\dot{E}x_i$ kW
1	Wet Brick Clay	19536.01	kg/h	19.0	0.79	kJ/kgK	1251.82	-4.79	-20.93
2	Wet Brick Moisture	3704.55	kg/h	19.0	4.19	kJ/kgK	1257.81	-6.06	-19.78
3	Palette Iron	5264.00	kg/h	19.3	0.45	kJ/kgK	192.33	-5.76	2.00
4	Dryer Car Iron	2820.00	kg/h	31.3	0.45	kJ/kgK	107.27	6.23	-4.01
5	Kiln Car Refractory	7280.00	kg/h	52.3	0.79	kJ/kgK	519.68	26.12	17.49
6	Kiln Car Iron	8720.00	kg/h	40.5	0.45	kJ/kgK	341.72	15.11	1.78
7	Dry Brick Clay	17339.35	kg/h	49.3	0.79	kJ/kgK	1226.36	23.36	69.10
8	Dry Brick Moisture	52.17	kg/h	49.3	4.19	kJ/kgK	19.55	23.36	-21.89
9	Dry Air	7599.62	kmol/h	40.0	29.14	kJ/kmolK	19251.78	14.63	907.97
10	W.V.	99.12	kmol/h	40.0	33.77	kJ/kmolK	291.00	14.63	-0.69
11	Coal Moisture	206.02	kg/h	42.0	4.19	kJ/kgK	75.46	16.53	-12.46
12	Coal Physical	1074.40	kg/h	42.0	0.25	kJ/kgK	23.50	16.53	-15.26
13	Coal Chemical	HHV			20590.93	kJ/kg			6145.24
$\dot{W}$									372.13
Total							30703.52	139.92	7420.69

Table 3.Control Volume Output Exergy Flows

No	Input	$\dot{m}$		T ˚C	C_p		$\dot{H}$ kW	$T_0\Delta\dot{s}$ kW	$\dot{E}x_i$ kW
1	Dry Brick Clay	19536.45	kg/h	51.2	0.79	kJ/kgK	1389.90	25.11	87.21
2	Dry Brick Moisture	19.74	kg/h	51.2	4.19	kJ/kgK	7.44	25.11	-24.51
3	Iron Metal Palette	5264.00	kg/h	38.7	0.45	kJ/kgK	205.10	13.39	-4.38
4	Iron Dryer Car	2820.00	kg/h	49.3	0.45	kJ/kgK	113.61	23.36	-14.79
5	Kiln Car Refractory Part	7280.00	kg/h	85	0.96	kJ/kgK	695.00	54.67	61.81
6	Kiln Car Iron Part	8720.00	kg/h	75	0.45	kJ/kgK	379.32	46.22	8.28
7	Fired Brick	16503.84	kg/h	50	0.79	kJ/kgK	1169.80	24.01	66.53
8	Kiln Chimney O_2	337.09	kmol/h	49.6	29.68	kJ/kmolK	896.68	23.64	44.74
9	Kiln Chimney CO_2	29.14	kmol/h	49.6	38.17	kJ/kmolK	99.67	23.64	-16.04
10	Kiln Chimney CO	0.13	kmol/h	49.6	28.10	kJ/kmolK	0.33	23.64	-23.61
11	Kiln Chimney SO_2	0.10	kmol/h	49.6	40.80	kJ/kmolK	0.38	23.64	-23.61
12	Kiln Chimney NO	0.02	kmol/h	49.6	29.91	kJ/kmolK	0.06	23.64	-23.63
13	Kiln Chimney N_2	1384.15	kmol/h	49.6	29.14	kJ/kmolK	3614.16	23.64	251.96
14	Kiln Chimney Dust	1.80	kg/h	49.6	0.79	kJ/kgK	0.13	23.64	-23.63
15	Kiln Chimney W.V.	86.53	kmol/h	49.6	33.84	kJ/kmolK	262.39	23.64	-3.63
16	Dryer Chimney1 O_2	745.57	kmol/h	38.6	29.11	kJ/kmolK	1878.47	13.30	68.69
17	Dryer Chimney1 CO_2	0.00	kmol/h	38.6	37.73	kJ/kmolK	0.00	13.30	-13.30
18	Dryer Chimney1 CO	0.05	kmol/h	38.6	28.09	kJ/kmolK	0.12	13.30	-13.29
19	Dryer Chimney1 SO_2	0.03	kmol/h	38.6	40.40	kJ/kmolK	0.12	13.30	-13.29
20	Dryer Chimney1 NO	0.00	kmol/h	38.6	39.44	kJ/kmolK	0.01	13.30	-13.30
21	Dryer Chimney1 N_2	2812.41	kmol/h	38.6	29.11	kJ/kmolK	7085.89	13.30	295.97
22	Dryer Chimney1 Dust	2.34	kg/h	38.6	0.79	kJ/kgK	0.16	13.30	-13.29
23	Dryer Chimney1 W.V.	154.38	kmol/h	38.6	33.76	kJ/kmolK	451.06	13.30	6.39
24	Dryer Chimney2 O_2	488.04	kmol/h	38.6	29.56	kJ/kmolK	1248.82	13.30	41.21
25	Dryer Chimney2 CO_2	0.00	kmol/h	38.6	37.73	kJ/kmolK	0.00	13.30	-13.30
26	Dryer Chimney2 CO	0.03	kmol/h	38.6	28.09	kJ/kmolK	0.07	13.30	-13.30
27	Dryer Chimney2 SO_2	0.01	kmol/h	38.6	40.40	kJ/kmolK	0.03	13.30	-13.30
28	Dryer Chimney2 NO	0.00	kmol/h	38.6	39.44	kJ/kmolK	0.00	13.30	-13.30
29	Dryer Chimney2 N_2	1840.96	kmol/h	38.6	29.11	kJ/kmolK	4638.31	13.30	189.14
30	Dryer Chimney2 Dust	1.31	kmol/h	38.6	0.79	kJ/kgK	0.09	13.30	-13.30
31	Dryer Chimney2 W.V.	136.80	kmol/h	38.6	33.76	kJ/kmolK	399.70	13.30	4.15
32	Ash Moisture	8.55	kg/h	90	4.19	kJ/kgK	3.61	58.80	-58.15
33	Dry Ash Physical	270.90	kg/h	90	0.25	kJ/kgK	6.83	58.80	-57.58
34	Ash Chemical	HHV			10649.00	kJ/kg	801.32		801.32
Total							25289.34	731.36	1520.87

V. Conclusions

The energy efficiency of the control volume is found as 82.56 %. This high rate is due to the high amount of heat recovery. High rate of oxidation in metals constitutes the price paid for this high rate of efficiency. This is due to the low flue gas temperature at the furnace chimney.

The exergy efficiency is found as 20.49%. This low value is due to the exergy losses in the burning and evoparation processes. The electrical exergy of 372kW used to transfer heat and accelerate drying, contributes to low exergy efficiency.Further research is planned for the exergoeconomic analysis of the control volume.

References

Energy Efficiency Programme in the Brick Sector in Latin American to Mitigate Climate Change – EELA, 2015, Manual Energy Efficiency in the Brick Industry

Japan International Cooperation Agency (JICA), 1997, the Study on Rational Use of Energy in Industry in the Republic of Turkey, Main Report for Dev Blok.

Caliskan, H., Hepbasli, A., 2010, Exergetic Analysis and Assessment of Industrial Furnaces, Journal of Energy Resources Technology, vol.132.

Hasanuzzaman, M.,Saidur, R., Rahim, N. A.,2011, Energy, Exergy and Econmic Analysis of an Annealing Furnace, International Journal of the Physical Sciences Vol. 6(6), pp. 1257-1266.

Bejan, A., Moran, M., Tsatsaronis, G., 1996. Thermal Design and Optimization.John Wiley & Sons, Inc, NJ.

Bejan, A., 2006, Advanced Engineering Thermodynamics, John Wiley & Sons

Kotas, T. J., 1985.The Exergy Method of Thermal Plant Analysis, Butterworths, 1985.

Çengel, Y. A., and Boles, M. A., 2006. Thermodynamics: An Engineering Approach, McGraw-Hill.

Rosen, M.A., 2002. Exergy and Economics: Is Exergy Profitable, Exergy-An International Journal, 1-3pp.

Midilli, A., 2014. Chemical Exergy Calculations: Examples, Summer Course on Exergy and Its Applications

Morosuk, T., Tsatsaronis, G. and Koroneos, C., 2016, Environmental İmpact Reduction Using Exergy-Based Methods, Journal of Cleaner Production, 118:118-123pp.

Hepbasli, A. and Kecebasi, A., 2013, A Comparative Study On Conventional And Advanced Exergetic Analyses Of Geothermal District Heating Systems Based On Actual Operational Data, Energy and Buildings, 61:193–201pp

Rosen, M.A. and Dıncer, I., 2003, Exergoeconomic Analysis of Power Plants Operating on Various Fuels, Applied Thermal Engineering, 23:643-658pp.

Atul, T. B., Dandge, S. S., Energy and Exergy Analysis of Boiler in 6MW Cogeneration Coal Power Plant, Int. Journal for Research neering Technology, Vol 5: 680-691pp.

Kaya, S., Kucukada, K. and Mancuhan, E., 2008, Model-Based Optimization Of Heat Recovery İn The Cooling Zone Of A Tunnel Kiln, Applied Thermal Engineering 28: 633–641pp.

Kaya, S., Mançuhan, E. and Küçükada, K., 2009, Modelling And Optimization Of The Firing Zone Of A Tunnel Kiln To Predict The Optimal Feed Locations And Mass Fluxes Of The Fuel And Secondary Air, Applied Energy, 86:325–332pp.

Oba, R., Possamai, T.S. and Nicolau, V.P., 2014, Thermal Analysis Of A Tunnel Kiln Used To Produce Roof Tiles, Applied Thermal Engineering, 63:59–65pp.

ENHANCEMENTS IN COAL BURNING IN A TUNNEL FURNACE

[1]Gürhan Tahtalı, [2]Hayati Olgun

[1]Dev Blok Brick Factory, Ege University, Solar Energy Institute, Bornova, Izmir, 35100, Turkey
[2]Ege University, Solar Energy Institute, Bornova, Izmir, 35100, Turkey,

[1]gurhantahtali@devblok.com, [2]hayatiolgun1958@gmail.com

Abstract
It is always hard to burn coal. Since climate change is an energy problem and burning fossil fuels to produce electricity or heat is responsible for roughly half of global warming pollution, it becomes a challenge to burn the coal efficiently. In this research; the effects of particle size distribution, coal humidity, coal crusher system and excess air are investigated in terms of burning efficiency and cost saving. It is found out that the amount of unburnt coal is directly proportional with the coal particle size. Particle size reduction is related with the performance of the coal crusher. It is experienced that the more the coal is crushed, the faster the hammers of the crusher wear. The compromise in increasing wear and labour is exceeded by increasing the surface hardness of the hammers. The return on investment (ROI) of a energy efficient coal crusher system is found out to be 6.7 months. The grain size distribution was found to be the most effective energy efficiency factor in coal combustion. The burning efficiency is inversely proportional with the grain size distribution of coal. It was experienced that by increasing the coal crushing performance, heat losses were decreased by 17 %.

Keywords: "coal burning, tunnel furnace, coal crusher, coal humidity, excess air, return on investment, energy efficiency"

I.Introduction

It is projected that total world energy consumption will increase by 36% between 2015 and 2035, and coal will account for 34.4% of the expected increase (Speight,2005). Low specific energy consumption will lead to low energy related emissions. This phoneme is consistent with the Bridge scenario proposed by International Energy Agency which plans to increase energy efficiency in the industry (IEA, 2015). Considering the high firing temperature which is around 900˚C and the mass production, furnace uses 90 % of total energy need of a brick factory. Being the energy dense production systems, the furnace in a brick factory should be the first item to be focused on in terms of energy efficiency and environmental emissions.

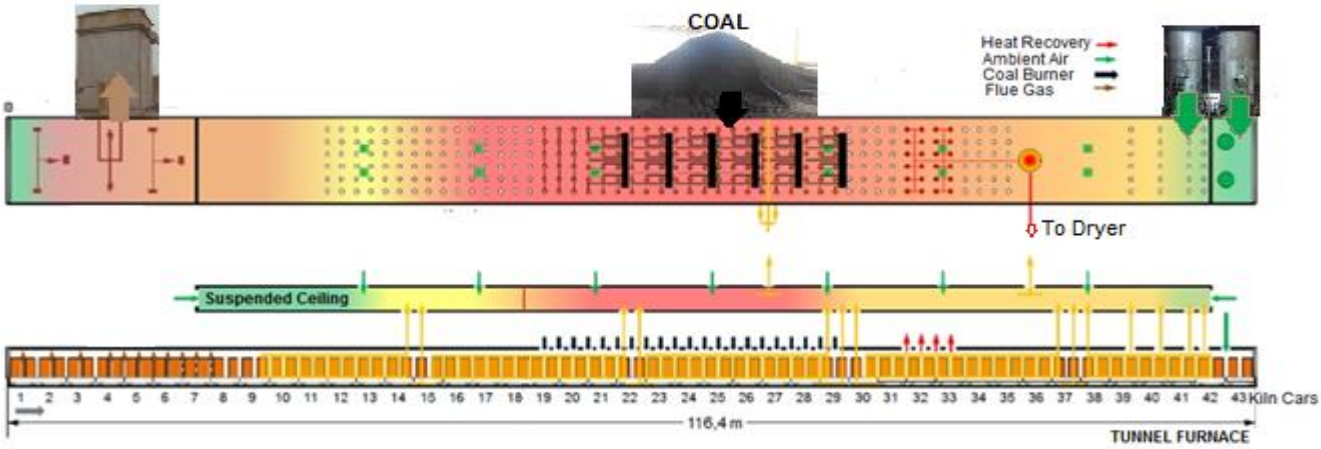

Fig1. Tunnel Furnace Structure

Tunnel furnace is an energy efficient way of burning in brick industry (Oral and Mistikoglu, 2007). Tunnel furnace ranks better in terms of environmental parameters and quality of bricks produced (Rajarathnam et. al. 2014) .In a tunnel furnace, the products to be fired are moved through the pre-heating, firing and cooling zones by the kiln cars. The firing air enters from the exit so that the firing air is heated by meeting the hot bricks on the kiln cars on the way to the firing zones. The fuel is injected in the firing zone from the fuel burners. The heat recovered from the end of the fire zone is sent to the dryer for efficient use of waste energy. Such a tunnel furnace is shown in Figure 1. When

coal is mixed with the clay as admixed coal (AC) in brick production to lower the coal consumption, the calorific value is found to be critical factor in fuel optimization (Kaya et. al.2009) .High calorific value AC should be preferred to decrease the atmospheric emissions, to satisfy uniform firing of the bricks and to decrease slightly fuel cost (Mancuhan and Kucukada, 2006). The specific energy consumption (SEC) for brick production is reported to be between 1427 kJ and 1766 kJ (EELA 2015). It is known that the size distribution of coal, the moisture of coal, excess air amount affect the combustion performance (Smoot, L.D., Smith, P.J. Plenum 1985). In this research paper, the effect of those in terms of heat losses and SEC are investigated experimentally.

II. Experimental Procedure

The coal was carried to the crusher by trucks after weighed by the truck weight scale. The quantity of consumed coal was calculated when the coal stack has finished. The coal samples were taken from the top of the tunnel furnace just before the coal entered the burners. Samples were mixed before analyzed. The moisture of the coal samples was measured via electronic moisture analyzer. The grain size analysis of coal samples were obtained by sieveing. The ash samples were collected from the top surface of the kiln cars. The coal and the ash samples were sent to the external accredited laboratory for ultimate analysis. The flue gas was measured by flue gas analyzer.

III. Analysis

The control volume was selected as the tunnel furnace. The heat losses related with coal were calculated by indirect method of energy analysis. In this method, the efficiency is the difference between the losses and the energy input. When the related amount of heat loss is divided into the energy input, the percentage of the loss under consideration is calculated. The heat losses due to: dry flue gas, H_2 Content of Coal, Moisture of Coal, CO in Flue Gas and ash can be calculated (Bathe and Dandge, 2017) as follows,

a) Heat Loss Due To Dry Flue Gas (L_1)

$$L_1 = \frac{m x C_p x (T_f - T_a)}{H_{HHV,c}} \quad (1)$$

Where,
m= Actual dry air mass for the combustion of 1 kg coal in kg.

C_p= Specific heat coefficient of flue gas in kJ/kg˚C.
T_f=Flue gas temperature in ˚C.
T_a=Ambient temperature in ˚C.
$H_{HHV,c}$=Higher heating value of coal in kJ/kg.

$$EA = \frac{O_2\%}{21 - O_2\%} \quad (2)$$

Where,
EA=Excess air ratio
Actual air supply per kg coal can be expressed as;

$$AAS = \left(1 + \frac{EA}{100}\right) \times TAS \quad \text{kg / kg coal} \quad (3)$$

Where,
AAS= Actual air supply in kg /kg coal
EA=Excess air ratio
TAS= Theorical air supply in kg / kg coal
TAS can be expressed as;

$$TAS = \frac{1}{23}\left[2{,}67C + 8\left(H_2 - \frac{O_2}{8}\right) + S\right] \text{ kg/kg coal} \quad (4)$$

Where,
C,H_2, O_2 and S are carbon, hydrogen, oxygen and sulfur content of coal as stated in the ultimate analysis of coal.

b) Heat Loss Due to H_2 Content of Coal (L_2)

$$L_2 = \frac{9 x m_{H_2} x (2250 + C_p(T_f - T_a)] x 100}{H_{HHV,c}} \quad (5)$$

Where,
m_{H_2}=H_2 present in 1 kg of coal in kg,
2250= Latent heat value of water in kJ/kg,
C_p=Specific heat coeeficient of water vapour in kJ/kg ˚C,
T_f= Temperature of flue gas in ˚C,
T_a=Ambient temperature in ˚C,
$H_{HHV,c}$=Higher heating value of coal in kJ/kg.

c) Heat Loss Due to Moisture of Coal (L_3)

$$L_3 = \frac{m_{H_2O} x [2250 + C_p(T_f - T_a) x 100}{H_{HHV.c}} \quad (6)$$

Where,
m_{H_2O}= Moisture of 1 kg coal in kg,
2250= Latent heat value of water in kJ/kg,
C_p=Specific heat coeeficient of water vapour in kJ/kg ˚C,
T_f= Temperature of flue gas in ˚C,
T_a=Ambient temperature in ˚C,
$H_{HHV,c}$=Higher heating value of coal in kJ/kg.

d) Heat Loss Due to the CO in Flue Gas (L_4)

For complete combustion and incomplete combustion, the energy released per kg Carbon can be expressed by (7) and (8) respectively.

$C+O_2 \rightarrow CO_2$ + 33.823,456 kJ/ (kg Carbon) (7)

$2C+O_2 \rightarrow 2CO$ + 10.167,12 kJ/ (kg Carbon) (8)

Since heat loss for each kg CO measured will be 23656,336 kJ / (kg Carbon), then heat loss due to the CO in flue gas can be calculated as;

$$L_3 = \frac{\dot{m}_{CO} x E_{l,CO}}{\dot{m}_c x H_{HHV.c}} \quad (9)$$

Where,
$\dot{m}_{CO}$= CO mass flow measured in flue gas in kg/h,
$E_{l,CO}$=Heat loss per kg CO in kJ/kg,
$\dot{m}_c$= Coal consumed in the control volume in kg/h,
$H_{HHV.c}$= Higher heating value of coal in kJ/kg.

e) Heat Loss Due to the Ash (L_5)

$$L_5 = \dot{m}_a x ((C_{p,s} x T_a) + H_{HHV,a}) \quad (10)$$

Where,
$\dot{m}_a$=Mass flow of ash in kg/h,
$C_{p,s}$=Specific heat coefficient of ash in kJ/kg ˚C (for sensible heat calculation),
T_a= Ambient temperature in ˚C,
$H_{HHV,a}$= Higher heating value of ash.

IV. Results and Discussions

Two flue gas measurements taken were compared in terms of heat losses related with coal combustion. After the first measurement, the coal crusher was replaced. The moisture of the coal, the grain size distribution of coal and the coal consumption was measured. The ultimate analysis for coal, ultimate analysis for ash was performed at an external laboratory for the two flue gas measurement occasions. The measured values and the heat loss percentages are shown in Table 1.

Table1. Measured Values and Heat Losses For Measurement No I And II

Measurements	I		II	
Feature	Measured	Heat Loss (%)	Measured	Heat Loss (%)
O_2 In Flue Gas (% v/v)	19.04	0.91	19.79	0.92
CO In Flue Gas (kg/h)	3.677	0.32	2.321	0.24
Moisture in Coal (%)	18.68	2.15	16.09	1.80
H_2 In Coal (%)	2.40	2.48	2.40	2.40
Ash Output (kg/h)	512	28.75	283	12.69
Coal Consumption (kg/h)	1379		1121	
HHV of Coal (kJ/kg)	19920		20581	
HHV of Ash (kJ/kg)	15405		10318	
SEC (kj/kg Fired Brick)	1624		1389	
Total		34.61		18.05

The highest difference in heat losses was seen in the heat loss due to ash. This difference was caused by the unburnt coal in the ash. Unburnt coal is directly proportional with the grain size of the coal. The grain size distributions of coal for measurements I and II where old coal crusher and new coal crusher was used respectively are shown in Fig2. Similarly, the grain size distributions of ash for measurement I and II are shown in Fig3.

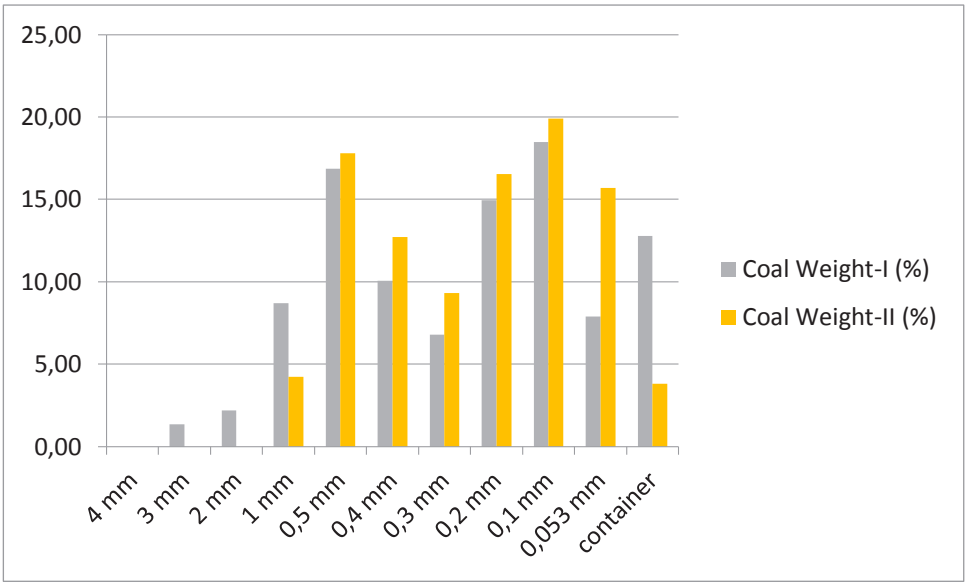

Fig2. Grain Size Distributions of Coal for Measurement I and II

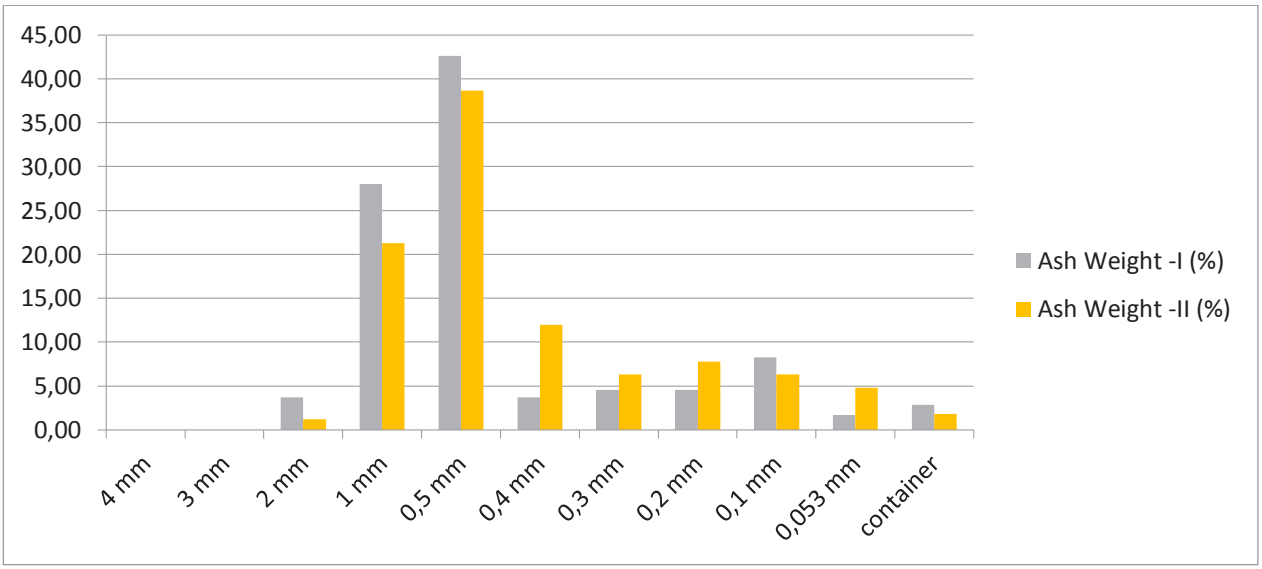

Fig3. Grain Size Distributions of Ash for Measurement I and II

V. Conclusions

The result of the enhancements in excess air, coal moisture and coal grain size evaluated by two performance measurements. When the heat losses related with the coal combustion were evaluated, the heat loss due to the dry flue gas was the lowest. Although the excess air ration measured at the chimney was high, it did not yield much heat loss since the flue gas temperature was low (around 50 ˚C). The increase in the moisture of coal increased the heat loss more than calculated in practice, since it was one of the sources of unburnt coal. It was found out that the highest heat loss was due to the ash with a significant calorific value. The replacement of the coal crusher system with a new one, increased the coal crushing performance by enabling better combustion of lower grain sized coalThe specific energy consumption (SEC) was decreased from 1624 kJ/ kg fired brick to 1389 kJ / kg fired brick which is below than the reported SEC values. The SEC value can even be decreased more by recycling the ash into the production as an admixed coal. The return of investment for the new coal crusher system was found to be 6.7 months. This short return time is due to the combustion enhancement with smaller grain sized coal and less electric power consumption.On the other side, the wearing of the hammers was faster in the new coal crusher. The service requirement period was optimized by increasing the surface hardness of the hammers to 41 HRC. Carbon emission trading schemes and carbon taxation schemes are the main approaches adopted by countries and regions to seek to achieve their emission reduction goals (Huisingh, et. al., 2015). These approaches will speed up the enhancements in coal combustion.

References

Smoot, L. D., Smith, P. J., 1985 . Coal Combustion and Gasification. Plenum Press, NY.

Speight, J. G.,2005 . Handbook of Coal Analysis, Wiley, NJ.

International Energy Agency, IEA, World Energy Outlook Special Report.,2015, Paris, www.iea.org

Oral, E. L., Mistikoglu, G., 2007. Competitive Analysis of the Turkish Brick Industry—a Case Study for Developing Countries, Building and Environment 42, 416-423

Rajarathnam, U., Athalye, V., Ragavan, S., Maithel, S., Lalchandani, D., Kumar, S., Baum,E., Weyant, C., Bond, T., 2014 Assessment of Air Pollutant Emissions from Brick Kilns. Atmospheric Environment 98 549-553.

Kaya, S., Mancuhan, E., Kucukada, K., 2009. Modelling and Optimization of the Firing Zone of a Tunnel Kiln to Predict the Optimal Feed Locations and Mass Fluxes of the Fuel and Secondary air. Applied Energy 86 325–332.

Mancuhan, E.,Kucukada, K.,2006. Optimization of Fuel and Air Use in a Tunnel Kiln to Produce Coal Admixed Bricks. Applied Thermal Engineering 26 , 1556–1563.

Huisingh, D., Zhang, Z., Moore J. C., Qiao, Q., Li, Q., 2015. Recent Advances in Carbon Emissions Reduction: Policies, Technologies, Monitoring, Assessment and Modeling. Journal of Cleaner Production 103 1-12.

Bathe, A., Dandge, S. S., 2017. Energy and Exergy Analysis of Boiler in 6MW Cogeneration Coal Power Plant. Int. J. for Research in Appl. Science & Eng. Tech. (IJRASET). ISSN:2321-9653. Vol.5

Energy Efficiency Programme in the Brick Sector in Latin American to Mitigate Climate Change – EELA, 2015. Manual, Energy Efficiency in the Brick Industry.

Miller, B. G.,2005 . Coal Energy Systems, Elsevier, MA.

Gomes, E., Ijaz, H., 2003. Transition from Traditional Brick Manufacturing to More Sustainable Practices, Energy for Sustainable Development, Vol. VII, No2.

Campell, R. J., 2013. Increasing the Efficiency of Existing Coal-Fired Power Plants. Congressional Research Service, www.crs.gov.

Effects of microstructure shape parameters on water removal in a PEMFC lotus-like flow channel

[1*]Xuan Xie, [1*]Bifeng Yin, [1*]Sheng Xu, [1]Hekun Jia, [1]Fei Dong, [1]Xin Chen,
[1] Jiangsu University, School of Automotive and Traffic Engineering, Department of Power Engineering and Engineering Thermal physics, 301 Xuefu Road, Zhenjiang, 212013, China

* E-mails: xiexuanujs@163.com
ybf@ujs.edu.cn
xushengujs@126.com

Abstract
Water removal in proton exchange membrane fuel cell (PEMFC) can prevent the water flooding and reduce the wall corrosion, hence improving the PEMFC performance. In this study, the chief object is to improve the anti-corrosion and drag reduction performances of the flow channel wall. The predicted water behavior in a PEMFC lotus-like flow channel was investigated. The influence of the microstructure shape parameters (height, radius and spacing) were studied. The investigation carried out has revealed the lotus-like flow channel can not only effectively accelerate the velovity of the water droplet on the wall surface of the flow channel, but also speed up their transport because the air exists at the bottom of the flow channel. As the height increases, the water is removed effectively. However, excessive microstructure height contributes to the water accumulation at the bottom of the microstructure. The pressure drop of the lotus-like flow channel is higher than that of the conventional straight flow channel, which leads to a higher requirement for the air compressor. In addition, the pressure drop shows an upward trend as the height increases. As the radius increases, the velocity of the water transport increases slowly. The variation of the radius brings out a bulge in the front of the water droplet. The spacing has an obvious influence on the water accumulation while it has an inapparent effect on the water removal and the water transport. The lotus-like flow channel has good anti-corrosion and drag reduction performances with the microstructure height of 50μm, the radium of 50μm and the spacing of 200μm.

Keywords: Proton exchange membrane fuel cell, water management, water removal, lotus-like flow channel, anti-corrosion performance, drag reduction performance, pressure drop

I. Introduction

Bipolar plate in PEMFC has the functions of separating oxygen and hydrogen, collecting and conducting current and removing the water. However, the flow channel on the bipolar plate is relatively narrow. The water is removed tough in the flow channel, leading to the water flooding. Meanwhile, the water on the surface can corrode the bipolar plate (Liu, H.C., 2018). Therefore, water management is is critical to PEMFC.

At present, many researches have been carried out on water behavior in the flow channel. Liu et al. (Liu, H.C., 2005) and Soong et al. (Soong, C.Y., 2005) inserted a baffle in the flow channel to improve the mass transfer in a PEMFC. M. Andersson (Andersson, M., 2018) studied the water behavior in the flow channel, and verified it by the results of synchrotron radiation x-ray imaging and tomography. Qin et al. (Qin, Y., 2018) studied water behavior in the flow channel having a hydrophilic needle. Yan et al. (Yan, X., 2019) proposed and developed two flow fields with three-dimensional channel geometry. It has been revealed that the waved flow channel with gradient channel depth can increase flow velocity accommodating the uneven distribution of oxygen concentration.

In previous studies, it has been found that three-dimensional flow channel can greatly enhance oxygen supply and remove water from the flow channel. However, the two-phase flow behavior of three-dimensional flow channel needs to be further studied. In addition, the influence of the microstructure on water behavior needs to be further studied. In this study, a lotus-like flow channel was designed with purpose of improving the anti-corrosion and drag reduction performance of the flow channel. The numerical investigation was carried out via VOF method. The effects of the microstructure shape parameters (height, radius and spacing) on the water removal were investigated.

II. Model Formulation

1. Computation domain and assumptions

The computation domain is a lotus-like flow channel with the length of 4mm, width of 0.7874mm and depth of 1mm. The lotus-like microstructures are distributed on the surface of the topwall, as shown in Fig. 1. The diameter and height of the microstructure are d and h respectively. The spacing between the microstructures is S, as shown in Fig. 2.

The laminar and incompressible flow is assumed. The velocity of the gas inlet is constant. The comstant temperature of the gas is assumed. The phase change of water is ignored. The surface tension coefficient between air and water is constant. The dynamic wettability effect and the gravity is neglected.

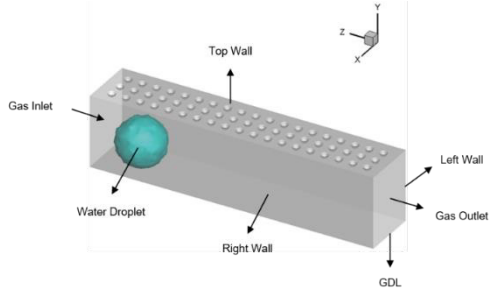

Fig. 1: Schemetic of the lotus-like flow channel

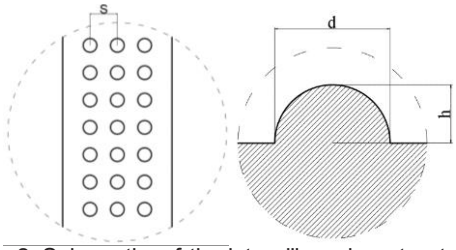

Fig. 2: Schemetic of the lotus-like microstructures

2. Numerical method

The 3D numerical model was set up combining with the interface reconstruction algorithm method. VOF method can predict water behavior and capture the surface tension effects.

3. Boundary and initial conditions

The uniform velocity was assigned to 10m/s at the gas inlet. A constant pressure at the gas out was fixed at 0.1MPa. The surfaces of the flow channel and GDL were non-slip. The static contact angles of the flow channel surface and GDL surface were 45° and 153° respectively. The surface tension coefficient of water-air interface was 0.07191N/m. A water droplet with a diameter of 0.6 mm was initially introduced on the GDL surface of the flow channel at a distance of 0.4mm from the gas inlet.

4. Discrete method

The pressure-based solver was used to solve the unsteady governing equations, and the VOF method based on an explicit scheme was selected for multiphase simulation. The time step in the simulation was 10^{-5}s. The meshes in the model were tetrahedral meshes. The number of the meshes are 0.6 million.

5. Numerical scheme

The simulation scheme was carried out as shown in Table 1.

Table 1. Simulation scheme

Cases	d(μm)	h(μm)	S(μm)
1	-	-	-
2	*100*	*25*	*200*
3	*100*	*50*	*200*
4	*100*	*75*	*200*
5	*50*	*50*	*200*
6	*100*	*50*	*200*
7	*150*	*50*	*200*
8	*100*	*50*	*150*
9	*100*	*50*	*200*
10	*100*	*50*	*250*

III. Results and discussions

1. Model vertification

Fig.3 shows the comparisons of the pressure drop obtained from the present study and the past study (Qin, Y., 2018). As shown in this figure, there is a good agreement for pressure drop.

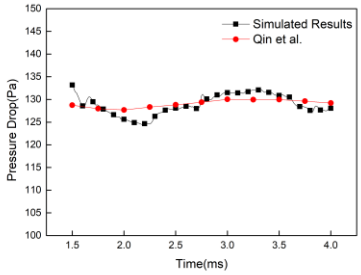

Fig. 3: Comparisons of the pressure drop obtained from the present study and literature

2. Effect of the microstructure height

The microstructure height investigated includes the conventional straight flow channel and the microstructure height of 25μm, 50μm and 75μm, respectively. It can be seen from Fig. 4(a) that the lotus-like flow channel can accelerate the velovity of the water droplet on the wall surface of the flow channel due to the existence of air at the bottom of the microstructure. With the increase of the height, the water is removed more effectively. However, excessive height contributes to the water accumulation. When the height is 50μm, the water is removed effectively. It can be seen from Fig. 4(b) that the pressure drop of the lotus-like flow channel is higher than that of the conventional straight flow channel. When the microstructure height varies from 25μm to 75μm, the pressure drop increases.

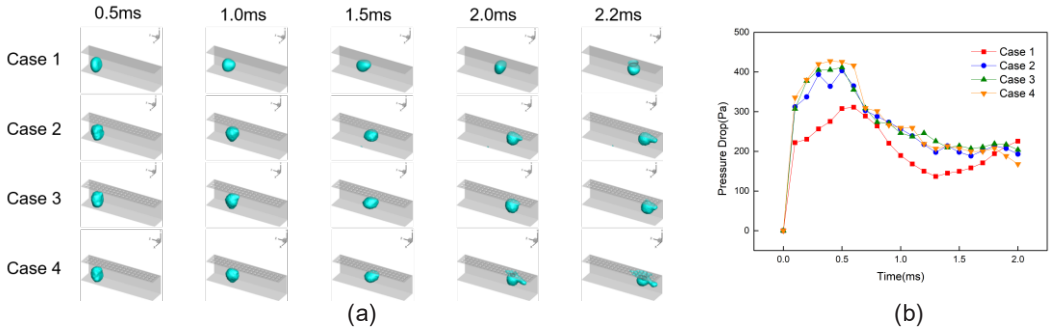

(a) (b)

Fig. 4: Comparisons of (a) the predicted behavior of water droplets and (b) the pressure drop in case 1～case 4

3. Effect of the microstructure radius

The microstructure radius investigated includes the conventional straight flow channel and the microstructure radius of 25μm, 50μm and 75μm, respectively. It can be seen from Fig. 5(a) that the decrease of the radius brings out a bulge in the front of the water droplet. Too small radius contributes to the water accumulation. When the radius is 50μm, the water is removed effectively. It can be seen from Fig. 5(b) that the mocrostructure radius has an inapparent influence on the pressure drop.

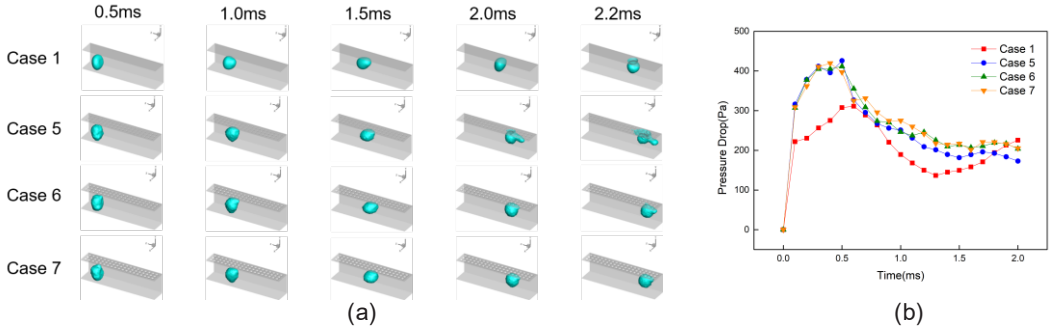

(a) (b)

Fig. 5: Comparisons of (a) the predicted behavior of water droplets and (b) the pressure drop in case 1 and case 5～case 7

4. Effect of the microstructure spacing

The microstructure spacing investigated includes the conventional straight flow channel and the microstructure spacing of 150μm, 200μm and 250μm, respectively. It can be seen from Fig. 6(a) that the variation of the spacing brings out a bulge in the front of the water droplet. When the spacing is 200μm, the water is removed effectively. It can be seen from Fig. 6(b) that the mocrostructure spacing has an inapparent influence on the pressure drop.

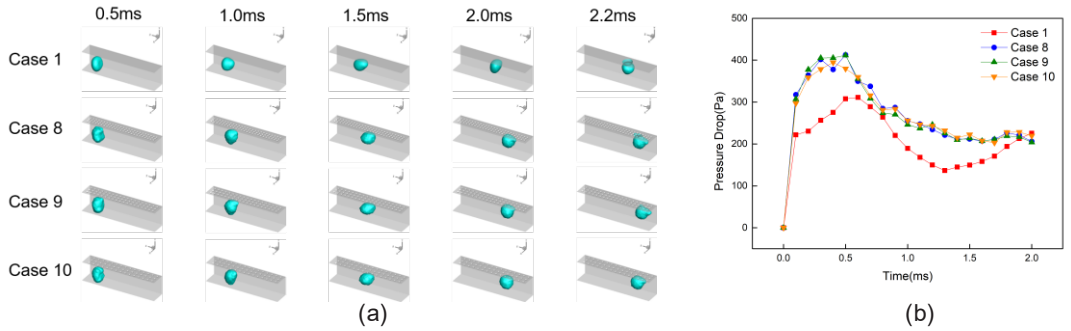

(a) (b)

Fig. 6: Comparisons of (a) the predicted behavior of water droplets and (b) the pressure drop in case 1 and case 8～case 10

IV. Conclusions

In this paper, a three dimentional numerical simulation of water behavior in the lotus-like flow channel was carried out. The influence of the microstructure shape parametres (height, radius and spacing) was carried out. Salient conclusions arising from this study are summarized below:

(1) The lotus-like flow channel can accelerate the water removal and water transport due to the existence of the water at the bottom of the mocrostructire.

(2) With the increase of the mocrostructure height, the velocity of water removal and pressure drop increase. However, excessive microstructure height contributes to the water accumulation at the bottom of the flow channel.

(3) The decrease of the radius brings out a bulge in the front of the water droplet. In addition, too small radius can result in the water accumulation. Inapparent impacts of scanning speed on the water removal are observed.

(4) The variation of the spacing brings out a bulge in the front of the water droplet. It has a subtle influence on pressure drop. The lotus-like flow channel has excellent anti-corrosion and drag reduction performances with the microstructure height of 50μm, the radium of 50μm and the spacing of 200μm.

Acknowledgements

This research was supported by Key Research and Development Project of Jiangsu Province (grant BE2019006).

References

Liu, H.C., Yang, W.M., Tan, J., Cheng, L.S., 2018. A Fin-shaped Flow Channel Enhances Water Removal Performance in a Proton Exchange Membrane Fuel Cell. Fuel Cells 19, 51–59. https://doi.org/10.1002/fuce.201800079

Liu, H.C., Yan, W.M., Soong, C.Y., Chen, F., 2005. Effects of baffle-blocked flow channel on reactant transport and cell performance of a proton exchange membrane fuel cell. J. Power Sources 142, 125–133. https://doi.org/10.1016/j.jpowsour.2004.09.037

Soong, C.Y., Yan, W.M., Tseng, C.Y., Liu, H.C., Chen, F., Chu, H.S., 2005. Analysis of reactant gas transport in a PEM fuel cell with partially blocked fuel flow channels 143, 36–47. https://doi.org/10.1016/j.jpowsour.2004.11.055

Andersson, M., Mularczyk, A., Lamibrac, A., Beale, S.B., Eller, J., Lehnert, W., Büchi, F.N., 2018. Modeling and synchrotron imaging of droplet detachment in gas channels of polymer electrolyte fuel cells. J. Power Sources 404, 159–171. https://doi.org/10.1016/j.jpowsour.2018.10.021

Qin, Y., Yin, Y., Jiao, K., Du, Q., 2018. Effects of needle orientation and gas velocity on water transport and removal in a modified PEMFC gas flow channel having a hydrophilic needle. Int. J. Energy Research 43, 2538–2549. https://doi.org/10.1002/er.4116

Yan, X., Guan, C., Zhang, Y., Jiang, K., Wei, G., Cheng, X., 2019. Flow field design with 3D geometry for proton exchange membrane fuel cells. Appl. Therm. Eng. 147, 1107–1114. https://doi.org/10.1016/j.applthermaleng.2018.09.110

Qin, Y., Li, X., Yin, Y, 2018. Modeling of liquid water transport in a proton exchange membrane fuel cell gas flow channel with dynamic wettability. Int. J. Energy Research 42, 3315–3327. https://doi.org/10.1002/er.4084

Chen, R., Qin, Y., Ma, S., Du, Q., 2019. Numerical simulation of liquid water emerging and transport in the flow channel of PEMFC using the volume of fluid method. Int. J. Hydrogen Energy. https://doi.org/10.1016/j.ijhydene.2019.07.169

Ferreira, R.B., Falcão, D.S., Oliveira, V.B., Pinto, A.M.F.R., 2017. 1D + 3D two-phase flow numerical model of a proton exchange membrane fuel cell. Appl. Energy 203, 474–495. https://doi.org/10.1016/j.apenergy.2017.06.048

Niu, Z., Jiao, K., Zhang, F., Du, Q., Yin, Y., 2015. Direct numerical simulation of two-phase turbulent flow in fuel cell flow channel. Int. J. Hydrogen Energy 41,3147–3152. https://doi.org/10.1016/j.ijhydene.2015.11.026

Parametric study and ANN modeling of Liquid feed Direct Ethanol Fuel cells

[1*]Vineesh Ravi , [1]Caraline Ann Jacob, [1]Sreeja P, [1]Yohans Varghese
[1] Department of chemical engineering, National Institute of Technology, Calicut
* E-mails: vineeshravi@nitc.ac.in

Abstract
Direct ethanol fuel cells (DEFCs) have emerged as an attractive solution to the present-day energy crisis. As a fuel, ethanol shows great promise in the field of Alcohol Fuel Cells. In this research endeavor, the experimentation of a liquid fed ethanol fuel cell was carried out to study the effect of various parameters on the performance of the fuel cell. The effect of operating parameters such as cell temperature, ethanol concentration, anode and cathode flow rate, humidity were studied. An artificial neural network (ANN) was also employed to model the performance of the DEFC. The model employed a feedforward topology with backpropagation. The neural network was trained using the experimental results obtained. The model is able to sufficiently predict the performance of the DEFC and the predicted target values are in good agreement with the experimental output values. The regression coefficient value was 0.992. The maximum performance was obtained at a cell temperature of 80ºC. The optimum power density was obtained at a concentration of 2M beyond which ethanol crossover decreases the cell performance. Anode and cathode optimum flow rates were obtained as 1.5ml/min and 2000ml/min, respectively.

Keywords: Artificial Neural Network, Current Density, Direct Ethanol Fuel Cell, Modeling, Power Density, Voltage.

I. Introduction
Since time immemorial, energy has been a fundamental prerequisite for sustenance. It is considered as an inevitable part of our daily needs and applications. Presently, the earth is fueled by polluting and non-renewable sources of energy, namely coal and oil. According to the United States Environmental Protection Agency, the total emission in the country in the past year was 6,587 Million Metric Tons of CO_2 equivalent. Of this, electricity production contributes to about 29% of the total amount. Fuel cells provide a simple solution to this conundrum. They are emission-free and more efficient than fossil fuel sources and have the capability to guarantee sustainability. Many types of fuels are being developed according to their applications. For many of these applications, hydrogen appears to be the most appropriate fuel. However, it has to be produced from different sources such as water, fossil fuels, etc. Furthermore, the production of hydrogen, its storage and distribution pose difficulties that outweigh the advantages (Barbaro, 2009). Alcohols, due to their many advantages, can be used as energy-efficient fuels. Storage and distribution of alcohols are easier to manage than that of hydrogen. Alcohols have a better octane rating that makes them better candidates for use in IC engines. Some of the fuels commonly used are methanol, ethanol and ethylene glycol (M. Z. F. Kamarudin,2013). Ethanol is a desirable fuel, as it can be abundantly produced by the fermentation of raw materials from agriculture or from different wastes. For portable electronics, ethanol can be used as a substitute for methanol. Ethanol has a lower level of toxicity compared to methanol. Ethanol has a higher energy density (6.28kWhr/L) compared to that of methanol (4.82kWhr/L). Furthermore, ethanol has a lower crossover rate and, consequently, lesser effects of mixed potential than methanol (Z. Zakaria,2016). The Direct Ethanol Fuel Cell (DEFC) directly converts the chemical energy of ethanol into electricity. The crux of a DEFC is the use of a proton exchange membrane such as Prefluorinated sulfonic acid electrolyte membrane (Nafion® membrane, manufactured by DuPont) as the electrolyte. A DEFC converts ethanol into carbon dioxide. This conversion takes using a complete oxidation reaction. This complete oxidation produces 12 electrons. Notwithstanding, this complete oxidation seldom takes place. Thus further research is required to find methods to remedy the incomplete oxidation and increase the efficiency per mole of the fuel (Z. Zakaria,2016).
Modeling of DEFCs can be done by many methods. These methods require the knowledge of many intricate details such as parameter values, equations pertaining to each of the losses, and the physical and chemical relationship between the various phenomena taking place within the system. However, using ANN can be quite simple and also proves to be cost effective. The performance of the fuel cell can be predicted. The ANN had a feedforward topology with backpropagation. This network employs the Levenberg-Marquardt algorithm for training the data. MATLAB software was used to perform the ANN computations. The model can be validated by experimental data to reinforce its credibility. Some of the main advantages of using neural networks are that it can solve a variety of nonlinear problems and loss of neurons does not result in total failure of the system. It also uses distributed memory, contrary to the localized memory employed by a digital processor. However, this method also has its limitations. It requires a large data pool for the network to generate satisfactory outputs. These systems also do not provide sufficient explanation for the outputs they produce. They can also be computationally intensive to train.

II. Experimental study
The system consisted of a fuel cell assembly structure, a compressor, a humidifier unit, a peristaltic pump, a vaporizer unit, and an electronic load subject to adjustment. The ethanol solution was given as feed to the fuel cell and it was prepared prior to experimentation, according to the concentration desired for testing. This solution was fed to the peristaltic pump, from where it was then supplied to the anode side of the fuel cell.
Air, after compression, passes through the humidifier and is supplied to the cathode side of the fuel cell. The operating conditions for the fuel cell were adjusted on the above equipment. The temperature was adjusted on the electronic load. The flow rate of ethanol was adjusted on the peristaltic pump, and the flow rate of air was regulated on the rotameter system present as part of the humidifier. The data was measured using an Electrochemical Work Station. The tests were performed on a single fuel cell unit. The cell consisted of a membrane electrode assembly placed between two graphite blocks having dimensions of 1mmx1mm etched with double serpentine flow channels to supply ethanol and air to the respective compartments. The fuel cell had an active area of 25cm^2. The diffusion

layers employed were made of carbon paper. A catalyst loading of 4 mg/cm^2 was used on the anode side (Pt-Ru) and a loading of 4 mg/cm^2 was used on the cathode side. The membrane used was Nafion® 117, procured externally. The MEA was commercially manufactured elsewhere. The MEA and graphite blocks were held between aluminium end plates and gold-plated collector plates were also used. The margins and surface of the end plates were connected and held in place by means of an intricate nut and bolt system.

The MEA was activated for operation at various conditions to study different effects. Initially, Open Circuit Voltage was determined at the beginning of each run using the Electrochemical Workstation. The OCV was recorded after allowing the voltage value to become stable for almost an hour. The polarization curve was obtained by plotting various data points.

II. Modelling of DEFC using ANN

A network was developed to model the relation between the cell parameters and its output. This was done by using the experimental data obtained from the previous section. The ANN had a feedforward topology with backpropagation. MATLAB software was used to perform the ANN computations.

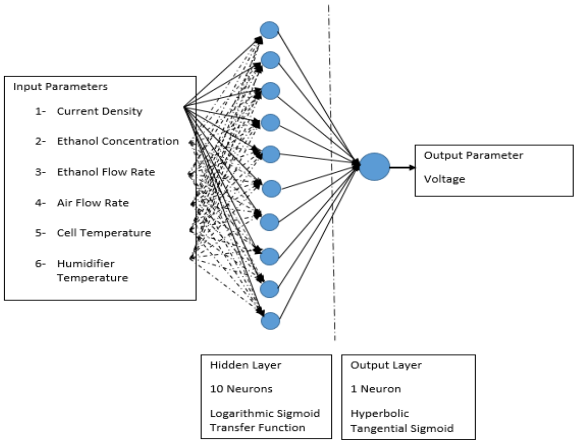

Fig.1. The Network Architecture

Fig.1. depicts the network architecture. The network has two layers, the hidden layer, and the output layer. Six input parameters were fed to the ANN and the output parameter was the voltage. A 6-10-1 architecture was selected with 10 neurons in the hidden layer and 1neuron in the output layer. The transfer function for the hidden layer was taken as the logarithmic sigmoid transfer function. The activation function for the output layer was the non-linear hyperbolic tangential sigmoid transfer function. A large set of data was selected and fed to the ANN, out of which, 70% of the data was used for the training of data, 15% for testing purpose, and another 15% was used for validation. The input values and target values were imported to the ANN toolbox and a network with the above-mentioned characteristics was created. The network was then allowed to train after adjusting the training parameters. Once the training process was completed through a series of iterations, the performance plots and regression values are examined. A regression coefficient value very close to 1 was obtained for the system.

Effect of Concentration

The effect of concentration was studied by experimenting with ethanol solutions of different concentrations from 0.5M to 4M. This was carried out at 60ºC, at an air flow rate of 1500ml/min, and an ethanol flow rate of 1ml/min. Figure 2 shows the effect of ethanol concentration on the performance of the fuel cell. It can be seen that as concentration increases, the performance increases up to 2M. At higher concentrations, the performance reduces. This is because a lower concentration gives rise to a lower value of crossover. Though higher concentrations of ethanol have better mass transport, a low concentration gives low crossover, which in turn causes better kinetics at the cathode side. As the concentration increases from 1M to 2 M, the activation overpotential is also reduced which resulted in a good performance. At 3M concentration and above, the ethanol molecules clog the active sites on the catalyst, thereby denying water molecules access to these active sites. Thus, the performance decreases. The power density curves are illustrated in Figure 3. A maximum power density of 5.78mW/cm^2 was obtained at 2M concentration.

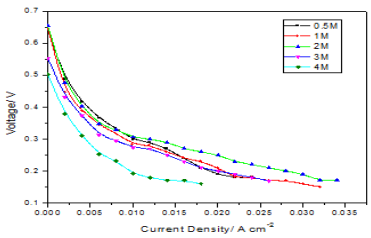

Fig.2. Polarization curves for different concentrations

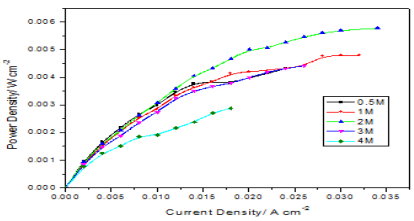

Fig.3. Power density curves for different concentrations

Effect of Cell Temperature

An increase in temperature of the fuel cell results in an increase in performance. This is due to a reduced value of activation overpotential and the enhanced reaction kinetics of the system. The conductivity of the membrane, the electrode kinetics, and the transport properties of the cell, are all functionally dependent on temperature. Another potential change is in the diffusivity of the ethanol molecules with an increase in the temperature. An increase in temperature could also give better OCV values Figure 4 and Figure 5 show the polarization and power density curves for various temperatures from 40°C-80°C, respectively. The experiments were carried out for 2M ethanol solutions at an air flow rate of 2000ml/min and an ethanol flow rate of 1.5ml/min. it is obvious that a temperature of 70°C-80°C seems ideal for the best performance of the DEFC.

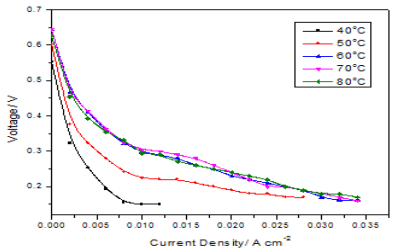

Fig.4. Polarization curve for different temperature

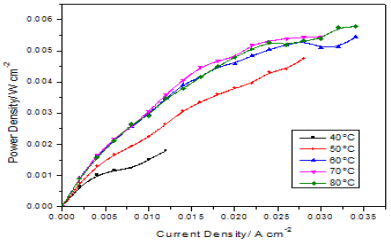

Fig.5. Power density curve for different temperature

Effect of Ethanol flow rate

Figure 6 and Figure 7 show the polarization and power density characteristics, respectively for different flow rates at a temperature of 60°C, for 2M concentration and for an air flow rate of 2000ml/min. The effect of flow rate is almost indistinguishable. 0.5ml/min, however, gives a very low value of power density. This is due to low transport of reactants at the surface of the catalyst, thus low utilization of catalyst sites, in turn reducing performance significantly. The maximum power density in this study was obtained at a flow rate of 1.5ml/min.

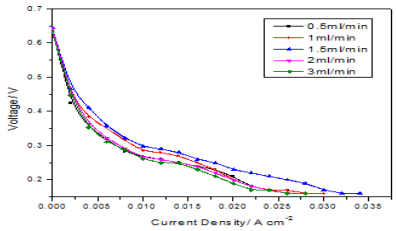

Fig.6.Polarization curve for different ethanol flow rate

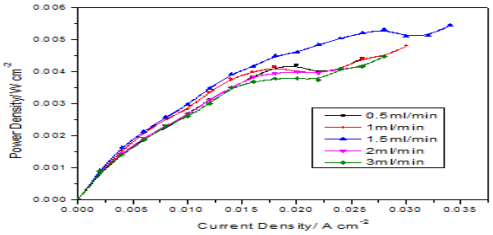

Fig.7. Power density curve for different ethanol flow rate

Effect of Humidity

The effect of humidity on the performance of the fuel cell was studied by varying the temperature on the humidifier. The change in temperature correspondingly changes the humidity. The moisture content influences the proton conductivity and the process of electro-osmosis. Thus better performance is seen at higher humidity. This is illustrated in Figure 8 and Figure 9.

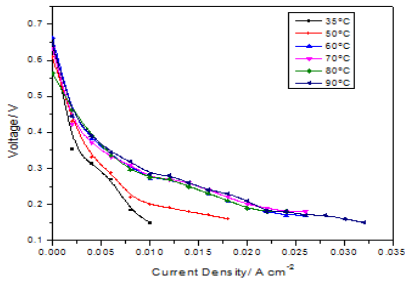

Fig.8.Polarization curve for the effect of humidity

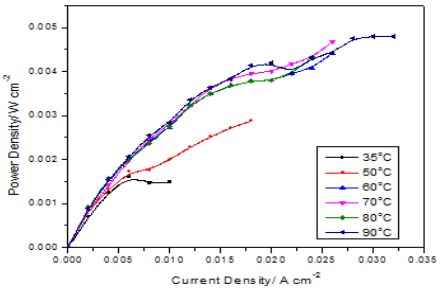

Fig.9.Power density for the effect of humidity

Modelling using ANN

The Neural Network developed was able to predict the different voltage values as the output for the different sets of input values. These output values were then compared to the output values obtained experimentally. Figure 10. compares the polarization characteristics obtained from the experimental data and from the ANN model for the effect of cell temperature. It can be seen the predicted data is in good agreement with the experimental data. The regression coefficient value was 0.992. The maximum performance was obtained at a cell temperature of 80ºC. Figure 11 shows the polarization characteristics for the effect of the ethanol concentration. The plots are quite similar with a regression coefficient of 0.9955. An ideal concentration of 2M gives the best performance in this case. Thus, it can be seen that the performance of the DEFC was modeled accurately enough. This shows that ANN is an efficient tool for anticipating the effect of various input parameters on the voltage of the fuel cell.

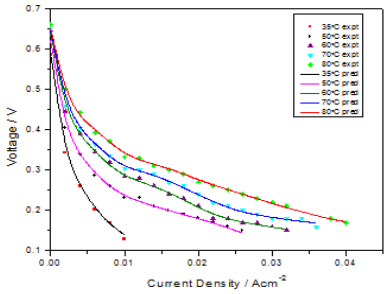

Fig.10.I–V curves for the effect of cell temperature

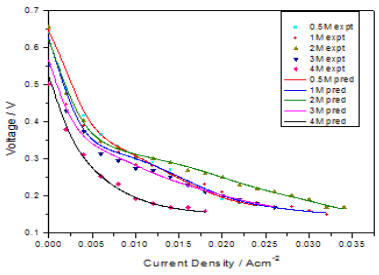

Fig.11.I–V curves for the effect of ethanol concentration

IV. Conclusions

In this research, the experimentation was carried out using liquid fed ethanol to study the effect of various parameters on the performance of fuel cell. An artificial network was used to model the performance of the DEFC. The solution to the model was determined by suitable numerical methods. Based on this model, a code was written and executed in MatLab. This model was used to study the effect of different parameters on the voltage-current density characteristics. The effect of concentration on the performance of the fuel cell was studied by changing the value of concentration in the model. It was found that an ethanol concentration of 0.25M gave the best value of power density. The best performance was obtained at 2000ml/min with a power density of 5.44mW/cm^2 . The performance increased with the increase in temperature. A temperature of 80°C gave the highest power density. The effect of concentration was studied and the optimum concentration was found to be 2M ethanol. On further increase of the concentration, the performance greatly reduces.The effect of humidity on the performance of the fuel cell shows that a higher humidity gave a better performance as the membrane remained better hydrated.Similarly the effect of air flow rate was studied, The best performance was obtained at 2000ml/min with a power density of 5.44mW/cm^2 . the polarization characteristics obtained from the experimental data and from the ANN model for the effect of cell temperature, ethanol concentration, ethanol flow rate, air flow rate and humidity were compared.It was seen that the predicted data is in good agreement with the experimental data. The R^2 value obtained was very close to 1, which implies that the predicted data was in good agreement with the experimental data. Thus it can be concluded that the performance of the DEFC was modeled accurately enough which shows that ANN is an efficient tool for anticipating the effect of various input parameters on the voltage of the fuel cell.

V. References

Alzate, V., Fatih, K., & Wang, H. (2011). Effect of operating parameters and anode diffusion layer on the direct ethanol fuel cell performance. *Journal of Power Sources*, *196*(24), 10625-10631. https://doi.org/10.1016/j.jpowsour.2011.08.080.

Andreadis, G., Stergiopoulos, V., Song, S., & Tsiakaras, P. (2010). Direct ethanol fuel cells: The effect of the cell discharge current on the products distribution. *Applied Catalysis B: Environmental*, *100*(1-2), 157-164. https://doi.org/10.1016/j.apcatb.2010.07.025.

Barbaro & P Bianchini, C.,. (Eds.). (2009). *Catalysis for sustainable energy production*. Wiley-Vch. https://doi.org/10.1021/cr800404j.

Battirola, L. C., Schneider, J. F., Torriani, I. C., Tremiliosi-Filho, G., & Rodrigues-Filho, U. P. (2013). Improvement on direct ethanol fuel cell performance by using doped-Nafion® 117 membranes with Pt and Pt–Ru nanoparticles. *international journal of hydrogen energy*, *38*(27), 12060-12068. https://doi.org/10.1016/j.ijhydene.2013.06.126.

M. Z. F., Kamarudin, Kamarudin, S. K., Masdar, M. S., & Daud, W. R. W. (2013). Direct ethanol fuel cells. *International Journal of Hydrogen Energy*, *38*(22), 9438-9453.

Pramanik, H., & Basu, S. (2007). A study on process parameters of direct ethanol fuel cell. *The Canadian Journal of Chemical Engineering*, *85*(5), 781-785. https://doi.org/10.1002/cjce.5450850524.

Zakaria, Z., Kamarudin, S. K., & Timmiati, S. N. (2016). Membranes for direct ethanol fuel cells: an overview. *Applied Energy*, *163*, 334-342. https://doi.org/10.1016/j.apenergy.2015.10.124.

Zignani, S. C., Baglio, V., Sebastián, D., Siracusano, S., & Aricò, A. S. (2016). Enhancing ethanol oxidation rate at PtRu electro-catalysts using metal-oxide additives. *Electrochimica Acta*, *191*, 183-191. https://doi.org/10.1016/j.electacta.2016.01.085.

Potential of Biocrude Production from Camel Manure via Hydrothermal Liquefaction: A Qatar Case Study

[1]Mohammad Alherbawi, [1]Prakash Parthasarathy, [1,2]Tareq Al-Ansari, [1*]Gordon Mckay
[1] Division of Sustainable Development, College of Science and Engineering, Hamad Bin Khalifa University, Qatar Foundation, Doha, Qatar.
[2] Division of Engineering Management and Decision Sciences, College of Science and Engineering, Hamad Bin Khalifa University, Doha, Qatar.
* E-mail: gmckay@hbku.edu.qa

Abstract
Livestock manure is a significant contributor to methane emissions which are released upon the decomposition of manure under anaerobic conditions. Besides, the mismanagement of manure may lead to serious water and soil contamination. In Qatar, camels are commonly domesticated for their meat and milk. Its camel population generates around 120,000 tonnes of manure annually, resulting in nearly 4 kilotonnes of CO_2 eq emissions. Meanwhile, Hydrothermal Liquefaction (HTL) has emerged as a promising technology for the valorization of wet wastes, as it does not require the energy-intensive drying step as in gasification and pyrolysis technologies. As such, this study investigates the potential of biocrude production from camel manure in Qatar, and potentially other similar areas, using HTL. Proximate and elemental analysis of manure samples is conducted, while the process is simulated using Aspen Plus® software with an optimal feed capacity to completely utilize most of Qatar's camel manure. Moreover, an economic assessment is conducted using Aspen Process Economic Analyzer (APEA). The demonstrated results are encouraging; whereby, a biocrude yield of 37.9% (dry, ash-free basis) is achieved, with a minimum selling price of 72 US$/bbl. Nevertheless, the presence of well-established oil refineries in Qatar makes it feasible to upgrade biocrude into drop-in transportation fuels via co-processing with petroleum crude, which has been recently certified by the American Society for Testing and Materials.

Keywords: Hydrothermal Liquefaction, Camel manure, Qatar, Biocrude.

I. Introduction

In Qatar, camels have been long domesticated for their meat, milk and fur. Recently, they have been tamed for racing which is becoming a very popular sport in this part of the world. According to the Planning and Statistics Authority of Qatar, there are around 126,000 camels in Qatar (Agriculture Statistics, 2018). These camels roughly produce around 120,000 tonnes of manure (Lensch, 1999), which is responsible for nearly 4 kilotonnes of CO_2 eq (Sowunmi et al., 2015). Camel manure of such magnitude is often disposed into landfill dumps, which may cause serious degradation and contamination of soil and water resources. Hence, a more efficient approach for the valorization of manure needs to be identified.

Although camel manure can be processed using different thermochemical processes such as pyrolysis and gasification, it is believed that the hydrothermal liquefaction technology (HTL) can better handle high moisture content feedstocks. HTL is a process that converts any carbonaceous material into biocrude oil, making use of hot and high pressurized water. Usually, the process is performed at a temperature between 250 and 400°C, a residence time up to 60 min, an operating pressure ranging between 4 and 25 MPa (Chen et al., 2019). Along with biocrude, the process also generates an aqueous phase rich liquid product, char and gases. The performance and the outputs of the HTL process are greatly influenced by factors such as temperature, pressure, residence time, feedstock type, nature of solvents and catalysts used (Al-Ansari et al., 2020; Alherbawi et al., 2021).

Several studies on HTL of different livestock manures have been reported, including cattle dung (Yin et al., 2010), poultry litter (Ghanim et al., 2016) and swine manure (Vardon et al., 2011). However, no studies on HTL of camel manure have been found in literature, as far as the authors are aware. Hence, this study focuses on the HTL of camel manure, with an objective to estimate the biocrude production potential of Qatar using Aspen Plus (V.9) software. Besides, Aspen Process Economic Analyzer (APEA) is employed to conduct a preliminary economic assessment of the implementation of HTL technology in Qatar.

II. Methodology

The fresh camel manure is procured from a local farm in Qatar. The proximate analysis of the manure is conducted using a thermogravimetry analyzer (TA Instruments SDT 650). The analysis is done according to ASTM D7582-12. While the elemental analysis of the manure is performed in (Euro-vector Euro EA 3000) CHN elemental analyzer according to ASTM D 3176 – 89.

Besides, Aspen Plus (V.9) is used to develop the HTL process. The NRTL package is used as a property method, while the camel manure is defined as a non-conventional component based on the proximate and elemental analysis performed in the former experimental step. The manure is simulated in correlation to coal's enthalpy and density built-in characteristics. Char is defined as 100% carbon (C). The developed process flowsheet is shown in Fig. 1. Camel manure is initially processed in a decomposition reactor to convert it into conventional components using a Fortran code adapted from (Alnouss et al., 2018). A slurry is created by mixing the biomass stream and water, with the presence of a sodium hydroxide alkali catalyst to enhance the possibility of the formation of oil-like products (Cao et al., 2017). The slurry is then pumped to the HTL reactor.

Block "RGibbs" is used to simulate the main reaction of the HTL process based on the principle of minimizing Gibbs free energy. The reaction is carried out at 300°C and 175 bars. Possible products are defined based on earlier experimental works (Magdeldin et al., 2018; Pedersen et al., 2017). The water content of the slurry is maintained in a sub-critical state at the given operating conditions, which has a lower viscosity and therefore higher solubility of organic compounds. Upon the completion of the reaction, the stream is purified by separating the solids using a solid separator, and splitting the remaining stream into gas, biocrude and aqueous phases using a three-stage flash drum.

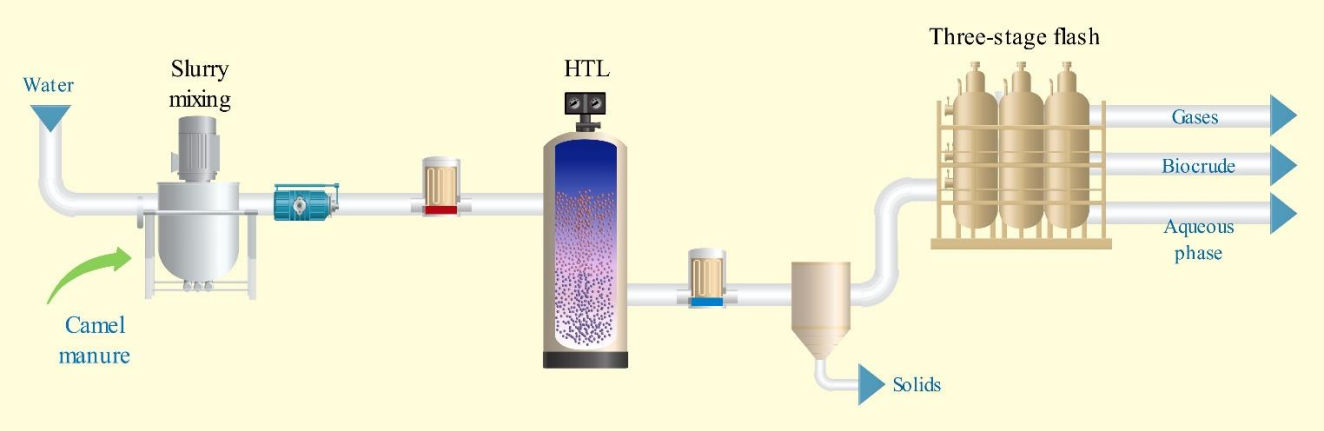

Fig. 1: Hydrothermal liquefaction process' flow diagram.

An economic assessment of the process is conducted using Aspen Plus Process Economic Analyzer (APEA) based on the following assumptions:

1) Plant lifespan of 30 years.
2) Annual feed capacity of 120,000 tonnes (wet basis).
3) Startup period of 6 months.

Besides, the flow prices are defined as presented in Table 1, while the utilities' prices in Qatar are considered. The minimum selling price of biocrude is calculated using the following standard levelized cost of fuel (LCOF) formula (International Energy Agency, 2010):

$$LCOF\ \left(\frac{U.S.\$}{bbl}\right) = \frac{\sum_1^t((K+O\&M+R)(1+d)^{-t})}{\sum_1^t((P(1+d)^{-t})} \quad (1)$$

Where, (t) is the plant lifespan,(K) is the annualized capital cost, (O&M) is the annual operating costs, (R) annual materials costs, (P) is the annual biocrude produced in barrels (bbl) and (d) is the discount rate (set at 10%).

Table 1. Raw materials and utility prices.

Item	Price	Unit	Ref.
Camel manure	*25* [a]	*$/tonne*	-
Sodium Hydroxide	*350*	*$/tonne*	(Alibaba, 2020)
Electricity (for industry)	*0.035* [b]	*$/kWh*	(Kahrama, 2020)
Water (for industry)	*1.479* [b]	*$/m³*	(Kahrama, 2020)

a) Camel manure is free of charge, while estimated handling and transportation charges are considered.
b) Currency conversion is based on the fixed local rate (US$ 1 = QAR 3.65).

III. Results and discussion

The proximate and elemental analysis of camel manure samples are presented in Table 2. The results indicate high volatile matter and considerable carbon contents.

Regarding the simulation results, the product composition of the HTL process is presented in Fig.2 on a dry and ash-free basis (daf.%) of feedstock. Significant yields of biocrude (37.9%) and hydrochar (19%) are obtained. Besides, the process released a mixture of gases including CO_2, CO, H_2, CH_4 and NH_3, which can be purified into syngas at a later stage. The biocrude yield from camel manure presented in this study is slightly higher than most of other livestock manure reported earlier under similar conditions as presented in Table 3, which is possibly due to higher carbon contents of camel manure.

Table 2. Proximate and elemental analysis of camel manure.

Proximate analysis		Elemental analysis (wt.%)	
Moisture (as received %)	*38.00*	C	*27.83*
Fixed carbon (db.%)	*12.53*	H	*1.02*
Volatile matter (db.%)	*66.25*	O	*47.75*
Ash (db.%)	*21.22*	N	*2.18*

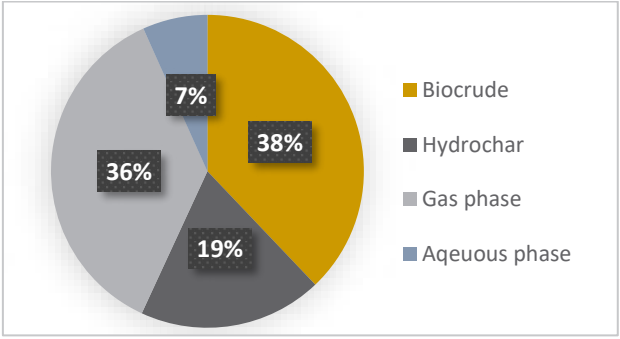

Fig. 2: Products distribution of hydrothermal liquefaction (dry and ash-free basis).

Table 3. Biocrude yield of HTL of camel manure (this study) as compared to other livestock manure reported in literature.

Biomass	Camel manure (this study)	Swine manure (Vardon et al., 2011)	Cattle manure (Yin et al., 2010)	Beef manure (Li et al., 2018)	Sheep manure (Li et al., 2018)
Biocrude Yield (daf.%)	*37.90%*	*30.20%*	*27.97%*	*20.20%*	*25.47%*

In terms of the product's quality, the characteristics of biocrude are believed to be advantageous over pyrolysis oil in terms of its chemical and physical properties as presented in Table 4. Whereby, the biocrude heating value is close to that of biodiesel, while its boiling point is close to that of gasoline. Moreover, its low oxygen content grants it a high potential to be upgraded into drop-in transportation fuels at mild refining conditions.

Table 4. Physical and chemical properties of biocrude.

Property	Value	Unit
Density @15°C	*880*	*Kg/m^3*
Average boiling point	*135.6*	*°C*
Average molecular weight	*100.6*	*g/mol*
Lower heating value	*38*	*MJ/kg*
Specific gravity	*0.87*	-
H/C ratio	*1.68*	-
O/C ratio	*0.13*	-

Table 5 presents a summary of HTL plant's economic assessment. The minimum selling price (MSP) of biocrude is calculated to be nearly US$ 72.3 per barrel, which is slightly lower than earlier studies (Kirtania, 2018), mainly due to lower utilities' tariff in Qatar for the industrial sector, as well as the lower biomass price and handling charges. The obtained MSP of biocrude can be enhanced if the produced gases are further purified into useful syngas while the biocrude is upgraded into drop-in transportation fuels, which can be a feasible pathway for countries with an established oil-refining infrastructure like Qatar. Whereby, the American Society for Testing and Materials (ASTM) has already certified the co-processing of fossil crude with up to 5 vol.% bio-components (Prussi et al., 2019).

The breakdown of capital and operating costs is presented in Fig. 3. The graphs demonstrate that biomass cost is the major operating cost component, with nearly (47%) of the net costs, followed by utilities (11.2%) and catalysts (10.12%). On the other hand, the purchased equipment cost accounts for the highest share of the capital costs (~40%), followed by equipment setting (11.25%) and contingencies (10%).

Table 5. Summary of plant's economic assessment.

Item	Value
Total capital cost ($)	*14,224,370*
Total operating cost ($/year)	*6,431,563*
Total raw materials cost ($/year)	*3,651,000*
Total utilities cost ($/year)	*720,031*
Equipment cost ($)	*5,756,997*
Minimum biocrude selling price (US$/bbl)	*72.3*

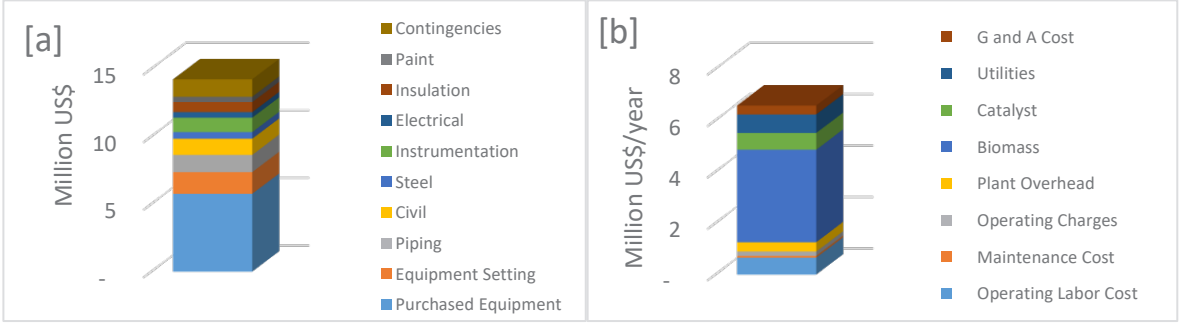

Fig. 3: Breakdown of (a) capital costs, and (b) operating costs.

IV. Conclusions

In this study, camel manure samples have been analyzed in a laboratory, while the HTL processing of the manure has been simulated in Aspen Plus using the HTL plant specifications that corresponds to the Qatari scenario. The results demonstrate a satisfactory biocrude yield of (37.9 daf.%) with a relatively high quality, while its minimum selling price of (72 US$/bbl) is encouraging.

Although HTL technology still requires further enhancement to be implemented at the industrial scale, it proved to have a high potential to produce higher quality bio-oils from the high-moisture containing biomass. This study is to be expanded to assess the potential of biocrude upgrading in existing fossil crude oil refineries in Qatar, with an expanded economic assessment.

Acknowledgements

The authors are grateful to Hamad Bin Khalifa University (HBKU) and Qatar Foundation (QF) for their financial support.

References

Agriculture Statistics, 2018. Planning and Statistics Authority, Qatar. Doha.

Al-Ansari, T., AlNouss, A., Al-Thani, N., Parthasarathy, P., ElKhalifa, S., Mckay, G., Alherbawi, M., 2020. Optimising Multi Biomass Feedstock Utilisation Considering a Multi Technology Approach, in: Pierucci, S., Manenti, F., Bozzano, G.L., Manca, D.B.T.-C.A.C.E. (Eds.), 30 European Symposium on Computer Aided Process Engineering. Elsevier, pp. 1633–1638.

Alherbawi, M., AlNouss, A., McKay, G., Al-Ansari, T., 2021. Optimum sustainable utilisation of the whole fruit of Jatropha curcas: An energy, water and food nexus approach. Renew. Sustain. Energy Rev. 137, 110605.

Alibaba, 2020. Sodium hydroxide powder supply. URL https://bit.ly/37TIK7w (accessed 1.1.20).

Alnouss, A., Mckay, G., Al-ansari, T., 2018. Optimum Utilization of Biomass for the Production of Power and Fuels using Gasification, in: 28th European Symposium on Computer Aided Process Engineering. Elsevier Masson SAS, pp. 1481–1486.

Cao, L., Zhang, C., Chen, H., Tsang, D.C.W., Luo, G., Zhang, S., Chen, J., 2017. Hydrothermal liquefaction of agricultural and forestry wastes: state-of-the-art review and future prospects. Bioresour. Technol. 245, 1184–1193.

Chen, Lin, Liu, Chen, Hung, Chen, Ong, 2019. A comprehensive analysis of food waste derived liquefaction bio-oil properties for industrial application. Appl. Energy 237, 283–291.

Ghanim, B.M., Pandey, D.S., Kwapinski, W., Leahy, J.J., 2016. Hydrothermal carbonisation of poultry litter: Effects of treatment temperature and residence time on yields and chemical properties of hydrochars. Bioresour. Technol. 216, 373–380.

International Energy Agency, 2010. Projected Costs of Generating Electricity. OECD/ IEA/NEA, Paris.

Kahrama, 2020. Utilities tariff. URL https://www.km.com.qa/CustomerService/Pages/Tariff.aspx (accessed 1.1.20).

Kirtania, K., 2018. Chapter 4 - Thermochemical Conversion Processes for Waste Biorefinery, in: Bhaskar, T., Pandey, A., Mohan, S.V., Lee, D.-J., Khanal, S.K.B.T.-W.B. (Eds.), . Elsevier, pp. 129–156.

Li, H., Lu, J., Zhang, Y., Liu, Z., 2018. Hydrothermal liquefaction of typical livestock manures in China: Biocrude oil production and migration of heavy metals. J. Anal. Appl. Pyrolysis 135, 133–140.

Magdeldin, M., Kohl, T., Järvinen, M., 2018. Techno-economic Assessment of Integrated Hydrothermal Liquefaction and Combined Heat and Power Production from Lignocellulose Residues. J. Sustain. Dev. Energy, Water Environ. Syst. 6, 89–113.

Pedersen, T.H., Jensen, C.U., Sandström, L., Rosendahl, L.A., 2017. Full characterization of compounds obtained from fractional distillation and upgrading of a HTL biocrude. Appl. Energy 202, 408–419.

Prussi, M., O'Connell, A., Lonza, L., 2019. Analysis of current aviation biofuel technical production potential in EU28. Biomass and Bioenergy 130, 105371. https://doi.org/https://doi.org/10.1016/j.biombioe.2019.105371

Sowunmi, A., Bastidas-Oyanedel, J.-R., Schmidt, J.E., 2015. Carbon Emissions from Livestock Manure in Arid Regions - Technical Study on the United Arab Emirates. Environ. Nat. Resour. Res. 5, 1–10.

Vardon, D.R., Sharma, B.K., Scott, J., Yu, G., Wang, Z., Schideman, L., Zhang, Y., Strathmann, T.J., 2011. Chemical properties of biocrude oil from the hydrothermal liquefaction of Spirulina algae, swine manure, and digested anaerobic sludge. Bioresour. Technol. 102, 8295–8303.

Yin, S., Dolan, R., Harris, M., Tan, Z., 2010. Subcritical hydrothermal liquefaction of cattle manure to bio-oil: Effects of conversion parameters on bio-oil yield and characterization of bio-oil. Bioresour. Technol. 101, 3657–3664.

Comparison of Multi-Input Single-Output Isolation-free DC-DC Converter Topologies for Hybrid Power Plants

[1]Sakir Kuzey, [2*]Muhammet Tahir Guneser, [2]Cihat Seker
[1] Giresun University, Sebinkarahisar Vocational Schools of Tech.Sciences, Electricity and Energy Department, Giresun, Turkiye
[2] Karabuk University, Engineering Faculty, Electrical and Electronics Engineering Department, Demir Celik Campus, Karabuk, 78100, Turkiye

* E-mails: sakirkuzey@giresun.edu.tr , mtguneser@karabuk.edu.tr , cihatseker@karabuk.edu.tr

Abstract
Today it is an obvious fact that energy consumption tends to increase due to technological developments, population growth, and increasing living standards. In last two decades, renewable energy sources are accepted the most convenient way. However, most of these alternative systems are not considered sufficient to supply whole demand alone. But hybrid systems with some of alternative energy sources, such as solar, wind and biomass appear to be a solution to supply the energy needs in the future. In hybrid systems, the dc-dc converter structure is the main device when converting energy for the proper loads. Single / multiple input single / multiple output dc-dc converter topologies vary in design according to the energy demand of the load. Particularly, topologies with bi-directional power flow and less circuit elements come to the fore.
In this study, the simulation of multi-input single output dc-dc converter topologies was performed in Matlab / Simulink software. Induction current and voltage, output current and voltage, as well as output power used in the determined topologies were analysed.

Keywords: MIC topologies, hybrid systems, Matlab / Simulink, two-input converters, V-I characteristics

I. Introduction

Today, transformers alone are insufficient in meeting the needs of loads with different profiles and in connection of renewable energy sources such as solar and wind to the grid. Additional mechanisms are needed to overcome power quality problems such as voltage rise and fall, ripple or harmonics (Dujić, 2012). With the advances in semiconductor technology, power electronics has emerged as a promising solution to dealing with the problems of complex power systems. High-power and controllable solid-state switches triggered the development of various power electronic converters that find application in both transmission and distribution systems. Power electronic circuits and mechanisms, initially created with the help of transistors, were primarily used in industry. This process, which started with motor control units, went beyond the industry thanks to the developing semiconductor technologies and went to electric vehicles (Du, 2011; Lee, 2009), micro grids (Wang, 2011; Rocabert, 2012), renewable energy sources (Sri Revathi, 2016; Zhao, 2012), home, office, agriculture and animal husbandry (Buning, 2010; Burmester, 2017) has found use in many places. Power electronic circuits, whose production and consumption increased with the increasing demand, made it necessary to minimize the effect of load effect on the source and peripheral devices and to be compatible with each other. In addition, the quality and uninterrupted energy demands of the users (Hemetsberger, 2003) made it necessary to provide power quality, efficiency, safety and insulation features. It is necessary to prevent wide-ranging power outages that occur in case of malfunctions, to dampen disturbing effects and to keep the power factor level that creates load on the grid at the optimum level.

Power converters that result from the combination of conventional transformers and semiconductor converters are defined as power electronics transformers (PET). PET's were first patented by Murray in 1970 (Mcmurray, 1970). Using conventional transformers in PETs provides easy conversion between different voltage levels as well as electrical insulation. However, transformers used in the network frequency (50Hz / 60Hz) have disadvantages such as very large weight and dimensions depending on the power. Brooks suggested in 1980 that by increasing the frequency of the insulation barrier, the size of the system could be reduced and more power could be transferred with a smaller transformer (Brooks, 1980). Thus, together with transformers that can be operated within the frequency application limits, the way for very high energy conversions from very small dimensions has been opened. It has started to widespread the use of PET instead of low frequency transformer (LFT), especially at low and medium voltage levels. Safe and efficient power control is provided in a wide range by properly controlling the power electronic elements in the PET's structure.

In this study, the studies on multi-input converters (MICs) are examined and MIC topologies, which are widely included in the literature, are summarized. MIC topologies are grouped under four subtitles as AC / AC, AC / DC, DC / AC and DC / DC. Topology structures are generally examined and detailed with a sample application. The developed MIC was simulated in Matlab / Simulink environment. The findings obtained from the design criteria and simulation are presented in the second section of the study.

II. Multi Input Single Output DC/DC Converter Topologies

There are many multi-input (MI) dc-dc converter topologies in the literature. However, this study will focus on two different topologies. In such systems, power transfer with a common circuit using more than one source and a single inductor is performed either in one way or two-ways.

Multi-input single output (MISO) dc-dc converter topology is given in [10]. The pulsating voltage source cells (PVSC) structure formed by the parallel connection of diodes to the sources forms the basis of the system. In the topology, the power flow is provided in one way with a converter with a single output filter and a single control system. The circuit model was generated in the simulation environment. There are two voltage sources and two switches in the circuit that can provide power to the load both separately and at the same time. By applying pulse width modulation (PWM) signal switching, four different operating modes were created at fixed switching frequency. Mode 1; It is the time interval when switch S_1 is on and switch S_2 is in off position. In this time interval, the energy from the V_1 source feeds the load through the inductor. Mode 2; It is the time interval when switch S_1 is off and switch S_2 is on. During this time, the V_2 source charges the inductor. The output capacitor supplies power to the load. Mode 3; It is the interval when both switches are off. In this time interval, it provides its load power from the energy stored in the inductor and the capacitor. Mode 4;It is the time interval when both switches are on. During this time, both sources work at the same time. The sources charge the inductor and the power of the load is provided by the capacitor. Since it has four different operating modes, the PWM signal applied to the switches must be applied in a way that creates these modes. Switches are operated at the same frequency.

If the source with high voltage value is defined as V_H and the source with low voltage value as V_L, there is a relationship between input voltages and output voltage as $V_H > V_o > V_L$. The parameters used in the simulation environment are listed in Table 1.

The signals used in the simulation study of two input dc-dc converter topology are given in Figure 1.

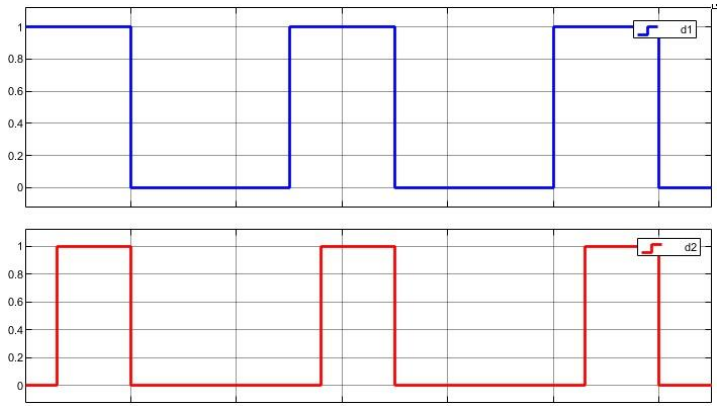

Figure 1: d_1 and d_2 duty cycle graph

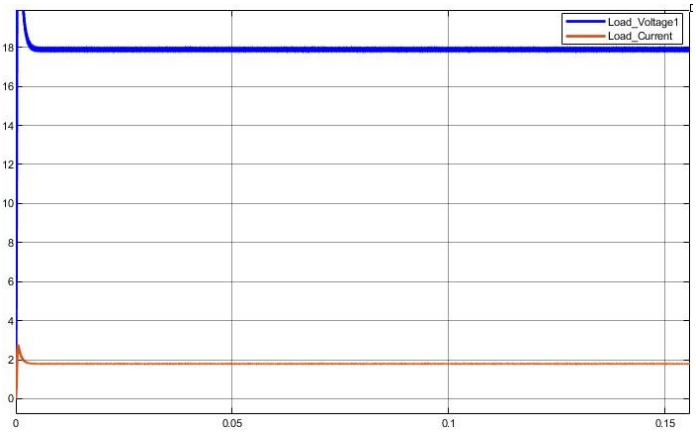

Figure 2: V_o vs I_o graph

When the power control relationship of the circuit is examined, it is seen that three different situations occur. The V_1 or V_2 source will be the main source that provides the power needed by the load, and the remaining power will be supplied from another source. The third case is that both sources will provide power to the load and always provide the highest power to the output by controlling the input currents. Figure 2 shows the output current and output voltage graph.

The circuit structure with common converter structure by means of a single inductor that provides two-way power flow analyzed is installed in simulation environment. Contrary to the topology abovementioned, it provides two-way power flow. This is particularly desirable for electric vehicle applications. For example; The power to be generated during regenerative braking in electric vehicles (EVs) is desired to be recovered. This situation points out that there should be a converter that can provide two-way power in EVs systems. In the literature, many studies have been done for different modes of this topology [8].

4 switches are used in the circuit. S_1 and S_2 switches determine which source will provide power, S_3 switch to determine whether the converter will operate in buck, boost or buck-boost modes, and the power flow way with the S_4 switch. One-way power flow is preferred in buck-boost converter mode for the system to be analyzed. There are

four operating modes due to the fact that there are two voltage sources and whether these sources are in transmission or not. Since the switching modes and PWM signal strategies to be applied to the switches are explained in detail in the mentioned studies, there is no need for explanation in this study. A fixed frequency is applied to the switches.

The parameters used in the simulation environment are listed in Table 1. The switching frequency is set at 20 kHz and the load at 5 Ω.

The output voltage, current and power graph obtained in the simulation environment are given in Figure 3. When the graphs are examined, it is seen that there are small differences according to the mathematical equations. The reason is that the circuit elements used in Simulink software are not ideal and have internal resistances.

Inductor voltage and inductor current graph is given in Figure 4. When the inductor voltage graph is investigated, it is clearly seen that it is proper for the PWM switching strategy used. Medium synchronous switching strategy is used in this study.

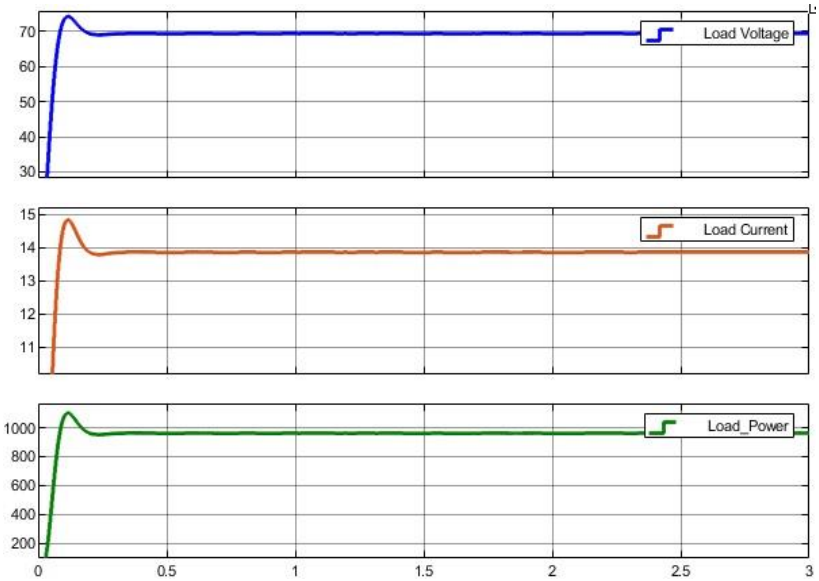

Figure 3: Output voltage, current and power graph

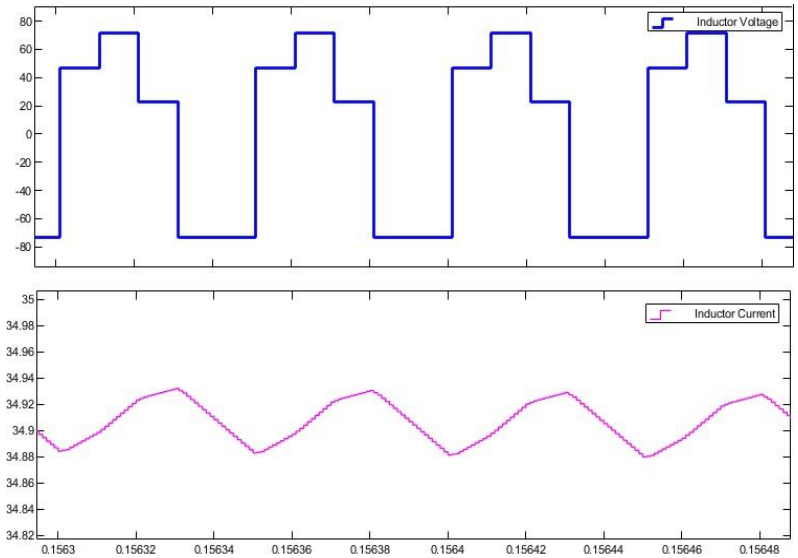

Figure 4: Inductor voltage and current graph.

IV. Conclusions

Two different MIC topologies were analyzed, and circuit models were installed in the simulation environment. In the first topology, the model with a single inductor common converter circuit is handled. The advantage of this topology is that it has a single inductor and a common converter circuit. However, one-way power flow is provided in this topology. This situation can be considered as the disadvantage of topology. In the second topology, two-way power flow is provided with the S4 switch. In terms of this feature, the second topology is different from the other topology. Two-input single-output buck-boost converter topology has come to the fore especially in terms of providing two-way power. Considering that the use of renewable energy sources will increase in order to meet the energy needs in the future, it is predicted that new topologies will be needed to be created with dc-dc converter combinations with multiple inputs or multiple outputs. Thus, it will be useful to work on the power flow control of multi-input single output

dc-dc converter systems using photovoltaic energy sources in future studies.

Table 1: Circuit parameters

Circuit parameters for first topology		Circuit parameters for second topology	
Parameter	Value	Parameter	Value
V_1	24 V_{DC}	V_1	48 V_{DC}
V_2	12 V_{DC}	V_2	24 V_{DC}
d_1	40 %	d_1	40 %
d_2	28 %	d_2	40 %
L	82 uH	d_3	60 %
C	160 uF	d_{12}	20 %
R	10 Ω	L	28.8 mH
f	20 kHz	C	4.32 mF
		R	5 Ω
		f	20 kHz
		Δ_i	5 %
		Δ_c	10 %

References

Brooks, J.L., 1980. Solid State Transformer Concept Development, Civil Engineering Laboratory - Naval Construction Battalion Center.

Buning, E. A. (2010). Electric drives in agricultural machinery-approach from the tractor side. Journal of Agricultural Engineering, 47(3), 30-35.

Burmester, D., Rayudu, R., Seah, W., Akinyele, D., 2017. A review of nanogrid topologies and technologies. Renew. Sustain. Energy Rev. https://doi.org/10.1016/j.rser.2016.09.073

Du, Y., Lukic, S., Jacobson, B., Huang, A., 2011. Review of high power isolated bi-directional DC-DC converters for PHEV/EV DC charging infrastructure, in: IEEE Energy Conversion Congress and Exposition: Energy Conversion Innovation for a Clean Energy Future, ECCE 2011, Proceedings. https://doi.org/10.1109/ECCE.2011.6063818

Dujić, D., Kieferndorf, F., Canales, F., 2012. Power electronic transformer technology for traction applications-An overview. Electronics. https://doi.org/10.7251/ELS1216050D

Hemetsberger F. A. (2003). An Investigation Of Power Quality Problems In A Remote Mine Site, M.S. Thesis, The University of Queensland.

Lee, Y.J., Khaligh, A., Emadi, A., 2009. Advanced integrated bidirectional AC/DC and DC/DC converter for plug-in hybrid electric vehicles. IEEE Trans. Veh. Technol. https://doi.org/10.1109/TVT.2009.2028070

Mcmurray, W. (1970). U.S. Patent No. 3,517,300. Washington, DC: U.S. Patent and Trademark Office.

Rocabert, J., Luna, A., Blaabjerg, F., Rodríguez, P., 2012. Control of power converters in AC microgrids. IEEE Trans. Power Electron. https://doi.org/10.1109/TPEL.2012.2199334

Sri Revathi, B., Prabhakar, M., 2016. Non isolated high gain DC-DC converter topologies for PV applications – A comprehensive review. Renew. Sustain. Energy Rev. https://doi.org/10.1016/j.rser.2016.08.057

Wang, F., Duarte, J.L., Hendrix, M.A.M., 2011. Grid-interfacing converter systems with enhanced voltage quality for microgrid applicationconcept and implementation. IEEE Trans. Power Electron. https://doi.org/10.1109/TPEL.2011.2147334

Zhao, Z., Xu, M., Chen, Q., Lai, J.S.J., Cho, Y., 2012. Derivation, analysis, and implementation of a boost-buck converter-based high-efficiency PV inverter. IEEE Trans. Power Electron. https://doi.org/10.1109/TPEL.2011.2163805

Large Scale Synthesis of Hexagonal Boron Nitride Nanosheets and their Utilization in Thermally Conductive Nanocomposites

[1]Mehamed Ali, [1*]Ahmed Abdala
[1] Texas A&M University at Qatar, Chemical Engineering, Education City, Doha, 00000, Qatar

* E-mails: ahmed.abdala@qatar.tamu.edu

Abstract
Despite their isostructural similarity to graphene, large scale preparation of hexagonal boron nitride nanosheet (h-BNNS) has been challenging. This is mainly due to their strong interlayer interactions initiated by the electronegativity difference in their elemental components. In this study, large scale h-BNNSs were prepared *via* ball milling (BM) technique. The h-BN exfoliation was optimized by studying the effect of ball to powder ratio, milling frequency, and milling time. Due to the relatively large particle sizes and the high h-BNNS yield, 10:1 ball to powder ratio, 250 rpm rotation rate, and 1.5 hours milling time were chosen as the optimum milling conditions. h-BNNSs prepared at the optimum milling conditions were examined with regards to yield, stability, structure, and surface chemistry characterizations. The yield of h-BNNS was impressively high ranging from ~ 38 % to ~ 60 % at 30 min and 4.5 hours milling times, respectively, implying very high efficiency. h-BNNS prepared at the optimum milling conditions were utilized for the fabrication of thermally conductive polyethylene (PE) nanocomposites. The ultimate application of these nanocomposites being in replacing metal evaporators in multi-effect distillation desalination it is not only prerequisite to have high thermal conductivity but also very essential to have enhanced mechanical durability, thermal stability, and wettability. Therefore, the performance of these nanocomposites was compared with those containing bulk h-BN in terms of processability, thermal conductivity, mechanical properties, and wettability. Finally, mitigation methods to alleviate BM induced defects and amorphizations were proposed and investigated. These treatments were found to be very essential in alleviating defects as well as enhancing the thermo-mechanical properties of PE nanocomposites making them very good candidates for their ultimate application.

Keywords: polyethylene, thermal conductivity, nanocomposite, h-BN, ball milling

I. Introduction

Seawater desalination provides 99 % of the total domestic water demand in Qatar (Rahman and Zaidi, 2018), mainly by utilizing thermal desalination processes such as multistage flash (MSF) and Multi-Effect Distillation (MED) desalination (Alhaj et al., 2017). Metal heat exchangers used in these processes suffers from extreme corrosion, scaling, and fouling due to the high salinity of the Arabian Gulf Sea. These problems are currently mitigated by using corrosion-resistant exotic metals or metal alloys, such as Cu-Ni alloy and Titanium, and by frequent cleaning and scale removal leading to a high capital and operating cost. A less common but a very good alternative to metals are polymers, being relatively resistant to seawater corrosion, fouling, and scaling. Furthermore, other polymer attributes such as lightweight, low cost, and ease of fabrication provide additional benefits, which play role in the reduction of the total cost. However, polymers have poor thermal and mechanical properties. Nevertheless, these properties can be enhanced by the incorporation of thermally conductive fillers, i.e. h-BN.

h-BN is an isoelectronic analogue to graphite. Like graphite, h-BN can be exfoliated to few layered h-BN nanosheets with better properties. Consequently, several techniques have been developed to exfoliate bulk h-BN to a single or few layered h-BNNS, including but not limited to mechanical cleavage (Meng et al., 2015), solvent assisted sonication (Zhang et al., 2017), chemical vapor deposition (Meng et al., 2015), and thermal exfoliation (Ko et al., 2016). Most of these methods are inefficient and produce low yield, making them costly for large scale production (Zhang et al., 2017)(Wang et al., 2018).

In this work, ball milling (BM) method was used for h-BN exfoliation. Ball milling is one of the easiest and efficient methods for h-BN exfoliation (Ding et al., 2018). However, ball milling method is known to create defects and reduce the particle size severely (Huang et al., 2000). Nevertheless, these problems can be mitigated by controlling: ball size, ball to powder ratio, milling frequency, and milling time. Another solution is wet ball milling, in which h-BN is milled in a solution (Ding et al., 2018)(Mochalin et al., 2015). Here, the effect of milling time on the h-BNNS yield was investigated. In addition, the impact of adding LLDPE to h-BN, mitigation treatment, during the BM process on the h-BNNS properties was investigated. Finally, the effect of incorporating h-BNNS on the thermal and mechanical properties of PE nanocomposites was studied.

II. Experimental Procedure

Material

Hexagonal boron nitride (h-BN) powder was provided by Asbury Carbon with 6 µm (h-BN6) and 35 µm (h-BN35) average particle sizes and 99.0% purity. Linear low density polyethylene (LLDPE) powder with density and melting point of 0.916 g/ cm3 and ~122 °C, respectively, was kindly supplied by QAPCO. Isopropanol (IPA), 99% purity, was purchased from Research Lab, India.

h-BNNS Preparation

h-BNNS was prepared by Retsch Mill CryoMill (Ball Mill). 3 g of bulk h-BN and 8 mm diameter steel balls

(~ 2 g) were loaded to steel vial at a ball to powder ratio of 10:1. The milling frequency was set at 30 Hz, and the h-BN powder was milled for various milling time ranging from 30 min – 4.5 h.

Nanocomposite Fabrication

h-BN or h-BNNS/PE composites were prepared by melt blending using Xplore Twin Screw 15 ml Micro-Compounder. In each batch, 9 g of the composites (h-BN powder and PE), were premixed and fed to the extruder; at a uniform temperature of 210°C, a rotation rate of 100 rpm, and residence time of 10 min. Afterwards, the extruded composite was then compression molded using Craver Bench Top Heated Manual Press (Model 4386) at 180°C and 10 bar for 5 min.

Filler and Composite Characterization

SEM images were obtained using FEI VERSA 3D. XRD was performed by Ultima IV X-RAY DIFFRACTOMETER. TGA was conducted using Discovery TGA under nitrogen atmosphere at a heating rate of 10 ℃/min and temperature range of 25 ℃ -700℃. DSC was done using Q2000 DSC at a heating and a cooling rate of 10 ℃/min and temperature range of 25 ℃ - 200 ℃. The thermal conductivity (λ) at room temperature were obtained using LINSEIS LFA 500.

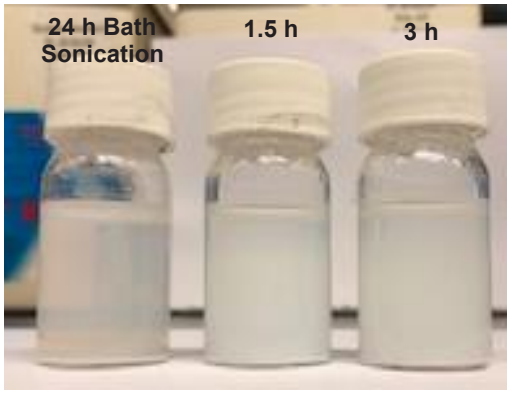

Fig. 1: h-BNNS6 stability (1 week) prepared by liquid exfoliation (24 h of bath sonication) and by BM for 1.5 and 3 hours.

III. Results and discussions

The yield of h-BNNS6 (h-BNNS exfoliated from h-BN6) was surprisingly high, ranging from 38 % at 0.5 h to 61 % at 4.5 h. The high yield in this work, however at shorter milling time, is comparable to the reported yield of BM (Lee et al., 2015)(Mochalin et al., 2015)(Posudievsky et al., 2016). Also, the yield was much higher than h-BNNS yield prepared by liquid exfoliation (Zhang et al., 2017). Moreover, h-BNNS6 exhibited high stability in aqueous solution, appearing as a milky solution in Fig. 1. In contrast, h-BNNS prepared by 24 hours of bath sonication, liquid exfoliation, showed poor stability as the result of incomplete exfoliation.

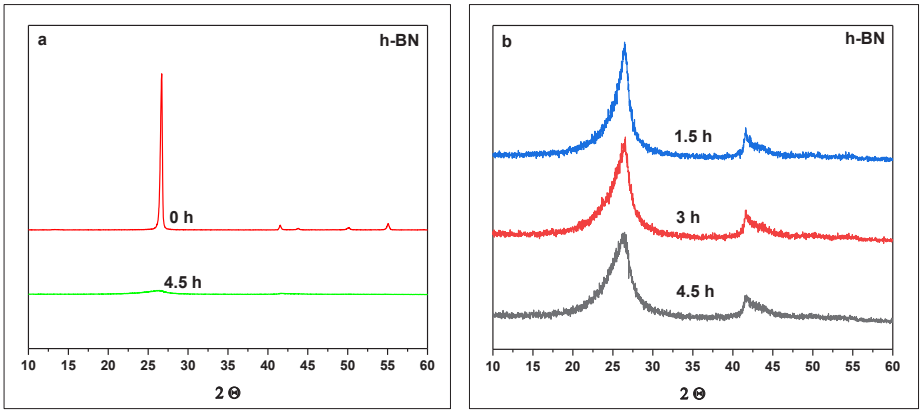

Fig. 2: XRD spectra of bulk h-BN (0 h) and h-BN milled for 1.5 h, 3 h, and 4.5 h.

The XRD patterns of bulk h-BN6 (0 h), as well as h-BN6 milled for several durations are shown in Fig. 2. The pattern of bulk h-BN6 exhibits peaks at 2θ of 26.66, 41.7, 43.9, 50.2, and 55.4º, which corresponds to the (002), (100), (101), (102), and (004) planes, respectively (Namba et al., 2019). These peaks have significantly diminished or disappeared with increasing milling time. Also, clear reduction in the (002) peak intensity was observed when milling time was increased from 0.5 to 1.5 h. However, no significant reduction in intensity was observed for milling beyond 1.5 h, i.e. at 3 or 4.5 h, suggesting that most h-BNNSs were formed at or below 1.5 h. In addition, the (002) peak was broader and shifted to the left as the milling time increases. Compared to the bulk h-BN6, milled h-BN6 exhibited higher d-spacing and FWHM. For example, the d-spacing and FWHM increased from 3.341 and 0.274 for bulk h-BN6 (0 h) to 3.389 and 3.526 for h-BN6 4.5 h, respectively. Moreover, the average crystallite sizes of h-BN6-

0h and h-BN6-4.5 h were found to be ~29 nm and 2.3 nm as calculated by Scherrer's equation (Monshi et al., 2012). Furthermore, the average number of layers was significantly reduced from 90 for bulk h-BN6 to 7 for BN6-4.5 h.

Fig. 3 (a-d) shows the SEM images of h-BN6 before and after BM. Bulk h-BN6 appears as agglomerated sheets of different particle sizes with an average of ~ 4-6 µm. Clearly, the average particle size decreased significantly with milling time and the average particle size of h-BN6-0.5 h was similar to the pristine h-BN6, however at 1.5 and 3 h, the average particle size dropped drastically to < 500 nm accompanied by the reduction in the sheet thickness as indication of h-BN exfoliation. As confirmed by XRD, yield, and stability results, the average particle size demonstrated no variation between h-BN6-1.5 h and h-BN6-3 h, suggesting sufficient exfoliation at 1.5 h. As a result, 1.5 h was selected as the optimum time for h-BNNS production.

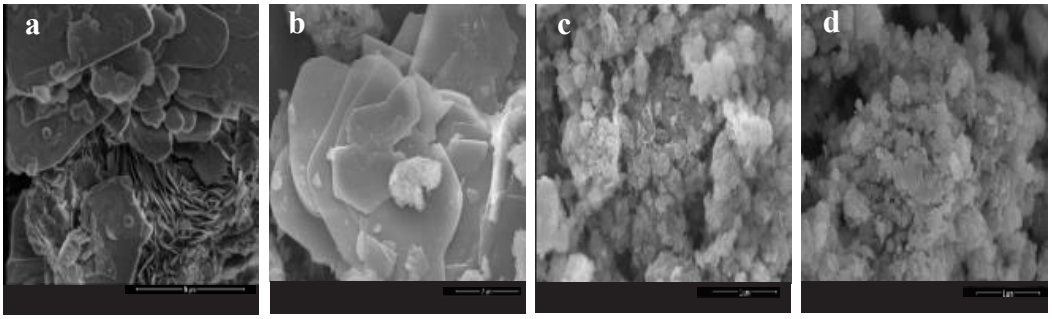

Fig. 3: SEM images of bulk h-BN6 and h-BN6 milled for various hours. (a) Bulk h-BN6 (0 h), (b) 0.5 h, (c) 1.5 h, and (d) 3 h.

The reduction in the h-BN particle size during milling was associated with appearance of asymmetrical XRD peaks. Peak asymmetry is frequently reported in BM treatment and it is attributed to defects and amorphizations (Huang et al., 2000)(Evin et al., 2014)(Evin et al., 2015). Therefore, large particle h-BN (h-BN35) was used to further study the defects and amophization during ball milling. In addition, LLDPE powder was mixed with h-BN35 in a ratio of 1 to 4 prior to BM to alleviate the BM induced stresses. Milled h-BN35 in the absence and presence of LLDPE were labeled as BMD-BN35 and BMD-BN35/LLDPE, respectively.

The dispersion of hBN-35, BMD-hBN35, and BMD-hBN35/LLDPE in LLDPE was examined using SEM and the results are shown in Fig. 4 (c) for composites containing 30 vol.% filler. The mixing of h-BN with LLDPE before ball milling has clearly improved the dispersion of h-BN in the LLDPE matrix compared to the composites prepared by direct melt blending with hBN35 (Fig 4.a) or melt blending of BMD-hBN35 with LLDPE (Fig 4.b).

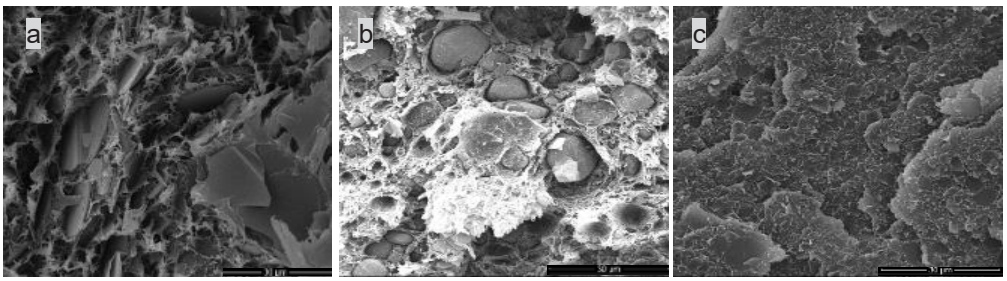

Fig. 4: SEM images of 30 vol. % h-BN35/PE composites. Bulk h-BN (a) and h-BN milled in the absence (a) and presence (b) of LLDPE.

Moreover, this enhanced dispersion has led to improved thermal conductivity and mechanical properties as shown in Table 1.

Table 1: effect of hBN type on the properties of hBN-LLDPE composite properties

	Pure LLDPE	LLDPE composite with 22.5 vol.% of		
		hBN35	BMD-hBN35	BMD-hBN35/LLDPE
Thermal Conductivity, W/m.K	0.269	0.805	0.737	1.31
Yield Stress, MPa	8.2	13.4	13.1	18.5
Young Modulus, MPa	319	924	731	2216
Elongation at Break, %	643	3.3	13.8	8.1

IV. Conclusions

h-BNNS was successfully produced by BM exfoliation of hBN with high yield and nano-crystallite sizes, but suffered from agglomeration and presence of structural defects. Nevertheless, incorporation of LLDPE during the ball milling exfoliation has reduced the structural defects and was extremely beneficial to the enhancement of thermal conductivity and mechanical properties. Finally, nanocomposites of LLDP with 30 vol.% hBNNS exhibited over 450% increase in thermal conductivity, over 124% increase in yield strength, and over 590% increase in modulus.

Acknowledgements

This publication was made possible by a NPRP award [NPRP # 10-0205-170349] from the Qatar National Research Fund (a member of Qatar Foundation). The statements made herein are solely the responsibility of the authors. The authors would like to acknowledge Dr. Said Mansour the Director of the Imaging and Characterization at Qatar Environmental and Energy Research Institute (QEERI) and his technical team for the support with SEM analysis.

References

Alhaj, M., Mohammed, S., Darwish, M., Hassan, A., 2017. A review of Qatar ' s water resources , consumption and virtual water trade. Desalin. Water Treat. 70, 70–85. https://doi.org/10.5004/dwt.2017.21246

Ding, J., Zhao, H., Yu, H., 2018. High-yield synthesis of extremely high concentrated and few-layered boron nitride nanosheet dispersions High-yield synthesis of extremely high concentrated and few-layered boron nitride nanosheet dispersions. 2D Mater. 5, 045015–045021.

Evin, E., Aksoy, M., E.EVİN, GÜLER, Ö., 2014. The effect of milling parameters on synthesis of high yield boron nitride nanotube. Journals Optoelectron. Adv. Mater. 16, 831–836.

Evin, E., Selen, V., GÜLER, S.H., SELEN, V., YARDIMCI, S., KELEŞ, A., 2015. Synthesis of C-BN hybride nano structures. J. Optoeletronics Adv. Mater. 17, 795–798.

Huang, J.Y., Yasuda, H., Mori, H., 2000. HRTEM and EELS Studies on the Amorphization of Hexagonal Boron Nitride Induced by Ball Milling. J. Am. Ceram. Soc. 83, 403–409.

Ko, W.Y., Chen, C.Y., Chen, W.H., Lin, K.J., 2016. Fabrication of Hexagonal Boron Nitride Nanosheets by Using a Simple Thermal Exfoliation Process. J. Chinese Chem. Soc. 63, 303–307. https://doi.org/10.1002/jccs.201500335

Lee, D., Lee, B., Park, K.H., Ryu, H.J., Jeon, S., Hong, S.H., 2015. Scalable exfoliation process for highly soluble boron nitride nanoplatelets by hydroxide-assisted ball milling. Nano Lett. 15, 1238–1244. https://doi.org/10.1021/nl504397h

Meng, J., Tajaddod, N., Cranford, S.W., Minus, M.L., 2015. Polyethylene-Assisted Exfoliation of Hexagonal Boron Nitride in Composite Fibers: A Combined Experimental and Computational Study. Macromol. Chem. Phys. 216, 847–855.

Mochalin, V.N., Liu, D., Qin, S., Gogotsi, Y., Lei, W., Chen, Y., 2015. Boron nitride colloidal solutions, ultralight aerogels and freestanding membranes through one-step exfoliation and functionalization. Nat. Commun. 6, 1–8. https://doi.org/10.1038/ncomms9849

Monshi, A., Foroughi, M.R., Monshi, M.R., 2012. Modified Scherrer Equation to Estimate More Accurately Nano-Crystallite Size Using XRD. World J. Nano Sci. Eng. 02, 154–160. https://doi.org/10.4236/wjnse.2012.23020

Posudievsky, O.Y., Khazieieva, O.A., Cherepanov, V. V, Dovbeshko, G.I., And, V.G.K., Pokhodenkoa, V.D., 2016. Efficient dispersant-free liquid exfoliation down to the graphene-like state of solvent-free mechanochemically delaminated bulk hexagonal boron nitride. RSC Adv. 6, 47112–47119. https://doi.org/10.1039/c6ra08312a

Rahman, H., Zaidi, S.J., 2018. Desalination in Qatar : Present Status and Future Prospects. Civ. Eng. Res. J. 6, 555700–555707. https://doi.org/10.19080/CERJ.2018.06.555700

Shoichiro Namba, Atsushi Takagaki, Keiko Jimura, Shigenobu Hayashi, R.K. a and S.T.O., 2019. Effects of ball-milling treatment on physicochemical properties and solid base activity of hexagonal boron nitrides. Catal. Sci. Technol. 9, 302–309. https://doi.org/10.1039/c8cy00940f

Wang, X., Yang, Y., Jiang, G., Yuan, Z., Yuan, S., 2018. A facile synthesis of boron nitride nanosheets and their potential application in dye adsorption. Diam. Relat. Mater. 81, 89–95. https://doi.org/10.1016/j.diamond.2017.11.012

Zhang, B., Wu, Q., Yu, H., Bulin, C., Sun, H., Li, R., Ge, X., Xing, R., 2017. High-Efficient Liquid Exfoliation of Boron Nitride Nanosheets Using Aqueous Solution of Alkanolamine. Nanoscale Res. Lett. 12, 596. https://doi.org/10.1186/s11671-017-2366-4

Sustainable energy use and decarbonization potential in the Hungarian residential building sector

[1*]Tamas Palvolgyi [1*]Attila Buzasi
[1] Budapest University of Technology and Economics, Faculty of Economic and Social Sciences, Department of Environmental Economics, Magyar tudósok krt. 2., Budapest, H-1117, Hungary

* E-mails: palvol@eik.bme.hu, buzasi@eik.bme.hu

Abstract
The residential buildings form a crucial sector of climate change mitigation in Hungary. Household heating is responsible for almost 25% of the overall CO_2 emissions and represents significant potential for future emission reductions. The primary objective of the paper is to identify the long term tendencies and future perspectives of decarbonization of household's heating energy use in Hungary. Methodology for spatial and temporal analysis of GHG emissions from household heating is developed; moreover, the essential characteristics of the residential building stock and structure of household heating fuel use are summarized. The comparative analyses of carbon-intensity of the household's heating among the EU member states are presented as well. The paper provides a detailed assessment of energy use and CO_2 emissions related to district heating of multi-dwelling residential buildings and heating fuel mix in detached houses, separately. Driving factors (such as fuel switch, energy efficiency improvements, housing's retrofit) in historical emission reductions are identified, as well as future decarbonization potentials and options in household heating are estimated. Results suggest that significant CO_2 emission reduction has been realized in heat production and district heating consumption and moderate future decarbonization potential can be expected. Nevertheless, in the case of detached houses (more than 2 million in Hungary), the primary source of decarbonization is the fuel switch to solid biofuel (fuelwood), and emission reduction options in housing energy efficiency improvement are still not adequately exploited. Finally, the paper focuses on the sustainability context of fuelwood use in household's heating, especially in rural regions, since fuelwood use leads to local air quality problems and related respiratory health risks. Furthermore, fuelwood use is strongly interlinked with energy poverty and other social circumstances. Concluding remarks and suggestions are summarized to achieve sustainable energy use.

Keywords: residential buildings, decarbonization potential, sustainable energy use

I. Introduction

Hungary, as an EU member state has committed to achieve significant CO_2 emission reduction by 2030 and full carbon neutrality by 2050 (National Energy Strategy of Hungary, 2020). It is known that the household's energy use is one of the leading causes of climate change. There is strong consensus that the residential sector has significant mitigation potential (Bai et al., 2018) by implementing energy efficiency measures, especially in developing and emerging economics (Miao et al., 2019; Serrano et al., 2017). Almost 3,4 million dwellings (which of 60% are single family houses) represents cca. 25% of total CO_2 emissions in Hungary. According to recent studies (Csoknyai et al., 2019; Novikova et al., 2018; Pombo et al., 2016) and policy documents (National Energy and Climate Plan of Hungary, 2018) dwelling's energy retrofit may lead to significant reduction of heating energy use and related CO_2 emissions. Our research aim is to identify the main drivers, trends in decarbonization of household's heating energy use in Hungary

II. Methodology and analysis

The methodology for spatial and temporal analysis of GHG emissions from household heating is based on the energy-related residential building's typology (Table 1.). According to the characteristics of national residential building stock (see in Table 1), the use of natural gas and fuelwood in the residential sector and district heating of multifamily houses represents more than 96% of the dwellings.

Table 1. Proportion of dwellings by building's typology and heating energy sources in Hungary (2017)

heating energy sources	Single family houses	Multi family houses	
		multi dwellings	apartment blocks
natural gas only	*23.6%*	*18,9%*	*2,1%*
natural gas and fuel wood	*18,2%*	*6,1%*	
fuel wood only	*13,8%*	*0,3%*	
district heating	*1,1%*	*5%*	*10,6%*
others	*0,2%*	*0,1%*	

Source: Central Statistical Office, Hungary
Note: other energy source: electricity, coal, oil

The evaluation methodology is based on the following steps:
(a) Comparative analyses of carbon-intensity of the household's heating among the EU member states.

(b) Long term tendency analysis of CO_2 emissions from the residential sector's heating fuel mix.

(c) Identification of driving factors (such as fuel switch, energy efficiency improvements, housing's retrofit) in historical emission.

d) Determination of future decarbonization potentials and options in household heating.

The primary sources of information of our study were the databases of annual energy balances and CO_2 emissions produced by Eurostat[1]. Additional CO_2 related data (i.e., emission factors) were given from the UNFCCC National Inventory Report of Hungary[2]. Household and energy statistics of the Central Statistical Office of Hungary were also used.

General description of residential building stock in Hungary

The residential building stock in Hungary has been measured and evaluated during the development of the National Building Energy Performance Strategy of Hungary by many Hungarian researchers (Csoknyai et al., 2016; Hrabovszky-Horváth et al., 2013). The elaborated building typology distinguishes 15 different types of residential buildings based on their building technology, structure, and date. These 15 building types cover the whole Hungarian residential building sector appropriately and get the chance to evaluate detailed analyses regarding their energy efficiency-related issues and to make further renovation-oriented recommendations.

According to this typology, the largest share of residential buildings is related to family houses with more than 80m^2 floor areas built in the Soviet era from 1946 to 1980, with almost 20% proportion of the total number of buildings. The energy demand for heating in the case of these buildings is relatively high: an average 250 kWh/m^2 energy needs yearly to heat the completely energy-inefficient buildings. Most dwellings in Hungary was built from 1946 to 1990, with a considerable amount of housing stocks (multi-flat buildings, built with industrialized technology). These housing estates have a tremendous potential of decarbonization since their net energy need for heating is appr. 150 kWh/m^2 yearly, moreover the average energy efficiency of these flats is decreasing sharply. The total energy need for heating concerning before mentioned two most relevant building types is almost 130 PJ/year, which represents cca. 50% of the total energy need for heating of residential buildings in Hungary. The third most relevant residential building type is family houses built before World War II with a considerable amount of energy need for heating. 13% of the total number of Hungarian residential buildings was built in this era; however, the total primary energy need for heating exceed 300 kWh/m^2 yearly, which represents a large share of total energy needs compared to other types of residential buildings.

III. Results and discussions

Recently, the proportion of household's heating in total CO_2 emissions has been stagnated at 13 % (8.3 million tonnes/year) based on weather corrected residential heating energy uses. Fig.1 compares the per capita household's heating-related CO_2 emissions among the EU Member States. Relatively high per capita value of Hungary can partially be explained by continental climate (i.e., severe winters) of the Carpathian Basin. Another important reason is the obsolete residential building's stock. According to the most recent information (National Energy Strategy of Hungary, 2020), more than 60% of the Hungarian residential buildings do not comply with the existing energy performance standards.

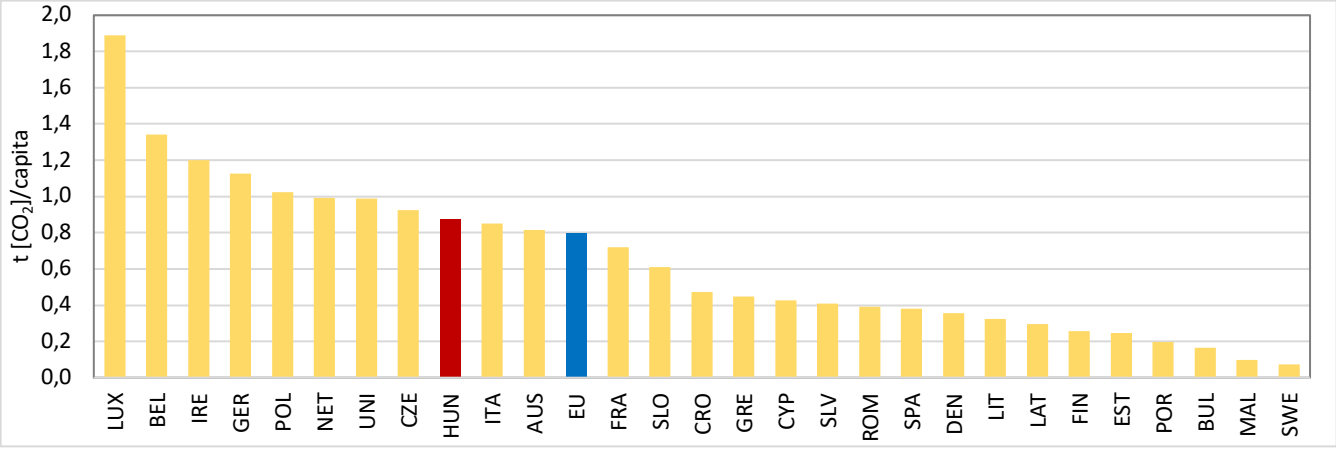

Fig. 1: Per capita CO_2 emissions of residential heating in EU member states (2017)

Certain countries (such as Croatia, Slovakia, Romania) having similar climatological conditions than Hungary can be attributed to significantly lower per capita residential CO_2 emissions. It highlights the importance of EU funded residential retrofit programs implemented in these countries.

Fig.2 presents the energy sources used in residential heating in Hungary. It is shown that the use of coal (lignite) and heating oil has almost ceased, which has led to reduce the CO_2 emissions by cca. 10 million tonnes/year

[1] http://ec.europa.eu/eurostat/web/energy/data/database
[2] https://unfccc.int/documents/194931

since 1990. However, no further potential in phasing out of coal and oil is expected.

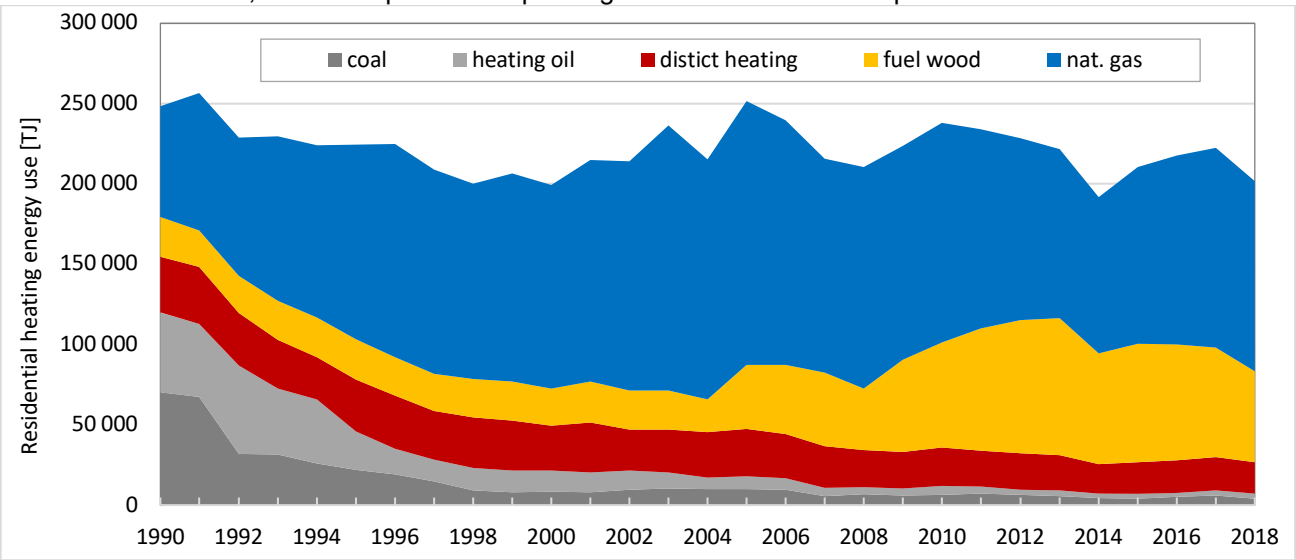

It should be noted that the use of fuelwood has been triplicated for the early 2010s. The spread of fuelwood in residential heating is a crucial factor in decarbonization, which gives almost 2.5 million tonnes/year savings in CO_2 emissions since 1990. Almost 80% of the residential heating-related CO_2 emissions are coming from the use of natural gas in single- and multi-family houses; therefore, this energy source forms the primary driver of CO_2 emissions from the residential sector. Although a slightly decreasing tendency is shown up in residential consumption of natural gas, a more intensive drop should be expected, mainly due to the fuel switch (from natural gas to fuelwood) that happened in the last decade. This reconfirms that penetration of building retrofit programs aiming at energy efficiency improvement in residential buildings is still insufficient.

District heating

As it is shown in Fig.3., the overall district heating energy use has significantly reduced (by 2,5%/year on average) since the late 1990s. Almost two-thirds of this reduction is attributed to modernization of production and distribution of district heating, as well as successful retrofit programs in apartment blocks.

It is a definite tendency that the coal and oil energy sources have practically been disappeared from the district heating energy mix. In parallel, the ratio of natural gas is stabilized at a high level of 75-80%, which means severe import dependency and high vulnerability in energy security of supply. The ratio of renewable energy sources in heat production in 2018 is only 18% in Hungary, while the EU average is 32% Due the growing biomass (fuelwood) prices and the high investment cost in geothermal installations the fuel switch to biomass and geothermal energy sources is relatively slow (the growth rate in renewables ratio is less than 2%/year).

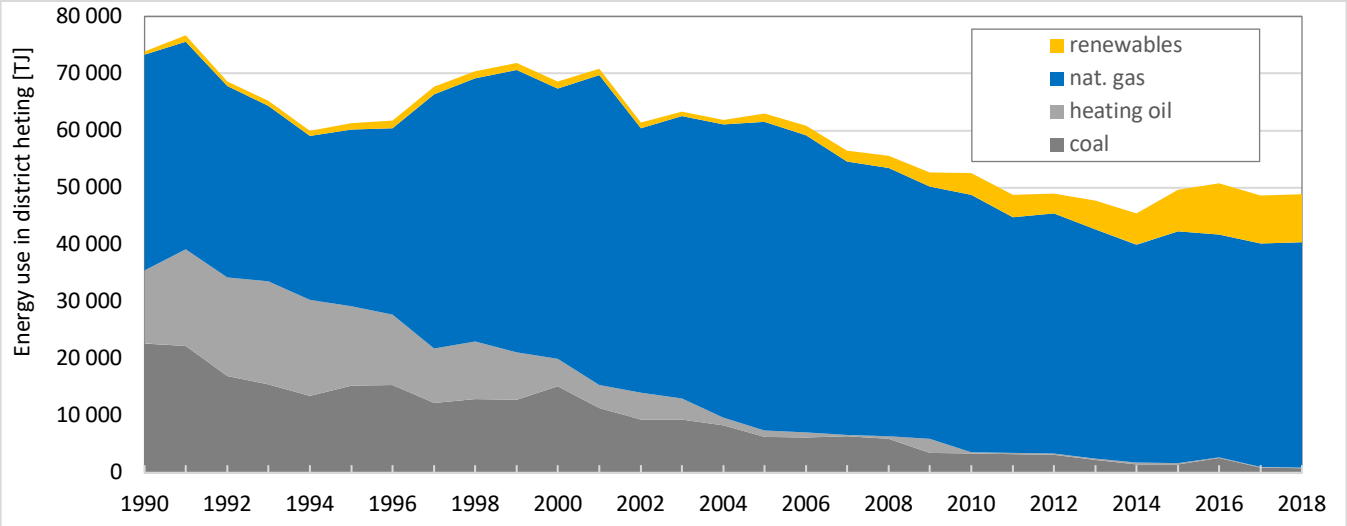

Fig. 3: Energy sources of district heating Hungary
(Note: renewables are consisting of biomass and geothermal energy use. Heat generation from nuclear source is neglected.)

The main driving force of decarbonization already realized in the district heating sector was the switch from coal and oil to natural gas, which has resulted in 3.6 million tonnes/year savings in CO_2 emissions. The energy efficiency improvements in energy infrastructure and building retrofits in apartment blocks have also brought 0.9 million tonnes/year CO_2 emission reductions.

V. Conclusions

Based on the previously introduced results, main conclusions can be highlighted in the followings. Firstly, it can be stated that there is undeniable high decarbonization potential in residential building's retrofit. According to our estimation, if 30% of the residential building stocks would be renovated (with an average energy savings of 50% per dwellings), it would enable an additional 1 million tonnes/year CO_2 reductions. Secondly, the high ratio of fuelwood (cca. 30%) in the household's heating makes it likely that it could not grow in the future; therefore, no further decarbonization potential may be exploited. Additionally, reduction in the use of natural gas in thermal power stations by 50% would lead to an additional 1.1 million tonnes/year CO_2 emission savings. Finally, further reduce in district heating demand may be reached by an extended building's renovation program in the apartment blocks. If the relevant target values of the National Building Performance Strategy of Hungary were reached, an additional 0,9 million tonnes/year CO_2 reduction could be realized.

Besides the general conclusions, it is worth mentioning that previously introduced spread of the use of fuelwood in residential heating cause serious sustainability challenges. First of all, it shall be noted that biomass production with agricultural techniques requires a tremendous amount of energy, pesticides, and fertilizers to ensure economic profitability. Extensive monocultural biomass production is facing several sustainability-related issues due to its adverse effects in terms of soil and groundwater degradation and the potential collapse of surrounding ecosystems. From a social point of view, increasing air pollution due to ineffective and insecure use of biomass for residential heating is a continually worsening issue, especially in the poorest rural regions in Hungary. Additionally, energy poverty, lack of financial sources, and appropriate heating technology are all increasing sustainability challenges due to decreasing well-being. Finally, rising PM_{10} concentration contributes to worsening respiratory and cardiovascular diseases in the less developed north-eastern regions of Hungary, posing these areas as the most polluted ones in the EU-28.

Acknowledgements

The research reported in this paper was supported by the Higher Education Excellence Program of the Ministry of Human Capacities in the frame of the Water sciences & Disaster Prevention research area of the Budapest University of Technology and Economics (BME FIKP-VÍZ).

References

Bai, X., Dawson, R.J., Ürge-Vorsatz, D., Delgado, G.C., Salisu Barau, A., Dhakal, S., Dodman, D., Leonardsen, L., Masson-Delmotte, V., Roberts, D.C., Schultz, S., 2018. Six research priorities for cities and climate change. Nature 555, 23–25. https://doi.org/10.1038/d41586-018-02409-z

Csoknyai, T., Hrabovszky-horváth, S., Georgiev, Z., 2016. Building stock characteristics and energy performance of residential buildings in Eastern-European countries. Energy Build. 132, 39–52. https://doi.org/10.1016/j.enbuild.2016.06.062

Csoknyai, T., Legardeur, J., Akle, A.A., Horváth, M., 2019. Analysis of energy consumption profiles in residential buildings and impact assessment of a serious game on occupants' behavior. Energy Build. 196, 1–20. https://doi.org/10.1016/j.enbuild.2019.05.009

Hrabovszky-horváth, S., Pálvölgyi, T., Csoknyai, T., Talamon, A., 2013. Generalized residential building typology for urban climate change mitigation and adaptation strategies : The case of Hungary. Energy Build. 62, 475–485. https://doi.org/10.1016/j.enbuild.2013.03.011

Miao, L., Gu, H., Zhang, X., Zhen, W., Wang, M., 2019. Factors causing regional differences in China's residential CO2 emissions—evidence from provincial data. J. Clean. Prod. 224, 852–863. https://doi.org/10.1016/j.jclepro.2019.03.271

National Building Energy Performance Strategy of Hungary, 2015. Available online: https://ec.europa.eu/energy/sites/ener/files/documents/2014_article4_hungary_en%20translation.pdf

National Energy and Climate Plan of Hungary, 2019. Draft version, online available: https://ec.europa.eu/energy/sites/ener/files/documents/ec_courtesy_translation_hu_necp.pdf

National Energy Strategy of Hungary, 2020. Online available in Hungarian: https://www.kormany.hu/download/b/40/c1000/Stratégiák_20200116.zip

Novikova, A., Csoknyai, T., Szalay, Z., 2018. Low carbon scenarios for higher thermal comfort in the residential building sector of South Eastern Europe. Energy Effic. 11, 845–875. https://doi.org/10.1007/s12053-017-9604-6

Pombo, O., Allacker, K., Rivela, B., Neila, J., 2016. Sustainability assessment of energy saving measures: A multi-criteria approach for residential buildings retrofitting - A case study of the Spanish housing stock. Energy Build. 116, 384–394. https://doi.org/10.1016/j.enbuild.2016.01.019

Serrano, S., Ürge-Vorsatz, D., Barreneche, C., Palacios, A., Cabeza, L.F., 2017. Heating and cooling energy trends and drivers in Europe. Energy 119, 425–434. https://doi.org/10.1016/j.energy.2016.12.080

Sintering Inhibitors of Iron Powder Particles used for Hydrogen Production

[1*]Fotouh Al-Ragom
[1] Kuwait Institute for Scientific Research, Jamal Abdul Nasser Street, Safat, 13109, Kuwait

* E-mail: fragom@kisr.edu.kw

Abstract
Thermochemical hydrogen production utilizing iron reduction oxidization (Redox) reactions is a promising high-efficiency route to renewable fuels. This work considers oxidation of iron by steam to produce hydrogen using a fluidized bed reactor. The oxidation of fluidized iron powder results in sintering and deactivation. Sintering adversely affects the hydrogen production process and inhibits the recycling of the iron/iron oxide. Therefore, an investigation has been taken to develop a way to hinder sintering during repeated Redox cycles so that the reactivity of the iron powder remains stable for hydrogen production in solar thermochemical reactors.
Elemental iron is used for experimental investigations. A laboratory testing facility is constructed. Bed temperature varied between 630 – 970°C and the steam mass flow rate is 2 g/min. To inhibit sintering, crystalline, and amorphous silica are utilized. The incorporation of inhibitors within the iron sample involved mixing the iron powder with silica. Mixing iron with silica hinders the sintering but reduces the hydrogen yield. Mixing iron with crystalline silica with apparent volume fraction to 0.5, 0.67, and 0.75 reduces the hydrogen yield compared to pure iron by 25%, 34% and 47%, respectively for silica particle size of 200-300 µm. Mixing iron with amorphous silica reduces the hydrogen yield by 19% and 6%, as compared to pure iron, for iron (0-250 µm) and (125-355 µm) particle size distribution respectively. The hydrogen production rate for Iron/amorphous silica mixtures surpassed that of the crystalline silica.

Keywords: Redox, sintering, hydrogen, water splitting.

I. Introduction

Hydrogen is abundantly available in the universe in its non-elemental form due to its reactivity. Sources for hydrogen include water and hydrocarbons. To recover hydrogen from its available resources, various methods are developed. Some of these methods are commercially available such as Steam methane reforming (SMR), and others are still in research and development. In 2018 about 95% of Hydrogen was produced by SMR, methane partial oxidation, and coal gasification. In 2019, it was reported that 70 million tons of hydrogen are being produced and used in several applications including ammonia and ethanol production, oil refining and transportation fuel (David, 2018 and Ogden, 1999). Recently interest in hydrogen as an energy carrier and feedstock increased as a solution for decarbonization. In countries where solar energy is abundant and because of the decline in the cost of solar energy technologies, green hydrogen (hydrogen produced by using renewable energy) is being evaluated and several projects and feasibility studies are being conducted. Other countries are going through a transitional stage in which blue hydrogen production is being considered or even actually generated (Gielen et al., 2019). It is anticipated that in 2024, the global hydrogen market will reach USD191.8 billion with a total production volume of 122.58 million tonnes (GlobeNewswire, 2020).
Direct thermal water splitting requires very high temperatures, around 2227°C (2500 K), to dissociate water into H_2 and O_2. Thermochemical water splitting (TCWS) through secondary reactions of reactive metals/metal oxides enables water splitting at lower temperatures (Neises et al., 2008). This method can split water to its elemental constituents', hydrogen and oxygen, through Reduction and Oxidation (REDOX) cycles of some reactive metals/metals' oxides. But this method faces several challenges including, material stability issues, hazardous or corrosive reactants, and/or products that necessitate the need for materials that can withstand corrosive environments and high temperatures of 1000 °C (Abanades, 2019 and Hossain, 2019). The high temperature required for REDOX cycles can be either provided by utilizing nuclear energy or renewable energy sources. The latter can provide a pathway for green hydrogen production.
TCWS cycles have the potential to deliver overall system efficiencies over 40% (T-Raissi, 2003). Various thermochemical cycles can be used to split water and ultimately produce hydrogen. Over 350 cycles are identified (Charvin et al., 2006). Abanades et al. screened water splitting cycles available in the literature that are suitable for utilization with solar energy. They have established a database for 280 cycles. Based on set criteria and with an objective to reduce the number of cycles to a manageable number, accordingly, 30 solar-driven water-splitting thermochemical cycles are identified. In general, the TCWS cycles are represented by the following equations:

$$MO_{oxidized} \rightarrow MO_{reduced} + O_2 \quad \text{Reduction Step} \quad (1)$$

$$MO_{reduced} + H_2O \rightarrow MO_{oxidized} + H_2 \quad \text{Oxidation Step} \quad (2)$$

M refers to the used metal, and MO refers to the corresponding metal oxide. The first step, reduction, represents the solar dissociation of the metal oxide to a lower-valence metal oxide or elemental metal. The second step is an exothermic hydrolysis reaction with a metal in which H_2 is liberated, and a corresponding metal oxide is formed (Steinfeld, 2002 and DOE, 2007). Both steps require high temperatures, usually 227°C (500 K), depending on the reactive metal.

Several cycles were thermodynamically examined and tested in solar reactors, including zinc and its oxides (ZnO/Zn) and iron oxide (Fe_3O_4/FeO) redox pairs. Other redox pairs such as titanium oxide (TiO/TiOx), Cobalt Oxide (Co_3O_4/CoO), and Manganese Oxide Mn_3O_4/MnO (Kreider et al., 2011) have been considered, but the yield of hydrogen production is too low (Steinfeld, 2002). Of particular interest is non-volatile iron oxide redox pairs (Fe_3O_4/FeO). Iron oxides are widely available, cheap, non-toxic and can provide high pure hydrogen yield. The TCWS using iron oxides can be realized through the following reactions:

$$Fe_3O_4 \rightarrow 3Fe + 2O_2 \quad (3)$$

$$3Fe + 4H_2O \rightarrow Fe_3O_4 + 4H_2 \quad (4)$$

Iron oxide used in the TCWS can be in various forms and structures, including powder, rod, and monolithic structure. The powder can be used either in a fixed or a fluidized bed reactor. The latter can provide higher reactivity, hence more hydrogen yield. Yet this method is faced with the challenge of the iron powder particles sintering (Cohesion) that can hinder the particle's fluidization and hydrogen yield in the repetitive reactions' cycles.
The research described in this paper discusses the possibility of using silica (crystalline and amorphous) as sintering inhibitors.

II. Experimental Procedure/Methodology/System Description

An experimental testing facility was developed to investigate the reactivity of the various iron/sintering inhibitor powders combinations. The experimental facility diagram is shown in Fig.1.

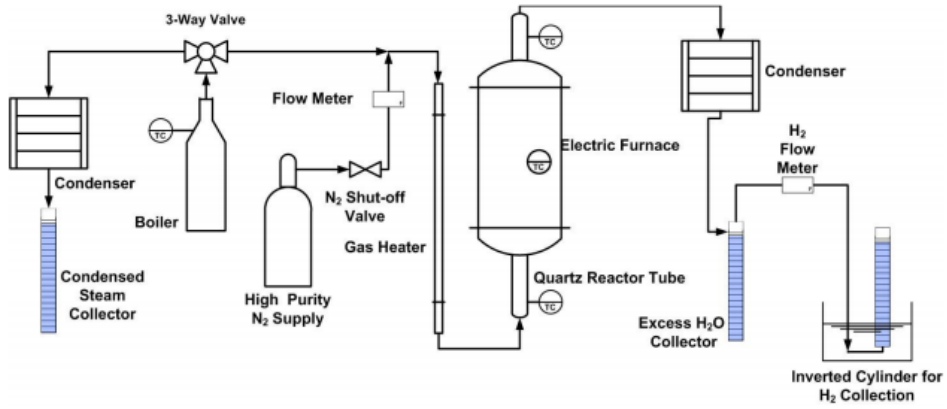

Fig.1 Experimental hydrogen production facility.

The powder is placed in a quartz tube in an electrical furnace and supported by a distributor made of a ceramic thermal insulation material that can withstand temperatures up to 1650 °C. The powder is then fluidized by superheated steam, which is partially used for hydrogen production. The outlet gas from the reactor is directed through a condenser, in which excess steam is condensed from the hydrogen gas flow. This condenser emptied into a sealed cylinder (water trap) to collect the condensate. The hydrogen gas is then directed into a flow meter and then to an inverted water-filled graduated cylinder where the rate of hydrogen production is recorded by a mass flow meter. The volume of hydrogen is visually logged by the amount of displaced water in the graduated cylinder at normal conditions NTP (Normal Temperature and Pressure; 20 °C and 101 kPa). Stainless-steel sheathed thermocouples are used to monitor and record the gas temperatures entering/exiting the quartz reactor chamber and the fluidized bed area.

For each set of tests, initial runs are conducted that included reacting fresh iron powder as a base case to compare against. The used iron powder is 99.56% pure and porous, with a mean particle size of 98 μm and a wide particle size distribution (0-250 μm). Each sample included 25 g (9 mL) of iron powder. To inhibit sintering silica, both crystalline and amorphous are used. Crystalline Silica (SiO_2) is regarded as an effective anti-sintering agent (Olsen, 1986).
Crystalline silica in the iron/silica mixture apparent volume fractions (Φ) is 0.33, 0.5, 0.67 and 0.75. The crystalline silica particle size distribution included three sets, 0-45 μm, 45-106 μm, and 200-300 μm. The amorphous silica in the iron/silica mixture represented 0.67 volume fraction, and iron particles (25 g) are separated into two sets 40-250 μm and 125-355 μm. The details of the experimental investigations are listed in Tables 1 and 2 for crystalline silica and amorphous silica respectively. The steam mass flow rate is set to 2 g/min in all experiments.

Table 1. Experiments for iron and crystalline silica mixture.

Experiment	Bed Temp. °C	Exp. Time Min	Sintering condition	Silica apparent volume fraction ϕ	SiO_2 Size µm	H_2 yield (20 min.) NL
Iron-1	652	28	S	-	-	7.6
Iron-2	871	35	S	-	-	12.6
Iron-silica-1	644	31	S	0.5	200-300	5.6
Iron-silica-2	642	33	S	0.5	200-300	5.8
Iron-silica-3	650	35	PS	0.67	200-300	5
Iron-silica-4	643	29	PS	0.75	200-300	4
Iron-silica-5	645	27	C	0.33	0-45	3.6
Iron-silica-6	632	57	S	0.33	0-45	3.7
Iron-silica-7	640	42	C	0.67	0-45	3.6
Iron-silica-8	961	23	S	0.67	45-106	6.2
Iron-silica-9	962	36	S	0.67	45-106	10.4
Iron-silica-10	968	26	S	0.67	45-106	8.5

S: Sintered (hard solid ≥ 95%), PS: Partially Sintered (hard solid < 95%), C: Clumped, soft, and can be easily restored to powder condition with minimum pressing.

Table 2. Experiments for iron and amorphous silica mixture.

Experiment	Bed. Temp. °C	Exp. Time Min	Sintering condition	H_2 yield (20 min.) NL
Iron-2	871	35	S	12.6
DE-0-250-1	854	35	C	10.0
DE-0-250-2-OX-1	845	35	C	11.0
DE-0-250-2-OX-2	900	36	C	4.1
DE-0-250-3	845	35	C	9.8
DE-125-355-1	857	35	C	11.4
DE-125-355-2	846	36	C	12.4

S: Sintered (hard solid ≥ 95%), PS: Partially Sintered (hard solid < 95%), C: Clumped, soft and can be easily restored to powder condition with minimum pressing. DE: Diatomaceous Earth.

III. Analysis

Ten experiments are conducted to evaluate the effectiveness of crystalline silica in hindering iron/iron oxide powder sintering.

Fig. 2 (left) displays the hydrogen yield for iron mixed with 200-300 µm silica powder with different silica (SiO_2) volume fractions with a set bed temperature of 650 °C. It is shown that the hydrogen yield decreases as the SiO_2 volume fraction is increased. Increasing the silica apparent volume fraction decreases the hydrogen yield. Increasing the silica apparent volume fraction to 0.5, 0.67, and 0.75 reduces the hydrogen yield compared to pure iron by 25%, 34% and 47%, respectively.

Fig.2 (middle) shows the hydrogen yield for iron (0-45 µm) and silica for various silica volume fractions at a set bed temperature of 650 °C. As observed, the hydrogen yield appears to be independent of silica volume fraction, although it is reduced by an average of 52% as compared with pure iron at 20 minutes of experiment time. It is believed that the smaller silica particles block the pores of the iron powder and inhibit sintering and hydrogen production. For Iron-silica-5 and Iron-silica-7, the powder clumps but does not sinter. Simple mechanical agitation is sufficient to break up the clumped powder. Fig.2 (right) shows the hydrogen yield for iron (45-104 µm) and silica with 0.67 volume fraction at temperatures over 900 °C (1173 K). It is found that the average hydrogen production yield over 20 minutes is about 0.03 $gH_2/g_{Fe,}$ and it reached 0.045 gH_2/g_{Fe} at 35 minutes.

From Fig.2, it is deduced that mixing iron with two different silica particle sizes (0-45 µm and 200-300 µm) at the same apparent volume fraction of 0.67 gives essentially the same hydrogen yield. In both cases, the average production yield over 30 minutes is 0.018 gH_2/g_{Fe}. Further investigations were carried out at higher temperatures

over 900 °C (1173 K). The operational conditions are included in Table 1. In all cases, the sample sinters after the reaction. The average hydrogen production yield over 20 minutes is about 0.03 g_{H2}/g_{Fe}. The maximum hydrogen production rate varied between 25-35 $Ncm^3/min/g_{Fe}$.

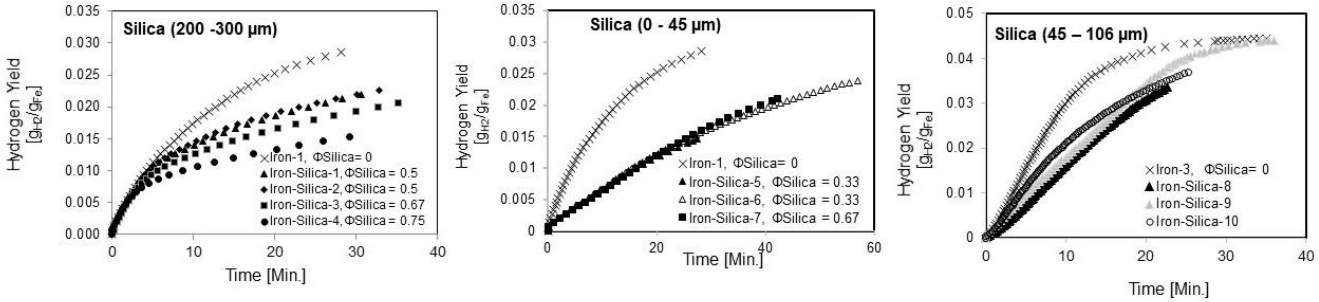

Fig.2 Hydrogen yield for mixed iron and silica with various silica volume fractions and particle size distribution at 650 °C (left and middle) and 960 °C (right).

Another type of silica was investigated, and that is amorphous silica, commonly known as diatomaceous earth. Diatomaceous earth (DE) is a naturally available silica source composed of skeletons of prehistoric plants, or diatoms, containing less than one percent crystalline silica. The DE has irregularly shaped diatoms; hence it is amorphous and exhibits a very small apparent density of 260 g/L and melts at 1700 °C (ILO and WHO, 2017). The operational conditions for iron and DE experiments are listed in Table 2. The experiments included using 25 g iron particles 0-250 µm and 125-355 µm mixed with DE with 0.67 volume fraction. One Redox cycle was carried out (DE-0-250-2-OX-1 and 2). The reduction cycle was carried out at a set bed temperature of 850 °C using carbon monoxide (CO) at 0.1 sLPM for 2:15 hours.

The maximum hydrogen production yield of iron/DE, as shown in Fig.3 (left), varied between 34-40 $Ncm^3/min/g_{Fe}$. This represents a 35% drop of that of the unmodified pure iron case for iron particle size of 0-250 µm. The production rate surpassed that of the crystalline silica that climaxed at 30 $Ncm^3/min.g_{Fe}$. The hydrogen production rate when diatomaceous earth is used as a sintering inhibitor was still lower than that for the unmodified iron (48 $Ncm^3/min/g_{Fe}$). Further analysis of the DE utilization with 125-355 µm iron revealed that the maximum hydrogen production yield of iron/DE, as shown in Fig.3 (middle), averaged 43% $Ncm^3/min.g_{Fe}$. The production rate surpassed that of the crystalline silica (30 $Ncm^3/min/g_{Fe}$). The hydrogen production rate was still lower than that for the unmodified iron (48 $Ncm^3/min/g_{Fe}$). Redox cycles were investigated. Two samples underwent a full Redox cycle. The hydrogen production rate for these experiments is shown in Fig.3 (right) DE-0-250-OX-1 and 2. The maximum hydrogen production rate was 40 $Ncm^3/min/g_{Fe}$ in the first oxidation step. In the second oxidation, the rate was 35 $Ncm^3/min/g_{Fe}$.

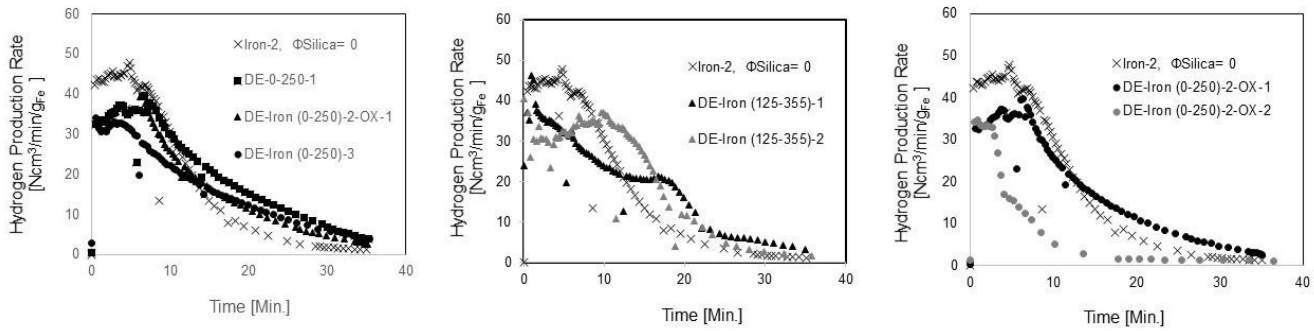

Fig.3 The rate of hydrogen production for Iron/DE Redox experiments (left and middle) and 960 °C (right).

IV. Results and discussions

Incorporating silica in the iron powder and mixing it in various volume fractions shows promising results in terms of hindering sintering in the oxidation step as compared to reacting pure iron powder. Sintering is found to be hindering hydrogen production in the repetitive REDOX cycles. Mixing iron with silica reduces the hydrogen yield in the first oxidation step, and this is mainly because the silica particles tend to clog some of the pores in the porous iron hence reducing the reactive surface area. Moreover, increasing the silica apparent volume fraction decreases the hydrogen

yield. When the crystalline silica apparent volume fraction varied between (0.5-0.75) the hydrogen yield reduced by (25% - 457%). In the case of the DE, amorphous silica, it is observed that the hydrogen yield appears to be independent of silica volume fraction, although it is reduced by a maximum of 19% compared with pure iron. It is believed that the smaller silica particles block the pores of the iron powder and inhibit sintering and hydrogen production. When the clumped DE/iron oxide sample was inspected, it was found that the DE particles cling to the surface of the iron particles preventing it from sintering, leading to soft clumping. When comparing the hydrogen production rate for the tested samples, it is noted that it is higher for the case when the iron is mixed with the amorphous silica as compared to the case of the crystalline silica and this might be attributed to the porosity for the amorphous silica.

V. Conclusions

Sintering can hinder hydrogen production in iron REDOX cycles. Sintering can be retarded if inhibitors are introduced to the iron/iron oxide powder. Silica, both crystalline and amorphous, were tested as sintering inhibitors in iron REDOX cycles for hydrogen production. Various iron/silica powder combinations were tested that included different silica volume fractions, iron particles distributions and silica type. The results of the tests show that using amorphous silica can yield a higher hydrogen rate as compared to crystalline silica. In the case of crystalline silica, the smaller the particle size and the less the volume fraction reduced the sintering of the iron/iron oxide. The utilization of silica as a sintering inhibitor can be further inspected to arrive at the optimum combination that can allow better hydrogen generation in repetitive iron REDOX cycles.

References

Abanades S., 2019. Metal Oxides Applied to Thermochemical Water-Splitting for Hydrogen Production Using Concentrated Solar Energy. Chemengineering. ChemEngineering 3, 63. doi:10.3390/chemengineering3030063doi:10.3390/chemengineering3030063.

Charvin, P., Abanades, S., Flamant, G., Neveu, P., and Lemort, F., 2006. Screening and testing of promising solar thermochemical water splitting cycles for hydrogen production. Proceedings of World Hydrogen Energy C.

David R., 2018. The “hydrogen economy” may be a thing after all. https://www.vox.com/energy-and-environment/2018/2/16/16926950/hydrogen-fuel-technology-economy-hytech-storage

Department of Energy (DOE), 2007. FY 2007 annual progress report. II.F Solar HiTemp Thermochemical Water Splitting DOE hydrogen program. http://www.hydrogen.energy.gov/annual_progress07.html.

Hossain, A., Sakthipandi, K., Ullah, A. K. M. Atique, Roy, S., 2019. Recent Progress and Approaches on Carbon-Free Energy from Water Splitting. Nano-Micro Letters 11:103. https://doi.org/10.1007/s40820-019-0335-4.

Gielen, D., Taibi, E., and Miranda, R., 2019. Hydrogen a renewable energy perspective. IRENA report prepared for the 2nd Hydrogen Energy Ministerial Meeting in Tokyo, Japan.

ILO and WHO, 2017. Diatomaceous earth (Uncalcined). 2012. http://www.inchem.org/documents/icsc/icsc/eics0248.htm

Kreider, P. B., Funke, H.H., Cuche,K., Schmidt, M.,Steinfeld, A., Weimer, A.w., 2011. Manganese oxide based thermochemical hydrogen production cycle. International Journal of Hydrogen Energy. 36, 7028-7037.

Neises, M, Roeb, M., Schmücker, M., Sattler, C., and Pitz-Paal, R., 2008. Kinetic Investigations of Two-Step thermochemical water s.plitting cycle using mixed iron oxides fixed on ceramic substrates. Proceedings of ES2008 Energy Sustainability, August 10-14.

Ogden, J.M., 1999. "Prospects for building a hydrogen energy infrastructure". Annual Review of Energy and the Environment. 24: 227–279.

Olsen, K., 1986. Mechanism of sintering inhibition in silica treated iron oxide recording particles. Journal of Magnetism and Magnetic Materials 54-57:1691-1692.

Steinfeld A., 2002. Solar hydrogen production via a two-step water splitting thermochemical cycle based on Zn/Zno redox reaction. International Journal of Hydrogen Energy. 27: 611-619.

T-Raissi, A., 2003. Analysis of solar thermochemical water splitting cycles for hydrogen production. Progress report, University of Central Florida.

Energy Saving in an Academic Instituion through Passive Daylighting Strategy

[1]Manju G Nair, [2]Aparna S, [3*]Abhilash Suryan, [4]Sandro Nizetic,
[1] Associate Professor and Head, Department of Architecture,
Rajiv Gandhi Institute of Technology, Kottayam, Kerala, India - 686501.
[2] Assistant Professor, Department of Architecture,
[3] Assistant Professor, Department of Mechanical Engineering,
College of Engineering, Trivandrum, 695016, India.
[4] Professor, LTEF- Laboratory for Thermodynamics and Energy Efficiency, Faculty of Electrical Engineering, Mechanical Engineering and Naval Architecture, University of Split, RudjeraBoskovica 32, 21000 Split, Croatia

* E-mail: suryan@cet.ac.in

Abstract
Passive daylighting strategies minimize artificial lighting resulting in a reduction in energy consumption of a building as well as the operating cost. Vernacular tropical architecture, with its focus on climate responsiveness, has always focussed on passive strategies of lighting and and thermal comfort. Techniques interpreted from vernacular strategies are widely used in building design in Kerala, as evidenced in the lighting interventions included in the design of the Department of Architecture, College of Engineering Trivandrum. However, owing to the unique terrain, there are design studios in the Ground-minus-one floor wherein there exists a shortage of natural daylighting. This paper focuses on the analysis and design recommendations for improving daylighting in spaces without access to typical passive lighting strategies.
A design studio room at the basement floor in the architecture department was taken for study in lighting levels. Simulation studies using IES Virtual Environment was done with the room at different times of the day. The daylighting level distribution within each part of the room was obtained. The daylighting levels were compared with the required light levels for the classroom. Though the design of the studio was ideal for thermal comfort, the lighting inside the classrooms was poor due to the orientation and the obstructions in the vicinity. The reduction in daylighting levels had to be supplemented to obtain good luminous comfort. As a passive daylighting strategy horizontal light pipes were proposed which provide outside daylighting to the interiors. The number and arrangement of light pipes were determined to have the optimum light intensity which can provide the required lighting level.
Keywords: Energy saving, Passive daylighting, Lightpipes.

I. Introduction

The tropics are the region of the Earth delimited in latitude by the Tropic of Cancer in the Northern Hemisphere and the Tropic of Capricorn in the south. Characterized by the sun passing directly overhead, this area around the equator receives more direct sunlight than any other region of the planet. Falling in Class A of Koppen's Climate classification, the tropical climate has a mean of above 18 degrees Centigrade all round the year. Generally hot and wet, the climate requires an architectural response of letting in light without the heat and wind without the rain.
Vernacular architecture is one that has evolved over centuries as a direct response to the place, including the climate, the culture and the geography. The typical climate responsive strategies adopted in tropical architecture features verandahs, courtyards, solar and rain shading, etc. (Arvind Krishan, 2014) Taking a detailed look at the passive lighting strategies followed, the most commonly used strategies are as illustrated below:

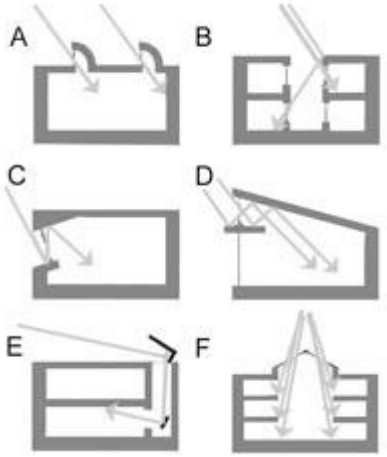

Fig. 1 Daylighting strategies

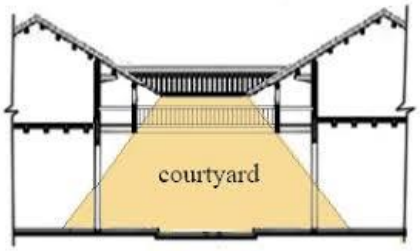

Fig. 2 Courtyard lighting

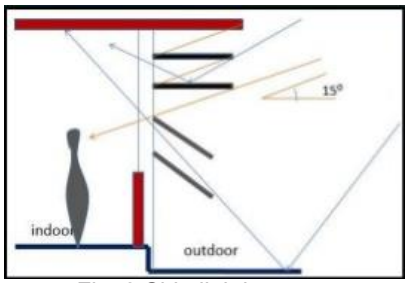

Fig. 3 Side lighting

Fig. 1 illustrates the typical lighting strategies adopted in tropical climates allowing for lighting without glare and heat (Thorpe, 2020), while Fig.2 shows the typical daylighting effect produced upon incorporating courtyards into the built form (Jie TAN, 2016). Figures 3 and 4 showcase the various sidelighting and toplighting strategies commonly adopted as stated by literature (Butera, 2014) (Kiamba, 2014)

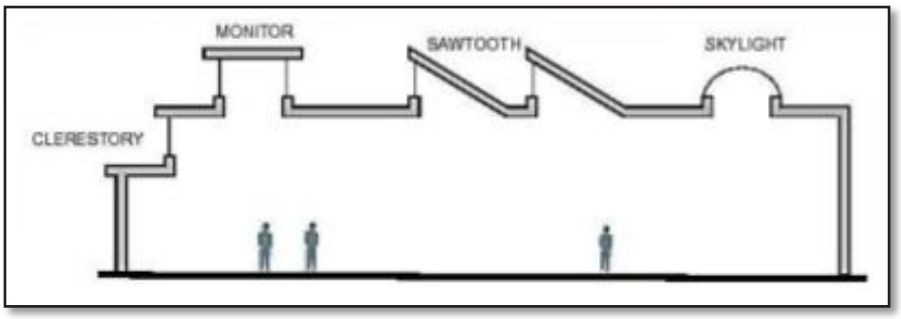

Fig. 4 Top lighting

While the vernacular strategies evolved primarily in residential architecture, they have been adopted and adapted in buildings of other occupancies as well. Taking the case of an academic building, specifically the Department of Architecture, College of Engineering Trivandrum, Kerala, India, the climatic conditions are as below:
Classification – Tropical Savanna (Aw); Yearly Mean Temperature – 27 degrees Celcius (Trivandrum, India)
The passive strategies adopted in the architectural design include orientation of building, north lighting, diffused lighting, courtyards, sun shades as illustrated by the building plans and photographs. A design studio room at basement floor in architecture department was taken for study in lighting levels. Simulation studies using (Butera, 2014) IES Virtual Environment (IESVE) was done with the room at different times of the day.

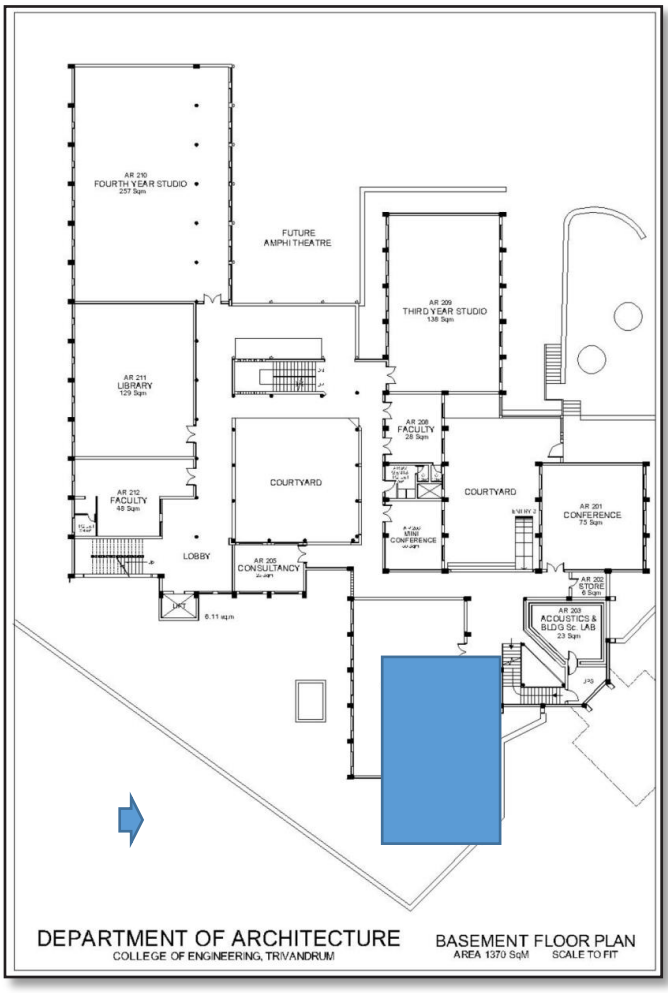

Fig. 5 Floor Plan – Basement Level

Fig. 6 Courtyard

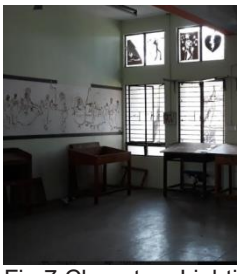

Fig.7 Clerestory Lighting

Fig. 8 & 9 Lighting levels on Upper Floors

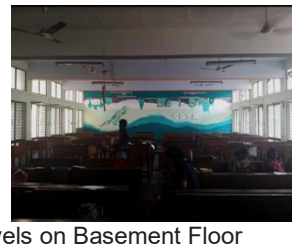

Fig. 10 & 11 Lighting levels on Basement Floor

The strategies used effectively cut off the heat and the glare and lets in passive daylighting as required in workspaces. However, one particular room, in the Basement level 1, due to its specific siting, faces a dearth of natural passive lighting, as evident from the picture above.
This is owing to the retaining walls on one side, and vegetation and building shadow on the other side. This room, where in the typical passive strategies have not been successful was chosen for the purpose of testing out light pipes as an alternative approach for daylighting.

II. Methodology

Simulation studies were undertaken to study the day light levels on the studio room as marked in blue colour in figure 5 on a typical day in February. Though the studio room at the basement floor had windows on the southern side it had little lighting inside due to the presence of a retaining wall nearby. The IES Virtual Environment (IESVE) was used for simulation of daylighting level. A study was undertaken with varying external illumination level with hour of the day. The date was taken as 10th February and the day lighting levels inside the classroom was calculated at intervals from 9 am,11 am,1 pm and 4 pm. Figure 12 to Figure 15 represents the daylighting levels in square grids in the plan of the studio room.

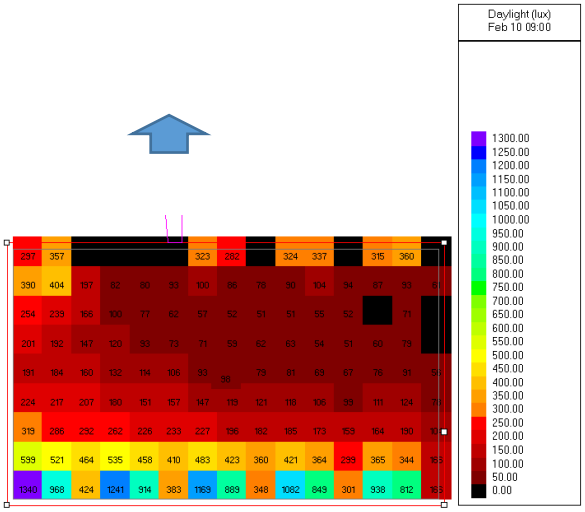

Fig.12 Daylight levels at 9 am, 10thFeb

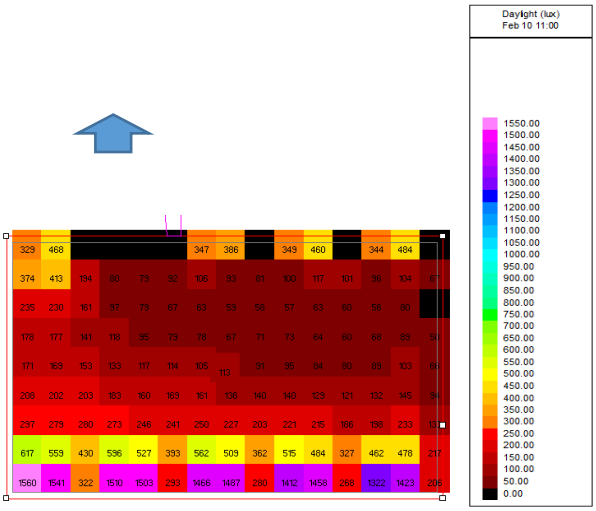

Fig.13 Daylight levels at 11 am, 10th Feb

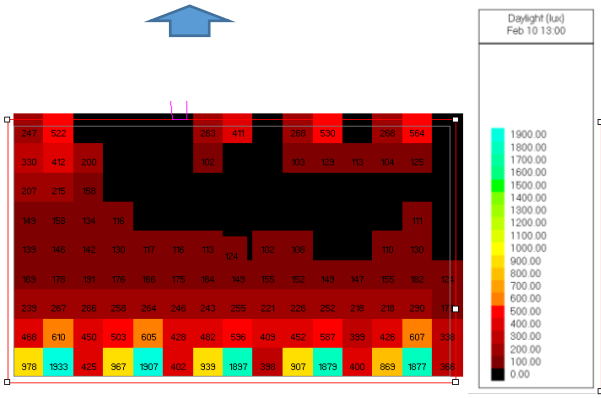

Fig.14 Daylight levels at 1pm, 10th Feb

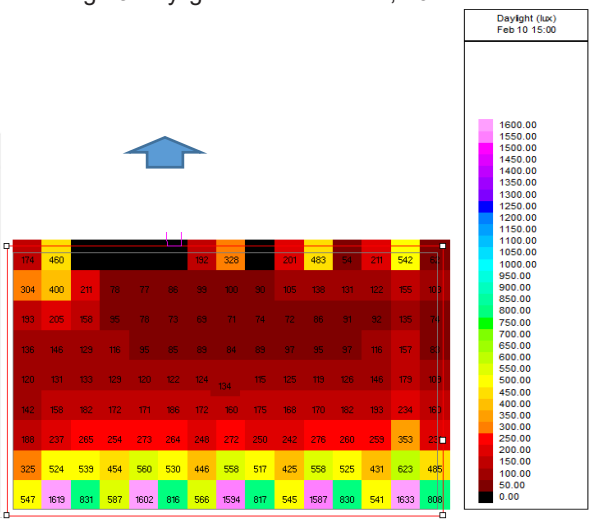

Fig.15 Daylight levels at 3pm, 10th Feb

III. Analysis and Results

According to SP: 41 (S&T)-1987 “Functional requirements of buildings (other than industrial buildings)” - Day lighting Part-4 the daylighting level for classroom should be a minimum of 300 lux.The daylighting level (lux) is found to be very high exceeding 300 lux near the window area at the southern side. The reverse happened at the rear side of the room with very low lighting level. The illuminance level was found to be less than 300 lux in the part of the room further from the windows.
A horizontal light pipe (fig 16) with the collection device at the southern side outside the classroom is proposed which can bring daylighting into the interiors to the side where the illuminance is low (Ganesan, 2014). Three light pipes with a cross section of 30 cm can bring sufficient daylighting to the interiors as seen in figure 17. Simulation

has been done with three light pipes bringing in daylight with help of diffusers. The expected lumen output of the diffusers is 2000 lumens. The simulated result with the three diffusers at 9 am is shown in figure 18, and is the lighting effect with windows open and with light pipes. The lighting levels will improve when the external illumination increases as the day progresses providing sufficient and uniform lighting inside.

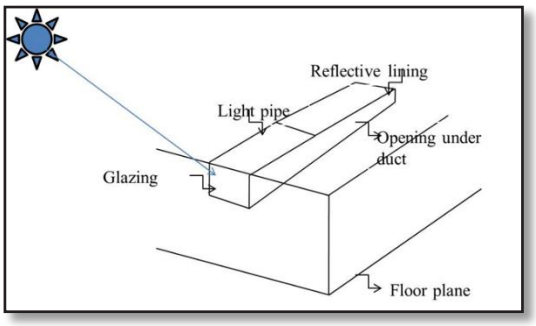

Fig. 16 Horizontal light pipe (Ganesan, 2014)

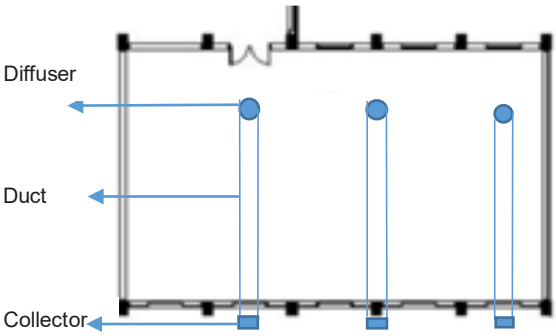

Fig.17 Plan of the classroom with diffusers, duct and the external collector of horizontal light pipes

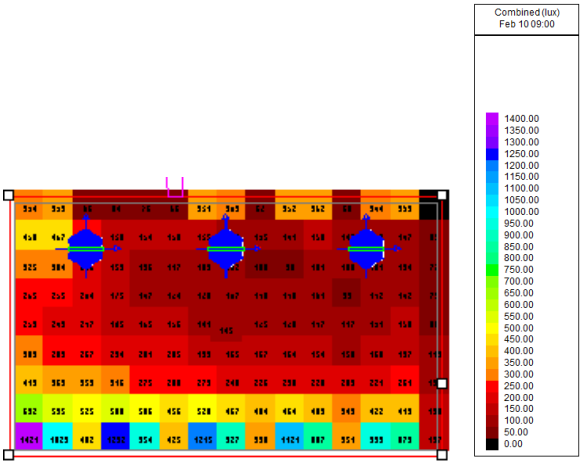

Fig.18 Daylight levels at 9 am, 10th Feb with light pipes

IV. Conclusion

As a preliminary investigation for improving the energy efficiency within academic institutions, a particular portion of a building in the campus is identified for analysis. The room was found to have thermal comfort, however the lighting inside the classrooms was poor due to the orientation and the obstructions in the vicinity. The reduction in daylighting levels has to be supplemented with horizontal light pipes to obtain good luminous comfort. The number and arrangement of light pipes were determined having the optimum light intensity which can provide the required lighting comfort.The study has demonstrated that the use of light pipes results in significant energy saving in buildings within academic institutions.

References

Arvind Krishan, N. B. (2014). Climate Responsive Architecture – A Design Handbook for Energy Efficient Buildings. New Delhi: Tata McGraHill.
Butera, F. M. (2014). Sustainable Building Design for Tropical Climates. Nairobi: UN Habitat.
Ganesan, A.R., Nair, M. G and Ramamurthy, K. 2014. Classification of Daylight enhancement systems, Lighting Research and Technology, 46, 245-267. https://doi.org/10.1177/1477153513483299
Jie Tan, X. G.-p. (2016). The Influence of the Courtyard Geometry on the Passive Lighting Energy Savings. 2nd International Conference on Sustainable Energy and Environmental Engineering (SEEE 2016).
Kiamba, L. R. (2014). Climate-responsive Vernacular Swahili Housing.
Thorpe, D. (2020). 10 Stages to a Passive Solar Building from Design to Build. Retrieved February 10, 2020, from SmartCitiesDive: https://www.smartcitiesdive.com/ex/sustainablecitiescollective/10-stages-passive-solar-building-design-build/1026136/
(SP: 41 [S&T] 1987, Handbook on Functional Requirements of Buildings (other than industrial buildings), Bureau of Indian Standards, CBRI Roorkee).
Trivandrum, India. (n.d.). Retrieved February 07, 2020, from weatherbase: http://www.weatherbase.com/weather/weather-summary.php3?s=17334&cityname=Trivandrum%2C+Kerala%2C+India&units=metric

Enhanced thermal conductivity of polyethylene composites using granulated graphene

[1]Chaudhry Usman, [1]Abdelnasser Mabrouk, [2*]Ahmed Abdala
[1] Qatar Environment & Energy research institute, Hamad Bin Khalifa University, Qatar
[2] Chemical Engineering program, Texas A & M at Qatar, Qatar

* E-mails: ahmed.abdala@qatar.tamu.edu

Abstract
Polymer heat exchangers may offer replacement to metal evaporators in Multi-Effect Distillation (MED) desalination because of their better resistance to corrosion, fouling and scale formation. However, the low thermal conductivity of polymers is a bottle neck for its application as a heat transfer surfaces, which require high thermal conductivity along with improved mechanical properties and wettability. Nevertheless, the Thermal conductivity, mechanical properties and wettability of polymers can be enhanced through addition of graphene-based fillers of very high thermal conductivity. In this article, the thermal conductivity of Polyethylene (PE)-graphene composites is controlled by several filler characteristics such as size, inherited thermal conductivity, loading, directionality, number of polymer-filler interfaces etc. In this work, nanocomposites of high- and low-density PE with granulated graphene having lateral dimensions in range of 100s of nm to few mm were prepared by melt mixing using different volume ratios of fillers followed by hot pressing. The morphological analysis of the composites' fractured surface releveled the random oriented of the graphene in the PE matrix. However, the melt processing greatly reduced the filler lateral size. At ~22 vol. % of granulated graphene, the thermal conductivities of the composites were 2.9 and 3.2 W/m.K indicating the very high enhancement of ~950% and ~800% for low-density and high-density polyethylene respectively. Moreover, stiffness of PE was improved significantly, but the ductility was reduced drastically. Finally, the impact of the composite processing time and extrusion speed on thermal conductivity and mechanical properties were investigated to establish the structure-processing-properties correlation.

Keywords: Composites, Evaporator, Polyethylene, Thermal conductivity, granulated graphene

I. Introduction

With growing demand of micro and nanotechnology in modern electronics systems, space, water and energy industry, thermally enhanced polymer can be beneficial as heat sink, thermal interface materials, heat exchanger etc. Polyethylene having simple basic structure is the highest volume engineering plastic produced globally because of its low price, excellent mechanical properties, and chemical resistance etc. (Patel, 2016; Ronca, 2017). Among wide range grades of PE, high density polyethylene (HDPE) and low-density polyethylene (LDPE) are among commodity thermoplastics and commonly used for many applications ranging from water pipes to flexible packing. HDPE is characterized by less branching and higher crystallinity while LDPE grades have ranges from longer and shorter chain branching. Increasing the poor thermal conductivity (κ) (0.1- 0.5 Wm-1K-1) of PE can be revolutionary in the field of engineering thermoplastic. The lower κ of the polymer can be tailored to obtain higher values by addition of highly conductive fillers such as carbon black, graphite, hexagonal boron nitride, carbon nanotubes graphene (Gulrez et al., 2014). Moreover, composites prepared from these fillers also exhibit excellent mechanical properties. Enhancement in κ of polymer composites (κc) reported in the literature is relatively low compared to the predicted κc based on the intrinsic filler conductivity (κ_f) and filler loading. This lower measured κc can be attributed towards large interfacial thermal /thermal boundary resistance between the conductive filler and the surrounding polymer chains leading to phonon scattering (Han and Fina, 2011). Moreover, the κc of the resulted composites (κc) profoundly rely on the several factors such as filler size, inherited κ, dispersion, loading, directionality, polymer inherited κ, conductive network, number of polymer-filler interfaces etc (Chen et al., 2016).

Inspired from the fractal root system of tree-shaped flows, the constructal-theory deals with the designing of conducting paths with improved access i.e. minimum flow resistance. In this theory, the mode of transport with the highest and lower resistivity are placed at the small and large construct respectively (Bejan, 2002)

It was reported that use of filler systems having different shape and size provide synergistic effect by offering better thermally conductive network formed bridges between fillers. Liu et al. fabricated HDPE composite incorporated with several size of graphite-based fillers. The highest κ about 2.51 W/(m·K) was found by incorporating a combination of 15 wt. % 500 μm, 10 wt. % 200 μm, 10 wt. % 20 μm, 4.0 wt. % 2.0 μm, and 1.0 wt.% graphene (total filler 40 wt. %) (Liu et al., 2018).

Therefore, in this research work, we studied the effect of LDPE and HDPE κ filled with granulated (GG) graphene with different volume content of GG. The as received GG particles used in this study were fabricated by rolling graphene nanopowder into large particles having lateral dimensions in range of 100s of nm to few mm. It can be believed that during melt processing large size GG will break down to smaller or optimized filler size to get high κc.

II. Experimental Procedure

Local grade of LDPE and HDPE from QAPCO and Q-Chem respectively and granulated graphene (GG) with density 0.3 g/cm^3 from Graphene supermarke, USA, were procured and used as supplied. Melt blending (200 C, 15 min) was used for the composite fabrication using Xplore MC-15 micro-compounder with different volume ratio of GG

followed by hot pressing (180 C, 4-ton clamping force, 5 min) using Craver hot press. The thermal diffusivity (δ) of neat polymer and composites was obtained at room temperature using Linseis LFA 500 Xenon flash. The κ of the neat polyethylenes and the composites is calculated as follows: $\kappa = \delta c_p \rho$ where c_p is specific heat capacity and ρ is the density.

III. Results and discussions

SEM images shown in Fig. 1 confirms the presence of graphene with different lateral dimensions consisting of several nanometers to few milimeters. The as received GG was fabricated by physical joining of the graphene nanopowder using rolling technique to produce large sheets. At higher magnification clusters of loosely bounded graphene particles were also observed. In FTIR spectrum (Fig. 1) of GG the peaks and assignment are as follow: 3443 (O-H stretching of the COOH group), 2924, 2850 (C-H stretch vibrations of the methylene group respectively), 1742 (C=O stretch of the COOH/carbonyl group), 1630 (aromatic C=C bending), 1463 and 1340 cm^{-1} (carboxyl O–H and C–O respectively). The GG was further analyzed by X-ray photo-electron spectroscopy (XPS) to confirm the chemical states of various elements and the presence of functional groups. The survey scan of GG showed mainly the presence of carbon (~ 96 wt. %) with small amount of oxygen (~3.0 wt. %). Fig. 1 also shows deconvoluted high resolution XPS spectra of O1s region. The deconvoluted peaks showed peak binding energies of 531.28, 533 and 536.37 eV which correspond to C-O (54.6 at. %), C=O (34.4 at.%), and chemisorbed oxygen (10.9 at.%), respectively (Al-Gaashani et al., 2019).

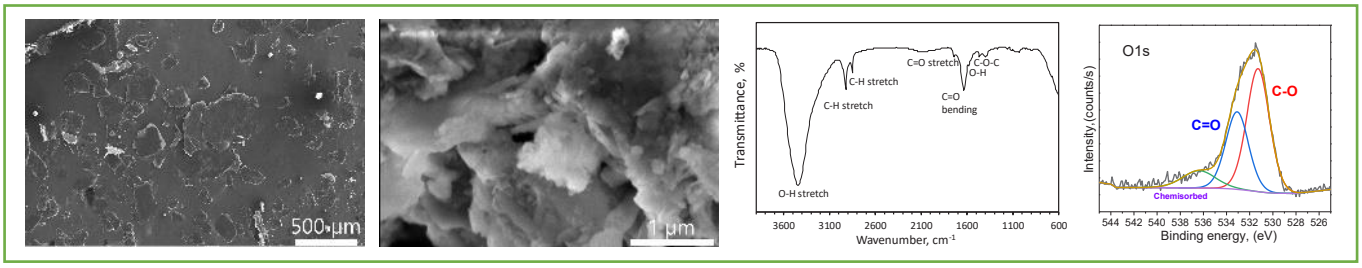

Fig. 1. SEM image of aggregated granulated graphene obtained at low and high magnifications, *and R*aman spectrum

SEM images of the fracture surfaces for the LDPE/GG and HDPE/GG composites are shown in Fig. 2. It can be seen from SEM that GG has been strongly affected by the fabrication process as relatively smaller particle size can be observed in the polymer matrix. It is clear that the shear mixing forces have broken down the large particles into smaller fragments. Also, the it can be observed that GG particles are reasonably distributed and forming interconnests within the polymer matrix. Fig. 2 also shows that the thermal conductivity of LDPE and HDPE based composites have increased with the increasing content of GG in the matrix. This probably resulted from the presence of filler with different particle sizes offering better thermally conductive network owing to the formation of bridges between larger and smaller lateral size particles where the larger fillers act like backbones and the smaller fillers represent the branches. The addition of GG has caused great improvement in the κ_c compared to previous studies where much lower κ_c were observed when graphene was used (Noorunnisa Khanam et al., 2016).
Fig. 2 indicates the tensile properties of of the composites. It was found that the addition of GG to HDPE, has improved the stiffness of the composite significantly. The incorporation of 22 vol. % GG to HDPE has caused an improvement of Young's Modulus of almost 300%.

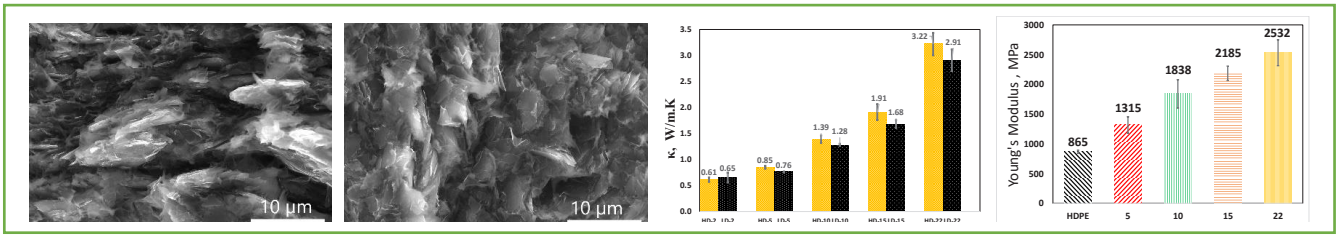

Fig. 2 SEM images of fractured surface of LDPE (Left) and HDPE (right) composites containing 22 vol.% granulated graphene and Thermal conductivity of LDPE and HDPE composite containing various loading of granulated graphene

IV. Conclusions

In this research, GG reinforced LDPE and HDPE composites with high thermal conductivity were produced by melt-extruding method. The SEM of composite fractured surfaces indicated presence of randomly orientated granulated graphene with different particle sizes in the polymer matrix. It was also found that the melt processing has greatly reduced the filler lateral size. The composites thermal conductivity was also affected by the graphene loading. At ~22 vol. % of granulated graphene, the thermal conductivities of the composites were 2.9 and 3.2 W/m.K indicating the very high enhancement of ~950% and ~800% for low-density and high-density polyethylene respectively. Addition of 22 vol. % of granulated graphene to polyethylene has increased the modulus by over 300%. Thus, the melt blended graphene reinforced PE composites with improved thermal conductivity and mechanical properties

could expand the area of thermally conductive polymers, replacing metals and ceramics in heat transfer devices and equipment, leading to energy saving.

Acknowledgements

"This research was supported by NPRP grant # NPRP10-0205-170349 from the Qatar National Research Fund (a constituent member of the Qatar Foundation). The authors would like to acknowledge Dr. Said Mansour the Director of the Imaging and Characterization at Qatar Environmental and Energy Research Institute (QEERI) and his technical team for the support with SEM and XPS analysis.

References

Al-Gaashani, R., Najjar, A., Zakaria, Y., Mansour, S., Atieh, M.A., 2019. XPS and structural studies of high quality graphene oxide and reduced graphene oxide prepared by different chemical oxidation methods. Ceramics International 45(11), 14439-14448.

Bejan, A., 2002. Constructal theory of organization in nature: dendritic flows, allometric laws and flight. WIT Transactions on Ecology and the Environment 57.

Chen, H., Ginzburg, V.V., Yang, J., Yang, Y., Liu, W., Huang, Y., Du, L., Chen, B., 2016. Thermal conductivity of polymer-based composites: Fundamentals and applications. Progress in Polymer Science 59, 41-85.

Gulrez, S.K.H., Ali Mohsin, M.E., Shaikh, H., Anis, A., Pulose, A.M., Yadav, M.K., Qua, E.H.P., Al-Zahrani, S.M., 2014. A review on electrically conductive polypropylene and polyethylene. Polymer Composites 35(5), 900-914.

Han, Z., Fina, A., 2011. Thermal conductivity of carbon nanotubes and their polymer nanocomposites: A review. Progress in Polymer Science 36(7), 914-944.

Liu, Z., Tu, R., Liao, Q., Hu, H., Yang, J., He, Y., Bian, H., Ma, L., Liu, W., 2018. High Thermal Conductivity of Flake Graphite Reinforced Polyethylene Composites Fabricated by the Powder Mixing Method and the Melt-Extruding Process. Polymers 10(7), 693.

Noorunnisa Khanam, P., AlMaadeed, M.A., Ouederni, M., Mayoral, B., Hamilton, A., Sun, D., 2016. Effect of two types of graphene nanoplatelets on the physico–mechanical properties of linear low–density polyethylene composites. Advanced Manufacturing: Polymer & Composites Science 2(2), 67-73.

Patel, R.M., 2016. 2 - Polyethylene, in: Wagner, J.R. (Ed.) Multilayer Flexible Packaging (Second Edition). William Andrew Publishing, pp. 17-34.

Ronca, S., 2017. Chapter 10 - Polyethylene, in: Gilbert, M. (Ed.) Brydson's Plastics Materials (Eighth Edition). Butterworth-Heinemann, pp. 247-278.

Evaluation of regional climate innovation potential in Hungary

[1*]Mária Szalmáné Csete, Ph.D. habil. , [2]Orsolya Barna
[1] Budapest University of Technology and Economics, Faculty of Economics and Social Sciences, Department of Environmental Economics, Magyar tudosok krt. 2., Budapest,1117, Hungary
[2] Budapest University of Technology and Economics, Faculty of Economics and Social Sciences, Department of Environmental Economics, Magyar tudosok krt. 2., Budapest,1117, Hungary

* E-mails: csete@eik.bme.hu

Abstract
Climate change can have extremely diverse impacts on different spatial levels depending on regional characteristics, adaptive capacity, and vulnerability of a territory. Nowadays, it is pivotal to be able to tackle climate change in a sustainable way on a regional level, also considering the UN Sustainable Development Goals (SDGs). Hungary is located in the center of the Carpathian Basin with special spatial and natural environment-related characteristics that also influences the possible impacts of climate change according to socio-economic development perspectives. Among several different regional development pathways, climate oriented spatial planning at the regional level can play a pivotal role in enhancing long-term sustainability. Climate innovation-related activities can foster the effectiveness of both mitigation or adaptation-oriented tasks and interventions on a regional level. Based on the international scientific literature review, several different types of innovation can be found, and some of them also can consider climate change-related issues. This paper gives an overview and a typology about climate innovation options from the regional development perspective considering the recent state of climate planning on the NUTS-3 level in Hungary. There is a lack of knowledge related to the comprehensive climate oriented spatial planning assessment on the county level in Hungary, mainly in connection with climate innovation; however, all of the 19 Hungarian counties and also the capital has accepted climate strategies. Among examined climate innovation-related solutions, this evaluation also highlights the crucial role of environmental education and training. Recent research evaluates the current status of climate strategies, tools, and practices in Hungary, considering the potential pathways according to the forthcoming activities. Based on the in-depth analysis mitigation, adaptation, and awareness-raising related climate innovation interventions can be distinguished in different sectors. The results of the evaluation show state-of-art knowledge concerning climate innovation as a support tool for sustainable regional development.

Keywords: climate innovation, regional development, sustainability management, environmental education, awareness-raising

I. Introduction

Nowadays, all societies are facing the climate challenge, which can enhance the possible impacts of other environmental problems and damage the recent ecological and socio-economic conditions. Due to these more intense and frequent phenomena, there is an urgent need for transformation also on global, regional and local levels. Innovation systems and management tools are able to support climate-related developments and sustainable development pathways at the same time. It is pivotal to share burdens and opportunities on a global and regional level as well. All countries and each region depending on the socio-economic and spatial characteristics, should play a crucial role in efforts related to mitigation and adaptation perspectives. The 'Europe 2020: A European strategy for smart, sustainable and inclusive growth' entitled strategy has a significant focus on innovation. It was endorsed by the European Council in June 2010. The Europe 2020 Strategy contains seven flagship initiatives to accelerate progress and long-term growth, also considering the re-thinking of innovation systems and processes concerning regional innovation potential. Innovation is the most significant and increasing source of growth in OECD countries. The term innovation can be described in many ways. Innovation and innovation systems have a significant role in finding solutions we need for our common sustainable, climate-oriented, resource and also cost-efficient future. Climate innovations are often associated with mitigation issues. However, they are also strictly related to adaptation and awareness-raising activities in the form of innovative technologies, education-oriented solutions, collaborations, financing instruments etc. There are different types of innovation systems. A regional innovation system can be identified as the group of research institutions, companies, entrepreneurs, networks, policymakers, local decision-makers etc. (Tödtling-Trippl, 2018) and these actors shape the regional innovation capacity and performance (Asheim-Gertler, 2005). Considering the regional innovation system related literature, those are mainly focusing on successful and innovative regions. There is a lack of investigations according to failing or developing a regional innovation system (Phelps et al., 2017). The recent paper delivers a reality check through strategy assessment considering the conditions of innovation aspects in the Hungarian climate-related spatial development. For a high-performing climate innovation system several conditions should be fulfilled. According to special WWF Report (WWF, 2011) for instance the basic environmental legal and regulatory systems (including intellectual property rights), economic solutions, efficient policy-making, institutionalized background and national platform for climate innovation, fostering stakeholder involvement and strengthening collaborative attitude, administration and entrepreneurs support are also crucial. This paper deals with the policy development side of climate innovation systems with a particular focus on climate change strategy development on the NUTS-3 level.

II. Methodology

Innovation is considered as one of the most effective and important strategies to tackle climate change challenges. In the last couple of decades, it became a term frequently used by all kinds of stakeholders. In general, innovation is understood as something new - it can mean a significant improvement or a radical change to how a problem, the challenge is solved (WWF, 2011). OECD refers to innovation as 'the implementations of a new or significantly improved product (good or service), or process, a new marketing method or a new organizational method in business practices, workplace organization or external relations' (OECD, 1997). There is an urgent need for innovation to address climate change and the transition to a low carbon economy. Climate innovation definition from WWF determines it as 'a transformative non-fossil fuels and non-nuclear product, service or system that given favourable conditions, will generate >20 million tons of annual greenhouse gas reduction in ten years if applied at scale.' (WWF, 2011). The system map of climate innovation (Figure 1) shows innovation differentiated as incremental or disruptive innovation, and also indicates the level of changes from products and processes to value systems (EIT Climate-KIC, 2016) This is a very effective structure to show the system of climate innovation, however considering the importance and impact of regional and spatial characteristics regarding innovation - these aspects are missing from the figure. In our paper, we focus on these aspects by evaluating the regional climate strategies from each Hungarian county - as these are the best sources to understand the regional climate innovation needs, potentials and plans.

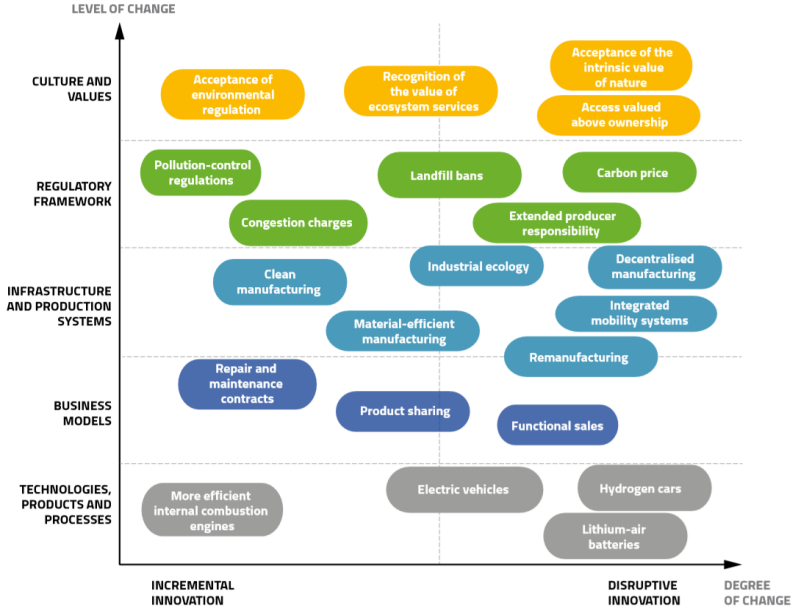

Fig. 1: Mapping climate innovation (Climate-KIC, 2016)

Hungary has altogether 19 counties that have an increasingly important role in regional development, especially in finding innovative and sustainable pathways. The financing of recent regional development is clearly EU-centered; thus, the relevance of the flagship initiatives of the Europe 2020 Strategy is undoubted including innovation and sustainable regional development as well. The capital of Hungary (Budapest) was also in the scope of the evaluation considering its economic and social role and significance in Hungary and especially its special rights according to the law that ensure the similarity with the county level, particularly in case of the possible effects of strategic documents. Beyond the national level, however, the main territorial level of planning and programming is now clearly in the planning role of the county as an essential coordinator and supporter of the sub-regional levels (district, city, and country). This underpins the mapping and assessment of climate-related innovations related to this spatial level. Different types of climate-related planning and strategic documents are existing (e.g. SEAP, SECAP, LCP etc.) that can be evaluated from various aspects. Considering mitigation or adaptation processes several in-depth analysis can be found (Heidrich et al., 2013; Reckien et al., 2014, 2015, 2019). The lack of innovation-oriented assessment can be observed in the case of these evaluations.

Based on the literature review the main steps of the evaluation are the following: 1. Identification of the existing development and planning strategies; 2. Selection of the relevant documents and examination of the availability; 3. Climate-innovation oriented questionnaire development for further in-depth evaluation; 4. Online collecting form development and conduct the survey; 5. Results and recommendations phase. Considering the Hungarian county level, the identified relevant documents are the regional development plans, climate change strategies. These are the latest spatial planning-related strategies and the first ones with a climate change focus. The analysis was focusing on climate change strategies from the aspect of innovation-related activities that can play a crucial role in sustainable and effective regional development perspectives. The examined strategies are available online and all of them were developed due to a proposal (KEHOP-1.2.0-15-2016-00001) supported by the European Union. The main goal of the supported projects was to foster effective adaptation activities with the development of climate change strategies on the county level and also guideline development. Another additional task was to establish a Climate Change Platform in the county that can ensure stakeholder involvement not only in strategy development

but in the implementation and monitoring phase.

The main research question deals with the recent knowledge and state of climate change-related innovation in regional planning and development perspectives on the NUTS-3 level in Hungary. The main structure of the questionnaire is the following: I.) General information: a. Name of the county, b. Availability of the evaluated document (weblink, c. Year of document development, d. The developers of the climate change strategy; II.) Content related information: a. Spatial Characteristics: i. The vision of the document, ii. Climate-related regional characteristics, iii. Identification of county-specific climate-related impacts, iv. Planned innovations connected to the regional; b. Main aims and intervention: i. Role of innovation in the mitigation/adaptation/awareness-raising strategic objectives, ii. Role of innovation in the mitigation/adaptation/awareness-raising strategic interventions, iii. Number of innovations in the mitigation/adaptation/awareness-raising strategic interventions, iv. Role of climate innovation in main aims and interventions; c. Stakeholder involvement: i. Stakeholders connected to innovation, ii. Educational institutions connected to innovation, iii. Climate innovation-related stakeholders. An online collecting form was developed and used for the analysis. The data collection was conducted in December 2019 and January 2020.

III. Analysis

The spatial characteristics of the counties were our first focus in the analysis of the climate strategies of the 19 Hungarian counties and the capital. 80% out of the 20 evaluated documents were developed in 2018, the others in 2017. Their visions, their climate-related characteristics, and their impacts identified were examined, and whether connections were established between the impacts and the planned innovations. Each county formulated its vision for a sustainable future for the climate strategy. These visions are usually concise and can act as a motto for the county. In general, the strategies also provide a longer explanation of the vision and the most important fields the county prioritized for action. Out of the 20 examined strategies, 8 strategies contained innovation in their vision, another 3 only mentioned innovation in their explanation. Nine strategies did not have any innovation-related items nor in their vision, nor in the explanation of their main aims, which means almost half of the strategies do not consider innovation as an element to achieve their climate change-related objectives. Regarding climate-related regional characteristics, most strategies (16) regarded as past analysis, present impacts, and future forecasts as well (the rest only examined some combinations of these) when creating their climate-related assessment. All the 20 documents identified as specific climate-related impact the increase of temperature, droughts, and heavy storms. Sixteen counties identified the rainfall pattern, 14 the floods, and 11 waterlogging (the geographical locations determine these impacts). Only 5 out of the 20 strategies connected their planned innovations to their regional and spatial characteristics. These five are typically connected to agriculture (agro innovation) and the energy sector.

The second part of our research related to the role of innovation in the main aims and interventions of the strategies related to mitigation, adaptation and awareness-raising. Our results show that innovation-related items are insignificant in proportion to the overall objectives, and interventions (e.g.: 1 out of 20 strategies involves innovation in their mitigation and adaptation objectives, and 1 out of 220 mitigation interventions is connected to innovation). Very low number still (5 out of 20 strategies), but innovation appears more related to the awareness-raising aims and action plans, especially when it comes to horizontal aims. Both Heves county and Jász-Nagykun-Szolnok (JNSZ) county claim that by 2030, the number of environmental interventions will be growing at a rate above the national average by reaching 40% (Heves) and 20% (JNSZ) of their population - with a special focus on their beneficiary districts; and climate-conscious interventions will become the engines of local innovations. These, however, do not appear at the level of the planned interventions.

The last part of our research examined whether the climate strategies identified any stakeholders to play an active role in stimulating and producing innovations. Two counties (Szabolcs-Szatmár-Bereg and Bács-Kiskun) declare that one of the tasks of all local stakeholders is to participate in the technological and innovation development and common thinking. Szabolcs-Szatmár-Bereg and Győr-Moson-Sopron counties also mention the National Center of Agricultural Research and Innovation that has been involved in developments for local foresters.

IV. Results and discussions

Many strategies mention the Climate Protection Platforms. These Platforms were created to support the elaboration of the climate strategies in the counties and helped the local decision-makers to widen their knowledge related to climate change. The role of the Platforms is to ensure the long-term co-ordination of activities at the county level, and the conditions for awareness-raising. These platforms could play also a key role in introducing climate innovation in the counties.

All strategies emphasize the importance of local universities and research institutions in the field of research, development and innovation especially related to awareness-raising. As this is the only result associated with innovation that is common in the strategies, this could be a good starting point for future actions: the introduction and application of educational innovations. Some researches and the results of school-level surveys show that the educational systems in Hungary and in other countries of Central Eastern European region (especially the Visegrad 4 countries) might not be as effective as in other parts of Europe. These systems might restrict creativity and innovativeness, as they still promote memorization and respect for teacher's authority instead of a debate, critical thinking and creativity. There is lack of developing independent thinking and an interdisciplinary and holistic approach is not typical. The interventions in this area could support the countries to reach their full economic and innovative potential. Considering growth models focusing on social and environmental sustainability different spatial levels can play a crucial role in shaping innovation systems, trajectories and in mobilizing introductory regional

potential for national growth. In the present chapter, the main results and recommendations according to the evaluated climate change strategies and the recent situation of regional innovation potential aspects are presented.

The characteristics of innovation in the era of digitalization (such as faster innovation cycles, data as core input, servitization, collaborative innovation) (OECD, 2020) can be taken into account on county level. Digital transformation is changing not only the nature of business innovation but regional development perspectives.

V. Conclusions

Based on the scientific literature review and the conducted evaluation, it can be stated that in Hungary, the climate change-related planning documents and strategies on the county level can not support the practical implementation of the Europe 2020 Strategy according to innovation. Based on the evaluated strategies, two types of sector innovation were identifiable, namely R&D&I activities related to the energy sector and agriculture. Building capacities and increasing resources are crucial in fostering regional innovation potential at the examined spatial level. The initiative of establishing Climate Change Platforms on the county level can favour coordination and transition management considering mitigation, adaptation and awareness raising-related innovation activities. The climate-related regional innovation potential development is in the initial phase in Hungary; thus it can ensure the implementation of an effective structure related to the system of climate innovation and not ad-hoc and partial development activities.

Acknowledgements

The research reported in this paper was supported by the Higher Education Excellence Program of the Ministry of Human Capacities in the frame of the Water sciences & Disaster Prevention research area of the Budapest University of Technology and Economics (BME FIKP-VÍZ).

References

Asheim, B., Gertler, S., 2005. The geography of innovation: Regional innovation systems, in: J. Fagerberg, D. Mowery, & R. Nelson (Eds.), The Oxford handbook of innovation. Oxford: Oxford University Press. pp. 291–317.Bejan, A., 2006. Advanced engineering thermodynamics, 3rd Edition. Wiley, New York, NY. https://doi.org/10.1109/TNSRE.2003.814453

Climate-KIC, 2016. System Climate Innovation for a Transformative Impact, Climate Innovation Insights, Series 1.3., Climate-KIC Grätzel, M., 2001. Photoelectrochemical cells. Nature 414, 338–344. https://doi.org/10.1038/35104607

Heidrich, O., Reckien, D., Olazabal, M., Foley, A., Salvia, M., de Gregorio Hurtado, S., Orru, H., Flacke, J., Geneletti, D., Pietrapertosa, F., Hamann, J.J.P., Tiwary, A., Feliu, E., and Dawson, R.J., 2016. National climate policies across Europe and their impacts on cities strategies. Journal of Environmental Management, 168, 36–45. http://doi:10.1016/j.jenvman.2015.11.043Morris, D.R., Szargut, J., 1986. Standard chemical exergy of some elements and compounds on the planet earth. Energy 11, 733–755. https://doi.org/10.1016/0360-5442(86)90013-7

OECD, 1997. Oslo Manual, The measurement of scientific and technological activities, Proposed guidelines for collecting and interpreting technological innovation data. European Commission, Eurostat http://www.oecd.org/science/inno/2367614.pdf

OECD, 2020. The Digitalisation of Science, Technology and Innovation: Key Developments and Policies, OECD Publishing, Paris, https://doi.org/10.1787/b9e4a2c0-en

Phelps, N., Atienza, M., Arias, M. 2017. An invitation to the dark side of economic geography. Environment and Planning A, 50(1), 236–244. doi: 10.1177/0308518X17739007

Reckien, D., Flacke, J., Dawson, R.J., Heidrich, O., Olazabal, M., Foley, A., Hamann, J.J.P., Orru, H., Salvia, M., de Gregorio Hurtado, S., Geneletti, D., and Pietrapertosa, F., 2014. Climate change response in Europe: What's the reality? Analysis of adaptation and mitigation plans from 200 urban areas in 11 countries. Climatic Change, 122, 331–340. http://doi:10.1007/s10584-013-0989-8

Reckien, D., Flacke, J., Olazabal, M., and Heidrich, O., 2015: The influence of drivers and barriers on urban adaptation and mitigation plans-an empirical analysis of European Cities. PLoS ONE, 10, 1–21. http://doi:10.1371/journal.pone.0135597

Reckien, D., Salvia, M., Pietrapertosa, F., Simoes, S.G., Olazabal, M., De Gregorio Hurtado, S., Geneletti, D., Krkoška Lorencová, E., D'Alonzo, V., Krook-Riekkola, A., Fokaides, P.A., Ioannou, B.I., Foley, A., Orru, H., Orru, K., Wejs, A., Flacke, J., Church, J.M., Feliu, E., Vasilie, S., Nador, C., Matosović, M., Flamos, A., Spyridaki, N.A., Balzan, M. V., Fülöp, O., Grafakos, S., Paspaldzhiev, I., and Heidrich, O., 2019. Dedicated versus mainstreaming approaches in local climate plans in Europe. Renewable and Sustainable Energy Reviews, 112, 948–959. http://doi:10.1016/j.rser.2019.05.014

Tödtling, F., Trippl, M., 2018. Regional innovation policies for new path development – beyond neo-liberal and traditional systemic views. European Planning Studies. 26:9, 1779-1795. http://DOI:10.1080/09654313.2018.1457140

WWF, 2011. Enabling the Transition, Climate Innovation Systems for a Low Carbon Future, WWF Report, WWF Sweden, Ulriksdals Slott, http://www.climatesolver.org/sites/default/files/110607.pdf

Direct synthesis of formic acid energy carrier from captured carbon dioxide and utilization in a direct formic acid fuel cell

Nour Mardini and Yusuf Bicer
Division of Sustainable Development (DSD), College of Science and Engineering (CSE), Hamad Bin Khalifa University (HBKU), Qatar Foundation (QF), Education City, Doha, Qatar

Emails: nkmardini@hbku.edu.qa

Abstract
The objective of this work is to develop a process flow modeling for the synthesis of formic acid from CO_2 and hydrogen for energy storage and transport purposes. The use of formic acid as an energy storage medium is promising due to difficulties in hydrogen storage, where formic acid can be stored for a longer time with minimal losses, and then can be utilized in a direct formic acid fuel cell for cleaner power generation. The process flow is developed using Aspen Plus and Engineering Equation Solver to obtain the energy and mass balances, efficiency, fuel utilization, and Nernst voltage of the direct formic acid fuel cell. The model is validated against data available in the literature for operating parameters. The results show that the operation parameters such as formic acid formation rate, heat duty, and work values, fuel cell efficiency and Nernst voltage have a significant influence on the overall performance. The proposed system forms formic acid from gaseous H_2 and CO_2 with an energy efficiency of about 19%. The formed formic acid is initially stored in a tank for energy storage and then used in a direct formic acid fuel cell to produce about 157.5 kW power with an energy efficiency of 15% at 0.7 V, 25℃ and 1 bar.

Keywords: Formic acid, direct formic acid fuel cell, carbon capture, hydrogen, energy storage.

I. Introduction

The extracted raw natural gas in the world is accompanied by other components, most notably, water vapor and non-hydrocarbon elements, which are classified as impurities. These elements include hydrogen sulfide, oxygen, carbon dioxide, nitrogen, and other rare gases. Therefore, such contaminated gas needs treatment before sending it to the commercial sale gas for consumer consumption. It is well known that fossil fuels are non-renewable sources, oil, coal, and natural gas. This can sustain only for the next few decades, and the accumulation of carbon dioxide in the atmosphere results in global warming.

In the future, hydrogen storage will have a strong demand for safe and renewable energy carrier for transportation and other energy-related applications. Energy storage can play an important part in improved system integration. Electricity cannot be stored in large amounts for extended periods, unlike hydrogen as chemical storage in the form of hydrogen. For that reason, hydrogen produced on an industrial scale could play an important part in the energy transition. To overcome the issues related to hydrogen storage, there are several hydrogen storage techniques such as chemical hydrides, methanol, ammonia, and formic acid (Müller et al., 2017).

Formic acid (FA) is an important strong organic acid that can be found in textiles, pharmaceuticals agriculture, leather, and food chemical applications. In adition, it is used mainly as a preservative and antibacterial agent in livestock feed due to reduction properties and acidic nature. Formic acid is most commonly found in nature in the bites and stings of insects and it is found in several industrial organic syntheses, biomass processing and as a by-product of petroleum refining (Singh et al., 2016). FA is the simplest carboxylic acid which makes it easy to bio-degradable, for this reason, it is environmentally sustainable. Recently, formic acid has been proposed as an important fuel. It could serve as one of the better fuels for portable devices, vehicles and other energy-related applications in the future.

Recent technological improvement in fuel cells and renewable energy helps increase the demand for FA. One of the main advantages of using FA as a hydrogen carrier is that under ambient conditions, FA is a non-toxic and environmentally benign liquid with low flammability (Eppinger & Huang, 2017a). It is very important for its effect on global warming because producing FA directly from the captured CO_2, will reduce CO_2 accumulation. Several studies describe the potential of FA for H_2 storage, as a non-toxic and easy-to-store chemical. Formic acid is widely explored as a possible fuel for fuel cells because of several reasons:

- Hydrogenation/dehydrogenation are usually less energy efficient than chemical storage method (FA) (Müller et al., 2017)
- Non-toxic, liquid at room temperature, with low flammability
- Normal handling conditions (8.4–100.8 °C) (Singh et al., 2016)
- Energy efficiency for storing hydrogen in bound form as molecules of formic acid as high as 60% compares with that of existing methods for hydrogen storage (Williams et al., 1978)
- A significant alternative in terms of reducing costs and scaling up, compared to the use of compressed hydrogen gas (van Putten et al., 2019)

In the literature, one of the studies showed that formic acid-based fuel cell can produce 7000 kWh yearly by use one liter of FA which can carry 590 liters of hydrogen, this will be equivalent to 200 smartphones being recharged (ICIS, 2019. In 2003 is accounting for 25% of global applications FA finds in several applications like textiles, pharmaceuticals and food chemicals(*Product Profile: Formic Acid | ICIS*, n.d.). As mentioned before, FA is

used in leather tanning, which deemed for 32% of 579 kT and 34% for silage animal feed. FA can be found in the market at various concentrations 85, 90, 95, 98 and 99 wt %, with 85% being the most common (Schmidt et al., 2014).

The several ways of producing FA synthesis are methyl formate (MF) hydrolysis, preparation of FA free from formats, oxidation of hydrocarbons and hydrolysis of formamide(Hladiy et al., 2004). The first route is the most common in Europe. There are three FA processes by methyl formate (MF) hydrolysis: BASF, USSR and Kemira-Leonard (KL) process. Formic acid plants based on this process were started up at BASF (Federal Republic of Germany) in 1981 and Kemira (Finland) in 1982. However, USSR had the processes in Saratov (Ukraine), and the other in Lesogorsk (North-West Russia). The most common processes are BASF and Kemira-Leonard (KL) process (Bressmann, 2004).

II. System Description

In the beginning, CO_2 will be taken from the acid gas removal unit and purified from other impurities like H2S then go to the compression stage. Formic acid synthesis stage is modeled and simulated by Aspen Plus, then the result will be collected. Formic acid is stored in a storage tank so that it can be stored for a long time, unlike hydrogen. Then, it can be used in DFAFCs which convert formic acid and oxygen into CO_2 and water to produce energy as the complete system diagram is shown in Figure 1. H_2O and CO_2 will be recycled to synthesis the formic acid process to produce formic acid again. The formation of liquid HCOOH from gaseous H_2 and CO_2 is thermodynamically unfavorable. This means Gibbs energy is positive (nonspontaneous reaction) for that formation of FA from CO_2 and H_2 needs electricity or heat to execute a forward direction or by adding Reaction Coupling which makes reaction treating with a weak organic base to neutralize the acid formed (Xu et al., 2011).
The main stages of the study can be listed as follows:

- Initially, separated and captured CO_2 is purified. The hydrogen generated from photochloralkali process will be reacted with CO_2 for synthesizing formic acid.
- Some portion of the hydrogen will also be used for formic acid reaction, where hydrogen and CO2 are simultaneously required. The required CO_2 will be obtained from the acid gas removal unit (that is normally rejected to ambient air or sent to the incinerator.). In this way, the cost of formic acid production will be further decreased.
- After producing formic acid, it will act as fuel and the chemical energy will be converted into electrical energy via fuel cells. Formic acid fuel cell has a higher electromotive force (1.45 V) compared to other polymer electrolyte membrane fuel cells and direct methanol fuel cells (1.18V) (Rejal et al., 2014).
- There is a net-zero CO_2 emission process because formic acid is decomposed in fuel cells to produce electricity with H2 and CO_2 which will be recycled to formic acid process to produce formic acid again.

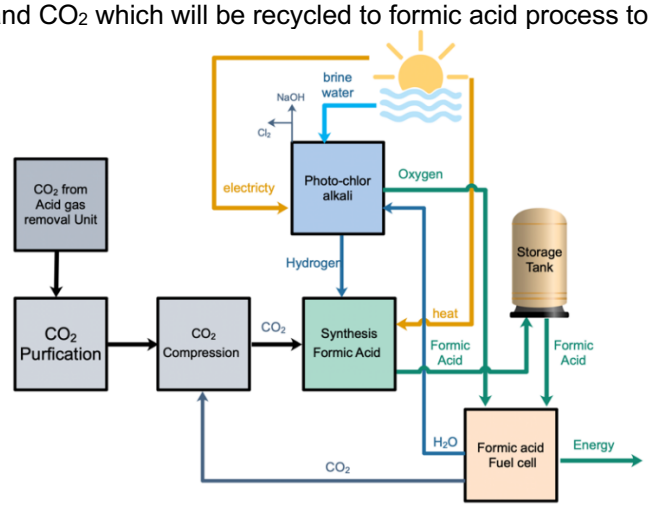

Figure 1. The complete system diagram for formic acid synthesis and utilization

In the compression stage, the CO_2 feed stream (100 kmole/h) is at atmospheric pressure and ambient temperature. Hence, it is pressurized to 60 bar and the H2 feed stream at the same flow rate and enters the process at 30 bar as it comes from high-pressure electrolysis and further pressurized to 60 bar.
As shown in figure 2. CO_2 and H_2 enter as a mixture at 600 kPa and 50℃ with 200 kmole/h flow rate, then arrive at the conversion reactor to produce formic acid at 19% of conversion ratio [10]. Formic acid is formed at 122℃ and 600 kPa. The formation of liquid HCOOH from gaseous H_2 and CO_2 is thermodynamically unfavorable. This means Gibbs energy is positive (nonspontaneous reaction) for that formation FA from CO_2 and H_2 need electricity or heat to execute a forward direction or by adding Reaction Coupling which makes reaction treating with a weak organic base to neutralize the acid formed. In this case, we add heat to form formic acid which leads to a high temperature of 122 ℃.

$$CO_2 + H_2 \rightarrow HCOOH$$

The challenge of storing hydrogen can be easier by formic acid as a hydrogen carrier. It is much easier and safer than hydrogen storage because hydrogen needs to be compressed at high pressures 700 bars or liquefied at -253°C. However, formic acid is storable as a liquid at 1 bar, which is significantly lower than hydrogen (Eppinger & Huang, 2017b).
The Aspen Plus flow sheet of the system is depicted in Figure 2 where it presents a brief description of the unit operation blocks. It gives the Aspen Plus name, which is the name given to each unit operation block by the software developers.
The Aspen Plus flow sheet of the system is depicted in Figure 2 where it presents a brief description of the unit operation blocks. It gives the Aspen Plus name, which is the name given to each unit operation block by the software developers.
The purpose of a fuel cell is to produce electricity by using chemical flow as raw material. DFAFC converts formic acid and oxygen into CO_2 and water to produce energy as shown in Figure 3. Formic acid oxidation occurs at the anode. Formic acid enters fuel cell ambient conditions with 0.23 kg/s. CO_2 and H_2O are recycled to be used in the FA plant. Therefore, the complete system is environmentally friendly and allows long-term storage of renewable energy.

$$\text{Anode: } HCOOH \rightarrow CO_2 + 2\,H^+ + 2\,e^-$$

$$\text{Cathode: } \frac{1}{2}\,O_2 + 2\,H^+ + 2\,e^- \rightarrow H_2O$$

$$\text{Overall reaction: } HCOOH + \frac{1}{2}\,O_2 \rightarrow CO_2 + H_2O$$

The model is based on the following main assumptions: isothermal and steady-state operation, zero-dimensional, all working fluids treated as ideal gases, pressure drops are neglected.

III. Analysis

In this study, the impact of flow rate of CO_2 in formation formic acid is shown in Figure 3. The Aspen Plus flowsheet of system is depicted in Figure 2 where it presents a brief description of the unit operation blocks. It gives the Aspen Plus name, that is the name given to each unit operation block by the software developers. The model is based on the following main assumptions: isothermal and steady state operation, zero-dimensional, all working fluids treated as ideal gases, pressure drops are neglected and ion cross over through fuel cell cannot be modelled in Aspen Plus, therefore the overall oxidation of formic acid was considered instead of the cell half reactions. Fluid package was used to synthesize formic acid is NTRL-HOC, which is used for nonideal chemical systems. The specific assumptions for the analysis of system are listed below:

- Conversion reactor for formation of formic acid works with 85% of CO_2 conversion.
- The pressure of conversion reactor is 60 bar.
- Heat duty of the conversion reactor is about 0.3 kW.
- The storage temperature of FA is equal to the ambient temperature.
- The separator efficiency is 100%.

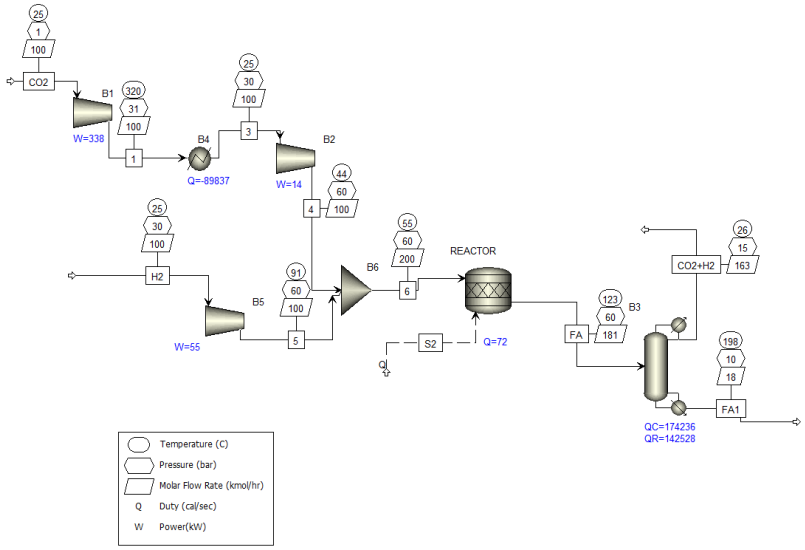

Figure 2. Process flow diagram simulation of FA synthesis and utilization in fuel cells

IV. Results and discussions

The process of validating the model and method used to synthesize FA and use in DFAFC was accomplished through a direct comparison of available data in the literature. The main criteria to make direct comparison are FA formation rate, FA fuel cell heat duty, work values, fuel cell efficiency and Nernst voltage. The literature studies form formic acid by adding Reaction Coupling (Amine) at temperatures of 180℃.
the efficiency for the conversion reactor and the fuel cells are calculated as 19.6 % and 15%, respectively. In the conversion reactor producing formic acid, there is a need for energy input to reaction. The cell is provided with fuel

through the stream via the O_2 stream, which will oxidize part of the fuel. Fuel utilization is an important parameter to indicate how much fuel will be utilized in this system, which is assumed to be 85% meaning that most of the fuel is reacted. The fuel cell has two output streams; gas and water as liquid. The gas consists of unreacted formic acid, CO_2 and H_2.

The thermodynamic properties for the fuel cell are listed in Table 1 Direct formic acid fuel cell has 150 cm^2 and 3 cells with current 0.5 A/cm^2 and 0.7 V will produce 156.5 kW power. Considering 16 hours fuel cell operation will produce about 2520 kWh electricity. In addition, the fuel cell produces about 130.9 kW heat. The power which DFAFC produced could be considered as attractive alternatives to replace batteries in portable power devices and clean energy generation.

Stream 6 contains CO_2 and H_2, and by increasing the mole flow rate of CO_2, the formed amount of formic acid will increase as well. However, the conversion will not change because of being a conversion reactor. The temperature will not affect information formic acid because the reaction occurs by adding heat and as assumed it needs 0.3 kW. The impact of the flow rate of CO_2 in the formation of formic acid is shown in Figure 3

Table 1. Mass and Energy balance of formic acid fuel cell

State	Entropy (s)	Temperature (T)	Pressure (P)	Enthalpy (h)	Mass flowrate (m)
Unit	kJ/mol-K	℃	kPa	kJ/kg	kg/s
0	0.11	25	101.3	32.26	0.23
1	6.41	25	101.3	0.00	0.10
2	0.22	40	1000.0	65.56	0.23
3	0.37	25	101.3	104.90	0.29
4	4.86	25	101.3	-8941.00	0.03
5	0.11	-	-	-1633.00	0.00

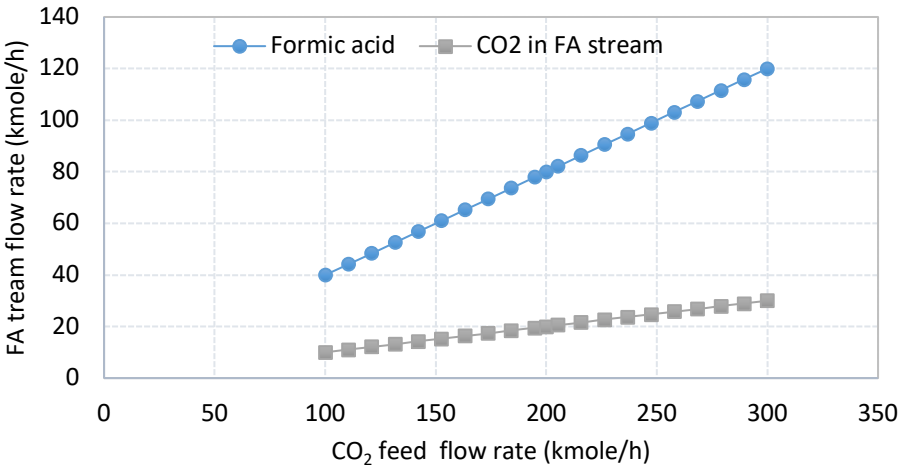

Figure 3. FA formation rate by changing CO_2 feed rate in the FA synthesis

V. Conclusions

Hydrogen storage as formic acid can play an important part in improved system integration. In hydrogen storage, energy can be stored in large amounts for extended periods. In the present work, the developed model for formic acid formation is analyzed using ASPEN plus software and Engineering Equation Solver. Furthermore, formic acid production by using CO_2 and H_2 as raw materials is a big challenge because the formation reaction is thermodynamically unfavorable. In this paper, it is proposed to solve this issue by adding heat to produce formic acid when the feed flow rate for CO_2 and H_2 100 kmole/h chosen as base flow rate. Hence, 100 kmole/h of CO_2 and H_2 can produce 874 kg/h formic acid which is capable of generating 157.5 kW with 85% fuel utilization ratio. Finally, the synthesis of FA from CO_2 and H_2 has the potential to be part of the CO_2 abatement options of the future, involving less fossil fuel consumption and alternative way of electricity storage. DFAFC produces about 157.5 kW with an efficiency of 15%. A set of sensitivity analyses was performed on understanding the impacts of the Nernst voltage and efficiency. In future work, we will consider producing formic acid by utilizing a photovoltaic system to produce energy for photochloralkali and the formic acid process and applying heat integration scenarios to be able to determine the minimum heating and cooling requirements for maximum heat recovery.

Acknowledgements

The authors acknowledge the support provided by the Hamad Bin Khalifa University, Qatar Foundation. This publication was made possible by an award from Qatar National Research Fund (a member of Qatar Foundation) with scholarship number GSRA6-2-0529-19049. The contents herein are solely the responsibility of the authors.

References

Bressmann, T. (2004). Self-inflicted cosmetic tongue split: A case report. *Journal of the Canadian Dental Association*, *70*(3), 156–157.

Eppinger, J., & Huang, K. W. (2017a). Formic Acid as a Hydrogen Energy Carrier. In *ACS Energy Letters* (Vol. 2, Issue 1, pp. 188–195). American Chemical Society. https://doi.org/10.1021/acsenergylett.6b00574

Eppinger, J., & Huang, K. W. (2017b). Formic Acid as a Hydrogen Energy Carrier. In *ACS Energy Letters* (Vol. 2, Issue 1, pp. 188–195). American Chemical Society. https://doi.org/10.1021/acsenergylett.6b00574

Hladiy, S., Starchevskyy, M., Pazderskyy, Y., & Lastovyak, Y. (2004). *Method for production of formic acid* (United States Patent No. US6713649B1). https://patents.google.com/patent/US6713649B1/en

Müller, K., Brooks, K., & Autrey, T. (2017). Hydrogen Storage in Formic Acid: A Comparison of Process Options. *Energy & Fuels*, *31*(11), 12603–12611. https://doi.org/10.1021/acs.energyfuels.7b02997

NEW ATLAS. (2018, March 22). New Atlas. https://newatlas.com/formic-acid-fuel-cell/53887/

Pérez-Fortes, M., Schöneberger, J. C., Boulamanti, A., Harrison, G., & Tzimas, E. (2016). Formic acid synthesis using CO2 as raw material: Techno-economic and environmental evaluation and market potential. *International Journal of Hydrogen Energy*, *41*(37), 16444–16462. https://doi.org/10.1016/j.ijhydene.2016.05.199

Product profile: Formic acid | ICIS. (n.d.). Retrieved November 16, 2019, from https://www.icis.com/explore/resources/news/2003/07/04/500868/product-profile-formic-acid/

Reis, A., & Mert, S. O. (2015). Performance assessment of a direct formic acid fuel cell system through exergy analysis. *International Journal of Hydrogen Energy*, *40*(37), 12776–12783. https://doi.org/10.1016/j.ijhydene.2015.07.131

Rejal, S. Z., Masdar, M. S., & Kamarudin, S. K. (2014). A parametric study of the direct formic acid fuel cell (DFAFC) performance and fuel crossover. *International Journal of Hydrogen Energy*, *39*(19), 10267–10274. https://doi.org/10.1016/j.ijhydene.2014.04.149

Schmidt, I., Müller, K., & Arlt, W. (2014). Evaluation of formic-acid-based hydrogen storage technologies. *Energy and Fuels*, *28*(10), 6540–6544. https://doi.org/10.1021/ef501802r

Singh, A. K., Singh, S., & Kumar, A. (2016). Hydrogen energy future with formic acid: A renewable chemical hydrogen storage system. In *Catalysis Science and Technology* (Vol. 6, Issue 1, pp. 12–40). Royal Society of Chemistry. https://doi.org/10.1039/c5cy01276g

van Putten, R., Wissink, T., Swinkels, T., & Pidko, E. A. (2019). Fuelling the hydrogen economy: Scale-up of an integrated formic acid-to-power system. *International Journal of Hydrogen Energy*. https://doi.org/10.1016/j.ijhydene.2019.01.153

Williams, R., Crandall, R. S., & Bloom, A. (1978). Use of carbon dioxide in energy storage. *Applied Physics Letters*, *33*(5), 381–383. https://doi.org/10.1063/1.90403

Xu, W., Ma, L., Huang, B., Cui, X., Niu, X., & Zhang, H. (2011). Thermodynamic analysis of formic acid synthesis from CO2 hydrogenation. *ICMREE2011 - Proceedings 2011 International Conference on Materials for Renewable Energy and Environment*, *2*, 1473–1477. https://doi.org/10.1109/ICMREE.2011.5930612

Kinetic studies of camel manure using thermogravimetric analysis

[1]Prakash Parthasarathy, [1]Samar El-Khalifa, [1,2]Tareq Al-Ansari, [1]Hamish Mackey, [1*]Gordon Mckay
[1] Division of Sustainable Development, College of Science and Engineering, Hamad Bin Khalifa University, Qatar Foundation, Doha, Qatar.
[2] Division of Engineering Management and Decision Sciences, College of Science and Engineering, Hamad Bin Khalifa University, Doha, Qatar.
* E-mail: gmckay@hbku.edu.qa

Abstract
Camel manures are often disposed of by landfill dumping. The dumping of the manure causes many health and environmental issues. To mitigate the ill-effect of the manure and to dispose of it in a safer way, pyrolysis treatment has been considered. However, prior to pyrolysis the thermal behavior of the manure needs to be studied. Hence, in this study, the thermal degradation of camel manure was studied using a Thermogravimetric Analyzer. The TG-DTG curve of the analysis exhibited three distinct reaction zones corresponding to moisture dehydration, hemicellulose–cellulose degradation, and lignin degradation. The kinetic parameters- pre-exponential factor, activation energy, and order of the reaction for the above zones were determined using a modified form of Arrhenius Equation. The pre-exponential factor was determined to be $3.51*10^9$, $1.59*10^9$, and $4.21*10^2$ 1/s for moisture dehydration, hemicellulose-cellulose degradation, and lignin degradation respectively. The activation energy was calculated to be 34.45, 58.34, and (-) 9.77 kJ/mol for moisture dehydration, hemicellulose-cellulose degradation, and lignin degradation respectively. The order of the reaction was determined to be 0.65, 0.95, and 0.33 for moisture dehydration, hemicellulose-cellulose degradation, and lignin degradation respectively. The knowledge on the kinetics of camel manure degradation will be helpful: for the design and fabrication of pyrolysis reactors, in the chemical reaction engineering, process modelling and simulation, and optimisation of the camel manure pyrolysis process.

Keywords: Camel manure, Thermal degradation, Thermogravimteric analysis, Arrhenius equation, Kinetic parameters.

I. Introduction

Qatar being a desert is not bestowed with plant biomass. However, there is a huge potential of generating animal biomass (manure) as it houses many species of livestock such as cattle, sheep, goats, camels, horses, and poultry. Among all the livestock manures, with respect to energy recovery, camel manure is considered the best as it can undergo degradation (thermochemical/biochemical) very easily. Further, the manure can be directly used as a fuel due to its low moisture content. Qatar houses about 126,029 camels ("Agriculture Statistics," 2018). Assuming that an adult camel excretes 0.95 T of manure per year, the camels in Qatar are generating approximately 120,000 T of manure every year (Lensch, 1999). The manure of such quantity is often disposed of in landfill sites which affects human health and causes serious environmental issues. Hence, an appropriate disposal method that can also recover useful energy and chemicals from the manure need to be identified.

Pyrolysis is one such treatment method that can effectively dispose and generate useful energy/chemicals from livestock manures like camel manure. By pyrolysis, the camel manure can be converted into useful products such as char, bio-oil, and syngas. Nonetheless, the composition of these products depends on the type of pyrolysis employed namely slow, fast, and flash. As Qatar is rich in natural gas and crude oil, Qatar shall focus on generating bio-char by slow pyrolysis from its available sources like camel manure as there is a strong demand for natural fertilizers in Qatar.

Camel manure, is composed of components such as moisture, cellulose, hemicellulose, lignin, and ash (Chen et al., 2017). Before performing pyrolysis studies, it is essential to understand the thermal behaviour of the above components as these components significantly influence the composition of the products as well as the kinetics of the degradation process. Hence, a Thermogravimetric analysis (TGA) on camel manure was performed. The TGA is a testing method conducted on samples to determine the change in weight with respect to change in temperature and time, and the results can be used to comprehend the thermal decomposition characteristics of the samples.

There are many works of literature on TGA of many livestock manures such as cattle, horse, swine, goat (Zhang et al., 2019), and chicken (Xu and Chen, 2013). However, to the best of the authors' knowledge, the TGA study on camel manure has not been undertaken so far. Hence, in this study, the TGA of camel manure has been carried out. The objective of the work is to conduct TGA of camel manure and to determine (i) the degradation temperature range of biomass components, (ii) the kinetic parameters (activation energy, pre-exponential factor and order of reaction) of the biomass components decomposition.

II. Materials & Methods

The fresh camel manure was procured from a local farm in Qatar. The camel manure as such had a moisture content of 38.00 %. The proximate analysis of the camel manure was conducted using a thermogravimetry analyser (TA Instruments SDT 650). The analysis was done according to ASTM D7582-12. The results of the proximate analysis are presented in **Table 1**.

Table 1. Results of proximate analysis of camel manure

Analysis	Sample 1
Proximate analysis (wt. %)	Air-dried-basis
Moisture	11.07
Volatile matter	58.92
Fixed carbon*d	11.14
Ash	18.87

*d – calculated by difference

The air-dried camel manure sample was sieved using a 125 μ sieve (Haver & Boecker make) and the samples that passed into the sieve was taken for the TGA. The TGA was performed using TA Instruments SDT 650 analyser. The operating conditions of the TGA is presented in **Table 2**.

Table 2. The operating conditions of the TGA study

Parameters	Values
Heating rate	10°C/min
Purge gas	Nitrogen
Purge gas rate	100 ml/min
Final temperature of decomposition	950.0°C
Residence time at the final decomposition temperature	30 min

III. Results and discussions

The obtained TG-DTG (Thermogravimetry-Derivative Thermogravimetry) curve of the camel manure is presented in **Fig. 1**.

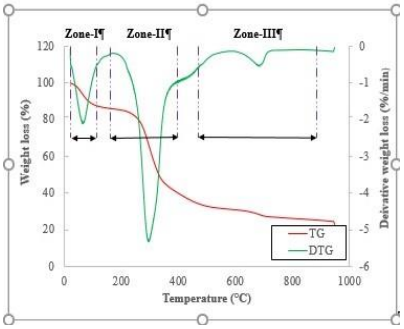

Fig. 1.-The TG-DTG curve of camel manure

From the curve, three distinct endotherms can be noticed. As illustrated in the figure, based on these endotherms the thermal decomposition of the sample is divided into three zones: Zone I, Zone II, and Zone III. The temperature range of these zones are presented in **Table 3**.

Table 3. The temperature range of the identified zones

Zones	Components	Initial temperature (°C)	Final temperature (°C)	Weight loss (%)
I	Moisture	21.27	107.00	12.15
Buffer zone (I & II)	Moisture & Hemicellulose-Cellulose	107.00	172.95	2.13
II	Hemicellulose-Cellulose	172.95	418.85	47.73
Buffer zone (II & III)	Hemicellulose-Cellulose & Lignin	418.85	483.78	4.87
III	Lignin	483.78	947.52	10.62
Residue	Ash			22.50

As discussed earlier, camel manure is composed of moisture, cellulose, hemicellulose, lignin, and inorganics. Zone-I could be due to the dehydration of water from the manure as the evaporation of water take place close to 100°C. An earlier study on pyrolysis of biomass reports that degradation of hemicellulose takes place below 350°C, while degradation of cellulose occurs between 250 and 500°C and the degradation of lignin happens above 400°C (Bo et al., 2009). Zone-II could be due to the decomposition of hemicellulose and cellulose. As hemicellulose and cellulose decompose at the same temperature range, no distinct endotherms could be observed for them. Zone-III could be due to the decomposition of lignin. Since the lignin molecules are complex, they have a long degradation temperature range. The residue left after the lignin decomposition could be due to the ash present in the manure. The region between Zone I and II could be due to the overlapping of decomposition of moisture and hemicellulose-cellulose. Similarly, the region between Zone II and III could be due to the overlapping of decomposition of hemicellulose-cellulose and lignin.

In general, biomass components undergo degradation at different rates based on their inherent nature. This is clearly evident from the three endotherms of the TG-DTG curve. Hence, the same kinetic parameters cannot be used to predict the thermal behaviour of the samples throughout its thermal transition (Kumar et al., 2008). Hence, in this study, the kinetic parameters such as pre-exponential factor, activation energy, and order of the reaction were determined for each zones considering their decomposition temperature range using a modified form of Arrhenius

equation.

Global kinetics of the devolatlization reaction can be written as (Ghaly and Mansaray, 1999)

$$-\frac{dX}{dt}=kX^{n}, \quad (1)$$

where $k=Ae^{-E/RT}$ (Arrhenius equation) and X can be given as $X=\frac{w-w_f}{w_0-w_f}$

Substituting the value of k and X in Eq. (1), then the equation becomes

$$\ln\left[\frac{-1}{w_0-w_f}\frac{dw}{dt}\right]=\ln A-\left(\frac{E}{RT}\right)+n\ln\left(\frac{w-w_f}{w_0-w_f}\right) \quad (2)$$

Eq. (2) is of the form, $y=B+Cx+Dz$ (3)

The parameters y, x, z, B, C and D in Eq. (3) can be given as

$$y=\ln\left[\frac{-1}{w_0-w_f}\frac{dw}{dt}\right],\quad x=\frac{1}{RT},\quad z=\ln\left(\frac{w-w_f}{w_0-w_f}\right)$$

$$B=\ln A,\quad C=-E,\quad D=n$$

The constants B, C, and D were determined by Multiple-linear regression equation using Linest function in Microsoft excel. The values of the pre–exponential factor, activation energy and order of the reaction for each zone is presented in **Table 4**.

Table 4. The kinetic parameter values of the identified zones

Zones	Components	Pre-exponential factor (1/s)	Activation energy (kJ/mol)	Order of the reaction (-)
I	Moisture	$3.51*10^9$	34.45	0.65
II	Hemicellulose-Cellulose	$1.59*10^9$	58.34	0.95
III	Lignin	$4.21*10^2$	-9.77	0.33

It can be noted from the table that the pre-exponential factor of the moisture dehydration is slightly higher than the hemicellulose-cellulose degradation while the pre-exponential factor of the moisture and hemicellulose-cellulose decomposition is significantly higher than that of lignin. This indicates that the evaporation of moisture and decomposition rate of hemicellulose-cellulose is much faster than the decomposition rate of lignin. From the table, it can also be observed that the activation energy of moisture dehydration is lower than the activation energy of hemicellulose-cellulose decomposition. This indicates that the energy required to decompose the hemicellulose-cellulose is higher than the energy required to liberate the moisture from the sample. It is interesting to observe that a negative activation energy value is obtained for the lignin decomposition. This negative energy could be due to the decrease in the decomposition rate of lignin in spite of the increase in temperature (David W. Oxtoby, H. Pat Gillis, 2016). The negative activation energy could also be due to the low order value of the lignin decomposition. The order of reaction for the hemicellulose-cellulose degradation is the highest indicating that the decomposition rate of hemicellulose-cellulose is faster. The order of reaction for the lignin decomposition is the lowest indicating that the decomposition rate of lignin is slower.

These kinetic parameters are very important as they can definitely be used in chemical reaction engineering, process simulation and modelling, and optimization of the camel manure pyrolysis process.

IV. Conclusion

The thermal degradation study of camel manure was conducted using a Thermogravimetric Analyzer. The TG-DTG curve exhibited three distinct reaction zones corresponding to moisture dehydration, hemicellulose–cellulose degradation, and lignin degradation. The dehydration of moisture occurred between 21.27 and 107.00°C, while the decomposition of hemicellulose–cellulose happened between 172.95 and 418.85°C and the decomposition of lignin occurred between 483.78 and 947.52°C. The kinetic parameters- activation energy, pre-exponential factor, and order of the reaction for the above zones were determined using a modified form of Arrhenius Equation. The pre-exponential factor was determined to be $3.51*10^9$, $1.59*10^9$, and $4.21*10^2$ 1/s for moisture dehydration, hemicellulose-cellulose degradation, and lignin degradation respectively. A high pre-exponential factor for moisture dehydration and hemicellulose-cellulose degradation indicates that their decomposition rate is faster than the decomposition rate of lignin. The activation energy was calculated to be 34.45, 58.34, and (-) 9.77 kJ/mol for moisture dehydration, hemicellulose-cellulose degradation, and lignin degradation respectively. A high activated energy value for the hemicellulose-cellulose degradation indicates that the energy required for the hemicellulose-

cellulose degradation is higher than the energy required for the moisture dehydration. A negative activation energy value was noticed for the lignin degradation. This could be due to the decrease in decomposition rate of lignin with respect to the temperature increase. The order of reaction for moisture dehydration, hemicellulose-cellulose degradation, and lignin degradation was found to be 0.65, 0.95, and 0.33 respectively. A higher order of reaction for the hemicellulose-cellulose degradation indicates that their decomposition rate is faster, while a lower order of reaction for the lignin degradation indicates that their decomposition rate is slower.

The knowledge on the kinetics parameters of the camel manure degradation will be helpful for the design and fabrication of pyrolysis reactors. It will also be helpful in the chemical reaction engineering, process modelling and simulation, and optimisation of the camel manure pyrolysis process. Future works should focus on studying the effect of the variable parameters such as heating rate, atmosphere, and particle size of samples on the kinetic parameters of camel manure decomposition.

Acknowledgements

The authors are grateful to Hamad Bin Khalifa University (HBKU) and Qatar Foundation (QF) for their financial support.

Nomenclature

A	:	Pre–exponential or frequency factor (min^{-1})
dw/dt	:	The ratio of change in weight to change in time
E	:	Activation energy of the decomposition reaction (kJ mol^{-1})
K	:	reaction constant
n	:	Order of reaction (–)
R	:	Universal gas constant (kJ $mol^{-1}K^{-1}$)
T	:	Absolute temperature (K)
t	:	Time (min)
w	:	Weight of sample at time t (kg)
wf	:	Weight of residue at the end of the reaction (kg)
wo	:	Initial weight of sample (kg)
X	:	Weight of sample undergoing reaction (kg)

References

Agriculture Statistics, 2018. Planning and Statistics Authority, Qatar. Doha.

Bo, L.H., Guang-yu, Z., J, C.-X., 2009. Analysis on TG-FTIR and kinetics of biomass pyrolysis, in: Sustainable Power Generation and Supply, SUPERGEN'09. IEEE, Nanjing.

Chen, G., He, S., Cheng, Z., Guan, Y., Yan, B., Ma, W., Leung, D.Y.C., 2017. Comparison of Kinetic analysis methods in Thermal Decomposition of Cattle Manure by Themogravimetric Analysis. Bioresour. Technol. 243, 69–77.

David W. Oxtoby, H. Pat Gillis, L.J.B., 2016. Principles of Modern Chemistry. Cengage Learning, Boston, USA.

Ghaly, A.E., Mansaray, K.G., 1999. Comparative study on the thermal degradation of rice husks in various atmospheres. Energy Sources 21, 867–881. https://doi.org/10.1080/00908319950014254

Kumar, A., Wang, L., A.Dzenis, Y., D.Jones, D., A.Hanna, M., 2008. Thermogravimetric characterization of corn stover as gasification and pyrolysis feedstock. Biomass and Bioenergy 32, 460–467.

Lensch, J., 1999. The two-humped camel (Camelus bactrianus). World Anim. Rev. 92, 36–41.

Xu, Y., Chen, B., 2013. Investigation of thermodynamic parameters in the pyrolysis conversion of biomass and manure to biochars using thermogravimetric analysis. Bioresour. Technol. 146, 485–493.

Zhang, J., Liu, J., Evrendilek, F., Zhang, X., Buyukada, M., 2019. TG-FTIR and Py-GC/MS analyses of pyrolysis behaviors and products of cattle manure in CO2 and N2 atmospheres: Kinetic, thermodynamic, and machine-learning models. Energy Convers. Manag. 195, 346–359.

Assessment of Three Electrochemical Energy Storage Methods for Residential Applications in Hot Climates

* Manal Alshafi and Yusuf Bicer
Division of Sustainable Development (DSD), College of Science and Engineering (CSE),
Hamad Bin Khalifa University (HBKU), Qatar Foundation (QF), Education City, Doha, Qatar

* E-mails: malshafi@mail.hbku.edu.qa, ybicer@mail.hbku.edu.qa

Abstract
Global warming plays an increasing role in our world, as the share of renewable energy sources in the overall production of electricity has witnessed exponential growth over the past years. Consumer demands are required to be met at any moment at a feasible price. Therefore, sources of renewables e.g. solar and wind power are potential options, however, production strongly relies on weather and is not fully capable of tracking the demand peaks. The need for high capacitive techniques of energy storage is strongly required to fill up the production deficiency of green energy at a convenient time of a given period. Storage is a significant issue with the advancement in renewable energy because of promoting decentralized energy production. Countless solutions exist to enhance system security, but they vary in terms of specifications. Thus, introducing a group of technical criteria can assist in understanding the performance of each storage technique. Such criteria can serve in proper comparison of different storages where the most suited technique is determined. Specifically, storing energy in hot arid climate regions is a sensitive matter as it is critical to consider appropriate technologies to implement to avoid unnecessary causalities caused by extreme temperatures. Most researches have primarily focused on understanding and defining how each storage system behaves and identifying the main specification of each system e.g. capacity and energy density or efficiency of the whole system. In addition to the literature, this study compares three different storage methods, namely; flow batteries, lithium-ion batteries and reversible fuel cells for a residential application located in hot arid regions in terms of water usage, energy density, location dependency, and temperature degradation. A selection approach regarding prior criteria was carried out among the three storage methods: lithium-ion batteries, flow batteries, and reversible fuel cells and obtained rankings were: 6.45, 6.43, and 6.13, respectively. Lithium-ion concluded to have the leading ranking in comparison with the other two methods, whereas the rankings are very close to each other and over the average, implying the potential application of these methods in hot climates.

Keywords: Electricity storage; renewable energy; fuel cell; battery; chemical storage

I. Introduction

It is undeniable nowadays that energy industries are continuously developing and are being innovative in response to the overwhelming energy demands, and its technologies. A massive interest has grown in the production of renewable energy as it can mitigate climate change. Systems of renewable energy, in which it can incorporate different types of renewable sources, are recognized as an ideal solution when it comes to the off-grid supply of power choices in rural places [1]. Due to the unpredicted behaviour of renewable sources, the benefits of these systems of energy (fuel savings, costs and emissions, efficiency), could be reachable if these systems are integrated with storage units [1]. Thus, various energy storage techniques are essential to consider in terms of being beneficial in fulfilling the climate change targets [2]. Renewable energy sources are the ultimate solutions to climate change in the world. Their wide implementation depends on sustainable energy storage techniques. A strong emphasis is invested in renewable energy as technologies targeting the relation of projects with the comprehensive sustainability of a specific system or community [3]. Countless types of renewable energy sources e.g. solar and wind are all the time replenished and could never run out and that is an advantage. Sun is what most renewable energy comes from, either indirectly or directly. Therefore, renewable energy sources are user-friendly and cost-effective as they can readily overcome the excessive use of fossil fuels [4]. There is an expansion for the requirement of energy, and its associated services to obtain economic and social development as well as enhancing health and human welfare. Energy services are undoubtedly required in all societies to satisfy basic human demands and to assist in production processes. The global use of fossil fuels has significantly dominated energy supply, in which it caused noticeable growth in emissions of carbon dioxide. Greenhouse gas emissions caused by energy services provisions have remarkably assisted in the historic rise in the concentration of atmospheric greenhouse gas. Renewable energy to contribute to economic and social development, obtain energy supply, energy access and decreasing unfavourable impacts on the health and environment, if properly implemented [5].

The increased significance of energy storage as well as management of power can be referred to numerous countries placing utmost emphasis on the production of electricity that is obtained from sources of renewable [6]. Energy storage systems are considered to be a solution that leads to the integration of renewable energy generation to existing power networks [6]. The global need for electricity is great, and its spreading by 3.6% per year, approximately, however, the wind does not always blow neither is the sun shines all the time [7]. Over the past decade, climate change is believed to be an anthropogenic origin. Great consumption of fossil fuels has caused a critical increase in the concentration of GHGs e.g. NO_2, CO_2, etc, that are considered as a major result of the rise in global average temperature. The residential sector has remarkable electricity consumption in most systems power. Variation in consumption of electricity in this sector is associated with weather conditions changes as they

often result in unfavourable peaks in overall power consumption in system powers. Therefore, it is observed that high peaks in power consumption exists associated with low and high-temperature peaks [8]. Since the hot arid climates have challenges with the implementation of energy storage techniques, the main objective of this study is to define and conduct an assessment for three optimal electrochemical storage methods for residential applications in hot and arid climates.

II. Energy Storage Systems (ESS)

Systems of energy storage are significant when it comes to power systems operation, as they assure continuity of energy supply as well as enhancing system reliability [9]. Energy storage systems vary in terms of their forms and sizes, as the scalability, cost, and size of energy storage systems strongly rely on the stored energy form [9]. Energy can be stored in various forms such as thermal, electromagnetic, kinetic, chemical, etc. Some forms are recommended for systems of small-scale, and others could be for large ones [9]. Furthermore, to compare various energy storage techniques, here, Table 1 is formed to summarize the differences among them concerning several critical energy criteria mentioned in the literature.

II. I Electrochemical storage

Electrochemical energy storage is considered as a potential technology, to store power, where a reversible chemical reaction inactive material by electrolyte is required [10]. Currently, battery storage is the second-highest storage method after pumped hydro storage. This method emits less harmful emissions and requires less maintenance [11]. Types of this storage considered here are Lithium-ion, redox flow batteries, and reversible fuel cells.

II.I. I Lithium-Ion Battery

These batteries commonly consist of an anode of graphite carbon, as well as lithiated metal oxide [12]. Salts are what the electrolyte made of [12]. In times of charging these batteries from flows of the cathode by electrolyte, to the anode [12]. In the case of discharging, the process is the opposite [12]. In the literature, a study was conducted to achieve the target of long cycle life, precise assessment for the battery of lithium-ion degradation is needful in energy management of hybrid [13]. A specific filter that is the data-focused framework is as well constructed to track states and differentiation of model parameters in times of process cycling [13]. Methods for both long and short term degradation predictions are later done to explain the significant parameters related to battery health [13].

II.I. II Redox Flow Battery

These batteries consist of a system of two electrolytes, where chemical compounds utilized to store energy are in the state of liquid, with electrolyte in solution [14]. Standard accumulators of electrochemical restrictions are overcome in such a way that reactions of electrochemical establish solid compounds, where electrodes immediately store them [14]. This system is considered a limited mass system, which restricts standard battery capacity [14]. Different types of electrolytes have been made by bromine usage as a central element, e.g. with sodium (NaBr), vanadium (VBr), zinc (ZnBr), and additional one recently, such as sodium polysulfide [14]. The efficiency of this storage within a range of 65-85% as given in Table 1.

II.I.III Reversible Fuel Cells Storage

Fuel cells are electrochemical conversion devices for producing energy through a fuel and oxidant supply. They are also used to make hydrogen by electrolysis of water in reverse mode, which becomes a reversible fuel cell [12]. This system produces hydrogen by the usage of electrolysis for off-peak consumption and securing adequate resources in times of demand by adopting a hydrogen buffer tank [12]. Then, when there is a demand, the devices operate in reverse mode of the fuel cell by supplying hydrogen and oxygen for power generation. This method shows comparatively lower round-trip efficiency as presented in Table 1. Note that in Table 1, the efficiency of fuel cell represents single-mode (electrolysis or fuel cell), whereas it should consider round-trip efficiency for electrical energy storage. In the literature, a case study was done using a numerical model to study systems of hybrid-focused storage and their combination with fuel cells was established: two high and low-temperature hydrides were chosen, considering their behaviour in metal hydrides as it was simulated and compared with the assistance of selected model [15]. This was a critical step in recognizing hydrides that are best suited to the picked situation [15].

Table 1. Comparison of different energy storages using several criteria

Electrochemical Energy Storage Method	Capacity (W/kW/MW)	Energy Density (Wh/kg, Wh/L or kWh/m^3)	Anticipated Lifetime (years)	Response Time	Energy Cost ($/kWh)	Power Cost ($/kW)	Efficiency (%)
Lithium-ion battery	1 kW-10 MW [12]	75 to 200 Wh/kg [16]	5-15 [16]	Minutes-days [16]	600-2500 [16]	1200-4000 [16]	90-95% [12]
Fuel Cells	kW to MW	800-10,000 Wh/kg [16]	5-15 [16]	Hours-months [16]	NA	10000+ [16]	60-70% [17]
Redox Flow Batteries	25 kW-10 MW [12]	NA	5-10 [16]	Hours-months [16]	NA	NA	65-85% [12]

III. Methodology

Hot climate regions have critical factors to consider when implementing systems of energy storage e.g. location, water use, temperature degradation, and energy density as all systems are compared and three of them are selected, and the decision is finalized for constructed selection criteria as shown in **Error! Reference source not found.**, where rank of 10 means best and 0 means poor with respect to each criteria column.

III. I Location

Some energy storage methods are highly dependent on specific locations. For example, PHES requires special reservoirs and vast water resources. CAES may require underground caverns. Therefore, energy storage techniques are ranked based on their specific location needs. Among selected options, the location is somehow not a limiting factor since they are chosen based on residential applications.

III. II Water use

Water shortage can curtail power production that is hydro-based and by expansion, businesses that depend on such power sources. In general, regions that lack water sources can show specific risks. Some ESS strongly relies on water use e.g. Pumped hydro requires a huge amount of water to be implemented in a site. Among the selected electrochemical routes, water is required as the source of hydrogen in reversible fuel cells. In addition, it will be required as a coolant in the battery units.

III.III Temperature degradation

Temperature affects the performance of the storage negatively. For instance, batteries storage negatively influenced by extreme heat as once it's damaged by heat, batteries capacities are difficult to restore. Over 50℃, lithium-ion batteries degrade more whereas the flow batteries can resist at slightly higher temperature. On the other hand, fuel cells can operate higher temperatures, in which PEM fuel cells operate optimally at about 80℃ temperature.

III. IV Energy density

Each energy storage system has an energy density in which it is the amount of energy stored in a system per unit volume or mass. The higher it is, the more energy to be transported or stored for the same volume or mass quantity. Lithium-ion batteries have in fact quite low energy densities compared to fuel cells as given in Table 1.

III. V Weighting Factors

Weighted Arithmetic Mean aggregates values and is used where each indicator assigns particular weights, in which overall indicators total in 100%, and such weighting scheme is determined based on the significance of the criteria that is obtained from the conducted survey. Different aggregation method is the weighted geometric mean. This type of method points to the central tendency of a set of values utilizing the product of such values instead of their sum (arithmetic mean). The arithmetic mean is preferable as it is easily calculated and understood with a lack of complexity. Besides, data separation and arrangement are not required unlike other measures of central tendencies.

IV. Results and Discussion

A survey was conducted based on the hot climate critical criteria which are water use, location, energy density and temperature degradation for all three energy storage systems. Various academic experts in energy storage systems field from different countries: Canada, Turkey, Qatar, Pakistan, and Australia have participated in answering this survey. All participants received the same questions in the same survey. The survey was simply direct; therefore, it did not include any lengthy discussions or complexity. It was divided into two parts, where the first one assists in assigning weighted factor for each criterion and the second one specifies a ranking number from 0-10 for each energy storage system for considered hot climate criteria as provided in Table 2. For instance, if 10 is given for one of the techniques concerning water use, then it means that this technology requires minimal water to be implemented. The survey aims to decide on the optimal storage techniques that are best suited for extreme temperature conditions. Table 3 shows the calculated weighted factor as the average was taken from responses obtained for each criterion.

Table 2. Weighting factors for hot climate criterion

Responses	Location	Water use	Temperature degradation	Energy Density
Participant 1	43%	9%	35%	13%
Participant 2	31%	26%	15%	28%
Participant 3	29%	16%	26%	29%
Participant 4	0%	32%	26%	42%
Participant 5	40%	10%	25%	25%
Participant 6	5%	30%	30%	35%
Participant 7	10%	20%	20%	50%
Average	**23%**	**20%**	**25%**	**32%**

After determining weighted factors as shown in Table 2 above, the second part of the survey was carried out to finalize the ranking number for each energy storage system with respect to each criterion and then decide on

the optimal techniques. Similarly, an average was calculated for all seven responses for each ESS, and then weighted arithmetic mean calculation was done in order to obtain a final ranking number for every system. For the purpose of determining the level of importance (ranking number) for every technology, a scale of 1 to 10 was adopted (10 is most and 0 is least) as shown in Table 3.

Table 3. Selection criteria (10 is the most and 0 is the least)

Energy Storage Method	Location	Water Use	Temperature Degradation	Energy Density	Overall Ranking
Weighting factor	23%	20%	25%	32%	
Lithium ion battery (Electrochemical)	7	8	4	7	**6.45**
Fuel Cells (Electrochemical)	8	4	5	7	**6.13**
Redox flow batteries (Electrochemical)	7	7	6	6	**6.43**

The optimal energy storage techniques as obtained from the conducted survey are lithium-ion batteries, fuel cells, and redox flow batteries for having an overall highest level of importance. When considering the location, lithium-ion batteries are the reasonable choice for applications that run in extreme weather. Water use is not much an issue for lithium-ion as unlike fuel cells, it does not significantly rely on water availability and can store storage even in arid regions. Furthermore, lithium-ion batteries have bear high round-trip efficiency, more flexible, and easier installation. However, among all, their temperature degradation is the highest.

In terms of fuel cells, higher temperature fuel cells are capable of making high-grade process heat in addition to electricity and are appropriate for combined power and heat/cooling for residential use. Although the system requires water (or other hydrogen source) for hydrogen production, the reversible reaction of hydrogen and oxygen yields water again, which can be recycled. Therefore, water use is also very limited for reversible fuel cell method. Besides, an outstanding energy density of 800-1300 Wh/kg as indicated in Table 1. Redox flow batteries consist of batteries types that have non-flammable electrolytes and lack the tendency of ignition or explosion e.g. vanadium redox flow battery. Additionally, its system is not as temperature-sensitive as lithium-ion batteries and can be implemented in hot regions. Water is not significantly required and it is also safe to say that this method delivers higher capacity power than lithium-ion batteries.

V. Conclusion

The purpose of conducting this study is to define and identify the three optimal energy storage systems for residential applications in hot climates. Storage is a considerable issue with the advancement in renewable energy, especially for decentralized applications. Countless solutions exist to enhance system security, but they vary in terms of specifications and are hard to compare. Thus, introducing a group of technical criteria could assist in understanding the implementation potential of each technique especially when considering sensitive regions that are hot and arid. Three optimal storage methods, namely; Lithium-ion battery, reversible fuel cells, and redox flow batteries vary in values as obtained from the survey and lithium-ion proved to have the highest overall ranking among the three with a value of 6.45 whereas other methods also yield similar results. Lithium-ion is hard to withstand extreme temperatures unless proper cooling techniques are implemented. But, they have a high efficiency of 90-95%. Although, each system characteristic was not described in detail in this study, however, the possibility of storing electrical energy was presented, whenever they are needed. Therefore, future work can focus on analyzing hot regions' behaviour, and developing efficient, and comprehensive assessments of these sources to be able to accurately compare various ESS for better implementation in hot arid climates.

References

[1] A. Petrillo, F. De Felice, E. Jannelli, C. Autorino, M. Minutillo, A.L. Lavadera, Life cycle assessment (LCA) and life cycle cost (LCC) analysis model for a stand-alone hybrid renewable energy system, Renew. Energy. 95 (2016) 337–355. doi:10.1016/j.renene.2016.04.027.

[2] S. Kapila, A.O. Oni, E.D. Gemechu, A. Kumar, Development of net energy ratios and life cycle greenhouse gas emissions of large-scale mechanical energy storage systems, Energy. (2019) 592–603. doi:10.1016/j.energy.2018.12.183.

[3] A. Mardani, A. Jusoh, E.K. Zavadskas, F. Cavallaro, Z. Khalifah, Sustainable and renewable Energy: An overview of the application of multiple criteria decision making techniques and approaches, Sustain. 7 (2015) 13947–13984. doi:10.3390/su71013947.

[4] N.K.M.A. Alrikabi, Renewable Energy Types, J. Clean Energy Technol. (2014) 61–64. doi:10.7763/jocet.2014.v2.92.

[5] IPCC, Special report on renewable energy sources and climate change mitigation: The fifth assessment report, 2011.

[6] N. Garimella, N.K.C. Nair, Assessment of battery energy storage systems for small-scale renewable energy integration, IEEE Reg. 10 Annu. Int. Conf. Proceedings/TENCON. (2009). doi:10.1109/TENCON.2009.5395831.

[7] B. Zohuri, B. Zohuri, Energy Storage Technologies and Their Role in Renewable Integration, 2019. doi:10.1007/978-3-319-92594-3_8.

[8] S. Jovanović, B.S. , Zorica Djordjević , Milorad Bojić , Slobodan Savić, Weather Conditions Impact on Electricity Consumption, in: 2012: pp. S438-47. http://www.ncbi.nlm.nih.gov/pubmed/10416545.

[9] B. Novakovic, A. Nasiri, Introduction to electrical energy systems, Electr. Renew. Energy Syst. (2015) 1–20. doi:10.1016/B978-0-12-804448-3.00001-3.

[10] IEC, Electrical energy storage: white paper, 2011. doi:10.1007/978-3-319-52311-8_1.
[11] J. Cho, S. Jeong, Y. Kim, Commercial and research battery technologies for electrical energy storage applications, Prog. Energy Combust. Sci. 48 (2015) 84–101. doi:10.1016/j.pecs.2015.01.002.
[12] R. Östergård, Flywheel energy storage - a conceptual study [Thesis], 2011.
[13] C. Liu, Y. Wang, Z. Chen, Degradation model and cycle life prediction for lithium-ion battery used in hybrid energy storage system, Energy. (2019) 796–806. doi:10.1016/j.energy.2018.10.131.
[14] H. Ibrahim, A. Ilinca, J. Perron, Energy storage systems-Characteristics and comparisons, Renew. Sustain. Energy Rev. 12 (2008) 1221–1250. doi:10.1016/j.rser.2007.01.023.
[15] M. Gambini, T. Stilo, M. Vellini, Hydrogen storage systems for fuel cells: Comparison between high and low-temperature metal hydrides, Int. J. Hydrogen Energy. 44 (2019) 15118–15134. doi:10.1016/j.ijhydene.2019.04.083.
[16] H. Chen, T.N. Cong, W. Yang, C. Tan, Y. Li, Y. Ding, Progress in electrical energy storage system: A critical review, Prog. Nat. Sci. 19 (2009) 291–312. doi:10.1016/j.pnsc.2008.07.014.
[17] C. Doetsch, J. Burfeind, Vanadium Redox Flow Batteries, Storing Energy With Spec. Ref. to Renew. Energy Sources. (2016) 227–246. doi:10.1016/B978-0-12-803440-8.00012-9.

Energy use identification for adapted production in Africa frameworks

[1,2]Aminata Kanta, [1]Rachid Outbib, [2]Lounès Tadrist

[1] (LIS) Laboratoire d'Informatique et Systèmes, 52 Avenue Escadrille Normandie Niemen, Marseille, 13013, France
[2] (IUSTI) Institut Universitaire des Systèmes Thermiques Industriels, 5 Rue Enrico Fermi, Marseille, 13013, France

* E-mails: aminata.kanta@etu.univ-amu.fr; lounes.tadrist@univ-amu.fr; rachid.outbib@lis-lab.fr

Abstract

This paper is a contribution to the analysis of the current energy access situation in sub-Saharan African regions. More precisely, the study concerns the areas remote from the main grid connection. The goal is to set up a large-scale electrification strategy to satisfy the load required and thus meet the minimum daily energy demand. Besides, the system must be technically and economically feasible according to the energy resources available in the considered area. This implies a deep assessment of the real need. Studies show a residential electrical demand of about 30% of the total electricity consumption. Exixting supply capacity efficiencies are evaluated for a great electrification improvement. Finally, some policies and recommendations are provided to improve sustainaible energy access for all.

Keywords: Energy use, Sub-Sahara Africa, Remote areas electrification, Total capacity produced

I. Introduction

The population of Sub Saharan area is estimated to more than one billion. Whereas this area remains among the places having more than 50% of its population with very low access to energy including electrification (Doorsamy, 2015) (IEA, 2019). It should be noted that, nowadays, electricity access is crucial to the region's social and economic development.

The region's energy survey has been the subject of numerous studies and assessments, particularly with regard to energy demand in remote areas. These areas sometimes face a higher electrification tariff due to the connection to the main grid over long distances. In addition, the electrical connection is less reliable for those who have access to it.

The focus of this paper is to determine the real need of the population in energy consumption and then prioritize them. Indeed, studies show that demand priorities are depending on the locality. Rural communities, for example, have a low electicity demand compared to urban communities, because of the close access to the main grid for these latters. However, rural communities and a large proportion of city dwellers still depend on the use of fuelwood due to low income in developing countries. For this, we propose here an assessment of the total energy demand both quantitatively and qualitatively including the annual consumption of traditional energy (firewood) and commercial energy (electricity, oil or others). Especially, in this period when the energy transition is a real necessity in order to mitigate climate change. the goal is, on the one hand, to have an overview of the different techniques used in order to meet the needs, on the other hand, to examine the performanace and the efficiency of the means available and then to find possible improvements for further optimization.

II. Overview of energy sector in the Sub-Sahara Africa

1. Energy demand

It should be noted that Africa, and in particular the sub-Saharan region, has a high poverty rate. This poverty is accentuated in rural areas where daily income is very low compared to the world average. The majority of the population therefore cannot afford the luxury of electrification. Their consumption remains very low. However, sustainable energy demand is constantly increasing and strongly concerns residential services. Residential accounts for 30% of total electricity consumption (Ponce de Leon Barido, 2017) (Ouedraogo, 2017). In addition, we have energy demand in schools, health centres, and small commercial activities. Residential energy demand mainly concerns cooking, lighting and recharging of electrical appliances. Electric load demand is low at about 10% (Tucho & Nonhebel, 2017), (Gebrehiwot, 2019), and more based on lighting and electrical appliances powering. In addition, this demand is dominated by lighting. Cooking energy is used from traditional fuels and remains the most consumed by households, accounting for more than 90% of total household energy consumption in remote areas.

An average SSA household have a size of five people. At least each inhabitant possesses one cellphone. Due to their low income, we can consider that the average household possesses a small Light-emitting Diode (LED) TV and a radio for informations access. LED TVs have a low load ranging between 20 and 60 watts with a rest load of 0,3 watt. This typical household generally have a minimum of three rooms including a master bedroom, girls' room and boys' room and an open space where is place for cooking, relaxing or watching TV. Supposing each place

lighted by one compact fluorescent bulb, table 1 gives the daily average residential electrical demand, cooking energy demand is not considered, as the demand is more thermal than electrical.

	Quantity	*Load (watts)*	*Operation time (hour)*	*Total energy (kwh)*
Lighting	4	11	4	0,176
Cell	4	5	2	0,040
Tv (LED type)	1	50	4	0,200
Radio	1	5	2	0,010
Total				0,426

Table 1 Average Sub Saharan African household's daily electrical demand

Based on literatures, the estimated annual net useful energy demand for cooking is 6 GJ, which corresponds to an equivalent daily consumption of about 16 MJ, or 4kWh electrical power or 10 kg or firewood burned (Tucho & Nonhebel, 2015). In addition to emit CO2, the wood fuel provides an energy that remains both insufficient and inefficient because only a maximum of 12% of the burning energy is obtained for the operation due to the humidity inside logs.

Currently, the African average annual electricity demand is estimated at 700 Terawatt- hours (TWh) with a part demand of more than 70% for the northern countries and South Africa, and with an estimated daily consumption of 4,5 kWh. This consumption includes as well housheols as health center, school and whorship place.

Agriculture is the main activity of farmers in rural areas and is one of the key factors of economic growth in sub-Saharan countries. Thus, some countries are facing the demand for electricity for agricultural productivity through advanced irrigation techniques in rural communities. And, according to the IEA, cold storage facilities powered by renewable electricity could be a reliable way to reduce post-harvest losses (estimated at 20–50%) in agricultural production. This can be satisfied by solar cooling systems.

2. Supply and installed capacity

Inadequate transport networks limit the availability of “sustainable” energy at the level of rural communities, so they resort to the traditional use of biomass for heating and cooking. Firewood accounts for 70% of energy consumption (Pillot, 2014), followed by oil which represents less than 30%. South Africa is excluded from these given data since the consumption is dominated by coal. Hydropower is the main source of electricity supply in sub-Saharan Africa. It currently provides more than 80% of the electricity supply in Ethiopia, Mozambique and parts of the western region. For example, in 2015, the total capacity installed in Ethiopia reached 4200 MW with a large source of hydroelectric power (3743 MW; 89%), followed by wind (337 MW; 8%) and thermal (126 MW; 3%) energy sources (Gebrehiwot, 2019). While the installed capacity of Ghana‘s power plant, based respectively on hydroelectric, thermal and solar energy, was about 3700 MW with an annual electricity generation of 11500 GWh in the same year (Agyarko, 2019). This latter’s thermal supply production is based on a predominant use of charcoal (39%), biomass (36%) and Liquefied Petroleum Gaz (24%) according to the IEA (IEA, 2019).

More available in the eastern part of the region, power generation is from the geothermal began to be introduced in the market, but remais less exploited. The largest producer today is Kenya with an estimated production over 700 MW. The geothermal power plants provide energy that is renewable, clean and more efficient when running without interruption. The current total energy is estimated to 250 TWh (IEA, 2019).

The development of agriculture throught use of advanced technologies is a key path to the transformation of residues into biofuels like bioethanol to replace actual industrial fuels, or renewable biomass fuel that burn with similar characteristics and heating values of coal. This process of crop residues transformation already exists in some western countries but the production remains very low due to these localities conditions.

III. Décentralized electrification

Inadequate Access to electricity and clean cooking strategies are being studied in selected villages, in order to reduce both premature deaths due to indoor air pollution and the reduction of physical tasks such as fetching, transporting firewood and water collection. The research time is estimated at 10 hours and is rather a chore for women and children, especially school-age girls. The latter are therefore deprived of their right to schooling.

In addition, both transmission and distribution are marked by losses on the main lines that connect to the central grid. This also reduces energy efficiency in the receiving electricity in rural communities. Due to this grid limitation, many business owners have a back-up generator using either diesel or fuel oil.

The sub-Saharan region has a vast reservoir of renewable energy resources, although these resources remain under-exploited due to the high capital cost of the energy conversion systems they require. The most important of these resources is the solar energy, with an average radiation of between 5 and 7 kWh/day (Pillot, 2014), depending on the country. It is very favourable to the production of electricity through conversion by means of photovoltaic solar panels. Solar energy plays a very important role in the energy transition. Another resource - that is little exploited - is wind power, with at least some installations in countries such as Kenya, Senegal and Ethiopia.
Thus, in order to find an alternative to satisfy the needs of the population, several schemes of combination of renewable energy sources are being evaluated through simulations (Pillot, 2014). The implementation of mini-grid (<10 MW of energy production) and off-grid (0-100 W) installations is then proposed according to the availability of resources, the energy demand and the appropriate technologies for greater efficiency and reliability. Off-grid includes stand-alone systems for households and micro-commercial shops. Off-grid and mini-grid are generally PV solar farms, or a combination of PV with either diesel generator or wind energy systems or both. These kinds of systems are very favourable to small business and households.

	Potential renewable energy resource		*(Existing / planned*) projects*
	Solar irradiation average (kWh/m²/day)	*Wind verage (m/s)*	
Djibouti	5.8	7.1	(IRENA, 2015) 300 kilowatt-peak grid connected PV plant 20 MW wind farm in Ghoubet*
Ethiopia	6.1	4.7	(Technology, 2013) 1 20 MW wind farm in Ashegoda
Ghana	4.2	4.4	(Mainstream Renewable Power, 2014) 225 MW wind farm in ayitepa*
Kenya	5.7	5.6	(Energy & Petroleum Regulatory Autority, 2012) 5.1 MWwind farm in Ngong 198 MW geothermal plant
Mozambique	5.5	4.8	(IRENA, 2012) 1.3 MW grid connected solar plant in Niassa

Table 2 Table 2 Renewable energy Projects in some countries of Sub-Sahara Africa

V. Discussion

The insuffiency of the electricity production induces a significant difference between the annual electricity supply and the demand. While the supphy is estimated to about 250 TWh in 2020, representing 2,8 times very low compared to the current annual electicity demand, which, currently, account to 700 TWh.

Based on the above data, it follows that improvement of access to electricity and clean cooking, either in rural and urban communities, necessitates affordable development and access to non-polluting fuels and modern technologies. This will considerably reduce the firewood fletching time spent by women and children. Non-polluting fuels include for example natural gas or biogas (by the use of agricultural waste and wood residues), they can be used for heating or even for electricity production. Electricity converters such as PV, wind power generators, or hydropower's last state-of-art technologies define modern technologies.

Each part of the region must put in place policies to reduce energy consumption and improve energy efficiency through the establishment of standards and labels for electrical appliances (Agyarko, 2019). Experiences of attempts to popularize solar cookers have shown reluctance in some localities. This is mainly due to unsuitable cooking habits. Thus, the dissemination of new technologies must involve upstream social impact studies and a consumer association in the development of innovation (IEA, 2019) in order to guarantee the penetration of products and the appropriation of technologies by users.

VI. Conclusion

The paper describes the real energy needs, and in particular the demand for electricity in the developing countries of sub-Saharan Africa. Existing plants are no longer sufficient to meet the increased demand. This is, on the one hand, related to the accentuated poverty rate, and, on the other hand, to the poor development of modern technologies enabling sustainable energy development, including full access to electricity and to a clean kitchen and the reduction of pollution problems linked to the use of traditional fuels. In order to facilitate this access, the solutions of means available have a great tendency towards decentralized electrification.

Acknowledgements

The first author would like to acknowledge the support of the Ministry of Higher Education and Scientific Research for the grant of the research fellowship.

References

Agyarko, K. A. (2019). Removing barriers and promoting demand-side energy efficiency in households in Sub-Saharan Africa. *Energy Policy, 137*, 111149.

Doorsamy, W. a. (2015). Sustainabil- ity of decentralized renewable energy systems in Sub- Saharan Africa. *978-1-4799-9982-8/15/$31.00 © 2015 IEEE*.

Energy & Petroleum Regulatory Autority. (2012). *Renewable energy portal*. Retrieved from Energy & Petroleum Regulatory Autority: www.epra.go.ke

Gebrehiwot, K. a. (2019). Optimization and cost-benefit assessment of hybrid power systems for off-grid rural electrification in Ethiopia. *Energy, 177*, 234-246.

IEA. (2019). *Africa Energy Outlook 2019.* Paris.

IRENA. (2012). *Mozambique renewable readiness assessment*. Retrieved from International Renewable Energy Investment: https://www.get-invest.eu/

IRENA. (2015). *International Renewable Energy Agency.* Retrieved from Djibouti renewable readiness assessment: https://www.irena.org/

Mainstream Renewable Power. (2014). *Ghana : 150 MW Ayitepa plant*. Retrieved from https://www.mainstreamrp.com/

Ouedraogo, N. S. (2017). Alternative scenarios and their implications for sustainable development strategies. *Africa energy future, 106*, 457-471.

Pillot, B. (2014). *Planification de l'électrification rurale décentralisée en Afrique subsaharienne à l'aide de sources renouvelables d'énergie : le cas de l'énergie photovoltaïque en République de Djibouti.* Université Pascal Paoli. tel-01127072.

Ponce de Leon Barido, D. a. (2017). The natural and capital infrastructure of potential post-electrification wealth creation in Kenya. *Energy, Sustainability and Society, 7*, 28.

Technology, P. (2013). *EEPCO begins operations of 120MW Ashegoda wind farm in Ethiopia*. Retrieved from Technology, Power: https://www.power-technology.com/

Tucho, G. T., & Nonhebel, S. (2017). Alternative energy supply system to a rural village in Ethiopia. *Energy, Sustainability and Society*.

Tucho, G., & Nonhebel, S. (2015). Bio-Wastes as an Alternative Household Cooking Energy Source in Ethiopia. *Energies, 8*, 9565-9583.

Cost and Thermal Aspects of Solar Driven Heating Assistance Options for Residential Buildings

[1*]Ümit Deniz Akyavuz, [2]Hasan Özcan
[1] Kilis 7 Aralık University, Vocational School of Technical Sciences, Electric and Energy Department, Mehmet Sanlı Mah. Doğan Güreş Paşa Bulvarı No:134 KİLİS
[2] Yıldırım Beyazıt University, Faculty of Engineering and Natural Sciences, Mechanical Engineering Department, Ayvalı Mah. Takdir Cad.150 Sk. No:5 Etlik-Keçiören /ANKARA

* E-mails: udakyavuz@kilis.edu.tr

Abstract
Turkey is a country that imports energy and its annual natural gas (adopted in the cleanest of fossil fuels) consumption is over 50 billion m^3. Every year 12-15 billion m^3 of natural gas is used in residential heating. Energy from renewable energy systems can reduce both CO_2 emissions and national energy imports. In this study, storage of sensible heat, hydrogen and electricity is compared in four different systems to be integrated to existing heating systems utilizing solar energy for heating assistance. Vacuum tube collector system and parabolic thermal collector (PTC) system are selected for sensible heat storage, photovoltaic (PV) panel system is selected for hydrogen storage and electrical energy storage via batteries. According to calculations for an area where 300 kW of solar energy falling for 8 hours, the highest heating support is PTC with approximately 5800 MJ. Its natural gas equivalent is approximately 160 m^3/day. PTC system is followed by thermal energy storage with vacuum tube, battery and hydrogen storage respectively. However, PTC system requires additional power generation system for power to grid when there is no thermal energy requirement. Cost aspects of the studied cases are also taken into account where hydrogen storage system represents the highest capital costs and increase the thermal energy cost for heating assistance.

Keywords: Energy storage, renewable energy, solar energy, heating system

I. Introduction

It is desirable that the fuel to be used in building heating is both cheap and that emits the least emission to the environment. It is known that natural gas is more suitable fuel than fuel oil, coal and engine. Thermal energy unit cost comparison is given in Table 1 (International Renewable Energy Agency, 2020; Journal of Natural Gas, 2020). In 2016 to meet the energy demand in Turkey, 87% of fossil fuels are provided. National natural gas consumption is 53.86 billion m3 for 2017, 25.1% of this was realized in residential buildings. (Energy Market Regulatory Authority, 2020). Application areas of renewable energy systems have increased due to technical, environmental and economic benefits, as they will not be exposed to fuel costs, unlike systems using fossil fuels (Adefarati ve Bansal, 2016). Energy storage methods have been developed because the discontinuity of energy from renewable energies such as the sun requires storage (Kronhardt vd., 2014; Ma vd.,2014).

Table 1. Thermal energy unit cost comparison

Fuel/Energy type	Unit thermal energy cost $\$/kWh_t$	Fuel/Energy type	Unit thermal energy cost $\$/kWh_t$
Natural gas	0,028	LPG	0,126
Domestic lignite coal	0,027	Biomass	0,034-0,050
Imported Siberian coal	0,035	Solar-thermal	0,020-0,040
Fuel Oil No:4	0,067	Electric heating	0,100-0,110
Bulk gas	0,117	Geothermal	0,004-0,100
Diesel	0,100		

A variety of materials are used to store thermal energy. It is desired that these materials have thermophysical properties such as melting point, high latent heat, high specific heat and high thermal conductivity for the given thermal application (Alva et al., 2017). One of the first projects that uses mineral oil as a thermal storage medium is SEGS-I, which allows for 3 hours of storage. Nominal operating temperatures between the high and cold temperature tanks of mineral oil, which correspond to 42% of the cost, are 307 °C and 240 °C (Barnes & Levine, 2011; Herrmann & Kearney, 2002). In solar heating operation using vacuum tube, the solar radiation on the collector surface is absorbed. Then the water gets warmer and passes to the radiator in the indoor unit with natural circulation. The heating rate approaching 50% has been achieved (Alpaydın and Küçüka, 2017). In the system study where hydrogen energy is stored with the help of PV panel for use in the cooling system, 2.27 kg of hydrogen is stored during 10 hours of sunbathing (Özcan ve Akyavuz, 2017).

In this study, storage of sensible heat, hydrogen and electricity is compared in four different systems to be integrated to existing heating systems utilizing solar energy for heating assistance. Vacuum tube collector (VTC) system and parabolic thermal collector (PTC) system are selected for sensible heat storage, photovoltaic (PV) panel system is selected for hydrogen storage and electrical energy storage via batteries.

II. System Description

In Figure 1, the configuration of the four systems is given in one diagram. Line 1-2-3 is the current heating system. Line of B1 and B2 are followed in the battery system. In thermal storage systems, T1 and T2 lines are followed. The electrical energy produced by the first system PV panel is stored in the battery group. It is used for heating the water if needed. This system is represented by line 4-5-6-7. In the second system, the electrical energy produced by the PV panel is used in electrolysis and stored as hydrogen. This system is represented by line 4-8-9-10. In the third system, solar energy concentrated by the parabolic mirrors is used to heat the fluid in the thermal tank. This system is represented by line 11-12-13-14. The thermal energy stored in the fourth system is provided by the thermal fluid heated in the solar energy system with vacuum tube. This system is represented by line 11-15-16-14.

The main purpose of each system that uses 8 hours of sunlight a day is to obtain thermal energy in the thermal tank. Then the thermal energy in the thermal tank is used to heat the water in the combined heating system.

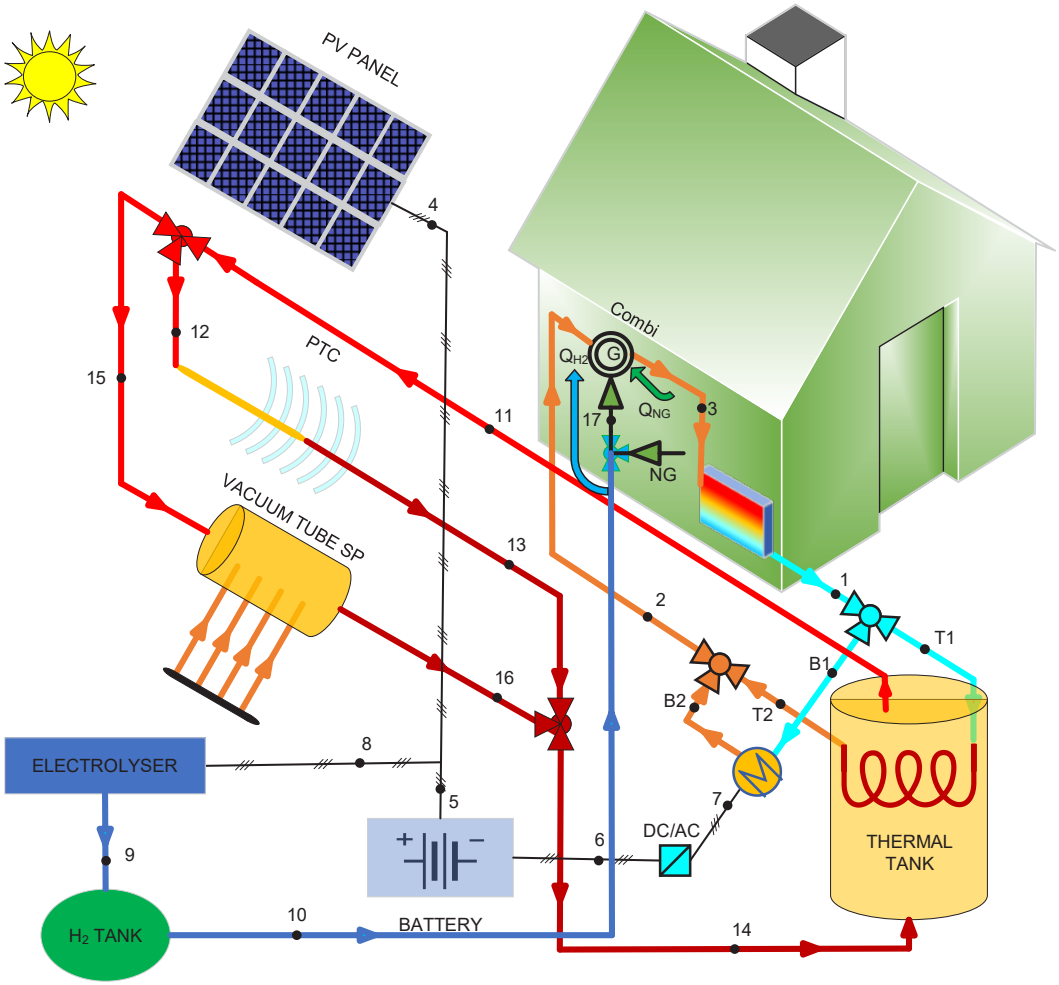

Figure 1. Systems description

III. Analysis

Q is the maximum useful energy from the collectors, A is collector area, I_N is the global solar radiation received as $1000\ W/m^2$ in calculations. The efficiency express is

$$\eta_{th} = \frac{Q}{I_N \times A} \quad (1)$$

Thermodynamic and cost equations of the components are given below as titles (Dinçer and Zamfirescu, 2014; Özcan and Akyavuz 2017; Wang and et al., 2019).

PV Panel

Energy efficiency in photovoltaic system is different from thermal systems. It is the ratio of that maximum power to solar radiation and area are multiplied.

$$\eta_{pv} = \frac{IV}{I_N A} \quad (2)$$

Electrolyser- Hydrogen Tank

The electrolyser efficiency is calculated with the following equation. Where $E_{tot,elec}$ depends on reversible, activation and concentration overpotentials.

$$\eta_{elec} = \frac{146.96}{E_{tot,elec}} \quad (3)$$

$$\eta_{elec} = \dot{m}_{H2,prod} \times \frac{HHV_{H2}}{\dot{W}_{elec}} \quad (4)$$

The total mass of H_2 to be stored for 8 hours is expressed with the following equation:

$$H_{2,stored} = 8 \times 3600 \times \dot{m}_{H2,prod} \quad (5)$$

The specific volume of hydrogen in storage conditions is used for the tank volume.

$$V_{tank} = H_{2,stored} \times v \quad (6)$$

Parabolic Through Collector (PTC)

Optimum PTC efficiency can be obtained 0.75. In this case, $I_N \times A$ corresponds to 300 kW.

$$\dot{Q}_{abs} = I_N \times A \times \eta_{opt} \quad (7)$$

Vacuum Tube Collector (VTC)

T_f is average inlet and outlet temperature, T_i denotes the inlet temperature, T_O represents the outlet temperature ($T_f = (T_i + T_O)/2$), T_{amb} refers to the ambient temperature, and I_N indicates the solar irradiance. The expression of vacuum tube solar energy efficiency is written as follow:

$$\eta = \frac{Q}{A \times I_N} \quad (8)$$

$$\eta = 0.8520 - 5.2618 \times T_f^* \quad (9)$$

$$T_f^* = \left(\frac{T_f - T_{amb}}{I_N}\right) \quad (10)$$

Natural gas heating system

LHV is natural gas upper heat value received as $8000\ kcal/m^3$. , V_{NG} is the amount of natural gas used. Natural gas total thermal value is as follows:

$$Q = LHV \times V_{NG} \quad (11)$$

Economic Analyses

The cost of energy from thermal or photovoltaic systems can be calculated by the capital costs of the system and the total energy produced.

$$C_{th}(\$/kWh) = \frac{C_{total}}{Q_u \times T_{life} \times T_{cap} \times 3600} \quad (12)$$

The total cost of all equipment used in the system is C_{total}. Interest rates and maintenance-repair costs are also included. Where, T_{life} is facility life and T_{cap} is facility capacity.

Table 2. Cost correlations for the studied systems components (in USD).

Component	Cost equation	Explanation
PV Panels	$C_{PV}(\$) = 310 \times A_{PV}$	A_{PV}: Panel area. Varies with the studied systems.
Battery	$C_{BAT}(\$) = 150 \times P$	P: Battery power
Electrolyser	$C_{EL}(\$) = 940 \times \dot{W}_{elec}$	$\dot{W}_{elec}$:Required power to produce adequate amount of hydrogen
H_2 Tank	$C_{TANK,H2}(\$) = 240 \times m_{H_2} \times SF$	SF: Safety factor (1.1)
PTC	$C_{PTC}(\$) = 227 \times A_{PTC}$	A_{PTC}: PTC area. Varies with the studied systems.
Vacuum Tubes	$C_{VT}(\$) = 120 \times A_{VT}$	A_{VT}: Vacuum tube area
Thermal fluid	$C_{FL}(\$) = 10 \times m_{FL}$	m_{FL}: Thermal fluid mass
Thermal Tank	$C_{TANK,TH}(\$) = 8437 \times V_T$	V_T: Thermal tank volume
Natural gas	$C_{NG}(\$) = 0.028 \times Q_{NG}$	Q_{NG}: Natural gas thermal value

The cost formula of each component in USD is shown in Table 2.

IV. Results and discussions

Values in Figure 2 were obtained, if PV efficiency is in the range of 20-25%, Battery and inverter efficiency is in the range of 85-95%, electrolyser efficiency is in the range of 60-70%, PTC efficiency is in the range of 70-75%, VTC efficiency is in the range of 50-70%, tank efficiency is 90%. The highest thermal energy value among the four systems is obtained as 5832 MJ in PTC system. Thermal energy unit cost is in the range of 0.06-0.16 $/kWh$_{th}$. PTC is the highest in system costs. This is because the cost of thermal oil and thermal tank corresponds to 80% of the total cost.

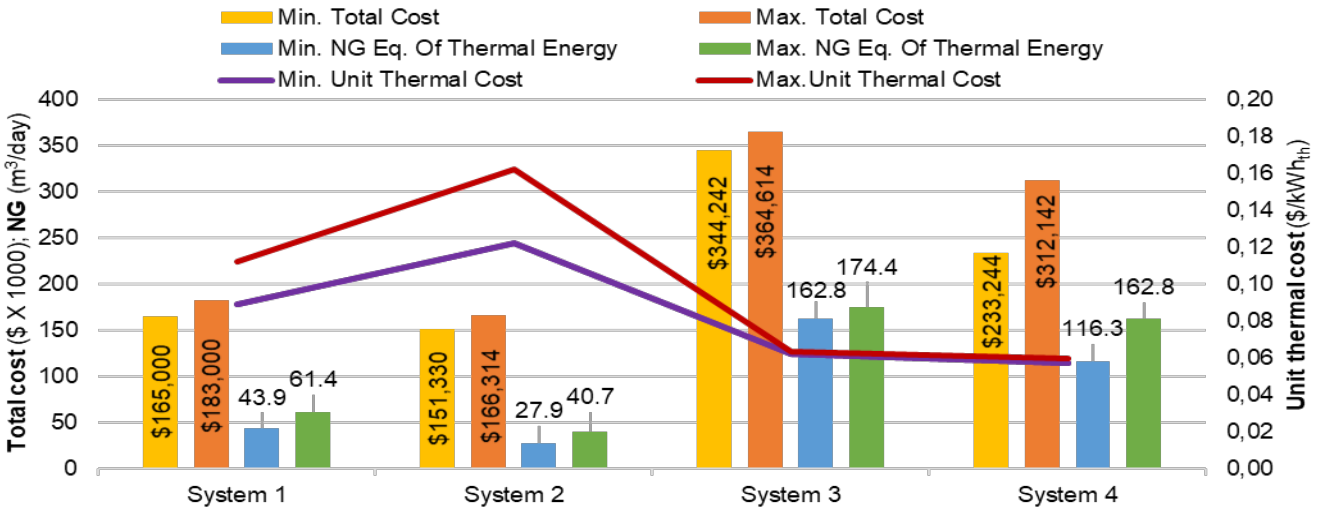

Figure 2. Results of systems in terms of cost and NG equivalent

V. Conclusions

Storage of solar energy as direct thermal energy is more efficient than other systems. In addition, if stored thermal energy is used during the day, it will reduce the cost of storage components. However, thermal storage requires higher temperature solar harvesting and a power production system might be required when there is no thermal energy need. A transient analysis may provide a better insight for cost assessment of the considered cases for solar driven heating assistance to help circular economy and decrease import energy.

References

Adefarati, T., and R.C. Bansal. 2016. Integration of Renewable Distributed Generators into the Distribution System: A Review. IET Renewable Power Generation 10 (7): 873–84. https://doi.org/10.1049/iet-rpg.2015.0378

Alpaydın, G.U. and Küçüka, S. 2017. Thermal Performance of Solar Room Heater with Evacuated Glass Tubes. 13. Ulusal Tesisat Kongresi, 697-706

Alva, G., L. Liu, X. Huang, and G. Fang. 2017. Thermal Energy Storage Materials and Systems for Solar Energy Applications. Renewable and Sustainable Energy Reviews 68: 693–706. https://doi.org/10.1016/j.rser.2016.10.021

Barnes, F.S., and J.G. Levine. 2011. Large Energy Storage Systems. Boca Raton: Taylor and Francis Group

Dinçer, İ. and Zamfirescu, C. 2014. Advanced power generation systems. Elsevier

Energy Market Regulatory Authority. Doğalgaz Piyasası 2017 Yılı Sektör Raporu. https://www.epdk.org.tr/Detay/DownloadDocument?id=nEv8WXcSskU=

Geyer, M., Lüpfert, E., Osuna, R., Esteban, A., Schiel, W., Schweitzer, A., Zarza, E., Nava, P., Langenkamp, J. and Mandelberg, E.,2002. EUROTROUGH-Parabolic Trough Collector Developed for Cost Efficient Solar Power Generation. 11th Int. Symposium on Concentrating Solar Power and Chemical Energy Technologies

Herrmann, U., and D.W. Kearney. 2002. Survey of Thermal Energy Storage for Parabolic Trough Power Plants, Journal of Solar Energy Engineering 124 (2): 145. https://doi.org/10.1115/1.1467601

International Renewable Energy Agency. Renewable Power Generation Costs in 2017. https://www.irena.org/-/media/Files/IRENA/Agency/Publication/2018/Jan/IRENA_2017_Power_Costs_2018.pdf

Journal of Natural Gas. Çeşitli Yakıtların Maliyet Karşılaştırma Tablosu. http://www.dogalgaz.com.tr/edergi/frame.asp?mag_id=4&sayi=213

Kronhardt, V., S. Alexopoulos, M. Reißel, J. Sattler, B. Hoffschmidt, M. Hänel, and T. Doerbeck. 2014. High-Temperature Thermal Storage System for Solar Tower Power Plants with Open-Volumetric Air Receiver Simulation and Energy Balancing of a Discretized Model. Energy Procedia 49: 870–77. https://doi.org/10.1016/j.egypro.2014.03.094

Özcan, H. and Akyavuz, Ü.D. 2017. Thermodynamic and economic assessment of off-grid portable cooling systems with energy storage for emergency areas", Applied Thermal Engineering 119. 108–118. https://doi.org/10.1016/j.applthermaleng.2017.03.046

Wang, T., Zhao, Y., Diao, Y., Ren, R., Wang, Z. 2019. Performance of a new type of solar air collector with transparent-vacuum glass tube based on micro-heat pipe arrays. Energy. 177, 16-28

The Energetic and Enviromental Parameters' effect on The Valuation of Bulk Carriers.

[1*]Murat Koray, [2]M.Ziya Söğüt

[1] Piri Reis University MHVS,Tuzla, Istanbul, Turkey
[2] Piri Reis University, Maritime Faculty,Tuzla, Istanbul, Turkey

* E-mail: nmkoray@pirireis.edu.tr

Abstract

Depending on the weather and the sea condition, all duty processes of dry cargo vessels consume energy depending on the device / system configuration that is either activated or deactivated. These processes affecting energy consumption can be defined as maneuvering in the port with full load on the port, open coastal waters and narrow waters, succession on the open sea, approaching the port of arrival, piloting the ship, pocketing or hoisting abdomen with pushing and pulling means and finally load handling. However, there is also a loss of energy wasted in direct proportion to the abilities of the ship's personnel. As a result of the development of environmentally sensitive systems and the regulations imposed by regulatory authorities such as the International Maritime Organization, Flag and Port State, shipping companies are under severe conditions for developing environmentally sensitive behavior as well as coping with low freight rates. This study is based primarily on the energy analysis and environmental effects of the power transmission system used in a dry bulk carrier, based on the operating parameters. Then, considering the performance data, the effects on the ship valuation processes are also questioned. At the end of the study, taking into account the fuel cost, which is the biggest impact on the Operational Expenditures costs, the relationship between the ship operation processes and valuation is presented. As a result of the study, it has been found that the total amount of fuel at 20°C has a value of 31.54% when 30 voyages are considered. A one-degree savings rate in this load distribution has yielded a 5.27% savings, with 510.31 tons. These savings increase the ship' value up to 2.7 million USD at the end of the economic life.

Keywords: dry cargo carriers, ship, energy, efficiency, ship valuation

I. INTRODUCTION

The maritime industry is one of the most important players in the logistics sector and reaches 90% of the potential for transportation. In the sector, which has basically fossil fuel-based energy consumption, the limitations imposed by national and international standards have forced all stakeholders to work on energy-efficient management. Especially, fossil-laden consumption can be seen as a major problem area that causes environmental threats such as CO_2, SO_x and NO_x. In addition to these, physical wastes, chemical wastes used for various purposes, ballast water pollution which balances load effects can also be considered as subjects to be studied in the sector. The International Maritime Organization (IMO) has developed a global approach based on the efficient use of energy and the reduction of emissions in fossil-based systems. The Energy Efficiency Design Index (EEDI), Energy Efficiency Operational Index (EEOI) and Ship Energy Efficiency Management Plan (SEEMP) management programs developed by the IMO sector in the context of sustainable energy efficiency policies can be seen as pioneering work in this respect. In addition to these studies, market-based measures (MBMs) based on the marine industry and sectoral studies have been taken into consideration (Pike, 2011).

The maritime sector, together with its stakeholders, is considered an important parameter in the development of sustainable policies. In this respect, not only the investment costs but also the maintenance costs of the vessels are important as well as the operating and voyage costs of the vessel. As a matter of fact, in the sector, many cost functions that define valuation are developed, which are basic components such as initial investment costs, fuel costs, repair and maintenance costs, personnel and insurance. Criteria assessed in this context greatly affect the costs of the vessel directly. In particular, it shows that fuel consumption is an important parameter for the measures considered in an economic appraisal.

The energy consumption of a commercial ship using the same trade routes may vary depending on sea and weather conditions. Important reasons for varying fuel consumption are operational parameters and energy management.

Technological features can be seen as a significant influence in valuation. Optimizations based on efficiency in energy consumption processes, conditions based on productivity in operational parameters, reveal the most efficient use of technology and affects the life cycle of the ships's expectancy. Therefore, technological features affect the valuation costs positively.

In studies related to cost analysis based on valuation for a ship, the size of the ship, the fuel consumption performance and the operational maintenance costs can be seen as key components. In this study, the energy and environmental performance of a main

propulsion system belonging to a bulk carrier referenced to parameters is examined. Then, considering the performance data, the ship valuation process effects are also defined.
At the end of the study, the relationship between shipbuilding processes and ship's appraisal will be introduced, taking into account the fuel cost, which is the biggest impact of Operational Expenditures (OPEX costs).

III. MATERIALS AND METHODS

III.1 Shipping Industry and Energy Productivity

The major part of world transport has reached a potential of 90% with tanker trade and dry cargo trade. Since 2008, the distribution of world transport and sea transport have been realized as in Fig. 1.

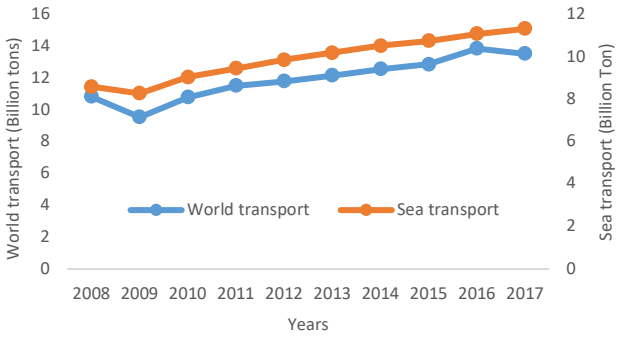

Fig.1: World and Sea Transport Changes (DTO, 2017)

The seaborne trade was at an average of 83.02% between 2008-2017. Although the change has ranged between 79% and 84% since 2008, this followed an upward trend with a change of 4.44% after the 2016 crisis. According to the United Nations Trade and Development Organization (UNCTAD) reports (2017), the distribution of the world's maritime trade fleet over 100 gross tonnes is as follows (DTO, 2017).

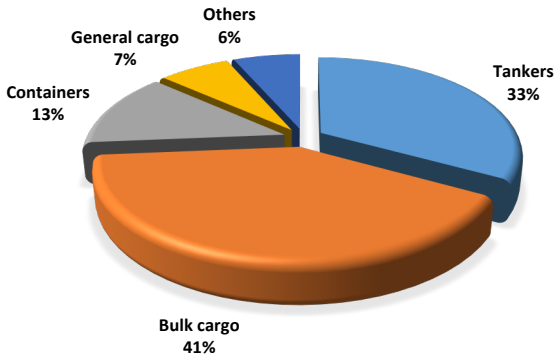

Fig. 2: Distribution of World Merchant Fleet (DTO, 2017)

Dry bulk shipping has the largest share in maritime transportation and includes general cargo, bulk dry cargo, and container transportation. Dry Bulk Carriers have had a maximum tonnage increase from 27% to 40% according to the UNCTAD' 30-year data. The share of container vessels has fallen from 17% to 6.5% due to the inability to compete with general cargo ships and freight with high costs. Although, the share of container ships increased from 1.6% to 13% (DTO, 2017).
The maritime sector, which consumes about 10% of the world's energy consumption, is a sector with mostly fossil fuel consumption. In the sector where the individual load effect is quite high, the main engines are mainly diesel engines. As fuel consumption has increased since the 1970s, improvements are seen towards lower fuel consumption. In diesel engines, stroke / bore ratio, peak pressure effects, low speed and average speed management, and reductions oriented towards oil consumption are at the top of these (GEA, 2012).
The maritime industry is seeing specific reductions in average impact pressures in diesel engines and fuel injection technologies. Also in fuel systems, control mechanisms based on fuel injection direction, spray runs, injector nozzle improvements, direct NO_x and SO_x reduction have become a priority.

III.2 Vessel Valuation

In the maritime sector, the economy of scale is a decisive factor in the formation of ship supply and demand, while the excessive volatility of the freight market makes ship valuation difficult. It is not enough to know only the age, tonnage and market price of ships in order to make a vessel appraisal close to the correct value. Factors such as the amount of production, the supply and demand situation of these goods, the gross national product of the countries, and the amount of each item transported by sea, which are the subjects of the trade, provide the predictability of the annual carrying capacity and the type of goods that these vessels can carry. These factors are taken into consideration when freight rates are calculated. However, freight rates are also affecting the profitability of the trade, as it is exposed to serious fluctuations in the maritime market, which is extremely fragile. Freight rates are an important decision support data for valuation of vessels. Current freight rates and estimated freight rates in the future; provides a significant input at the choice of new shipbuilding purchase, second hand ship purchase, hot / cold laid-up or out of service preferences.

Operational costs are utmost important in periods when freight rates are low. Large size carriers need to transport long distances at once, and relatively small vessels should be used at short distances. Especially during these periods, the high prices of the fuels consumed by the vessels cause them not to be profitable. For dry cargo vessels, operation costs, periodic maintenance costs, voyage costs, cargo handling costs and capital costs are important variables in terms of operating costs.

Energy efficiency emerges as a distinctive factor to determine the performance of variables affecting operating costs. In terms of operational costs, the quality of the lubricating oil used in the main and auxiliary machines affects the insurance values as well as the frequency of use of spare materials, failure rates due to the age of the ship and the usage pattern,

periodical or selected maintenance, repair and overhaul applications affect the value of the vessels. In terms of voyage costs for a Capesize dry bulk carrier, the performance of the main and auxiliary machines of the ship and the speed-dependent fuel consumption (approximately 66% fuel oil and 10% diesel oil) have an important place in the total cost of the voyage (Martin, 2009).

Fuel consumption depending on the design of the ship, the capacity of the crew on the ship, and the type of freight has different variables during the handling period at the port. Cargo handling of dry bulk carriers are much more laborious and costly than a container ship or a Ro-Ro ship, since dry bulk carriers have heavy and large-scale bulk cargoes. According to Clarkson data considering the capital costs, maintenance-repair costs, voyage and operation costs of vessels for 5, 10 and 20 years old, the cost of capital decreases as the ship age increases, complex faults arise and maintenance-repair costs rise. Approximate voyage costs increase by 7%, operating costs increase by 13%. Operation and voyage costs for dry cargo vessels up to 10 years range from 2% to 4%, with a radical increase of 5% to 8% over the second decade.

For vessels over 20 years old, there is no commercial profitability during periods when there are particularly low freight rates, and it is considered to be a suitable way of getting out of service in the age range of 20-25 years. 20 years is a critical age for ships. During this period, options for renovation or modernization should be considered. However, the rapid progress of the technology reveals that the strict rules laid down by the regulatory authorities in particular for environmental protection are not a rational solution at the end of a ship's life cycle (maximum 10 years at high cost modernizations). As a result of the splashing of shipbuilding technology in the next 20-30 years, it may be possible to get the vessels out of service perhaps every 10 years (LTAV, 2018). Depending on the dwt tonnage of a dry bulk carrier, the total cost is expressed by the following formula:

$$Ctm = \frac{OC+PM+VC+CHC+K}{DWT} \qquad (1)$$

where: C_{tm}: Cost per dwt per annum (t: year, m: stands for the m^{th} ship), OC: Operational Cost per annum, PM: Periodic Maintenance per annum, CHC: Cargo Handling Cost per annum, K: The capital cost per annum. DWT: The Ship's deadweight (LTVA, 2018).

As can be seen from the cost formula, fuel consumption plays a decisive role in total cost per deadweight because each cost item has a variable that affects fuel consumption. If the ship's valuation formula in the context of the "Discounted Cash Flow Method" developed by the Hamburg Ship Brokers Association is looked at; the difference between revenues and expenditures, and the residual value of the ship, taking into consideration the discount rate years to year, long-term value of the ship can be estimated. As can be understood from this form, the OPEX costs and the discount rates are at the forefront.

$$DCFV = \sum_{t=1}^{T} \left(\frac{(Ct-Bt)}{(1+i)^{t-p}} + \frac{RVT}{(1+i)^{T-p}} \right) \qquad (2)$$

C_t = Charter Income, C_1 = Current Net-TC Rate in running year, $C_{2\text{-}T}$ = Average Net-TC Rate of the past 8-10 years (If possible, otherwise shorter), Bt = Average OPEX of the last 8-10 years, i = Discount Rate, t = period, t_1 : current year, $t_{2\text{-}T}$: period end, Average 10 year charter rate), T = Remaining period until Age 20/25, RV_T = Residual Value, In this formula the exponent t–p can be fractional, which enables the discount rate to correspond to the appropriate period (LTAV,2018).

After the dry cargo vessels have passed 10 years of age, it is now possible to articulate the residual value of these vessels. However, when it comes to ship valuation, due to the rising volatility of vessels' value, especially ships older than 10 years, it is seen that the same notation of vessels value can be different from each other in respect to cost-effectiveness. In this sense, comparing only the previous sales values of similar vessels, looking at only market values could lead to a miscalculation.

The physical condition of the tanks' interior coatings, the deficiencies in the criteria of seaworthiness and cargoworthiness of the ships, the compatibility with the newly published regulations by authorities, having a few purchasers, such as chemical tankers in the niche market, the availability of complex faults with high cost repairs or the need to equip with new systems / devices, require additional calculations to determine the value of these vessels. Therefore, as the ship ages, a more balanced and reasonable relationship can be established between freight rates and charter rates as a result of the reduction of total energy loss and to prevent the misuse of the ship.

Given the high OPEX costs in older ships, it would be possible for the ship to operate with a profit margin above charter rates for vessels between 10 and 25 years of age with a holistic energy approach instead of laid-up or out of service options. In particular, reducing fuel consumption to a minimum during the periods at the cylical bottom (trough) of the economy could be an important part of the holding strategies. As the tonnage of ships is reduced, the cargo capacity will also be decreased, so Handysize-type dry cargo ships can only be covered with their operating costs in adverse economic conditions and may have worked unprofitably. In this situation, owners's choice will be Aframax or Capesize Dry Bulk Carriers, but, their carrying capacity will not be complete with maximum freight because of the lessened production capacity of the world in any time. Although it is possible to manning of a vessel with a qualified crew to ensure safety and security at sea, there is no difference between Handymax and the Capesize Dry Bulk Carriers in terms of personnel costs.

The daily average fuel consumption of a dry cargo ship with a capacity of 30,000 DWT is around 21 ton / day. The fuel consumption of a dry cargo ship of 170,000 DWT is around 50 tons/day. The annual USD / DWT costs are reduced by 62% compared between two dry bulk carriers, which is about 2.5 times the fuel

consumption. When the fuel cost is examined, Capesize Dry Bulk Carriers are 42% more economical than Handysize Dry Bulk Carriers (LTAV, 2017).

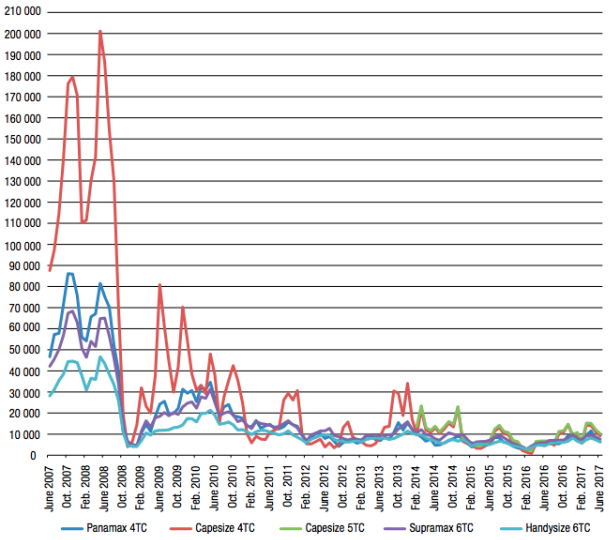

Fig. 3: Distrubitions of world merchant fleet (UNCTAD, 2014)

However, according to UNCTAD data, Freight rates of $200,000/pday for Capesize in 2008 fell to $10,000/pday in June 2017 (UNCTAD, 2014). According to the estimation of 25th April of 2018 by the brokerage firm of Alibra Shipping Limited, Time Charter Rate is calculated as $19750/pday. The highest volatility occurred in $160,000/pday in August 2008, $80,000/pday in September 2008, $15,000/pday in October 2008 and $5,000/pday in November 2008 (Kyong, 2013). Capesize Dry Bulk Carriers are mainly used to carry iron ore (70-80%), partly coal (30-40%) and grain (0-5%). Handysize Dry Bulk Carriers carry mainly grain loads. Hence, major maritime trade routes are determined by the supply and demand of major loads. According to the Baltic Dry Index (BDI), the index decreased from 3,000 in 2010 to 1363 on 28th April of 2018 (Malcome, 2017). This means that if the daily index multiplier is assumed to be 0.110345333, then the freight value can be calculated as 12353 USD / day for the index of 1363. Assuming that the TCR values are 19,000 USD / day, there will be a loss of approximately 7000 USD / day for Capesize Dry Bulk Carriers. In this case, it may be necessary to take some economic measures, such as changing major commercial routes, lowering crew salaries or reducing the number of personnel, attenuating the quality of the given provision. In addition, some options might be preferred such as laid up or out of service. The most important consideration in the decision-making process is to focus on fuel consumption and energy efficiency, which have the greatest effect on voyage costs and operating costs. Measures such as lowering the ship's speed by 11 kts, adaptation of the integrated energy management system to the vessels, reconsideration of the concept of ship use, and the gradual reduction of the number of personnel before realizing the unmanned ship technologically will reduce fuel consumption. An important factor here is not willing to the amount of lubricating oils consumption allowed in the tolerances fixed by law for main and auxiliary machines, but rather to ensure the lubricating oil consumption closer to the factory settings via selected maintenance-repair procedures, as much as possible, in a vessel with a daily consumption of 50 tons of fuel. While 0.1-0.2 grams of lubricating oil consumption per kilowatt is considered normal, every 1.5% savings in fuel consumption will cause the lubricating oil consumption to be reduced up to 50% (Malcome, 2017). If Capesize Dry Bulk Carrier which consumes 17,000 kW/pday energy reduces her speed from 14.7 mil/hour to 13 mil/hour, the daily amount of fuel consumption can be reduced from 55 tonnes/pday to 45 tonnes/pday. Depending on the age of the ship, the economic fuel consumption should be determined by comparing the Energy Efficiency Design Index (EEDI) with the Energy Efficiency Operation Index (EEOI) to calculate the optimum speed. In order to prevent overheating of main and auxiliary machines, to prevent lubricating oil leaks and to increase the quality of lubricating oil, maintenance and repair of cooling water systems, making system isolations and using protective oils should be considered. In such an economic environment, subsidies of the states for the fuel and the lubricating oil will be one of the measures to relieve the sector.

III. RESULTS AND DISCUSSION

From vessel operating costs to valuation processes, energy consumption is one of the fundamental issues that must be managed in institutional strategies. Although climate conditions are prioritized within the scope of energy consumption strategies, freight distributions, ballast water management, economic speed of the ship and operating criteria for Dry Bulk Shipping should be considered.

Priority holistic approaches are important for all these parameters. In this respect, sustainable energy management strategies are formed for each ship's business model. For dry bulk carriers with a direct voyage traffic has been considered according to two criteria, namely unit load consumption and total distance.

Analysis of consumption of a ship for thirty times distance by unit load provides effective ballast management with direct load. The energy consumption distribution of a freight ship with reference to this study is given in Fig. 4.

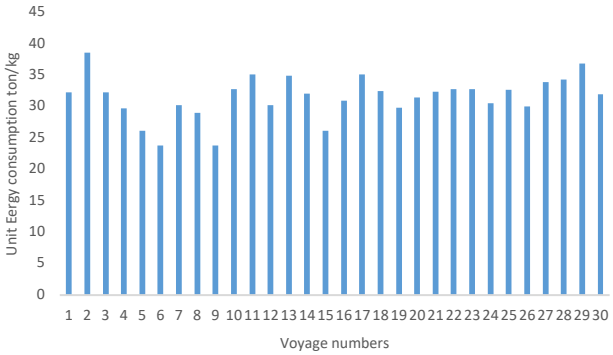

Fig. 4: Unit energy consumption based on unit tonne

According to this distribution, it is seen that average consumption is 31.57 kg / ton. However, it is seen that consumption distribution has a consumption change of 14.85 kg / ton with a minimum of 23.48 kg / ton and 38.67. Only in this way the rate of change due to load is examined according to the average consumption. The results are given in Fig. 5

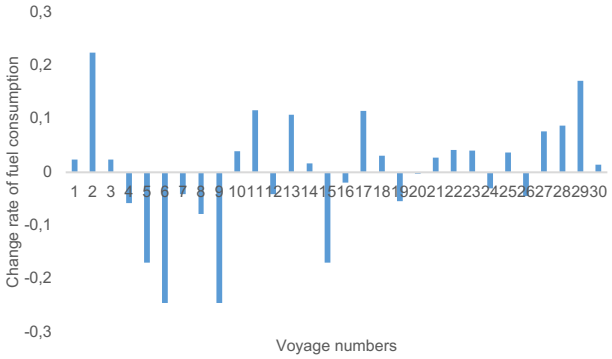

Fig. 5: Unit energy consumption change rate considering unit load

According to the distribution of consumption, there was a change of 24.49% in the negative direction and a change of 22.48% in the positive direction. In this respect, the consumption histogram of the ship was examined. The highest average consumption was 29.31 tons / kg for 8 value and 31.33 tons / kg for 11 value. When 29.31 ton / kg is taken as a reference in all of this distribution, a saving potential of 7.17% in current consumption is determined. It was seen that the unit could achieve this consumption target in unit load. This means 625.18 tons of fuel savings when total travel loads and consumption are taken into consideration. Similarly, the current load values were fixed and evaluated based on the energy consumed per mile. Accordingly, the consumption distributions for unit miles are given in Fig. 6.

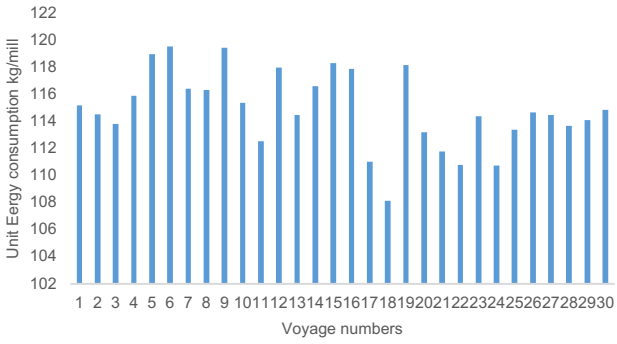

Fig. 6: Unit energy consumption based on unit mile

The energy consumption per mile according to the voyage conditions was found to be 114.89 kg / mile. The minimum energy consumption per mile in voyage conditions is 108.16 kg / mile, while the maximum consumption is 119.52 kg / mile. In this distribution, the difference between the peak values was found to be 11.36 kg / mile difference. Distribution of these mile changes according to voyage numbers are examined and the results are given in Fig. 7.

Fig. 7: Unit energy consumption change rate considering unit mile

When the peak differences due to mileage consumption are examined, a total of 9.89% is noticeable. When the general average consumption is taken into consideration, a distribution of 4.03% in the positive direction and 5.85% in the negative direction is observed. In this context, the distribution histograms were examined, and a specific value was determined for the unit mile. In this context, a total of 297.56 savings potential draws attention when efficiency analyzes are evaluated by accepting 111.25 kg / mile reference from the histogram. In this respect, it has been seen that only significant savings can be achieved in energy consumption over the two parameters.

The choice of diesel engines is most noticeable on ships. In this way, remarkable savings can be achieved in operational operating parameters for a diesel engine. Similarly, savings in main engine performance can be achieved. However, energy consumption should not be considered only in terms of fuel and other diesel fuels. For example, changing the sea water temperature can be seen as a significant saving point. Sea water temperature is an important parameter for cooling the main engine. Sea water has a range of 5°C to 32°C. At these temperature changes, the amounts of fuel consumption consumed for cooling a main motor at 12.6 MW power are given in Figure-8.

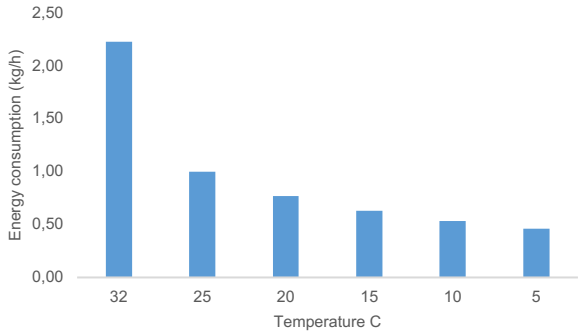

Fig. 8: Energy consumption of cooling process

Cooling energy consumption for an average cooling water temperature of 20°C has an effect of 0.77 kg/h. For each °C grade, the cooling savings potential has an effect of 2.68%. Only the total amount of savings that can be provided on 1°C temperature control when above 30 voyages are examined. In this context, it has been found that the total amount of fuel at 20°C has a

value of 31.54% when 30 voyages are considered. A one-degree savings rate in this load distribution has yielded a 5.27% savings, with 510.31 tons.

IV. CONCLUSIONS

Developing local solutions for energy efficiency in ships will not be accurate in terms of holistic strategies. In addition, planning or prioritization of management tools needs to be considered together with a process analysis. The energy efficiency analyses mentioned above are important processes for holistic strategies, that need to be managed.

Total energy management will have a very positive contribution to ship valuation. Although the vessels are equipped with environmentally sensitive and energy efficient technologies due to the new regulations, they are naturally affecting voyage and operating costs due to possible faults in the use of vessels.

Since the freight rates and operating expenditures will increase in periods when the economy is volatile, it is estimated that this will seriously lower the value of the vessels. Until the unmanned vessels are realized, studies to reduce misusing of ships will help to ensure energy efficiency.

REFERENCES

DTO, Turkish and world maritime transport, Maritime Sector and Statistics by Numbers (Part 1), Journal of Maritime commercial, Chamber of Maritime Commerce, Istanbul, Turkey (TR), February 2017.

GEA, Global Energy Assessment Chapter 9 - Toward a Sustainable Future, Cambridge University Press, Cambridge, UK and New York, NY, USA and the International Institute for Applied Systems Analysis, Laxenburg, Austria (2012).

Kim, K. H., Forecasting the capesize freight market, World Maritime University Dissertations. 161 (2013), http://commons.wmu.se/all_dissertations/161

Latarche M., An overview of engine lubricants on ships, 12.04.2017, ShipInsight, https://shipinsight.com/an-overview-of-engine-lubricants-on-ships

LTAV, Long term assest value (LTAV), Association for promotion of the Long Term Asset Value method - c/o VHSS e.V. Schopenstehl 15 20095 Hamburg Germany, (2018), http://www.long-term-asset-value.de/uploads/document/Anlage_2_b_LTAV_Engl.pdf

Stopford M., Maritime Economics, Routladge Taylor & Francis Group, 2009, pp.250.

Pike K., Butt N., Johnson D., Walmsley S., Global Sustainable Shipping Initiatives: Audit and Overview 2011 A REPORT FOR WWF", Southampton Solent University, School of Maritime and Technology, East Park Terrace, Southampton SO14 0YN, UK. http://awsassets.panda.org/downloads/sustainable_shipping_initiatives_report_1.pdf

UNCTAD, Review of Maritime Transport 2014,(2014), http://unctad.org/en/pages/PublicationWebflyer.aspx?publicationid=1068

Economic Analysis of Various Liquefied Energy Carriers Based on Ocean Transport Costs

*Mohammed Al-Breiki and Yusuf Bicer
Division of Sustainable Development (DSD), College of Science and Engineering (CSE), Hamad Bin Khalifa University (HBKU), Qatar Foundation (QF), Education City, Doha, Qatar

E-mails: *malbreiki@mail.hbku.edu.qa

Abstract
The energy of natural gas can be transported in forms of liquefied energy carriers (chemicals), pipelines, hydrates, compressed natural gas, and others. For large scale energy transport, forms of liquefied chemicals can be used to transport the energy of natural gas due to a reduction in volume compared to gaseous forms. However liquefied energy carriers have commonly low boiling temperatures. Therefore, some portion of liquefied energy carriers' mass is lost continuously due to the temperature difference between the storage and the ambient temperature, these losses are called boil-off gas (BOG). BOG is an obvious problem when the energy of natural gas is stored and transported in a liquefied form. These losses reduce the quantity of the liquefied energy carrier, which directly affect their economic value. Therefore, this study presents an economic analysis of three liquefied energy carriers produced from natural gas, namely; liquified natural gas (LNG), methanol, liquid ammonia (NH_3). The economic approach focusses on determining the total ocean transport costs, which are dependent on capital costs, operational costs, and BOG costs. The transport distance (km) and ship capacity (m^3) are fixed for the three energy carriers for a fair comparison. The total transport costs of LNG, liquid ammonia, and methanol are 0.75 $/GJ, 1.10 $/GJ, and 0.76 $/GJ, respectively. Liquid ammonia yields a lower cost of transportation per unit mass (kg) but due to lower calorific value, it has a slightly higher cost of transportation per unit energy (GJ). BOG generated during LNG transport contributes to 12% of the total costs whereas, BOG generation during methanol transport does not exceed 1%. To reduce the total costs of transporting the energy of natural gas, proper handling of BOG by economical methods is required during transporting the energy as LNG or transporting the energy of natural gas as methanol can be more economically efficient.

Keywords: Economic analysis, boil-off gas, energy carriers, natural gas, transport costs, transportation.

I. Introduction

The energy of natural gas can be transported in large scale quantity either by pipelines in gaseous forms or by chemicals in liquefied forms. Transporting the energy of natural gas by pipeline is not commercially feasible for distance over 2000 km, however, liquefied forms such as liquefied natural gas (LNG) becomes more advantageous for long distances (Pospíšil et al., 2019). Liquefied natural gas is the most common form to export the energy of natural gas in large proven natural gas reserves countries such as Qatar and Australia. For example, Qatar converts 70% of it produced natural gas yearly into LNG for exportation purposes (Shah, 2017). LNG is favorable to be used to transport the energy of natural gas due to the reduction in the volume of about 600 times compared to gaseous forms (Nwaoha and Wood, 2014). However, transporting the energy as LNG has two unfavorable disadvantages that have made LNG export countries to invest more in transporting sector to find alternatives for higher efficient transport method; LNG has a low boiling temperature of about -162^{o}C and LNG contains for carbon atoms which pollute the environment (Kurle et al., 2017). A liquefied form with a low boiling temperature continuously loses some portion of its mass due to temperature difference between the liquefied energy carriers and the ambient, these losses are called boil-off gas (BOG). BOG is an unavoidable problem when the energy of natural gas is transported in a liquefied form. Researchers proposed different solutions to eliminate the generated BOG during ocean transport. For example, a reliquefication facility that captures the generated BOG and sends back to storage tanks or used as fuel for the propulsion system of the ship (Moon et al., 2007). Whereas other researchers proposed to transport the energy of natural gas by other liquefied energy forms such as ammonia, methanol, and hydrogen(Seddon, 2006). Furthermore, the amount of BOG generated during LNG ocean transport is dependent on the voyage length and it is around 2.5% to 3% of the quantity shipped(Seddon, 2006). These losses reduce the quantity of the liquefied energy carriers, which directly affect their economic values. The cost of shipping LNG is (0.5-1.8$/MMBtu) based on the capital and operational costs of the ship with an assumption of 1% BOG generation (Cho et al., 2018). From the

literature, the majority of the researches mainly focuses on LNG therefore, this study presents an economic analysis to show the cost of transporting the energy of natural gas by other liquefied energy carriers such as liquid ammonia and methanol. The cost of transporting liquid ammonia and methanol is determined based on capital costs, operational costs and BOG losses costs. The costs of transporting liquid ammonia and methanol are then compared with the cost of transporting LNG.

II. Methodology

The three energy carriers; LNG, liquid ammonia, and methanol are used to transport the energy of natural gas. To estimate the total cost of transporting these liquefied energy carriers, capital costs, operational costs, and BOG losses costs are needed to be determined as shown in Figure 1. Since there are three energy carriers with different characteristics and boiling temperatures, three different ships are selected based on the energy carriers' requirements. The capital costs represent the cost of the ship while the operational costs cover labor, port charges, maintenance, insurances, fuel costs, and miscellaneous charges. The capital costs for each ship are defined based on the capacity of the tanker (m^3) and tanker costs($/$m^3$). While the labor costs, ports charges, percentage of maintenance, insurances, and miscellaneous charges are estimated based on the ship requirements for each energy carries. Moreover, heavy fuel oil (HFO) is used to fuel the ship and the cost of the total required HFO is added to the operational costs. The BOG costs are the costs of the total amount of loss of liquefied energy carriers during the voyage duration. For a fair comparison, the three ships are sailed for the same distance of 12000 km. Addition of the three costs; capital costs, operational costs and BOG costs determine the total costs. The ratio of the total costs and the quantity shipped estimate the costs of each energy carrier in ($/GJ).

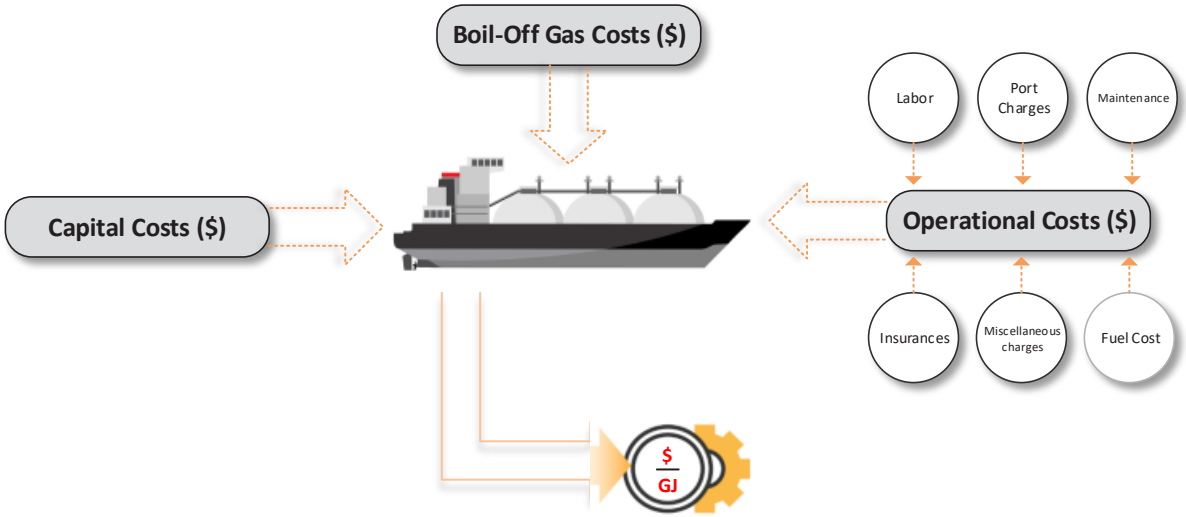

Figure 1: Key contributions to the cost of liquefied energy carriers' ocean transport

III. Analysis

To estimate the total transporting costs for the three carriers, capital costs, and operational costs, and BOG costs are needed to be accumulated. LNG, ammonia, and methanol have different thermophysical properties such as storage temperature, density lower heating value (LHV) and BOG as shown in Table 1. The capacity of each energy carrier is calculated based on the density while the carried energy is estimated by LHV.

Table 1: Significant thermophysical properties of LNG, ammonia, and methanol

Thermophysical Properties	LNG	Liquid Ammonia	Methanol
Storage Temperature (°C)	-162	-34	5
Density (kg/m^3)	423.1	682.8	805
LHV (MJ/kg)	48.6	18.6	19.9
Boil Off Gas per Day (%)	0.12	0.025	0.005

Source: Engineering Equation Solver (Klein, 2018)

The capital costs, operational costs, and BOG costs used parameters are shown in Table 2. The capital costs for the same ship capacity with 15 years lifespan and 10% discount factor are estimated based on the cost of the tank per metric cube. Operational costs differ from each energy carrier due to the required fuel which is dependent on the carried capacity. Each energy carrier has a different daily BOG rate therefore the quantity of lost mass differs.

Table 2: Statistics for transporting LNG, Ammonia, and Methanol

	LNG	**Liquid Ammonia**	**Methanol**
Ship Capacity (m3)	150,000	150,000	150,000
Capacity (kg)	63,465,000	102,420,000	120,750,000
Tanker costs ($/m3)	1200	1016	700
Logistics			
Days/year	350	350	350
Distance (km)	12000	12000	12000
Speed (knots)	20	20	20
Sailing time (days)	13	13	13
Turnaround (h)	36	36	36
Trips/year	24.14	24.14	24.14
Sailing days/year	313.79	313.79	313.79
Capital Costs			
Capital costs ($)	180,000,000	152,400,000	105,000,000
ROC(15 years,10% DFC) %	15.19	15.19	15.19
Total Capital costs ($)	**27,342,000**	**23,149,560**	**15,949,500**
Operataionl Cost			
Labor ($)	2,520,000	2,520,000	2,520,000
Required Fuel (kg)	6,869,569	11,086,130	13,253,003
Cost of HFO ($/kg)	0.58	0.58	0.58
Fuel Costs ($)	3,984,350	6,429,955	7,686,742
Port Charges ($)	3,610,000	3,610,000	3,610,000
Miantenance(4% Capex) ($)	7,200,000	6,096,000	4,200,000
Insurance (15% Opex) ($)	2,597,152	2,798,393	2,702,511
Misc (10% Opex) ($)	1,731,435	1,865,596	1,801,674
Total Operating Cost ($)	**21,642,937**	**23,319,944**	**22,520,927**
BOG Cost			
BOG shipping (kg)	23,897,855.17	8,034,672.41	192,102.27
Cost of BOG ($)	**6,887,314.06**	**4,214,346.37**	**64,223.63**
Quantitiy Transported (kg)	1,531,913,793.10	2,472,206,896.55	2,561,363,636.36
Energy (GJ)	**74,451,010.34**	**45,983,048.28**	**50,971,136.36**

IV. Result

The ocean transport costs for LNG, liquid ammonia, and methanol are calculated based on the addition of capital costs, operational costs and BOG costs. The capital costs of LNG are 15% and 40% higher than ammonia and methanol respectively due to higher storage temperature which requires higher insulated materials. The reason for high operational costs for ammonia and methanol is that the capacity of these energy carriers is higher compared to LNG. The LNG BOG rates are 0.12% which results in 76,158 kg of loss per one trip. Even though LNG losses reduce the quantity shipped per trip, LNG still delivers more energy due to its high energy content (heating value). Moreover, the total transport costs of LNG, liquid ammonia, and methanol in ($/m^3) are shown in Table 3. Costs breakdown of total transport costs of LNG, liquid ammonia, and methanol is presented in Figure 2A and 2B. Figure 2A presents costs of capital costs, operational costs and BOG costs in ($/GJ) whereas Figure 2B shows the total costs in ($/kg).

Table 3: Total transport costs of LNG, ammonia, and hydrogen

	LNG	**Liquid Ammonia**	**Methanol**
($/m^3)	15.43	14.00	12.11

Total transport cost of liquid ammonia is 1.10 $/GJ which is highest however, the cost of liquid ammonia is 0.02 $/kg which is lower cost compared to LNG per unit mass. Total costs of LNG and methanol

is 0.75 $/GJ and 0.76 $/GJ, respectively. BOG costs contribute significantly to the total costs of LNG of about 12% of the total costs. This indicates that BOG during LNG transport needs to be properly handled, hence other liquefied energy carriers with better thermophysical characteristics can be also used for transporting the energy of natural gas.

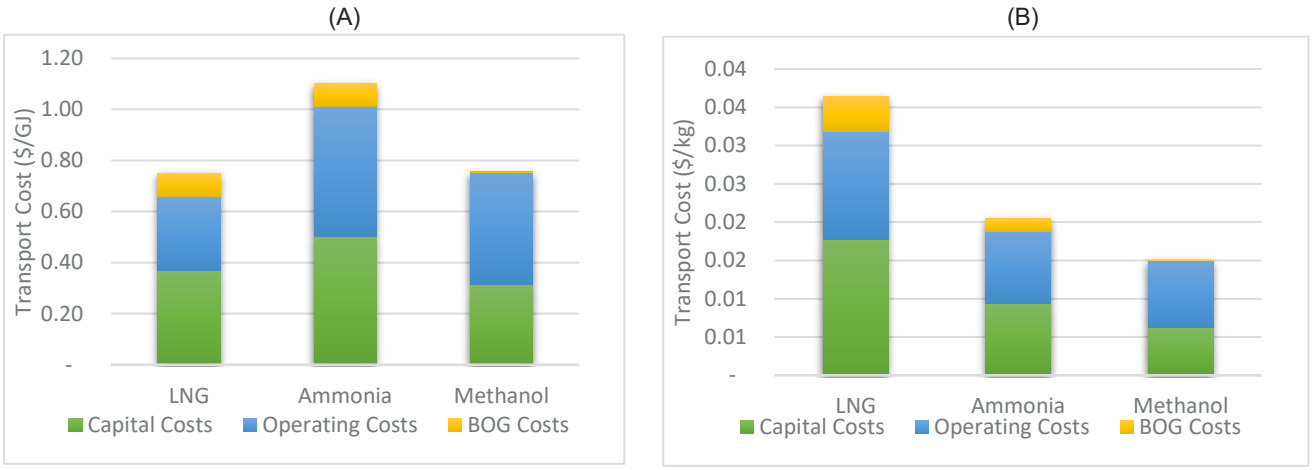

Figure 2: Breakdown total transportation costs of LNG, ammonia, and methanol, (A) per GJ and (B) per kg

V. Conclusion

Three energy carriers; LNG, liquid ammonia, and methanol are proposed to transport the energy of natural gas for the same distance and with the same ship, capacity to estimate the total costs of ocean transport. The transport costs of liquefied energy carriers consist of capital costs, operational costs, and BOG costs. The total transport costs of LNG, liquid ammonia, and methanol are 0.75 $/GJ, 1.10 $/GJ, and 0.76 $/GJ accordingly. BOG contributes to 12% of the total costs of LNG cost transport. Thus, proper handling of the BOG generation can reduce the total costs or transporting the energy of natural gas vie methanol can be more effective.

Acknowledgment

The authors acknowledge the support provided by the Hamad Bin Khalifa University, Qatar Foundation, Qatar (210009034).

References:

Cho, J., Lim, G.J., Kim, S.J., Biobaku, T., 2018. Liquefied natural gas inventory routing problem under uncertain weather conditions. Int. J. Prod. Econ. 204, 18–29. https://doi.org/10.1016/j.ijpe.2018.07.014

Klein, 2018. EES: Engineering Equation Solver | F-Chart Software : Engineering Software.

Kurle, Y.M., Wang, S., Xu, Q., 2017. Dynamic simulation of LNG loading, BOG generation, and BOG recovery at LNG exporting terminals. Comput. Chem. Eng. 97, 47–58. https://doi.org/10.1016/j.compchemeng.2016.11.006

Moon, J.W., Lee, Y.P., Jin, Y.W., Hong, E.S., 2007. Cryogenic Refrigeration Cycle for Re-Liquefaction of LNG Boil-Off Gas. Cryocoolers 14 629–635.

Nwaoha, C., Wood, D.A., 2014. A review of the utilization and monetization of Nigeria's natural gas resources: Current realities. J. Nat. Gas Sci. Eng. https://doi.org/10.1016/j.jngse.2014.03.019

Pospíšil, J., Charvát, P., Arsenyeva, O., Klimeš, L., Špiláček, M., Klemeš, J.J., 2019. Energy demand of liquefaction and regasification of natural gas and the potential of LNG for operative thermal energy storage. Renew. Sustain. Energy Rev. 99, 1–15. https://doi.org/10.1016/j.rser.2018.09.027

Seddon, D.D., 2006. Gas Usage and Value: The Technology and Economics of Natural Gas Use in the Process Industries.

Shah, Y.T., 2017. Chemical energy from natural and synthetic gas, Chemical Energy from Natural and Synthetic Gas. https://doi.org/10.1201/9781315302355

A Survey of International Security Standards for Smart Grids, Industrial Control System and Critical Infrastructure

[1*]İsa Avcı, [2]Cevat Özarpa, [3]Muhammed Ali Aydın
[1] Istanbul University-Cerrahpasa, Engineering Faculty, Department of Computer Engineering, Avcılar, 34315, Istanbul, Turkey.
[2] Karabuk University, Engineering Faculty, Mechanical Engineering, Balıklarkayası Mevkii, 78050, Karabuk, Turkey.
[3] Istanbul University-Cerrahpasa, Engineering Faculty, Department of Computer Engineering, Avcılar, 34315, Istanbul, Turkey.

* E-mails: *isaavci@ogr.iu.edu.tr, cevatozarpa@karabuk.edu.tr, aydinali@istanbul.edu.tr

Abstract
International security standards used in smart grids, Industrial Control Systems and critical infrastructures have become important for institutions and organizations. Within the framework of these standards, it is aimed to increase the security and durability of smart networks, Industrial Control systems and critical infrastructures. When determining the most useful best practice standards and guidance for implementing effective cybersecurity and information security, it is important to determine the role and scope of each, and how it will interact with other standards and guidance. Cyber security and information security standards are applied to all organizations in which they operate, regardless of sector and institution, regardless of their size. This study provides general information about international information and cyber security standards used and referenced in the detection and protection of security vulnerabilities in smart grids, Industrial Control systems and critical infrastructure systems. In this study, we investigate 26 international security standards in smart grids, Industrial Control Systems and critical infrastructures and in which country it was developed and years of development. The research study covers the years from 1971 to 2020. According to our research results, 19 security standards were developed in the USA. It also provides general information on smart grids, Industrial Control Systems and critical infrastructures.

Keywords: Smart Grids, Industrial Control Systems, Critical Infrastructures, Security Standards, Cyber Security

I. Introduction

Smart grids, Industrial Control Systems and critical infrastructures are important issues many countries and throughout world in case of protecting systems in nowadays and future. Many standards have been developed worldwide for the safe protection of critical systems by institutions. It should be made more reliable especially for vital systems. In order to protect such systems, USA has been determined as a result of our research that European countries pay more attention to the development of these standards.

In this study, 26 security standards were investigated around the world about smart grids, industrial control systems and critical infrastructures. This review was made on security standards developed from 1971 to 2020. In addition, in this study, the institution information belonging to the standards, the country and the year of its extraction were also investigated in detail. In this article, smart grids, Industrial Control Systems and critical infrastructures are briefly described. With this study, the importance of such critical systems in terms of cyber and other security measures are emphasized. In addition, the standards examined have been shown for which systems they are developed.

II. Smart Grids

Infrastructure services have an important position as an indispensable element for city life. Control of these infrastructure services has gained vital importance due to the increase in the urban population. The growing population has made it impossible to use and control infrastructure without Information Technology (IT) applications (Nam, 2011).

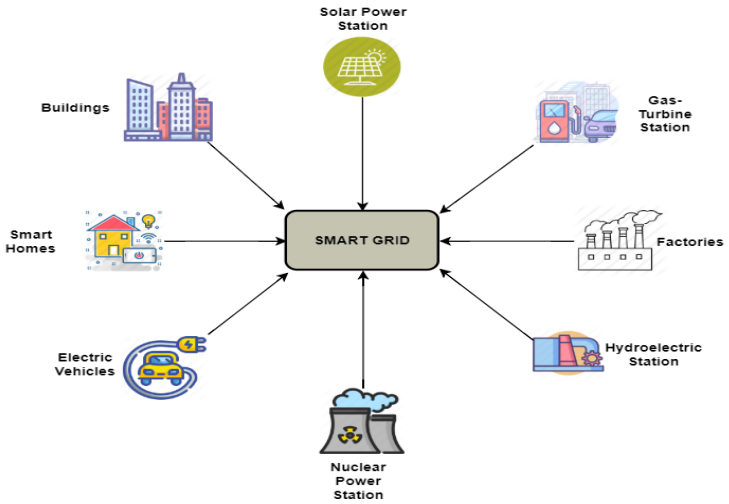

Fig. 1.Smart grid overview (Feroze and Javaid, 2017).

ISO (International Organization for Standardization), which is concerned with optimal management of physical assets, indicates that infrastructure management should be holistic, systematic, risk-based, optimum and sustainable (Minnaar and Basson, 2013). The smart grid field communication is based on the IEC 61850 standard. The IEC 61850 protocol standard for the sub-station allows all protection, calculation, testing and monitoring to be combined with a single standard protocol (Baigent and Adamiak, 2004). Otherwise, devices of different manufacturers will not be able to use a large number of protocols and interfaces that do not mutually fit or are not parallel to each other. In the technical field, equipment standardization and interoperability have been implemented for a long time (Dönmez, 2013).

III. Industrial Control Systems

Industrial Control Systems (ICS) are used within various industries on a global scale, for the automation and control of operational plants. ICS industries include electricity, water, wastewater, food, and transportation (Stouffer et al. 2013). It is a general term that includes many control systems including Industrial Control System (ICS), controller control and data acquisition (SCADA) systems, Distributed Control Systems (DCS) and Programmable Logic Controllers (PLC) (NIST, 2020).

IV. Critical Infrastructures

The critical infrastructure includes all energy-related generation and storage facilities, transmission lines and routes, and consumption facilities and systems. Platforms and natural gas wells used in the production of energy sources such as oil and natural gas, all pipelines and LNG terminals from the main transmission lines that play a role in the transportation of these resources to the secondary transmission lines reaching the homes, tankers, refineries, pump stations, renewable energy facilities, dams and conversion power generation control and protection systems, nuclear power plants, and all kinds of power generation systems, including power plants (Özertem, 2012).

Critical infrastructure consists of three main parts: natural gas, oil and electricity (Feroze, F. and Javaid, 2017). These are the basic vital elements of world society and the needs for these elements for the future should be taken into consideration.It is essential to implement a sustainable, environmentally compatible safety rule and policy based on uninterrupted flow and supply security and non-leakage in oil and gas pipeline facilities (The White House, 2003).

The economic welfare and development of the modern state, the use of advanced technology and the development of the level of production and development to ensure the effective use of energy resources and infrastructure security is an indispensable element of national security policies (Caşın, 2014). In addition to coal, oil and natural gas, the widespread use of nuclear energy, the information technologies that ensure the use of energy and the critical infrastructures that make up the distribution systems, ensure the safety and security of the critical infrastructures, making the continuous flow of fuel, gas and electricity used in daily life. The International Energy Agency (IEA) redefines the three vital elements of balanced energy policies as energy security, economic development and environmental protection (CRS Report, 2005).

V. Investigation of International Security Standards the Systems

Our study have investigated the international security standards developed worldwide, from 1971 to 2020, are given below in Table 1. This study covers cyber security, information security, business continuity and security in general, especially developed for smart networks, critical infrastructures and ICS.

Table 1. International Security Standards

	Standards	Description	Year	Institution	Country
1	ILTA	The LegalSEC of the International Legal Technology Association provides the legal community with guidance for risk-based information security programs (iltanet, 2018).	1971	ILTA	USA
2	NIST SP 800	Publications in NIST's Special Publications (SP) 800 series provide information that concerns the computer security community. This series includes the guidelines, recommendations, technical specifications and annual reports of NIST's cyber security activities (NIST, 2020).	1990	NIST	USA
3	ISO/IEC 27031	This Standard closes the gap between the event itself and overall business continuity and creates a key link in the cyberspace flexibility chain (Itgovernance, 2020).	2000	ISA	USA
4	DHS	Department of Homeland Security-It is a security standard that provides advice to developers to increase security in ICS systems of various industrial organizations (Timpson, 2020).	2002	DHS	USA
5	BSIMM	Building Security in the Maturity Model is geared towards software security and provides a framework for organizing a range of activities to help manage and measure enterprise security initiatives (BSIMM, 2020).	2006	BSIMM	USA
6	IEC 62351	IEC 62351 is an industry standard aimed at improving safety in automation systems in the field of power systems. (Ipcomm, 2020).	2007	IEC	Switzerland
8	CIS 20	The Internet Security Center has a standard 20 control that is originally developed by SANS (Cisecurity, 2020).	2008	CIS	USA

9	ISO/IEC 15408:2009	ISO / IEC 15408 defines the software and hardware security evaluation criteria of these standard information security devices consisting of 3 standards: information technologies, security techniques and evaluation criteria for information security (Timpson, 2020).	2009	ISO	Switzerland
10	ISO/IEC 27032	These standard, although the recommended controls ISO / IEC 27001 is not certain given up or prescriptive, cyber attacks, including those outside the cyber space itself recognizes that confidence vectors (Itgovernance, 2020).	2012	ISA	USA
11	ISO/IEC 27001	It is a meticulous and comprehensive guide to protect your information within the principles of privacy, integrity and usability (Itgovernance, 2020).	2013	ISA	USA
12	ISO/IEC 27002	It provides helpful, practical guidance on the implementation of ISO / IEC 27001 (Itgovernance, 2020).	2013	ISA	USA
13	ISO/IEC 22301	ISO / IEC 22301 is an international standard for business continuity management systems (BCMS) and forms the final part of cyber flexibility (Itgovernance, 2020).	2012	ISO	Switzerland
14	PAS 555	PAS 555 adopts an approach to explain the appearance of effective cybersecurity and can be used to verify that solutions are comprehensive (Itgovernance, 2020).	2013	BSI	England
15	NERC CIP	NERC has approved version 5 of critical infrastructure protection cyber security standards (CIP Version 5), which represents significant progress in reducing cyber risks to the collective power system (NERC, 2020).	2013	NERC	USA
16	NIST SP 800-53	This publication provides a catalog of security and privacy controls for federal information systems and organizations and for various threats such as organizational operations, organizational assets, individuals, other organizations and hostile cyber attacks, natural disasters, structural failures and human errors (NIST, 2020).	2013	NIST	USA
17	NISTIR 7628	NISTIR 7628 is a comprehensive document for security designers / practitioners in smart grid research and implementation. NISTIR 7628 covers top-down and bottom-up approaches in risk assessments and security analysis (NIST, 2020).	2014	NIST	USA
18	NIST SP 800-82 Rev. 2	This document Audit SCADA systems, DCS and PLC such other control system configurations, including the unique performance, reliability and security requirements in terms of Industrial Control Systems (ICS) on how to protect provides guidance (NIST, 2020).	2015	NIST	USA
19	ISO/IEC 27035	ISO / IEC 27035 is an international standard for incident management. This standard also includes guidance to update policies and processes and to minimize the risk of repetition to strengthen existing controls following analysis of the event.	2016	ISA	USA
20	ISA/IEC 62443 (ISA99)	The ISA99 committee will set up standards, proposed practices, technical reports and related information to define procedures for the implementation of electronically safe production and control systems and safety practices and the evaluation of electronic safety performance (ISA, 2020).	2017	ISA	USA
21	ISO/IEC 27019:2017	It provides guidance for the control of processes applied to process control systems used in the energy company industry for the production, transmission, storage and distribution of electrical energy, gas, oil and heat (ISO, 2020).	2017	ISA	USA
22	CSA V4.0	The Cloud Security Alliance provides Security Guidelines for Critical Focus Areas in Cloud Computing v4.0 to increase security and reduce risk in the adoption of cloud computing technologies.	2017	CSA	USA
23	NIST 800-53/CSF	Special Publication 800-53 of the National Institute of Standards and Technology (NIST) provides controls for federal information systems, but can be used by commercial organizations (NIST, 2020).	2018	NIST	USA
24	BS 7799-3 2017	Information security management systems and Guidelines for information security risk management	2017	BSI	England
25	GB/T22239:2019	GB/T22239 is “Information Security Technology-Basic Rule for Classified Protection of Information System Security” (Timpson, 2018).	2019	GB	China
26	IEC 61850:2020	The IEC 61850 standard has been developed to standardize communication in the high-voltage substation.	2020	IEC	Switzerland

VI. Conclusions

The study is conducted to investigate security standards developed in the context of vital and critical systems, infrastructure and smart grids from past to present.With this study, we want to present our scientific contribution to researchers by researching the security standards developed and by showing their historical development and which countries are doing more studies on these issues.

The study investigates 26 standards and shows in which year and in which countries they were developed. Especially, 19 of the studies are shown to be developed in USE and the others are developed in Switzerland, England and China. It is recommended that other countries should attach importance to these issues and support international standards.

The aim of this study is to provide researchers convenience in their research and to take security precautions on the systems used by the institutions by applying specially prepared standards in related fields in cyber security and other security issues.

References

Aminu Bature, A., Melville, L. and etc. 2018, An Investigation into the Effects of Risks and Risk Management of Bioenergy Projects, ICREN.

Baigent, D., Adamiak, M. and Mackiewicz, R., 2004, IEC 61850 communication networks and systems in substations: an overview for users.

BSIMM, 2020, https://www.bsimm.com/framework.html, (ET: 05.01.2020).

Caşın, M.H.,2014, 'Kritik Enerji Altyapı Güvenliğinin Kurumsal Çerçevesi-Kritik Enerji Altyapı Güvenliği', Hazar Strateji Enstitüsü, İstanbul,ss. 5-6.

Cisecurity, 2020, https://www.cisecurity.org/controls/, (ET: 18.01.2020).

Channelpostmea, 2017, http://www.channelpostmea.com/2017/03/02/dubai-wants-to-become-a-global-benchmark-for-smart-cities, (ET: 02.03.2017).

CRS Report for Congress, 'Risk Management and Critical Infrastructure Protection: Assessing, Integrating, and Managing Threats, Vulnerabilities and Consequences', Şubat 2005, ss. 5.

Dönmez, M., 2013, Smart grids, and integration, BTC Business Technology.

Eia, 2020, https://www.eia.gov/outlooks/ieo/.

Elkind, J., 2010, "Energy Security, Call for a Broader Agenda", Energy Security, Economics, Politics, Stategies and Implications (Derl: Carlos Pascual ve Jonathan Elkind), Bölüm 6, ss. 119-149, Brookings Institution Press, Washington, D.C.

Erdal, L. and Karakaya, E., 2012, ENERJİ ARZ GÜVENLİĞİNİ ETKİLEYEN EKONOMİK,SİYASÎ VE COĞRAFÎ FAKTÖRLER, Uludağ Journal of Economy and Society.

Feroze, F. and Javaid, N., 2017, Towards Enhancing Demand Side Management using Evolutionary Techniques in Smart Grid, ResearchGate.

Iltanet, 2020, https://www.iltanet.org/resources/legalsec (ET: 08.01.2020).

Ipcomm, 2020, https://www.ipcomm.de/protocol/IEC62351/en/sheet.html, (ET: 11.01.2020).

ISA, 2020, https://www.isa.org/isa99/, (ET: 08.01.2020).

ISO, 2020, https://www.iso.org/standard/68091.html, (ET: 08.01.2020).

Itgovernance, 2020, https://www.itgovernance.co.uk/cybersecurity-standards (ET: 10.01.2020)

Kruyt B., Vuuren D.P.,Van de Vries H.J.M. and Groenenberg H., 2009, "Indicators for energy security", Energy Policy, c. 37, ss. 2166–2181.

Minnaar, J. R., Basson, W., and Vlok, P. J., 2013, Quantitative methods required for implementing pas 55 or the ISO 55000 series for asset management. South African Journal of Industrial Engineering, 24(3):98-111.

Mutasim, M. and etc., 2019, Novel Approach of Quantifying Energy Security in terms of Economic, Environmental and Supply Risk Factors, Journal of Advanced Research in Fluid Mechanics and Thermal Sciences 57, Issue 1 (2019) 100-109.

Nam, T., & Pardo, T. A., 2011, Conceptualizing smart city with dimensions of technology, people, and institutions. In Proceedings of the 12th Annual International Digital Government Research Conference: Digital Government Innovation in Challenging Times (pp. 282–291). ACM.

NERC, 2020, https://www.nerc.com/pa/CI/Pages/Transition-Program.aspx (ET: 09.01.2020)

NIST, 2020, https://csrc.nist.gov/publications/detail/nistir/7628/archive/2010-08-31 (ET: 08.01.2020)

NIST, 2020, https://nvd.nist.gov/.

Özertem,H.S.,2012,https://www.academia.edu/2449511/Critical_Energy_Insrastructure_Project_Final_Report_Kritik_Enerji_Altyap%C4%B1_G%C3%BCvenli%C4%9Fi_No_3.

Stiller, C., Seydel, P., Bunger, U. and Wietschel, M. (2008) "Early Hydrogen User Centres and Corridors As Part Of The European Hydrogen Energy Roadmap (Hyways)", International Journal Of Hydrogen Energy, c.33, s.41, ss. 4193- 4208.

Stouffer, K., Falco, J., and Scarfone, K. (2013) Guide to industrial control systems (ICS) security. NIST Special Publication, 800. 82.

The White House, 2003,'Risk Management and Critical Infrastructure Protection: Assessing, Integrating, and Managing Threats, Vulnerabilities and Consequences', ss. 5-6.

Timpson D., Moradian E., 2018, A Methodology to Enhance Industrial Control System Security, 22nd International Conference on Knowledge-Based and Intelligent Information & Engineering Systems, Procedia Computer Science 126 (2018) 2117–2126.

Thermodynamic Comparison of Cooling Options for Clean SOFC-Powered Locomotives

[1] Khaled H.M. Al-Hamed and [1,2] Ibrahim Dincer
[1] Clean Energy Research Laboratory, Faculty of Engineering and Applied Science, University of Ontario Institute of Technology, 2000 Simcoe Street North, Oshawa, Ontario, L1H 7K4, Canada
[2] Yildiz Technical University, Faculty of Mechanical Engineering, Istanbul, 34349 Turkey
E-mails: khaled.alhamed@ontariotechu.net, Ibrahim.Dincer@uoit.ca

Abstract
In this paper, an energy and exergy efficiency based-comparison of two space cooling options for locomotives, powered by an integrated SOFC system, is presented. System 1 uses a reversible heat pump that has space and operating weight advantages, while System 2 uses an absorption chiller to recover waste heat for providing space cooling that is more exergetically efficient. Both energy and exergy analyses are employed to model the present systems. The obtained results show that the energy and exergy efficiencies of System 2, with an absorption chiller operating at a cooling load of 105 kW, have slightly higher values than System 1 by a difference of around 1%. Therefore, using an absorption chiller as a cooling option is less attractive compared to a reversible heat pump due to the space requirements advantages of using a reversible heat pump.

Keywords: Energy, exergy, efficiency, cooling, locomotives, solid oxide fuel cell.

1. Introduction

It is important to note that the current practice in Ontario, Canada is still with diesel-electric powering systems (Railway Association of Canada, 2015). This needs to be changed to more environmentally friendly solutions, such as SOFC based powering systems for locomotives. Solid-oxide fuel cells (SOFCs) are considered potential powering drivers for future locomotives (Azizi et al., 2019). They consume cleaner fuels, like methane, ammonia, and hydrogen.

One of the main objectives of using a powering system is really to move a passenger locomotive. Another objective is to cover the space cooling and heating for thems. The current practice for space heating is to use furnaces that burn propane, and for space cooling, air conditioners are used. A recent investigation by (Al-Hamed and Dincer, 2020) considered the advantages of using a reversible heat pump that offers a higher Coefficient of Performance (COP) than other options, like absorption chillers with a heat exchanger, and air conditioner with a furnace. A reversible heat pump requires six times less space to install than an absorption chiller at the same cooling load of 105 kW. Also, it requires half the operating weight of an absorption chiller.

The only disadvantage of the reversible heat pump is the consumption of mechanical power that can be used for the primary objective (i.e. moving the locomotive). On the other hand, absorption chillers consume a low-temperature heat source to provide space cooling which should increase the overall energy and exergy efficiencies of the SOFC-based powering system. The purpose of this paper is to compare these two cooling options in terms of thermodynamic performance energetically and exergetically and to see if it is justifiable to use an absorption chiller instead of a reversible heat pump.

2. System Description

The description of System 1 shown in Fig. 1 is first mentioned. Methane fuel enters the integrated system through the fuel regenerator to be preheated for the SOFC and the combustor. At the same time, a fresh charge of air is compressed by the air compressor and then preheated at the air regenerator. Air and most of the methane enter the SOFC and react electrochemically to produce a DC-type electric power to run the locomotive. The exhaust gases leaving the fuel cell are then completely combusted with the redirected fresh charge of methane in the combustor. 10% of the high-temperature exhaust gases, leaving the combustor, go to the fuel regenerator while the rest gets expanded in the gas turbine. The exhaust gases of the methane combustion leave the SOFC-GT subsystem through the air and fuel regenerators. The exhaust gases leaving the air regenerator go through the boiler of the Steam Rankine Cycle (SRC) to use the waste heat for further power production, which is bottomed with an ammonia-Organic Rankine Cycle (NH3-ORC). Part of the power produced by the SRC is supplied to compressor 2 of the reversible heat pump to produce either space heating or cooling. The exhaust gases, leaving the fuel regenerator, get expanded and then mixed with the other stream of exhaust gases to provide heat to the heater for hot water production. More details on this integrated system are available in this paper (Al-Hamed and Dincer, 2020).

System 2 presented in Fig 1 defers from System 1 in which it replaces the reversible heat pump with an absorption chiller. This chiller uses exhaust gases that contain thermal energy to produce the cooling effect. This makes this cycle exergetically more efficient than a reversible heat pump because lower grade source of energy is used to produce the cooling effect, unlike the heat pump which consumes mechanical power to produce either heating or cooling effects. The heating effect is generated by utilizing a regular heat exchanger after the hot water production cycle, namely HX1. The operation of the absorption chiller is described. When the system is in the cooling mode, Pump 3 is turned on and it pumps a mixture of refrigerant and absorbent to the regenerator for preheating before it enters the generator. This mixture could be a mixture of water-Li/Br or ammonia-water. In the generator, the mixture is separated into refrigerant vapor and liquid absorbent by means of heating supplied by a hot stream of exhaust gases leaving the fuel regenerator. The liquid absorbent flows back to the absorber after it passes through the regenerator and the expansion valve. The refrigerant vapor proceeds to Condenser 2 and Expansion valve 2 to reduce its pressure and temperature. This low-temperature liquid enters the evaporator to absorb heat from the

cycle is turned off and a fan is turned on instead to blow cold air across the pipes of HX1. The heat is supplied from the exhaust gases leaving the heater from the hot water production cycle.

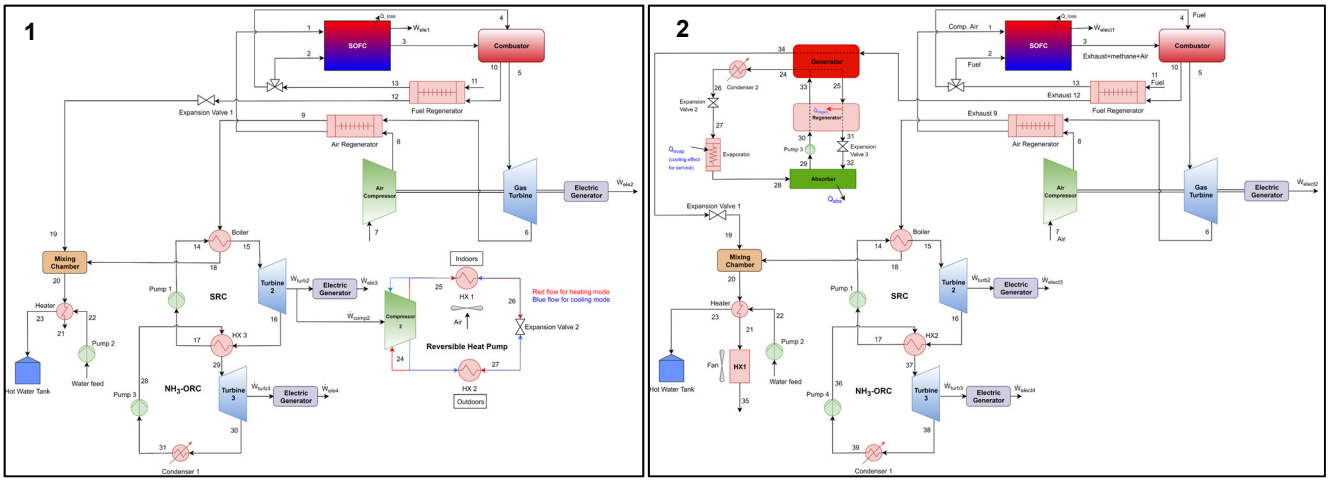

Fig. 1: Schematic diagrams of the studied integrated systems for locomotives.1) System 1 with a reversible heat pump taken from (Al-Hamed and Dincer, 2020). 2) System 2 with an absorption chiller.

3. Thermodynamic Analysis

The balance equations are applied to every component under the assumption of steady-state uniform flow conditions. The other assumptions are made for the analysis as follows:

- The pressure losses are neglected across heat exchangers and connecting pipes.
- The changes in specific kinetic and potential energy values are ignored.
- The chemical reaction in the combustor is assumed complete and all the methane is burned.

Now, the balance equations, namely mass balance, energy balance, entropy balance, and exergy balance are expressed in their rate form. Starting with the mass balance equation, it is expressed mathematically as

$$\sum_{inlet} \dot{m}_{inlet} = \sum_{outlet} \dot{m}_{outlet} \quad (1)$$

which basically states that the addition of mass flow rates of inlet streams of a component is equal to the addition of mass flow rates of outlet streams of the same component. Next, the energy balance equation is written as follows when the kinetic and potential energies are ignored

$$\dot{Q} + \sum_{inlet} (\dot{m}_{inlet} h_{inlet}) = \sum_{outlet} (\dot{m}_{outlet} h_{outlet}) + \dot{W} \quad (2)$$

where the heat is positive when it is added to the component and work is positive when it is produced by the component. The entropy balance equation in the rate form can be written as

$$\sum_{k} \frac{\dot{Q}_k}{T_k} + \sum_{inlet} (\dot{m}_{inlet} s_{inlet}) + \dot{S}_{gen} = \sum_{outlet} (\dot{m}_{outlet} s_{outlet}) \quad (3)$$

The entropy generation rate term on the left side of this equation must be positive which is the statement of the second law of thermodynamics. Finally, the exergy balance equation is stated as

$$\sum_{k} (1 - \frac{T_o}{T_k}) \dot{Q}_k + \sum_{inlet} (\dot{m}_{inlet} ex_{inlet}) = \sum_{outlet} (\dot{m}_{outlet} ex_{outlet}) + \dot{W} + \dot{E}x_d \quad (4)$$

In addition to the balance equations, the electrochemical reaction that takes place in the fuel cell is expressed by Haseli et al. (Haseli et al., 2008) in a chemical reaction formula as

$$CH_4 + 2\lambda\cdot(O_2 + 3.76N_2) \longrightarrow U_f\cdot CO_2 + (1-U_f)\cdot CH_4 + 2U_f\cdot H_2O + 2(\lambda-U_f)\cdot O_2 + 7.52\lambda\cdot N_2$$

From this formula, we notice that the products have some excess oxygen and some remaining methane which is completely burned in the combustor according to the chemical reaction stated below

$$\alpha\cdot CH_4 + U_f\cdot CO_2 + (1-U_f)\cdot CH_4 + 2U_f\cdot H_2O + 2(\lambda-U_f)\cdot O_2 + 7.52\lambda\cdot N_2 \longrightarrow$$
$$(1+\alpha)\cdot CO_2 + 2(1+\alpha)\cdot H_2O + 2(\lambda-(1+\alpha))O_2 + 7.52\lambda\cdot N_2$$

where α is a mass flow rate ratio of methane defined as

$$\alpha = \frac{\dot{m}_4}{\dot{m}_2} \quad (5)$$

To get more details on the thermodynamic analysis of these integrated systems, please refer to the corresponding section in a previous paper published by the authors in (Al-Hamed and Dincer, 2020).

4. Results and Discussion

The system 1 thermodynamic results have been already published, but System 2 results were not. For this reason, we present the thermodynamic performance results of System 2 and compare it to System 1. In Table 1, the output power values and energy and exergy efficiencies of the overall system and the subsystems are listed. As can be seen, the power output of SOFC is the highest at a value of 2194 kW, followed by GT, Turbine 2, and Turbine 3. The SOFC provides 70.12% of the total power driving the locomotive. The other 29.88% is recovered by the three turbines. In this integrated system, an absorption chiller with a heat exchanger subsystem is used instead of a reversible heat pump. Although we have shown a good case for the advantages of using reversible heat pump

cycles, it is interesting to see the effect of this choice on the overall energy and exergy efficiencies. From this table, the overall energy and exergy efficiencies are 68.83% and 67.24%, respectively. These are around 1% higher than System 1 reported in (Al-Hamed and Dincer, 2020), which means that using an absorption chiller with a heat exchanger subsystem is not much worth it when compared to space and weight advantages of reversible heat pumps mentioned earlier.

Table 1. Calculated parameters for the thermodynamic analysis of system 2.

Parameter	Value
SOFC electric power	*2194 kW*
Gas Turbine (GT) electric power	*582.7 kW*
Turbine 2 electric power	*265.2 kW*
Turbine 3 electric power	*86.50 kW*
Total electric power of the integrated system	*3129 kW*
Total power required by the train at maximum load	*3100 kW*
Evaporator heat transfer rate (cooling mode)	*105 kW*
SOFC-GT energy efficiency	*59.08%*
SOFC-GT exergy efficiency	*59.11%*
SRC energy efficiency	*24.38%*
SRC exergy efficiency	*52.87%*
ORC energy efficiency	*10.52%*
ORC exergy efficiency	*63.56%*
Overall energy efficiency	*68.83%*
Overall exergy efficiency	*67.24%*

Now, we present a parametric analysis to compare the effects of cooling load met by the reversible heat pump in system 1, or the absorption chiller in system 2 on the overall performance of the integrated systems and the Steam Rankine Cycle. Also, cooling load effects on state 34 temperature, in system 2, are studied. In Fig. 2, the cooling load effects on the overall energy and exergy efficiencies of systems 1a and 2 are shown. As the cooling load increases from zero to 120 kW, the overall energy and exergy efficiency values of system 2 increase from 66.59% and 66.60% to 69.14% and 67.33%, respectively. On the other hand, for system 1, as the cooling load increases, only the overall energy efficiency increase from 67.01% to 68.71%, while the overall exergy efficiency decrease from 67.02% to 66.25%. This is due to the increase in heat output and the decrease in total power produced, especially from turbine 3 of SRC.

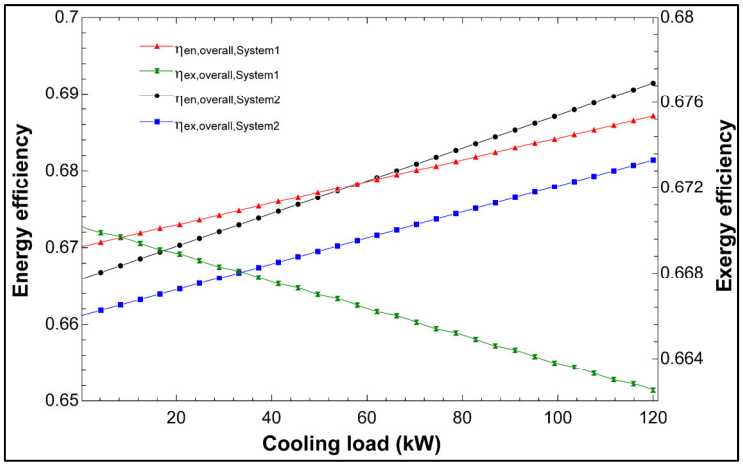

Fig. 2: Energy and exergy efficiencies comparison of systems 1a and 2 versus the cooling load.

5. Conclusions

The comparison between System 1 and System 2 presented above show that the use of an absorption chiller for mobile applications in terms of energy and exergy efficiencies is slightly favorable to the absorption chiller option. The increase in exergy efficiency is around 1% for a cooling load of 105 kW which does not justify its use when considering the space and weight requirements of absorption chillers compared to reversible heat pumps.

References

Al-Hamed, K.H.M., Dincer, I., 2020. A novel integrated solid-oxide fuel cell powering system for clean rail applications. Energy Convers. Manag. https://doi.org/https://doi.org/10.1016/j.enconman.2019.112327

Azizi, A., Ahrend, P., Samuelsen, S., Brouwer, J., 2019. Prototype Design and Evaluation of Hybrid Solid Oxide Fuel Cell Gas Turbine Systems for Use in Locomotives.

Haseli, Y., Dincer, I., Naterer, G.F., 2008. Thermodynamic modeling of a gas turbine cycle combined with a solid oxide fuel cell. Int. J. Hydrogen Energy 33, 5811–5822. https://doi.org/10.1016/j.ijhydene.2008.05.036

Morris, D.R., Szargut, J., 1986. Standard chemical exergy of some elements and compounds on the planet earth. Energy 11, 733–755. https://doi.org/10.1016/0360-5442(86)90013-7

Railway Association of Canada, 2015. Locomotive Emissions Monitoring Program, Environment.

Rosen, M.A., Dincer, I., 2001. Exergy as the confluence of energy, environment and sustainable development. Exergy, an Int. J. 1, 3–13.

AN EXPERIMENTAL STUDY ON GAS-TO-LIQUIDS (GTL) AND BIOGAS DUAL FUEL OPERATION OF A DIESEL ENGINE

[1*]Saket Verma, [2]L.M. Das and [2]S.C. Kaushik
[1]Department of Mechanical Engineering, BITS-Pilani, Pilani Campus, Rajasthan 333031, India
[2]Centre for Energy Studies, Indian Institute of Technology (IIT) Delhi, Hauz Khas, New Delhi, 110016, India

* E-mails: saket.verma@pilani.bits-pilani.ac.in, saketverma@hotmail.com

Abstract

An experimental study of dual fuel operation of a conventional diesel engine using biogas as the main and GTL (gas-to-liquids) as the pilot fuel is presented in this work. It is significant as alternative and renewable fuels can be ustilized in the existing diesel engines using minor hardward modifications. The presented fuel combination has great potential, however not been extensively studied. In this study, the fuel delivery methods are: convetional directly injection for pilot fuel (GTL) and intake manifold induction for main fuel (biogas). The dual fuel operations were studied at steady state conditions with variable engine loads. The performance characterization of dual fuel engine was performed using energy and exergy analyses. On the emission side, oxides of nitrogen (NOx), hydrocarbon (HC), carbon monoxide (CO) and smoke emissions were analysed. These results were compared with the standard single fuel operations of the diesel engine. As a result of this study, it was found that the engine efficiency with GTL fuel was slightly higher as compared to diesel in single fuel operation. The dual fuel operation showed up to 80% pilot fuel replacement by biogas, however, some reduction in engine efficiency was observed. The major reason for loss in efficiency with biogas is its lower calorific value. At the full load, the exergy efficiencies with diesel, GTL and GTL-biogas operations were 28.4%, 30.2% and 23.6% respectively. At the above operating conditions, exergy destructions were 36.5%, 33.4% and 47.7% respectively. On the emissions side, GTL showed slight improvements in NOx, HC and CO emissions as compared to diesel. The dual fuel operation showed significant reduction in NOx and smoke emissions, though the HC and CO emissions were increased.

Keywords: Dual fuel, GTL, Biogas, Diesel, Exergy, Irreversibility

I. Introduction

The deployment of renewable fuels in various primemovers is not a new idea, however, its importance has been better understood in the past few decades. The energy demand rose sharply with fast industrial growth and modernization causing tremendous amount of fossil fuel exploration and consumption. The result of which was environmental degradation and energy scarcity. It has been suggested by many scientists that all sources of renewable energies should be explored and utilized in the various energy systems to create a sustainable future. In this regard, GTL and biogas are potential renewable fuels to replace the fossil fuel in diesel engines. GTL is a hydrocarbon fuel, which can be produced from various carbonaceous materials including both fossil fuels, such as coal and natural gas, and renewable fuels, such as biogas and biomass. The physical and chemical charateristics of GTL closely match with the diesel fuel and therefore it can run any compression ignition (CI) engine without hardware modifications. The main fuel, biogas is produced from anaerobic digestion of organic waste. A raw biogas usually contains methane (CH_4), carbon dioxide (CO_2) and small amount of other gases. The auto-ignition temperature of biogas is very high (600-650 °C) (Barik and Murugan, 2014) so that its compression ignition (CI) in diesel engine is very difficult. Therefore, small amount of liquid fuel with low auto-ignition temperature is used to initiate the combustion, and the bulk combustion takes place with biogas-air mixture. This technique is termed as dual fuel (DF) combustion, which is an effective method to utilize the gaseous fuels in CI engines. The effect of GTL as an alternative to diesel has been studied by (Abu-Jrai et al., 2009) on the combustion, performance, and emissions of a diesel engine with addition of simulated reformer product gas (hydrogen-rich gas, referred to as reformed EGR). It was observed that the GTL improved the brake thermal efficiency and an optimal ratio of GTL and reformer was found beneficial. Furthermore, GTL fuel without reformer showed NO_x and smoke emission reductions up to 75% and 60%, respectively as compared to the diesel fuel. (Du et al., 2014) studied the effect of GTL/diesel blends on combustion and particle size distribution of a turbocharged intercooled common-rail direct injection (DI) diesel engine. It was found that as the GTL volume was increased in the GTL/diesel blends, the combustion was advanced and the premixed phase was shortened. This resulted in higher peak cylinder pressures, however, at high loads the rate of pressure rise was decreased. The GTL fuel tends to produce more accumulation mode particles and reduces the nucleation mode particles emission. Another study with synthetic diesel fuel was performed by (Labeckas and Slavinskas, 2013) on a naturally aspirated, direct injection, diesel engine (60 kW). They found higher ignition delay (4.3°) and higher cylinder pressures (1.8%) with the synthetic diesel fuel as compared to conventional diesel. This was caused due to the lower cetane number of the synthetic diesel (49.7) as compared to the conventional diesel fuel (51.6). (Szybist et al., 2007) analysed the premixed ignition behaviour of GTL, biodiesel and n-heptane fuels as compared to the diesel fuel. In this study, highest low-temperature heat release was obtained by GTL as compared to other fuels. (Soltic et al., 2009) compared diesel, GTL, rapeseed

methyl ester, neat soybean and neat rapeseed oil as fuels in a direct injection on-road CI engine. The results indicated that GTL and oxygenated fuels showed higher efficiency and lower emissions as compared to diesel fuel when calibrated to equal NO_x levels. (Stanley, 2009) studied the prospect of GTL technology in the utilization of natural gas that is otherwise being flared. It was shown that with the GTL technology, natural gas can be converted into synthetic fuel having much better properties than the petroleum distillates. Considering the wide variety of high quality products and proven technology, GTL was suggested as a prominent technology for alternative fuels. With this background, present paper investigates the performance and emission behaviours of a GTL-biogas DF engine. The performance of the engine is studied with help of second-law of thermodynamics that is energy and exergy analyses. On the emission side, oxides of nitrogen (NO_x), hydrocarbon (HC), carbon monoxide (CO) and smoke emissions are analysed. The results of dual fuel engine are compared with the standard single fuel operations of the diesel engine.

II. Experimental Procedure

The schematic diagram of the experimental setup is given in Fig. 1. The experiments were performed for three cases, viz. single fuel diesel operation, single fuel GTL operation and dual fuel GTL-biogas operation. In the cases of single fuel operations, the liquid fuel was directly injected into the combustion chamber with the help of a conventional (mechanically-actuated) diesel injector. The liquid fuel injection is automatically controlled by a mechanical governor based on the load requirements and engine speed. On the other hand, the gaseous main fuel (biogas) in dual fuel operation was supplied with the intake air in the intake manifold and the liquid pilot fuel was directly injected into the combustion chamber. The engine operation was started with single fuel operation and at this point the intended engine load was applied with the help of loading panel. Thereafter, the main fuel (biogas) supply was initiated with the help of a precise control valve causing slight increase in the engine speed. As a result of this, the engine governing system was actuated, which slightly reduces the quantity of injected pilot fuel. In this manner the biogas supply was progressively increased and stoped when further addition of biogas led to abnormal engine operation. This condition corresponds to the maximum pilot fuel substitution because maximum diesel is being replaced by biogas. At this operating point the readings such as, fuel flow rates, air flow rate, temperatures, engine speed, engine power and emissions were recorded. This procedure was repeated by varying the engine load and other data points were recorded.

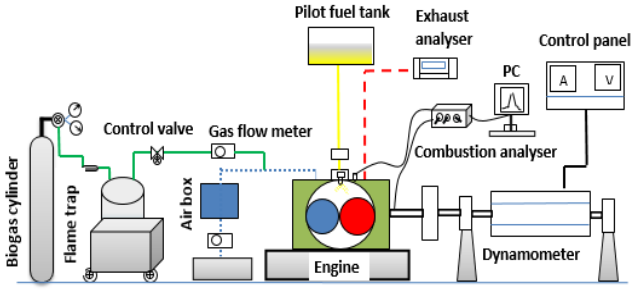

Fig. 1: Experimental set-up

III. Exergy Analysis

Exergy analysis is based on the second-law of thermodynamics, which analyses the system in terms of quality of energy. Based on second-law of thermodynamics, exergy balance for the dual fuel engine system can be given as: the rate of exergy destruction ($\dot{X}_{des}$) in the engine system should be equal to the input exergy to the engine minus sum of exergy flow out of the system.

$$\dot{X}_{des} = \dot{X}_{in} - (\dot{X}_W + \dot{X}_Q + \dot{X}_{ex}) \quad (1)$$

In the above equation, the chemical exergy of the liquid pilot fuel ($x_{ch,p}$) can be calculated using empirical correlation. The specific chemical exergy of main fuel (biogas) ($x_{ch,BG}$) is calculated from the following equation:

$$x_{ch,BG} = \sum_i x_i x_{ch,i}^{\ o} + T^0 \sum_i x_i R \ln x_i \quad (2)$$

for any i^{th} species in the biogas mixture, x_i is mole fraction and $x_{ch,i}^{\ o}$ is standard specific chemical exergy in the above equation.

The rate of total input fuel exergy ($\dot{X}_{in}$) to the engine is given the sum of rate of pilot fuel and main fuel exergies:

$$\dot{X}_{in} = (\dot{m}_p x_{ch,\,p} + \dot{m}_m x_{ch,\,BG}) \quad (3)$$

The exergy output ($\dot{X}_W$) from work transfer is same as that of energy output ($\dot{E}_W$).

$$\eta_{II} = (\dot{X}_W / \dot{X}_{in}) \times 100 \quad (4)$$

IV. Results and Discussions

Fig. 2 depicts the variation of fuel flow rates in diesel, GTL and GTL-BG dual fuel cases against the engine loads. It shows that the fuel flow rates for all the cases increase with the engine loads. This is because higher engine loads put higher energy demands and therefore input energy is increased in the form of fuel flow rates. It is also observed that GTL fuel shows slightly lower fuel requirements as compared to diesel fuel throughout the engine load spectrum. It can be caused by higher calorific value and better combustion properties of GTL as compared to diesel, which lead to lower fuel requirements at the same engine loads. In case of DF operation, the major part of energy is provided by the main fuel (biogas) and small part is provided by the pilot (GTL) fuel. Therefore, the fuel flow rates required for GTL were found smaller than for biogas (also lower than the fuel flow rates with single fuel operations). Pilot fuel substitution (% by mass) and energy share of pilot fuel (% of total input exergy) are depicted in Fig. 3 against the engine load. Pilot fuel substitution shows decreasing trend with the increasing engine loads and therefore, pilot fuel energy share is increased. At the low load, small quantity of pilot fuel is required, mainly to start the combustion and the bulk combustion of premixed main fuel (biogas) cater the power requirements. However, at high loads, due to relatively low calorific value and flame speed of biogas, additional amount of pilot fuel is required to supplement engine power requirements. The increased amount of pilot fuel also helps in improving the heat release rate and therefore, combustion of the charge mixture. The pilot fuel substitution varied from 80.20% to 61.27% when the engine operation was studied from no load to full load.

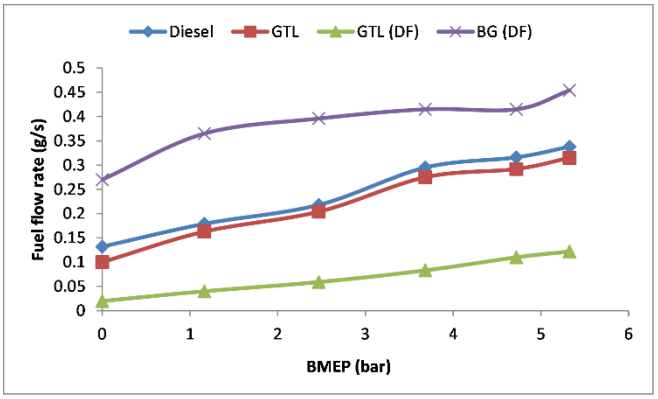

Fig. 2: Fuel flow rates with engine loads for diesel, GTL and GTL-BG DF cases.

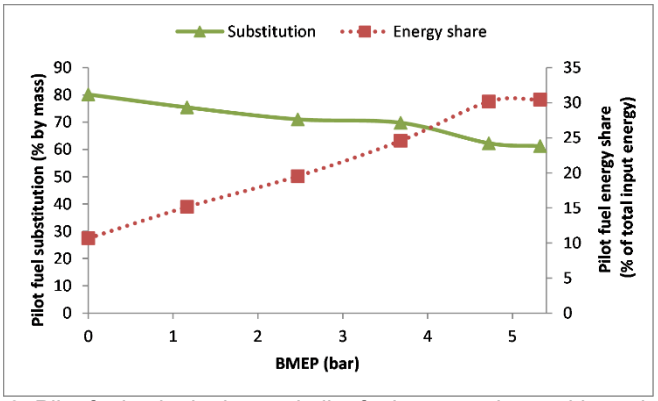

Fig. 3: Pilot fuel substitution and pilot fuel energy share with engine loads.

The trend of exergy efficiency is shown in Fig. 4. The highest exergy efficiencies of 28.4%, 30.2% and 23.6% where calculated at the full load condition for diesel, GTL and GTL-BG DF cases respectively. On the other hand, exergy destruction showed the opposite trend. The exergy destruction decreased with the engine load for all the cases. This is because of improved combustion of gaseous fuel (biogas) at high load conditions. The high temperature and pressure condition at high load render lesser entropy generation and hence lower exergy destruction. It was found that the GTL-BG DF case represents highest exergy destruction, whereas, the exergy destruction with diesel and

GTL cases were comparable. The high exergy destruction with BG-DF case can be attributed to low temperature and poor combustion of the gaseous fuel in dual fuel engine.

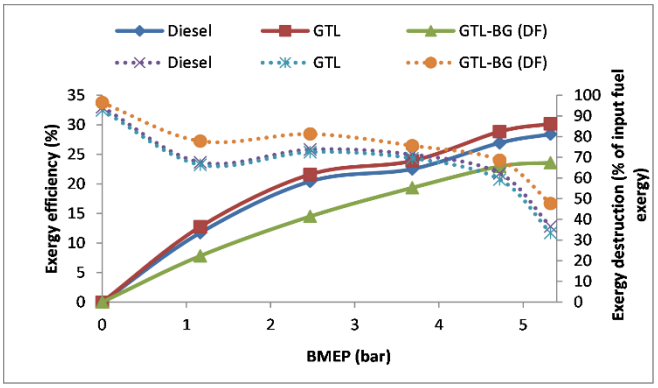

Fig. 4: Exergy efficiency and exergy destruction with engine loads.

V. Conclusions

In this work, GTL-BG DF operation has been experimentally studies and compared with the standard single fuel operations with diesel and GTL as the fuels. The results of the investigation are presented with performance and emission characteristics of the engine. The results showed that GTL is a better alternative to conventional diesel from the prospects of its improved performance and emission characteristics in a diesel engine. As a result of replacing diesel with GTL, 1.8% improvement in the exergy efficiency and 3.1% improvement in exergy destruction were observed. The GTL-BG DF operation resulted in 28.4% exergy efficiencies at full load condition. It is suggested to employ single fuel operation at low loads and DF operations at high loads for overall better efficiency. The dual fuel operation with GTL and biogas offers great flexibility and convenient way to utilize renewable fuels in the existing diesel engines.

Acknowledgements

We would like to acknowledge the support of Council of Scientific & Industrial Research (CSIR), New Delhi, India for granting research fellowship. Research facility provided by Indian Institute of Technology Delhi (IITD) is also gratefully acknowledged.

References

Abu-Jrai, A., Rodríguez-Fernández, J., Tsolakis, A., Megaritis, A., Theinnoi, K., Cracknell, R.F., Clark, R.H. “Performance, combustion and emissions of a diesel engine operated with reformed EGR: Comparison of diesel and GTL fuelling.” Fuel Vol. 88 No. 6 (2009): pp. 1031-41.

Barik, D., Murugan, S. “Investigation on combustion performance and emission characteristics of a DI (direct injection) diesel engine fueled with biogas-diesel in dual fuel mode.” Energy Vol. 72 (2014): pp. 760–71.

Du, J., Sun, W., Wang, X., Li, G., Tan, M., Fan, L. “Experimental study on combustion and particle size distribution of a common rail diesel engine fueled with GTL/diesel blends.” Applied Thermal Engineering Vol. 70 No. 1 (2014): pp. 430-40.

Labeckas, G., Slavinskas, S. “Performance and emission characteristics of a direct injection diesel engine operating on KDV synthetic diesel fuel.” Energy Conversion and Management Vol. 66 (2013): pp. 173-88.

Soltic, P., Edenhauser, D., Thurnheer, T., Schreiber, D., Sankowski, A. “Experimental investigation of mineral diesel fuel, GTL fuel, RME and neat soybean and rapeseed oil combustion in a heavy duty on-road engine with exhaust gas aftertreatment.” Fuel Vol. 88 No. 1 (2009): pp. 1-8.

Stanley, I.O. “Gas-to-Liquid technology: Prospect for natural gas utilization in Nigeria.” Journal of Natural Gas Science and Engineering Vol. 1 No. 6 (2009): pp. 190-4.

Szybist, J.P., Boehman, A.L., Haworth, D.C., Koga, H. “Premixed ignition behavior of alternative diesel fuel-relevant compounds in a motored engine experiment.” Combustion and Flame Vol. 149 No. 1-2 (2007): pp. 112-28.

Catalytic Hydrolysis of mixtures of Sodium Borohydride and Ammonia Borane for Hydrogen Generation

[1]Deniz Lim, [1]Gülay Özkan, [2]Göksel Özkan,
[1] Ankara University, Faculty of Engineering, Department of Chemical Engineering, Ankara, 06100,Tandoğan, Turkey
[2] Gazi University, Faculty of Engineering, Department of Chemical Engineering, Ankara, 06570 Maltepe , Turkey

* E-mails: gozkan@eng.ankara.edu.tr, gozkan@gazi.edu.tr

Abstract
Catalytic hydrolysis of mixtures of sodium borohydride (NaBH4) and ammonia borane (NH3BH3) was studied for hydrogen production. For hydrolysis, novel tri-metallic (Ni-B-Zr) and bimetallic (Ni-B) catalysts was prepared and used. Experiments conducted at different reactant molar ratios and temperatures. Comparing Ni-B and Ni-B-Zr for pure NaBH4 and pure NH3BH3 reactions, positive effect on hydrogen production provided by Zr on Ni-B catalyst was obtained. SEM, BET Kinetic analysis for hydrolysis reactions were carried out and activation energies of hydrolysis reactions of pure NaBH4, pure NH3BH3, and NaBH4/NH3BH3 molar ratios were calculated

Keywords: Keywords: Hydrogen production, Dehydrogenation, catalytic hydrolysis, ammonia borane, sodium borohydride,

I. Introduction

Hydrogen is the fuel with the highest energy content per unit mass of known fuel types. The safe and efficient transport and storage of hydrogen is one of the most important requirements for the development of hydrogen economy along with production. Hydrogen can be stored physically and chemically. Chemical storage is the storage of hydrogen in hydrides, amides/imides, hydrocarbons, and boron-based materials (Moussa, et al 2019,). From these substances, hydrogen can be released by hydrolysis, thermolysis or alcoholysis (Murathan, et al, 2018). The most remarkable aspect of the hydrolysis, half of the produced hydrogen is obtained from water. Catalytic hydrolysis provides high hydrogen generation yields in low temperatures. Catalysts can be pre-synthesized or can be synthesized in situ in hydrolysis reactor. In this study, sodium borohydride ($NaBH_4$) and ammonia borane (NH_3BH_3) were selected as hydrogen containing material, because both $NaBH_4$ and NH_3BH_3 can release a large amount of hydrogen (10.8% by weight, 19.5% by weight), respectively, through hydrolysis reactions.

In addition, studies have shown that the hydrolysis of these two materials together provides improved results. The hydrolysis of the composites was found to be better than the pure substances. Studies on hydrolysis of $NaBH_4$-NH_3BH_3 composites without catalyst having different $NaBH_4$/NH_3BH_3 molar ratios were concluded that the maximum yields obtained from the pure samples were lower than the maximum yield achieved by the composite (Huang, Z., et al.,2012, Xu, Yanmin,2014). Moreover, hydrolysis of $NaBH_4$ and NH_3BH_3 together as composites having different molar ratios accelerated with $AlCl_3$ showed that all ratios gave similar results due to the pH lowering effect of NH_3BH_3 on the solution pH become insignificant besides the similar effect of $AlCl_3$ and higher yield and higher hydrogen production rate were obtained with increasing $AlCl_3$ content (Xu, Yanmin,2016). The effect of sodium borohydride addition on the reaction mechanism and kinetics of ammonia borane hydrolysis with FeB catalyst were investigated. It is obtained that; as the molar ratio of $NaBH_4$ / NH_3BH_3 increased, the rate of hydrogen production was also increased, and the addition of $NaBH_4$ reduced the activation energy from 52.11 kJ / mol to 27.19 kJ / mol (Figen, A. K., et al,2018). In another work in which $NaBH_4$-NH_3BH_3 mixture was investigated, it was observed that the NH_4^+ ions from NH_3BH_3 contributed to the distribution of catalyst nanoparticles formed in-situ. Fe-B, Co-B and Ni-B catalysts were found to be economical and effective catalysts for $NaBH_4$ (Singh, P. K., et al., 2017).

In the studies, various catalysts were used in the hydrolysis of NH_3BH, $NaBH_4$ and mixtures of both , such as noble or non-noble metals (Demirci, U.B. , Miele, P. 2009, Özgür, D., et al. 2018), metal alloys (Kim,et al .,2009) and acids (Akdim, O.,et al., 2009, Akkuş, S. et al, 2018, Akkuş, S. et al, 2019). These studies have mainly focused on the preparation of catalysts, development of active, durable catalytic materials. Also, preparation of catalysts is sometimes complicated or expensive, which limits the application of catalytic hydrolysis of NH_3BH_3 and $NaBH_4$. So it is significantly valuable to develop a simple and cost-effective hydrolysis method for both NH_3BH and $NaBH_4$. Also, it is significantly valuable to sea a synergetic effect on hydrolysis of these two materials together.

In this study, first, hydrolysis of $NaBH_4$ and NH_3BH_3 with Ni-B-Zr catalyst, which was prepared in-situ, at different temperatures and with $NaBH_4$ /NH_3BH_3 different mole ratios were aimed to be examined and kinetic analysis was carried out. Secondly, the effect of presence of Zr was examined by conducting hydrolysis experiments with Ni-B and comparing with Ni-B-Zr.

II. Experimental Procedure/Methodology/System Description

Nickel(II) chloride hexahydrate ($NiCl_2.6H_2O$ Merck), $ZrCl_4$ (*Merck-Schuchardt),* Sodium Borohydride ($NaBH_4$, 98%, Sigma-Aldrich) and ammonia borane (NH_3BH_3, synthesized in laboratory) were optained and used . Using the deionized water, All of the aqueous solutions were prepared. The hydrolysis of mixtures of $NaBH_4$ and NH_3BH_3 with the help of an in-situ catalyst occurs in two steps, catalyst formation reactions and hydrolysis reactions, which are occurring in the same reactor (Figure 1), respectively. Dilute solution of $NiCl_2$ and $ZrCl_4$ was put on the reactor (catalyst contains 10%zr and 90% Ni-B by weight and total active substance amount is 0.0023g). One outlet of the reactor was connected to the feed burette, which was filled with reactant solution having desired $NaBH_4$:NH_3BH_3 molar ratio. The amount of SBH required for catalyst formation was calculated stochiometrically, and the reagent volumes required for 40 ml hydrogen formation were calculated and their total was put into the hopper. As shown in Figure 2after the determined amount of solution required for the catalyst formation was fed to the reactor, waited until hydrogen generation was finished, then the remaining solution, for hydrolysis reaction, was fed in one time. Hydrogen output rates were recorded. Experiments were carried out by keeping the temperature constant different temperature. Moreover, in order to obtain the effect of $ZrCl_4$ addition, same procedure was applied for pure $NaBH_4$ and NH_3BH_3 hydrolysis reactions using $NiCl_2.6H_2O$, without $ZrCl_4$ solution.

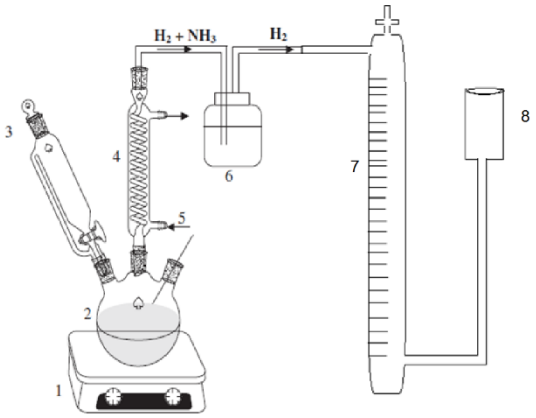

Figure 1. The reaction apparatus for hydrogen generation (1) hot plate (2) fifty milliliters three-necked round-bottom flask (3) addition funnel with a pressure equalized arm (4) condenser (5) coolant in and out (6) washing bottle (7) gas burette, (8) leveling bottle (Deniz et al.,2019)

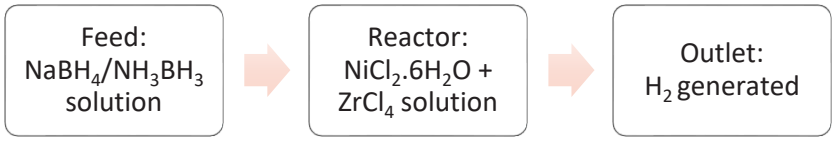

Figure 2. Experimental procedure

As a result of the experiments, some catalysts were selected and SEM and BET analysis were performed. When selecting the catalysts to characterize, it was aimed to investigate the difference of Ni-B and Ni-B-Zr catalysts and the situation before and after hydrolysis. SEM images of the samples taken from selected catalysts were taken by QUANTA 400F Field Emission SEM high resolution scanning electron microscope. SEM measurements of the samples were performed at 30kV, x25000 - x200000 magnification and 500 nm-4µm range. In addition, elemental contents in the structure of the samples were determined in percent by EDX analysis. Surface and pore characterization of samples was performed using Quantachrome Autosorb 1C-MS BET analyzer. The samples were degassed at 120 ° C for 4 hours. Multi-point BET area and pore size distribution analyzes were performed.

III Results and Discussions

Hydrolysis

Hydrolysis of mixtures consisting of SB and AB was studied in the presence of Zr-Ni-B /Ni-B catalyst. Samples different reactant ratios were spontaneously hydrolyzed at different temperatures
Hydrolysis reactions of reactants can be described as given in Eq. (1-2).

$$NH_3BH_3 + 2H_2O \xrightarrow{\text{catalyst}} NH_4BO_2 + 3H_2 \quad (1)$$

$$NaBH_4 + 2H_2O \xrightarrow{\text{catalyst}} NaBO_2 + 4H_2 \quad (2)$$

The mechanisms of hydrolysis reactions given in Equation 1 and 2 have been proposed in different ways in the literature. According to those experiments, effect of molar ratio and effect of temperature are obtained. H_2 production yield of each experiment is calculated as given in Eq. (3). In this equation, mol $H_{2,theoretical}$ is calculated by taking into account the SBH/AB molar ratio and stoichiometry reactions. Also, mol $H_{2,experimental}$ refers to all hydrogen collected during in-situ catalyst formation and hydrolysis reactions.

$$H_2\ production\ yield\ (\%) = \frac{mol\ H_{2,experimental}}{mol\ H_{2,theoretical}} * 100\% \quad (3)$$

By comparing Ni-B and Ni-B-Zr for pure $NaBH_4$ and pure NH_3BH_3 reactions, positive effect of Zr on Ni-B catalyst is determined. In the composition of trimetallic cataliyst (Zr is used) yields are increased.

Reaction Kinetics

Reaction kinetics of hydrolysis reactions of $NaBH_4$, NH_3BH_3 and their mixtures having different $NaBH_4/NH_3BH_3$ molar ratios accelerated by using tri-metallic Ni-B-Zr catalyst, were studied according to the exponential kinetics

Catalyst Characterization

The in bimetallic and trimetallic catalysts used in the experiments were removed from the solution phase in the reactor and subjected to the characterization process. After the in-situ catalysts formed in the reactions are filtered and dried, Multi-point BET area and pore size distribution analyzes were performed. Results are given in Table 1. Zr addition to the Ni-B catalyst is caused an great increase in surface area and raised the pore volume. It can observed that metallic-boron compound has been formed as Zr-B structure.

Table 1. Surface area, Pore volume and Pore size of Ni-B and Ni-B-Zr catalyst.

Catalyst	BET SURFACE AREA (m^2/g)	AVERAGE PORE SIZE (Å)
Ni-B	44.33	4.292
Ni-B-Zr	175.5	32.160

SEM images of the samples taken from selected catalysts were taken at 30kV, x25000 - x200000 magnification and 500 nm-4µm range. Results of SEM are given in Figure 2, which shows the morphologies of the Ni-B and Ni-B-Zr catalyst. As it can be seen from (a), structure in Ni-B catalyst is there is porous, amorphous and homogeneous. And from (b), there is also a porous structure in Ni-B-Zr catalyst. Ni-B is more crystalline when compared with Ni-B-Zr and it has bigger pores. In Ni-B-Zr, micro structure is more obvious. It was shown that the particles in the Ni-B sample were distributed more homogeneously than those in the Ni-B-Zr sample.

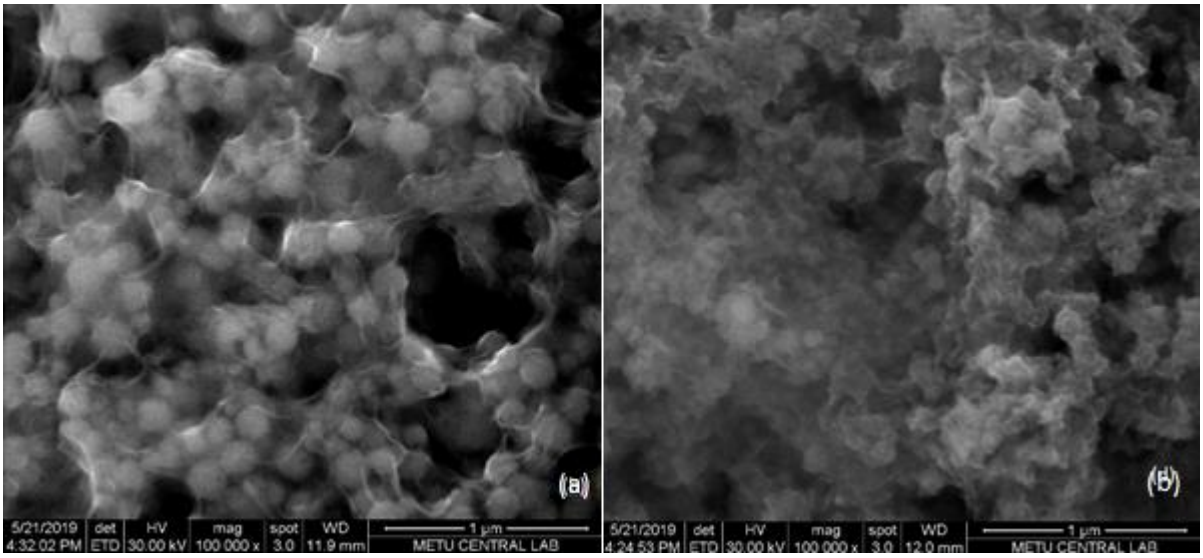

Figure 2. SEM images of a) NiB catalyst after hydrolysis reaction, b) NiBZr catalyst after hydrolysis reaction.

V. Conclusions

In this work, hydrolysis of sodium borohydride, ammonia borane and their mixtures in presence of in-situ catalyst were studied. First in-situ solution-state catalysts were prepared and then the hydrolysis reactions were occurred. According to the experiments, sodium borohydride/ammonia borane provide higher rate and yield compared to pure sodium borohydride and pure ammonia borane. Thus, Zr addition to Ni-B is found to be an effective. Since studies for different SBH/AB mole ratios are limited in literature, this work investigating different SBH/AB mole ratios and two different catalysts may provide useful data for future studies.

Acknowledgements

This work was financially supported by Ankara University (A.U.B.A.P) under the Project No: 19L0443012.

References

Akdim, O., Demirci, U.B., Miele P., 2009, Acetic acid, a relatively green single-use catalyst for hydrogen generation from sodium borohydride, Int J. Hydrogen Energy, 34, pp.7231-7238

Akkuş, M.S, Murathan, H.B, Özgür, D., Özkan, G, Özkan, G., 2018, New insights on the mechanism of vapour phase hydrolysis of sodium borohydride in a fed-batch reactor, Int J Hydrogen Energy, 43,(23),pp 10734-10740

Chen, Y., & Kim, H.,2008, Use of a nickel-boride–silica nanocomposite catalyst prepared by in-situ reduction for hydrogen Production from hydrolysis of sodium borohydride. Fuel Processing Technology, 89(10), pp 966-972.

Deniz L, Özkan, G.,Özkan, G., 2019, Hydrogen Generation from Sodium Borohydride, Ammonia Borane and Their Mixtures Using Ni-B-Zr In-Situ Catalyst 4th International Hydrogen Technologies Congress (IHTEC-2019),(24-26 June 2019) Trakya University, Edirne

Demirci, U. B., 2017, Ammonia borane, a material with exceptional properties for chemical hydrogen storage. International Journal of Hydrogen Energy, 42(15), pp. 9978-10013

Figen, A. K., Taşçi, K., & Filiz, B. C., 2018, Synergetic Effect of Sodium Borohydride Addition in Ammonia Borane Hydrolysis Reaction Mechanism and Kinetics. Kinetics and Catalysis, 59(2), pp 128-135

Huang, Z., Wu, C., Chen, Y., & Wang, X., 2012,The catalyst-free hydrolysis behaviors of $NaBH_4$–NH_3BH_3 composites. International Journal of Hydrogen Energy, 37(6) pp. 5137-5142.

Kim, D.R., Cho, K.W. , Choi, Y.I., Park C.J., 2009, Fabrication of porous Co–Ni–P catalysts by electrodeposition and their catalytic characteristics for the generation of hydrogen from an alkaline $NaBH_4$ solution Int J Hydrogen Energy, 34 pp.2622-2630

Loghmani, M. H., & Shojaei, A. F., 2013, Hydrogen generation from hydrolysis of sodium borohydride by cubic Co–La–Zr–B nano particles as novel catalyst. International Journal of Hydrogen Energy, 38(25): 10470-10478

Moussa, G. & Moury, R., Demirci, U. Şener, T.,Miele, P., 2013, Boron-based hydrides for chemical hydrogen storage, . International Journal of Energy Research, 37(8)pp. 825-842

Murathan, H.B, Özkan, G., Akkuş, M.S, Özgür, D.Ö, Özkan, G., 2018, Hydrogen production from the methanolysis of ammonia borane by Pd-Co/Al_2O_3 coated monolithic catalyst, Int J. Hydrogen Energy,43(23)pp. 10728-10733

Özkan, G. Akkuş, M.S, Özkan, G., 2019,The effects of operating conditions on hydrogen production from sodium borohydride using Box-Wilson optimization technique, Int J. Hydrogen Energy 44(20), pp. 9811-9816

Özgür, D.Ö, Şimşek, T, Özkan, G, Akkuş, M.S, Özkan, G.,2018, The Hydroloysis of ammonia borane by using Amberlyst-15 supported catalysts for hydrogen generation, Int J. Hydrogen Energy ,43(23),pp. 10765-10772

Singh, P. K., & Das, T., 2017, Generation of hydrogen from NaBH4 solution using metal-boride (CoB, FeB, NiB) catalysts. International Journal of Hydrogen Energy, 42 (49): 29360-29369

Xu, Y., Wu, C., Chen, Y.,Huang, Z., Luo, L., Wu, H., Liu, P., 2014. Hydrogen generation behaviors of NaBH4–NH3BH3 composite by hydrolysis. Journal of Power Sources; DOI: 261. 7–1310.1016/j.jpowsour.2014.03.038.

Xu, Y., Chen, J., Wu, C., Chen, Y., Jiafei, Li, Li, Z., 2016, Hydrogen generation from hydrolysis of $NaBH_4$/NH_3BH_3 composite promoted by AlCl3. International Journal of Hydrogen Energy. DOI: 41.10.1016/j.ijhydene.2016.05.234.

Zhang, L., Zhou, L., Yang, K., Gao, D., Huang, C., Chen, Y., Xia, Q., 2016, Pd Ni nanoparticles supported on MIL-101 as highperformance catalysts for hydrogen generation from ammonia borane. Journal of Alloys and Compounds.677,pp: 87-95

Investigation of Ni_2B as an additive in the molten carbonate fuel cell anode materials

[1]Erdi Başarır, [1]Gülay Özkan, [2]Göksel Özkan,
[1] Ankara University, Faculty of Engineering, Department of Chemical Engineering, Ankara, 06100 Tandoğan, Turkey
[2] Gazi University, Faculty of Engineering, Department of Chemical Engineering, Ankara, 06570 Maltepe, Turkey

* E-mails: gozkan@eng.ankara.edu.tr, gozkan@gazi.edu.tr

Abstract
Molten carbonated fuel cells are notable as power generation systems because of its high efficiency and relatively clean conversion of chemical energy into electrical energy. In this work, the anode electrode for molten carbonate fuel cell was synthesized. The positive effect of nickel boride as an additive in nickel anode electrode was investigated. Nickel boride was synthesized by chemical reduction with solvo-thermal route. Reduction reaction of nickel chloride hexahydrate salt with sodium borohydride was performed for nickel boride synthesis. Result of reaction, both nickel boride and hydrogen were produced and then nickel boride was put into reactor kept at 350 °C for 12 hours to provide solvo-thermal conditions. Obtained nickel boride was added to green sheet. Green sheets were subjected to sintering operation to get anode electrodes. As a result of SEM analysis, average particle size for without and with additive anode electrodes were calculated as 4,4 µm and 3,4 µm respectively. According to EDAX results, atomic percent of nickel for without/with additive anode electrods were found %44,34 and %83,13 respectively.

Keywords: Keywords: Plastic material, Anode, metals, molten carbonate fuel cell, nickel boride

I. Introduction

The fuel cell technology is an important part of the energy equation to reduce CO_2 emissions and to decrease our carbon footprint in sectors where the contribution to global CO_2 emissions are the highest by reducing fuel consumption in transportation, by increasing the efficiency in power generation, and by simplifying the transition from fossil to renewable fuels on the market (Iyidir et al, 2015). The Molten Carbonate Fuel Cells (MCFC), which are constant energy production systems and which have fuel consumption flexibility (H_2, natural gas, reformer gas including CO_2 up to 20%) work between 600-750 °C. A single fuel cell is composed of electrolyte, polymeric electrolyte or ceramic matrix, and permeable-pore type anode and cathode electrodes that are in touch with every surface of them. Nickel and Nickel oxide catalysts are also used as anode and cathode electrodes in molten carbonate fuel cells because of their cheaper than platinum and high durability (Özkan, 2017). Electrolyte is compose of the mixture of Li_2CO_3/K_2CO_3 or Li_2CO_3/Na_2CO_3. Molten carbonate fuel cell components are exposed to back dissolution of nickel oxide cathode electrode; electrolyte loss; corrosion of separator plates; lectrolyte holding capacity; catalyst deactivation; matrix breakage or degradation; corrosion of porous electrodes due to high temperature; impurities and pollution-related problems. To ensure long-term stability of such stack components above considerations need to be taken into account in material selection. Anode properties that will be suitable for MCFC are listed as; Should be electronically conductive; Electrochemical and catalytically preserved for a long time; It should form porous structure; Should be durable; Should show thermal compatibility with other components; Should be resistant to creep fatigue; Be chemically stable and compatible in electrolyte and fuel flow environments in operating and non-operating conditions. In order to ensure these phenomena, nickel can be combined with various metals (Cr, Al, Cu, etc.), in order to have binary metal alloys with good improvements of electrode microstructure, as reported in literatüre (Li et al 2015). Among these issues, creep and sintering mechanisms have the main effect on the anode degradation and shrinkage. Pure Ni anodes have a creep strain around 40% during the first 100 h of operation, with a decrease of surface area and shrinkage due to sintering (Kulkarni, et al,2012). To really improve stress resistance and cell's performance, the research of alternative anode materials with high performances is required (Frattini et al,2017)).

In this work, the positive effect of nickel boride in nickel anode was investigated.

II. Experimental Procedure/Methodology/System Description

Experimental studes, the schematic flow diagram given in Figure1, consist of three parts: nickel boride synthesis, green sheet synthesis and anode synthesis. Nickel boride synthesis was done according to eq(1).

$$8NaBH_4 + 4NiCl_2 \cdot 6H_2O \rightarrow 2Ni_2B + 6B(OH)_3 + 8NaCl + 25H_2 + 6H_2O \quad (1)$$

Nickel boride synthesis was performed two steps. In the first part, the nickel borides was sentesised using analytical reagent nickel chloride. Solutions of 0.183 grams of sodium boron hydride was prepared with 10 mL of distilled

water. 0.576 grams of nickel chloride in 10 ml of distilled water was placed in a double-mouthed flask in the ice bath (0 ^{0}C) and then Sodium boro-hydride solution was added very slowly with stirring over 30 min. It has been observed that there was gas releasition in every drop. A black precipitate appeared immediately upun the first additiyion of Sodium boro-hydride solution. After the reac-tion, the solution was kept stirring for another 30 min. At the end of 30 minutes, the double-mouthed flask was taken to the water bath kept at 60 ° C in order to formation B(OH)3 to pass filter paper. The aqueous phase was decanted from the granular black solid. It was filtered and washed with distilled water at 80 °C, and latter washed with methanol at the laboratory conditions and then with distilled water for 3 times.

In the second part; The black particles were taken into a 35 mL reactor and after adding 28 mL of pure water, the reactor was immersed in a vertical tube oven at 350 ° C and kept for 12 hours. It was filtered, washed once with hot distilled water, once with methanol and three times with cold distilled water in order to remove impurities and boric acid that may be occur in it. The filter paper was dried in the oven kept at 105 ° C for 12 hours and black particles were obtained. The particles obtained were characterized by XPS, SEM and EDAX (Energy dispersive X-ray analysis) analysis. SEM images of the samples taken from selected catalysts were taken by QUANTA 400F Field Emission SEM high resolution scanning electron microscope. SEM measurements of the samples were performed at 30kV, x25000 - x200000 magnification and 500 nm-4µm range. In addition, elemental contents in the structure of the samples were determined in percent by EDX analysis.

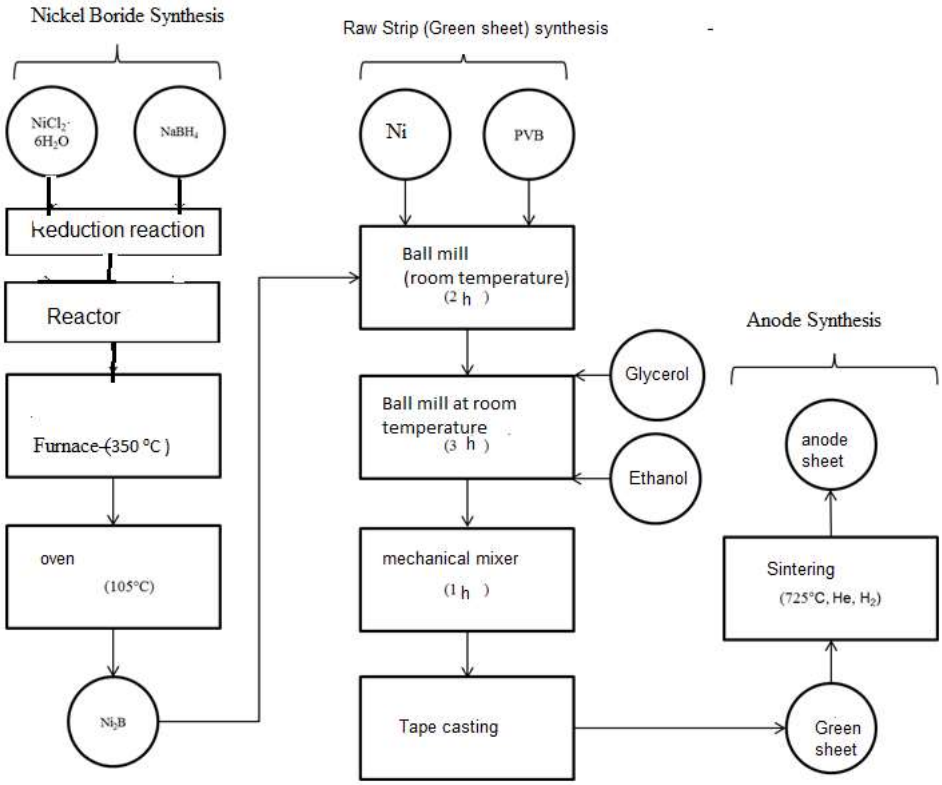

Figure 1. Schematic representation of experimental studies for Anode

In the second study, the green sheets of the anode of the Molten Carbonate Fuel Cells system was prepared by the tape casting technique using the Dr-Blade. Slurry solutions whose proportional and percentage composition (active material (Ni, NiO), binder (polyvinyl butyral, PVB), plasticizer (polyethylene glycol, PEG), organic solvent (ethanol), dispersant (glycerol)) was optimized according to Özkan et. al 2016. Schematic representation of experimental studies for anod was shown in Figure1. Nickel powder and PVB chemicals were grinded in the ball mill for 2 hours to ensure homogeneous and size distribution of solid chemicals. After 2 hours, Ethanol and PEG were added. The sludge obtained at the end of the mixing process, which lasted for 3 hours, was mixed with the mechanical mixer with 120 rpm at 1 hour in an atmospheric environment in order to increase its consistency due to the fact that it was too fluid for tape casting. The green sheet was obtained on the glass surface with a doctor blade. The green sheet was subjected to drying at room temperature for 1 day. Finely, sintering was carried out in the ash furnace at 725 $_o$C using He and H_2 gases.

III Results and Discussions

The result of XPS analysis of the black product (Ni_2B) was shown in Figure 2. As can be seen from this figure, Ni(2p3) at 853 eV, B (1s) at 189 eV were observed. The value of the nickel was 22.6% and the value of the boron was 11.3%, and Ni_2B formation was clearly revealed from these peaks.

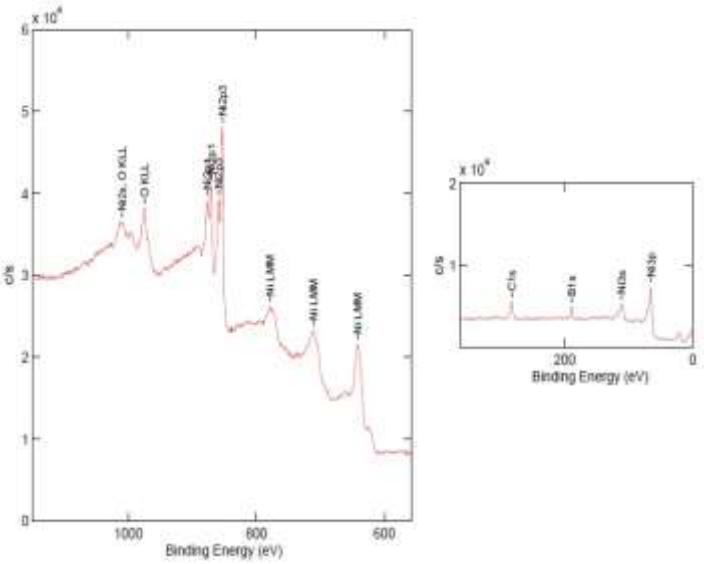

Figure 2. Solvo-Termal yol ile sentezlenen siyah ürünün XPS analizi sonucu

In the second part of the study, Nickel boride synthesized was added to get the green sheets. The weight distribution of chemicals in recipes for synthesizing green sheets were given in Table1. Drying processes was completed for each. The thickness of Ni_2B doped green sheet was measured as1.48 mm. After that sintering processes was completed. The thickness Ni_2B doped sheet was measured as1.45 mm. It was observed that the level of reduction of approximately 0.03 mm in the thickness of the materials after sintering was a fairly good green sheet recipe. Other studies were shown that the thickness reduction was around 0.05-0.5 mm (Tomimatsu 1997). This means that the nickel in the green sheet was sintered without collapsing as a result of adding Ni_2B.

Oxidation problem of Nickel is known as one of the critical problems in the literature.TGA-DTA analysis of the green sheets with and without additive were made to clarify oxidation problem of Nickel. In the range of 400-900 °C, Ni_2B doped plays a role in preventing the oxidation of the Ni anode.

Table 1. The weight distribution of chemicals in recipes prepared for green sheets

Chemicals	Without Ni_2B	% 3 Ni_2B
PVB	1	1
PEG	0.5	0.5
Ethanol	14	14
Glycerol	0.5	0.5
Nickel	20	20
Nickel boride	0.00	0.63

Acording to SEM analysis images of with/without additive anode sheeds, It was observed that the average particle size decreases as the percentage of additive increases. Also, homogeneous dispersions were observed in the anode structure. From the EDAX analysis spectrum of with/without additive anode sheeds, as the percentage of additives increased, the amount of impurities in the structure decreased by 4 -8 times.

V. Conclusions

As a result, it was observed that Ni2B in anode sheetssignificantly reduced the oxidation of nickel, one of the problems of nickel-based anode electrodes, and caused to decrease in particle size and more homogeneous dispersion of the particles.

Acknowledgements

This work was financially supported by Ankara University (A.U.B.A.P) under the Project No:17HO443008

References

Frattini D, Accardo G, Moreno A, Yoon S. P, Han H.J, Nam W.S, 2017 Strengthening mechanism and electrochemical Characterization of ZrO2 nanoparticles in Nickel–Aluminum alloy for Molten Carbonate Fuel Cells, Journal of Industrial and Engineering Chemistry 56 pp. 285–291

Li W, J. Chen, H. Liang, C. Li, 2015 Research on high-temperature compression and creep behavior of porous Cu-Ni-Cr alloy for molten carbonate fuel cell anodes Mater. Sci. 33 pp. 356

Kulkarni A, Giddey S, 2012, Materials issues and recent developments in molten carbonate fuel cells J. Solid State Electrochem. 16 pp.3123

Özkan G, Gemici S, Başarır E, Özkan G, 2016. Determination of Optimum Production Conditions of Casting Slurry in the Manufacture of Molten Carbonate Fuel Cell Electrodes with the Tape Casting Technique, CET, 52 pp. 871-878

Özkan G, Gemici S, Erkay C, Başarır E, Özkan G, 2017. Application of Response Surface Optimization Technique to the Preparation of Cathode Electrode for the Molten Carbonate Fuel Cell, JCSP, Vol: 39 ,3 pp.361-365

İyidir, U., Ozkan G., Ozkan G**.,** 2015.Synthesis and characterization of molten carbonate fuel cell anode materials., Energy Sources, Part A: 37 (22), pp. 2487-2495

Tomimatsu, N., Ohzu, H., Akasaka, Y., Nakagawa, K., Tateishi, H. 1997. US005595832A

Exergetic investigation of a new integrated ammonia based system

[1] Osamah Siddiqui and [1,2] Ibrahim Dincer
[1] Clean Energy Research Laboratory, Faculty of Engineering and Applied Science, University of Ontario Institute of Technology
2000 Simcoe Street North, Oshawa, Ontario L1H 7K4, Canada
[2] Yildiz Technical University, Faculty of Mechanical Engineering, Istanbul, 34349 Turkey
E-mail: osamah.siddiqui@ontariotechu.net, ibrahim.dincer@uoit.ca

Abstract
In this study, a newly developed integrated ammonia synthesis and fuel cell system is presented for hybrid solar and wind power plant applications. The system is incorporated with a novel type of three-way thermal energy storage, electrochemical ammonia synthesis and direct ammonia fuel cell subsystem operating with single alkaline molten electrolyte salt. The excess solar thermal energy is stored in this subsystem and the molten salt acts as both the storage medium and electrolyte for electrochemical ammonia synthesis as well as power generation through direct ammonia fuel cells. The energy and exergy efficiencies of the electrochemical ammonia synthesis system are evaluated to be 38.2% and 41.1% respectively. Further, the direct ammonia fuel cell entails an energy efficiency of 61.5% and an exergy efficiency of 57.8%. Several parametric studies are also conducted to investigate the effects of varying operating conditions and system parameters on the system performance.

Keywords: ammonia synthesis; ammonia fuel cell, integrated system, energy, exergy, efficiency

1. Introduction

The utilization of clean energy resources requires the development of new effective systems that can provide solutions to the current problems faced by these resources. Solar and wind energy resources, which are considered to be the most prominent clean energy options entail the challenge of intermittency. Both solar intensities as well as wind velocities are variable in nature. Solar radiation intensities entail a predictive pattern where the amount of solar intensities in a given location can be estimated through various empirical relations. However, several factors such as visibility, clouds, rain etc. effect the amount of solar radiation intensities falling on the surface of the earth in an unpredictable way. Further, wind velocities also entail high variability in speed and can range from very low values to considerably high values for a given location. Harnessing solar and wind energy is vital for advancement of the clean energy era, where several countries across the globe have adopted the usage of solar and wind plants for power generation. In addition, these are considered the most prominent options that will be used for clean power generation in the upcoming future. Thus, the main challenge of intermittency associated with solar and wind energy resources need to be addressed.

The main focus of energy storage methods in solar and wind power plants has been battery storage. Batteries allow the storage of electrical energy in the form of chemical energy. However, there are various problems associated with the usage of batteries. Firstly, they are not suitable for long term energy storage and need to be replaced after a set number of charging cycles. Thus, storing excess energy in the form of ammonia needs to be investigated that can act as a clean energy storage medium. Some studies have considered this route. Zhou et al. (2019) studied the usage of ammonia for energy storage. Clean ammonia was synthesized using renewable energy through solar and wind resources. Moreover, several applications of using ammonia such as power generation as well as fertilizer production were considered. The overall system analysis through energy and exergy approaches was not considered. Chen et al. (2019) investigated the usage of ammonia for energy storage. The operating principle entailed a thermochemical system where release and absorption of energy was used in a cyclic manner. The energy release accompanying the ammonia synthesis process and the energy absorption during the ammonia dissociation process were employed cyclically. Giddey et al. (2017) investigated a transportation system that was based upon ammonia fuel to mitigate the environmental emissions. Hydrogen required to synthesize ammonia was obtained from renewable energy resources. In addition to this, different routes of using ammonia for power generation were studied. These included the combustion of ammonia to generate thermal energy that can be used to produce mechanical power. The energy efficiency was evaluated to be 39% considering the route of ammonia decomposition. Further, the route of ammonia combustion was reported to have an efficiency of 21%. Although some studies were performed on ammonia-based energy storage options, no studies conducting comprehensive energy and exergy analyses of such systems for solar and wind power applications are found. Thus, in this study a newly developed integrated ammonia synthesis and fuel cell system is presented for hybrid solar and wind power plants. The specific objectives of this study include: (i) developing an integrated ammonia synthesis and fuel cell system for energy storage, (ii) conducting thermodynamic analyses on the developed system, (iii) determining the energy and exergy efficiencies of system components as well as subsystems, (iv) performing a parametric study to investigate the effects of changing operating system parameters on the efficiencies of the overall system as well as subsystems.

2. System description

The developed integrated ammonia synthesis and fuel cell system for hybrid solar and wind power plants is shown in Fig. 1. The solar tower based solar thermal technology is utilized that absorbs incoming solar energy through a molten salt medium. An alkaline molten salt of a mixture of sodium and potassium hydroxide (NaOH+KOH) is utilized

that acts as both an electrolyte for the electrochemical ammonia synthesis (EAS) and direct ammonia fuel cell (MEAFC) as well as the thermal energy storage medium. The wind turbines are connected to the proton exchange membrane (PEM) water electrolysis subsystem as well as the pressure swing adsorption (PSA) air separation unit. The PEM electrolysis produces hydrogen from water and electrical input whereas PSA generates nitrogen via air separation through an electrical input.

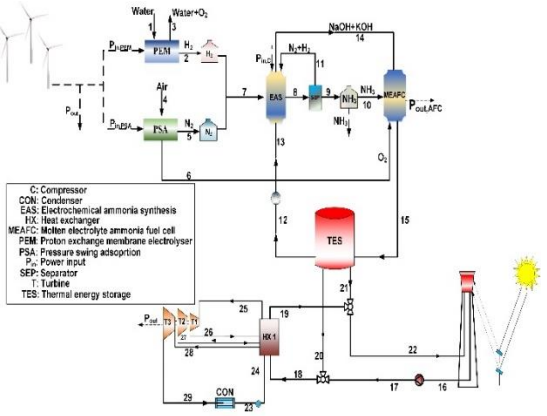

Fig. 1: Schematic of the developed integrated ammonia synthesis and fuel cell system

3. Analysis

The new system developed is assessed through thermodynamic analyses. Both EES and ASPEN Plus simulation software are utilized for the modelling. The ASPEN Plus simulation flowsheet is shown in Fig. 2.

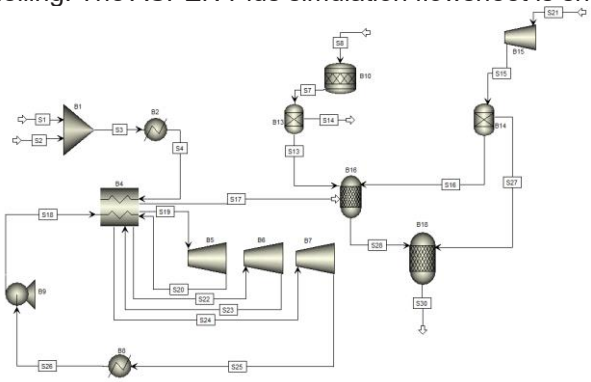

Fig. 2: A simulation flowsheet of the developed system

The electrochemical ammonia synthesis process is considered to operate at a temperature of 250°C and the direct ammonia fuel cell is considered to operate at 400°C. Moreover, the maximum pressure of the re-heat steam Rankine cycle is set at 3 MPa and the minimum pressure is 10 kPa.

The general mass, energy, entropy and exergy balance equations are expressed as

$$\sum_{in} \dot{m}_{in} = \sum_{ex} \dot{m}_{ex} \quad (1)$$

$$\dot{Q} + \sum_{in} \dot{m}_{in} \left(h_{in} + \frac{V_{in}^2}{2} + g Z_{in} \right) = \dot{W} + \sum_{ex} \dot{m}_{ex} \left(h_{ex} + \frac{V_{ex}^2}{2} + g Z_{ex} \right) \quad (2)$$

$$\sum_{in} \dot{m}_{in} s_{in} + \sum_{k} \frac{\dot{Q}_k}{T_k} + \dot{S}_{gen} = \sum_{ex} \dot{m}_{ex} s_{ex} \quad (3)$$

$$\dot{E}x^{Q} + \sum_{i} \dot{m}_i \, ex_i = \sum_{e} \dot{m}_e \, ex_e + \dot{E}x_w + \dot{E}x_d \quad (4)$$

The overall water splitting reaction in the PEM electrolyser is written as

$$H_2O + \dot{W}_{in,PEM} \rightarrow H_2 + \frac{1}{2} O_2 \quad (5)$$

The relation between the power input ($\dot{W}_{in,PEM}$), voltage (V_{PEM}) and current (I_{PEM}) is denoted as

$$\dot{W}_{in,PEM} = V_{PEM} I_{PEM} A_{PEM} \quad (6)$$

The PEM voltage (V) is dependent on several voltage losses occurring due to polarization and the overall voltage can be written as

$$V_{PEM} = V_{OCV,PEM} + V_{Ohmic,PEM} + \left(V_{act,a} + V_{act,c} \right)_{PEM} + \left(V_{conc,c} + V_{conc,a} \right)_{PEM} \quad (7)$$

where the concentration, activation and Ohmic, polarization losses are added to the open circuit voltage and the open circuit voltage is expressed as

$$V_{OCV,PEM} = \frac{RT}{nF}\ln\left(\frac{(p_{H_2})(p_{O_2})^{0.5}}{p_{H_2O}}\right) + \frac{\Delta G}{nF} \quad (8)$$

Moreover, the overall ammonia synthesis reaction is written according to

$$N_2 + 3H_2 \leftrightarrow 2NH_3 \quad (9)$$

Furthermore, the half-cell electrochemical reactions occurring during this process at the cathode and anode are written respectively as:

$$N_2 + 6e \rightarrow 2N^{3-} \quad (10)$$

$$2N^{3-} + 3H_2 \rightarrow 2NH_3 + 6e \quad (11)$$

In addition, in the MEAFC, ammonia reacts electrochemically to generate power. The anodic and cathodic reactions for this process are expressed as

$$2NH_3 + 6OH^- \rightarrow N_2 + 6H_2O + 6e \quad (12)$$

$$\frac{3}{2}O_2 + 3H_2O + 6e \rightarrow 6OH^- \quad (13)$$

The electrical power output from the ammonia fuel cell can also be written according to

$$\dot{P}_{out,MEAFC} = V_{AFC} I_{AFC} A_{AFC} \quad (14)$$

where the actual cell voltage (V_{AFC}) is a function of several voltage polarization losses and is written as

$$V_{FC} = V_{OCV} - V_{Ohmic} - V_{conc} - V_{act} \quad (15)$$

Also, the voltage of MEAFC under open circuit condition can be written as

$$V_{OCV,AFC} = \frac{-\Delta G}{nF} + \frac{\bar{R}T}{nF}\ln\left[\frac{(P_{NH_3})^2(P_{O_2})^{1.5}}{(P_{H_2O})^3(P_{N_2})}\right] \quad (16)$$

where n denotes the number of electrons transferred during the electrochemical reaction, T is the operating temperature of the fuel cell, P represents the partial pressures of the reactants or products, ΔG represents the change in Gibbs free energy and F is Faraday's constant.

The efficiencies of the EAS system considering energetic and exergetic performances are written as

$$\eta_{en,EAS} = \frac{\dot{N}_{NH_3}\overline{LHV_{NH_3}}}{\dot{W}_{in,EAS} + \dot{N}_{H_2}\overline{LHV_{H_2}}} \quad (17)$$

$$\eta_{ex,EAS} = \frac{\dot{N}_{NH_3}\overline{ex_{NH_3}}}{\dot{W}_{in,EAS} + \dot{N}_{H_2}\overline{ex_{H_2}}} \quad (18)$$

Also, the efficiencies of the direct ammonia fuel cell system are determined as

$$\eta_{en,AFC} = \frac{\dot{W}_{AFC}}{\dot{N}_{NH_3}\overline{LHV_{NH_3}}} \quad (19)$$

$$\eta_{ex,EAS} = \frac{\dot{W}_{AFC}}{\dot{N}_{NH_3}\overline{ex_{NH_3}}} \quad (20)$$

The overall system energy efficiency is evaluated as

$$\eta_{en,ov} = \frac{\dot{W}_{AFC} + \dot{W}_{RC} + \dot{W}_{WT}}{\dot{Q}_S + \frac{1}{2}\rho A V^3} \quad (21)$$

The overall system exergy efficiency is determined as

$$\eta_{ex,ov} = \frac{\dot{W}_{AFC} + \dot{W}_{RC} + \dot{W}_{WT}}{\dot{Q}_S\left(1 - \frac{T_0}{T_S}\right) + \frac{1}{2}\rho A V^3} \quad (22)$$

4. Results and Discussion

The energetic performance of the EAS subsystem is determined to entail an efficiency value of 38.2%. The corresponding EAS exergetic performance is assessed to have an efficiency value of 41.1%. Moreover, the energy efficiency of the MEAFC subsystem is determined to entail a value of 61.5% and the exergy efficiency is evaluated as 57.8%. These values are obtained under the considered operating conditions of EAS temperature of 250°C. Also, the MEAFC operating temperature considered for the analysis is set at 400°C. However, these major subsystems are also analysed at varying system conditions and operating parameters.

Fig. 3 shows the effect of varying EAS current densities on the ammonia synthesis rate as well as efficiencies. The efficiencies are observed to decrease with increasing current densities. Especially, at low current densities in the region of activation polarization, the efficiencies drop significantly. This can be attributed to high activation polarization voltage losses that result in higher power input requirements and thus lower efficiencies. The EAS energy efficiency varies between a value of 47.1% and 43.1% when the current density is varied between 0 and 10000 A/m^2. Also, the exergy efficiency decreases from 50.9% to 46.5% for the same rise in current densities. However, the ammonia synthesis rates increase linearly with rising currents. Further, the effect of EAS temperature on the energetic and exergetic performances are depicted in Fig. 4. Rising temperatures are observed to decrease the efficiencies. This can be attributed to the overall nature of the ammonia synthesis reaction that entails an exothermic nature. In such reactions, increasing temperatures favour the backward reaction and lowering temperatures favour the forward reaction.

However, other factors such as electrolyte conductivity should also be considered. With rising temperatures, the conductivity rises leading to lower polarization losses and thus lower voltage losses. This should also be taken

into account to analyse the effects of temperature on EAS performance. The energy efficiency is observed to decrease from 38.2% to 34.5% when the temperature rises from 250°C to 500°C. Similarly, the exergy efficiency reduces from 41.1% to 37.1% for the same rise in temperature. These results are obtained at an operating current density value of 8000 A/m^2.

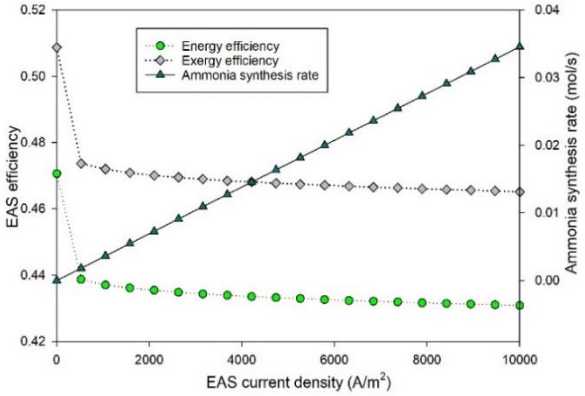

Fig. 3: Effect of varying current density on EAS performance

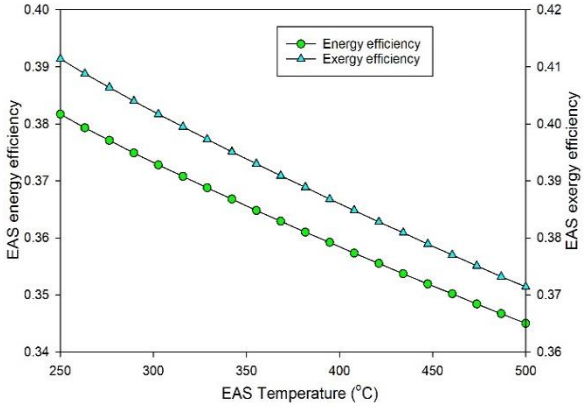

Fig. 4: Effect of EAS temperature on the efficiencies

Fig. 5 depicts the effect of varying the operating temperature of the molten electrolyte based direct ammonia fuel cell on its energetic and exergetic performance. Both energetic and exergetic performances are observed to enhance with rising temperatures. This can be attributed to several factors. Firstly, higher electrolyte temperatures would lead to lower polarization losses. The Ohmic losses would be lower due to higher electrolyte conductivity. Also, the concentration polarization would be lower due to higher diffusion coefficients at higher operating temperatures. The energetic performance of the MEAFC is observed to rise from an efficiency value of 59.6% to a value of 63.4% when the operating temperature is raised from 300°C to 500°C. In addition to this, the exergetic performance is also observed to rise from 56% to 59.5% for the same rise in AFC temperature. Thus, as the usage of higher temperatures lowers the efficiency of the EAS subsystem and rises the MEAFC efficiencies, it is recommended to perform an optimization study on the integrated ammonia synthesis and fuel cell (ASFC) system to investigate the optimum temperature that would provide the highest overall efficiencies.

This will allow to better understand the performance of the system under primarily actual operating conditions where both solar intensities and wind speeds vary every hour. Moreover, further economic studies should be conducted in the developed system considering different life cycle stages as well energy storage phases to determine the energy storage cost associated with the present system and how it stands in comparison with other energy storage methods. The power output results of the reheat Rankine cycle as a function of the steam mass flow rate are depicted in Fig. 6. A 3-stage steam turbine system is utilized where the steam is reheated after exiting turbines 1 and 2. The individual and cumulative power outputs of these turbines can be inferred from Fig. 6. The total power output at a low mass flow rate of 0.2 kg/s is evaluated to be 229 kW where the largest contribution is by turbine 3 that entails a power output of 149 kW. This is followed by turbine 1, which entails a power output of 53 kW. Turbine 2 has the least contribution of 27 kW. This can be attributed to the change in pressures at each turbine stage. In turbine 1, the first stage comprises of a pressure drop from 3 MPa to 1 MPa, whereas the second turbine entails a pressure drop from 1 MPa to 600 kPa. Since a higher pressure drop is associated with turbine 1, a higher power output is obtained. It is thus recommended to investigate the effects of varying operating pressures for the multi-stage turbine subsystem, where the pressure ratio of each turbine stage should be set at the optimum value such that the system provides both higher useful power output as well as higher overall energetic and exergetic efficiencies.

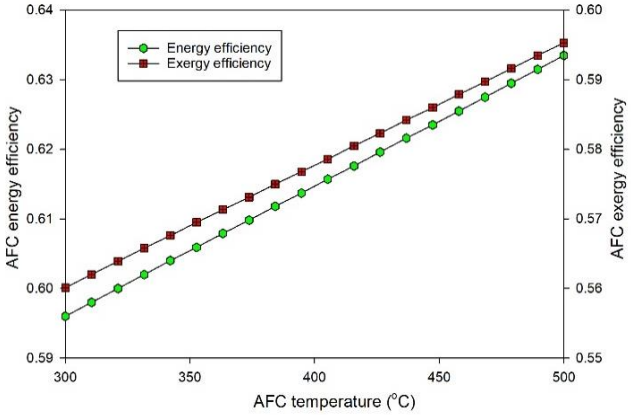

Fig. 5: Effect of AFC temperature on the efficiencies

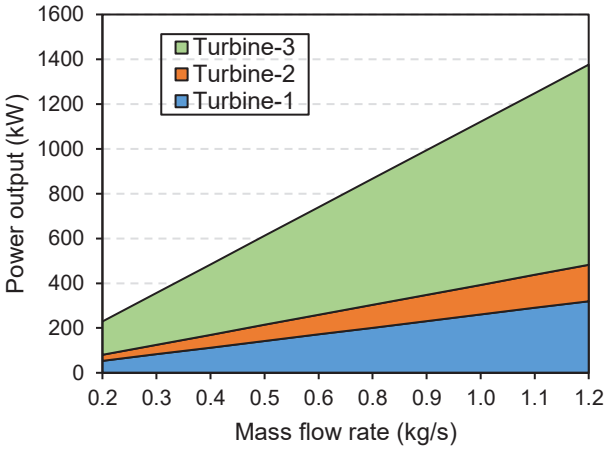

Fig. 6: Power output results of reheat Rankine cycle

5. Conclusions

In the present study, a new integrated ammonia synthesis and fuel cell system is designed for hybrid solar and wind power plants. The system entails a novel type of hybrid thermal energy storage, electrochemical ammonia synthesis and direct ammonia fuel cell subsystem operating with alkaline molten salt. The energetic and exergetic efficiencies of the ammonia synthesis subsystem are found to be 38.2% and 41.1% respectively. Also, the direct ammonia fuel cell entails an energy efficiency of 61.5% and an exergy efficiency of 57.8%. Several parametric studies are also conducted to investigate the effects of varying operating conditions and system parameters on the system performance.

Nomenclature

A	area (m^2)
ex	specific exergy (kJ/kg)
F	Faradays constant
G	Gibbs free energy (J)
h	specific enthalpy (kJ/kg)
J	current density (A/m^2)
LHV	lower heating value (kJ)
$\dot{m}$	mass flow rate (kg/s)
P	Pressure (kPa)
PEM	proton exchange membrane
s	specific entropy (kJ/kgK)
T	temperature (°C)
V	voltage (V)
$\dot{W}$	work rate (kW)

Greek letters

η	efficiency

Subscripts

a	anode, aerosols
act	activation
d	destroyed
en	energy
ex	exergy
ov	overall
P	pump
PEM	proton exchange membrane

References

Chen, C., Liu, Y., Aryafar, H., Wen, T., Lavine, A.S., 2019. Performance of conical ammonia dissociation reactors for solar thermochemical energy storage. App. Energy 255, 113785.

Giddey, S., Badwal, S.P.S., Munnings, C., Dolan, M., 2017. Ammonia as a Renewable Energy Transportation Media. ACS Sust. Chem. Eng. 5, 10231-10239.

Zhou, M., Wang, Y., Chu, Y., Tang, Y., Tian, K., Zheng, S., Chen, J., Wang, Z., 2019. Ammonia as an environmentally benign energy carrier. Energy Procedia 58, 4986-4991.

Performance investigation of the reactor cascading effect on ammonia synthesis

[1]Haris Ishaq and [1,2]Ibrahim Dincer
[1]Clean Energy Research Laboratory, Faculty of Engineering and Applied Science, University of Ontario Institute of Technology
2000 Simcoe Street North, Oshawa, Ontario L1H 7K4, Canada
[2]Yildiz Technical University, Faculty of Mechanical Engineering, Istanbul, 34349 Turkey
Emails: haris.ishaq@uoit.net, Ibrahim.Dincer@uoit.ca

Abstract
This study develops the concept of cascaded ammonia synthesis and investigates the three different configurations of ammonia synthesis including single-stage, double-stage and triple stage cascaded systems. The concept of using multiple cascaded reactors in series is investigated in this study which can eliminate the cost of reheat and repressurizing the unreacted gases to recycle back in the synthesis reactor and to reduce the number of recycle loops. All three proposed configurations are simulated using Industrial software Aspen Plus V11. The results revealed that the exergetic and energetic efficiencies increase with the reactors cascading ammonia synthesis. The exergetic and energetic efficiencies for the single-stage configuration are found to be 20.2% and 18.6%, for double-stage configuration, 35.35% and 32.6% and for triple-stage configuration, 46.71% and 43.09% respectively. Furthermore, the sensitivity results are presented and discussed.

Keywords: Cascaded reactors, ammonia synthesis, energy, exergy, efficiency

1. Introduction

Ammonia synthesis plays a vital role in the development of chemical industry. The leading sector for natural gas consumption is industry as Haber Bosch process uses natural gas reforming for hydrogen production and finally ammonia synthesis (Leigh, 2004). This Haber Bosch is energy-intensive process which consumes 1-2% of global energy every year (Erisman, Sutton, Galloway, Klimont, & Winiwarter, 2008). Haber bosch process is carried out at very high temperature 350-400 ℃ and 150-250 bar and traditional iron oxide catalysts yield the fractional conversion of 20-30% which grasps the attraction of more appealing solutions to achieve higher fractional conversion. The unreacted gases are separated from ammonia, reheat, repressurized and recycled back to the synthesis reactor. The researchers and scientists are looking toward the transition of traditional energy systems with renewable energy based system (Uyar and Beşikci, 2017). The present ammonia synthesis system can be converted to the clean and environmentally benign process by switching the hydrogen production process with a sustainable energy system. This study proposes a unique approach of cascading ammonia synthesis reactors to achieve high fractional conversions. This process may increase the cost of additional reactor by it can cut down the cost of repressurizing and reheating the unreacted gases. This study develops three different configurations of ammonia synthesis system and explores their performances and efficiencies.

A unique approach of cascading ammonia synthesis reactors to achieve high fractional conversions is proposed in this study. This process may increase the cost of additional reactor by it can cut down the cost of repressurizing and reheating the unreacted gases. It can also eliminate the number of recycle stages. Three different configurations including single-stage, double-stage and triple stage for ammonia synthesis are developed in this study and results obtained from the simulation study are presented and discussed.

2. System Description

This study presents three different configurations of ammonia synthesis using cascading reactors including single-stage, double-stage and triple stage approaches. All three proposed configurations are simulated using industrial software Aspen Plus V11. Figure 1 displays the schematic layout of the proposed configuration while Figure 2 shows the Aspen Plus simulation flowsheet.In the single-stage ammonia synthesis system with reference to Fig.2, compressor C1A compresses nitrogen at 150 bar while compressor C1C compresses input hydrogen at the same operating pressure. The valves C1B and C1D are installed to resist the pressure drop and backflows. The mixer C1E mixes the input nitrogen and hydrogen and feeds them to the synthesis reactor C1F. The synthesis reactor is operating at 150 bar and 350 ℃. The synthesized ammonia is separated from the unreacted gases through separator C1G.

In the triple-stage ammonia synthesis configuration, compressor C3A compresses nitrogen at 150 bar while compressor C3C compresses input hydrogen at the same operating pressure. The valves C3B and C3D are installed to resist the pressure drop and backflows. The mixer C3E mixes the input nitrogen and hydrogen and feeds them to the synthesis reactor C3F. The output of the first synthesis reactor passes through the separator C2G which separates formed ammonia to maintain the partial pressure and feeds the unreacted gases to the second synthesis reactor C3H. In the same way, the output of the second synthesis reactor passes through the separator C3I and reaches to the third synthesis reactor C3J. The slight pressure drop which can be caused by the partial pressure of ammonia in the inlet feed of the next reactor is eliminated by separating ammonia from the unreacted gases before entering the next cascaded reactor. Synthesis reactors are operating at 150 bar and 350 ℃. The synthesized ammonia is separated from the unreacted gases through separator C3K. The following reaction takes place during ammonia synthesis with $N_2 + 3H_2 \rightarrow 2NH_3$.

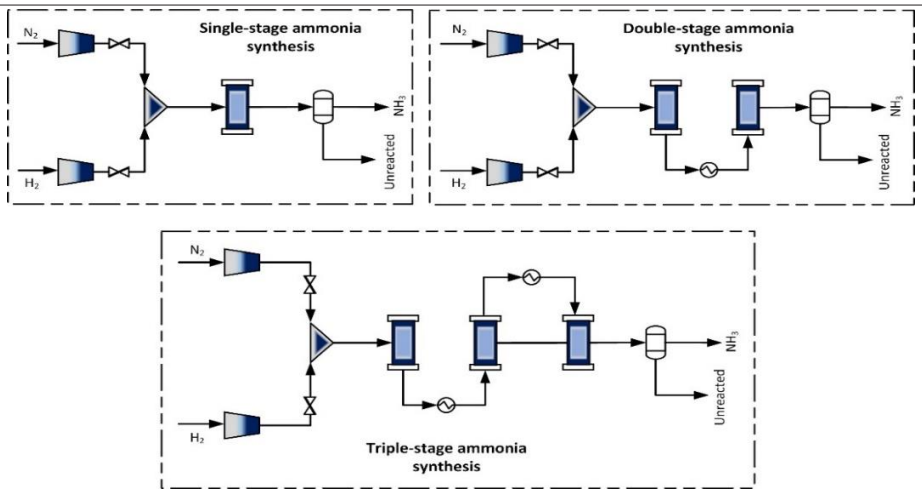

Fig. 1: Schematic diagram of the three proposed configurations

3. Analysis

The proposed configurations are simulated and analysed using thermodynamic approach. The proposed configurations are simulated using industrial software Aspen Plus V11 under the property method of PENG-ROB. Numerous parametric studies are conducted to explore the system performance. This section describes the thermodynamic equations used for each significant component of the proposed configuration. The general equations followed during the analysis are as follows:

$$\dot{Q}_i + \dot{W}_i + \sum_i \dot{m}_i \left(h_i + \frac{V_i^2}{2} + gZ_i\right) = \dot{Q}_e + \dot{W}_e + \sum_e \dot{m}_e \left(h_e + \frac{V_e^2}{2} + gZ_e\right) \quad (1)$$

$$\sum_i \dot{m}_i ex_i + \dot{Q}_i \left(1 - \frac{T_0}{T}\right) + \dot{W}_i = \sum_e \dot{m}_e ex_e + \dot{W}_e + \dot{Q}_e \left(1 - \frac{T_0}{T}\right) + \dot{E}x_{dest} \quad (2)$$

Both physical and chemical exergies and enthalpy of formations are calculated during the system analysis. The thermodynamic equations of significant components such as nitrogen and hydrogen compressor, mixer, synthesis reactor and separator are described with the reference of single-stage ammonia synthesis system in Fig.2.

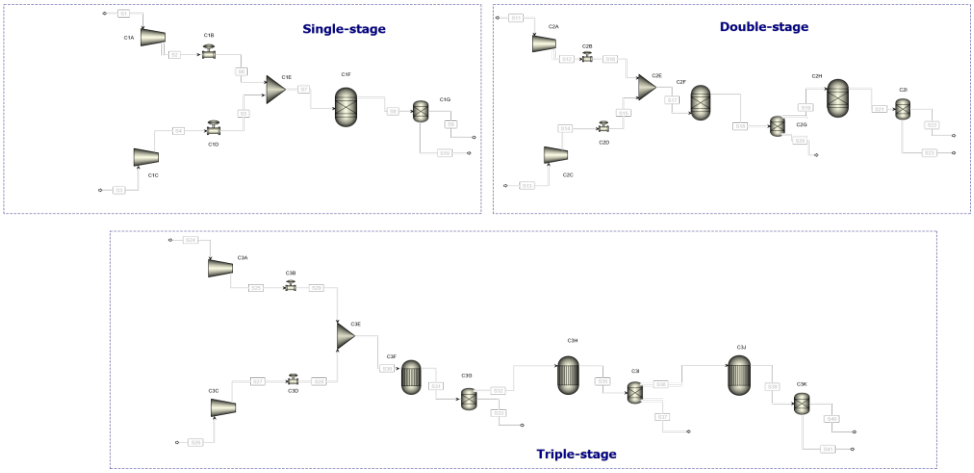

Fig. 2: Aspen plus flowsheet of the three proposed configurations for ammonia synthesis

Compressor

$$\dot{m}_{S1} h_{S1} + \dot{W}_{comp} = \dot{m}_{S2} h_{S2} \quad (3)$$

$$\dot{m}_{S1} ex_{S1} + \dot{W}_{comp} = \dot{m}_{S2} ex_{S2} + \dot{E}x_{dest} \quad (4)$$

Mixer

$$\dot{m}_{S5} h_{S5} + \dot{m}_{S6} h_{S6} = \dot{m}_{S7} h_{S7} \quad (5)$$

$$\dot{m}_{S5} ex_{S5} + \dot{m}_{S6} ex_{S6} = \dot{m}_{S7} ex_{S7} + \dot{E}x_{dest} \quad (6)$$

Synthesis reactor

$$\dot{m}_{S5} h_{S5} + \dot{m}_{S6} h_{S6} = \dot{m}_{S8} h_{S8} + \dot{Q}_{out} \quad (7)$$

$$\dot{m}_{S5} ex_{S5} + \dot{m}_{S6} ex_{S6} = \dot{m}_{S8} ex_{S8} + \dot{Q}_{out} \left(1 - \frac{T_0}{T}\right) + \dot{E}x_{dest} \quad (8)$$

Separator

$$\dot{m}_{S8} h_{S8} = \dot{m}_{S9} h_{S9} + \dot{m}_{S10} h_{S10} \quad (9)$$

$$\dot{m}_{S8} ex_{S8} = \dot{m}_{S9} ex_{S9} + \dot{m}_{S10} ex_{S10} + \dot{E}x_{dest} \quad (10)$$

The overall exergetic and energetic efficiencies are

$$\eta_{ov} = \frac{\dot{m}_{NH_3} LHV_{NH_3}}{\dot{m}_{N_2} h_{N_2} + \dot{m}_{H_2} LHV_{H_2} + \dot{W}_{comp1} + \dot{W}_{comp2}} \quad (11)$$

$$\psi_{ov} = \frac{\dot{m}_{NH_3} ex_{NH_3}}{\dot{m}_{N_2} ex_{N_2} + \dot{m}_{H_2} ex_{H_2} + \dot{W}_{comp1} + \dot{W}_{comp2}} \quad (12)$$

4. Results and discussion

This system proposes three different configurations of single-stage, double-stage and triple-stage ammonia synthesis. Aspen Plus industrial software is employed to simulate the proposed configurations. Numerous sensitivity analyses and parametric studies have been conducted and discussed on each proposed configuration.

The effect of input flowrates on the ammonia synthesis reactors is significant to be investigated under different operating capacities. Figure 3 displayed the effect of input hydrogen and nitrogen flowrates on ammonia production capacities. The range of nitrogen is taken 0.1 to 1 mol/s and hydrogen range is taken 0.1 to 3 mol/s. The legends are representing the ammonia production capacity increases from 0.1 to 0.5 mol/s at fractional conversion of 0.25. The gradual increase in ammonia production capacity can be depicted from the figure. The effect of input flowrates on the heat rate of ammonia synthesis reactors is significant to be investigated under different operating capacities. Figure 4 shows the effect of input hydrogen and nitrogen flowrates on heat rate of ammonia production reactor. The hydrogen range is taken 0.1 to 3 mol/s and range of nitrogen is taken 0.1 to 1 mol/s. The legends are representing the different levels of heat rate of ammonia production reactor C1F. Ammonia synthesis is an exothermic reaction which releases heat. The heat rate of ammonia synthesis reactor increases from 7.18 to 117.1 kW.

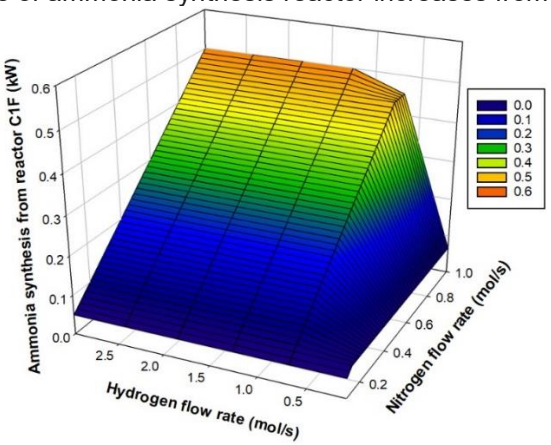

Fig. 3: H_2 and N_2 input flowrates effect on ammonia production capacity of reactor C1F

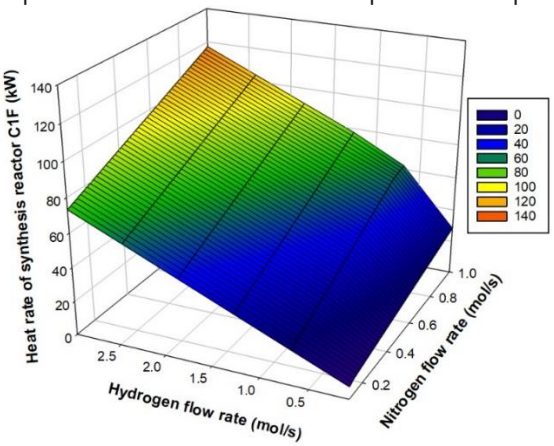

Fig. 4: H_2 and N_2 input flowrates effect on heat rate of NH_3 synthesis reactor C1F

The effect of input flowrates on the heat rate of ammonia synthesis reactor C2H is significant to be investigated under different operating capacities. Figure 5 displays the effect of input hydrogen and nitrogen flowrates on heat rate of ammonia production reactor C2H. The legends are representing the different levels of heat rate of ammonia production reactor C1F. It can be observed that heat rate of the synthesis reactor does not increase in the beginning to meet the heat required to initiate the reaction. The heat rate of ammonia synthesis reactor increases from 0.91 to 26.1 kW. It is important to investigate the effect of input flowrates on the ammonia synthesis from the reactors employed to the double-stage configuration. Figure 6 exhibits the effect of input hydrogen and nitrogen flowrates on ammonia production capacities from the reactors employed to the double-stage configuration. The range of nitrogen is taken 0.1 to 1 mol/s and hydrogen range is taken 0.1 to 3 mol/s. The legends show the ammonia production flowrates from reactors C2F and C2H. It is clear that ammonia production capacity increase with the cascading of second reactor in series. Ammonia production from first reactor C2F increases from 0.05 to 0.5 mol/s and 0.08 to 0.87 mol/s from second reactor C2H. Figure 7 shows the effect of nitrogen input flowrate on ammonia synthesis from triple-stage configuration at different intervals of hydrogen flowrates. The legends represent the respective line at the defined flowrate of hydrogen from 0.36 to 10.8 kmol/h. The range of nitrogen input flowrate taken is 0.36 to 5.4 kmol/h. It is clear that ammonia production flowrate increases with the rise in input flowrates of nitrogen and hydrogen.

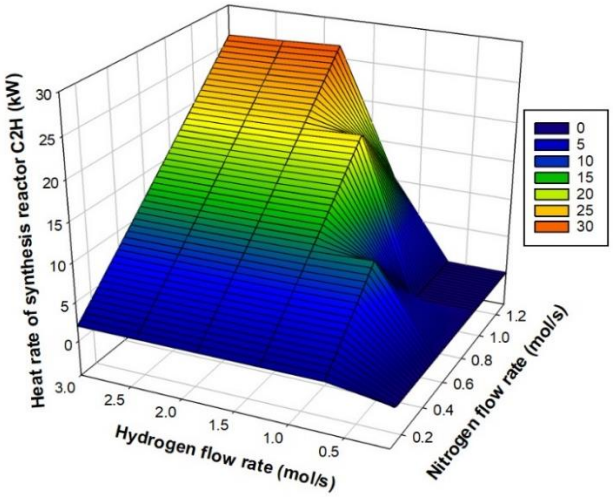

Fig. 5: H_2 and N_2 input flowrates effect on heat rate of NH_3 synthesis reactor C2H

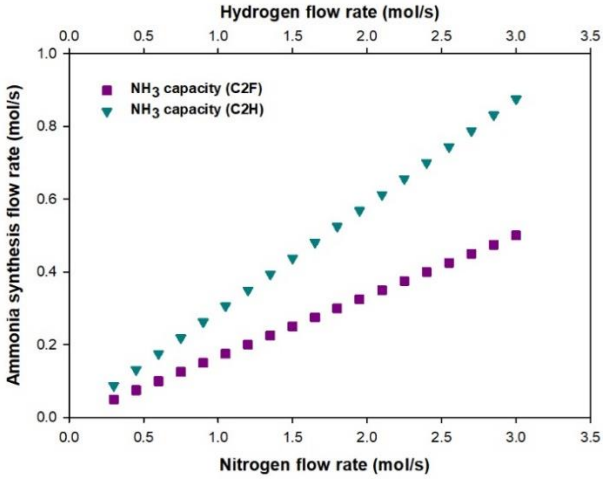

Fig. 6: Effect of H_2 and N_2 input flowrates effect on ammonia production capacity from double-stage configuration

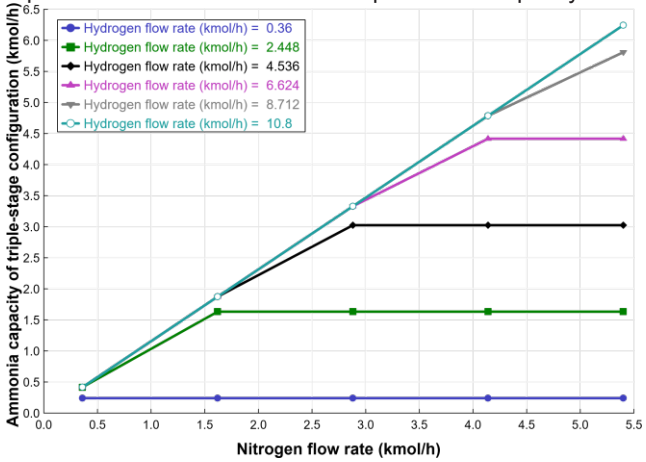

Fig. 7: Effect of H_2 and N_2 input flowrates effect on ammonia production capacity from triple-stage configuration

Figure 7 shows the effect of nitrogen input flowrate on heat rate of ammonia synthesis reactor C3F employed to the triple-stage configuration at different intervals of hydrogen flowrates. The legends represent the respective line at the defined flowrate of hydrogen from 0.36 to 10.8 kmol/h. The range of nitrogen input flowrate taken is 0.36 to 5.4 kmol/h. Figure 8 displays the effect of input hydrogen and nitrogen flowrates on heat rate of ammonia production reactor C3F. It can be clearly stated that heat rate of the reaction increases with the input flowrates as ammonia synthesis increases. The maximum heat rate of 141.59 kW is found at 5.4 kmol/h of nitrogen and 10.8 kmol/h of hydrogen. Table 1 displays the significant outcomes of the designed configurations.

Table 1 Some results of the designed configurations

Parameters	Results	Units
Heat rate of reactor C1F	-117.106	kW
Heat rate of reactor C2F	-126.89	kW
Heat rate of reactor C3H	-19.95	kW

Heat rate of reactor C3F	-141.59	kW
Heat rate of reactor C3H	-30.26	kW
Heat rate of reactor C3J	-23.28	kW
H_3 output flow rate of single-stage system	1.8	kmol/h
NH_3 output flow rate of double-stage system	3.15	kmol/h
NH_3 output flow rate of triple-stage system	4.16	kmol/h
Energy efficiency of single-stage system	18.6	%
Exergy efficiency of single-stage system	20.2	%
Energy efficiency of double-stage system	32.6	%
Exergy efficiency of double-stage system	35.35	%
Energy efficiency of triple-stage system	43.09	%
Exergy efficiency of triple-stage system	46.71	%

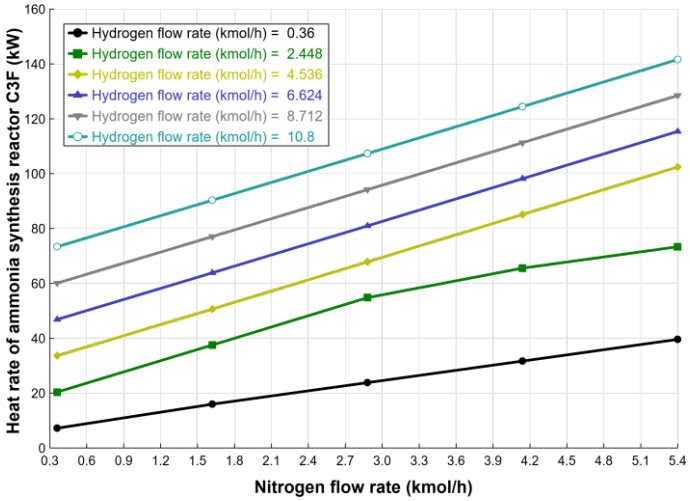

Fig. 8: Effect of H_2 and N_2 input flowrates on heat rate of NH_3 synthesis reactor C3F

5. Conclusions

Three new cascaded configurations for ammonia synthesis including single-stage, double-stage and triple stage cascaded systems are proposed is this study. The concept of using multiple cascaded reactors in series is investigated under different operating conditions and capacities. The reactors cascading can eliminate the cost of reheat and repressurizing the unreacted gases to recycle back in the synthesis reactor and to reduce the number of recycle loops. The results revealed that the exergetic and energetic efficiencies increase with the reactors cascading ammonia synthesis and triple-stage configuration shows the maximum efficiencies of 46.71% and 43.09% respectively. The ammonia production rates from the single-stage, double-stage and triple-stage configurations are found to be 1.8, 3.15 and 4.16 kmol/h respectively.

References

Erisman, J. W., Sutton, M. A., Galloway, J., Klimont, Z., & Winiwarter, W. (2008). How a century of ammonia synthesis changed the world. *Nature Geoscience*, *1*(10), 636–639. https://doi.org/10.1038/ngeo325

Frattini, D., Cinti, G., Bidini, G., Desideri, U., Cioffi, R., & Jannelli, E. (2016). A system approach in energy evaluation of different renewable energies sources integration in ammonia production plants. *Renewable Energy*, *99*, 472–482. https://doi.org/10.1016/J.RENENE.2016.07.040

Lan, R., Irvine, J. T. S., & Tao, S. (2013). Synthesis of ammonia directly from air and water at ambient temperature and pressure. *Scientific Reports*, *3*. https://doi.org/10.1038/srep01145

Leigh, G. J. (2004). Haber-Bosch and Other Industrial Processes. In *Springer*. https://doi.org/10.1007/978-1-4020-3611-8_2

Marnellos, G., & Stoukides, M. (1998). Ammonia synthesis at atmospheric pressure. *Science*, *282*(5386), 98–100. https://doi.org/10.1126/science.282.5386.98

Uyar, T. S., & Beşikci, D. (2017). Integration of hydrogen energy systems into renewable energy systems for better design of 100% renewable energy communities. *International Journal of Hydrogen Energy*, *42*(4), 2453–2456.

Revisit of Modeling Techniques for Foam Flow in Porous Media

[1] Mirna MAKLAD, [1] Lei DING, [1*] Dominique GUERILLOT
[1] Texas A&M University at Qatar, Department of Petroleum Engineering, Doha, PO Box 23874, Qatar

* E-mails: mirna.maklad@qatar.tamu.edu

Abstract

There are generally two approaches for modeling foam in porous media, namely, the texture implicit local equilibrium (LE) foam model and texture explicit population balance (PB) mode. Both models need to solve the mass conservation equation and the momentum conservaton equation.

The LE model uses an empirical algebraic formula to correlate the gas mobility reduction with certain local conditions, such as surfactant concentration, water saturation, shear-rate, and oil saturation. Contrastively, the PB model correlates the gas mobility reduction with foam texture, i.e., the number of bubbles per unit pore volume, which is calculated dynamically with exact functions of lamellae generation and destruction. The physics behind PB foam model is clearer. Thus, the PB model is capable to capture the foam entrance effect and transient foam behavio. However, it needs to solve an additional partial differential equation (PDE) for foam texture, which makes the PB model more complex and computationally costly than the LE model. Another restriction for the application of PB model is the difficulty for determining a number of kinetic parameters in foam generation and destruction terms. Although both models could be used at lab scale and reservoir scale in principle, only the LE model is considered practically at reservoir scale. The most widely used LE foam model is the STARS™ foam model developed by Computer Modeling Group (CMG).

In this abstract, both models are revistited and a short review of the capacities of the commercial reservoir simulator is given.

Keywords: Foam, Local Equilibrium, Population Balance, Numerical Simulation

Introduction

There are generally two approaches for modeling foam in porous media, namely, the texture implicit local equilibrium (LE) foam model and texture explicit population balance (PB) model (Rossen, 1996; Ma, 2016). Both models need to solve the mass conservation equation for various components and the momentum conservaton equation for different phases (Darcy's law) (Kovscek, 1994). The LE model uses an empirical algebraic formula to correlate the gas mobility reduction with certain local conditions, such as surfactant concentration, water saturation, shear-rate, and oil saturation (Farajzadeh, 2015). Contrastively, the PB model dynamically calculates the foam texture, i.e., the number of bubbles in unit pore volume, with exact expressions to descibe lamellae generation and destruction (Chen, 2010).

The physics behind PB foam model is clearer. Thus, the PB model is capable to capture the foam entrance effect and transient foam behavior (Ma, 2016). However, it needs to solve an additional partial differential equation (PDE) for foam texture, which makes the PB model more complex and computationally costly than the LE model. Another restriction for the application of PB model is the difficulty for determining a number of kinetic parameters in foam generation and destruction terms. Although both models could be used at lab scale and reservoir scale in principle, only the LE model is considered practically at reservoir scale (Zeng, 2016).

In this abstract, both models are revistited and a short review of the capacities of the commercial reservoir simulator is given.

Conservation of Mass

Based on mass balance over a representative elementary volume, conservation equation (Eq. 1) of species *i* (can be surfactant, water or gas) is:

$$\frac{\partial W_i}{\partial t} + \vec{\nabla} \cdot \vec{N}_i = R_i \qquad \text{Eq. 1}$$

- Where W_i is the overall concentration of i in units of mass of i per unit bulk volume (Eq. 2).

$$W_i = \emptyset \sum_{j=1}^{N_p} \rho_j S_j w_{ij} + (1-\emptyset)\rho_s w_{is} \quad \text{Eq. 2}$$

- $\vec{N}_i$ is the flux of species i (Eq. 3).

$$\vec{N}_i = \sum_{j=1}^{N_p} [\rho_j \vec{u}_j w_{ij} - \emptyset S_j \vec{\vec{D}}_{ij} \cdot \vec{\nabla}(\rho_j w_{ij})] \quad \text{Eq. 3}$$

Then, the conservation equation (Eq. 4) of species i is:

$$\frac{\partial}{\partial t}\left[\emptyset \sum_{j=1}^{N_p} \rho_j S_j w_{ij} + (1-\emptyset)\rho_s w_{is}\right] + \vec{\nabla} \cdot \left\{\sum_{j=1}^{N_p} [\rho_j \vec{u}_j w_{ij} - \emptyset S_j \vec{\vec{D}}_{ij} \cdot \vec{\nabla}(\rho_j w_{ij})]\right\} = 0 \quad \text{Eq. 4}$$

where $\emptyset$ is the porosity, ρ is the density, S is saturation, w is the mass concentration of component i in phase j, $\vec{\vec{D}}$ is the dispersion coefficient. The subscript i denotes component i, j denotes phase j, and s denotes solid phase.

Conservation of Momentum

For incompressible and creeping flow, the conservation of momentum can be described by Darcy's law after neglecting the inertial terms (Eq. 5):

$$\vec{u}_j = -\frac{\vec{\vec{K}} k_{rj}}{\mu_j} \vec{\nabla} \Phi_j \quad \text{Eq. 5}$$

where $\vec{u}_j$, μ_j, Φ_j and k_{rj} are the superficial velocity, dynamic viscosity, flow potential and relative permeability of phase j, respectively.

Foam Flow in Porous Media

As discussed in the previous sections, foam can largely reduce the mobility of gas in two aspects: one is to decrease the gas relative permeability and the other is to increase the gas apparent viscosity. Due to the fact that the relative permeability and viscosity are always being together in the flow equations, one may only modify one of the two aforementioned equations. The texture-explicit population balance (PB) model correlates gas mobility reduction with foam texture, while the texture-implicit local equilibrium (LE) model take gas mobility reduction as a function of several local conditions of interest.

Texture-Explicit Population-Balance (PB) Foam Model

Because the reduction in gas mobility rely heavily on foam texture (n_f), typically, the PB model commits to quantify the bubble density and correlate it to gas mobility. A general form of bubble population balance equation is as following (Eq. 6):

$$\frac{\partial}{\partial t}[\emptyset(S_{g,f} n_f + S_{g,t} n_t)] + \vec{\nabla} \cdot (\vec{u}_{g,f} n_f) = \emptyset S_g (r_g - r_c) + Q_b \quad \text{Eq. 6}$$

Where $S_{g,f}$ is the flowing gas saturation, $S_{g,t}$ is the trapped gas saturation, n_f is the foam texture in the flowing gas, n_t is the foam texture in trapped gas, $\vec{u}_{g,f}$ is the flux of flowing gas, S_g is the gas saturation ($S_g = S_{g,f} + S_{g,t}$), r_g and r_c are the lamellae generation rate and lamellae coalescence rate, respectively, expressing in per unit volume of gas, Q_b is the source or sink term. The population balance model is sometimes called full physics model, and r_g as well as r_c may have different expressions.

Texture-Implicit Local Equilibrium (LE) Foam Model

Though there is no explicit foam generation and coalescence function, but the physics of foam behavior in porous media is reported to be equally honored in the LE model (Lotfollahi, 2016; Gassara, 2017). The most widely used LE foam model is the STARS™ foam model developed by Computer Modeling Group (CMG).

In this model, the gas relative permeability in the presence of foam is calculated by multiplying a dimensionless interpolated factor (FM) with the gas relative permeability in the absence of foam (Eq. 7 and 8). FM can be calculated as a function of different variables, e.g., salinity, oil saturation, surfactant concentration, water saturation and capillary number, etc. A detailed description of these effects can be found in Figure 1.

$$k_{rg}^{f} = k_{rg}^{nf} * FM \quad \text{Eq. 7}$$

$$FM = (1 + Fmmob * F_1 * F_2 * F_3 * F_4 * F_5 * F_6 * F_7 * F_{dry})^{-1} \quad \text{Eq. 8}$$

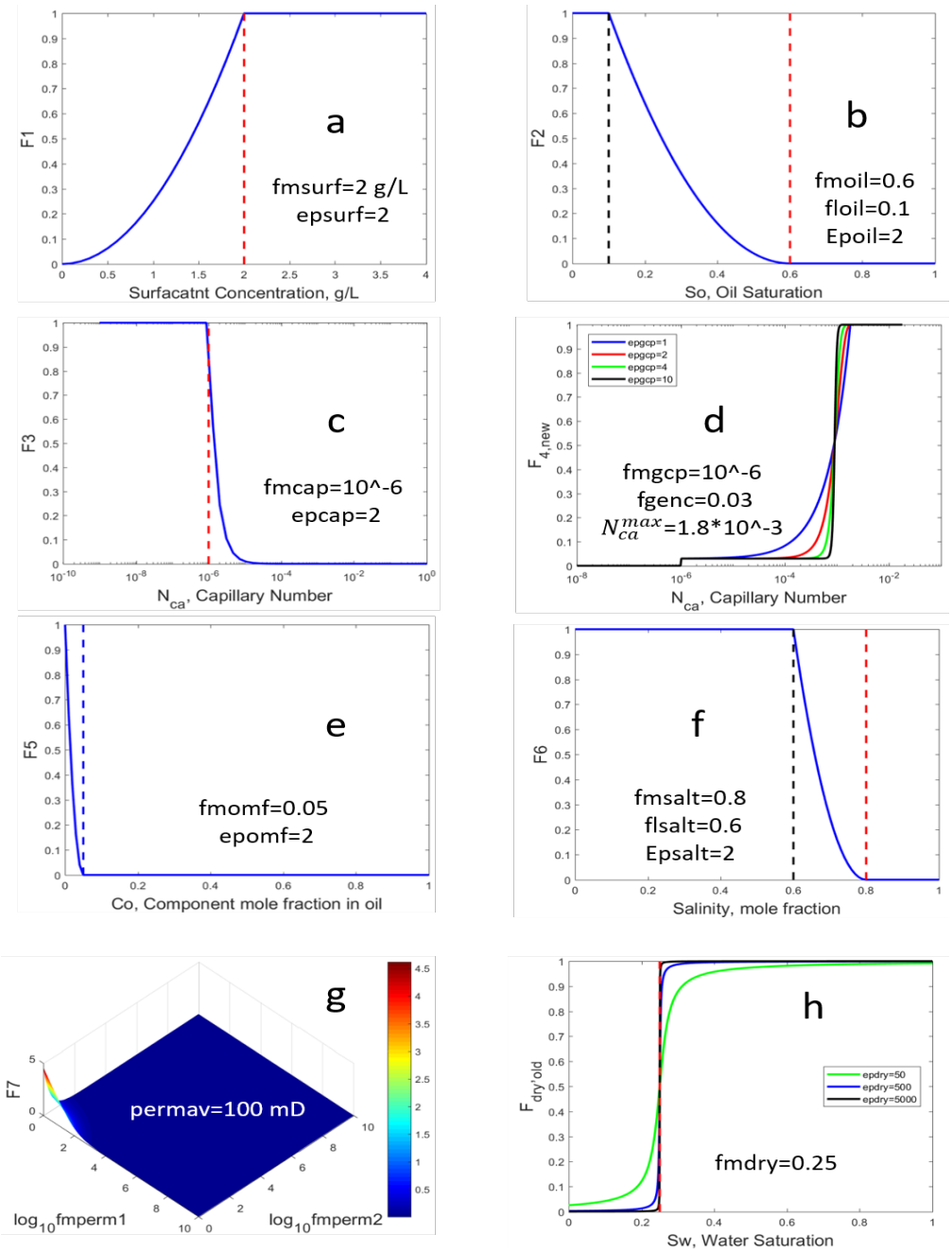

Figure 1. F_1-F_{dry} in CMG STARS

(a). F_1 as a function of surfactant concentration; (b). F_2 as a function of oil saturation; (c). F_3 as a function of capillary number; (d). F_4 as a function of capillary number; (e). F_5 as a function of oil composition; (f). F_6 as a function of salinity; (g). F_7 as a function of fmperm1 and fmperm2; (h). F_{dry} as a function of water saturation

The LE model embedded in ECLIPSE (in both ECLIPSE 100 and ECLIPSE 300 modules in the 2016 version) is similar to STARS foam model in CMG with modified function on surfactant concentration (F_s), oil saturation (F_o),

capillary number (F_c) and dry-out effect (F_w). There is also a tabulated model (E100 Tab model) describing the decay of foam as a function of water and oil saturation based on the table values inputted, which is mechanistically a PB model.

Conclusions

Different foam models, i.e., PB models and LE models, have been reviewed.

Acknowledgements

Financial supports from the startup funding from Texas A&M University at Qatar is greatly acknowledged.

References

Chen, Q. K. (2010). Modeling foam displacement with the local-equilibrium approximation: theory and experimental verification. SPE Journal, 171-183.
Farajzadeh, R. L. (2015). Effect of permeability on implicit-texture foam model parameters and the limiting capillary pressure. Energy & fuels, 3011-3018.
Kovscek, A. R. (1994). Fundamentals of Foam Transport in Porous Media. In S. L.L., Foams: Fundamentals and Applications in the Petroleum Industry (pp. 115-163). ACS.
Ma, K. R. (2015). Modeling techniques for foam flow in porous media. SPEJ, 453-470.
Rossen, W. (1996). Foams in enhanced oil recovery. In R. Prud'homme, Foams: Theory, Measurements and Applications (pp. 413-464). New York.
Zeng, Y. M.-B. (2016). Insights on foam transport from a texture-implicit local-equilibrium model with an improved parameter estimation algorithm. Industrial & Engineering Chemistry Research, 7819-7829.

RELIABILITY ANALYSIS OF V-TROUGH SOLAR AIR HEATER (VTSAH) WITH THERMAL STORAGE USING HOURLY AVERAGE SOLAR INSOLATION (HASI) DATA

[1*]Sunil Raj B A, [2]M.Eswaramoorthy
[1] [1]Department of Mechanical Engineering, ACS College of Engineering, Bengaluru-560074, Karnataka, India
[2] School of Mechanical Engineering, Sri Matha Vaishno Devi University, Katra, J&K, India

E-mail: [1]sunilaswath@gmail.com, [2] rmeswar@yahoo.com

Abstract
The present investigation is performed by using Hourly Average Solar Insolation (HASI) data and standard deviation to study the reliability performance of V-Trough Solar Air Heater (VTSAH) over a year by using Monte Carlo simulation (MCS) technique with help of MATLAB package. This paper is organized as two sections; the first section deals the various solar insolation prediction models along with hourly average solar insolation (HASI) method are compared. The comparison is carried on the basis of predicted hot air generation by solar air heater. Estimation of heated air using HASI method is close to the actual heated air generated by solar air heater. The deviation in monsoon month is due to the cloud cover. In later part of the paper various reliability indices are obtained by HASI method using MCS technique. Reliability indices, auxiliary energy hours (AEH) and auxiliary thermal energy (ATE) reduce exponentially with increase in load indicates that a solar air heater with thermal storage system, source will offset maximum fuel when all of its generated energy is utilized. Fuel saving calculation is also investigated. Case studies are presented for ACS College of Engineering in Bangalore, Karnataka State, India.

I. Introduction

The Solar radiant energy is carbon free source among different renewable resources; the uncertainty on solar energy availability causes reliability of standalone system. Energy storage system incorporation is notable options to meet energy needs at non availability of solar insolation. The factors responsible for thermal energy storage dependence availability of solar insolation, type of the load, component cost used in the process. Solar air heater has a potential for low temperature of agricultural drying applications and the suitable key to save the fossil fuels and minimize the carbon emission during drying process. The majority of fruits and agricultural vegetables contain more than 75% of liquid (water) and therefore they are highly consumable. The solar air heater with thermal storage system is used to avoid the spoilage of the fruits, vegetables and agricultural produces. The solar drying system is divided as natural air circulation *i.e.* free convection and forced convection solar air heater. The VTSAH systems helps to enhance the availability of solar insolation input with addition of V trough reflector on conventional solar air heater with storage; it is subjected to various failure modes, the performance reduction on VTSAH is due to leakage between the flow pipe joints, blower failure, controller failure, dust on glazing surface etc., The forced convection based solar air heater significantly increases the thermal efficiency and increases the operating cost. The performance of solar wind system is used to forecast the nature which depends on availability of wind, solar and load data which is illustrated by Nehru *et al.* (2000). Billiton and Kari (2001) presented the reliability assessment on corresponding solar air heater economic analysis. Many researchers attempted on reliability analysis on different solar thermal systems. Bagmen and Billiton (2005) extended usual chronological series method to find the reliability performance of solar power system. Billiton and Bagmen, (2006) studied the reliability of small integrated thermally heat generating system. Kekezoglu and Arikan (2013) studied the reliability analysis on a hybrid system with the series of PV panel integrated system. Setien, M. Frasquet (2015) carried out reliability analysis of Tower with dual receiver system (solar and gas) mathematical model developed which conclude that the design life of the system will be up to 30 years. Hassan Bin Nasir (2017) performed the techno-economic evaluation has been carried out for solar air heater (SAH) with dimple shaped protrusions to make energy and economics efficient SAH.

The ASHRAE model is suitable for of Indian location and used to estimate the solar insolation data. India is geographically located in latitude from 7° N to 37° N and collects an annual average solar insolation from 16,710 kJ/m^2/day to 29,265 kJ/m^2/day. The reliability of a solar air heater is an important economical aspect related to increased useful life and therefore demonstrate better contest in the marketplace. Numerous studies evaluated on the reliability analysis of different solar thermal product under dissimilar environmental circumstances. As the reliability increases the useful life of the product also increases therefore it exhibit better competition in the market. The research literature review on the reliability analysis of various solar thermal systems makes an evident that there is certainly a need of study on estimating reliability and life time of solar thermal systems. In recent year numerous reliability studies on solar thermal system were carried out from the available source of information. It is the first time; the reliability of VTSAH is carried out based on hourly average solar insolation technique over a period of year. The objective is to evaluate the reliability of VTSAH with thermal energy storage system. The suggested system consists of two major parts V-trough reflector and a flat absorber plate. The primary task of the V trough reflector is to capture the incident solar insolation. Additionally, the flat absorber plate is responsible to take up solar radiant energy and transfer heat into the working fluid with a minimum temperature difference. The study will proceed by calculating the temperature using a thermal modeling and indicates the thermal behavior. The site located in Kengeri which is in southern part of Bangalore, Karnataka, India and geographically located at 12.9°N 77.48°E having the elevation of 826 meters.

II. Experimental Setup

The VTSAH are systems that collect radiant energy emitted by the sun and stored it, translate the heat to moving air in flow channel for space heating. The absorber plates are often black to absorb more of the sun's radiant energy, often metal acts as a heat exchange with flowing air. There are many different designs and systems that may include blower to increase the speed of flowing air. The VTSAH with latent heat storage is as shown in Fig. 1; the solar heater air is used more effectively for drying under manageable conditions. The V trough solar air heater is developed to use paraffin wax as PCM (stored in the back side of absorber plate in metal container) to enhance its productivity. The excess energy is stored in the PCM energy storage container, this process continuous throughout the night by using the additional thermal energy stored in the paraffin wax material during day time. The Table 1 shows the detailed specification of VTSAH.

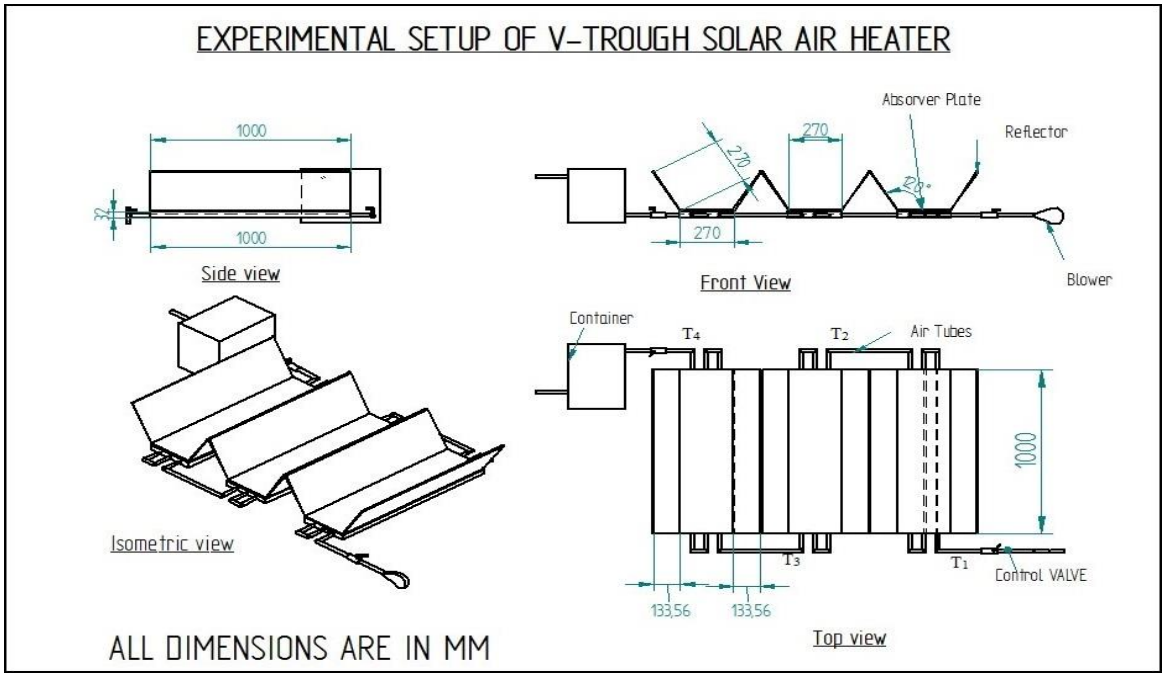

Fig1: Experimental Setup of VTSAH

Tabel 1 : Specification of VTSAH

Set up	Values
The numberof mirror in V-trough reflector	2
Mirror Dimensions	Width of 0.27 × Length of 1 m × thickness of 0.005 m
Area of Reflectivty	0.54 m^2
Mirror Reflectivity	0.9 (or 90%)
Mirror Inclined angle	60
Absorber Plate Dimensions	0.27 m(width) × 1m(length)0.001m (thick)
Orientation of VTSAH	Along East-West direction
Latitude of the site	12.96 North
Longitude of the site	77.63 East
Standard time zone meridian	120 East
PCM duct dimension	0.27 m(width) × 1 m(Length) × 0.025 m(thick)
The total weight of PCM is used for set up	5 Kg
Air Blower	1

III. Evaluation Model

The heat output obtained from a VTSAH depends on the operating parameters like availability of radiant energy from the sun, incident solar insolation angle, atmospheric temperature, reflectance and its design parameter. The reliability analysis on VTSAH involves three stages; solar insolation data modeling, VTSAH energy conversion and VTSAH reliability modeling.

a. Solar insolation Data Modeling

The radiant energy from the sun which is falling on a collector surface is a composition of direct beam insolation, diffused insolation and reflected insolation. The assessment of monthly average daily solar insolation on clear day is given by modified Angstrom regression equation, which is given by Eq. (1), Eq.(2) – Eq.(4) for the known latitude and longitude of location (Sukhatme, 2004)

$$\frac{\bar{H}_g}{\bar{H}_a} = a + b\left(\frac{\bar{S}}{\bar{S}_{\max}}\right) \quad (1)$$

$$\frac{\bar{I}_g}{\bar{I}_a} = \frac{\bar{H}_g}{\bar{H}_a}(a_1 + b_1 \cos\omega) \quad (2)$$

$$I_g = I_{bn} \operatorname{Cos}\theta_z + I_d \quad (3)$$

$$I_T = I_b r_b + I_d r_d + (I_b + I_d) r_r \quad (4)$$

According to ASHRAE model, it is recommended that

$$I_{bm} = A \exp\left[-B / \cos\theta_z\right] \quad (5)$$

$$I_d = C I_{bn} \quad (6)$$

The site steady factor a, b is given by, $a = 0.4091 + 0.5017 \sin(\omega_s - 60°)$' $b = 0.6610 - 0.4768 \sin(\omega_s - 60°)$, the steady factor A is meant for apparent solar insolation in (W/m^2), the steady factor *B* is meant for atmospheric extinction coefficient which were determined on the monthly basis.

Table 2:
Constant values of A, B, C of Indian cities for predicting hourly solar insolation (Sukhatme, 2004)

Sl. No.	Day	A (W/m^2)	B	C
1	21st Jan	707	0	0.193
2	21st Feb	731.2	0.012	0.210
3	21st Mar	766.86	0.0506	0.230
4	21st Apr	712.35	0.132	0.386
5	21st May	797.39	0.16	0.26
6	21st June	441.71	0.397	1.109
7	21st July	223.87	0.172	1.722
8	21st Aug	241.8	0.149	1.623
9	21st Sept	395.21	0.075	0.749
10	21st Oct	644.73	0.025	0.257
11	21st Nov	665.6	0.009	0.212
12	21st Dec	693.52	0	0.192

$p = m - 3.5$ for $m = 6$
$p = m - 9.5$ for $m > 6$ (7)

For Medium Rain (MR)

$$\left.\begin{aligned} \lambda_b &= 0.8885 - 0.0545p + 0.0035p^2 + 0.0073p^3 && m \le 6 \\ \lambda_d &= 1.0460 - 0.0629p + 0.0078p^2 + 0.0045p^3 && m \le 6 \\ \lambda_b &= 0.9319 - 0.2928p + 0.0298p^2 + 0.0319p^3 && m > 6 \\ \lambda_d &= 1.0664 + 0.0949p + 0.0178p^2 + 0.0038p^3 && m > 6 \end{aligned}\right\} \quad (8)$$

The equation for suitable time correction factor of beam and diffused insolation are as shown below:

$q = LAT - 12$ (9)

$$\left.\begin{aligned} \mu_b &= 1.0043 + 0.0694q - 0.0091q^2 - 0.0009q^3 \\ \mu_d &= 1.233 + 0.0243q - 0.0288q^2 - 0.0002q^3 \end{aligned}\right\} \quad (10)$$

$I_{bhc} = I_b \times \lambda_b \times \mu_b$ (11)

$I_{dhc} = I_d \times \lambda_d \times \mu_d$ (12)

$I = I_{bhc} + I_{dhc}$ (13)

The beam and diffused insolation on hourly basis is computed from January to December month individually by applying Equation (1) to Equation (13).

The input data consists of hourly average solar insolation (HASI), standard deviation, monthly maximum and minimum hourly values of the month, the total bright sun shine hour. The random hourly solar insolation is given by Eq. (14). The solar insolation output for 365 days is obtained, Fig. 2 shows the step by step procedure involved in HASI technique.

$$(G_h)_{rnd} = normrnd(G_h)_{mean}, std) \quad (14)$$

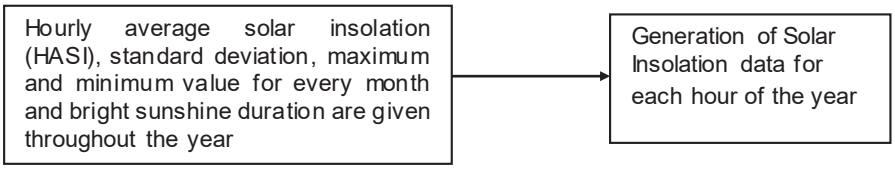

Fig 2. Fundamental steps of HASI Method

b. VTSAH thermal energy conversion

The energy obtained from the VTSAH is given by

$$E = SIF \times CA \times \eta_c \quad (15)$$

The important factor that pointing out the energy obtained from VTSAH are (i) The conversion efficiency of VTSAH system (ii) insolation intensity and (iii) thermal storage system temperature. Thermal efficiency of VTSAH system means the thermal output energy of SAH per unit solar insolation falling on VTSAH. Thermal efficiency of VTSAH system is depending on solar insolation and operating temperature of collector. The increase in temperature above the value of cited temperature which leads to decrease in the thermal storage system output.

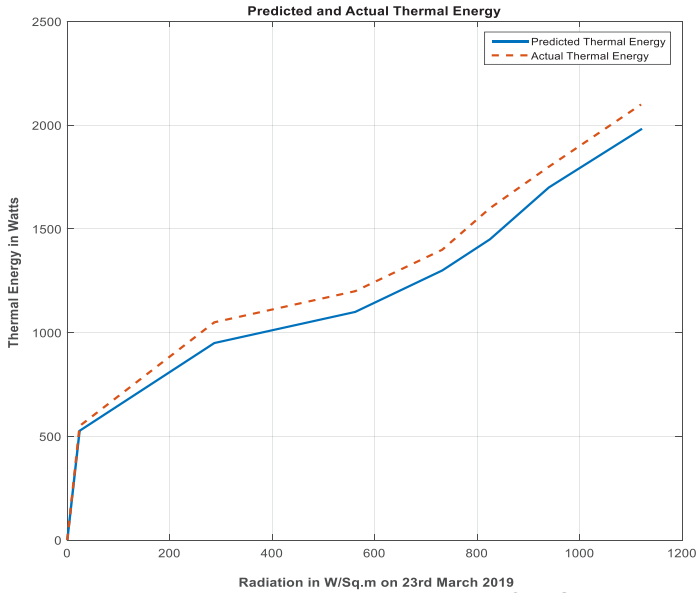

Fig 3: Actual and predicted energy of VTSAH

The thermal effectiveness of VTSAH system improves with the increase in solar insolation intensity. Fig 3 shows the typical energy curve of VTSAH system, for distinct insolation brings out notable rise in the thermal efficiency of VTSAH, solely. After a few insolation points is known as knee point, further improvement in insolation produces a relatively small increase in the energy (Patel, 2006; Cha et al., 2004).

$$E = -0.0622.(G_h)^2 + 36.5073.(G_h) + 351.29 \qquad 0 < G_h < 287$$

$$= (0.002 - (G_h) + 4.8821)10 \qquad 288 < G_h < 1000 \quad (16)$$

The predicted energy from VTSAH is calculated by using Eq. (16). The actual and predicted graph was plotted for 02 kWh solar air heater array. The graphical representation is as shown by taking solar insulation of 287W/m^2 as a knee point. The available knee point value is explained by empirical relationship (Moharil and Kulkarni, 2009). The thermal energy obtained by VTSAH arrangement is explained by:

$$E_d = E\eta_i\eta_b \quad (17)$$

c. VTSAH Reliability modeling

The VTSAH contains two subcomponents and for each subcomponent a probabilistic models is developed. Fig 4 shows the reliability models of conventional and VTSAH with thermal storage system. The VTSAH system three state models include a thermal storage system in addition to the rated capacity and zero capacity state. The HASI technique is proficient to consider thermal energy storage losses. The available solar insolation helps to generated heat from VTSAH system, V trough reflector and blower unit are working satisfactorily to enhance the performance. The losses of VTSAH thermal storage due to failure of latent heat storage materials kept bottom side of absorber plate as in container, dust accumulation on the reflector and solar air heater transparent cover surface, shadow on parts of solar air heater array. A combined probability model and the index ELOL for the entire period are given below.

$$P(X) = \sum_{i=1}^{n} p_i E^{'}(X - C_i) \quad (18)$$

$$ELOL_i = P_i(C_{ia}(L_{ia})) \quad (19)$$

$$ELOL_i = \sum_{i=1}^{nds} ELOL_i \quad (20)$$

The capability outage possibility desk and ELOL index is calculated using Eqs. (18) – (20). The load hour losses (LHLO) and expected loss of load (ELOL) are shown at a particular time that the VTSAH system is unable to meet the energy needs. The expected loss of energy (ELOE) is calculated using Eq. (21)

$$ELOE = \sum_{j=1}^{u} EC_j P_j \quad (21)$$

$$P(H) = \sum_{i=1}^{n(H)} t(H)_i / N \quad (22)$$

The probability value is obtained using Eq.(22). The expected loss of health (ELOH) is an index. The dirt, snow, or other foreign matter which will be action as a fouling factor which occupies on the front surface of the VTSAH reflector and absorber plate glass surface is reduces the amount of solar insolation reaching the collector surface of VTSAH. ELOH value is computed by Eq. (23) (Billiton and Kari, 2003)

$$ELOH = (1 - P(H)) \quad (23)$$

The auxiliary thermal energy (ATE) and auxiliary energy hour (AEH) available is obtained when the energy supply is for fixed number of hours and thermal energy generation is more than energy necessity for that day using an Equ.(24) and Equ.(25)

$$ATE = E_{GD} - E_{Dd} \quad (24)$$

$$AEH = ATE / E_{Dmh} \quad (25)$$

The fuel energy saved for year i[th] by considering the sample year N and knowing the rate of heat transfer (RH) is calculated by Eq. (26) (Billiton and Kari, 2003)

$$FS = \frac{\sum_{i=1}^{N} PC_i}{N.HR} \quad (26)$$

The method involved for the reliability analysis of VTSAH system by using Monte Carlo simulation is briefly explained in the following steps as shown below (Billiton and Li, 1994)

(i) Specify the initial state of conventional SAH and VTSAH with thermal storage. Usually it is believed that all elements are beginning in the upstate.

(ii) The inverse transform method $f(t) = \lambda e^{-\lambda t}$ is used to simulate the length of each element which is at present state and also distribute the component failure rates functions. The state duration (T) sample values is $T_i = -\ln(U_i) / \lambda i$, where U_i is the uniformly distributed random number [0 1] corresponding to the *i* th element, λ_i is a failure rate depending on the current state of the *i* th element.

A sequential *'up'* and *'down'* state for each element is constructed in a given time period. The HASI simulation process flowchart is as shown in the fig.5..

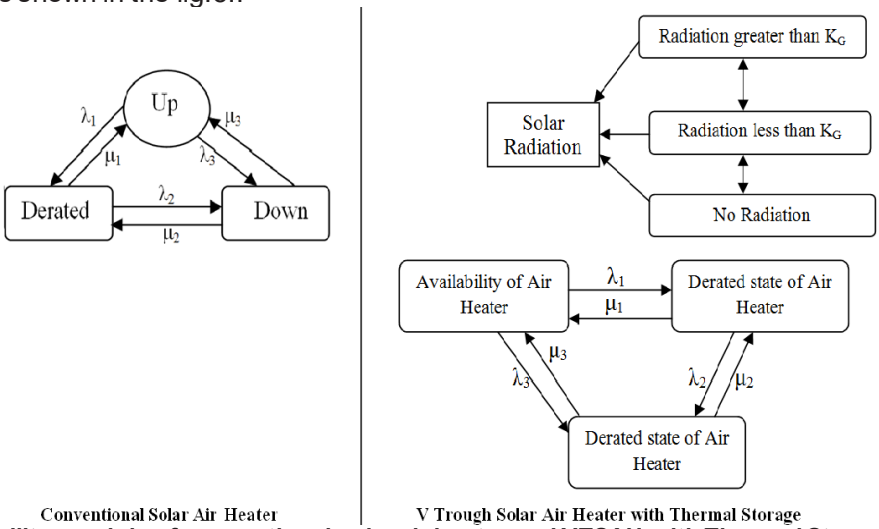

Fig 4: Reliability models of conventional solar air heater and VTSAH with Thermal Storage system

IV Simulation results

The system are simulated for the site at Kengeri (12.9° N, 77.48° E) and an elevation of 826 meters having annual average rainfall of 858 mm which is considered as a low rainfall category is placed for the rainfall correction factor. The constant *a* and *b* taken as 0.28 and 0.42 respectively. The constant *A, B* and *C* are selected from Table 1. To plot ABC rainfall correction, Eqs. (7) – (13) are used. The VTSAH system predicted thermal energy output by different solar insolation methods and actual thermal energy generation are measured. It is verified that the following methods namely *a-b* constant, *A–B–C* no rain and *A–B–C* rainfall have high heat generation evaluation with respect to actual values. The method ABC without rainfall analyzed has the maximum predictable energy

produced with actual energy. The proposed HASI approach the estimated VTSAH output energy of single iteration of MCS. The thermal energy storage estimations by HASI technique is various ±12% from actual energy generation for the months January to May and October to December. The estimation deviates 15–20% during for June to September month due to non-availability of solar insolation.

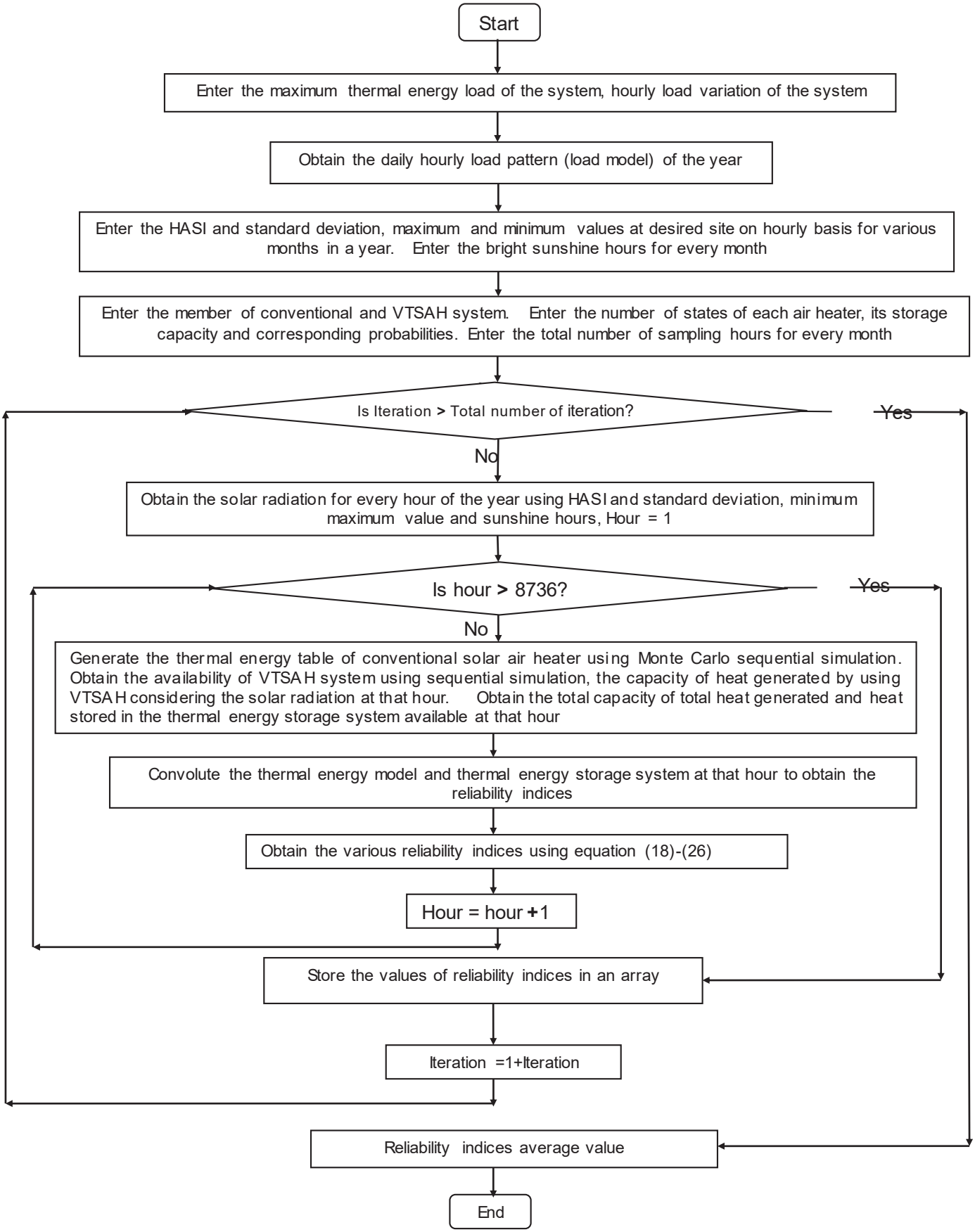

Fig 5: Flow diagram of MCS method for HASI technique

Monte Carlo Simulation Technique using HASI method for VTSAH

The VTSAH is utilized for agricultural procedure drying products, it promote employments generation to enhance the farmer income from weaker section in India and other countries, saving of fossil fuel usage. The various reliability indices of ELOL, LHLO and ELOE achieved by HASI technique using MCS method on VTSAH with the maximum thermal load of 2kW$_t$ are shown in Table 3. The linear increase of ELOL for lowers energy storage loads and saturates at higher energy storage loads. The linear increase of ELOL for increase in thermal energy storage loads. An exponentially increases of ELOE initially for lower energy storage load and linearly for higher energy storage load.

Table 3:
Reliability indices using MCS technique on 02 kW VTSAH system for different maximum heat transfer

Maximum energy (kW)	ELOL (days/year)	LHLO (h)	ELOE (kWh/year)	AEH (h)	ATE (kW)
0.25	145.25	335	1586	325.2	80.72
0.5	178.32	438	2286	185.2	55.32
0.75	225.5	552	3185	92.5	36.25
1.0	278.6	685	4298	36.8	24.58
1.25	328.6	815	5680	10.8	11.68
1.5	355.2	938	7218	1.78	4.89
1.75	361.23	1052	8854	0.224	1.15
2.0	362.5	1132	10,452	0.0015	0.0250

AEH and ATE are exponentially reduced with increase in thermal energy storage load and becomes zero for thermal energy storage load of more than 1.5 kW. ATE reduction with increase in thermal energy storage indicates that VTSAH is utilized all its stored thermal energy. The energy available in VTSAH source is not consumed fully due to lower demand energy. The result of rise in VTSAH system capacity on various reliability indices for 2 kW energy on the system is as shown in Table 3. It is proved from Table 4 that as the increase in thermal energy increased by 60%, the reliability indices ELOL, LHLO, ELOE reduces to 33% of their base value and AEH and ATE increases 7 times to their base value.

Table 4:
Reliability indices using MCS technique with increase in capacity of VTSAH system on thermal energy load of 02 kW

Maximum energy (kW)	ELOL (days/year)	LHLO (h)	ELOE (kWh/year)	AEH (h)	ATE (kW)
1.0	223.5	556	3231	90.2	182.8
1.2	186	448.7	2653	172.5	331.2
1.4	153.5	372	2231	275	492.5
1.6	132.5	310.2	1780	372	656
1.8	116.8	265.2	1452	492	816.2
2.0	102.3	224.5	1256	610.2	971.5

The LHLO during different months of the year, the thermal load of 1 kW and 2 kW are considered for the VTSAH system, respectively, with a maximum energy load of 02 kW. It is noticed that as the capacity increase, the LHLO reduces by one hour during the rainy season and by two hours during sunshine hours. It indicates that just the increase in the capacity of VTSAH system is not the solution to improve the reliability during the rainy seasons, but the use of some other medium of source is the solution.

V. Conclusions

In this paper, the HASI technique is projected for the forecast of VTSAH. The results calculated by HASI technique varies ±12% from actual values. The deviations in monsoon months are more due to non availability of solar insolation. The benefit of HASI technique is used as a probabilistic method for MCS method. The reliability analysis based HASI technique is accomplished that the increase in VTSAH installed capacity, which reduces the LHLO during rainy seasons and additional hours of thermal energy storage is available during the summer period. AEH and ATE reduce exponentially with raise in energy load and becomes zero at maximum load. The HASI technique with MCS method was presented together with related economic analysis, should prove useful as valuable inputs for the system design and planning.

References

B. Kekezoglu ; O. Arikan 2013 Reliability Analysis of hybrid energy systems: Case study of Davutpasa Campus ISBN: 978-1-4673-2230-0 IEEE publisher. Pg 1141 -1144

Billiton, R., Allan, R.N., 1996. Reliability Evaluation of Power Systems, second ed. Plenum Press, New York.

Billiton, R., Bagmen, 2006. Generating capacity adequacy evaluation of small stand alone power system containing solar energy. Reliability Engineering System Safety 91, 438–443

Billiton, R., Kari, R., 2001. Maintaining supply reliability of small isolated power systems using renewable energy. IET Proc. Gener.Transm. Distrib. 148 (6), 530–534.

Billiton, R., Kari, R., 2003. Reliability/cost implications of utilizing photo voltaic in small isolated power systems. Reliability Engineering System Safety 79, 11–16.

Billiton, R., Li, W., 1994. Reliability Assessment of Electric Power System using Monte Carlo Methods. Plenum Press, New York.

Cha, S.T., Jeon, D.H., Bae, I.S., Lee, R., Kim, J.O., 2004. Reliability evaluation of distribution system connected photovoltaic generation considering weather effects. Proceedings of 8th International Conference on Probabilistic Methods Applied to Power System. Iowa State University, Ames, Iowa, pp. 451–456.

E. Setien, M. Frasquet 2015 Reliability Analysis of Solar Gas Hybrid Receiver for central tower plants Energy Procedia 69 pg no. 1558 – 1567

Hassan Bin Nasir 2017 Techno-Economic Analysis of a Solar air heater with dimple shaped protrusions on the surface , India ISSN (Print): 2393-8374, , Volume-4, Issue-6, 2017

Jain, A., Tripathy, S.C., Balasubramanian, R., 1995. Reliability and economic analysis of a power generation system including a photovoltaic system. Energy Conversion Management 36 (3), 183–189.

Mani, A., 1980. Handbook of Solar radiation Data for India. Allied Publishers, New Delhi.

Messenger, R., Ventre, J., 2000. Photovoltaic System Engineering. CRC Press, New York.

Moharil, R.M., Kulkarni, P.S., 2006. Design and performance of solar photovoltaic water pump. J. IE(I) Interdis. Div. 87 (2), 25–32.

Moharil, R.M., Kulkarni, P.S., 2009. A case study of solar photovoltaic power system at Sagardeep Island, India. Renewable Sustainable Energy. Rev. 13, 673–681.

Nehru, M.H., LaMeres, B.J. 2000. An approach to evaluate the general performance of standalone wind/photovoltaic generating system. IEEE Trans. Energy Conversion. 15 (4), 433–439.

Page, J.K., 1961. New sources of energy. Proc. UN Conf. Rome 4, 378.

Parishwad, G.V., Bhardwaj, R.K., Nema, V.K., 1997. Estimation of hourly solar radiation for India. Int. J. Renewable Energ. UK 12 (3), 303–313.

Shrestha, G.B., Goel, L., 1998. A study on optimal sizing of stand-alone photovoltaic stations. IEEE Trans. Energ. Convers. 13 (4), 373–378.

Sukhatme, S.P., 2004. Solar Energy: Principles of Thermal Collection and Storage, second ed. Tata McGraw Hill, New Delhi, India.

Influence of boundary conditions on the exergetic optimization of a Thermal Energy Storage Unit combined with an Organic Rankine Cycle

Andreas König-Haagen, Dieter Brüggemann*
Chair of Engineering Thermodynamics and Transport Processes (LTTT), Center of Energy Technology (ZET), University of Bayreuth, Universitätsstraße 30, 95447 Bayreuth, Germany

*Corresponding author: dieter.brueggemann@uni-bayreuth.de , andreas.koenig-haagen@uni-bayreuth.de

Abstract
Within this work the promising combination of a Thermal Energy Storage (TES) with an Organic Rankine Cycle (ORC) – named ORCTES – is analyzed and optimized from an exergetic point of view. The investigated application is waste heat recovery and the TES is used to overcome the temporal mismatch between heat supply and electricity demand. A numerical model was set up in MATLAB Simulink to describe the ORCTES facility with a thermal storage capacity of approximately 1.5 MWh. Air is used as heat transfer fluid (HTF) for the horizontal flow TES consisting of a packed sand bed with a maximum charging temperature of 600 °C. Within the numerical model all relevant material properties of the TES and the HTF are implemented temperature dependently and convection, diffusion and radiation as well as heat and pressure losses are included in the simulations. The ORC is represented by characteristic curves taken from literature. Parameter variations regarding several boundary conditions including the charging temperature and the mass flow of the HTF are performed with the implemented numerical model. A recently developed detailed exergetic evaluation method for TES in systems is applied to identify the optimization potential of the TES and its interactions with the remaining system. Later on, a mathematical optimization concerning the TES dimensions etc. is carried out for two characteristic sets of boundary conditions. The results reveal that the effect of physical aspects on the exergetic performance strongly depends on the boundary conditions and might be different for the TES itself compared to the effect on the overall system. Furthermore, the optimum of some of the TES parameters is also dependent on the boundary conditions. For the two cases analyzed in detail, the exergetic efficiencies of the optimized system are about 43 % and 28 %.

Keywords: Exergetic Evaluation, Optimization, Thermal Energy Storage, Organic Rankine Cycle

I. Introduction

If an Organic Rankine Cycle (ORC) is used for the utilization of fluctuating waste heat, a combination with a Thermal Energy Storage (TES) allows to downsize the ORC and to run it less in off-design. Even though the combination of an ORC and a TES is a promising approach, there is only a very limited number of studies found in literature dealing with this specific case (Dal Magro et al., 2015; Manfrida et al., 2016; Nardin et al., 2014). Exergetic analyses are well suited to study and optimize such systems, but in most studies found in literature the TES is strongly simplified. Hence, the exergetic analysis cannot be performed on a detailed level. In general, detailed second law analyses of TES in systems have only recently attracted attention due to e.g. pumped thermal electricity storage (McTigue et al., 2015). Before, the TES were mostly studied strongly simplified and the containing systems were not considered (Bejan, 1978; Bjurström and Carlsson, 1985). More recently a TES in combination with an air conditioning system has been analyzed with the help of a so-called advanced exergetic analysis (Mosaffa et al., 2014). The combination of an ORC with sensible and latent TES (König-Haagen et al., 2014) and a high temperature fixed bed TES in combination with an ORC – called ORCTES – was studied and optimized by the authors with the help of a detailed exergetic evaluation method (König-Haagen et al., 2020). The present paper continues the work regarding the ORCTES by investigating the influence of boundary conditions on the exergetic efficiency, on the exergetic losses and on the optimization result. According to the previous paper (König-Haagen et al., 2020) a numerical model is set up in MATLAB Simulink. For different boundary conditions, extensive exergetic evaluations are carried out which show the optimization potential of the ORCTES. Subsequently, a mathematical optimization is performed to optimize the TES system. Finally, the results for different boundary conditions are analyzed together.

II. System Description

One module of the ORCTES developed by the enolcon GmbH and set up at the University of Bayreuth (see Figure 1) will be studied numerically. About 4.7 t of sand with a diameter of 2 mm are placed in the six sections with a size of about 1.1 m x 1.1 m x 0.4 m in depth, height and length.

Figure 1: Storage modules of the ORCTES facility at the University of Bayreuth

The vertical flow-through TES is operated with air as heat transfer fluid (HTF) and coupled to an ORC. The pipes of the periphery have an inner diameter of 0.2 m, are made of stainless steel and are, like the TES, insulated with mineral wool and plates of 0.2 m thickness. The maximum charging temperature of the TES is 600 °C leading to a thermal storage density of 0.75 MWh per module. A more detailed description of the ORCTES system can be found in literature (König-Haagen et al., 2020; Schlipf et al., 2017). Applying the numerical model described later, variation simulations are performed. The varied parameters are listed in Table 1. For each variation the overall exergetic efficiency in the swung-in state is calculated and for two characteristic cases a detailed exergetic analysis and a mathematical optimization are carried out.

Table 1. Varied boundary conditions

parameter	value	unit
charging temperature	400, 500, 600	°C
standard volume flow	1/3, 2/3, 1	$m^3\ s^{-1}$
pipe length	twice 5, 10, 20	m
storage time	0, 1, 2, 5, 10	h

The TES, its periphery and the ORC are included in the numerical model. All components are modelled physically, except for the ORC, which is implemented by means of characteristic curves (Preißinger and Brüggemann, 2017). The model of the TES is primarily based on the Schumann model. Herein, the HTF and the sand are coupled by source terms (q_{HTF} and q_{Par}) that account for the heat transfer between both phases. Each phase is modelled one-dimensionally and the energy equation for the HTF is

$$\psi c_p \rho \frac{\partial T}{\partial t} + \psi u c_p \rho \frac{\partial T}{\partial x} = \psi \frac{\partial}{\partial x}\left(\Lambda \frac{\partial T}{\partial x}\right) + q_{HTF} \tag{1}$$

and for the particles it is

$$(1 - \psi) c \rho \frac{\partial T}{\partial t} = (1 - \psi) \frac{\partial}{\partial x}\left(\Lambda \frac{\partial T}{\partial x}\right) + q_{Par}. \tag{2}$$

Herein, the porosity is ψ, the temperature is T, the time is t, the density is ρ, the velocity is u and the specific heat capacity of the HTF and the particles is c_p and c respectively. In equation (1) and (2) Λ is an effective thermal conductivity that is calculated by (VDI, 2013)

$$\Lambda = \lambda_{eff} + \frac{\mathrm{Pe}_0}{2} \lambda_{HTF} \tag{3}$$

The second term on the right hand side with the heat conductivity of the HTF λ_{HTF} and the Peclet number of the superficial velocity Pe_0 accounts for disperse effects. The detailed model of Bauer/Zehner/Schlünder (VDI, 2013) is used to determine the effective heat conductivity of the packed bed without through flow λ_{eff}.
The correlation based on the heat transfer of a single sphere (VDI, 2013) is used to calculate the heat transfer coefficient between the particles and the HTF. This model is extended for small Peclet numbers with the correlation found in Kunii and Suzuki (Kunii and Suzuki, 1967). Determining the pressure drop in the fixed bed is done by using the model of Molerus described in the VDI Heat Atlas (VDI, 2013). To calculate the energy transport in the pipes of the periphery

$$c_p \rho \frac{\partial T}{\partial t} + u c_p \rho \frac{\partial T}{\partial x} = \frac{\partial}{\partial x}\left(\lambda \frac{\partial T}{\partial x}\right) + q_{pipe-HTF} \tag{4}$$

is used for the HTF and

$$c \rho \frac{\partial T}{\partial t} = \frac{\partial}{\partial x}\left(\lambda \frac{\partial T}{\partial x}\right) + q_{pipe-wall} \tag{5}$$

for the pipe walls. The pressure drop of pipes, valves, bends and branches as well as the heat transfer between the HTF and the pipe is taken into account (VDI, 2013). Equation (1), (2), (4) and (5) are discretized with the method of lines and the resulting time-dependent ordinary differential equations can be efficiently treated by solvers provided by MATLAB Simulink. All important material properties are implemented temperature dependently.

III. Analysis

A previously developed exergetic evaluation method is applied in this work (König-Haagen et al., 2020; König-Haagen et al., 2014). The method is somewhat similar to the concept of the advanced exergetic analysis (Morosuk and Tsatsaronis, 2019) and an approach based on structure coefficients (Beyer, 1970). However, the difference consists in the fact that the influence of physical aspects and the influence of the considered component on the remaining system is studied. The aim of the detailed exergetic evaluation method is to strengthen the understanding of the process, to show optimization potentials and to check the results of mathematical optimizations for plausibility. To achieve this the individual components are once studied as they are – called real – and also idealized – called ideal. The real exergetic efficiency of one component, parts of the system or the overall system ε^{real} is given by

$$\varepsilon^{real} = \frac{E_P}{E_F} \tag{6}$$

and the idealized efficiency ε^{ideal} is generally defined as

$$\varepsilon^{ideal} = \frac{E_P^{ideal}}{E_F}. \quad (7)$$

In equation (6) and (7) the fuel exergy is E_F, the product exergy is E_P and the product exergy resulting from an idealization is E_P^{ideal}. Determining the influence of a particular physical aspect y is in general done using equation

$$y = \frac{\varepsilon^{ideal}}{\varepsilon^{real}}. \quad (8)$$

The described method is well suited to illustrate the influence of physical aspects on the respective component itself, other components of the system or the overall system. However, only the influence on the overall system will be considered in detail in this paper. Table 2 lists the physical aspects studied in this work.

Table 2. Idealized physical aspects

idealized physical aspect	components
heat loss to the surrounding	storage / periphery
heat resistance from the heat transfer fluid (HTF) to the particles and inside the particles	storage
effective thermal conduction in flow direction	storage
pressure drop	storage / periphery

IV. Results and discussions

For the variation computations (see Table 1) with the TES in the design state, the highest exergetic overall efficiency of 36 % was obtained for a standard volume flow of 0.67 m^3s^{-1}, a pipe length of 5 m, an inlet temperature of 600 °C and a storage time of 0 h. The lowest exergetic efficiency of 8 % resulted for a standard volume flow of 1 m^3s^{-1}, a pipe length of 20 m, an inlet temperature of 400 °C and a storage time of 10 h. The scenario with the highest efficiency is referred to as case 1 and the scenario with the lowest efficiency as case 2. In order to achieve the highest possible overall exergetic efficiency, the parameters given in Table 3 were subsequently optimized for both cases with a downhill simplex algorithm combined with a branch and bound method. After the optimization the overall exergetic efficiencies increased to 43 % and 28 %. The optimal parameter values, their boundaries and the initial values are shown in Table 3. Interestingly, the optimized parameters concerning the TES are in general similar for both optimized cases. However, the pipe diameter differs by about 43 %. Before the optimization the highest influence on the overall exergetic efficiency of case 1 could be seen for the heat transfer resistance, the pressure drop of the periphery and the heat conduction with y being 1.09, 1.06 and 1.05 respectively. For case 2 the highest influence occurred for the pressure drop of the periphery with y = 2.56, the heat transfer resistance with y = 1.63 and the heat loss of the TES with y = 1.57. The above results indicate that a heuristic optimization should aim at reducing these influences. After the mathematical optimization of case 1, the heat transfer resistance, the heat conduction and the heat loss of the periphery have the highest influence. The heat loss of the periphery, the heat loss of the TES and the heat transfer resistance have the highest influence on the optimized case 2. In general, the influences are much lower after the optimization and more even (see Figure 2). Due to the optimization the TES including the periphery has an exergetic efficiency of about 90 % for case 1 and about 75 % for case two and the exergetic efficiency of the ORC is always below 50 %.

Surprisingly, the influence of a physical aspect is sometimes very different for a considered component in comparison to the overall system. For example, the pressure loss of the periphery can sometimes increase the exergetic efficiency of the ORC a little bit, but in return it may drastically reduce the exergetic efficiency of the entire system.

Table 3. As-is state, boundaries and optimum of the varied parameters

	storage length in m	number of segments	cross sectional area in m²	pipe diameter in m	particle diameter in m	porosity
minimum	0.945	1	1	0.18	0.002	0.3
maximum	7.56	9	2.84	0.5	0.02	0.5
as-is state	3.78	6	1.21	0.2	0.00207	0.419
optimum case 1	2.50	1	2.64	0.5	0.00876	0.5
optimum case 2	2.51	1	2.84	0.35	0.00819	0.499

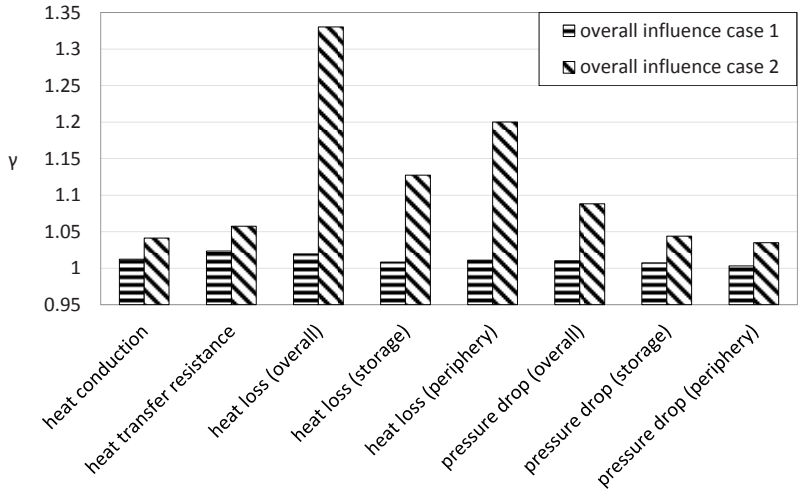

Figure 2: Influence of different physical aspects on the exergetic overall efficiency after the optimization

V. Conclusions

Within this paper a detailed exergetic analysis and an optimization are performed for the ORCTES system (a combination of a high temperature TES and an ORC) under different boundary conditions. The exergetic analysis reveals that the pressure drop of the periphery and the heat transfer resistance are mainly responsible for the exergy loss before optimization. After the optimization the influence of the studied physical aspects is much smaller as well as more even and the exergetic overall efficiency was raised from 36 % to 43 % and from 8 % to 28 %. This optimization was achieved by varying different parameters of the TES and its periphery. Interestingly, the optimal TES parameters are mostly similar for both cases studied, but the parameters of the periphery differ. Future work will include a detailed analysis of the interactions within the system and an investigation including the influence of the boundary conditions in more detail.

Acknowledgements

The authors thank the staff of enolcon GmbH and STORASOL GmbH for their support and Prof. Markus Preißinger for providing the data for the characteristic curves of the ORC.

References

Bejan, A., 1978. Two thermodynamic optima in design of sensible heat units for energy-storage. Journal of Heat Transfer 100, 708–712.

Beyer, J., 1970. Strukturuntersuchungen - notwendiger Bestandteil der Effektivitätsanalyse von Wärmeverbrauchersystemen. Energieanwendungen 19, 358–361.

Bjurström, H., Carlsson, B., 1985. An exergy analysis of sensible and latent heat storage. Journal of heat recovery systems 5, 233–250.

Dal Magro, F., Meneghetti, A., Nardin, G., Savino, S., 2015. Enhancing energy recovery in the steel industry: Matching continuous charge with off-gas variability smoothing. Energy Conversion and Management 104, 78–89.

König-Haagen, A., Höhlein, S., Brüggemann, D., 2020. Detailed exergetic analysis of a packed bed thermal energy storage unit in combination with an Organic Rankine Cycle. Applied Thermal Engineering 165, 114583.

König-Haagen, A., Rösler, F., Brüggemann, D., 2014. Exergetic analysis of thermal energy storages in thermodynamic systems, in: Eurotherm Seminar #99: Advances in Thermal Energy Storage.

Kunii, D., Suzuki, M., 1967. Particle-to-fluid heat and mass transfer in packed beds of fine particles. International Journal of Heat and Mass Transfer 10, 845–852.

Manfrida, G., Secchi, R., Stańczyk, K., 2016. Modelling and simulation of phase change material latent heat storages applied to a solar-powered Organic Rankine Cycle. Applied Energy 179, 378–388.

McTigue, J.D., White, A.J., Markides, C.N., 2015. Parametric studies and optimisation of pumped thermal electricity storage. Applied Energy 137, 800–811.

Morosuk, T., Tsatsaronis, G., 2019. Advanced exergy-based methods used to understand and improve energy-conversion systems. Energy 169, 238–246.

Mosaffa, A.H., Garousi Farshi, L., Infante Ferreira, C. A., Rosen, M.A., 2014. Advanced exergy analysis of an air conditioning system incorporating thermal energy storage. Energy 77, 945–952.

Nardin, G., Meneghetti, A., Dal Magro, F., Benedetti, N., 2014. PCM-based energy recovery from electric arc furnaces. Applied Energy 136, 947–955.

Preißinger, M., Brüggemann, D., 2017. Thermoeconomic Evaluation of Modular Organic Rankine Cycles for Waste Heat Recovery over a Broad Range of Heat Source Temperatures and Capacities. Energies 10, 269.

Schlipf, D., Faust, E., Schneider, G., Maier, H., 2017. First operational results of a high temperature energy storage with packed bed and integration potential in CSP plants. AIP Conference Proceedings 1850, 80024.

VDI, 2013. VDI-Wärmeatlas, 11., bearb. und erw. Aufl. Springer-Verlag, Berlin, Heidelberg.

Economic and social sustainability in low-carbon energy transitions: Computer simulations of a proof-of-concept study

[1*]Ibrahim Ari and [2]Muammer Koc

[1,2] Division of Sustainable Development (DSD), College of Science and Engineering (CSE), Hamad bin Khalifa University (HBKU), Qatar Foundation (QF), Education City, Doha, Qatar.
* E-mail: iari@hbku.edu.qa

Abstract
Global efforts have considerably raised in the low-carbon energy transition to reduce CO2 emissions for the last decade, hence protect the nature of the world. The transition from fossil fuels to renewable resources has broadly investigated in many studies in terms of environmental sustainability and technological development. However, economic and social outcomes of clean energy investment have been usually overlooked in the energy literature, whereas sustainable development requires a holistic approach by considering the economy and society along with the environment. There is a dramatic financing gap in energy investment, and conventional financing models fail to fill the gap. The financing tools depending on excessive debt ultimately and negatively affect social welfare by increasing wealth inequality. This study proposes an innovative proof-of-concept financing model for building solar powerplants that provides insights into wealth inequality and social welfare. To this end, a closed economic system is designed as an agent-based computational model with the proposed policy rules and the equity-foundation-based financing model. Then, the proposed model is simulated for fifty years to evaluate and compare the wealth inequality with a conventional financing mechanism. As a proof-of-concept, the key finding shows that the proposed policy settings radically reduce wealth inequality to 0.434 throughout simulation time, which is lower than the lowest value in the world. In conclusion, there is a need for innovative financing models to achieve environmental sustainability together with economic and social pillars.

Keywords: Sustainable finance, solar powerplant, wealth inequality, agent-based modeling.

I. Introduction

Energy investment, which is highly connected to the sustainable development goals (SDGs) (Ari and Koc, 2018), has a significant influence on economic growth and development, as discussed broadly in the literature (Munnell, 1992; Samouilidis and Mitropoulos, 1983). Global energy investment, amounted to USD 1.8 trillion in 2018 (IEA, 2019), has been increasing and shifting towards sustainability by harnessing renewable power. Renewable energy investment has a profound role in building a sustainable future and a better planet for everyone. To meet long-term sustainability goals, renewables investment would need to expand two-and-a-half times with increasing its share to 65% by 2030 (IEA, 2019). Therefore, renewables recently attracted more attention and accounted for two-thirds of power generation investments while hitting the record level on spending solar photovoltaics (PVs) in 2017 (IEA, 2018). However, there was a considerable amount of gap for financing energy infrastructure, including renewables, which is approximately USD 1.7 trillion in 2017 (IEA, 2019; OECD/IEA and IRENA, 2017). Renewables require much more investment than the current trend, although the rapid advancements in technology reduce the cost of harnessing clean energy significantly. The need for renewable investment was estimated that the annual increase must be at least 150% between 2015 and 2050 (OECD/IEA and IRENA, 2017). These numbers confirm that obtaining the necessary capital for financing energy plants is a challenge faced by governments and private entities.

II. Methodology

The objective of this study is to develop a policy framework substantially decreasing wealth inequality by redistributing the wealth through the foundation institution, and reducing the debt burden on society by mobilizing the domestic savings. In line with this objective, this study attempts to provide evidence for the following question. What kind of a financial intermediary and policy rules for sustainable financing should be developed for sustainable development, without reducing the total capital in the market and social development? In this regard, this study provides a proof of concept analysis on alternative foundation-based financings for renewable energy investments. To this end, equity-foundation-based model is designed and simulated in an agent-based computational economics (ACE) with simple, yet powerful, policy regulations (see (Ari and Koc, 2019) for the details of the methodology). Besides, a banking system is also modeled to compare the proposed models with conventional financing. Project developers and the government sign a power purchasing agreement (PPA) that is a legal contract stipulating that the government buys all the electricity generated by the power plant during its lifetime. This study chooses Puerto Vallarta, Jalisco, Mexico as the place of the case study. Table 1 summarizes all the inputs, and assumptions given below.

Table 1. Configuration of the experiment on the agent-based model.

Agent	Variable	Unit	Value
Power Plant	Overnight capital cost	US$	100,000,000
	Lifetime	year	25
	Construction period	year	2

	Power capacity	MWp	100
	Azimuth of PV panels[1]	degree	180
	Tilt of PV panels[1]	degree	23
	Energy yield[1]	MWh/MW	1724
	Estimated O & M cost	US$/kW/year	8
	Decrease rate of O&M (first yr)	-	0.01
	Rate of plant availability	-	0.99
	Degradation factor (first year)	-	0.03
	Degradation factor (others)	-	0.002
	Land lease	US$	0
	Rate of asset management cost	-	0.30
	Rate of insurance cost	-	0.15
	Rate of other expenses	-	0.15
Depositor/Investor	Initial capital (IN)	US$	150,000,000
	Initial capital (LE)	US$	450,000,000
	Population (IN)	people	250,000
	Population (LE)	people	10
Loan	Interest rate	-	0.05
	Loan period	year	10
	Grace period	year	2
Bank	Central bank rate	-	0.0225
	Interest of required reserves	-	0.0220
	Prime-deposit interest rate	-	0.0105
	Default-deposit interest rate	-	0.0095
Environment	Carbon intensity (NG)	g CO2eq/kWh	46
	Carbon intensity (Solar)	g CO2eq/kWh	469
	Construction frequency	year	1

Notes: 1. The inputs for Puerto Vallarta, Jalisco, Mexico are obtained from the "Global Solar Atlas 2.0, a free, web-based application is developed and operated by the company Solargis s.r.o. on behalf of the World Bank Group, utilizing Solargis data, with funding provided by the Energy Sector Management Assistance Program (ESMAP). For additional information: https://globalsolaratlas.info.

The results will be given in the following section. The policy scenarios are summarized in Table 2.

Table 2. The summary of policy scenarios.

	Project Developer	Loan (%)	Equity (%)	Shareholder List	Project Shares [Shareholder Limits]	Non-Profit EBIN	Found. Share
1	LE	100	0	(LE,Bank,IN, EBIN)[1]	(1.0, 0.0, 0.0, 0.0)	-	-
2	LE	70	30	(LE,Bank,IN,EBIN)	(1.0, 1.0, 1.0, 1.0)	False	0.0
3	LE	0	100	(LE,Bank,IN,EBIN)	(1.0, 1.0, 1.0, 1.0)	False	0.0
4	EBIN	0	100	(EBIN,IN,LE,Bank)	(1.0, 1.0, 1.0, 1.0)	False	0.0
5	EBIN	0	100	(EBIN,IN,LE,Bank)	(0.20, 1.0, 1.0, 1.0)	False	0.0
6	EBIN	0	100	(EBIN,IN,LE,Bank)	(0.20, 1.0, 1.0, 1.0)	True	0.5

Notes: 1. LE, EBIN, and IN stand for large enterprises, equity-based financial intermediary, and individuals, respectively.

III. Results

Table 3 summarizes the results of wealth accumulation and Gini index for the scenarios. These results show that the proposed policy in Scenario 6 outperforms the other scenarios in terms of Gini index minimization and the wealth maximization at the same time.

Table 3. Results of the seven policy scenarios.

Results	Policies for Comparison			Proposed Policy Implications		
	Scenario 1	Scenario 2	Scenario 3	Scenario 4	Scenario 5	Scenario 6 (PCP)
WA—Bank [1]	3,325.79	2,898.76	2,161.94	1,491.84	1,705.73	1,715.44
WA—EBIN	0.00	759.95	1,325.82	7,075.56	3,572.83	498.00
WA—LE	6,652.95	6,766.31	8,491.56	1,337.78	1,537.01	1,567.50
WA—IN	240.66	240.66	240.66	1,106.57	4,578.85	4,578.85
WA—FND[2]	0.00	0.00	0.00	0.00	0.00	3,051.33
WA—Total	10,219.39	10,665.68	12,219.97	11,011.75	11,394.41	11,411.11
Gini Index	0.976	0.977	0.980	0.899	0.598	0.434

Notes: 1. The WA stands for Wealth Accumulation, US$ in Millions. 2. The FND stands for foundation.

In Scenario 6, which is the proposed model, there is a sharp decrease in the Gini index in the first year of the simulation, as in Scenarios 4 and 5. Despite the erratic rise of the wealth inequality from 2021 to 2024, there is a dramatic decrease from 0.688 in 2024 to 0.434 in 2070 throughout the simulation time. The resulting value is less than the lowest Gini coefficient, 0.498, among 174 countries reported in the Global Wealth Databook, 2018 (Credit Suisse, 2018). In the meantime, Mexico's Gini index in 2018 was reported at 0.80, which is significantly higher than

0.483 (Credit Suisse, 2018). Scenario 6 is the optimum policy framework among all the scenarios in terms of simultaneously minimizing the Gini index and maximizing the total wealth in society. As a proof of concept, the proposed model overcomes social stress by spending towards the benefit of the public through the foundation pool; and it also reduces social and economic inequality by delivering a more equitable wealth distribution.

IV. Conclusions

Global efforts have considerably raised in the low-carbon energy transition to reduce CO2 emissions for the last decade, hence protect the nature of the world. The transition from fossil fuels to renewable resources has broadly investigated in many studies in terms of environmental sustainability and technological development. However, economic and social outcomes of clean energy investment have been usually overlooked in the energy literature, whereas sustainable development requires a holistic approach by considering the economy and society along with the environment. There is a dramatic financing gap in energy investment, and conventional financing models fail to fill the gap. The financing tools depending on excessive debt ultimately and negatively affect social welfare by increasing wealth inequality. This study proposes an innovative proof-of-concept financing model for building solar powerplants that provides insights into wealth inequality and social welfare. To this end, a closed economic system is designed as an agent-based computational model with the proposed policy rules and the equity-foundation-based financing model. Then, the proposed model is simulated for fifty years to evaluate and compare the wealth inequality with a conventional financing mechanism. As a proof-of-concept, the key finding shows that the proposed policy settings radically reduce wealth inequality to 0.434 throughout simulation time, which is lower than the lowest value in the world. In conclusion, there is a need for innovative financing models to achieve environmental sustainability together with economic and social pillars.

References

Ari, I., Koc, M., 2019. Sustainable Financing for Sustainable Development: Agent-Based Modeling of Alternative Financing Models for Clean Energy Investments. Sustainability 11, 1967. https://doi.org/10.3390/su11071967

Ari, I., Koc, M., 2018. Sustainable financing for sustainable development: Understanding the interrelations between public investment and sovereign debt. Sustainability 10. https://doi.org/10.3390/su10113901

Credit Suisse, 2018. Global Wealth Databook 2018.

IEA, 2019. World Energy Investment 2019. Int. Energy Agency.

IEA, 2018. World Energy Investment 2018. Int. Energy Agency.

Munnell, A.H., 1992. Policy Watch : Infrastructure Investment and Economic Growth. J. Econ. Perspect. 6, 189–198.

OECD/IEA, IRENA, 2017. Perspectives for the Energy Transition: Investment Needs for a Low-Carbon Energy System. Int. Energy Agency 204.

Samouilidis, J.-E., Mitropoulos, C.S., 1983. Energy investment and economic growth. Energy Econ. 5, 237–246. https://doi.org/10.1016/0140-9883(83)90028-2

Simulation Model for Designing an Optimal Site Specific Renewable Energy Based Electric Vehicle (EV) Charging Station – a Case Study in Qatar

Abdulla Al Wahedi, Yusuf Bicer
Division of Sustainable Development (DSD), College of Science and Engineering (CSE), Hamad Bin Khalifa University (HBKU), Education City, Doha, Qatar

* E-mails: amalwahedi@mail.hbku.edu.qa

Abstract
E-Mobility deployment has become of increasing interest during recent years in various countries all over the world targeting mainly for reducing the reliance on fossil fuel-based means of transportation and decrease harmful emissions produced from transportation. Securing the required electricity to satisfy Electric Vehicles' (EVs) charging needs without increasing power generation sources that are based on fossil fuels nor expanding or overloading the exiting electricity infrastructure, standalone charging stations powered by renewable sources are considered as the ultimate solution for securing the electricity needed. This paper investigates modeling, simulation and optimization of a proposed grid-independent multigeneration charging station in the State of Qatar comprising of hybrid solar, wind and biomass sub-systems with ammonia, hydrogen, and battery storage systems where real metrological data inputs related to the incorporated renewable subsystems are used. The objective of the proposed design is to fast charge minimum 50 EVs per day and produce sufficient mass of H_2 and NH_3 to produce 200 kW power considering multiple constraints such as site-specific metrological conditions for the power generated by solar system and wind turbine and their intermittent nature as well as restricted land area not exceeding 1,500 m^2 to meet typical fuel station land requirement. The results showed that the selection of 1,440 kWh/day CPV/T system and 250 kW rated wind turbine along with 650 kW Li-ion battery storage system and 11 kW biomass-driven steam turbine can achieve the desired target of daily EVs fast charging with operational consideration of total shutdown of H_2 and NH_3 production during the months of October and November and 25% shutdown during the month of December.

Keywords: Grid-independent, fast-charging station, electrical vehicle, modeling, simulation, optimization.

I. Introduction

The roll out of grid-independent renewable energy-based fast charging stations to fulfil the rapid expansion of EVs adoption around the globe seems to be a promising solution from the technical, economic and environmental perspectives. However, such systems require deep examinations from the feasibility point of view prior to go for practical implementation where the proposed designs must be modeled, simulated and optimized considering real-life conditions. Since limited studies related to investigation and modeling of off-grid charging stations was performed (Mehrjerdi, 2019), this paper proposes and optimizes through modeling and simulation an off-grid renewable-based charging station in the State of Qatar.

With a population of about 2.64 million (State of Qatar Goverment, 2019), area of 11,521 km^2 (Hukoomi, 2015) and over 1.5 million fossil fuel-based conventional vehicles (CEIC, 2019), Qatar announced "Green Car Initiative" in May 2017 to promote the roll out of carbon free car usage. Targeting for 10% EVs by 2030 (The Peninsula Qatar, 2017), triggers securing the required electricity for EV charging stations from non-fossil fuels sources as a critical challenge.

From 2012 to 2017, the number of vehicles in Qatar has grown by 12% where the reported number of vehicles was 1.5 million in 2017 (CEIC, 2019). With the same percentage increase, the number of vehicles will reach 2.7 million by 2022. By the same year, the number of charging stations is reported to become 400 stations (Sachin, 2019) out of which 2 to 4% will be EVs (Qana, 2017). In order to secure the considerable additional energy demand required to charge the anticipated number of EVs without expanding conventional power generation plants nor degrading the existing network in a timely manner, grid-independent EV charging stations powered by renewable energy sources proposal along with an optimization, simulation and modeling tool to assist in designing and distributing EVs charging stations all over the country are required.

Assuming in 2022, 3.5% of the overall vehicles in Qatar will be EVs, 108,000 EVs will be on the road. Considering 80% of the EVs shall satisfy their charging needs at workplaces and homes (Sokorai et al., 2018), the rest 20% which is 21,600 EVs need in the city and on the road fast charging stations. Distributing this number over 400 charging stations, each station must charge over 50 EVs as minimum number on daily basis.

Assuming the dominant number of EVs will be of medium size with 50 kWh battery capacities which is the upper range of this size (Lokesh and Hui Min, 2017) and most on the move EV drivers start to search for a charging station when the State of Charge (SoC) of their EVs' batteries reaches 20% aiming for charging up to 80% SoC level in 15 to 20 minutes (Lokesh and Hui Min, 2017), this work considers 35 kWh daily charging demand per EV.

II. System Model

The proposed hybrid fast charging station model is shown in Figure 1 which is a multi-generation design with wind, solar and biomass renewable sources to provide the daily fast charging demand by EVs. The system has H_2 and NH_3 storage systems in addition to the battery storage system to ensure uninterruptable supply of needed power if there is no sufficient wind or during cloudy days or night times.

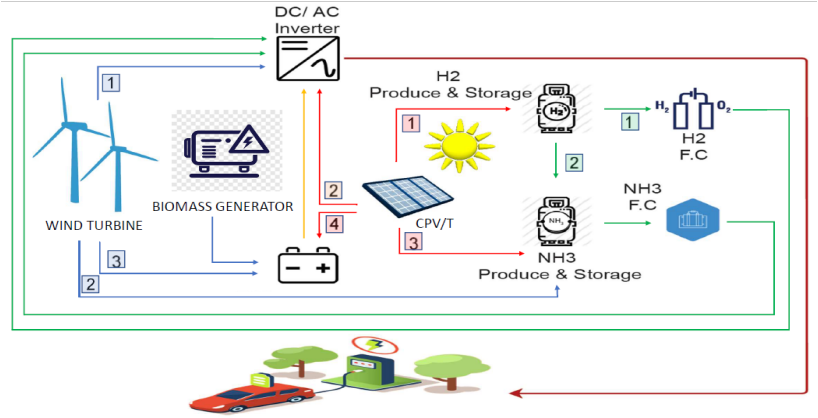

Figure 1: System Schematic Diagram

The proposed design consists of the following subsystems:

- Solar system: supplying power mainly to an electrolyzer and the rest is used for EV charging and battery storage.
- Wind Turbine: used for EV charging, N_2 and NH_3 production, and battery storage.
- Biomass Combustion: Municipal Solid Waste (MSW) is burnt only during unfavorable weather conditions to complement the above two electricity sources where the generated heat is used in the Rankine cycle to generate the required electricity for meeting the shortfall demand during unfavorable periods only.
- Electrolyzer Unit: to decompose H_2O into H_2 and O_2. H_2 is used for producing ammonia and generating power through hydrogen FC.
- NH_3 production: N_2 is produced through cryogenic air separation which is used with H_2 to synthesize NH_3 through Haber-Bosch process.
- H_2 Fuel Cell: the earlier produced H_2 and O_2 are used for producing energy for charging during night times or unfavorable periods through H_2 FC.
- NH_3 FC: The stored NH_3 is used as input for NH_3 FC to produce energy for charging during night times or unfavorable periods.
- Battery System: The excess daily energy whether from biomass, wind and/or solar systems is stored in the batteries for later use whenever needed.

III. Methodology

After calculating the electricity required to charge a minimum 50 EVs, PVSyst software (PVsyst 6.7.8 software, 2018) was used to determine the maximum possible electricity production per day with different available solar systems and associated battery storage capacities considering the metrological conditions of Qatar and typical charging station space limitation. The required mass and storage tank volumes of H_2, NH_3, N_2, O_2 and H_2O for producing 200 kW of electricity by H_2 and NH_3 fuel cells along with electricity required for producing the determined H_2, NH_3 and N_2 was calculated using Engineering Equation Solver (EES) program (Klein, 2018). From the literature review, the total electricity requirements for producing the respective mass of H_2 and NH_3 were calculated which must be considered along with the electricity required for fast charging 50 EVs.

A 250 kW wind turbine system was selected from the market as an optimal size and capacity considering the wind speed in Qatar and a typical charging station aesthetic and space characteristics. The priority hierarchy levels indicated in Figure 2 were developed based on which the designed system shall operate.

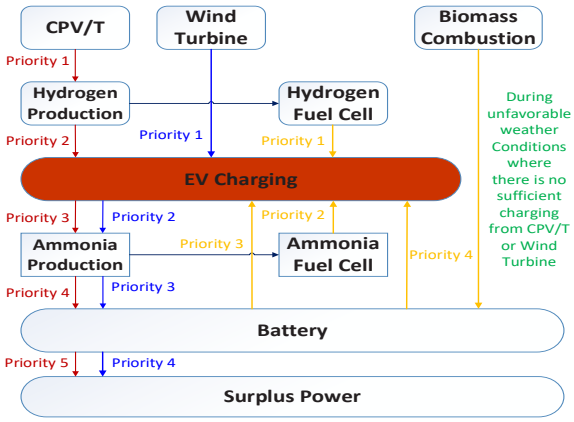

Figure 2: Priority hierarchy level

To simulate the produced and consumed energy by the proposed model in Qatar, a comprehensive model is developed in Excel using Visual Basic programming code considering the objective functions and constraints stated earlier in this report as well as developed formulas and algorithms based on priority hierarchy levels in Figure 2 to determine the hourly energy produced by the proposed subsystems and the hourly power consumption considering stochastic daily flow of electric vehicle to the proposed charging station for a complete year.

IV. Results and Discussions

To determine the optimal battery size for the system considering the additional power required to produce 200 kW from H_2 and NH_3 FCs, random battery capacities were simulated where 650 kWh battery size was determined as the optimal capacity for the battery system. Battery size reduction will increase the number of daily EVs not being charged by the charging station against desired while size increase is not feasible since power shortage is only faced through few months of a year as reflected in Figure 3 so the rest of the year the extra capacity will be ideal.

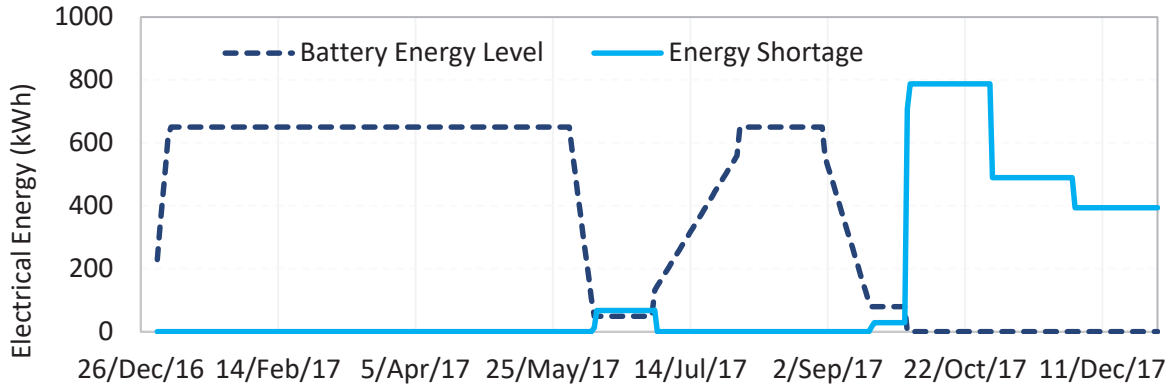

Figure 3: Yearly battery energy storage behavior in a Charging Station

However, the obtained results with the PV system showed % 9.51 of the total targeted annual EVs are not met as shown in Figure 4.

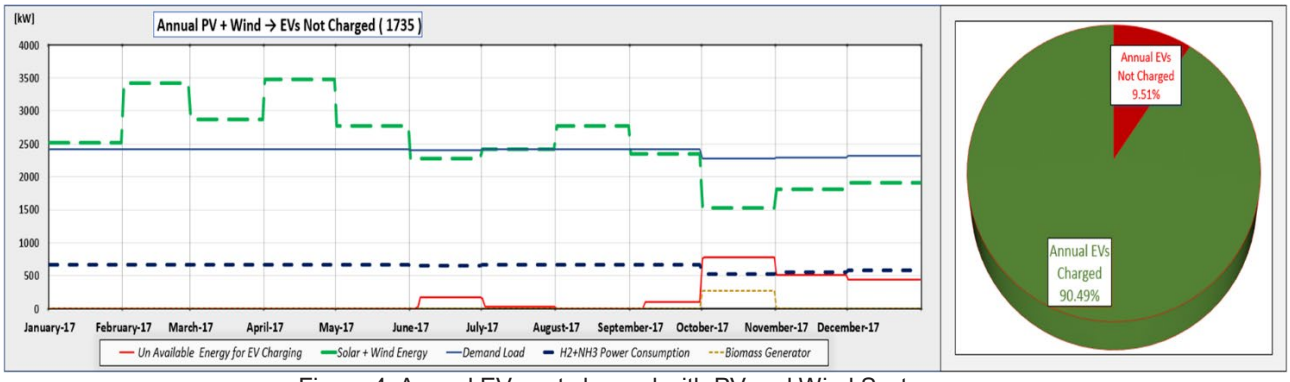

Figure 4: Annual EVs not charged with PV and Wind System

The simulation showed that replacing the PV system with CPV/T has improved the results and decreased the shortage down to % 5.78 as shown in Figure 5.

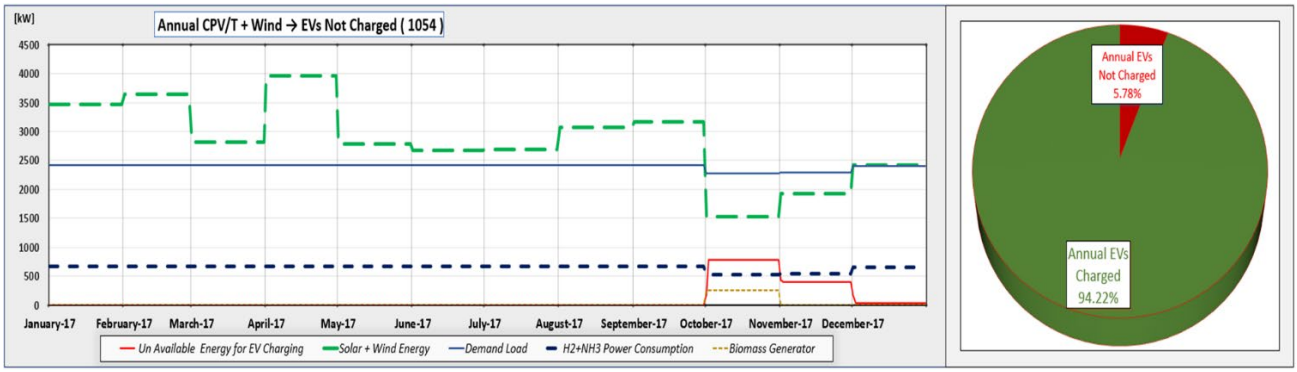

Figure 5: Annual EVs not charged with CPV/T and Wind System

To improve the results further, optimizing the operation of H_2 and NH_3 production during the last 3 months of a year where there is energy shortage was considered due to their high energy consumption. The results showed a further decrease in the shortage down to % 1.25 by shutting down H_2 and NH_3 production during the months those

months as shown in Figure 6.

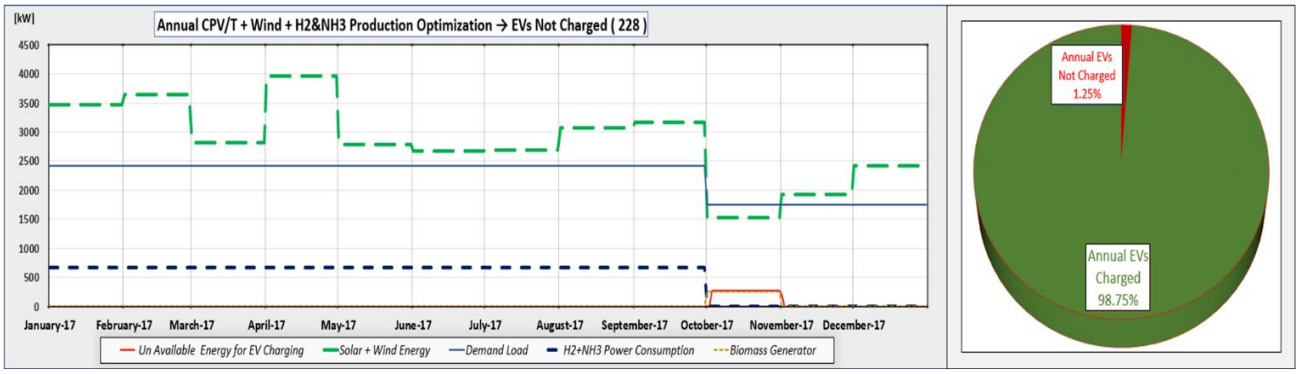

Figure 6: Annual EVs not charged with CPV/T + Wind System + H_2 and NH_3 production reduction

To eliminate the shortage completely, random biomass driven generator capacities were simulated and the results showed that operating 11 kW biomass-driven generator during the months of October and November shall eliminate the shortage with H_2 and NH_3 production operation enhancement where only %25 production reduction in the month of December is required to achieve the desired minimum target by a charging station in a year as shown in Figure 7.

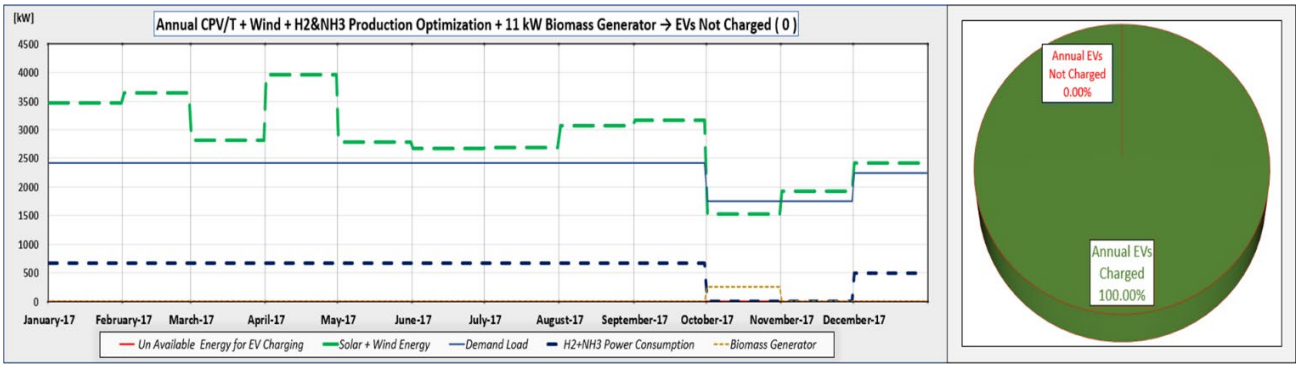

Figure 7: Annual EVs not charged with CPV/T + Wind System + H_2 and NH_3 production reduction + biomass generator

V. Conclusions

This study aims to model, simulate and optimize a renewable energy-based stand-alone electric car charging station in a country with harsh weather conditions such as Qatar by utilizing solar, wind and biomass sources along with electro-chemical and chemical energy storage systems. The results showed that minimum 50 EVs can be fast-charged daily with CPV/T system and 250 kW rated wind turbine along with 650 kWh Li-ion battery storage system and 11 kW biomass-driven generator with the total shutdown of H_2 and NH_3 production during the months of October and November and 25% shutdown during the month of December due to energy optimization within the charging station.

Acknowledgements

Authors acknowledge the support extended by both Hamad Bin Khalifa University (HBKU) and Qatar Electricity and Water Corporation (KAHRAMAA) and more specifically Engr. Mazan Al Masri to deliver this study.

References

CEIC, C. and E.I.C., 2019. Number of Registered Motor Vehicles in Qatar [WWW Document]. URL https://www.ceicdata.com/en/qatar/number-of-registered-motor-vehicles/number-of-registered-motor-vehicles (accessed 7.26.19).

Hukoomi, 2015. About Qatar 1–2.

Klein, 2018. EES: Engineering Equation Solver | F-Chart Software : Engineering Software.

Lokesh, B.T., Hui Min, J.T., 2017. A Framework for Electric Vehicle (EV) Charging in Singapore. Energy Procedia 143, 15–20. https://doi.org/10.1016/j.egypro.2017.12.641

Mehrjerdi, H., 2019. Off-grid solar powered charging station for electric and hydrogen vehicles including fuel cell and hydrogen storage. Int. J. Hydrogen Energy 44, 11574–11583. https://doi.org/10.1016/j.ijhydene.2019.03.158

PVsyst 6.7.8 software, 2018.

Qana, D., 2017. Qatar aims to reach 10% Green Cars by 2030. Lusailnews, Online Main Page_Diverse.

Sachin, K., 2019. 400 electric car charging stations by 2022 in Qatar. Penins. Qatar, Online Home_News_Qatar.

Sokorai, P., Fleischhacker, A., Lettner, G., Auer, H., 2018. Stochastic Modeling of the Charging Behavior of Electromobility. World Electr. Veh. J. 9, 44. https://doi.org/10.3390/wevj9030044

State of Qatar Goverment, P. and S.A., 2019. Monthly Figures on Total Population [WWW Document]. June. URL https://www.mdps.gov.qa/en/statistics1/Pages/population.aspx (accessed 7.26.19).

The Peninsula Qatar, 2017. Qatar aims to increase electric cars to 10%. Penins. Qatar, Online Home_News_Qatar.

Preliminary investigation of the experimental CO_2 Cascade Heat Pump System from exergetic point of view

[1*]Mansour Ndiaye, [2*]Onder Kizilkan, [1]Koshiro Uchi, [3]Petter Neksa, [1]Hiroshi Yamaguchi
[1] Department of Mechanical Engineering, Doshisha University, Kyo-Tanabeshi, Kyoto 610-0321, Japan
[2] Department of Mechanical Engineering, Faculty of Technology, Isparta University of Applied Sciences, Isparta, Turkey
[3] SINTEF Energy Research, Sem Sælands vei 11, 7034 Trondheim, Norway

* E-mails: onderkizilkan@isparta.edu.tr

Abstract
Thermodynamic properties and heat transfer characteristics of CO_2 is essential to investigate for new refrigeration systems. This study presents a preliminary investigation of a CO_2 cascade heat pump system that can achieve the ultra-low temperature below the CO_2 triple-point temperature of -56°C and thermal energy above 100°C. It is known that the system performance of this heat pump system can be optimized by an exergy analysis of the system. Exergy can be considered as an indicator to measure how nearly the efficiency of a process approaches the ideal condition. Therefore, this study has pointed out the specific weakness of the heat pump with an exact method over the system to evaluate the inefficiencies. The primary purpose of this study is to apply the conventional exergy analysis to the CO_2 cascade heat pump system in order to improve our understanding of the system components and to provide useful information for optimizing the heat pump performance. The results show that the exergy efficiency of the Cool Water Gas Cooler is very low in both the high-pressure and low-pressure sides. However, it has seen that the efficiency of the Cool Water Gas Cooler increase when the inlet water temperature increase. Therefore, the performance of this CO_2 cascade heat pump system can be optimized with an appropriate inlet water temperature of the cold water gas cooler.

Keywords: Carbon dioxide, Exergy Analysis, cascade heat pump, system performance

I. Introduction

Research and development of refrigeration systems using natural refrigerants as working fluid have increased. The use of natural refrigerants is on the rise, creating a new set of challenges for refrigeration and heat pump technologies. The physical properties of CO_2 are favorable for its use in heat pumps and refrigeration systems (Afroz et al., 2008; Neksa, 2002). As an ecological natural refrigerant, CO_2 has no ozone depletion potential (ODE), low global warming potential (GWP), no toxicity, no flammability, and excellent inertness. In terms of its acceptable heat transfer characteristics and substantial pressure drop, the thermodynamic and transport properties of CO_2 are also beneficial for its use as a refrigerant. Besides, it has a low critical temperature (31.1°C) and pressure (7.38 MPa). (Liao and Zhao, 2002). Because of these advantages, CO_2 is selected to be used as a natural refrigerant in heat pumps and refrigeration systems and the development and application of CO_2 in refrigeration and heat pump technologies has become a research focus because CO_2 is a safe, economical and environmentally sustainable refrigerant (Liu et al., 2017; 2018; Hua et al., 2009). For the last decades, several investigations have been performed about CO_2 based refrigeration and heat pump systems by numerous researchers. In these studies about refrigeration systems, the cooling temperatures were generally varied between -30 °C to 0 °C, accomplished by the evaporation process of CO_2. However, a refrigeration temperature of below -30°C and below is required for some essential industrial applications such as fishing industry (Japanese fishing vessels operate with freezers at -50 to -60°C) and biomedical engineering (very low temperature from -40 to -80°C is needed for storage of medical and biological samples in clinical, pharmaceutical and biotechnology applications).

Recently, the interest in achieving ultra-low temperature below the CO_2 triple point temperature has gained considerable importance. Yamaguchi et al. (2008), proposed a refrigeration method utilizing CO_2 as a working fluid that can achieve a cryogenic temperature below the CO_2 triple point by expanding CO_2 into the solid-gas two-phase flow (CO_2 flows in both liquid and gas state with some dry ice particles) through a horizontal circular tube. According to their results, the experimental system reached an ultra-low temperature which was below -56.6°C, promising a successful cryogenic refrigeration operation. In addition, it was found that the solid particles were uniformly distributed during the high flow velocity ranges of the CO_2. In contrary to this, for the slower flow velocity ranges of the CO_2, it was observed that there were CO_2 sedimentations inside the horizontal tube (dry ice particles), which was thought to be caused due to the growth of particle size because of the CO_2 particles' collision. They concluded that, in order to further understand the phenomenon in detail, more researches had to be performed to investigate the effects of the CO_2 temperature and pressure and expansion valve type.

Later on, Yamaguchi and Zhang (2009) have proposed a novel refrigeration system working with CO_2 as described in Fig. 1. The refrigeration system consists of a high-pressure cycle (HPC) and a low-pressure cycle (LPC) forming a cascade cycle. The low and high-pressure cycles are connected by a brine loop for transferring the rejected heat from the evaporator of HPC to the condenser of LPC. In the LPC, solid-gas two-phase of CO_2 is utilized in order to maintain an ultra-low temperature environment below -56.6 °C and thermal energy above 100°C. The HPC of the experimental set-up is designed to be comprised of five main components such as a compressor

(CP1), a hot water gas cooler (HGC1), a cool water gas cooler (CGC1), an expansion valve (EV1) and a brine evaporator (Evp1). The LPC which is connected to the HPC by brine fluid cycle is designed to be comprised of six main components such as a compressor (CP2), a hot water gas cooler (HGC2), a cold water gas cooler (CGC2), a brine gas cooler (BGC), an expansion valve (EV2) and an evaporator (Evp2). To optimize the performance of this heat pump system, exergy analysis is advocated.

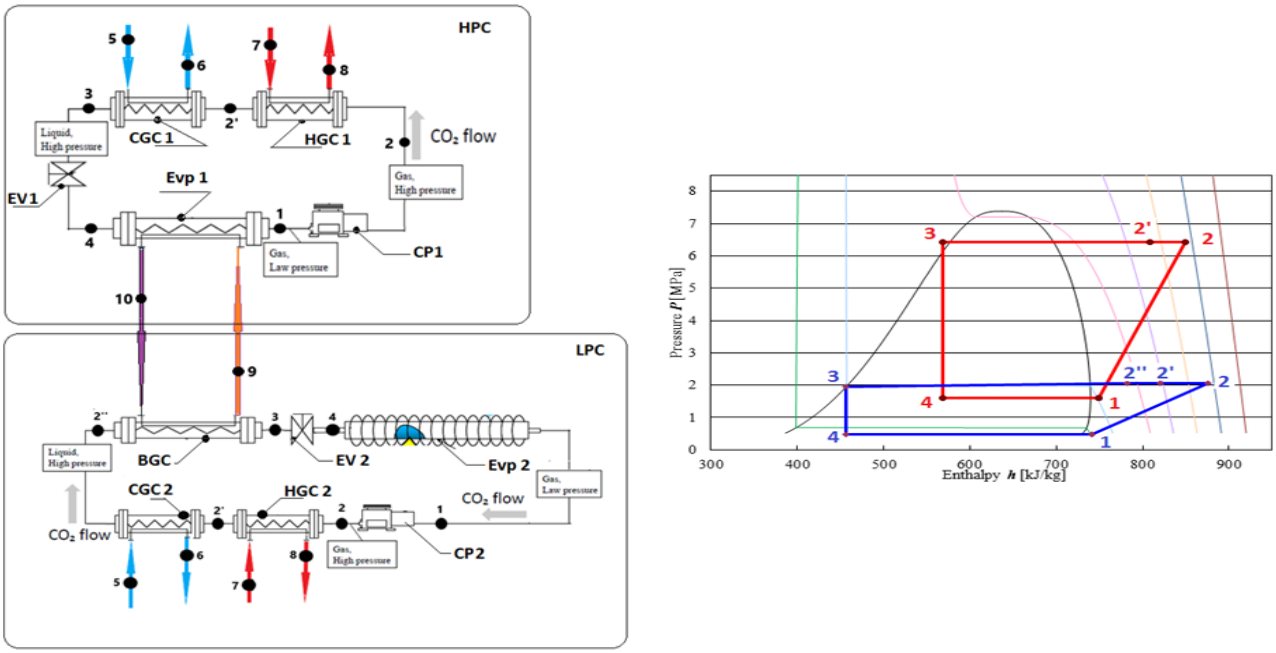

Fig. 1. CO_2 based experimental cascade heat pump system and P-h diagrams of HPC and LPC

In order to optimize and improve the system performance of the CO_2 cascade refrigeration system for ultra-low temperatures, exergy analysis is a very useful tool for determining the system failures, causes, locations, and magnitudes of process inefficiencies. Thus, in this study, a preliminary investigation of the experimental system is performed from the exergetic point of view. For this aim, energy and exergy analyses of the heat pump system are carried out using experimental data. The exergy destruction rates are calculated for all system elements with exergy efficiency. Finally, a parametric analysis was conducted to investigate the effect of inlet water temperature on exergy efficiency.

II. Methodology

This study proposes an exergy analysis of the components in both HPC and LPC. All components of the heat pump system are affected by exergy destruction, and the exergy destruction is the main reason imperfections of the overall system performance. The aim of the study presented here is, using exergy analysis, to systematically show where the losses in the heat pump occur, how large they are and, also how these losses affect the performance of the heat pump system. According to the second law of thermodynamics, exergy analysis equations are shown as following (Cengel and Boles):

$$\dot{E}_i = \dot{m}\left(h_i - h_0 - T_0(s_i - s_0)\right) \quad (1)$$

In the above equation, $\dot{E}_i$ is the specific exergy in any i^{th} state, T is the temperature, h and s are enthalpy and entropy, respectively, and subscript 0 represents reference state. The exergy destruction in each component of the HPC and LPC are calculated based on the equations specified below (Cengel and Boles, 2015; Moran et al., 2014):

HPC
Compressor:

$$\dot{E}_{d,CP1} = \dot{W}_{CP1} - (\dot{E}_2^H - \dot{E}_1^H) \quad (2)$$

Hot water Gas Cooler:

$$\dot{E}_{d,HGC1} = (\dot{E}_2^H - \dot{E}_{2'}^H) - (\dot{E}_8^H - \dot{E}_7^H) \quad (3)$$

Cool water Gas Cooler:

$$\dot{E}_{d,CGC1} = (\dot{E}_{2'}^H - \dot{E}_3^H) - (\dot{E}_6^H - \dot{E}_5^H) \quad (4)$$

Expansion Valve:

$$\dot{E}_{d,EV1} = \dot{E}_3^H - \dot{E}_4^H \quad (5)$$

Brine evaporator:

$$\dot{E}_{d,Evp1} = (\dot{E}_4^H - \dot{E}_1^H) - (\dot{E}_{10}^H - \dot{E}_9^H) \quad (6)$$

LPC
Compressor:

$$\dot{E}_{d,CP2} = \dot{W}_{CP2} - (\dot{E}_2^L - \dot{E}_1^L) \quad (7)$$

Hot water Gas Cooler:

$$\dot{E}_{d,HGC2} = (\dot{E}_2^L - \dot{E}_{2'}^L) - (\dot{E}_8^L - \dot{E}_7^L) \quad (8)$$

Cool water Gas Cooler:

$$\dot{E}_{d,CGC2} = (\dot{E}_{2'}^L - \dot{E}_{2''}^L) - (\dot{E}_6^L - \dot{E}_5^L) \quad (9)$$

Brine Gas Cooler:

$$\dot{E}_{d,BGC} = (\dot{E}_{2''}^L - \dot{E}_3^L) - (\dot{E}_{10}^L - \dot{E}_9^L) \quad (10)$$

Evaporator:

$$\dot{E}_{d,Evp2} = (\dot{E}_1^L - \dot{E}_4^L) + \dot{E}_{Qh} \quad (11)$$

$$\dot{E}_{Qh} = -\dot{Q}_h \left(1 - \frac{T_0}{T_s}\right) \quad (12)$$

The exergy destruction $\dot{E}_d$ and the exergy efficiency η_{ex} of the considered component are calculated respectively based on the following equations:

$$\dot{E}_d = \dot{E}_{in} - \dot{E}_{out} \quad (13)$$

$$\eta_{ex} = \frac{\dot{E}_{out}}{\dot{E}_{in}} \quad (14)$$

III. Results and Discussion

Conventional exergy analysis method was performed for the HPC and the LPC of the CO_2 cascade heat pump system. The results shown in Table 1 indicate the values of exergy input and output, the exergy destruction (irreversibility) and the exergy efficiency of each component in both HPC and LPC. In addition, the results are given in Fig. 2 comparatively.

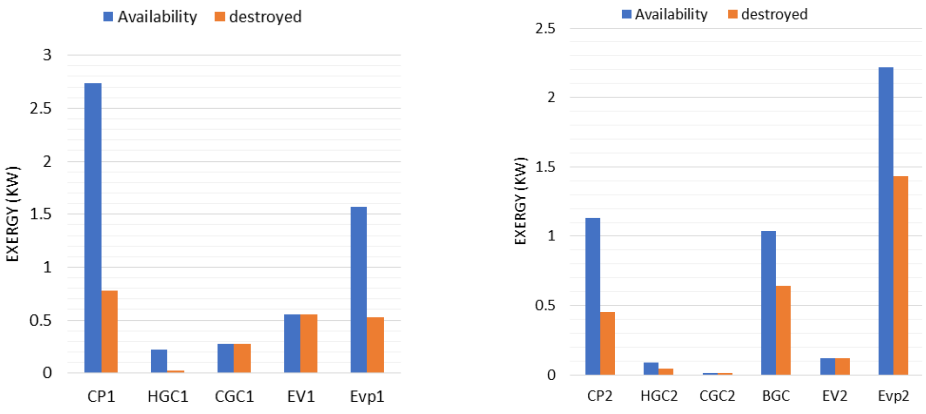

Fig. 2. Availability and exergy destruction within each component of a)HPC b) LPC

Table 1. Results of the exergy analyses of the HPC and LPC

HPC	$\dot{E}_{in}$ (kW)	$\dot{E}_{out}$(kW)	$\dot{E}_d$(kW)	η_x(%)	LPC	$\dot{E}_{in}$ (kW)	$\dot{E}_{out}$(kW)	$\dot{E}_d$(kW)	η_x(%)
CP1	2.74	1.96	0.780	71.5	CP2	1.133	0.679	0.454	60
HGC1	0.225	0.197	0.028	88	HGC2	0.090	0.047	0.043	52.2
CGD1	0.275	0.028	0.273	10.2	CGC2	0.016	0.002	0.014	8
					BGC	1.04	0.400	0.640	38.46
EV1	0.551	-	0.551	-	EV2	0.123	-	0.123	-
Evp1	1.572	1.04	0.532	66.15	Evp2	2.216	0.785	1.431	35.42

According to the results, the exergy efficiency of the Cool Water Gas Cooler is very low in both the high-pressure and low-pressure sides. Therefore, this low efficiency decreases the performance of the heat pump system. However, this low performance can be improved by optimizing the exergy efficiency of the cold water gas cooler in both HPC and LPC. Fig. 3. As shown in Fig. 3a, the exergy efficiency of the CGC1 increases when the inlet water temperature increases. This result is useful to optimize the system performance of this heat pump because when the exergy efficiency of the CGC1 increase, the exergy efficiency of the HPS increase as well (see Fig.3b). In fact, in many industrial applications, water at the temperature between the ranges of 25 to 35°C is available. Therefore, this available water can be used in the cold water gas cooler of the HPC and the LPC to optimize the heat pump performance.

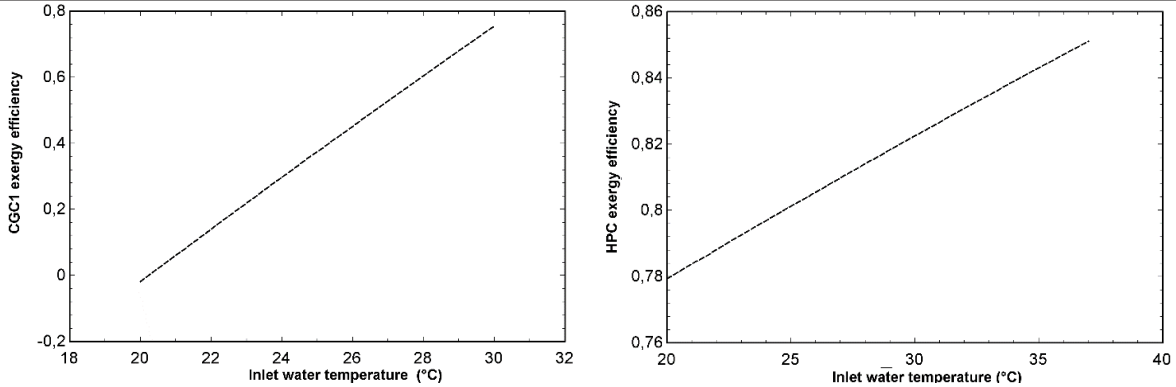

Fig.3. The variation of exergy efficiency with inlet water temperature for a) CGC1 b) HPC

Besides, the exergy efficiency of each system component are given in Fig. 4. The results show that the exergy efficiency of some components in the low-pressure side particularly the evaporator and the brine gas cooler are quite low. Therefore, to improve the system performance, more study should be performed in order to reduce the exergy loss within the cold water gas cooler in both high-pressure and low-pressure side, the brine gas cooler and the evaporator in the low-pressure side. Reducing that part of the exergy destroyed within those components can significantly increase the efficiency of this CO_2 heat pump system.

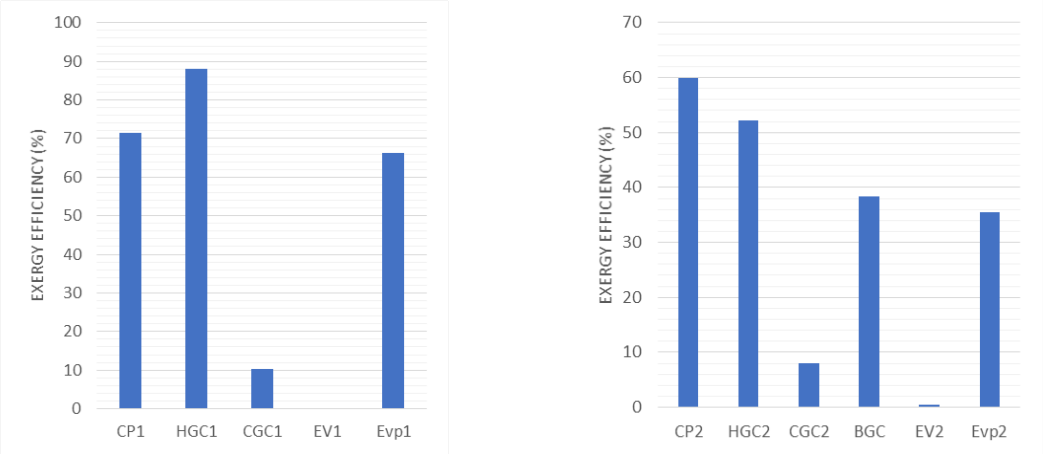

Fig.4. The exergy efficiency of each component of a) HPC b) LPC

References

Afroz, H. M. M., Miyara, A., Tsubaki, K., 2008. Heat transfer coefficients and pressure drops during in-tube condensation of CO_2 -DME mixture refrigerant. International Journal of Refrigeration 31, 1458-1466.

Liao S.M., Zhao, T.S., 2002. An experimental investigation of convection heat transfer to supercritical carbon dioxide in miniature tubes. International Journal of Heat Mass Transfer 45, 5025-5034.

Neksa, P., 2002. CO_2 heat pump systems. International Journal of Refrigeration 25, 421–427.

Liu, F., Zhu, W., Cai, Y., Eckhard, A.G., Ren, J., Lei, Y., 2017. Experimental performance study on a dual-mode CO_2 heat pump system with thermal storage. Applied Thermal Engineering 115, 393–405.

Liu, F., Zhu, W., Zhao, J., 2018. Model-based dynamic optimal control of a CO_2 heat pump coupled with hot and cold thermal storages. Applied Thermal Engineering 128, 1116–1125.

Hua, T., Zhao, Y., MinXia, L., YiTai, M., 2009. Research and application of CO_2 refrigeration and heat pump cycle. Sci China Ser E-Tech Sci 52(6), 1563-1575.

Yamaguchi, H., Zhang, X.R., Fujima, K., 2008. Basic study on new cryogenic refrigeration using CO_2 solid-gas two-phase flow. International Journal of Refrigeration 31, 404-410.

Yamaguchi, H., Zhang, X.R., 2009. A novel CO_2 refrigeration system achieved by CO_2 solid-gas two-phase fluid and its basic study on system performance. International Journal of Refrigeration 32, 1683-1693.

Cengel, Y.A., Boles, M.A., 2015. Thermodynamics, an engineering approach, 8th edition. McGraw-Hill Education, New York, NY.

Moran, M.J., Shapiro, H.N., Boettner, D.D., Bailey, M.B., 2014. Fundamentals of engineering thermodynamics, 8th edition. John Wiley & Sons, Hoboken, NJ.

CSP-hybrid staged-gasification of solid waste to produce hydrogen: ASPEN Plus simulation

[1]Shahid H. Ansari, [1]Baraka C Sempuga, [1]Diane Hildedbrandt, [1*]Xinying liu,
[1] Institute for the Development of Energy for African Sustainability (IDEAS), University of South Africa, 5th floor Phapha building, Science campus, Florida, Johannesburg, South Africa

* e-mail: liux@unisa.ac.za

Abstract
Hydrogen (H_2) production from solid waste through concentrated solar power (CSP)-hybrid staged-gasification is an attractive technology because of environmental benefits and economic issues. In this study, the effects of gasification temperature and steam to biomass ratio on yield of syngas are investigated to predict the optimum operating conditions with maximum H_2 productivity. ASPEN Plus® is used to develop a simple model for gasification followed by reforming of syngas and water gas shift (WGS) reaction. Heat load of a gasifier is balanced by injection of solar energy while heat load of a reformer is balanced by combustion of produced syngas. Main objective of this study is to compare the benefits of reforming of syngas, WGS reaction and incorporation of CSP. The feed of 1000 kg/h feedstock is gasified at 700-900°C @ 1 bar_a. Simulation results showed that with increase in temperature of the gasifier and steam flow rate to the gasifier significantly increased the carbon conversion, yield of hydrogen and yield of syngas. Simulation results revealed that H_2 production efficiency with CSP is around 12.5 kmol/MW_{th} for PW as a feedstock while it 13.2 kmol/MW_{th} in case of MSW. It is noted that adding CSP into the system can boost H_2 production up to 50% to 146 g/kg of wet pinewood sawdust (PW) as a feedstock while 61% to 224 g/kg of municipal solid waste (MSW). Simulation results from all the cases indicate that CSP-hybrid staged-gasification is a promising alternative process to produce secondary fuel in the form of H_2.

Keywords: Solid waste, Cocentrated solar power, Gasification, Reforming, Water gas shift reactions, Hydrogen production efficiency

I. Introduction

Solid waste (PW and MSW) has potential to produce H_2 via. staged-gasification process(Gu et al., 2019) which is a thermochemical process to convert solid waste into syngas with various gasifying agents like carbon dioxide (CO_2), oxygen (O_2), steam (H_2O) or air(Meng et al., 2019; Sadhwani et al., 2018), followed by steam reforming and/or WGS reaction. There has been some experimental study to produce H_2 via. gasification. The H_2 yield is in the range of 30-165 gH_2/kg of wet biomass. The yield of syngas per unit biomass can be increased by using pure H_2O or pure O_2 as a gasifying agent(AlNouss et al., 2020a). Steam gasification has higher H_2 concentration, higher product gas efficiency and higher heating value per unit of biomass as compared to air or O_2 gasification (Samimi et al., 2020; Singh Siwal et al., 2020). However, steam gasification requires a significant amount of external heat to carry out a series of endothermic reactions as compared to air or O_2 gasification(Hu et al., 2020). CSP can play a key role to balance the enthalpy of reaction of gasification process and the entire biomass can be converted into H_2 and CO (Milani et al., 2017). By combining CSP and biomass gasification, it shows great potential to convert solar energy into H_2.

Because gasification is a complex process (Al-Zareer et al., 2018) simulation models are essential to investigate the effects of operating conditions on the performance of gasification and to predict process behavior. It will save time and money to conduct a series of costly experiments and allow us to study different scenarios to optimize the process. Many researchers have developed the simplest possible models in ASPEN Plus®(Acar and Böke, 2019; Li et al., 2019; Tavares et al., 2020; Terrell and Theegala, 2019). These models have considered the complex chemical reactions, characteristics of the reactor and important physical characteristics of feedstock. Because of extensive range of published literature, simulation-based study has been applied to design a hybrid biomass gasification for H_2 production. Such hybrid process provides an opportunity to convert solar energy to H_2(Chen et al., 2019; Zhao et al., 2019). The proposed system has considered of two distinct section to balance the heat load: (1) the injection of CSP-thermal energy to the gasifier and (2) the addition of heat of combustion of a fraction of produced syngas to the reforming section. However, main technical challenges with gasification are endothermic gasification reactions, higher tar in syngas and lower H_2 contents in syngas.

The H_2 contents can be boosted by adding reforming or WGS reaction following by the gasification. The aim of this study is to investigate gasification at lower temperature which will ease the injection of CSP as an external thermal energy input to the gasifier unit. The significance of present study is its focus on utilization of renewable energy resource like solar energy to increase the H_2 production efficiency. In this study, the effect of temperature, steam to biomass (S/B) ratio and effects of CSP on H_2 production efficiency has been investigated in terms of yield of syngas, H_2/CO ratio, CO/CO_2 ratio, higher heating value of syngas, H_2 boost up by CSP and H_2 production efficiency in terms of kmol/$MW_{solar\ thermal\ energy}$. The best operating parameters for the proposed system have been determined and compared with the experimental results presented by other researchers to find out a sustainable pathway to produce H_2 from solar and solid waste resources via. CSP-hybrid staged-gasification approach.

II. System Model Description

The PW and MSW were selected as the feedstock to produce H_2. ASPEN Plus® was used to develop a simple model and generate simulation results for the steam gasification. The anticipated findings in this study are in agreement with published work done by other researchers(Cao et al., 2019; Gao et al., 2009; Terrell and Theegala, 2019). A simple model was developed on the basis of Gibbs free energy minimization for gasification and reforming followed by equilibrium reactor for WGS reaction(Han et al., 2017; Tavares et al., 2020) as described in Figure 1.

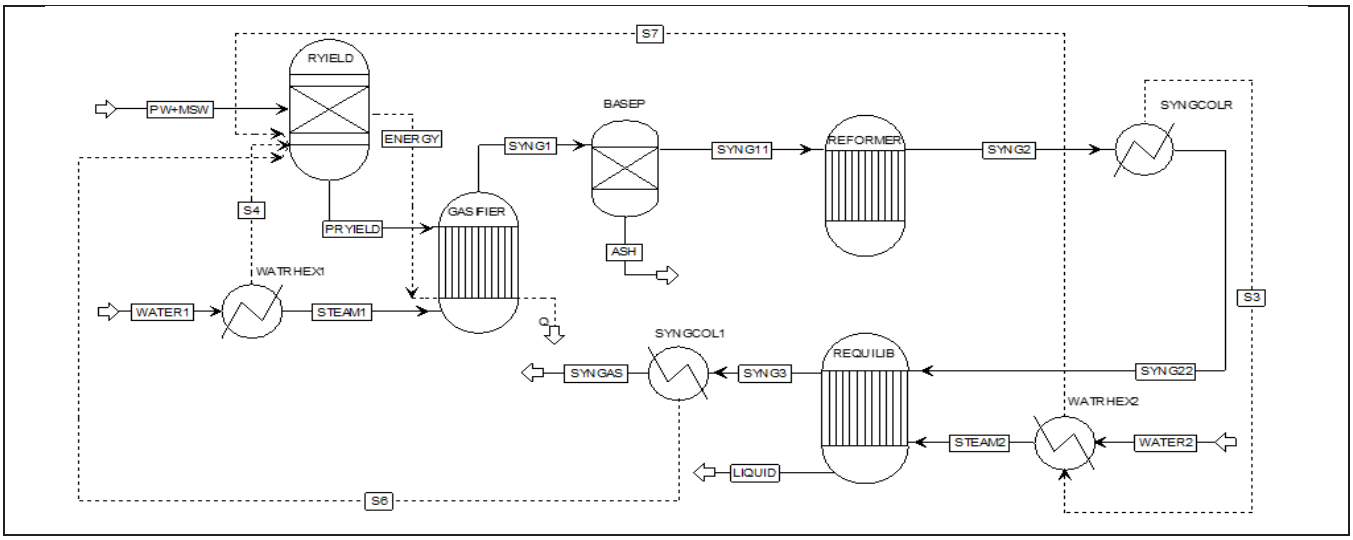

Fig. 1: Process flowsheet for the staged-gasification of pinewood sawdust or municipal solid waste

In the RGibbs block, the gasification temperature was varied from 700 to 900℃ with the increment of 50℃ and pressure of 1 bar_a. In the reformer section, reforming temperature was kept constant at 900℃ and 1 bar_a. While in REquil block, temperature was kept at 200℃ and 1 bar_a for WGS reaction. 1000 kg/h feedstock was fed to the RYield reactor at 25℃ and 1 bar_a. The water was fed to the heat exchanger at 25℃ and 1 bar_a to generate steam at 100℃ and 1 bar_a sent to the RGibbs reactor as gasification agent. The steam flowrate fed to the gasifier was set to the minimum value so that no solid carbon is formed in the gasifier at different gasification temperature. The heat needed by the gasifier was supplied by CSP-solar-thermal energy. When no CSP is available, then a fraction of syngas is combusted to produce heat to meet the heat load of the gasifier. The produced syngas was cleaned in the cyclone separator to remove out the ash and cleaned syngas was further reformed to increase the H_2 content in the syngas. The reformed syngas was followed by WGS reaction to produce H_2.

III. Results and discussions

The obtained yield of gH_2 per kg of wet biomass from gasification of PW and MSW was compared with literature as presented in Table 1. The optimum H_2 production at 800℃ is 98 gH_2 per kg of wet biomass which is higher than as reported by other reseachers. Similarly, the yield of H_2 from gasification of MSW at 800℃ is 140 gH_2 per kg of wet MSW which is way better than as reported by experimental work. After steam gasification and reforming of syngas, the HHV has slightly increased from 10.80 to 12.50 MJ/Nm^3 at 700-900℃ in agreement with experimental data(Hernández et al., 2012). Although this trend is not reported by other authors(Shayan et al., 2018). In the literature, the higher heating value of produced syngas from solid waste gasification with different gasifying agents is presented in Table 2.

Table 1. H_2 yield per kg of biomass on wet basis

Feedstocks	gH_2/kg biomass	Reference
Pinewood sawdust	*80*	(Gao et al., 2009)
Municipal solid waste	*32*	(Chen et al., 2020)
Pinewood sawdust without CSP	*98*	*This study*
Municipal solid waste without CSP	*140*	*This study*
Pinewood sawdust with CSP	*146*	*This study*
Municipal solid waste with CSP	*224*	*This study*

Table 2. Higher heating value of syngas produced from solid waste gasification with different gasifying agents

Feedstocks	Gasifying agent	HHV (MJ/Nm^3)	Reference
PW	*Oxygen and steam*	*9-11*	*(Lv et al., 2007)*
MSW	*Steam and air*	*9-13*	*(Chen et al., 2020)*
Combined MSW and biomass	*Steam*	*6-10*	*(Cao et al., 2019)*
PW	*Steam*	*11-13*	*This study*
MSW	*Steam*	*12-13*	*This study*

Effect of Temperature, CSP and steam to biomass ratio on H_2 productivity

Figure 2 (a-c) illustrates the effect of gasification temperature and S/B ratio on the yield of syngas and composition of syngas from gasification of PW with S/B ratio of 0.15 to 0.39 (w/w). The S/B ratio is calculated as steam flowrate (kg/h) fed to the gasifier divided by the biomass flowrate introduced into the gasifier in terms of kg/h. Figure 2 (d) illustrates the effect of gasification temperature on the higher heating value (HHV) of syngas. Figure 2 (e-f) describes the effect of adding CSP-thermal energy on H_2 productivity, H_2 boost up (in %) and H_2 production efficiency ($kmol/MW_{solar\ thermal\ heat}$) with respect to temperature in the gasifier. Herein, the H_2 productivity is calculated as amount of H_2 incraesed by adding CSP-thermal energy into the gasifier. H_2 boost up (in %) is calculated as the percent increase in H_2 with addition of solar-thermal energy to the gasifier. While H_2 production efficiency is calculated as amount of H_2 produced with CSP divided by the heat load of the gasifier.

From figure 2(a), it can be seen that H_2 concentration slightly decreasing with temperature while CO concentration increasing with temperature. Similarly, the conecentration of CO_2 decreasing at the higher temperature. After reforming of syngas, the concentration of CH_4 drops down to the minimum value. But the concentration of CO has increased with reforming of methane. The concentration of H_2 was maximized by the WGS reaction with addition of more water. Figure 2(b) shows the effect of gasification temperature on molar ratio of H_2/CO and CO/CO_2. Gasification with reforming and WGS reaction, the H_2/CO molar ratio can be increased up to 73.0 while the CO/CO_2 molar ratio can be decreased up to 0.03. The CO/CO_2 ratio increases with temperature because CO_2 content decreases with higher temperature. Adding reforming and WGS reaction can boost up the H_2 production. By incorporating CSP-thermal energy to the gasifier, 30-35% of syngas can be saved(Ansari et al., 2020). It is clearly shown in the figure 2 (e-f) that when no CSP is available, then maximum amount of H_2 is around 49.0 kmol/h at 700-900℃. When CSP is available, the produced amount of H_2 can reached to 73.0 kmol/h at same temperature range. It is clear that adding CSP thermal energy into the gasifier can increase the H_2 productivity up to 24.0 kmol/h. The proposed system shows that an opportunity to convert solar energy into H_2 fuel. It is noted that adding CSP into the system can boost H_2 production up to 50% at 700-900℃. Results showed that with increasing temperature H_2 productivity has decreased from value of 13.30 to 11.70 kmol/h. H_2 productivity with reforming and WGS reaction has slightly decreased from 24.90 to 23.0 at 700-900℃. The maximum H_2 production efficiency with reforming and WGS reaction is 12.50 $kmol/MW_{th}$, which indicating that 750℃ is best gasification temperature for this operation.

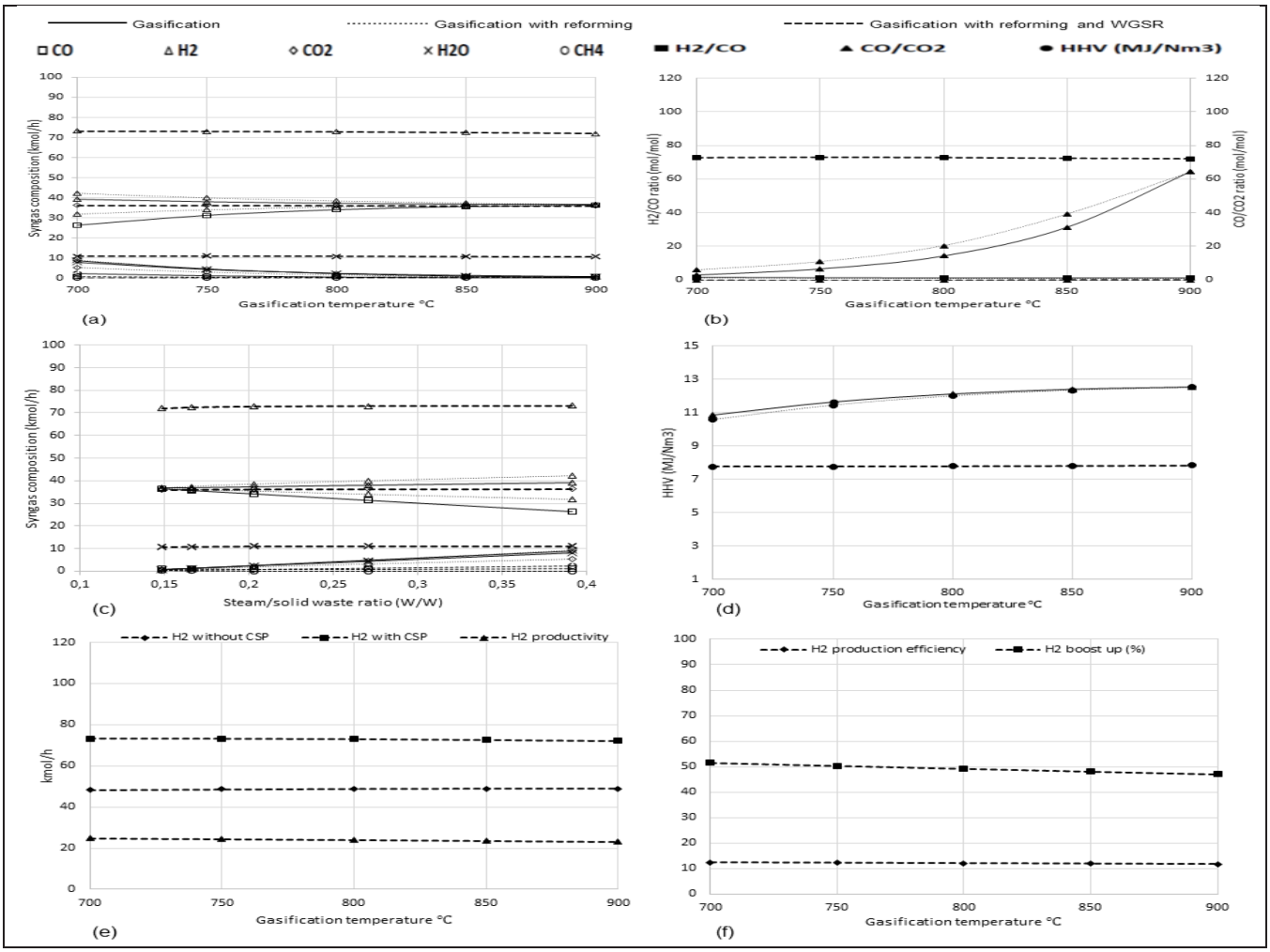

Fig. 2: Simulation results from steam gasification of PW (a) the effect of temperature on the yield of syngas and composition of syngas (b) the effect of temperature on the H_2/CO molar ratio and CO/CO_2 molar ratio (c) the effect of S/B ratio on the yield of syngas and composition of syngas (d) the effect of temperature on the HHV of syngas (e) the effect of temperature on the yield of H_2 without CSP, H_2 with CSP and H_2 productivity (f) the effect of temperature on H_2 production efficiency and H_2 boost up

It is shown that when no CSP is available, maximum amount of H_2 is 70.0 kmol/h in case of MSW. When CSP is available, the produced amount of H_2 can reached to 112.0 kmol/h. It is convincing that adding CSP into the gasifier can increase H_2 productivity up to 42.0 kmol/h. It is noted that adding CSP can boost H_2 production up to 61%. Results showed that with increasing temperature H_2 productivity has slightly decreased from value of 13.30 to 11.70 kmol/h. The H_2 productivity with reforming and WGSR has slightly decreased from 42.60 to 39.40. The maximum H_2 production efficiency with reforming and WGS reaction is 13.20 kmol/MW_{th}. It is conluded that both MSW and PW has potential to produce fuel gas to be used in the existing combustion engines without any modification.

IV. Conclusions

In conclusion, a new configuration of a CSP-hybrid solid waste gasification is proposed to produce clean and green H_2 from biomass and solar energy resources. This study showed that the H_2 production efficiency is around 13 kmol/MW_{th}. This number shows that a good potential to convert solar into H_2 fuel. It is noted that adding CSP into the system can boost H_2 production up to 50% for PW as a feedstock while 61% in case of MSW. From solid waste gasification of 100% MSW as compared to 100% PW, the concentration of H_2 increased from 73.0 to 112.0 kmol/h while same trends for CO_2 and CH_4. As the limitation of the available CSP technology, 700–800°C might be the best temperature for the CSP-hybrid solid waste-gasification. It can be observed that the present model shows acceptable values of H_2 production as found in the experiments. It shows that both PW and MSW has an acceptable potential to produce H_2 in order to be used in combustion engines. As predicted that there is no significant increase in HHV of H_2 enriched syngas. Follow up studies can analyze other operating conditions like catalyst and residence time to improve H_2 production efficiency. The results are promising, which makes the hybrid CSP steam gasification process a good option to convert renewables resources (biomass and solar) into H_2 fuel. This study provides a parametric analysis to transform biomass and solar into valuable and carbon-neutral alternative fuels. Steam gasification with WGS reaction is a promising technology to produce H_2 enriched syngas as an alternative fuel.

Acknowledgements

The authors would like to acknowledge the University of South Africa (UNISA) and the financial support from National Research Foundation (NRF) with grant number 113648.

References

Acar, M.C., Böke, Y.E., 2019. Simulation of biomass gasification in a BFBG using chemical equilibrium model and restricted chemical equilibrium method. Biomass and Bioenergy 125, 131–138. https://doi.org/10.1016/j.biombioe.2019.04.012

AlNouss, A., McKay, G., Al-Ansari, T., 2020a. A comparison of steam and oxygen fed biomass gasification through a techno-economic-environmental study. Energy Convers. Manag. 208, 112612. https://doi.org/10.1016/j.enconman.2020.112612

Ansari, S.H., Ahmed, A., Razzaq, A., Hildebrandt, D., Liu, X., Park, Y.K., 2020. Incorporation of solar-thermal energy into a gasification process to co-produce bio-fertilizer and power. Environ. Pollut. 266, 115103. https://doi.org/10.1016/j.envpol.2020.115103

Cao, Y., Fu, L., Mofrad, A., 2019. Combined-gasification of biomass and municipal solid waste in a fluidized bed gasifier. J. Energy Inst. 92, 1683–1688. https://doi.org/10.1016/j.joei.2019.01.006

Chen, G., Jamro, I.A., Samo, S.R., Wenga, T., Baloch, H.A., Yan, B., Ma, W., 2020. Hydrogen-rich syngas production from municipal solid waste gasification through the application of central composite design: An optimization study. Int. J. Hydrogen Energy 45, 33260–33273. https://doi.org/10.1016/j.ijhydene.2020.09.118

Gao, N., Li, A., Quan, C., 2009. A novel reforming method for hydrogen production from biomass steam gasification. Bioresour. Technol. 100, 4271–4277. https://doi.org/10.1016/j.biortech.2009.03.045

Han, J., Liang, Y., Hu, J., Qin, L., Street, J., Lu, Y., Yu, F., 2017. Modeling downdraft biomass gasification process by restricting chemical reaction equilibrium with Aspen Plus. Energy Convers. Manag. 153, 641–648. https://doi.org/10.1016/j.enconman.2017.10.030

Hernández, J.J., Aranda, G., Barba, J., Mendoza, J.M., 2012. Effect of steam content in the air-steam flow on biomass entrained flow gasification. Fuel Process. Technol. 99, 43–55. https://doi.org/10.1016/j.fuproc.2012.01.030

Hu, Y., Cheng, Q., Wang, Y., Guo, P., Wang, Z., Liu, H., Akbari, A., 2020. Investigation of Biomass Gasification Potential in Syngas Production: Characteristics of Dried Biomass Gasification Using Steam as the Gasification Agent. Energy and Fuels 34, 1033–1040. https://doi.org/10.1021/acs.energyfuels.9b02701

Li, Q., Song, G., Xiao, J., Sun, T., Yang, K., 2019. Exergy analysis of biomass staged-gasification for hydrogen-rich syngas. Int. J. Hydrogen Energy 44, 2569–2579. https://doi.org/10.1016/J.IJHYDENE.2018.11.227

Lv, P., Yuan, Z., Ma, L., Wu, C., Chen, Y., Zhu, J., 2007. Hydrogen-rich gas production from biomass air and oxygen/steam gasification in a downdraft gasifier. Renew. Energy 32, 2173–2185. https://doi.org/10.1016/j.renene.2006.11.010

Meng, F., Ma, Q., Wang, H., Liu, Y., Wang, D., 2019. Effect of gasifying agents on sawdust gasification in a novel pilot scale bubbling fluidized bed system. Fuel 249, 112–118. https://doi.org/10.1016/j.fuel.2019.03.107

Milani, R., Szklo, A., Hoffmann, B.S., 2017. Hybridization of concentrated solar power with biomass gasification in Brazil's semiarid region. Energy Convers. Manag. 143, 522–537. https://doi.org/10.1016/j.enconman.2017.04.015

Samimi, F., Marzoughi, T., Rahimpour, M.R., 2020. Energy and exergy analysis and optimization of biomass gasification process for hydrogen production (based on air, steam and air/steam gasifying agents). Int. J. Hydrogen Energy 45, 33185–33197. https://doi.org/10.1016/j.ijhydene.2020.09.131

Shayan, E., Zare, V., Mirzaee, I., 2018. Hydrogen production from biomass gasification; a theoretical comparison of using different gasification agents. Energy Convers. Manag. 159, 30–41. https://doi.org/10.1016/J.ENCONMAN.2017.12.096

Tavares, R., Monteiro, E., Tabet, F., Rouboa, A., 2020. Numerical investigation of optimum operating conditions for syngas and hydrogen production from biomass gasification using Aspen Plus. Renew. Energy 146, 1309–1314. https://doi.org/10.1016/j.renene.2019.07.051

Terrell, E., Theegala, C.S., 2019. Thermodynamic simulation of syngas production through combined biomass gasification and methane reformation. Sustain. Energy Fuels 3, 1562–1572. https://doi.org/10.1039/c8se00638e

Development of an Assessment Methodology for Smart Cities: Canadian Cities as Case Studies

[1] Azzam Abu-Rayash and [1,2] Ibrahim Dincer
[1] Faculty of Engineering and Applied Science, University of Ontario Institute of Technology, 2000 Simcoe Street North, Oshawa, Ontario, L1H 7K4, Canada.
[2] Yildiz Technical University, Faculty of Mechanical Engineering, Istanbul, 34349 Turkey
Corresponding author email: Azzam.abu-rayash@uoit.ca

Abstract
The urge to develop and innovate net zero energy systems for smart city applications has never been more pressing. As the world population is rapidly growing, the global energy demand expands exponentially. The setback with higher energy consumption is the substantial greenhouse gas emissions associated with using fossil-based fuels, which make up the primary energy sources in the world today. The concept of net zero energy has been investigated for various applications including homes, farms, and communities. However, the concept of net zero energy city is seldom explored in the literature, making this paper more valuable and addressing an important research gap. This paper introduces a novel concept to assess cities for their smartness. A smart city is characterized by assessing the economy, environment, society, governance, energy, infrastructure and transportation aspects. Each domain is evaluated by assessing a number of key parameters that reflect the condition of that domain in any given city. All indicators can be numerically evaluated and assessed, which gives this approach more credibility and accuracy. Toronto achieved the highest in smart governance and smart energy with 92.7% and 77% respectively; while it was the lowest in the smart environment with 71.6%. On the other hand, Montreal's smart governance and smart energy were the second highest with 90.1% and 75.6% respectively. Toronto and Montreal achieved the highest smart governance while Vancouver scored the most in smart infrastructure. The economies throughout the different cities need significant improvements, while the smart society domain is also open for further improvement. The energy domain needs substantial improvements for these cities to be characterized as smart cities.

Keywords: Smart Cities, Energy Sustainability, Energy Systems, Clean Fuels, Energy Storage

1. Introduction
Cities are important and critical metropolitan hubs that drive the economic, social and environmental aspects of societies. Understanding the various aspects that could transform and assess our cities for their smartness therefore becomes critical. Metropolitan areas act as a hub for significant segments of society to come close together and initiate civilizations. Despite the fact that these metropolitan areas or cities only occupy less than 5% of the earth's land area, they consume more than 75% of its natural resources and emit 60-80% of the global greenhouse gases (GHG) (Musango et al., 2017). It is evident that the world population is experiencing significant increase, which demands special attention to cities development in order to be able to handle these dynamic changes. Giffinger et al. (2007) developed a model to assess smart cities by considering six characteristics, 31 factors and 74 indicators; providing an integrated assessment that attempted to include the opinions of decision makers. Lund et al. (2016) investigated optimal solutions for integrating renewable energy. They used an integrated cross-sector approach to argue the most efficient and least-cost storage options for the entire renewable energy system. Dincer and Acar (2017) investigated the smart energy systems and identify the expectations of such systems to be exergetically sound, energetically secure, environmentally benign, economically feasible, commercially viable, socially acceptable, integrated, and reliable. Finally, Victoria et al. (2018) developed a holistic framework for assessing and interrelating smart city projects and urban challenges in a specific region and for evaluating the projects' potential to generate effects. This paper aims to develop a conceptual model of a net zero energy smart city that can realistically be implemented. The specific objectives of this thesis are as follows: to develop a novel methodology to characterize smart cities and assess their smart performance based on seven main domains and to develop a comprehensive smart city concept by integrating various domains

2. Model Development and Methodology
Past research was limited to introducing aspects to smart cities and evaluating local and regional projects based on smart cities objectives. This research expands on the aspects of a smart city by including critical components such as energy and resources as part of the assessment. These aspects and their consequent indicators are assessed and categorized into five levels of increasing smartness. Together, they form the smart city matrix. As cities integrate more smart initiatives, they transition from level 1 to level 5. The aspects considered in the smart city concept for this thesis are comprised of seven main sub-indexes. Each aspect constitutes a number of indicators that can be quantified for further analysis using this methodology. These aspects are described in detail in Figure 1 and are as follows:

- Smart Environment
- Smart Economy
- Smart Society
- Smart Governance
- Smart Energy
- Smart Infrastructure
- Smart Transportation

These sub-indexes and corresponding indicators will be used to assess cities for their smartness. The Smart City Index (SCI) is the metric used to assess cities in their smartness. This index is composed of seven main domains including the smart environment index, smart economy index, smart society index, smart governance index, smart energy index, smart infrastructure index, and transportation index. These indexes are further assessed with specific indicators. This comprehensive concept is illustrated further in Figure 1. It is critical for a smart city to be environmentally benign and inclusive. The domains and indicators selected are aligned with the UN's SDGs as well as the WCCD. For instance, SDG 1 is no poverty, and for this model, poverty rate is evaluated as a percentage. Furthermore, a smart economy takes into account the GDP per capita, R&D expenditure, unemployment rate and the Gini coefficient. A smart society is characterized based on the educational level, poverty rate, gender equality, and the healthcare index within the society.

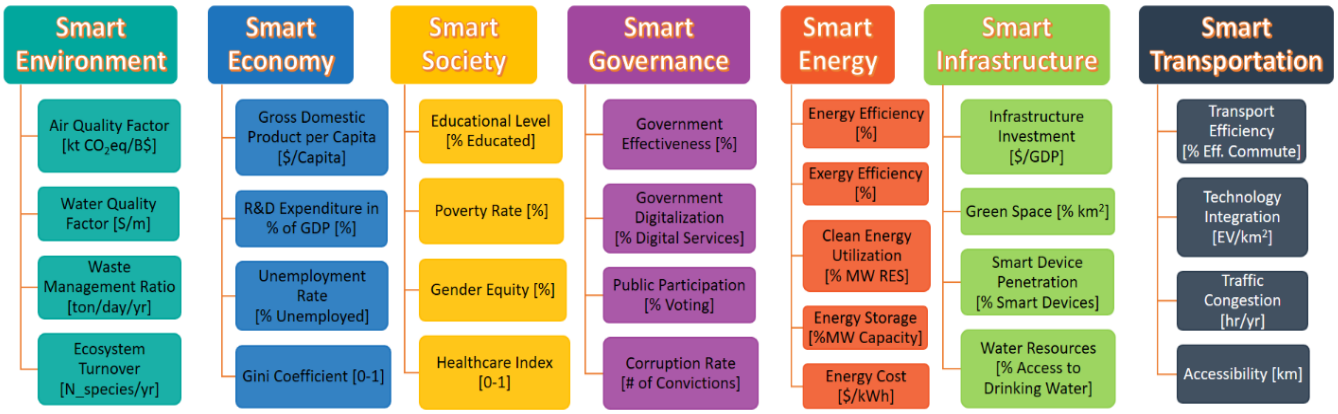

Fig. 1 Aspects of smart cities including main indicators for each sub-index

Smart governance is assessed based on government effectiveness, digitalization, public participation and the corruption rate within the government. Smart energy takes into consideration the energy efficiency of the systems, utilization of clean energy, energy storage, and the overall cost of energy. As for the rest of the domains, further details about their characterization and assessment is elaborated later in their respective sections. Furthermore, the economic aspect must be both viable as well as inclusive, allowing for growth and economic prosperity. Smart cities without smart people and high level of innovation, creativity and education is virtually impossible. Moreover, smart cities have laws, bylaws and written policies to ensure the longevity and sustainability of measure that the city takes regardless of political turnover. The energy sector for a smart city must rely on clean, abundant and reliable energy sources coupled with efficient, integrated and multigenerational systems to provide dependable and reliable services. Finally, a smart city is one with efficient mobility and reliable transportation. It is important to mention that such an assessment is complex and integrated various disciplines together. The smart city index is evaluated using the weighted geometric mean for each sub-index as per the various schemes, such as the panel, egalitarian, individualist or hierarchist weighting schemes. The following function is used to assess the main smart city index:

$$WGM_{(\gamma,\omega)} = \prod_{i=n}^{m} \gamma_i^{\omega_i}$$

where γ represents the dimensionless normalzied value for the respective domain and ω represents the weight associated with each domain. The following function is also used:

$$Smart\ City\ Index = \gamma_{SEnv}{}^{\omega_{Env}} \times \gamma_{SEco}{}^{\omega_{Eco}} \times \gamma_{SSoc}{}^{\omega_{Soc}} \times \gamma_{SGov}{}^{\omega_{Gov}} \times \gamma_{SEn}{}^{\omega_{En}} \times \gamma_{Infra}{}^{\omega_{Infra}} \times \gamma_{STrans}{}^{\omega_{Trans}}$$

3. Results and Discussion

Four Canadian cities have been examined to evaluate them based on the smart city index methodology that has been developed. Indicator data for each city has been collected and analyzed to compare their performance and benchmark their smartness to each other. While governance and the environment domains can be considered smart and satisfactory, substantial improvements in the energy and infrastructure domains are required throughout all cities. Furthermore, the economies of all cities along with the energy and environment domains need to be significantly improved in order to attain smart energy and smart environment characterizations. Figure 2 shows these domains along with the priority factors and evaluated measures for each domain.

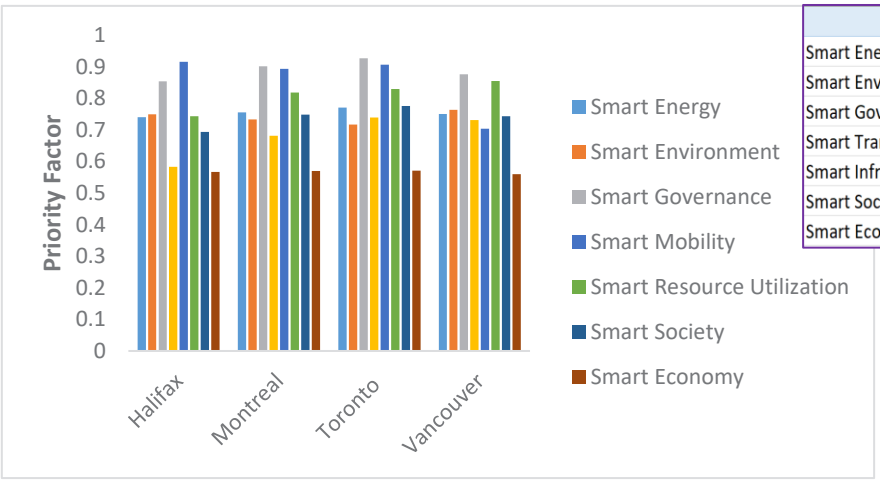

	Halifax	Montreal	Toronto	Vancouver
Smart Energy	0.740646445	0.75591002	0.770668172	0.750497564
Smart Environment	0.749492796	0.732831119	0.716639973	0.76401725
Smart Governance	0.854102742	0.901622024	0.927153568	0.875995379
Smart Transportation	0.915707308	0.893196193	0.906835826	0.703925702
Smart Infrastructure	0.770315495	0.784438687	0.795406359	0.820096499
Smart Society	0.693582729	0.748709804	0.776321676	0.743303997
Smart Economy	0.566798529	0.569993154	0.571082874	0.559469558

Fig 2. Main domains and the priority factor for each domain throughout the studied cities

4. Conclusions

A novel and integrated methodology to assess smart cities has been deployed and implemented to assess Canadian cities. The methodology characterizes smart cities by assessing various aspects including the economy, environment, society, governance energy, infrastructure and transportation. Several indicators are used to evaluate each aspect. Toronto achieved the highest in smart governance and smart energy with 92.7% and 77% respectively; while it was the lowest in the smart environment with 71.6%. On the other hand, Montreal's smart governance and smart energy were the second highest with 90.1% and 75.6% respectively. The economic aspect needs significant improvements for these cities to become smarter. Furthermore, transportation and governance are the two aspects that have improved performance based on the results. Toronto houses the smartest society at 77.6%, followed by Montreal and Vancouver at 74.9% and 74.3% respectively.

References

Dincer, I., & Acar, C. (2017). Smart energy systems for a sustainable future. *Applied Energy*, *194*, 225–235. https://doi.org/10.1016/J.APENERGY.2016.12.058

Fernandez-Anez, V., Fernández-Güell, J. M., & Giffinger, R. (2018). Smart city implementation and discourses: An integrated conceptual model. the case of vienna. Cities, 78, 4-16. doi:10.1016/j.cities.2017.12.004

Giffinger, R., Fertner, C., Kramar, H., Kalasek, R., Pichler-Milanović, N., & Meijers, E. (2007). Smart cities: Ranking of european medium-sized cities. vienna, austria: Centre of regional science (srf), vienna university of technology.

Hoornweg, D. A. (2016). Cities and sustainability: A new approach. London;New York;: Routledge, Taylor & Francis Group.

Lund, H., Duic, N., Østergaard, P. A., & Mathiesen, B. V. (2016). Smart energy systems and 4th generation district heating. *Energy*, *110*, 1–4. https://doi.org/https://doi.org/10.1016/j.energy.2016.07.105

Musango, J. K., Currie, P., & Robinson, B. (2017). *Urban metabolism for resource efficient cities: from theory to implementation*. Retrieved from www.sustainabilityinstitute.net

Natural Resources Canada. (2016). Energy Efficiency Trends Analysis Tables - Transportation Sector - Energy Use Analysis.

Skaaning, S.-E. (2018). The Global State of Democracy Indices Methodology. Conceptualization and Measurement Framework, Version 2. https://doi.org/10.31752/idea.2018.66

Statistics Canada. (2017). Table 14-10-0287-03 Labour force characteristics by province, monthly, seasonally adjusted. https://doi.org/https://doi.org/10.25318/1410028701-eng

Wendling, Z. A., Emerson, J. W., Esty, D. C., Levy, M. A., de Sherbinin, A., et al. (2018). 2018 Environmental Performance Index. New Haven, CT: Yale Center for Environmental Law & Policy. Retrieved from https://epi.yale.edu/

Model and Flow Sheet Improvements for Coal fired Power Plants Equipped with a CO2 Capture Process Using Monoethanolamine

[1] Tanguy HAHN, [2] Jian CHEN, [2] Weiyang FEI, [1,3*] Fethi ALOUI

[1] Polytechnic University Hauts-de-France, Engineering School INSA Hauts-de-France,
Campus Mont Houy, Valenciennes, F-59313, France
[2] Tsinghua University, State Key Laboratory of Chemical Engineering, Department of Chemical Engineering
30 Shuangqing Rd Haidian Qu, Beijing, 100 084, China
[3] Polytechnic University Hauts-de-France, LAMIH CNRS UMR 8201, Campus Mont Houy, Valenciennes, F-59 313, France

* E-mail: Fethi.Aloui@uphf.fr

Abstract
The present paper follows two prior works by Liu et al. (2015) and Liu et al. (2017), conducted on the subject of CO_2 capture with a monoethanolamine based process. The study presented in this article is about the improvements brought to the flow sheet of a supercritical coal fired power plant aiming to reduce as much as possible the efficiency penalty created by the CO2 capture process.
MEA based capture processes require a lot of energy, extracted from the steam cycle, in order to regenerate the solvent, hence the loss of efficiency. Reducing the efficiency penalty is operated through several methods. The first one is reducing the energy consumed by the reboiler in the MEA capture process itself by splitting the rich solvent and using a kettle type heat exchanger for the heat exchanges bewteen the rich and lean MEA solvent. The second method consists of getting heat from the lean solvent back into the steam cycle by pre-heating the water after the low pressure turbine to 327K. The pre-heating can be improved with a water-ammonia Absorption Heat Transformer. The pre-heating is first being conducted with heat coming from the vapor and liquid phases generated by the AHT and in a second simulation, only the liquid phase is being used for the pre-heating and the vapor is send through a turbine to generate an additional 6.17 MW of power.

Keywords: Carbon dioxide, Monoethanolamine, Flow sheet, Efficiency penalty, Coal fired power plant, Modelling.

I. Introduction

Since the beginning of the industrial era, CO2 emissions have been on the rise and are now reaching dangerous level in the Earth's atmosphere. In order to avoid catastrophic consequences on the environment and to keep the global warming below 1.5°C, as suggested in the latest report published by the Intergovernmental Panel on Climate Change (Allen et al., 2018), the CO_2 emissions must be significantly reduced, and reducing these emissions is one of the biggest challenges of the upcoming decade.

In 2017, coal represented 38% of all the CO2 emissions coming from the electricity generation, and with the current global warming context, ways to reduce the CO2 cost of each kWh have been studied in the past few years. In these improvements, we can find modifications made to the steam cycle such as operating the steam cycle in a supercritical state, and using CO2 instead of water steam, allowing the efficiency of power plants to reach 50 % (Li et al., 2019). However, supercritical power plants are improving the efficiency of the steam cycle, and as the plant produces more energy for the same amount of coal being burned, the CO2 cost of the kWh produced is being decreased, but this CO2 cost still remains quite important. In order to drastically reduce the CO2 cost of each kWh, several capture processes, with excellent capture rates, have been developed.

Post-combustion capture processes based on absorption with MEA are part of the most known and studied capture techniques. Its flexibility and easy integration in power plants (Liu et al., 2015) makes it one of the primary choices when it comes to capture processes. Furthermore, numerous studies (Le Moullec and Kanniche, 2011) have been conducted on the improvement of the process flowsheet, as well as the interactions between these modifications, in order to reduce the energy consumption of the stripper's reboiler, which is the main energy consumption unit in a MEA capture process.

A previous work conducted by Liu et al. (2015), uses a 600 MW coal fired power plant with an efficiency of 41.6% as a reference. It has been shown that the integration of a MEA absorption process to the power plant generates an efficiency penalty of 12.29%. This work has been completed by studying different scenarios of flow sheet modifications in the steam cycle and the MEA capture process (Liu et al., 2017), and the lowest efficiency penalty that has been reached was 8.07% with some approximations made to the models.
This paper has three objectives. The first one is to improve the models in order to be as close as possible from real power plant operating conditions, the second one is to study the impact of a reduced capture rate, going from 90% to 50% with 10% steps in order to reach the CO2 emissions of a gas fired power plant (Gonzalez-Salazar et al., 2018), and the third one is to improve the flow sheet of the steam cycle and of the capture process to reduce the efficiency penalty generated by the capture process as welle as increasing the power generation.

II. Presentation of the previous models

II.1. General overview

Several models with different flow sheet improvements have been created in Aspen+ in order to reduce and compare the efficiency penalties (Liu et al., 2017).

The models are divided in two groups depending on the extraction point of the steam used for the PCC's reboiler. The steam is either extracted from the Low-Pressure turbine or bewteen the LP and IP turbine. The following names have been given to the models (where x is the number of the model) :

- xA: models with steam extraction from the LP turbine.
- xB: models with steam extraction between IP and LP turbines.

The difference between the two extraction points is the pressure of the extracted steam. In xA models the extraction pressure is 3.64 bar and in xB models the pressure is 9.1 bar. This directly leads to a higher temperature for the steam extracted at 9.1 bar.

Furthermore, 5 flowsheet improvements have been made, and each one was tested with both scenarios presented above, for a total of 10 models:

- case 1: Basic integration of PCC into supercritical CFPP,
- case 2: Recovery of waste heat generated during CO_2 compression,
- case 3: Reduction of the throttling losses at the entrance of the LP turbine,
- case 4: Adding a lean vapor recompression to the capture process,
- case 5: Reducing the temperature pinch in the heat exchangers from 10K to 5K.

In these previous Aspen+ models, the heat exchanger were modeled by "Heaters" block, leading to uncertainties about the results as the physical properties (flow rate, temperatures, heat capacity, ...) are not taken into account. This approximation may lead to an over estimation of the results obtained by runing the simulations.

Parameters of the simulations for the CO_2 capture process are presented in the table below:

Table 1: Parameters of the simulation for the capture process.

Flue gas flowrate (kg/s)	*707.80*	**Solvent MEA content (wt%)**	*30*
Flue gas CO_2 content (wt%)	*19.54*	**Lean solvent inlet temperature (K)**	*313*
Flue gas inlet temperature (K)	*317*	**Lean solvent loading (mole CO2/mole MEA)**	*0.269*
CO_2 capture rate (%)	*90*	**CO_2 stream temperature (K)**	*328*

II.2. Steam cycle

The steam cycle (figure 1) is composed of 3 main turbines (high, intermediate and low pressure) an auxiliary turbines (for the steam being extracted to the reboiler) and a heat recovery system. Depending on the case studied, the flowsheet can be different from a model to another.

The steam exiting the boiler is at 242 bar and 839 K. Some steam is extracted from the HP and IP turbines in order to pre-heat the water ready to enter the plant's boiler.

The recovery heat system is using heat coming from the CO_2 compression. Each compression stages generates hot CO_2 and this energy is being transfered to the water from the steam cycle in order to pre-heat the water before in enters the boiler, thus reducing the coal consumption required to create the steam.

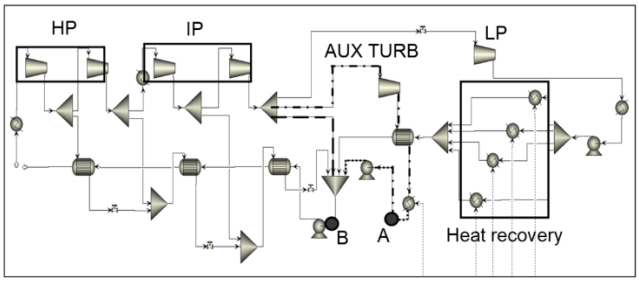

Fig. 1: Steam cycle for case 4B.

II.3. Capture process

The CO_2 capture process uses MEA solvent as a solvent. The design of the Absorber and Stripper columns have been calculated in order to be used in a 600 MW supercritical CFPP (Liu et al., 2015), and the obtained results will be used for all the following simulations in this paper.

Table 2: Absorber and Stripper design parameters.

	Absorber	Stripper		Absorber	Stripper
Pressure drop (mm water/m)	*42*	*42*	**Packing height (m)**	*30*	*30*
Column diameter (m)	*11.66*	*10.78*	**Number of stages**	*20*	*20*
Column number	*3*	*2*	**Column pressure (bar)**	*1*	*1.7*
Column packing	*IMTP no.40*	*Flexi Pac1Y*			

In the previous work (Liu et al., 2017), the capture process has been improved with a lean vapor recompression. The lean solvent is being flashed, and the vapor obtained is being compressed and sent back to the Stripper. This allows the process to reuse some of the heat from the lean solvent.

III. Improvements brought to the models

III.1. Reduction of the CO_2 capture rate

In order to reach the same CO_2 emission level as a gas fired power plant, the CO_2 capture rate of the model 4B has been reduced from 90% to 50% (Gonzalez-Salazar et al., 2018) with 10% steps. Two methods of capture rates have been studied: a partial flue gas treatment and a reduction of the capture rate inside of the Absorber. To achieve a partial flue gas treatment, a split block has been added to the flue gas stream, before it enters the Absorber, in order to chose the ratio of flue gas that enters the column. In this case, one part of the flue gas enters the Absorber and the other part is being released directly in the atmosphere.

The reduction of the capture rate inside of the Absorber has been done by creating a User Defined Function to let a certain amount of CO2 leave at the top of the column. The results are presented in the figure 2. These results show that the efficiency penalty decreases quite linearly for both methods. But an offset of 1.16% for the Absorption column method and 1.27% for the partial flue gas treatment can be observed. The offset can be generated by flaws in the modelling of the capture process and by the resolution algorithms selected. With the efficiency penalty reaching 5.53% at a 50% capture rate, the overall efficiency of a supercritical coal fired power plant with an original 41.6% efficiency would drop to 36.1%. In comparison, a gas fired power plant can average 39% if operated in a simple cycle and 57% if operated in a combined cycle (Gonzalez-Salazar et al., 2018).

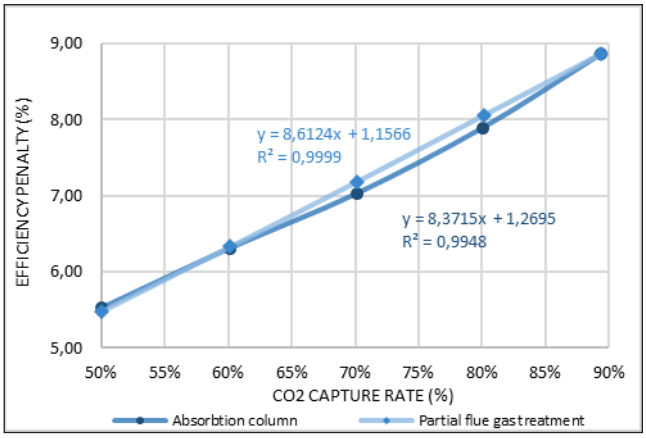

Fig. 2: Efficiency penalty for different capture rates

III.2. Replacement of "Heater" blocks by real heat exchanger

A first approximation has been made in the simulations with the help of "Heater" type blocks in order to model the heat exchangers from the heat recovery system. These blocks do not take into account the physical properties of the fluids who are exchanging heat, and this leads to a "best case scenario", as the fluids are cooled or heated at the desired temperatures.

The efficiency penalty is calculated with the following formula:

$$\Delta\eta = \eta_{ref} - \frac{\sum W_{turb} - \sum W_{pumps} - \sum W_{comp}}{E_{boil}}$$

The efficiency penalty has been calculated before and after the modifications in order to compare the variations.

As the "Heater" blocks are replaced by real heat exchangers in the simulations, and after flow rates optimization, thanks to User Designed Functions, the efficiency penalty is increased in all the cases (+0.23 % of mean increase over all scenarios), except for the scenario 4B (Fig. 3).

This efficiency penalty increase was expected as the simulations are now more precise when it comes to heat exchanged between the steam cycle and the compressed CO_2. The heat exchanges being reduced in most of the cases, less energy is available for the steam cycle and the work outputs generated by the steam turbines are being reduced. As the energy consumption by the capture process remains unchanged by the changes made from one scenario to the improved scenario, the overall efficiency of the power plant decreases.

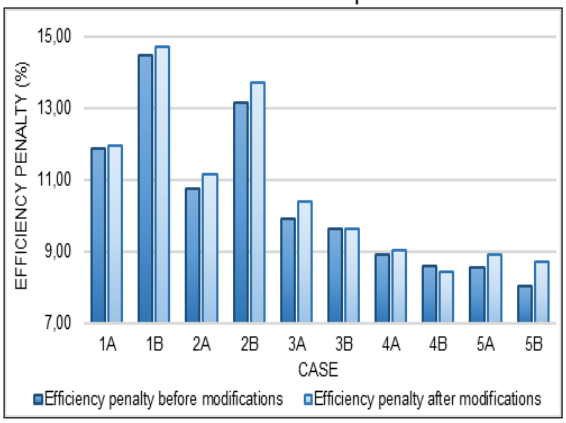

Fig. 3: Efficiency penalty before and after replacing the "Heaters" by heat exchangers and after optimization, for each case.

The scenario 4B has the lowest efficiency penalty of all the cases after the modifications (efficiency penalty of 8.46%) and will be used as the basis for the other improvements made to the simulations.

Some of the properties of the capture process are being presented in the table below:

Table 3: Results of the optimized 4B scenario.

Efficiency penalty (%)	*8.46*	**Condenser's duty (GJ/t_{CO2})**	*0.6*
Reboiler's duty (GJ/t_{CO2})	*3.5*	**Lean solvent flow rate (kg/s)**	*2369*

III.3. Improvement of the capture process flowsheet

This improvement focuses on the reduction of the reboiler's duty in order to reduce the energy consumption of the capture process.

To achieve a reduction of the reboiler's duty, an advanced capture flowsheet is being implemented in Aspen+, the rich solvent coming out of the Absorber is being split. One part is being kept at the same temperature, the other part is being heated up with a kettle type heat exchanger (Jung et al., 2013). To simulate the Kettle heat exchanger, a classic heat exchanger is paired with a flash tank (Fig. 4).

At the outlet of the kettle heat exchanger, two stream are available: a liquid stream and a vapor stream. The liquid stream is being injected at the stage number 6 of the Stripper as it is the best compromise bewteen reducing the reboiler's duty and increasing the condenser's duty. The vapor stream is being compressed at 2 bar, thus increasing the temperature of the vapor to 448K. This extra temperature is going to reduce the reboiler's duty, as it will increase the temperature of the solvent inside of the Stripper.

Finaly, the cold stream is entering at the top of the Stripper. Its low temperature will help reduce the Condenser's duty. As the reduction of the reboiler's duty is not reduced by a linear ratio with the amount of work required to compress the vapor, it is necessary to keep the compressor's outlet pressure quite low in order to avoid consuming to much energy in the compressor. The strippper's operating pressure is 1.7 bar, and the compressor's outlet pressure has been set to 2 bar. The operating conditions of the advanced process are being presented in the following table:

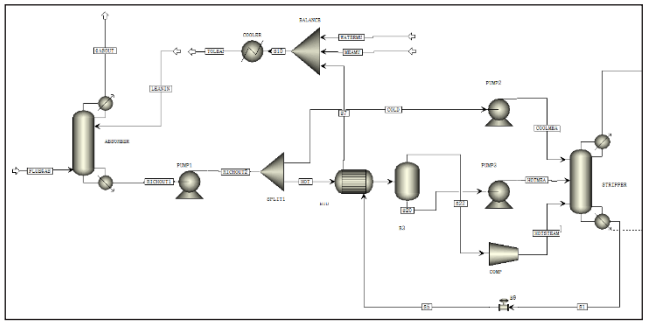

Fig. 4: Advanced capture process flowsheet.

Table 4: Parameters of the advanced capture process.

Heat/cool split ratio	*0.5*	**Hot liquid MEA injection stage number**	*6*
Flash tank temperature (K)	*424*	**Compressor outlet pressure (bar)**	*2*
Flash tank pressure (bar)	*1*		

With this simulation, the reboiler's duty has been brought down quite significantly to 2.1 GJ/tCO_2, a reduction of 40%. However, the counter part is a high increase of the condenser's duty. Despite the cold MEA flow entering at the top of the Stripper, the condenser's duty has increased to 1.5 GJ/tCO_2, almost three times the initial duty.
When integrated to the whole power plant, the reduction of the reboiler's duty brings the efficiency penalty down to 8.03% (-0.43%) for the model named 6B.

III.4. Pre-heating of the steam using residual heat from the lean solvent

The second flow sheet modification from this paper consists of a pre-heating of the water before it enters the heat recovery system by using the remaining heat from the lean solvent once it exchanged its energy with the rich solvent. In the heat exchanger, the lean solvent outlet temperature is 332K and the water before the heat recovery system is at 305K. The pre-heating will allow the temperature to reach higher levels when exchanging heat with the compressed CO_2, therefore increasing the amount of energy being reused by the steam cycle and increasing the efficiency of the power plant.
With this heat exchanger, the water is pre-heated at 327K, however, the reboiler's duty remains unchanged from the 4B case. To use the heat of the lean solvent, an absorption heat transformer has been considered (Wakim and Rivera-Tinoco, 2019 and Jawahar et al., 2010). To implement this process water has been selected as an absorbant and ammonia as a refrigerant (Yokozeki, 2005).

The liquid ammonia is being pumped at a high pressure and is being transformed into vapor inside an Evaporator with the heat coming from the hot source, which is the lean solvent in the case studied in this paper. This vapor enters an Absorber where it will be absorbed into the lean water-ammonia liquid. The absorption is exothermic and will produce a higher temperature than the hot source (which is the heat from the lean solvent), and this temperature will be used to achieve a pre-heating in the steam cycle. The rich solvent will leave the absorber, enter a heat exchanger and go through an expansion valve. The outlet pressure should be low enough to create ammonia vapor when the liquid is being heated in the Generator by the hot source.

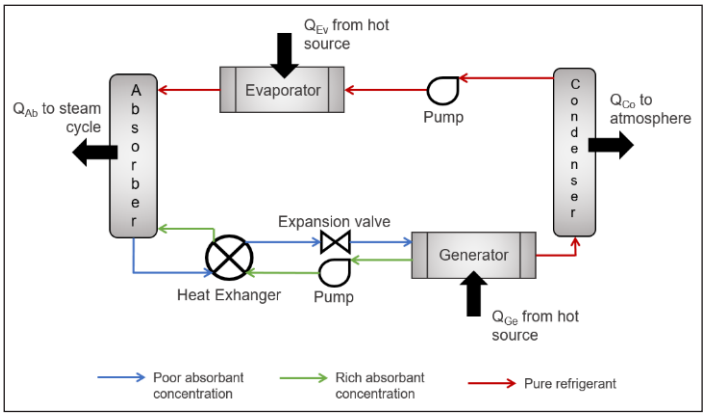

Fig. 5: Basic absorbtion heat transformer process

The lean solvent is being pumped back at high pressure and sent back to the Absorber while the ammonia will enter a condenser to go back into liquid state before being pumped back at high pressure.
The operating conditions of the AHT are being presented in the following table 5:

Table 5: Parameters of the AHT process

H_2O/NH_3 ratio	*1.31*
High pressure (bar)	*17*
Low pressure (bar)	*1.55*
Hot source temperature (K)	*332*

To use this energy, the steam and liquid phases of the hot water/ammonia mix is being send to the steam cycle. A second LP turbine is being added to the steam cycle, and the pre-heating is happening between the two LP turbines in order to give extra energy to the steam. A sensitivity analysis conducted on the outlet pressure of the LP 1 has shown that the power generated by the two turbines is maximal for an outlet pressure of 0.21 bar. The outlet pressure of the second LP turbine remains the same as in the models with only one LP turbine, 0.0588 bar.

III.5. Addition of a turbine in the AHT process

The AHT process presented in the previous section can be improved by using the steam coming from the Absorber and use it to generate power by sending it through a turbine (Hernández-Magallanes et al., 2018).

Tab. 6: Parameters of the AHT turbine

Inlet steam pressure (bar)	*17*
Outlet team pressure (bar)	*1.55*

With these operating conditions, the turbine is generating an additional 6.17 MW of power to the power plant. The new efficiency penalty with this addition is 7.45% (-1.01%) and this model is called 8B.

III.6. Combining the Kettle heat exchanger and the AHT process

The final improvement porposed in this paper is the combination of the kettle type reboiler and the AHT process with the turbine. This will allow the reduction of the energy consumption of the CO_2 capture process as well as the generation of additional power by the power plant.
The parameters of the two process were already set in the previous paragraphs of this paper and are being conserved for this simulation. The User Defined Functions previously created avoid errors when runing the simulations when the two processes are being combined. By doing so, the efficiency penalty of the power plant is reduced to 6.70% (-1.76%) for the model 9B.

IV. Conclusion

This paper has been focusing on the study of efficiency penalty and on improving the flowsheet of a CFPP equipped with a PCC process, and provide a complete CFPP model instead of isolated blocks.
The CO2 capture rate of the CFPP has been reduced from 90% to 50% in order to reach the same level of emission as a GFPP. The efficiency penalty is being reduced linearly with the CO2 capture rate and a CFPP, with a MEA PCC process emiting the same CO2 levels as a GFPP, would have a 36.1% efficiency. Compared to the higher efficiency of a GFPP (between 39% and 57%), reducing the capture rate does not seem economicaly interesting, but considering the reserve of coal, and when taking the environment into account, this efficiency may seem acceptable. With a better moddeling and flowsheet optimization, the prior models can be more representative of real operating conditions of a CFPP. The last model improvement is the combination of the kettle type heat exchanger with the AHT process and its turbine and reduces the efficiency penalty to 6.70%, which represents a 1.76% decrease compared to the best scenario of the previous work.

Acknowledgements

This research work was supported by the National Science and Technology Support Program of China (No. 2015BAC04B02), the State Key Laboratory of Chemical Engineering of Tsinghua University and LAMIH (UMR CNRS 8201) of the Polytechnic University Hauts-de-France (Valenciennes, France). These supports are gratefully acknowledged.

References

Gonzalez-Salazar, M.A., Kristen T., Prchlik, L., 2018. Review of the operational flexibility and emissions of gas- and coal-fired power plants in a future with growing renewables, Renewable and Sustainable Energy Reviews. 82(1):1497-1513.

Hernández-Magallanes, J.A., Heardb, C.L., Besta, R., Rivera, W., 2018. Modeling of a new absorption heat pump-transformer used to produce heat and power simultaneously, Energy. 165:112-133.

Jawahara, C.P., Raja, B., Saravanan, R., 2010. Thermodynamic studies on NH3–H2O absorption cooling system using pinch point approach, International Journal of Refrigeration. 33(7):1377-1385.

Jung J., Jeong, Y.S., Lim, Y., Lee, C.S., Han, C., 2013. Advanced CO_2 Capture Process Using MEA Scrubbing: Configuration of a Split Flow and Phase Separation Heat Exchanger, Energy Procedia. 37:1778-1784.

Le Moullec, Y., Kanniche, M., 2011. Screening of flowsheet modifications for an efficient monoethanolamine (MEA) based post-combustion CO2 capture, International Journal of Greenhouse Gas Control. 5(4):727-740.

Li, H., Zhang, Y., Yang, Y., Han, W., Yao, M., Bai, W., Zhang, L., 2019. Preliminary design assessment of supercritical CO_2 cycle for commercial scale coal-fired power plants, Applied Thermal Engineering. 158:113785.

Liu, X., Chen J., Luo X., Wang M., Meng H., 2015. Study on heat integration of supercritical coal-fired power plant with post-combustion CO2 capture process through process simulation, Fuel. 158:625-633.

Liu, X., Yu, Y., Chen, J., 2017. Upgrading the integration of supercritical coal-fired power plant with post-combustion CO2 capture process through process simulation, International Journal of Global Warming. 12:149-163.

Ritchie, H., Roser, M., 2015. When will we run out of fossil fuels? Ourworldindata.org.

Wakim, M., Rivera-Tinoco, R., 2019. Absorption heat transformers: Sensitivity study to answer existing discrepancies, Renewable Energy. 30:881-890.

Yokozeki, A., 2005. Theoretical performances of various refrigerant-absorbent pairs in a vapor-absorption refrigeration cycle by the use of equations of state, Applied Energy. 80(4):383-399.

Theoretical Investigations of Stirling Engine Performances for Different Working Fluids

[1] Houda HACHEM, [1] Ramla GHEITH, [2]* Fethi ALOUI

[1] University of Monastir, National Engineering School of Monastir (ENIM), LESTE Laboratory
Avenue Ibn El Jazzar 5019 Monastir, Tunisia
[2] Polytechnic University Hauts-de-France (UPHF), LAMIH, CNRS UMR 8201, F-59313 Valenciennes, France

E-mail: houdahachem@yahoo.fr
*Corresponding author e-mail: Fethi.Aloui@uphf.fr

Abstract
Present paper is performed to investigate the effect of working fluids on a double acting Stirling engine performance. A numerical model that includes major thermal losses that decreases the Stirling output power and efficiency was developed. The influences of tree monatomic gases (helium, Neon and Argon) and one diatomic gas (nitrogen) on optimal compression ratio and optimal regenerator form factor as well as optimal frequency of the Stirling engine are studied. It was found that the optimal design of regenerator, allowing the maximum output power, depends on the working fluid characteristics. Results shown that, the compression ratio corresponding to the optimum power depends on the working fluid used. It was shown that to achieve a high output power of the Stirling engine, it is preferable to use a monoatomic gas having the highest heat capacity and thermal conductivity and the lowest density as working fluid.

Keywords: Working fluids, Double acting Stirling engine, Rotational speed, Compression ratio, Regenerator form factor.

I. Introduction

Given the energy and environmental problem, many companies from various sectors rediscover forgotten Stirling technology and adapt it to their own process. Nowadays, Stirling installations are patterned and commercialized such as Microgen installation, Whispergen unit, Stirling Dish, etc. The Stirling technology provides a good solution, since it can work with any external heat source such as solar, combustion of any fuel, nuclear and even warmth. The Stirling engine is characterized by a silent mode of operation, easy maintenance, lower NOx, HC, and CO emission and a good efficiency (Derviş, 2017).
The Stirling engine is working in a closed cycle. It takes periodically four transformations, representing the Stirling cycle: two isothermal processes and two isochoric processes as shown in figure1. The Stirling engine is mainly composed by five compartments: 2 working spaces and three heat exchangers (Heater, cooler and regenerator). The regenerator (porous medium) characteristics are determinant for the whole engine performances (Hachem et al., 2015a). Compared to the Ericsson engine, at nearly the same working conditions, the Stirling engine presents higher global performances (specific indicated work, thermodynamic and exergetic efficiencies), due to the presence of a regenerator (Hachem et al., 2015b).
Different working fluids are used in Stirling machines even for Stirling generators and Stirling coolers. Robert Stirling used carbon dioxide and nitrogen instead of air as the working fluid in some of the engines that he manufactured (Derviş, 2017). Several research projects determine the effect of working gas (nitrogen, helium, hydrogen or other) on the output power of the Stirling engine or on the cooling power of the Stirling refrigeration machine. Otaka et al. (2002) investigated a 100W Beta type Stirling machine. They found that the refrigeration produced by nitrogen was 28% less than that produced by helium. Tekin and Ataer (2010) studied the effect of working fluid (Hydrogen, Air, Helium) inside a V-type Stirling-cycle Refrigerator (VSR).
They found that when the hydrogen is used as the working fluid, the COP of the VSR is higher than the VSR that uses helium or air. This is due to low pressure drop and high specific heat of the hydrogen. The cooling load of the VSR are 662, 653 and 624 W respectively when hydrogen, helium and air are used for the working fluid, at a rotational speed 1400 rpm. Chen et Ju (2015) tested the effect of three working fluids (Nitrogen, Argon, Helium) on the optimal operating frequency, minimal onset temperature differences and mean pressure inside a thermo-acoustic Stirling heat engine (TASHE). Their results show that a Stirling engine using helium has a much wider range of mean pressure than an engine using nitrogen or argon. There was an optimal mean pressure for the minimum onset temperature for each working fluid. The achieved minimal onset temperature differences for argon, helium and nitrogen were respectively 525°C at 0.51 MPa, 470°C at 1.1 MPa and 454°C at 0.35 MPa. The estimated operating frequencies for the three tested working gases were 40 Hz for argon, 44 Hz for nitrogen and 127 Hz for helium. Ni et al. (2015) investigated heat transfer proprieties inside a Stirling engine with U-shaped tubes heater for three working fluids (helium, nitrogen and carbon dioxide). Their results show that helium has the highest heat transfer coefficient in the heater and the lowest temperature difference. Carbon dioxide has the greatest volumetric heat capacity and the highest temperature difference and has the second highest heat transfer coefficient among the three working fluids. Wang et al. (2016) experimented GPU-3 Stirling engine when using Helium and Hydrogen. Their experimental results show that the indicated power of the Stirling engine is about 2.31kW for helium, while it is 3.47 kW for hydrogen. Despite the good performance, use of hydrogen as working fluid in Stirling engines presents safety risks.
The aim of this work is focused on improving the performances of the double acting Stirling engine of the

Whispergen unit. Therefore, the effect of different working gases on the efficiency and the output power are performed. The effect of several parameters such as compression ratio, regenerator form factor (length /diameter), rotational speed, charge pressure, and hot end temperature was investigated for four gases. The gases are divided into main two categories based on their behaviour and atomic number which are: Monatomic gases (Helium He, Argon Ar, Neon Ne) and diatomic gases (Nitrogen N_2).

2. Experimental facility

The double acting Stirling engine (Fig. 1) consists of 4 interconnected cylinders in which oscillate four up and down pistons depending on the expansion and compression cycle of the working fluid. This engine is kinematic type. It is a compact and powerful engine, reliable and robust. This engine is integrated into the Whispergen micro-CHP unit. The double-acting Stirling engine uses Nitrogen as a compressed working fluid at a pressure of 20 bar. Its rotational speed is about 1500 rpm. It is connected to a generator (4-pole single-phase induction motor) to produce electricity so that its nominal electrical power output reaches up to 1kW. It is driven by a Wobble-yoke training system (Valenti et al, 2014; Valenti et al., 2015). Table 1 summarizes different geometrical characteristics of this engine.

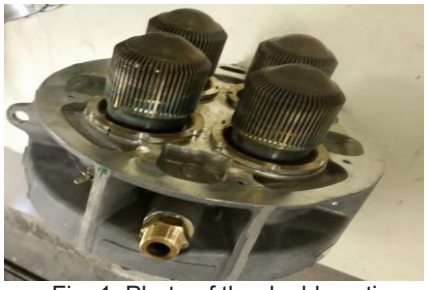

Fig. 1: Photo of the double acting Stirling engine.

Table 1: Geometrical characteristics of the double acting Stirling engine.

Working conditions		**Regenerator**	
Rotational speed (rpm)	1500	Type	Annular
Working gas	Nitrogen	Annular external diameter [m]	0.0636
Average pressure (bar)	20	External diameter [m]	0.0566
One cylinder dimensions		Internal diameter [m]	0.0435
Dead volume of the compression space [cm^3]	19.1	Annular internal diameter [m]	0.0415
swept volume of the compression space [cm^3]	27.4	Length [m]	0.02
Dead volume of the expansion space [cm^3]	19.9	Porosity	0.69
swept volume of the expansion space [cm^3]	28.4	Mesh diameter	6E-5
stroke (m)	0.021	Total wet surface [m^2]	0.35
Hot heat exchanger		**Cold heat exchanger**	
Type	Fins	type	Fins
Length [m]	0.049	Length [m]	0.052
Number of fins	84	Number of fins	180
Fins height [m]	0.003	Fins height [m]	0.0018
Fin-to fin width [m]	5.00E-4	Fin-to fin width [m]	5.55E-4
Heater average cross section [m^2]	1.26E-4	Heater average cross section [m^2]	1.8E-4

III. Theoretical model description

In previous studies, Hachem et al. (2015a) reconsidered the quasi-steady model proposed by Urieli (1984) and propose a general model including all parameters that decrease the engine's brake power and considering the most important phenomenon recorded in Stirling engine (thermodynamic phenomenon, thermal and mechanical losses). This model is modified and it is used to estimate the mechanical energy produced by the double acting Stirling engine. The basic assumptions made are that the working gas is considered as an ideal gas and having constant properties, the physical properties of the porous medium (regenerative) are uniform and constant. The most important heat losses governing the Stirling engine, described in table2, are added to the classical quasi-steady model. Numerical values of the input data issue from simulation, are related for a single cylinder among the four cylinders of the Stirling engine (Fig. 2). The calculated output power is simply multiplied by four to estimate the total power of the double acting Stirling engine.

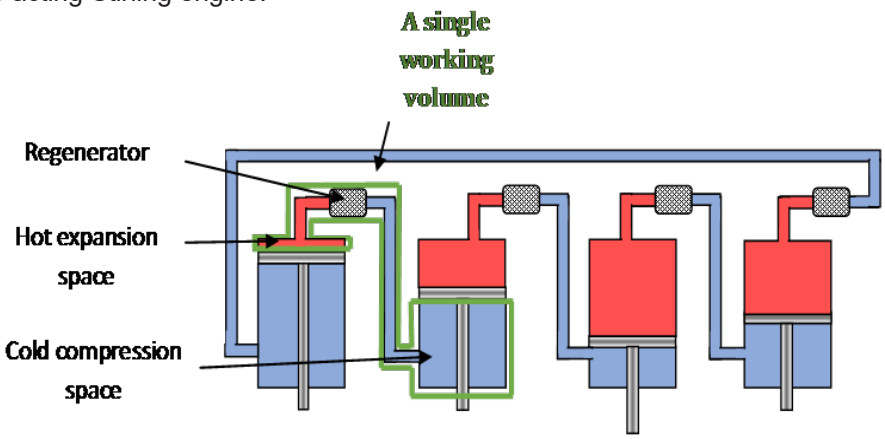

Fig. 2: Schema of the double acting Stirling engine.

Table 2: Thermal losses expressions considered in the double acting Stirling engine modelling.

Thermal loss	Expression	Ref.
Loss due to internal conduction in heater, cooler and regenerator	$\delta\dot{Q}_{Cd} = \frac{\lambda_m A.\Delta T}{L}$ λ_m: Thermal conductivity of the material through which heat conduction occurs (W m^{-1} K^{-1}) ΔT: Temperature difference between the two interfaces of the heat exchanger (K). A: Cross area through the heat exchanger L: Length of the heat exchanger λ_m: Conductivity of the heat exchanger material (W $m^{-1}K^{-1}$)	Reader and Hooper (1983)
Loss due to pressure drop in heater, cooler and regenerator	$\delta\dot{Q}_v = -\frac{\dot{m}\left(\frac{2f\mu_g u_g V}{A d_{hyd}^2}\right)}{\rho_m}$ ρ_m: Density of solid material (kgm^{-3}) $\dot{m}$: Mass flow rate through the heat exchanger (kg s^{-1}) f: Viscous friction coefficient μ: Dynamic viscosity of the working fluid (kg $m^{-1}s^{-1}$) u: Axial velocity (m s^{-1}) V: Volume of the heat exchanger (m^3) A: Fluid cross section through heat exchanger (m^2) d_{hyd}: Hydraulic diameter (m).	Tlili et al. (2008)
Loss due to heat exchanger imperfection in heater, cooler and regenerator	$\dot{Q}_{irr} = (1-\varepsilon\ )\dot{Q}_r$ $\dot{Q}_r$: the effective thermal power exchanged in each heat exchanger ε : the efficiency of each heat exchanger	Tlili et al. (2008)
Shuttle loss in compression and expansion spaces	$\delta\dot{Q}_{St} = \frac{\pi s_p^2 \lambda_g d_{cyl}}{8xL_p}\ \Delta T$ ΔT: Difference of working gas temperatures between the PMB and the PMH of the cylinder S_p: Stroke of the piston (m) dcyl: Internal diameter of the cylinder (m) L_p: Length of the piston (m) x: Annular gap between the piston and the cylinder (m) λ_g: Gas thermal conductivity (W m^{-1} K^{-1})	Kolin (1991)

VI. Results and discussions

VI.1. Modelling of the double acting Stirling engine

When working with nitrogen under 20 bar, 1500 rpm, 1100 K, 300 K respectively as initial charge pressure, rotational speed, hot end temperature and cold end temperature. The produced work by one cylinder of the Stirling engine is estimated about 21.8 J/cycle at a rotational speed of 1500 rpm. P-Ve and P-Vc diagrams are plotted in Fig. 3 and the evolution of the produced work by one cylinder versus shaft angle over one shaft revolution is plotted in Fig. 4.

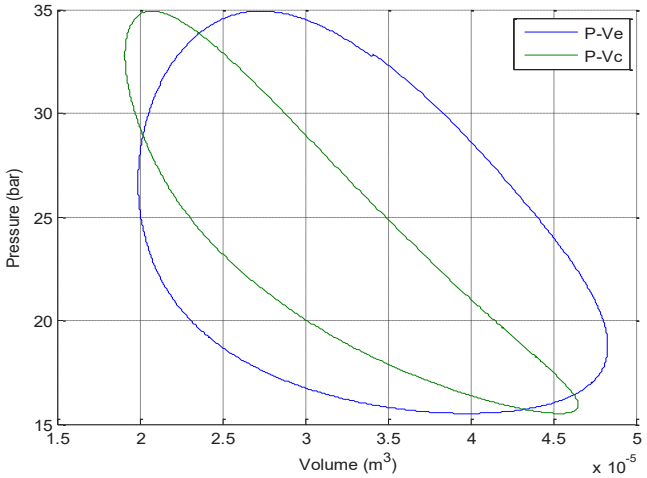

Fig. 3: P-Ve and P-Vc diagram inside one cylinder of the Double acting Stirling engine for an initial working gas pressure of 20 bar.

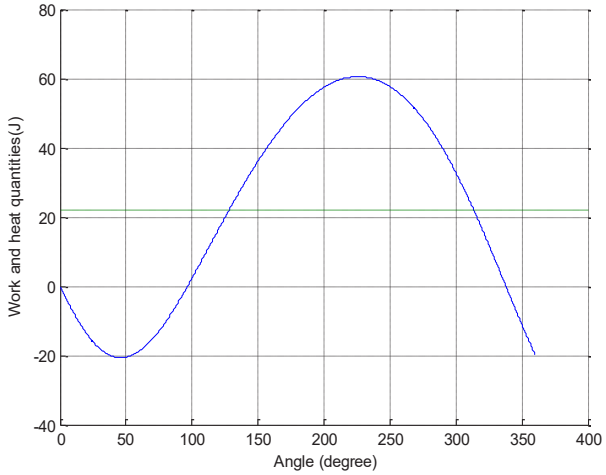

Fig. 4: Evolution of the produced work by one cylinder of the double acting Stirling engine without considering losses for an initial working gas pressure of 20 bar.

An important difference between both cycles (experimental and theoretical) can be noted. These differences are essentially explained by:

- Losses by friction and by singular pressure drop when the working fluid going through heat exchangers,
- The real movements of the pistons are different from the theoretical movements,
- The great heterogeneity of the instantaneous temperatures in the thermal machine and to the irreversibility presents in the Stirling machine,
- The regenerator cannot follow the temperatures variations from the hot side to the cold one, and vice-versa. Indeed, the temperature of the regenerator reaches that of the hot source and does not fall anymore because of its big thermal inertia,

- The loss of the pressure drop recorded in the regenerator is important. It is due to its geometric aspects (weak diameter) and to its physical characteristic (weak porosity).

IV.2. Parametric study

IV.2.1. Rotational speed effect

The rotational engine speed is a critical parameter for the Stirling engine performances. The increase of rotational engine speed reduces heat loss by internal conduction, reduces heat exchange time and increases viscous friction loss inside each heat exchanger.
The heat transferred from the working fluid to compression and expansion areas depends on the nature of the working fluid. Thermo-physical characteristics of four working fluids (one diatomic gas and three monatomic gases), are given in table 3.

Tab.3: Proprieties of common Stirling engine working fluids at 20°C and 1atm.

	Thermal conductivity λ (W. m^{-1}. K^{-1})	Density ρ (kg. m^{-3})	Heat capacity $\bar{C}_P$ (J.kg^{-1}K^{-1})	Dynamic viscosity μ (Pa.s)	$\gamma=\frac{\bar{C}_P}{\bar{C}_V}$	$r = \bar{C}_P - \bar{C}_V$
N_2	0.02583	1.250	1040	0.0178	1.3994	296.8
He	0.1513	0.178	5190	0.0190	1.667	2077
Ar	0.01772	1.669	520	0.0228	1.667	208
Ne	0.0486	0.842	1030	0.0316	1.667	412

Results show that an optimum value of rotational speed is expected for each working fluid. From Fig. 5, it is clearly seen that helium presents the highest mechanical output power compared to argon, neon and nitrogen. Results show that optimal rotational speeds corresponding to the highest output power respectively of Ar, N_2 and Ne are 1100 rpm, 1500 rpm and 3500 rpm. However the output power helium curve follows a monotonous increase with rotational speed. Because, among the four working gases, helium is the heaviest gas (lowest density value). Even when increasing rotational speed, helium absorb higher amount of heat in each heat exchanger thus its output power increases.

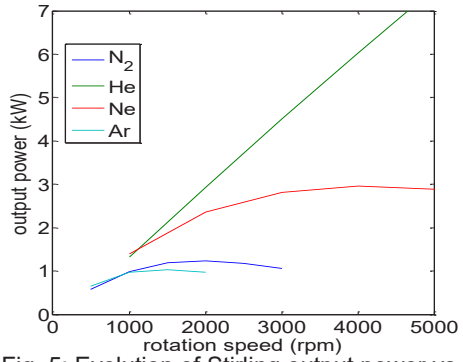

Fig. 5: Evolution of Stirling output power vs. rotational speed.

VI.2.2. Compression ratio effect

In a Stirling machine, the compression ratio is defined as the ratio between the compression volume Vc and the expansion volume Ve. The compression ratio is determined by the combination of a number of geometrical parameters such as strokes and radius of displacer and power pistons. However, engines designed with the same compression ratio, but through different combinations of these parameters could work differently (Chen et al., 2015). Figure 6 presents the evolution of mechanical output power and thermodynamic efficiency of the double acting Stirling engine for different compression ratio values as well as for different working fluids. The output power decreases with the compression ratio increase for He and Ne as working fluids. However a parabolic evolution of output power versus compression ratio is observed when using N_2 and Ar.

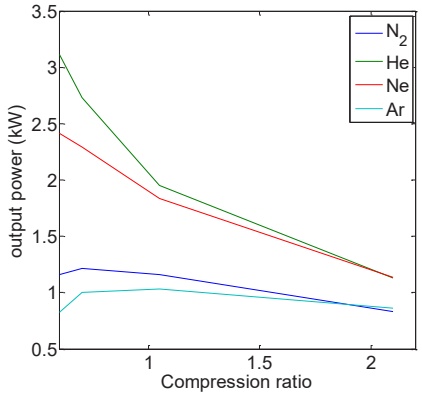

Fig. 6: Evolution of Stirling engine output power vs. compression ratio for different working fluids.

It is shown, also, that the compression ratio corresponding to the optimum efficiency depends on the working fluid used. It is about 1.1 for N2 and 0.7 for He. This can be explained by the huge heat capacity ratio of helium compared to other gases. At higher values of the working fluid mass, the production of work becomes lower. This can be explained by the approximation of the high and low temperatures of the working fluid.

IV.2.3. Regenerator design effect

A polynomial function is proposed to fit the output power as well as the efficiency as follow:

$$y = ax^6 + bx^5 + cx^4 + dx^3 + ex^2 + fx + g$$

where *a*, *b*, *c*, *d*, *e*, *f* and *g* are constants (coefficients of fit curve equations) shown in tables 4 and 5 respectively for the output power and the efficiency and x is the regenerator form factor.
The form factor is defined as the regenerator length devised by its diameter. . From figure 7, it is clearly seen that Ar and N2 reaches nearly the same optimum form factor value around 0.15. Using Ar as working fluid allow to reach 1.65kW and 35.5% as output power and efficiency. However, the use of Ne at 0.3 as optimum form factor resulted in 2.09kW and 34% as output power and efficiency. It was found that an optimal form factor is expected for the regenerator design, allowing the maximum mechanical output power and efficiency depends on the working fluid characteristics.

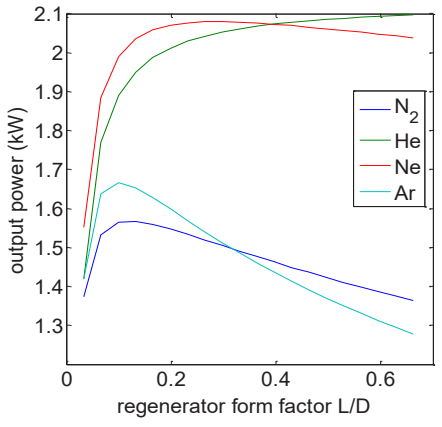

(a)

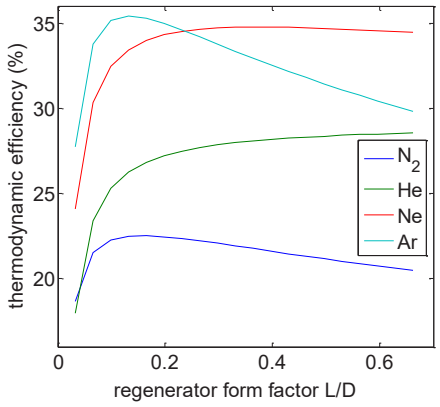

(b)

Fig. 7: Evolution of Stirling engine vs. the Output power (a) and the Efficiency regenerator form factor (b) for different working fluids.

Table 4: Coefficients of output power fit curve equation.

Working fluid	a	b	c	d	e	f	g
N_2	-371.07	867.33	-803.28	374.42	-91.777	10.686	1.1156
He	-650.19	1523.8	-1417.5	666.19	-166.63	21.428	0.88213
Ne	-654.31	1532.2	-1423.4	667.44	-166.08	20.832	1.0349
Ar	-572.62	1335.8	-1233.3	571.41	-138.13	15.39	1.053

Table 5: Coefficients of efficiency fit curve equation.

Working fluid	a	b	c	d	e	f	g
N_2	-6132.1	14355	-13327	6238.6	-1543.4	186.39	14.105
He	-10034	23524	-21891	10294	-2577.2	331.99	9.6582
Ne	-11768	27600	-25700	12094	-3028.9	386.36	14.451
Ar	-13660	31965	-29651	13851	-3406.7	402.62	17.92

V. Conclusion

A key issue in designing and optimizing Stirling engines is to conduct a precise thermodynamic study to predict its performances under different working fluids. Numerical results show that:

- Helium is more advantageous over other tested gases,
- An optimal rotational speed is expected for each working gas,
- An optimal compression ratio corresponding to the maximum power depends on the working fluid used,
- A regenerator optimal form factor is expected for each working gas.

Consequently, in order to obtain a higher output power and efficiency in Stirling engines, monatomic gases with high thermal conductivity, high specific heat, low density, and low viscosity should be preferred as working fluid. As a perspective of this study, our next researches will consider the change of the thermodynamic properties of these working fluids according to temperature and pressure.

Acknowledgments

This research was supported by the laboratories LESTE of ENIM (university of Monastir, Tunisia) and LAMIH (UMR CNRS 8201) of the Polytechnic University Hauts-de-France (Valenciennes, France). These supports are gratefully acknowledged.

References

Chen, M., Ju, Y.L., 2015. Effect of different working gases on the performance of a small thermoacoustic Stirling engine. Refrigeration. 51:41-51.
Chen, W.L., Yang, Y.C., Salazar, J.L., 2015. A CFD parametric study on the performance of a low-temperature differential γ-type Stirling engine. Energy Conversion and Management: 106:635-643.
Cinar, C, Yucesu, S, Topgul, T, Okur, M., 2005. Beta-type Stirling engine operating at atmospheric pressure. Applied Energy. 81(1):351-357.
Derviş, E., Hayri, Y., Battal, D., 2017. A review development of rhombic drive mechanism used in the Stirling engines. Renewable and Sustainable Energy Reviews. 78:1044-1067.
Hachem, H., Gheith, R., Aloui, F., Ben Nasralla, S., 2015a. Global numerical characterization of a γ-Stirling engine considering losses and interaction between functioning parameters. Energy Conversion and Management. 96-532-543.
Hachem, H., Creyx, M., Gheith, R., Delacourt, E., Morin, C., Aloui, F., Ben Nasrallah, S., 2015b. Comparison based on exergetic analyses of two hot air engines: a Gamma type Stirling engine and an open Joule cycle Ericsson engine. Entropy. 17:7331-7348.
Kolin, I., 1991. Stirling motor: History-theory-practice (Contributions to the 5th Int. Stirling Engine Conference), Inter University Center, Dubrovnik.
Ni, M., Shi, B., Xiao, G, Luo, Z., Cen, K., 2015. Heat transfer characteristics of the oscillating flows of different working gases in U-shaped tubes of a Stirling engine. Applied Thermal Engineering. 89:569-577.
Otaka, T, Ota, M., Murakami, K., 2002. Study of performance characteristics of a small Stirling refrigerator. Heat Transfer Asian Research. 31 (5).
Reader, G.T., Hooper, C., 1983. Stirling engines. London & New York: E&FN Spon.
Tekin, Y., Ataer, O.E., 2010. Performance of V-type Stirling-cycle refrigerator for different working fluids. Refrigeration. 33:12-18.
Tlili, I., Timoumi, Y., Ben Nasrallah, S., 2008. Analysis and design consideration of mean temperature differential Stirling engine for solar application. Renewable Energy. 33:1911-1921.
Valenti, G., Silva, P., Fergnani, N., Di Marcoberardino, G., Campanari, S., Macchi, E., 2014. Experimental and numerical study of a micro-cogeneration Stirling engine for residential applications. Energy Procedia. 45:1235-1244.
Valenti, G., Silva, P., Fergnani, N., Campanari, S., Ravidà, A., Di Marcoberardino, G., Macchi, E., 2015. Experimental and numerical study of a micro-cogeneration Stirling unit under diverse conditions of the working fluid. Applied Energy. 160:920-929.
Wang, K., Dubey, S., Choo, F.H., Duan, F., 2016. A transient one-dimensional numerical model for kinetic Stirling engine. Applied Energy. 183:775-790.

Spectral Analysis of LBM-LES Numerical Data on Lid-driven Cavity

[1] Insaf MEHREZ, [1] Ramla GHEITH, [2]* Fethi ALOUI

[1] University of Monastir, National Engineering School of Monastir (ENIM), LESTE Laboratory
Avenue Ibn El Jazzar 5019 Monastir, Tunisia
[2] Polytechnic University Hauts-de-France (UPHF), LAMIH, CNRS UMR 8201, F-59313 Valenciennes, France

E-mail: mehez.insaf@gmail.com
*Corresponding author e-mail: Fethi.Aloui@uphf.fr

Abstract
The lid-driven cavity is an important fluid mechanical system work for as a benchmark for testing numerical methods and for examining fundamental aspects of incompressible flows in confined volumes which are driven by the tangential motion of a bounding wall. A numerical study is provided of lid-Driven cavity flows focusing on the evolution of the flow for high Reynolds number. A spectral analysis and a fluctuation velocity are performed on the numerical data obtained from Lattice Boltzmann method (LBM) and large-eddy simulation (LES) of the turbulent flow. The analyzed data or signals are picked at two specific points inside the cavity allowing investigating three drastically different flow regimes over time: laminar, transitional and turbulent. In comparison with direct numerical simulation, LBM-LES model not only have a reduced resolution in space but also in time. In this context, the background of LBM is presented and the construction of Navier-Stokes equations from Boltzmann equation is discussed. The LBM-LES model for solving transition is developed and turbulence modeling is implemented. In the second part, a Fourier transform is chosen to study signals from LBM-LES model, to provide a local analysis of transient turbulent events.

Keywords: Lid-driven cavity, Turbulence, LBM-LES model, Spectral analysis.

1. Introduction

The first numerical investigation of the flow in a lid-driven cavity is due to (Kawaguti, 1961) who performed simulations for creeping as well as for nonlinear flows for Reynolds numbers up to Re=128, investigating three aspect ratios Γ=0.5, 1 and 2. Only after the more extensive theoretical and numerical study of (Bruneau and Saad, 1977) the lid-driven cavity became a benchmark problem for Navier–Stokes solvers (Schreiber and Keller, 1983; Ghia et al., 1982, 1977; Botella and Peyret, 1998; Albensoeder and Kuhlmann, 2005) as well as a paradigm for investigating vortex dynamics in closed systems.

In recent years LBM has undergoes rapid development since it is a relatively new method and attracts an increasing amount of attention (Succi, 2001; Yuang et al., 2014).Its main assets are its simple algebraic manipulation, its easy solution procedure and its implementation of boundary conditions with its ability of dealing with complex fluids. It may explain why LBM is a very promising and competitive numerical tool in solving heat transfer process (Mishra and Lankadasu, 2005), turbulent flows (Teixeira, 1998; Yu et al., 2005) micro-flows (Nie et al., 2002), nanofluids flows (Zhou and Yan, 2015) porous media (Guo and Zhao, 2002) .and multiphase flow (He et al., 2003). However, this apparent simplicity still has some limitations. When trying to simulate turbulent flow, these methods cannot be directly applied. Teixeira (1998) presented a lattice Boltzmann method for turbulent flows when the single relaxation time is modified. The large eddy simulation (LES) can efficiently simulate vorticity larger than a prescribed scale. The Smagorinsky (Smagorinsky ,1962) is applied to simulate flow turbulence, which spread out to be the simplest x and most accurate for turbulence flows. (Hou et al., 1996) demonstrate that the standard Smagorinsky model can be included into the lattice Boltzmann equation for turbulence modeling when the single relaxation time is modified as a variable relaxation time. It is directly attached with the distribution function without any calculations of derivatives.

The analysis of sampled signals of turbulent fluid flows through wavelet analysis is now common practice. Such analysis often provides tremendous insight into the flow behavior otherwise difficult to apprehend with more conventional statistical signal analysis methods (example: Fourier transform). The use of wavelet analysis to study signals from LES is not as common, because of the intrinsic high level of non-physical noise introduced by the subgrid models and the reduced resolution both in time and in space. However, depending on the subgrid model and the numerical method used, these difficulties may be overcome.

LBM-LES model has been employed and is reported here for the aim of this work of the time histories of the velocity and other fluctuating quantities in the turbulent regime of the lid-driven cavity flow.

2. Numerical methods

The incompressible Navier-Stokes equations are numerically solved:

$$\frac{\partial \overline{u_j}}{\partial x_j} = 0 \quad (1)$$

$$\frac{\partial u_i}{\partial t} + u_j \frac{\partial u_i}{\partial x_j} = -\frac{1}{\rho}\frac{\partial p}{\partial x_i} + \nu \frac{\partial}{\partial x_j}\left(\frac{\partial u_i}{\partial x_j} + \frac{\partial u_j}{\partial x_i}\right) \quad (2)$$

Lattice Boltzmann method (LBM) is carried out by solving the above governing equations, using large eddy simulation (LES).

2.1. Standard LBM

The lattice Boltzmann model proposed to solve the axial and radial velocities by (Qian et al., 1992). The equation of the particle velocity distribution function f_k can be written:

$$f_k(\boldsymbol{r}+\boldsymbol{e}_k\Delta t, t+\Delta t) = f_k(\boldsymbol{r},t) - \frac{\Delta t}{\tau}\left[f_k(\boldsymbol{r},t) - f_k^{eq}(\boldsymbol{r},t)\right] \quad (3)$$

where, f_k is the distribution function denoting the number of particles at lattice node $\boldsymbol{r}$ and time t, τ is the relaxation time, f_k^{eq} is the equilibrium distribution function and Δt is the time step.

For the D_2D_9 lattice arrangement, τ and f_k^{eq} are given by the following expressions:

$$\tau = \frac{3\nu}{|\boldsymbol{e}_k|^2} + \frac{\Delta t}{2} \quad (4)$$

$$f_k^{eq}(\boldsymbol{r},t) = w_k\rho(\boldsymbol{r},t)\left[1 + \frac{\mathbf{3}\ \boldsymbol{e}_k\boldsymbol{U}}{c_s^2} + \frac{\mathbf{9}\ \boldsymbol{e}_k\boldsymbol{U}}{2c_s^4} - \frac{3\boldsymbol{U}^2}{2c_s^2}\right] \quad (5)$$

where ν is the viscosity, U is the velocity vector. The nine velocities $\boldsymbol{e}_k$ and their corresponding weights w_k in the $D2Q9$ lattice are defined as:

$$e_0 = (0,0), e_1 = (\pm1,0).c, \quad e_{2,4} = (0,\pm1).c, e_{5,6,7,8} = (\pm1,\pm1).c \quad (6)$$

$$w_0 = \frac{4}{9}, w_{1,2,3,4} = \frac{1}{9}, w_{5,6,7,8} = \frac{1}{36} \quad (7)$$

where $c = \frac{\Delta x}{\Delta t}$; c_s is the speed of sound and Δx is the grid size.

At each node, the macroscopic density ρ and velocity U are calculated from the values of f_k over all directions:

$$\rho(\boldsymbol{r},t) = \sum_{k=0}^{8} f_k(\boldsymbol{r},t) \quad (8)$$

$$u(\boldsymbol{r},t) = \frac{1}{\rho}\sum_{k=0}^{8} f_k(\boldsymbol{r},t) \quad (9)$$

2.2. LBM assembling with LES

LBM-LES is implementing to simulate turbulent flow. To simplify the problem in this study, we assembled the standard Smagorinsky sub-grid scale model (Smagorinsky, 1962) into the LBM. By the LES theory, the viscosity is the sum of the molecular and eddy viscosities, v and v_t, respectively:

$$\nu_{tot} = \nu + \nu_t \quad (10)$$

ν_t is determined as follows:

$$\boldsymbol{\nu_t} = \boldsymbol{C_s}\Delta * |\bar{\boldsymbol{S}}| \quad (11)$$

Here, Cs represents the Smagorinsky constant, Δ is the filter width, and $\bar{\boldsymbol{S}}$ is the strain rate tensor at the grid-scale. Meanwhile, according to LBM theory, the total viscosity ν_{tot} is calculated as:

$$\boldsymbol{\tau_{tot}} = \mathbf{3}\boldsymbol{\nu_{tot}}\frac{\Delta t}{\Delta x^2} + \frac{\mathbf{1}}{\mathbf{2}} \quad (12)$$

where τ_{tot} is the total relaxation time and it is obtained from ν_{tot}, and is used to replace the original relaxation time **τ** in Eq. (4). As the solution of the lattice Boltzmann (Eq. 3) is the solution to the flow (Eq.1) and (Eq.2), the flow turbulence can be simply and naturally modeled in the standard lattice Boltzmann equation with the total relaxation time which includes the eddy relaxation time from Eq. (10). By using the Chapman-Enskog analysis, it can be shown that the following 2D incompressible turbulent flow can be recovered from the lattice Boltzmann.

3. Geometry and boundary conditions

The two-dimensional flow in the (x, y) plane can be thought of being implanted in the three-dimensional problem by ejecting the two-dimensional flow field u = (u, v, 0) in z direction and by letting Lz → ∞. The numerical calculation of two-dimensional cavity flows requires little resources. The system thus provides a good test bed for numerical codes and for studying two-dimensional flows physics.

The geometry at stake is shown in Figure 1. We are dealing with a square cavity consisting of three rigid walls with Bounce-Back scheme and a lid moving with a tangential unit velocity. We are interested in the velocity distribution for a Reynolds number equal to 5000. The corresponding Mach number is Ma=U/cs =0.14. The simulation used 325x325 uniform meshes. The distance between adjacent nodes was δx = 1 lattice units (lu) = 0.001m. The time step was set to be δt = 0.001 s. The time for one complete circulation of the fluid in the cavity

required approximately 2.9 s or 2900 time steps. Following Equation (10), the viscosity of the fluid was $v = 3.1\times10^{-6}$ m^2/s with a relaxation parameter value of 1.9683.

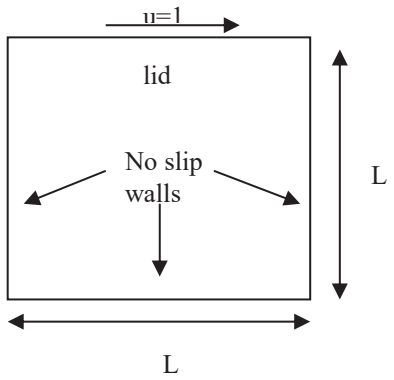

Fig. 1: Geometry of the lid-driven cavity

4. Results and discussions

4.1. Code validation

Typical streamline patterns of the two-dimensional global recirculation vortex driven by the moving wall for Re = 5×10^3 are shown in figure 2. The results of LBM-LES model is in good agreement with the results of (Ghia et al., 1982).

The figure shows a two separated eddies in the bottom corners are signaled by the two separating streamlines. Even a second separated vortex is visible in the bottom right corner. For even higher Reynolds numbers (equal to 5000) the core of the vortex approaches a solid-body rotation with circular streamlines and constant vorticity.

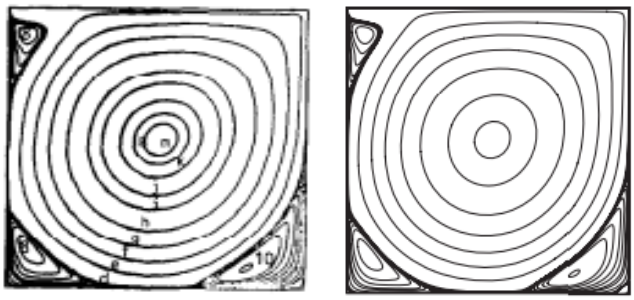

(a) (b)

Fig. 2: Streamline a) results of (Ghia et al., 1982) b) LBM-LES model for Re=5000

4.2. Fluctuations

Two points have been carefully and purposely elected inside the cavity with a location corresponding to the center and the bottom vortex. For the LES, only the resolved part have been used. The point P1 is located at the center of the cavity with coordinates

P1=(0.5, 0.5, 0.0) **(13)**

The point P2 is located in the BD1 vortex with coordinates

P2=(0.07, 0.07, 0.0) **(14)**

In addition, the statistical analysis of the temporal fluctuations of the velocity field allows one to study the vortically-intense regions of the flow. The vortical structures are therefore connected to the rapid changes in the temporal signal of the velocity field. The same profile is observed for different position P1 and P2.

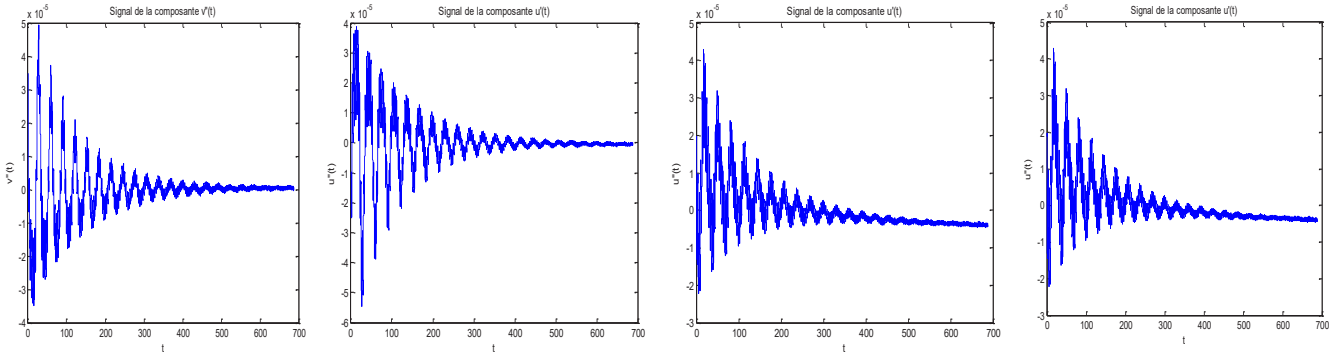

(a) **(b)**

Fig. 3: Velocity fields for the x-y components at b) the point P1b) the point P2

4.3. Spectral analysis

The time series of the x- y components of the velocity field have been extracted from the LBM-LES databases at

the two distinct locations inside the cavity introduced in previous section. The groundbreaking work of Kolmogorov (Kolmogorov, 1941) highlights the fact that the velocity fluctuations of a turbulent flow can be characterized and analyzed based upon the behaviors of the scales of the spatial increment of the Eulerian velocity or the temporal increment of the Lagrangian velocity. A pre-analysis of the simulated system consists in the Fourier transform computation applied to the velocity signal at the points P1 and P2 of maximum mean turbulence production within the cavity. The Fourier transform can be written as:

$$S(\nu) = \int s(t) e^{-2i\pi\nu t} dt \qquad (15)$$

The results of the spectral analysis for the intensity in a Log-Log scale are shown in Figure 4 where a -5/3 slope is observed for the velocity signals. These results which are characteristics of the developed turbulence region of the cavity flow are in good agreement with those predicted by the statistical theory of the turbulence (Kolmogorov, 1941). Slopes were conventionally estimated using a linear regression method. It is worth noting that these spectra lack smoothness at high frequencies due to the limited size of our databases of turbulent flow samples.
The above results for the turbulent region of the flow, for different positions, provide structures possessing a clear fractal signature.
At the point P1 have a very small frequencies correspond of the gravity force.
At the point P2 corresponds to very large depressions associated with the turbulent bursts occurring when a pair of counter-rotating vortices is produced. At this position, we note the absence of the small frequencies.

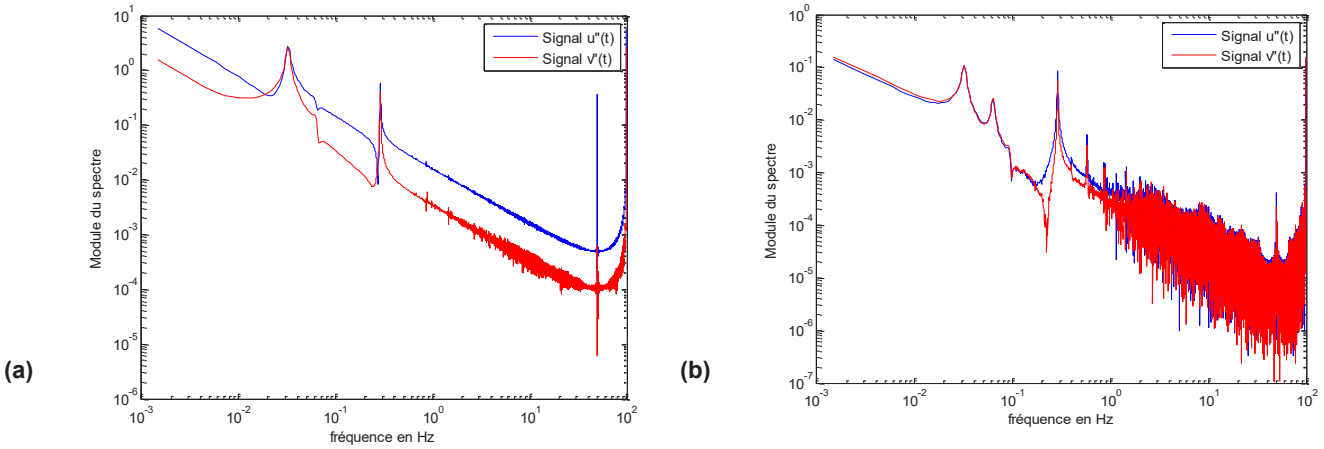

Fig. 4: Fourier transforms of the time histories of the LBM-LES velocity signals maximum mean turbulence production within the cavity at a) the point P1 and b) the point P2

5. Conclusion

In this study, the LBM method is used to conduct an LES of turbulent flow in Lid-Driven cavity. The fluctuation of the instantaneous velocity fields inside the cavity are then used to investigate the complex vortical structures which characterise this flow. The LBM-LES is an alternative approach to the Navier–Stokes equation (NSE) to solve fluid flow problems. This method is capable of modelling applications such as turbulent flow. Solution of the lattice Boltzmann equation (LBE) uses a simple stream and collide computational procedure. Although the most popular formulation of the LBE is the Boltzmann equation with the so called Bhatnagar Gross Krook (BGK) approximation based on the use of a single relaxation time (SRT). The simple and traditional spectral (Fourier) analysis presented provides interesting initial results. However, such spectral analysis is known to provide limited insight.

Acknowledgments

This research was supported by the laboratories LESTE of ENIM (university of Monastir, Tunisia) and LAMIH (UMR CNRS 8201) of the Polytechnic University Hauts-de-France (Valenciennes, France). These supports are gratefully acknowledged.

References

Albensoeder, S., Kuhlmann, H.C., 2005. Accurate three-dimensional lid-driven cavity flow. J. Comput. Phys., 206:536–558.
Bruneau, C.H., Saad, M., 1977. The 2d lid-driven cavity problem revisited. Comp. Fluids, 35:326–348, 2006
Botella, O., Peyret, R., 1998. Benchmark spectral results on the lid-driven cavity flow. Comp. Fluids, 27:421–433.
Guo, Z., Zhao, T.S., 2002. Lattice Boltzmann model for incompressible flows through porous media, Phys. Rev. E, vol. 66, 036304.
Ghia, K., Ghia, N., Shin, C.T. 1982. High-Re solutions for incompressible flow using the Navier-Stokes equations and a multigrid method. J. Comput. Phys., 48: 387–411, 1982.
He, X.Y., Chen, S.Y., Zhang, R, 2003. A Lattice Boltzmann Scheme for Incompressible Multiphase Flow and Its Application in Simulation of Rayleigh-Taylor Instability, J. of Computational Physics. vol. 152, pp.642-663.
Hou S., Sterling J., Chen S., Doolen G.D., 1196. A lattice Boltzmann subgrid model for high reynolds number flows. Fields Inst. Commun, Vol. 6, pp. 151–166
Kawaguti, M., 1961. Numerical solution of the Navier–Stokes equations for the flow in a two-dimensional cavity. J. Phys. Soc.Jap., 16:2307–2315.
Kolmogorov, AN., 1941. The local structure of turbulence in incompressible viscous fluid for very large Reynolds numbers. CR Acad Sci USSR, 299–303.
Mishra, S.C., Lankadasu, A., 2005. Application of the lattice Boltzmann method for solving the energy equation of a 2-D transient conduction–radiation problem, Numer. Heat Transfer A, vol. 47, pp. 935-954.

Nie, X., Doolen, G.D., Chen, S., 2002. Lattice Boltzmann simulation of fluid flows in MEMS, J. of Statistical Physics. vol. 107, pp. 279-289.

Qian Y. H., d'Humières D., Lallemand P., 1992. Lattice BGK models for Navier-Stokes equation, Europhysics Letters, Vol. 17, no. 6 pp. 479-484.

Schreiber, R., Keller, H.B., 1983. Driven cavity flows by efficient numerical techniques. J. Comput. Phys., 49:310–333, 1983

Smagorinsky J., 1963. General circulation experiments with the primitive equations. Mon. Weather Rev, Vol. 91, pp. 99–164.

Succi, S. 2001. The Lattice Boltzmann Equation for Fluid Dynamics and Beyond, Oxford University Press, Oxford.

Yuang, H.Z., Niu, X.D.,Shu. S, Li, M. J., Yamaguchi, H., 2014. A momentum exchange-based immersed boundary-lattice Boltzmann method for simulating a flexible filament in an incompressible flow, Computers and Mathematics with Applications vol. 67, pp. 1039-1056.

Teixeira, C. M., 1998. Incorporating Turbulence Models into the Lattice-Boltzmann Method, Int. J. Modern Physics C, vol. 9, No. 8, pp. 1159-1175.

Yu, H., Girimaji, S.S., Luo, L.S, 2005. DNS and LES of decaying isotropic turbulence with and without frame rotation using lattice Boltzmann method, J. of Computational Physics, vol. 209, pp. 599–616

Zhou, W.N., Yan, Y.Y., 2015. Numerical investigation of the effects of a magnetic field on nanofluid flow and heat transfer by the lattice Boltzmann method, Numer. Heat Transfer A, vol. 68, pp. 1-16

The Effect of Entering Angle on Machinability of PH 13-8 Mo

[1*]Ahmet Serdar Güldibi, [2]Halil Demir
[1] Karabuk Univeristy, Technology Faculty, Manufacturing Department, Baliklarkayasi mevkii, Karabuk, 78050, Turkey
[2] Karabuk Univeristy, Technology Faculty, Manufacturing Department, Baliklarkayasi mevkii, Karabuk, 78050, Turkey

* E-mails: aserdarguldibi@karabuk.edu.tr

Abstract
PH 13-8 Mo steel is an attractive steel for air and space industry as well as medical sector due to its greater strength and better corrosion immunity. High strength and good ductility steels have great importance for industry because of lightweight engineering designs and CO_2 savings. On the other hand, machining of high strength and hard materials causes high energy consumption and CO_2 production. Determining cutting force is an essential factor for minimizing power consumption in metal cutting process. For cleaner production the consumption should be eliminated. In this study, the effect of entering angle on machinability of PH 13-8 Mo was investigated for the solution heat treated (A0), solution heat treated and then aged at 400℃ (A4), 525℃ (A525) and 600℃ (A6) samples. All samples were machined at different cutting speeds and at different feed rates at a 1 mm constant cutting depth. The results show, increasing entering angle decreases cutting forces, rising cutting speed reduces cutting forces and improving feed rate boosts cutting forces. The lowest cutting force was measured at 150 m/min cutting speed, at 0.04 mm/dev feed rate and at 95° entering angle for A0 sample and the cutting force is 56% higher at 75° entering angle.

Keywords: PH 13-8 Mo, Machining, Cutting Forces

I. Introduction

Energy efficiency is the most important subject of this century because of its effect on economy and environment. High energy consumptions cause air and environmental pollutions. Manufacturing industry is one of the highest energy consumers in the world. Casting, forging, rolling, bending and machining operations cause excessively energy consumptions. According to Statistics Canada the manufacturing sector consumed 2172 petajoules of energy in 2017 in Canada. To reduce energy consumption in machining operations it is needed to reduce cutting forces which affected by workpiece material, tool geometry, cutting speed, feed rates, chip load and cutting fluid. In this study two different cutting tools were used to machine samples at various cutting speeds and feed rates.

PH 13-8 Mo is a member of maraging steels which is used for many applications, such as landing gear parts, nuclear reactor components, petrochemical applications and medical parts (Guo et al., 2003). This steel is very attractive for many industry sectors because of its high strength and hardness which ensue of the developed precipitations in the microstructure while aging treatment. However aging treatments affect machinability of the steels and cause high energy consumption. To reduce energy consumption the cutting forces must be reduced. Entering angle has affect on cutting forces and on tool life. The purpose of this study determining the effect of entering angle on cutting forces under different cutting conditions.

II. Experimental Procedure

PH 13-8 Mo steel is a low carbon steel. The chemical composition was analyzed by the GNR Atlantis optical emission spectrometry. The workpieces were supplied from Uddeholm Company in diameter of 35 mm and length of 350 mm. The samples were solution heat treated at 850℃ for 0.5 h and subsequenlty air cooled. All samples except one aged at different temperatures (400, 525, 600 ℃) for 4 hour and cooled in room temperature. After heat treatment four sets of samples were prepared: Solution heat treated (A0), aged at 400℃ (A4), aged at 525℃ (A525) and aged at 600℃ (A6).

Grinding and polishing were applied to heat treated samples for the microstructural investigations. Kalling's reagent was used for etching the samples at different etching times depend on material hardness. Microstructural investigations were carried out using Nikon Epiphot 200 optical microscope and Carl Zeiss Ultra Plus Fesem SEM. The machining tests were performed under dry machining at 1 mm constant cutting depth, at different cutting speeds and at various feed rates. Two different cutting inserts and two different tool holders were used for the machining tests. The cutting insters have CNMG120408 and SNMG120408 geometries. CNMG (C) is PVD multi-layer coated and SNMG (S) is CVD multi-layer coated cemented carbides. The tool holders have same angles except entering angle. DCLNR (C) has 95° entering angle and DSBNR (S) has 75° entering angle. The geometry of the tool holders was given at fig. 1. The rake and the inclination angle of the tool holders are -5°. The tool with 75° entering angle is marked as (S) and the tool with 95° entering angle is marked as (C).

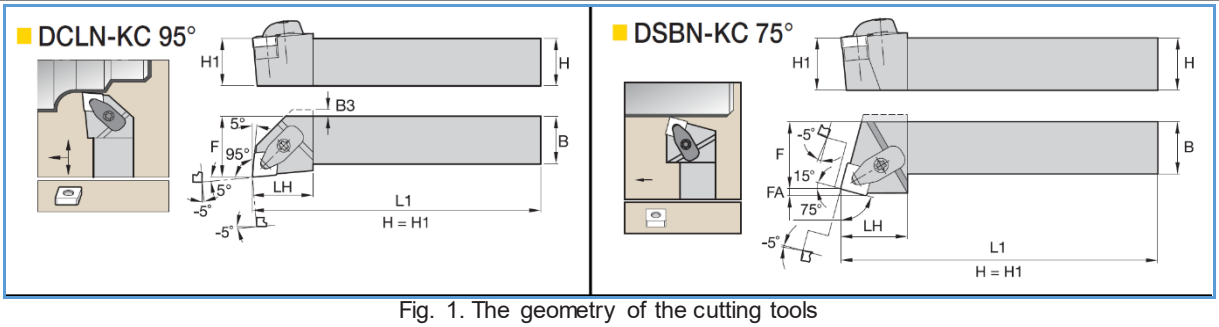

Fig. 1. The geometry of the cutting tools

III. Microstructure and EDS analyses

PH 13-8 Mo steel is maraging steel which consist Cr, Ni, Mo, Al and C to form precipitations in the microstructure. Maraging steels are precipitation hardenable martensitic steels and designed to form complete matertensitic structure and austenite transforms completely into martensite during cooling.

Table 1. Chemical Composition of Corrax Steel

Element	C	Si	Mn	P	S	Cr	Mo	Ni	Al
%	0.048	0.203	0.012	0.026	12.24	13.88	1.388	9.064	1.582

Maraging steels can be hardened through aging process. PH 13-8 Mo steel reaches the highest hardness value after aging at 525℃ for 4 hours. Rockwell hardness measurements were given at table 2 below. Higher temperatures than 525℃ decrease the hardness of the workpiece material because of the growth of the precipitations and reverted austenite formation in the martensite boundaries (Schnitzer et al., 2010). Reverted austenite also cause decrease on toughness and strength for maraging steels (Viswanathan et al., 2005).

Table 2.Rockwell hardness results

Sample	Rockwell Hardness
A0	30.5
A4	38.7
A525	50.3
A6	41.2

The microstructures of the samples after heat treatment can be seen in fig. 2. As seen in the microstructure, solution heat treated A0 sample has lath martensite structure. After aging treatment the lath martensite structure transform to plate martensite because of NiAl precipitations and reverted austenite formation in the martensite boundaries (Guldibi and Demir, 2020; Sha et al., 2012).

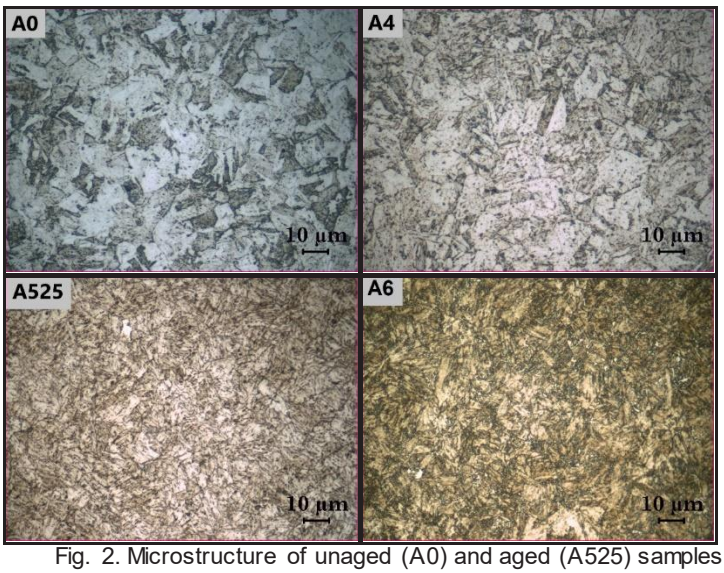

Fig. 2. Microstructure of unaged (A0) and aged (A525) samples

Precipitations are not visible under light microscope. Fig. 3 shows the EDS analysis with the sprectrum points 1-5 black marked on the SEM image of A525 sample. The marked points contain varios percentage of C, Cr, Ni, Al and Mn elements. The chemical composition of the market points was given at table 3. The precense of these elements indicates a small amount of CrC, NiAl, MoC and NiMn precipitations. The precipitations hinder the movements of the dislocations and enhances the strength and hardness of the material. Reverted austenite occurs

in the martensite boundaries and cause decrease on hardness, strength and toughness of the material.

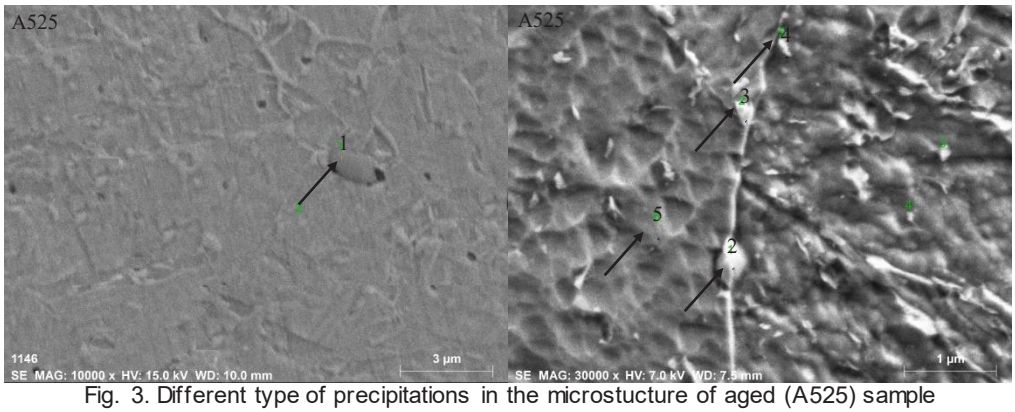

Fig. 3. Different type of precipitations in the microstucture of aged (A525) sample

Table 3. Chemical composition of the precipitations in the microstructure of aged (A525) sample

Element	C	Al	Cr	Mn	Ni	Mo	Fe
1	5.33	1.13	10.55	6.41	5.93	14.28	Balance
2	17.22	1.35	20.20	2.11	6.26	1.14	Balance
3	6.95	1.11	23.16	2.82	10.64	1.32	Balance
4	3.89	1.55	18.67	1.02	11.19	1.19	Balance
5	2.50	1.48	18.83	4.41	9.89	0.46	Balance

IV. Cutting forceses

The cutting tests were carried out under dry cutting conditions at different cutting speeds and feed rates. The effect of feed rates on cutting forces for two different entering angles were given at Fig. 4. As can be seen in the figure increasing feed rate increase the cutting forces excessively. Increments on feed rate cause growth on shear plane area which is responsible for the increase on cutting forces.

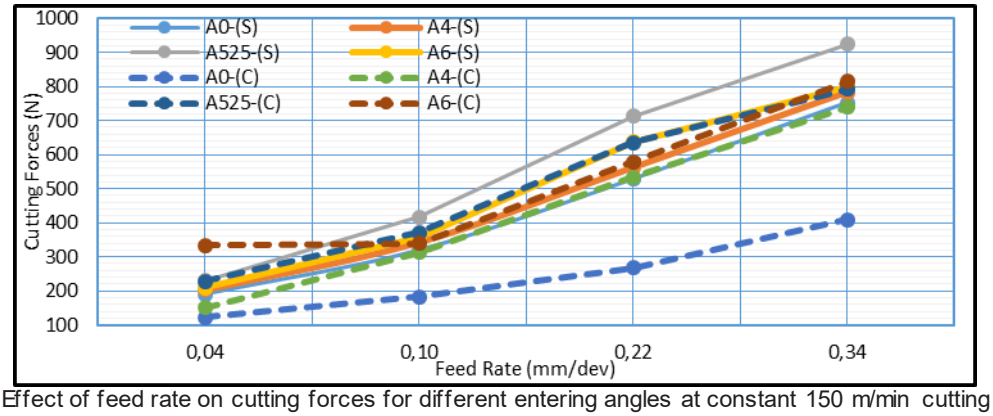

Fig. 4. Effect of feed rate on cutting forces for different entering angles at constant 150 m/min cutting speed

The machining tests at 150 m/min cutting speed and at 0.04 mm/dev feed rate show that the cutting forces for A0-(S) is 56% higher than A0-(C), A4-(C) is 36% higher than A4-(S), A525-(C) has the same result with A525-(S) and A6-(C) is 59% higher than A6(S).

The results at 0.34 mm/dev is, A0-(S) 84% higher than A0-(C), A4-(S) 6% higher than A4-(C), A525-(S) 17% higher than A525-(C) and A6-(S) 2% lower than A6-(S). A525-(S) has significant tool wear therefore the cutting forces higher than A525-(C). 95° entering angle offers more durability for tool life than 75° entering angle. This can be explained by the enlargement of the cutting edge. 75° entering angle cause 4% larger cutting edge than 95° enterince angle at the same cutting depth.

Tool manufacturers claim that the low entering angles offer more durability for tool life and low cutting forces. However, the tests show the exact opposite results. This can be explained by the hardness, ductility and strength of PH 13-8 Mo Steel and enlargements on cutting edge of the tool because of low entering angle.

The effect of cutting speed on cutting forces for different entering angles were given in fig.5. as can be seen in the figure increasing cutting speed decrease cutting forces until 200 m/min cutting speed because of heat formation in the cutting zone which softens the workpiece material and ease the cutting process. Higher cutting speeds then 200 mm/min increase cutting forces because of tool wear and vibration formation (Kayhan and Budak, 2009).

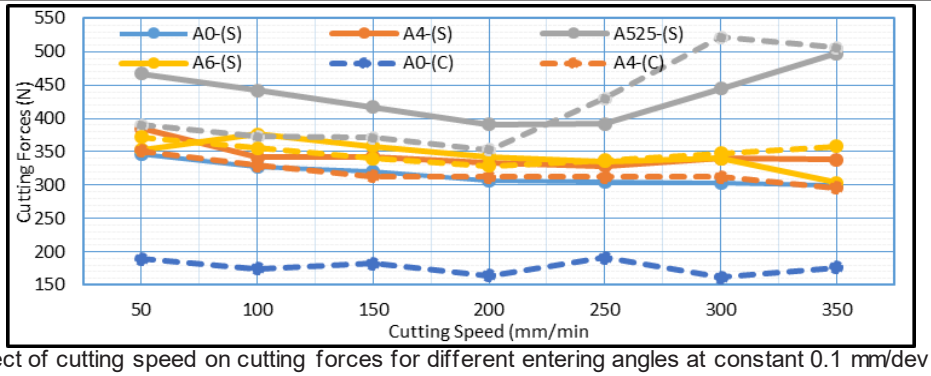

Fig. 5. Effect of cutting speed on cutting forces for different entering angles at constant 0.1 mm/dev feed rate

Low cutting speeds increase cutting forces because of BUE and low heat formation in the cutting zone. In addition to that low cutting speeds also responsible for the vibration which cause increments on cutting forces. As cutting speed increases, cutting temperature increases which softerns the workpiece materials leads to reduce the flow stress affecting the tool and lowers cutting force (El-Hossainy et al., 2010). However high cutting speeds cause also tool wear which increase the cutting forces and damage the workpiece surface. The results show that the lowest cutting forces were measured at 200 m/min cutting speed for A0-(C) which machined under 95° entering angle. A0 sample has 30.5 HRC hardness which is relative less than other samples. The small increments and decrements on the cutting forces for A0-(C) sample depend on vibration formation during machining. The results at 200 m/min show that the A0-(S) is 86% higher than A0-(C), A4-(S) is 7% higher than A4-(C), A525-(S) is 10% higher than A525-(C) and A6-(S) is 4% higher than A6-(C). Higher cutting speeds than 200 m/min cause tool wear which increase cutting forces excessively. As seen in the results, increasing feed rate increase the cutting forces and increasing cutting forces decrease cutting forces until 200 m/min cutting speed.

V. Conclusions

This study investigated the influence of entering angle on cutting forces at different cutting speeds and feed rates for PH 13-8 Mo samples at various hardness. Machining tests were carried out for A0 (30.5 HRC), A4 (38.7 HRC), A525 (50.3 HRC) and A6 (41.2 HRC). The results indicated that:

- Aging treatments cause increase on hardness of the material. Higher aging treatments than 525℃ cause decrease on hardness because of overaging which is responsible for reverted austenite formation and precipitation growth.
- Increasing cutting speed decrease cutting forces until 200 m/min. Higher cutting speeds cause increments on cutting forces.
- Enhancements on feed rates rise the cutting forces excessively.
- Low entering angles cause higher cutting forces to compare with higher entering angles.

Acknowledgements

Sciencetific Research Projects Department of Karabuk University (BAP) was supported this research with project no KBÜBAP-18-KP-145.

References

El-Hossainy, T.M., El-Zoghby, A.A., Badr, M.A., Maalawi, K.Y., Nasr, M.F., 2010. Cutting Parameter Optimization when Machining Different Materials. Mater. Manuf. Process. 25, 1101–1114. https://doi.org/10.1080/10426914.2010.480998

Guldibi, A.S., Demir, H., 2020. Aging Effect on Microstructure and Machinability of Corrax Steel 10, 5168–5174.

Guo, Z., Sha, W., Vaumousse, D., 2003. Microstructural evolution in a PH13-8 stainless steel after ageing. Acta Mater. 51, 101–116. https://doi.org/10.1016/S1359-6454(02)00353-1

Kayhan, M., Budak, E., 2009. An experimental investigation of chatter effects on tool life. Proc. Inst. Mech. Eng. Part B J. Eng. Manuf. 223, 1455–1463. https://doi.org/10.1243/09544054JEM1506

Schnitzer, R., Zickler, G.A., Lach, E., Clemens, H., Zinner, S., Lippmann, T., Leitner, H., 2010. Influence of reverted austenite on static and dynamic mechanical properties of a PH 13-8 Mo maraging steel. Mater. Sci. Eng. A 527, 2065–2070. https://doi.org/10.1016/j.msea.2009.11.046

Sha, W., Leitner, H., Guo, Z., Xu, W., 2012. Phase transformations in maraging steels, in: Phase Transformations in Steels. Elsevier, pp. 332–362. https://doi.org/10.1533/9780857096111.2.332

Viswanathan, U.K., Dey, G.K., Sethumadhavan, V., 2005. Effects of austenite reversion during overageing on the mechanical properties of 18 Ni (350) maraging steel. Mater. Sci. Eng. A 398, 367–372. https://doi.org/10.1016/j.msea.2005.03.074

Heating Rate Effect on Tetrapak Paper Pyrolysis: Thermogravimetric Analysis

[1] Afef BOUAZIZI, [2] Emna BERRICH, [2] Imene BEKRI, [3] Ezzedine SRASRA, [4*] Fethi ALOUI

[1] Al-Manar University, Faculty of Sciences, El-Manar, 2092 El Manar Tunis, Tunisia.
[2] University of Nantes, GEPEA, CNRS UMR6144, Institute Mines-Telecom (IMT), Nantes - France.
[3] National Center of Materials Sciences, Technopole of Borj Cedria, BP 73, 8027 Soliman, Tunisia.
[4] Polytechnic University Hauts-de-France (UPHF), LAMIH (UMR CNRS 8201)
Campus Mont Houy, F-59313 Valenciennes Cedex 9 - France.

* Corresponding author e-mail: Fethi.aloui@uphf.fr

Abstract

Biomass and the plastics are considered to be ones of the most important renewable sources in nature. The typical composition of a tetrapak is 70% of cardboard (Kraft paper), 25% of low-density polyethylene (LDPE) and 5% of aluminium foil. In this paper, we present the heat rate effect on tetrapak pyrolysis using thermogravimetric TG analysis. Three heating rates (5°C/min; 10°C/min; 20°C/min) and three Nitrogen flow rates (20, 40 and 60 ml/min) were used. The Tetra Pak is composed of 47.46% of carbon, 7% of hydrogen and 0,325% of nitrogen. The derivative TG curves function of time and temperature for the different heating rates and Nitrogen flow rates were illustrated and discussed.

Keywords: Tetrapak paper wastes, Energetic valorization, Pyrolysis, Heating rate, Thermogravimetric analysis.

I. Introduction

The multi-layer polycoated paperboards, called often tetrapaks based on the name of their first and largest producer company, are widely used as aseptic packages for beverages like milk, juice or wine. This packaging system allows products to be distributed without refrigeration for relatively long time. For this reason, used tetrapaks create a significant part of Municipal Solid Waste (MSW). Tetrapak is generally composed of 70% of cardboard (Kraft paper), 25% of low-density polyethylene (LDPE) and 5% of aluminum foil. Biomass is considered to be one of the most important renewable sources in nature. It is estimated that the world's annual biomass production is up to 146 billion tons (Gillet et al., 2017). At the same time, biomass (cellulose 'CL') is largely produced as a by-product of industry, agriculture and forestry such as bioethanol fermentation, pulp and paper manufacturing, grain planting, and forest mining (Barbarias et al., 2018). For example, biomass waste derived from agricultural production is estimated to be as many as 30 billion tons per year and that those from pulp and paper industry can reach 70 million tons per year (Leyva-Porras et al., 2013). On the other hand, plastics are extensively used in our daily life to bring us considerable convenience. It is reported that the global annual production of plastics in 2015 was estimated to have come to 322 million tons (Ahn et al., 2016). Low-density polyethylene (LDPE) is an important commodity plastic of high output among all polymer resins, which can be manufactured into products including film, package… (Haydary et al., 2013; Ahn et al, 2016).

In this study, our main aim is to understand the thermal degradation behaviour of the Tetrapak wastes and to find the optimal CL-LDPE pyrolysis parameters. The sample to study was obtained from Tetra Pak paper formed by cellulose, polyethylene and aluminium, so the cellulose and polyethylene (CL-LDPE) are coupled.

II. Materials

The waste Tetra Pak sample was obtained from garbage, those wastes were washed with water and they are dried in the oven on 105°C while 24hours to eliminate any trace of moisture. The paper was cut into small parts of 3-4mm. The composition of the raw material is showed in table 1.

Table 1: Tetrapak wastes composition (wt %).

Cardboard	Polyethylene	Aluminum
75	25	5

III. Elementary analysis

The tetrapak paper was crushed in order to get a homogeneous powder. The elemental analysis was carried out with an apparatus of the type "Flash EA 1112 Series, CHNS-O Analyzer", the percentage of the elements is determined by performing the average of three tests. The Tetra Pak is composed of 47.46% of carbon, 7% of hydrogen and 0,325% of nitrogen (table 2). The elemental analysis results are similar to the result in the study of pyrolysis of aseptic packages (Wu et al., 2002).

Table 2: Tetrapak composition on Carbon, Hydrogen and Nitrogen using Elementary analysis.

% N	% C	% H
0.325	47.46	7

IV. Results and discussions

IV. 1. Thermogravimetric analysis

The raw material was tested for moisture content, and proximate analysis and TGA/DTA analyses were performed. The moisture content was counted as 6% after overnight drying at 105 °C into the oven. Thermogravimetric analysis was performed under N_2 atmosphere. The flowrate of purge gas was kept at different values: 20, 40 and 60 ml/min and with different heating rate: 5, 10 and 20°C/min. The sample was heated from the ambient temperature up to 600°C. From the thermal gravimetric analysis (TGA), in all the curves there are two important mass degradation peaks detected at temperatures below 600°C, which indicates the paper and polyethylene thermal degradation temperatures ranges. Paper is known to start degradation at temperatures above 200°C, which corresponds to the first degradation region, whereas polyethylene degradation begins at temperatures above 400°C, which corresponds to the second degradation region.

Table 3: Material conversion rate for each heating rate.

Heating rate (°C/min)	Nitrogen flow (ml/min)	Material conversion rate (%w)
20	20	77.38%
	40	62.5%
	60	60%
10	20	71.25%
	40	72.5%
	60	62.5%
5	20	68.75%
	40	80%
	60	60%

The conversion rate values increase while the heating rates decrease. For a heating rate of 5°C/min and a Nitrogen flow rate of 40ml/min, the highest conversion rate is then obtained. It reaches 80%.

IV. 2. Heating rate effect on Tetrapak degradation

The heating rate effect on Tetrapak pyrolysis has been studied using thermogravimetric analysis. The derivative TG (DTG) curves are presented on figures 1 to 3. It can be seen that the cardboard layer is decomposed at a lower temperature than plastic layer. Clearly separate peaks of degradation are always observed for the cellulose and plastics. The DTG curves of tetrapak thermal degradation shows two mass loss temperatures ranges between 200 and 500°C. As we can see, the first devolatilization took place between 200 and 400°C.

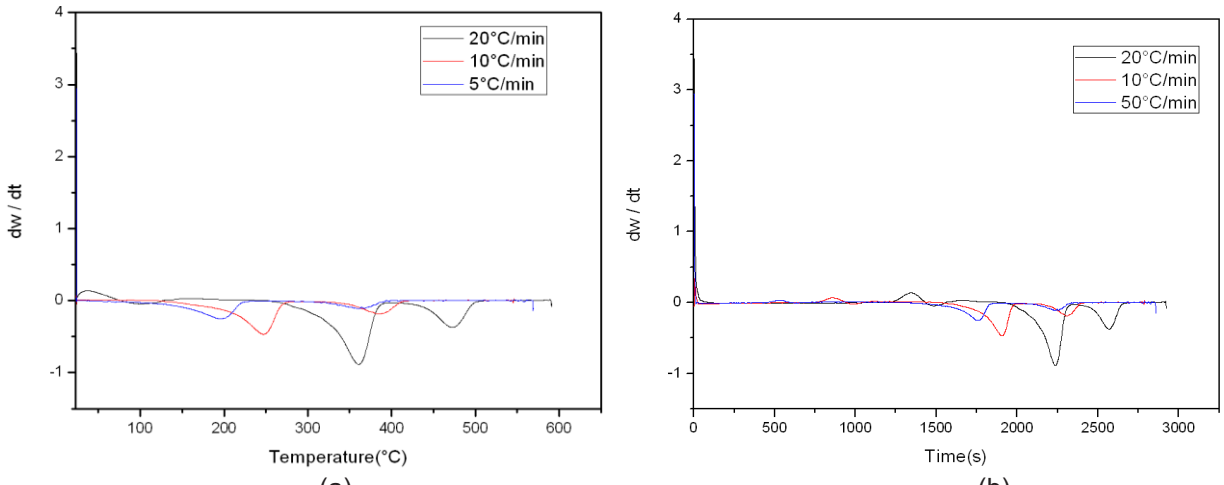

Fig. 1: DTG for a flowrate of 60 ml/min and different heating rates (5, 10 and 20°C/min): (a) vs. temperature and (b) vs. time.

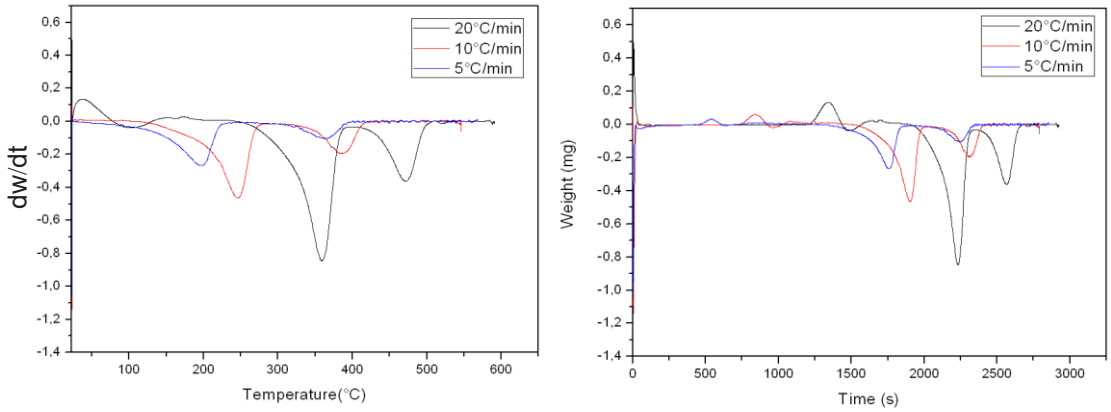

(a) (b)

Fig. 2: DTG and weight evolutions for a flowrate of 40ml/min and different heating rates (5, 10 and 20°C/min): (a) vs. temperature and (b) vs. time.

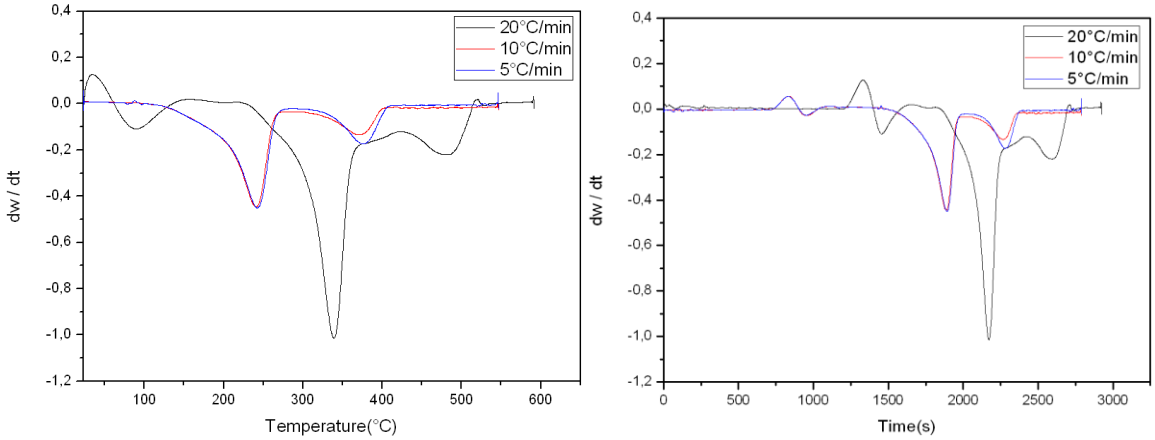

(a) (b)

Fig. 3: DTG evolutions for a flowrate of 20ml/min and for different heating rates (5, 10 and 20°C/min): (a) vs. temperature and (b) vs. time.

The tetrapak thermal decomposition begins at temperature around 220°C after 30 minutes of heating, taking into account the isothermal time to remove moisture, which equal to 20 min. And the second devolatilization taken place between 400 and 500°C with a maximum peak temperature at 445°C. The first peak is as corresponding to the thermal degradation of cardboard layer while the second one to the decomposition of the low density polyethylene. TG/DTG results showed that weight loss of tetrapak was over at the temperature of 500°C. For example, for the tetrapak degradation at 20°C/min for 20 ml/min begins at T_{11} equals to 231.44 °C after t_{11} equals to 30.95 minutes of heating. This first peak finishes at T_{13} equals to 361.98 °C after t_{13} equals to 37.41 minutes. The conversion rate reaches at the end of this peak x_{13} equals to 54 (%W). While the flow rate increases to 60 ml/min begins at T_{11} equals to 249.17 °C after t_{11} equals to 31.8 minutes of heating. This first peak finishes at T_{13} equals to 379.82 °C after t_{13} equals to 38.25 minutes. The conversion rate decreases at the end of this peak x_{13} equals to 39 (%W). This first peaks corresponds to Cellulose peak degradation.

Table 4: Tetrapak first peak degradation at 20°C/min for different nitrogen flow.

	Nitrogen flow (mL/min)			
	20	40	60	100
T_{11} (°C)	231.44	247.34	249.17	244.32
T_{13} (°C)	361.98	383.46	379.82	385.11
t_{11} (min)	30.95	31.7	31.8	31.15
t_{13} (min)	37.41	38.4	38.25	38.56
x_{13} (%W)	54	41	39	41

The cardboard is mainly responsible for the char formation of tetrapak. Since the principal components in tetrapak are Kraft paper, polyethylene and aluminium foil, the residue consisted of char and aluminium. It is clear that the degradation of single components in tetrapak (cellulose and LDPE) are independent during heating. Our result is in

good agreement with the studies carrying out using print-free tetrapak (Wu et al., 2002), cellulose-PE and cellulose-PP (Sharypov et al., 2002). The results obtained from DTG shows that during the thermal degradation of tetrapak, the degradation of cellulose is almost completed before beginning of the mass loss of LDPE. DTG results over different heating rates (5°C/min, 10°C/min and 20°C/min) show that devolatilization finishes quickly. The thermal degradation of cellulose took place between 230 and 400 °C, the degradation of CL at heating rate 20 °C/min finishes after 37.41min while for 10 °C/min and 5 °C/min the degradation finishes successively after 54.35 min and 54.75 min. Our results are similar to that of (Zheng et al., 2018) in the study of the thermal behaviour of cellulose mixed by polyethylene. The peak of CL decomposition begins at 225°C and finishes at 353°C, the degradation takes place after 20.6 minutes of heating. In the other hand, the thermal decomposition of LDPE occurred between 400-500°C. The degradation of LDPE begins after 56 minutes of heating and finishes after 1 hour and 5min. The thermal decomposition of polyethylene begins at 388°C and finishes at 495°C. The maximum temperature of the peak is equals to 461°C. The decomposition of polyethylene is occurred after 4.63 minutes of heating. The thermal degradation of LDPE depend on heating rate, it can be observed that at 20°C/min the degradation time is lower than the other heating rates. Our results are in agreement with the study of thermal degradation behaviours of plastics by (Das et al., 2017).

V. Conclusion

The obtained results illustrate that tetrapak pyrolysis consisted of two distinct stages. The different ranges temperatures and durations were identified. The conversion rates of the Tetrapak thermal degradation were also determined. The first stage (below 400°C) corresponds to the primary degradation reaction of cardboard. The degradation of polyethylene was significant in the second stage. Aluminium foil was easily separated from the solid product. At temperatures below 600°C, the Aluminium foil was obtained without any visible structural or chemical changes.

Acknowledgments

This work was supported by the GEPEA laboratory, IMT Atlantique (Nantes, France), El-Manar University and CERTE Borj Cedria (Tunis, Tunisia) and Polytechnic University Hauts-de-France (Laboratory LAMIH UMR CNRS 8201) at Valenciennes (France). These supports are gratefully acknowledged.

References

Gillet, S., Aguedo, M., Petitjean, L., Morais, A.R.C., Da Costa Lopes, A.M., Łukasik, R.M., Anastas, P.T., 2017. Lignin transformations for high value applications: towards targeted modifications using green chemistry. Green Chem. 19(18):4200-4033.

Barbarias, I., Lopez, G., Artetxe M., Olazar, M., 2018. Valorisation of different waste plastics by pyrolysis and in-line catalytic steam reforming for hydrogen production. Energy Convers. Management. 156:575-584.

Leyva-Porras, C., Esneider-Alcala, M.A., Toxqui-Teran, A., Marquez-Lucero, A., Aguilar-Martinez, J.A., 2013. Effect of molding parameters on young's modulus of an injection molded low-density polyethylene (LDPE). Ind. Eng. Chem. Res. 52:5666-5671.

Ahn, Y., Jeon, J.H., Park, J.H., Thenepalli, T., Ahn, J.W, Han, C., 2016. Effects of modified LDPE on physico-mechanical properties of HDPE/CaCO3, composites. Korean J. Chem. Eng. 33:3258-3266.

Haydary, J., Susa, D., Dudas, J., 2013. Pyrolysis of aseptic packages (tetrapak) in a laboratory screw type reactor and secondary thermal/catalytic tar decomposition. Waste Management. 33(5):1136-1141.

Wu, C., Chang, H., Tseng, C., 2002. Pyrolysis products of uncoated printing and writing paper of MSW. Fuel. 81:719-725.

Sharypov, V.I., Marin, N., Beregovtsova, N.G., Baryshnikov, S.V., Kuznetsov, B.N., Cebolla, V.L., Weber, J.V., 2002. Co-pyrolysis of wood biomass and synthetic polymer mixtures. Part I: influence of experimental conditions on the evolution of solids, liquids and gases. J. Anal. Appl. Pyrolysis. 64:15-28.

Pallab Das, Pankaj Tiwari, 2017. Thermal degradation kinetics of plastics and model selection. Thermochimica Acta. 654:191-202.

Zheng, Y., Tao, L., Yang, X., Huang, Y., Liu, C., Zheng, Z., 2018. Study of the thermal behavior, kinetics, and product characterization of biomass and low-density polyethylene co-pyrolysis by thermogravimetric analysis and pyrolysis-GC/MS. Journal of Analytical and Applied Pyrolysis. 133:185-197.

Renewable Penetration to Turkey's Electric Power Grid

[1]İzzet Alagöz, [2*]Mehmet Bulut, Mehmet Biçer

[1,2]Electricity Generation Company Inc., Ankara, 06510, Turkey
* E-mail:mehmet.bulut@euas.gov.tr

Abstract

Turkey's demand for energy and industrial development, in parallel to urbanization and growing population,are constantly increasing along with electricity demand. In order to meet this demand, there are limited hydrocarbon resources, nonetheless, Turkey has a huge potential for renewable resources that can meet this demand instead of imported coal and natural gas in electricity generation. The use of renewable energy sources, including wind and solar power, has increased rapidly in recent years in Turkey and record growth in renewable power generation has been recorded in a short time where solar power installed capacity reached 5062 MW and wind power reached to 7005 MW by the end of 2018. This trend has the potential to continue and the country's cleaner renewable energy sources can be the main source of electricity generation. This study examines the penetration of renewable energy sources to the grid by analyzing the current grid situation. The results show that the estimated installed capacity for electricity generation capacity of Turkey is about 111.710 MW and 127.754 MW, respectively for the years 2024 and 2029.

Keywords: Electrical energy, Renewable, Hydroelectric, Wind energy, Solar energy

I. Introduction

Turkish economy and industry are growing more rapidly with an increase in population resulting in more demand for energy continuously. For this reason, in order to sustain the development of the country, it needs high quality, continuous, cheap and reliable energy sources to meet the demand. Although Turkey has many sources of energy, it does not have a high potential for hydrocarbon reserves, but renewable energy resources such as solar and wind have great potential due to the geographic location. This benefit brings the potential for renewable energy in electricity production to reduce its dependence on external hydrocarbon sources such as imported natural gas. In addition, environmental awareness is needed to take advantage of these resources to the maximum extent. In addition to wind energy, which started to be used 20 years ago, there has been avery important step to generate electricity from geothermal and solar energy resources as well.

The amount of energy consumed per person is used as a measure of the development and welfare level of the countries. When developed countries are evaluated from this point of view, it is observed that the average energy consumption of OECD is about 6500 kWh/person and the annual energy consumption per person is 10,000 kWh/year in European countries. As shown in Fig. 1, the electricity gross generation per capita in Turkey is 3700 kWh/year and net consumption is about 2855 kWh/year. When electricity consumption per capita is assessed by considering Turkey's process of development, it is evident that the demand will increase continuously in the coming years.

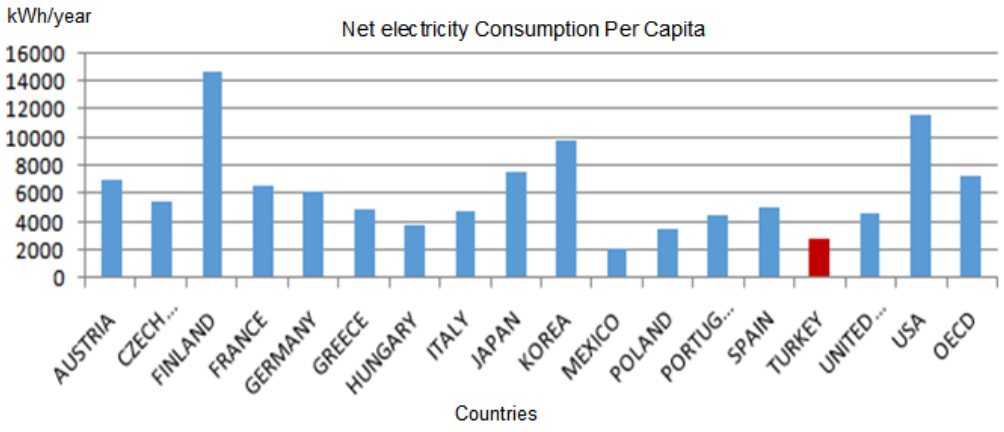

Figure 1. Net electricity consumption per capita of OECD countries in 2017 (Data from TEIAS, 2020)

Each year about 300 TWh of electricity is consumed in Turkey, which is almost a fifth of the amount of primary energy used in Turkey. The gross electricity consumption in Turkey in 2018 was 304,8 billion kWh. Turkey's energy use is expected to increase by 50% over the next decade. The demand for electricity in 2018, with an increase of 3.8% reached 306.7 billion kW has shown in Fig. 2.

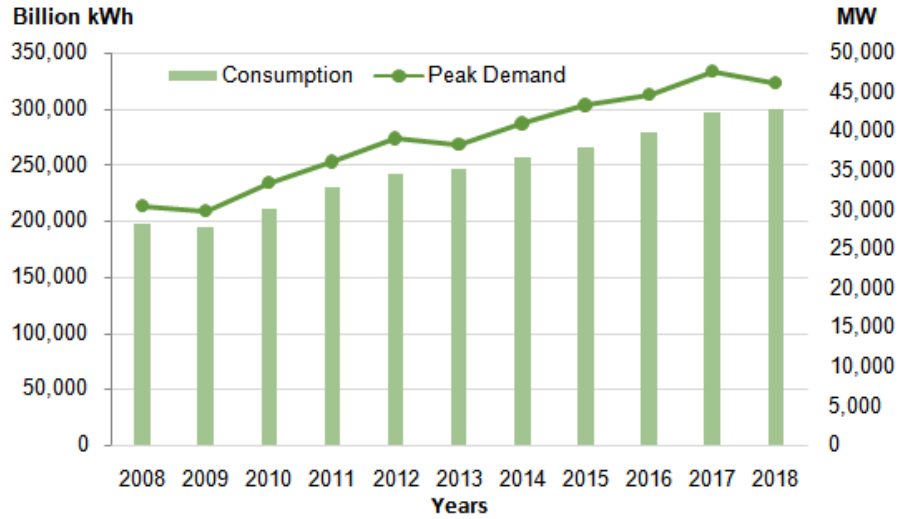

Figure 2. Changes in Turkey's electricity generation and peak demand values

In 2018, 37.3% of Turkey'selectricity production was supplied from coal, 29.8% from natural gas, 19.8% from hydraulic energy, 6.6% from wind power, 2.6% from the solar energy, 2.5% from geothermal energy and 1.4% are from other resources. (MENR, 2020)

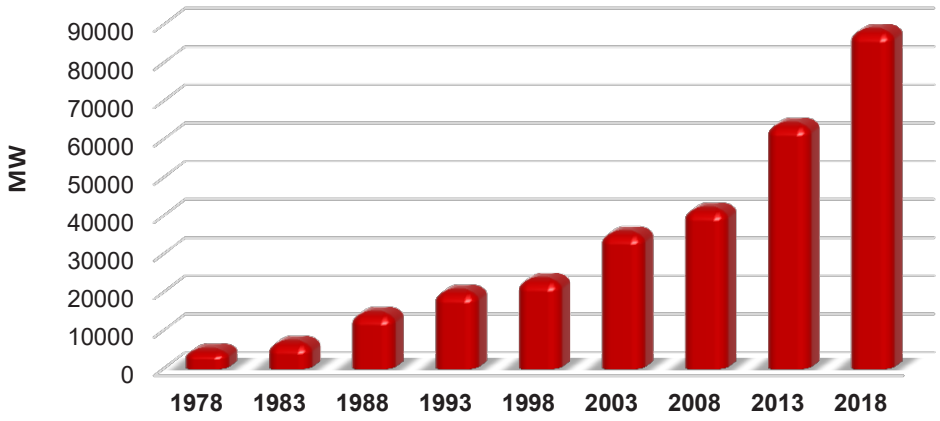

Figure 3. Annual installed power capacity increase of Turkey

As of the end of September 2019, Turkey's installed power reached 90,720 MW, which represents a threefold increase in 15 years. Distribution of Turkey's installed power by resources as of the end of September 2019 are as follows; 31.4% hydraulic energy, 28.6% natural gas, %22.4 coal, 8.1% wind power, %6.2 solar energy, 1.6% geothermal and 1.7%is in the form of other resources. Investigating the installed power capacities per source type, it is seen that the solar power plants increased by 48% to 5,068 MW and the wind power plants increased by 7.5% to 7.005 MW. The share of renewable power plants in installed capacity is 47.8% including hydropower plants, and the solar power plants have the highest increase in installed capacity.

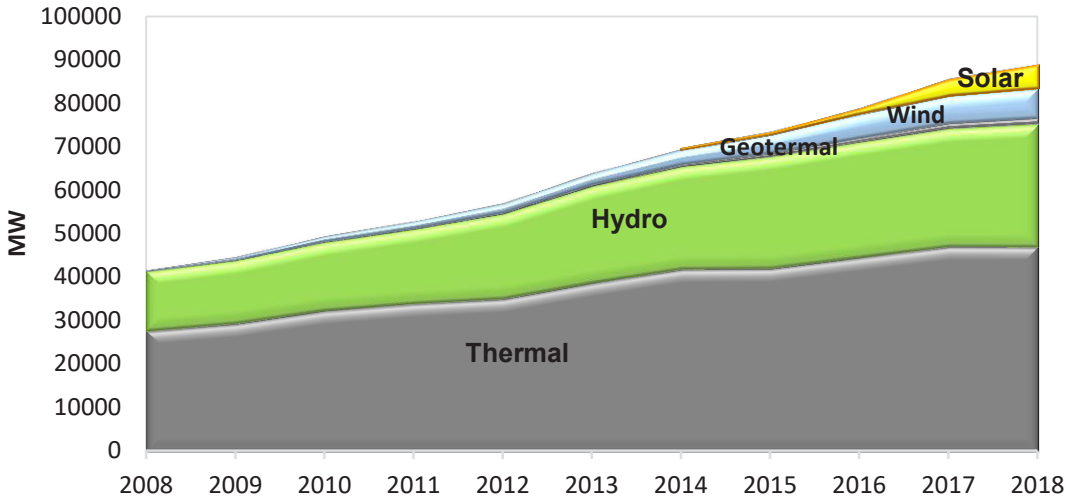

Figure 4. The change of Turkey's electricity installed capacity by years based on resources

II. Renewable Energy Potential in Turkey

Turkey is in fortunate geography in terms of renewable energy sources. It is particularly rich in hydraulic, solar, wind, geotherma land biomass energy potentials.

a) Hydraulic Energy

The average annual precipitation is about 642.6 mm in Turkey, this value corresponds to 501 billion m^3 of water per year (DSİ, 2020). However, within the framework of today's technical and economic conditions, the surface water potential that can be consumed for various purposes is an average of 98 billion m^3 per year, including 95 billion m^3 from domestic rivers and 3 billion m^3 from rivers from neighboring countries.

In determining the hydroelectric potential, gross potential, technical potential, and economic potential concepts are important. Turkey's theoretical hydropower potential is about 433 billion kWh whereas the technical potential is about 216 billion kWh and both technically and economically viable potential was calculated to be 130 billion kWh. Turkey's gross potential is 1% of the world total potential (433,000 GWh/year), and 16% of the European total. Figure 5 shows the increase in the installed capacity from hydraulic power plants in Turkey. As can be seen, there is a regular increase in hydraulic energy installed power.

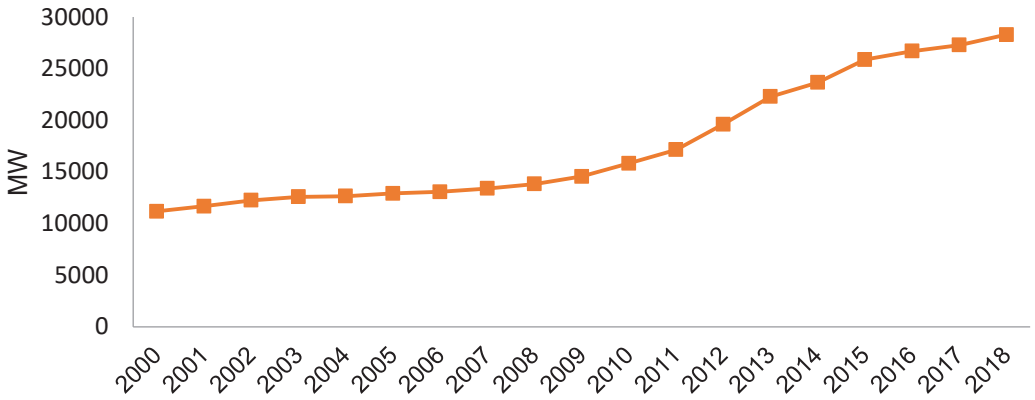

Figure 5. The development of hydraulic power installed capacity in Turkey

b) Solar Energy

Due to the geographical location of Turkey, the average annual sunshine time of 2640 hours and annual average day light duration in Turkey is 7.5 hours and the average annual radiation is 1,527 kWh/m^2, which is higher than most of the European countries as Fig. 6a shows.

Nevertheless, Turkey's installed solar capacity is only around 5.53 GW.According to estimates, Turkey's potential for electricity generation from solar power is 380 TWh per year and has apotential of about 56,000 MW installed. As seen in Fig. 6b, solar energy capacity is constantly increasing and reached 5062 MW by the end of 2018. This value corresponds to 0.5% of the total power installed capacity. Turkey constitutes a rate of 0.5%, which is quite inadequate. However,in the near future, Turkey is expected to reach higher capacities in terms of renewable generation (Fig. 6).

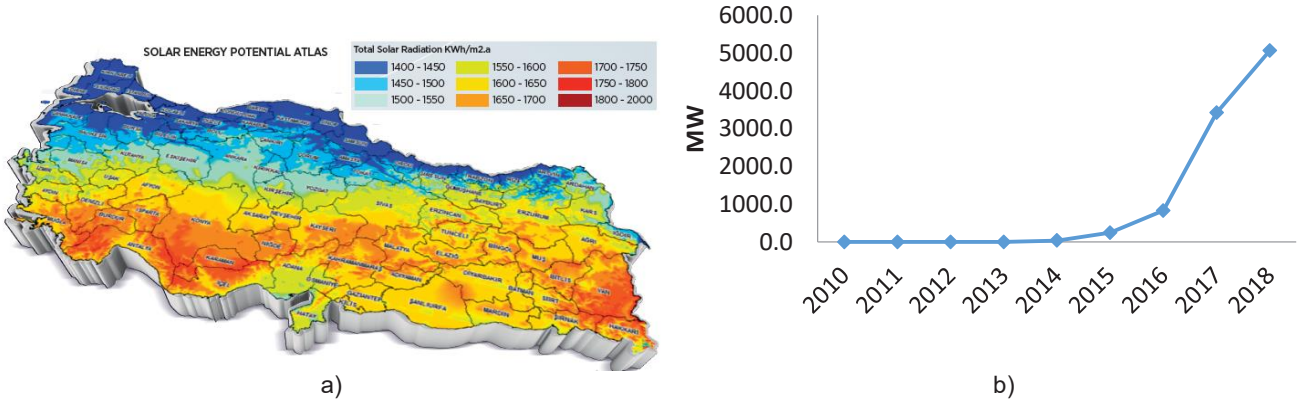

a) b)

Figure 6. a) Turkey's solar energy potential atlas, b) The changes of solar power installed capacity inTurkey

c) Wind power

Wind energy today is also one of the most important topics in the Turkish energy mix.Turkey's wind energy potential was prepared in 2007 and Turkey has about 5000 MW potential in the zone of 8.5 m/s and has a potential of 48,000 MW in the zone 7.0 m/s speeds. Fig. 7 shows the changes in Turkey's wind power install capacity. As can be seen, Turkey shows a significant increase in wind power installations in recent years.

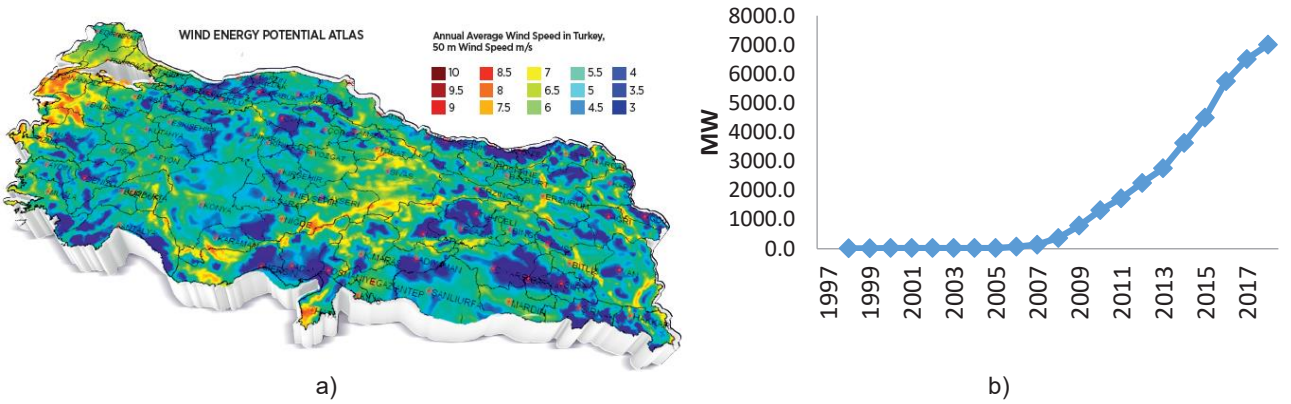

a) b)

Figure 7. a) Turkey's wind power potential map b) The changes of wind power installed capacity in Turkey

Turkey implemented a unique procedure for areas with solar and wind energy resources called the Regulation for renewable energy resource area (RERA). RERA aims to create large-scale (1000 MW) renewable energy resource sites in the state. Through RERA, it is planned that an additional 20,000 megawatts installation will be added to the energy mix in the following 10 years.

Turkey's offshore wind potential is also evident with the possibility of reaching 32 GW. Because of difficulties in application, Turkey's offshore wind energy potential is estimated to be around 11.000 MW. Bozcaada, Bandirma, Gokceada, Inebolu, and Samandag coastlines are the most suitable locations for offshore wind farm development.

III. Utilization of Electricity Production from Renewable Sources in Turkey

It is anticipated that more than 50% of the electricity used in Turkey will be coming from renewable resources, which currently corresponds to 150 billion kWh of electricity. As illustrated in Fig. 8, Turkey's hydroelectric generation differs in some years, consistent with the total electricity production shows that there is a continuous upward trend in installation and generation. Electricity generation from wind and solar energy started in 2008, showing a logarithmic increase over the years. It is predicted that electricity production from wind and solar will reach hydroelectric production capacity in the coming years.

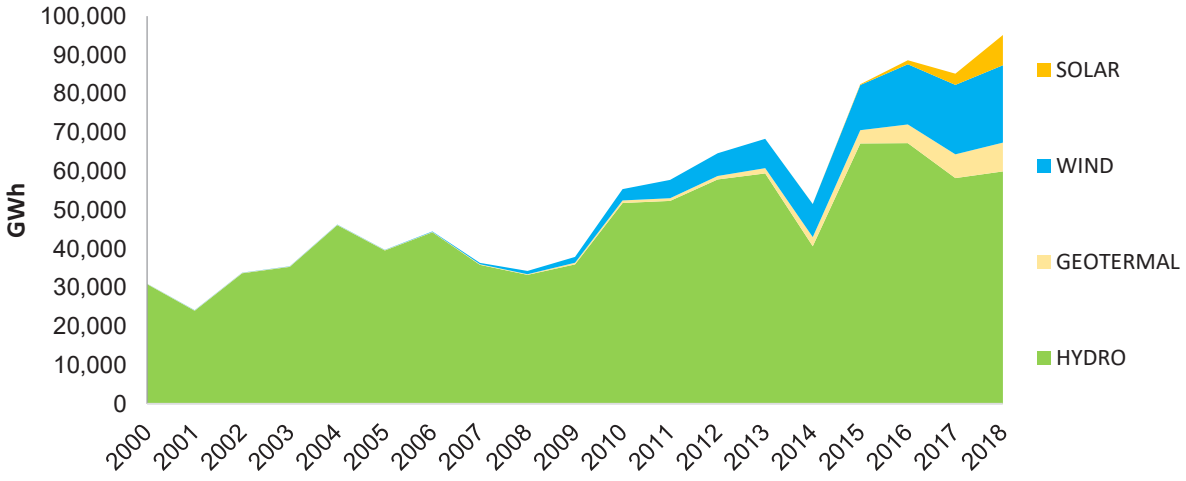

Figure 8. Turkey's electricity generation from various renewables including dam type hydros between 2000-2018 years

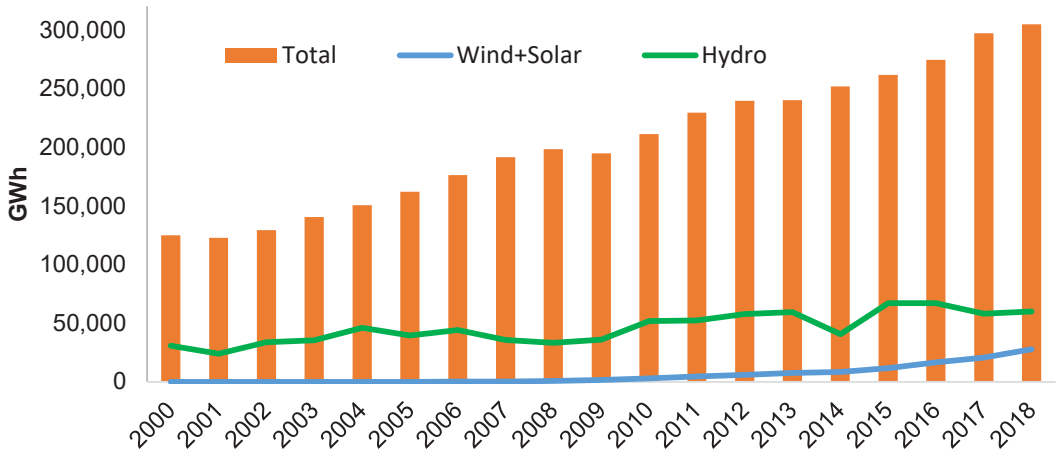

Figure 9. Turkey's total electricity generation comparison with renewable resources between 2000-2018 years

According to the estimation results, in parallel with the development of the gross consumption estimates the capacity of grid in 2030 is expected to be 453,000 GWh with an average increase of 2.7% compared to the low scenario, 481,000 GWh with an average increase of 3.2% according to the base (reference) scenario, and 515,000 GWh an average of 3.8% according to the high scenario.

The estimated installed capacity for the electricity generation in Turkey for the year 2024 is 111.710 MW, while for the year 2029 is 127.754 MW.

IV. Conclusions

Although Turkey shows a continuous increase inelectricity demand,electricity production is largely dependent on external sources such as natural gas and imported coal. Therefore, it gives a great opportunity for the implementation of renewable energy sources, especially solar and wind energy in the country.

Turkey's total installed capacity is about 91,341.7 MW by the end of 2019. Among this capacity, 28.36% of the installed power is composed of natural gas power plants, 22.60% hydroelectric power plants with dams, and 11.06% of lignite power plants. While the installed power capacities of renewable energy sources including dam types hydros are about 44.477.8 MW in total where this ratio corresponds to 48.7% of the total installed power.Based on Turkey's electricity demand projections, in order to meet the demand,there is a need of about 37,000 MW power capacity in addition to the existing installed capacity by 2030. This amount corresponds to 40% of the current capacity. Hence, obtaining the expected power from solar and wind energy will contribute greatly to both the evaluation of domestic resources and the reduction of emissions.

References

MENR , 2020,Ministry of Energy and Natural Resources, www.enerji.gov.tr, Turkey

TEIAS, 2020, Turkish Transmission Operator Co. www.teias.gov.tr, Turkey

Guide , 2019, Investor's Guide For Electricity Sector In Turkey, MENR, 2. Edition.

EPIAS, 2018, Electricity Market Summary Information Report, Energy Markets Operator (Epiaş)

European Commission, 2013, Bringing Europe and third countries closer together through renewable energies.

A. Ilhan, M. Bilgili, 2016, An Overview of Turkey's Offshore Wind Energy Potential Evaluations, J. of Sci. Reviews 9(2): 55-58

MENR, 2019, Turkey Electricity Demand Projections Report, 2019-2039, www.enerji.gov.tr

DSİ, 2020,General Directorate of State Hydraulic Works, www.dsi.gov.tr

E. A. Yilmazca, N. Ozi, 2018, Renewable Energy Potential and Future Aims of Turkey, J. of Soc. Sci. Research, 8(3), 525-535.

Parametric Study of a Parabolic Trough Collector Based Solar Thermal System for Improving Asphalt Paving Sustainability

[1*]Yassine Hrimech, [1]Abdallah Saad, [2]Radia Ait EL Cadi, [3]Moaad Aboumalik, [4]Mohamed Essaaidi

[1] ENSEM, University of Hassan II, "Route El Jadida", km 7, Po. Box. 8118, Oasis, Casablanca, 20 000, Morocco
[2] Materials and Renewable Energies Lab., Faculty of Science, IbnZohr University, BP8106, Agadir, 80 006, Morocco
[3] Physics Dept., Faculty of Science, Abdelmalek Essaadi University, Av_Sebta, Mhannech II, Tetouan, 93 002, Morocco
[4] ENSIAS, University of Mohamed V, Madinat al Irfane, Po. Box. 713, Rabat, 10 106, Morocco

* Biblioyassine@gmail.com * Moad.aboumalik@uae.ac.ma

Abstract

This paper presents a proposed design of a Parabolic Trough Collector based solar thermal system, for improving the asphalt pavement installations. The purpose is to heat the bitumen used to coat the aggregates intended for the construction of road pavements. The asphalt mixture needs about 10% of bitumen mixed with 85% of aggregates, which must be dried beforehand at 165 °C to remove moisture. Each ton of asphalt needs 10 liters of fuel to reach the mixing temperature Tɵ. As the thermal process was very fossil with a large amounts of CO2 emissions, the proposed solar heat system will replace the conventional process by using the Parabolic Trough Collector technology, which increase the temperature of the heat transfer fluid at the collector outlet to T_{HTF} = 230 °C, in order to reach the desired bitumen temperature gradient (From T = 70 °C to Tɵ = 165 °C). A parametric study has been established, with the measurements taken from Casablanca meteorological data. The system has been designed under TRNSYS 17 software, and the simulation results show the effectiveness of the heat production part, which contributes to minimize the cost and decreases CO2 emissions.

Keywords: Sustainability, Asphalt pavement industry, Solar energy, Parabolic Trough Collector (PTC).

I. Introduction

Due to the concern of the global warming effects, the development of clean energies becomes a priority for many countries. Morocco as a leader in renewable energies in Africa, has invested 30 billion dollars to produce at least 10,100 MW of additional electricity from renewable energy sources in 2021. While solar energy will contribute 20%, wind energy and hydropower will contribute around 32% (Ministry of Energy, Mines and Environment. 2020), (Moaad Aboumalik et al, 2019).
The aim of this work is to be part of the implementation of the Moroccan strategy, especially in the industrial heating process, through renewing the current asphalt pavement installations. Indeed, in the current system, the asphalt mixture is heated before being laid on the ground, allowing the bitumen to liquefy and coat the gravel. The mixture needs about 10% of bitumen mixed with 85% of aggregates, according to the manufacturer data information.
Figure 1 shows an example of the pavement layer of a bituminous mixture, while Figure 2 shows a synoptic diagram of the asphalt plant types that are usually used in the pavement layer. Generally, there is two types: the batch heater and the drum mix plants. For our case study we used the batch heater which is designed for small capacity productions from 50 to 200 ton per hour (apa-mi.org. 2019). The aggregates were previously heated and dried before mixing them with the hot-bitumen at 165 °C.

Fig. 1. Building the pavement layer of a bituminous mixture (adapted from (apa-mi.org. 2019)).

Furthermore, the process needs 10 liters of fuel for each ton of bitumen, which is expensive and pollutant. For this reasons, a parametric study was established, and a Parabolic Trough Collector based technology within the proposed solar system was selected, for a more sustainable technology in the asphalt pavement industry.

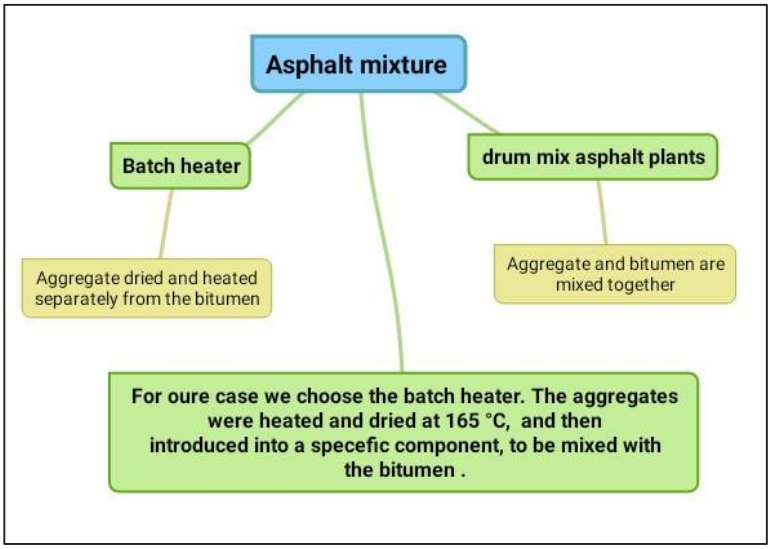

Fig. 2. Synoptic diagram of two asphalt plant types: (batch heater and drum mix plant).

II. Parametric analysis

The case study is carried out in an asphalt pavement construction site in Casablanca, focusing only on heating the bitumen and heat transfer fluid (HTF), without introducing any other process operations in the system. Figure 3 shows the proposed scheme of the heat production part for an asphalt pavement installation:

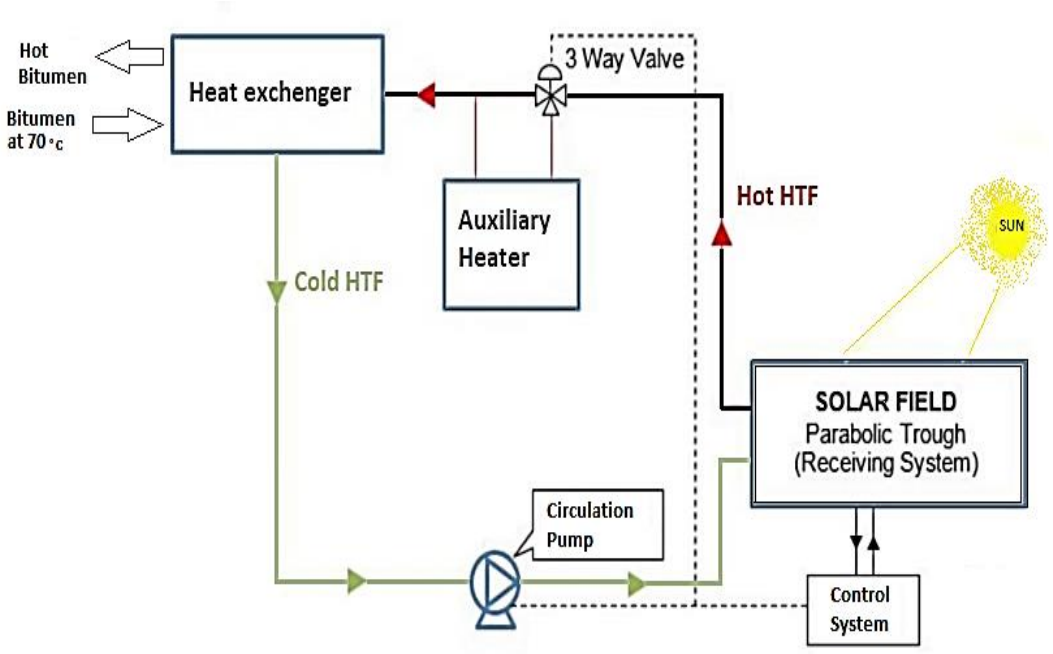

Fig. 3. The proposed scheme of the heat production part, for an asphalt pavement installation

Simulated behaviors were performed using Transient System Simulator 17 (TRNSYS 17), which is one of the most widely used software tools in the thermodynamic field. It was developed and marketed by the University of Wisconsin in the US to provide dynamic simulations of transient behaviors within the established parametric study.

The components are mathematically modeled and solved for each time interval, and can be programmed by the FORTRAN language (Antonio Marcos et al. 2019). Furthermore, researchers have the possibility of creating their own components, which is a determining criteria in the simulation of their system designs (Vassiliki Drosou et al. 2018), (Badreddine El Ghazzani et al. 2017).

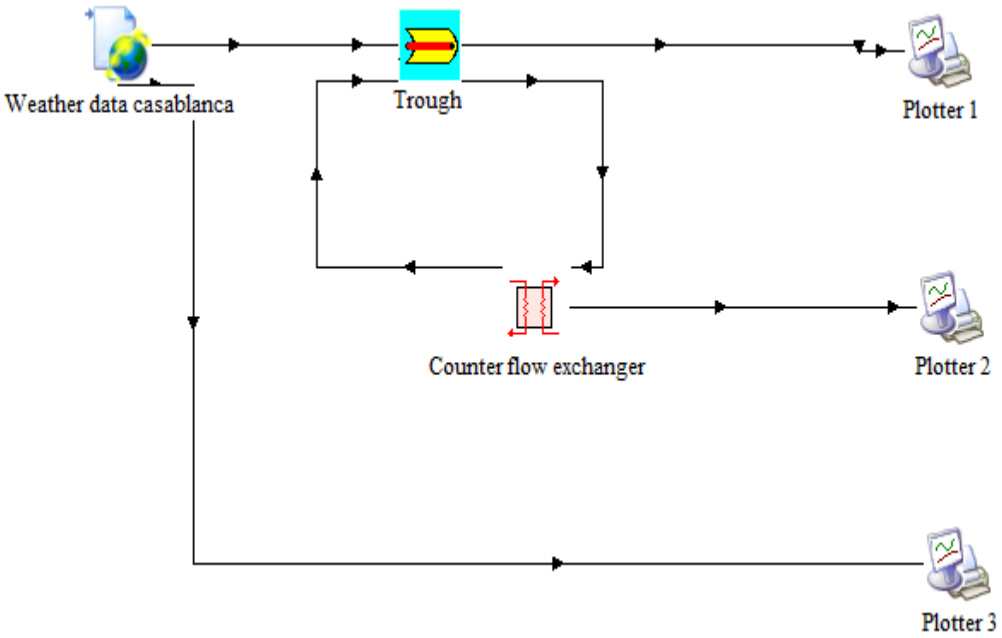

Fig. 4. Model of the heat production part basing on the parabolic trough station

As depicted in Figure 4, a typical model of the heat production part was designed under TRNSYS 17. The Meteorological data (TMY2) of a site in Casablanca city was obtained from the METEONORM 7 software, and loaded at TRNSYS-17 by using the component TYPE 526 (Vassiliki Drosou et al. 2018). The data consisted of total and diffuse horizontal irradiation every hour (I, Id), ambient temperature (Ta) and also the bitumen temperature (70 °C) before entering to the heat exchanger.

Table 1. Parabolic trough collector characteristics

Parameters	Value
Clean Reflectivity	*0.94*
Broken Mirror Fraction	*0.0*
Length of SCA	*47 m*
Aperature Width of SCA	*5 m*
Focal Length of SCA	*5 m*
Rowspacing	*15 m*
Total Field Area	*8000 m^2*
Pump Max Power	*1600 W*
Pump Max Flow Rate	*18647.99 kg/hr*
Demanded Outlet Temperature	*390 °C*
Inlet Temperature Solar Field	*70 °C*
Cleanliness Solar Field	*0.95*
Specific Heat HTF	*2.15 kJ/kg.K*

The PTC characteristics were integrated (see Table 1) in order to assess the HTF temperature. The desired temperature at the outlet of the heat exchanger was obtained behind and presented in each hour of January during a year.

IV. Simulation results

Figure 5 presents the TRNSYS simulation results, which calculates in every hour the PTC mass flow and the outlet temperature of the exchanged energy in the heat transfer fluid (HTF) within a closed loop. Weekly weather data was built using the METEONORM 7 software:

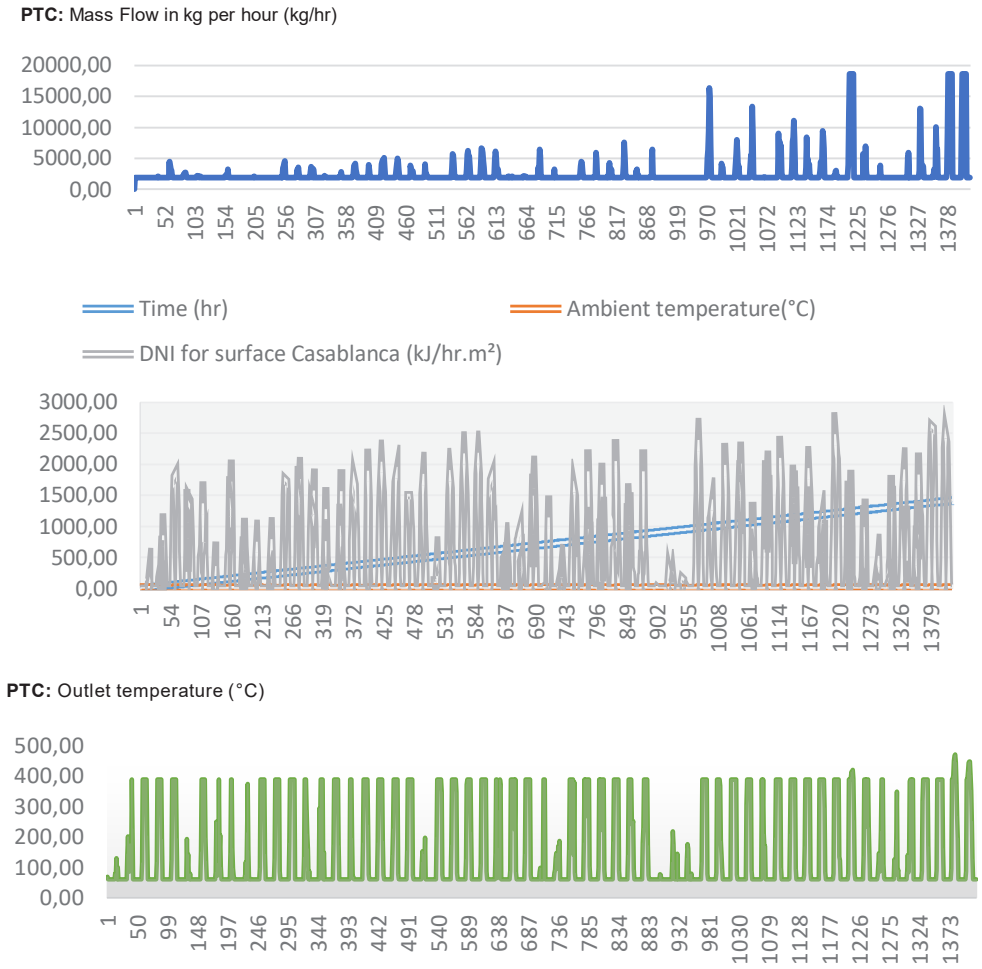

Fig. 5. Simulation results of the PTC based station under Casablanca meteorological data

V. Conclusion

With the advance in PTC based solar thermal technologies, solar energy has the potential to become financially competitive compared to fuel-based generation resources. A parametric study of heating bitumen process has been presented in this paper, to identify PTC performances of the proposed system. The model of the simulation carried out by TRNSYS 17 helps to analyze the constraints to which the heat production part is subjected. Thus, the results presented in Figure 5 (automatically transferred to Excel) show that the proposed PTC based solar station is efficient compared to the conventional system. It also contributes to optimize the cost of the asphalt paving industry and to reduce CO2 emissions.

VI. References

Antonio Marcos de Oliveira Siqueira, Gabi Antoine Altabash, Rayan Fadi Barhouche, Gabriel Siqueira Silva, and Fábio Gonçalves Villela. (2019). “Simulation Study Of Parabolic Trough Solar Power Plants In Brazil.” International Journal of Research - Granthaalayah, 7(8), 17-28. https://doi.org/10.5281/zenodo.3379638.

APA Michigan. What is hot mix asphalt [Internet]. Asphalt Pavement Association of Michigan; c2008. [Available from] : http://www.apa-mi.org/what_is_hot_mix_asphalt_paveme.php

Badreddine El Ghazzani, Diego Martinez Plaza, Radia Ait El Cadi, Ahmed Ihlal, Brahim Abnay, Khalid Bouabid, “Thermal plant based on parabolic trough collectors for industrial process heat generation in Morocco”, Renewable Energy, 113 (2017) PP 1261 – 1275.

Moaad Aboumalik, Mohamed EL Brak, and Mohamed Essaaidi. (2019). “Moving toward a smarter power grid: A proposed strategy for strengthen smart grid roadmaps through a case study.” International Journal of Smart Grid and Clean Energy 8 (2), 131-139. 2019. DOI: 10.12720/sgce.8.2.131-139

Official website of the Ministry of Energy, Mines, and Environment; [Availibale from] : https://www.mem.gov.ma/en/Pages/rapports.aspx

Vassiliki Drosou, Loreto Valenzuela & Argiro Dimoudi (2018) A new TRNSYS component for parabolic trough collector simulation, International Journal of Sustainable Energy, 37:3, 209 – 229, DOI: 10.1080/14786451.2016.1251432

Integrated sustainability assessment of a multigeneration system

[1,2]Ugur Akbulut,[2,3]Ibrahim Dincer
[1] Department of Mechanical Engineering, Faculty of Engineering, Recep Tayyip Erdogan University, 53100 Rize, Turkey
[2] Faculty of Engineering and Applied Science, Ontario Tech. University, 2000 Simcoe Street North, Oshawa, Ontario L1H 7K4, Canada
[3] Yildiz Technical University, Faculty of Mechanical Engineering, Istanbul, 34349 Turkey

* E-mails: ugur.akbulut@erdogan.edu.tr, Ibrahim.dincer@uoit.ca

Abstract
In this study, a solar-geothermal hybrid multigeneration system integrated with the Cu-Cl cycle for hydrogen production and absorption chiller for cooling is analyzed based on the integrated sustainability assestment. A specific model containing energy, exergy, environmental, economical, technological, social and educational aspects developed for the proposed system. LCA results of concentrating solar power and geothermal power generating systems from the literature are used as input parameters to carry out the analysis. The proposed system is quantitively evaluated giving a score between 0 and 1 to each category. The economic (0.93), exergy (0.90) and educational (0.90) aspect scores are found confirming the system is being highly profitable, sustainable an innovative. Also, system's overall integrated sustainability assessment score is found to be 0.74 which is higher than the sustainability index of the PV system ranged from 0.54 to 0.63 as presented in the literature.

Keywords: Exergy, energy, environment, sustainability, integrated sustainability index.

1. Introduction

Sustainability has become a major highlight in modern civilization and gained priority in the society. It can be defined as to avoid the depletion of the natural resources in order to maintain the ecological balance for future generations. One of the challenges to achieve a sustainable society is to have a quantitative assessment of the sustainability of a system. There are many kind of studies on measuring sustainability in the literature but universal approaches are very few. Quantitative indicators for sustainability assessment are being developed and used. In the context of evaluating the sustainability of energy sytems some studies comment on from a thermodynamic or greenhouse gas perspective, others focus on the role of social indicators in sustainability assessment, some methods rank indicators without normalization with respect to sustainability target values (Hacatoglu et al., 2014).

The Integrated Sustainability Index (ISI) which is proposed by Hacatoglu et al. (2014) is used for energy systems combines selected indicators from multiple dimensions to create a single-score assessment of sustainability. The ISI of an energy system is determined from individualist, egalitarian, or hierarchist perspectives by normalization, weighting, and aggregation of of non-dimensional sub-indicators. Aggregation yields an ISI between zero and one, where one represents a sustainable system. Hacatoglu et al. (2014) compared a wind-battery system with a gas-fired system and showed that, wind-battery system produces fewer potential global warming, stratospheric ozone depletion, air pollution, and water pollution impacts. Moreover, Nitrous oxide contributes more than 90% of the stratospheric ozone depletion potential of gas-fired and wind-battery systems. Hacatoglu et al. (2015) applied the ISI to a hybrid energy system with hydrogen-based storage to meet the energy needs of a small community in southern Ontario.That was a trigeneration system and can provide the heating, cooling, and electrical energy needs of the 50-household community.Solar and wind are used as energy resources. The Global Warming Potential and Stratospheric Ozone Depletion Potential sub-indicators have the most significant impacts. The results showed that the proposed affordable system has low-carbon emission and potential to improve standart of living for a typical household in southern Ontario. Hacatoglu et al. (2016) applied ISI to assess the sustainability of a wind energy system with hydrogen-based storage. The ISI of the wind-hydrogen system is also compared to the ISI of a conventional gas-fired system from individualist, egalitarian and hierarchist perspectives. A comparative assessment revealed that there are very little differences in the ISI of each system for each perspective. Abu-Rayash and Dincer (2019) introduced a new integrated sustainability assessment model for energy sytems which includes energy, exergy, economy, environment, society, technology, education, and the system size indicators. In this model, target values are used to normalize the data and various aggregation and weighting methods are used to obtain objectivity in the assessment. Also, a solar-PV system to provide the residential demand for electricity, heating, cooling and hot water for 150 Ontarian homes is analyzed with the proposed model as a case study. The sustainability index for the PV system ranged from 0.54 to 0.63 depending on the used scheme (individualist, egalitarian or hierarchist). Moreover, all schemes give the economic index a higher priority over other indexes.

Resulting a detailed literature review, it is noticed that there is a lack of case studies for integrated sustainability assessment of multigeneration systems. The absence of specific targets and reference values to compare with the actual values is a big handicap. In this study, it is aimed to develop a sustainability assestment model containing energy, exergy, environmental, economical, technological, social and educational aspects for the proposed system. Assumptions are given in Table 1, input parameters for the system are given in Table 2, and equations which are used for calculation are given in Table 3.

2. System Description

Analysed system is a solar-geothermal hybrid multigeneration system integrated with the Cu-Cl cycle for hydrogen production and absorption chiller for cooling. Fig. 1 presents the schematic layout of the stated system. It is a combination of four sub-systems named as solar heliostat field, geothermal power generation system, copper-chlorine (Cu-Cl) cycle and absorption cooling system (Siddiqui et al., 2019).

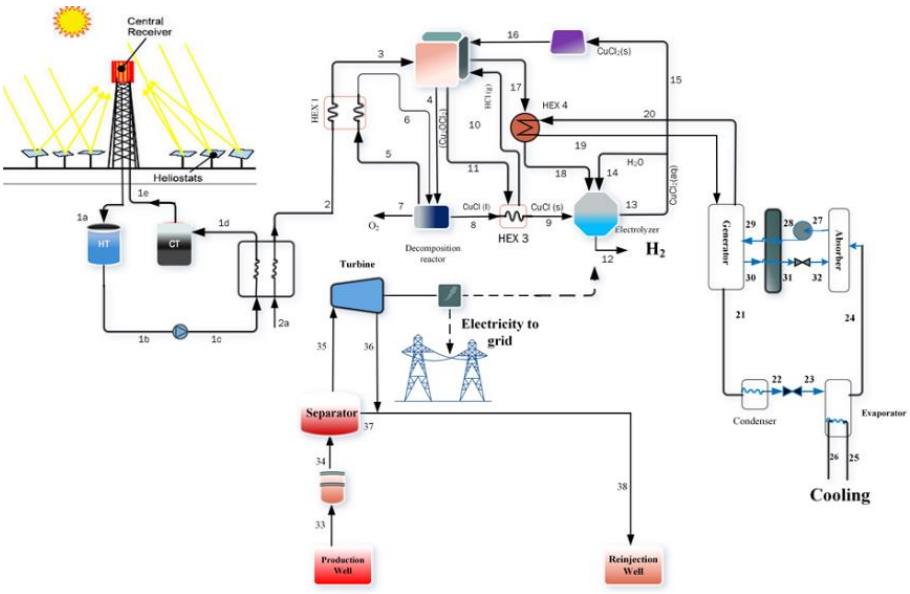

Fig. 1: The schematic layout of the integrated system (Siddiqui et al., 2019).

Hydrogen and electricity production and cooling are the major system objectives. The solar heliostat source provides the heat which is necessary to be used in CuCl cycle for hydrogen production. Also, the CuCl cycle needs electrical input in electrolyzer. The geothermal source is connected with the turbine-generator system to achieve the electrical output. Produced electrical load is used to run electrolyzer while remaining electric power is transferred to the grid. Also, the heat recovered from the system is used tovemploy the absorption chiller to provide cooling.

3. Analysis

In the analysis and assessment, the following criteria are considered:

- **Energy Aspect**

The energy aspect is assessed using two indicators, energy efficiency ratio (η) and productivity ratio (Y_{PR}) . Since the target efficiency is always larger than the actual efficiency, the value of energy efficiency ratio is between 0 and 1 (Hacatoglu, 2014). It can be calculated by Eq.1, where η_{rev} and η_{act} refers to reversible (target) and actual energy efficiency achieved by the system. Y_{PR}, is used to compare the design value of the system. Energy systems that produce electricity at higher rates are more sustainable than the systems that are intermittent or having low production rates Abu-Rayash and Dincer (2019). Y_{PR}, is obtained by using Eq.2, where $X_{PR,act}$ and $X_{PR,target}$ shows actual and target values for production rate (tones/year). Total score of energy aspect (Y_{ER}), is estimated with the Eq.3 which is given in Table 3, where W_{η} and W_{PR} are the weights of η and Y_{PR} respectively.

- **Exergy Aspect**

The exergy efficiency ratio (ε) includes target exergy efficiency (ε_{tar}) and actual exergy efficiency (ε_{act}) values of the system. The ε_{act}, considers the exergy losses (ε_{loss}) thus it is always smaller than ε_{tar} . Therefore, ε is always between 0 and 1 and can be calculated by Eq.4 (Hacatoglu, 2014). Exergy destruction ratio (ε_D) and the total score of exergy aspect (Y_{EXR}) can be estimated by using Eq. 5 and Eq. 6 respectively, where W_{ε} and W_D shows the weights of ε and ε_D respectively.

- **Environmental impact**

In this study, various indicators are used in order to comprehensively reflect the total score of environmental impact (Y_{ENV}) such as, global warming potential (Y_{GWP}), acidification potential (Y_{AP}), eutrophication potential (Y_{EP}), photochemical ozone creation potential (Y_{POCP}) and water consumption (Y_{WC}). Values of these environmental impacts are calculated by using Eqs. 7-11, where $X_{GWP,act}$ and $X_{GWP,target}$ presents actual and target values for global warming potential, $X_{AP,act}$ and $X_{AP,target}$ presents actual and target values for acidification potential, $X_{EP,act}$ and $X_{EP,target}$ presents eutrophication potential, $X_{POCP,act}$ and $X_{POCP,target}$ presents photochemical ozone creation potential and $X_{WC,act}$ and $X_{WC,target}$ presents actual and target values for water consumption, respectively. Y_{ENV} is estimated by using Eq. 12 where W_{GWP}, W_{AP}, W_{EP}, W_{POCP} and W_{Wc} are the weights of Y_{GWP}, Y_{AP}, Y_{EP}, Y_{POCP} and Y_{WC} respectively.

- **Economic impact**

Energy systems are economically sustainable if they are profitable, serviced at lower cost for the consumer and contain the elements of a successful business idea. There are several economical methods can be chosen as an

economic impact indicator. For example, benefits-cost ratio, the payback period, levelized cost of energy etc. In this study, payback period is chosen as the economic impact indicator. Logically, energy systems with shorter payback periods are more economically favorable and sustainable than those with longer payback periods. Eq. 13 is used to determine the payback period (PBT), where PI shows the total project investment and PCF shows the periodic cash flow, respectively.

- **Technological aspect**

The technological indicators assist in analyzing the performance, design and production aspects of the energy system in question. Commercializability (Y_{COMM}), technology readiness (Y_{TR}) and innovation (Y_{IN}) are the indicators that will be used to assess the score of technological aspect of the system (Y_{TECH}) in this study. Commercialization refers to the system or technology to be commercially viable and sustainable. Non-commercialized systems are still in the R&D stage. Multigenerational energy systems provide more commercial outputs, which increases their commercializability (Dincer and Acar, 2017). A system is technologically ready if it has already been been well established and are currently operational. Also, technologies that promote innovation and constantly enhance their development, research and technology competitiveness are considered more favorable and sustainable. The score of technological aspect (Y_{TECH}), can be calculated by Eq.14 where W_{COMM}, W_{TR} and W_{Wc} are the weights of Y_{COMM}, Y_{TR} and Y_{IN} respectively.

- **Social aspect**

Social aspect considers indicators such as job creation (Y_{JC}), public awareness (Y_{PA}), social acceptance (Y_{SA}), social cost (Y_{SC}), human welfare (Y_{HW}) and human health (Y_{HH}) Abu-Rayash and Dincer (2019). In this study, considering the International Renewable Energy Agency Report (IRENA, 2013), the job creation factor is assessed based on the number of jobs created after each newly installed MW in unit (jobs/MW). Also, being well known by the community is considered positive for public awareness (Ramírez et al., 2017). The power of the people is immense and thus for an energy system to be sustainable and operational, it must be accepted and perceived positively by society. Agreement with RES in a direct neighbourhood can be considered as an indicator for social acceptance (GEO ELEC, 2013). Adding that, energy systems usually come with a cost socially. This indicator has been assessed by calculating the social cost of carbon. Finally, energy systems that take into consideration the welfare of society are more favorable and thus more sustainable and the human health criteria is a social indicator used to assess energy systems on the effects of any toxic substances on human health. In this study, the score of social aspect (Y_{SOC}), is calculated by Eq.15 where W_{JC}, W_{PA}, W_{SA}, W_{SC}, W_{HW} and W_{HH} are the weights of Y_{JC}, Y_{PA}, Y_{SA}, Y_{SC}, Y_{HW} and Y_{HH} respectively.

- **Education aspect**

Education aspect is assesed with three main indicators such as staff training (Y_{TRAIN}), educational level of staff (Y_{EL}) and educational innovation (Y_{EI}). The number of trained people required by the industry is an indicator that can help us assess the educational aspect of the systems. If the energy system requires specific skilled staff, specific education and rare talents, the system is perceived as less sustainable. The educational level can be considered as three categories such as simple, moderate and advanced. Advanced educational level is considered most sustainable among these three. Also, innovation in education is an indictor reflecting sustainable development and energy systems that requires creativity in their education stand out as most sustainable. The calculation of educational aspect score (Y_{EDU}) is given with the Eq. 16 where W_{TRAIN}, W_{EL} and W_{EI} refers the weights of Y_{TRAIN}, Y_{EL} and Y_{EI} respectively.

Table 1. Assumptions made for the analysis (Abu-Rayash and Dincer, 2019)

Proposed model is confined to energy systems that are in operation
The target energy efficiency is always assumed to be greater than the actual energy efficiency
LCA is an effective tool for assesment of the environmental aspect.
This assessment methodology does not take into account all environmental indicators
The target environmental indicators have lower values than the actual indicators
Technology is assumed to be regularly evolving and competitive
Assessment of technology is open to all concepts regardless of location
In assessment of social aspects survey results are considered a reliable source of information. Therefore, the size and quality of surveys should be of high quality.
Assessments of technological aspects is qualitative and may be subjective.
Equal weighting is used to aggregate values within each category.

Table 2. Input parameters

Parameter	Description	Value
Energy Impact	Overall system energy efficiency (η_{act})	0.196 (Siddiqui et al., 2019)
	The actual value of production rate (Y_{PR})	0.80 accepted
	The weight of efficiency (W_{η})	0.5 (equal weighting)
	The weight of productivity ratio indicator (W_{PR})	0.5 (equal weighting)
Exergy Impact	Actual exergy efficiency (ε_{act})	0.191 (Siddiqui et al., 2019)
	Target exergy efficiency (ε_{tar})	0.191 (Siddiqui et al., 2019)
	Energy losses (ε_{loss})	Omitted (Siddiqui et al., 2019)

	The weight of exergy efficiency ratio indicator (W_ε)	0.5 (equal weighting)
	The weight of exergy destruction ratio indicator (W_D)	0.5 (equal weighting)
Environmental Impact	Actual CO_2 emission ($X_{CO2,act}$)	150 g CO_2 eq/kWh (Asdrubali et al., 2015)
	Target CO_2 emission ($X_{CO2,target}$)	45 g CO_2 eq /kWh (Asdrubali et al., 2015)
	The weight of global warming potential (W_{GWP})	0.2 (equal weighting)
	Actual acidification potential ($X_{AP,act}$)	0.6 g SO_2 eq /kWh (Asdrubali et al., 2015)
	Target acidification potential ($X_{AP,target}$)	0.3 g SO_2 eq /kWh (Asdrubali et al., 2015)
	The weight of acidification potential (W_{AP})	0.2 (equal weighting)
	Actual eutrophication potential ($X_{EP,act}$)	0.075 g PO_4^{3-}eq /kWh (Asdrubali et al., 2015)
	Target eutrophication potential ($X_{EP,target}$)	0.040 g PO_4^{3-}eq /kWh (Asdrubali et al., 2015)
	The weight of eutrophication potential (W_{EP})	0.2 (equal weighting)
	Actual photochemical ozone creation potential ($X_{POCP,act}$)	0.050 g C_2H_4 eq/kwh (Asdrubali et al., 2015)
	Target photochemical ozone creation potential ($X_{POCP,target}$)	0.020 g C_2H_4 eq/kwh (Asdrubali et al., 2015)
	The weight of photochemical ozone creation potential (W_{POCP})	0.2 (equal weighting)
	Actual water consumption ($X_{WC,act}$)	1500 g/kWh (Asdrubali et al., 2015)
	Target water consumption ($X_{WC,target}$)	700 g/kWh (Asdrubali et al., 2015)
	The weight of water consumption (W_{GWP})	0,2 (equal weighting)
Economic Impact	Cost of CSP system	6000 $/kW (IRENA, 2017)
	Cost of geothermal power system	4000 $/kW (Ni et al., 2016)
	Hydrogen production	32.1 mol/s (55kW used per 1 mol/s H_2 production) (Siddiqui et al., 2019)
	Cooling effect provided (COP_C)=0.69	603,9 kW (Siddiqui et al., 2019)
	Electricity provided to grid	1632,5 kW(Siddiqui et al., 2019)
	Electricity selling price	0.39 $/kWh accepted
	Hydrogen selling price	13.99 $/kg accepted
	The score of economic impact (Y_{ECO})	$Y_{ECO} = 0.926$ accepted (Abu-Rayash and Dincer, 2019)
Technological Aspect	Commercializability (Y_{COMM})	$Y_{COMM} = 0.55$ accepted (Abu-Rayash and Dincer, 2019)
	The weight of commercializability (W_{COMM})	0.333 (equal weighting)
	Technology readiness (Y_{TR})	$Y_{TR} = 0.90$ accepted (Abu-Rayash and Dincer, 2019)
	The weight of technology readiness (W_{TR})	0.333 (equal weighting)
	Innovation (Y_{IN})	$Y_{IN} = 0{,}90$ accepted (Abu-Rayash and Dincer, 2019)
	The weight of innovation (W_{IN})	0.333 (equal weighting)
Social Aspect	Job creation (Y_{JC})	$Y_{JC} = 0.55$ accepted (IRENA, 2013)
	The weight of job creation (W_{JC})	0.166 (equal weighting)
	Public awareness (Y_{PA})	$Y_{PA} = 0.74$ accepted (Ramírez et al., 2017)
	The weight of public awareness (W_{PA})	0.166 (equal weighting)
	Social acceptance (Y_{SA})	$Y_{SA} = 0.70$ accepted (GEO ELEC, 2013)
	The weight of public awareness (W_{SA})	0.166 (equal weighting)
	Social cost (Y_{SC})	$Y_{SC} = 0.50$ accepted (Samadi, 2017)
	The weight of social cost (W_{SC})	0.166 (equal weighting)
	Human welfare (Y_{HW})	$Y_{SC} = 0.80$ accepted (Abu-Rayash and Dincer, 2019)
	The weight of human welfare (W_{HW})	0.166 (equal weighting)
	Human health (Y_{HH})	$Y_{SC} = 0.70$ accepted
	The weight of human health (W_{HH})	0.166 (equal weighting)
Educational Aspect	Staff training (Y_{TRAIN})	$Y_{TRAIN} = 0.70$ accepted (Abu-Rayash and Dincer, 2019)
	The weight of staff training (W_{TRAIN})	0.333 (equal weighting)
	Educational level of staff (Y_{EL})	$Y_{EL} = 0.80$ accepted (Abu-Rayash and Dincer, 2019)
	The weight of educational level (W_{EL})	0.333 (equal weighting)
	Educational innovation (Y_{EI})	$Y_{EL} = 0.90$ accepted (Abu-Rayash and Dincer, 2019)
	The weight of educational innovation (W_{EI})	0.333 (equal weighting)

Table 3. Equations which are used for analysis

Number	Parameters considered	Equation
1	Energy efficiency ratio (η)	$\eta = \frac{1-\eta_{rev}}{1-\eta_{act}}$
2	Productivity ratio (Y_{PR})	$Y_{PR} = \frac{X_{PR,act}}{X_{PR,target}}$
3	Total score of energy aspect (Y_{ER})	$Y_{ER} = \eta W_\eta + Y_{PR} W_{PR}$
4	Exergy efficiency ratio (ε)	$\varepsilon = \frac{1-\varepsilon_{tar}}{1-\varepsilon_{act}}$
5	Exergy destruction ratio (ε_D)	$\varepsilon_D = (1-\varepsilon_{act}-\varepsilon_{loss}) = (1-\varepsilon_{tar})$
6	Total score of exergy aspect (Y_{EXR})	$Y_{EXR} = \varepsilon W_\varepsilon + \varepsilon_D W_D$
7	Global warming potential (Y_{GWP})	$Y_{GWP} = \frac{X_{GWP,target}}{X_{GWP,act}}$

8	Acidification potential (Y_{AP})	$Y_{AP} = \frac{X_{AP,target}}{X_{AP,act}}$
9	Eutrophication potential (Y_{EP})	$Y_{EP} = \frac{X_{EP,target}}{X_{EP,act}}$
10	Photochemical ozone creation potential (Y_{POCP})	$Y_{POCP} = \frac{X_{POCP,target}}{X_{POCP,act}}$
11	Water consumption (Y_{WC})	$Y_{WC} = \frac{X_{WC,target}}{X_{WC,act}}$
12	Total score of environmental aspect (Y_{ENV})	$Y_{ENV} = Y_{GWP}W_{GWP} + Y_{AP}W_{AP} + Y_{EP}W_{EP} + Y_{POCP}W_{POCP} + Y_{WC}W_{WC}$
13	Payback time (PBT)	$PBT = \frac{PI}{PCF}$
14	The score of technological aspect (Y_{TECH})	$Y_{TECH} = Y_{COMM}W_{COMM} + Y_{TR}W_{TR} + Y_{IN}W_{IN}$
15	The score of social aspect (Y_{SOC})	$Y_{SOC} = Y_{JC}W_{JC} + Y_{PA}W_{PA} + Y_{SA}W_{SA} + Y_{SC}W_{SC} + Y_{HW}W_{HW} + Y_{HH}W_{HH}$
16	The score of educational aspect (Y_{EDU})	$Y_{EDU} = Y_{TRAIN}W_{TRAIN} + Y_{EL}W_{EL} + Y_{EI}W_{EI}$

4. Results and discussion

Fig.2 shows that, energy ratio is low (0.24) because proposed system's actual overall energy efficiency is (19.6%) too small considering the target energy efficiency (0.81). Production ratio is 0.8 as accepted. Exergy impact score (0.90) and environmental impact score (0.59) together prove that system is highly sustainable and compatible with the environment. Exergy loss is too small which could be omitted in the calculations so actual exergy efficiency is equal to the target exergy efficiency (19.1%). In accordance with the used renewable sources and system components global warming potential (150 g CO_2 eq/kWh), acidification potential (0.6g SO_2 eq /kWh), eutrophication potential (0.075 g PO_4^{3-} eq /kWh), photochemical ozone creation potential (0.050 g C_2H_4 eq/kwh) and water consumption (1500 g/kWh) are extremely lower than their accepted target values (45gCO_2 eq/kWh, 0.3gSO_2 eq/kWh, 0.040 g PO_4^{3-}eq /kWh , 0.020 g C_2H_4 eq/kwh and 700 g/kWh), respectively. Analyzed system has a very strong sustainability in the economic aspect (0.93) because of its multi-generational character and valuable hydrogen output (32 kg/s). The short payback period (1.48 years) will attract investors' attention to this system. System is innovative (0.9) and its technology readiness (0.9) is high. However, its commercializability is low (0.5) because there is still no market competition for the system. Job creation (0.55) and social cost (0.50) indicators has average values although public awareness (0.74), social acceptance (0.77), human welfare (0.8) and human health (0.7) indicators having high scores. When it comes to education dimension, it can be said that, staff training (0.7), educational level of staff (0.8) and educational innovation (0.9) indicators' scores are high because system is an extremely new and innovative technology.

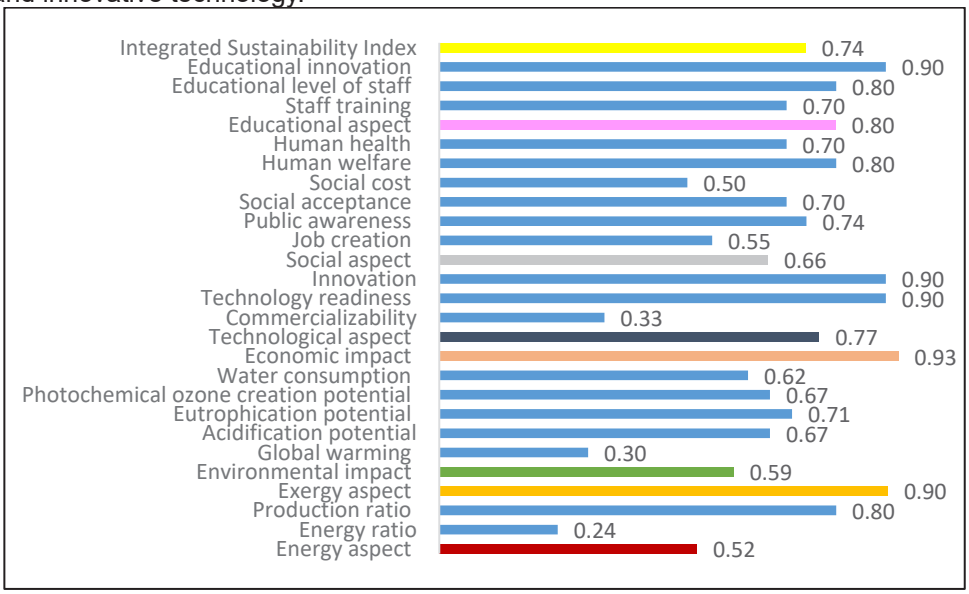

Fig. 1. Calculated values of the main indicators used for the integrated sustainability assessment model

5. Conclusions

In this study, a novel solar and geothermal based energy system for producing electricity, hydrogen and cooling is analyzed by using integrated sustainability assessment model. Finally, proposed system's total sustainability index is calculated as 0.74 is higher than the sustainability index of the PV system ranged from 0.54 to 0.63 (Abu-Rayash and Dincer, 2019). As a result, proposed system is found to be economically profitable, exergetically efficient, environmentally friendly, socially well-known and accepted. Also, this innovative system has potential to bring welfare to the humanity although it has low social cost. Such innovative systems should become widespread due to their high technological and educational outcomes to ensure the sustainability of science and humanity.

References

Abu-Rayash, A., Dincer I., 2019. Sustainability assessment of energy systems: A novel integrated model. Journal of Cleaner Production 212, 1098-1116. https://doi.org/10.1016/j.jclepro.2018.12.090

Acar, C., Dincer, I., 2017. Environmental impact assessment of renewables and conventional fuels for different end use purposes. Int. J. Global Warming 13, Issue 3-4. https://doi.org/10.1504/IJGW.2017.087197

Asdrubali, F., Baldinelli, G., D'Alessandro, F., Scrucca, F., 2015. Life cycle assessment of electricity production from renewable energies: Review and results harmonization. Renewable and Sustainable Energy Reviews 42,1113–1122. http://dx.doi.org/10.1016/j.rser.2014.10.082

GEO ELEC, 2013. Public acceptance of geothermal electricity production. https://www.researchgate.net/publication/255791445

Hacatoglu, K., Dincer, I., Rosen, M.A., 2014. A new model to assess the environmental impact and sustainability of energy systems. Journal of Cleaner Production 103, 211-218. https://doi.org/10.1016/j.jclepro.2014.06.050

Hacatoglu, K., Dincer, I., Rosen, M. A., 2015. Sustainability assessment of a hybrid energy system with hydrogen-based storage. International Journal of Hydrogen Energy 40(3), 1559-1568. https://doi.org/10.1016/j.ijhydene.2014.11.079

Hacatoglu, K., Dincer, I., Rosen, M. A. 2016. Sustainability of a wind-hydrogen energy system: Assessment using a novel index and comparison to a conventional gas-fired system. International Journal of Hydrogen Energy 41(19), 8376-8385. https://doi.org/10.1016/j.ijhydene.2016.01.135

IRENA, 2013. Renewable Energy and Jobs. https://www.irena.org/publications/2013/Dec/Renewable-Energy-and-Jobs-(2013)

IRENA, 2017. Renewable Power Generation Costs in 2017. https://www.irena.org/publications/2018/Jan/Renewable-power-generation-costs-in-2017

Ni, O., Velasquez, R., Gonzalez, G., 2016. Sustainability assessment, case of study: Geothermal power plant. 14th LACCEI International Multi-Conference for Engineering, Education, and Technology: "Engineering Innovations for Global Sustainability", 20-22 July 2016, San José, Costa Rica. https://www.academia.edu/31464619

Ramírez, E, Macías, J, Pineda, J, Martínez, K, Malo, M, López-Sánchez, J, Raymond, J, Blessent, D., 2017. Public awareness and perception on deep geothermal energy: Preliminary results from an international survey. Conference: IGCP636 2017 Annual Meeting. https://www.researchgate.net/publication/323971485

Samadi, S., 2017. The social costs of electricity generation—categorising different types of costs and evaluating their respective relevance. Energies 10, 356; https://doi.org/10.3390/en10030356

Siddiqui, O., Ishaq, H., Dincer, I., 2019. A novel solar and geothermal-based trigeneration system for electricity generation, hydrogen production and cooling. Energy Convers. Manag.198,111812. https ://doi.org/10.1016/j.enconman.2019.111812

Application of Artificial Neural Networks for Solar Multi-parameters Prediction; A Case Study of Nigeria

[1*]Olusola Bamisile, [2]Ariyo Oluwasanmi, [3]Taiwo Ajagunsegun,[4]Mustapha Mukhtar, [5]Olufunso Alowolodu, [2]Philip Adjei, [1]Qi Huang

[1] University of Electronic Science and Technology of China, School of Mechanical and Electrical Engineering, Electronics Science and Technology Department, Chengdu, 611731, China.

[2] University of Electronic Science and Technology of China, School of Software Engineering, Chengdu, 611731, China.

[3] Shaheed Udham Singh College of Engineering and Technology, Department of Computer Science and Engineering, Tangori Mohali, India.

[4] Guangdong University of Petrochemical Technology, School of Economics and Management, Maoming 525000, China.

[5] Federal University of Technology Akure, Computer Science Department, 704, Ondo State, Nigeria.

* E-mails: boomfem@gmail.com

Abstract

In this research, the use of three artificial neural network (ANN) models for solar irradiance and solar PV parameters forecasting in Nigeria is presented. Although solar irradiance prediction exists in literature, the use of ANN for solar PV parameter prediction is limited in previous studies. Six different locations are selected in Nigeria and datasets from these locations have been used to train, and the ANN models developed. This research aims to model ANN algorithms that can forecast solar irradiance and solar PV parameters based on an hourly time-step. A deep learning regression model built on the Levenberg-Marquardt backpropagation algorithm is used to train and test the ANN model for all the locations considered. Three different ANN models were developed for each location in Keras python using all the input parameters. The evaluation metrics used in this study are; R, R-squared, RMSE, and MAE. The models developed are capable of predicting solar irradiance and solar PV parameters. The R values for the ANN models range from 0.9046 – 0.9777 for solar irradiance and 0.7768 – 0.8739 for solar PV multi-parameters prediction.

Keywords: Deep Learning, Artificial Neural Network, Solar Irradiance, Solar PV.

I. Introduction

The enormous amount of greenhouse gases being emitted daily is a major contributing factor to amplified global temperature vulnerabilities. Although the development and utilization of renewable energy (RE) have increased in recent years, fossil fuels still dominate global energy production (Wang et al., 2019). RE sources (RES) like wind, solar, hydro, geothermal, and tidal can recycle themselves in nature and also replenish themselves within a short time frame. The use of RES for electricity generation and other sources have been researched and many are in wide application globally.

In addition to air temperature, wind speed, humidity, and precipitation, one of the most important outdoor climatic conditions in recent years is solar radiation (SR). This is due to its usefulness in different fields such as architecture, energy, agriculture, and meteorology (Kaba et al., 2018). Detailed knowledge about spatial and temporal variability of SR is vital for both present and future planning. Although SR is one of the most monitored meteorological data, the availability of measurement stations is limited especially in underdeveloped and developing countries. Nigeria as a developing country has 36 states and about 54 weather observation stations (Ogungbenro and Morakinyo, 2014). According to Nigeria's Meteorological Agency (NiMet), the country requires about 9,000 weather stations and this is highly unachievable at the moment. It is therefore imperative that a means to measure or predict solar radiation and some other meteorological data in the country is devised.

In literature, machine learning techniques such as artificial neural network (ANN), has been used for different forecasting and prediction tasks. Nourani et al. used an ANN-based estimation to predict the interval for the downscaling of hydro-climatologic parameters. Prediction interval width and coverage probability were reported to be 2 – 10 % higher and 10 – 40 % lower in comparison to the Bootstrap method for different general circulation models (Nourani et al., 2019). The application of machine learning or deep learning methods for solar radiation prediction has been found more accurate than traditional methods. The prediction of global solar irradiance with hybridized k-means and SVR algorithms resulted in overall values of 0.9842, 0.434 MJ/m^2/day, 2.7498 %, and 1.795 % for R^2, RMSE, RRMSE, and MAPE respectively (Ayodele et al., 2019).

In this research, the use of ANN models for solar PV parameters forecasting in Nigeria is presented. According to PVGIS, the important parameters required to calculate the performance of a PV system are solar irradiance, sun elevation, wind speed, and ambient temperature. This research aims to model ANN algorithms that can forecast these parameters. The forecast for solar irradiance is first modeled and then the forecast of other solar PV parameters. Twelve years of input data based on an hourly time-step will be used to train and test the models developed. The evaluation metrics of the model accuracy will be based on R, R-squared, RMSE, and MAE value. The model will be used to forecast data for seven different locations within Nigeria and the best model for each location will be proposed.

II. Methodology

ANNs exist typically as organized layers made up of interconnected input nodes, hidden layers, and output nodes. In this study, the ANN structure used consists of an input layer, a hidden layer, and an output layer (Karabacak and Cetin, 2014). The Input and output layers are different for solar irradiance and solar PV multi-parameters forecast. Following literature (Deo et al., 2019), a feed-forward neural network which contains multilayer perceptron neurons is employed for forecasting task in this study. The ANN models used eight input parameters for the solar irradiance and solar PV multi-parameters prediction. Although a one-layer model is common in literature, ANN with two, and three hidden layers are considered in the scope of this research. A feed-forward neural network with a multilayer perceptron (FFN-MLP) is mostly used for solar irradiance prediction/forecast in existing studies (Ghimire et al., 2019). The input parameters are used to train the network until it is capable of approximating a function and the theory of gradient descent is applied for weight adjustment. The mathematical representation of a neural network model can be written as :

$$y(x) = L\left(\sum_{j=1}^{N} w_j(p).x_j(p) + c\right) \quad (1)$$

Where $y(x)$ is the forecasted solar irradiance, $L(.)$ is the hidden transfer function, $w_j(p)$ is the weight that connects neurons in the input layer, $x_j(p)$ is the input variable in discrete-time t and c is the neuronal bias.

In this study, three ANN models will be compared to determine the best forecasting model for different locations. The parameters used to estimate solar PV performance are in-plane irradiance (G_i), sun elevation (A_S), ambient temperature (T_{amb}), and 10m total wind speed (W_{10}). These are measured respectively as Gi in W/m^2, As in deg., T_{amb} in deg. C, and W_{10} in m/s. These parameters are crucial to the estimation of solar PV electricity production but are not readily available at many locations. Twelve years of data for these parameters based on hourly time-step have been downloaded from the PVGIS website (Commission, 2019). These will be used for both training and testing of deep and machine learning models used in this research. A total of seven different locations namely; Sokoto, Lagos, Abuja, Port Harcourt (PH), Maiduguri, and Taraba are considered in the scope of this study. These include locations with (1) very high solar radiation such as Kano, Sokoto, and Maiduguri, (2) relatively average solar radiation distribution (Abuja and Taraba), and (3) relatively low solar radiation distribution (Lagos and Port Harcourt). The specifics of these locations in terms of longitude and latitude are presented in Table 1.

Table 1: Location specifics of case studies

Location (State)	Longitude (decimal degree)	Latitude (decimal degree)
Lagos	6.562	3.376
Port Harcourt	7.025	4.747
Taraba	10.387	8.055
Abuja	7.403	9.032
Sokoto	5.232	12.978
Maiduguri	13.138	11.809

Table 2 highlights the segregation of the training and testing data set. Following literature (Afram et al., 2017), the predictors and objective variables are normalized using the standard normalization method. A total of 48 ANN models were constructed and Keras regression model was implemented to provide high-level building blocks based on model-level library. To examine the performance of the prediction models developed, statistical indicators are used to compare and validate models. These include; correlation coefficient (r), mean absolute error (MAE), regression coefficient (R^2), root mean square error (RMSE), will serve as an indicator for the testing datasets (Meenal and Selvakumar, 2018; Yadav et al., 2014).

Table 2: Segregation of the testing and training data

		Number of Feature Points	Percentage
Solar Irradiance Prediction	Testing	(10512, 8)	10 %
	Training	(94608, 8)	90 %
Solar PV Multi-parameter Prediction	Testing	(8757, 8)	0.0833 %
	Training	(96363, 8)	91.67 %

III. Results and discussions

MAE is a quantity that can be used to measure how close the predicted values are in comparison to the real data while RMSE indicates the level scatter produced by the ANN model (Premalatha and Valan Arasu, 2016). The R-value shows the relationship between the predicted values and the real dataset. The closer the R-value is to 1 the more accurate the model is said to be. The summary of the RMSE, MAE, and R-values for the solar irradiance prediction training and test are presented in Table 3. The R scores for each ANN model are presented in the extended version of this paper, so also, the hyperparameters that include; the number of hidden layers, number of neurons in each hidden layer, and number of epochs. The best model for each location will be chosen based on the

model that satisfies most of the following criteria; highest R-value, least MAE, and least RMSE.

The performance of all the ANN models showed that these models are suitable for solar irradiance prediction as the R-value for all the locations considered in Nigeria is between 0.904 and 0.978. However, the best model for solar irradiance prediction in Abuja, Maiduguri, Lagos, PH, and Taraba is ANN-3 while ANN -2 has the best performance for Sokoto (Table 3). In comparison to existing literature (Ghimire et al., 2019; Yang et al., 2020), the performance of the ANN models in this study is superior to the ones presented in their research. While the R values for the models developed by Ghimire et.al. range from 0.600 to 0.937 and that of the models developed by (Premalatha and Valan Arasu, 2016) is between 0.6755 and 0.9545, the R values of this present study are between 0.94046 and 0.9777.

ANN-1 has the best prediction performance out of all the models for Abuja, Maiduguri, Lagos, and PH for solar PV multi-parameters prediction. ANN-2 is the best fit for Sokoto and Taraba. The training and test R-value, MAE, RMSE for all the locations are presented in Table 4. The R-squared values and λ_{MAE} and λ_{RMSE} are presented in the extended version of this paper. The trend of the ANN performance for solar PV parameter prediction is similar to that of solar radiation prediction. The ANN models' performance is better for regions with high G_i, A_S, T_{amb}, and W_{10}. Also, the MAE and RMSE are smaller in comparison to solar irradiance prediction cases.

Table 3: Solar irradiance performance metrics summary

		RMSE (W/m²)		MAE (W/m²)		R	
Location	**Model**	**Training**	**Test**	**Training**	**Test**	**Training**	**Test**
Abuja	ANN-1	88.571	89.70501	41.24926	41.89888	0.963654	0.963666
	ANN-2	89.70271	89.92378	41.30736	41.96733	0.963498	0.963485
	ANN-3	88.88534	**89.63443**	39.15941	**39.62474**	0.963345	**0.963724**
Lagos	ANN-1	115.3526	114.516	59.30018	58.78947	0.920623	0.923442
	ANN-2	112.3027	113.0029	54.42512	54.61101	0.92467	0.925532
	ANN-3	112.2451	**112.8876**	55.09339	55.31314	0.925013	**0.925690**
Maiduguri	ANN-1	82.0475	83.2643	35.18284	35.3061	0.974302	0.948972
	ANN-2	78.14875	81.7164	31.84112	33.0205	0.97672	0.975116
	ANN-3	82.10793	82.6447	31.35719	**31.2167**	0.974264	**0.97454**
PH	ANN-1	120.4929	120.9866	62.82689	63.382	0.901252	0.90459
	ANN-2	119.9492	120.5427	62.33092	63.14022	0.902189	0.905323
	ANN-3	118.823	**120.2826**	60.01105	**61.03538**	0.904114	**0.905753**
Sokoto	ANN-1	75.23825	77.20032	32.60505	33.10191	0.978149	0.977432
	ANN-2	73.71575	**76.7851**	30.03823	**31.0103**	0.979034	**0.977677**
	ANN-3	75.71128	77.8905	32.5493	33.1657	0.977871	0.977022
Taraba	ANN-1	88.75959	91.4881	40.69629	41.6181	0.9644	0.962881
	ANN-2	86.94432	91.50793	39.11635	40.76196	0.965867	0.962865
	ANN-3	89.05307	91.55137	39.71769	40.58797	0.96416	**0.962829**

Table 4: Solar PV multi-parameter performance metrics

		RMSE		MAE		R	
Location	**Model**	**Training**	**Test**	**Training**	**Test**	**Training**	**Test**
Abuja	ANN-1	46.12166	46.51183	12.29065	12.48156	**0.855843**	**0.855224**
	ANN-2	45.54318	45.85322	11.05598	11.22394	0.849157	0.848264
	ANN-3	45.80834	46.12113	11.28507	11.41138	0.852934	0.853155
Lagos	ANN-1	58.9642	58.56698	16.84522	16.78166	**0.836441**	**0.83501**
	ANN-2	58.70492	58.64047	14.84908	14.88823	0.829877	0.82941
	ANN-3	58.56107	58.6011	14.96323	14.9978	0.807039	0.806358
Maiduguri	ANN-1	42.24084	42.4465	10.45274	10.4183	**0.877547**	**0.876877**
	ANN-2	42.02454	42.2318	9.860988	9.82206	0.857641	0.856881
	ANN-3	41.92515	42.2301	8.935582	8.88484	0.867909	0.867491
PH	ANN-1	63.24347	62.9726	17.23945	17.3672	**0.801604**	**0.801719**
	ANN-2	63.14804	62.8757	16.71214	16.8149	0.783305	0.781272
	ANN-3	63.01409	62.98399	16.71582	16.85408	0.778825	0.776847
Sokoto	ANN-1	42.77417	44.1062	13.55283	13.8287	0.852532	0.849392
	ANN-2	38.93149	40.4886	8.311102	8.52791	**0.877107**	**0.873904**
	ANN-3	38.99871	40.3774	8.84921	9.08048	0.86997	0.864494
Taraba	ANN-1	45.61537	46.6163	11.45749	11.6268	0.856936	0.854254
	ANN-2	45.69499	46.55918	11.22593	11.38143	**0.859021**	**0.855646**
	ANN-3	46.0494	47.0669	11.38845	11.5918	0.857318	0.856351

IV. Conclusions

In this study, three artificial neural network models have been developed for solar irradiance and solar PV multi-parameters prediction based on hourly timestep. These models were trained and tested on the dataset from six different states within Nigeria. Three ANN models were developed for each location in Keras python using

different input parameters. The prediction R-value for all the locations considered respectively are; 0.9046 – 0.9777 for solar irradiance and 0.7768 – 0.8739 for solar PV multi-parameters. ANN models with three hidden layers (ANN-3) have the best performance for solar Irradiance prediction in five of the six locations considered. Similarly, ANN models with one hidden layer (ANN-1) have the best prediction performance for four of the six locations considered. The ANN model's performances are high for regions with high solar irradiance (Sokoto and Maiduguri) while the models have difficulty learning for regions with relatively low solar irradiance (PH and Lagos).

The accuracy of the ANN models for solar irradiance prediction is better when compared to solar PV multi-parameters prediction. However, it is noteworthy that the performance of all the models presented in this study is an improvement to the performance of models in existing literatures. The improvement in performance for this present study can be attributed to the data size and the specificity of the ANN models.

Acknowledgments

This research is supported by Sichuan Youth Science and Technology Innovation Team Fund under Grant No. 2017TD0009.

References

Afram, A., Janabi-Sharifi, F., Fung, A.S., Raahemifar, K., 2017. Artificial neural network (ANN) based model predictive control (MPC) and optimization of HVAC systems: A state of the art review and case study of a residential HVAC system. Energy Build. 141, 96–113. https://doi.org/10.1016/j.enbuild.2017.02.012

Ayodele, T.R., Ogunjuyigbe, A.S.O., Amedu, A., Munda, J.L., 2019. Prediction of global solar irradiation using hybridized k-means and support vector regression algorithms. Renew. Energy Focus 29, 78–93. https://doi.org/10.1016/j.ref.2019.03.003

Commission, E., 2019. PHOTOVOLTAIC GEOGRAPHICAL INFORMATION SYSTEM [WWW Document]. URL https://re.jrc.ec.europa.eu/pvg_tools/en/tools.html#TMY (accessed 10.11.19).

Deo, R.C., Şahin, M., Adamowski, J.F., Mi, J., 2019. Universally deployable extreme learning machines integrated with remotely sensed MODIS satellite predictors over Australia to forecast global solar radiation: A new approach. Renew. Sustain. Energy Rev. 104, 235–261. https://doi.org/10.1016/j.rser.2019.01.009

Ghimire, S., Deo, R.C., Downs, N.J., Raj, N., 2019. Global solar radiation prediction by ANN integrated with European Centre for medium range weather forecast fields in solar rich cities of Queensland Australia. J. Clean. Prod. 216, 288–310. https://doi.org/10.1016/j.jclepro.2019.01.158

Kaba, K., Sarıgül, M., Avcı, M., Kandırmaz, H.M., 2018. Estimation of daily global solar radiation using deep learning model. Energy 162, 126–135. https://doi.org/10.1016/j.energy.2018.07.202

Karabacak, K., Cetin, N., 2014. Artificial neural networks for controlling wind-PV power systems: A review. Renew. Sustain. Energy Rev. 29, 804–827. https://doi.org/10.1016/j.rser.2013.08.070

Meenal, R., Selvakumar, A.I., 2018. Assessment of SVM, empirical and ANN based solar radiation prediction models with most influencing input parameters. Renew. Energy. https://doi.org/10.1016/j.renene.2017.12.005

Nourani, V., Jabbarian Paknezhad, N., Sharghi, E., Khosravi, A., 2019. Estimation of prediction interval in ANN-based multi-GCMs downscaling of hydro-climatologic parameters. J. Hydrol. 579, 1–18. https://doi.org/10.1016/j.jhydrol.2019.124226

Ogungbenro, S.B., Morakinyo, T.E., 2014. Rainfall distribution and change detection across climatic zones in Nigeria. Weather Clim. Extrem. https://doi.org/10.1016/j.wace.2014.10.002

Premalatha, N., Valan Arasu, A., 2016. Prediction of solar radiation for solar systems by using ANN models with different back propagation algorithms. J. Appl. Res. Technol. 14, 206–214. https://doi.org/10.1016/j.jart.2016.05.001

Wang, H., Lei, Z., Zhang, X., Zhou, B., Peng, J., 2019. A review of deep learning for renewable energy forecasting. Energy Convers. Manag. 198, 111–799. https://doi.org/10.1016/j.enconman.2019.111799

Yadav, A.K., Malik, H., Chandel, S.S., 2014. Selection of most relevant input parameters using WEKA for artificial neural network based solar radiation prediction models. Renew. Sustain. Energy Rev. https://doi.org/10.1016/j.rser.2013.12.008

Yang, L., Cao, Q., Yu, Y., Liu, Y., 2020. Comparison of daily diffuse radiation models in regions of China without solar radiation measurement. Energy 191. https://doi.org/10.1016/j.energy.2019.116571

THERMODYNAMIC ANALYSIS OF A NOVEL SOLAR ASSISTED MULTIGENERTAION SYSTEM

[1, 4]Muhammad Sajid Khan, [2*]Muhammad Abid, [1]Mi Yan, [3]Tahir Abdul Hussain Ratlamwala
[1]Institute of Energy and Power Engineering, Zhejiang University of Technology, Hangzhou, Zhejiang 310014, China
[2]Cyprus International University, Faculty of Engineering, Department of Energy Systems Engineering, Nicosia, North Cyprus via Mersin 10, Turkey
[3]National University of Sciences and Technology, Islamabd, Pakistan
[4]Mechanical Engineering Department, Mirpur University of Science & Technology, (MUST) Mirpur (10250), AJK, Pakistan

* E-mails: mabid@ciu.edu.tr

Abstract
In the present study, a novel solar assisted multi-generation system is proposed and thermodynamically analysed for multiple outputs. The system consists of solar tower with heliostat, a combined cycle, single effect absorption chiller, heat pump, water-based thermal energy storage system and an electrolyzer for hydrogen production. Supercritical carbon dioxide is the heat transfer fluid in the central tower receiver, while atmospheric air is used as a working fluid in the gas cycle and R410A is utilized in heat pump. The entire system is investigated thermodynamically and performances of the system are evaluated and compared considering energetic and exergetic efficiencies, specifically for four scenarios; single generation system, co-generation system, tri-generation system and multi-generation system. Results show that energy efficiency of single and multi-generation systems are approximately 20.93% and 51.62%, while exergy efficiency is almost 22.51% and 53.45%, respectively. The location of any sub-system integrated with the main system is influenced on the performance of whole system.

Keywords: multi-generation, exergy, Heliostat, electrolyzer, heat transfer, energy.

I. Introduction

The use of renewable energy resources instead of fossil fuels to generate power, heating and cooling etc. has drawn much attention due to the harmful effect on the environment produced by the fossil fuels. The fundamental source of renewable energy is the solar energy and amongst the renewable energy resources, solar energy is clean, abundantly available and can be easily harnessed for multigenerational purpose (Tian and Zhao 2013). In addition, various outputs like electricity, heating, cooling, etc. can be achieved through solar thermal systems, like, PTC, solar tower, solar dishes (Suleman et al. 2014b). Although there are many technologies that can be used to convert solar energy into electricity but central receiver tower is the most attractive and deployed concentrated solar power (CSP) technology, discussed by (Tian and Zhao 2013).

Tri-generation and multi-generation are helpful to overcome energy challenges utilizing energy resources in an efficient way (Khalid et al. 2015). Multi-generation systems and processes have great potential to gain higher exergy and energy efficiencies at less operating costs and low emissions to the environment as waste heat of high temperature cycle is used to drive other integrated cycles. A multi-generation system (solar energy integrated with coal gasification) to generate hydrogen, electricity, hot water, heating and cooling was studied by Ozturk and Dincer (2013). Al-Ali and Dincer (2014) conducted another study, using energy and exergy analysis of integrated solar-geothermal system for multi-generation purpose. It was concluded that exergy efficiency increased up to 10%, whereas, energy efficiency enhanced from 16.4% to 75% by shifting single generation to multi-generation system. Multi-generation systems powered by renewable energy are sustainable and predict better efficiency as compared to the single or co-generation systems (Ahmadi et al. 2014; Dincer and Zamfirescu, 2012). Okonkwo et al. (2018) studied a solar tower assisted combined cycle power plant using sCO_2 as a heat transfer fluid in solar collector. The investigation was carried out using first and second law analysis along with exergo-economics optimization. The study showed a payback period of 10 years and 0.31$/kWh of levelized energy cost that proved its economic viability. Combined environmental and exergy analysis have been performed by Abid et al. (2018); Ahmadi et al. (2012) investigated a tri-generation ORC from exergo-environmental point of view, while a small scale integrated hydrogen and power generation system was exergo-economically analyzed by Caliskan et al. (2013). Parham et al. (2017) accomplished the comprehensive thermodynamic and environmental analysis of a multi-generation system having an ORC, an internal heat exchanger, an open absorption heat transformation system and an electrolyzer. Hydrogen can be used as a fuel offers exceptional advantages that helps hydrogen to become one of the most important energy carrier of the future (Abid et al. 2020). According to the research reported to-date, multigenerational systems are proposed to enhance the performance with less hazardous on the environment. There exist studies that are reported about the energy and exergy analysis of solar-assisted multi-generation systems but according to the best knowledge of authors, the comparative assessment of the best configuration of multi-generation system is almost rare. Therefore, a novel multi-generation system is proposed for multiple outputs that consists of heliostat with solar tower to drive combined gas cycle (topping Brayton cycle, while bottoming Rankine cycle) to generate power and an electrolyzer for hydrogen production, an absorption chiller, heat pump and a thermal energy storage

II. System Description

Fig. 1 shows the proposed multi-generation system that is composed of six sub-systems (solar tower with heliostat, combined cycle, single effect absorption chiller, heat pump, electrolyser and a thermal energy storage system). The solar radiations fall on the heliostat field that reflects solar radiations onto the central receiver mounted on the top

of the tower. In the present study, supercritical CO_2 is the heat transfer fluid circulating in the receiver which has thermal properties quite similar to the air. Heat exchanger 1 gets thermal energy of the heated s-CO_2 and exchanges its heat to the secondary fluid (air) in the Brayton cycle. After the expansion process in the gas turbine, there is another heat exchanger 2, which transfers the thermal heat of air to the working fluid (water) for the steam cycle. The fluid turns into super-heated steam by absorbing heat from the air and it drives high-pressure steam turbine. The steam leaving the high-pressure turbine (HPT) is reheated and used to drive a low-pressure turbine at the same temperature. The high temperature working fluid of gas cycle at state point 7 is used to drive a single effect absorption chiller. The remaining energy of hot working fluid after chiller generator is used to drive the heat pump to produce heating. Hot fluid at state point 40 passes through the evaporator of the heat pump between state pump 41 and 42. Here, the working fluid R410 A absorbs the heat and rejects between the state points 43 and 44 tot further maintain the suitable temperature of the required heated area. The low-grade heat of the condenser of rankine cycle is used to heat the water of thermal energy storage system.

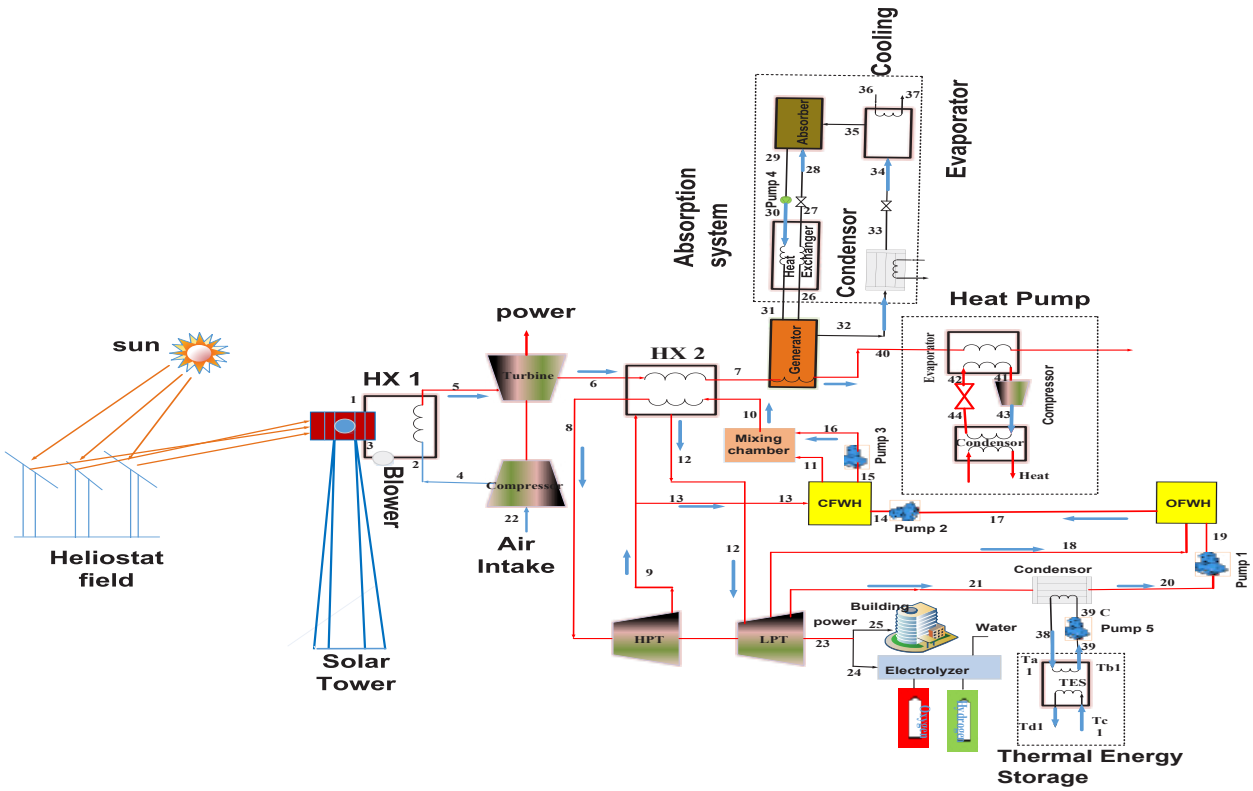

Fig. 1: Schematic of solar integrated multi-generation system

III. Analysis

This section presents the equations used to carryout the thermodynamic analysis of proposed multigeneration system. Engineering Equation Solver (EES) by Klein (2009), is employed for the comprehensive analysis of the whole integrated system. Considering a control volume with a steady state process (Xu et al. 2011).

$$\dot{Q}_{c.v} - \dot{W}_{c.v} + \sum \dot{m}_{in} h_{in} - \sum \dot{m}_{out} h_{out} = 0 \quad (1)$$

$$\dot{X}_d = \dot{E}_{x_{in}} - \dot{E}_{x_{out}} \quad (2)$$

The energy efficiency of single generation, co-generation, tri-generation and multi-generation systems can be defined by the following relations.

$$\eta_{en,sing-gen} = \frac{W_{net,single\ gen}}{\dot{Q}_{sun}} \quad \text{(Single generation includes power cycle only)} \quad (3)$$

$$\eta_{en,co-gen} = \frac{W_{net,co-gen} + Q_e}{\dot{Q}_{sun}} \quad \text{(Co-generation includes power cycle plus absorption chiller)} \quad (4)$$

$$\eta_{en,\ tri-gen} = \frac{W_{net,tri-gen} + Q_e + \dot{Q}_{TES}}{\dot{Q}_{sun}} \quad \text{(Tri-generation includes power cycle, chiller plus TES)} \quad (5)$$

$$\eta_{en,\ multi-gen} = \frac{W_{net,multi-gen} + Q_e + \dot{Q}_{TES} + \dot{Q}_{hp}}{\dot{Q}_{sun}}$$

(Multi-generation involves power cycle, chiller, TES plus heat pump) (6)

Now, the relationships used to find the exergy efficiency of single, co, tri and multi-generation systems can be defined as (Islam and Dincer 2017):

$$\eta_{ex,sing-gen} = \frac{w_{net,single\ gen}}{\dot{Q}_{sun}\times\left(1-\frac{T_o}{T_{sun}}\right)} \quad (7)$$

$$\eta_{ex,co-gen} = \frac{w_{net,co-\ gen}+\dot{E}x_{th,e}}{\dot{Q}_{sun}\times\left(1-\frac{T_o}{T_{sun}}\right)} \quad (8)$$

$$\eta_{ex,\ tri-gen} = \frac{w_{net,tri-\ gen}+\dot{E}x_{th,e}+\dot{Q}_{TES}\left(1-\frac{T_o}{T_{source}}\right)}{\dot{Q}_{sun}\times\left(1-\frac{T_o}{T_{sun}}\right)} \quad (9)$$

$$\eta_{ex,\ multi-gen} = \frac{w_{net,multi-\ gen}+\dot{E}x_{th,e}+\dot{Q}_{TES}\left(1-\frac{T_o}{T_{source}}\right)+\dot{Q}_{hp}\left(1-\frac{T_o}{T_{source}}\right)}{\dot{Q}_{sun}\times\left(1-\frac{T_o}{T_{sun}}\right)} \quad (10)$$

IV. Results and discussions

In the recent work, a solar tower assisted combined power plant (Brayton cycle is topping cycle and steam cycle as a bottoming cycle) is suggested, producing power and hydrogen via electrolyser. A comprehensive energy and exergy analysis is performed along with the exergo-environmental analysis by varying the certain operating parameters. It can be seen from fig. 2 that energy efficiencies of single generation, co-generation and tri-generation systems are 20.93%, 32.06% and 44.55%, respectively, while exergetic efficiencies are 22.51%, 35.18% and 49.65%, accordingly. It is also evident that higher energy efficiencies of tri-generation and multi-generation are due to the higher COP value of heat pump and TES heat gain. Fig. 3 depicts the influence of increasing the solar radiation from 500 to 1100 W/m2 on the efficiencies of single generation, co-generation, tri-generation and multi-generation systems, respectively. Energy efficiency of single generation increases from 15.92% to 24%, while exergy efficiency improves to almost 50.77% against rise in solar radiation. This is due to the reason that only network output from the power cycle is required in single generation system, so availability of more solar flux promotes higher useful heat gain to the heat transfer fluid from receiver.

The inlet temperature of heat transfer fluid varies from 500 K to 800 K as shown in fig. 4 and energy efficiencies of single generation, co-generation, tri-generation and multi-generation systems rises from 17.34% to 24.99%, 26.56% to 38.28%, 36.91% to 53.19% and 42.77% to 61.64%, respectively. The higher work output from the power cycle is the main sharing factor of the efficiencies of single generation system. Fig. 5 presents the graphical interpretation of heliostat receiver energetic and exergetic efficiencies and hydrogen production rate against increase in the concentration ratio. All the performance parameters increase gradually, energy efficiency rises from 28.32% to 77.8%, exergy efficiency from 23.3% to 64.02%, while hydrogen production rate enhances from 0.00289 kg/s to 0.00796 kg/sec.

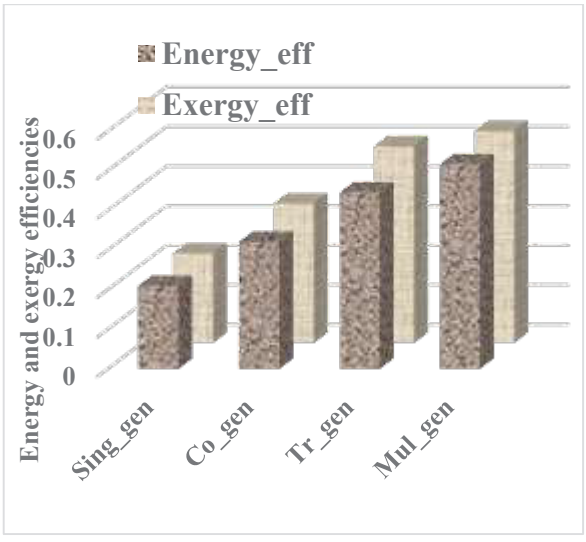

Fig. 2. Comparison of efficiencies

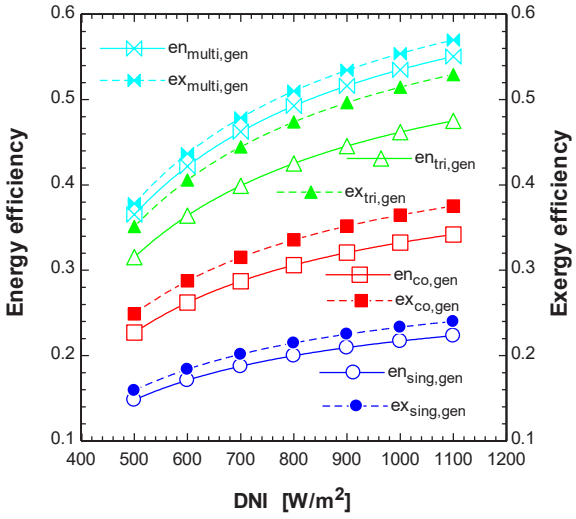

Fig. 3: DNI effect on efficiencies

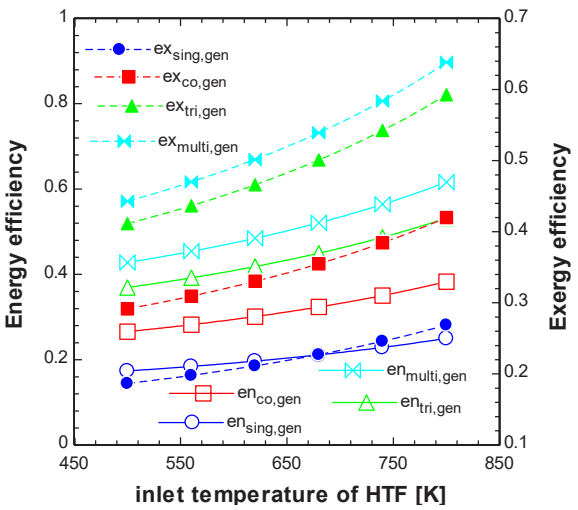

Fig. 4: Inlet temperature impact on efficiencies

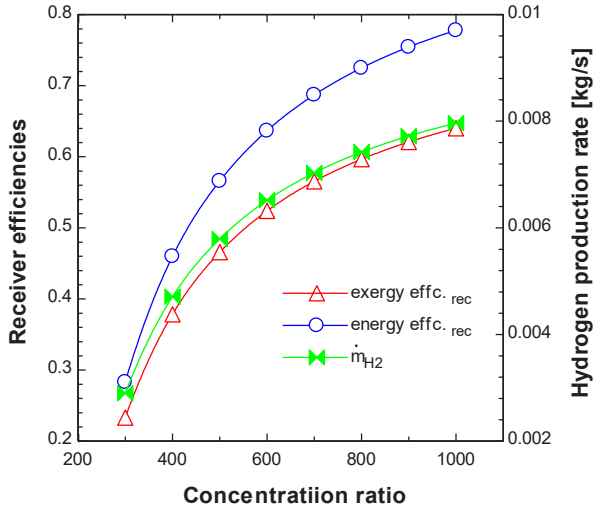

Figure 5: Effect of concentration ratio

V. Conclusions

A comprehensive thermodynamic analysis and comparison of novel solar tower assisted multi-generation system producing multiple outputs are carried out in the present study. Main findings of the study include that the energy and exergy efficiencies of single generation system are 20.93% and 22.51% respectively, while for co-generation system these are 32.06% and 35.18%, accordingly. An appreciable improvement is found in the case of multi-generation system, as its efficiencies are 51.62% and 53.45%.. Increase in the concentration ratio also increases the area of heliostat that further improves the performance of the solar receiver.

References

Al-Ali, M., Dincer, I., 2014. Energetic and exergetic studies of a multigenerational solar-geothermal system. Appl. Therm. Eng. 71, 16–23.

Ahmadi, P., Dincer, I., Rosen, M.A., 2014. Performance assessment of a novel solar and ocean thermal energy conversion based multigeneration system for coastal areas. J. Sol.Energy Eng. 137 (1), 11013.

Abid, M., Khan, M. S., & Hussain Ratlamwala, T. A. (2019). Thermodynamic Performance Evaluation of a Solar Parabolic Dish Assisted Multigeneration System. Journal of Solar Energy Engineering, 141(6).

Abid, M., Khan, M. S., & Ratlamwala, T. A. H. (2020). Comparative energy, exergy and exergo-economic analysis of solar driven supercritical carbon dioxide power and hydrogen generation cycle. International Journal of Hydrogen Energy, 45(9), 5653-5667.

Abid, M., Khan, M. S., & Ratlamwala, T. A. (2018). Techno-environmental analysis of a parabolic dish assisted recompression with and without reheat s-CO2 Brayton cycle. International Journal of Exergy, 27(4), 527-552.

Caliskan H, Dincer I, Hepbasli A. Exergoeconomic and environmental impact analyses of a renewable energy based hydrogen production system. Int J Hydrogen Energy 2013; 38(14):6104-11.

Dincer, I., Zamfirescu, C., 2012. Renewable-energy-based multigeneration systems. Int. J. Energy Res. 36 (15), 1403–1415.

Islam, S., & Dincer, I. (2017). Development, analysis and performance assessment of a combined solar and geothermal energy-based integrated system for multigeneration. Solar Energy, 147, 328-343.

Okonkwo, E.C., Okwose, C.F., Abid, M., and Ratlamwala, T.A.H. (2018). “Second-Law Analysis and Exergoeconomics Optimization of a Solar Tower–Driven Combined-Cycle Power Plant Using Supercritical CO2”. Journal of Energy Engineering, 144(3): 04018021.

Ozturk, M., Dincer, I., 2013. Thermodynamic assessment of an integrated solar power tower and coal gasification system for multigeneration purposes. Energy Convers. Mange. 76, 1061–1072.

Parham K, Alimoradiyan H, Assadi M. Energy, exergy and environmental analysis of a novel combined system producing power, water and hydrogen. Energy 2017; 134:882-892.

Suleman, F., Dincer, I., Agelin-Chaab, M., 2014b. Energy and exergy analyses of an integrated solar heat pump system. Appl. Therm. Eng. 73, 557–564.

Tian Y, Zhao C-Y. A review of solar collectors and thermal energy storage in solar thermal applications. Appl Energy 2013; 104:538–53.

Xu, C., Wang, Z., Li, X., and Sun, F. (2011). “Energy and exergy analysis of solar power tower plants.” Applied Thermal Engineering, Elsevier Ltd, 31(17–18), 3904–3913.

Thermodynamic Analysis of a Hydrogen Solid Oxide Fuel Cell (SOFC) Integrated Absorption Chiller & Organic Rankine Cycle for Cooling and Power production

Victor Adebayo[1], Muhammad Abid[1], Michael Adedeji[1], Tahir Abdul Hussain Ratlamwala[2]
[1] Energy systems engineering department, Cyprus International University, Nicosia, North Cyprus, Mersin 10, Turkey
[2] National University of Sciences and Technology (NUST) Islamabad, Pakistan

* E-mail: mabi@ciu.edu.tr

Abstract
As climate change concerns continue to rise and the ever-increasing cost and scarcity of fuel resources, fuel cells with their high electrical efficiency, reduced emissions and useful heat output have been identified as key technological solution for both energy efficiency for buildings and emission reduction. In this work, thermodynamic analysis was carried out to investigate the incorporation of a hydrogen solid oxide fuel cell (SOFC) with a lithium bromide-water (LiBr-H_2O) absorption chiller and the Organic Rankine cycle for the simultaneous production of electricity and cooling. The system's physical and thermodynamic components include an SOFC, an ORC, heat exchangers for the heating process, and a double-effect absorption chiller for cooling. The SOFC exhaust gases are used to drive the ORC, and the generator of the absorption chiller. The heat exchangers are also used to preheat the SOFC reactant streams with the exhaust gases in order to enhance the energy consumption efficiency of the overall system. The system is simulated under steady state conditions and the performance of the entire system was also observed under various operating conditions.

Keywords: SOFC, Hydrogen, ORC, Thermodynamic

I. Introduction
The use of more efficient power plants has become a major challenge for power plant designers and operators today with the depletion of fossil fuels and their consequent effect on global warming. Conventional thermal plant efficiency is typically less than 39% where most of the electricity is expended as waste heat. Evaluation of an efficient system that can efficiently utilize waste heat is therefore important for improving the overall performance of the plants.
Combined power and cooling production (co-generation) is a viable method utilizing waste heat. This improves efficiency of the plant and thus reduces emissions of greenhouse gases.
The primary driver is an important part of a system of co-generation which makes its selection essential. Gas turbines, internal combustion engines, external combustion steam turbines, engines, micro-turbines and fuel cells are the major drivers. Among these, fuel cell-based cogeneration also achieves higher energy efficiency, possibly because the fuel cell avoids constraints on Carnot's efficiency limitations (Ranjbar et al., 2014). In addition, when fuelled with pure hydrogen, fuel cells are completely zero emission devices with the only by-product being water vapour (Sieres, 2011).
In a fuel cell, a fuel and an oxidant transform their chemical energy directly into electrical energy. Even though fuel cells are not heat engines, heat is still generated, must be extracted from them. There are various types of fuel cells available, distinguished by the electrolyte used which, in effect, depends on the temperature at which it operates (Sieres, 2011).
Nearly all currently designed SOFC systems employ a zirconia electrolyte stabilized by yttria. This is because it shows good stability in both oxidizing and reducing atmospheres as well as good oxygen ion conductivity, and is unreactive to other materials used in the SOFC (Ormerod, 2003). Usually, the anode of a SOFC is made of a nickel cermet, such as Ni-YSZ, while the cathode is made of strontium (Sr) doped with lanthanum manganite (LaMnO3). The fact that all the components in a SOFC are solid structures allows the cells to be formed in any configuration. The SOFC works within the range 600–1000ºC so it can be integrated with other conventional thermal cycles (Milewski and Budzianowski, 2014).
While the concentration of actual research is on single cells and stack operation, models of global systems for combined production of power and cooling from a fuel cell are essential to identifying appropriate designs and operating conditions.
This study provides findings from a thermodynamic study of the integration of a hydrogen solid oxide fuel cell (SOFC) with a double effect Li-Br-H_2O absorption chiller and an ORC for the co-production of electricity and cooling. Using engineering equations solver software, a steady state mathematical model was developed to simulate the efficiency of the entire integrated energy system and of the various subsystems. Also, to evaluate optimal operating conditions, the effects of some system parameters have been investigated.

II. Integrated System configuration and description/ Methodology
Figure 1 provides a schematic illustration of the integrated system. It consists of a hydrogen solid oxide fuel cell (SOFC), a double-effect Li Br-H_2O absorption chiller, an ORC, an air heater and a hydrogen preheater. The system can simultaneously produce electricity and refrigeration. The Integrated System operating concept can be summed

up as follows. The fuel of the SOFC, which is pure Hydrogen, is preheated by the hydrogen heat exchanger (H_2 HX), and injected into the anode of the SOFC. Likewise air in the heat exchanger (Air HX) is preheated and circulated into the SOFC cathode. The fuel's chemical energy (H_2) and the oxidant (O_2 in the atmosphere) are transformed to electrical power and heat in the SOFC.

To improve the overall thermodynamic efficiency of the SOFC, the high temperature exhaust gases exiting the SOFC are used to preheat the SOFC's reactant streams. These exhaust gases are then used to run the absorption system and an ORC where cooling and additional power are produced. The circulation of the solution is accomplished by a pump in the double-effect LiBr absorption cycle. The weak solution in LiBr leaving the absorber is made to flow through the two heat exchangers to the high- and medium-temperature generators (HTG and MTG). The solution is then heated in the HTG by the hot air from the Air heat exchanger and refrigerant water vapor is produced as a result. Used as a source of heat input to the MTG is the vapor leaving the HTG vapour. Once the vapor is condensed it is throttled at the condenser pressure and then throttled further into the evaporator.

To evaluate the performance of the integrated energy system a lumped steady state model was developed. Such types of models are ideal for the current study because emphasis is not centered on either the fuel cell, the components of the absorption system or that of the ORC, but on how the operating conditions influence the efficiency of the entire system.

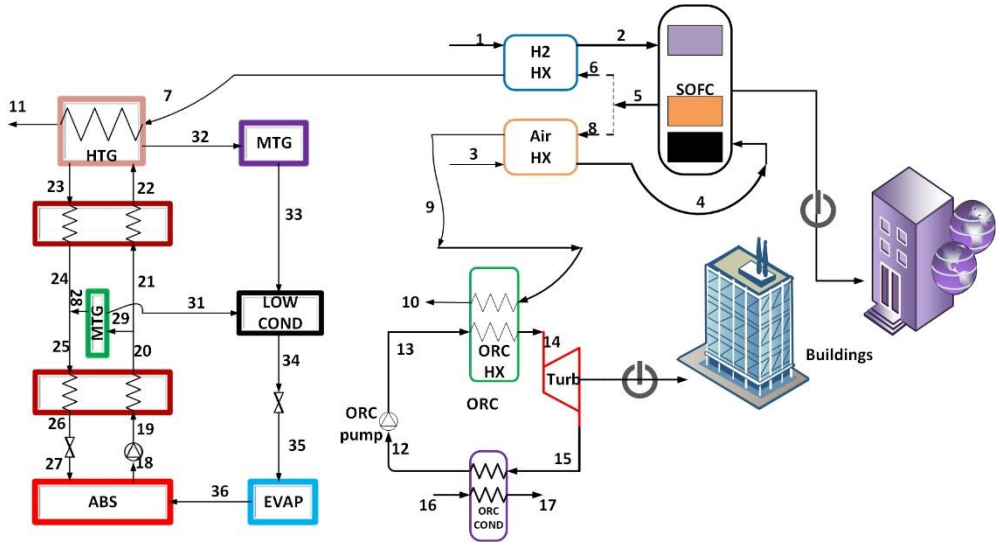

Fig. 1 Schematic diagram of the integrated system

The mathematical model described above was developed using the Engineering Equation Solver (EES). The model was used to simulate and evaluate the performance of an integrated hydrogen solid oxide fuel cell with a double-effect absorption system using LiBr-H_20 pair and working fluid and an ORC for combined electricity and cooling production.

Some of the input parameters and operating conditions considered for the analysis are listed below in Table 1 below

Table 1. Input parameters and operating conditions

Parameter	Value	Reference
Inlet temperature of H_2 and Air	*25°C*	(Sieres, 2011)
Operating pressure	*100 kPa*	(Sieres, 2011)
Fuel composition	*100% H_2* *21% O_2* *79% N_2*	(Sieres, 2011)
Operating temperature of SOFC	*900°C*	(Sieres, 2011)
Fuel utilization ratio of SOFC	*100%*	(Sieres, 2011)

III. Analysis

The integrated system's mathematical model is based on the application of global mass, energy balance and basic heat and mass transfer calculations. The following general assumptions were taken into account for the entire system: the system operates under steady-state conditions, pressure drops are insignificant except in the pumps and expansion systems, heat transfer between the heat exchangers and the atmosphere is minimal, the fuel of the SOFC is pure H_2 under atmospheric conditions, the ambient air entering the SOFC is 79% N and 21% O, reactants and SOFC products can be considered as ideal gases.

(i) The Solid Oxide Fuel Cell

The basic assumptions for the SOFC are: the SOFC works under steady state conditions, the pressure is unchanged, there is an ideal and full stoichiometric reaction, and the fuel cell is inside a thermal sink to ensure the needed operating temperature. The exit gas temperatures are equal to the SOFC temperature, all heat transfer

between the cell and its surroundings typically occurs at fuel cell temperature boundaries, the kinetic and gravitational potential changes in energy are negligible, and the SOFC works under thermodynamically reversible conditions so that the entropy production rate due to irreversibility is zero (Sieres, 2011).
The electrochemical reaction occurring within the solid oxide fuel cell anode and cathode is defined in the following terms (Sieres, 2011):

$$H_2 + 2.381(0.21O_2 + 0.79N_2) \rightarrow \dot{Q}_{sofc} + \dot{W}_{sofc} \quad (1)$$

Where $\dot{W}_{sofc}$the work rate of the fuel cell and $\dot{Q}_{sofc}$ is is the amount of heat transmitted from the surrounding to the fuel cell.
The first and second laws of thermodynamics for the fuel cell can be summarized thus (Li, 2007):

$$\dot{N}_{H_2} \cdot (h_{in} - h_{out}) + \dot{Q}_{sofc} - \dot{W}_{sofc} = 0 \quad (2)$$

$$\dot{N}_{H_2} \cdot (s_{in} - s_{out}) + \frac{\dot{Q}_{sofc}}{T_{sofc}} - \dot{S}_g = 0 \quad (3)$$

Where h_{in} the amount of enthalpy per mole of H is carried by reactant inflow into the system and h_{out} is the amount of enthalpy per mole of H_2 extracted from the system by the exhaust stream containing the reaction products. Respectively the variables s_{in} and s_{out} are identical to h_{in} and h_{out},

$$h_{in} = (h_{H_2} + 0.5 \cdot h_{O_2} + 1.881 \cdot h_{H_2})_{in} \quad (4)$$

$$h_{out} = (h_{H_2O} + 1.881 \cdot h_{H_2})_{out} \quad (5)$$

(ii) The Organic Rankine Cycle

In steady state conditions, the components of the ORC are also taken as control volume components and devices therefore a typical mass balance equation can be written.

Work done by the ORC turbine: $\dot{W}_{turb} = \dot{m}_{14}h_{14} - \dot{m}_{15}h_{15}$ (6)

Heat rate into the ORC: $\dot{Q}_{in\ ORC} = \dot{m}_9 h_9 - \dot{m}_{10}h_{10}$ (7)

(iii) The Double-Effect Absoription Chiller

In steady state conditions, the components of the absorption chiller are also taken as control volume components and devices therefore a typical mass balance equation can be written.
The Coefficienct of performance of the double effect chiller is given as:

$$COP_{en} = \frac{\dot{Q}_{evp}}{\dot{Q}_{HTG} + \dot{W}_{pump,a}} \quad (8)$$

IV. Results and discussions

In this segment, findings from the system analysis are discussed. Certain assumptions were made and established earlier, and then the graph is discussed. Table 2 show the output form the system analysis, and is given below.

Table 1. System output results

Parameter	Value
Work rate of SOFC	*190363 kW*
Work done by the ORC turbine	*662.8 kW*
Cooling load	*219.5 kW*
COP of absorption chiller	*1.324*
Overall energy efficiency	*66.9%*
Total work delivered by the integrated system	*190992 kW*

Figure 2 shows the effect of varying the mass flow rate of the hydrogen fuel into the Solid oxide fuel cell and observing this effect on the net power output and overall energy efficiency of the integrated system.

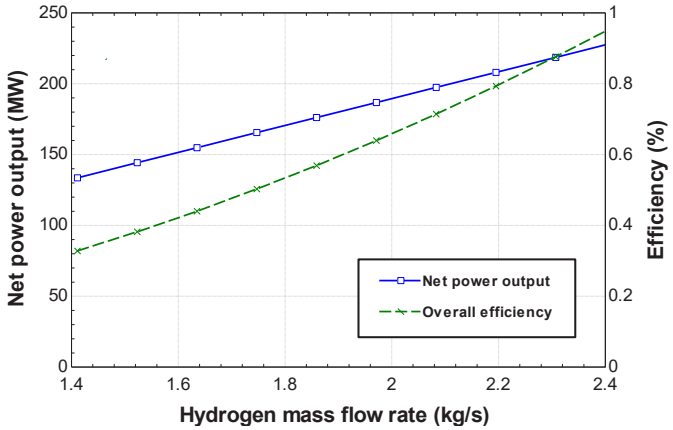

Fig. 2. Effect of hydrogen mass flow rate on system performance

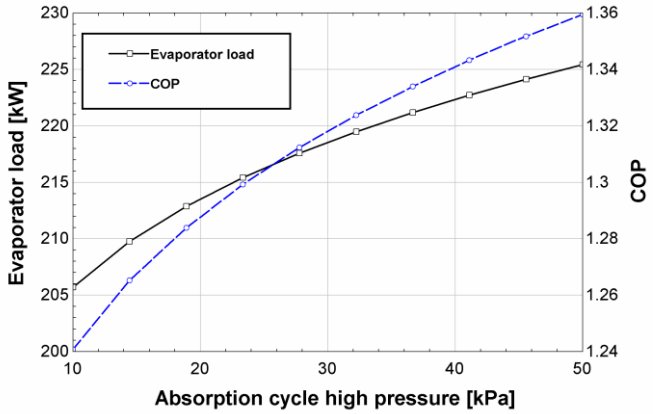

Fig. 3. Effect of Absorption cycle hgh pressure on evaporator load and COP

As observed from figure 2, the net power output and overall system efficiency increases as the mass flow rate of the hydrogen fuel entering the SOFC increases. Figure 3 also shows the effect of the high-level pressure of the absorption chiller and observing its effect on the evaporator load and COP of the chiller. As the pressure increases, the evaporator load and subsequently the COP also increases.

V. Conclusions

A mathematical model was introduced in this paper to model an integrated hydrogen solid oxide fuel cell with a double effect LiBr-H_2O chiller and ORC for combined electricity generation and cooling. The performance of the entire system was also observed under various operating conditions such as hydrogen fuel mass flow rate nad high level pressure of the absorption chiller. Net power production and overall system performance are observed to improve as the mass flow rate of the hydrogen fuel entering the SOFC increases.

References

Li, X., 2007. Thermodynamic performance of fuel cells and comparison with heat engines, in: Advances in Fuel Cells. Elsevier, pp. 1–46.

Milewski, J., Budzianowski, W., 2014. Recent key technical barriers in solid oxide fuel cell technology. Arch. Thermodyn. 35, 17–41.

Ormerod, R.M., 2003. Solid oxide fuel cells. Chem. Soc. Rev. 32, 17–28.

Ranjbar, F., Chitsaz, A., Mahmoudi, S.M.S., Khalilarya, S., Rosen, M.A., 2014. Energy and exergy assessments of a novel trigeneration system based on a solid oxide fuel cell. Energy Convers. Manag. 87, 318–327.

Sieres, J., 2011. Simulation of an integrated hydrogen fuel cell with NH3-water absorption system for combined production of electricity, cooling / heating and hot water.

Energy and Exergy Analysis of a Solar Driven Trigeneration System for Ammonia Synthesis, Electricity Generation and Fresh Water Production

[*1,2]Murat Emre Demir, [1,3]Ibrahim Dincer
[1]Clean Energy Research Laboratory, University of Ontario Institute of Technology, Faculty of Engineering and Applied Science, 2000 Simcoe Street North, Oshawa, Ontario L1H 7K4, Canada
[2] Faculty of Naval Architecture and Ocean Engineering, Istanbul Technical University, Maslak-Sariyer, Istanbul, 34469, Turkey
[3] Yildiz Technical University, Faculty of Mechanical Engineering, Istanbul, 34349 Turkey
E-mail: medemir@itu.edu.tr

Abstract
This research paper designs and analyzes a new integrated solar-driven system for ammonia synthesis, fresh water production, and power generation. The trigeneration system consists of a solar thermal subsystem, a thermal energy storage system where the molten salt is used as a heat transfer fluid and storage medium, a solar energy-driven Rankine cycle, a multi-stage flash distillation, a proton exchange membrane electrolyser array, and an ammonia synthesis unit. The proposed integrated system uses solar energy to charge the molten salt, which flows through a heat exchanger and generates steam for the topping cycle. The exhaust stream of the steam turbine provides heat for the multi-stage flash distillation (MSF) process. A 20 stage MSF unit is proposed where the seawater is utilized as the feedwater in this study. A portion of the produced fresh water is sent to PEM electroylzer array for hydrogen production, which is used for ammonia production via the Haber-Bosch process. The thermodynamic analysis of the integrated system is analyzed by using Engineering Equation Solver and Aspen plus software packages. The performance assessments based on energy and exergy efficiencies are carried out for all the system components. Power generation, fresh water production, and ammonia synthesis capacities are also determined. The overall exergy efficiency of the system is determined as 11.0% where the ammonia synthesis, power generation, and fresh water production capacities are 0.85 kg / h, 17.6 MW, and 143.97 kg / h respectively. The results show that the solar receiver is responsible for the highest exergy destruction plus exergy losses as 70.8 MW.
Keywords: Desalination, heat storage, ammonia synthesis, power production, efficiency.

1. Introduction
In today's world, sustainable development has a huge interest in meeting the demand for increasing global needs such as energy and clean water due to population growth and higher living standards. Renewables could be the primary solution for a cleaner and more prosperous environment instead of conventional sources. However, most of the renewable energy sources should be assisted with an energy storage/carrier medium due to their intermittent nature. In this context, hydrogen is the most promising content based on its favorable features such as high heating value, carbon-free molecular structure, and high feedstock availability when it is produced from water. On the other hand, issues regarding the storage and transportation of the hydrogen still constitute a significant concern for the commercialization of the hydrogen economy. One of the methods to tackle the aforementioned problems is to synthesize alternative fuels from hydrogen. Ammonia can be considered as an energy carrier as well as a feedstock. It can be used for storing hydrogen due to its physical characteristics, or it can directly be burned without any emission of carbon in an internal combustion engine. Although ammonia can be synthesized via a variety of methods, the Haber-Bosch process is dominantly used for commercial production. More than 90% of global ammonia production is currently performed by the Haber-Bosch synthesis process, which combines hydrogen with nitrogen via a high-temperature and pressure iron oxide catalyst (Bicer, Dincer, Zamfirescu, Vezina, & Raso, 2016).

This research study develops and thermodynamically analyzes a new integrated solar-energy based system for ammonia synthesis, freshwater supply, and electricity generation. Using Engineering Equation Solver and Aspen plus software, the thermodynamic analysis of the integrated system is analyzed. For all system components, performance assessment based on energy and exergy efficiencies is calculated. The capacities for generating electricity, producing freshwater and synthesizing ammonia are also determined.

2. System description
The proposed system in this study is presented in Fig. 1. The trigeneration system consists of a solar thermal subsystem with a heliostat field, a two-tank storage system in which the molten salt acts as a heat transfer fluid and a storage medium, a solar-powered Rankine cycle, a multi-stage flash distillation unit for freshwater production, a proton exchange membrane electrolyser array to provide hydrogen for ammonia synthesis and an ammonia synthesis unit. After the molten salt passes through the solar

receiver, the excessive portion of it goes directly to the hot storage tank. To maintain the generated power at a specific rate, the molten salt in the hot storage tank offset the energy deficit for the cases where the DNI is inadequate. Upon sunset, the integrated system is fed only by the molten salt from storage. The required amount of freshwater is provided via the MSF process with the seawater. A 20 stage MSF unit is used in this study. A portion of the produced freshwater is sent to the PEM electrolyzer array for hydrogen production which is used for ammonia production via Haber ammonia via the Haber-Bosch process. The produced hydrogen gas and the nitrogen gas coming from the air separator unit are compressed and sent to the ammonia synthesizer at 300 bar and 180 ˚C. The temperature rises to 468 ˚C in the ammonia synthesizer. The hot ammonia gas and unreacted gasses are directed to the expander, where the pressure and temperature gradually decrease while the expander generates power. After the condensation process, the liquid ammonia is collected in the storage tank, and the unreacted gases are sent to another loop for better conversion efficiency. The overall system performance is assessed via a comprehensive thermodynamic analysis. The sub-systems' production capacities of freshwater, hydrogen, electricity, and ammonia are calculated. The exergy destructions throughout the system are obtained. The authors investigate a similar configuration for solar hydrogen production in their previous study (Demir & Dincer, 2018). For further information about the theoretical steps about the solar desalination/hydrogen production subsystem, the research paper can be examined .

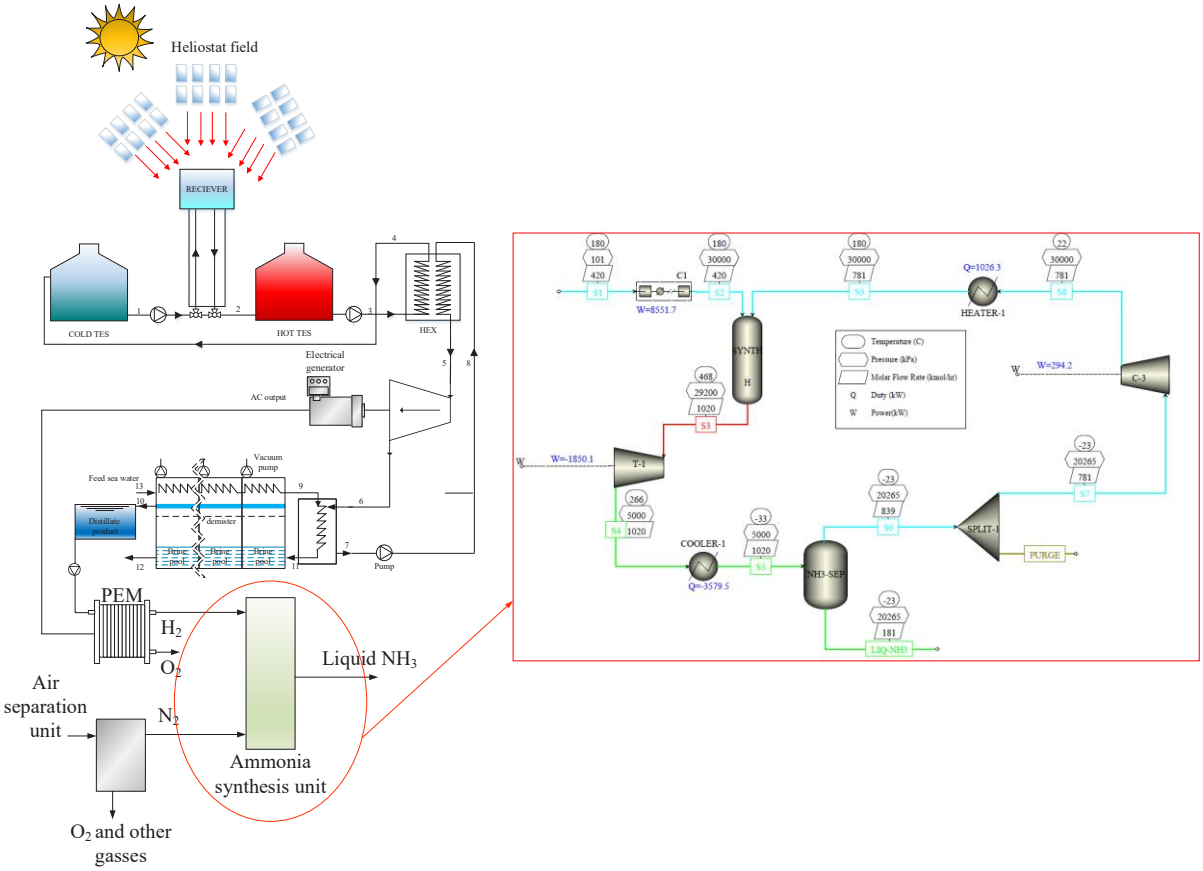

Fig.1 Solar driven integrated system layout

3. Analysis

The proposed system will be evaluated for five subunits, namely the field of heliostat — solar receiver, thermal energy storage, multi-stage flash distillation (MSF), Rankine cycle, PEM electrolyzer stack, and ammonia synthesis unit. This section describes the calculation order of all system elements. First, the quantity of solar radiation reaches the heliostat field and reflects the receiver is calculated. The daily average DNI level is assumed as 7.43 kWh/m^2/day. Moreover, it is assumed that the daylight is available 12h in a day. Then, the heat losses of the storage tanks determined and the capacity of the Rankine cycle is calculated accordingly. The condenser load of the Rankine cycle corresponds to the heat input of the multi-stage flash distillation sub-system. A mathematical model is used to obtain freshwater output of the desalination process where a part of the products is sent to the PEM electrolyzer. A mathematical model is used to determine hydrogen production in the electrolyzer. The produced hydrogen is sent to the ammonia synthesize bottom cycle. The ammonia production cycle is modeled in ASPEN plus while EES performs the rest of the modeling. The calculations are done based on the assumptions of study

state steady flow, negligible changes in potential and kinetic energies, no chemical reactions take place except for electrolyzer and ammonia synthesizers. The overall energy and exergy efficiencies of the system are defined by taking into account the system inputs and outputs as follows (Demir & Dincer, 2018):

$$\eta_{en} = \frac{\dot{W}_{net} + \dot{m}_{NH_3} LHV_{NH_3} + \dot{m}_{water}\Delta h_{water}}{\dot{Q}_{solar} + \dot{m}_{N_2} h_{N_2}}$$

$$\psi = \frac{\dot{W}_{net} + \dot{m}_{NH_3} ex_{NH_3} + \dot{m}_{water}\mathrm{ex}_{\mathrm{water}}}{Ex^{\dot{Q}_{solar}} + \dot{m}_{N_2} ex_{N_2}}$$

4. Results and discussion

Table 1 tabulates the thermodynamic properties of the corresponding state points. The overall energy and exergy efficiency of the system is determined as 11.0% and 70.3% respectively. The significant difference between the energy and exergy efficiencies can be attributed to the high production rate of the water by the system. The water comes out from the system at 40 ˚C with a mass flow rate of 3307 kg/s. The heat is mostly preserved within the system, on the other hand, the water temperature drops drastically compare to the heat source temperature. Hence it results in a higher energy efficiency accompanied by a relatively low exergy efficiency. Another two overall exergy and energy efficiencies of the system can be described which not take into account water as a useful output to see the impact of the ammonia and electricity production on the overall system performance.

Table 1. Thermodynamic properties of state points.

	$\dot{m}$	T	P	h	s	$\dot{E}x$
State #	kg/s	K	kPa	kJ/kg	kJ/kg K	kW
0		298,2	101,3	104,9	0,3672	
0`		298,2	101,3	-396,3	-0,8951	
1	789,6	658,7	101,3	37	0,05643	118108
2	789,6	942,3	101,3	377,9	0,4877	285720
3	789,6	940	101,3	375,1	0,4848	284260
4	789,6	660	101,3	38,53	0,05876	118764
5	94,64	620	3000	3109	6,733	104648
6	94,64	343,3	31,35	2484	7,339	28472
7	94,64	343,3	31,35	293,5	0,9565	1222,4
8	94,64	344,3	3000	300,1	0,9669	1554,4
9	3306,8	323,3	101,3	209,9	0,7052	13844
10	143,08	313,2	7,385	167,5	0,5724	204,88
11	3306,8	338,3	101,3	272,6	0,895	34276
12	3164	313,2	7,385	167,5	0,5724	4532
13	3306,8	298,2	101,3	104,9	0,3672	0

Based on these alternative definitions, the energy and exergy efficiencies are calculated as 10.0% and 10.1% respectively. This also shows that only 14% of the useful outputs are energetically responsible for ammonia production and electricity generation.

Fig. 2 shows the exergy destruction plus loss rates of the system components. As expected, the highest exergy destruction rates occur at the receiver surface, and the steam generator where heat transfer takes place at higher temperatures and the temperature difference between the heat source and heat sink remains high. The lowest exergy destruction plus loss rates are obtained at hot and cold storage tanks by 657 kW and 1458 kW respectively. It can be contributed to the well insulation of the tank walls. Since the function of these tanks is not convert nor transfer the heat, the irreversibilities related to the second law of thermodynamics are limited compared to the other system components here.

The power production capacity of the system is determined as 17583 kW where the Rankine cycle generates 58364 kW of it and the bottoming cycles for hydrogen and ammonia production are responsible for 40781 kW of consumption. The fresh water production rate is calculated as 143.97 kg/s on average which corresponds to 12439 tons per day. The fresh water production rate of the system can meet the demand of a community with a population of over 40,000 people. The PEM electrolyzer stack`s capacity of hydrogen production is calculated as 0.17 kg/sec. The produced hydrogen is directly sent to the ammonia synthesis unit with a first loop conversion rate of 42.8% at 30 MPa compressor pressure. At a steady-state conversion process, 0.85 kg/s of ammonia is produced by the system.

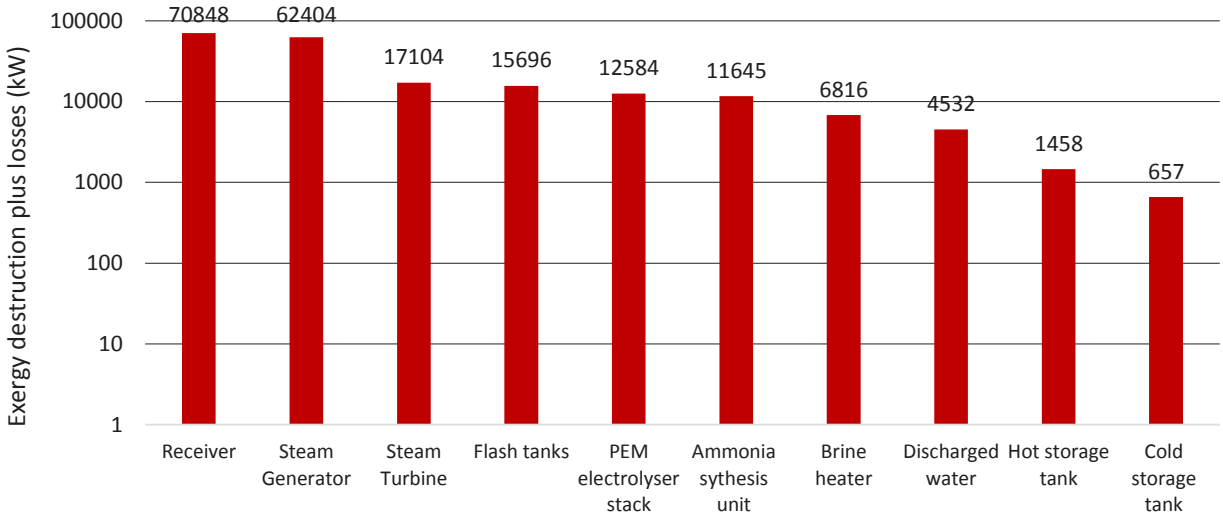

Fig.2. Exergy destruction plus exergy loss rates of the system components

5. Conclusions

In this study, a solar-driven system for ammonia production, electricity generation, fresh water production and heating is designed and analyzed thermodynamically. The main findings of this study can be listed as follows:

- The energy and exergy efficiency of the system is calculated as 11.0% and 70.3% respectively.
- The net power production capacity of the system is determined as 17.6 MW
- The ammonia production capacity of the system is determined as 0.85 kg/s
- The fresh water production capacity of the system is determined as 143.97 kg/s
- The solar receiver is responsible for the highest exergy destruction as 70.8 MW.

Acknowledgement

The authors acknowledge the support provided by the Turkish Academy of Sciences (TÜBA).

References

Bicer, Y., Dincer, I., Zamfirescu, C., Vezina, G., & Raso, F. (2016). Comparative life cycle assessment of various ammonia production methods. *Journal of Cleaner Production*, *135*, 1379–1395. https://doi.org/10.1016/j.jclepro.2016.07.023

Demir, M. E., & Dincer, I. (2018). Development and analysis of a new integrated solar energy system with thermal storage for fresh water and power production. *International Journal of Energy Research*, *42*(9), 2864–2874. https://doi.org/10.1002/er.3846

Energy analysis of vapor compression cooling system combined with desiccant wheel regenerated by auxiliary solar cycle in sultry weather

[1] Jafar Mahdavi, [1] Ali Pourahmadiyan, [2]Pouria Ahmadi, [3*]Nader Javani

[1] K. N. Toosi University of Technology, Department of Mechanical Engineering, No. 19, Pardis Street, Molla Sadra Ave., Vanak Sq, Tehran, P.O. Box 19395-1999, Iran
[2] School of Mechanical Engineering, College of Engineering, University of Tehran, P.O. Box 11155-4563, Tehran, Iran
3 Faculty of Mechanical Engineering, Yildiz Technical University, Besiktas, Istanbul, 34349, Turkey

* E-mails: Pahmadi@ut.ac.ir"

Abstract

One of the main challenges of achieving thermal comfort in a hot and humid climate is tackling the latent heat of humidity in addition to the sensible heat of air exerting excessive load on cooling systems. Desiccants are moisture absorbent materials settled in the way of humid air inside a rotating wheel in air conditioning systems (ACS). These substances are considered energy efficient since they can be regenerated by low-grade heat sources for continuous performance. In this investigation, the energy consumption of a hybrid desiccant cooling system (HDCS) is compared with the conventional vapor compression system (VCS) by dynamic simulation in TRNSYS. The case study is a four-story Office building with 8.86 tons of refrigeration load located in Bandar-Abbas, the southern part of Iran, in which the highest temperature and relative humidity (RH) recorded in July are 42 C° and 85% respectively. Results show that using solid silica-gel desiccant and heat recovery wheels along with common VSC contributes to a maximum reduction of 51.43% in electric energy consumption. Besides, due to the high potential of location in absorbing solar radiation, evacuated tube collectors with an area of 28.56 m^2 are used in an alternative cycle in order to provide a portion of required heat for desiccant wheel regeneration, leading up to 42.13% decrease in heater energy consumption.

Keywords: Desiccant Cooling System, Solar Energy, Energy Consumption, TRNSYS

I. Introduction

The ever increasing rate of energy usage has become a global concern due to its environmental implications and limited fossil fuel sources. Many efforts have been paid to stop this trend by replacing green energies. Meantime, cooling systems are more focused since their electrical energy consumption accounts for more than 10% of overall in the world ("The Future of Cooling - IEA"). Among different climate conditions, hot-humid weather comprises more latent heat for its high humidity, which exerts additional load along with sensible heat on cooling systems. For this reason, in these areas cooling systems are using excessive energy to provide thermal comfort. Having the ability to remove humidity, Desiccants empower hybrid cooling systems to offer favorable conditioned air in these areas. For continuous performance, it is essential to regenerate desiccants, which requires a low-grade heat source that can be supplied by renewable energies such as solar energy richly available in sultry weather (Wu et al., 2018).

Many studies regarding HDCS and its components have been carried out numerically and experimentally. Fong et al. (Fong et al., 2011a) compared VCS with a desiccant absorption cooling system using solar energy for both desiccant regeneration and chiller generator. They reported a 36.5% reduction in annual energy consumption for heavily crowded areas with hot-humid weather. In another case, they coupled a VCS with a solid silica-gel desiccant wheel and found that using desiccants cuts the chiller energy usage by 45.5% for a restaurant zone while the same assessment for a store showed just 13.3% reduction due to its low humidity versus that of the restaurant (Fong et al., 2011b). Hurdogan et al. (Hürdoğan et al., 2012) evaluated the performance of HDCS regenerated by a heater and assisted by solar energy as an auxiliary source of heat in Adana, Turkey. Results indicate that the COP experienced improvement between 50% to 120% based on absorbed radiation around the year. The experiment conducted by Lou et al. (Luo et al., 2019) in Taichung, Taiwan, showed that integration of solar collectors with the desiccant regeneration cycle of VCS enhances the overall performance in terms of energy consumption by 10%. Based on Rehman et al. (Rehman et al., 2020) investigation among 32 cities in Saudi Arabia hot climate, the energy-saving factor increases up to 34.6% while using HDCS instead of conventional VCS.

In this study, the performance of a proper cooling system in terms of energy is considered for a four-story office building with 8.86 tons of refrigeration load. The location is Bandar-Abbas, Iran, and the simulation period is July in which the lowest temperature is 31C°. Although evaporative cooling systems are widely used in most of the moderate areas in Iran, these types of systems are not suggested for selected location since the average temperature of the area is above 25C° (Daou et al., 2006) and as a result, a VCS is proposed. Moreover, due to the high amount of humidity in ambient air, a desiccant wheel is coupled with the system so that the latent load can be reduced or completely removed prior to its entrance to the cooling system. To take the most advantage of weather condition, in addition to the heater, an auxiliary solar cycle is added for desiccant regeneration. Eventually, a heat recovery wheel is taken to account, to make the process air cooler and lessen the sensible load of the chiller.

II. System Description

The main goal of this study is comparing the performance of common cooling systems, and those are utilizing dehumidifier components and renewable energies in sultry weather. So that three different configurations are considered as follows, (a) a conventional VCS, (b) a HDCS regenerated by a heater, (c) a HDCS regenerated by a heater and, using solar cycle as an alternative regenerator.

As shown in Fig. 1 in configuration (a), once the ambient air has been mixed with process air proportionately, it enters the cooling coil, then its temperature and humidity are decreased by the cold water, which is sent from the evaporator. After the zone is conditioned, a determined portion of the process air is sent out to continue the cycle. In configuration (b), there is installed a desiccant wheel receiving hot and humid air at point 1 to lessen the humidity. At point 2 the air temperature is higher in comparison with point 1, so a heat recovery wheel is used to facilitate the heat transfer between process and regeneration air while the humidity remains constant. Following this, the process air is directed to the coil, and the regeneration air is heated so as to be used in desiccant wheel.

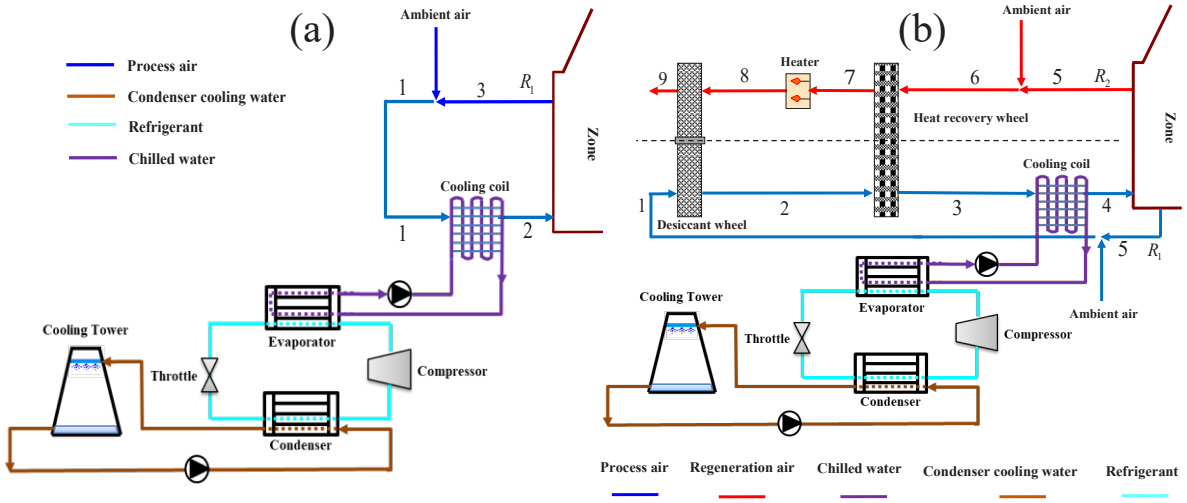

Fig. 1: arrangement of (a) a conventional VCS, (b) a HDCS regenerated by a heater

According to Fig. 2, in configuration (c), the procedure of regeneration is assisted by a solar cycle using evacuated tube collectors. After being heated in an air-water heat exchanger, regeneration air is sent to the heater. At that point, a controller calculates the appropriate temperature for desiccants regeneration, and the required energy from the heater is determined consequently. After this occurs, hot air makes desiccants ready for resuming the dehumidification process. Additionally, R_1/R_2 which is indicative of return air quantity is assumed to be 1/3 based on (Heidarinejad and Pasdarshahri, 2010).

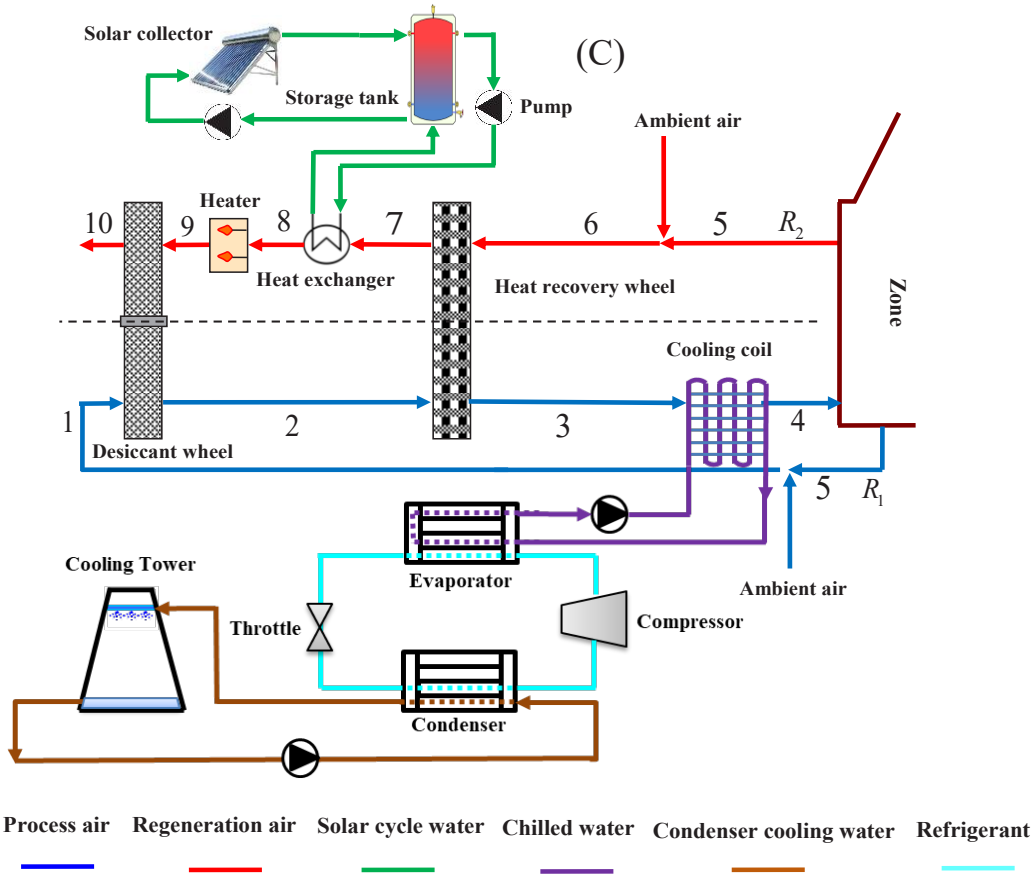

Fig. 2: arrangement of a HDCS regenerated by a heater and solar cycle

The psychrometric chart of configuration (c) is depicted in Fig. 3 showing that thermal comfort condition is fulfilled at point 5 representing the temperature and humidity of air inside zone. In summary, processes in this chart can be described as below:

- (1-2) the humidity of process air is decreased, and its temperature is raised inside the desiccant wheel.
- (2-3) the temperature of the process air is decreased through the heat recovery wheel.
- (3-4) VCS decreases the temperature and humidity of process air.
- (4-5) the temperature and humidity of process air are increased inside the zone.
- (5-1) the ambient air is mixed with the return air.
- (5-6) the ambient air is mixed with the exhaust air.
- (6-7) the temperature of regeneration air is increased through the heat recovery wheel with constant humidity.
- (7-8) the temperature of regeneration air is increased inside the air-water heat exchanger with constant humidity.
- (8-9) the heater increases the temperature of regeneration air with constant humidity.
- (9-10) the humidity of regeneration air is increased by absorbing the moisture of process air, and the temperature is raised.

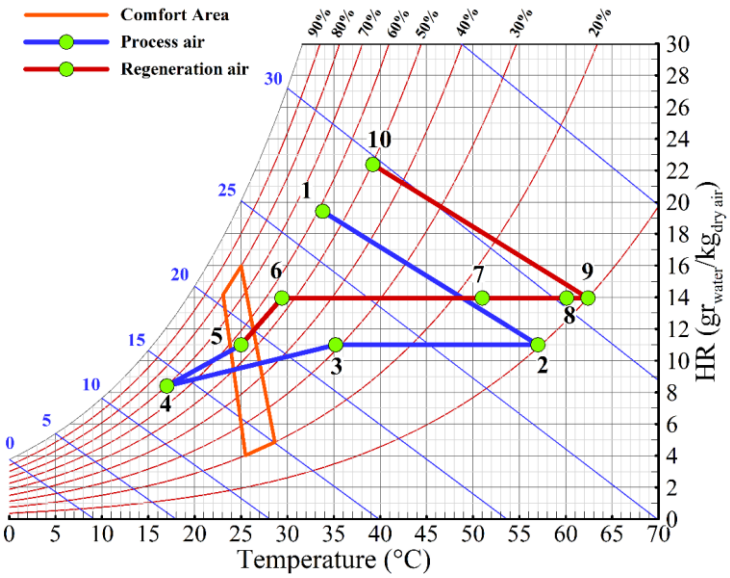

Fig. 3: psychrometric chart of configuration (c).

III. Analysis

The transient performance of proposed systems was simulated using TRNSYS software. Simulation time is July which, is the hottest month for selected location. For dehumidification process in desiccant wheel, a model developed by Jurinak (Jurinak, 1983) was used. This model is based on $F_1 - F_2$ potentials, and the set of equations are as below:

$$F1 = \frac{-2865}{T^{1.490}} + 4.344\omega^{0.8624}$$

$$F2 = \frac{T^{1.490}}{6360} - 1.127\omega^{0.07969} \quad (1)$$

Where T is the air temperature (k) and ω is the humidity($kg_{water}/kg_{Dry\ air}$). For heat recovery wheel the maximum heat transfer rate was calculated as following (Klein et al., 2006).

$$\dot{Q}_{sens} = \varepsilon_{sens} \times C_{min} . (T_{P,in} - T_{R,in}) \quad (2)$$

Where $\dot{Q}_{sens}$ is the sensible heat transfer rate (kJ/h), ε_{sens} is the heat recovery wheel sensible effectiveness and the subscripts P, R and in are indicative of process air, regeneration air and inlet in turn. Furthermore, C_{min} is defined as:

$$C_{min} = min\{(\dot{m}C_p)_P, (\dot{m}C_p)_R\} \quad (3)$$

Where $\dot{m}$ is the air mass flow rate (kg/h) and C_p is specific heat at constant pressure (kJ/kg.k).The solar cycle contains different components namely solar collector, fluid storage tank, heat exchanger and pump. the solar collector efficiency can be obtained from Hottel-Whiller general equation (Duffie and Beckman, 2013).

$$\eta = a_0 - a_1 \frac{(\Delta T)}{I_T} - a_2 \frac{(\Delta T)^2}{I_T} \quad (4)$$

Where ΔT is the difference of temperature between ambient and fluid (k), I_T is global radiation incident on collectors (kJ/h.m^2), and parameters a_0, a_1 (w/$m^2.K$) and a_2 (w/$m^2.K^2$) are expressing intercept, first order and second order efficiency respectively.

The heat transfer rate in cooling coil was calculated as (Wisconsin-Madiso, 1988):

$$\dot{Q}_{coil} = \varepsilon_{coil}\dot{m}_a C_{pa}(T_{a,in} - T_{w,in}) \quad (5)$$

Where ε_{coil} is coil effectiveness and subscripts a and w indicate air and water respectively.

IV. Results and discussions

For the purpose of study, three configurations of cooling systems are examined in terms of energy. Results show that owing to the ability of dehiumidifier materials in absorbing moisture, a desiccant wheel gives a significant reduction in chiller load when it is added to the VCS. According to Fig. 4, a conventional VCS working in hot-humid weather condition requires nearly 35 tones of refrigeration load while a HDCS cuts the maximum load by 51.43%.

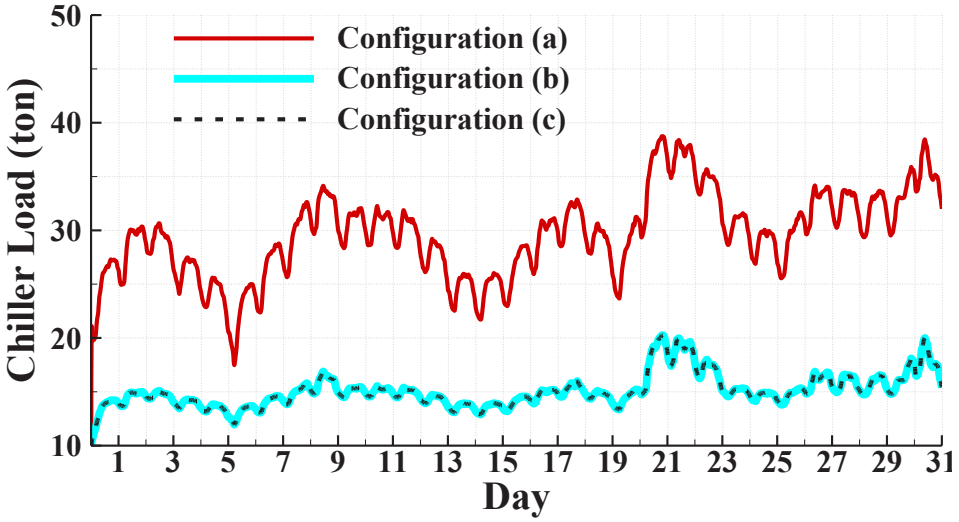

Fig. 4: required chiller load of three different configurations.

It is important to note that using an auxiliary solar cycle does not affect the chiller load since solar energy is used only for the regeneration process. As shown in Fig 5 when a solar cycle is integrated with configuration (b) the required energy from heater for desiccant regeneration is decreased during 7 AM to 6 PM, particularly at 11 AM when solar gain is peaked by the amount of 15 kW which means that 42.13% of regeneration energy is obtained from solar cycle. Due to space limitation, the solar fraction in configuration (c) is 0.6, which is equivalent to 28.56 m^2 surface of solar collectors.

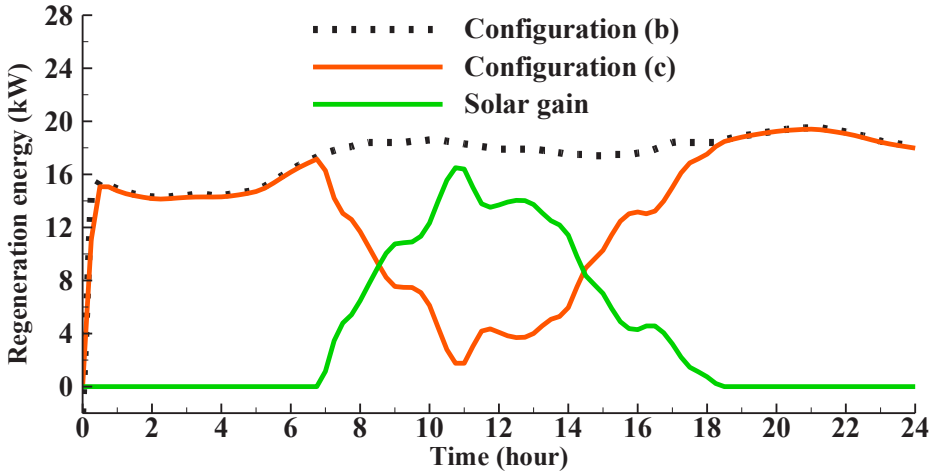

Fig. 5: solar gain and required regeneration energy of configuration (a) and (b).

V. Conclusions

Desiccant wheel is a favorable component of hybrid cooling systems used for coming to terms with high humidity of air in sultry weather. This study shows that utilization of HDCS in Bandar-Abbas, Iran, decreases chiller capacity by more than half, which is a great advancement in terms of both energy and system compactness. Moreover, based on obtained results, combination of the regeneration process with solar cycle leads to a maximum reduction of 42.13% in energy consumption of this procedure.

References

Daou, K., Wang, R.Z., Xia, Z.Z., 2006. Desiccant cooling air conditioning: A review. Renew. Sustain. Energy Rev. https://doi.org/10.1016/j.rser.2004.09.010

Duffie, J., Beckman, W., 2013. Solar engineering of thermal processes. Hoboken.

Fong, K.F., Chow, T.T., Lee, C.K., Lin, Z., Chan, L.S., 2011a. Solar hybrid cooling system for high-tech offices in subtropical climate - Radiant cooling by absorption refrigeration and desiccant dehumidification. Energy Convers. Manag. 52, 2883–2894. https://doi.org/10.1016/j.enconman.2011.04.005

Fong, K.F., Lee, C.K., Chow, T.T., Fong, A.M.L., 2011b. Investigation on solar hybrid desiccant cooling system for commercial premises with high latent cooling load in subtropical Hong Kong. Appl. Therm. Eng. 31, 3393–3401. https://doi.org/10.1016/j.applthermaleng.2011.06.024

Heidarinejad, G., Pasdarshahri, H., 2010. The effects of operational conditions of the desiccant wheel on the performance of desiccant cooling cycles. Energy Build. 42, 2416–2423. https://doi.org/10.1016/j.enbuild.2010.08.011

Hürdoğan, E., Büyükalaca, O., Yilmaz, T., Hepbasli, A., Uçkan, I., 2012. Investigation of solar energy utilization in a novel desiccant based air conditioning system. Energy Build. 55, 757–764. https://doi.org/10.1016/j.enbuild.2012.02.017

Jurinak, J., 1983. OPEN CYCLE SOLID DESICCANT COOLING--COMPONENT MODELS AND SYSTEM SIMULATIONS.

Klein, S., Newton, B., Thornton, J., Bradley, D., 2006. TRNSYS Reference Manual: Mathematical Reference.

Luo, W.J., Faridah, D., Fasya, F.R., Chen, Y.S., Mulki, F.H., Adilah, U.N., 2019. Performance enhancement of hybrid solid desiccant cooling systems by integrating solar water collectors in Taiwan. Energies 12, 1–18. https://doi.org/10.3390/en12183470

Rehman, S., Rafique, M.M., Alhems, L.M., Mahbub Alam, M., 2020. Development and implementation of solar assisted desiccant cooling technology in developing countries: A case of Saudi Arabia. Energies 13. https://doi.org/10.3390/en13030524

The Future of Cooling – Analysis - IEA [WWW Document], n.d. URL https://www.iea.org/reports/the-future-of-cooling (accessed 2.5.20).

Thesis, J.B.-P.D., Wisconsin-Madison, U. of, 1988, undefined, n.d. Methodologies for the design and control of chilled water systems. ci.nii.ac.jp.

Wu, X.N., Ge, T.S., Dai, Y.J., Wang, R.Z., 2018. Review on substrate of solid desiccant dehumidification system. Renew. Sustain. Energy Rev. 82, 3236–3249. https://doi.org/10.1016/j.rser.2017.10.021

Exergy Loss Calculation in a Power Generation System for a Research Hospital

[1*]Murat Hacıosmanoğlu and [2]Adnan Midilli,
[1]Recep Tayyip Erdogan University, Faculty of Engineering, Department of Mechanical Engineering, Rize, 53100, Turkey
[2]Yildiz Technical University, Faculty of Mechanical Engineering, Department of Mechanical Engineering, Besiktas, İstanbul, 34349, Turkey

* E-mails: murat.haciosmanoglu@erdogan.edu.tr"

Abstract
The main objective of this study is to calculate total exergy losses in a power generation system designed for a research hospital in Rize, Turkey. For this porpuse a multigeneration system is designed and all aqupments are taken into consideration for the analysis. Considering all the parameters, exergy loses of each component of the system are calculated. The results from this study show that the maximum and minimum value of exergy loss in the gas turbine powered system are found to be 2750 kW in the combustion chamber and to be 25 kW in gas turbine. In this regard, it can be said that there is a need to enhance the exergetic performance of the processes in the system.

Keywords: "Exergy, Gas Turbine, Hospital"

I. Introduction

Today, the reduction in conventional energy sources and atmospheric degradation in terms of global warming and air pollution necessitate the development of more efficient system designs and the use of alternative energy sources (Dincer, and Rosen, 2005). The production of useful product such as electricity, oxygen, hydrogen and thermal energy needed by the facilities from a single source and at the location where the need is reduced both the energy production costs of the facilities and the loss of efficiency caused by the electricity and heat produced separately. Technologies developed for this purpose are being tested by many countries today (Dincer et al., 2014).

The multigeneration processes comprising cogeneration and trigeneration can make significant differance owing to their potential for high efficiencies additionally low operating costs and contamination per energy output (Ahmadi et al. 2011). Complexes such as medium and large-scale industrial establishments, hospitals, universities have basic needs such as electricity, heating and cooling (Dincer et al., 2014). For this reason, over the past few years the establishing of cogeneration systems for both heating and power production or trigeneration systems for combined power production, heating and cooling has increased significantly to supply the thermal and power needs of facilities (Gopisetty, and Treffinger, 2013). Multigeneration render possible to generate power such as electricity and useful thermal energy like hot water from single energy resource. Multigeneration system including cogeneration contribute significantly to the environment and considerably reduces energy consumption thanks to their high efficiency in the production of cheap and clean energy, low operating costs and low emission values per unit of energy produced (Ghaebi et al., 2011).

The systems to be developed should be examined according to thermodynamic rules and their efficiency should be evaluated. In studies conducted for this purpose, energy analysis look at the amount of energy and exergy analysis is interested in the quality of energy. With the energy analysis, it is possible to compare the energy efficiency of a system with the maximum efficiency that can be achieved if that system is reversible. In exergy analysis, it is possible to determine the highest efficiency that a system can reach within the limits of operating conditions (Kaya et al., 2016). In this way, the irreversibilities in the system and the enhancement capability of the system can be revealed. In addition, exergy analysis gives clues about whether the efficiency of the system is realistic or not during the design phase (Coban et al., 2017).

As a result, many researchers and scholars state that thermodynamic productivity can be best measured with exergy analysis since exergy analysis gives more ideas and is more advantageous in studies of increasing efficiency compared to energy analysis (Dincer, and Rosen, 2005; Aydin et al., 2012). For this reason, meeting the energy needs of hospitals that need both electricity and heat with cogeneration and trigeneration systems is an important attempt to increase efficiency. In the present work, exergy loss per component of the the system designed to meet the electricity, hot and cold water, oxygen and hydrogen needs of the research hospital in Rize was determined and the results obtained were evaluated.

II. System Description

In order to understand the system designed to meet the needs of the hospital, the schematic diagram which is developed is shown Fig. 1. According to this design, there are five subsidiary systems following the gas turbine. These systems are after burner, distiller, heat exchanger, chiller, electrolyzer.

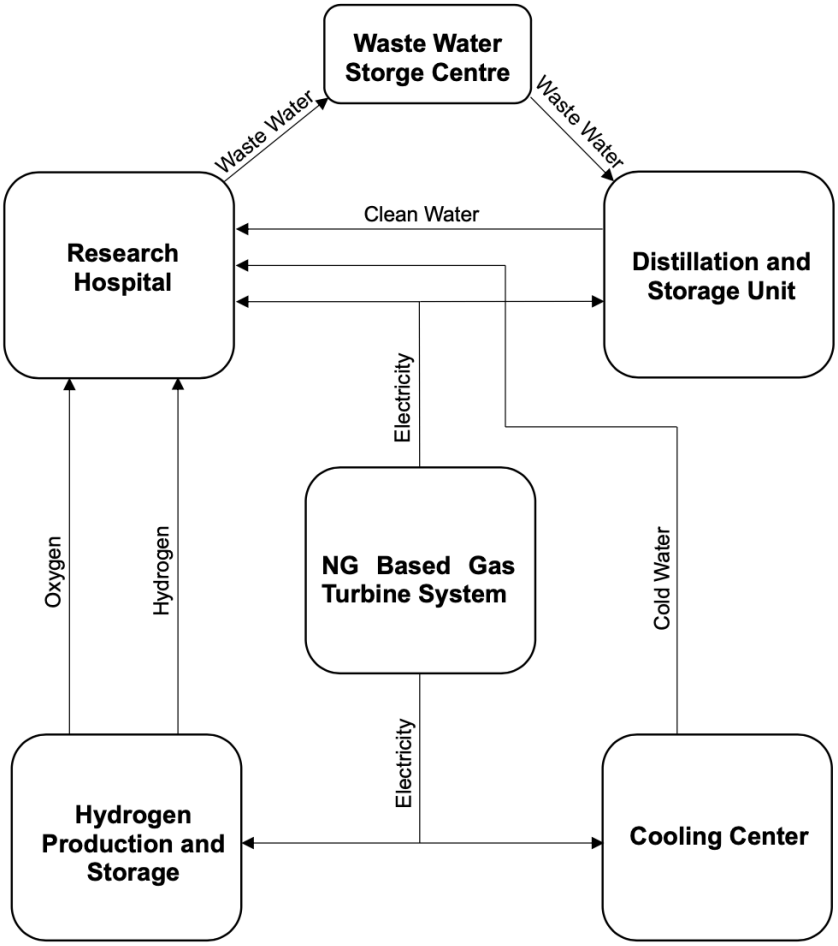

Fig. 1: Schematic illustration of the system

III. Energy and Exegy Analysis

The thermodynamic analysis of the power generation system of the research hospital is based on the following assumptions:

- ❖The system is always open with steady flow.
- ❖Exhaust gases are supposed to be air as working fluid.
- ❖Complete combustion is considered to have occurred.
- ❖Compressor and chiller are adiabatic.
- ❖Potential energy and exergy changes are negligible.x
- ❖Kinetic energy and exergy changes are negligible.

If the energy balance of each one of all the elements according to the first law of thermodynamics is written in accordance with the above assumptions (Inac et al., 2019):

$$\dot{Q} - \dot{W} + \sum \dot{m}_{in} h_{in} - \sum \dot{m}_e h_e = 0 \quad (1)$$

where $\dot{Q}$ and $\dot{W}$ are the heat transfer and work rate, $\dot{h}$ is the specific enthalpy, $\dot{m}$ is the mass flow rate for given state point.

If the exergy balance of each element is written in accordance with the second law of thermodynamics with the above assumptions:

$$\sum \dot{m}_{in} ex_{in} - \sum \dot{m}_e ex_e + \dot{E}x_Q - \dot{E}x_W - \dot{E}x_{dest} = 0 \quad (2)$$

where $\dot{E}x_{dest}$ is exergy destruction rate. $\dot{E}x_Q$and $\dot{E}x_W$ are the exergy rate as a consequence of work and heat transfer, respectively. The exergy terms in the second equation can be expressed as given:

$$\dot{E}x_Q = Q\left(1 - \frac{T_0}{T}\right) \quad (3)$$

$$\dot{E}x_W = \dot{W} \quad (4)$$

Flow exergy at each point can be defined as follows:

$$\dot{E}x_f = \dot{E}x^{ph} + \dot{E}x^{ch} \quad (5)$$

where $\dot{E}x^{ph}$ and $\dot{E}x^{ch}$ symbolize specific physical exergy and chemical exergy, respectively.

$$\dot{E}x^{ph} = \dot{m}\left[(h - h_0) - T_o(s - s_0)\right] \quad (6)$$

The chemical exergy can be given as follows:

$$\dot{E}x^{ch} = \dot{m}\,(ex^{ch}) \quad (7)$$

IV. Results and discussions

As seen in Figure 2, the exergy loss occurred in the distiller and combustion chamber with 2399.78 kW and 2749.66 kW, respectively. This is because of the high irreversibility of the combustion process and distillers. On the other hand, owing to very high exergy efficiency of turbine the lowest exergy loss occured in this element with 24.84 kW. Exergy losses in the compressor, afterburner, waste heat boiler and chiller were 1602.21 kW, 1645.65 kW, 831.16 kW and 114.76 kW, respectively.

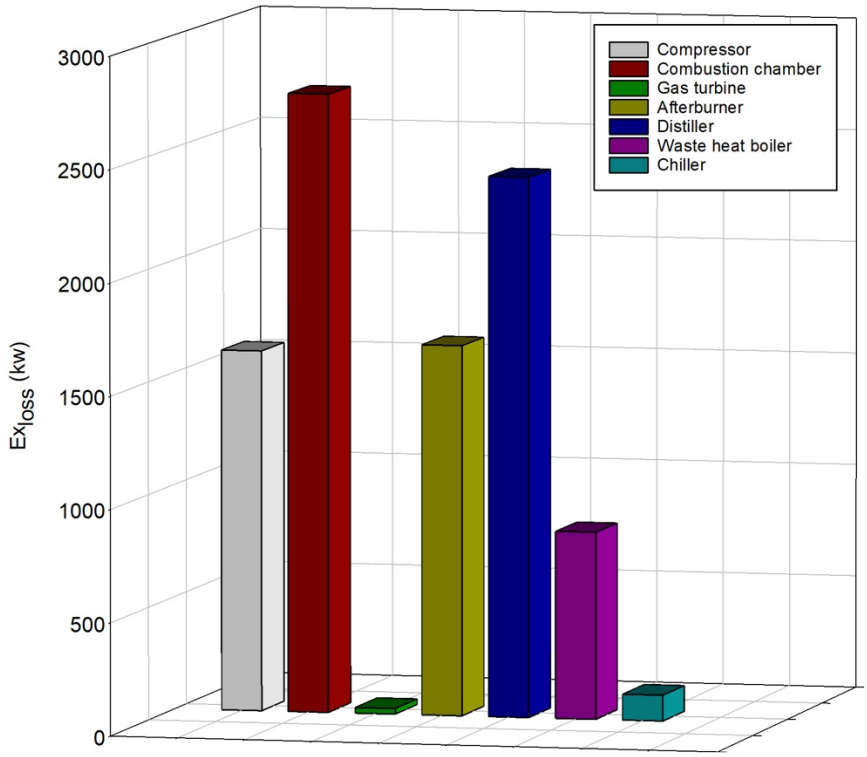

Fig. 2. Exegy loss of power generation system components

V. Conclusions

In the present study, energy and exergy analyzes of a multigeneration system developed for the research hospital were made in line with the thermodynamic principles and the exergy loss of each component was calculated.

As a result of this work;

- The thermodynamic performance parameters of the power generation system that can be installed for the research hospital have been revealed.
- A method has been put forward for future thermodynamic analysis studies.

In the continuation of this study, necessary thermodynamic analyzes will be carried out to minimize exergy losses in each component.

References

Ahmadi, P., Rosen, M. A., & Dincer, I. (2011). Greenhouse gas emission and exergo-environmental analyses of a trigeneration energy system. International Journal of Greenhouse Gas Control, 5(6), 1540-1549. https://doi.org/10.1016/j.ijggc.2011.08.011

Aydin, H., Turan, O., Midilli, A., & Karakoc, T. H. (2012). Exergetic and exergo–economic analysis of a turboprop engine: a case study for CT7–9C. International Journal of Exergy, 11(1), 69-88. https://doi.org/10.1504/ijex.2012.049089

Çoban, K., Şöhret, Y., Çolpan, C. Ö., & Karakoç, T. H. (2017). Küçük bir turbojet motorun farklı yakıt kullanımlarında ekserjetik ve eksergoekonomik performansının karşılaştırılması. *Sürdürülebilir Havacılık Araştırma Dergisi,* 2(2). https://doi.org/10.23890/SUHAD.2017.0202.

Dincer, I., & Rosen, M. A. (2005). Thermodynamic aspects of renewables and sustainable development. *Renewable and Sustainable Energy Reviews*, *9*(2), 169-189. https://doi.org/10.1016/j.rser.2004.02.002

Dincer, I., Midilli, A., & Kucuk, H. (Eds.). (2014). Progress in exergy, energy, and the environment. Springer. https://doi.org /10.1007/978-3-319-04681-5

Ghaebi, H., Amidpour, M., Karimkashi, S., & Rezayan, O. (2011). Energy, exergy and thermoeconomic analysis of a combined cooling, heating and power (CCHP) system with gas turbine prime mover. *International Journal of Energy Research*, *35*(8), 697-709. https://doi.org/10.1002/er.1721

Gopisetty, S., & Treffinger, P. (2013, May). Energy analysis of trigeneration based on scarce data. In *2013 10th International Conference on the European Energy Market (EEM)* (pp. 1-7). IEEE. https://doi.org/ 10.1109/EEM.2013.6607394

Inac, S., Unverdi, S. O., & Midilli, A. (2019). A parametric study on thermodynamic performance of a SOFC oriented hybrid energy system. International Journal of Hydrogen Energy, 44(20), 10043-10058. https://doi.org/ 10.1016/j.ijhydene.2019.01.247

Kaya, N., Turan, O., Midilli, A., & Karakoc, T. H. (2016). Exergetic sustainability assessment of a HALE UAV using dodecene fuel. *International Journal of Exergy*, *21*(1), 87-109. https://doi.org/10.1504/IJEX.2016.078514

Urban sprawl and its impact on the environment: case of the Greater El Jadida, (Morocco)

[1*] Ikram El Mjiri, [1] Abdelmejid Rahimi, [2] Abdelkrim Bouasria
[1] Laboratory of Geodynamics and Geomatics, Department of Geology, Faculty of Sciences, Chouaib Doukkali University, BP. 20, 24000, El Jadida, Morocco.
[2] Laboratory of Geosciences and Environmental Technology, Faculty of Sciences, Chouaib Doukkali University, BP. 20, 24000, El Jadida, Morocco.

* E-mails: elmjiri.ikrame@gmail.com

Abstract
This study conducted on the great El Jadida (between 8° and 10° West longitude and 33°.5' and 32°.5' North latitude) located on the Atlantic coast of Morocco, treats on the one hand the dynamics of urban sprawl and on the other hand, changes in surface temperature between 1985 and 2019. It is based on the diachronic analysis of a time series of satellite images (Landsat), supplemented by field checks. The aim of this work is to evaluate the spatio-temporal mutations of the surface temperature that this region is experiencing as a result of urban expansion and its impact on the environment. The data used are five satellite images including Landsat TM for the two scenes of 1985 and 1995, Landsat ETM for the scene of 2005 and Landsat OLI for the two scenes of 2016 and 2019. This methodology allowed the spatio-temporal comparison of the different tele-analytical maps of surface temperatures and urban and peri-urban extension between 1985 and 2019. Thus, over this period, the built-up areas of the great El Jadida, experienced an increase of 5121 ha, an increase rate of 247% in 35 years. During the same period the surface temperature underwent changes in the distribution of the different temperature intervals, marked essentially by an increase in the areas where the surface temperature is between 25 and 30°C and a decrease in those where the temperature is above 30°C. The juxtaposition of the two maps, that of the evolution of urban sprawl and that of changes in surface temperature, allows us to suggest the impact of urban sprawl on the spatial distribution of surface temperature.

Keywords: environment, the great El Jadida, Landsat images, urban sprawl, surface temperature.

I. Introduction

Soil artificialisation is a fundamental variable for regional planning as well as for the study and understanding of many fields related to the environment (Béchet et al., 2017). To control the spatio-temporal dynamics of certain environmental phenomena, it is necessary to carry out regular monitoring using satellite imagery (Abutaleb et al., 2015), which has become indispensable in most cartographic inventories and monitoring of these phenomena. It provides basic data for monitoring and mapping the spatiotemporal evolution of these phenomena over several decades by qualifying and quantifying the observed changes.

The great El Jadida, considered as the second industrial pole in Morocco after Casablanca, has known especially these last three decades an important urban extension. This urban sprawl, which is to the detriment of the forest environment and agricultural land, generates negative impacts by increasing pressure on the environment (Chéry et al., 2014). It is presumably to be at the root of environmental problems and climate change marked mainly by erratic rainfall and unprecedented periods of drought. In order to assess the impact of urban sprawl and changes in the spatial distribution of surface temperature in the city of El Jadida and its outskirts, it was necessary to carry out a diachronic study based on a time series of satellite images (Landsat) (Kafy et al., 2019).

II. Study area

The great El Jadida is a coastal area, which includes the city and its surroundings. It is located about 96 km from the economic capital Casablanca (Fig 1). The coordinate of this area falls between longitudes 8° and 10° West and latitudes 33°.5' and 32°.5' North, covering an area of approximately 356 Km^2. The dominant climate is semi-arid with mild temperate winters and a generally hot and dry summer with oceanic influences in the coastal areas. The rainy season with an estimated annual average of 317 mm decreases from the coast to the interior.

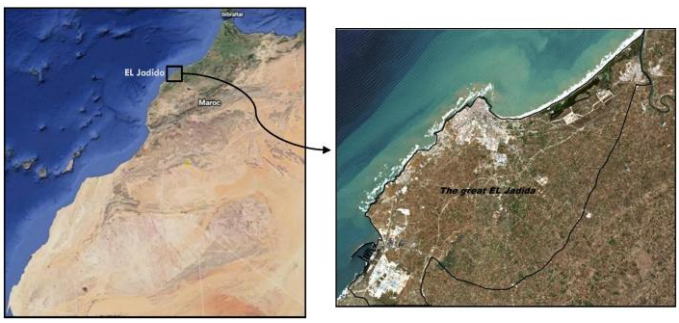

Fig. 1. Location of the study area

II.Data and Methodology

Data:

The dataset used in this work consists of five Landsat 5, 7 and 8 satellite images (sensors: TM for the two scenes of 1985 and 1995, ETM for the scene of 2005 and OLI for the two scenes of 2016 and 2019). These images were acquired almost at the same time of the year (between April and May) in order to reduce problems related to differences in sun angles, ecological changes in vegetation and differences in soil moisture.

Methodology:

The methodology adopted is based on a succession of pre-processing and treatments applied to satellite images in order to elaborate the maps necessary for the evaluation of the spatio-temporal evolution of large EL Jadida (Abd El-Kawy et al. 2019). Thus, these orthorectified satellite images were pre-processed (geometrically and radiometrically corrected, mapped and georeferenced) and cut out over the study area. In order to evaluate the impact of urban sprawl on the environment, several treatment methods have been tested, including classification supervised by the Support Vector Machine (SVM) algorithm (El Mjiri et al. 2020) and temperature extraction from large El Jadida surfaces between 1985 and 2019.

IV. Results and discussions

Urban sprawl using the SVM classification method:

The application of classification SVM (Maulik and Chakraborty.2017), whose overall relevance varies between 94% and 99%, on the various satellite images, has made it possible to produce derived images characterizing urban sprawl for each year (Fig 2). The presentation of these derived images facilitates the visual comparison and identification of areas of urban sprawl between 1985 and 2019. As a result, the maps prepared show that the total urban extension represents 2072 ha in 1985; 3114 ha in 1995; 4547 ha in 2005; 6498 ha in 2016 and 7193 ha in 2019 (Table 1).

Thus, it can be seen that between 1985 and 2019, built-up areas increased by 5121 ha, a growth rate of 247% in 35 years. In absolute terms, the largest increase is recorded between 2005 and 2016.

Table 1. Spatial and temporal evolution of the buildings in the large el jadida (1985-2019) by using svm.

	1985		1995		2005		2016		2019	
	(ha)	%	(ha)	%	(ha)	%	(ha)	%	(ha)	%
B	2072	5,82	3114	8,75	4547	12,8	6498	18,3	7193	20 ,2
KC	0,96		0.91		0,92		0.98		0.98	
OA	97		94%		93.86%		98.44%		99.16%	

B: Buildings, KC: Kappa Coefficient, OA: Overall Accuracy

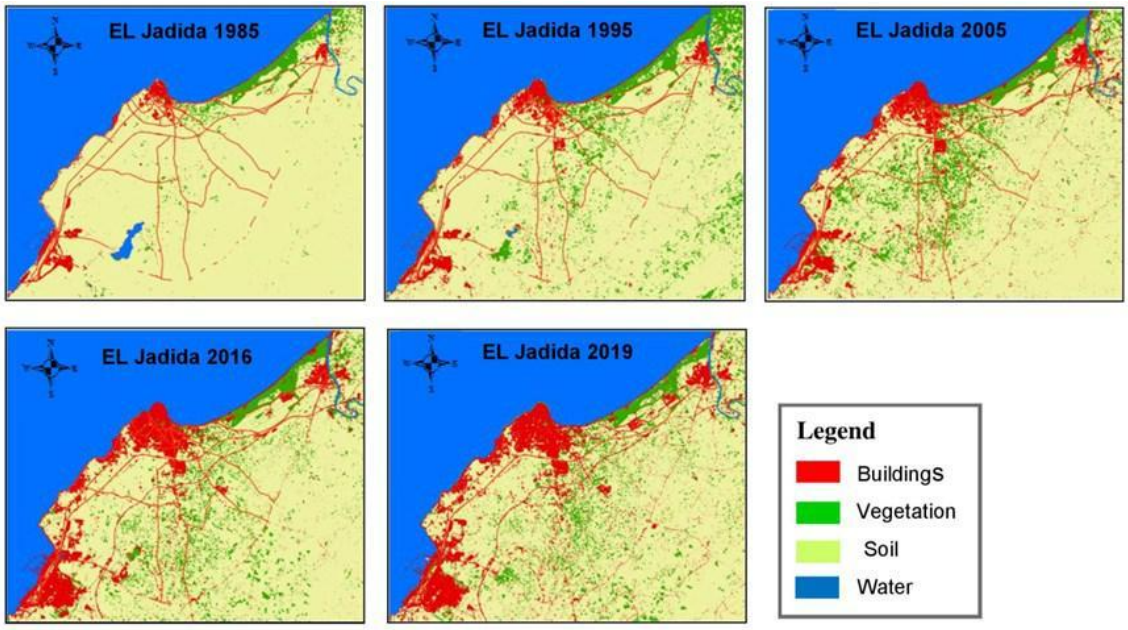

Fig. 2. Mapping of urban areas in the great EL Jadida based on SVM classification

Mapping of surface temperature:

The extraction of the surface temperature of the large EL Jadida, is based on the techniques of thermal remote sensing (TIR) (Avdan and Jovanovska, 2016). These techniques are the only possible approach to surface temperature extraction (Coll et al., 2005). Thus, the tele-analytical surface temperature maps obtained by the threshold values (Fig. 3), show the spatial distribution of the different temperature intervals, characterized by moderate temperatures along the Atlantic coast and becoming higher and higher towards the interior.

The confrontation between these different tele-analytical maps shows that each temperature interval evolves at its own pace in time and space. Therefore, the analysis, consisted in highlighting the substantial mutations in the spatial distribution of surface temperature that occurred between 1985 and 2019. These mutations result in a regression of the areas where the temperature is above 30°C and an increase of those where the surface temperature is between 25 and 30°C. These maps also show a disappearance between 2005 and 2016 of areas where the surface temperature is higher than 35°C and which will reappear in 2019 in the southeast of the region studied. These changes were relatively small between 1985 and 1995, but more marked between 1995 and 2019.

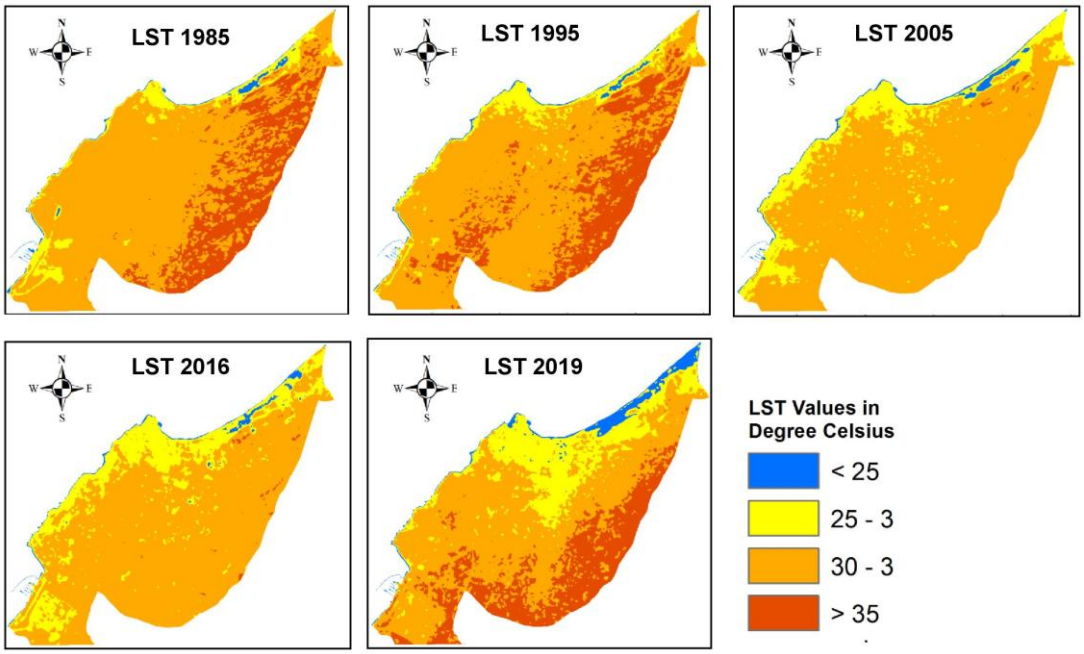

Fig. 3. Surface temperature variation in great El Jadida from 1985 to 2019.

The impact of urban sprawl on the environment:

The superposition of the two maps, that of the evolution of urban sprawl (Fig. 4) and that of the changes in surface temperature (Fig. 5), reflects the extent of the environmental changes experienced by this region between 1985 and 2019. Therefore, urban sprawl and all that accompanies it in terms of greenhouse gas emissions, the unbridled consumption of agricultural and natural land and the increased vulnerability of territories, causes disruptions to the ecosystem and damages biodiversity (Lai and Cheng, 2011).

This suggests the determining role of urban extension in the changes in the spatial distribution of surface temperature in the great El Jadida which is considered as the second industrial pole in Morocco after Casablanca.

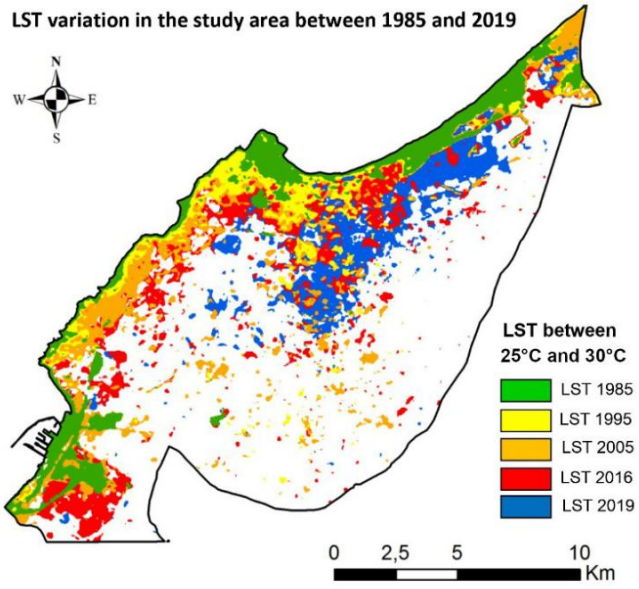

Fig. 4. LST variation between 1985 and 2019

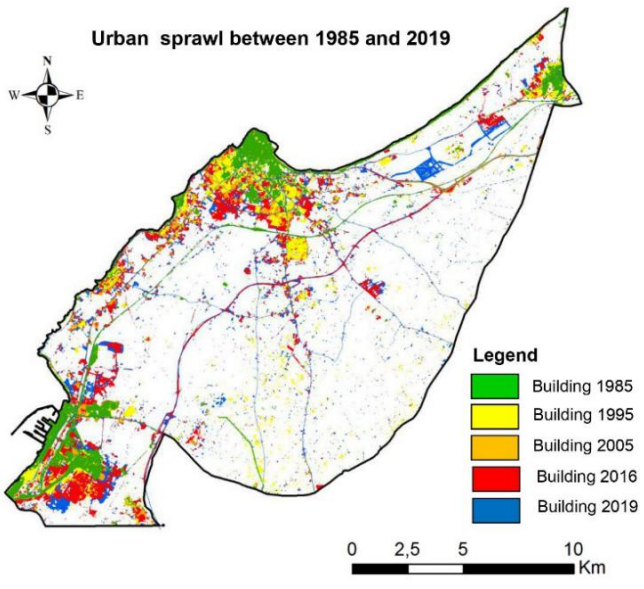

Fig. 5. Evolution of urbain sprawl between 1985 and 2019

V. Conclusions

This study shows that the great El Jadida is subject, between 1985 and 2019, to increasing anthropic pressures. The latter, which are essentially marked by a very accentuated urban sprawl, have contributed to the disturbance of the ecosystem. These perturbations are essentially marked by irregular pluviometry and unprecedented periods of drought.Thus, during this period (between 1985 and 2019), the built-up areas of the great El Jadida, increased by 5121 ha, a growth rate of 247% in 35 years. The mapping of the surface temperature between 1985 and 2019 in the greater El Jadida area has revealed some changes with an increase in areas where the surface is between 25 and 30°C and a regression of areas where the temperature is above 30°C. The analysis of the two maps, that of the evolution of urban extension and that of the changes in surface temperature, allows us to suggest the impact of urban extension on the spatial distribution of surface temperature.

References

Abd EL-kawy, O.R., Ismail, H.A., Yehia, H.M., Allam, M.A., 2019. Temporal detection and prediction of agricultural land consumption by urbanization using remote sensing. Egypt. J. Remote Sens. Sp. Sci. https://doi.org/10.1016/j.ejrs.2019.05.001

Abutaleb, K., Ngie, A., Darwish, A., Ahmed, M., Arafat, S., Ahmed, F., 2015. Assessment of Urban Heat Island Using Remotely Sensed Imagery over Greater Cairo, Egypt. Adv. Remote Sens. 04, 35–47. https://doi.org/10.4236/ars.2015.41004

Avdan, U., Jovanovska, G., 2016. Algorithm for Automated Mapping of Land Surface Temperature Using LANDSAT 8 Satellite Data. J. Sensors 2016, 1480307. https://doi.org/10.1155/2016/1480307

Béchet, B., Le Bissonnais, Y., Ruas, A., Aguilera, A., André, M., Andrieu, H., Ay, S., Baumont, C., Barbe, E., Vidal Beaudet, L., BELTON-CHEVALLIER, L., Berthier, E., Billet, P., Bonin, O., Cavailhes, J., Chancibault, K., Cohen, M., Coisnon, T., Colas, R., CORNU, S., Cortet, J.J., Dablanc, L., Darly, S., Delolme, C., Fack, G., Fromin, N., GADAL, S., Gauvreau, B., Geniaux, G., Gilli, F., Guelton, S., Guérois, M., Hedde, M., Houet, T., Humbertclaude, S., Jolivet, L., Keller, C., LeBerre, I., Madec, P., Mallet, C., Marty, P., Mering, C., Musy, M., Oueslati, W., Paty, S., Polèse, M., Pumain, D., Puissant, A., Riou, S., Rodriguez, F., Ruban, V., Salanié, J., Schwartz, C.C., Sotura, A., Thébert, M., Thévenin, T., Thisse, J., Vergnes, A., Christiane, W., Werey, C., Desrousseaux, M., 2017. Sols artificialisés et processus d'artificialisation des sols : déterminants, impacts et leviers d'action.

Philippe Chéry, Alexandre Lee, Loïc Commagnac, Anne-Laure Thomas-Chery, Stéphanie Jalabert et Marie-Françoise Slak, « Impact de l'artificialisation sur les ressources en sol et les milieux en France métropolitaine », Cybergeo : European Journal of Geography [En ligne], Aménagement, Urbanisme, document 668, mis en ligne le 28 février 2014, consulté le 30 novembre 2020. URL : http://journals.openedition.org/cybergeo/26224 ; DOI : https://doi.org/10.4000/cybergeo.26224

Coll, L., Messier, C., Delangrange, S. et Berninger, F. (2005) Belowground competition between hybrid poplar and the herbaceous vegetation in plantation established on previously logged forest sites in southern Quebec, en soumission.

El Mjiri I., Rahimi A., Bouasria A., 2020. Urban sprawl evolution and soil artificialization assessment by using satellite data from 1985 to 2019: case of El Jadida metropolitan in Morocco, 2020 Second International Sustainability and Resilience Conference: Technology and Innovation in Building Designs, November 11-12 2020, University of Bahrain.

Kafy, A.-A., Islam, M., Khan, A.R., Ferdous, L., Hossain, M.M., 2019. Identifying Most Influential Land Use Parameters Contributing Reduction of Surface Water Bodies in Rajshahi City, Bangladesh: A Remote Sensing Approach. Remote Sens. L. 2, 87–95. https://doi.org/10.21523/gcj1.18020202

Lai, W.-T., Chen, C.-F., 2011. Behavioral intentions of public transit passengers—The roles of service quality, perceived value, satisfaction and involvement. Transp. Policy 18, 318–325. https://doi.org/https://doi.org/10.1016/j.tranpol.2010.09.003

Maulik, U., Chakraborty, D., 2017. Remote Sensing Image Classification: A survey of support-vector-machine-based advanced techniques. IEEE Geosci. Remote Sens. Mag. 5, 33–52. https://doi.org/10.1109/MGRS.2016.2641240

Thermodynamic Analysis of an Automobile's Air Conditioning System Assisted by Exhaust Gas and Solar Energy

[1]Santi Sarkar, [1*]Goutam Khankari, [3]Sujit Karmakar
[1] Department of Simulator Training Centre, Mejia Thermal Power Station, DVC, Bankura, West Bengal-722183, India
[2] Department of Mechanical Engineering, National Institute of Technology, Durgapur, India

* E-mail: goutam_khankari@yahoo.co.in

Abstract
Most of new automobile engines used all over the world, converts nearly 30 % of developed power into useful work. The rest is found as losses and major losses found in the cooling and exhaust system. A novel automobile's air conditioning (AAC) system assisted by engine exhaust and solar energy is proposed in the present research study. The system is modeled in Cycle-Tempo modelling software and R22 and ammonia rich NH_3-H_2O binary mixture are used as a working fluid for the existing and proposed automobile's AC system, respectively. Result shows that the proposed system can produce about 1.64 kW of electric power which will help in reducing the total power requirement of AC system after maintaining constant cooling effect of about 10.5 kW. As a result, the COP of an Automobile's AC system is increased from 2.453 to 2.793. The net combined energy and exergy efficiencies of the proposed system are about 4.30 % and 15 %, respectively. The energy and exergy efficiencies of the system are increased with increase in pressure. About 25 bar is the optimum value of operating pressure as per given boundary conditions of the present study. Exergy analysis of the system discloses the different locations of exergy destruction in the system. By this novel system, the fuel saving of the automobile can be done by about 2.17 kg/day and CO_2 emission can be avoided by about 6.78 kg /day. Economic analysis is also carried out for techno-commercial feasibility.

Keywords: Air conditioning system, COP, Energy, Exergy, Environment, Economic, Engine exhaust, Solar energy

I. Introduction

Higher atmospheric temperature enhances the use of air conditioning system in the passenger vehicles. It enhances the energy consumption of the vehicles and also increases the environmental hazarads. Different thermodynamic refrigeration cycles are being used in vehicles to get thermal comfort and out of them; vapour compression refrigeration system is one of the best suited efficient technologies. Designing an energy efficient Automobiles Air Conditioning (AAC) system is a great challegenge to the energy professionals through out the world. Various research works related to AAC have been carried out by different researchers during last few decades [Alkan and Hosoz, 2010; Buonocore et al.,2020]. Yang et al., 2020 studied the defogging and dewing process of a truck and found the maximum human comfort and maximum efficiency of the system at the humidity range of about 20-60 % and temperature range of about 292 -298 K. Yu et al.,2019 proposed the CO_2/R41 mixture for automobiles AC and heat pump systems and concluded that the improvement inenergy efficiency of the heating and cooling mode was about 14.5 % and 25.7 %, respectively. The flameability study of CO_2/R41mixture was also carried by the researcher for safety point of view. Venkataraman et al.,2020 have carried out a rigorous review on the Vapour Absorption Refrigeration System (VARS) for automobiles application by considering engine exhaust and fuel cell exhaust as a separate heat source. They found that the use of engine exhaust in the VARS is a challenging job and suggested to use the fuel cell coupled VARS system in automobiles. Muztuza Ali and Chakraborty,2015 proposed an adsorption cooling system for cars driven by engine exhaust and results found that an engine exhaust of 3000cc car can produce cooling effect of 3 kW and the performance of CaCl -in-silica gel–water system was more than the other adsorbents-water systems. A compound cycle system was proposed by Zhang et al.,2018 for automobiles waste heat recovery and air conditioning system and their analysis results showed that the maximum power output of about 13.01 kW can be achieved by the independent system with R245fa-R134a working fluid and the smallest heat transfer area found in the compound system with R1234yf working fluid. Buonocore et al., 2020 assessed the thermal comfort of air-conditioned and naturally ventilated university class room under hot and humid condition and they found that in the natural ventilation, about 80% thermal comfort could be achieved at temperature set of 25 ^{0}C and about 23-25 ^{0}C for the air-conditioned system.

There is derth of literature for the combined use of engine's exhaust and solar energy for assisting to run the automobiles air conditioning system as the engine's exhaust carries about 25-30 % of total supplied heat at a temperature of about 300-400 ^{0}C and the availability of solar energy in India is large during day time hours.
The present study proposes a novel automobile's air conditioning (AC) system assisted by high grade engine's exhaust gas and solar energy. The key novelty of the work is solar energy integration and working fluid of existing system i.e. R22 is replaced by the ammonia rich binary mixture for getting more TG power output. The existing and proposed systems are thermodynamically modeled by using of Cycle-Tempo computer modelling softwatre [Cycle-Tempo, 2007] at different operating conditions. Performance studies of the systems are carried out based on Energy, Exergy, Environment and Economic (4E) analyses.

II. Proposed System

Figure 1(a) describes the flow diagram of a existing automobile's AC system and Figure1(b) shows the proposed automobile's AC system assisted by engine's exhaust and solar energy. The main components of the proposed air conditioning system are compressor, heat exchanger, flat Plate solar collector, turbine, condenser, expansion valve and evaporator. Cooling fan is used for condensing the working fluid in the condenser and circulating fan is used for cold air circulation inside the passenger area of the vehicles. Ammonia rich NH_3-H_2O mixture is used as working fluid for the proposed system.

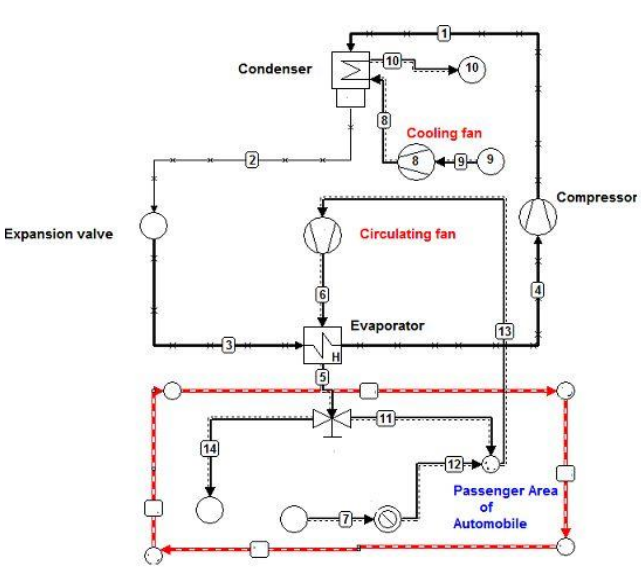

Fig.1(a)

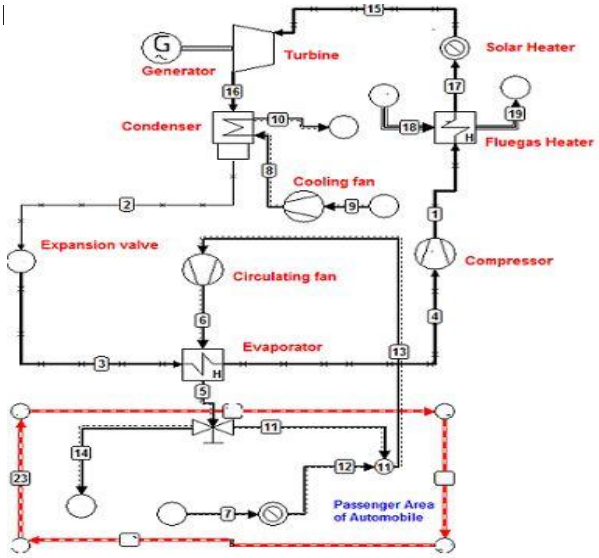

Fig.1(b)

Fig. 1. (a) Simplified diagram of existing automobile's AC system; (b) Proposed automobile's AC system assisted by engine's exhaust and solar energy.

III. Analysis Methodology

The proposed configuration is modeled in Cycle-Tempo Modelling Software [Cycle-Tempo, 2007]. Following assumptions are made for modeling the proposed system.

Assumptions

i. Ambient Pressure (P_o) is considered as 1.013 bar and Temperature (T_o) of environment is 298K.
ii. Mass and temperature of engine exhaust are 0.25 kg/s and 420^{0}C, respectively.
iii. Average speed of vehicle: 120KM/h; Fuel consumption (with AC of 10.5 kW): 2.5KM/litre.
iv. Operating pressure of existing AC system is considered as 15 bar.
v. R22 and ammonia rich NH_3-H_2O (95% NH_3) are used working fluid for existing and proposed AC system, respectively.

The simulation model of the components is done on the basis of conservation of mass and energy principles.

Performance parameters:

Conmbined net energy efficiency (η): $\frac{W_T+W_{cooling\ effect}-Auxiliary\ power}{Q_{HX}+Q_{Solar}}$ (1)

Conmbined net exergy efficiency (Ψ): $\frac{W_T+W_{cooling\ effect}-Auxiliary\ power}{Ex_{HX}+Ex_{Solar}}$ (2)

Auxiliary Power: $W_{Compressor} + W_{cooling\ fan} + W_{circulating\ fan}$ (3)

Coefficient of Performance of the system is given below;

$$C.O.P = \frac{W_{cooling\ effect}}{W_{COMP}-W_T} \quad (4)$$

IV. Results and discussions

A. Thermodynamic performance analysis of automobiles's AC system

Performance study of the existing and proposed AC system of automobiles is carried out based on simulated operating data. The operating parameters of the both systems are given in Table 1 and the performance report is given Table 2 and Fig.2. From Table 2, it is found that the cooling effect produced by the both systems are fixed at 10.5 kW and from the proposed system, additional 1.64 kW power may be produced from engine's exhaust gasses and solar energy. The novelty of the work is to use the waste high grade exhaust gas and solar energy as a supplementary energy source for producing the electricity which in turn is used for supplying the some portion of the compressor's consumed power. As a result, the COP of the Automobile's AC system is improved from 2.453 to 2.793. Thereby, it reduces the total fuel consumption of the vehicles and also environmental pollutants.

Table 1. Operating data of the both air conditioning systems

	Proposed Air Conditioning system			Existing Air Conditioning System		
Pipe no.	Pressure [bar]	Temperature [°C]	Mass flow [kg/s]	Pressure [bar]	Temperature [°C]	Mass flow [kg/s]
1	25	85.16	0.013	15	73.81	0.071
2	13	35.45	0.013	15	39.04	0.071
3	6.28	12.15	0.013	6.28	6.69	0.071
4	6.28	21.87	0.013	6.28	21.87	0.071
5	1.02	20	1.414	1.02	20	1.414
6	1.02	24.87	1.414	1.02	24.87	1.414
7	1.013	20	1.4	1.013	20	1.4
8	1.02	30.67	2.203	1.02	30.67	1.501
9	1.013	30	2.203	1.013	30	1.501
10	1.02	39.67	2.203	1.02	39.67	1.501
11	1.02	20	0.014	1.02	20	0.014
12	1.013	24.26	1.4	1.013	24.26	1.4
13	1.013	24.18	1.414	1.013	24.18	1.414
14	1.02	20	1.4	1.02	20	1.4
15	25	233.66	0.013	-	-	-
16	13	175.4	0.013	-	-	-
17	25	114.86	0.013	-	-	-
18	1.125	450	0.25	-	-	-
19	1.125	440	0.25	-	-	-

But, the compressor power of the proposed system is higher than the existing system due to higher operating pressure and the same is shown in Table 2. However, COP of the proposed system (about 2.793) is higher than the existing system (2.453).

Table 2. Performance report of the both automobiles AC systems

		Existing AC System	Proposed AC System
Components	**Unit**	**Value**	**Value**
Turbo-Generator(TG)	kW	-	1.64
Compressor	kW	2.05	2.63
Circulating fan	kW	1.06	1.06
Cooling water fan	kW	1.17	1.72
Cooling Effect	kW	10.5	10.5

B. Effect of operating parameters on the system performance

Effect of variation in operating pressures on the system performance is studied by fixing constant refrigeration effect of the vehicles and the result is shown in Fig.2. From Fig.2, it is cleared that the system both energy and exergy efficiencies are increased with increase in operating pressure and it is also observed that the increasing slope of efficiencies are decreased after the operating pressure of 24 bar. It is found that at higher pressure, losses in condenser and fluegas exit are less which causes more energetic performance of the system. It is also found in Table 3 that the exergy destruction in fluegas heater and solar heater are higher at lower operating pressure.

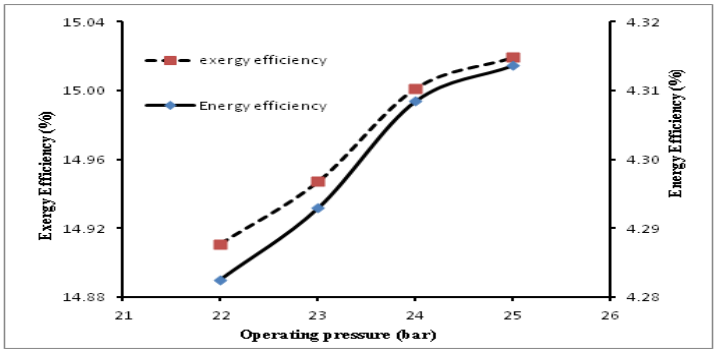

Fig. 2. Pressure vs. Efficiencies of the proposed system

.

Table 3. Exergy balance of the proposed system at different pressures

Pressure (bar)	power and Cooling effect (%)	Condenser loss (%)	FG exit loss (%)	Solar exergy loss (%)	FG heater loss(%)	Throttling loss (%)	Other losses (%)
22	1.169	2.917	73.885	7.434	2.211	0.132	12.252
23	1.367	2.913	73.885	7.392	2.184	0.132	12.127
24	1.566	2.909	73.885	7.352	2.157	0.132	11.999
25	1.747	2.905	73.884	7.313	2.132	0.132	11.885

C. Environmental impact of the proposed system

It is observed that at higher operating pressure, the fuel saving is more due to higher system performance. As a result, amount of CO_2 reduction is more at elevated pressure. The proposed system increases the fuel saving by about 2.17 kg/day and reduces the CO2 reduction by about 6.78 kg/day at 25 bar operating pressure and by considering vehicle operating hours of about 12 hrs.

D. Economic analysis

Techno-commercial feasibility of the Automobile's AC system assisted by engine exhaust and solar energy is carried out by considering vehicle life of 10 years and vehicle running time of 12 hours per day. It is found that the total investment cost of the proposed AAC is about Rs. 8, 51,651.50 at 25 bar operating pressure and about 10.5 kW cooling capacity of the AC system. The further study is also required for optimization of the cost as per market value. From Table 4, it is also concluded that the cost of electricity production and SPP of the additional power generating system is about Rs. 5.691 per kWh and 6.37 years, respectively.

Table 4. Economic analysis of the proposed power generation system(without ac)

Cost analysis of Proposed Power Generation System only Driven by Engine Exhaust and Solar Energy	
Annual O&M cost@1% of total cost i.r.o additional components for power generation (Rs.)	3036.51
Anuual depriciation cost @10% of total cost i.r.o additional components for power generation (Rs.)	30365.10
Interest charge on 70 % loan of total cost i.r.o additional components for power generation @14% (Rs.)	9471.80
Annual fixed cost for power generation only (Rs.)	42873.41
Annual total cost for additional components of power generation (Rs.)	346524.41
Annual fuel saving due to powergeneration (Litre)	635.75
Power generation cost (Rs./kWhr)	5.691
Annual fuel saving cost due to additional power generation (Rs.)	47681.01
Payback Period for the additional power generation system (years)	6.37
ROI (considering 10 years life)	0.57
Rate of Return (%)	13.76

V. Conclusions

Following are the major conclusions that could be drawn from the present research:

- The proposed system can produce additional 1.64 kW of electric power with design cooling effect of 10.5 kW. Thereby, the COP of the Automobile's AC system is improved from 2.453 to 2.793 which in turn reduce the total fuel demand of the vehicles.
- The net combined energy efficiency of the proposed system is about 4.30 % and the net combined exergy efficiency of the system is found about 15 %.
- The energy and exergy efficiencies of the proposed system are increased with increase in pressure and thereby it improves the COP of AC system. Energy and exergy balances of the system disclose the different location for energy losses and exergy destruction.
- The proposed system decreases the fuel saving by about 2.17 kg/day. It will reduce the different air pollutants and out of them, the CO_2 reduction is about 6.78 kg/day by considering the vehicle operating hours of about 12 hrs. This data is for a single passenger vehicle. The amount of reduction of pollutants and fuel consumption will be more in globally.
- The total capital cost of the proposed system is about Rs. 8, 51,651.50 at the pressure of 25 bar. The power generation cost and payback period of the power generation system (without chilling effect) are about Rs. 5.691 per kWh and 6.37 years, respectively.

References

Alkan A, Hosoz M.,2010. Comparative performance of an automotive air conditioning system using fixed and variable capacity compressors. International Journal of Refrigeration ,33, 487-495.

Buonocore C.,De Vecchi R., Scalco V. , Lamberts R.,2020. Thermal preference and comfort assessment in airconditioned and naturally-ventilated university classrooms under hot and humid conditions in Brazil, J. of Energy and Buildings, 211, 2020,. https://doi.org/10.1016/j.enbuild.2020.109783

Cycle-Tempo release 5.0, 2007, Delft University of Technology.

Khankari G., Karmakar S.,2018. Power generation from fluegas waste heat in a 500MW subcritical coal-fired thermal power plant using solar assisted KCS11. J. of Applied Thermal Engineering, 138, 235-245.

Khankari G., Karmakar S.,2020. A novel solar assisted Kalina Cycle System for waste heat utilization in thermal power plants, Int. Journal of Energy Research (Wiley Publication), pp. 1-13, DOI: 10.1002/er.5326.

Muztuza Ali S., Chakraborty A.,2015. Thermodynamic modelling and performance study of an engine waste heat driven adsorption cooling for automotive air-conditioning, Journal of Applied Thermal Engineering, 90, 54-63.

Supirattanakul P., Rittidech S., Bubphachot B.,2011. Application of a closed-loop oscillating heat pipe with check valves (CLOHP/CV) on performance enhancement in air conditioning system, Energy Build. 43, 1531–1535.

Venkataraman V., El-Kharouf A., Pandya B., Amakiri E., Steinberger-Wilckens R.,2020. Coupling of engine exhaust and fuel cell exhaust with vapour absorption refrigeration/air conditioning systems for transport applications: A review", J. of Thermal Science and Engineering Progress, 18. https://doi.org/10.1016/j.tsep.2020.100550.

Yua B., Yanga J., Wanga D., Shia J., Guoc Z., Chena J.,2019. Experimental energetic analysis of CO2/R41 blends in automobile airconditioning and heat pump systems , J. of Applied Energy, 239, 1142–1153.

Yang Y., Huang Y. , Zhao J.,2020. Optimization of the automotive air conditioning strategy based on the study of dewing phenomenon and defogging progress, Journal of Applied Thermal Engineering, 169, https://doi.org/10.1016/j.applthermaleng.2020.114932

Zhang Y., Han Y., Yan J., Chen R.,2018. Thermodynamic analysis of compound cycle system for automotive waste heat recovery and air conditioning refrigeration, J. of Energy Conversion and Management, 168, 32-48.

Using Bat Algorithms for Techno-Economic Analysis of a Grid-Connected PV System and Comparison with PSO and WOA Methods

[1]Muhammet Tahir Guneser, [1*]Abdurazaq Elbaz
[1] Karabuk University, Engineering Faculty, Eletrical and Electronics Department, Karabuk, 78100, Turkiye

abdalrazaklabz@gmail.com

Abstract
In this study, we propose an updated methodology based on an improved algorithm for the optimizing and sizing of a grid-connected PV system. We aim to minimize total net present cost using a novel optimization algorithm, the improved bat algorithm (IBAT), based on teaching and learning processes. To manage this optimization, several methods such as particle swarm optimization (PSO), the whale optimization algorithm (WOA), and cuckoo search (CS) are widely used. However, new approaches are needed to increase the efficiency. Optimized grid-connected PV systems can reduce production expenses, even in countries with large supplies of fossil fuel. The net present cost (NPC) and the cost of energy (COE) of the grid-connected PV system are $19595 and 0.134 $/kWh more efficient, respectively. To validate the proposed method and to ascertain the speed and accuracy of the IBAT, NPC and COE were measured and compared with the results of other common optimization algorithms, namely PSO, WOA, and CS. A policy for energy efficiency was then illustrated. The loss of power supply probability (LPSP) was evaluated to confirm operating stability. Since the IBAT is easy to build and requires fewer control parameters, it was deemed more feasible. The modeled system was tested on a grid-connected PV system installed at the Centre for Solar Energy Research and Studies (CSERS) in Tripoli, Libya. Annual data of irradiance, load profile, and temperature of the PV system were obtained and used for comparing the IBAT performance results and others. Obtained results proved that the proposed IBAT provides better optimal configuration than the commonly used algorithms. The LPSP value of the IBAT is 0.0965 compared with WOA, PSO, and CS values of 0.415, 0.625, and 0.845, respectively.

Keywords: Techno-economic analysis, PV Power System, IBAT Algorithm, PSO, WOA, CS

I. Introduction

The continuously increasing demands for electric energy, the significant rise of oil prices, and the shrinking of fossil fuel reserves, combined with the environmental pollution caused by conventional thermal electric energy-generating units, have led to worldwide concern about the development of alternative electric energy production methods. Aiming towards the achievement of this goal, grid-connected photovoltaic (GCPV) systems are widely used in order to inject the energy produced by photovoltaic (PV) modules into the electric grid (Swider et al., 2008) (Deb et al., 2007) .

Artificial intelligence techniques are becoming more common as alternative approaches to conventional methods. They can learn from instances, solve non-linear problems, and perform predictions very quickly. The particle swarm optimization (PSO) technique (Sawle et al., 2018), genetic algorithms, harmony search algorithm (Paulitschke, 2017), ant colony algorithms (Shiva and Mukherjee, 2015), cuckoo search (CS) (Nadjemi et al., 2017), artificial bee colony algorithm (Das et al., 2018), hybrid algorithms (Lasheen and Abdel-salam, 2018), and multi-objective optimization (Huang et al., 2019) are some of the most powerful optimization algorithms used in different studies and different systems. Because of the use of complex systems in such research, the initial cost of components is very high and, therefore, in some countries the use of the grid's electricity is significantly more cost-effective than such complex systems.

Considering that one of the most widely used renewable resources available at all locations is solar energy, and especially via PV panels, a PV system was selected as a power source in this study. Another reason to use this system is the suitability of solar radiation in Libya. All the meteorological data are real data that were collected from the Centre for Solar Energy Research and Studies (CSERS) in Tripoli, Libya, and the hourly loads were also collected as actual registered loads over the same period from the CSERS. Since this study is based on real data, it could be used for an actual feasibility study for implementation of the proposed system. In summary, this paper makes contributions to the literature in terms of analyzing the performance of a grid-connected PV system based on the concepts of loss of power supply probability (LPSP), net present cost (NPC),and cost of energy (COE). The ptimum system size and performance analysis of a grid-connected PV system has been determined using the improved bat algorithm (IBAT). Comparison of this algorithm with the whale optimization algorithm (WOA), CS, and PSO shows its superiority in solving optimization problems.

The rest of the paper is organized as follows: In Section II, the mathematical modeling of the grid-connected hybrid generation system is presented. In Section III, the study area's meteorological data and load profile are provided. In Section IV, the proposed optimization problem is introduced. In Section V, the simulation results of the proposed MATLAB program are discussed, and the final section concludes the work.

II. Mathematical Modeling of Grid-Connected Hybrid Generation System

The proposed grid-connected PV system consists of different components such as solar PV panels, a power inverter, a generator, and a utility grid, as shown in Fig. 1.

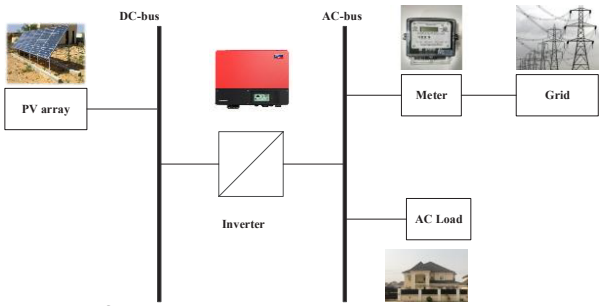

Fig. 1. Schematic diagram of the proposed hybrid grid-connected PV-biomass energy system.

III. Meteorological Data and Load Profile

In this study, we selected the location of the CSERS in Tripoli, which is located on the Libyan coast of the Mediterranean Sea (latitude: 32°48.9′ N, longitude: 13°26.3′ E; altitude: approximately 6 m above sea level). Real solar radiation and air temperature data for the location were obtained from the Climatic Database of the CSERS for 2019 (CSERS, n.d.). Global solar insolation ranged between 1.9 kWh/m^2 and 8.2 kWh/m^2. Minimum temperature was 3 °C and maximum was 45 °C. All data were collected at 5-minute intervals. In Fig. 2, the hourly load pattern is provided. With an average load of 17 kW, the actual load is around 34 kW.

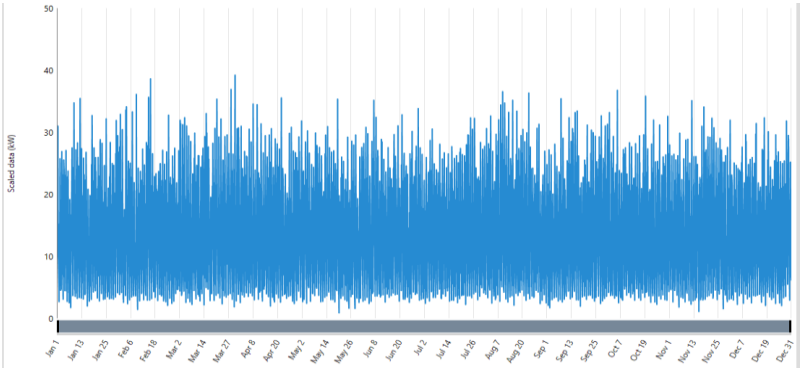

Fig. 2. Hourly load power profile for 2019.

IV. The Proposed Optimization Method

The proposed goal function, the plan for energy conservation, and the proposed steps adopted in this approach are explained in this section. The GCPV optimization algorithm's proposed method is summarized in Fig. 3. Among the most relevant design parameters of GCPV power plants are the seven decision variables shown here.

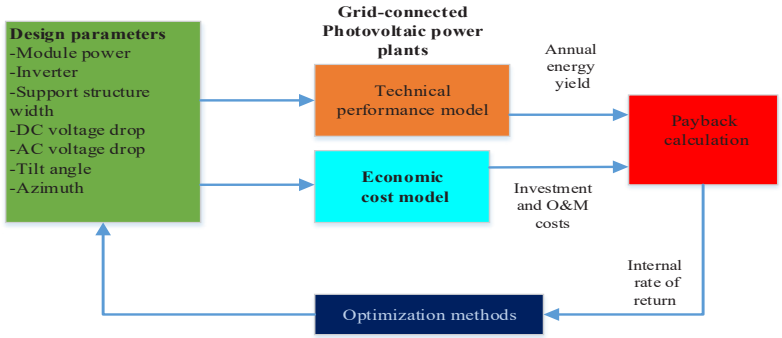

Fig. 3. Design optimization process of grid-connected photovoltaic power plants.

Parameters and Constraints for Optimization: -

1. Net present value (NPV)

This method has to do with approximating the net cash flows that can occur in the future, discounting said flows with a discount rate and using the risk level ''of the project and then subtracting the net initial investment from the present value of the net cash flows as shown in Eq. (1) (Gómez et al., 2010).

$$NPV = \left(Cash_{in} * \frac{1-(1+IRR)^{-n}}{IRR}\right) - (C_{in} + C_{gp}) \quad (1)$$

Here, IRR is the internal rate of return, projected to be 10% in this analysis, while n is the predicted number of years that this method is run, estimated to be 25 years. $Cash_{in}$ is the cash inflow, which can be measured as follows:

$$Cash_{in} = Kwh_{price} * Load \quad (2)$$

2. Cost of energy (COE)

This can be measured by the following formula:

$$COE = \frac{(Total\ cost\ of\ generated\ energy\ for\ one\ year)}{(Total\ energy\ supplied\ in\ one\ year\ Kwh)} \quad (3)$$

3. Loss of Power Supply Probability (LPSP)

In this model, LPSP is used to test the system's reliability. LPSP can be described as the load demand that the system is unable to satisfy in the study period divided by the total load. It is given by:

$$LPSP = \frac{\Sigma(P_{load} - P_{PV} - P_{GO})}{P_{load}} \quad (4)$$

The LPSP value is in the range of [0, 1] and it confirms the efficiency of the system until the total provided power from the integrated solar PV system-connected grid covers the load. LPSP values of 0 mean that the load is completely met at all times and a value of 1 indicates that the load is totally unmet. The permissible LPSP value is usually believed to be 0.05% or 5%. In order to minimize the COE with a stable method, the variable to be considered is NPV. The restrictions suggested are as follows:

$$N_{PVmin} \leq N_{PV} \leq N_{PVmax} \quad (5)$$

Here, N_{PVmin} and N_{PVmax} are the minimum and maximum number of PV panels (Fathy, 2016) (Xu et al., 2013).

V. Results and Discussion

The proposed algorithm has been applied to investigate an electrical autonomous grid-connected PV system located at the CSERS in Tripoli, Libya, with data obtained from the CSERS. The MATLAB environment was used to implement and code the proposed algorithm using an Intel Core i7-7500U CPU @ 2.9 GHz. For comparison of results, three other strong well-known algorithms have been run to assess the strength of the IBAT and the validity of our results. The IBAT results are compared with the outcomes of the WOA, PSO, and CS algorithms.

A population of particles travels in the search space of the optimization problem in the WOA, PSO, and CS approaches. The location of a particle represents a possible solution to the problem of optimization. Each particle scans the search space for better locations. In this study, a terminal criterion is a specific number of iterations. Each system size is equivalent to a final price and two objective functions are minimizing NPC and COE. The search space of all algorithms is the same and the variable is component size. Table 1 outlines the parameters of the algorithms and the statistical results for the different criteria. The minimum, maximum, and mean values of NPC and COE are respectively illustrated in this table. As shown, the IBAT algorithm has the best results in terms of the min, mean, and max values for the three objective functions.

Table1. Technical parameters and statistical results of CS, PSO, WOA, and IBAT.

Algorithm	NPC ($)			COE $/kWh			LPSP
	max	mean	min	min	mean	max	
IBAT	19760	19604.8	19595	0.134	0.136	0.14	0.0965
WOA	19761	19611	19600	0.151	0.153	0.158	0.415
PSO	19768	19617	19607	0.159	0.161	0.168	0.625
CS	19778	19620	19612	0.165	0.167	0.172	0.845

The NPC and COE trends in reaching the optimal solution are depicted in Figs. 4(a) and 4(b). As illustrated in these figures, the IBAT algorithm reaches the final answer faster than WOA, PSO, and CS; this shows IBAT's advantage in convergence speed. As the algorithm progresses, new answers are found, and the values of NPC and COE are decreased. IBAT's progress is depicted with a black line and this algorithm shows the fastest tendency towards the minimum solution. Similarly, to its performance for NPC, IBAT has the best convergence speed for the COE criterion. Along with its ease of implementation, these advantages make IBAT one of the most powerful algorithms.

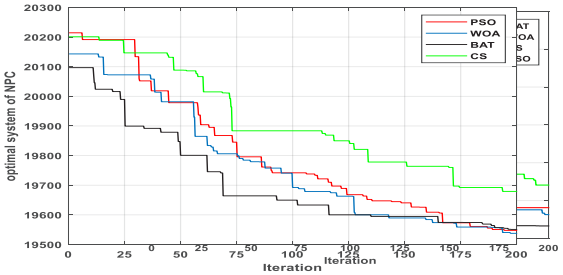

Fig. 4. (a) Comparison of algorithms' convergence speeds for min COE ($/kWh). (b) Comparison of algorithms' convergence speeds for min NPC ($).

VI. Conclusions

In this paper, a grid-connected PV system has been considered as a power generation system to contribute electricity for public places during business hours. Since PV systems with batteries are very expensive in comparison with PV systems without batteries, the most reasonable use of PV system equipment involves grid-connected PV system installation with the electricity demand met just for the daytime period. For optimum techno-economic analysis of the method, the IBAT algorithm was used and the final objective function was to minimize NPC and COE. A comparison of IBAT with WOA, CS, and PSO demonstrated IBAT's superiority in solving optimization problems. The optimally sized system for the CSERS had average PV system consumption of 26% and the electrical grid supplied the rest of the electrical load. In contrast to the three other algorithms, the NPC and COE obtained with IBAT had 12.7% and 13.4% increases, respectively.

The designed grid-connected PV system is installed at the CSERS in Tripoli, Libya. Annual real electrical and climatic data recorded by the CSERS were collected. The results obtained by IBAT have been compared to those of the WOA, PSO, and CS approaches. The proposed IBAT gives the optimal architecture of the grid-connected PV system with COE of 0.1349 $/kWh and LPSP of 0.0965. The IBAT approach consumes elapsed time of 497.326 seconds, which is the best performance among the presented approaches.

References

CSERS, n.d. Centre for Solar Energy Research and Studies. https://doi.org/Centre for Solar Energy Research and Studies.

Das, C.K., Bass, O., Kothapalli, G., Mahmoud, T.S., Habibi, D., 2018. Optimal placement of distributed energy storage systems in distribution networks using artificial bee colony algorithm. Appl. Energy 232, 212–228. https://doi.org/10.1016/j.apenergy.2018.07.100

Deb, J., Yohanis, Y.G., Norton, B., 2007. The impact of array inclination and orientation on the performance of a grid-connected photovoltaic system 32, 118–140. https://doi.org/10.1016/j.renene.2006.05.006

Drury, E., Denholm, P., Margolis, R., Drury, E., Denholm, P., Margolis, R., 2011. The Impact of Different Economic Performance Metrics on the Perceived Value of Solar Photovoltaics The Impact of Different Economic Performance Metrics on the Perceived Value of Solar Photovoltaics.

Fathy, A., 2016. A reliable methodology based on mine blast optimization algorithm for optimal sizing of hybrid PV-wind-FC system for remote area in Egypt. Renew. Energy 95, 367–380. https://doi.org/10.1016/j.renene.2016.04.030

Gómez, M., López, A., Jurado, F., 2010. Optimal placement and sizing from standpoint of the investor of Photovoltaics Grid-Connected Systems using Binary Particle Swarm Optimization. Appl. Energy 87, 1911–1918. https://doi.org/10.1016/j.apenergy.2009.12.021

Huang, Z., Xie, Z., Zhang, C., Hwa, S., Xie, Y., 2019. Modeling and multi-objective optimization of a stand-alone PV-hydrogen-retired EV battery hybrid energy system 181, 80–92. https://doi.org/10.1016/j.enconman.2018.11.079

Lasheen, M., Abdel-salam, M., 2018. Maximum power point tracking using Hill Climbing and ANFIS techniques for PV applications: A review and a novel hybrid approach. Energy Convers. Manag. 171, 1002–1019. https://doi.org/10.1016/j.enconman.2018.06.003

Nadjemi, O., Nacer, T., Hamidat, A., Salhi, H., 2017. Optimal hybrid PV / wind energy system sizing : Application of cuckoo search algorithm for Algerian dairy farms. Renew. Sustain. Energy Rev. 70, 1352–1365. https://doi.org/10.1016/j.rser.2016.12.038

Paulitschke, M., 2017. ScienceDirect ScienceDirect Comparison particle swarm and genetic based design The of on District algorithm Heating and Cooling algorithms for PV-hybrid systems with battery and hydrogen storage Assessing the feasibility of path using the heat demand-outdoor temperature function for a long-term district heat demand forecast. Energy Procedia 135, 452–463. https://doi.org/10.1016/j.egypro.2017.09.509

Sawle, Y., Gupta, S.C., Bohre, A.K., 2018. Review of hybrid renewable energy systems with comparative analysis of off-grid hybrid system Loss of Power Supply Probability Loss of Load Probability. Renew. Sustain. Energy Rev. 81, 2217–2235. https://doi.org/10.1016/j.rser.2017.06.033

Shiva, C.K., Mukherjee, V., 2015. A novel quasi-oppositional harmony search algorithm for automatic generation control of power system. Appl. Soft Comput. J. 35, 749–765. https://doi.org/10.1016/j.asoc.2015.05.054

Swider, D.J., Beurskens, L., Davidson, S., Twidell, J., Pyrko, J., Auer, H., Vertin, K., Skema, R., 2008. Conditions and costs for renewables electricity grid connection: Examples in Europe 33, 1832–1842. https://doi.org/10.1016/j.renene.2007.11.005

Xu, L., Ruan, X., Member, S., Mao, C., Member, S., Zhang, B., Luo, Y., 2013. An Improved Optimal Sizing Method for Wind-Solar-Battery Hybrid Power System 4, 774–785.

Entropy production and Human life cycle assessment for Indians with considering protein, fat, and carbohydrate

a) Arvind Kumar Patel, b) Dr S.P.S. Rajput

a) Research Scholar at the Department of Mechanical Engineering MANIT, Bhopal
b) Professor at the Department of Mechanical Engineering MANIT, Bhopal

Corresponding Author mailing address:
Arvind Kumar Patel
Department of Mechanical Engineering, Near Mata Mandir Square
MANIT, Bhopal (India)-462024
Corresponding Author E-mail-arvindpatel88@gmail.com

Abstract:

In present work, the thermodynamic life cycles of humans has been determined on the bases diurnal entropy generation with considering energy intake per day for people living in India. This study has been carried out on the food and energy intake data provided by the National Sample Survey Office (NSSO) and National institution of nutrition, Hyderabad. The protein, fat and carbohydrate intake of 18 Major Indian states are considered for the study. With the help of the second law of thermodynamics, entropy production is determined from protein, fat and carbohydrate in whole life duration. In this work, life spans of humans are calculated from entropy production living in different Indian states and, it is seen that people living in Tamilnadu has the maximum life span of 79 years, and Haryana has the least life span of 66 years. Remaining states vary in the range of 66-79 years. This life span of humans is validated by the NITI Aayog study on Life expectancy in India and shows a little variation in the range of 3-8 years.

Key Words: Energy, Entropy, Human body, Thermodynamics, Life span, food habits, NITI Aayog

1. Introduction:

From the last few decades, classical thermodynamics is used to develop a fundamental understanding of the biological systems. The exchange of mass, momentum, and energy are all obeyed by natural methods. The second law of thermodynamics is essential to understand the phenomena of evolution, growth, ageing, and death. The field of biological thermodynamics covers not only living plants and animals but also societies and corporations. To understand the growth, ageing and end of the natural system, one should know about entropy. Entropy is defined as the degree of randomness in a system. Entropy can be evaluated for living and non-living systems both. One can say that if a system has the perfect molecular order, then the entropy of this system is minimum and if a system has randomness on the higher side, then the entropy of the system is increasing. Entropy is also affected by the space between molecules if molecular area among particle is more, then the entropy of that system is more. (Ibrahim Dincer, 2001)[1] studied the concept of energy, exergy and entropy for all the thermodynamic system, and these concepts are equally applicable for living and non-living systems. (Prigogine, 1961)[2] consider the biological system as an open thermodynamic system and explain the dynamics of living organisms. He has described the many internal variables inside the natural species and their relation with the surrounding environment. (Alexei A. Zotin, 2018)[3] Investigated the growth and development of biological species in terms of various thermodynamic parameters. (Silva Carlos, 2008) [4] investigated the entropy production in males, females, and children. According to his investigation, entropy production in males is more than female. The methodology adopted by him applies to all species if the growth chart, energy consumption and diet composition are known. He has calculated the life span for males and females on the bases of physical activity level (PAL) and concluded that a person with light exercise has the highest lifespan and with intense exercise has a minimum lifecycle. (Ichiro, 1989)[9] Studied the entropy inflow and outflow from the human body in a naked position under the basal condition in the respiration calorimeter due to different modes of heat and mass transfer. His analysis is based on the data obtained by (Hardy D. James) [5]. Aoki concluded

that entropy production from the human body is nearly constant in the temperature range of 26-32^{0}C. (Rahman., 2007)[6] determined the entropy production from the human body with considering entropy flux to and from the human body. He has also considered the heat loss due to convection to and from the human body and physical activity level (rest and intense exercise). He has calculated the entropy production at rest, training and death are 21×10^{-5} kW/K, 219×10^{-5}kW/K and zero kW/K respectively. (K. Annamalai, 2002) et al. [7] analyzed the human body thermodynamically and determined the entropy production 10000 kJ/kg-K per person and predicted the life span 77 years. Kuddusi H. et al. [8] studied glucose oxidation in the human body and its consumption. Entropy production due to glucose oxidation is computed as 0.41×10^{-5} kW/kg-K and predicted the life span of 77.34 years. James Hardy et al. [5] calculated the heat loss from the human body on the bases of hardy radiometer and respiration calorimeter. In this work, the purely thermal loss was considered. A man in the dressed and undressed situation was put inside the calorimeter and losses are calculated. In hardy work rectal temperature and skin temperature also measured.

From the above literature, the researcher has concluded that many authors have attempted the entropy generation in humans. Entropy production has been computed for resting conditions, mild exercise, and heavy exercise through the indirect calorimetric system. Some authors also computed the entropy production from the individual human organs such as lungs and heart. Still, none has determined the entropy production and life cycle in the context for the Indian subcontinent.

3. Data collection: Various food and energy-related data are collected from a report "NUTRITIONAL INTAKE IN INDIA" [10] Published by National Sample Survey Office (NSSO) New Delhi. This food-related data is obtained from door to door surveys done by NSSO.

4. Methodology Adopted: Laws of thermodynamics are equally applicable for both living and non-living things. In present work laws of thermodynamics is applied for the humans and estimating the performance of the human body in terms of entropy production and life cycle analysis.

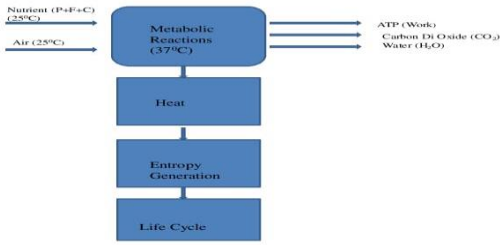

Fig.1- Schematic presentation of methodology adopted to find heat generation in the human body

4.1 First Law of Thermodynamics for Human Body: first law of the thermodynamic state that the change in enthalpy of a system equals the net heat transfer into the system minus the net work done by the system.

$$Q = H\text{-}W \quad (1)$$

$$Q = H_p - H_r \quad (2)$$

Where Q is the Heat, H is the Enthalpy, and W is the Work.

4.2 Entropy production from 1 kg of carbohydrate, palmitic acid, and 20 amino acids:

$$S_{g,glucose} = \Delta S_{sys} + \Delta S_{envi} = S_p - S_r + \frac{-Q_{s,glucose}}{T_{envi}} \quad (3)$$

$$= 29884 - 28586 + \frac{-(-1634820)}{310} = 6573 \text{ kJ/(K kmol glucose)}$$

Molar mass of glucose = 180 kg/kmol Glucose

$$S_{g,glucose} = \frac{6573}{180} = 36.51 \text{ kJ/(kg-K)} \quad (4)$$

By a similar process, entropy production of palmitic acid and 20 amino acid has been calculated.

$$S_{g,palmeticacid} = 86.4 \text{ kJ/(kg-K)} \quad (5)$$

$$S_{g,20\ amino\ acid} = 66.8 \text{kJ/(kg-K)} \quad (6)$$

These values of entropy production of glucose, palmitic acid and 20 types of amino acid have been calculated with the help of equation (2).

Equations (4), (5), and (6) show that the entropy production inside the human body due to chemical reaction takes place. All these values are in 1 kg of glucose, palmitic acid, and 20 amino acids, respectively. Factors such as water and airflow to and from the system are not impacting the entropy production. So these factors are not included in this work.

5. Result and Discussion:

Table-1 indicates the values of protein, fat, and carbohydrate intake of the people residing in various Indian states. With the help of table-I and equation (4-6), one can calculate the entropy production on the bases of protein, fat, and carbohydrate.

Entropy production due to protein intake in Andhra Pradesh:

$$\frac{59.3}{1000} \times 66.77 \frac{kJ}{K\ kg} = 3.95 \frac{kJ}{K\ kg\ food} \quad (7)$$

Entropy production due to fat intake in Andhra Pradesh:

$$\frac{55.2}{1000} \times 86.36 \frac{kJ}{K\ kg} = 4.76 \frac{kJ}{K\ kg\ food} \quad (8)$$

Entropy production due to carbohydrate intake in Andhra Pradesh:

$$\frac{356.7}{1000} \times 36.52 \frac{kJ}{K\ kg} = 13.02 \frac{kJ}{K\ kg\ food} \quad (9)$$

Total Entropy Production due to protein, fat, and carbohydrate

$$3.95+4.76+13.02 = 21.73 \frac{kJ}{K\ kg\ food}$$

Entropy production rate can be calculated by multiplying the food consumption rate in kg/sec per capita: (As per the NIN, Hyderabad, the average cooked food intake by the Indian Nationals is 1.25 kg/day per person).

$$21.73 \frac{kJ}{K\ kg\ food} \times (1.44 \times 10^{-5}) \frac{kg}{sec} = 31.29 \times 10^{-5} \frac{kW}{K} \quad (10)$$

Entropy Production rate per unit mass: (As per the world bank report the average mass of a human is 62 kg)

$$\frac{31.29 \times 10^{-5}}{62} \frac{kW}{K\ kg} = 0.504 \times 10^{-5} \frac{kW}{K\ kg} \quad (11)$$

Silva and Annamalai have estimated the value of entropy production in the whole life of human in per kg of human and that value is 11404 kJ/kg-K. With the assistance of this entropy production, one can determine the life cycle of the human body residing in any part of the world. Here life cycle has been calculated for Indian people living in different states of the nation.

Life cycle calculation for People of Andhra Pradesh:

$$\frac{11404}{0.504\times10^{-5}} \times \frac{1}{365\times24\times3600} = 71.74 \text{ Years}$$

Similarly life cycle of top five and least five Indian states have been determined and shown bellow.

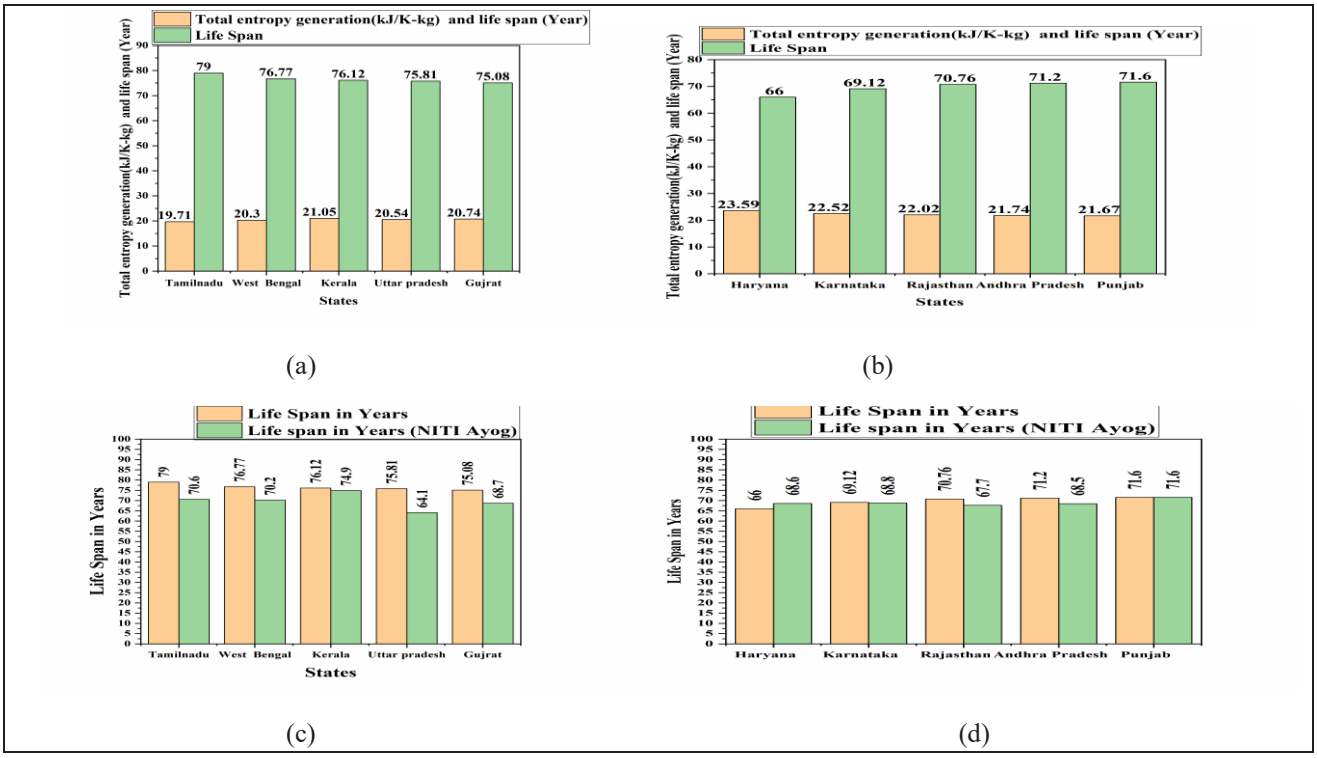

Figure-2. (a) Comparison of Entropy production and life span estimation for the top five states. (b) Comparison of Entropy production and life span estimation for the least five states. (c) Comparision of thermodynamic life span of human with NITI aayog life expectancy for top five states. (d) Comparision of thermodynamic life span of human with NITI aayog life expectancy for least five states.

Conclusion and Recommendations:

Entropy production in human is a unique problem and not address yet, especially in case of the human body with considering energy intake and food habits in Indian conditions. The life span of humans is determined in this work and compared with the established data and NITI Aayog report on life expectancy. On the bases of the above research work, the following conclusion may be drawn.

1. The total entropy production due to protein, fat, and carbohydrate is highest in Haryana and lowest in Tamilnadu.
2. Entropy production in kW/K is very much similar in case of Rajasthan, Punjab and Andhra Pradesh. The entropy production rate is highest in Haryana and lowest in Tamilnadu.
3. Life span estimation of Tamilnadu is highest among all Indian states, and lowest life expectancy is recorded in Haryana.
4. Life expectancy data of NITI Aayog is compared with current research work, and there is a minor difference of 1.22 years in case of Kerala when compared. The highest difference is recorded in Utter Pradesh.

References:

[1] Ibrahim Dincer and Yunus A. Cengel. Energy, Entropy and Exergy Concepts and Their Roles in Thermal Engineering. Entropy. Vol.3, issue-3. 2001, pp-116-149. https://doi.org/10.3390/e3030116

[2] I Prigogine, Introduction to thermodynamics of irreversible process, second revised edition, Inder science publication, NY-London 1961

[3] Alexei A. Zotin, Vladimir N. Pokrovskii. The growth and development of a living organism from the thermodynamic point of view. Physica A. Vol-512 (2018) pp-259-366

[4]. Silva Carlos, Annamalai Kalyan. Entropy production and human ageing: life span entropy and effect of physical activity level. Entropy 2008;10(2):100e23.http://dx.doi.org/10.3390/entropy-e10020100.

[5] Hardy D. James, DuBois F. Eugene. Regulation of Heat loss from the human body.Russell Sage Institute of Pathology in Affiliation with the Newyork Hospital and Department of Medicine, Cornell Medical College, NewYork. PHYSIOLOGY: HARDY AND DUBOIS pp- 624-630.

[6] M.A. Rahman. A novel method for estimating the entropy production rate in the human body. Thermal Science 2007;11(01);75-92. https://doi.org/10.2298/TSCI0701075R

[7] K. Annamalai, I Puri. Advanced thermodynamics engineering. Boca Raton, Florida, USA; CRC Press 2002

[8] H. Kuddusi, Thermodynamics analysis of different diets in the human body. Senior design product, food engineering department, Istanbul technical university 2011

[9] D. Nelson, M. Cox Lehninger principles of biochemistry. New-York USA; Worth-Worth 2003

[10] https://www.nin.res.in/scientific.html (National Institute of Nutrition, Hyderabad)

Entropy Generation and Exergy Analysis under transient condition for Large Diameter Natural Circulation Loops

[1*]Elton Dylan Nazareth, [2*]Arunachala U Chandavar, [3]Rajat A Chandavar,
[1] Manipal Academy of Higher Education, Research scholar, Department of Mechanical and Manufacturing Engineering, Manipal Institute of Technology, Udupi, 576104, India
[2] Manipal Academy of Higher Education, Sr. Associate Professor, Department of Mechanical and Manufacturing Engineering, Manipal Institute of Technology, Udupi, 576104, Karnataka, India
[3] Hexagon Capability Center India, Software Engineer, Madhapur, Hyderabad, 500081, Telangana, India

* E-mail: arun.chandavar@manipal.edu

Abstract
Natural circulation systems are the most reliable heat transportation systems applied widely in nuclear and solar thermal systems. Particularly in generation IV nuclear reactors, it is used as a decay heat removal system during accidental scenario and as a secondary power generating unit during normal operation. However, a stable power generation is of concern as instability in natural circulation loops (NCL) leads to unstable power. In case of single phase NCL, horizontal heater and horizontal cooler (HHHC) configuration delivers the highest flow rate compared to other arrangements with a penalty of least stability. The entropy generated in NCL is mainly due to the fluid friction, heat transfer across the cooler and heater. In the present experimental work with water as loop fluid, transient analysis (with instantaneous entropy generation) is done with and without orifice plates. Different operating procedures like startup from rest, power raising from a stable steady state and power step down from an unstable state are explored. The observation was that the system could switch from either an unstable to stable state, stable to unstable state, or remain in the stable/unstable state. This phenomenon is further quantified using the entropy generated in the system along with the exergy analysis. Further, the system stability is improved by using orifice plates and, entropy generation rate is observed to decrease with reduction in orifice diameter. This drop is attributed to the significant reduction in mass flow rate than increase in temperature difference across the legs. Also noted that the NCL with lower orifice diameter and high heater input lead to better exergy efficiency.

Keywords: Natural circulation systems, instantaneous entropy generation, instability, orifice plates, horizontal heater horizontal cooler, exergy analysis.

I. Introduction

NCL is highly reliable as it has no moving parts for fluid circulation. Among the various configurations of it, the heater and cooler being horizontal tends to be the most unstable. For efficient heat removal (either during accidental mode or power generation), the loop must be stable i.e., flow in one single direction for the heat input it receives.

The techniques used in stabilizing the loop are nanofluids (Nayak et al., 2009a) (Nayak et al., 2009b), flow restrictors (Misale and Frogheri, 1999), Tesla valve (Arunachala et al., 2019) (Wahidi et al., 2020), loop inclination (Basu et al., 2013), increasing the wall thickness (Vijayan et al., 1992) and so on. However, the cost effective and easy to use method is the addition of orifice plates in the flow line, which is extensively being used in single and two-phase NCLs. In the earliest works (Zvirin et al., 1981), the orifice plates were installed in the hot leg, with multiple holes along the circumference. (Misale and Frogheri, 1999) installed the orifices on both the legs of a horizontal heater and horizontal cooler (HHHC) loop of 22 mm diameter and observed a stable state with 6 mm diameter orifice plate for the entire operating condition compared to 10 and 14 mm plates. Further, (Misale and Frogheri, 2000) performed a similar study using 10, 22, 26, 30 and 36 mm orifice plates in a 40 mm loop, and found better stability at lower β ratio. (Elton et al., 2020) have identified various instability patterns in a large diameter HHHC loop, which are different from the ones found by (Vijayan et al., 2001). To attain the highest thermodynamic efficiency, the stability analysis should be complemented by the detraction of entropy generation. Hence, (Goudarzi and Talebi, 2015) have analytically studied the effect of loop geometry on entropy generation in a 30 mm loop. In a similar study, (Sahu and Sarkar, 2019) elaborated the role of loop diameter (20 – 30 mm), other geometries and hybrid nanofluid in energy and exergy performance.

Till date literature review includes different types of study on stability analyses of HHHC loop and stability restraining techniques. However, entropy generation studies are limited to analytical method as well to $\geq$ 30 mm size loop. Hence, the present experimental study focusses on entropy generation in larger diameter (38.89) HHHC loop under both stable and unstable condition.

II. System Description

The experimental set up includes HHHC, 38.89 mm uniform diameter loop (stainless steel seamless tube with a provision for insertion of orifice plate), power system and instrumentation as shown in Fig. 1. The entire loop is insulated by ceramic blanket followed by Polyvinyl Chloride pipe. The height and width of the loop is 1600 mm and 1100 mm respectively.

The thermostatic bath (Siskin, Profichill RCC – 400 ST – 40) recirculates water to the cooler (double pipe heat exchanger) through the mass flow meter (Rheonik, RHE26). Thermocouple of K-type (ϕ 1.5 mm, minerally insulated) are used to measure the temperature difference across the cooler, hot leg and cold leg. The heater section is made

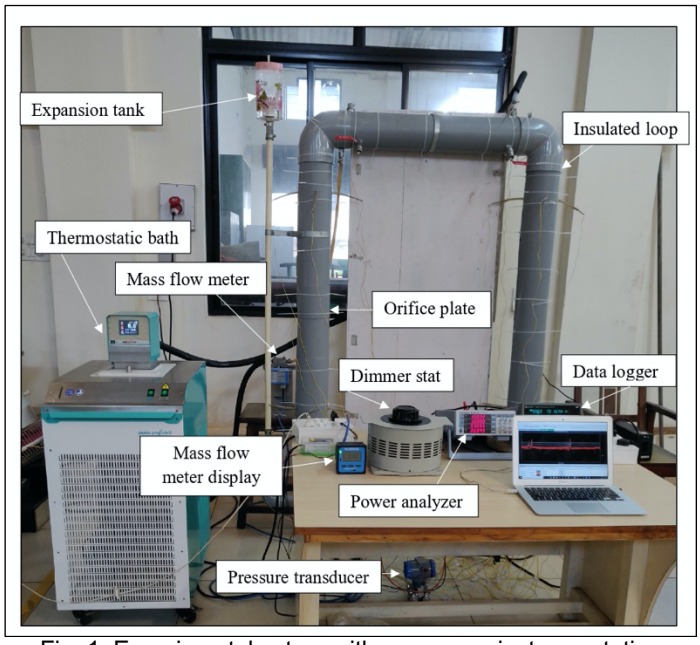

Fig. 1: Experimental set up with necessary instrumentation

of Nichrome winding and Dimmer stat (Automatic electric, 20D-1P) and power analyzer (Yokogawa, WT310E) supplies known amount of power. The loop mass flow rate is indirectly measured by referring to the differential pressure transmitter (Rosemount, 3051 CD) reading across the heater. All data are captured using data acquisition system (Keysight, 34972A). The orifice plates used are of 35, 30, 25 and 20 mm diameter representing β as 0.9, 0.77, 0.64 and 0.51 respectively.

III. Analysis

The entropy generated in the different sections of the system has been simplified and the equations are finalized by referring to (Goudarzi and Talebi, 2015). The entropy generated in the heater section due to the heat transfer in heater and the friction) are given as in Equation 1 and 2.

$$\dot{S}_{gen_1} = wC_P\Delta T \int_{T_{cl}}^{T_{hl}} \frac{dT}{T^2+T\Delta T} = -wC_P ln\left[\frac{1+{}^{\Delta T}/_{T_{hl}}}{1+{}^{\Delta T}/_{T_{cl}}}\right] \quad \text{where } \Delta T = \frac{WDC_P(T_{hl}-T_{cl})}{Nu_h k P_h L_h} \tag{1}$$

$$\dot{S}_{gen_2} = \frac{8fw^3L_h}{\rho_0^2\pi^2D_h^5}\left[\frac{ln\left[{}^{T_{hl}}/_{T_{cl}}\right]}{T_{hl}-T_{cl}}\right] \tag{2}$$

At the cooler section, the three entropy generation terms are heat exchanger ($\dot{S}_{gen_3}, \dot{S}_{gen_4}$) and friction ($\dot{S}_{gen_5}$).

$$\dot{S}_{gen_3} = wC_P \int_{T_{hl}}^{T_{cl}} \frac{dT}{T} = -wC_P ln\left[\frac{T_{cl}}{T_{hl}}\right] \tag{3}$$

$$\dot{S}_{gen_4} = \frac{wC_P}{T_{sec}} \int_{T_{hl}}^{T_{cl}} dT = \frac{wC_P}{T_{sec}}(T_{hl}-T_{cl}) \tag{4}$$

$$\dot{S}_{gen_5} = \frac{fw^3V_t}{2\rho^2D_cA_c^3St_mT_{sec}} ln\left[\frac{T_{sec}exp\left(\frac{St_mA_cL_c}{V_t}\right)+T_{hl}-T_{sec}}{T_{hl}}\right] \tag{5}$$

Further, the entropy generation in pipe (friction) is,

$$\dot{S}_{gen_6} = \frac{fw^3L_p}{2\rho_0^2DA_p^2T} \tag{6}$$

The total entropy generated in the NCL is the sum of all the terms as shown below,

$$\dot{S}_{total} = \sum_1^6 \dot{S}_{gen} \tag{7}$$

The dimensionless form of the entropy (ξ) is calculated (Goudarzi and Talebi, 2015) as,

$$\xi = \frac{\dot{S}_t}{{}^{Q_h}/_{(T_{hl}-T_{cl})}} \tag{8}$$

Even the exergy efficiency (second law efficiency) is calculated as follows (Cengel and Boles, 2011),

$$\eta_{II} = \frac{\dot{\chi}_{rec}}{\dot{\chi}_{sup}} \tag{9}$$

Where, $\dot{\chi}_{sup} = Q_h$ and $\dot{\chi}_{rec} = \dot{\chi}_c = w_c C_{p,c}\left[T_{c,out} - T_{c,in} - T_0 ln\left(\frac{T_{c,out}}{T_{c,in}}\right)\right]$

IV. Results and discussion

Here the entropy generated in the NCL for a fixed time period (after omitting the initial time transients) is discussed. In an NCL, there is a limiting power at which the loop switches from a stable to an unstable flow regime.

However, this limiting power increases with decrease in β. In (Elton et al., 2020), the loop was subjected to different operating conditions (without orifice) in order to find the stability point. Here, a constant power of 300 W is applied and referred to the operating procedure of start up from rest, which reflects the variation in the dynamic dimensionless entropy generation (ξ) with and without orifice plate as shown in Fig.2. The fluctuation of ξ reduces with β and the degree of fluctuation indicates the instability. For β=0.51 and 0.64, a steady flow is seen due to the added resistance in the flow line. The difference between the loop leg temperatures (T_{hl}-T_{cl}) flow rate (w) and effective length increase are the deciding factors for the entropy generation. With increase in β, the flow rate increases, whereas the T_{hl}-T_{cl} decreases. However, the difference in leg temperature reduction is marginal as compared to the increase in *w* (due to the higher diameter of the loop). Hence it leads to higher fluctuations in ξ in an unstable loop.

For the operating procedure of power rise from a steady state, the stability point for the system without orifice plates have been addressed in the study of (Elton et al., 2020). For a power rise of 100 W to 250 W, the ξ has been plotted against time, which shows (Fig. 3) the transition of the loop upon power rising. The ξ is increasing steadily and reaches a peak point, which shows the initiation of flow reversal. This peak is followed by lower value of entropy generation which shows that the loop has either uniform/non-uniform bi-directional fluctuations. During the next operating procedure of power step down from an unstable state, the initial power was set to 300 W and later decreased to 175 W (Fig. 4). During the initial power set, the increasing trend of entropy generation exhibits limit cycle oscillations. After a step down to 175 W, the entropy generated continuously decreases, which shows the loop is stabilizing, and uniform power extraction could be possible.

The exergy efficiency for all the stable flow cases in large diameter NCL (Elton et al., 2020) has been plotted as shown in Fig. 5. The exergy efficiency is better for lower β ratio and higher heater power. The loop with higher β causes instability when operated at higher heat input, hence aren't considered in the plot. The range of exergy efficiency obtained are all below 0.2 %, which shows a high loss of useful work in NCLs. This could be due to the low flow rate induced and the 3D flow pattern within the loop.

V. Conclusions

The outcome of the present analysis is summarized below.

1. The entropy generation is proportional to the degree of instability at a given heat input due to higher loop flow rate observed in large diameter NCL.
2. At higher heat input, a constant power generation would be possible for an NCL with low β due to higher stable operating range.
3. The optimum operating condition for an NCL would be at higher heater power and low β.

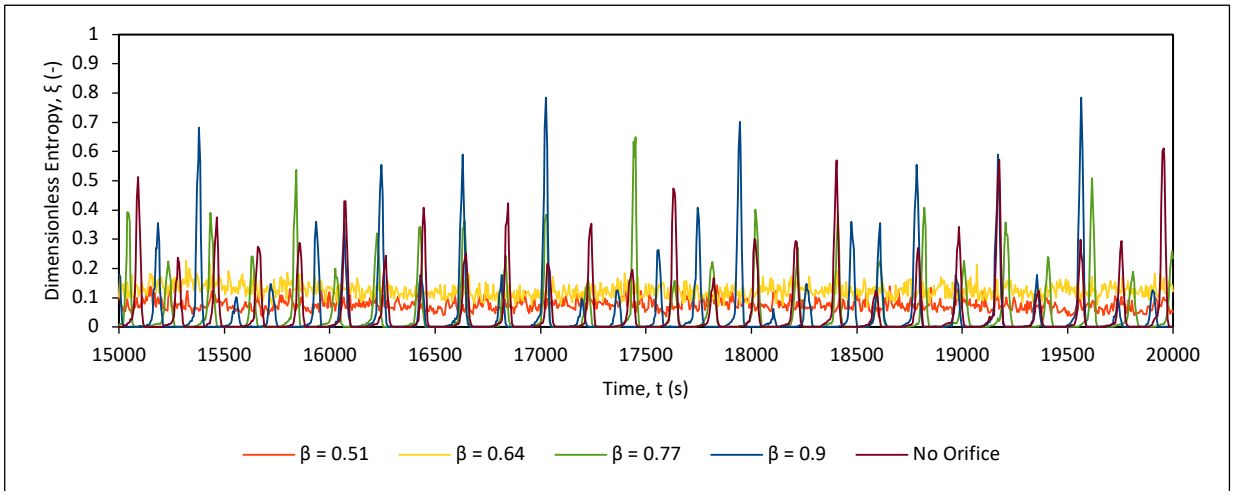

Fig. 2. Effect of β on dimensionless entropy

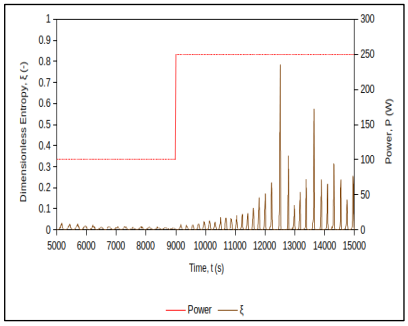

Fig. 3. Variation in dimensionless entropy (power rise from steady state)

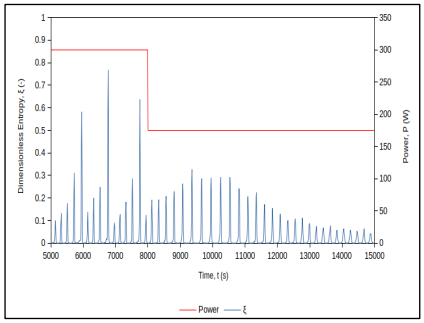

Fig. 4. Variation in dimensionless entropy (power step down from an unstable state)

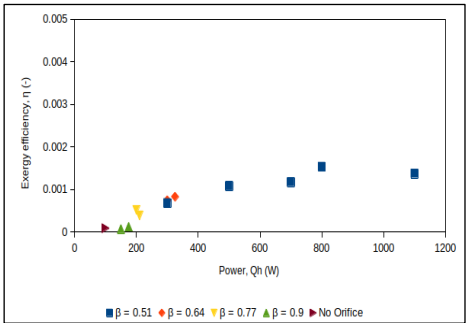

Fig. 5. Effect of β on exergy efficiency

Acknowledgements
The authors gratefully acknowledge the financial support from SERB, DST under core research grant scheme (CRG/2019/004429). The authors are also thankful to Dr. P K Vijayan, professor and Dean (R&C) IIT Jammu, for his unconditional guidance towards this concept.

Nomenclature

A	Area (m^2)	i	Inside
C_p	Specific heat (J/kg K)	in	Inlet
D	Diameter (m)	or	Orifice
f	Friction factor (-)	out	Outlet
Q	Power, (W)	p	Pipe
Re_{ss}	Steady state Reynolds number = $\frac{WD}{A\mu}$(-)	P	Perimeter (m)
$\dot{S}_{gen}$	Entropy generated (J/K)	rec	Recovered
St_m	Modified Stanton number = $\frac{4\,Nu}{Re_{ss}Pr}$ $(-)$	sec	Secondary
T	Temperature (K)	Sup	Supplied
V	Volume (m^3)	T	Total
w	Mass flow rate (kg/s)	*Greek*	
Subscript		β	Orifice ratio = D_{or}/D_i
0	Reference	$\dot{\chi}$	Exergy rate (W/K)
c	Cooler	Δ	Difference
cl	Cold leg	η	Exergetic efficiency (-)
h	Heater	μ	Dynamic viscosity (Pas)
hl	Hot leg	ρ	Density (kg/m^3)

References

Arunachala, U.C., Rajat, A.C., Shah, D. and Sureka, U., 2019. Stability improvement in natural circulation loop using tesla valve–an experimental investigation. *International Journal of Mechanical and Production Engineering Research and Development, 9 (6), 13*, *24*.

Basu, D.N., Bhattacharyya, S. and Das, P.K., 2013. Influence of geometry and operating parameters on the stability response of single-phase natural circulation loop. *International Journal of Heat and Mass Transfer*, *58*(1-2), pp.322-334.

Cengel, Y.A. and Boles, M.A., 2011. Thermodynamics: An Engineering Approach Seventh Edition.

Elton, D.N., Arunachala, U.C. and Vijayan, P.K., 2020. Investigations on the dependence of the stability threshold on different operating procedures in a single-phase rectangular natural circulation loop. *International Journal of Heat and Mass Transfer, 161*, p.120264.

Misale, M. and Frogheri, M., 1999. Influence of pressure drops on the behavior of a single-phase natural circulation loop: preliminary results. *International communications in heat and mass transfer*, *26*(5), pp.597-606.

Misale, M. and Frogheri, M., 2000. Stabilization of a single-phase natural circulation loop by pressure drops. In *ICHMT DIGITAL LIBRARY ONLINE*. Begel House Inc..

Nayak, A.K., Gartia, M.R. and Vijayan, P.K., 2009a. Nanofluids: A novel promising flow stabilizer in natural circulation systems. *AIChE journal*, *55*(1), pp.268-274.

Nayak, A.K., Gartia, M.R. and Vijayan, P.K., 2009b. Thermal–hydraulic characteristics of a single-phase natural circulation loop with water and Al2O3 nanofluids. *Nuclear Engineering and Design*, *239*(3), pp.526-540.

Vijayan, P.K., Bhojwani, V.K., Bade, M.H., Sharma, M., Nayak, A.K., Saha, D. and Sinha, R.K., 2001. *Investigations on the effect of heater and cooler orientation on the steady state, transient and stability behaviour of single-phase natural circulation in a rectangular loop* (No. BARC--2001/E/034). Bhabha Atomic Research Centre.

Wahidi, T., Chandavar, R.A. and Yadav, A.K., 2020. Stability enhancement of supercritical CO2 based natural circulation loop using a modified Tesla valve. *The Journal of Supercritical Fluids*, *166*, p.105020.

Zvirin, Y., Jeuck III, P.R., Sullivan, C.W. and Duffey, R.B., 1981. Experimental and analytical investigation of a natural circulation system with parallel loops. *Journal of Heat Transfer, 103,* pp. 645-652.

Study on challenges and opportunities of Dish type Solar Stirling engine utilization at UAE conditions

[1*]Ben Alex Baby, [1] N. M. Zajith Ali, [2] Y. Raja Sekhar, [2]M. Natarajan, [2]C. Chiranjeevi
[1] Mechanical Engineering Department, University of Bolton RAK Academic Centre, Ras Al Khaimah, 16038, UAE
[2] School of Mechanical Engineering, Vellore Institute of Technology, Vellore, Tami Nadu, 632014, India

* E-mails: b.baby@bolton.ac.uk

Abstract
Solar thermal power plants are gaining popularity in the Middle East region. They have the potential of revolutionizing the oil-independent power supply sector in the coming years Diversification of energy mix is critical in meeting the ambitious renewable energy targets and net zero emissions by 2050 for UAE. Although the Concentrated Solar Power (CSP) has widespread application, Solar thermal energy extraction using a point-focusing dish collector and power generation with the use of Stirling engine is studied numerically. A theoretical model of a solar dish Stirling system is modelled with MATLAB®, applying year-round weather conditions of UAE to analyze the overall system performance and study the opportunities and challenges of the technology in the region. The maximum overall efficiency is noted to be 27% for the maximum DNI and having an average total annual power output estimated to be 11.8 MW. Also, the peak power of more than 3KWe was attained for an average of 5.7 hrs a day. The offset CO_2 emissions account to 620 $kgCO_2/kWh$ for a 10kW_e dish Stirling engine. Cleanliness factor of the mirrors considerable reduced the net power output by up to 15%. Challenges in terms of ensuring the tracking efficiency, cleanliness of the mirrors, structural stabilities and limited energy storage possibility are discussed.

Keywords: Dish/Stirling engine, Solar thermal energy, Numerical Analysis, CO_2 emissions.

I. Introduction

Solar energy is still considered as the primary form of renewable energy, utilized in different ways from its light intensity to its heat energy. The PV technology is fast-growing, and so is the solar thermal applications. The total solar thermal capacity accounts to 479 GWth, offsetting 41.9MTOe and 135.1 million tons of CO2 emissions (Musi et al., 2017). Most of the solar thermal energy conversion has its application in heating applications such as solar water heating, solar drying. In contrast, the concentrated solar power and dish/Stirling engines convert solar energy to electric power. UAE in it's 'Energy Strategy 2050' (Ministry of Energy & Institute, 2020) aims at achieving 50% of its total energy mix from clean energy sources thereby contributing 70% less Carbon dioxide to the total carbon footprint. A dish/Stirling system consists of a collector and a Stirling engine that converts solar energy into mechanical energy and thereby to electrical energy using generators. This system is also deemed to have the highest efficiency with up to 30% efficiency (Mancini et al., 2003) in converting solar energy to electrical energy. Hafez et al., (2016) took into consideration various design parameters such as reflector material of the concentrator, geometric shape, solar radiation, concentration ratio, aperture area rim angle. They obtained a maximum power output for 990W/m^2, using numerical modelling by MATLAB®. A numerical and experimental study performed (Gholamalizadeh and Chung, 2017) on 1 kW Stirling engine to understand the energy and exergy efficiency, accounting to maximum energy loss in the receiver and Stirling engine. The parabolic dish collector and cavity receiver were mathematically modelled for a fixed focal length (Nazemi and Boroushaki, 2016), overall performance was compared against various design parameters(Ahmadi, 2012). Uzair et al. analyzed the effect of wind velocities to and varied elevation angles on a dish collector (Uzair et al., 2017).
All of these studies have pointed to one aspect of a dish/Stirling engine system, which is to strike that balance between technological viability and economic feasibility. A recent study (Malali et al., 2019) have studied the effect of circumsolar radiation, optical quality obtaining a modified system efficiency of up to 36%. Lai et al. (Lai et al., 2019) in a dynamic analysis of solar dish/Stirling engine considering the effect of solar flux intensity, wind velocity and an optimum charged gas mass, the overall efficiency of 44% was obtained with a modified theoretical proposed. A dynamic operation (Vahidi Bidhendi and Abbassi, 2020) simulated in TRNSYS® states desert climates have the best output of up to 24%, and humid climate has a reduced efficiency of 15%. Recent studies (Jabari et al., 2020) have shown how this can be applied to a zero energy building as a cogeneration unit of power and heat. Considering the gaining popularity as a more efficient means for harnessing electric power from solar energy using dish/Stirling engine, a theoretical model (Mendoza Castellanos et al., 2019, 2017) was considered for a 10 kWe power production and a suitability study for the UAE climate condition was made numerically using MATLAB® code. The dynamic study analysis includes the hourly variation in the performance, year-round considering an average day in each month.

II. Methodology/System Description

UAE experiences a good share of solar insolation throughout the year with and annual solar hour of 3568 h, an average of 9.7h/day and a total annual solar radiation o of 2285 kWh/m^2 i.e. approximately 6.3 kWh/m^2 daily average

(Assi et al., 2012), thus it is suitable to harness solar energy.

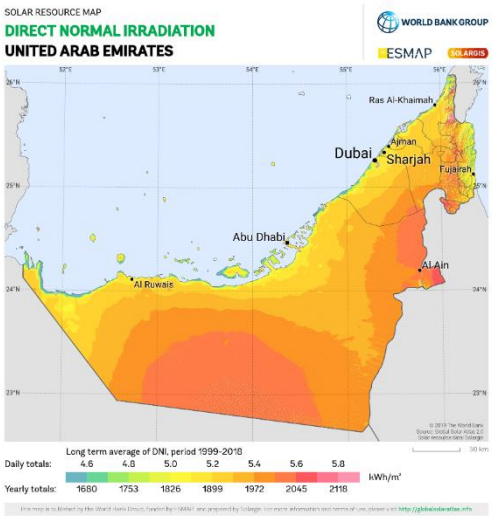

Fig. 1. DNI map of the UAE region

The weather data required for this study was assumed from the DView which uses the National Solar Radiation Database (NSRD) (Sengupta et al., 2018) as made available by National Renewable Energy Laboratory's (NREL's). A year-round analysis of the technology has been studied numerically considering one day, which had maximum DNI for all twelve months.

III. Numerical modelling and Analysis

MATLAB® code was generated based on the collector parameters and mathematical equations listed in Table 1 and Eqns. 1-13 of appendix. The results of the present numerical model were compared against the experimental values of Nepveu,2008 for validation. The comparision of system efficiency value from present analysis were deviating ±10% from experiment at different DNI conditions as shown in Fig. 2. The reason for deviation is the fact that variation in cleanlinesss index during experimentation, a factor accounting for optical efficiency of mirrorsand hence the numerical model is validated.

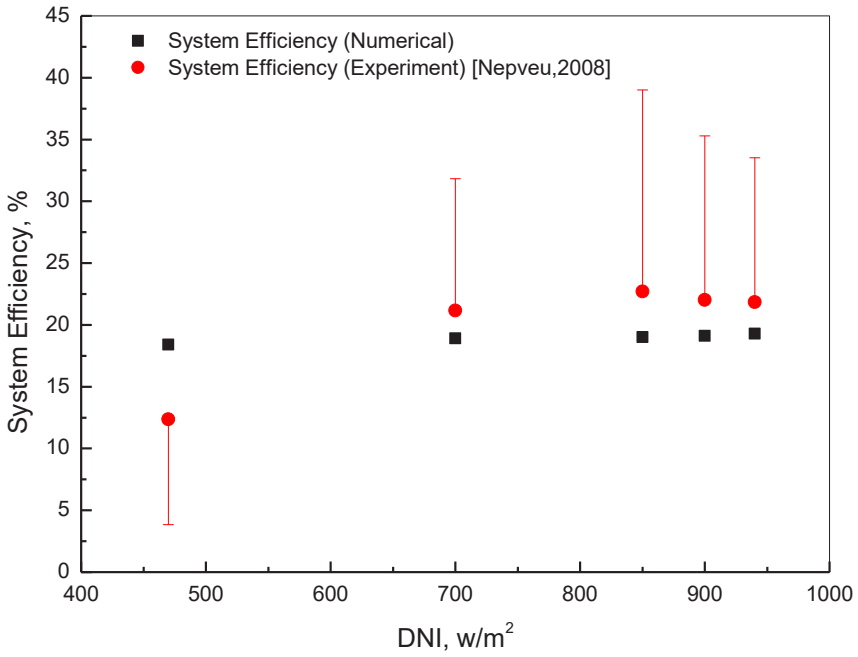

Fig. 2. Validation of present numerical simulationwith experiment data of literature for a Dish Stirling Engine

IV. Results and discussions

Evaluation of dish type solar collector with Stirling engine utilization against its performance and technological challenges for UAE conditions was analyzed in this study. The indicators to analyze the performance was power output and overall efficiencies.

A] Performance analysis

Power output: Considering a twelve-hour window to evaluate the performance, the net output power based on the solar insolation incident of the solar dish is plotted in Fig. 3. On an average 5.7 hours a day, the peak power of 3kWe was obtained, i.e. 2069 hours a year against 3568 annual solar hours in UAE. High production from morning to evening and not specifically around the peak sun hours like the noon part of the day, they are making it suitable for our application in UAE.

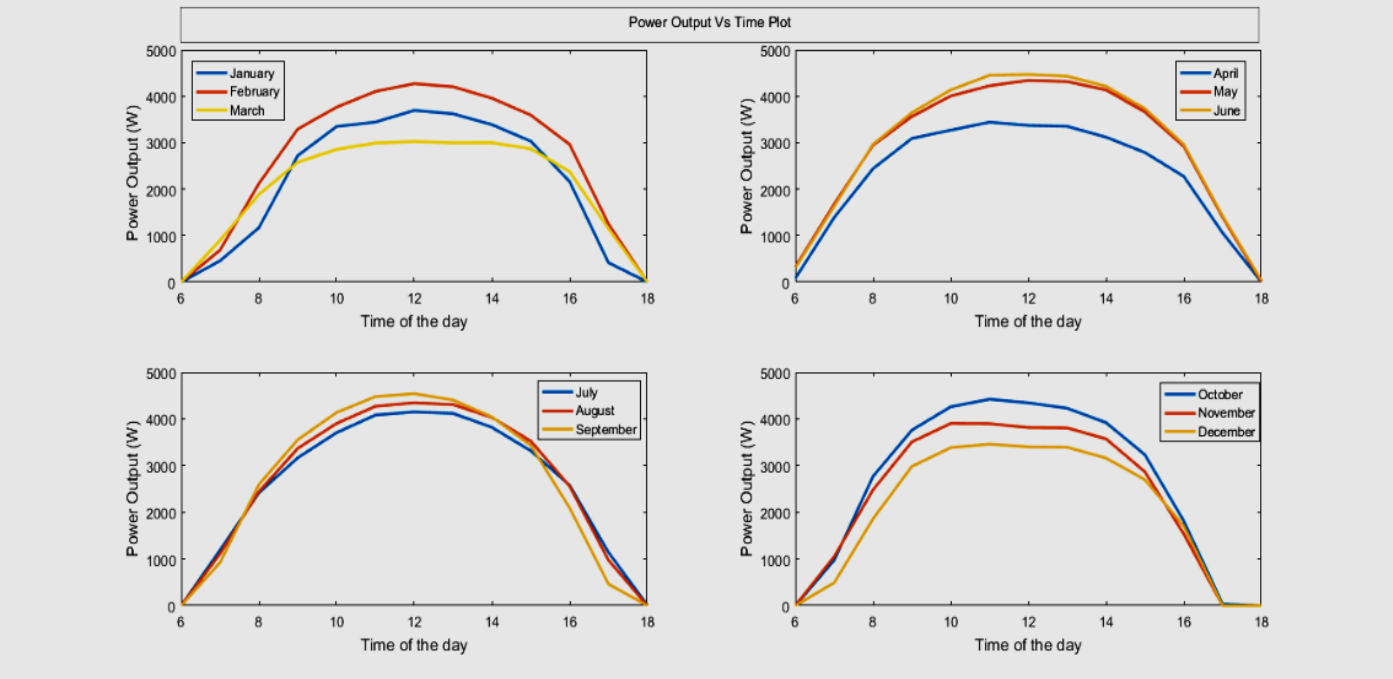

Fig. 3. Plot showing the variation in power output for different seasons and time of the day

Total Efficiency: The peak efficiencies were between 25% to 27% (Dadasaheb et al.,2019) and similarly for UAE conditions, for an average of 9.42 hr/day; all round the year. This accounts for 79% of the time in a day as shown in Fig.4. The maximum solar insolation was 960 W/m^2 and cavity temperature of 1927K. The net reduction in CO_2 emissions was calculated for the power output generated by the system. With an annual power generation of 11.8MW, an offset of 620 kgCO_2/kWh was achieved. For a monthly average of 1 MWh of power generated, 52 Kg of CO_2 emissions reduced monthly.

Net Power Output: The average daily power for every month is calculated for through-out the year and shown in Fig 5. Although June shows maximum average power generated, the peak power generated on the maximum DNI day of each month is higher than the average value. This shows the need for appropriate energy storage facility that can work towards taping the maximum potential of the system.

Cleanliness Factor and Power Output: The best and the worst month were identified from the daily averaged value, and the effect of the cleanliness factor is depicted in Fig. 6. The daily power output for the days considered, there was a maximum of up to 15% reduction in the power output when compared to clean mirrors.

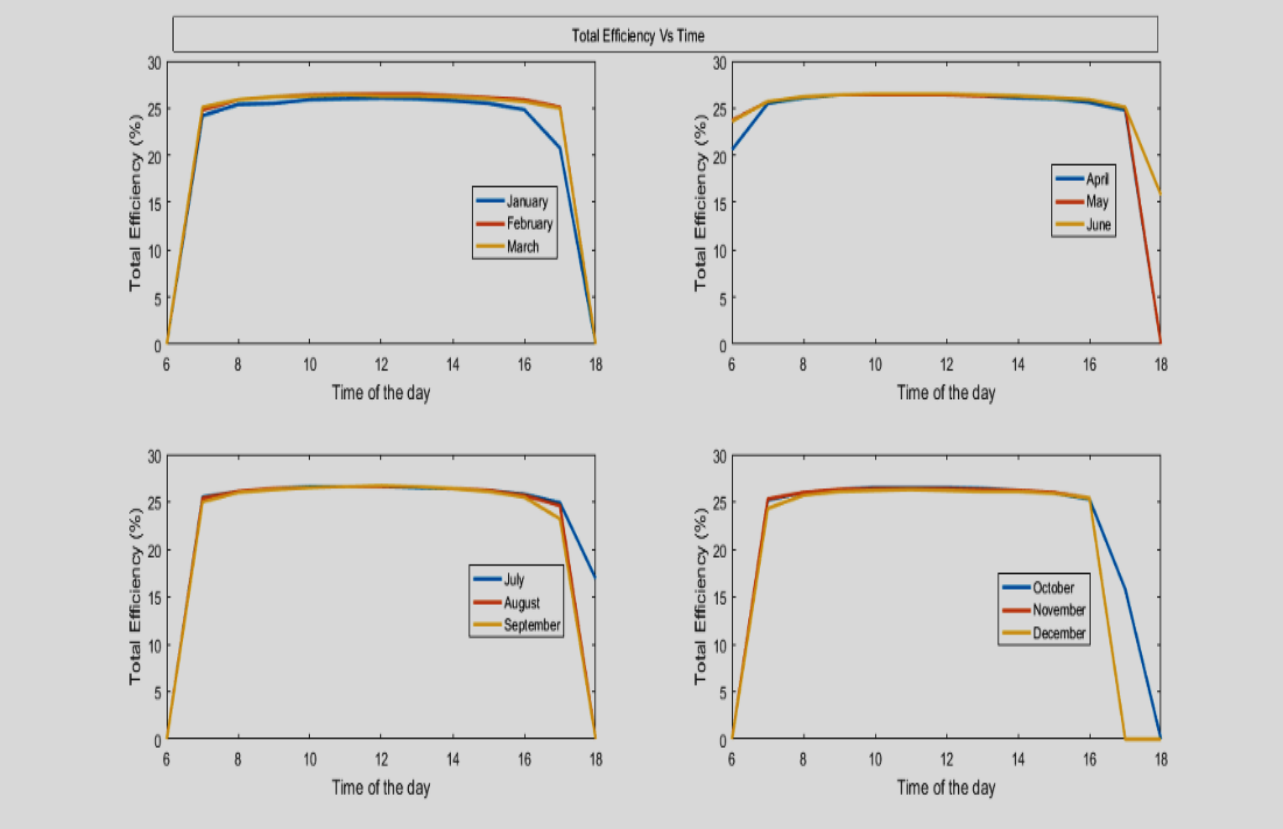

Fig. 4. Theoretical total system efficiency of dish Stirling engine for different seasons and time of the day

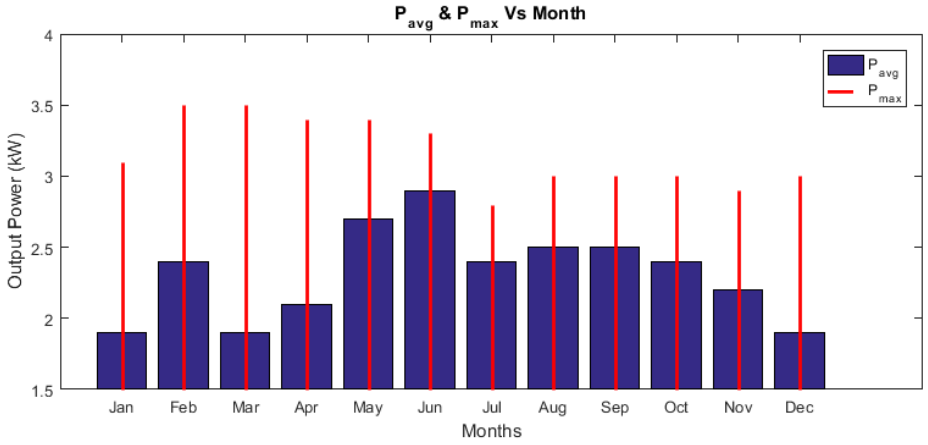

Fig. 5. Teoretical annual average and maximum power from Dish Striling engine

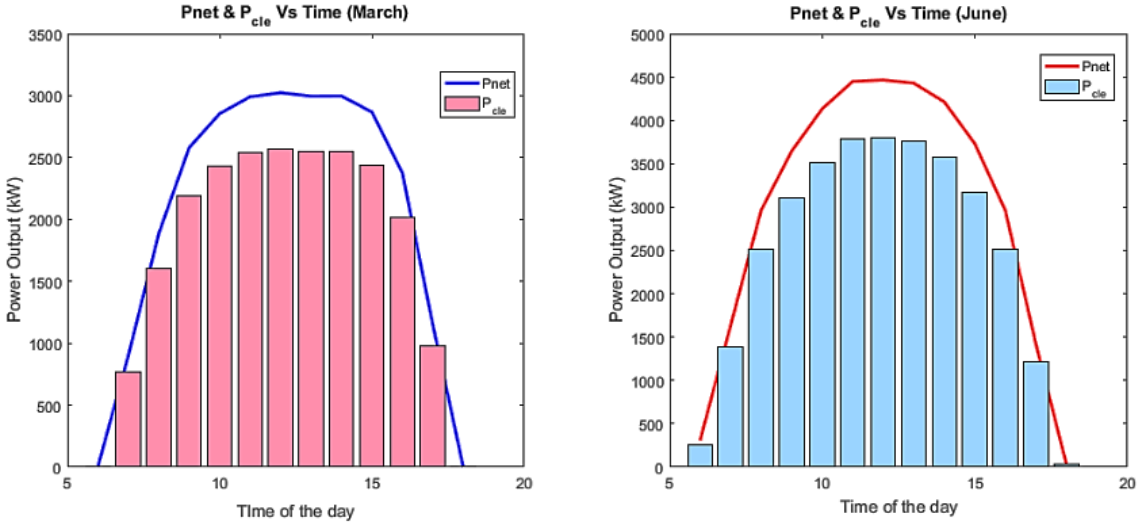

Fig. 6 Effect of Cleanliness factor on the Power output during a day for months of March and June

B) Technological advantages and challenges

Dish Stirling system is generally deemed to have the maximum solar to electricity conversion efficiency as the entire solar rays are concentrated to a point, and the use of a tracking system ensures it has maximum throughput for the whole sun hours. Although this is the general case, some advantages and challenges as applied to middle east countries are discussed below.

Advantages: *Net Water Use:* In arid countries where solar energy is high, easy availability of water for cooling and cleaning process is at stake. For an air-cooled solar dish type Stirling engine, the water use is less than the concentrated solar plant operations. The average water use water in CSP is 99.3% times higher than Dish/Stirling system (Macknick et al., 2012). Thus, making it technically challenging for the middle east countries.

Modular Design and Off-grid Applicability: The differences in design account considerably to Solar energy land-use footprint. Dish type Stirling engine is paralleled to a Solar PV in terms of readily available electric power at disposal. The modular design hence accounts to 2.8 acres/MW_{ac} while CSP would require 64% more land area. This accounts for 7.7 acres/MW_{ac} of a land requirement (Sean Ong, Clinton Campbell and Robert Margolis, 2013)

Challenges: *Cleanliness factor of mirrors:* One of the significant findings of this paper is the reduction in net power output accounting to the cleanliness factor of the mirrors, by about 14% in its annual power generation accounting to 1.71 MW of loss in net power production.

Solar tracking efficiency and structural features: Dual-axis tracking of the device will be in need for point concentrating solar collectors for maximum power output. An open-loop control system can be designed with for an already known sun path in case of a dish type collector. Monitoring the tracking system for a CSP would require a real-time analysis by having a closed-loop control system with feedback, on only alterations in orientation, positioning etc., thus adding to the structural complexity.

Energy Storage: Major disadvantage of dish type Stirling engine is the lack of energy storage in the system, thus making it similar to that of a PV panel, although battery storage is still a viable option. In case of a CSP, the use of appropriate energy storage method determines the operational efficiency and ability of function during off-peak solar hours.

V. Conclusions

Solar Dish type Stirling engine is studied extensively across various climatic conditions, and UAE is one of the major countries in the sunbelt countries; there lies a vast potential to tap the solar energy. This paper focuses on the suitability of using the Dish Stirling Engine to harness the solar thermal energy and converting it into usable power. The following are some of the findings,

- The net efficiency of the system was observed to rise to 27% for high insolation periods comparable with PV technologies.
- An average annual power generation of 11.8MW of power is estimated numerically.
- Some major opportunities of the technology lie in its modular design and power output readily available similar to that of a PV power generation and low water needs as compared to CSP technologies.
- Disadvantages are the cost investment required, lack of energy storage facilities and majorly from UAE's perspective the cleanliness factor of the reflecting surface.

References

Ahmadi, M.H., 2012. Investigation of Solar Collector Design Parameters Effect onto Solar Stirling Engine Efficiency. J. Appl. Mech. Eng. 01, 10–13. https://doi.org/10.4172/2168-9873.1000102

Assi, A., Jama, M., Al-Shamisi, M., 2012. Prediction of Global Solar Radiation in Abu Dhabi. ISRN Renew. Energy 2012, 1–10. https://doi.org/10.5402/2012/328237

Gholamalizadeh, E., Chung, J.D., 2017. Exergy analysis of a pilot parabolic solar dish-stirling system. Entropy 19, 1–12. https://doi.org/10.3390/e19100509

Hafez, A.Z., Soliman, A., El-Metwally, K.A., Ismail, I.M., 2016. Solar parabolic dish Stirling engine system design, simulation, and thermal Analysis. Energy Convers. Manag. 126, 60–75. https://doi.org/10.1016/j.enconman.2016.07.067

Jabari, F., Nazari-heris, M., Mohammadi-ivatloo, B., Asadi, S., Abapour, M., 2020. A solar dish Stirling engine combined humidification-dehumidification desalination cycle for cleaner production of cool, pure water, and power in hot and humid regions. Sustain. Energy Technol. Assessments 37, 100642. https://doi.org/10.1016/j.seta.2020.100642

Lai, X., Yu, M., Long, R., Liu, Z., Liu, W., 2019. Dynamic performance analysis and optimization of dish solar Stirling engine based on a modified theoretical model. Energy 183, 573–583. https://doi.org/10.1016/j.energy.2019.06.131

Macknick, J., Newmark, R., Heath, G., Hallett, K.C., 2012. Operational water consumption and withdrawal factors for electricity generating technologies: A review of existing literature. Environ. Res. Lett. 7. https://doi.org/10.1088/1748-9326/7/4/045802

Malali, P.D., Chaturvedi, S.K., Agarwala, R., 2019. Effects of circumsolar radiation on the optimal performance of a Stirling heat engine coupled with a parabolic dish solar collector. Appl. Therm. Eng. 159, 113961. https://doi.org/10.1016/j.applthermaleng.2019.113961

Mancini, T., Heller, P., Butler, B., Osborn, B., Schiel, W., Goldberg, V., Buck, R., Diver, R., Andraka, C., Moreno, J., 2003. Dish-stirling systems: An overview of development and status. J. Sol. Energy Eng. Trans. ASME 125, 135–151. https://doi.org/10.1115/1.1562634

Mendoza Castellanos, L.S., Carrillo Caballero, G.E., Melian Cobas, V.R., Silva Lora, E.E., Martinez Reyes, A.M., 2017. Mathematical modeling of the geometrical sizing and thermal performance of a Dish/Stirling system for power generation. Renew. Energy 107, 23–35. https://doi.org/10.1016/j.renene.2017.01.020

Mendoza Castellanos, L.S., Galindo Noguera, A.L., Carrillo Caballero, G.E., De Souza, A.L., Melian Cobas, V.R., Silva Lora, E.E., Venturini, O.J., 2019. Experimental Analysis and numerical validation of the solar Dish/Stirling system connected to the electric grid. Renew. Energy 135, 259–265. https://doi.org/10.1016/j.renene.2018.11.095

Ministry of Energy & Institute, 2020. UAE Energy Strategy 2050 [WWW Document]. U.ae. URL https://u.ae/en/about-the-uae/strategies-initiatives-and-awards/federal-governments-strategies-and-plans/uae-energy-strategy-2050 (accessed 8.15.20).

Musi, R., Grange, B., Sgouridis, S., Guedez, R., Armstrong, P., Slocum, A., Calvet, N., 2017. Techno-economic Analysis of concentrated solar power plants in terms of levelized cost of electricity. AIP Conf. Proc. 1850. https://doi.org/10.1063/1.4984552

Nazemi, S.D., Boroushaki, M., 2016. Design, Analysis and optimization of a solar dish/stirling system. Int. J. Renew. Energy Dev. 5, 33–42. https://doi.org/10.14710/ijred.5.1.33-42

Sean Ong, Clinton Campbell, P.D., Robert Margolis, and G.H., 2013. Land-Use Requirements for Solar Power Plants in the United States.

Sengupta, M., Xie, Y., Lopez, A., Habte, A., Maclaurin, G., Shelby, J., 2018. The National Solar Radiation Data Base (NSRDB). Renew. Sustain. Energy Rev. 89, 51–60. https://doi.org/10.1016/j.rser.2018.03.003

Uzair, M., Anderson, T.N., Nates, R.J., 2017. The impact of the parabolic dish concentrator on the wind induced heat loss from its receiver. Sol. Energy 151, 95–101. https://doi.org/10.1016/j.solener.2017.05.022

Vahidi Bidhendi, M., Abbassi, Y., 2020. Exploring dynamic operation of a solar dish-stirling engine: Validation and implementation of a novel TRNSYS type. Sustain. Energy Technol. Assessments 40, 100765. https://doi.org/10.1016/j.seta.2020.100765

Apendix:

A mathematical model of a dish type collector and Stirling engine is generated using the equations given below and input parameters defined in Table 1(Hamza W, 2019). The input parameters are the climatic conditions of UAE, the system configuration of the considered Stirling Engine and opto-geometric configuration of the dish type collector. This remains constant throughout the year-round performance.

Table 1. **Specifications of Concentrating collector**.

Parameter	Value
Diameter (m)	5
Depth (m)	0.2
Reflectivity	0.94
Focal length	7.81
Rim angle (rad)	0.32
Aperture's area (m2)	19.63
Receiver parameters	
Receiver's diameter (m)	0.25
Receiver's radius (m)	0.13
Receiver aperture' area (m^2)	0.05
Thermal conductivity insulation K (W/mk)	0.04
Thickness insulation(m)	0.05
Emissivity of cavity	0.86
cavity length (m)	0.1
cavity diameter (m)	0.15
cavity radius (m)	0.075
Effective absorptance	0.24

Cavity area (m^2)	0.024
Concentration ratio	400
Optical efficiency	
Shading efficiency (ɣ)	0.9975
Reflectivity (P)	0.94
Transmission / Absorption efficiency (Ɛ)	0.97
Spillage efficiency (Ə)	0.98
Optical efficiency (η_o)	0.9

The optical efficiency of the dish type concentrator is given in equation 1, which is dependent on the material of the mirror, geometrical configuration and also combining various collector losses as given in Table 1.

$$\eta_o = ɣ * P * Ə * Ɛ \quad (1)$$

The thermal efficiency of the dish/Stirling system

$$\eta_r = \frac{Qu}{\eta_o * Qs} \quad (2)$$

Solar radiation incident energy on the collector surface is given in equation (3)

$$Qs = DNI * Aa \quad (3)$$

The receiver energy at the Stirling engine

$$Qr = \eta_o * Qs \quad (4)$$

The heat loss at the receiver end accounts to the conductive, convective and radiative losses considering the insulating material, medium surrounding the receiver, wind velocity.

$$Ql = Qcond + Qconv + Qradi \quad (5)$$

The useful energy transmitted to the receiver is given by equation (6)

$$Qu = Qr - Ql \quad (6)$$

The losses due to conduction convection and radiation are given in equation (7) to (14) considering the insulation material and its thickness in case of conductive losses, the natural and forced convection by considering the surrounding medium and wind velocity and radiation losses.

$$Qcond = \frac{Tcav - Tamb}{\ln\left|\frac{\left(\frac{Dcav}{2}\right)+\delta ins}{\left(\frac{Dcav}{2}\right)}\right| / 2\pi * Kins * Lcav} \quad (7)$$

$$Tcav = 4\sqrt{\frac{Qr}{At * Ɛr * 6}} \quad (7a)$$

$$NU_{Natural} = 0.088 * Gr^{\left(\frac{1}{3}\right)} * \left(\frac{Tcav}{Tamb}\right)^{0.18} * \cos\theta^{2.47} * \left(\frac{Dap}{Dcav}\right)^{(-0.982*\left(\frac{Dap}{Dcav}\right)+1.12} \quad (8)$$

$$H = h_{natural} * h_{force} \quad (9)$$

$$h_{natural} = \frac{NU * \lambda}{Dcav} \quad (9a)$$

$$h_{force} = 0.1967 * V^{1.849} \quad (9b)$$

$$Qconvection = H * Acav * (Tcav - Tamb) \quad (10)$$

$$Qradiation = Ɛeff * Acav * 6 * (Tcav^4 - Tamb^4) \quad (11)$$

The overall efficiency is the result of all efficiencies, optical efficiency, thermal efficiency, Stirling engine efficiency and finally the generator efficiency. It will essentially be the result of complete efficiency, collector overall area Aa and the DNI.

$$\eta_{total} = \eta_o * \eta_r * \eta_{st} * \eta_{gen} \quad (12)$$

The overall power out of the system considers the cumulative effect of all the efficiencies to incident solar energy on the collector.

$$P = \eta_{total} * Qs \quad (13)$$

Synthesis and characterization of carbonized nano-micro materials from agricultural and industrial wastes

Maria Kanwal [1], *Rao Arsalan Khushnood [1], Abdul Ghafar Wattoo [2]
[1]NUST Institute of Civil Engineering (NICE), National University of Sciences and Technology (NUST), H/12, Islamabad, 44000, Pakistan
[2]Department of Physics, Khawaja Farid University of Engineering and Information Technology (KFUEIT), Rahim Yar Khan, 64200, Pakistan
* E-mails: mariakanwal63@gmail.com, * arsalan.khushnood@nice.nust.edu.pk, dragwattoo@gamil.com

Abstract

This research explored the potential of corn cobs (CC) and rubber tyre (RT) as the pyrolysis feedstock with a focus on the yield of biochar. These wastes were placed individually into the pyrolysis fixed-bed reactor and pyrolysis was performed at 500°C in the nitrogen (N_2) environment. Carbonized CC (CCC) and carbonized RT (CRT) were collected after this process with the yield of 47.43% and 50.05% by weight of biomass respectively. Various properties of these carbonized materials were characterized and compared with the commercially available activated charcoal (ACC). The laser granulometry, scanning electron microscopy with energy dispersive spectroscopy (SEM & EDS), thermal gravimetric analysis (TGA), X-ray diffraction (XRD) and Fourier transform infrared (FTIR) spectroscopy were performed to assess the particle size, morphology, elemental composition, thermal stability, crystallinity and functional groups corresponding to each sample. The D_{50} of all the biochars was in the range of 3.42 µm to 4.78 µm with key minerals of $CaCO_3$ and Graphite, similar to ACC. The biochars showed the erratic surface texture from irregular micro-sheets to round nano-particles. All of the characteristics of biochars were comparable to the ACC; thus they can be used as the replacement material of carbon to modify various properties and reduce the cost of composite materials.

Keywords: Biochar, pyrolysis, carbonized materials, activated charcoal, agricultural and industrial wastes

I. Introduction

Biochar is the solid product of the biomass carbonization process and it has extensively been used as the soil modifier, a properties enhancer for cementitious materials and a CO_2 sequester for the atmosphere. The idea of thermally decomposing the biomass, in limited amount or absence of O_2, spawned when some Amazonia soils were unusually productive than the many fenced unfertile plots. Then it was observed that there was a larger amount of black carbon added by the unintentional activities of the native population (Glaser et al., 2001). Specifically, biochar from different sources may improve the water penetration, soil water retention, capacity to exchange ions, nutrient retention, pH and N use efficiency. Biochar particles have a strong influence on the biological processes of soils with implications for their biochemistry (Enders et al., 2012).

In the construction sector, the use of carbon-based materials is also a growing trend. Carbonaceous materials are not only contributing to elevating the mechanical, chemical, and electrical properties of cementitious composites but also participating in the confiscation of CO_2 and reducing the carbon footprint. As the production of cement is the most energy-intensive process and is responsible for the degradation of the environment because 7% CO_2 of the total environmental CO_2 is emitted during this process. Therefore, it is desirous to have more sustainable, environmentally friendly, and cost effective substitute to partially replace the cement in the cementitious composites (Khalid et al., 2018; Mahmood et al., 2020). Up to 1% replacement of cement (by weight) does not significantly alter the mechanical properties of concrete, though it can reduce the production cost of concrete by 3.4% in addition to reducing the carbon footprint (Akhtar and Sarmah, 2018).

Environmental wastes produced from agriculture or industries are hindering to meet the desired sustainability, therefore they should be properly employed in different forms to achieve the ecological goals. Pyrolysis of such feedstock is one of the energy-efficient and reliable procedures among other methods (gasification, fermentation, digestion, combustion, liquefaction, enzymatic conversion and chemical conversion) to get the biochar and bio-oil from both hard and soft biomasses. Biochars yielded from different feedstock biomasses and produced under different conditions show diverse physical and chemical properties. Research shows that the crop yield ratios were different when biochar from dissimilar feedstock was employed, similarly, they do not show analogous properties in cementitious materials as well (Akhtar and Sarmah, 2018; Rodriguez-Uribe et al., 2016). Therefore, we need to characterize various agricultural and industrial feedstock to categorize them according to their suitability in enhancing the respective properties and their field of applications. In this research, we have performed the pyrolysis of two agricultural and industrial feedstock biomasses, which are corn cobs (CC) and rubber tyre (RT). Then physical, thermal, chemical, and morphological studies were conducted to ensure their stability and proficiency in different environments.

II. Material and Methods

Both of the wastes were collected from different sources and sun-dried to ensure the complete curtailment of moisture as represented in Table 1. Then the fully dried biomasses were crushed and ground up to a size of 0.4 to 1.8 mm. Because previous research suggests that the smaller size of biomass feedstock is promising for a homogenous distribution of heat during the pyrolysis (Iftikhar et al., 2019).

Pyrolysis of each feedstock (200gm) was performed individually and put in a fixed bed reactor of pyrolysis assembly. The slow pyrolysis with 500°C was selected because this temperature is sufficient for the complete combustion of cellulosic and hemicellulosic-based biomasses (Lee et al., 2013). For an initial 30 min, the Nitrogen gas (N_2) was supplied at the rate of 300 ml/min to purge out the present gases in the assembly. Then there was a continuous supply of N_2 at the rate of 50 ml/min in order to produce the biochars in the inert environment. The heating ramp was adjusted to rising with a rate of 20°C/min until reached to 500°C. Then sustained over there for 30 min and gradually reduced. When the pyrolysis assembly turned into room temperature the biochar was collected from the pyrolysis bed reactor.

Table 1. Biomass type, source, drying duration and percentage yield of biochar

Biomass Type	Source	Sun drying (days)	Biochar Yield (%)
CC	*Corn Farm, Okara, Pakistan*	*30*	*47.43*
RT	*Local Tire Puncture Shop, Islamabad, Pakistan*	*0*	*50.05*

III. Analysis

The collected carbonized materials (biochar) were weighed and calculated the percentage yield of carbonized corn cobs (CCC) and carbonized rubber tyre (CRT) out of the biomass by using the expression given in eq. (1).

$$Biochar\ Yield\ (\%) = \frac{w_2}{w_1} \times 100 \quad (1)$$

Where; w_1 and w_2 are the weights in grams of biomass placed in the pyrolysis chamber and of produced biochar respectively. The biochars were further pulverized for a continuous one hour using mortar and pestle to achieve the nano-micro size. Then different characterizations were performed to investigate the particle size, surface morphology, and texture, elemental composition, thermal stability, crystallinity, and vibrating behavior then each property was compared with the commercially available activated charcoal (ACC).

The particle size distribution (PSD) of all samples was carried out on PSD analyzer LA-920 (HORIBA Laser Scattering) after sonication of 30 min. Surface morphology and elemental composition of all the biochars was studied by scanning electron microscopy with energy dispersive spectroscopy (SEM & EDS) on FEI Quanta FEG 250. The thermal stability was also compared with the ACC by checking the mass loss behavior at elevated temperatures, on a thermal gravimetric analyzer (TGA). Then X-ray diffraction (XRD) and Fourier transform infrared (FTIR) spectroscopy was performed to investigate the minerals composition, crystallinity, grain size, dislocation densities, micro-strains and vibrational signatures of samples. The grain size (G), dislocation densities (d), and micro lattice strains (s_m) were calculated from the XRD spectra by using the Debye-Scherrer's and Williamson-Hall's expressions by taking the full width at half maximum (FWHM) of peaks by using Xpert Highscore software, eq. (2), (3) and (4).

$$G = \frac{0.97\lambda}{(FWHM)cos\theta} \quad (2)$$

$$d = \frac{1}{G^2} \quad (3)$$

$$S_m = \frac{(FWHM)\ cos\theta}{4} \quad (4)$$

IV. Results and Discussions

The PSD data of all three samples are presented in Table 2. The results showed the minimum D_{50} values for CCC which is 3.42 µm and the CRT sample showed a slight higher D_{50} value (4.78 µm) but there was a maximum size of ACC. The variation in the sizes of samples might be due to their composition (char, oil, and gaseous content), agglomeration or entanglements of the particles or hardness/softness values of the biomasses or the biochars.

Fig. 1 is representing the XRD patterns of all specimens where the sharp or wide peaks corresponding to different minerals are also marked over there. All samples have the similar peaks which were originating from $CaCO_3$ (C) with miller indices (3 0 0), Graphite (G) with miller indices (0 0 2) and (1 0 0). Compared to other samples, ACC has a higher intensity and sharper peaks which are representing the good crystallinity and purity of the reference material. The CRT sample was crystalline than the agricultural biochar with sharp and very clear peaks of G and $CaCO_3$. But the CCC was somewhat amorphous and showed the wider peaks, however, the peaks were corresponding to the same minerals which were detected from the other samples so the formation of biochar or carbonized material was confirmed. The grain size, dislocation densities and micro lattice strains of all samples are shown in Table 2. Just like the particle size the grain size of CCC is also minimum, but the CRT and ACC has the same values of G, d, and S_m which is confirming that crystalline structure of the industrial waste produced biochar is analogous to the ACC.

Table 2. Evaluation of particle size and crystallinity of biochars

Sample Name	D_{50} (µm)	G (nm)	d (nm^{-2})	S_m
ACC	*13.61*	*5.193323*	*0.037077*	*0.07191*
CCC	*3.42*	*3.861702*	*0.067057*	*0.096706*
CRT	*4.78*	*5.193323*	*0.037077*	*0.07191*

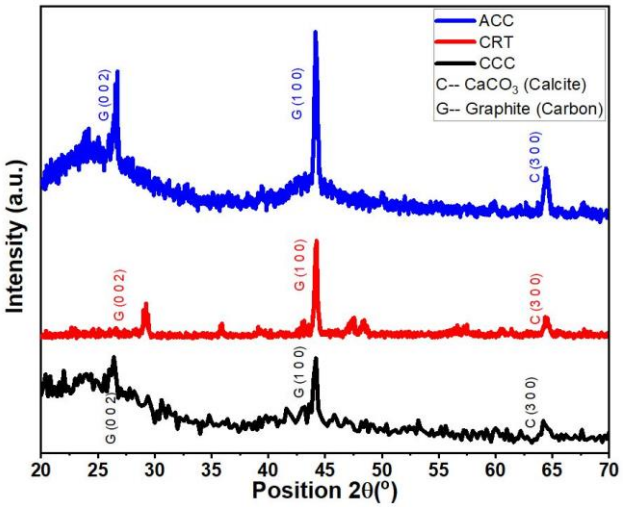

Fig. 1. XRD spectra of all samples

The FTIR spectra of all specimens are shown in Fig. 2. There was no prominent absorbance peak at 3650cm^{-1} which indicates the absence of stretching frequency of O-H (Khan et al., 2015). A major absorbance peak at 3423cm^{-1} is representing the N-H stretching frequency or it might be due to the O-H vibrations of carboxylic and phenolic groups (Zhang et al., 2019). The peaks in all biochars at 2925cm-1 was originating from asymmetric stretching of ammonia (CH_3) and primary amines majorly present in the agricultural biomasses or it might be due to the stretching of aliphatic functional groups (O-H). Other major peaks detected in all biochars at different absorbance bands were due to the existence of N-H at 1610 cm^{-1}, C=C Aromatic group or C-H aliphatic group at 1444 cm^{-1} and minor peaks of aromatic bending of C-H at 882 cm^{-1}. All these absorbance bands were closer to the ACC sample which confirms the formation of carbonaceous material during the pyrolysis.

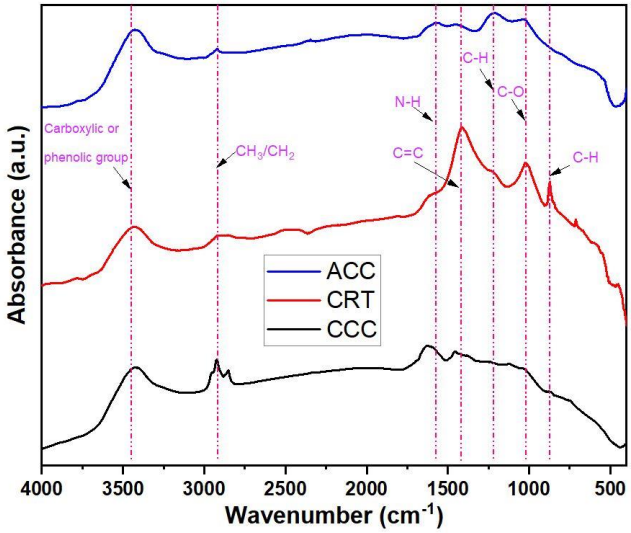

Fig. 2. FTIR spectra of all specimens

The TGA of both biochars along with ACC was also carried out, according to their mass loss behavior, the combustion process can be divided into three phases which are evaporation of moisture phase, combustions phase and burning out phase respectively (Qin et al., 2020). The initial mass loss up to 105°C is usually attributed to the evaporation of moisture but it was not consistent for each sample. The CRT sample having the industrial origin has the least moisture content which was 0.605% only by the weight of the sample. But the agricultural biochar (CCC) showed 2.16%, which is closer to the moisture content of the reference sample (3.13% by weight). The main combustion of fixed carbon and evaporation of volatiles is usually happened in the next phase from 105°C to onward till the burning. The CCC showed closer thermal stability to the ACC, both of these materials were highly stable even at 900°C but CRT was decomposed just around the 814°C.

Fig. 3(a-c) is representing the SEM micrographs and elemental composition of all samples. SEM images are confirming the particle sizes of all specimens as depicted by PSD. The CCC sample has a micro-sheets-like structure in addition to nano-micro particles but CRT has irregular and round shape nano-micro particles only. CRT has minimum particle size and it has seemed that all of the particles are in the nano range which was not clear during the PSD analysis due to the agglomerations of particles. The EDS analysis showed the carbon content of 90.99%, 62.91% and 91.37% for ACC, CRT, and CCC samples respectively. Therefore, it can be said that the CCC sample has similar Carbon as for ACC and can be used in place of carbon in various applications.

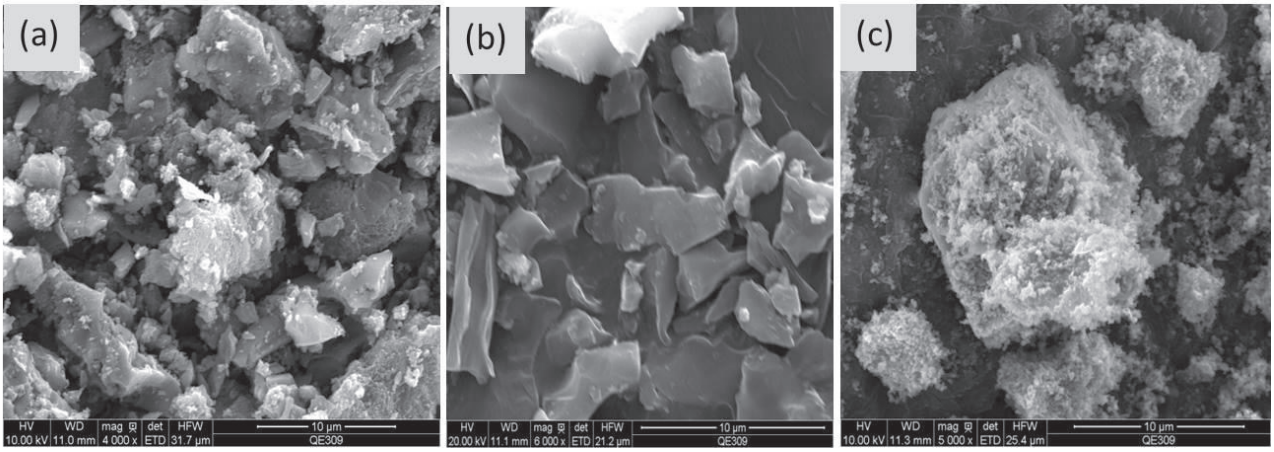

Fig. 3. (a) SEM image of ACC, (b) SEM image of CCC and (c) SEM image of CRT

V. Conclusion

In this study, the biochars from agricultural and industrial wastes have been synthesized and their characteristics are compared with the ACC. So, the following conclusions can be drawn from this study;

- The pyrolysis of agricultural and industrial biomasses is a competent way to produce green, carbonized materials with an approximate average yield of 47 to 50% by weight of biomasses. The one hour grinding of produced biochars is sufficient to convert them into nano-micro range with D_{50} of 3.42 and 4.78 µms of CCC and CRT respectively but proper sonication is recommended before performing the PSD.
- The crystallinity and presence of carbon-based minerals confirm the formation of carbonized materials (biochar) from all wastes with rhombohedral and hexagonal crystal structures. The higher absorbance of the C=C aromatic group in both biochars confirmed their close proximity to ACC.
- The CCC can sustain very high temperatures compared to other biochars due to the presence of higher carbon content which is 91.37%. The biochars from different sources represent the different morphology but they all are exceptional consists of maximum proportions of carbon.

Acknowledgement

The research was funded by Higher Education Commission (HEC), Pakistan, under the project of National Research Programme for Universities (NRPU), Project# 10232. Therefore, the authors would like to greatfully acknowledge to HEC, Pakistan.

Reference

Akhtar, A., Sarmah, A.K., 2018. Novel biochar-concrete composites: Manufacturing, characterization and evaluation of the mechanical properties. Sci. Total Environ. 616–617, 408–416. https://doi.org/10.1016/J.SCITOTENV.2017.10.319

Enders, A., Hanley, K., Whitman, T., Joseph, S., Lehmann, J., 2012. Characterization of biochars to evaluate recalcitrance and agronomic performance. Bioresour. Technol. 114, 644–653. https://doi.org/10.1016/j.biortech.2012.03.022

Glaser, B., Haumaier, L., Guggenberger, G., Zech, W., 2001. The "Terra Preta" phenomenon: A model for sustainable agriculture in the humid tropics. Naturwissenschaften 88, 37–41. https://doi.org/10.1007/s001140000193

Iftikhar, H., Zeeshan, M., Iqbal, S., Muneer, B., Razzaq, M., 2019. Co-pyrolysis of sugarcane bagasse and polystyrene with ex-situ catalytic bed of metal oxides/HZSM-5 with focus on liquid yield. Bioresour. Technol. 289, 121647. https://doi.org/10.1016/J.BIORTECH.2019.121647

Khalid, A., Khushnood, R.A., Mahmood, A., Ferro, G.A., Ahmad, S., 2018. Synthesis, characterization and applications of nano/micro carbonaceous inerts: A review. Procedia Struct. Integr. 9, 116–125. https://doi.org/10.1016/j.prostr.2018.06.019

Khan, S., Waqas, M., Ding, F., Shamshad, I., Arp, H.P.H., Li, G., 2015. The influence of various biochars on the bioaccessibility and bioaccumulation of PAHs and potentially toxic elements to turnips (Brassica rapa L.). J. Hazard. Mater. https://doi.org/10.1016/j.jhazmat.2015.06.050

Lee, Y., Park, J., Ryu, C., Gang, K.S., Yang, W., Park, Y.K., Jung, J., Hyun, S., 2013. Comparison of biochar properties from biomass residues produced by slow pyrolysis at 500°C. Bioresour. Technol. 148, 196–201. https://doi.org/10.1016/j.biortech.2013.08.135

Mahmood, A., Khushnood, R.A., Zeeshan, M., 2020. Pyrolytic carbonaceous reinforcements for enhanced electromagnetic and fracture response of cementitious composites. J. Clean. Prod. 248, 119288. https://doi.org/10.1016/J.JCLEPRO.2019.119288

Qin, L., Wu, Y., Hou, Z., Jiang, E., 2020. Influence of biomass components, temperature and pressure on the pyrolysis behavior and biochar properties of pine nut shells. Bioresour. Technol. 313, 123682. https://doi.org/10.1016/j.biortech.2020.123682

Rodriguez-Uribe, A., Misra, M., Behazin, E., Ogunsona, E., Anyia, A.O., Mohanty, A.K., 2016. Mechanical, Chemical, and Physical Properties of Wood and Perennial Grass Biochars for Possible Composite Application. BioResources 11. https://doi.org/10.15376/biores.11.1.1334-1348

Zhang, C., Zhang, N., Xiao, Z., Li, Z., Zhang, D., 2019. Characterization of biochars derived from different materials and their effects on microbial dechlorination of pentachlorophenol in a consortium. RSC Adv. https://doi.org/10.1039/C8RA09410A

The Effect of Air Layer Thickness on Insulation Thickness Applied to Buildings with Sandwich Walls

[1]Okan KON, [2*]İsmail CANER
[1,2] Balikesir University Engineering, Faculty Department of Mechanical Engineering,
Cagis Campus, Balikesir, 10145, Turkey

* ismail@balikesir.edu.tr

Abstract
In this study, the effect of different air layer thickness between two brick walls called the Sandwich wall on insulation thickness to be applied was investigated. The recommended heat transfer coefficients for each climate zone were taken from the Turkish Insulation Standart (TS 825). It has been taken into consideration that the wall surfaces between the two walls are unpainted and painted with aluminum-containing. Conduction, convection, and radiation heat transfers are used to calculate the thermal resistances of the air layer of different thicknesses. The temperature values of January, which is the coldest month and given for each climate zone in outdoor temperatures are used. Indoor temperature is accepted as 19 ^{0}C given in TS 825. Rock wool is used as an insulation material. Firstly, the minimum insulation thicknesses for rock wool insulation material with unpainted wall surfaces and painted with aluminum-containing are calculated for each climate zone recommended. Secondly, minimum insulation thicknesses for rock wool insulation material between two walls without using the air layer were determined. Finally, differences in insulation thickness and cost-saving due to insulation material were investigated.

Keywords: Sandwich wall, heat insulation, air layer, cost saving

I. Introduction

The aim of the study is to investigate the effect of the thickness of the air layer between two brick walls on insulation thickness. The application of unpainted brick with an emissivity value of 0.93 and painted with aluminum-containing with an emissivity of 0.27 on the wall surfaces between the two walls was examined. The heat resistance of the air layer used in the calculations was calculated by taking the month of January with the lowest outdoor temperature value. Air layer thickness is accepted as 5, 10, 15, 20, 25 cm. Rock wool with a conduction heat transfer coefficient of 0.04 W/m.K has been taken as an insulation material. The calculations were made for five climate zones given in TS 825. The thickness of the rock wool insulation material was calculated for unpainted sandwich walls and painted sandwich walls with aluminum-containing (Al painted). Then, the insulation thickness was calculated without an air layer between the two walls directly applying rock wool insulation material. Insulation thickness difference and insulation material cost saving have been investigated. The effect of applying paint with different emissivity between the air layer and this layer for the buildings with sandwich walls on the insulation material to be applied was investigated.

II. Methodology

II. I. Calculation of air layer thermal resistance

To find the convection heat transfer coefficient of the air layer, the formulations given below were used.

Grasshof sayısı (Cengel, 2014 ; Al-Sibai, Hillemacher et al.; 2013)

$$Gr=\frac{g.x^3.\beta.(T_s-T_0)}{\vartheta^2} \quad (1)$$

Here, g is gravitational acceleration, T_s is surface temperature, T_0 is outdoor temperature, ϑ is kinematic viscosity, β is film temperature and x is air layer thickness.

Raleigh number;

$$Ra=Gr.Pr \quad (2)$$

Here, Gr is grasshof number and Pr is prandatl number.

Nusselt number;

If $Ra<10^3$ $Nu=1$ (3)

If $10^3<Ra<10^4$ and $\frac{H}{x}<83$ $Nu=0.38.Ra^{0.25}.(\frac{H}{x})^{-0.25}$ (4)

For $10^4<Ra<10^7$ and $\frac{H}{x}<83$ $Nu=0.42.\ Pr^{0.012}.Ra^{0.25}.(\frac{H}{x})^{-0.25}$ (5)

For $10^7<Ra<10^9$ $Nu=0.049.Ra^{0.33}$ (6)

Convection heat transfer coefficient;

$$h_{conv.}=\frac{Nu.\lambda_a}{x} \quad (7)$$

Here, λ_a is conduction heat transfer coefficient, x is air layer thickness and H is the height of the air layer. When, Nu=1 olduğunda conduction heat transfer occurs.

The radiation heat transfer coefficient for air layer (Cengel, 2014; Lewandowski, and Lewandowska-Iwaniak; 2014)

$$h_{rad.}=\sigma.\varepsilon.(T_1+T_2).(T_1^2+T_2^2) \quad (8)$$

Where, σ is Stefan Boltmann constant, ε is emissivity, T_1 and T_2 are surface temperatures between walls. The equations for combine heat transfer coefficient according to convection and radiation heat transfer and thermal resistance are given below (Cengel, 2014; Holman, 2014, Lewandowski, and Lewandowska-Iwaniak; 2014, TS 825, 2013);

$$h_{comb.}=h_{conv.}+h_{rad.} \quad (9)$$

$$R_{comb.}=\frac{1}{h_{comb.}} \quad (10)$$

II. II. The overall heat transfer coefficient calculation

Overall heat transfer coefficient for the wall,

$$U=\frac{1}{(R_i+R_w+R_{comb.}+\left(\frac{y}{\lambda}\right)_{ins}+R_o)} \quad (11)$$

Total thermal resistance for non insulation wall according to $R_{t,w}$ is the overal heat transfer coefficient of the wall,

$$U=\frac{1}{(R_{t,w}+\left(\frac{y}{k}\right)_{ins})} \quad (12)$$

Here, R_i and R_0 are indoor and outdoor surface thermal resistances. y is insulation thickness; λ is insulation materials conduction heat transfer coefficient. (y/λ) is insulation layers' thermal resistance (Bolattürk, 2006; Kaynaklı and Yamankaradeniz, 2007, Kon, 2017).

II. III. Values used in calculations

Outdoor air temperature for January and indoor air temperature given in TS 825 are shown in Table 1. External wall structures and properties are given in Table 2. Table 3 shows the external wall heat transfer coefficients for five climate zones recommended in TS 825. Rock wool is used as an insulation material. The conduction heat transfer coefficient value of the rock wool insulation material is 0.04 W/m.K and the cost is 80 $/m^3$. (Kürekçi,2016).

Table1. Outdoor air temperature for January and indoor air temperature (TS 825, 2013)

Climate zone	Outdoor Temperature (^{0}C)	Indoor Temperature (^{0}C)
Zone 1	*8.4*	
Zone 2	*2.9*	
Zone 3	*-0.3*	*19*
Zone 4	*-5.4*	
Zone 5	*-10.5*	

Table 2. External wall structes and properties (TS 825, 2013)

External wall construction component	Thickness (m)	Thermal Conductivity λ (W/mK)
Thermal resistance of inner surface *(R_i=0.130 m^2.k/W)*		
lime-cement mortar interior plaster	*0.020*	*1.000*
Horizontal perforated brick	*0.085*	*0.330*
Air layer	---	---
Rock wool Insulation	---	*0.040*
Horizontal perforated brick	*0.135*	*0.330*
Cement mortar exterior plaster	*0.030*	*1.600*
Thermal resistance of external surface *(R_0=0.04 m^2.k/W)*		

Table 3. The heat transfer coefficients for five climate zones recommend in TS 825 (TS 825, 2013)

Climate zone	External wall Heat transfer coefficient (W/m^2.K)
Zone 1	*0.66*
Zone 2	*0.57*
Zone 3	*0.48*
Zone 4	*0.38*
Zone 5	*0.36*

IV. Results and discussions

In Table 4, insulation thicknesses recommended for each climate zone are given to TS 825 without the air layer. In Figure 1, the thermal resistances for five climate zones based on air layers of different thicknesses and unpainted and Al painted wall surfaces are shown. In Figure 2, insulation thicknesses based on air layers of different thicknesses and unpainted and Al painted wall surfaces in five climatic regions are given. In Figure 3, a) difference in insulation thicknesses depending on air layers of different thicknesses and unpainted and Al painted wall surfaces in five climate regions, b) insulation material cost saving is shown.

Table 4. Recommended insulation thickness according to TS 825 without air layer

Climate zone	Insulation Thickness (m)
Zone 1	*0.026*
Zone 2	*0.035*
Zone 3	*0.049*
Zone 4	*0.070*
Zone 5	*0.076*

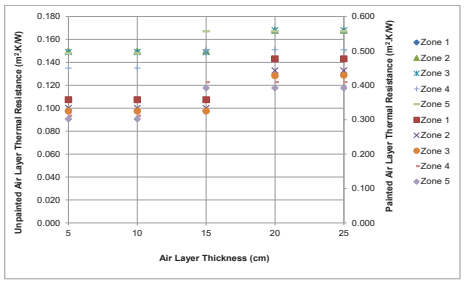

Fig. 1. Thermal resistances of five climate zones due to different thickness of air layers and unpainted and Al painted wall surfaces

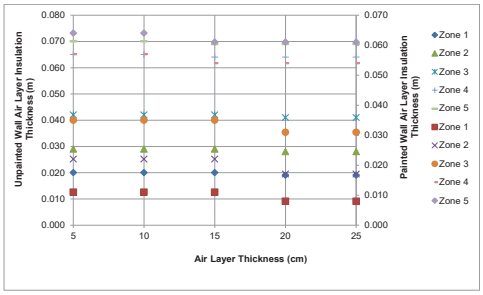

Fig. 2. The insulation thicknesses of five climate zones due to different thickness of air layers and unpainted and Al painted wall surfaces

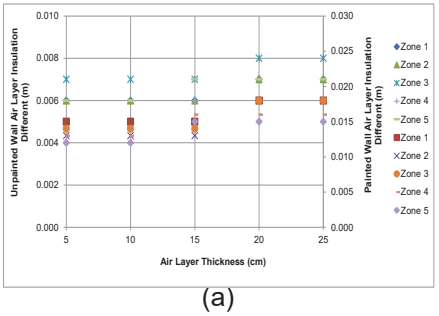

(a)

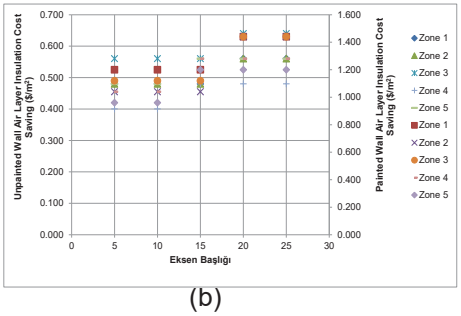

(b)

Fig. 3. Depending on air layers of different thickness in five climatic zones and unpainted and Al painted wall surfaces a) difference in insulation thickness b) insulation material cost saving

In different air layer thicknesses for sandwich walls with unpainted bricks; thermal resistances were calculated between 0.135 to 0.170 m^2.K/W in five climate zones. For different air layer thicknesses for Al painted wall surfaces between the air layers; thermal resistances were calculated between 0.302 to 0.477 m^2.K/W. Since the emissivity values of the Al painted wall surfaces are lower, the thermal resistance values are determined much higher than the unpainted wall surfaces.

Insulation thicknesses recommended in TS 825 for rock wool insulation material in different air layer thicknesses, for sandwich walls with unpainted brick between the airs layers were calculated between 0.019 to 0.070 m. Insulation thicknesses for the sandwich wall with Al painted between the air layers of different thicknesses were calculated between 0.008 to 0.064 m in five climate zones. Since the thermal resistance values of the paint containing aluminum are much higher than the unpainted air layer, the rock wool insulation thickness is much lower at Al painted wall.

The recommended insulation thickness values according to TS 825 for sandwich walls with rock wool insulation without an air layer are 0.026 m for the first climate zone, 0.035 m for the second climate zone, 0.049 m for the third climate zone, 0.070 m for the fourth climate zone and It is calculated as 0.076 m for the fifth climate zone

The difference in insulation thickness recommended in TS 825 for rock wool insulation material without air layer and with different air layer thicknesses, for sandwich walls with unpainted brick between air layers were calculated between 0.006 to 0.008 m. The difference in insulation thicknesses for the sandwich wall with Al painted on the wall surfaces between the air layer and without air layer was calculated between 0.012 to 0.018 m in five climate zones. In this case, the cost-saving value for the rock wool insulation material is calculated between 0.480 to 0.560 $/m^2 for the rock wool insulation material with different air layer thicknesses, and the non-painted brick walls between the air layers. The insulation thicknesses of the rock wool cost saving are calculated between 0.960 to 1.440 $/m^2 for the sandwich wall with Al painted on the wall surfaces between different air layers and without air layer.

V. Conclusions

For each climate zone, the thermal resistance of the air layer generally increases as the air layer increases. However, while in the first, second and third climate zones, it remains fixed separately at 5, 10 and 15 cm air layer thickness and 20 and 25 cm thickness, while in the fourth and fifth climatic zone, it is separately fixed at 5 and 10 cm thickness and 15, 20 and 25 cm thickness. The difference in thermal resistance value for each climate zone in the air layer with an unpainted wall surface is lower than the thermal resistance difference for each climate zone in the air layer with an Al painted wall surface.

The difference in thickness of the insulation between the rock wool insulation thickness with the unpainted wall and rock wool insulation without the air layers was found to be 1 cm and the cost-saving related to this was found below 1 $/m^2. The difference in insulation thickness between the sandwich wall with Al painted wall and insulated with rock wool and the rock wool insulation wall without air layer was determined to be around 2 cm and the cost-saving related to this was determined to be around 1.5 $/m^2. Considering the cost-saving value of rock wool insulation material, it can be seen that it will provide a significant saving when the entire external wall surface area is considered. The importance of different emissivity paint application of the air layer for the sandwich walls is seen.

In the future study, cost saving and energy saving calculations based on different insulation thickness calculation methods and air layer will examined.

References

Al-Sibai, F., Hillemacher, B., Burghold, M. and Kneer, R., 2013. Untersuchung zur dämmwirkung von wärmedämm-materialien mit ınfrarot reflektierenden oberflächen. Bauphysik, 35, 4, 225-234. https://doi.org/10.1002/bapi.201310071

Bolattürk, A., 2006. Determination of optimum insulation thickness for building walls with respect to various fuels and climate zones in Turkey. Applied Thermal Engineering, 26,11-12,1301-1309. https://doi.org/10.1016/j.applthermaleng.2005.10.019

Cengel, Y., 2014, Heat and mass transfer: fundamentals and applications. McGraw-Hill Higher Education.

Holman, J.P., 2014, Heat transfer, McGraw-Hill Higher Education.

Kon, O. 2017. Ekolojik sürdürülebilirlik kapsamında binalarda kullanılan çevre dostu ısı yalıtım malzemeleri ve bunlara bağlı yenilenebilir yakıt tüketimi, Academia Journal of Engineering and Applied Sciences, Vol. 1, Issue 3, 143-155.

Kaynaklı, Ö.,Yamankaradeniz, R., 2007, Isıtma süreci ve optimum yalıtım kalınlığı hesabı, VII. Tesisat Mühendisliği Kongresi, İzmir, Türkiye, 25-28 Ekim, 187-195.

Lewandowski, W. M. and Lewandowska-Iwaniak, W. 2014. The external walls of a passive building: A classification and description of their thermal and optical properties, Energy and Buildings. Elsevier B.V., 69, 93–102. https://doi.org/10.1016/j.enbuild.2013.10.021

Kurekci, N. A., 2016. Determination of optimum insulation thickness for building walls by using heating and cooling degree-day values of all Turkey's provincial centers', Energy and Buildings. https://doi.org/10.1016/j.enbuild.2016.03.004

Türk Standardı, TS 825, Thermal Insulation Regulations in Buildings, December 2013.

Comfort as the dead state of buildings: a preliminary discussion.

Valentina Bonetti
University of Strathclyde, Department of Mechanical and Aerospace Engineering, 75 Montrose St, Glasgow, G1 1XJ, UK

E-mail: valentina.bonetti@strath.ac.uk

Abstract:
Exergy is typically defined as the maximum work that can be extracted from a system when reaching equilibrium with its “reference environment” - a large region unaffected by the interactions - and derives from Gibbs’ original concept of “available energy of a body and medium”. The reference environment definition plays a key role in exergy analysis but is still controversial, especially in the case of buildings; the most popular choice is the local outdoor air, because readily available and largely unaffected by the presence of the building, but its fluctuating conditions pose various challenges. The controversy around the reference environment arguably remains one of the main blockers for the practical application of building exergy methods. However, going back to the origins, Gibbs defined available energy not only for a “body and medium”, but also for the case of a “body alone”, a system formed by subsystems in non-equilibrium conditions. Later, exergy too was defined for this second case, as the subsystem contribution to the body available energy. In the case of the “body alone”, the reference is the “dead state” (or “thermostatic state" of the body), in place of the reference environment. The main idea of this article is that building exergy analysis can be based not only, as currently, on the exergy definition originated by Gibbs’ case of the “body and medium”, but alternatively on the exergy definition originated by the case of the “body alone”, for which a large environment is not needed. The outdoor reference environment can thus be substituted by an indoor “dead state”, making the analysis simpler and “warm" and “cool" exergies more relevant to practical heating and cooling applications. The study discusses typical fluctuations of indoor conditions and the impact on exergy values, and proposes a fixed dead state as the exergy reference.

Keywords: Exergy, reference environment, dynamic analysis.

I. Introduction

Building exergy analysis is an interesting concept, but it is hardly applied or even known in practice. The controversy on the reference state definition, the complexity of the analysis and the lack of convincing practical benefits are possibly the biggest obstacles to its utilisation. In the author’s opinion, the main problem is the adoption of the varying outdoor air conditions as the reference state. First of all, outdoor fluctuations, combined with the inertia of the building envelope, make the outdoor environment not directly available; secondly, the meaning of “warm" and “cool" exergies based on the variable outdoor temperature can be misleading, especially because they are often treated as if they were always usable for heating and cooling. For instance in Choi et al. (2020) (left of page 11), energy stored at 25°C when the outdoor air is at 30°C is proposed as cool exergy useful for indoor cooling, and energy stored at 15°C when the outdoor air is at 10°C is considered as warm exergy that could be used for indoor heating, in a case where the indoor temperature is 20°C; this is misleading because defining energy as “warm" or “cool" because it is less cold or less hot than the outdoor air does not necessarily make it useful for heating or cooling purposes, but at most for some fresh air pretreatment. As already observed in Bonetti (2017) (where some of the benefits of an exergy reference based on indoor comfort are discussed), defining warm and cool exergies on the base of outdoor variable conditions is not compatible with the common meaning of “warm" and “cold", and cannot be directly translated into heating or cooling.

One alternative to the variable outdoor air reference is the use of indoor conditions. In the past, indoor air has been considered as a reference state for building exergy analysis, but the main argument against its use has been the fact that indoor air is not a large environment, as required by the definition of exergy (Schmidt & Torio 2011). But where did this requirement come from? Answering the question requires going back to the origins.

Gibbs (1873) was the first to incorporate the first and second law of thermodynamics in one equation, in his paper "Graphical Methods in the Thermodynamics of Fluids"; the combination of the first and second law led him to introduce the concept of “available energy". Gibbs distinguished two cases: a "body alone", in internal non-equilibrium conditions, and a "body and medium", in non-equilibrium conditions with each other.

In the case of the “body alone", the available energy of the body is the greatest amount of mechanical work that ideally can be obtained by taking the body, without any net contributions of energy from external objects, from the initial non-equilibrium condition to its point of stable or neutral equilibrium (on its “surface of dissipated energy") that

various forms, like a difference in the pressure of some of its part, or a gradient in temperature, or even different chemical compositions. It is important to observe that the term “body" refers not necessarily to a single entity but to a system that is potentially including several subsystems and processes (Gaggioli 2012). In the case of the “body and medium", the medium is supposed to be at uniform pressure and temperature and it is defined as “reference environment": a large subsystem that is not affected by the interactions with the other components of the overall system, and is represented by a plane in Gibbs’ energy-entropy-volume space. The available energy in this case is the distance (on the energy axis) from the point corresponding to the initial conditions of the body to the point with the same entropy and volume on the reference plane. Even if the body is in internal equilibrium, the combination between body and medium can still have available energy, unless they are in the same conditions.

The vast majority of exergy analysis is based on the second case, the “body and medium", and relies on the definition of a reference environment (the medium). However, Gaggioli (2012) examined in depth the meaning of “dead state" and highlighted that exergy can be based on Gibbs’ “available energy of a body" (the first case mentioned above), which does not require a reference environment. The exergy of each subsystem of an overall system (in which no large one is required) was defined by Gaggioli (1998) as the subsystem contribution to the available energy of the overall system, with the reference being the overall system “dead state" - its “thermostatic" conditions, when all the sub-parts are in equilibrium, subject to the given constraints. Such subsystem exergy is additive, and exergy balances can be used to perform exergy analysis. According to Gaggioli (2012), If subsystems are free to exchange entropy S and volume V, the exergy content Ex_i of each subsystem i is $Ex_i = E + p_f - T_f S$, where the subscript f indicates the dead state.

The main idea of this study is that building exergy analysis can be based on Gibbs’ case of the “body alone" and does not require a large environment, but can rather use, as reference, a definition of dead state related to indoor comfort. In order to make the “body alone" relevant to building design, its boundaries include the indoor air and all the inner parts of the envelope that have a direct impact on indoor conditions (in practice, the depth of thermal mass that effectively contributes to the envelope interior storage). The dead state here proposed as a reference is a fixed “target comfort" state, in order to avoid all the problems linked to reference fluctuation described by Pons (2019). This choice makes the definition of “warm" and “cool" exergies more straightforward to understand and relevant to heating and cooling strategies. This brief article starts the discussion on how different the models of realistic cases are from Gibbs’ “body alone", how distant the thermostatic temperature of a typical system could be from a fixed dead state, and what impact discrepancies have on exergy values based on this reference.

II. The dead state of a “box" building

Gibbs’ “body alone" was a closed and isolated system - although Gaggioli mentioned the possibility of having an open system (Gaggioli 1961), where the dead state might vary. The closest real system which could be considered closed and isolated is a building with external high insulation, no openings and no internal loads, like the one in Fig. 1a, modelled with ESP-r for the UK climate. The outdoor has very low impact on its indoor conditions: considering system boundaries that include the envelope inner layers and the indoor air (the red rectangle on the right of Fig. 1b), thermostatic conditions (that can adopted as “dead state") are reached after a short heating intervention, and freely maintained very stable for a long time (4 weeks are represented in Fig. 1b). Model and data are available at Bonetti (2020).

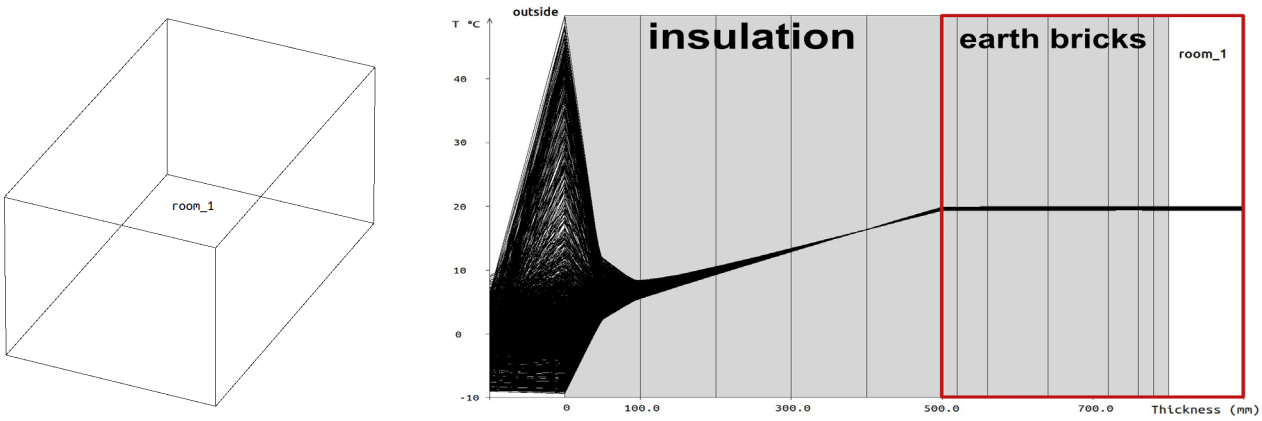

(a) ESP-r box model in a UK climate.

(b) Cumulative values of intra-construction T in a wall of the box model (February).

Fig. 1: The first case study: a box model with 500 mm of external high insulation and 300 mm of earth on the internal layers.

Real buildings, especially in case of low performances, are not closed and isolated because of transmission losses, internal loads, solar gains, air exchanges. Consequently, the system constituted by the inner envelope layers and indoor air has a variable thermostatic state (the point at which all the subsystems are in equilibrium). However, the internal variations are much more limited than the outdoor air fluctuation, particularly for good envelopes; it is interesting to calculate the thermostatic state of real buildings for different zones and control strategies.

In this brief article, the average-performing case of Fig. 2 is sufficient to illustrate the point (data available from Bonetti (2020)). The system boundaries are defined through an approximate estimate of “periodic penetration depth" of 10 cm (or less, if an insulation layer is encountered) as suggested by the Standard DIN 4108. Different control strategies impact significantly. The thermostatic temperature T_{eq} comes from the system energy balance:

$T_{eq}(t) = \sum_i m_i c_i T_i(t) / \sum_i m_i c_i$ (where i = subsystem, m = mass, c = specific heat, t = hourly timestep).

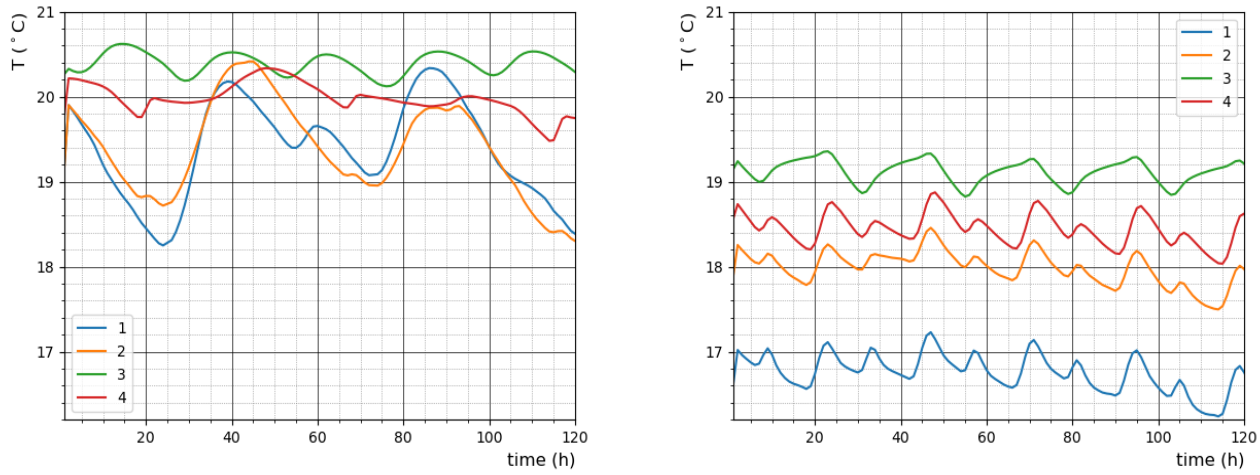

(a) Radiant wall heating, set-point 21°C at night-time (9pm-6am) (b) Basic air ideal heating, set-point 22°C (6am-8am + 6pm-10pm)

Fig. 2: Thermostatic temperature T_{eq} of 4 different thermal zones of a realistic model (5-11 Feb, UK winter typical week).

IV. Thermal exergy sensitivity

Rosen & Dincer (2004) introduced the sensitivity σ, a measure of how exergy is impacted by variations in the reference state. In the case of thermal exergy, if heat Q is exchanged at T with a reference T_0 that varies by ΔT_0:

$$\sigma = \frac{Ex(T_0 + \Delta T_0) - Ex(T_0)}{Ex(T_0)} = \frac{Q\left(1 - \frac{T_0 + \Delta T_0}{T}\right) - Q\left(1 - \frac{T_0}{T}\right)}{Q\left(1 - \frac{T_0}{T}\right)} = \frac{\Delta T_0}{T_0 - T} \quad (1)$$

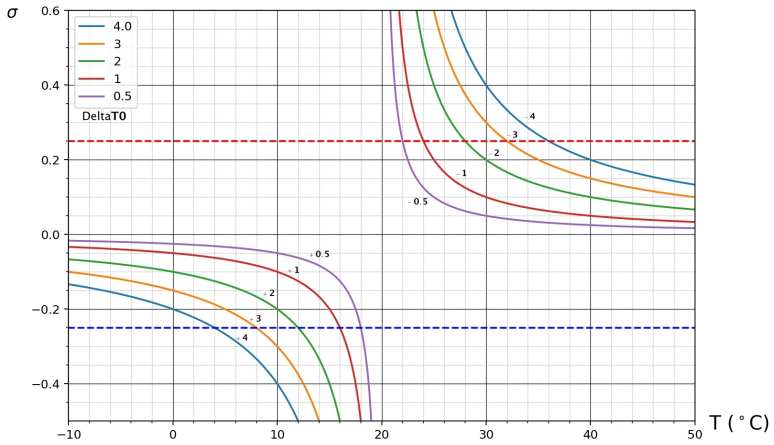

Fig. 3: Thermal exergy sensitivity σ against heat temperature T, for $T_0 = 20°C$ and different reference variations ΔT_0.

even for temperatures quite close to the reference ($\pm 10\%$ around $15°C$ and $25°C$). For relatively large variations ($\pm 4°C$), only exergies at temperatures under $4°C$ or over $36°C$ remain reasonably accurate ($\pm 25\%$). The acceptance criteria depends on the aim of the analysis and should be investigated more in depth case by case.

V. Discussion: dead state and comfort targets

In most buildings the indoor environment, including the inner layers of the envelope, is in relatively stable conditions, dictated by comfort targets and control strategies. As soon as the temperature falls out of an acceptable range, the HVAC system intervenes to bring the conditions back to the desired value. If we define an overall system with boundaries that include the inner part of the envelope, the HVAC distribution (e.g. radiators) and the indoor and fresh air, its subsystems change dynamically to adapt to loads and chase the desired comfort. Although the thermostatic state of such a system is fluctuating, its conditions are generally fairly close to the comfort target, and adding all the internal loads and fluxes takes them even closer. We could then define a fixed dead state equal to the comfort requirements and obtain exergy values that are easy to calculate and interpret, and not far from the instantaneous reality of the indoor ambient (and thus relatively accurate, as discussed in section IV). An in-depth discussion of why the exergy reference state should be fixed has been already presented by Pons (2019). It could be useful to consider whether the building exergy dead (or reference) state would be better defined through a fuzzy logic, to reflect the intrinsic nature of comfort as a range rather than a single value.

VI. Conclusions and future work

The main idea of this article is that building exergy analysis can be based on a fixed reference equal to the target indoor comfort conditions - a sort of “design dead state" of the indoor environment. The theoretical justification of this choice comes from the fact that exergy does not need a large reference environment to be defined, but can instead be based on the Gibbs’ case of the “body alone". Some advantages of this selection, focus of past and future work, are an easier and clearer analysis - the meaning of “warm" and “cold" exergies now coincides with the common meaning of “warm" and “cold" - and a shifted attention to the energy quality of the indoor ambient, which could for instance facilitate the design of demand-offer decoupling strategies.

Acknowledgements

The author thanks the Engineering and Physical Sciences Research Council U.K. (EPSRC, Grant No.1586601) and the Building Research Establishment (BRE) for the past financial support.

References

Bonetti, V., 2017. Dynamic exergy analysis for the built environment: fixed or variable reference?, *in* ‘9th International Exergy, Energy and Environment Symposium (IEEES-9)’, Split, Croatia.

Bonetti, V., 2020. ‘GitHub repository: The dead state of buildings (models and data)’.
URL: *https://github.com/ValentinaBonetti/TheDeadStateOfBuildings (accessible from January 2021)*

Choi, W., Ooka, R. & Shukuya, M., 2020. ‘Unsteady-state exergetic performance comparison of externally and internally insulated building envelopes’, *International Journal of Heat and Mass Transfer* **163**.

Gaggioli, R., 2012. ‘The Dead State’, *International Journal of Thermodynamics* **15**(4), 191–199.

Gaggioli, R. a., 1961. ‘The concept of available energy’, *Chemical Engineering Science* **16**, 87 – 96.

Gaggioli, R. A., 1998. ‘Available Energy and Exergy’, *International Journal of Applied Thermodynamics* **1**, 1–8.

Gibbs, J., 1873. ‘A Method of Geometrical Representation of the Thermodynamic Properties of Substances by Means of Surfaces’, *Transactions of the Connecticut Academy of Arts and Sciences* pp. 382–404.

Pons, M., 2019. ‘Exergy Analysis and Process Optimization with Variable Environment Temperature’, *Energies* **12:4655**.

Rosen, M. A. & Dincer, I., 2004. ‘Effect of varying dead-state properties on energy and exergy analyses of thermal systems’, *International Journal of Thermal Sciences* **43**(2), 121–133.

Schmidt, D. & Torio, H., 2011. ECBCS Annex 49: Low Exergy Systems for High-Performance Buildings and Communities, Technical report, Fraunhofer IBP.

Geospatial assessment of *Jatropha curcas* plantation in Qatar: A GIS modelling approach

[1]Mohammad Alherbawi, [1]Maryam Haji, [1]Hazrath Bilal Khan, [1]Gordon McKay, [1,2*]Tareq Al-Ansari
[1] Division of Sustainable Development, College of Science and Engineering, Hamad Bin Khalifa University, Qatar Foundation, Doha, Qatar.
[2] Division of Engineering Management and Decision Sciences, College of Science and Engineering, Hamad Bin Khalifa University, Doha, Qatar.
* E-mail: talansari@hbku.edu.qa

Abstract
Qatar is one of the largest producers and exporters of fossil-based fuels including natural gas. Though, the country is striving to diversify its energy resources by incorporating renewables to mitigate associated emissions and expand its fossil reserves lifetime for the coming generations. Energy crops are believed to be amongst the prominent resource for biofuel production for being carbon neutral. However, no attempts were made to grow energy crops due to the extremely limited arable land area as well as the water scarcity in this part of the world. Meanwhile, *Jatropha curcas* is preferred over other energy crops due to its superior agronomical traits, where it can grow in non-arable lands and harsh climates with minimal water requirements. Besides, it proved to yield higher seeds with the supply of treated sewage effluent, which is widely available and not completely utilised in Qatar. According to the UN's Food and Agricultural Organisation, *Jatropha* can grow within 30°N and 35°S latitudes. Yet, there is a need to investigate suitable sites to grow *Jatropha* across Qatar. As such, this study utilises the Geographic Information System (GIS) and Analytical Hierarchy Process (AHP) to identify the suitable sites based on multicriteria including soil type, depth and pH contents, as well as average annual humidity and temperature. The combination of these methods and criteria may provide a better insight on the potential of biofuel production from *Jatropha* in Qatar. The GIS-based spatial analysis identified wasteland area of 6779 km^2 in Qatar as highly suitable to grow *Jatropha*. In addition, 1564 km^2 are identified as moderately suitable sites. The obtained results indicate a high potential to grow *Jatropha* in Qatar for biofuel production with no competition on land and water resources.

Keywords: Qatar, *Jatropha curcas*, GIS, Geospatial modeling, Site suitability, Biofuel.

I. Introduction

Qatar is a peninsula located in the Arabian Gulf with an area of ~11,500 km^2 and an elevation of below 100 m above the sea level. Its arid-desert climate is characterised by an average daily temperature of 13 – 42 °C (Cheng et al., 2017), a highly fluctuating rainfall of about 80 mm (Food and Agriculture Organisation, 2008), a strong wind and a high relative humidity (Abu Sukar et al., 2007). While evapotranspiration ranges from as low as 2 mm/day in December, up to 10 mm/day in June (Food and Agriculture Organisation, 2008).

The arable area in Qatar is about 65,000 ha, which is only 0.6% of the country's total area (Department of Agricultural and Water Research, 2002). Besides, the soils of Qatar belongs to "aridisol" category that distinguish the areas of an arid climate (Qatar Statistics Authority, 2013). Four types of soil are found in Qatar including rawdha, lithosol, sabkha and sandy soil (Ministry of Municipal Affairs and Agriculture, 2005). Rawdha soil or farm soil is found in around 850 land depressions, and made up of sandy-loam, sandy-clay-loam or calcareous-loam, with a depth of 30-150 cm. Whereas lithosol is a shallow soil with a typical depth of (10-30 cm), composed of calcareous-sandy-loam and mostly covered with limestone and rock debris. Sandy soil is composed of coarse-sand and calcareous-loamy-sand with a considerable depth of at least 120 cm (Baalousha, 2016). Besides, sabkha soil is a highly saline soil that is found in coastal areas and mainly composed of clay, slit and mud with a considerable depth (Baalousha, 2016; Food and Agriculture Organisation, 2008).

Meanwhile, Qatar is suffering from land degradation, whereby 191,000 ha of its arable lands were affected by wind erosion, while this area is gradually increasing due to the movement of sand dunes towards agricultural and populated areas (Abahussain et al., 2002). Nevertheless, dust or sandstorms are a regular phenomenon in the Arabian Peninsula (Hermida et al., 2018). This phenomenon results in severe health problems, crop damages, traffic accidents, soil degradation, solar systems malfunction and disorder in many public sectors (Beegum et al., 2018).

On the other hand, Qatar has one of the highest GDP per capita worldwide (TheWorldBank, 2019), with oil and natural gas being the main source of the government revenues (US-Qatar Business Council, 2018). Although Qatar has the third largest proven reserve of natural gas, the country strives to invest in renewables to diversify its energy resources and mitigate its carbon footprint. Whereby, Qatar's GHG emissions have increased with an annual average of 6.38% over the period 1999-2018 (Knoema, 2018a).

Energy crops are the most prominent source of carbon-neutral energy. Though, due to the poor soil and harsh climate of Qatar, no attempts to grow energy crops have been made earlier to the best knowledge of the authors. However, *Jatropha curcas* proved to be one of the most promising energy crops that tolerates arid climates and thrives in marginal and non-arable lands, leaving fertile soils for food crops (Singh et al., 2008; Tomar et al., 2014).
The Food and Agriculture Organisation (FAO) revealed that *Jatropha* can best thrive within 30°N and 35°S latitudes (Ismail and Rossi, 2010), as such, it is believed to have the potential to grow in Qatar. Furthermore, *Jatropha* has been used earlier to enhance soil, mitigate wind erosion and as a live fence (Tomar et al., 2014). While the *Jatropha* fruit and oil can be utilised to produce different fuel products (Alherbawi et al., 2020a, 2020b). Therefore, as an added value, *Jatropha* can be grown in Qatar for multiple purposes; not only for biofuel production, but also to preserve the soil against wind erosion, combat desertification and sandstorms and enhance the air quality by capturing carbon emissions and dust.

Jatropha can grow in different soil types including saline, arid and marginal lands (Prasad et al., 2017; Tomar et al., 2014). However, well-aerated sandy-loam or clay-loam soils with good drainage and a pH of 5.2-8.5 are reported to contribute to higher yields (Tomar et al., 2014). Clay soils may limit root system development (Valdés-Rodríguez et al., 2013), while salinity may suppress the *Jatropha* fruit yield (Tomar et al., 2014). Preliminary site assessment is crucial to ensure the success of *Jatropha* biofuel projects, as the lack of sufficient agronomic experience was the main reason behind the failure of different projects earlier (Wahl et al., 2012). In this regard, the analytical hierarchy process (AHP) has emerged as an effective tool for multicriteria weighing and is being increasingly used for optimal sites selection (Taddese, 2014). Meanwhile, several GIS-based spatial assessments of *Jatropha curcas* have been conducted in different countries including Brazil (Yamada and Sentelhas, 2014), Ethiopia (Taddese, 2014), India (Sunil et al., 2009), Malaysia (Shabanimofrad et al., 2011), Pakistan (Khan and Hasan, 2020) and Thailand (Qasim et al., 2015). While Trabucco et al. (Trabucco et al., 2010) conducted a global mapping of *Jatropha* yields in response to different climates.

Since *Jatropha curcas* has never been cultivated before in Qatar, there is a need to evaluate the land suitability to grow it prior to actual plantation trials. As such, this study utilises the geographic information system (ArcGIS) combined with the AHP decision-making tool to select *Jatropha* plantation sites that may possibly contribute to the highest yields. Identification of optimal plantation sites may provide a broader insight on the potential of biofuel production, carbon capture and soil enhancement through the cultivation of *Jatropha* in Qatar.

II. Methodology

The key criteria that are expected to influence the growth and yield of *Jatropha* in Qatar are selected carefully based on published cultivation experiences worldwide and considering the topographic and climate conditions. The selected factors include soil type, depth and pH, as well as the average annual temperature and humidity.

The annual precipitation is not considered in this study due to the limited and highly fluctuating levels, therefore, an irrigated *Jatropha* crop is assumed. While other topographic features such as land elevation and slope are also ignored due to their marginal variations. Besides, the ranges of the key factors are grouped into three classes of suitability, labelled as: highly suitable, moderately suitable, and marginally suitable as presented in Table 1.

Table 1: Definition of key criteria and their ranges (adapted from (Alherbawi et al., 2021; Maes et al., 2009; Tomar et al., 2014; Trabucco et al., 2010; Valdés-Rodríguez et al., 2013)).

Criteria		Suitability classes		
		Highly suitable	**Moderately suitable**	**Marginally suitable**
Soil factors	Soil type	Rawdha/Lithosol	Sandy	Sabkha
	Soil depth (cm)	>45	20-45	<20
	Soil pH	5.5 – 8.5	4.5 – 5.5, 8.5 – 9.5	<4.5 & >9.5
Climate factors	Annual average temperature (°C)	<28	28-38	>38
	Annual average Humidity (%)	>60	40-60	<40

The relative importance of the selected criteria is evaluated using analytical hierarchy process (AHP) (Saaty, 1999). Whereby a pair-wise comparison is conducted as presented in Table 2. The AHP tool facilitates the breakdown of complex problems into a hierarchical structure, in which the qualitative and quantitative aspects of the problem are collectively considered (Haji et al., 2020). Initially, each criterion in the extreme left column of the pair-wise matrix is compared with the criteria in the top row in terms of their importance in the problem and is given a value based on the extent of importance. 1 is given for equal importance, 3 for moderate importance, 5 for strong importance, 7 for very strong importance and 9 for extreme importance.

The normalised pair-wise comparison is then estimated by dividing each element in the matrix by the sum of its own column. Finally, the average of each row in the normalised matrix is calculated which represents the weight of the corresponding criterion in the row.

Table 2: AHP's pair-wise comparison matrix.

Criteria	Soil type	Soil depth	Soil pH	Temp.	Humidity
Soil type	**1.00**	3.00	7.00	5.00	5.00
Soil depth	0.33	**1.00**	5.00	3.00	5.00
Soil pH	0.14	0.20	**1.00**	0.30	0.33
Temp.	0.20	0.33	3.33	**1.00**	1.00
Humidity	0.20	0.20	3.00	1.00	**1.00**
Total	1.88	4.73	19.33	10.30	12.33

In addition, the consistency of the pair-wise comparison is tested and validated using consistency ratio approach developed by Saaty (1988) to ensure their suitability to be used in the decision-making process. Only consistency ratios (CR) below 10% are considered as acceptable values and indicate a reasonable consistency of the pair-wise comparison.

ArcGIS (V.10.7.1) is used to plot five maps representing the selected criteria with three suitability classes based on data retrieved from Qatar Atlas (Qatar Statistics Authority, 2013) and the Atlas of soils for the State of Qatar (Ministry of Municipal Affairs and Agriculture, 2005), as well as the geospatial network of the UN's Food and Agriculture Organisation (Food and Agriculture Organisation, 2020). While a composite suitability map is generated considering the criteria weights that are estimated earlier using the following formula (Taddese, 2016):

$$\textit{Site suitability} = \sum_{i=1}^{5}(W_i \; x \; C_i) \quad (1)$$

Where, W_i: is the relative weight of criterion C_i

III. Results and discussion

The obtained AHP's criteria weights are presented in Table 3. The process granted soil types the highest importance with approximately 50%, followed by the soil depth. While the average annual temperature and humidity are given almost equal importance. Besides, the criteria pair-wise comparison achieved a consistency ratio of 5%, which indicate a reasonable consistency.

Table 3: Definition of criteria weight using AHP.

Criteria	Soil type	Soil depth	Temp.	Humidity	Soil pH
Criteria weight	0.48	0.27	0.11	0.10	0.05
Ranking	1	2	3	4	5

Soil type and depth are the decisive factors in identifying the optimal plantation sites. Whereby, temperature and humidity have minimal variation across the different locations. While the pH of Qatar's soil falls within the high suitability range for *Jatropha*.

The generated composite suitability map is presented in Fig.1. Where the high suitability sites dominated around 75% of the evaluated area.

The GIS-model identified around 6779 km^2 of the total Qatar area as highly suitable to grow *Jatropha*. The former figure accounts only for arid and wastelands and excludes the area of arable lands that are reserved for food cultivation (~650 km^2). Besides, the model has also identified around 1564 km2 as moderately suitable sites for *Jatropha* cultivation. While the remaining area showed low suitability mainly due to soil salinity, as well as limited depth which may suppress the fruit yield and limit roots development, respectively. The northern part of Qatar exhibited higher suitability as compared to the southern part, while the central region has shown better performance than the coastal areas.

Considering a fruit yield of 10 tonnes/ha, the area which is identified as highly suitable can generate over 6.5 million tonnes of *Jatropha* biomass, including 1.7 million tonnes of oil per year. Upon upgrading, the oil alone can perfectly cover the gasoline demand in the state of Qatar, which is estimated by 1.25 million tonnes/year (Knoema, 2018b). As such, *Jatropha curcas* is proved to have a high potential to be utilised in the State of Qatar as a carbon sink and an alternative source of energy.

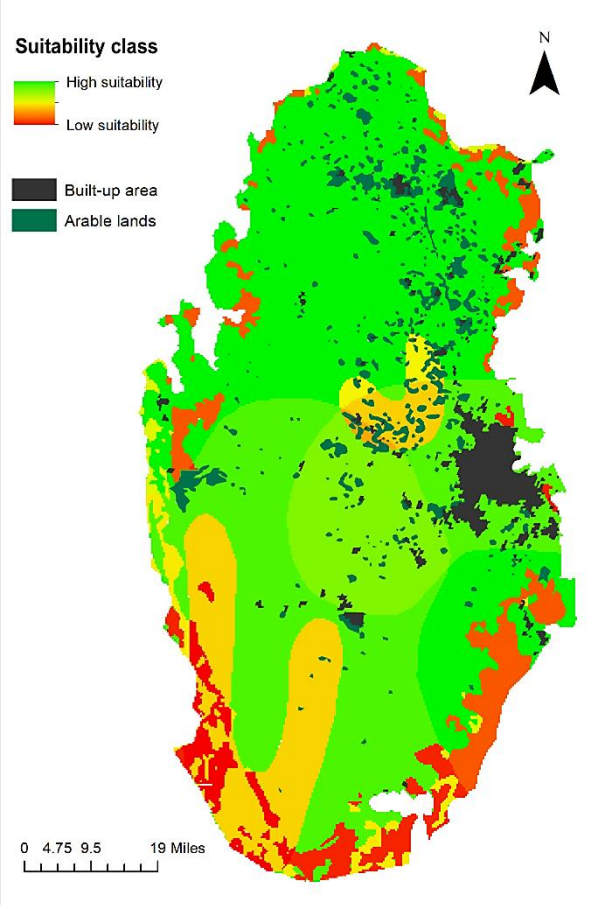

Fig.1: Composite suitability map of Jatropha in Qatar.

IV. Conclusions

This study utilised the Geographic Information System (GIS) and Analytical Hierarchy Process (AHP) to identify the optimal cultivation sites of *Jatropha curcas* in Qatar based on multicriteria including soil type, depth and pH contents, as well as average annual humidity and temperature. The GIS-based spatial analysis identified wasteland area of 6779 km^2 in Qatar as highly suitable to grow *Jatropha*. In addition, 1564 km^2 are identified as moderately suitable sites. The highly suitable sites can possibly generate over 1.7 million tonnes of oil, which is sufficient to completely meet the gasoline demand of Qatar. As such, *Jatropha curcas* showed high potential to be cultivated in Qatar for biofuel production and GHG emissions mitigation.

References

Abahussain, Ali, A., Abdu, A.S., Al-Zubari, W.K., El-Deen, N.A., Mahmmod, A.-R., 2002. Desertification in the Arab Region: analysis of current status and trends. J. Arid Environ. 51, 521–545.

Abu Sukar, H.K., Almerri, F.H., Almurekki, A.A., 2007. Agro-hydro-meteorological data book for the State of Qatar. DAWR, Canberra.

Alherbawi, M., Al-Ansari, T., Mckay, G., 2020a. Potential Integrated Pathways for Jet Biofuel Production from Whole Fruit of Jatropha, in: Pierucci, S., Manenti, F., Bozzano, G.L., Manca, D.B.T.-C.A.C.E. (Eds.), 30 European Symposium on Computer Aided Process Engineering. Elsevier, pp. 235–240.

Alherbawi, M., AlNouss, A., Mckay, G., Al-Ansari, T., 2020b. Optimum Utilization of Jatropha Seedcake Considering the Energy, Water and Food Nexus, in: Pierucci, S., Manenti, F., Bozzano, G.L., Manca, D.B.T.-C.A.C.E. (Eds.), 30 European Symposium on Computer Aided Process Engineering. Elsevier, pp. 229–234.

Alherbawi, M., McKay, G., Mackey, H.R., Al-Ansari, T., 2021. Jatropha curcas for jet biofuel production: Current status and future prospects. Renew. Sustain. Energy Rev. 135, 110396. https://doi.org/https://doi.org/10.1016/j.rser.2020.110396

Baalousha, H.M., 2016. Groundwater vulnerability mapping of Qatar aquifers. J. African Earth Sci. 124, 75–93.

Beegum, S.N., Gherboudj, I., Chaouch, N., Temimi, M., Ghedira, H., 2018. Simulation and analysis of synoptic scale dust storms over the Arabian Peninsula. Atmos. Res. 199, 62–81.

Cheng, W.L., Saleem, A., Sadr, R., 2017. Recent warming trend in the coastal region of Qatar. Theor. Appl. Climatol. 128, 193–205.

Department of Agricultural and Water Research (DAWR), 2002. Agricultural census results 2000/2001. Doha, Qatar.

Food and Agriculture Organisation (FAO), 2008. Irrigation in the Middle East region in figures – AQUASTAT Survey 2008.

Food and Agriculture Organisation of the United Nations (FAO), 2020. GeoNetwork. URL http://www.fao.org/geonetwork/srv/en/main.home (accessed 10.10.20).

Haji, M., Govindan, R., Al-Ansari, T., 2020. Novel approaches for geospatial risk analytics in the energy–water–food nexus using an EWF nexus node. Comput. Chem. Eng. 140, 106936.

Hermida, L., Merino, A., Sánchez, J.L., Fernández-González, S., García-Ortega, E., López, L., 2018. Characterization of synoptic patterns causing dust outbreaks that affect the Arabian Peninsula. Atmos. Res. 199, 29–39.

Ismail, M., Rossi, A., 2010. A Compilation of Bioenergy Sustainability Initiatives. Rome.

Khan, M.J., Hasan, S.A., 2020. GiS-Based Screening Model of coastal city Karachi for plantation of Biofuel Source. Sci. Rep. 10, 1–7.

Knoema, 2018a. Qatar - CO2 emissions [WWW Document]. URL https://knoema.com/atlas/Qatar/CO2-emissions (accessed 9.10.20).

Knoema, 2018b. Gasoline consumption in Qatar. URL https://knoema.com/data/qatar+consumption+gasoline (accessed 1.10.19).

Maes, W.H.A., Trabucco, A., Achten, W.M.J., Muys, B., 2009. Climatic growing conditions of Jatropha curcas L. Biomass and bioenergy 33, 1481–1485.

Ministry of Municipal Affairs and Agriculture, 2005. The Atlas of Soils for The State of Qatar.

Prasad, S., Nirala, D.P., Sinha, A., Kumar, J., Kumari, P., 2017. Oil content analysis of Jatropha curcas L. seeds under agronomical treatment with N, P, K and Gypsum. J. Pharmacogn. Phytochem. 1132–1134.

Qasim, S., Qasim, M., Shrestha, R.P., Phongaksorn, N., Gyawali, R., 2015. GIS Based Land Suitability Assessment for Jatropha Curcas L. Cultivation in Phetchaburi Province, Thailand. J. Sci. Technol. 10, 4666.

Qatar Statistics Authority, 2013. Qatar Atlas.

Saaty, T.L., 1999. Basic theory of the analytic hierarchy process: How to make a decision. Rev. la Real Acad. Ciencias Exactas Fis. y Nat. 93, 395–423.

Saaty, T.L., 1988. What is the analytic hierarchy process?, in: Mathematical Models for Decision Support. Springer, pp. 109–121.

Shabanimofrad, M., Yusop, M.R., Saad, M.S., Wahab, P.E.M., Biabanikhanehkahdani, A., Latif, M.A., 2011. Diversity of Physic Nut ('Jatropha curcas') in Malaysia: Application of DIVA-Geographic Information System and Cluster Analysis. Aust. J. Crop Sci. 5, 361.

Singh, R.N., Vyas, D.K., Srivastava, N.S.L., Narra, M., 2008. SPRERI experience on holistic approach to utilize all parts of Jatropha curcas fruit for energy. Renew. Energy 33, 1868–1873. https://doi.org/https://doi.org/10.1016/j.renene.2007.10.007

Sunil, N., Sivaraj, N., Anitha, K., Abraham, B., Kumar, V., Sudhir, E., Vanaja, M., Varaprasad, K.S., 2009. Analysis of diversity and distribution of Jatropha curcas L. germplasm using Geographic Information System (DIVA-GIS). Genet. Resour. Crop Evol. 56, 115–119.

Taddese, H., 2016. Application of Geographic Information Systems in identifying accessible sites for Jatropha curcas production in Ethiopia. Energy Procedia 93, 82–88.

Taddese, H., 2014. Suitability analysis for Jatropha curcas production in Ethiopia-a spatial modeling approach. Environ. Syst. Res. 3, 25.

TheWorldBank, 2019. Countries GDP per capita. URL https://data.worldbank.org/indicator/NY.GDP.PCAP.CD?year_high_desc=true (accessed 1.10.20).

Tomar, N.S., Ahanger, M.A., Agarwal, R.M., 2014. Jatropha curcas: An Overview, in: Ahmad, P., Wani, M.R. (Eds.), Physiological Mechanisms and Adaptation Strategies in Plants Under Changing Environment: Volume 2. Springer New York, New York, NY, pp. 361–383. https://doi.org/10.1007/978-1-4614-8600-8_13

Trabucco, A., Achten, W.M.J., Bowe, C., Aerts, R.A.F., ORSHOVEN, J.O.S.V.A.N., Norgrove, L., Muys, B., 2010. Global mapping of Jatropha curcas yield based on response of fitness to present and future climate. Gcb Bioenergy 2, 139–151.

US-Qatar Business Council, 2018. Economics in Qatar.

Valdés-Rodríguez, O.A., Sánchez-Sánchez, O., Pérez-Vázquez, A., Caplan, J.S., Danjon, F., 2013. Jatropha curcas L. Root Structure and Growth in Diverse Soils. Sci. World J. 2013.

Wahl, N., Hildebrandt, T., Moser, C., Lüdeke-Freund, F., Averdunk, K., Bailis, R., Barua, K., Burritt, R., Groeneveld, J., Klein, A.-M., Kügemann, M., Walmsley, D., Schaltegger, S., Zelt, T., 2012. Insights into Jatropha projects worldwide: key facts & figures from a global survey. Leuphana University of Lüneburg, Lüneburg.

Yamada, E.S.M., Sentelhas, P.C., 2014. Agro-climatic zoning of Jatropha curcas as a subside for crop planning and implementation in Brazil. Int. J. Biometeorol. 58, 1995–2010.

Techno-Economic Analysis of a 500MW$_e$ Supercritical Coal-based Thermal Power Plant with Solar Assisted MEA-based CO_2 Capture

[1]Rajesh Kumar, [1*]Sujit Karmakar
[1] National Institute of Technology Durgapur, Department of Mechanical Engineering, West Bengal-713209, India

* E-mail:sujitkarmakar@yahoo.com

Abstract
Coal-based thermal power plants are the largest emitter of CO_2 in the atmosphere. Emissions of CO_2 in the atmosphere increase its concentration level and leads to global warming. The integration of the post-combustion CO_2 capture system (CCS) with coal-fired power plants has the techno-economical potential to mitigate CO_2 but a large energy penalty resulting in a decrease of plant efficiencies. The present study copes with Energy, Exergy, Environment, and Economic analysis (4E analysis) of a coal-fired Supercritical thermal power plant with solar assisted Monoethanolamine (MEA) based post-combustion CCS. The thermodynamic analysis of the plant configurations is carried out with a computer simulation program, 'Cycle-Tempo'. It is found that the maximum energy and exergy losses take place in cooling water and combustor, respectively. The addition of solar energy for MEA regeneration helps in increasing, energy and exergy efficiencies of the plant by about 2.2% and 5% points, respectively, and contributing 26% of the total energy demand for the CO_2 capture unit. The Levelized Cost of Electricity (LCoE) and the payback period of the proposed plant are 4.96 INR/kWh and 4.18 years, respectively. Moreover, CO_2 avoided of the novel plant configuration is increased by 12.5%. The study also shows that the total area required for installing the solar trough is about 326 acres.

Keywords: Energy, Exergy, CO_2 capture, MEA, Solar energy

I. Introduction

In the world energy scenario, coal power plants are the major sources of electricity generation. Thermal power plants are the largest emitter of CO_2 in the atmosphere and contribute around 75 percent of the total emission. As per the World Metrological Organization (WMO), the Greenhouse gas bulletin average concentration of CO_2 reached 421.5 ppm in 2019. CO_2 is the key greenhouse gas, and its emission to the atmosphere creates an adverse effect on the climate. To keep a safe environment, CO_2 emission has to be minimized. CO_2 capture and storage (CCS) system has the potential to reduce the CO_2 emission from coal power plants. Basically, CCSs are of three types. (I) Oxy-fuel CCS, (II) Pre-combustion CCS, (III) Post-combustion CCS(Kanniche et al., 2010).MEA absorption-based CO_2 capture system is best for old existing coal-based power plants(Olajire, 2010). The study reveals that retrofitting of MEA based post-combustion CCS decreases the plant efficiency by 8-12% points(Karmakar and Kolar, 2013). They also suggest that at the optimum absorber-stripper configuration, the reboiler heat duty is 3.77 MJ_{th} per kg of CO_2 capture. (Goto et al., 2013)found that with the CO_2 capture plant, the efficiency is reduced by about 10% points, and the ratio of efficiency reduction by CO_2 capture to the total efficiency reduction is 0.67. They also found that about 2% efficiencyis improved by reduction of thesolventregeneration energy by 1GJ/t of CO_2.

Solar energy, major renewable energy, is a viable option to reduce the energy penalty. Solar energy for feed water heating reduced 62000t-65000t of CO_2 yearly from the coal power plants(Suresh et al., 2010).Solar parabolic trough collector (PTC) has higher efficiency than linear Fresnel reflector (LFR)(Wang et al., 2015). The present study copes with the thermodynamic analysis (energy and exergy-based) of a 500MWe Supercritical coal power plant with solar aided MEA absorption-based CO_2 capture in Indian climatic conditions (33°C ambient temperature and 1.013 bar atmospheric pressure) with high ash (HA) Indian coal. Solar energy is considered as the energy source for MEA regeneration, and the results are also compared with published literature (Karmakar, 2016). The plant is simulated with the computer programme "Cycle-Tempo" (Cycle tempo, 2007).

II. Plant Configuration

A 500 MW$_e$ coal-fired Supercritical thermal power plant is considered for the study. The plant has one high HP turbine with two HPFWHs, one dual flow IPturbines with three IPFWHs, and two dual-flow LPTurbines with two LPFWHsand a re-heater with 565°C final temperature. The steam parameters used for the operation are 242.2 bar/537°C/565°C(Suresh et al., 2010)**.** The plant is integrated with a solar aided MEAbased CO_2 capture system. A solar parabolic trough is used for harvesting solar energy. The plant layout is shown in Fig. 1, which is modeled in "Cycle-Tempo". The CO_2 capture unit is integrated with the main plant after ID fan and before the chimney. In the present study, the total energy required for MEA regeneration is given by solar energy. From the hot well of the condenser, some fraction of condensate water is tapped and sent through the solar parabolic trough collector fields to produce steam at a pressure of 2.8bar and temperature of 132°C in the stripper column to regenerate MEA. After re-boiler, it is again mixed with the main plant condensate cycle. The reboiler heat duty has been considered as 3.8 MJ_{th}/kg of CO_2 capture inthe present study**.** In India, the intensity of direct solar irradiation ratevaries from 510 to 1005 W/m^2 on the earth's surface at day time. It strongly depends on the latitude, altitude of the place, and

season. The analysis of the present work is carried out considering different values, and maximum performance improvement is found in the summer season. However, the present study is carried out by considering the low solar irradiation rate of about 500 W/m^2(Suresh et al., 2010). The annual average direct irradiation and efficiency (η_c) areconsidered as 500 W/m^2,60% respectively.

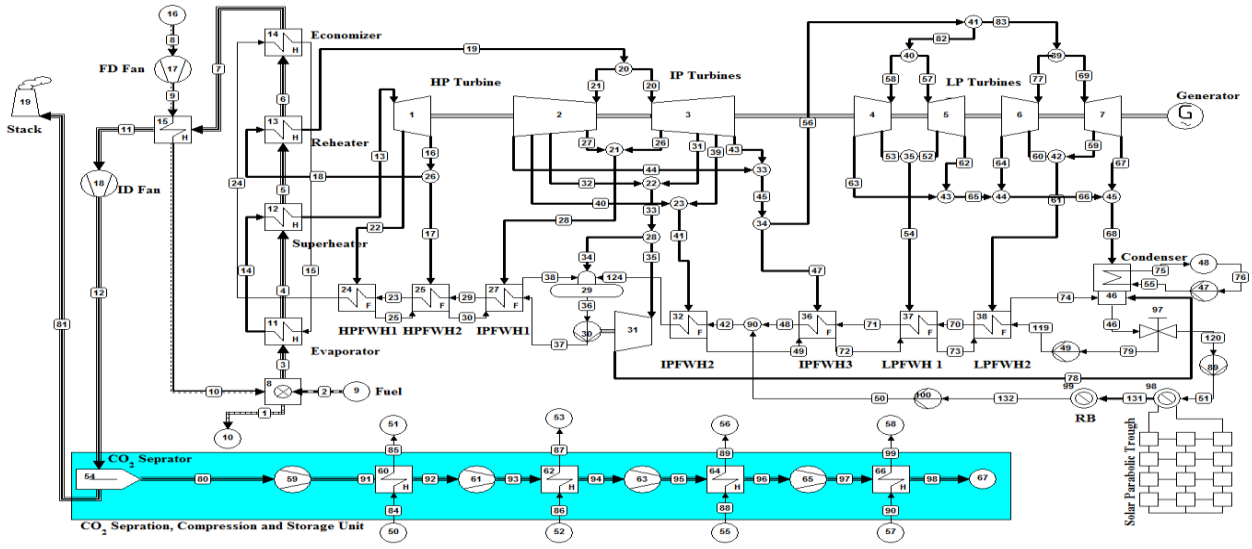

Fig.1:SupC plant with solar aided MEA based CO2 capture

III. Simulation Procedure

Cycle-Tempo is a software tool that helps in the analysis and optimization of various kinds of thermodynamic systems. The thermal power plant has a huge number of subsystems, which form a very complex network of mass and energy flows. This type of huge network takes lots of time while solving manually, but Cycle-Tempo has the facility to solve such a complex network very easily in less time. All the calculations are based on the basic equations of mass, energy, and chemical species balance.

The basic thermodynamic equations are given as follows which are used for the study:

$$\sum \dot{m}_i = \sum \dot{m}_e \quad (1)$$

$$\sum \dot{m}_i h_i + \dot{Q}_{cv} = \sum \dot{m}_e h_e + \dot{W}_{cv} \quad (2)$$

$$\sum \dot{m}_i \psi_i + \dot{X}_{heat} = \sum \dot{m}_e \psi_e + \dot{W}_{cv} + \dot{I} \quad (3)$$

$$\sum_e \dot{N}_j = \sum_i \dot{N}_j + \dot{N}_p \quad (4)$$

Where equation (1) shows the mass balance, eq. (2) shows the energy balance, eq. (3) shows the exergy balance, and equation (4) shows the chemical species balance of the system (Suresh et al., 2010).

Performance Parameters

The performance parameters are used to determine the performance of power plant. This gives the idea to choose the suitable system with better performance. The following parameters are used for performance analysis:

Energy and Exergy Efficiency

$$\text{Energy effiency}(\eta) = \frac{(\text{Netelectricity})_{\text{Output}}}{\text{Energyinputthroughfuel}} \quad (5)$$

Exergy efficiency is defined as follows:

$$\text{Exergy efficiency } (\varepsilon) = \frac{(\text{Netelectricity})_{\text{Output}}}{\text{Exergy input through fuel}} \quad (6)$$

IV. Results and Discussion

Performance analysis (Based on Energy and Exergy)

Thermodynamic analysis of a 500 MW_ecoal-fired Supercriticalcoal power plant is carried out energetically and exegetically by using HA Indian coal. Addition of solar aided CO_2 capture unit increases the plant energy and exergy efficiencies by 2.2%, and 4.9%points, respectivelyin comparison with theSupC plant integrated with CO_2 capturewithout solar assistance. This improvement is due to save of fuel consumption by using solar energy for regeneration of MEA.Table 1 and Table 2 show the comparative energy and exergy balances, respectively. From Table 1, it is found that the cooling water or the condenser energy loss of solar-assisted CO_2 capture plant (about 52 %) is higher than the without solar-assisted CO_2 capture plant (18.8 %). Some part of the steam is used for amine regeneration resulting in less steam supply in the condenser for MEA based CO_2 capture plant without solar assistance. On the other side, solar assisted CO_2 capture unit uses solar energy for steam generation to be used

for MEA regeration which increases the steam flow rate in the condenser. Moreover, the stack loss is found slightly less in solar assisted CO_2 capture unit contributing about 4.3 % of total energy input compared to MEA based CO_2capturewhich contributes about 4.6 % of total energy input. This may be inferred that integration of solar energy reduces the fuel consumption of the plant and thereby, it reduces heat loss through the dry flue gas.Moreover, the reduction in the amount of flue gas helps in reducing the flue gas cooling losses from 5.4 % to 5.1 %.

Table 2 shows the exergy balance of the configured plant and helps to point out the actual place of irreversibility in plants. The exergy efficiency of SupC plant with solar-assisted CO_2 capture is about 29.9 %, which is 4.9 %-points higher than the SupC plant with CO_2 capture (without solar assistance). Maximum exergy destruction founds in the combustor, followed by the steam generator. The major difference in exergy destruction between two cases plant with CC and plant with solar aided CC is due to cooling water and reboiler exergy losses. Exergy loss in reboiler decreases and condenser loss increases in the present work compared to the SupC plant with MEA based CO_2 capture.The novelty of the proposed plant is lying with solar integration for amine regeneration system, which helps not only to reduce the CO_2 emission but also the other major pollutants like SO_x,NO_x, and Suspended Particulate Matter (SPM). The CO_2 avoided of the coal power plant with and without solar aided CO_2 capture systemare about 0.68 and 0.58 kgCO_2)/ kWh of electricity generation, respectively.

Table 1. Energy balance

Components (%)	Supercritical (Karmakar, 2016)	Supercritical with CO_2 capture (Karmakr, 2016)	Supercritical with Solar assisted CO_2 capture (Present work)
Energy efficiency	36.7	28.4	30.6
Cooling water	49.3	18.8	52.0
Stack	10.1	4.6	4.3
Bottom Ash	0.8	0.8	0.8
Reboiler	0	29.9	3.9
CO_2 compression	0	3.0	3.0
Flue gas cooling	0	5.4	5.1
Desuperheater	0	5.5	-
Other losses (by difference)	3.1	3.6	0.3

Table 2. Exergy balance

Components (%)	Supercritical (Karmakr, 2016)	Supercritical with CO_2 capture (Karmakar, 2016)	Supercritical with Solar assisted CO_2 capture (Present Work)
Exergy efficiency	33.6	25	29.9
Combustor	33.3	33.3	31.5
Steam generator(Economizer+ Evaporator +S heater + Re-heater)	18.9	18.8	17.6
Compressed CO_2 stream	0	5.4	5.0
Condenser and cooling water	0.7	1.0	4.8
Turbines	3.8	2.6	3.3
Stack	3.8	1.3	1.6
Feed water heaters	0.7	0.6	0.6
Flue gas cooling	0	0.4	0.6
Re-boiler	0	6.7	0.6
CO_2 compression	0	0.5	0.5
Bottom Ash	0.5	0.5	0.5
Desuperheater	0	0.7	-
Others(by difference)	4.7	3.2	3.5

Environmental analysis

Coal combustion for power generation is the primary cause of environmental pollution where the products of emission is released into the atmosphere. The combustion products consist mainly of CO_2, SO_x,NO_x, and SPM. However, high concentration of CO_2 in the environment is the main cause of global warming. The study shows thatthe Specific Fuel Consumption (SFC) of the MEA based CO_2 capture plant (without solar) is about 0.58 kg/kWh, which is slightly more than the stand-alone SupC power plant (0.56kg/kWh). Auxiliary power consumption for the CO_2 Capture unit decreases the net plant output, and also the auxiliary steam requirement for the regeneration of MEA increases the fuel consumption of the boiler. Thereby, the SFC of the plant is higher thanthe stand-alone plant. The solar integration with the MEA based CO_2 capture unit reduces the SFC, which is about 0.57 kg/kWh. Moreover, the power plant emissions are directly linked with the SFC of the plant.Thespecific CO_2emissionsfor SupC plant is 0.81kg/kWh, for SupCwith CCS is 0.14 kg/kWh, and SupCwith solar aided CO_2 capture unit is 0.12 kg/kWh. The result shows that SupC plant with solar aided CO_2 capture unit contributes the minimum specific CO_2emission.

Economic analysis

Economic analysis of the different plant configurations is carried out based on the Levelized Cost of Electricity (LCoE) generation, and the results are shown in Table 9.
The assumptions which have been made for cost analysis of the plant are as follows:
Plantlife- 25 years, Discount rate- 12 %, Plant capacity factor-0.85, Cost of solar collector area (indirect heating) - INR 13,800/m^2, Cost of solar collector area (indirect heating) - INR 13,800/m^2, Fixed operation and maintenance cost-2.5 percent of capital cost, Variable operation and maintenance cost-0.10 per unit. Capital cost- INR 55000 /kW, CO_2 capture plant cost -75 percent of capital cost (Karmakar, 2016).
The(Suresh et al., 2010) study shows that the LCoE of the 500 MW_e coal-fired power plant with solar-assisted MEA based CO_2 capture system is about 4.96 INR/kWh, which is slightly higher than the plant without solar-assisted MEA based CO_2 capture. The payback period of the proposed plant is about 4.18 years; whereas about 3.49 INR/kWh is found in the plant without solar-assisted MEA based CO_2 capture system.The cost per tonne of CO_2 avoided for SupC with solar aided CO_2 capture plant is about 2300 INR, which is more than the supC plant without solar-assistedMEA based CO_2 capture system by about 630 INR. However, the use of solar energy can be promoted for safeguarding the environment instead of the high cost of CO_2 avoided and a marginal increase in payback period.

V. Conclusions

The present study shows the thermodynamic of a solar-assisted MEA based CO_2 capture system when integrated with a 500 MW_eSupCcoal power plant. The major conclusions of the study are as follows:

- There is 2.2% point improvement in thePlant energy efficiency, and 4.9%-points improvement in exergy efficiency with solar assisted MEA based CO_2 capture plant.
- Maximum energy loss takes place in the condenser, and Maximum exergy loss takes place in the combustor.
- CO_2 avoided of the plant increases by 12.5% with respect to Supercritical plant with MEA based CO_2 capture.
- The LCoE of the 500 MW_e coal plant with solar assisted MEA based CO_2 capture system is about 4.96 INR/kWh.326 acres of solar parabolic area is needed for this capacity, and the payback period of the proposed plant is about 4.18 years.

References

Ahmed M.H., Amin M.A., and BannaFath H. El., 2018. “Modeling of solar power plant for electricity generation and water desalination”, J. of Solar Energy, ASME, 141 (1) 011015, pp.1-6, doi: 10.1115/1.4041260.
Cycle-Tempo release 5.0, 2007, Delft University of Technology.

Goto, K., Yogo, K., &Higashii, T., 2013. “A review of efficiency penalty in a coal-fired power plant with CO_2 capture”, Appl. Energy111, pp. 710-720.

Han W., JinH.Jin and Lin R., 2011. “A novel multifunctional energy system for CO_2 removal by solar reforming of natural gas", J. of Solar Energy, ASME, 133(4)041004, pp.1-8, doi:10.1115/1.4004034.

Kanniche, M., Gros-Bonnivard, R., Jaud, P., Valle-Marcos, J., Amann, J. M., &Bouallou, C, 2010. “Pre-combustion, post-combustion, and oxy-combustion in thermal power plant for CO_2 capture”,Appl. Therm. Eng. 30, pp.53-62.

Karmakar, S., &Kolar, A. K., 2013. “Thermodynamic analysis of high-ash coal-fired power plant with carbon dioxide capture”, Int. J. Energy Res. 37, pp.522-534.

Karmakar S., 2016. “4-E (Energy, Exergy, Environment, and Economic) analysis on advanced coal technologies for power generation with CO_2 capture”, Ph.D. thesis, Dept. of Mechanical Engineering, IIT Chennai, India.

Olajire, A. A.,2010. “CO_2 capture and separation technologies for end-of-pipe applications–a review”, Energy 35, pp.2610-2628.

Reich L., Melmoth L., Yue L., Bader R., Gresham R., Simon T. and Lipiński W.,2017. “A solar reactor design for research on calcium oxide- based carbon dioxide capture”, J. of Solar Energy, ASME, 139(5), pp. (1-5), doi: 10.1115/1.4037089.

Skorek-Osikowska, A., Bartela, L., &Kotowicz, J., 2017.“Thermodynamic and ecological assessment of selected coal-fired power plants integrated with carbon dioxide capture”, Appl. Energy200, pp. 73-88.

Suresh, M. V. J. J., Reddy, K. S., &Kolar, A. K.,2010. “4-E (Energy, Exergy, Environment, and Economic) analysis of solar thermal aided coal-fired power plants”, Energy Sustain. Dev.14, pp. 267-279.

Suresh, M. V. J. J., Reddy, K. S., &Kolar, A. K.,2010. “3-E analysis of advanced power plants based on high ash coal”,Int. J. Energy Res. 34, pp.716-735.

Wang, F., Zhao, J., Li, H., Li, H., Zhao, L., & Yan, J.,2015. “Experimental study of solar assisted post-combustion carbon capture”, Energy Procedia75, pp. 2246-2252.

3-E (Energy, Exergy, and Environmental) based comparative analysis of 500 MWe SuperCritical Air-Coal ,Oxy-Coal ,and Partial Oxy-Coal Combustion based Thermal Power Plants with CO_2 Capture

[1]Soumya Jyoti Chatterjee, [1*]Sujit Karmakar,
[1] National Institute of Technology Durgapur, Department of Mechanical Engineering, West Bengal-713209, India

* e-mail:sujitkarmakar@yahoo.com

Abstract
In this study comparative performance analysis is done of a 500MW_e Partial Oxy-Coal Combustion (POCC) based Supercritical (SupC) power plant having a CO_2 Capture Unit (CCU) which is membrane based, at a fixed furnace temperature by varying the amount of oxygen rich air (varying from 0% to 100%) supplied in the combustor. Also, the results are compared with a similar kind of Air Coal Combustion (ACC) based power plant. On the basis of 3-E (Energy, Exergy and Environment) analysis detailed thermodynamic study is done and by using 'Cycle-Tempo' which is a computer based software at different operating conditions different plant configurations are modeled. From the results we can see that in case of ACC power plant the net energy is about 35.07 % and net exergy efficiency is about 30.88 %, respectively which is higher than the POCC plant by about 8 % and 7.04 %-points, respectively at 70% oxygen rich air supply. The reason is inferred by the huge auxiliary power consumption in the Air Separation Unit (ASU) of POCC based plant which is higher than the ACC based power plant by about 2.113 times. However, the CO_2 emission in case of POCC based plant is about 0.861 kg/kWh and it is about 3.198 times lower than the ACC based power plant due to lower volume of flue gas emission with higher concentration of CO_2 present in it. Further, the result shows that the performance of CCU for the POCC based plant is about 45.54% and contributing 2.07 times higher performance than the ACC based plant. In the flue gas there is a high concentration of CO_2 which reduces the auxiliary power consumption of POCC based plant per kg of CO_2 captured.

Keywords*:* Air-Coal Combustion, CO_2 Capture, Partial Oxy-Coal Combustion, Supercritical Power Plant

I. INTRODUCTION

Several environmental issues has been there due to increase in CO_2 concentration in atmosphere, among them one is global warming which is increase in global temperatures and it is is one of the notable features [1–3].In this context a key role must be played by Carbon Capture and Storage (CCS) for its mitigation in this context [4,5] along with Carbon Capture and Utilization (CCU) technology. There are 3 categories of CO_2 capture technology , first is Post-Combustion, second one is Pre-Combustion and the third one is Oxy-Fuel Combustion [4, 5]. The cost of the CCS technologies are very high and these technologies has not been previously used in industrial units and for the above factors are main reason for the technologies not been applied. For producing pure O_2 the air separation unit (ASU) consumes huge amount of energy, due to which there is significant amount of energy penalty and it is the main opposing factor for large-scale deployment of oxy-combustion [7]. A hybrid configuration is there which is termed as partial oxy fuel also can be called as partial oxy combustion and this can also be a good compromise between the post combustion technology and oxy fuel combustion technology and for short-term commercial applications this technology has been proposed [8]. The dilution of flue gas needs to be reduced by using nitrogen to enhance the CO_2 concentration if flue gas and it can be done by burning primary fuel in an oxygen rich environment. The ASU requirement for oxygen separation is smaller than the ASU required for oxy fuel combustion and for this in partial oxy combustion in terms of both capital cost and also energy penalty there is a lower incidence, also we require minor modifications for flue gas recirculation in conventional boilers; in parallel, amount of flue gas which is need to be treated is lower due to less dilution by nitrogen and as compared to conventional post-combustion processes, CO_2 partial pressure is higher [9].

II. METHODOLOGY

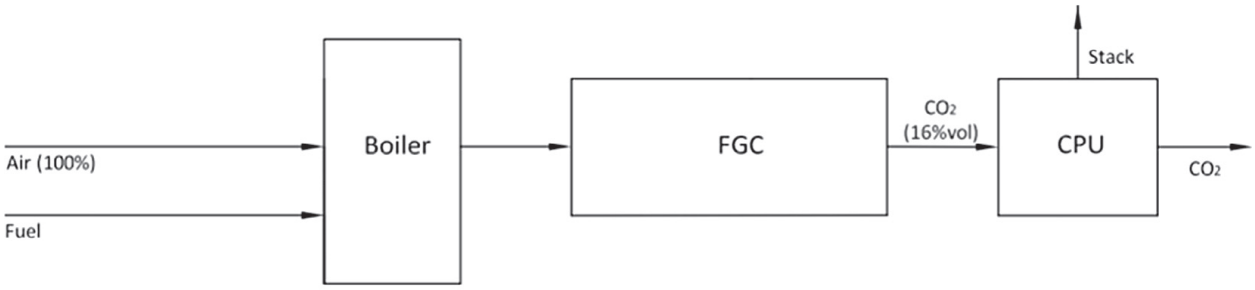

Fig.1: Conceptual diagram of an ACC based 500 MW_e Supercritical power plant with CO_2 capture

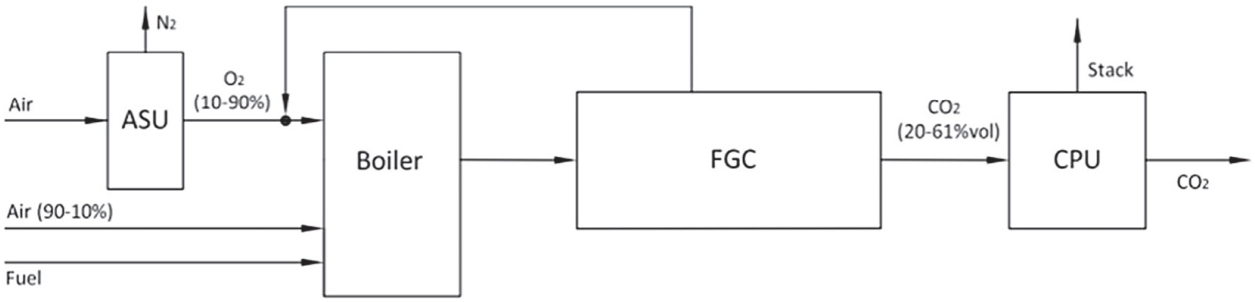

Fig.2: Conceptual diagram of an OCC based 500 MW_e Supercritical power plant with CO_2 capture

Schematic diagram of a Partial oxy coal combustion based Supercritical (SupC) power plant of capacity 500 MWe with CO_2 capture is shown in Fig.2. In the plant the parameters of the steam are 242.2 bar/537°C/565°C, reheating is done in single stage with final temperature of feed water at 280°C. In the SupC plant there is one number single-flow HP turbine, one number dual-flow IP turbine, and two numbers of double-flow LP turbines. The number of HP FWHs and LP FWHs are three, four respectively. ASU consists of two stage air compressors with intercoolers to obtain mole purity of O_2 at 95%. At the exit of ESP the flue gas passes through the Flue Gas Desulfurization (FGD) and Flue Gas Condenser (FGC). The flue gas at the exit of ESP passes through the Flue Gas Desulfurization (FGD) and Flue Gas Condenser (FGD) to obtain 0.85 mole purity of CO_2 with a CO_2 capture efficiency of 85%. Four-stages of compression and intercooling is done by compressing CO_2 to achieve pressure of 110 bar and to reach 35°C temperature with intercoolers for ease of transportation and storage. The Indian coals used in the power plants are of low grade (due to high mineral matter ~ 43%) and high quality as sulphur content is low (low sulfur content < 0.6%). The coal used here has high ash content and LHV value 15234 KJ/Kg.

III. ANALYSIS

Thermodynamic analysis of the ACC and POCC based 500MW SupC coal-fired steam power plants are done under steady state condition and analysis is done on the basis of exergy and energy. 'Cycle-Tempo' which is a computer flow sheet programme is used here, [6] the proposed power plants are simulated at different operating conditions. The required input parameters are pressure, temperature of all the pumps, different fans and HP,IP and LP turbines used and also their fuel quality and efficiencies, all the different operating conditions of the plant and also of the equipments and path of the process.

IV. RESULTS AND DISCUSSION

Overall, the net plant energy efficiency and net plant exergy efficiency of ACC based 500MW SupC steam power plant with CO_2 capture are about 35.07 % and 30.88 %, respectively and it is higher compared to the POCC based power plant by about 8 % and 7.04 %, points respectively. Moreover, higher auxiliary power consumption of POCC based power plant which is about 2.113 times more than ACC based power plant causes less energetic and exergetic plant performances compared of ACC based power plant. For the environment protection, POCC based power plant may be promoted over the ACC based power plant instead of poor plant performance.

Environmental impact of the ACC and POCC based power plants are studied and results of the analysis are given in Fig. 3 and Fig. 4. From Fig.3, it can be seen that the environmental benefits of POCC based power plant is more compared to the ACC based power plant as the amount of atmospheric emission and the CO_2 captured is drastically reduced to about 0.861 kg/kWh and 0.72 kg/kWh, respectively. Amount of dry fluegas at the inlet of membrane based CO_2 Capture Unit (CCU) is lower than the ACC based plant and thereby amount of CO_2 capture is reduced by about 0.06 kg/kWh compared to ACC based power plant. It is also analyzed that the performance of CCU for the POCC and ACC based plants are about 0.4554 and 0.2205 point, respectively and the same is shown in Fig.3. The performance of CCU for the POCC based power plant is higher than the ACC based power plant which is about 2.065 times as the CO_2 concentration increases in the fluegas stream. From Fig.4, it is found that the auxiliary power consumption of the POCC based power plant is about 31.12 % of total generation and as compared to the ACC based power plant it is higher due to additional power consumed by the Air Seperation Unit (ASU). It is also analyzed from Fig.4 that the power consumption per kg of CO_2 capture for the POCC based power plant is about 407.148 kW/kg which is about 1.335 times lower than the ACC based plant and this reduction is due to increase the performance of CO_2 Capture Unit (CCU) of OCC based plant.

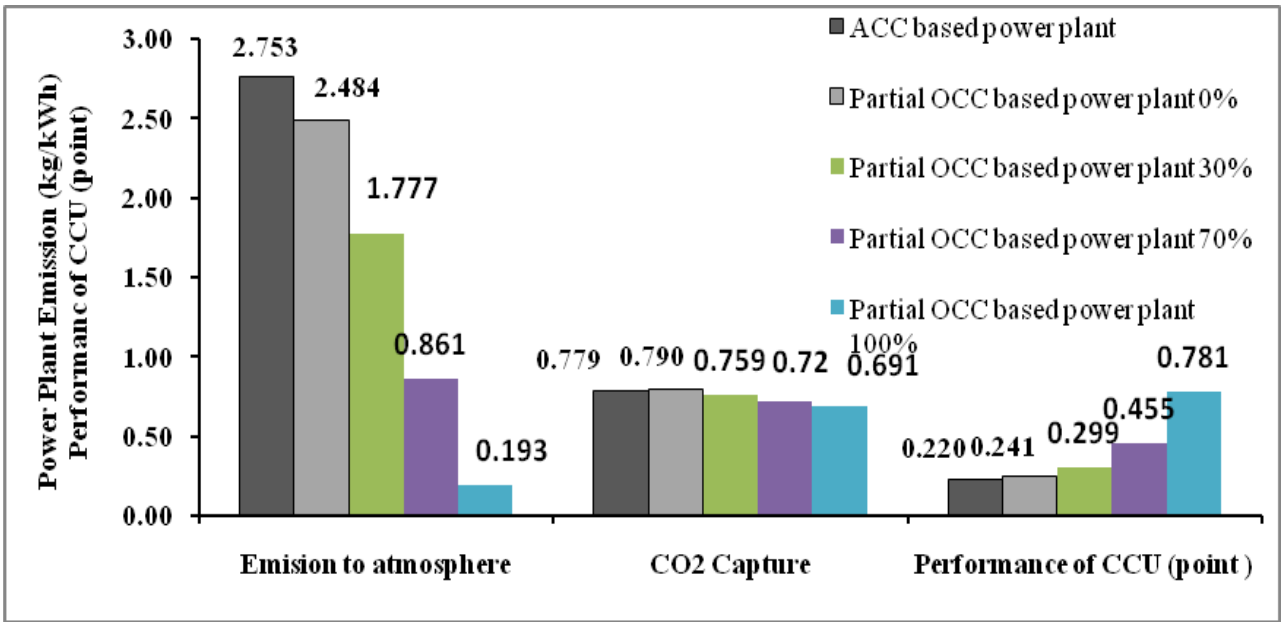

Fig.3 Environmental impact of the plants

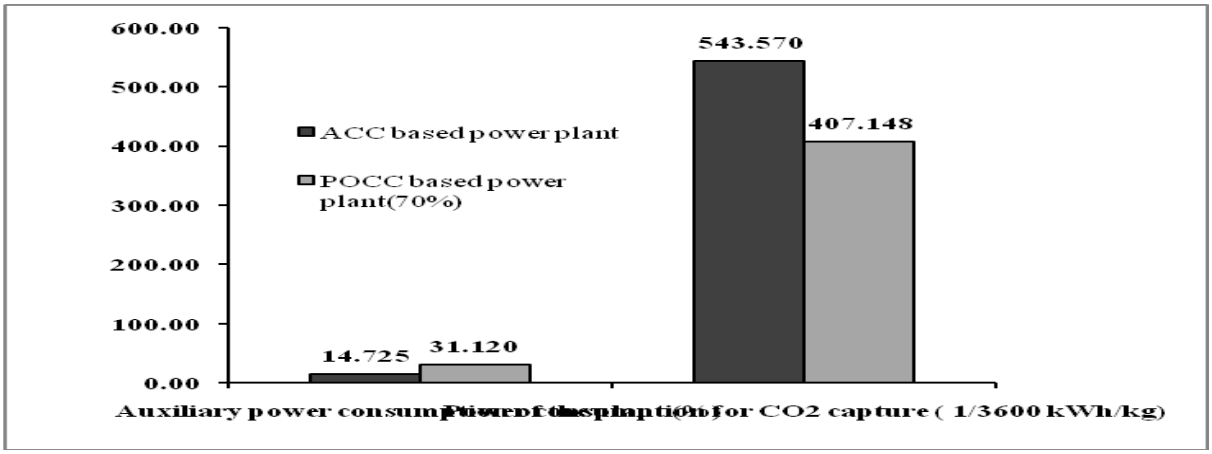

Fig.4 Comparative study on auxiliary power consumption of the plants

V. CONCLUSIONS

Major conclusions which can be drawn from the present study are as follows;

- 35.07 % and 30.88 % are the net plant energy and exergy efficiencies respectively of ACC based 500MW SupC steam power plant with CO_2 capture which is higher than the POCC based power plant by about 8 % and 7.04 %-points, respectively at 70% oxygen rich air supply. Additional power consumption by the ASU and fluegas recirculation of POCC based power plant cause poor energetic and exergetic performances of the plant.
- Compared to ACC based plant the environmental effect of POCC based plant is less as emission of CO2 to the atmosphere for POCC based plant is about 0.861 kg/kWh which is about 3.198 times lower than the ACC based power plant due to lower volume of flue gas emission with higher concentration of CO_2 present in it.
- The performance of CCU for the POCC based plant is about 45.54% and contributing 2.07 times higher performance than the ACC based plant due to increase in the CO_2 concentration in the fluegas stream.
- Due to higher performance of CCU auxiliary power consumption of the CO2 capture unit of the POCC based plant is about 1.34 times less than that for ACC based plant and the figure comes to 407.148 kW/Kg.

REFERENCES

1. BP Statistical Review of World Energy, June 2017.
2. Central Electricity Authority (CEA). Monthly review of power sector (executive summary): September 2017 Highlights of power sector, Government of India, 2017.
3. IPCC special report, Carbon dioxide capture and storage –Technical Report, 2005.
4. Buhre, B.J.P., Elliott, L.K., Sheng, C.D., Gupta, R.P., and Wall, T.F., Oxy-fuel combustion technology for coal-fired power generation, Progress in Energy and Combustion Science, Vol.31, PP.283-307, 2005.
5. Suresh, M.V.J.J., K.S. Reddy, and Kolar, A.K., 3-E analysis of advanced power Plants based on high ash coal, International Journal Energy Research, Vol.34, PP.716-735, 2010.
6. Cycle-Tempo. Release 5.0, Delft University of Technology, 2007.
7. Ortiz C, Valverde JM, Chacartegui R, Benítez-Guerrero M, Perejón A, Romeo LM. The Oxy-Coal process: a novel CO_2 capture system by integrating partial oxy-combustion with the calcium-looping process. Appl Energy 2017; 196:1–17.
8. Doukelis A, Vorrias I, Grammelis P, Kakaras E, Whitehouse M, Riley G. Partial O_2-fired coal power plant with post-combustion CO_2 capture: a retrofitting option for CO_2 capture ready plants. Fuel 2009; 88:2428–36.
9. Vega F, Navarrete B, Cano M, Portillo E. Development of partial oxy-combustion technology: new solvents applied to CO2 capture in fossil-fuels power plants. Energy Procedia 2014;63:484–9.

Investigation of Using Hemp as a Thermal Insulation Material in the Building Envelope in Terms of Thermal Comfort

[1]Okan KON, [2,*]İsmail CANER, [3]Samet ARDA

[1,2] Balikesir University Engineering, Faculty Department of Mechanical Engineering,
Cagis Campus, Balikesir, 10145, Turkey
[3]BHR Building Project Engineering San. Tic. Ltd. Şti. Bursa/Turkey

*E-mail: ismail@balikesir.edu.tr

Abstract:
In this study, the use of hemp as an insulation material in building envelopes such as external walls, ceilings, and floors has been investigated in terms of thermal comfort. For thermal comfort; the temperature difference between the inner surface of the external wall and the indoor environment and the difference between the ceiling surface temperature and the floor surface temperature is very important. In this study, thermal comfort analysis has been made for the building. The temperature difference between the inner surface of the external wall and the indoor temperature should be below 3 ^{0}C for an acceptable thermal comfort environment. The temperature difference between the ceiling and floor should be below 8 ^{0}C. For the values below these temperature differences, occupants can comfortably lead their lives in their buildings. In the study, thermal comfort analysis has been investigated according to the heat transfer coefficient which calculated depending on optimum insulation thickness and recommended values in TS 825. While the optimum insulation thickness was found, natural gas was used as an energy source for the heating period, and electricity was used for the cooling period.

Keywords: Hemp, insulation material, thermal comfort, surface temperature, building envelope

I. Introduction

The purpose of the study is to investigate the use of hemp as a thermal insulation material in building envelope in terms of thermal comfort depending on the inner surface temperatures. In the literature, thermal comfort analysis generally made for non-residential buildings. Residential and non-residential inspections are generally made based on the personal perceptions of the occupants living in the building. In this study, thermal comfort analysis has been carried out based on the differences in building envelope surface temperatures for buildings considering hemp as an insulation material. The lowest outdoor temperatures, soil temperatures, and attic temperatures used in the calculations were taken from Principles for the preparation of the projects of the central heating systems (TS 2164). The external wall heat transfer coefficient is calculated by accepting 20% column and 40% column.

II. Methodology

II. I. Calculation of Degree-day

For heating degree-day, T_i is indoor air temperature and taken as 19 ^{0}C and for cooling degree-day, indoor air temperature is taken as 22 ^{0}C. Degree-day values calculations are as follows (Ulaş, 2010, Kon, 2014),

If ($T_0 \leq T_i$) $\quad HDD=30\sum_1^{12}(T_i-T_0)$ (1)

if ($T_0 > T_i$) $\quad CDD=30\sum_1^{12}(T_0-T_i)$ (2)

II. II. Insulation thickness calculation depending on the insulation material recommended in TS 825

Overall heat transfer coefficient for building envelope,

$$U=\frac{1}{(R_i+R_w+\left(\frac{x}{k}\right)_{ins}+R_0)}$$ (3)

Total thermal resistance for non-insulated building envelope according to $R_{t,w}$ is the overall heat transfer coefficient of building envelope,

$$U=\frac{1}{(R_{t,w}+\left(\frac{x}{k}\right)_{ins})}$$ (4)

Here, R_i and R_0 are indoor and outdoor surface thermal resistances. x is insulation thickness; k is insulation materials' conduction heat transfer coefficient. (x/k) is insulation layers' thermal resistance (Bolattürk, 2006; Kaynaklı and Yamankaradeniz, 2007, Kon, 2017). When calculating U_a which is average heat transfer coefficient ($U_a=A.U_w+B.U_{col.}$); A is wall ratio and B is column ratio (Huang J. at all, 2020).

II. III. Calculation of surface temperatures

$$q=U.(T_i-T_0)$$ (5)

$$T_{si}=T_i-R_i.q$$ (6)

Here T_{si} is surface temperature of building envelope element, T_i is indoor air temperature, T_0 is outdoor air temperature and q is heat flux (TS 825, 2013).

II. IV. Optimum insulation thickness calculation

Optimum insulation thickness for heating + cooling can be calculated from the equation below;

$$x_{opt,\,H.C}=293.94\left(\frac{HDD.C_f.k.PWF.\,a}{H_u.C_i.\eta}+\frac{CDD.C_e.k.PWF.a}{C_i.COP}\right)^{1/2}-k.R_{t,w} \quad (7)$$

Here HDD is heating degree-day, CDD is cooling degree-day, H_u is lower heating value, COP is coefficient of cooling performance, η is heating system efficiency, C_f is fuel price, C_e is electricity price, C_i is cost of insulation material, a is constant for building envelope (for external wall=1, for floor=0.5 and for roofed ceiling=0.8) , k is conduction heat transfer coefficient of insulation material, PWF is present wort factor (Aslan, 2010; Bolatturk, 2006; Kon, 2014; TS 825, 2013). Where i is interest rate, g is inflation rate and N is life (Dombaycı et al., 2006).

If i<g real interest rate is $r=\frac{g-i}{1+i}$ (8)

If g<i real interest rate is $r=\frac{i-g}{1+g}$ (9)

Then $PWF=\frac{(1+r)^N-1}{r(1+r)^N}$ (10)

II. V. The values used in calculations

In Table 1, the heating and cooling degree-day values are given which calculated depending on the outdoor air temperatures given in the TS 825. Table 2 shows the lowest outdoor temperatures, temperatures between ceilings, soil temperatures, and unused basement given in TS 2164 for the selected cities, . In Table 3, fuel properties and financial values used in calculations for the heating and cooling period are given. The structural components of the sample building are shown in Table 4.

Table 1. Heating and cooling degree-day values

Zone	Heating Degree-day (HDD)	Cooling Degree-day (CDD)
1. Zone	*1430*	*556*
2. Zone	*2573*	*176*
3. Zone	*3248*	--
4. Zone	*4074*	--
5. Zone	*5052*	--

Table 2. The lowest outdoor temperatures, ceilings, soil and unused basement temperatures for selected cities (°C) (TS 2164, 200)

Zone	City	The lowest outdoor temperatures	The unused ceiling temperatures	The unused basement temperatures	Soil temperatures
1. Zone	Adana	*0*	*9*	*12*	*9*
2. Zone	Bursa	*-6*	*2*	*9*	*6*
3. Zone	Afyon	*-12*	*-3*	*6*	*6*
4. Zone	Yozgat	*-15*	*-6*	*6*	*6*
5. Zone	Ağrı	*-24*	*-12*	*3*	*3*

Table 3. Fuel characteristics and financial values (Ucar, Balo, 2010; Yılmaz, Koçlar Oral, 2018; Caner, 2020; Dlimi at all., 2019)

Parameter	Value
Natural gas price (C_f)	*0.385 $/m^3*
Natural gas lower heating value (H_u)	*34.485 10^6 J/m^3*
Heating system efficiency (η)	*% 93*
Annual price increase of natural gas (i)	*% 9.52*
Electricity price (C_e)	*0.107 $/kWh*
Inflation rate of increase (g)	*% 9.85*
Cooling system performance coefficient (COP)	*2.5*
Depending on the annual price increase of natural gas and inflation rate present worth factor (PWF)	*10.0*
Hemp insulation material price (C_i)	*100 $/m^3*
Life (N)	*10 year*

Table 4. Example building envelope components

Component	Thickness (m)	Conduction Heat Transfer Coefficient (W/m.K)
	External wall	
Internal surface thermal resistance (R_i=0.13 m^2.K/W)		
Lime mortar, lime cement mortar internal plaster	*0.02*	*1.00*
Perforated brick	*0.20*	*0.36*
Hemp Insulation material	*Table 5*	*0.04*
Cementm external plaster	*0.03*	*1.60*
External surface thermal resistance (R_0= 0.04 m^2.K/W)		

Table 4. Example building envelope components (continue)

Ceiling		
Roof space surface thermal resistance (R_i=0.08 m^2.K/W)		
Hemp Insulation material	*Table 5*	*0.04*
Floor covering	*0.01*	*0.19*
Cement mortar screed	*0.02*	*1.40*
Concrete floors	*0.15*	*2.20*
Lime mortar, lime cement mortar internal plaster	*0.02*	*1.00*
Internal surface thermal resistance (R_i=0.13 m^2.K/W)		
Floor		
Internal surface thermal resistance (R_i=0.13 m^2.K/W)		
PVC synthetic material coating	*0.01*	*0.23*
Leveling screed	*0.05*	*1.40*
Concrete floors	*0.12*	*2.20*
Hemp Insulation material	*Table 5*	*0.04*
Lean concrete	*0.10*	*1.65*
External surface thermal resistance (R_0=0)		
Column		
Internal surface thermal resistance (R_i=0.13 m^2.K/W)		
Lime mortar, lime cement mortar internal plaster	*0.02*	*1.00*
Concrete	*0.30*	*2.20*
Hemp Insulation material	*Table 5*	*0.04*
Cement mortar internal plaster	*0.03*	*1.60*
External surface thermal resistance (R_0= 0.04 m^2.K/W)		

III. Results and discussions

Insulation thicknesses are given in Table 5. In Table 6, heat transfer coefficients of the building envelope are shown which are recommended in TS 825 and depend on the optimum insulation thickness. In Table 7, average heat transfer coefficients of the external wall for two different column ratios are given. Table 8 shows the temperature differences of the indoor environment and the inner surface of the external wall depending on the different column ratios.

Table 5. Insulation thicknesses

Zone	External wall (U_{DD}) (Column ($U_{col.}$))	Ceiling ($U_{Cei.}$)	Floor (U_{Floor})
Recommend in TS 825 (m)			
Zone 1	*0.030*	*0.079*	*0.046*
Zone 2	*0.040*	*0.091*	*0.056*
Zone 3	*0.053*	*0.128*	*0.078*
Zone 4	*0.075*	*0.159*	*0.091*
Zone 5	*0.081*	*0.176*	*0.097*
Optimum insulation thickness (m)			
Zone 1	*0.060*	*0.067*	*0.050*
Zone 2	*0.076*	*0.081*	*0.061*
Zone 3	*0.086*	*0.089*	*0.068*
Zone 4	*0.100*	*0.102*	*0.077*
Zone 5	*0.115*	*0.115*	*0.088*

Table 6. The heat transfer coefficients of building envelope

Zone	External wall (U_{DD})	Ceiling ($U_{Cei.}$)	Floor (U_{Floor})
Recommend in TS 825 (W/m^2.K)			
Zone 1	*0.660*	*0.430*	*0.660*
Zone 2	*0.570*	*0.380*	*0.570*
Zone 3	*0.480*	*0.280*	*0.430*
Zone 4	*0.380*	*0.230*	*0.380*
Zone 5	*0.360*	*0.210*	*0.360*
Depending optimum insulation thickness (W/m^2.K)			
Zone 1	*0.442*	*0.490*	*0.619*
Zone 2	*0.375*	*0.418*	*0.529*
Zone 3	*0.343*	*0.386*	*0.484*
Zone 4	*0.306*	*0.343*	*0.437*
Zone 5	*0.275*	*0.309*	*0.390*

Table 7. Average heat transfer coefficients of external wall-column rate

Zone	Column	External wall	%20 Column %80 External wall	%40 Column %60 External wall
Depending on TS 825 (W/m^2.K)				
Zone 1	*0.913*	*0.660*	*0.711*	*0.761*
Zone 2	*0.744*	*0.570*	*0.605*	*0.640*
Zone 3	*0.599*	*0.480*	*0.504*	*0.528*
Zone 4	*0.451*	*0.380*	*0.394*	*0.409*
Zone 5	*0.422*	*0.360*	*0.373*	*0.385*
Depending optimum insulation thickness (W/m^2.K)				
Zone 1	*0.542*	*0.442*	*0.462*	*0.490*
Zone 2	*0.446*	*0.375*	*0.389*	*0.404*
Zone 3	*0.400*	*0.343*	*0.355*	*0.366*
Zone 4	*0.352*	*0.306*	*0.315*	*0.325*
Zone 5	*0.311*	*0.275*	*0.282*	*0.290*

* Considering the workmanship, the same insulation thickness is applied to the external walls and columns.

Zone	%20 Column %80 External wall	%40 Column %60 External wall	Inner surface of unused under-ceiling	Inner surface of unused above-ground	Temperature difference
Depending on TS 825 (^{0}C)					
Zone 1	*1.70*	*1.82*	*18.44*	*11.74*	*6.70*
Zone 2	*1.92*	*2.03*	*18.16*	*11.78*	*6.38*
Zone 3	*1.99*	*2.09*	*18.20*	*6.0*	*12.20*
Zone 4	*1.71*	*1.77*	*18.25*	*6.0*	*12.25*
Zone 5	*2.05*	*2.12*	*18.15*	*3.0*	*15.15*
Depending optimum insulation thickness (^{0}C)					
Zone 1	*1.14*	*1.19*	*18.36*	*11.69*	*6.67*
Zone 2	*1.27*	*1.31*	*18.08*	*8.73*	*9.35*
Zone 3	*1.43*	*1.48*	*17.90*	*6.0*	*11.90*
Zone 4	*1.39*	*1.44*	*17.89*	*6.0*	*11.89*
Zone 5	*1.58*	*1.62*	*17.76*	*3.0*	*14.76*

IV. Conclusions

Since the columns have surfaces both outside and inside, they should be considered together in thermal comfort calculations depending on the proportions of the external wall and the column. It has been observed that the temperature difference between indoor and indoor surface temperatures due to optimum insulation thicknesses is much lower. Especially for 20% column and 80% outer wall area, this temperature difference is even lower. It is calculated that it is half the temperature difference of 3 ^{0}C recommended in TS 825. It has been determined that the optimum insulation thickness for external walls is much more suitable in terms of thermal comfort.

It has been determined that there is not a big difference between the temperature difference between the unused under-ceiling inner surface calculated based on heat transfer coefficients and the inner surface temperature difference above the unused floor and the temperature difference between the internal environment and the inner surface of the wall depending on the optimum insulation thickness according to each climate zone recommended in TS 825. The temperature difference between the unused under-ceiling inner and the unused above-ground inner surface temperature was found only in the first and second climatic zones below 8 ^{0}C recommended in the literature. Especially in the fifth climate zone, it can reach twice the value with 15 ^{0}C. This is an undesirable situation in terms of thermal comfort.

References

Aslan, A., 2010, Investigation of energy and thermoeconomic efficiency of Gonen geothermal district heating system, PhD Thesis, Balikesir University Institute of Science, Balikesir. Turkey.

Bolattürk, A., 2006. Determination of optimum insulation thickness for building walls with respect to various fuels and climate zones in Turkey. Applied Thermal Engineering, 26,11-12,1301-1309. https://doi.org/10.1016/j.applthermaleng.2005.10.019

Caner, I., 2020, Optimization of heating and cooling load in hospitals in terms of thermal comfort and energy consumption, Ph.D. thesis, Balikesir University Institute of Science. Turkey.

Dlimi M., Iken O., Agounoun R., Zoubir A., Kadiri I., Sbai K., 2019, Energy performance and thickness optimization of hemp wool insulation and air cavity layers integrated in Moroccan building walls, Sustainable Production and Consumption , 20, 273–288. https://doi.org/10.1016/j.spc.2019.07.008

Dombaycı, Ö. A.,Gölcü, M., Pancar, Y., 2006, Optimization of insulation thickness for external walls using different energy-sources, Applied Energy, 83, 9, 921-928. https://doi.org/10.1016/j.apenergy.2005.10.006

EVS-EN ISO 7730 Ergonomics of the thermal environment –Analytical determination and interpretation of thermal comfort using calculation of the PMW and PPD indices and local thermal comfort criteria, 2006.

Huang, J., Lv, H., Feng, W., Qu, P., Huang, Z., 2020, Determination of economical thermal insulation thickness for a building wall with two parallel structures, Energy Sources, Part A: Recovery, Utilization, And Environmental Effects, 42,4, 339-409. https://doi.org/10.1080/15567036.2019.1587086

Kaynaklı, Ö.,Yamankaradeniz, R., 2007, Isıtma süreci ve optimum yalıtım kalınlığı hesabı, VII. Tesisat Mühendisliği Kongresi, İzmir, Türkiye, 25-28 Ekim, 187-195.

Kon, O. 2017. Environment-Friendly heat insulation material used in the scope of ecological sustainability and use of renewable energy related to these factors , Academia Journal of Engineering and Applied Sciences, 1, 3, 143-155.

Kon O., 2014, Determining theoretically and practically the optimum insulation thickness of buildings used for different purposes according to heating and cooling loads, PhD Thesis, Balikesir Universty, Balikesir University Institute of Science, Turkey.

Türk Standardı, TS 825, Thermal insulation regulations in buildings, December 2013.

Türk Standardı, TS 2164, Principles for the prefaration of the projects of the central heating systems, 2000.

Ucar, A. and Balo, F., 2010, Determination of the energy savings and the optimum insulation thickness in the four different insulated exterior walls, Renewable Energy. 35, 1, 88-94. https://doi.org/10.1016/j.renene.2009.07.009.

Ulaş, A., 2010, Basen on TS 825 directivce, analysis of heat loss, fuel consumption, carbondioksit emission and cost for buldings, M.Sc. Thesis, Gazi University Institute of Science And Technology, Ankara, Turkey.

Yılmaz, Y. Oral, K. G., 2018, An approach for an educational building stock energy retrofits through life-cycle cost optimization, Architectural Science Review, 61, 3, 122–132. https://doi.org/10.1080/00038628.2018.1447438

Impact of Fossil Fuel Subsidies on Renewable Energy Sector

[1*]Sikandar Abdul Qadir, [2]Furqan Tahir, [1]Luluwah Al-Fagih,
[1] Division of Engineering and Management Sciences, College of Science and Engineering, Hamad Bin Khalifa University, Doha - 34110, Qatar
[2] Division of Sustainable Development, College of Science and Engineering, Hamad Bin Khalifa University, Doha - 34110, Qatar

* E-mail: sqadir@hbku.edu.qa

Abstract
The incessant growth of carbon emissions from fossil fuel based power plants need to be controlled in order to limit the global temperature rise. Energy subsidies are one of the reasons for the over consumption of fossil fuel all over the world. Instead of providing benefits, they are damaging the environment. In comparison, subsidies for renewable energy (RE) are very low which is one of the factors for the laggard growth. Additionally, subsidies data for the renewables is not available, unlike fossil fuel. In this work, we discussed that by providing subsidy the cost of environmentally damaging fuel is decreased hence excess usage. Subsidies for renewable may provide long term benefits, are also discussed and some policy recommendations are put forward to accelerate the growth of RE across the world.

Keywords: Fossil Fuels, Subsidies, Barriers, Renewable Energy, Incentives

I. Introduction
It has been a known fact that for many years that the consumption of fossil fuel (FF) is damaging the environment (Ali et al., 2018; Imteyaz and Tahir, 2019; Tahir, 2014). However, after many years of research and studies that discourage fossil fuel use, the World is still consuming the FF for the energy needs (Tahir et al., 2019). The term "Fossil-Fuel" is composed of two-word, Fossil, which means the preserved remains of animals and plants on the Earth for millions of years. Fuel, any substance used to produce energy for useful work, i.e., heat engines, electricity generators, etc. There are different kinds of fossil fuel in different states which exist in Earth's crust, such as (i) Petroleum, (ii) Coal, and (iii) Gas. These three are the major categories of fossil fuel and have varying emissions levels depending on the composition of the material. Their presence in the Earth's crust also varies based on the type of fuel that is extracted. Extraction is also an energy-intensive process as drilling is required to find the deposits of the FF. World's largest FF deposits were found in the Middle East (Charles et al., 2014). The abundance of FF in the region has led to the overuse of the resource. Furthermore, all states in the region have support mechanisms such as subsidy to support consumers and producers. Additionally, subsidies for FF are the driving factor for economic activity, particularly in the GCC region (Charles et al., 2014). One of the main reasons to discourage FF use is due to CO_2 and other gases emitted when any FF is burned. When more FFs is burned, ultimately CO_2 emission will increase which is main cause for environmental damage.

It has been projected that energy demand will rise by 12% between 2019 and 2030. Although the rise will not be the same for energy after the pandemic, and it is anticipated that the global demand will increase by 9% till 2030 (IEA, 2020a). To achieve this 9% target of energy demand with minimal FFs is challenging for the global community. Since complete removal for FF usage will not reduce due to the economic growth, specifically in Brazil, China, Russia and India (Apergis, 2019). Therefore, policies must be formulated in such a way that discourages the use of FFs. One of the key policy measures to reduce the use of FF is to promote the use of renewable energy (RE) with support mechanism to encourage investment but so far we have not reached the levels where we can assure that we can manage the climate crisis. United Nations sustainable development goal (SDG-7) is related to the use of clean energy resources (United Nations, n.d.); it has been reported in the annual review that the target set for 2030 for clean energy resources will not be achieved due to less deployment of RE resource worldwide (Nemitallah et al., 2020). The lower installation of renewables is due to subsidy present still for the FFs; therefore, power generation is still based on FFs. In this study, we have first discussed the FFs subsidies in detail. FFs subsidies are one of the significant barriers in shifting the World towards renewable energy. We have then enlightened the potential of renewable energy to overcome the growing energy needs of the World. Policies related suggestions are highlighted in the discussion section with concluding remarks.

II. Fossil Fuel Subsidies
A subsidy is defined as the government's additional amount to lower the actual of the FF (Hayer, 2017). From IEA data for total energy supply we can observe that in 2018, oil and coal were the major source of fuel supply to the world as shown in Fig. 1 (IEA, 2018). Use of fossil fuel for the energy needs all overall the world signifies that priority is still the FF for energy needs. Subsidy for the FF has decreased in the recent years and it is expected it will be around $181.9 Billion this year as shown in Fig. 2 (IEA, 2020b). Fig. 3 represents the total amount in USD for the subsidy provided in 42 countries extracted from IEA Data from 2010 to 2019 (IEA, 2020b). In 2019, $317.5 Billion has been spent on fossil fuel subsidies, as reported in the IEA Database (IEA, 2020b).

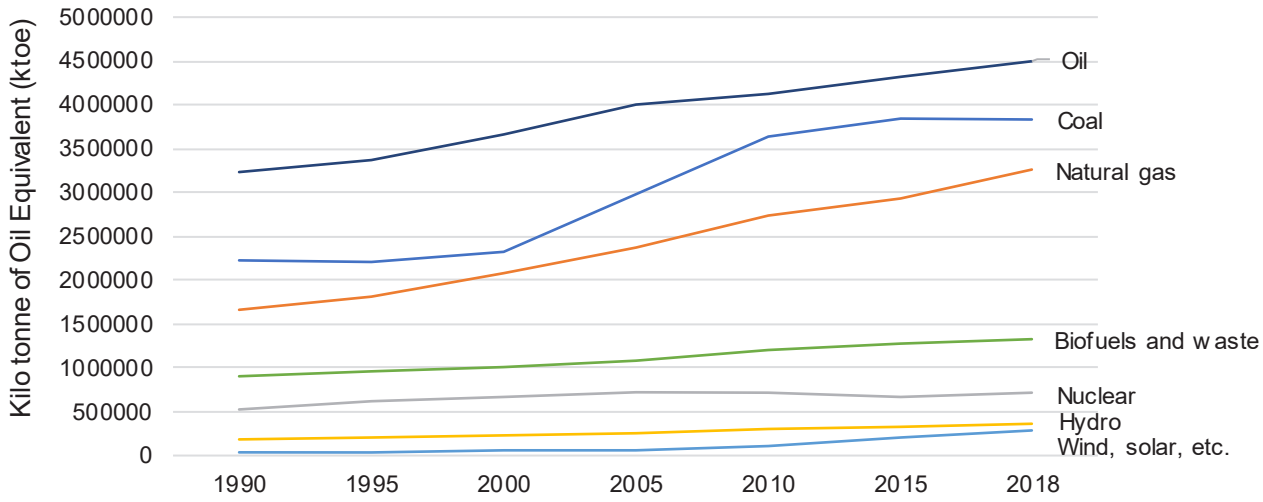

Fig. 1: Total Energy Supply by Fuel Source (IEA Data 1990 - 2018)

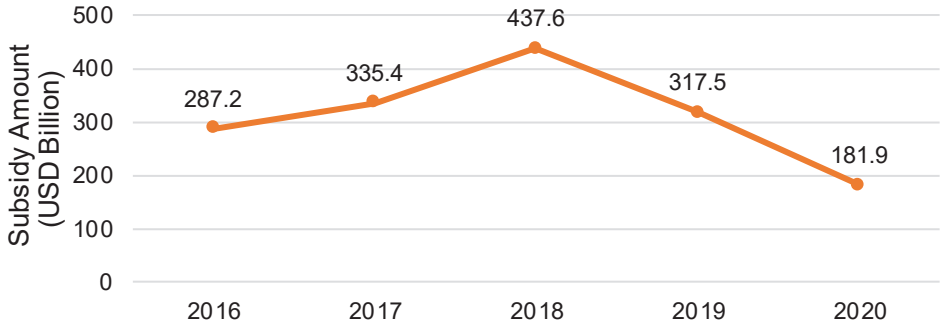

Fig. 2: Downward trend in the Subsidy for Fossil Fuel since 2018 (IEA)

III. Replacing Fossil Fuel Subsidies with Renewable

Renewable energy subsidies are not well documented, unlike FFs subsidies. FFs subsidies data is widely available on different sources such IEA due to their preeminence in the energy sector (IEA, 2020b). Therefore, it is difficult to calculate how much support is provided to renewable energy projects in the recent years. A 2017 report from IRENA "Energy subsidies: Evolution in the global energy transformation to 2050" reported about the renewable energy subsidy for the world's major energy consumers nation represented in Fig. 4 (Taylor, 2020). If we compare the RE subsidy data to the FFs subsidy it is almost half of FFs subsidy. Additionally, it should be noted that subsidy provided for the renewable is not directly for the consumers but rather for encouraging the investment in renewable energy sector such as tax benefits, energy related services at cost lower than actual etc.

With the post-pandemic growth rate mentioned in the "IEA World Energy Outlook 2020", there is still a need to discover clean energy resources to meet the world demand in the future. More investment is needed to ensure that the 2030 SDG target is achieved (Nemitallah et al., 2020). Renewable energy potential worldwide can be estimated from the fact that currently 26.2% of electricity is produced from RE and it had the potential to reach 45% of global electricity generation by 2040. This potential for RE is estimated using Solar, wind and hydropower (C2ES, 2019). At present, solar and wind project cost have become low-priced due to mature technology. There is a debate that subsidies for renewables, which are already low, should be wholly removed ("It's Time to End Subsidies for Renewable Energy - America's Power," 2020; Perry et al., 2020). Investors finance renewable energy projects because, with support mechanisms from the states, selling cheap electricity to the grid is still financially feasible for them. As solar and wind both are a variable source of energy, the selling price is already low to grid compared to a conventional energy source, i.e., fossil fuel (Perry et al., 2020).

To keep renewable energy price low and minimize the damage to environment, FFs subsidies should be directed for the renewables. It will significantly impact on the overall transition to RE. Few of the advantages are listed below (Bridle et al., 2019):

- Revenue stream for government will increase once the FFs subsidies are removed, and actual energy price will be charged for FFs.
- With emission reduction targets, there is a need to shutdown gradually non clean energy resource, reduction in subsidies for FFs should decrease any new investment in the FFs based plants and business will ultimately shift towards clean energy plants.
- This replacement of energy subsidy will not only help now to reach climate change targets but will help

countries in future to have cheap energy resource which is directly linked to the economic development. Industries will have abundant energy resources to manufacture more with clean and cheap energy which makes them more competitive in the international market.

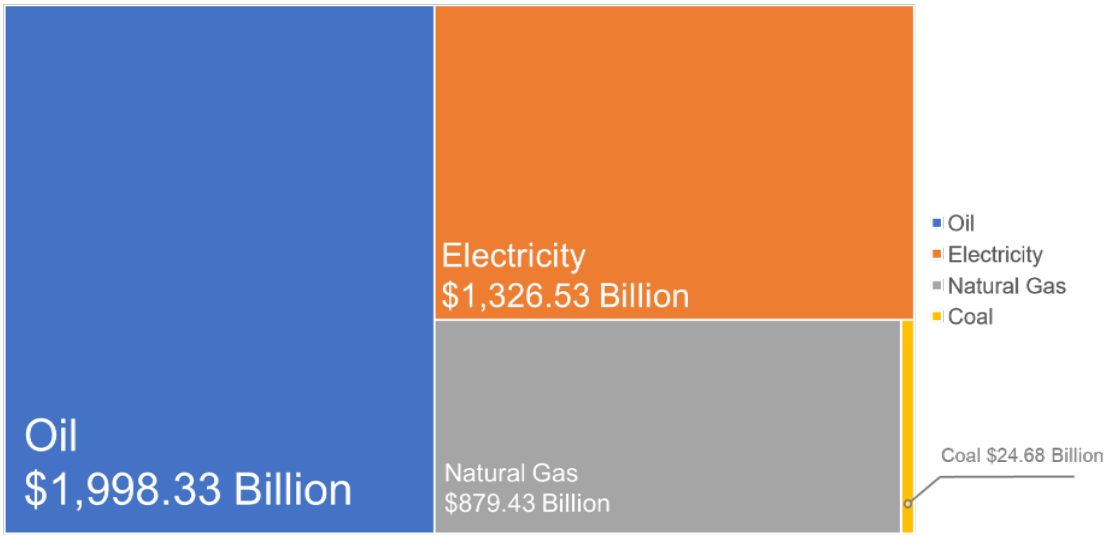

Fig. 3: Total Fossil Fuel Subsidies 2010 - 2019

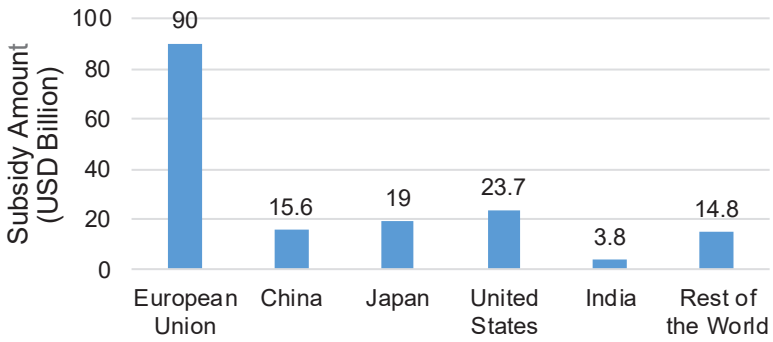

Fig. 4: Renewable Energy Subsidy 2017 (IRENA)

IV. Discussion

With the current fossil fuel subsidy, it is expected that the oil industry will remain profitable and it may extract the half of domestic oil reserves in the US which leads to the higher production rate and more CO_2 will be emitted to the atmosphere (Coleman and Dietz, 2019; Erickson et al., 2017). Therefore, it should be stressed that policies to diverge the FFs subsidies towards Renewables are formulated. Two methodologies can be applied for such transformation either by selling cheap renewable electricity to the final consumer or by providing support for investment in building the RE plants infrastructure. By providing the support for the renewable, two objectives can be achieved. First, Electricity will reach in rural underdeveloped areas where transmission lines are not available. They can generate their own electricity from various means such as solar, wind and hydro. This will ultimately improve the quality of life in the rural areas. Second, job opportunities will be created for the locals due the renewable energy plants. Few of the policy directions for renewable energy promotion are mentioned below:

- Comprehensive database for RE subsidy should be available like FF subsidy for the comparison.
- International monitoring body such as IRENA should work with UN to monitor progress of SDG – 7 i.e. usage of clean energy resources.
- Role of IRENA in promoting and prioritizing renewable usage should be made more inclusive.
- Innovative fiscal incentives should be provided to increase the share of RE in energy usage and reduce the FFs consumption and subsidies in general.
- Gradual plan for the removal of FF subsidies and closure of non-clean energy plants should be prepared with discussion from all stakeholder.

V. Conclusion

As we are experiencing difficult times now due to the COVID-19 pandemic, it is essential to save the taxpayers money by diverting the capital allocated for the subsidies to other stimuli such as healthcare or the promotion of renewable energy. The World economies were shut down or are partially open at present; energies usage has been significantly reduced, which also paves the way to reduce subsidies gradually. Governments across the World can

use this time to align their resources to mitigate the climate change issue. Since the start of the pandemic, it has been noticed GHG has been reduced during this time, but if strict measures are not taken to curb the GHG emissions, the rate of emissions will be higher as people are more likely to go out after the lockdown restrictions are eased.

References

Ali, H., Tahir, F., Atif, M., AB Baloch, A., 2018. Analysis of steam reforming of methane integrated with solar central receiver system, in: Qatar Foundation Annual Research Conference Proceedings. p. EEPD969.

Apergis, N., 2019. Chapter 6 - Renewable Energy and its Finance as a Solution to the Environmental Degradation, in: Özcan, B., Öztürk, I. (Eds.), Environmental Kuznets Curve (EKC). Academic Press, pp. 55–63. https://doi.org/https://doi.org/10.1016/B978-0-12-816797-7.00006-0

Bridle, R., Sharma, S., Mostafa, M., Geddes, A., 2019. Fossil Fuel to Clean Energy Subsidy Swaps: How to pay for an energy revolution GSI REPORT.

C2ES, 2019. Renewable Energy — Center for Climate and Energy Solutions [WWW Document]. Cent. Clim. Energy Solut.

Charles, C., Moerenhout, T., Bridle, R., 2014. The Context of Fossil-Fuel Subsidies in the GCC Region and Their Impact on Renewable Energy Development.

Coleman, C., Dietz, E., 2019. Fossil Fuel Subsidies: A Closer Look at Tax Breaks and Societal Costs [WWW Document]. EESI.

Erickson, P., Down, A., Lazarus, M., Koplow, D., 2017. Effect of subsidies to fossil fuel companies on United States crude oil production. Nat. Energy 2, 891–898. https://doi.org/10.1038/s41560-017-0009-8

Hayer, S., 2017. Fossil Fuel Subsidies.

IEA, 2020a. World Energy Outlook 2020 [WWW Document]. IEA, Paris.

IEA, 2020b. Energy subsidies Tracking the impact of fossil-fuel subsidies [WWW Document]. IEA, Paris.

IEA, 2018. Data & Statistics - IEA [WWW Document]. IEA, Paris.

Imteyaz, B., Tahir, F., 2019. Thermodynamic analysis of premixed and non-premixed oxy-methane combustion cycle with membrane assisted oxygen separation, in: 8th Global Conference on Global Warming (GCGW), Doha, Qatar. p. 33.

It's Time to End Subsidies for Renewable Energy - America's Power [WWW Document], 2020. . Am. Power.

Nemitallah, M.A., Abdelhafez, A.A., Habib, M.A., 2020. Approaches for Clean Combustion in Gas Turbines, Fluid Mechanics and Its Applications.

Perry, A., Cleary, M., Wyman, O., 2020. Why It's Too Soon To Sunset Renewable Energy Subsidies [WWW Document]. Forbes.

Tahir, F., 2014. Experimental & Numerical Investigations of Oxy-fuel Combustion Using Porous Plate Reactor. King Fahd University of Petroleum and Minerals.

Tahir, F., Ali, H., Baloch, A.A.B., Jamil, Y., 2019. Performance Analysis of Air and Oxy-Fuel Laminar Combustion in a Porous Plate Reactor. Energies 12, 1706. https://doi.org/10.3390/en12091706

Taylor, B.Y.M., 2020. Energy subsidies: Evolution in the global energy transformation to 2050, International Renewable Energy Agency.

United Nations, n.d. Sustainable Development Goals [WWW Document]. Sustain. Dev. Knowl. Platf.

Simulation of Heavy Duty Electric Vehicle Powertrain with Wheeled and Half Tracked Alternatives

[1*]Mustafa Umut Karaoğlan
[1]Dokuz Eylul University, Engineering Faculty, Department of Mechanical Engineering, Buca, Izmir, 35390, Turkey

* E-mails: mustafa.karaoglan@deu.edu.tr

Abstract
Electric vehicles offer clean and efficient options in transportation and heavy duty applications. Electrification of heavy vehicles which can be used in transportation, construction and military applications, can reduce fuel consumption and exhaust emissions more than small sized vehicle. In this study, drive cycle analysis of heavy duty electric vehicle is performed using Matlab/Simulink for both wheeled and half tracked powertrain alternatives. Battery power requirements and SOC (State of Charge) history is determined according to the drive cycle of HHDDT (Heavy Heavy-Duty Diesel Truck) Transient Mode for constant vehicle weight and battery capacity. On the other hand, gradebility of vehicles is calculated as slope potential during the drive cycle. According to the results, it is clearly shown that, higher vehicle range is achieved by wheled alternative but half track vehicle offers higher climbing potential.

Keywords: Electric vehicle, heavy duty, half tracked, wheeled

I. Introduction

Many studies about heavy duty vehicles are conducted with electric powertrain technology for cleaner environmental impacts and reduced fuel consumptions with efficient way in the literature. However, there are not many studies in the literature on electrical options for heavy vehicles operating in difficult terrain conditions that are specially prepared for them to maintain their movements. The simulations of the vehicle model created in the developed computer programs can be compared with the types of electric drive vehicles that are widely used today.

Over the years, empirical and theoretical models developed to predict the performance of tracked and wheeled heavy vehicles on off road conditions. Consequently, the mechanics of vehicle-terrain interaction is of importat for the proper selection of vehicle configuration and design parameters to meet specific operational requirements (Wong, 2008). In order to present important aspects of the tracked vehicles, dynamic modelling of the powertrain system for a tracked vehicles has been simulated for fuel economy and vehicle performance (Switonski, Kciuk, 2011). A five degree-of-freedom steering model of a tracked vehicle has been developed theoretically to determine handling behavior during non-stationary motion at high and low speeds individually (Janarthanan and Padmanabhan,2011). The powertrain of a dual-motor driven hybrid electric tracked-vehicles are modeled using Double Deep Q-learning algorithm for the fuel economy (Han, Xuefeng, et al., 2019). A sliding mode control was simulated using MATLAB/Simulink based on active co-operative braking strategy for an electrified heavy commercial road vehicles (Subramaniyam and Subramanian, 2020).

According to the literature survey, there are many studies on modeling wheeled and tracked vehicles in Matlab/Simulink environment individually. However, studies about the half-tracked vehicles have been focused on vehicle mechanics for conventional heavy vehicles. In this study, wheeled and half-tracked drive types of an electric heavy vehicle is modelled individually and the results of the powertrain analysis are compared for vehicle performance.

II. Simulation Methodology for Wheeled and Half Tracked Powertrains

Heavy vehicles moving under difficult operating conditions for the best performance in all terrain. In this study, the power requirement of the batteries for an electric wheeled heavy vehicle and a half-tracked heavy vehicle, which have same weight, was determined in Matlab/Simulink environment. Battery power requirement output has been used for the vehicle range and the SOC of the battery depending on the simulation time. Simulation model is created in Matlab/Simulink, which includes vehicle motion resistance submodel, battery submodel and drive cycle inputs.

In the simulation model, the battery power requirement of both types of electric heavy vehicles was calculated the resistive forces acting on the vehicle. These resistance forces for wheeled heavy vehicle are; rolling resistance force (F_R), air resistance force (F_L) and acceleration resistance (F_a) force. Half-tracked vehicle which is driven by the track, is considered as a rear-drive heavy vehicles and F_R is the rolling resistance acting on the wheels on the front axle of the vehicle, R_{in} is the internal resistance of the track at the rear and R_c is the tracked motion resistance, F_L is air resistance and F_a is acceleration resistance. F_a^- is regenerative braking force which is included for both types of vehicles. The battery power requirement including these resistance forces was modeled using Eq. 1.

$$\begin{Bmatrix} P_B = \frac{(F_R+F_L+F_a+F_a^-.\eta_{EM}.\eta_M.\eta_B)}{\eta_{EM}\ .\eta_M\ .\eta_B}.\ V_w \\ P_B = \frac{(F_R+R_{in}+R_c+F_L+F_a+F_a^-.\eta_{EM}.\eta_M.\eta_B)}{\eta_{EM}\ .\eta_M\ .\eta_B}.\ V_{ht} \end{Bmatrix} \quad (1)$$

where V_w is the speed of the wheeled vehicle (m/s), V_{ht} is the speed of half-tracked vehicle (m/s for the speed profile shown in Fig.1. η_{EM} is the electric motor efficiency, η_m *is the* mechanical efficiency and η_B is the battery efficiency. The front axle forces are used the calculation of F_R rolling resistance for front axle of half-tracked heavy vehicle. R_{in} is the internal resistance (N) of the track and suspension system where are in the rear axle of half-tracked vehicle. Due to the complexity of these structures, it is very difficult to determine the internal resistance by analytical methods. The average internal resistance approach developed by (Bekker,1956) is used for the rear axle resistance forces in the calculations. R_c (N) is the resistance resulting from the vehicle-terrain interaction and is calculated using the sinking amount of the track at the rear side of the vehicle. The power requirement ofthe battery was calculated as a result of the resistance powers of the vehicle. The state of charge ($SOC(t)$) and the vehicle range ($X_{w,ht}$) are calculated from battery energy requirement during the drive cycle of both types of vehicles and the equations are shown in Eq. 2 and Eq. 3, respectively.

$$SOC(t) = SOC_i - \frac{1}{Q_{bat}} \int_0^t I_{bat} \, . \, dt \tag{2}$$

where SOC_i is the initial battery charge, Q_{bat} is the battery capasity (kWh) and I_{bat} is the battery current (A).

$$X_{w,ht} = x_{tot} . \frac{Q_{bat}}{E_{bat}} \tag{3}$$

where x_{tot} *(m)* is the amount of distance the vehicle travels through the cycle andE_{bat} is the required energy in the battery during the cycle.

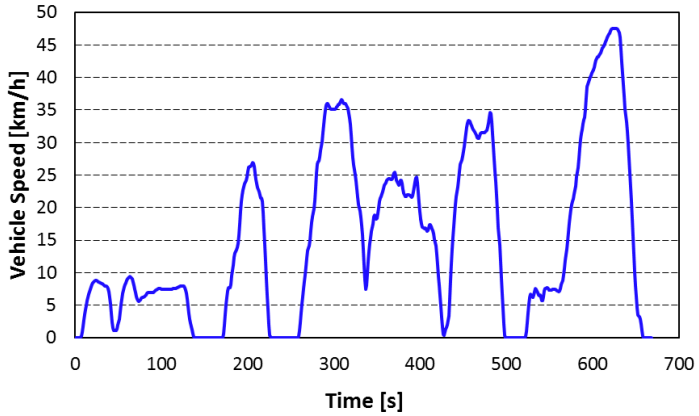

Fig. 1. Speed profile of HHDDT-Transient Mode drive cycle for the powertrain simulation

The simulation models created in this study were created using the formulations that given and the results were obtained by defining the parameters shown in Table 1 as input to the model.

Table 1.Parameters for simulation models of wheeled and half tracked vehicle

Definitions	Parameters	Value	Unit
Vehicle Mass	m	8000	kg
Gravitational Acceleration	g	9,81	m/s^2
Electric Motor Efficiency	η_{EM}	0,9	-
Mechanical Efficiency	η_M	0,9	-
Battery Efficiency	η_B	0,92	-
Initial Battery Charge (SOC_i)	SOC_i	0,8	-
Battery Capacity	Q_{bat}	250	kWh
Adhesion Coefficient For Wheeled Vehicle	μ_w	0,7	-
Adhesion Coefficient For Half-Tracked Vehicle	μ_{ht}	0,8	-

The simulation modelwere designed to calculate the climbing performance in Matlab/Simulink for both drive types of the heavy vehicles. α_w is the maximum angle of climbing performance for the wheeled vehicle and α_{ht} is the maximum angle of climbing performance for the half-tracked vehicle and the equaitions of the angles are shown in Eq. 4 and Eq. 5 according to the road adhesion coefficients (μ_w and μ_{ht}), respectively.

$$\alpha_w = \sin^{-1}[(G.\mu_w.\cos\alpha_w) - (F_R.\cos\alpha_w + F_L + F_a)] \tag{4}$$

$$\alpha_{ht} = \sin^{-1}[(G.\mu_{ht}.\cos\alpha_t) - (F_R \, .\cos\alpha_t + R_{in} + R_c + F_L + F_a)] \tag{5}$$

where G is the vehicle weight

Powertrain models have been created for both types of vehicles in Matlab/Simulink. The sub-blocks where the vehicle resistances and related battery energy requirement were calculated, the vehicle range was calculated and the SOC was calculated were included in the model. The output results obtained according to the input parameters of speed profile values.

III. Results and discussions

In this study, Matlab/Simulink model was created to calculate the power consumption for determining vehicle performance of both wheeled and half-tracked heavy vehicles. Speed profile of HHDDT-Transient Mode drive cycle defined as the input parameter for the simulation model. Battery power requirements of the vehicle for two different types of electric heavy vehicle parameters were calculated and shown in the Fig.2a. Additionally, the SOC history was calculated by using the battery power requirement and shown in the Fig.2b.

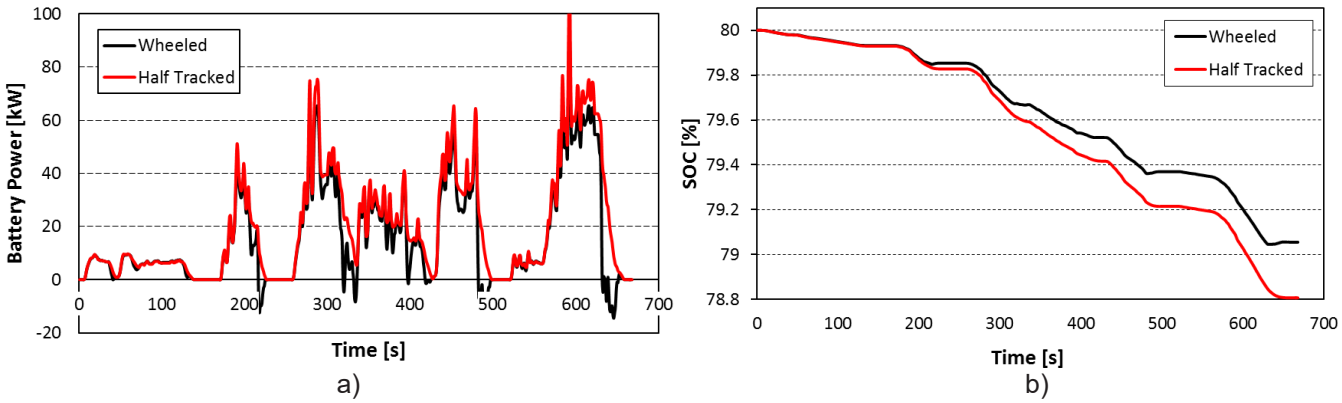

a) b)

Fig. 2. Battery power requirements (a) and SOC history (b) of wheeled and half tracked alternatives of the vehicle

As a result of the resistance forces, the battery power requirement of half-tracked vehicle is higher than wheeled type of a heavy vehicle. The maximum power requirement for the half-tracked vehicle was occurred as about 100 kW during the drive cycle. However, 89 kW power was required in the battery for the wheeled heavy vehicle. As a result of the selected road profile and battery capacity parameters, the energy requirement for a half-tracked heavy vehicle was calculated as 3.7 kWh as a result of the cycle time. However, the energy requirement was calculated as 2.95 kWh was for wheeled heavy vehicles. Fig. 2b shows the SOC values of two different types of vehicle batteries. As can be seen,the state of charge of the battery decreases faster as a result of the higher power requirement during the cycle time given in the speed profile of the half-tracked vehicle. The SOC of battery, which was 80% at the beginning, droped to 79.05% in the wheeled vehicle and to 78.8% in the half-tracked vehicle as a result of one cycle. The range values calculated based on the energy values required by the vehicle batteries were calculated as 241.4 km for a wheeled vehicle and 191.1 km for a half-tracked vehicle.

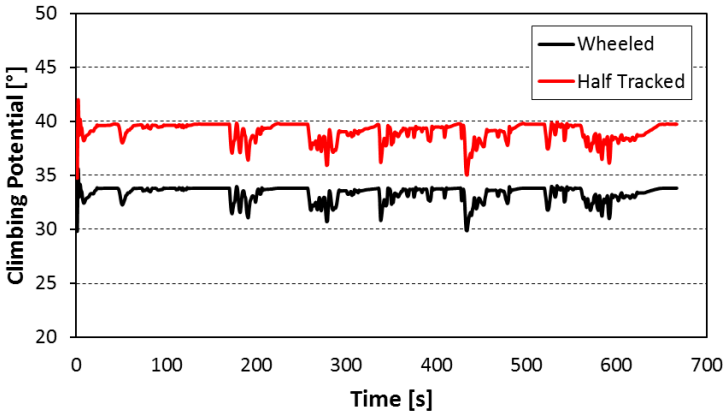

Fig. 3. Climbing potential of wheeled and tracked alternatives of the vehicle during the drive cycle

Maximum slope angle is an important factor in vehicle performance, especially of the heavy off-road vehicles. Fig.3 shows climbing potential of the wheeled and the tracked types of vehicles according to the Eq. 4 and 5. The results show that maximum 34 degrees climbing angle potential could be achieved for wheeled vehicle. However, this potential was calculated as maximum 40 degrees for the half-tracked vehicle. Although a half-tracked vehicle require more power and their rangeis lower than a wheeled vehicle, their ability to climb potential is better than wheeled vehicle.

IV. Conclusions

The heavy duty vehicle powertrain was simulated by Matlab/Simulink for both wheeled and half tracked types as vehicle alternatives. To determine vehicle range, which is one of the main vehicle performance criteria for electric vehicles, battery power requirements and SOC of the battery were calculated for the drive cycle. Additionally, climbing potential of the vehicle alternatives are calculated for dry concrete road as an important vehicle performance parameter. Main conclusions are listed below:

- 241.4 km vehicle range is calculated for wheeled type as s concquence of batter powers and SOC alternatives. On the other hand, the range of half tracked vehicle is calculated as 191.1 km.
- Wheeled vehicle alternative can reach nearly 34 degree climbing angle during the cycle time. However, maximum 40 degree of climbing angle can be achieved by the half tracked version.

It can be explained that, the wheeled type adventegous for vehicle range but the wheeled type has disadvantage in terms of climbing angle potential compared to the half tracked type. On the other hand advanced and comprehensive results can be aimed by developing simulation method including additional drive cycles, additional vehicle architecture, battery capacities, road conditions and steering effect as future works.

References

Wong, J. Y., 2008. *Theory of ground vehicles*. John Wiley & Sons.

Han, Xuefeng, et al.,2019. Energy management based on reinforcement learning with double deep Q-learning for a hybrid electric tracked vehicle. *Applied Energy* , 254: 113708. https://doi.org/10.1016/j.apenergy.2019.113708

Switonski, E., Lawomir Kciuk, S., & Klein, W., 2011. Modelling and investigation of dynamic parameters of tracked vehicles. *Mechanics and Mechanical Engineering*, *15*(4), 115-130.

Subramaniyam, K. V., & Subramanian, S. C. (2020). Wheel Slip Regulation Of Electrified Heavy Road Vehicles Using Regenerative Braking. *IFAC-PapersOnLine*, *53*(1), 422-427.

Janarthanan, B., Padmanabhan, C., & Sujatha, C., 2011. Lateral dynamics of single unit skid-steered tracked vehicle. *International Journal of Automotive Technology*, *12*(6), 865-875. https://doi.org/10.1007/s12239−011−0099−4

Bekker, M. G. (1956). Theory of Land Locomotion. The University of Michigan Press. Ann Arbor. Crosheck, J. E. (1975). Skid steering of crawlers. SAE Paper No. 750552, 1−15.

Prospects of CO_2 Utilization after Carbon Capture Process

[1]Binash Imteyaz, [2*]Sikandar Abdul Qadir, [3]Furqan Tahir
[1] Center of Excellence in Energy Efficiency, Research Institute, King Fahd University of Petroleum and Minerals, Dhahran-31261, Saudi Arabia
[2] Division of Engineering and Management Sciences, College of Science and Engineering, Hamad Bin Khalifa University, Doha - 34110, Qatar
[3] Division of Sustainable Development, College of Science and Engineering, Hamad Bin Khalifa University, Doha – 34110, Qatar
* E-mails: sqadir@hbku.edu.qa

Abstract
It has been estimated that keeping the global temperature rise below 1.5 °C as per Paris agreement would be difficult to achieve; unless the efforts are significantly scaled up. For this purpose, both renewable energy resources and carbon capture should be employed to restrict the global warming effects. The carbon capture utiliz ation and storage (CCUS) involves three stage: (i) carbon capture (ii) transportation and (iii) CO_2 utilization or storage. The CO_2 transportation is well established and would not significantly affect the overall CCUS project cost. Therefore, in-depth analysis is required to enhance the efficiency of carbon capture and CO_2 utilization processes in order to make CCUS projects financially viable. In this study, available and proposed CO_2 technologies are reviewed and analyzed. It is found that the enhanced oil recovery (EOR) and enhanced coal bed methane (ECBM) recovery are more feasible and can be further improved. While other utilization processes are still in the development phase but have room for improvements that can make them feasible in the future.

Keywords: Carbon Capture, CO_2 Utilization, CCUS, Feasibility

I. Introduction
In order to combat global warming threat, it was agreed in the Paris agreement to restraint the global temperature rise below 1.5 °C as compared to pre-industrial levels. However, in a report by Intergovernmental Panel on Climate Change (IPCC), concerns were made for keeping the global temperature rise below 1.5 °C (Nemitallah et al., 2020). The likelihood of extreme events due to climatic change will be intensified in case the global temperature rise surpasses the 1.5 °C threshold. Furthermore, in the yearly review meeting of UN Sustainable Development Goal 7 (SDG-7), it was concluded that the additional steps should be taken in order to meet 2030 SDG-7 objectives for energy efficiency, carbon emissions and renewable resources.

The contribution of renewable resources for the cumulative energy usage was 18.1 % in 2017. However, the renewable energy share is growing but the fossil fuels based energy will remain the major contributor in the future. Therefore, only the deployment of renewable energy will not be sufficient and efforts need to be made in enhancing energy efficiency, usage of low carbon fuels and biofuels, and carbon capture techniques (Ali et al., 2018; Tahir, 2014). This reflects importance of deploying carbon capture technologies and it can help in minimizing the risk associated with the global temperature rise. The carbon capture technology is still in the research and development phase and requires more focus for achieving viable carbon free systems (Nemitallah et al., 2020). The carbon capture utilization and storage (CCUS) involves separating CO_2 from the fossil fuels based power plants, which is then transported for sequestration, enhanced oil recovery or the production of chemicals/fuels (Habib et al., 2015; Tahir et al., 2019). The processes involving CCUS are shown in Fig. 1.

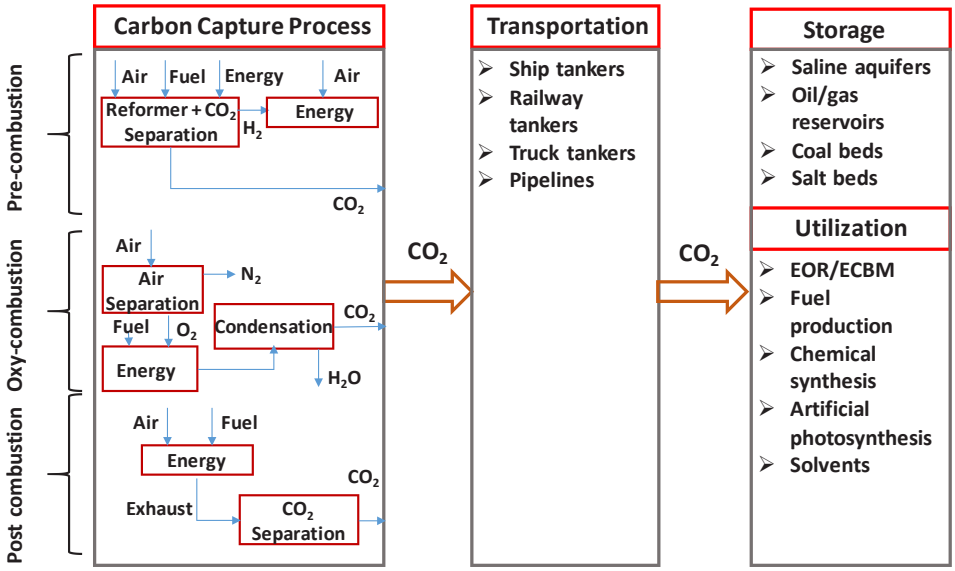

Fig. 1: Stages and processes in CCUS

There are three configurations of carbon capture namely (i) pre-combustion (ii) oxy- fuel combustion and (iii) post-combustion (Imteyaz and Tahir, 2019). These processes raises the overall cost of the power plant by 70 % – 80 % (Leung et al., 2014). For transportation, the impurities from captured CO_2 are removed to avoid corrosion and added cost (Wang et al., 2011). The CO_2 is then compressed and transported via pipelines, tanker trucks, railway tankers or ships. The CO_2 transportation by pipelines has the minimal cost of around 5 – 8 USD/ton (Chandel et al., 2010). However, the transportation cost does not significantly affects the CCUS project cost. The collected CO_2 can be stored in geological sites or can be utilized for enhanced oil recovery or in chemical industries. The CO_2 utilization techniques are young and significant research is needed to make these processes economic viable. In this work, available and proposed CO_2 utilization techniques available in the literature are presented. In addition, the feasibility of these techniques are discussed, and challenges and recommendations are highlighted at the end. The CO_2 storage is not included in this survey.

II. Review of CO_2 utilization techniques

The carbon dioxide can be utilized as the raw material for producing chemicals and fuels. In addition, it can also be used as the solvent in an industrial process or can be used for enhanced oil and fuel gas recovery as shown in Fig. 2 (Baena-Moreno et al., 2019). These utilization techniques can have a positive impact on overall CCUS project.

For chemicals production, the CO_2 reacts with organic compounds to form carbonates/carbamates via carboxylation process (Yuan et al., 2017). Although the conventional processes are broadly used, the CO_2 reaction with organic substances give better fixation with less energy requirements. Feroci et al. (Feroci et al., 2003) analyzed the electrochemical production of carbamate esters and they found that the CO_2 utilization can reduce the cost of raw materials with better yield and low energy requirements. The use of phosgene to produce isocyanates is well established, cost-effective and efficient. However, because of health and environmental effects, alternatives should be established. One of which is CO_2 for isocyanate production; but the most of the related studies are not yet commercialized and are limited to pilot-scale (Wang et al., 2017). Another application of CO_2 utilization is urea production, which primarily needs ammonia and carbon dioxide. Generally, natural gas is the primary raw material to produce both ammonia and carbon dioxide; however, additional CO_2 can be used as stripping agent to further enhance the urea yield (Pérez-Fortes et al., 2014). The other processes involving CO_2 include linear and acyclic carbonates, and polymers production that shows eco-friendly synthesis (Martín et al., 2015). One of the key advantage of producing polymers from CO_2 is that they are biodegradable but the thermal/mechanical properties and the process efficiency needs to be improved for commercialization (Taherimehr and Pescarmona, 2014). In addition, the polycarbonate synthesis can be entirely renewable.

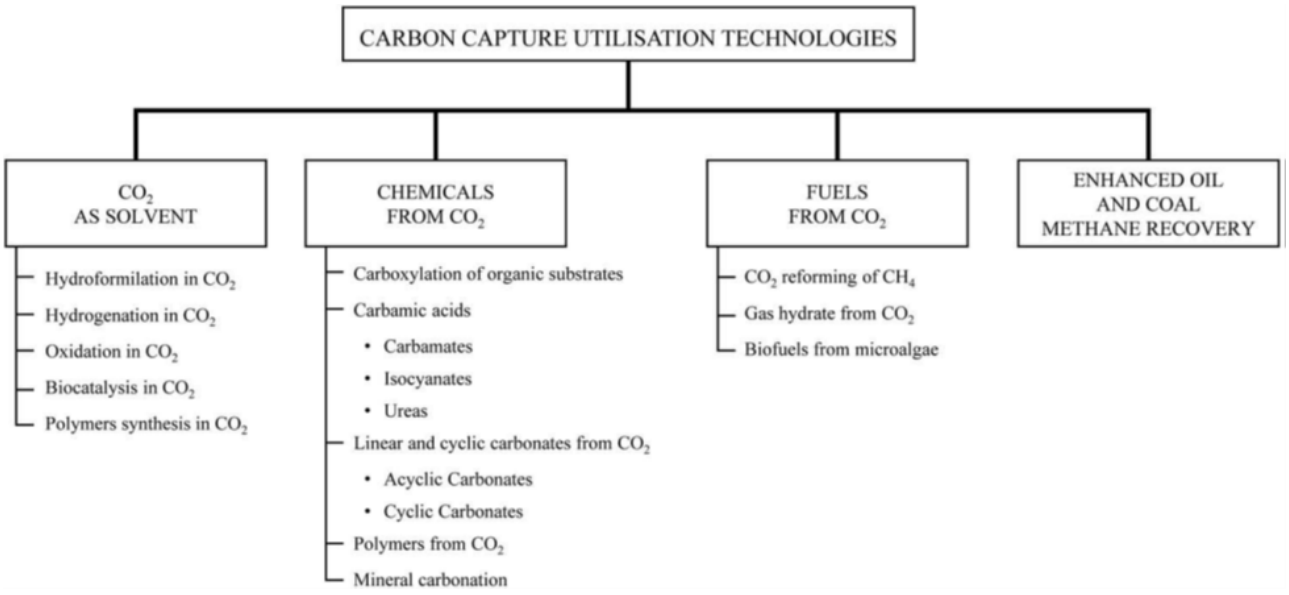

Fig. 2: CO_2 utilization techniques (Baena-Moreno et al., 2019)

For solvent application, both liquid and supercritical states ($scCO_2$) can be used. Generally, the solvents used in industries are organic based and have higher environmental effects as well as most of them are toxic and flammable. CO_2 can be a suitable candidate as it is non-flammable and non-toxic. Marriott et al. (Marriott et al., 2015) studied the feasibly of employing $scCO_2$ and found that the capital cost would be higher as compared with conventional solvents setup; however, the lower energy requirements and environmental benefits makes it a suitable choice. Hydrogenation, hydroformylation, biocatalysis, polymer synthesis and oxidation are some processes, where the CO_2 application has been established (Aresta, 2010).

From fuel production prospective, CO_2 can be used to synthesize hydrates, biofuels and syngas. The reforming

of methane with CO_2 exhibit two main advantages: (i) both are greenhouse gases and this process can reduce overall carbon emissions, and (ii) more economical as gas separation process is not required (Selvarajah et al., 2016). However, the process is more endothermic than the steam reforming that makes it energy intensive process. In addition, stable catalysts need to be developed to make this process viable. Another application of CO_2 consist of extracting methane from methane hydrates in the deep ocean by injecting CO_2 that will replace the methane and will be stored (Ota et al., 2005). The feasibility study is needed to assess the economic and environmental aspects. The algae farming requires significant amount of CO_2 that can be from atmosphere or captured from an industrial process (Demirbaş, 2008). For the algae cultivation, open ponds is the cheaper option as compared to bioreactors; however, the process require large land area (Cuéllar-Franca and Azapagic, 2015). The artificial photosynthesis can be used to convert/store solar energy in to chemical energy. The efficient conversion systems, cost and suitable catalysts are the main the hurdles for this technique (Aresta et al., 2013).

The most developed CO_2 utilization techniques is the enhanced oil recovery (EOR) and enhanced coal bed methane (ECBM) to recover remaining oil/gas from the field (Panwar et al., 2017). It has been estimated that the 40 % of the remaining oil can be can be produced after primary extraction (Blunt et al., 1993). The EOR is more developed than the ECBM process and has been employed in many regions. The economic viability of EOR by CO_2 strongly depends on CO_2 cost (Baena-Moreno et al., 2019).

III. Discussion

There are numerous options to utilize CO_2 after the carbon capture process. The CO_2 utilization in different processes has the potential to significantly reduce the carbon emissions. With the recent advances, the productivity and process efficiency of some techniques have been improved. This could lead to feasible CCUS implementation. Some of the key challenges and recommendations for the CO_2 utilization are as follows:

- Most of the studies were focused on analyzing the CO_2 utilization technique and the comparison with the conventional processes in terms of energy and economics, is lacking in the literature.
- The life cycle assessment (LCA) should be involved while assessing the feasibility of CO_2 utilization technique.
- Among the demonstrated CO_2 utilization techniques, EOR and ECBM are more economically viable; however, these have inadequate CO_2 storage capacity hence they require storage capacity improvements (Saghafi, 2010).
- The EOR process with CO_2 can be further improved financially.
- Currently the large scale artificial photosynthesis for methane and methanol production is not financially feasible and exhibit a technical challenge (Roy et al., 2010). For this purpose, more focus has been given to establish new catalysts based on nano-technology (Liu and Maroto-Valer, 2012; Tan et al., 2012).
- The chemical production from CO_2 require small CO_2 quantities that would not significantly reduce the CCUS cost (Huang and Tan, 2014).
- With respect to climate financing, the CCUS ventures are underfinanced as compared to the renewable energy resources.

IV. Conclusion

The several options available for the CO_2 utilization after the carbon capture process are discussed in this study. The captured CO_2 can be utilized to produce chemicals and fuels, can be used as solvents and to convert solar energy in to chemical energy via artificial photosynthesis. Furthermore, CO_2 can be used for enhanced oil recovery (EOR) and enhanced coal bed methane (ECBM) recovery. These technologies are well developed than the others; however, these processes can be made more efficient. Most of the CO_2 utilization techniques are still in the development phase and require more analysis and resources to make them financially viable. For the feasibility assessment, the CO_2 utilization technique should analyzed with respect to energy, economics and environmental. Furthermore, the CCUS projects are underfinanced as compared to the renewable energy ventures.

References

Ali, H., Tahir, F., Atif, M., AB Baloch, A., 2018. Analysis of steam reforming of methane integrated with solar central receiver system, in: Qatar Foundation Annual Research Conference Proceedings. p. EEPD969.

Aresta, M. (Ed.), 2010. Carbon Dioxide as Chemical Feedstock. Wiley. https://doi.org/10.1002/9783527629916

Aresta, M., Dibenedetto, A., Angelini, A., 2013. The changing paradigm in CO2 utilization. J. CO2 Util. 3–4, 65–73. https://doi.org/10.1016/j.jcou.2013.08.001

Baena-Moreno, F.M., Rodríguez-Galán, M., Vega, F., Alonso-Fariñas, B., Vilches Arenas, L.F., Navarrete, B., 2019. Carbon capture and utilization technologies: a literature review and recent advances. Energy Sources, Part A Recover. Util. Environ. Eff. 41, 1403–1433. https://doi.org/10.1080/15567036.2018.1548518

Blunt, M., Fayers, F.J., Orr, F.M., 1993. Carbon dioxide in enhanced oil recovery. Energy Convers. Manag. 34, 1197–1204. https://doi.org/10.1016/0196-8904(93)90069-M

Chandel, M.K., Pratson, L.F., Williams, E., 2010. Potential economies of scale in CO2 transport through use of a trunk pipeline. Energy Convers. Manag. 51, 2825–2834. https://doi.org/10.1016/j.enconman.2010.06.020

Cuéllar-Franca, R.M., Azapagic, A., 2015. Carbon capture, storage and utilisation technologies: A critical analysis and comparison of their life cycle environmental impacts. J. CO2 Util. 9, 82–102. https://doi.org/10.1016/j.jcou.2014.12.001

Demirbaş, A., 2008. Production of Biodiesel from Algae Oils. Energy Sources, Part A Recover. Util. Environ. Eff. 31, 163–168. https://doi.org/10.1080/15567030701521775

Feroci, M., Casadei, M.A., Orsini, M., Palombi, L., Inesi, A., 2003. Cyanomethyl Anion/Carbon Dioxide System: An Electrogenerated Carboxylating Reagent. Synthesis of Carbamates under Mild and Safe Conditions. J. Org. Chem. 68, 1548–1551. https://doi.org/10.1021/jo0266036

Habib, M.A., Tahir, F., Nemitallah, M.A., Ahmed, W.H., Badr, H.M., 2015. Experimental and numerical analysis of oxy-fuel combustion in a porous plate reactor. Int. J. Energy Res. 39. https://doi.org/10.1002/er.3323

Huang, C.-H., Tan, C.-S., 2014. A Review: CO2 Utilization. Aerosol Air Qual. Res. 14, 480–499. https://doi.org/10.4209/aaqr.2013.10.0326

Imteyaz, B., Tahir, F., 2019. Thermodynamic analysis of premixed and non-premixed oxy-methane combustion cycle with membrane assisted oxygen separation, in: 8th Global Conference on Global Warming (GCGW), Doha, Qatar. p. 33.

Leung, D.Y.C., Caramanna, G., Maroto-Valer, M.M., 2014. An overview of current status of carbon dioxide capture and storage technologies. Renew. Sustain. Energy Rev. 39, 426–443. https://doi.org/10.1016/j.rser.2014.07.093

Liu, Q., Maroto-Valer, M.M., 2012. Studies of pH buffer systems to promote carbonate formation for CO2 sequestration in brines. Fuel Process. Technol. 98, 6–13. https://doi.org/10.1016/j.fuproc.2012.01.023

Marriott, R., Jessop, P., Barnes, M., 2015. CO2-based Solvents, in: Carbon Dioxide Utilisation. Elsevier, pp. 73–96. https://doi.org/10.1016/B978-0-444-62746-9.00006-2

Martín, C., Fiorani, G., Kleij, A.W., 2015. Recent Advances in the Catalytic Preparation of Cyclic Organic Carbonates. ACS Catal. 5, 1353–1370. https://doi.org/10.1021/cs5018997

Nemitallah, M.A., Abdelhafez, A.A., Habib, M.A., 2020. Global Warming and Emission Regulations, in: Approaches for Clean Combustion in Gas Turbines. pp. 1–12. https://doi.org/10.1007/978-3-030-44077-0_1

Ota, M., Morohashi, K., Abe, Y., Watanabe, M., Smith, Jr., R.L., Inomata, H., 2005. Replacement of CH4 in the hydrate by use of liquid CO2. Energy Convers. Manag. 46, 1680–1691. https://doi.org/10.1016/j.enconman.2004.10.002

Panwar, D.S., Saxena, V.K., Suman, S., Kumar, V., Singh, A.K., 2017. Physicochemical study of coal for CBM extraction in Raniganj coal field, India. Energy Sources, Part A Recover. Util. Environ. Eff. 39, 1182–1189. https://doi.org/10.1080/15567036.2017.1314394

Pérez-Fortes, M., Bocin-Dumitriu, A., Tzimas, E., 2014. CO2 Utilization Pathways: Techno-Economic Assessment and Market Opportunities. Energy Procedia 63, 7968–7975. https://doi.org/10.1016/j.egypro.2014.11.834

Roy, S.C., Varghese, O.K., Paulose, M., Grimes, C.A., 2010. Toward Solar Fuels: Photocatalytic Conversion of Carbon Dioxide to Hydrocarbons. ACS Nano 4, 1259–1278. https://doi.org/10.1021/nn9015423

Saghafi, A., 2010. Potential for ECBM and CO2 storage in mixed gas Australian coals. Int. J. Coal Geol. 82, 240–251. https://doi.org/10.1016/j.coal.2010.01.002

Selvarajah, K., Phuc, N.H.H., Abdullah, B., Alenazey, F., Vo, D.-V.N., 2016. Syngas production from methane dry reforming over Ni/Al2O3 catalyst. Res. Chem. Intermed. 42, 269–288. https://doi.org/10.1007/s11164-015-2395-5

Taherimehr, M., Pescarmona, P.P., 2014. Green polycarbonates prepared by the copolymerization of CO 2 with epoxides. J. Appl. Polym. Sci. 131. https://doi.org/10.1002/app.41141

Tahir, F., 2014. Experimental & Numerical Investigations of Oxy-fuel Combustion Using Porous Plate Reactor. King Fahd University of Petroleum and Minerals.

Tahir, F., Ali, H., Baloch, A.A.B., Jamil, Y., 2019. Performance Analysis of Air and Oxy-Fuel Laminar Combustion in a Porous Plate Reactor. Energies 12, 1706. https://doi.org/10.3390/en12091706

Tan, J.Z.Y., Fernández, Y., Liu, D., Maroto-Valer, M., Bian, J., Zhang, X., 2012. Photoreduction of CO2 using copper-decorated TiO2 nanorod films with localized surface plasmon behavior. Chem. Phys. Lett. 531, 149–154. https://doi.org/10.1016/j.cplett.2012.02.016

Wang, J., Ryan, D., Anthony, E.J., Wildgust, N., Aiken, T., 2011. Effects of impurities on CO2 transport, injection and storage. Energy Procedia 4, 3071–3078. https://doi.org/10.1016/j.egypro.2011.02.219

Wang, P., Liu, S., Deng, Y., 2017. Important Green Chemistry and Catalysis: Non-phosgene Syntheses of Isocyanates - Thermal Cracking Way. Chinese J. Chem. 35, 821–835. https://doi.org/10.1002/cjoc.201600745

Yuan, G., Qi, C., Wu, W., Jiang, H., 2017. Recent advances in organic synthesis with CO 2 as C1 synthon. Curr. Opin. Green Sustain. Chem. 3, 22–27. https://doi.org/10.1016/j.cogsc.2016.11.006

Energy and Water Conservation Index Application for Optimizing the Conservation of Energy and Water at Facility

[1*]Andreas Prasetyadi, [1]Budi Setyahandana,
[1] Sanata Dharma University, Faculty of Science and Technology, Department of Mechanical Engineering, Jalan Affandi, Mrican, Depok, Sleman 55281, Indonesia

* E-mails: pras@usd.ac.id

Abstract
The sustainability of a system with challenge of economy and environment needs to be managed through integrating energy and water. Indexing energy and water with quantity and quality is proposed to show the conservation performance. A method consisting of water conservation index and energy conservation index is mentioned to show its ability for optimizing of energy and water in a facility. Analysis of the exergy destruction which is the main factor of exergy efficiency, mentions that reducing the exergy destruction in water processing effectively reduces the exergy supplied for the system. Minimization of water processed also determines exergy supplied. Namely, reducing water availability to as close as unity significantly reduces the cost of energy for water. The index optimization to as close as unity implies reducing water processed and exergy supplied.

Keywords: Exergy, Energy and Water Nexus, Energy and Water Conservation Index

1 Introduction

Trade-off between economical and environmental requirement becomes the concern of facilities development and management. The economical constraint is mostly blamed to limit the capability of running the system to be environmental friendly in term of energy, water, carbon footprint, and other resources. It is noted that conservation is a way of creating sustainable system [1]. Among them, the conservation of water and energy is important in a system operation.

The process of energy provision needs a quite amount of water [2]. Accordingly, water phases need energy [3]. Consumption process of energy and water also conveys both resources significantly. Interrelation of energy and water in consumption process tend to amplify each other. However, some water consumptions approaches have positive correlation with energy consumption. The metrics of water conservation tends to be biased of location due to uneven water distribution and energy price. It implies difficulty in comparing the approaches in different location.

In this article, optimization energy and water conservation using water conservation indexing as a mix of quantity and quality of the water during a usage is theoretically proposed in addition to exergy as the indexing method of energy. The index shows level of performance of the system in conserving water and energy during its process. The metric ability to be free of location bias with different water potential condition and energy value is expected.

2 Methods

Optimization is conducted through operation of the index of energy and water conservation. The water conservation index has two main features to show the quantity and quality. They are water availability and water accessibility. The concepts are based on Georgescu-Roegen [4] work about thermoeconomic. Generally, both metrics mention the ratio of actual over the ideal condition. Accordingly, energy is also indexed into quantity and quality. Exergy is applied for indexing that involves the system quality. The exergy efficiency is calculated for the index of energy at the proper system.

2.1 Conservation level of the water

The conservation level of water is defined as the score levelling system in preventing the water during the system process. It is calculated using equation (1), with W_{av}^{*} is determined by equation (2). WC is the water conservation level and W_{av}^{*} mentions the availability factor. W_{av} is water availability pointing out the ratio of available water over the amount of water provided for the process.

$$WC = W_{ac} * W_{av}^{*} \quad (1)$$

$$W_{av}^{*} = \begin{cases} W_{av}, 1 \le W_{av} \\ W_{av}^{-1}, 1 > W_{av} \end{cases} \quad (2)$$

The water conservation level shows the difference of input water and output water in term of quality and quantity. The conservation level 1 means that the system run fully with output water has equal quantity and quality of the input. It means

that the system releases water as good and as much as it withdraws. Moreover, it also mentions that the system withdraws the water as much as it needs.

2.2 Conservation level of the energy

The conservation level of the energy is determined as the exergy efficiency of the system as shown in equation (3). Ex_{dest}, Ex_{win}, and Ex_s are the exergy destruction, exergy of the input water, and exergy supply, respectively. The exergy destruction indicates amount of energy practically unused due to physical limitation. The exergy of input work shows the exergy of the water flowing to the system. The exergy supply points the energy needed for the process. Generally, a thermal system can be simplified as product of pump and heat exchanger system as done in former author's work [5].

$$\eta_{II} = 1 - \frac{Ex_{dest}}{Ex_s + Ex_{win}} \tag{3}$$

The level of conservation 1 indicates that the system uses energy only for work. In this case, there is not any exergy destruction. Such system is fully reversible and can recycle the supplied exergy.

2.3 Energy and water conservation level index

The conservation level index is defined as product of water conservation level and energy conservation level as shown in equation (4). The EWC, and WC are the energy and water conservation index, and the water conservation index, respectively. The energy and water conservation index also has maximum value of 1. The value mentions condition of water conservation level of 1 and exergy efficiency previously described.

$$EWC = \eta_{II} WC \tag{4}$$

2.4 Optimization of the energy and water conservation

There are two factors determining the energy and water conservation. They are energy used for water processing and the water for energy consumption. The energy used for water processing is determined from accessibility of the water components and availability of the water components. It can be calculated using equation (5), with EWF as energy for water factor that is energy used for water phases. Meanwhile, the water for energy consumption factor (WEF) can be traced from equation (6). Then, the economical factor can be determined by equation (7). It is assumed that economical factor is determined from the exergy supply which is a kind of primary energy supply.

$$EWF = \frac{W_{ac}}{W_{av}} \tag{5}$$

$$WEF = \frac{E_{win}}{E_{dest}} \tag{6}$$

$$Ex_s = Ex_{dest}\left(\frac{1}{(1-\eta_{II})} - WEF\right) \tag{7}$$

3 Results and Discussion

The water conservation level can show whether a system conserve water as reported in former author's work. The conservation level, namely water conservation index is free of the location bias as it doesn't allow the location factor give an advantage as shown in Figure 1. The unique location has its own advantage and drawback. However, the advantage and drawback should not limit to apply the best for the site. People have to adapt their system to meet the location factor. The availability defines the trend of water conservation level. Matching the availability to be unity gives the performance of the system to be on its peak. Meanwhile, accessibility determines maximum level that a system can reach. Accessibility limits the performance to be unity in the best condition. Therefore, it can be inferred that the conservation will be on their best if the availability and the accessibility are 1s. It happens when EWF = 1 as defined by equation (5).

When the water availability is higher than 1, the water conservation provides level index less than 1. It happens as the EWF < 1 due to water accessibility ≤ 1, both variables < 1, or water availability > 1. The water accessibility < 1 means that the system cannot provide the water as much and as good as the system needs. It makes the system runs in lower capacity. Meanwhile, the availability >1 implies that too much water is withdrawn for run the system.

Optimization of the water can be conducted from the energy for water factor regarding the water accessibility and availability

factor. Having specific water conservation index and EWF, the position of water conservation and water availability is clearly known. The combination of WC/EWF and WC < 1 tells that water availability is higher than its need and the accessibility is less than it needs. Adjustment on quality factor is important to increase the conservation factor of the system.

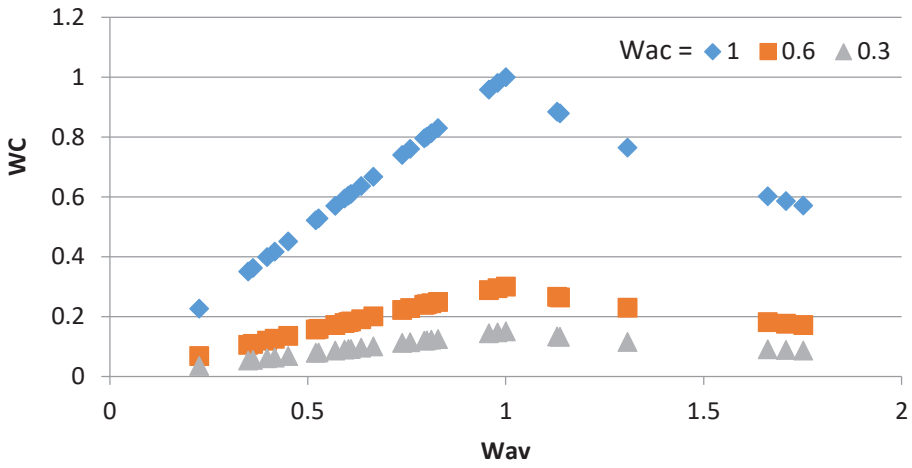

Figure 1. Water availability, water accessibility and the water conservation index. Maximum water conservation index happens when water is withdrawn as much as needed and processed as good as it should be.

The energy conservation level is determined as the effectiveness of energy supplied being transformed to be work. Regarding the energy for water phases, if the efficiency of the exergy is close to unity, equation (7) gives exergy supply close to E_{win}. It implies that the exergy supplied to the system is equal to the exergy of the water entering the system. This condition shows that the system is fully reversible, an ideal condition.

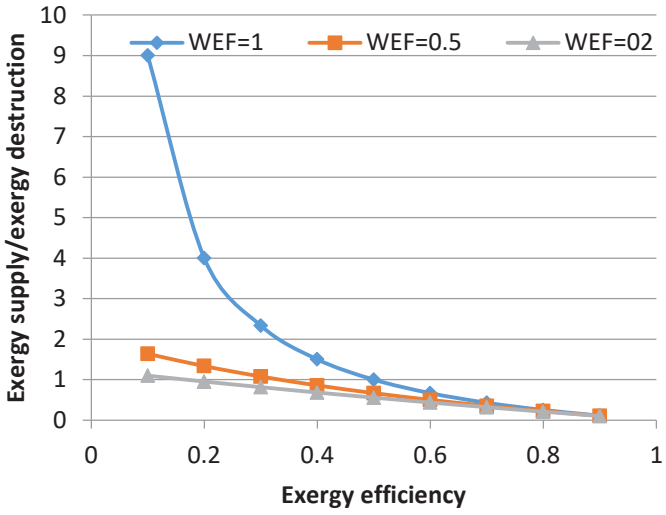

Figure 2. Exergy supply over exergy destruction as function of exergy efficiency in specific water of energy factor.

Optimization based of the energy and water conservation index can work for optimiziation of energy and water conservation. An index of energy and water conservation can be separated into an energy conservation index and water conservation index. The indexes can be derived from EWF and WEF. Equations (1), (2), and (5) imply that optimization of water conservation by increasing the EWF as close as unity, increases the WC accordingly as shown in Figure 3. It means that energy for the water will be more conserved as the water conservation index increases. Meanwhile, the efficiency of exergy as mentioned in equation (3) implies that the exergy destruction represents irreversibility. The Figure 2 indicates the ratio of exergy supplied to the system to exergy destruction as function of the exergy efficiency and WEF. The higher the WEF is, for less efficient exergy the exergy supply is higher. It means that more exergy should be supplied for the system for processing. As the efficiency increases, the ratio becomes closer to zero indicating less energy for processing. The pattern shows that optimization of the exergy efficiency should be accompanied with minimizing the exergy of the water flowing to the system. It means that more water processed needs more energy. In other word, minimum water supply is targeted to reduce the exergy supplied.

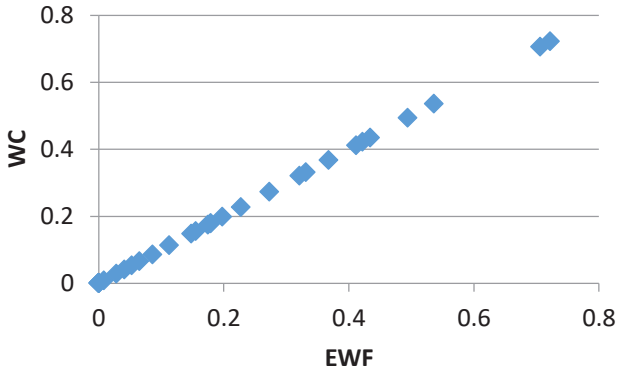

Figure 3. The WC is linear to EWF.

4 Conclusions

An optimization of the energy and water conservation index was developed and potentially can be applied for optimizing the energy and water conservation of a facility. Increase of the index shows the increase of the conservation indicated by energy for water factor and water for energy factor. Index of unity shows ideal condition of reversible process and conserved water in amount and quality.

References

[1] da Silva, L.C.C., Filho, D.O., Silva, I.R., V e Pinto, A.C., and Vaz, P.N.: Water sustainability potential in a university building – Case study. *Sustain. Cities Soc.* (47), 101489 (2019).

[2] Spang, E.S., Moomaw, W.R., Gallagher, K.S., Kirshen, P.H., and Marks, D.H.: Multiple metrics for quantifying the intensity of water consumption of energy production, *Environ. Res. Lett.* (9) 105002 (2014).

[3] Wakeel, M., Chen, B., Hayat, T., Alsaedi, A., and Ahmad, B.: Energy consumption for water use cycles in different countries: A review. *Appl. Energy*. (178), 868–885 (2016).

[4] Georgescu-Roegen, N.: Energy and Economic Myths. *South. Econ. J.* (41), 347–381 (1975).

[5] Prasetyadi, A. and Koonsrisuk, A., Second Law Analysis of the Centralized HVAC System of Suranaree University of Technology Hospital. in *Proceedings of the 14th Conference on Energy, Heat and Mass Transfer in Thermal Equipments and Processes*, (2019).

cse.hbku.edu.qa

General inquiries:
cse@hbku.edu.qa
inquiry@hbku.edu.qa

P.O. Box: 34110
Doha – Qatar


HBKU


HBKU


Hamad Bin Khalifa University


Hamad Bin Khalifa University


Hamad Bin Khalifa University


9 786254 098178